Curcumin and its transition metal complexes: Synthesis, characterization and investigation of their antibacterial activity through model DNA binding experiments coupled with an *in silico* molecular modeling approach

Thesis Submitted for the Degree of

Doctor of Philosophy (Science)

of Jadavpur University

Under the supervision of

Prof. Saurabh Das

by

TANMOY SAHA

Department of Chemistry

Jadavpur University

Kolkata-700 032

India

2024

যাদবপুর বিশ্ববিদ্যালয়
কলকাতা-৭০০০৩২, ভারত

*JADAVPUR UNIVERSITY
KOLKATA-700 032, INDIA

FACULTY OF SCIENCE: DEPARTMENT OF CHEMISTRY : INORGANIC CHEMISTRY SECTION

CERTIFICATE FROM THE SUPERVISOR

This is to certify that the thesis entitled **"Curcumin and its transition metal complexes: Synthesis, characterization and investigation of their antibacterial activity through model DNA binding experiments coupled with an in silico molecular modeling approach"** submitted by **Mr. Tanmoy Saha** who got his name registered on ***11th October, 2018*** for the award of Ph.D. (Science) degree of Jadavpur University is based on his own work that was performed under my supervision at the ***Department of Chemistry, Jadavpur University, Kolkata-700032*** and that neither this thesis nor any part of it has been submitted for any degree or diploma or for any other academic award anywhere before.

Saurabh Das 27.12.2024

(Signature of Supervisor and date with official seal)

Dr. Saurabh Das
Professor
Department of Chemistry
Jadavpur University
Kolkata-700 032

দূরভাষ: ২৪১৪-৬৬৬৬/৬১৯৪/৬৬৪৩/৬৪৯৫/৬৪৪৩ প্রসারণ: ২৪৬৯ Website:www.jadavpur.edu Phone:2414-6666/6194/6643/6495/6443 Extn.2469
দূরবার্তা: (৯১)-০৩৩-২৪১৪-৬৪১৪/৬২১০/২৪১৩-৭১২১ E-mail : hod@chemistry.jdvu.ac.in Fax: (91)-033-2414-6414/6210/2413-7121

JADAVPUR UNIVERSITY

KOLKATA-700 032

MARK SHEET

NO.: CW/16052/ 000723

(For Ph.D/M. Phil. Course Work)

Results of the PH.D. COURSE WORK EXAMINATION, 2020

In CHEMISTRY held in DECEMBER, 2019 - JANUARY, 2020

Name TANMOY SAHA Class Roll No. 201920104005

Examination Roll No. PHDCHEM20106 Registration No. of

Subject Code / Name	Credit Hr.(c_i)	Marks
COMPULSORY UNITS:: EX/CHEM/PHD/A & B RESEARCH METHODOLOGY & REVIEW OF RESEARCH WORK	4	86
ELECTIVE UNITS ::	4	86
EX/CHEM/PHD/I-1 :: APPLICATION OF SPECTROSCOPIC STUDIES IN CHEMICAL RESEARCH EX/CHEM/PHD/I-2 :: MATERIALS, CATELYSES & ELECTROCHEMICAL STUDIES EX/CHEM/PHD/I-3 :: METALS IN LIFE & REACTION DYNAMICS EX/CHEM/PHD/I-4 :: SINGLE CRYSTAL X-RAY STR. SUPRAMOLECULAR CHEM.& DFT COMPUTN.		

Total Marks : 172 (out of 200) **Remarks:** P

Prepared by : Checked by :

Date of issue : 15 / 09 / 2020

Controller of Examinations

DECLARATION

I do hereby declare, that the work embodied in the thesis entitled "**Curcumin and its transition metal complexes: Synthesis, characterization and investigation of their antibacterial activity through model DNA binding experiments coupled with an *in silico* molecular modeling approach"** submitted for the award of Doctor of Philosophy (Ph. D.) in Science is the completion of studies carried out by me under the supervision of Prof. Saurabh Das at the department of Chemistry, Jadavpur University. The work is original and has not been submitted in part or full for either any equivalent degree/diploma or any other academic award elsewhere.

In keeping with the general practice of reporting scientific observations, due acknowledgements have been made wherever the work described was done taking an active assistance of a laboratory that expertises in that particular field of investigation.

Tanmoy Saha 27.12.2024

Tanmoy Saha

Research Scholar

Department of Chemistry

Jadavpur University

Kolkata-700032

India

Dedicated

to

all my teachers

and

my parents

Acknowledgement

I would want to use this opportunity to sincerely thank everyone who has supported me during my doctoral study. Without their ongoing encouragement and support, my thesis would not have been feasible.

First and foremost, I would like to express my deepest gratitude to my supervisor, Prof. Saurabh Das, for his unwavering support, guidance and mentorship throughout my PhD journey. His insightful advice, patience and dedication have been invaluable in shaping my academic and personal growth. From the very beginning, he encouraged me to explore new ideas, challenge myself and strive for excellence in my work. He provided me with a great deal of autonomy to work on a variety of facets of chemistry and to investigate results related to chemical experiments in biology. He greatly encouraged me to investigate computational biology and chemistry and correlate these with my experimental findings. That ultimately played a significant role in my doctoral research. I consider it fortunate to have him as my Ph.D. advisor since he was there for me through the highs and lows of my research career and kept me motivated throughout.

I am grateful to all heads of the Department of Chemistry, Jadavpur University, who were in position during my doctoral studies for providing me with access to all departmental facilities. I am also grateful to all Section-in-Charge of the Inorganic Chemistry Section, who were in position, during my research work for the support and encouragement I received from them. I wish to extend my sincere gratitude to Prof. Chittaranjan Sinha, Dean, Faculty Council of Science, as well as all former Deans of the Science faculty and all members of staff at the faculty of Science office for their cooperation. I am very much thankful to all the non-teaching staff of the Department of Chemistry at Jadavpur University for their invaluable support and cooperation.

I extend my sincere gratitude to Prof. Kasturi Mukhopadhyay of the School of Environmental Sciences, Jawaharlal Nehru University, New Delhi, for the support that I received related to the investigations that were carried out in her laboratory on the applications of compounds prepared by me on various bacterial cell lines, achieved through a collaboration with my supervisor Prof. Saurabh Das. I would like

to express my gratitude to Dr. Prince Kumar, then a research scholar in the laboratory of Prof. Mukhopadhyay for his effort in conducting the experiments.

I would like to thank Prof. Sanjay Kumar of the Department of Physics, Jadavpur University for his assistance in performing thermogravimetric analysis. I am particularly grateful to one of his past research scholars Dr. Soumen Singha, for helping me in various aspects related to quantum calculations.

I would also like to express my heartfelt gratitude to Prof. Tapan Kumar Mondal of Department of Chemistry, Jadavpur University and his research scholars for assistance with the mass spectrometer (a departmental facility). I would like to convey my sincere thanks to Prof. Shouvik Chattopadhyay and his research scholars for invaluable assistance throughout my PhD studies.

I would like to express my heartfelt gratitude and respect for all my professors who influenced my academic path during my undergraduate studies at Gurudas College, Kolkata, University of Calcutta and during my postgraduate studies at Ramakrishna Mission Vivekananda Centenary College, Rahara, West Bengal State University. I wish to convey my sincere gratitude to late Dr. Arunava Sen and Prof. Gurunath Mukherjee for their steadfast guidance and mentorship during my postgraduate studies. Their profound knowledge and understanding of Coordination chemistry and Bioinorganic chemistry and the connection between the two, that was highlighted by them in their classes have significantly influenced my research and academic growth. Their insightful critiques, enduring patience and meticulous attention to detail have significantly contributed to my development as a researcher and as a discerning thinker. I am very thankful for the chances they gave me, the conversations that broadened my views and the support that I received when things were tough. I consider myself very fortunate to have them as my teachers.

In this context, I wish to express my sincere appreciation for Mr. Sujay Chakraborty one of my teachers in undergraduate study, whose mentorship and passion for chemistry have significantly influenced my undergraduate experience. I was impressed by his ability to take difficult ideas and make them approachable while encouraging a sense of wonder outside the classroom. I felt confident enough to talk about difficult topics because he believed in me and supported me. I will always be grateful for all the time he spent teaching and guiding me. He brought chemistry to

life and sparked a fervour for the subject that will endure throughout my scholarly and professional journey.

I express my sincere gratitude to my esteemed lab seniors, Dr. Ramesh Chandra Santra, Dr. Durba Ganguly, Dr. Sayantani Chatterjee, Dr. Partha Sarathi Guin and Dr. Tathagata Deb, from whom I acquired a wealth of knowledge at the onset of my work. I express my gratitude for their collaboration and insightful recommendations throughout the process. I would like to express my appreciation for Dr. Bitapi Mondal, Dr. Mouli Saha, Dr. Promita Nandy, Dr. Somenath Banerjee and Mr. Tushar Kanti Mondal, with whom I had the opportunity to work in the lab under exceptionally pleasant conditions receiving their assistance in all areas of laboratory activity. I share many life experiences with Dr. Mouli Saha, Dr. Durba Ganguly and Dr. Bitapi Mondal, particularly worth mentioning is, when they stood by me in difficult times. They still remain steadfast in their support towards me. These valued relationships have endured over time, offering unwavering backing through various life challenges and accomplishments. Their continuous presence and support have been a wellspring of strength and solace, aiding in overcoming both personal and career obstacles. The strong connection formed with these individuals has cultivated a sense of community and mutual comprehension that continues to enhance daily life.

While I did my research, I was a teacher at Sri Aurobindo Institute of Education in Saltlake Kolkata which is affiliated to ISCE/ISC board. My departmental colleagues, Mrs. Runa Choudhury and Mrs. Dipshikha Roy, were very helpful. They gave me all kind of support in school so that I could do my research work. I also received a positive support from my ex Principal, Mrs. Debolina Bhattacharya and ex vice principal, Mrs. Nandita Chandra, and other teaching and non-teaching staff members. This work would not have been possible without the cooperation and support that I received from the members of the Governing body of the school.

I would like to extend my heartfelt appreciation for Prof. Somen Sahu, Department of Fishery Economics and Statistics, West Bengal University of Animal and Fishery Sciences. His comprehensive support has been invaluable throughout my life. Prof. Sahu has consistently motivated me to explore novel and exceptional opportunities over the years. He has been a steadfast presence during both my triumphs and challenges. His confidence in my abilities has inspired me to excel and progress in life.

The unwavering backing and mentorship provided by Prof. Sahu have played a crucial role in moulding my personal and professional development. His faith in my capabilities has driven me to venture beyond my comfort zone and pursue excellence. His constant encouragement and wisdom were particularly crucial during difficult times serving as an indispensable source of support.

A special thanks to Dr. A.K. Bhattacharya (M.D. in medicine), my family physician, who also supported me during my poor health condition and motivated me to do my research work. I am really thankful to him. Dr. A.K. Bhattacharya's support extended beyond his role as a family physician, providing invaluable encouragement during challenging times. His unwavering belief in my research pursuits acted as a driving force, inspiring me to persevere despite health setbacks. This combination of medical care and emotional support exemplifies the profound impact a compassionate healthcare professional can have on a patient's overall well-being and academic journey.

Throughout my research endeavours, I experienced the profound loss of my father, late Mr. Hari Saha. Nevertheless, I sensed his unwavering presence and support surrounding me at all times. My mother, Mrs. Sukla Rani Saha, has been a steadfast source of support and encouragement throughout my life, serving as an enduring inspiration that has guided me on this journey, including my research career, culminating in the submission of this thesis. All that I have accomplished in life is a direct result of their unwavering love, selfless sacrifice and profound blessings. It is better to remain indebted to her instead of extending thanks. I also express my gratitude to my wife, Mrs. Antara Mondal Saha, for her direct or indirect invaluable support. I also express my profound gratitude for the unwavering love and support of my daughter, Miss Tanwita Saha, whose affection has been instrumental in my continued pursuit of writing this thesis.

Tanmoy Saha

Tanmoy Saha
Research Fellow
Department of Chemistry
Jadavpur University
Kolkata-700032
December 2024

Date: 27.12.2024
Place: Jadavpur, Kolkata

List of Abbreviation used

HCur	: Curcumin or LH_3
Cur	: Monoanion of Curcumin or Conjugate base of Curcumin
[Mn(Cur)]	: $[Mn^{II}(Cur)_2(HCur)]$ or Mn^{II}-Curcumin complex
[Cu(Cur)]	: $[Cu^{II}(Cur)(OCOCH_3)(OH_2)]$ or Cu^{II}-Curcumin complex
[Zn(Cur)]	: $[Zn^{II}(Cur)(OCOCH_3)(OH_2)]$ or Zn^{II}-Curcumin complex
DFT	: Density Functional Theory
TDDFT	: Time Dependent Density Functional Theory
NCI	: Non Covalent Interaction
HOMO	: Highest Occupied Molecular Orbital
LUMO	: Lowest Occupied Molecular Orbital
LLCT	: Ligand to ligand charge transfer
ESP	: Electrostatic Potential
ELF	: Electron localisation Function
LOL	: Localised Orbital Locator
RDG	: Reduced Density Gradient
UV-Vis	: Ultraviolet-Visible Spectroscopy
IR	: Infrared spectroscopy
MS	: Mass spectroscopy
DMF	: Dimethyl formamide
DMSO	: Dimethyl sulfoxide
DNA	: Deoxyribonucleic acid
CT DNA	: Calf thymus DNA
ROS	: Reactive Oxygen Species
MTT	: 3-(4,5-dimethylthiazol-2-yl)-2,5-diphenyltetrazolium bromide
PBS	: Phosphate buffered saline

DTT	: Dithiothreitol
BHI	: Brain heart infusion
MHB	: Mueller-Hinton broth
DMEM	: Dulbecco's Modified Eagle Medium
NADH	: Nicotinamide Adenine Dinucleotide-Hydrogen
SOD	: Superoxide Dismutase
NADPH	: Nicotinamide adenine dinucleotide phosphate
ADP	: Adinosine diphosphate
ATP	: Adinosine triphosphate
HPLC	: High-performance liquid chromatography
FTIR	: Fourier-transform infrared spectroscopy
PDB	: Protein Data Bank
PRL	: Proflavine
NT	: Netropsin
GDP	: Guanosine 5'-diphosphate
GTP	: Guanosine 5'-triphosphate
FtsZ	: Filamenting temperature-sensitive mutant Z
MDR	: Multidrug-resistant
9PC	: 3-[(6-chloro[1,3]thiazolo[5,4-b]pyridin-2-yl)methoxy]-2,6-difluorobenzamide or PC190723
PDBQT	: Protein Data Bank , Partial Charge and Atom Type
MD	: Molecular Dynamics
RMSD	: Root mean square deviation
RMSF	: Root mean square fluctuation
ROG	: Radius of Gyration
SASA	: Solvent accessible surface area
H-BOND	: Hydrogen Bond
MMGBSA	: Molecular mechanics with generalised born and surface area solvation

Abstract

Curcumin is a polyphenolic compound found in the rhizomes of Curcuma longa and is referred to as turmeric. Recognized as a yellow pigment, it has attracted a substantial amount of interest owing to several pharmacological qualities that it possesses, like anti-inflammatory, antioxidant and anticancer activities. However, the potential of this substance to operate as an antibacterial agent, particularly in the form of metal complexes is not yet fully explored. It was demonstrated through this study that metal complexes of Curcumin have improved stability, solubility and bio-availability, all of which have the potential to boost antibacterial capabilities of the compound. As a part of this study, some metal complexes of Curcumin were synthesized, characterized and antibacterial activity were evaluated on gram positive and gram negative bacteria. In addition, *in silico* modeling studies were conducted concurrently to compare results obtained from *in vitro* investigations.

Over the last four decades, researchers have been involved in carrying out studies to learn about effects of Curcumin in pharmacology. The reason why researchers had their focus on this pigment goes beyond its function as a food colorant; it is used against multiple chronic diseases and is also a chemo-preventive agent. Although identified for the first time in powdered rhizome of *Curcuma longa* Linn in 1815, until the 1970s, there was little progress related to research with this pigment pertaining to its structure and activities as an antioxidant. Little was known on biochemical properties of Curcumin. However, as time passed, the science associated with Curcumin became popular and it is now a topic of discussion in different branches of chemistry (analytical, inorganic, organic and physical).

Although Curcumin is a multifaceted molecule, owing to its hydrolytic instability and aqueous insolubility it is poorly bio-available, which is a major obstacle for achieving its full therapeutic

potential? In 1997, Y. J. Wang et al. showed that under physiological conditions the molecule breaks down in solution into several smaller fragments. Therefore, whatever pharmacological reports are available on Curcumin, it becomes extremely difficult to believe these are due to Curcumin present in solution as a single unit. Rather it could be a collective effect of all fragments formed from it in solution. Most researchers concentrating on the pharmacological or medicinal aspects of the molecule have remained largely silent on an important issue.

In an attempt to overcome its inherent limitations three metal complexes of Curcumin, one with Mn(II), another with Cu(II) and a third with Zn(II) having formulae $[Mn^{II}(Cur)_2(HCur)]$, $[Cu^{II}(Cur)(OCOCH_3)(OH_2)]$ and $[Zn^{II}(Cur)(OCOCH_3)(OH_2)]$ respectively were synthesized. Physico-chemical studies performed in solution using manganese(II) chloride, copper(II) acetate and zinc(II) acetate with Curcumin indicate the formation of a 1:3 Mn^{II}: Curcumin complex, a 1:2 Cu^{II}:Curcumin complex and 1:2 Zn^{II}:Curcumin complex. However, in case of Cu^{II} and Zn^{II}, attempts to synthesize a complex based on physicochemical studies always led to the formation of a 1:1 Cu^{II}:Curcumin and a 1:1 Zn^{II}:Curcumin species, if Cu^{II}-acetate and Zn^{II}-acetate were used as starting materials.

Owing to poor solubility in water, the UV spectrum of the complexes were recorded in DMSO. λ_{max} was obtained at 400 nm for Mn^{II} complex, at 428 nm for Cu^{II} and at 426 nm for Zn^{II} complexes respectively. Curcumin itself has a λ_{max} at 432 nm with a molar extinction coefficient $\varepsilon = 2.85 \times 10^4\ M^{-1}\ cm^{-1}$. Mass spectrum of the Cu^{II} complex henceforth referred to as Cu(Cur), shows a molecular ion peak at m/z = 507.3225 (m/z_{theo}= 507.39 considering ^{63}Cu). In case of the Mn^{II} complex, henceforth referred to as Mn(Cur), the molecular ion peak was obtained in a cluster of peaks having m/z 1157.4994, 1156.4755 and 1155.3969 [m/z (theo) being 1158.05]. Mass spectrum of the Zn^{II} complex, henceforth referred to as Zn(Cur) shows molecular ion peaks at m/z = 508.4731, 510.5261, 512.2132 owing to the three

relatively abundant isotopes of Zn (m/z_{theo} being 508.38 for ^{64}Zn; 510.38 for ^{66}Zn; 512.38 for ^{68}Zn) In all three cases, TGA indicate formulae mentioned above. Since single crystals were not obtained and powder X-ray diffraction patterns did not yield a structure employing Reidfelt analysis the structure was determined using DFT based on spectroscopic evidence. Structure of all the complexes was optimized by B3LYP functional. For C, H, and O 6-311+G basis sets were used. For Mn and Zn LanL2Dz basis set and for Cu SDD basis set was used. All quantum-chemical calculations were performed using Gaussian 09 for Zn and Cu and Gaussian 16 for Mn.

Before proceeding with *in vitro* studies, it was important to check whether the complexes are stable in various biological milieu and/or buffer medium. The synthesized Mn(Cur), Cu(Cur) Zn(Cur) were found to be stable in different buffer systems and in different biological milieu when Curcumin present alone, degrades within 20 minutes.

Hence, with such improved stability in biological milieu, that were obtained as a part of this study, all complexes were tried for their DNA binding ability and showed effective binding with calf thymus DNA. It was found that Cu(Cur) had a reasonably strong affinity for DNA realized from its binding constant value with calf thymus DNA at different temperatures in the temperature range 25°C to 35°C.

Metal complexes exhibit potent and significant enhancement in activity over that of Curcumin when tried on *E. coli* and *S. aureus. These were carried out in the laboratory of* Prof. Kasturi Mukhopadhyay at Jawaharlal Nehru University (JNU), New Delhi. *Bacterial killing assay showed when targets were exposed to 25 μM metal complexes for 60 minutes around 97-98% killing was achieved while for the same concentration and exposure time, Curcumin could kill only 36-37%. On increasing concentration to 50 μM, complexes were able to kill approximately 99% cells in 60*

minutes while a similar concentration of Curcumin could only kill 66-67% in that time. All complexes showed significant improvement in antibacterial activity in comparison to Curcumin.

Calcein leakage assay that was also performed through a collaboration in the laboratory of Prof. Kasturi Mukhopadhyay at JNU New Delhi revealed that complexes triggered immediate membrane permeabilization in *S. aureus*. Excellent potency of complexes was supported by its safe toxicological profile, being non-hemolytic and non-cytotoxic towards mammalian cells making them suitable candidates for further *in vivo* investigations.

In silico molecular docking and molecular dynamics simulation support the interaction of prepared complexes with DNA, *E. coli* and *S. aureus* With that aim, the investigation of FTSz inhibiting activity was checked thoroughly. The protein of *E. coli* and *S. aureus* were taken from the RCSB protein data bank and confirmed by docking studies, after analyzing them according to Ramachandran plot and other necessary parameters. All docking calculations were performed using Autodock 4.2 and Autodockvina algorithm. From docking studies, it was confirmed that in all cases, prepared complexes showed more negative binding energy than Curcumin. After molecular dynamics, analysis was done through RMSD, RMSF, ROG, SASA, H-Bond and MMGBSA. All results were satisfactory.

Therefore, this study provides a scientific basis for the development of Curcumin based metal complexes as effective antibacterial agents. Given the rise of antibiotic-resistant bacteria, novel antibacterial agents are a need of the hour. The findings presented in this dissertation might contribute to new therapeutic strategies against bacterial infections and advance the field of medicinal chemistry.

Content

		Page No
Chapter 1	**Introduction**	**1-17**
	1.1. A concise introduction to bacterial origins and its impact on mankind	3
	1.2. The need for Antibiotics and their role in health care	4
	1.3. Research on Curcumin–a natural occurring flavonoid as Antibacterial agent	5
	1.4. Exploring antibacterial mechanism	6
	References	8
Chapter 2	**Review on Curcumin and its medicinal applications**	**18-77**
	2.1. Curcumin: A brief historical background	20
	2.2. Chemical properties of Curcumin	23
	2.2.1. The aspect of degradation of Curcumin	27
	2.3. Interaction of Curcumin with biomolecules	32
	2.3.1. Interaction with proteins	33
	2.3.1.1 By non-covalent interaction	34
	2.3.1.2 By covalent interaction	36
	2.3.2. Interaction with nucleic acids	37
	2.3.3. Interaction with membranes	38
	2.4. Medicinal properties of Curcumin	39
	2.4.1. Antioxidant property	39
	2.4.2. Anti-inflammatory activity	40
	2.4.3. Anticancer activity	42
	2.4.4. Antibacterial activity	44
	2.5. Understanding of Antibacterial activity of Curcumin through various mechanism	46
	2.5.1. Disruption of Cell Membrane	46
	2.5.2. The suppression of bacterial quorum sensing system and prevention of biofilm formation.	47
	2.5.3. Inhibition of cell division	49
	2.5.4. Induction of Oxidative Stress and Programmed Cell Death (PCD)	51

2.5.5. Phototoxicity 52
2.5.6. Perturbation of bacterial cell metabolism 53
2.5.7. Regulation of intracellular bacterial proliferation 54
References 55

Chapter 3 Review on metal complexes of Curcumin and their medicinal applications 78-114

3.1. Metal ions in Biology 80
3.2. Significance of transition metal ions in research related to Curcumin 81
3.3. Stoichiometry of Metal-Curcumin complexes 83
3.4. General procedure for synthesis of Curcumin based metal complexes 84
3.5. Medicinal properties of metal complexes of Curcumin 86
3.5.1. Antioxidant property 86
3.5.2. Anticancer property 89
3.5.3. Antimicrobial activity 93
References 96

Chapter 4 Review on in-silico approaches in Inorganic Chemistry: DFT, Molecular Docking & Molecular Dynamics 115-184

Introduction 117
4.1. Quantum Chemical Calculations: Density Functional Theory 119
4.1.1. Some Theoretical Background of DFT 120
4.1.1.1 The Fundamental Wave Equation in Quantum mechanics 120
4.1.1.2 Time independent Schrödinger equation into Many-Body problem 120
4.1.1.3 Introduction of Hartree-Fock approximation 122
4.1.1.4 Foundation of DFT and Hohenberg-Kohn theorem 123
4.1.1.5 Introduction of Kohn-Sham Equations 125
4.1.1.6 Different Density Functionals 126
4.1.2. Application of DFT in Coordination Chemistry 128
4.2. Molecular Docking Simulations 132

4.2.1. Some Theoretical Background of Docking 133
4.2.1.1 Mathematical viewpoint of Docking 134
4.2.2. Types of Docking methodologies 139
4.2.2.1 Rigid receptor-Rigid ligand docking 140
4.2.2.2 Rigid receptor-Flexible ligand docking 140
4.2.2.3 Flexible receptor-Flexible ligand docking 141
4.2.2.4 Blind docking 142
4.2.2.5 Active site docking 143
4.2.3. Different models of Docking Study 143
4.2.4. Basic steps involved in protein-ligand Docking Study 145
4.2.5. Application of Docking Study 148
4.3. Molecular Dynamics Simulations 149
4.3.1. Theoretical aspects of Classical MD simulations 150
4.3.1.1 Force Field in MD simulation 151
4.3.1.2 Thermodynamic Ensembles 153
4.3.2. Methodology of MD Simulation 154
4.3.2.1 Creation of simulation environment 154
4.3.2.2 Minimisation of Energy 155
4.3.2.3 Heating the system and equilibration 155
4.3.2.4 Production Run 156
4.3.2.5 Analysis of MD trajectories 156
4.3.3. Application of Molecular Dynamics 159
References 160

Chapter 5 Genesis and Scope 185-200
References 192

Chapter 6 Experimental: Materials and Methods 201-235
Introduction 203
6.1. Materials used: 203
6.2. Experimental
6.2.1. Determination of stoichiometry of metal complexes of Curcumin 204
6.2.1.1 By mole ratio method 204

6.2.1.2 By Job's method of continuous variation 205
6.2.2. Determination of pK_a of Curcumin in the absence and presence of metal ions 205
6.2.3. Synthesis of transition metal complexes Of Curcumin 207
6.2.3.1 Synthesis of the Mn^{II} complex of HCur 207
6.2.3.2 Synthesis of a Cu^{II} complex of Curcumin 208
6.2.3.3 Synthesis of a Zn^{II} complex of Curcumin 208
6.2.4. Instrument used for different experiments 209
6.2.4.1 Instrument used for characterization of the complexes 209
6.2.4.2 Instrument used *for in silico* experiments of the metal complexes and HCur 209
6.2.5. Quantum Chemical Calculations for the structure determination of the metal complexes 209
6.2.5.1 Non-covalent interaction (NCI) and bond critical point analysis 210
6.2.5.2 Analysis of ELF and LOL 211
6.2.6. Analysis of chemical stability of Curcumin and its metal complexes in physiological buffer conditions 212
6.2.6.1 Using UV-Vis spectroscopy 212
6.2.6.2 Using HPLC 212
6.2.7. Biophysical interactions of metal complexes with calf thymus DNA 213
6.2.7.1. Titration of metal complexes of Curcumin with calf thymus DNA 213
6.2.7.2. Titration of Cu^{II} complex of Curcumin with DNA at different temperatures and evaluation of thermodynamic parameters 215
6.2.8. Superoxide dismutase activity of the Mn^{II} complex of Curcumin 216
6.2.9. In silico molecular modelling of Curcumin (HCur) and its metal complexes 217

with selected DNA and bacterial FtsZ protein model
6.2.9.1 Molecular Docking 217
6.2.9.2 Molecular Dynamics 220
References 225

Chapter 7 Characterization of Curcumin through different Spectroscopy and Quantum Chemical calculations **236-257**
Introduction 238
7.1. Determination of pKa of Curcumin 239
7.2. Characterization of Curcumin 240
7.2.1. UV-Vis spectroscopy 240
7.2.2. IR spectra of Curcumin 240
7.3 Quantum Chemical calculations based on spectroscopic evidence 241
7.3.1. Frontier molecular orbitals 242
7.3.2. Molecular electrostatic potential surface analysis 244
7.3.3. Quantum descriptor analysis 245
7.3.4. NCI-RDG analysis 246
7.3.5. ELF and LOL analysis 248
7.4 Stability of Curcumin under physiological buffer system 250
7.4.1 Followed by UV-Vis spectroscopy 250
7.4.2. Followed by High Pressure Liquid Chromatography 251
References 253

Chapter 8: Synthesis, characterization, structural analysis through quantum chemical computations of a Mn^{II}-Curcumin complex and an investigation of superoxide dismutase like activity & DNA binding **258-302**
Introduction 260
8.1. Stoichiometry of complex formation for Mn^{II} and HCur by mole ratio and Job's method of continuous variation. 261
8.2. Determination of stability constant of Mn^{II}-Curcumin in solution 264

8.3. Characterization of the complex 266
8.3.1. Analysis mass spectrum 266
8.3.2. Thermo-gravimetric analysis of the complex 267
8.3.3. Molar conductance of the complex 268
8.3.4. Magnetic susceptibility measurements 268
8.3.5. UV-Vis spectra of Curcumin and its Mn^{II} complex in DMSO 268
8.3.6. Analysis of IR spectra 269
8.4. Quantum Chemical calculations based on experimental evidence 270
8.4.1. MO composition analysis 277
8.4.2. Quantum descriptor analysis 281
8.4.3. Molecular electrostatic potential surface analysis 282
8.4.4. Non-covalent interactions (NCI) & Reduced density gradient (RDG) analysis 283
8.4.5. Analysis of ELF and LOL 285
8.5. Analysis of stability of $[Mn^{II}(Cur)_2(HCur)]$ in different biological media 287
8.6. Interaction of $[Mn^{II}(Cur)_2(HCur)]$ with calf thymus DNA. 288
8.7. Hypoxanthine to xanthine, xanthine oxidase-inhibiting activity of $[Mn^{II}(Cur)_2(HCur)]$ 292
8.8. Biological applications of the prepared $[Mn^{II}(Cur)_2(HCur)]$ complex 293
References 295

Chapter 9: Synthesis, characterization, structural elucidation using, Quantum Chemical calculations and temperature-dependent DNA binding studies of a Cu^{II}–Curcumin complex **303-351**

Introduction 305
9.1. Physicochemical studies on the formation of a Cu^{II} complex of Curcumin 307
9.2. Characterization of the Cu^{II} complex of Curcumin 308
9.2.1. Analysis of the mass spectrum 308
9.2.2. Thermo-gravimetric analysis 309

9.2.3. UV-Vis spectra of Curcumin and its Cu^{II} complex in DMSO 310
9.2.4. Analysis of IR spectra 310
9.3. Determination of stability constant of [Cu(Cur)] in solution. 311
9.4. DFT calculations based on experimental evidence 313
9.4.1. FMO composition analysis 316
9.4.2. Opto-electronic absorption property 321
9.4.3. Natural orbital transition analysis 323
9.4.4. Quantum descriptor analysis 325
9.4.5. MEP surface analysis 326
9.4.6. Non-covalent interactions (NCI) & Reduced density gradient (RDG) analysis 327
9.4.7. ELF and LOL analysis 329
9.5. Comparative stability analysis of the Cu^{II} complex under physiological conditions 330
9.5.1. Followed by UV-Vis spectroscopy 330
9.5.2. Followed by HPLC 332
9.6. Interaction of $[Cu^{II}(Cur)(OCOCH_3)(OH_2)]$ with calf thymus DNA. 334
9.6.1 Interaction of $[Cu^{II}(Cur)(OCOCH_3)(OH_2)]$. with calf thymus DNA at different temperatures 337
9.7. Biological applications of the prepared $[Cu^{II}(Cur)(OCOCH_3)(OH_2)]$ complex 340
References 342

Chapter10: Synthesis, characterization, establishment of structure through Quantum Chemical calculations of a Zn^{II} Complex of Curcumin and its efficacy as a DNA binding agent **352-396**
Introduction 354
10.1. Physicochemical studies on the formation of a Zn^{II} complex with Curcumin 356
10.2. Characterization of the Zn^{II} -Curcumin complex 357
10.2.1. Analysis of the mass spectrum 357
10.2.2. Thermo-gravimetric analysis 358

10.2.3. UV-Vis spectra of Curcumin and $[Zn^{II}(Cur)(OCOCH_3)(OH_2)]$ in DMSO 359

10.2.4. Analysis of IR spectra 360

10.3. Stability constant determination of Zn^{II} -Curcumin in solution. 361

10.4. Quantum chemical calculations for $[Zn^{II}(Cur)(OCOCH_3)(OH_2)]$ 363

10.4.1. Frontier molecular orbital analysis 365

10.4.2. Opto-electronic absorption analysis 369

10.4.3. Natural transition orbital (NTO) analysis 371

10.4.4. Analysis of quantum descriptor 372

10.4.5. Analysis of MEP surface 373

10.4.6. Non-covalent interactions (NCI) & Reduced density gradient (RDG) analysis 374

10.4.7. ELF and LOL analysis 377

10.5. Comparative stability analysis of $[Zn^{II}(Cur)(OCOCH_3)(OH_2)]$ under physiological conditions 378

10.5.1. Followed by UV-Vis spectroscopy 378

10.6. Interaction of $[Zn^{II}(Cur)(OCOCH_3)(OH_2)]$ with calf thymus DNA. 380

10.7. Biological applications of the prepared $[Zn^{II}(Cur)(OCOCH_3)(OH_2)]$ complex 385

References 387

Chapter11: *In silico* molecular modeling experiments to elucidate the DNA binding modes of Curcumin and its metal complexes **397-439**

Introduction 399

11.1. Molecular docking interaction of DNA models with Curcumin & its metal complexes to examine binding mechanism 401

11.2. Analysis of Molecular Dynamics trajectories by examining the mode of DNA interaction with Curcumin and its metal complexes 418

11.2.1. Analysis of RMSD 418

11.2.2. Analysis of RMSF 422

11.2.3. Analysis of Radius of gyration (Rg) 423
11.2.4. Analysis of Solvent accessible surface area (SASA). 424
11.2.5. Analysis of Hydrogen bond during simulation. 425
11.2.6. Calculations of Molecular Mechanics Generalized. Born Surface Area (MM-GBSA) 426
11.2.7. Trajectory snapshots analysis during MD simulation. 429
References 431

Chapter12: *In silico* molecular modeling investigations for the establishment of antibacterial properties of Curcumin and its metal complexes through FtsZ inhibition **440-482**
Introduction 442
12.1. Structure and function of FtsZ 443
12.2. Molecular docking interaction of FtsZ with Curcumin & its metal complexes 445
12.3. Analysis of molecular dynamics trajectories examining FtsZ's interactions with Curcumin and its metal complexes 461
12.3.1. Analysis of RMSD 461
12.3.2. Analysis of RMSF 465
12.3.3. Analysis of Radius of gyration (Rg) 467
12.3.4. Analysis of Solvent accessible surface area (SASA). 468
12.3.5. Analysis of Hydrogen bond during simulation. 470
12.3.6. Calculations of Molecular Mechanics Generalized. Born Surface Area (MM-GBSA) 471
12.3.7. Trajectory snapshots analysis during MD simulation. 474
References 477

Chapter 13: Summary and Conclusion **483-490**

APPENDIX-I List of publication

APPENDIX-II List of Conference proceedings

APPENDIX-III Online workshop and trainings

APPENDIX-IV Reprint of Publications included in the thesis

CHAPTER 1

Introduction

1.1 A concise introduction to bacterial origins and its impact on mankind

With a history stretching back more than 3.5 billion years, bacteria are among the most ancient forms of life on our planet. In their early stages of colonization, these tiny creatures had a significant impact on the biosphere and ecosystem evolution.[1-6] Around 4.5 billion years ago, Earth had extreme weather conditions, that included frequent volcanic eruptions, low oxygen levels and scorching temperatures.[6,7] Life continued to exist in spite of these harsh circumstances. It is highly probable that the first forms of life were bacteria or other basic, single-celled creatures. These primordial bacteria multiplied and evolved by harnessing the energy of substances found in their immediate surroundings.[1-8] Beginning of the bacterial era can be better understood via the lens of abiogenesis, an idea that states non-living materials underwent natural processes to give rise to life.[9] This theory proposes that protocells, the ancestors of bacteria, evolved from more basic organic molecules that underwent a process of progressive structural modification. These first cells eventually learned to multiply and develop, leading to a wide variety of bacterial species.[9-12] During the formation of Earth's atmosphere and aspects related to it, bacteria were pivotal players. Photosynthesis by cyanobacteria, a kind of photosynthetic bacteria triggered the "Great Oxygenation Event" around 2.4 billion years ago.[13-15] This critical event altered Earth's atmosphere in a way that allowed sophisticated life to evolve, first by way of plants, then animals and finally human beings.[1-17]

While microbes helped to shape life on Earth, their connection with humans is quite complicated. The human body contains billions of microorganisms that are collectively known as microbiome.[18] These promote digestion, produce key vitamins and fight against hazardous infections, all of which contribute to our well-being. *Lactobacillus* and *Bifidobacterium* are two types of helpful bacteria present in the gut that help to maintain a healthy digestive tract.[19,20] Unfortunately, not all bacteria are helpful. Some of them can cause illness resulting in variety of diseases ranging from mild skin irritations to life-threatening disorders like tuberculosis,

pneumonia or sepsis.[21] Such pathogenic bacteria penetrate and exploit body's resources causing damage to tissues and organs. Diseases caused by *Vibrio cholerae*, plague (*Yersinia pestis*) and strep throat (*Streptococcus pyogenes*) are some of the dangers of bacterial infections.[22]

1.2 The need for Antibiotics and their role in health care

Discovery of antibiotics may be said to be the most important turning point in the fight against bacteria caused illnesses.[23] In 1928, Alexander Fleming discovered penicillin that is considered to be the beginning of the antibiotic era. An organism called *Penicillium notatum* produces this first naturally occurring antibiotic (penicillin) which was effective against bacteria having no adverse effects on human cells.[24] This discovery changed our approach to medicines by giving people a way to cure potentially deadly bacterial infections.[23-25] Prior to discovery of antibiotics, bacterial illnesses were the major cause of mortality across the world. Infectious diseases that included pneumonia, meningitis and wound infections were common. They either caused death or created major complications with regard to human health.[26,27] Antibiotics revolutionized healthcare by significantly lowering death rates.[28] On account of the fact that antibiotics continue to be the foundation of therapy for bacterial infections, demand for antibiotics is enormous. Whether it's a nominal infection in the urinary tract or a serious one like sepsis, antibiotics are there to help today.[29] However, a major problems confronting contemporary medicine is an emergence of microorganisms that are resistant to antibiotics.[30,31] It enables bacteria to thrive even in the presence of antibiotics. Certain bacteria evolve defence mechanisms against antibiotic therapy, making the medications useless.[32] These resistant bacteria proliferate and spread over time making illnesses more difficult to cure. A number of reasons contribute to the acceleration of antibiotic resistance like overprescription of antibiotics and discontinuation of antibiotic therapy.[33] There are several bacteria that are resistant to multiple drugs including *methicillin-resistant Staphylococcus aureus* (MRSA) and multi-drug resistant *Mycobacterium tuberculosis* which pose significant danger to the public health.[34-36]

These infections are more difficult to cure; they necessitate lengthier hospital stays, more costly medicine and in certain situations no effective therapy at all. The health industry has stressed on the significance of infection prevention, prudent antibiotic use and discovery of novel antibiotics in the fight against antibiotic resistance.[34-36] To combat the rising tide of antibiotic resistance, fresh antibiotic development is of utmost importance. Conventional antibiotics work by interfering with a particular bacterial process. However, bacteria develops resistance mechanisms to such medication for which new strategies are required. Novel approaches to antibiotic discovery have emerged as a result of recent developments in biotechnology aided with computational chemistry.[38-43] Consequently, research in the form of herbal cure and plant-based medicines are now potential substitutes for pharmaceutical antibiotics and have gained a lot of momentum.[44-46] The antibacterial characteristics and a long history of use of natural herbs in traditional medicine provide great promise. Secondary metabolites of many plants and herbs have potent antibacterial characteristics. These include alkaloids, flavonoids, terpenes and phenols.[44-46]

1.3 Research on Curcumin–a natural occurring flavonoid as Antibacterial agent

An important component of turmeric (*Curcuma longa* Linnaeus) is Curcumin (HCur), a yellow pigment, recognized as a lipophilic polyphenolic molecule.[47-50] Besides its historic usage as a cooking ingredient in many Asian societies it has been a key component of Ayurveda and is utilized in wound healing, inflammation, arthritis etc.[47-51] In addition to numerous pharmacological qualities that it exhibits, HCur also possess antibacterial activity that is effective against a broad variety of pathogens. Results from several *in vitro* studies show HCur is effective against a wide variety of Gram-positive and Gram-negative bacterial species.[52,53] However, due to low water solubility and poor physiological stability, it has not been possible to realize its full potential as a therapeutic agent.[54–56] HCur degrades quickly in most physiological buffers and cell culture medium with the fact in the latter it is somewhat more stable owing to presence of

serum.[57,58] Research is yet to definitely establish whether the molecule's biological properties may be attributed to the molecule itself or it is the consequence of the molecule itself and its hydrolyzed products like vanillin, vanilic acid, ferulic acid etc.[57,58] Formation of complexes with metal ions inhibits hydrolysis of HCur, suggesting that biological properties of complexes may be attributed to HCur in conjunction with the respective metal ion, while excluding any influence from hydrolyzed products.[59-61] Numerous studies on complexes of HCur demonstrate that the presence of a metal ion in conjunction with HCur leads to the emergence of new characteristic features that are not observed in HCur alone, many of which have proven beneficial in biological contexts.[59-62]

1.4 Exploring antibacterial mechanism

It is now essential to investigate the factors contributing antibacterial activity. The antibacterial activity of HCur and its complexes has been examined through various studies like bacteria killing kinetics , membrane permeabilization through calcein leakage assay etc.[63,64] Bacterial membrane permeabilization is a crucial process that supports several antimicrobial methods, including as antibiotic action, host immunological responses, and antimicrobial peptide (AMP) activity.[65-67] The integrity of the bacterial membrane is critical for sustaining crucial cellular processes such as nutrition transport, energy production, and structural support.[68,69] Disruption of this membrane causes loss of cell viability, making membrane permeabilization an important target in the development of innovative antimicrobial medicines.[70] Bacterial membranes are conventionally categorized into two types based on the Gram stain method.[71,72] Gram-negative bacteria have inner cytoplasmic membrane, a thin peptidoglycan layer, and an outer membrane, whereas Gram-positive bacteria do not have an outer membrane but have a thicker peptidoglycan layer outside a single lipid bilayer.[73] The outer membrane of Gram-negative bacteria has lipopolysaccharides (LPS), which enhance the membrane's stiffness and impermeability to certain deleterious chemicals. The structural distinctions are essential for

evaluating the processes of membrane permeabilization.[70,73] Membrane permeabilization is becoming increasingly important in the development of novel antimicrobial medicines, particularly against drug-resistant bacteria.[65-70] Novel therapies are being developed to target bacterial membranes with greater precision while reducing harm to host cells.[74,75] Furthermore, combination therapy that utilize membrane-targeting drugs alongside standard antibiotics can improve antimicrobial effectiveness.[76,77] In this thesis all the studies was carried out on both Gram-positive and Gram-negative bacterial strain. Morphology of bacterial cell membrane upon exposure on Curcumin and its complexes was monitored thoroughly under various spectroscopic technique. Bacterial cell permeabilization may be a significant mechanism through which such compounds exhibit antibacterial activity, indicating complexes surpass HCur in this regard.

The other way to show antibacterial mechanism is FtsZ inhibition; which represents a significant and well-established mechanism for bacterial cell death, functioning by disrupting the activity of FtsZ a crucial bacterial cytoskeletal protein involved in cell division.[78-82] Inhibition of FtsZ disrupts the formation of the Z-ring, which is essential for bacterial cytokinesis, resulting in the failure of cell division and subsequent cell death.[78-85] FtsZ, a member of tubulin superfamily demonstrates structural and functional similarities to eukaryotic tubulin that is essential for bacterial growth and present in various bacterial species. It is identified as a potential target for the development of new antimicrobial agents, particularly in the context of rising antibiotic resistance as a global health concern.[78,79] Conversely, small-molecule inhibitors are significant as they can be designed to target specific binding sites on FtsZ, thereby obstructing its GTPase activity or its polymerization capability. Exploring FtsZ in drug discovery research demonstrates significant potential for developing novel antibiotics effective against bacterial infections.[78-85] A significant number of molecules that specifically target FtsZ were identified. Certain substances exhibit antibacterial properties against various bacteria including drug-resistant strains and can inhibit polymerization of FtsZ.[78-85]

Computational modeling is an increasingly utilized technique that facilitates the achievement of objectives that may be challenging to accomplish experimentally and without ambiguity. It is a process that facilitates the development and discovery of new drugs. This dissertation aims to investigate bacterial membrane permeabilization activity through laboratory experiments and FtsZ inhibition using an *in silico* approach.[78-85]

References:

1. J.L. Bada; How life began on Earth: a status report. *Earth and Planetary Science Letters*, **2004**, 226, 1-5.
2. T. Cavalier-Smith; Cell evolution and Earth history: stasis and revolution. *Philosophical Transactions of the Royal Society B: Biological Sciences*, **2006** , 361, 969-1006.
3. H.C. Urey; On the early chemical history of the earth and the origin of life. *Proceedings of the National Academy of Sciences*, **1952**, 38, 351-363.
4. J. Errington; L-form bacteria, cell walls and the origins of life. *Open biology*, **2013**, 3, 120143.
5. W. Altermann, J. Kazmierczak, A. Oren, D.T. Wright; Cyanobacterial calcification and its rock-building potential during 3.5 billion years of Earth history. *Geobiology*, **2006**, 4, 147-166.

6. G. Wächtershäuser; From volcanic origins of chemoautotrophic life to Bacteria, Archaea and Eukarya. *Philosophical Transactions of the Royal Society B: Biological Sciences*, **2006** 361, 1787-808.

7. J.K. Fredrickson, T.C. Onstott; Microbes deep inside the earth. *Scientific American*, **1996** 275, 68-73.

8. L.E. Dietrich, M.M. Tice, D.K. Newman; The co-evolution of life and Earth. *Current Biology*, **2006**, 16, 395-400.

9. B.S. Palmer ; A review on the spontaneous formation of the building blocks of life and the generation of a set of hypotheses governing universal abiogenesis. *International Journal of Astrobiology*, **2013**, 12, 39-44.

10. J. Bergman ; Why abiogenesis is impossible. *Creation Research Society Quarterly*, **2000** 36, 195-207.

11. G.T. Javor ; Life, An Evidence for Creation. *In Proceedings of the International Conference on Creationism*, **1998** , 4, 31.

12. J.S. Hernandez, J.H. Osorio, J.E. Perez ; Origins of life before the cell: echos from the past with broad implications in our future. *Brazilian Journal of Biological Sciences*, **2015** , 2, 179-192.

13. J.F. Kasting, J.L. Siefert ; Life and the evolution of Earth's atmosphere. *Science*, **2002** , 296, 1066-1068.

14. N.H. Sleep, D.K. Bird ; Evolutionary ecology during the rise of dioxygen in the Earth's atmosphere. *Philosophical Transactions of the Royal Society B: Biological Sciences*, **2008** 363, 2651-2664.

15. J. Olejarz, Y. Iwasa, A.H. Knoll, M.A. Nowak; The Great Oxygenation Event as a consequence of ecological dynamics modulated by planetary change. *Nature communications*. **2021**, 12, 3985.

16. P. Sánchez-Baracaldo, T. Cardona ; On the origin of oxygenic photosynthesis and Cyanobacteria. *New Phytologist*. **2020** , 225, 1440-1446.

17. G.D. Smith, N. Thanh Doan ; Cyanobacterial metabolites with bioactivity against photosynthesis in cyanobacteria, algae and higher plants. *Journal of Applied Phycology*, **1999**, 11, 337-344.

18. L.K. Ursell, J.L. Metcalf, L.W. Parfrey, R. Knight ; Defining the human microbiome. *Nutrition reviews*, **2012**, 70, 38-44.

19. R. Tojo, A. Suárez, M.G. Clemente, C.G. de los Reyes-Gavilán, A. Margolles, M. Gueimonde, P. Ruas-Madiedo ; Intestinal microbiota in health and disease: role of bifidobacteria in gut homeostasis. *World journal of gastroenterology: WJG*, **2014** 20, 15163.

20. F. Turroni, M. Ventura, L.F. Buttó, S. Duranti, P.W. O'Toole, M.O. Motherway, D. van Sinderen; Molecular dialogue between the human gut microbiota and the host: a Lactobacillus and Bifidobacterium perspective. *Cellular and Molecular Life Sciences*, **2014** 71, 183-203.

21. C.H. Lin, C.J. Lin, Y.W. Kuo, J.Y. Wang, C.L. Hsu, J.M. Chen, W.C. Cheng, L.N. Lee ; Tuberculosis mortality: patient characteristics and causes. *BMC infectious diseases*, **2014**, 4, 1-8.

22. D.G. Moriel, D. Piccioli, M.M. Raso, M. Pizza ; The overlooked bacterial pandemic. *In Seminars in Immunopathology, Berlin/Heidelberg: Springer Berlin Heidelberg*, **2024**, 45, 481-49.

23. E.J. Culp, N. Waglechner, W. Wang, A.A. Fiebig-Comyn, Y.P. Hsu, K. Koteva, D. Sychantha, B.K. Coombes, M.S. Van Nieuwenhze, Y.V. Brun, G.D. Wright ; Evolution-guided discovery of antibiotics that inhibit peptidoglycan remodelling. *Nature.* **2020**, 578, 582-587.

24. R. Haider ; Penicillin and the Antibiotics Revolution Global History. *Asian Journal of Pharmaceutical Research*, **2023**, 13, 55-62.

25. G. B. Mahady ; Medicinal plants for the prevention and treatment of bacterial infections. *Current pharmaceutical design*, **2005**, 11, 2405-2427.

26. C. Dye ; After 2015: infectious diseases in a new era of health and development. *Philosophical Transactions of the Royal Society B: Biological Sciences*, **2014**, 369, 20130426.

27. A.R. Tunkel, R. Hasbun, A. Bhimraj, K. Byers, S.L. Kaplan, W.M. Scheld, D. van de Beek, T.P. Bleck, H.J. Garton, and J.R. Zunt; 2017 Infectious Diseases Society of America's clinical practice guidelines for healthcare-associated ventriculitis and meningitis. *Clinical Infectious Diseases*, **2017**, 64, e34-e65.

28. R. D'Amico, S. Pifferi, V. Torri,, L. Brazzi, and E. Parmelli ; Antibiotic prophylaxis to reduce respiratory tract infections and mortality in adults receiving intensive care. *Cochrane Database of Systematic Reviews*, **2009**, 4.

29. J. V. Eng, R. Marcus, J.L. Hadler, B. Imhoff, D. J. Vugia, P. R. Cieslak, E. Zell, V. Deneen, K. G. McCombs, S.M. Zansky, and M. A. Hawkins ; Consumer attitudes and use of antibiotics. *Emerging infectious diseases*, **2003**, 9, 1128.

30. A.J. Alanis ; Resistance to antibiotics: are we in the post-antibiotic era? *Archives of medical research*, **2005** , 36, 697-705.

31. E. Oldfield, and X. Feng ; Resistance-resistant antibiotics. *Trends in Pharmacological Sciences*, **2014**, 35, 664-674.

32. J.M.T. Hamilton-Miller.; Immunopharmacology of antibiotics: direct and indirect immunomodulation of defence mechanisms. *Journal of chemotherapy*, **2001**, 13, 107-111.

33. Q. Zhang, G. Lambert, D. Liao, H. Kim, K. Robin, C.K. Tung, N. Pourmand, and R.H. Austin ; Acceleration of emergence of bacterial antibiotic resistance in connected microenvironments. *Science*, **2011**, 333, 1764-1767.

34. A.U. Khan, A. Sultan, A. Tyagi, S. Zahoor, M. Akram, S. Kaur, M. Shahid and C.V. Vaishnavi ; Amplification of mecA gene in multi-drug resistant Staphylococcus aureus strains from hospital personnel. *The Journal of Infection in Developing Countries*, **2007**, 1, 289-295.

35. L.M. Assis, M. Nedeljković, A. Dessen ; New strategies for targeting and treatment of multi-drug resistant Staphylococcus aureus. *Drug Resistance Updates*, **2017**, 31, 1-14.

36. P. Bradley, N.C. Gordon, T.M. Walker, L. Dunn, S. Heys, B. Huang, S. Earle, L.J. Pankhurst, L. Anson, M. De Cesare, P.Piazza ; Rapid antibiotic-resistance predictions from genome sequence data for Staphylococcus aureus and Mycobacterium tuberculosis. *Nature communications*, **2015**, 6, 10063.

37. K. Bhattarai, R. Bastola, B. Baral ; Antibiotic drug discovery: Challenges and perspectives in the light of emerging antibiotic resistance. *Advances in genetics*, **2020**, 105, 229-292.

38. N.C. Mohana, H.Y. Rao, D. Rakshith, P.R. Mithun, B.R. Nuthan, S. Satish; Omics based approach for biodiscovery of microbial natural products in antibiotic resistance era. *Journal of Genetic Engineering and Biotechnology*, **2018**. 16, 1-8.

39. M.Q. Zhang, B. Wilkinson; Drug discovery beyond the 'rule-of-five'. *Current opinion in biotechnology*, **2007**, 18, 478-488.

40. A.K. Bansal; Role of bioinformatics in the development of new antibacterial therapy. *Expert Review of Anti-Infective Therapy*, **2008**, 6, 51-65.

41. I.J.D.S. Nascimento, T.M. de Aquino, E.F. da Silva-Júnior ; The new era of drug discovery: The power of computer-aided drug design (CADD). *Letters in Drug Design & Discovery*, **2022**. 19, 951-955.

42. P. Bultinck, H. De Winter, W. Langenaeker, J.P. Tollenare, *Computational medicinal chemistry for drug discovery*. CRC Press**. 2003**.

43. C.N. Cavasotto, M.G. Aucar, N.S. Adler ; Computational chemistry in drug lead discovery and design. *International Journal of Quantum Chemistry*, **2019**. 119, e25678.

44. H.M.A. AlSheikh, I. Sultan, V. Kumar, I.A. Rather, H. Al-Sheikh, A. Tasleem Jan, , Q.M.R. Haq; Plant-based phytochemicals as possible alternative to antibiotics in combating bacterial drug resistance. *Antibiotics*, **2020**, 9, 480.

45. D. Savoia; Plant-derived antimicrobial compounds: alternatives to antibiotics. *Future microbiology*, **2012**, 7, 979-990.

46. H. Chandra, P. Bishnoi, A. Yadav, B. Patni, A.P. Mishra, A.R. Nautiyal; Antimicrobial resistance and the alternative resources with special emphasis on plant-based antimicrobials—a review. *Plants*, **2017**, 6, p.16.

47. B.B. Aggarwal, C. Sundaram, N. Malani, H. Ichikawa; Curcumin: the Indian solid gold. The molecular targets and therapeutic uses of curcumin in health and disease, **2007**. 1-75.

48. J. S. Jurenka; Anti-inflammatory properties of curcumin, a major constituent of Curcuma longa: a review of preclinical and clinical research. *Alternative Medicine Review*, **2009**, 14, 141-153.

49. S. Y. Teow, K. Liew, S. A. Ali, A. S. B. Khoo, S. C. Peh; Antibacterial action of curcumin against Staphylococcus aureus: a brief review. *Jour. Trop. Med*., **2016** Article ID 2853045, 10 pages

50. M. D. Cas, R. Ghidoni; Dietary Curcumin: Correlation between bioavailability and health potential, *Nutrients*. **2019**, 11, 2147.

51. S. B. de Souza Ferreira , M. L. Bruschi; Improving the bioavailability of curcumin: is micro/nanoencapsulation the key?, *Ther Deliv*., **2019**, 10, 83-86.

52. M. R. Agel, E. Baghdan, S. R. Pinnapireddy, J. Lehmann, J. Schaefer, U. Bakowsky; Curcumin loaded nanoparticles as efficient photoactive formulations against gram-

positive and gram-negative bacteria. *Colloids and Surfaces B: Biointerfaces*, **2019**. 178, 460-468.

53. T. Haukvik, E. Bruzell, S. Kristensen, H.H. Tønnesen; Photokilling of bacteria by curcumin in different aqueous preparations. Studies on curcumin and curcuminoids XXXVII. *Die Pharmazie-An International Journal of Pharmaceutical Sciences*, **2009**, 64, 666-673.

54. Z. Stanić; Curcumin, a compound from natural sources, a true scientific challenge–a review. *Plant Foods for Human Nutrition*, **2017**, 72,1-12.

55. Y. Hussain, W. Alam, H. Ullah, M. Dacrema, M. Daglia, H. Khan, C.R. Arciola; Antimicrobial potential of curcumin: therapeutic potential and challenges to clinical applications. *Antibiotics*, **2022,** 11, 322.

56. L. Slika , D. Patra; A short review on chemical properties, stability and nano-technological advances for curcumin delivery.*Expert opinion on drug delivery*, **2020** , 17, 61-75.

57. Y.J. Wang, M.H. Pan, A.L. Cheng, L.I. Lin, Y.S. Ho, C.Y. Hsieh, J.K. Lin; Stability of curcumin in buffer solutions and characterization of its degradation products. *Journal of pharmaceutical and biomedical analysis*, **1997**, 15, 1867-1876.

58. P. Anand, A. B. Kunnumakkara, R. A. Newman, B. B. Aggarwal; Bioavailability of Curcumin: Problems and promises, *Mol. Pharmaceutics.*, **2007**, 4, 807–818.

59. S. Wanninger, V. Lorenz, A. Subhan, F. T. Edelmann; Metal complexes of curcumin–synthetic strategies, structures and medicinal applications. *Chem. Soc. Rev.,***2015**, 44, 4986-5002.

60. S. Banerjee, P. Prasad, A. Hussain, I. Khan, P. Kondaiah, A. R. Chakravarty; Remarkable photocytotoxicity of curcumin in HeLa cells in visible and arresting its degradation on oxovanadium (IV) complex formation. *Chem. Comm*., **2012**, 48, 7702-7704.

61. S. Banerjee, A.R. Chakravarty; Metal complexes of curcumin for cellular imaging, targeting, and photoinduced anticancer activity. *Accounts of chemical research*, **2015**, 48, 2075-2083.

62. M.A. Subhan, K. Alam, M.S. Rahaman, M.A. Rahman, R. Awal; Synthesis and characterization of metal complexes containing curcumin ($C_{21}H_{20}O_6$) and study of their anti-microbial activities and DNA binding properties. *J. Sci. Res*., **2014**, 6, 97-109.

63. P. Garcia-Penarrubia, A.D. Bankhurst, F.T. Koster; Experimental and theoretical kinetics study of antibacterial killing mediated by human natural killer cells. *Journal of immunology (Baltimore, Md.: 1950)*, **1989** , 142, 1310-1317.

64. P. Tyagi, M. Singh, H. Kumari, A. Kumari, K. Mukhopadhyay; Bactericidal activity of curcumin I is associated with damaging of bacterial membrane. *PloS one*, **2015**, 10, e0121313.

65. B. Skerlavaj, D.O.M.E.N.I.C.O. Romeo, R. Gennaro, Rapid membrane permeabilization and inhibition of vital functions of gram-negative bacteria by bactenecins. *Infection and immunity*, **1990**, 58, 3724-3730.

66. S. Thennarasu, D.K. Lee, A. Poon, K.E. Kawulka, J.C. Vederas, A. Ramamoorthy; Membrane permeabilization, orientation, and antimicrobial mechanism of subtilosin A. *Chemistry and physics of lipids*, **2005**, 137, 38-51.

67. K. Matsuzaki; Membrane permeabilization mechanisms. *Antimicrobial Peptides: Basics for Clinical Application*, **2019** , 9-16.

68. J.G. Hurdle, A.J. O'neill, I. Chopra, R.E. Lee ; Targeting bacterial membrane function: an underexploited mechanism for treating persistent infections. *Nature Reviews Microbiology*, **2011** , 9, 62-75.

69. J. Sun, S.T. Rutherford, T. J. Silhavy , K.C. Huang; Physical properties of the bacterial outer membrane. *Nature Reviews Microbiology*, **2022**, 20, 236-248.

70. F. Guilhelmelli, N. Vilela, P. Albuquerque, L.D.S. Derengowski, I. Silva-Pereira, C.M. Kyaw; Antibiotic development challenges: the various mechanisms of action of antimicrobial peptides and of bacterial resistance. *Frontiers in microbiology*, **2013,** 4, 353.

71. J.W. Bartholomew , T. Mittwer ; The gram stain. *Bacteriological reviews*, **1952**, 16, 1-29.

72. S. Halebian, B. Harris, S.M. Finegold, R.D. Rolfe; Rapid method that aids in distinguishing Gram-positive from Gram-negative anaerobic bacteria. *Journal of clinical microbiology*, **1981 ,** 13, 444-448.

73. M.R.J. Salton; Studies of the bacterial cell wall: IV. The composition of the cell walls of some gram-positive and gram-negative bacteria. *Biochimica et biophysica acta*,**1953 ,** 10, 512-523.

74. A.E. Clatworthy, E. Pierson, D.T. Hung ; Targeting virulence: a new paradigm for antimicrobial therapy. *Nature chemical biology*, **2007**. 3, 541-548.

75. J. Fernebro; Fighting bacterial infections—future treatment options. *Drug Resistance Updates*, **2011 ,**14, 125-139.

76. M. Liao, C. Wu, K. Shen, X. Hu, J.R. Lu; Combinatorial therapies of surfactant-like antimicrobial peptides and antibiotics for improved therapeutic efficacy. *Current Opinion in Colloid & Interface Science*, **2024**. 101829.

77. C. Dias, A.P. Rauter ; Membrane-targeting antibiotics: recent developments outside the peptide space. *Future Medicinal Chemistry*, **2019**. 11, 211-228.

78. S. Zorrilla, B. Monterroso, M-Á Robles-Ramos, W. Margolin, G. Rivas; FtsZ Interactions and biomolecular condensates as potential targets for new antibiotics, *Antibiotics*, **2021**, 10 254

79. K. Haranahalli, S. Tong, I. Ojima; Recent advances in the discovery and development of antibacterial agents targeting the cell-division protein FtsZ. *Bioorganic & medicinal chemistry*, **2016** , 24, 6354 – 6369.

80. S. Tripathy, S. K. Sahu ; FtsZ inhibitors as a new generation of antibacterial agents. *Bioorganic chemistry*, **2019**; 91, 103169.

81. S. Kapoor, D. Panda; Targeting FtsZ for antibacterial therapy: a promising avenue. *Expert opinion on therapeutic targets*, **2009** , 13, 1037–1051.

82. R. McQuillen, J. Xiao; Insights into the structure, function, and dynamics of the bacterial cytokinetic FtsZ-ring. *Annual Review of Biophysics*, **2020**, 49, 309–341.

83. S. Kifayat, V. Yele, A. Ashames, D.K. Sigalapalli, R.R. Bhandare, A.B Shaik, et al. Filamentous temperature sensitive mutant Z: a putative target to combat antibacterial resistance. *RSC advances*, **2023**, 13, 11368–11384.

84. N. Sun, L. Ban, M. Li, Z. Fang, X. Li, W. Yao, et al. Probing the benzofuroquinolinium derivative as a potent antibacterial agent through the inhibition of FtsZ activity. *Jour. Pharmacol. Sci.*, **2018** , 138, 83–85.

85. N. Sun, Y-J. Lu, F-Y. Chan, R-L. Du, Y-y. Zheng, K. Zhang, et al. A thiazole orange derivative targeting the bacterial protein FtsZ shows potent antibacterial activity. *Frontiers in microbiology*. **2017**, 8, 855.

CHAPTER 2

Review on Curcumin and its medicinal applications

2.1 Curcumin: A brief historical background

Curcumin, also known as diferuloylmethane [(1E,6E)-1,7-bis-(4-hydroxy-3-methoxyphenyl)-hepta-1,6-diene-3,5-dione] is a polyphenol that serves as the principal constituent within a herbal remedy and culinary spice turmeric (Curcuma longa Linn belonging to Zingiberaceae), a member of the ginger family and native to southern and south-western tropical Asia.[1] This resplendent yellow spice, extracted from rhizome of the botanical specimen boasts a rich lineage of utilization within ancient healing practices of China and India.[1,2] For over two millennia, pulverized rhizome of turmeric has been employed in various facets of Asian culinary practices, medicinal applications, cosmetic formulations and in the art of fabric dyeing.[2] The advent of the 14th century witnessed the introduction of this pivotal spice in the western hemisphere by intrepid European explorers who embarked upon their ventures to the Asian continent.[3] The enduring utilization of Curcumin as a traditional remedy persists in contemporary times as well. Within the realm of the venerable Indian medical tradition (Ayurveda), a concoction consisting of a paste derived from the turmeric plant is employed for the purpose of remedying prevalent ocular infections. Additionally, the same preparation is utilized in dressing wounds, amelioration of bites, burns, acne and sundry dermal afflictions.[4]

Its commercialization started when Johnson & Johnson, the prominent pharmaceutical house, ventured into production of turmeric-infused band-aids specifically tailored for the Indian market.[5] In northern India, it is customary for women to partake in a regimen involving consumption of a concoction comprised of freshly prepared turmeric paste, powdered dried ginger roots and honey, diluted in a vessel of heated milk. This elixir is typically imbibed twice daily following childbirth. The application of a turmeric poultice to the perineum is known to facilitate the recuperation process of any laceration present in the birth canal.[6] Utilization of powdered turmeric in conjunction with boiled milk as a remedy for cough and other respiratory afflictions as

well as incorporation of roasted turmeric as an essential component in the treatment of dysentery among children is documented.[4] This time-honored remedy is additionally employed for management of dental ailments, gastrointestinal maladies like dyspepsia and hyperacidity, impaired digestion, excess gas formation, gastric ulcers as well as for mitigating hallucinogenic manifestations associated with hashish and other psychotropic substances.[7] Curcumin presently finds application in the realms of gastronomy and industrial production. It serves as an ingredient for perfumes, imparting a natural yellow hue to the final product. It has today gained approval as a food additive lending its distinct flavour to a diverse range of dishes and mustard preparations.[8] The contemporary focus on utilization of natural and complementary medicines in the realm of western medicine has captivated the scientific community's interest in this time-honored therapeutic solution.

Over the course of more than four decades, scientists have proven many of Curcumin's pharmacological actions, establishing its ability to function as a chemo-preventive agent and a possible therapeutic agent for a number of chronic diseases.[9-14] Although studies on Curcumin dates back to over two centuries, they were initially pursued at isolated places of the world[15-16]. However, today, scientists from all over the world have become interested in it for its multi-faceted behavioral benefits. From only a few papers on the structure of Curcumin, its production, biochemistry and antioxidant activity that appeared between 1815 and 1970, there was a substantial increase in publications related to it with several groups of researchers probing diverse biological aspects of the compound. However, since the publication by Aggarwal and co-workers in nineties, on possible anticancer activity of Curcumin, research in this regard picked up on an altogether different scale.[17] While most scientists focused on biological aspects of Curcumin others sought to understand the chemistry that underlies the compound's remarkable biological action. Researchers having training in organic, inorganic, physical and analytical chemistry were able to achieve a lot

of success in their effort to study Curcumin. The primary focus of organic chemists was on the isolation and synthesis of Curcumin and related novel compounds (synthetic or natural). Inorganic chemists took advantage of the compound's diketo group, its metal chelating ability to create novel structural entities with altered biological activity. Complex formation had three impacts i) it could overcome the natural degradation of Curcumin in biological milieu, ii) increase bio-availability and iii) overcome drug resistance by virtue of being a new moiety with completely different physico-chemical properties. Curcumin's interactions with micro-heterogeneous systems and biomolecules have been the attention of physical chemists owing to highly sensitive spectroscopic abilities. It's distinctive absorption and spectroscopic features were exploited by analytical chemists to identify and quantitatively estimate trace elements like boron.[18] Curcumin's chemical reactivity with reactive oxygen species (ROS), addition reactions, degradation and creation of nano-conjugates and formulations are several areas of chemistry that have contributed to our understanding of its biological activity. Extensive research unveiled the remarkably diverse array of advantageous attributes that Curcumin possesses encompassing anti-inflammatory, antioxidant, chemo-preventive and chemotherapeutic abilities. These activities were later exemplified through *in vitro* cellular systems and *in vivo* animal models laying the foundation for ongoing human clinical trials.[19-21]

This review succinctly summarizes the comprehensive body of research pertaining to multifaceted activities of Curcumin, elucidating intricate mechanism of action and delineating its chemical composition and clinical attributes. In the light of the burgeoning fascination surrounding Curcumin and the copious body of literature emerging on it, it would be prudent to regard reports cited in this review as merely illustrative in nature, rather than all-encompassing.

2.2 Chemical properties of Curcumin

Curcumin ($C_{21}H_{20}O_6$) is the primary bioactive compound accountable for physiological effects that are observed in turmeric. In 1910, Lampe and Millipedes were the first to characterize the structure and chemistry of Curcumin. After another three years, in 1913, they announced that they successfully synthesized the molecule and confirmed its structure.[22] Using chromatography, Srinivasan was able to separate and quantify various components of Curcumin way back in 1953.[23] Demethoxycurcumin (DMC), bis-demethoxycurcumin (BDMC) and Curcumin are the three hydrophobic Curcuminoids that make up majority of Curcumin and is found in the ratio 17:3:77 (Fig. 1).[24] In another study, proportion Curcuminoids in Curcumin were approximately 5% for bisdemethoxycurcumin (BDMC), 15% for demethoxycurcumin (DMC) and 80% for Curcumin itself (Fig.1). Hence, Curcumin is a mixture largely composed of three hydrophobic Curcuminoids, Curcumin, DMC and BDMC. They are similar in the sense that their chemical structures include two aromatic feruloyl rings connected to orthomethoxy phenolic OH groups.

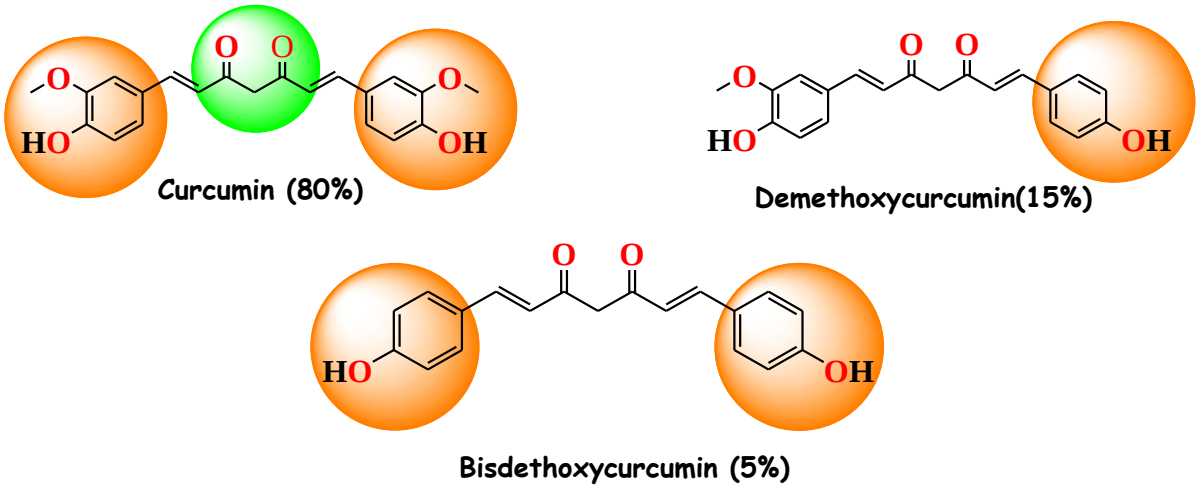


Figure 1: Chemical structures of different Curcuminoids

Curcumin is classified as a member of diaryl hepatanoid compounds, characterized by linkage of two aromatic rings through a chain consisting of seven carbon atoms. The two aryl groups exhibit

symmetrical substitution with methoxy and phenolic –OH groups at ortho positions. Additionally, the seven-carbon chain demonstrates conjugation featuring an enone moiety and a 1,3-diketone group. The structure is occasionally referred to as diferuloyl methane consisting of two aryl but-2-ones. The highly polar aromatic rings are connected to one another in a symmetrical fashion by means of a seven-carbon aliphatic chain and two unsaturated carbonyl groups (Fig. 2).[25]

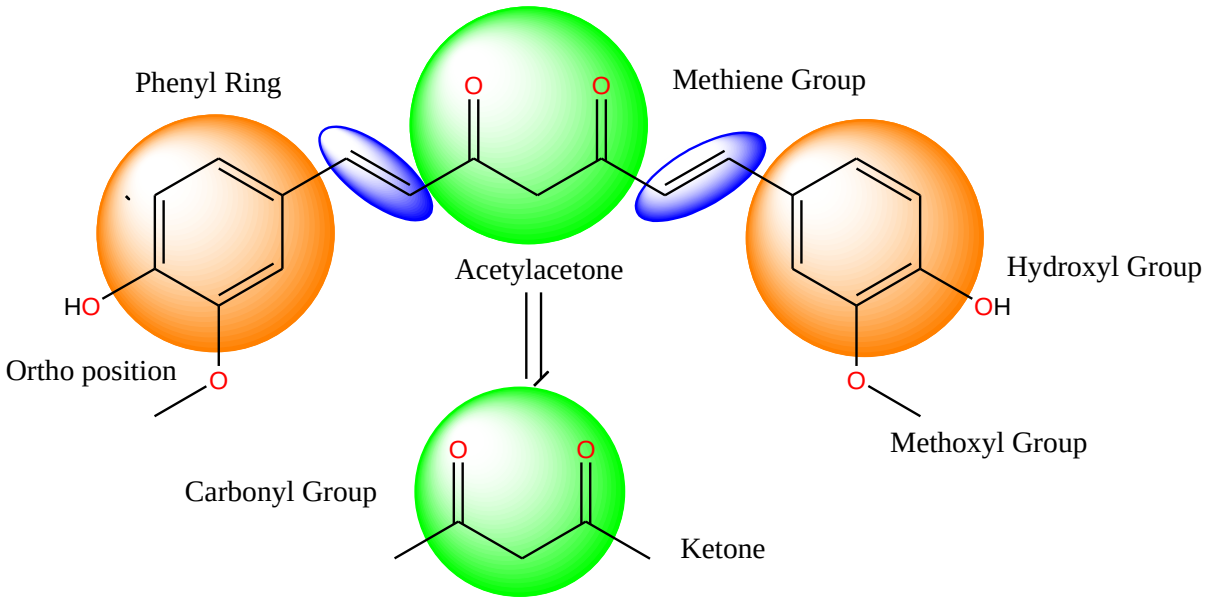


Figure 2: Different functional groups in the molecular structure of Curcumin

This seven-carbon aliphatic chain structure is responsible for the hydrophobic nature of Curcumin making it practically insoluble in water. However, solubility is observed in ethanol, dimethyl sulfoxide (DMSO), methanol and acetone.[25] Presence of two feruloyl aromatic rings in Curcumin allows it to exhibit an UV-Vis absorption at 430 nm.[25]

Findings from X-ray diffraction analysis of Curcumin revealed that its molecular structure in solid state consists of three planar groups with substitution that are interconnected by double bonds.[26,27] In the crystalline state, molecular symmetry is disrupted by a rotation of -162° between the planes of two aryl moieties. On the other hand, presence of a 1,3-diketone functionality leads to formation of intra-molecular hydrogen bonding that in turn induces keto-enol tautomerism,

resulting in the existence of both di-keto and enolate configurations in the molecule. The di-keto form predominates under conditions that are acidic or neutral. When the compound exists in solid state the enol form predominates; the same is true under alkaline conditions as well (Fig. 3).[25,26] In crystalline phase, it predominantly exists in cis-enol configuration with enolic hydrogen equally distributed over the two oxygen atoms of the keto-enol moiety (Fig. 3).[26]

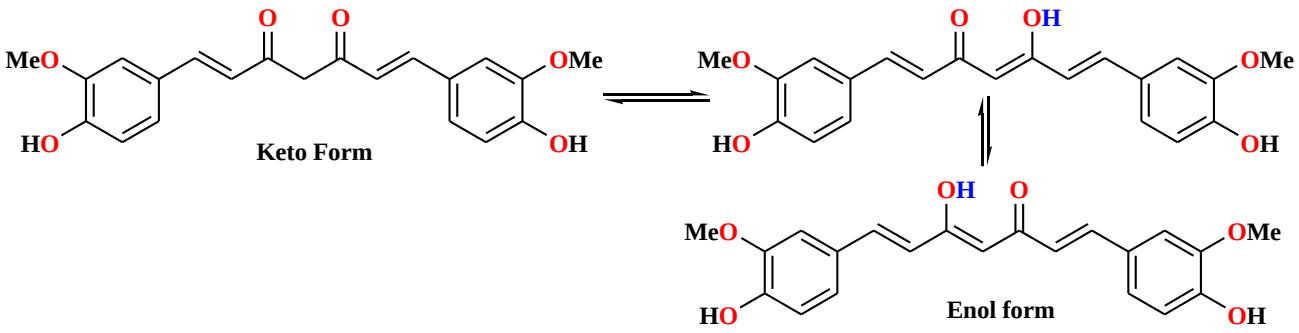


Figure 3: Keto-enol tautomerism of Curcumin

Typically, unsaturated diketones have the ability to exist in nine distinct forms as a result of keto-enol tautomerism and *cis-trans* isomerism.[28] Influence of environmental and structural factors affect their relative contributions. Several computational studies conducted by multiple research groups have investigated the stability of keto and enol forms of similar compounds both in gas and solution phases.[29-33] These studies have consistently indicated that the enol form exhibits greater stability compared to the keto form having a difference of approximately 5 to 8 kcals/mol. Additionally, it has also been calculated that the keto form exhibits a twisted conformation whereas the enol form adopts a planar conformation with a dihedral angle of 180°. This conformation allows for resonance stabilization across two phenyl rings.[31] Curcumin exhibits an electron cloud distribution throughout its structure while phenolic OH groups form intramolecular hydrogen bonds with o-methoxy units (Fig. 4).

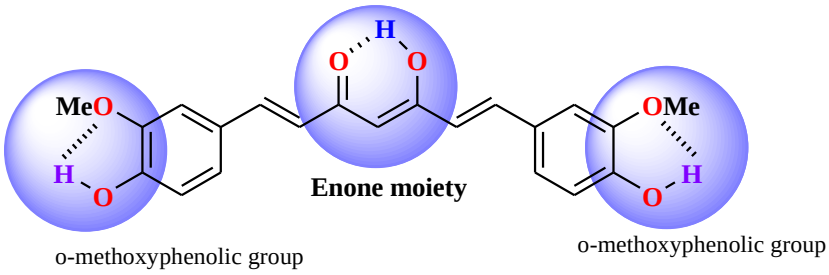


Figure 4 : Intramolecular hydrogen bonding (-----) within Curcumin molecule

According to recent quantum chemical investigations it was suggested that the trans conformer with lowest energy is characterized by the presence of two phenol-methoxy groups located on two opposite sides of the Curcumin backbone. Additionally, the linker group exhibits free rotation resulting in minimal energy barrier between *trans* and *cis* forms.[30] Extensive nuclear magnetic resonance (NMR) investigations utilizing both proton (^{1}H) and carbon-13 (^{13}C) spectroscopy conducted in solution provide confirmation that Curcumin predominantly exists in the enol form in majority of non-polar organic solvents (Fig. 3).[32-34] ^{1}H nuclear magnetic resonance (^{1}H-NMR) spectrum of Curcumin in a solution of deuterated dimethyl sulfoxide (DMSO-D6) exhibit a clearly discernible peak at 16.4 ppm attributed to the presence of enolic hydrogen. The observed low field peak may be attributed to a combined influence of strong intramolecular hydrogen bond and a conjugated system. In the presence of polar protic solvents and low pH conditions, the observed peak becomes indiscernible suggesting predominance of the keto form. This phenomenon is attributed to the influence of these conditions on intra-molecular hydrogen bonding interactions that in turn affects intermolecular hydrogen bonding.

Curcumin exhibits three acidity constant values due to the presence of ionizable protons in the form of phenolic and enolic OH groups. Three acidity constants were reported based on a combination of experimental and theoretical studies. The enol proton exhibits highest acidity

compared to two phenolic protons.[35-38] The calculated ground state dipole moment of Curcumin is 10.77 D. [35-38] Additionally, hydrophobicity parameter log(P) falls in the range 2.5 to 3.6 that supports its limited solubility in water.[39] The predicted water solubility of Curcumin is approximately 3 to 6 g/ml. These parameters additionally corroborate the fact that Curcumin exhibits a polarity that enables solubility in lipids and proteins.

Antimicrobial, antioxidant, anti-inflammatory, neuro-protective, anticancer and immuno-modulatory activities are among the well documented biological activities of Curcumin.[40] It was put to extensive use in traditional medicine for the treatment of a wide range of diseases that include autoimmune, neurological, diabetic, cardiovascular and various infectious diseases. Through the following discussion, an effort would be made to go into greater detail regarding antibacterial activities of Curcumin, its mechanism of action and different barriers associated with its clinical application as an antibiotic.

2.2.1 The aspect of degradation of Curcumin:

The metabolic process of Curcumin results in a variety of compounds. According to existing literature, it was suggested Curcumin undergoes conversion to glucuronides and various other conjugates *in vivo*. Curcumin is thought to be conjugated to a sulphate moiety assisted by sulphotransferase. Such Curcumin sulphate is thereafter converted to Curcumin by putative enzymes inside cells, which is why sulphates were found as a product of degradation of Curcumin.[41] Additionally, reduced derivatives of Curcumin like tetrahydro Curcumin, hexahydro Curcumin and octahydro Curcumin were also identified.[42-46] All the compounds could be synthesized and subsequently subjected to independent examination to assess their potential biological influence. The extent of independent action of metabolites in comparison to Curcumin remains uncertain and there are different viewpoints in the literature on activity of such molecules.

Today it is well documented that tetrahydro Curcumin has superior antioxidant properties and demonstrates less anticancer activity compared to Curcumin.[43,47]

Curcumin exhibits fast degradation under neutral and alkaline conditions. It is somewhat more stable in acidic milieu. When pH decreases the equilibrium tends to favour the neutral form, characterized either by poor or negligible solubility. Consequently, investigations conducted in buffered solvents often entail the initial step of dissolving the substance in a polar protic organic solvent like methanol followed by subsequent dilution with water.[48,49]

The conjugated structure of Curcumin exhibits absorption throughout the visible range between 408 and 500 nm.[50] This characteristic feature was employed to monitor the degradation of Curcumin in different buffers utilizing either spectroscopy and/or HPLC. At pH ~ 7.5 and ambient temperature conditions in aqueous buffer solutions, half-life ($t_{1/2}$) for the degradation of Curcumin was approximately 20 minutes.[51] When temperature was elevated to 37°C, the observed half-life at pH 7.2 was found to be less than 10 minutes.[48] Increased breakdown upon exposure to heat prompted a comprehensive examination of degradation products of Curcumin.[48] It was established that Curcumin exhibits photo-reactivity evidenced by 5% decrease of the parent compound, when samples were prepared in clear glass containers compared to amber glass containers.[48] The breakdown of Curcumin occurs through two primary mechanisms, namely solvolysis and oxidative degradation (Fig. 5). Breakdown of heptadienedione chain by solvolysis specifically through nucleophilic substitution or elimination facilitated by solvent molecules occur in aqueous alkaline buffer and leads to 90% decrease in concentration in an investigation comprising 30-minutes. The primary products were identified as vanillin, ferulic acid and feruloylmethane (Fig. 5).[48] Variation in incubation of pH and/or temperature results in a difference in relative abundance of degradation products. Additionally, incubation of Curcumin in cell culture medium (specifically RPMI 1640, Roswell Park Memorial Institute medium) and human blood

also lead to an observation of these degradation products.[48] According to recent spectroscopic investigation it was determined that solvolysis is rather insignificant; the primary chemical breakdown product resulting due to autoxidation is a bicyclopentadione (Fig. 5).[51] Incorporation of O_2 by a spontaneous, free-radical-driven process results in oxygenation and double cyclization of the heptadienedione chain that connects two methoxyphenol rings.[52] Additional degradation products that are anticipated during bicyclopentadione synthesis were identified via further investigation of the kinetics of disintegration of radiolabeled Curcumin.[53] Oxidative degradation described above does not require photochemical initiation. However, photochemical degradation has also been observed both in crystalline and soluble forms of Curcumin. This suggests that the light induced degradation pathway is probably not oxidative in character and that it might perhaps contribute to documented antioxidant capabilities attributed to Curcumin. The aforementioned degradation routes indicate it is important to take into account dynamic redox cycling (as mentioned earlier) while analyzing results of bioassays using Curcumin. Exposure to sunlight leads to degradation of crystalline Curcumin, resulting principally in the formation of vanillin, ferulic acid, ferulic aldehyde and vanillic acid (Fig. 5).[54] Breakdown of Curcumin in organic solvents is consistent when exposed to light. A number of products that depend on solvent for their formation are generated. An internal cyclization product is generated in methanol, isopropanol and in chloroform. Isopropanol has the potential to function as a reactive substrate resulting in the synthesis of a guaiacol derivative.[55] The process of photochemical degradation mostly arises from type I and type II reactions involving molecular oxygen and this is extensively discussed in the literature.[56]

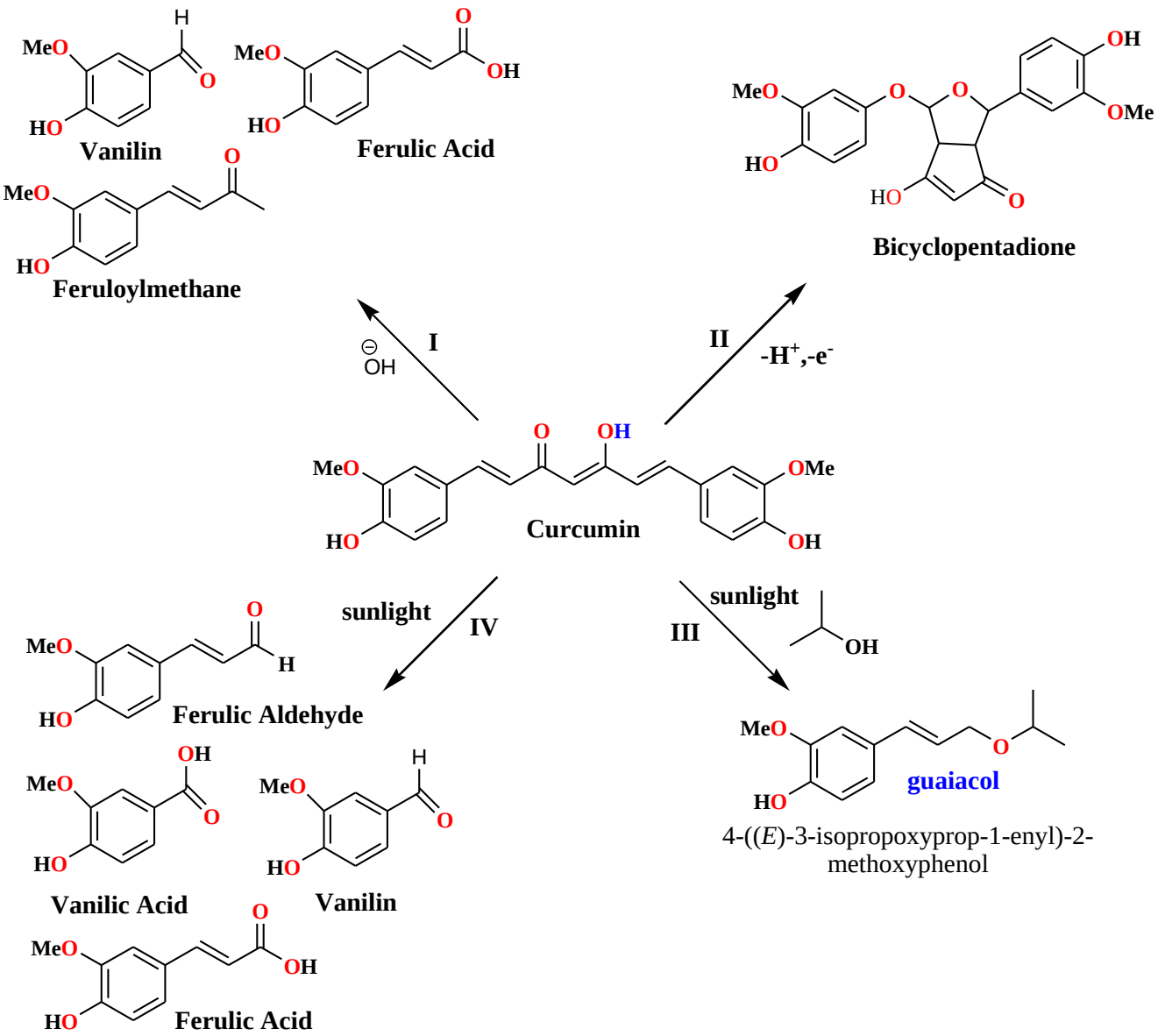


Figure 5: Major chemical breakdown mechanisms of Curcumin: (I) Solvolysis at an alkaline pH in a buffered aqueous solution quickly results in the formation of multiple fragmented byproducts, (II) Autooxidation in buffered environment produces a significant degradation product, a bicyclopentadione, under aqueous conditions, (III) when Curcumin is dissolved in specific organic solvents such as isopropanol, photodegradation can involve a reaction with the solvent as substrate, (IV) Photodegradation of Curcumin can occur when in crystalline form and dissolved in organic solvent.

Addition of surfactants, albumins, cell culture media and biological fluids prevent the breakdown of Curcumin dramatically.[35] Degradation is not affected by presence or alteration of substitution on the aromatic ring suggesting that it mostly occurs via keto-enol linkage. Encapsulation with

lipids or nanoparticles has been shown to enhance the chemical stability of Curcumin.[57,58] Additional efforts to enhance stability involved artificial modifications aimed at eliminating or safeguarding oxidation sites[59] (namely, phenolic and enolic hydroxyl groups) and altering the β-diketone structure to diminish reactivity of an enolate Michael acceptor.[60,61] Fast deterioration of Curcumin necessitates further exploration both *in vitro* and *in vivo* environments. It is therefore imperative to consistently show the stability of Curcumin under the given assay conditions.

Several scholarly articles have employed computational methodologies to either forecast the efficacy of Curcumin or to elucidate its observed bio-activity through experiments.[62,63] Owing to a probable absence of Curcumin in its original state or at the very least its bioactivity being influenced by the existence of various reactive and/or bioactive degradation products these models have limited relevance to intended targets. Despite inclusion of binding features of degradation products in computational studies several aspects still make these models distant from a real life situation in relation to bio-activity of Curcumin.[64] In a recent publication, Shen and Ji posed an inquiry on the potential role of degradation products like ferulic acid and vanillin in contributing to the overall activity of Curcumin, more specifically in terms of enhanced bio-availability and antioxidant properties[65]. Similar to Curcumin, both ferulic acid and vanillin have promising therapeutic potential in treatment of disorders like Alzheimer's disease (AD) and cancer. Additionally, both compounds display comparable binding affinities to various proteins and enzymes. However, a majority of these experiments were conducted placing a major emphasis on Curcumin when actually it is not present as a single unit, also utilizing far greater dose than those that may be anticipated under situations of limited bio-availability.[65, 66] Hence, further investigations are needed to ascertain the precise impact of degradation and metabolic products on *in vivo* bioactivity of Curcumin.[65, 66]

A fundamental prerequisite for majority of medicines is their capacity to maintain stability when exposed to physiological conditions which serve as a representative model for *in vivo* environments. Additionally, it is crucial for medications to exhibit stability while stored or incorporated into other formulations. In this context, physiological circumstances are defined as aquatic environments, ideally having pH ~ 7.4 and temperature 37°C. Curcumin does not possess any of these features and exhibits significant chemical instability.[64-66]

2.3 Interaction of Curcumin with biomolecules

The pleiotropic effect of Curcumin is a result of its ability to interact with several target molecules within cells that might include protein, DNA, lipids, metals and metallo-proteins that are considered common molecular targets.[66-69] These biomolecules can have covalent or non-covalent interactions with Curcumin. Its biological activity is altered irreversibly through covalent interactions; weaker interactions being reversible.[70] Hydrophobic contacts, π-π interactions and hydrogen bonding are non-covalent interactions. Depending on the type of biomolecule, all three functional groups of Curcumin that is the phenolic moiety, keto-enol tautomer group and the seven-carbon linker group are implicated in such interaction. The phenolic moiety and keto-enol group can take part in hydrogen bonding interactions while aromatic functionality causes π-π interactions. Owing to adaptability afforded by its seven-carbon linker, Curcumin can readily adopt a shape that maximizes its hydrophobic interactions. The keto-enol group serves as a Michael acceptor or electron donor in reactions that involve protein thiols and metals that result in covalent bonds.[70]

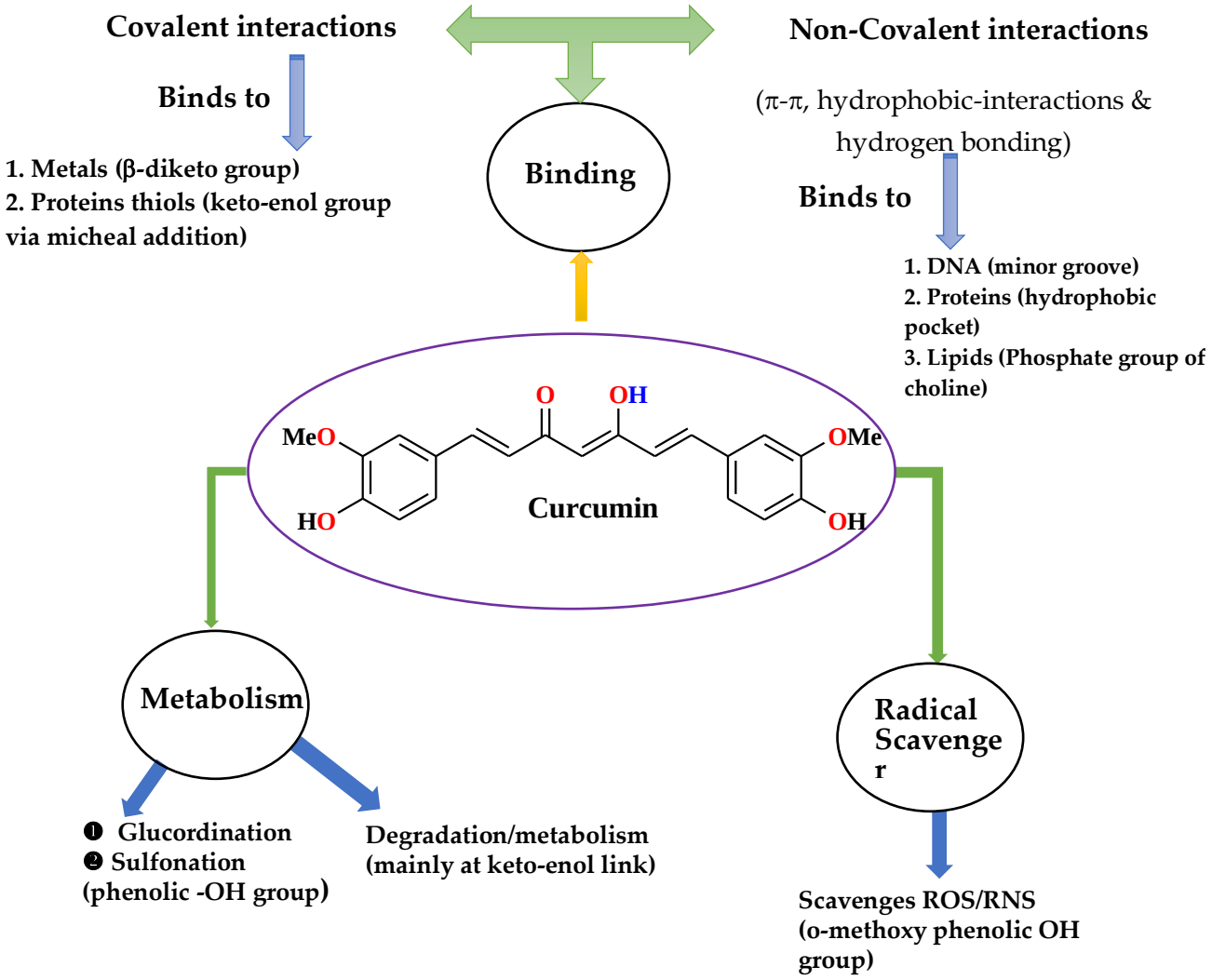


Figure 6: Structural features involved in the biological activity of Curcumin

2.3.1 Interaction with proteins:

Curcumin interacts with numerous proteins involved in cellular signaling processes that are essential for progression and regulation of diseases. Curcumin can either up-regulate or down-regulate a specific protein depending on the nature of interaction. Curcumin interacts with proteins like different transcription factors, inflammatory molecules, enzymes, kinases, drug resistance proteins, adhesion molecules, growth factors, receptor proteins, cell survival & cell-cycle regulatory proteins, carrier proteins, FtsZ (Filamenting temperature-sensitive mutant Z) protofilaments, prion proteins, tubulins and amyloid-beta (Aβ) aggregates.[70] Recent experimental

and computational studies indicate Curcumin binds to several proteins through non-covalent interactions.[50,71] These interactions result in a small but favorable free energy of association.[50,71]

2.3.1.1 By non-covalent interaction:

Albumins are a type of transport proteins that were studied by various research groups in terms of interactions with Curcumin. It was found to bind to both human serum albumin (HSA) and bovine serum albumin (BSA).[72-78] Addition of albumin to an aqueous solution not only enhances its solubility but also improves its stability and bio-availability. Using absorption, fluorescence and circular dichroism (CD) techniques researchers confirmed that Curcumin binds to human serum albumin (HSA) at two different sites. The site with highest affinity for Curcumin is located in domain IIA, approximately 2.74 nm away from a tryptophan residue TRP214; the binding being primarily driven by hydrophobic interactions. Curcumin binds to BSA through hydrophobic interactions specifically in the vicinity of Trp212 and Trp314 in domains I and II. Binding of Curcumin was found to induce partial unfolding of albumin proteins.[75,78] Other Curcumin analogues like isooxazolcurcumin (modified at the diketo moiety) and diacetylcurcumin (modified at the phenolic moiety), were found to bind albumins in a similar manner i.e. through hydrophobic interactions.[77] Based on these results, it can be inferred that binding of Curcumin to albumins is not attributed to any single functional group. Instead, the entire molecule interacts within hydrophobic regions of albumins.

Another protein that has been extensively studied for its interactions with Curcumin is amyloid beta (Aβ). It plays a significant role in the development of Alzheimer's disease. Epidemiological studies show that the Indian population who regularly consume turmeric are less likely to develop Alzheimer's disease. Researchers were prompted by this intriguing observation to investigate the potential therapeutic role of Curcumin in Alzheimer's disease, a progressive

neuro-degenerative disease characterized by the formation of Aβ plaques in the brain; formed due to aggregation of Aβ fibrils.[80-84] In a study, mice with advanced amyloid accumulation were fed with Curcumin that was identified to cross the blood-brain barrier and bind to amyloid plaques.[82] Although the mechanism is not fully understood yet, existing reports suggest Curcumin inhibits aggregation of Aβ and promotes disaggregation of fibrils through binding. Reineke and Gestwicki[83] conducted a structure-activity study using a library of synthesized Curcuminoids. They proposed that in order to effectively bind with amyloid all ligands need to possess at least two phenyl groups. Additionally, they found that polar functional groups like aromatic hydroxyl groups are crucial for such binding. They mentioned in their study that the most effective inhibitors are compounds where two phenyl rings are connected by rigid linkers ranging in size from 8 to 16 Å. In another study, Masuda et al.[84] examined intermolecular dipole-dipole interactions between Curcumin and Aβ fibrils and found that binding is not specific to a particular site but rather Curcumin recognises the repetitive structures that make up the intermolecular β-sheet. Binding activity of Curcumin was confirmed as being decreased when phenolic hydroxyl groups were methylated, indicating the importance of polar aromatic hydroxyl groups.[84] Further research aimed at understanding specific binding mechanism and types of interactions involved would greatly contribute to a practical application of Curcumin that could then be used for prevention or treatment of Alzheimer's disease. Some of the interactions mentioned could be realized by solid-state NMR.[84]

2.3.1.2 By covalent interactions:

α, β-unsaturated carbonyl compounds have a propensity to engage in conjugation with glutathione (GSH) and therefore it is likely that Curcumin being a member of this class may undergo reaction with GSH.[85,86] Presence of GSH results in an augmentation of Curcumin depletion in a solution and it was seen that presence of GST (Glutathione S transferase) accelerates the process. Curcumin was observed to deplete glutathione (GSH) to a greater extent in comparison to other α, β-unsaturated carbonyl compounds.[85] The veracity of this claim was substantiated through rigorous scientific methodologies like absorption spectrophotometry, high-performance liquid chromatography (HPLC) and mass spectrometry. These investigations have unequivocally demonstrated that Curcumin exhibits an ability to form conjugates with glutathione, known as Curcumin-glutathione conjugates as well as adducts with feruloylmethylketone and aldehyde that are further modified by glutathione (GSH).[85] Curcumin, in addition, exerts inhibitory effects on GST activity by forming Michael adducts with cysteine through covalent attachment to the diene moiety.[86] These interactions may potentially elucidate the rapid degradation of Curcumin in bio-fluids and its subsequent low plasma concentration.[42] Curcumin was found to covalently bind and inhibit the isoenzyme thioredoxin reductase (TrxR) that plays a crucial role in combating oxidative stress.[87] The observed inhibition was documented at micromolar concentrations of Curcumin in presence of NADPH. Utilization of mass spectrometry revealed Curcumin exhibits a propensity for engaging in covalent interactions with selenocysteine/cysteine residues within the active site through Michael addition. The aforementioned binding elicited permanent modifications, leading to the generation of reactive oxygen species in cellular systems.[87] Curcumin has been hypothesized to form covalent bonds with various proteins involved in inflammation and cancer like tumour necrosis factor alpha (TNF-α). However, it is important to note that these proposed associations lack sufficient experimental validation as yet.[70,88]

2.3.2 Interaction with nucleic acids:

Numerous *in vitro* and *in vivo* experiments have unequivocally demonstrated Curcumin manifests intricate interactions with cellular DNA. The confirmation of co-localization of Curcumin with nuclear selective fluorescent probes in both normal and tumour cells via fluorescence imaging provides compelling evidence of a direct interaction between Curcumin and nucleic acids. It is widely postulated that these interactions are of utmost importance in anti-neoplastic efficacy of Curcumin.[79,89] A series of investigations were undertaken to elucidate the intricate interplay between Curcumin and its derivatives with nucleic acids. These were conducted using model systems that involved utilization of calf thymus DNA and yeast RNA. It is worth noting that these investigations were performed under carefully controlled conditions that closely mimic the physiological environment.[90-94] Based on comprehensive investigation utilizing fluorescence, circular dichroism (CD) and molecular docking methodologies, it was possible to ascertain Curcumin does not undergo intercalation with DNA. Instead, it exhibits limited affinity for DNA grooves as evidenced by minimal groove binding properties.[90] Groove-binding properties of Curcumin analogues, specifically isooxazole Curcumin, diacetyl Curcumin and dimethoxy Curcumin were demonstrated to exhibit similarity with Curcumin.[91-93] This elucidates that interaction between Curcumin and grooves of DNA remain unaffected by any discernible structural element, instead it is primarily governed by hydrophobic interactions or hydrogen bonding. Based on scholarly investigations, it has been duly noted that Curcumin possesses an ability to establish hydrogen bonds with yeast RNA through interaction with oxygen and nitrogen atoms present in select nucleic acids, specifically uracil, guanine, and adenine.[94]

2.3.3 Interaction with membranes:

Over the past two decades, researchers also studied interaction of Curcumin with several different membrane models. Some of these studies led to the understanding that insolubility of Curcumin in water could be addressed by solubilization in lipid solutions. Investigations revealed such solubilization very efficiently limits the breakdown of Curcumin.[50,95-100] Curcumin demonstrates substantial deterioration within a short time frame when dissolved in aqueous methanol. About 95% of Curcumin is stable for more than two days when it is integrated into liposomal solutions like DMPC (1,2-dimyristoyl-sn-glycero-3-phosphocholine) and DPPC (1,2-dipalmotoyl-sn-glycero-3-phosphocholine). Owing to its antioxidant properties, Curcumin is able to prevent damage caused by reactive oxygen species (ROS) to lipids. Therefore, Curcumin is considered a lipid-soluble antioxidant that like vitamin E effectively scavenges lipid peroxyl radicals and interrupts chain reactions.[101,102] *In vivo* studies have confirmed that liposomal Curcumin is effective against tumors, with results that are consistent with those seen with free Curcumin.[97] Curcumin is now, also being studied for its potential use in liposomal and polymeric nanoparticle encapsulated formulations. Through a number of studies, these demonstrate that there is increased Curcumin bioavailability.[79, 98] Recent research by Barry et al.[99] examines Curcumin's binding to membranes. In this study, NMR spectroscopy and differential scanning calorimetry were employed to investigate how Curcumin alters structures of liposomal membranes. Curcumin, like cholesterol was shown to form hydrogen bonds at the choline phosphate group which allowed it to cross the membrane at low quantities. Polar O-H groups can also contribute to coupling. Curcumin has a strong effect on the structure of lipid membranes and produces trans-bilayer interactions with lipids. Curcumin's molecular length is roughly equal to that of a single leaflet of the lipid bilayer, allowing its high conjugation, planarity and rigid structure to align with the lipid

bilayer and facilitate binding processes. Previous research has shown membrane alterations generated by Curcumin affect intracellular exocytotic and membrane fusion processes.[99,100]

2.4 Medicinal Properties of Curcumin

In addition to its use in the food industry, as a flavoring and coloring ingredient, turmeric has also found widespread application in Ayurvedic medicine due to its anti-oxidant, antiseptic, analgesic, antimalarial, antibacterial and anti-inflammatory characteristics.[103] Since ancient times, people have used Curcumin as dietary supplement as it is considered safe from a pharmacological standpoint.[104]

2.4.1 Antioxidant property:

The Curcuminoids have antioxidant action due to their inherent chemical structure.[103-105] The Curcuminoids are composed of two methoxylated phenols linked by two α, β unsaturated carbonyl groups which exist in a stable enol configuration.[106] Research has demonstrated inhibitory effects of Curcumin on lipid peroxidation, specifically in relation to linoleate, a polyunsaturated fatty acid possessing an ability to undergo oxidation and generate a fatty acid radical. Previous studies provide evidence to support the notion Curcumin functions as a chain-breaking antioxidant at the 3' position. This leads to an intramolecular Diels-Alder reaction and subsequent neutralization of lipid radicals.[107] Furthermore, Curcumin exhibits free radical-scavenging activity in addition to its ability to reduce lipid peroxidation. Previous studies also demonstrate an ability of the compound to effectively scavenge several reactive oxygen species (ROS) generated by macrophages like superoxide anions, hydrogen peroxide and nitrite radicals. This efficacy was observed both in controlled laboratory settings (*in vitro*) and in living organisms (*in vivo*) with rat peritoneal macrophages serving as experimental models.[108,109] Enzyme inducible nitric oxide synthase (iNOS) is present in macrophages and is responsible for producing significant quantities

of nitric oxide (NO) to facilitate "oxidative burst" required for immune protection against pathogens. The induction of inducible nitric oxide synthase (iNOS) occurs in response to oxidative milieu, leading to generation of nitric oxide (NO). The formed NO can subsequently undergo a reaction with superoxide radicals resulting in the formation of peroxynitrite a highly cytotoxic species that poses a significant threat to cellular integrity. Previous studies have demonstrated Curcumin has the ability to decrease the activity of inducible nitric oxide synthase (iNOS) in macrophages, resulting in reduction in ROS production in response to oxidative stress.[110, 111] Subsequent investigations conducted on microglial cells, which serve as analogs to brain macrophages, have revealed a decrease in NO production and a consequent safeguarding of neural cells against oxidative stress subsequent to an administration of Curcumin. Consequently, this spice exhibits potential utility in mitigating neuroinflammatory processes linked to degenerative disorders including Alzheimer's disease.[112-114]

2.4.2 Anti-inflammatory activity:

The inducible transcription factor i.e. Nuclear Factor-Kappa B (NF-κB) that controls the expression of many inflammatory, proliferative and survival genes can be inhibited by Curcumin, as demonstrated in a number of studies.[115-119] NF-κB is responsible for the regulation of several genes including cyclooxygenase-2 (COX-2), IκBα, TNF-α, cyclin D1, intercellular adhesion molecule-1 (ICAM-1), Cellular-myc (C-myc), B-cells leukemia/lymphoma-2 protein (Bcl-2), matrix metallopeptidase-9 (MMP-9), inducible nitric oxide synthase (iNOS) and interleukins like inteleukin-6 (IL-6) and interleukin-8 (IL-8).[118-122]

NF-κB expression is connected to the fact how cells react to harmful substances like cytokines, UV exposure, free radicals, low oxygen levels (like those found in cigarette smoke) and infectious antigens.[123-127] Many malignancies get enhanced by NF-κB activation linked to anti-

apoptotic gene expression, angiogenesis, tumor growth and metastasis.[128] Research were conducted to show that head and neck squamous cell carcinoma exhibit constitutive expression of the transcription factor NF-κB. The heterodimeric protein NF-κB contains five subunits: RelA (p65), RelB, c-Rel, NF-κB1 (p50 and p105), and NF-κB2 (p52).[129] NF-κB is present in an inert state within the cytoplasm by IκB (inhibitor of NF-κB), an entity consisting of subunits α and β. Several steps are necessary to release NF-κB from this inhibitory binding after receiving appropriate chemical signals that trigger NF-κB activation. IκK (inhibitor kappa B kinase) must phosphorylate IκB at α subunit, which ubiquitinates and degrades IκBα releasing NF-κB from the cytoplasm. The unbound NF-κB can then enter the nucleus to bind DNA and trigger transcription.

Curcumin's anti-inflammatory benefits come from its inhibition of the NF-κB pathway. It prevents IκK-mediated phosphorylation and degradation of IκBα, preventing NF-κB from entering the nucleus and inducing transcription.[117,118,130] Research has shown that suppressing NF-κB activity reduces COX-2, iNOS and inflammatory markers.[116,119,131] Curcumin inhibits production of inflammatory cytokines by activated monocytes and macrophages including COX-2, lipoxygenase (LOX), iNOS, monocyte chemotactic protein-1(MCP-1), monocyte inflammatory protein-1 (MIP-1α) and interleukins like IL-1, -2, -6, -8 and -12.[132-133] It suppresses inflammatory pathways in addition to NF-κB activation. The arachadonic acid pathway for eicosanoid biosynthesis produces leukotrienes, prostaglandins, prostacyclins and thromboxanes that are involved in inflammatory response. Curcumin reduces arachadonic acid metabolism by downregulating LOX and COX-2 transcription and post-translational enzyme inhibition. It directly suppresses prostaglandin E2 biosynthesis[133-136], reduces oxidative stress and inflammatory cascade by scavenging free radicals. This was studied for its anti-inflammatory effects in Alzheimer's, cardiovascular, diabetes, asthma, inflammatory bowel, arthritis, pancreatitis and renal diseases.[137-140]

2.4.3 Anticancer Activity:

Curcumin has a number of attributes that points to the possibility that it could be used to treat cancer. These include both chemo-preventive and direct therapeutic applications. It was shown to be active in a variety of *in vitro* models with dose employed in these models being comparable to that used in case of human being.[141] However, results have so far been achieved on animal models. Studies conducted both *in vitro* and *in vivo* have shown Curcumin inhibits development of cancer by having an effect on two fundamental mechanisms of carcinogenesis namely angiogenesis and tumor growth.[141]

Curcuminoids and turmeric have an effect on tumor angiogenesis in a number of ways,[142] that are interdependent on each other. Some are

i) An intervention that involves modulating the activity of transcription factors like NF-κB and Activator Protein-1 (AP-1), known to be involved in inflammatory processes. Additionally early growth response protein 1 (EGR1) is targeted to reduce the expression of interleukin-8 (IL-8) in specific cancer cell lines found in pancreas or head & neck. This approach aims to prevent induction of VEGF (Vascular Endothelial Growth Factor) synthesis.[142]

ii) Another intervention focuses on impeding angiogenesis, which is the formation of new blood vessels by targeting the actions of nitric oxide (NO) and inducible nitric oxide synthase (iNOS).

iii) Furthermore, intervention includes inhibiting activity of COX-2 and 5-LOX, which are enzymes associated with the production of inflammatory molecules.[142]

iv) In the realm of angiogenic factors, it is noteworthy to mention the pivotal role played by VEGF. This factor serves as the primary catalyst for various crucial processes like migration, sprouting, survival and proliferation during the intricate process of angiogenesis.[142]

Curcumin was shown to cause cell death in several cell lines derived both from animals and human, including leukemia, melanoma and carcinoma of the breast, lung, colon, kidney, ovary and liver.[143]

It appears that it performs its role by caspase-dependent and independent (mitochondrial) pathways respectively related to the absence and presence of p53. Curcumin has biphasic activity that acts on the proteasome with an activation at lower dose and inhibition at higher levels.[143] It is therefore likely that Curcumin will result in either cell death or cell survival depending on the amount utilized. This is because inhibiting proteasome leads to apoptosis while stimulating it leads to cell survival. Hence, Curcumin in varying amounts may affect cell death. When present in low dose, it causes oxidative stress and apoptosis; in high dose it leads to reduction in the formation of reactive oxygen species and a decrease in ATP.[144]

Additionally, Curcumin demonstrates the capacity to induce cellular demise in diverse cell lineages that exhibit resistance towards apoptosis. This phenomenon is attributed to activation of alternate cellular demise pathways that are distinct from apoptosis like mitotic catastrophe, a process characterized by anomalous mitosis, resulting in the formation of multinucleated and massive cells. The mitotic catastrophe induced by Curcumin is intricately associated with downregulation of gene expression pertaining to diverse apoptotic inhibitor proteins.[145]

Another study indicated that injection of Curcumin was able to considerably lower the levels of cell cycle regulators CDK4-cylin D1 as well as inhibit expression of p53, an upstream regulator of CDK4-cylin D1 complex.[146] Recently, Vallianou et al.[147] highlighted the ability of Curcumin to promote apoptosis in tumor cells by producing severe endoplasmic reticulum stress that plays an essential role in apoptosis. According to results of that study, Curcumin may work by inhibiting activation of EGR1 but was unable to stop the progress of cancer nor could it stop it from invading other tissues.[147]

Curcumin has strong anti-oxidant and free-radical quenching properties that are crucial in inhibiting initial stages of carcinogenesis. Studies demonstrate it can effectively suppress DNA mutagenesis caused by UV irradiation and activation of cellular SOS functions.[148] Curcumin not

only inhibits production of nitric oxide (NO) and scavenges DNA-damaging superoxide radicals but also impacts both Phase I and Phase II enzymes of hepatic cytochrome p450.[149, 150] These enzymes are responsible for the oxidation and detoxification of harmful substances and are typically induced in response to toxin exposure being responsible for producing carcinogenic metabolites that form DNA adducts during the oxidation processes of these substances.[149] On the other hand, Curcumin was found to stimulate the activity of Phase II enzymes glutathione like S-transferase, glutathione peroxidase and glutathione reductase responsible for detoxifying harmful metabolites.[150]

2.4.4 Antibacterial Activity:

Bacterial infections have a prominent position among infectious ailments. Hence, comprehensive investigations spanning over half a century were undertaken to attain novel antimicrobial pharmaceuticals derived from diverse origins. In the light of advancement made in the realm of antibacterial agents, it remains imperative to address pressing requirement for novel antimicrobial agents as a consequence of the emergence and proliferation of multidrug-resistant bacterial strains.[151]

Antibacterial properties of Curcumin were first reported by Schraufstatter and colleagues in 1949.[151] Over the past seventy years multiple successful studies have been conducted to examine the wide-ranging inhibitory effect of Curcumin against various gram-negative and gram-positive bacteria.[152-156] Investigations on the aqueous extract of Curcuma longa rhizome revealed noteworthy findings regarding its antibacterial properties. Specifically, studies determined minimum inhibitory concentration (MIC). These were made on bacterial strains *S. epidermis* ATCC 12228, *Staph. aureus* ATCC 25923, *Klebsiella pneumoniae* ATCC 10031 and *E. coli* ATCC 25922.[157] A methanolic extract derived from turmeric exhibited minimum inhibitory

concentration (MIC) values of 16 μg/mL and 128 μg/mL against *Bacillus subtilis* and *Staphylococcus aureus* respectively.[158] Investigations pertaining to hexane and ethanol extracts of turmeric and Curcuminoids derived from an ethyl acetate extract isolated from *Curcuma longa*, possessing 86.5% Curcumin was used to assess efficacy against 24 pathogenic bacteria (obtained from chicken and shrimp). These were *Vibrio harveyi, V. alginolyticus, V. vulnificus, V. parahaemolyticus, V. cholerae, Bacillus subtilis, B.cereus, Aeromonas hydrophila, Streptococcus agalactiae, Staph.aureus, Staph.intermedius, Staph.epidermidis* and *Edward siella tarda.*[159] Findings reveal ethanol extract exhibit the most potent antimicrobial activity as evidenced by its minimal inhibitory concentrations (MIC) ranging from 3.91 to 125 ppt.[159,160]

The efficacy of turmeric oil, a byproduct during manufacture of Curcumin has been observed on various bacterial strains including *B. subtilis*, *B. coagulans*, *B. cereus*, *Staph. aureus*, *E. coli*, and *P. aeruginosa*.[161] Curcumin, in addition, demonstrated inhibitory efficacy against methicillin-resistant *Staphylococcus aureus* (MRSA) strains as evidenced by minimum inhibitory concentration (MIC) found in the range 125-250 μg/mL[162]. The examination conducted *in vitro* on three novel Curcumin compounds specifically indium Curcumin, indium diacetyl Curcumin and diacetyl Curcumin exhibited their efficacy against *Staphylococcus aureus*, *Staphylococcus epidermis*, *Escherichia coli*, and *Pseudomonas aeruginosa*. Findings indicate indium Curcumin displays superior antibacterial properties in comparison to Curcumin alone suggesting its potential as a promising candidate for subsequent *in vivo* investigations. Nevertheless, it is worth noting that diacetyl Curcumin failed to demonstrate any discernible antibacterial properties with various strains of bacteria.[163] The findings have exhibited auspicious antimicrobial efficacy with different Curcumin derivatives.

Antibacterial drugs may target the stability and assembly of FtsZ protofilaments as a critical element for bacterial cytokinesis.[164] The cytokinesis of *B. subtilis* was effectively suppressed by

Curcumin due to its ability to induce filamentation. Furthermore, it was observed that intervention not only had a negligible impact on the segregation and arrangement of nucleoids but it effectively inhibited formation of the cytokinetic Z-ring in *B. subtilis*.[164] Experimental findings have elucidated that Curcumin exerts a diminishing effect on the aggregation of FtsZ protofilaments, that are closely linked to its capacity to bind to FtsZ with a dissociation constant of 7.3 μM. Findings further indicate Curcumin may have the ability to impede the assembly dynamics of FtsZ in Z-ring, potentially leading to suppression of bacterial cell proliferation. This represents one of the plausible mechanisms through which Curcumin exerts antibacterial effects as has been suggested by previous research.[164] The empirical investigation pertaining to *E. coli* and *B. subtilis* has elucidated that Curcumin through its inhibitory impact on FtsZ polymerization possesses the ability to repress the assembly of FtsZ thereby inducing disruption in the process of prokaryotic cell division.[165] Furthermore, it is noteworthy to mention Curcumin has demonstrated a considerable degree of antibacterial efficacy as evidenced by its minimum inhibitory concentration (MIC) ranging from 5 to 50 μg/mL against a total of 65 clinical isolates of *Helicobacter pylori*.[166]

2.5 Understanding of Antibacterial activity of Curcumin through various mechanism

2.5.1 Disruption of Cell Membrane:

Curcumin and its two analogs DMC and BDMC has demonstrated notable antibacterial efficacy against a diverse spectrum of bacterial strains.[155] Findings indicate it possesses the ability to impair the permeability and structural integrity of bacterial cell membranes in both Gram-positive and Gram-negative bacteria, ultimately resulting in demise of bacterial cells.[167] The lipophilic nature of Curcumin facilitates its direct integration into liposome bilayers thereby augmenting permeability of the said bilayers.[167] Utilization of solid-state nuclear magnetic

resonance (NMR) spectroscopy has provided valuable insights into the behaviour of Curcumin. Studies have demonstrated that Curcumin has the ability to penetrate deeply into lipid bilayers of membranes, assuming a trans-bilayer orientation. This insertion of Curcumin into the membrane was found to disrupt an orderly arrangement of 1,2-dipalmitoyl-*sn*-glycero-3-phosphocholine (DPPC) membranes. Furthermore, perturbation of membrane structure was observed to have an impact on exocytotic and membrane fusion processes.[168] The findings shed light on intricate interactions between Curcumin and cellular membranes contributing to our understanding of its biological effects. The study conducted by Tyagi et al. provide evidence supporting the notion that Curcumin when present at a concentration of 100 μM has the ability to induce permeabilization of cell walls of both *Staphylococcus aureus* and *Escherichia coli*.[169] The property of membrane permeabilization exhibited by Curcumin may potentially explain its ability to directly eradicate both Gram-positive and Gram-negative bacteria.[169] Undoubtedly, augmentation in bacterial membrane permeabilization instigated by Curcumin has the potential to enhance absorption of various pharmaceutical compounds.[171] Furthermore, explanation of the complex process acts as a method to explain substantial synergistic impact of Curcumin treatment with alternative antibiotic drugs or naturally occurring compounds.

2.5.2 The suppression of bacterial quorum sensing system and prevention of biofilm formation:

Quorum Sensing (QS) system represents a sophisticated mechanism of intercellular communication employed by microbial communities to effectively gauge their population density and dynamically respond to changes in their external surroundings.[171] Currently, there exist three primary quorum sensing (QS) systems. These are acylhomoserine lactone (AHL) QS system, predominantly found in Gram-negative bacteria; the autoinducing peptide (AIP) QS system prevalent in Gram-positive bacteria and autoinducer-2 (AI-2) QS system that manifests in both

Gram-negative and Gram-positive bacteria. The pivotal role of QS systems in the genesis and progression of bacterial biofilms, renowned for their involvement in approximately 80% of microbial infections is widely acknowledged.[172] Proliferation of bacteria within biofilms confers a substantial degree of resistance against both antibiotics and immune cells of the host, thereby resulting in an ineffectiveness of antimicrobial treatment.[172] Quorum sensing (QS) systems serve as principal regulators governing comprehensive progression of biofilm formation and encompassing pivotal stages like bacterial adhesion, biofilm development and maturation. Hence, identification of novel inhibitory compounds that specifically target bacterial quorum sensing (QS) systems represents a significant approach in the endeavor to regulate bacterial biofilm formation and combat resistance. Numerous scientific investigations have documented inhibitory effects of Curcumin on bacterial quorum sensing systems and formation of biofilms. Additionally, Curcumin was found to impede attachment of bacteria to host receptors in a diverse range of species like *Staphylococcus aureus*, *Enterococcus faecalis*, *Escherichia coli*, *Streptococcus mutans*, *Listeria monocytogenes*, *Helicobacter pylori*, *Pseudomonas aeruginosa*, *Serratia marcescens*, *Aeromonas hydrophila* and *Acinetobacter baumannii*. Such findings were reported in several studies.[170-174] Furthermore, Fig. 7 represents a comprehensive depiction of inhibitory mechanisms exerted by Curcumin in relation to biofilm formation, suppression of bacterial swimming and clustering behaviour as well as inhibition of virulence.[170-175] It is worth noting that Curcumin possesses the ability to stimulate the synthesis of lactate dehydrogenase (LDH) in several bacterial strains like *Pseudomonas aeruginosa*, *Staphylococcus aureus* and *Enterococcus f*aecalis. Remarkably, the resulting Curcumin/LDH complex has exhibited notable antimicrobial properties, effectively combating bacterial growth and inhibiting formation of biofilms.[175] Undoubtedly, inherent anti-

biofilm characteristics exhibited by Curcumin serve to enhance its prospects as a viable and effective anti-infective agent.

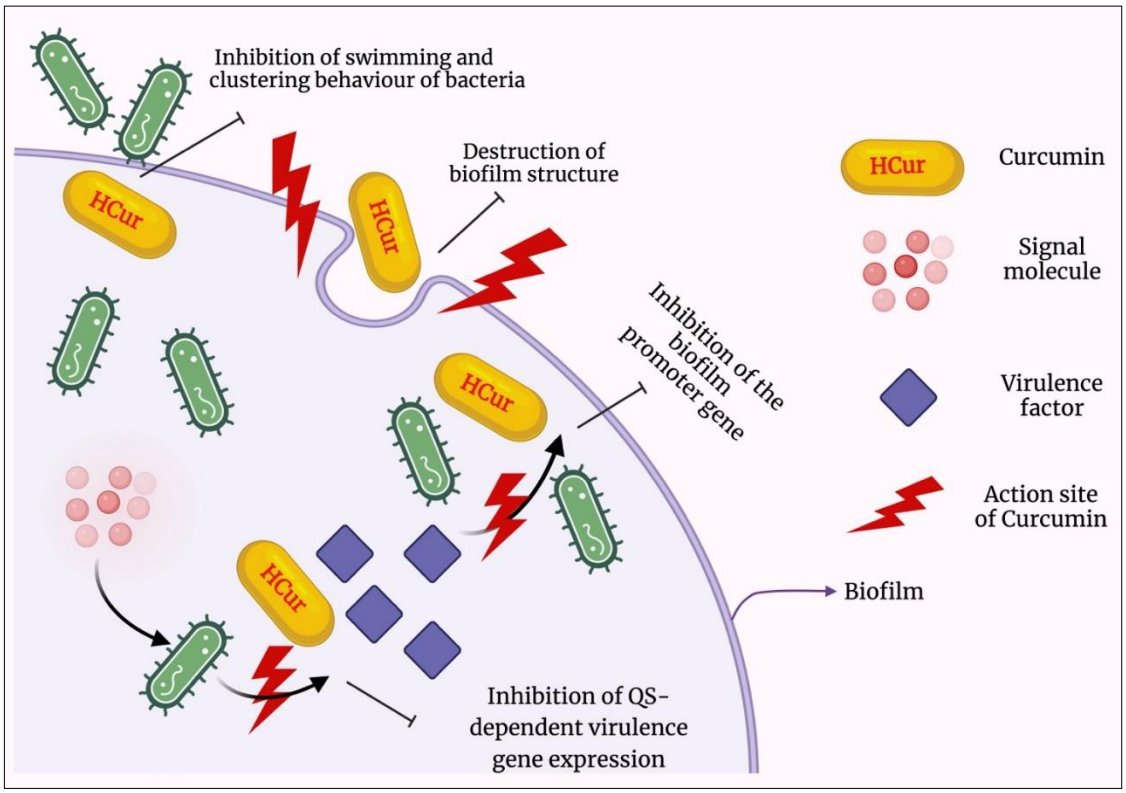


Figure 7: Inhibitory mechanism of Curcumin

2.5.3 Inhibition of Cell Division:

The inhibition of bacterial cell division is a significant mechanism by which Curcumin exhibits antibacterial activity.[155,164] The essential role of filamentous temperature-sensitive mutant Z (FtsZ) in bacterial cell division has been demonstrated in many studies.[164,165,176] The protein structure includes a polymerization domain at N-terminal which is connected to a conserved C-terminal peptide (CCTP) of approximately eight amino acids. This connection is made through a linker region that lacks a defined structure and can vary in length (around 50 amino acids in *E. coli*).

FtsZ forms polymers by associating with guanosine triphosphate (GTP).[164] The process is closely linked to the conversion between closed and open conformations of FtsZ and plays a crucial role in the formation of Z ring of FtsZ. The attachment of polymerized FtsZ filaments to the cytoplasmic membrane is facilitated by membrane anchors *ZipA* and *FtsA*. This attachment is mediated by conserved C-terminal peptide (CCTP) of FtsZ as shown in Figure 8. Rai et al. demonstrated Curcumin can inhibit the formation of cytokinetic Z ring by directly interacting with FtsZ in both *B. subtilis* and *E. coli*.[164] Furthermore, Curcumin was found to enhance guanosine triphosphate (GTPase) activity of FtsZ resulting in termination of the polymerization process.[164] Moreover molecular docking analysis of Curcumin to *E. coli* FtsZ structure indicates binding takes place in the GTPase catalytic pocket.[165]

In a more recent study, Morão et al. demonstrated that a simplified molecular version of Curcumin, in which the β-diketone part was replaced with a monocarbonyl group was able to disrupt the divisional septum of *B. subtilis*. Interestingly, this disruption occurred without directly inhibiting FtsZ. These findings indicate simplified form of Curcumin primarily exerts its antibacterial effect by permeabilizing the cell membrane. This disruption of membrane potential is crucial for proper localization of FtsZ within bacterial cells.[155]

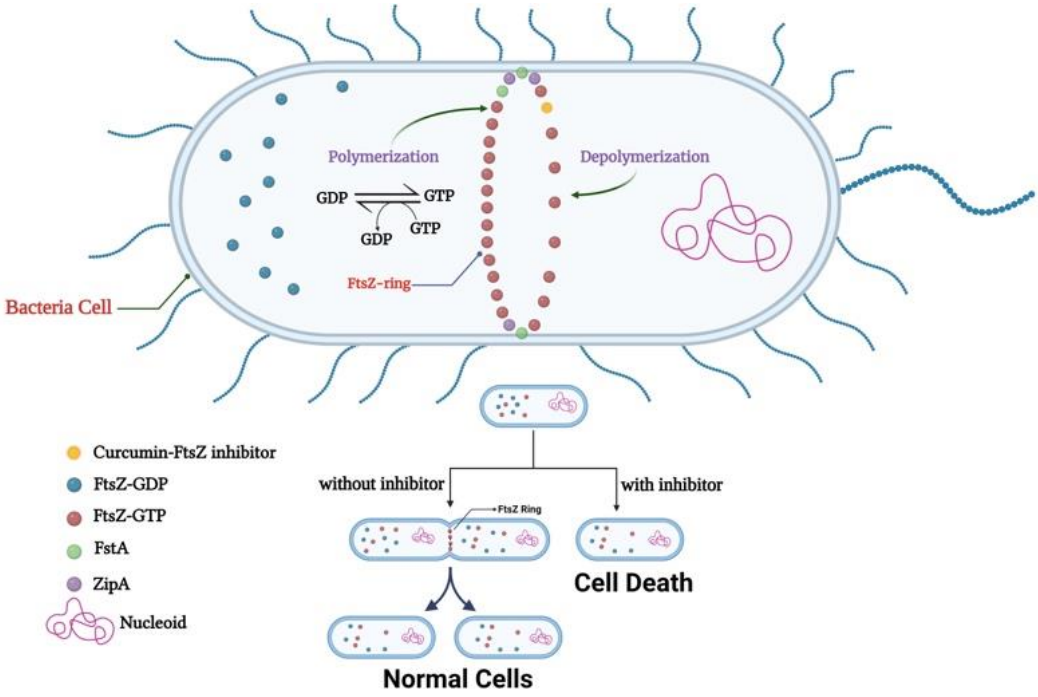


Figure 8: FtsZ inhibition activity of Curcumin by Z-ring formation

2.5.4 Induction of Oxidative Stress and Programmed Cell Death (PCD):

Throughout the history of multicellular eukaryotic creatures, programmed cell death (PCD) has been recognized as a crucial biological and pathogenic phenomenon.[177] Similarly, signaling pathways can be activated by monocellular organisms like bacteria resulting in cell death within a colony. There are a number of bacterial activities that can induce programmed cell death like stress response, developmental phase, genetic change and biofilm formation.[177] In terminally stressed *Escherichia coli*, apoptotic-like death is characterized by a number of biochemical and physiological changes including release of reactive oxygen species (ROS), condensation of chromosomes, exposure of phosphatidylserine outside of cells, DNA fragmentation, dissipation of membrane potential (DY) and loss of structural integrity.[178] ROS-induced cell death occurs due to the detrimental impact of superoxide anions ($O_2^{\bullet -}$), hydrogen peroxide (H_2O_2) and hydroxyl radicals ($OH^{\bullet}$) on several bacterial biological components including DNA, membrane lipids and proteins.[179]

Curcumin, when present at minimum inhibitory concentrations (MIC) triggers generation of reactive oxygen species (ROS) in bacterial cells. This leads to an apoptosis-like reaction in *E. coli* characterized by a build up of ROS, membrane depolarization and an increase in influx of Ca^{2+} ions.[170] Curcumin at the genetic level stimulated the increase in RecA protein expression that facilitates apoptotic-like death mechanisms in bacteria.[170] Consistent with this discovery, *E. coli* strains lacking RecA gene exhibit resistance to Curcumin confirming that Curcumin-induced cell death in *E. coli* relies on apoptotic pathways.[170] Furthermore, studies demonstrate Curcumin is able to decrease expression of genes responsible for initiating SOS (Save Our Souls) response in bacteria. This response helps cells recover from DNA damage and plays a role in the creation of biofilms and cell division.[178] LexA is a transcriptional repressor that binds to DNA and controls the activity of genes related to SOS response.[180] Recent research has shown Curcumin effectively prevents SOS reactions triggered by UV-induced DNA damage in *Salmonella typhimurium* and *E. coli*. This is achieved by reducing expression of LexA. The inhibitory effects of Curcumin on biofilm formation and cell division state that the above are likely connected with inhibitory effects on bacterial SOS responses. Curcumin has demonstrated an ability to directly interact with bacterial DNA resulting in bacteriostatic action.[170]

2.5.5 Phototoxicity:

Curcumin has the ability to absorb blue light in the wavelength range 455-460 nm. This makes it a useful photosensitizer for enhancing effectiveness of photodynamic processing.[25] This ability to induce phototoxicity in both Gram-positive and Gram-negative bacterial cells was utilized through exposure to blue light irradiation.[170,181] Gram-positive bacteria exhibit greater sensitivity and susceptibility to photosensitizers in comparison to Gram-negative bacteria.[170] This discrepancy may be attributed to a sturdier outer membrane structure of Gram-negative bacteria in contrast to more permeable cytoplasmic membrane structure of Gram-positive cells, which

facilitates easier entry of photosensitizers into cells.[182] A recent discovery revealed use of ethylene diamine tetraacetic acid (EDTA), a substance that makes cell membranes more permeable greatly enhance antibacterial properties of Curcumin activated by blue light in *S. aureus* and *S. mutans* cells.[183] Over the last decade, researchers have gained a functional comprehension of molecular mechanisms behind Curcumin-induced phototoxicity, while the exact mechanism remains largely uncertain.[25] Studies have shown antibacterial properties of Curcumin activated by blue light are a result of autoxidation that produces reactive oxygen species (ROS). The generated ROS then cause damage to lipids, proteins and DNA ultimately resulting in death of bacterial cells.[170] Jiang et al. demonstrated Curcumin triggered by blue light effectively elevated levels of intracellular reactive oxygen species (ROS) and induced membrane damage in *S. aureus*.[184] A recent study demonstrated Curcumin-induced phototoxicity directly causes DNA damage and protein degradation, eliminates biofilms and inhibits expression of virulence genes (such as inlA, hlyA, and plcA) in *Listeria* monocytogenes[185]. Chen et al. demonstrated temperature has a role to play in the phenomenon of Curcumin-induced phototoxicity.[186] Recently, it was reported Curcumin could be used as a coating on the surface of endotracheal tube which is known to be the main cause of ventilator-associated pneumonia. This coating has the ability to effectively kill *E. coli*, *S. aureus* and *P. aeruginosa* when exposed to blue light at a wavelength of 450 nm.[187] Photodynamic properties of Curcumin were found to have an unique potential in preventing ventilator-associated pneumonia in patients.

2.5.6 Perturbation of bacterial cell metabolism:

Several antibiotics like β-lactams, aminoglycosides and quinolones have been extensively utilized in clinical settings and their mechanism of action thoroughly studied.[188] Recent metabolomic studies using high-throughput technologies have shown apart from previously identified mechanisms, subsequent metabolic changes that occur after antibiotics interact with their primary targets also contribute significantly towards bacterial-killing mechanism.[189] According to

reports L-serine has the potential of increasing the sensitivity of *E. coli* to gentamicin. This is achieved by enhancing the generation of NADH and ROS that in turn facilitates the bacterial killing effect of Curcumin.[190] Adeyemi et al. found that treatment of S. aureus with Curcumin affects concentrations of kynurenine, nitric oxide and total thiol levels suggesting disruptions in these metabolic pathways have a role in Curcumin's antibacterial killing mechanism.[191] The activation of kynurenine pathway is expected to result in a reduction in cellular L-tryptophan supply, necessary for bacterial growth. This leads to deprivation of a critical nutrient for bacterial cells.[191]

2.5.7 Regulation of intracellular bacterial proliferation:

Curcumin is an effective immune-regulator and was shown to modify the body's natural defenses against bacterial infections occuring within cells.[191] Marathe et al. demonstrated that prior exposure of macrophages to Curcumin reduced severity of intracellular infection caused by *Listeria monocytogenes* and *Shigella flexneri*. However, Curcumin had an opposite effect on infection caused by *Salmonella enterica serovar Typhimurium, S. aureus* and *Yersinia enterocolitica*, exacerbating their impact.[192] The differential effect observed may be explained by the ability of Curcumin to stabilize cell membranes. This prevents fusion of the vacuole holding the pathogen with lysosomes. This mechanism has been shown in *S. enterica serovar Typhimurium, S. aureus*, and *Y. enterocolitica* since the group's researchers developed a machinery to hinder the fusion process.[193] In contrast, *Listeria* monocytogenes and *S. flexneri* have the ability to evade lysosomal breakdown by escaping into the cytoplasm of host cells.[194] Recent investigations have shown Curcumin has the ability to safeguard human macrophages from *Mycobacterium* TB infection by triggering apoptosis, autophagy and activation of NF-κB[195]. Currently, specific objectives of Curcumin in the host that regulate development and reproduction

of intracellular infections, remain uncertain and additional research is required to determine the exact molecular pathways involved.[195]

References

1. B. Kocaadam , N. Sanlier ; Curcumin, an active component of turmeric (curcuma longa), and its effects on health. Crit. Rev. *Food Sci. Nutr*., **2017**, 57, 2889–2895.
2. H. P.T. Ammon , M.A. Wahl; Pharmacology of Curcuma longa. *Planta Med*.,**1991**, 57, 1–7.
3. B. B. Aggarwal, C. Sundaram , N. Malani , H. Ichikawa; Curcumin: The Indian solid gold., *Adv. Exp. Med. Biol*., **2007**, 595, 1 – 75.
4. R. Thakur, H. S. Puri, A. Husain; *Major medicinal plants of India*, **1989**, 33, 585.
5. H.E. Macgregor; Out of the spice box, into the lab, *Los Angeles Times*, **2006**.
6. N. K. Pandeya; Old wives' tales: Modern miracles-Turmeric as traditional medicines in India, *Trees for Life Journal*.,**2005**,1:3.
7. J. Tilak, M. Banerjee, H. Mohan, T. P. A. Devasagayam; Antioxidant availability of turmeric in relation to its medicinal and culinary uses., *Phytother. Res.,* **2004**,18, 798 – 804.
8. S. Shishodia, G. Sethi, and B. B. Aggarwal; Curcumin: Getting back to the roots., *Ann. N. Y. Acad. Sci.,* **2005**, 1056, 206 – 217.
9. B.B. Aggarwal, A. Kumar, A. C. Bharti; Anticancer potential of Curcumin: Preclinical and clinical studies. *Anticancer Res*., **2003**, 23, 363–398.

10. R.Wilken, S.M. Veena, M.B. Wang, E.S. Srivatsan; Curcumin: A review of anticancer properties and therapeutic activity in head and neck squamous cell carcinoma. *Mol. Cancer.*, **2011**, 10, 1–19.

11. G. Grykiewicz, P. Silfirski; Curucmin and Curcuminoids in quest for medicinal status. *Acta Biochim. Pol.*, **2012**, 59, 201–212.

12. T. Esatbeyoglu, P. Huebbe, M.A. Insa, E. DawnChin, A.E. Wagner, G. Rimbach; Curcumin—From Molecule to Biological Function. *Angew. Chem. Int. Ed.*, **2012,** 51, 5308–5332.

13. S. Gupta, S. Prasad, H. K. Ji, S. Patchva, L. J. Webb, K. I. Priyadarsini, B. B. Aggarwal; Multitargeting by Curcumin as revealed by molecular interaction studies. *Nat. Prod. Rep.*, **2011**, 28, 1937–1955.

14. K.I. Priyadarsini; Chemical and structural features influencing the biological activity of Curcumin. *Curr. Pharm. Des.*, **2013**, 19, 2093–2100.

15. H. A. Vogel, J. Pelletier; Curcumin-biological and medicinal properties. *J. Pharma,***1815**, 2, 50.

16. O.P. Sharma; Antioxidant activity of Curcumin and related compounds. *Biochem. Pharmacol.* **1976**, 25, 1811–1812.

17. S. Singh, B. B. Aggarwal; Activation of transcription factor NF-κB is suppressed by Curcumin (Diferuloylmethane). *J. Biol. Chem.*, **1995,** 270, 24995–25000.

18. P.S. Ramanjaneyulu, Y.S. Sayi, V.A. Raman, K.L. Ramakumar ; Spectrophotometric determination of boron in nuclear grade uranium compounds with Curcumin and studies on effect of HNO_3. *J. Radioanal. Anal. Nucl. Chem.*, **2007**, 274, 109–114.

19. R. Marulasiddeshwara, M.S. Jyothi, K. Soontarapa, R.S. Keri, R. Velmurugan; Nonwoven fabric supported, chitosan membrane anchored with Curcumin/TiO_2 complex: Scaffolds for MRSA infected wound skin reconstruction. *Int. J. Biol. Macromol.,* **2020**, 144, 85–93.

20. Y. Panahi, O. Fazlolahzadeh, S.L. Atkin, M. Majeed, A.E. Butler, T.P. Johnston, A. Sahebkar; Evidence of Curcumin and Curcumin analogue effects in skin diseases: A narrative review. *J. Cell Physiol.,* **2019,** 234, 1165–1178.

21. E.M. Altundag, K. Toprak, S ̧anlıtürk, G. Güran, M. C. Özbilenler, N.R. Kerküklü, A.M. Yılmaz, S.A. Yalçın; Synergistic combination of histone deacetylase inhibitor suberoylanilide hydroxamic acid and natural flavonoid Curcumin exhibits anticancer and antibacterial activity. *Anticancer Agents Med. Chem.,* **2021,** 21, 1301–1308.

22. V. Lampe, J. Milobedzka; Studien über Curcumin. Berichte der deutschen chemischen Gesellschaft,**1913**,46,2235–2240.

23. K.R. Srinivasan; A chromatographic study of the Curcuminoids in Curcuma longa, *L. J. Pharm. Pharmacol.,* **1953,** 5, 448–457.

24. Z. Ma, N.Wang, H. He, X. Tang; Pharmaceutical strategies of improving oral systemic bioavailability of Curcumin for clinical application. *J. Control. Release.,* **2019,** 316, 359–380.

25. M. S. Damyeh, R. Mereddy, M.E. Netzel, Y. Sultanbawa ; An insight into Curcumin-based photosensitization as a promising and green food preservation technology. *Compr. Rev. Food Sci. Food Saf.,* **2020,** 19, 1727–1759.

26. H. H. Tonnesen, J. Karlsen, A. Mostad; Structural studies of Curcuminoids I. The crystal structure of Curcumin. *Acta Chemica Scabdinavica B*, **1982**,36, 475-479.

27. P.P. Sahoo, Y.V. Ramshankar, S. Suresh, T.N. Guru Row; Redetermination of Curcumin : (1E, 4Z,6E-5-hydroxy-3-methoxy-phenyl- hepta-1,4,6-triene-3-one). *Acta Crystal.,* **2007,** 63, 860–862.

28. J. Emsley; The composition, structure and hydrogen bonding of the β-diketones, *Springer-Verlag,* **1984,**148-191.

29. J.S. Wright; Predicting the antioxidant activity of Curcumin and Curcuminoids. *J Mol Stru (Theochem),* **2002,** 591,207-217.

30. T.M. Kolev, E.A. Velcheva, B.A. Stamboliyska, M. Spiteller; DFT and Experimental studies of the structure and vibrational spectra of Curcumin. *Int. Jour. Quant Chem,* **2005**,102, 1069-1079.

31. L. Shen, H. F. Ji, Theoretical study on physicochemical properties of Curcumin. *Spectrochim. Acta – Part A.,* **2007,** 67, 619-623.

32. R. Benassi, E. ferrari, S. Lazzari, F. Spagnolo, M. Saladini ; Theoretical study on Curcumin: A comparison of calculated spectroscopic properties with NMR, UV-Vis and IR experimental data. *Jour.Mol. Struc*., **2008** ,892,168-176.

33. K. Balasubramanian; Molecular orbital basis for yellow curry spice Curcumin: prevention of Alzheimer's disease. *Jour. Agric Food Chem.,***2006,** 54,3512-3520.

34. F. Payton, P. Sandusky, W. L. Alworth; NMR study of the solution structure of Curcumin. *Jour. Nat. Prod.*, **2007,**143-146.

35. K.I. Priadarsini; Photophysics, Photochemistry and Photobiology of Curcumin: Studies from organic solutions, bio-mimetics and living cells. *Jour. Photochem Photobiol C: Chemistry Reviews*, **2009**,10, 81-96.

36. H. H. Tonnesen, J. Karlsen; Studies on Curcumin and Curcuminoids VI. Kinetics of Curcumin degradation in aqueous solution. *VI. Z Lebensum Unters Forsch*, **1985**,180, 402-404.

37. F. Dietze, A. F. Arrieta, U. Zimmer; pKa stability constants and UV/VIS spectral behaviour of selected Curcumin analogues. *Pharmazie,* **1997**, 52,302-306.

38. M. Borsari, E. Ferrari, R. Grandi, M. Saladini; Curcuminoids as potential new iron-chemlating agents: spectroscopic, polarographic and potentiometric study on their Fe(III) complexing ability. *Inorg Chim Acta*, **2002**, 328, 61-68.

39. Y. Murakami, H. Ishi, N. Takada, S. Tanaka, M. Machino, S. Ito, S. Fujisawa; Comparative anti-inflammatory activities of Curcumin and tetrahydroCurcumin based on the phenolic-OH bond dissociation enthalpy, ionization potential and quantum chemical descriptor. *Anticancer Res*, **2008**, 28,699-707.

40. S. Prasad; S.C. Gupta,; A.K. Tyagi, B.B. Aggarwal; Curcumin, a component of golden spice: From bedside to bench and back. *Biotechnol. Adv.*, **2014,** 32, 1053–1064.

41. A. Pandey, M. Chaturvedi, S. Misra , P. Kumar , P. Somvanshi, R. Chaturvedi; Reductive metabolites of Curcumin and their therapeutic effects, *Heliyon,* **2020**, 6 ,11, e05469.

42. P. Anand, A.B. Kunnumakkara, R.A. Newman, B.B. Aggarwal; Bioavailability of Curcumin: problems and promises. *Mol. Pharmac. Rev.,* **2007**, 4, 807-818.

43. P. Anand, S.G. Thomas, A.B. Kunnumakkara, et al. ; Antioxidant, antiinflammatory, anticancer, anticarcinogenic, antidiabetic and neuroprotective effects of Curcumin analogues (Congeners) made by man and mother nature. *Biochem Pharmacol (Review)*, **2008**,76,1590-1611.

44. B. Wahlstrom, G. Blennow; A study on the fate of Curcumin in the rat. *Acta Pharmacol Toxicol* ,**1978**, 43, 86-92.

45. G. Garcea, D. J. Jones, R. Singh, et al. ; Detection of Curcumin and its metabolites in hepatic tissue and portal blood of patients following oral administration. *Br J Cancer*,**2004**,90, 1011-15.

46. S.I. Hoehle, E.P. feiffer, A.M. Solyom, M. Metzler ; Metabolism of Curcuminoids in tissue slices and subcellular fractions from rat liver. *Jour. Agric Food Chem.*, **2006**, 54, 756-64.

47. S.M. Khopde, K.I. Priyadarsini, S.N. Guha, J.G. Satav, P. Venkatesan, M.N. Rao; Inhibition of radiation induced lipid peroxidation by tetrahydroCurcumin: possible mechanisms by pulse radiolysis. *Biosci Biotech Biochem*, **2000**, 64, 503-509.

48. Y. J. Wang, M. H. Pan, A.L. Cheng, L.I. Lin, Y.S. Ho, C.Y. Hsieh, J.K. Lin; Stability of Curcumin in buffer solutions and characterization of its degradation products. *Jour. Pharm. Biomed. Anal.* **1997,** 15, 1867−1876.

49. R. Jagannathan, P.M. Abraham, P. Poddar; Temperature dependent spectroscopic evidences of Curcumin in aqueous medium: A mechanistic study of its solubility and stability. *Jour. Phys. Chem. B,* **2012,** 116, 14533−14540.

50. K. I. Priyadarsini; Photophysics, photochemistry and photobiology of Curcumin: Studies from organic solutions, bio-mimetics and living cells. *Jour. Photochem. Photobiol., C,* **2009,** 10, 81−95.

51. M. Griesser, V. Pistis, T. Suzuki, N. Tejera, D. A. Pratt, C. Schneider; Autoxidative and cyclooxygenase-2 catalyzed transformation of the dietary chemopreventive agent Curcumin. *Jour. Biol.Chem.*, **2011,** 286, 1114−1124.

52. O. N. Gordon, C. Schneider; Vanillin and ferulic acid: Not the major degradation products of Curcumin. *Trends Mol. Med.*, **2012,** 18, 361−363.

53. C. Schneider, O. N. Gordon, R. L. Edwards, P. B. Luis; Degradation of Curcumin: From mechanism to biological implications. *Jour. Agric. Food Chem.*, **2015,** 63, 7606−7614.

54. A. Khurana, C. T. Ho; High-performance liquid-chromatographic analysis of Curcuminoids and their photo-oxidative decomposition compounds in Curcuma longa l. *Jour. Liq. Chromatogr.*, **1988,** 11, 2295−2304.

55. H. H. Tønnesen, J. Karlsen, G. B. van Henegouwen; Studies on Curcumin and Curcuminoids. VIII. Photochemical stability of Curcumin. Z. *Lebensm.-Unters. Forsch.*,**1986,** 183, 116−122.

56. M. Heger, R. F. van Golen, M. Broekgaarden, M. C. Michel; The molecular basis for the pharmacokinetics and pharmacodynamics of Curcumin and its metabolites in relation to cancers. *Pharmacol. Rev.*, **2014,** 66, 222−307.

57. M. Ghosh, A. T. Singh, W. Xu, T. Sulchek, L. I. Gordon, R. O. Ryan; Curcumin nanodisks: Formulation and characterization. *Nanomedicine,* **2011,** 7, 162−167.

58. M. Sun, X., Su, B. Ding, X. He, X. Liu, A. Yu, H. Lou, G. Zhai; Advances in nantoechnology-based delivery systems for Curcumin. *Nanomedicine (London, U. K.)*, **2012**, 7, 1085−1100.

59. C. Tamvakopoulos, K. Dimas, Z. D. Sofianos, S. Hatziantoniou, Z. Han, Z. L. Liu, J. H. Wyche, P. Pantazis; Metabolism and anticancer activity of the Curcumin analogue, dimethoxy Curcumin. *Clin. Cancer Res.*, **2007**, 13, 1269−1277.

60. T. P. Robinson, R. B. Hubbard, T. J. Ehlers, J. L. Arbiser, D. J. Goldsmith, J. P. Bowen; Synthesis and biological evaluation of aromatic enones related to Curcumin. *Bioorg. Med. Chem.*, **2005,** 13, 4007−4013.

61. G. Liang, L. Shao, Y. Wang, C. Zhao, Y. Chu, J. Xiao, Y. Zhao, X. Li, S. Yang; Exploration and synthesis of Curcumin analogues with improved structural stability both in vitro and in vivo as cytotoxic agents. *Bioorg. Med. Chem.*, **2009,** 17, 2623−2631.

62. T.G. Lim, S.Y. Lee, Z. Huang, D.Y. Lim, H. Chen, S.K. Jung, A. M. Bode, K. W. Lee, Z. Dong; Curcumin suppresses proliferation of colon cancer cells by targeting CDK2. *Cancer Prev. Res.,* **2014,** 7, 466−474.

63. K. Balasubramanian; Molecular orbital basis for yellow curry spice Curcumin's prevention of Alzheimer's disease. *Jour. Agric. Food Chem.,* **2006,** 54, 3512−3520.

64. L. Ciccone, L. Tepshi, S. Nencetti, E.A. Stura; Transthyretin complexes with Curcumin and bromo-estradiol: Evaluation of solubilizing multicomponent mixtures. *New Biotechnol.*, **2015**, 32, 54−64.

65. L. Shen, H. F. Ji; The pharmacology of Curcumin: Is it the degradation products? *Trend Mol Med.,***2012,**18, 138–143.

66. P. Anand, A.B. Kunnumakkara, R.A. Newman, B.B. Aggarwal; Bioavailability of Curcumin: problems and promises. *Mol Pharmac. Rev.,* **2007**, 4, 807-818.

67. R. Wilken, S. M. Veena, M. B. Wang, E. S. Srivatsan; Curcumin: A review of anticancer properties and therapeutic activity in head and neck squamous cell carcinoma. *Mol Cancer.*, **2011**, 10, 1-19.

68. B.B. Aggarwal, C. Sundaram, N. Malini, H. Ichikawa, Curcumin: The Indian solid gold. *Adv Exp Med Biol.*, **2007**, 595, 243-305.

69. P. Anand, S.G. Thomas, A.B. Kunnumakkara, et al.; Antioxidant, anti-inflammatory, anticancer, anticarcinogenic, antidiabetic and neuroprotective effect of Curcumin analogues (Congeners) made by man and mother nature. *Biochem Pharmacol (Review)*, **2008**,76,1590-1611.

70. S. Gupta, S. Prasad, H.K. Ji et al.; Multitargeting by Curcumin as revealed by molecular interaction studies. *Nat. Prod. Rep.,* **2011**, 28, 1937-1955.

71. Y. Masuda, M. Fukuchi, T. Yatagawa, et al.; Solid-state NMR analysis of interaction sites of Curcumin and 42-residue amyloid - protein fibrils. *Bioorg Med Chem.*, **2011,** 19, 5967-5974.

72. F. Zsila, Z. Bikadi, M. Simonyi, Molecular basis of cotton effects induced by the binding of Curcumin to albumin. *Tetrahedron Asym.*, **2003**, 14, 2433-2444.

73. J. S. Mandeville, E. Froehlich, H. A. Tajmir-Riahi; Study of Curcumin and genistein intearctaion with human serum albumin. *Jour. Pharmac Biomed Anal.*, **2009**, 49, 468–474.

74. A. Barik, K.I. Priyadarsini, H.Mohan; Photophysical studies on binding of Curcumin to bovine serum albumin. *Photochem Photobiol.*, **2003**, 77, 597-603.

75. A. Barik, B. Mishra, A. Kunwar, K.I. Priyadarsini; Interaction of Curcumin with human serum albumin: Thermodynamic properties, fluorescence energy transfer and denaturation effects. *Chem Phys Letters.*, **2007**, 436, 239-243.

76. S.P. Mitra; Binding and stability of Curcumin in presence of bovine serum albumin. *Jour. Surf Sci Technol*., **2007**, 23, 91-110.

77. B.K. Sahoo, K.S. Ghosh, S. Dasgupta; Investigating the binding of Curcumin derivative to bovine serum albumin. *Biophys Chem*., **2008**, 132, 81-88.

78. A. C. Pulla Reddy, E. Sudharshan, A.G. Aappu Rao, B.R. Lokesh; Interaction of Curcumin with human serum albumin-a spectroscopic study, *Lipids*,**1999**,34,1025-1029.

79. A. Kunwar, A. Barik, R. Pandey, K.I. Priyadarsini; Transport of liposomal and albumin loaded Curcumin to living cells: an absorption and fluorescence spectroscopic study. *Biochim Biophys Acta.*, **2006**, 1760, 1513-1520.

80. S. Mishra, K. Palanivelu; The effect of Curcumin (turmeric) on Alzheimer's disease: an overview. *Ann Indian Acad Neurol*.; **2008**, 11, 13-19.

81. D. Yanagisawa, H. Taguchi, A. Yamamoto, N. Shirai, K. Hirao, I. Tooyama; Curcuminoid binds to amyloid-β1-42 oligomer and fibril. *Jour. Alzh Disease*., **2011**, 24 ,33-42.

82. F. Yang, G.P. Lim, A.N. Begum et al. Curcumin inhibits formation of amyloid beta oligomers and fibrils, binds plaques and reduces amyloid in vivo. *Jour. Biol Chem.*, **2005** ,280,5892-901.

83. A.A. Reinke, J.E. Gestwicki; Structure-activity relationships of amyloid beta aggregation inhibitors based on Curcumin: influence of linker length and flexibility. *Chem Biol Drug Des.*, **2007**, 70, 206-15.

84. Y. Masuda, M. Fukuchi, T. Yatagawa, et al.; Solid-state NMR analysis of interaction sites of Curcumin and 42-residue amyloid β-protein fibrils. *Bioorg Med Chem*, **2011**,19,5967-5974.

85. S. Awasthi, U. Pandya, S.S. Singhal et al. ; Curcumin-glutathione interactions and the role of human glutathione S-transferase $P_{1\text{-}1}$. *Chem Biol Inter*, **2000**,128,19-38.

86. M. L. Iersel, J.P. Ploemen, I. Struik et al.; Inhibition of glutathione S-transferase activity in human melanoma cells by unsaturated carbonyl derivatives. Effects of acrolein, cinnamaldehyde, citral, crotonaldehyde, Curcumin, ethacrynic acid and trans-2-hexanal. *Chem Biol Inter,* **1996**, 102, 117-132.

87. J. Fang, J. Lu, A. Holmegren; Thioredoxin reductase is irreversibly modified by Curcumin: A novel molecular mechanism for its anticancer activity. *Jour. Biol Chem.*, **2005**, 280, 25284-25290.

88. Y. Jung, X. Wanping, H. Kim, N. Ha, L. Neckers; Curcumin-induced degradation of $ErbB_2$: A role for the E3 ubiquitin ligase CHIP and the Michael reaction acceptor activity of Curcumin. *Biochim Bio- phys Acta*, **2007**,1773,383-390.

89. K. K. Gupta, S. S. Bharne, K. Rathinasamy, N. R. Naik, D. Panda; Dietary antioxidant Curcumin inhibits microtubule assembly through tubulin binding. *FEBS Journal*, **2006**, 273 ,5320-5332.

90. F. Zsila, Z. Bikadi, M. Simonyi; Circular dichroism spectroscopic studies reveal pH dependent binding of Curcumin in the minor groove of natural and synthetic nucleic acids. *Org Biomol Chem.*,**2004,** 2, 2902–2910.

91. R. Bera, B.K. Sahoo, K. Ghosh, S. Dasgupta; Studies on the interaction of isoxazole Curcumin with calf thymus DNA. *Int. Jour. Biol Macromolecules*, **2008**, 42, 14-21.

92. B.K. Sahoo, K.S. Ghosh, R. Bera, S. Dasgupta; Studies on the interaction of diacetylCurcumin with calf thymus-DNA. *Chem Phys*, **2008,** 351, 163-169.

93. A. Kunwar, E. Simon, U. Singh, et al.; Interaction of a Curcumin analogue dimethoxy Curcumin with DNA. *Chem Biol Drug Design*, **2011,** 77, 281-287.

94. S. Nafisi, M. Adelzadeh, Z. Norouzi, M.N. Sarbolouki; Curcumin binding to DNA and RNA. *DNA Cell Biol*, **2009**, 28, 201–208.

95. G. Began, E. Sudharshan, K. Udaya Sankar, A.G. Appu Rao; Interaction of Curcumin with Phosphatidylcholine: A Spectrofluorometric Study. *Jour Agric Food Chem*,**1999**,47,4992-4997.

96. Y. Sun, C.C. Lee, W.C. Hung, F.Y. Chen, M.T. Lee, H.W. Huang; The bound States of amphipathic drugs in lipid Bilayers: Study of Curcumin. *Biophys J*, **2008**,95,2318-2324.

97. L. Li, F.S. Braiteh, R. Kurzrock; Liposome-encapsulated Curcumin: in vitro and in vivo effects on proliferation, apoptosis, signaling, and angiogenesis. *Cancer*, **2005,**1041322-1331.

98. S. Mourtas, M. Canovi, C. Zona, et al.; Curcumin-decorated nanoliposomes with very high affinity for amyloid-β1-42 peptide. *Biomaterials*, **2011,** 32,1635-1645.

99. J. Barry, M. Fritz, J.R. Brender, P.E.S. Smith, D.K. Lee; A Ramamoorthy, Determining the effects of lipophilic drugs on membrane structure by solid state NMR spectroscopy: the case of the antioxidant Curcumin. *Jour Amer Chem Soc*, **2009**,131, 4490-4498.

100. H. I. Ingolfsson, R.E. Koeppe, O.S. Andersen; Curcumin is a Modulator of Bilayer Material Properties. *Biochemistry*, **2007**,46,10384–10391.

101. A.A. Gorman, V.S. Hamblett, V.S. Srinivasan, P.D. Wood; Curcumin derived transients: A pulsed laser and pulse radiolysis study. *Photo-chem Photobiol*,**1994**,59,389-398.

102. K.I. Priyadarsini; Free radical reactions of Curcumin in model membranes, *Free Radic Bio Med*,**1997**,23,838-84.

103. B.B. Aggarwal, C. Sundaram, N. Malani, H. Ichikawa; Curcumin: The Indian solid gold. *Adv Exp Med Biol*, **2007**,595,1-75.

104. H.P. Ammon, M.A. Wahl; Pharmacology of Curcuma longa. *Planta Med*,**1991**,57,1-7.

105. B.B. Aggarwal, A. Kumar, A.C. Bharti; Anticancer potential of Curcumin: preclinical and clinical studies. *Anticancer Res*, **2003**,23,363-398.

106. Sreejayan, M.N. Rao; Curcuminoids as potent inhibitors of lipid peroxidation. *J Pharm Pharmacol*,**1994**,46,1013-1016.

107. T. Masuda, T. Maekawa, K. Hidaka, H. Bando, Y. Takeda, H. Yamaguchi; Chemical studies on antioxidant mechanisms of Curcumin: analysis of oxidative coupling products from Curcumin and linoleate. *Jour Agric Food Chem*, **2001**, 49, 2539-2547.

108. B. Joe, M. Vijaykumar, B.R. Lokesh; Biological properties of Curcumin–cellular and molecular mechanisms of action. *Crit Rev Food Sci Nut*, **2004**, 44,97-111.

109. B. Joe, B.R. Lokesh; Role of capsaicin, Curcumin and dietary n-3 fatty acids in lowering the generation of reactive oxygen species in rat peritoneal macrophages. *Biochem Biophys Acta*,**1994**,1224,255-263.

110. I. Brouet, H. Ohshima; Curcumin, an anti-tumour and anti-inflammatory agent, inhibits induction of nitric oxide synthase in activated macrophages. *Biochem Biophys Res Commun*,**1995**, 206, 533-540.

111. M.M. Chan, H.I. Huang, M.R. Fenton, D. Fong; In vivo inhibition of nitric oxide synthase gene expression by Curcumin, a cancer preventive natural product with anti-inflammatory properties. *Biochem Pharmacol*, **1998**, 55,1955-1962.

112. K.K. Jung, H.S. Lee, J.Y. Cho, W.C. Shin, M.H. Rhee, T.G. Kim, J.H. Kang, S.H. Kim, S. Hong, S.Y. Kang; Inhibitory effect of Curcumin on nitric oxide production from lipopolysaccharide-activated primary microglia. *Life Sci,* **2006**,79, 2022-2031.

113. B. Ray, D.K. Lahiri; Neuroinflammation in Alzheimer's Disease: different molecular targets and potential therapeutic agents including Curcumin. *Curr Opin Pharmacol*, **2009**, 4 ,434-444.

114. L. F. He, H. J. Chen, L. H. Qian et.al.; Curcumin protects pre-oligodendrocytes from activated microglia in vitro and in vivo. *Brain Res*, **2010**, 1339, 60-69.

115. M.M. Chan; Inhibition of tumor necrosis factor by Curcumin, a phytochemical. *Biochem Pharmacol*,**1995**, 49,1551-1556.

116. S. Singh, B.B. Aggarwal; Activation of transcription factor NF-kB is suppressed by Curcumin (diferuloylmethane). *J Biol Chem*, **1995**, 270, 24995-25000.

117. P. Brennan, L.A. O'Neill; Inhibition of nuclear factor kappaB by direct modification in whole cells: Mechanism of action of nordihydroguaiaritic acid, Curcumin and thiol modifiers. *Biochem Pharmacol*,**1998**, 55, 965-973.

118. C. Jobin, C.A. Bradham, M.P. Russo, B. Juma, A.S. Narula, D.A. Brenner, R.B. Sartor: Curcumin blocks cytokine-mediated NF-kappa B activation and proinflammatory gene expression by inhibiting inhibitory factor I-kappa B kinase activity. *J Immunol*,**1999**, 163,3474-3483.

119. S.M. Plummer, K.A. Holloway, M.M. Manson, R.J. Munks, A. Kaptein, S. Farrow, L Howells: Inhibition of cyclo-oxygenase 2 expression in colon cells by the chemopreventive agent Curcumin involves inhibition of NF-kappaB activation via the NIK/IKK signalling complex. *Oncogene*, **1999**, 18:6013-6020.

120. J. S. Jurenka; Anti-inflammatory properties of Curcumin, a major constituent of Curcima longa: A review of preclinical and clinical research. *Altern Med Rev*, **2009**, 14,141-153.

121. P.J. Barnes, M. Karin; Nuclear factor-κB, a pivotal transcription factor in chronic inflammatory diseases. *N Engl J Med,* **1997**, 336, 1066-1071.

122. I.E. Wertz, K.M. O'Rourke, H.Zhou, M. Eby, L. Aravind, S.Seshagiri, P.Wu, C. Wiesmann, R. Baker, D.L. Boone, A. Ma, E.V. Koonin, V.M. Dixit: De-ubiquitination and ubiquitin ligase domains of A20 downregulate NF- kappaB signalling. *Nature*, **2004**, 430, 694-699.

123. T.D. Gilmore; Introduction to NF-κB: players, pathways, perspectives. *Oncogene*, **2006**, 25, 6680-6684.

124. A.R. Brasier; The NF-κB regulatory network. *Cardiovasc Toxicol*, **2006**, 6, 111-130.

125. N.D. Perkins; Integrating cell-signalling pathways with NF-κB and IKK function. *Nat Rev Mol Cell Biol.*, **2007**, 8, 49-62.

126. T.D. Gilmore; The Rel/NF-κB signal transduction pathway: introduction. *Oncogene*, **1999**, 18, 6842-6844.

127. R.J. Anto; A.Mukhopadhyay, S. Shishodia, C.G. Gairola, B.B. Aggarwal; Cigarette smoke condensate activates nuclear transcription factor-κB through phosphorylation and degredation of IκB(α): correlation with induction of cyclooxygenase-2. *Carcinogenesis*, **2002**, 23,1511-1518.

128. A. Garg, B.B. Aggarwal; Nuclear transcription factor-κB as a target for cancer drug development. *Leukemia*, **2002**, 16, 1053-1068.

129. S.Ghosh, M. Karin; Missing pieces of the NF-κB puzzle. *Cell*, **2002**, 109((Suppl)):S81-96.

130. D.Wang, M.S. Veena, K. Stevenson, C. Tang, B. Ho, J.D. Suh, V.M. Duarte, K.F. Faull, K. Mehta, E.S. Srivatsan, M.B. Wang; Liposome-encapsulated Curcumin suppresses growth of head and neck squamous cell carcinoma in vitro and in xenografts through the inhibition of nuclear factor kappaB by an AKT-independent pathway. *Clin Cancer Res*, **2008**, 14, 6228-6236.

131. S.S. Han, H.J. Seo, Y.J. Surh; Curcumin suppresses activation of NF-kappaB and AP-1 induced by phorbol ester in cultured human promyelocytic leukemia cells. *J Biochem Mol Biol*, **2002**, 35, 337-342.

132. Y. Abe, S. Hashimoto, T. Horie, Curcumin inhibition of inflammatory cytokine production by human peripheral blood monocytes and alveolar macrophages. *Pharmacol Res*, **1999**, 39, 41-47.

133. C.V. Rao; Regulation of COX and LOX by Curcumin. *Adv Exp Med Biol,* **2007**, 595,213-26.

134. M.T. Huang, T. Lysz, T. Ferraro, T.F. Abidi, J.D. Laskin, A.H. Conney ; Inhibitory effects of Curcumin on in vitro lipoxygenase and cyclooxygenase activities in mouse epidermis. *Cancer Res,* **1991**, 51, 813-819.

135. F. Zhang, N.K. Altorki, J.R. Mestre, K. Subbaramaiah, A.J. Dannenberg; Curcumin inhibits cyclooxygenase-2 transcription in bile acid- and phorbol estertreated human gastrointestinal epithelial cells. *Carcinogenesis*, **1999**, 20, 445-451.

136. A. Koeberle, H. Northoff, O. Werz; Curcumin blocks prostaglandin E2 biosynthesis through direct inhibition of the microsomal prostaglandin E2 synthase-1. *Mol Cancer Ther.*, **2009**,8,2348-2355.

137. G.P. Lim, T. Chu, F. Yang, W. Beech, S.A. Frautschy, GM Cole; The curry spice Curcumin reduces oxidative damage and amyloid pathology in an Alzheimer transgenic mouse. *J Neurosci*, **2001**,21,8370-8377.

138. F. Yang, G.P. Lim, A.N. Begum, O.J. Ubeda, M.R. Simmons, S.S. Ambegaokar, P.P. Chen, R. Kayed, C.G. Glabe, S.A. Frautschy, G.M. Cole; Curcumin inhibits formation of amyloid beta oligomers and fibrils, binds plaques, and reduces amyloid in vivo. *J Biol Chem*, **2005**, 280, 5892-5901.

139. D.O. Moon, M.O. Kim, H.J. Lee; Curcumin attenuates ovalbumin-induced airway inflammation by regulating nitric oxide. *Biochem Biophys Res Commun.*, **2008**, 375, 275-279.

140. B.B. Aggarwal, K.B. Harikumar; Potential therapeutic effects of Curcumin, the anti-inflammatory agent, against neurodegenerative, cardiovascular, pulmonary, metabolic, autoimmune and neoplastic diseases. *Int J Biochem Cell Biol*, **2009**, 41, 40-59.

141. R.K. Maheshwari, A.K. Singh, J. Gaddipati , R.C. Srimal; Multiple biological activities of Curcumin. *A short review. Life Sci*, **2006**, 78, 2081-2087

142. D.R.Y. Jr, S.M. Sagar ; Targeting angiogenesis with integrative cancer therapies. *Integr Cancer Ther.,* 2006, 5, 9-29.

143. D. Karunagaran, R.Rashmi, T.R. Kumar ; Induction of apoptosis by Curcumin and its implications for cancer therapy. *Curr Cancer Drug Targets*, **2005**, 5, 117-129.

144. L. Helson: Curcumin (diferuloylmethane) delivery methods: *A review Biofactors*, **2013**, 39, 21-26.

145. S. Salvioli, E. Sikora, E.L. Cooper, C. Franceschi ; Curcumin in cell death processes: A challenge for CAM of age-related pathologies. *Evid Based Complement Alternat Med*, **2007**, 4, 181-190.

146. J.Y. Yang, X.Zhong, H.W. Yum, H.J. Lee, J.K. Kundu, H.K. Na, Y.J. Surh; Curcumin inhibits STAT3 signaling in the colon of dextran sulfate sodium-treated mice. *J Cancer Prev*, **2013**, 18, 186-191.

147. N.G. Vallianou, A. Evangelopoulos, N. Schizas , C. Kazazis; Potential anticancer properties and mechanisms of action of Curcumin. *Anticancer Res*, **2015,** 35, 645-651.

148. Y. Oda; Inhibitory effect of Curcumin on SOS functions induced by UV irradiation. *Mutat Res*, **1995**, 348,67-73.

149. R. Thapliyal, G.B. Maru; Inhibition of cytochrome p450 isoenzymes by Curcumins in vitro and in vivo. *Food Chem Toxicol*, **2001**, 39, 541-547.

150. M. Iqbal, S.D. Sharma, Y. Okazaki, M. Fujisawa, S. Okada; Dietary supplementation of Curcumin enhances antioxidant and phase II metabolizing enzymes in ddY male mice: possible role in protection against chemical carcinogenesis and toxicity. *Pharmacol Toxicol*, **2003**, 92, 33-38.

151. E. Schraufstatter , H. Bernt ; Antibacterial action of Curcumin and related compounds. *Nature*, **1949**, 164, 456.

152. M. Liu, Y. Lu, P. Gao, X. Xie, D.Li, D. Yu, M. Yu; Effect of Curcumin on laying performance, egg quality, endocrine hormones, and immune activity in heat-stressed hens. *Poult. Sci. 2020*, **99,** 2196–2202.

153. J.Y. Sharahi, Z.A. Ahovan, D.T. Maleki, Z.R. Rad, M. Goudarzi, A. Shariati, N. Bostanghadiri, E. Abbasi, A. Hashemi; In vitro antibacterial activity of Curcumin-meropenem combination against extensively drug-resistant (XDR) bacteria isolated from burn wound infections. *Avicenna J. Phytomed*. **2020**, 10, 3–10.

154. S. Taghavifar, F. Afroughi, M. S. Keyvan; Curcumin nanoparticles improved diabetic wounds infected with methicillin- resistant staphylococcus aureus sensitized with hamlet. *Int. J. Low. Extrem. Wounds*., **2022**,2,141-153.

155. L. G. Morão ,C. R. Polaquini, M. Kopacz, G. S. Torrezan, G. M. Ayusso, G.Dilarri, L. B. Cavalca, A. Zielin´ska, D. J. Scheffers, L. O. Regasini, H. Ferreira; A simplified Curcumin targets the membrane of bacillus subtilis. *Microbiologyopen*, **2019**, 8, e00683.

156. A. Kaur, P. Sharma, N. Capalash; Curcumin alleviates persistence of acinetobacter baumannii against colistin. *Sci. Rep.*, **2018**, 8, 11029.

157. N. Niamsa and C. Sittiwet; Antimicrobial activity of Curcuma longa aqueous extract. *Journal of Pharmacology and Toxicology.*, **2009**, 4 ,173-177.

158. S. Ungphaiboon, T. Supavita, P. Singchangchai, S. Sungkarak, P. Rattanasuwan, A. Itharat; Study on antioxidant and anti-microbial activities of turmeric clear liquid soap for wound treatment of HIV patients. *Songklanakarin Journal of Science and Technology*, **2005**, 27, 269–578.

159. O.A. Lawhavinit, N. Kongkathip, and B. Kongkathip; Antimicrobial activity of Curcuminoids from Curcuma longa L. on pathogenic bacteria of shrimp and chicken. *Kasetsart Journal— Natural Science*, **2010**, 44, 364–371.

160. I. M. Hosny, W. I. El Kholy, H. A. Murad, and R. K. El Dairouty; Antimicrobial activity of Curcumin upon pathogenic microorganisms during manufacture and storage of a novel style cheese 'Karishcum'. *Journal of American Science*, **2011**, 7, 611–618,.

161. P. S. Negi, G. K. Jayaprakasha, L. J. M. Rao, and K. K. Sakariah; Antibacterial activity of turmeric oil: a byproduct from Curcumin manufacture. *Journal of Agricultural and Food Chemistry*, **1999,**47,4297–4300.

162. S. H. Mun, D. K. Joung, Y. S. Kim et al.; Synergistic antibacterial effect of Curcumin against methicillin-resistant Staphylococcus aureus. *Phytotherapy Research*, **2013**,19, 599–604.

163. S. Tajbakhsh, K. Mohammadi, I. Deilami et al.; Antibacterial activity of indium Curcumin and indium diacetylCurcumin. *African Journal of Biotechnology*, **2008**, 7, 3832–3835.

164. D. Rai, J. K. Singh, N. Roy, and D. Panda, Curcumin inhibits FtsZ assembly: an attractive mechanism for its antibacterial activity. *Biochemical Journal*, **2008,** 410, 147–155.

165. S. Kaur, N. H. Modi, D. Panda, N. Roy; Probingthebinding site of Curcumin in Escherichia coli and Bacillus subtilis FtsZ—a structural insight to unveil antibacterial activity of Curcumin. *European Journal of Medicinal Chemistry*, **2010**, 45, 4209–4214.

166. R. De, P. Kundu, S. Swarnakar et al.; Antimicrobial activity of Curcumin against helicobacter pylori isolates from India and during infections in mice. *Antimicrobial Agents and Chemotherapy*, **2009**, 53, 1592–1597.

167. G.K. Varshney, R.K. Saini, P.K. Gupta, K. Das; Effect of Curcumin on the diffusion kinetics of a hemicyanine dye, LDS-698, across a lipid bilayer probed by second harmonic spectroscopy. *Langmuir*, **2013**, 29, 2912–2918.

168. J. Barry, M. Fritz, J.R. Brender, P.E. Smith, D.K. Lee, A. Ramamoorthy, ; Determining the effects of lipophilic drugs on membrane structure by solid-state nmr spectroscopy: The case of the antioxidant Curcumin. *J. Am. Chem. Soc.* **2009**, 131, 4490–4498.

169. P. Tyagi, M. Singh, H. Kumari, A. Kumari, K. Mukhopadhyay,; Bactericidal activity of Curcumin I is associated with damaging of bacterial membrane. *PLoS ONE*, **2015**, 10, e0121313.

170. D. Zheng, C. Huang, H. Huang, Y. Zhao, M.R.U. Khan, H. Zhao, L. Huang,; Antibacterial mechanism of Curcumin: A review. *Chem. Biodivers.*, **2020**, 17, e2000171.

171. D. Deryabin, A. Galadzhieva, D. Kosyan, G. Duskaev; Plant-derived inhibitors of ahl-mediated quorum sensing in bacteria: Modes of action. *Int. J. Mol. Sci*., **2019**, 20, 5588.

172. G. Brackman, T. Coenye,; Quorum sensing inhibitors as anti-biofilm agents. *Curr. Pharm. Des.* **2015,** 21, 5–11.

173. D. Bonifácio, C. Martins, B. David, C. Lemos, M.G.P.M.S. Neves, A. Almeida, D.C.G.A. Pinto, M.A.F. Faustino, Â. Cunha,; Photodynamic inactivation of listeria innocua biofilms with food-grade photosensitizers: A Curcumin-rich extract of Curcuma longa vs commercial Curcumin. *J. Appl. Microbiol*. **2018**, 125, 282–294.

174. H. Darmani, E.A.M. Smadi, S.B.M. Bataineh,; Blue light emitting diodes enhance the antivirulence effects of Curcumin against helicobacter pylori. *J. Med. Microbiol*., **2020**, 69, 617–624.

175. B. Gayani, A. Dilhari, G.K. Wijesinghe, S. Kumarage, G. Abayaweera, S.R. Samarakoon, I.C. Perera, N. Kottegoda, M.M. Weerasekera, Effect of natural Curcuminoids-intercalated layered double hydroxide nanohybrid against staphylococcus aureus, pseudomonas aeruginosa, and enterococcus faecalis: A bactericidal, antibiofilm, and mechanistic study. *Microbiologyopen*., **2019**, 8, e00723.

176. S. Du, J. Lutkenhaus, At the heart of bacterial cytokinesis: The z ring. *Trends Microbiol*., **2019**, 27, 781–791.

177. N. Allocati, M. Masulli, , C. Di Ilio; V. De Laurenzi,; Die for the community: An overview of programmed cell death in bacteria. *Cell Death Dis*., **2015**, 6, e1609.

178. D. J. Dwyer, D.M. Camacho, M.A. Kohanski, J. M. Callura, J. J. Collins,; Antibiotic-induced bacterial cell death exhibits physiological and biochemical hallmarks of apoptosis. *Mol. Cell*., **2012**, 46, 561–572.

179. B. Ezraty, A. Gennaris, F. Barras, F.J. Collet, Oxidative stress, protein damage and repair in bacteria. *Nat. Rev. Microbiol.*, **2017**, 15, 385–396.

180. M. Butala, D. Zgur-Bertok, S.J.W Busby, The bacterial lexa transcriptional repressor. *Cell Mol. Life Sci.,* **2009,** 66, 82–93.

181. M. Ghasemi, K. Khorsandi, Z. Kianmehr,; Photodynamic inactivation with Curcumin and silver nanoparticles hinders pseudomonas aeruginosa planktonic and biofilm formation: Evaluation of glutathione peroxidase activity and ros production. *World J. Microbiol. Biotechnol.*, **2021**, 37, 149.

182. V.S. Ghate, W. Zhou, H. G. Yuk,; Perspectives and trends in the application of photodynamic inactivation for microbiological food safety. *Compr. Rev. Food Sci. Food Saf.*, **2019**, 18, 402–424.

183. G. Nima, J. Soto-Montero, L. A. Alves, R.O. Mattos-Graner, M. Giannini,; Photodynamic inactivation of streptococcus mutans by Curcumin in combination with edta. *Dent. Mater.*, **2021**, 37, e1–e14.

184. Y. Jiang, A.W. Leung, H. Hua, X. Rao, C. Xu,; Photodynamic action of LED-activated Curcumin against Staphylococcus aureus involving intracellular ROS increase and membrane damage. *Int. J. Photoenergy*, **2014**, 637601.

185. J. Huang, B. Chen, H. Li, Q.H. Zeng, J.J. Wang, H. Liu, Y. Pan, Y. Zhao,; Enhanced antibacterial and antibiofilm functions of the Curcumin-mediated photodynamic inactivation against listeria monocytogenes. *Food Control*, **2020**, 108, 106886.

186. B. Chen, J. Huang, Y. Liu, H. Liu, Y. Zhao, J.J. Wang,; Effects of the Curcumin-mediated photodynamic inactivation on the quality of cooked oysters with vibrio parahaemolyticus during storage at different temperature. *Int. J. Food Microbiol.*, **2021**, 345,109152.

187. A.C. Zangirolami, L.D. Dias, K.C. Blanco, C.S. Vinagreiro, N.M. Inada, L.G. Arnaut, M.M. Pereira, V. S. Bagnato,; Avoiding ventilator-associated pneumonia: Curcumin-functionalized endotracheal tube and photodynamic action. *Proc. Natl. Acad. Sci., USA*, **2020**, 117, 22967–22973.

188. U. Theuretzbacher, K. Outterson, A. Engel, A. Karlen,; The global preclinical antibacterial pipeline. *Nat. Rev. Microbiol.*, **2020**, 18, 275–285.

189. P. Belenky, J.D. Ye, C.B. Porter, N.R. Cohen, M.A. Lobritz, T. Ferrante, S. Jain, B.J. Korry, E.G. Schwarz, G.C. Walker, J. J. Collins; Bactericidal antibiotics induce toxic metabolic perturbations that lead to cellular damage. *Cell Rep.*, **2015**, 13, 968–980.

190. X. Duan, X. Huang, X. Wang, S. Yan, S. Guo, A.E. Abdalla, C. Huang, J. Xie; L-serine potentiates fluoroquinolone activity against escherichia coli by enhancing endogenous reactive oxygen species production. *J. Antimicrob. Chemother.*, **2016**, 71, 2192–2199.

191. O.S. Adeyemi, J.I. Obeme-Imom, B.O. Akpor, D. Rotimi, G.E. Batiha, A. Owolabi,; Altered redox status, DNA damage and modulation of l-tryptophan metabolism contribute to antimicrobial action of Curcumin. *Heliyon*, **2020**, 6, e03495.

192. S.A. Marathe, M. Sen, I. Dasgupta, D. Chakravortty,; Differential modulation of intracellular survival of cytosolic and vacuolar pathogens by Curcumin. *Antimicrob. Agents Chemother.*, **2012,** 56, 5555–5567.

193. E.D.R. Case, J.A. Smith, T.A. Ficht, J.E. Samuel, de Figueiredo, P. Space: A final frontier for vacuolar pathogens. *Traffic*, **2016,** 17, 461–474.

194. M. Ogawa, C. Sasakawa,; Intracellular survival of shigella. *Cell Microbiol.*, **2006**, 8, 177–184.

195. X. Bai, R.E. Oberley-Deegan,; A. Bai,; A.R. Ovrutsky,; W.H. Kinney,; M. Weaver,; G. Zhang,; J.R. Honda,; D.E. Chan,; Curcumin enhances human macrophage control of mycobacterium tuberculosis infection. *Respirology*, **2016**, 21, 951–957.

CHAPTER 3

Review on metal complexes of Curcumin and their medicinal applications

3.1 Metal ions in Biology

Today, it is fairly established that metal ions have a crucial role in different biochemical processes, and are necessary components that has been chosen by nature. Most importantly transition metal complexes have a significant role in catalysis, in the creation of new material, in photochemistry and within biological systems.[1-3] Medicinal inorganic chemistry utilizes some of the unique and distinct characteristic features of metal ions to create novel pharmaceuticals.[4-6] Metals ions in the form of salts were utilized for therapeutic applications since ancient times. Increasing significance of transition metal complexes as effective medicinal agents is driven by advances made in the field of inorganic chemistry and that of spectroscopic techniques. Recent breakthroughs have enabled the creation of several transition metal complexes using organic ligands that are of interest in biology. The complexes have the potential to be utilized as medicinal agents.[1-8]

Metals possess distinct attributes; like varying oxidation states leading to redox activity, various coordination modes and a reactivity for organic substrates etc. Owing to these, the properties of coordination complexes, whether used as pharmaceuticals or as pro-drugs are highly appealing tools in the field of medicinal chemistry. The complexes have a wide range of action that includes anti-inflammatory, anti-infective and anti-diabetic properties. Some possess beneficial benefits in the treatment of diseases like cancer, Alzheimer's etc.[9] As a result of an interaction between metal ions and ligands biological activity of the ligand in majority of cases undergo significant transformations. These either enhance the drug molecules' (ligands) efficacy and/or lead to reduction of adverse effects.[10] Compounds like cisplatin, carboplatin and oxaliplatin, examples of metal-based drugs, are well-known for their anticancer activity.[11] Various biological systems rely heavily on certain metal ions (like zinc and copper), for their

regular functioning.[12] Again, metal ions copper, iron and manganese have crucial roles in several biological processes, ranging from electron transport to catalysis to aspects related to structure. They are often found in active regions of proteins and enzymes.[13]

However, metal ions are subject to strict regulation due to their propensity to undergo different types of reactions; elevated levels of metal ions have been reported to be associated with many disorders that includes cancer.[5] These side effects restrict their use in drugs. Despite limitations and/or side effects, transition metal complexes, remain predominant chemotherapeutic agents playing a significant role in medical treatment.[6]

3.2 Significance of transition metal ions in research related to Curcumin

Curcumin and curcuminoids are perfectly suited to function as chelating ligands for various metal ions thus creating very stable complexes.[14-15] The functional groups present in Curcumin are α, β-unsaturated β-diketone moiety, an aromatic O-methoxy-phenolic group, and a seven-carbon linker unit (Fig. 1A).[14-16] β-diketones readily undergo deprotonation to generate enolates anion, while the unsaturated carbonyl compound acts as a Michael acceptor and undergoes nucleophilic addition.[16-18] The phenolic –OH group of Curcumin is responsible for its antioxidant effect whereas the carbon linker contributes to hydrophobicity (Fig. 1B).[19] Due to this hydrophobic nature, it has low intestinal absorption and quick metabolism.[20] Degradation of Curcumin in aqueous buffer (pH 7.5) and ambient temperature was estimated to take 20 minutes. At 37°C, half-life was less than 10 minutes, with primary products of hydrolysis being vanillin, ferulic acid and feruloylmethane.[21-24] Hence, limited bioavailability of Curcumin is a major obstacle to its therapeutic use. There are several ways to increase bioavailability and also to stabilize Curcumin in aqueous buffer. Among them utilization of nanoparticles, liposomes, micelles and phospholipid complexes plays a significant role.[25-27] Enhancement of bioavailability

of Curcumin can also be achieved through complex formation with transition metal ions. It could be utilized to sidestep some of the obstacles discussed earlier.[28-31]

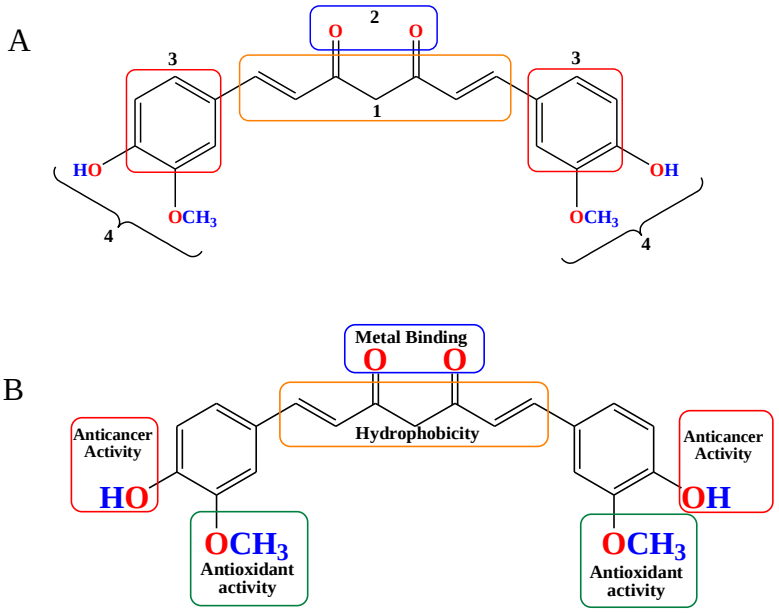


Figure 1: (A) Structural information of Curcumin, (B) different groups of Curcumin which has ve biological attributes

Over the past decade, there has been a significant rise in research focused on creating, analyzing, and studying biological effects of metal Curcumin complexes. It is evident that potential medicinal uses are just as varied as Curcumin itself. The three most captivating domains being selective cytotoxicity, anticancer activity and anti-Alzheimer's activity. Apart from this, metal Curcumin complexes have demonstrated significant potential in various areas that includes antioxidative/neuroprotective activity, antiarthritic/antirheumatic activity, antimicrobial/antifungal activity, anti-viral/anti-HIV activity and in biological imaging/ radioimaging.[8-13,32-40]

3.3 Stoichiometry of Metal-Curcumin complexes

Due to the presence of the α, β unsaturated β-diketo moiety, Curcumin functions as a potent chelating agent able to interact with different metal ions. Several techniques including UV-vis spectroscopy, nuclear magnetic resonance, mass spectrometry and atomic force microscopy (AFM) have been utilized to ascertain binding of metal ions to Curcumin.[40-43] Metal ions typically form a chelate with the keto-enol (β-di-ketone) moiety of Curcumin.[32-36,40-45] Chelation causes a change in the structure of Curcumin.[41] Typically, metals can bind with either one or two Curcumin molecules and may form both homoleptic and heteroleptic complexes. In case of homoleptic complexes Curcumin interacts with metal ions in ratios 1:1, 2:1, 3:1 (Ligand : Metal) where metal ions are coordinated via the enolic group, replacing the enolic proton.[32-45] IR responses at around 455 cm^{-1} confirms the presence of a metal oxygen bond while carbonyl peaks in these complexes show a slight shift of ~10 cm^{-1} in IR spectroscopy following coordination to metal centres.[32-45] There have been reports claiming binding of three Curcumin molecules like that in an octahedral complex with Fe^{3+}.[42] Complex formation of one metal with one Curcumin in 1:1 ratio results in a variation in case of all four metal-O bonds (Fig.2 A); however, these bond lengths are uniform in a 1:2 metal-Curcumin complex. The metal-Curcumin (1:1) combination induces orthorhombic symmetry in its structure whereas a 1:2 metal-Curcumin complex exhibits square planar coordination.[32-45] Furthermore, there have been reports of steric repulsion occurring between methoxy groups of phenolic rings of both Curcumins in the 1:2 metal-Curcumin complex (Fig 2B).[43] Formation of a complex of Curcumin with a metal ion has an impact on both physical and chemical characteristics of Curcumin as well as on the biological reactivity of the new species pertaining to the presence of a metal ion.[18]

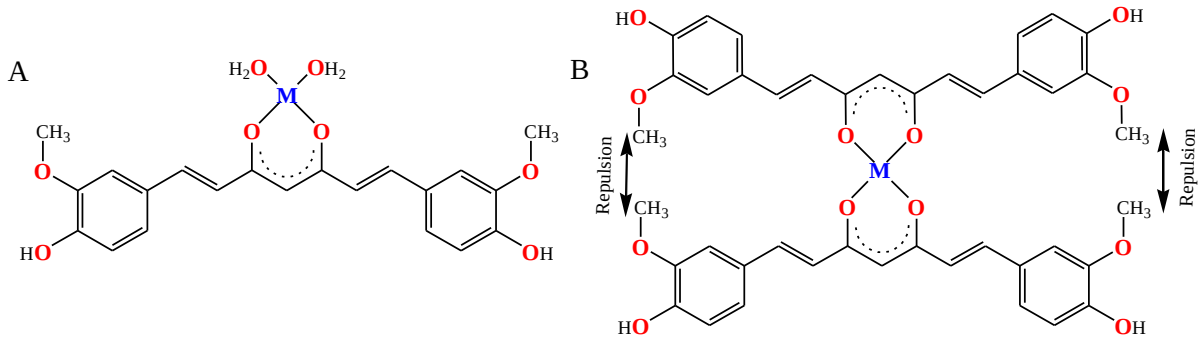


Figure 2: (A) Structure of 1:1 and (B) 1:2 metal:Curcumin complexes showing the β-diketone moiety of Curcumin as the metal binding site, M = Bivalent metal

3.4 General procedure for synthesis of Curcumin based metal complexes

Complex formation has been attempted either with free Curcumin or its derivatives like bis de-methoxycurcumin, dimethulcurcumin, triethylcurcumin.[77] A synthetic procedure is used to produce almost any metal complex that has Curcumin and its derivatives as ligands. The initial step most often is the deprotonation of unbound Curcumin using a suitable base. At the second stage, the anions produced are made to react with metal halides at correct molar ratios.[41-76] Complexation with Boron is the most extensively studied among the five major group elements.[46-48] Several descriptions of aluminum and gallium complexes with Curcumin as ligands was found in the literature.[49-51, 52-54] However, there are just a few examples of Curcumin complexes of indium, tin, and lead.[54] For Groups 3–6, there are known examples of Y, La, Zr, V and Cr with a notable abundance of vanadyl species containing the V=O unit.[55-57] On the other hand, Curcumin complexes have also been reported for all metals in Groups 7–12 excepting osmium. Most papers have reported that copper Curcumin complexes,[59-61] followed by zinc,[62-64] nickel,[65] iron,[66,67] manganese[68,69] and ruthenium.[70,71] Even technetium complexes containing Curcumin were reported.[72] Curcumin complexes have also been prepared for lanthanides and actinides.[73-76] Beck et al. prepared some homoleptic Curcumin complexes.[77] $Pd(Curc)_2$ and $M(Me_2Curc)_2$ (M = Ni, Cu) were synthesized using metal(II) acetates.[78,79] Homoleptic $Fe(Cur)_3$

was synthesized by reacting $FeCl_3$ with 3 equivalents of NaCur which was generated in situ.[80] Owing to poor solubility of Curcumin in water, there is the requirement of an use of organic solvents for the purpose of dissolution. Solvents frequently employed in this regard are methanol, ethanol and acetone. The metals employed in the form of soluble salts that may be dissolved in water.[40-76] Using the standard synthetic approach, with or without certain modifications, majority of Curcumin complexes are easily obtained. The products are usually obtained as precipitates with yields being reasonably high.[56-66] The products typically have low crystallinity and are poorly soluble in water and in common organic solvents. Pyridine, dimethylformamide (DMF) and dimethylsulfoxide (DMSO) are among the very few extremely polar solvents in which several Curcumin complexes show substantial solubility.[40-45,50-69] Consequently, as of now there were little availability of X-ray diffraction investigations that characterize the structures of metal Curcumin complexes.[41-53] In the realm of rare-earth elements and middle and/or late-transition metals homoleptic Curcumin complexes of $M(Curc)_2$ and $M(Curc)_3$ types have gained considerable attention. Curcumin complexes with homoleptic transition metals or lanthanides are often characterized by their insoluble precipitates.[76] According to results, homoleptic transition metal complexes of Curcumin as the only ligand are difficult to crystallize.[76] This is likely due to the fact that metal ions may form polymeric arrays when they make a contact with free phenolic -OH groups. This may be overcome by two techniques. One by blocking the unbound phenolic –OH groups located at the 4-positions of the phenyl rings. To do this, phenolic –OH groups can be transformed into –OR, –OC(O)R, or –OC(O)OR (where R represents Me or Et) functions. Based on this idea copper(II) acetate was reacted with 2 equiv. of alkylated Curcumins which results in the formation of two homoleptic complexes e. g. $[Cu(Et_2Curc)_2(1,4\text{-dioxane})]$ (Et_2CurcH = 1,7-bis(4-ethoxy-3-methoxyphenyl)-1,6-heptadiene-3,5-dione) and $Cu(Bu_2Curc)_2$ (Bu_2Curc = 1,7-bis-(4-n-butoxy-3-methoxyphenyl)-1,6-heptadiene-3,5-dione).[59,81] Both complexes were

characterized by X-ray single crystal method. The second alternative involves creating heteroleptic complexes that incorporate appropriate "spectator ligands" alongside Curcumin. The likelihood of isolating soluble and crystallizable Curcumin complexes appears to be higher when there is just one Curcumin ligand present in these heteroleptic complexes. The spectator ligands that can be used alongside Curcumin to complete the coordination sphere of the metal ions includes pyridine, 2,2'-bipyridine, phenanthroline, terpyridine derivatives, tertiary phosphines, pentamethylcyclopentadienyl or p-cymene and cyclopentadiene. Some oxovandaium complexes were synthesized by A. R.Chakraborty et al. where amalgamation of Curcumin and nitrogen based spectator ligands were reported.[56,57] Even larger series of new Curcumin complexes was prepared starting from organo-transition metal halides, including $[(R_3P)MCl_2]_2$ (M = Pd, Pt; R = Et, ^{n}Bu, Ph, tolyl) $[(\eta^5\text{-}C_5Me_5)MCl_2]_2$(M = Rh, Ir), $[(\eta^6\text{-p-cymene})RuCl_2]_2$ (p-cymene = p-isopropyltoluene) and $[(\eta^3\text{-}C_3H_5)PdCl]_2$.[71-73,78] Hieu et al. produced metal–Curcumin complexes by mechanically combining metal chloride salts with Curcumin (in the ratio, 1:1 mole for Zn^{2+} and Curcumin, and 1:3 mole for Fe^{3+}) in a mortar until a uniform powder mixture was achieved. A solution consisting of propylene glycol and water in a 1:1 volume ratio was added to the mixture. This was then mechanically shaken and dried at a temperature of 60^0C to obtain powdered complexes of Curcumin.[82]

3.5 Medicinal properties of metal complexes of Curcumin

3.5.1 Antioxidant property:

Metal-Curcumin complexes have been referred to as having "multiple-anti" effects[58] meaning they possess many pharmacological activities, including antioxidant actions that are superior either to free Curcumin or free metal ions. Curcuminoids, including Curcumin and its metabolite tetrahydrocurcumin has antioxidant properties beneficial for a range of health issues.[17]

Multiple authors have discovered metallocomplexes of bioactive chemicals that possess an ability to boost antioxidant activity. An example of this would be evaluation of antioxidant capacity of several flavonoid complexes like that having quercetin, rutin, catechin and galangin coupled with Cu^{2+}, Fe^{2+}, Al^{3+} and Zn^{2+}.[35] These studies indicates metals have a considerable impact on the chemical characteristics of flavonoids because antioxidant activities of flavonoid complexes were much more effective than that of free flavonoids.[35] Curcumin is considered one of the most significant herbs with antioxidant qualities, particularly in terms of its economic value. It is believed to function as a phenolic chain-breaking antioxidant by donating hydrogen atoms from its phenolic group.[83] Furthermore, Curcumin can augment functions and quantities of antioxidant enzymes such as catalase, superoxide dismutase and glutathione peroxidase, while also suppressing production of free radicals.[84] As a result, there has been several preclinical and clinical experiments conducted to demonstrate its effectiveness. Studies have demonstrated supplementing with Curcumin in case of humans has a notable ability for antioxidant properties and that it helps in reducing levels of malondialdehyde (MDA).[85] There is a possibility that the presence of two phenolic groups, the enol form of the diketone moiety and the extended conjugated structure of Curcumin are factors that are responsible for the molecules' free radical reaction centers.[37] Barik *et al.* demonstrated that the antioxidant activity of Curcumin in the β-keto-enol form is greater than that of Curcumin in β-diketone form.[37] The redox state of the biological environment, the presence of metal ions and substituents on the side chain are three parameters that have an effect on the antioxidant activity of Curcumin.[38] Antioxidant activity of several complexes of Curcumin, its derivatives, including diacetylbisdemethoxycurcumin, diacetylcurcumin, demethoxycurcumin and bisdemethoxycurcumin was examined by Mohammadi *et.al.*[54] These were complexes of In^{3+}, Ga^{3+} and VO^{2+} where authors demonstrated that free aromatic ring hydroxyl groups were essential to bestow the complexes that were stated

to possess excellent antioxidant characteristics.[54] Metal-Curcumin complexes effectively regulate oxidative stress by addressing the imbalance between free radicals and antioxidant levels in the body. This is achieved by reduction of free radicals, enhancement of antioxidant levels or a combination of both mechanisms. Multiple studies have shown Curcumin based metal complexes have enhanced antioxidant capacity compared to free Curcumin alone.[82,86-88] Using Mn^{2+}, Mg^{2+}, Cu^{2+}, Ni^{2+} and Co^{2+} as metal ions in these complexes, Priya et al. investigated the antioxidant activity of Curcumin and its metal complexes demonstrating antioxidant activity of the complexes is equivalent to that of free Curcumin. In a different study, a number of divalent metal ions, such as Cu^{2+}, Fe^{2+}, Mn^{2+}, Mg^{2+}, B^{2+}, Se^{2+} and Zn^{2+} were selected for complex formation with Curcumin to assess antioxidant activity.[88] According to the findings of their investigation, metal-Curcumin complexes exhibited superior DPPH radical scavenging and ferrous reduction power activity in comparison to freely available Curcumin. Curcumin-capped gold nanoparticles and Curcumin-silver nanoparticles have also demonstrated exceptional antioxidant activity, as evidenced by the DPPH radical test.[89,90] Using either Zn^{2+} or Cu^{2+} as coordination complexes has a number of benefits, the most important of which are their low toxicity and a limited number of adverse effects.[91] Since zinc is able to prevent lipid peroxidation, it is a crucial component in the process of shielding cells from the damaging effects of oxidative stress.[92] Additionally, it was observed that antioxidant activity of Curcumin was increased when chelated with metals like Fe^{2+}, Mn^{2+} and Zn^{2+}.[86] Superoxide dismutase, is an enzyme that plays a significant role in the process of scavenging reactive oxygen species (ROS). It accomplishes this by converting superoxide into hydrogen peroxide and oxygen, which are both less hazardous.[93] In this particular scenario, complex formation of Curcumin with Cu^{2+} leads to an increase in lipid peroxidation that was six times higher and increase in SOD activity that was ten times higher.[37] A study conducted on animals has discovered that introduction of a Zn^{2+}–Curcumin complex

effectively restores the reduced functionality of antioxidant enzymes and elevates the level of MDA induced by cold-restraint stress.[94] Fe^{2+}–Curcumin not only maintained antioxidant enzyme activity after chelation but also enhanced the antioxidant activity of Curcumin.[95] Therefore, this intricate compound has the capability to function as a medicinal agent by diminishing oxidation.

3.5.2 Anticancer property:

In vitro and *in vivo* assessments of anticancer potential of numerous metal complexes have been conducted in the past few decades. Several metal complexes with anticancer properties having metals like Pt, Au, As, Ru, Rh, Cu, V, Co, Mn, Gd and Mo, have been shown to interact with or alter cellular redox equilibrium, leading to increased oxidative stress.[96] Nevertheless, several metal-complexed anticancer drugs such as platinum compounds possess several drawbacks as a result of severe adverse effects, that includes the well-known toxicity to liver and kidneys often associated with heavy metals.[97] In order to address this issue, several researchers have directed their attention towards metal-containing pharmaceuticals derived from non-platinum natural products. Curcumin and its derivatives also exhibit anti-cancer properties against several forms of cancer that are melanoma, head and neck, breast, colon, pancreatic, genitourinary, gastrointestinal, lung, prostate, and ovarian in nature.[98] Multiple research conducted by various authors have shown that Curcumin effectively inhibits the growth and spread of cancer cells, that it suppresses formation of new blood vessels that support tumor growth (angiogenesis) and triggers cell death and apoptosis.[99-102] Consequently, directing efforts towards inhibiting angiogenesis might be an effective approach for cancer treatment.[100]

A study showed Curcumin-capped copper nanoparticles effectively suppress the growth of MDA-MB-231 human breast cancer cells and angiogenesis.[103] Another study showed when Cu^{2+} was complexed with Curcumin it enhanced therapeutic efficacy against both primary and

metastatic breast cancer. This was achieved by enhancing the stability of Curcumin, thus facilitating apoptosis and suppressing proliferation and angiogenesis.[104] Cu^{2+}–Curcumin also caused DNA photocleavage, photocytotoxicity and cellular localization in HeLa and MCF-7 cancer cells and demonstrated significant photocytotoxicity with little toxicity in the absence of light, resulting in notable photodynamic effects.[105] In yet another study, it was found Copper chelates of synthetic curcuminoids possessed improved ability to inhibit tumor growth. Additionally, it demonstrated efficacy in prolonging the lifespan of animals with ascites tumors and resulted in a reduction in the size of solid tumors in mice.[106] Cu^{2+}–Curcumin enclosed within liposomes resulted in enhancement of anticancer efficacy in an animal model of triple negative breast cancer.[107] This improvement was observed without any detrimental side effects. Therefore, Cu^{2+} complexes of Curcumin improve the transportation of drugs and boost the effectiveness of Curcumin in therapy. Copper complexes of Curcumin were shown to be more cytotoxic than iron complexes of Curcumin.[9] This was seen in the context of increased cytotoxic effects of Fe^{3+}-Curcumin and Cu^{2+}-Curcumin complexes on breast cancer cells like MCF-7, MDA-MB-231 and 4T1. Further investigation showed cytotoxicity of Curcumin was notably enhanced when it formed metal complexes with Cu^{2+}, Zn^{2+}, oxovanadium (VO^{4+}) and Ni^{2+} in comparison to when it was in its unbound form. Activity of metal complexes that were investigated could be ranked in the following order $Cu^{2+} > VO^{4+} > Ni^{2+} > Zn^{2+}$.[108] This study also examined protective effects of Curcumin complexed with Cu^{2+} and Zn^{2+} against H_2O_2-induced damage in PC12 cells.

Another study showed that a compound containing zinc (ZnO-3-mercaptopropionic acid–curcumin) effectively enhanced the solubility and transportation of Curcumin. Furthermore, this compound demonstrated a higher level of toxicity against breast cancer cells in comparison to unbound Curcumin.[109] Zn^{2+}–Curcumin complexes were observed to cause cytotoxicity in prostate cancer and neuroblastoma cell lines.[110] Studies have shown complexes formed between

Zn^{2+} and Curcumin could enhance mitochondrion-mediated apoptosis in a synergistic manner.[111] Zn^{2+}–Curcumin complexes not only decrease survival of cancer cells but also intensify cellular response to therapeutic medications like that due to doxorubicin, both in case of laboratory experiments and in living organisms. Evidence demonstrates that once internalized into cells, this compound undergoes degradation subsequently releasing Curcumin and Zn^{2+} ions.[112] Zn^{2+}–Curcumin combination caused structural alterations in mutated tumour protein 53 or p53 proteins (R175H and R273H) and reinstated the ability to induce programmed cell death in cancer cells. The intricate compound successfully penetrated the blood-tumor barrier and targeted the glioblastoma tissues in a mouse model resulting in regression of tumor development.[113]

Ni^{2+}–Curcumin complexes show anticancer properties in several cancer cells such as human cervical and lung carcinoma cells, mostly through cell cycle arrest, generation of reactive oxygen species (ROS) and disruption of mitochondrial membrane potential.[114]

The vanadium combination with Curcumin enhances therapeutic effectiveness of Curcumin. Furthermore, the compound has significant photodynamic treatment impact on HeLa and MCF-7 cancer cells under visible light while exhibiting lower toxicity in the absence of light.[115] In addition to HeLa cells, oxovanadium(IV)–Curcumin complexes demonstrate photocytotoxicity in hepatic Hep G2 cancer cells when exposed to visible light. This compound enhances the absorption of Curcumin by cancer cells leading to the production of reactive oxygen species when exposed to light and ultimately to programmed cell death of cancer cells.[116]

A Curcumin-manganese complex was synthesized and tested for its ability to inhibit cell growth in various cancer cell lines, including human osteosarcoma cells (HOS), human colon cancer cells (HT 29), human melanoma cells (A375) and human fibroblast cells (NHDF). The results demonstrate that the manganese complex had a notable impact on reducing IC_{50} for all

malignant cell lines tested in comparison to that due to curcumin alone; the effect being particularly pronounced for HOS and A375 cell lines.[117]

Several researchers have also explored possible anti-cancer properties of Pd^{2+} complexes due to their structural resemblance to Pt^{2+} complexes. Their studies have shown complexes have cytotoxic effects on tumor cells.[118,119] In general, Pd^{2+} complexes exhibit reduced anticancer efficacy compared to cisplatin because of their greater chemical reactivity.[120] Valentini et al. assessed the effectiveness of Pd^{2+} complexes of Curcumin in inhibiting cell growth, producing reactive oxygen species (ROS), activating C-Jun-N-Terminl Kinase (JNK) and inducing cell death by causing mitochondrial membrane depolarization.[121]

Studies with Co^{3+}–Curcumin complex demonstrated greater efficacy against cancer compared to unbound Curcumin. A study revealed binding of Co^{3+} with Curcumin improves resistance of Curcumin to hydrolysis and leads to an increased absorption by cells; it also shows increased cytotoxicity during exposure to light. Additionally, it has a notable photodynamic therapeutic impact under visible light conditions on MCF-7 cells, but its toxicity is significantly reduced in the absence of light. Studies have shown Curcumin, when released, functions as a phototoxin by generating intracellular reactive oxygen species (ROS), which leads to death of cancer cells.[122] Co^{3+}–Curcumin complexes have also been used to transport both metal ions and Curcumin to hypoxic tumor cells due to their high cellular absorption and function as cytotoxins.[110]

Ru^{2+}–Curcumin complexes have demonstrated cytotoxicity in several cancer cell lines at low doses.[123] A combination of Ru^{2+}–polypyridyl with Curcumin has exhibited superior antiproliferative activity and cytotoxicity against different cancer cells compared to curcumin or cisplatin alone. This compound induces apoptosis in cancer cells by interacting with DNA and blocking MEK/ERK signaling.[124] A Curcumin-containing ruthenium(II)–letrozole combination

induced cancer cell death perhaps by triggering autophagy.[125] Studies have demonstrated that another Ru^{2+}–Curcumin complex is more effective in inducing apoptosis than free Curcumin in colon cancer cells. This enhanced effect is achieved via inhibiting proteasomes. This Ru^{2+}–Curcumin combination exhibits superior suppression of isolated proteasomal activity compared to free curcumin.[126] In order to enhance anticancer properties of Ru^{2+}–Curcumin complexes, a modified form of Curcumin (where -OH groups in Curcumin were substituted by OCH_3) was employed. Anticancer activity of such a Ru^{2+} complex was shown to be superior to that of free Curcumin.[127]

3.5.3 Antimicrobial activity:

Curcumin demonstrates antimicrobial activity against a wide range of microbes, including various pathogenic gram-positive bacteria like *Bacillus cereus, Bacillus subtilis, Staphylococcus aureus, Streptococcus mutans, Staphylococcus epidermidis* and gram-negative bacteria like *Escherichia coli, Pseudomonas aeruginosa, Yersinia enterocolitica, and Shigella dysenteriae*. It is effective on fungi such as *Aspergillus níger, Candida albicans, and Penicillium notatum,* as well as on molds;[128] exhibiting a notably greater effectiveness on gram-positive bacteria than on gram-negative bacteria. The outer membrane of gram-negative bacteria contains hydrophilic lipo-polysaccharides which serve as a barrier against penetration of hydrophobic antimicrobial compounds.[129] Studies have demonstrated that Curcumin can effectively prevent the formation of biofilm in case of *Enterococcus faecalis* on tooth substrates *in vitro*. Additionally, Curcumin has been found to enhance antimicrobial effects of several drugs including gentamicin, cefixime, ciprofloxacin, cefepime, vancomycin, tetracycline and amikacin against *S. aureus*. Although there has been significant research on Curcumin precise mechanisms of its antimicrobial action can be thought to be due to disruption of cell membranes by inhibiting

ATPase activity, inhibiting bacterial cell proliferation by affecting the assembly of FtsZ protein in the Z-ring, permeabilization of membranes, production of reactive oxygen species (ROS) and depletion of antioxidants, interference with biofilm formation etc.[130-134] Properties of metal ions are crucial in influencing antimicrobial effects of Curcumin. Throughout history, various metal ions like mercury, arsenic, copper and silver have been valued for their ability to combat microbes.[135] Many among them belonging to the d-block of the periodic table (such as V, Ti, Cr, Co, Ni, Cu, Zn, Tb, W, Ag, Cd, Au, and Hg) possess antimicrobial properties. Additionally, some metal ions from groups 13-16, like Al, Ga, Ge, As, Se, Sn, Sb, Te, Pb and Bi also exhibit antimicrobial activity.[136] Antimicrobial efficacy of Curcumin with Cr^{3+}, Pd^{2+}, Y^{3+}, La^{3+}, Ce^{3+} and Eu^{3+} was assessed revealing Cr^{3+}, Pd^{2+} and Y^{3+} had antibacterial properties against *E. Coli*, *Klebsiella pneumonia* and *Pseudomonas sp*.[137] Antibacterial activity against *S. Pyogenes, S. aureus* and *E. coli* followed the order $Cu^{2+} > Ni^{2+} > Co^{2+}$ when bound to a Schiff base ligand.[138] However, for *P. aeruginosa* and *K. pneumoniae* order of activity was $Cu^{2+} > Co^{2+} > Ni^{2+}$ when bound to the same Schiff base ligand.[138] Furthermore, these compounds demonstrated anthelmintic efficacy against *Pheretima posthuma*.[138]

A Cu^{2+}–Curcumin complex demonstrated beneficial microbicidal action making it a potential candidate for the development of a vaginal microbicidal gel that could combat viral infections.[139] A separate investigation demonstrated Cu^{2+}–Curcumin complexes exhibit greater growth inhibition of *P. aeruginosa* in comparison to free Curcumin. (minimum inhibitory concentration of Cu^{2+}–Curcumin complexes and free Curcumin were 62.5 and 125 μg/mL respectively). In addition, the complexes formed between Cu^{2+} and Curcumin at a concentration of 62.5 μg/mL inhibited development of bacterial cells.[140]

A Co^{2+}-Curcumin, synthesised by Hatamie et al., increased antibacterial activity when compared to Curcumin alone.[141]

A compound formed by the binding of Zn^{2+} and Curcumin was shown to have significant toxicity against *P. aeruginosa*.[142] Furthermore, a combination of Curcumin complex and chitin glucan-zinc nanomaterial exhibited remarkable antibacterial efficacy.[143]

A Ru^{2+}–Curcumin complex demonstrates antibacterial properties, specifically against drug-resistant Gram-positive *S. aureus* bacteria. This compound exhibits potent inhibitory effect and demonstrats great specificity against a diverse range of methicillin and vancomycin resistant *S. aureus* strains.[144] Furthermore, it resulted in a reduction in average bacterial numbers in a mouse model of *Staphylococcus* infection when compared to vancomycin. These data suggest Ru^{2+}–Curcumin combination has strong antibacterial properties under both laboratory and live organism settings.[144,145]

A combination of silver nanoparticles with Curcumin demonstrated both excellent solubility in water and enhanced antibacterial properties. This compound demonstrated the capacity to prevent bacterial infections on wound sites.[90] Metal-Curcumin complexes not only have antimicrobial actions but they also prevent the production of bacterial biofilms. A research conducted to assess the possible inhibitory impact of an oxo-vanadium–Curcumin combination on bacterial biofilm formation demonstrated inhibition of biofilms that were associated with Gram positive bacteria *S. aureus* and Gram negative *E. coli*. This inhibition was shown to be positively connected with suppression of bacterial alkaline phosphatase activity as indicated by *in silico* experiments.[146]

Further investigation showed a complex formed by Cu^{2+} and Curcumin, when present at a concentration of 1/4 of minimum inhibitory concentration , effectively suppressed the development of biofilms. One of the Curcumin-ruthenium compound demonstrated strong antibiofilm action in comparison to several medicines licensed by FDA.[144] Furthermore, Zn^{2+}–Curcumin combination demonstrated effectiveness in inhibiting biofilm formation.[142] Findings of

these various forms of research suggest Curcumin-metal complexes have antimicrobial effects through the generation of toxicity, reducing growth and being able to limit the development of biofilms.

References

1. M. Moustakas; The role of metal ions in biology biochemistry and medicine. *Materials*, **2021**, *14*, 549.
2. D. Buccella, M. H. Lim, and J. R. Morrow; Metals in Biology: From Metallomics to Trafficking *Inorganic Chemistry*, **2019** , 58 , 13505-13508.
3. Robert R. Crichton, Ricardo O. Louro; Practical Approaches to Biological Inorganic Chemistry (Second Edition), *Elsevier*, **2020**, 1-16.
4. C. Orvig, M.J Abrams; Medicinal inorganic chemistry: introduction. *Chem Rev.*, **1999**, 99, 2201–2204.
5. M. Yaman, G. Kaya, H. Yekeler ; Distribution of trace metal concentrations in paired cancerous and non-cancerous human stomach tissues. *World J Gastroenterol*, **2007**, 13, 612–618.
6. A. A Warra; Transition metal complexes and their application in drugs and cosmetics – A Review. *J Chem Pharm Res.*, **2011**, 3, 951-958.
7. M. Frezza, S. Hindo, D Chen, et al.; Novel metals and metal complexes as platforms for cancer therapy. *Curr Pharm Des*, **2010**, 16, 1813–1825.

8. Y.K Yan, M. Melchart, A. Habtemariam, P.J Sadler; Organometallic chemistry, biology and medicine: ruthenium arene anticancer complexes. *Chem Commun*, 2005,14, 4764-4776.

9. S. Wanninger, V. Lorenz, A. Subhan, and F. T. Edelmann; Metal complexes of curcumin—synthetic strategies, structures and medicinal applications. *Chem. Soc. Rev*. **2015**, 44, 4986 – 5002.

10. J. Joseph, K. Nagashri, G. A. B. Rani; Synthesis, characterization and antimicrobial activities of copper complexes derived from 4-aminoantipyrine derivatives. *J. Saudi Chem. Soc.,* **2013**,17, 285–294.

11. U. Ndagi, N. Mhlongo, M. E. Soliman; Metal complexes in cancer therapy—an update from drug design perspective. *Drug Des. Devel. Ther*.,**2017**,11, 599–616.

12. H. Pasdar, B. H. Saghavaz, N. Foroughifar, and M. Davallo; Synthesis, characterization and antibacterial activity of novel 1,3-diethyl-1,3-bis(4-nitrophenyl)urea and its metal(II) complexes. *Molecules*, **2017**, 22, 2125

13. B. de Las Heras, A. Amesty, A. Estevez-Braun, and S. Hortelano; Metal complexes of natural product like-compounds with antitumoral activity. *Anticancer Agents Med. Chem.* **2018**

14. S.C. Gupta, B. Sung, J.H. Kim, S. Prasad, S. Li, B.B. Aggarwal; Multitargeting by turmeric, the golden spice: From kitchen to clinic. *Mol. Nutr. Food Res.* **2013**, 57, 1510–1528.

15. A.B. Kunnumakkara, D. Bordoloi, G. Padmavathi, J. Monisha, N.K. Roy, S. Prasad, B.B. Aggarwal; Curcumin, the golden nutraceutical: Multitargeting for multiple chronic diseases. *Br. J. Pharmacol.* **2017**, 174, 1325–1348.

16. S. Prasad, S.C. Gupta, A.K. Tyagi, B.B. Aggarwal; Curcumin, a component of golden spice: From bedside to bench and back. *Biotechnol. Adv.* **2014**, 32, 1053–1064.

17. B.B. Aggarwal, L. Deb, S. Prasad; Curcumin differs from tetrahydrocurcumin for molecular targets, signaling pathways and cellular responses. *Molecules,* **2015,** 20, 185–205.

18. K.I. Priyadarsini; The chemistry of curcumin: From extraction to therapeutic agent. *Molecules*, **2014**, 19, 20091–20112.

19. M. Salem, S. Rohani, E.R. Gillies; Curcumin, a promising anti-cancer therapeutic: A review of its chemical properties, bioactivity and approaches to cancer cell delivery. *RSC Adv*. **2014**, 4, 10815–10829.

20. A. Shakeri, A. F. G. Cicero, Y. Panahi, M. Mohajeri, A. Sahebkar; Curcumin: a naturally occurring autophagy modulator. *J. Cell. Physiol.* **2019**, 234, 5643–5654.

21. Y. J. Wang, M. H. Pan, A.L. Cheng, L.I. Lin, Y.S. Ho, C.Y. Hsieh, J.K. Lin; Stability of Curcumin in buffer solutions and characterization of its degradation products. *Jour. Pharm. Biomed. Anal.* **1997,** 15, 1867−1876.

22. R. Jagannathan, P.M. Abraham, P. Poddar; Temperature dependent spectroscopic evidences of Curcumin in aqueous medium: A mechanistic study of its solubility and stability. *Jour. Phys. Chem. B,* **2012,** 116, 14533−14540.

23. K. I. Priyadarsini; Photophysics, photochemistry and photobiology of Curcumin: Studies from organic solutions, bio-mimetics and living cells. *Jour. Photochem. Photobiol., C,* **2009,** 10, 81−95.

24. M. Griesser, V. Pistis, T. Suzuki, N. Tejera, D. A. Pratt, C. Schneider; Autoxidative and cyclooxygenase-2 catalyzed transformation of the dietary chemopreventive agent Curcumin. *Jour. Biol.Chem.*, **2011,** 286, 1114−1124.

25. O. N. Gordon, C. Schneider; Vanillin and ferulic acid: Not the major degradation products of Curcumin. *Trends Mol. Med.*, **2012,** 18, 361−363.

26. C. Schneider, O. N. Gordon, R. L. Edwards, P. B. Luis; Degradation of Curcumin: From mechanism to biological implications. *Jour. Agric. Food Chem.*, **2015,** 63, 7606−7614.

27. A. Khurana, C. T. Ho; High-performance liquid-chromatographic analysis of Curcuminoids and their photo-oxidative decomposition compounds in Curcuma longa l. *Jour. Liq. Chromatogr.*, **1988,** 11, 2295−2304.

28. S. Gupta, S. Prasad, H. K. Ji, S. Patchva, L. J. Webb, K. I. Priyadarsini, B. B. Aggarwal; Multitargeting by Curcumin as revealed by molecular interaction studies. *Nat. Prod. Rep.*, **2011**, 28, 1937–1955.

29. S. Banerjee, A.R. Chakravarty; Metal complexes of curcumin for cellular imaging, targeting, and photoinduced anticancer activity. *Acc Chem Res.* **2015**, 48, 2075-83.

30. S. Prasad, D. DuBourdieu, A. Srivastava, P. Kumar, R. Lall; Metal-Curcumin Complexes in Therapeutics: An Approach to Enhance Pharmacological Effects of Curcumin. *Int J Mol Sci*. **2021**, 22,7094.

31. T. Sarakar, S. Banerjee, A. Hussain; Remarkable visible light-triggered cytotoxicity of mitochondria targeting mixed-ligand cobalt(III) complexes of curcumin and phenanthroline bases binding to human serum albumin, *RSC Advances*,**2015**,22.

32. R. Sareen, N. Jain, and K. L. Dhar; Curcumin-Zn(II) complex for enhanced solubility and stability: an approach for improved delivery and pharmacodynamic effects. *Pharm. Dev. Technol.* **2016,** 21, 630–635.

33. R. Pallikkavil, M. B. Ummathur, S. Sreedharan, and K. Krishnankutty; Synthesis, characterization and antimicrobial studies of Cd (II), Hg (II), Pb (II), Sn (II) and Ca (II) complexes of curcumin. *Main Group Metal Chem.* **2013**, 36, 123–127.

34. M. Subhan, K. Alam, M. Rahaman, M. Awal; Synthesis and characterization of metal complexes containing curcumin ($C_{21}H_{20}O_6$) and study of their anti-microbial activities and DNA binding properties. *J. Sci. Res.* **2014**, 6, 97–109.

35. R. F. de Souza, W. F. De Giovani; Antioxidant properties of complexes of flavonoids with metal ions. Redox Rep.: *Commun. Free Rad. Res*. **2004** , 9, 97–104.

36. J. Daisy, Reactive centers of curcumin and the possible role of metal complexes of curcumin as antioxidants. *Univ. J. Phys. Appl.* **2015**, 9, 6–16.

37. A. Barik, B. Mishra, L. Shen, H. Mohan, R. M. Kadam, et al.; Evaluation of a new copper(II)–curcumin complex as superoxide dismutase mimic and its free radical reactions. *Free Rad. Biol. Med.* **2005,** 39, 811–822.

38. S. Dutta, A. Murugkar, N. Gandhe, S. Padhye; Enhanced antioxidant activities of metal conjugates of curcumin derivatives. *Metal-Based Drugs,* **2001**, 8, 183–188.

39. K. Mitra, S. Gautam, P. Kondaiah, and A. R. Chakravarty; Platinum (II) complexes of curcumin showing photocytotoxicity in visible light. *Eur. J. Inorg. Chem.* **2017**, 1753–1763.

40. A. Sahebkar, M. C. Serban, S. Ursoniu, M. Banach; Effect of curcuminoids on oxidative stress: a systematic review and meta-analysis of randomized controlled trials. *J. Funct. Foods.* **2015**,18, 898–909.

41. S. Vellampatti, G. Chandrasekaran, S.B. Mitta, V.K. Lakshmanan, S.H. Park, Metallo-curcumin-conjugated DNA complexes induces preferential prostate cancer cells cytotoxicity and pause growth of bacterial cells. *Sci. Rep*. **2018**, 8, 14929–14939.

42. M. I. Khalil, A. M. Al-Zahem, M.H. Al-Qunaibit; Synthesis, characterization, mössbauer parameters, and antitumor activity of Fe(III) curcumin complex. *Bioinorg. Chem. Appl*. **2013**, 2013, 982423.

43. A. Barik, B. Mishra, A. Kunwar, R.M. Kadam, L. Shen, S. Dutta, S. Padhye, A.K. Satpati, H.Y. Zhang, K. I. Priyadarsini; Comparative study of Copper(II)-curcumin complexes as superoxide dismutase mimics and free radical scavengers. *Eur. J. Med. Chem.* **2007**, 42, 431–439.

44. M. H. M. Leung, T. Harada, T .W. Kee; Delivery of curcumin and medicinal effects of the Copper(II)-curcumin complexes. *Curr. Pharm. Des.* **2013**, 19.

45. O. Vajragupta, P. Boonchoong, H. Watanabe, M. Tohda, N. Kummasud, Y. Sumanont; Manganese complexes of curcumin and its derivatives: Evaluation for the radical scavenging ability and neuroprotective activity. *Free Rad. Biol. Med.* **2003**, 35, 1632–1644.

46. M. R. Hayes, and J. Metcalfe. ;The boron-curcumin complex in the determination of trace amounts of boron. *Analyst*. **1962**, 87.1041, 956-969.

47. D. W. Dyrssen, Y. P. Novikov, & L. R. Uppström.; Studies on the chemistry of the determination of boron with curcumin. *Analytica Chimica Acta*, **1972** , *60*(1), 139-151.

48. Z. Sui, R. Salto, J. Li, C. Craik and P. R. Ortiz de Montellano.; Inhibition of the HIV-1 and HIV-2 proteases by curcumin and curcumin boron complexesBioorg. *Med. Chem.*, **1993**, 1, 415–422.

49. T. Jiang, G.-R. Zhou, Y.-H. Zhang, P.-C. Sun, Q.-M. Du and P. Zhou.; Effect of Al(III) and Curcumin on silk fibroin conformation and aggregation morphology, *RSC Adv.*, **2012**, 2,9106–9113.

50. T. Jiang, L. Wang, S. Zhang, P.-C. Sun, C.-F. Ding, Y.-Q. Chu and P. Zhou.; Interaction of curcumin with Al(III) and its complex structures based on experiments and theoretical calculations, *J. Mol. Struct.*, **2014**, 1004, 163–173.

51. F. Ahmadi, A. A. Alizadeh, N. Shahabadi and M. R. Nasrabadi.; Study binding of Al–curcumin complex to ds-DNA, monitoring by multispectroscopic and voltammetric techniques, *Spectrochim. Acta, Part A*, **2011**, 79, 1466–1474.

52. E. Ferrari, R. Benassi, S. Sacchi, F. Pignedoli, M. Asti and M. Saladini.; Curcumin derivatives as metal-chelating agents with potential multifunctional activity for pharmaceutical applications. *Jour. Inorg. Biochem*., **2014**, 139, 38–48.

53. M. Asti, E. Ferrari, S. Croci, G. Atti, S. Rubagotti, M. Iori, P. C. Capponi, A. Zerbini, M. Saladini and A. Versari, Synthesis and characterization of (68)Ga-labeled curcumin and curcuminoid complexes as potential radiotracers for imaging of cancer and Alzheimer's disease. *Inorg. Chem.*, **2014**, 53, 4922–4933.

54. K. Mohammadi, K. H. Thompson, B. O. Patrick, T. Storr, C. Martins, E. Polishchuk, V. G. Yuen, J. H. McNeill and C. Orvig, Synthesis and characterization of dual function vanadyl, gallium and indium curcumin complexes for medicinal applications. *J. Inorg. Biochem*., **2005**, 99, 2217–2225.

55. K. H. Thompson, K. B¨ohmerle, E. Polishchuk, C. Martins, P. Toleikis, J. Tse, V. Yuen, J. H. McNeill and C. Orvig.; Complementary inhibition of synoviocyte, smooth muscle cell or mouse lymphoma cell proliferation by a vanadyl curcumin complex compared to curcumin alone. *Jour. Inorg. Biochem*., **2004**, 98, 2063–2070.

56. B. Balaji, B. Balakrishnan, S. Perumalla, A. A. Karande and A. R. Chakravarty.; Photoactivated cytotoxicity of ferrocenyl-terpyridine oxovanadium(IV) complexes of curcuminoids. *Eur. J. Med. Chem*., **2014**, 85, 458–467.

57. B. Banik, K. Somyajit, G. Nagaraju and A. R. Chakravarty.; Oxovanadium(IV) complexes of curcumin for cellular imaging and mitochondria targeted photocytotoxicity. *Dalton Trans.*, **2014**, 43, 13358–13369.

58. M. S. Refat ; Synthesis and characterization of ligational behavior of curcumin drug towards some transition metal ions: Chelation effect on their thermal stability and biological activity. *Spectrochimica Acta Part A: Molecular and Biomolecular Spectroscopy*, **2013**, 105, 326-337

59. J. Wang, D. Wei, B. Jiang, *et al.* Two copper(II) complexes of curcumin derivatives: synthesis, crystal structure and in vitro antitumor activity. *Transition Met Chem.* **2014**,39, 553–558.

60. T. K. Goswami, S. Gadadhar, B. Gole, A. A. Karande, A. R. Chakravarty.; Photocytotoxicity of copper(II) complexes of curcumin and N-ferrocenylmethyl-l-amino acids. *Euro. Jour. of Med. Chem.*, **2013,** 63, 800-810.

61. A. Barik , B. Mishra, A. Kunwar , R.M. Kadam, L. Shen, S. Dutta, S. Padhye, A.K. Satpati, H.Y. Zhang, and K.I. Priyadarsini.; Comparative study of copper (II)–curcumin complexes as superoxide dismutase mimics and free radical scavengers. *European journal of medicinal chemistry*, **2007**, *42*, 431-439.

62. D. Pucci, T. Bellini, A. Crispini, I. D'Agnano, P. F. Liguori, P. Garcia-Ordun˜a, S. Pirillo, A. Valentini and G. Zanchetta, DNA binding and cytotoxicity of fluorescent curcumin-based Zn(II) complexes. *Med. Chem. Commun.*, **2012**, 3, 462.

63. D. Pucci, A. Crispini, B. Sanz Mendiguch´ıa, S. Pirillo, M. Ghedini, S. Morelli and L. De Bartolo,Improving the bioactivity of Zn(II)-curcumin based complexes. *Dalton Trans.*, **2013**, 42, 9679–9687.

64. M. I. Khalil, M. M. Al-Qunaibit, A. M. Al-zahem and J. P. Labis, Synthesis and characterization of ZnO nanoparticles by thermal decomposition of a curcumin zinc complex. *Arabian J. Chem.*, **2014**, 7, 1178–1184.

65. S. S. Nawaz, K.B. Manjunatha, S. Ranganatha, S. Supriya, Prabhat Ranjan, T. Chakraborty, D. Ramakrishna, Nickel curcumin complexes: Physico chemical studies and nonlinear optical activity, *Optical Materials*, **2023**, 136, 113450

66. N. Bicer, E. Yildiz, A.A. Yegani, and F. Aksu.; Synthesis of curcumin complexes with iron (III) and manganese (II), and effects of curcumin–iron (III) on Alzheimer's disease. *New Journal of Chemistry*, **2018**. 42, 8098-8104.

67. N.E. Rainey, A. Moustapha, A. Saric, *et al.* Iron chelation by curcumin suppresses both curcumin-induced autophagy and cell death together with iron overload neoplastic transformation. *Cell Death Discov.* **2019**, 5, 150.

68. Y. Sumanont, Y. Murakami, M. Tohda, O. Vajragupta, H. Watanabe, & K. Matsumoto, Effects of manganese complexes of curcumin and diacetylcurcumin on kainic acid induced neurotoxic responses in the rat hippocampus. *Biological and Pharmaceutical Bulletin*, **2007**, 30, 1732-1739.

69. O. Vajragupta, P. Boonchoong, H. Watanabe, M. Tohda, N. Kummasud, Y.Sumanont.; Manganese complexes of curcumin and its derivatives: evaluation for the radical scavenging ability and neuroprotective activity, *Free Radical Biology and Medicine*, **2003**, 35, 1632-1644.

70. R. Pettinari, F. Marchetti, F. Condello, C. Pettinari, G. Lupidi, R. Scopelliti, S. Mukhopadhyay, T. Riedel and P.J. Dyson.; Ruthenium (II)–arene RAPTA type complexes containing curcumin and bisdemethoxycurcumin display potent and selective anticancer activity. *Organometallics*, **2014.** 33,3709-3715.

71. F. Caruso, M. Rossi, A. Benson, C. Opazo, D. Freedman, E. Monti, M.B. Gariboldi, J. Shaulky, F. Marchetti, R. Pettinari and C. Pettinari.; Ruthenium–arene complexes of curcumin: X-ray and density functional theory structure, synthesis, and spectroscopic

characterization, in vitro antitumor activity, and DNA docking studies of (p-cymene) Ru (curcuminato) chloro. *Journal of Medicinal Chemistry*, **2012**. 55, 1072-1081.

72. C. Triantis, T. Tsotakos, C. Tsoukalas, M. Sagnou, C. Raptopoulou, A. Terzis, V. Psycharis, M. Pelecanou, I. Pirmettis, and M. Papadopoulos; Synthesis and characterization of fac-$[M(CO)_3(P)(OO)]$ and cis-trans-$[M(CO)_2(P)_2(OO)]$ complexes (M=Re,^{99m}Tc) with acetylacetone and curcumin as OO donor bidentate ligands. *Inorganic Chemistry*, **2013**. 52,12995-13003.
73. S.S. Zhou, X. Xue, J.F. Wang, Y. Dong, B. Jiang, D. Wei, M.L. Wan, and Y. Jia.; Synthesis, optical properties and biological imaging of the rare earth complexes with curcumin and pyridine. *Journal of Materials Chemistry*, **2012**, 22, 22774-22780.
74. A. Hussain, K. Somyajit, B. Banik, S. Banerjee, G. Nagaraju and A.R. Chakravarty.; Enhancing the photocytotoxic potential of curcumin on terpyridyl lanthanide (III) complex formation. *Dalton transactions*, **2013**, 42,182-195.
75. Y.M. Song, J.P. Xu, L. Ding, Q. Hou, J.W. Liu and Z.L. Zhu.; Syntheses, characterization and biological activities of rare earth metal complexes with curcumin and 1, 10-phenanthroline-5, 6-dione. *Journal of inorganic biochemistry*, **2009**, 103, 396-400.
76. M.A. Subhan, K. Alam, M.S. Rahaman, M.A. Rahman, and R. Awal.; Synthesis and characterization of metal complexes containing curcumin ($C_{21}H_{20}O_6$) and study of their anti-microbial activities and DNA binding properties. *J. Sci. Res*, **2014**. 6, 97-109.
77. F. Kühlwein, K. Polborn and W. Beck.; Übergangsmetallkomplexe des Curcumins und seiner Derivate. *Z. Anorg. Allg. Chem.*, **1997**, 623, 1211–1219.
78. M.A. Rodrigues, J. N. Fernandes, R. Ruggiero, W. Guerra.; Palladium Complex Containing Curcumin as Ligand: Thermal and Spectral Characterization. *American Journal of Chemistry*,2012, 2, 157-159.

79. A. Valentini, F. Conforti, A. Crispini, A. De Martino, R. Condello, C. Stellitano, G. Rotilio, M. Ghedini, G. Federici, S. Bernardini, D. Pucci.; Synthesis, oxidant properties, and antitumoral effects of a heteroleptic palladium (II) complex of curcumin on human prostate cancer cells. *Journal of medicinal chemistry*, **2009**, 52, 484-491.

80. T. Q. Huie , D. T. T. Thao , Enhancing the solubility of curcumin metal complexes and investigating some of their biological activities. Jour. of Chem., 2019,8082195

81. Z. Pi, J. Wang, B. Jiang, G. Cheng, S. Zhou, A curcumin-based TPA four-branched copper(II) complex probe for in vivo early tumor detection, *Materials Science and Engineering: C*, 2015, 46, 565-571.

82. T.Q. Hieu, D.T.T. Thao.; Enhancing the solubility of curcumin metal complexes and investigating some of their biological activities. *J. Chem.* **2019**, 1–9.

83. L.R.C. Barclay, M.R. Vinqvist, K. Mukai, H. Goto, Y. Hashimoto, A. Tokunaga, H. Uno.; On the antioxidant mechanism of curcumin: Classical methods are needed to determine antioxidant mechanism and activity. *Org. Lett.* **2000**, 2, 2841–2843.

84. N. Gupta, K. Verma, S. Nalla, A. Kulshreshtha, R. Lall, S. Prasad.; Free radicals as a double-edged sword: The cancer preventive and therapeutic roles of curcumin. *Molecules*, **2020**, 25, 5390.

85. K. Jakubczyk, A. Druüzga, J. Katarzyna, K. Skonieczna-zydecka.; Antioxidant potential of curcumin—A meta-analysis of randomized clinical trials. *Antioxidants*, **2020**, 9, 1092.

86. C.P.V. Mary, S. Vijayakumar, R. Shankar.; Metal chelating ability and antioxidant properties of curcumin–metal complexes—A DFT approach. *J. Mol. Gr. Modell.* **2018**, 79, 1–14.

87. R.S. Priya, S. Balachandran, J. Daisy, P.V. Mohanan.; Reactive centers of curcumin and the possible role of metal complexes of curcumin as antioxidants. *Univ. J. Phys. Appl.* **2015**, 9, 6–16.

88. A. Thakam, N. Saewan.; Antioxidant activities of curcumin–metal complexes. *Thail. J. Agric. Sci.* **2011**, 44, 188–193.

89. D. K. Singh, R. Jagannathan, P. Khandelwal, P.M. Abraham, P. Poddar.; In Situ synthesis and surface functionalization of gold nanoparticles with curcumin and their antioxidant properties: An experimental and density functional theory investigation. *Nanoscale,* **2013**, 5, 1882–1893.

90. Y. Lyu, M. Yu, Q. Liu, Q. Zhang, Z. Liu, Y. Tian, D. Li, M. Changdao.; Synthesis of silver nanoparticles using oxidized amylose and combination with curcumin for enhanced antibacterial activity. *Carbohydr. Polym.* **2020**, 230, 115573.

91. J. A. Drewry, and P. T. Gunning.; Recent advances in biosensory and medicinal therapeutic applications of zinc(II) and copper(II) coordination complexes. *Coord. Chem. Rev.*, **2011** 255, 459–472.

92. T. Ishida.; Anti-cancer effects of zinc (II) ion in tumor formation and growth, proliferation, metastasis and DNA damage. *Deg. Intellec. Develop. Disabilities*, **2017**, 1, 1–7.

93. A. M. Horspool, and H. C. Chang; Neuron-specific regulation of superoxide dismutase amid pathogen-induced gut dysbiosis. *Redox Biol*. **2018** 17, 377–385.

94. X. Mei, D. Xu, S. Xu, Y. Zheng, S. Xu; Gastroprotective and antidepressant effects of a New Zinc(II)-curcumin complex in rodent models of gastric ulcer and depression induced by stresses. *Pharmacol. Biochem. Behav*. **2011**, 99, 66–74.

95. A. Ahmed, M.N. Hasan, D Bagchi, H.M. Altass, M. Morad, R.S. Jassas, A.M. Hameed, J. Patwari, H. Alessa, A. Alharbi et al.; Combating essential metal toxicity: Key information from optical spectroscopy. *ACS Omega* **2020**, 5, 15666–15672.

96. U. Jungwirth, C. R. Kowol, B. K. Keppler, C. G. Hartinger, W. Berger et al. Anticancer activity of metal complexes: involvement of redox processes. *Antioxid. Redox Signal*. **2011**, 15, 1085–1127.

97. M. A. Jakupec, M. Galanski, and B. K. Keppler .; Tumour-inhibiting platinum complexes—state of the art and future perspectives. *Rev. Physiol. Biochem. Pharmacol*. **2003**, 146, 1–54.

98. H. Batra, S. Pawar, and D. Bahl.; Curcumin in combination with anticancer drugs: a nanomedicine review. *Pharmacol. Res*. **2019**, 139, 91–105.

99. H.T. Liu, and Y.S. Ho.; Anticancer effect of Curcumin on breast cancer and stem cells. *Food Sci. Human Wellness.* **2018**, 7, 134–137.

100. A. Shakeri, N. Ward, Y. Panahi, and A. Sahebkar.; Anti-angiogenic activity of curcumin in cancer therapy: a narrative review. *Curr. Vasc. Pharmacol.* **2019,** 17, 262–269.

101. B. Ricciuti, J. Foglietta, V. Bianconi, A. Sahebkar, and M. Pirro.; Enzymes involved in tumor-driven angiogenesis: a valuable target for anticancer therapy. *Semin. Cancer Biol*. **2017**,11, 005

102. B. Ricciuti, J. Foglietta, R. Chiari, A. Sahebkar, M. Banach et al.;Emerging enzymatic targets controlling angiogenesis in cancer: preclinical evidence and potential clinical applications. *Med. Oncol*. **2017**, 35, 4.

103. S. Kamble, B. Utage, P. Mogle, R. Kamble, S. Hese, et al.; Evaluation of Curcumin capped copper nanoparticles as possible inhibitors of human breast cancer cells and angiogenesis: a comparative study with native curcumin. *AAPS Pharm. Sci. Tech*., **2016** 17, 1030–1041.

104. S. Zhou, J. Li, J. Yu, Y. Wang, H. Liu, G. Lin, Z. He, Y. Wang.; Unique flower-like cur-metal complexes loaded liposomes for primary and metastatic breast cancer therapy. *Mater. Sci. Eng. C* **2021**, 121, 111835.

105. T.K. Goswami, S. Gadadhar, B. Gole, A.A. Karande, A.R. Chakravarty.; Photocytotoxicity of Copper(II) complexes of curcumin and N-Ferrocenylmethyl-l-amino acids. *Eur. J. Med. Chem.* **2013**, 63, 800–810.

106. V.D. John, G. Kuttan, K. Krishnankutty. ; Anti-tumour studies of metal chelates of synthetic curcuminoids. *J. Exp. Clin. Cancer Res.* **2002**, 21, 219–224.

107. K. Greish, V. Pittalà, S. Taurin, S. Taha, F. Bahman, A. Mathur, A. Jasim, F. Mohammed, I.M. El-Deeb, S. Fredericks, et al.; Curcumin–copper complex nanoparticles for the management of triple-negative breast cancer. *Nanomaterials* **2018**, 8, 884.

108. K. Krishnankutty, V. D. John.; Synthesis, characterization, and antitumour studies of metal chelates of some synthetic Curcuminoids. *Synth. React. Inorg. Metal-Organic Chem.* **2003**, 33, 343–358.

109. S.B. Ghaffari, M.H. Sarrafzadeh, Z. Fakhroueian, S. Shahriari, M.R. Khorramizadeh.; Functionalization of ZnO nanoparticles by 3- mercaptopropionic acid for aqueous curcumin delivery: Synthesis, characterization, and anticancer assessment. *Mater. Sci. Eng. C* **2017**, 79, 465–472.

110. S. Banerjee, A.R. Chakravarty.; Metal complexes of curcumin for cellular imaging, targeting, and photoinduced anticancer activity. *Acc. Chem. Res.* **2015**, 48, 2075–2083.

111. Q.P. Qin, Z.Z. Wei, Z.F. Wang, X.L. Huang, M.X. Tan, H.H. Zou, H. Liang.; Imaging and therapeutic applications of Zn(II)-cryptolepine-curcumin molecular probes in cell apoptosis detection and photodynamic therapy. *Chem. Commun.* **2020**, 56, 3999–4002.

112. R. Wu, X. Mei, Y. Ye, T. Xue, J. Wang, W. Sun, C. Lin, R. Xue, J. Zhang, D. Xu.; Zn(II)-curcumin solid dispersion impairs hepatocellular carcinoma growth and enhances chemotherapy by modulating gut microbiota-mediated zinc homeostasis. *Pharmacol. Res.* **2019**, 104454–104463.

113. A. Garufi, D. Trisciuoglio, M. Porru, C. Leonetti, A. Stoppacciaro, V. D'Orazi, M.L. Avantaggiati, A. Crispini, D. Pucci, G. D'Orazi.; A fluorescent curcumin-based Zn(II)-complex reactivates mutant (R175H and R273H) P53 in cancer cells. *J. Exp. Clin. Cancer Res.* **2013**, 32, 72–82.

114. A. Banaspati, M.K. Raza, T.K. Goswami.; Ni(II) curcumin complexes for cellular imaging and photo-triggered in vitro anticancer activity. *Eur. J. Med. Chem.* **2020**, 204, 112632.

115. U. Bhattacharyya, B. Kumar, A. Garai, A. Bhattacharyya, A. Kumar, S. Banerjee, P. Kondaiah, A.R. Chakravarty.; Curcumin "drug" stabilized in oxidovanadium(IV)-BODIPY conjugates for mitochondria-targeted photocytotoxicity. *Inorg. Chem.* **2017**, 56, 12457–12468.

116. B. Balaji, B. Balakrishnan, S. Perumalla, A.A. Karande, A.R. Chakravarty.; Photoactivated cytotoxicity of ferrocenyl-terpyridine oxovanadium(IV) complexes of curcuminoids. *Eur. J. Med. Chem.* **2014**, 85, 458–467.

117. B. A. Stoica, T. Petreus, O. Cioanca, and M. Hancianu.; ANtip- roliferative effects of a novel manganese mitochondrial targeted complex. *Farmacia*, **2015,** 63, 886–889.

118. R. Kontek, K. Matlawska-Wasowska, U. Kalinowska-Lis, B. Kontek, and J. Ochocki Evaluation of cytotoxicity of new trans-palladium(II) complex in human cells in vitro. *Acta Pol. Pharm.* **2011,** 68, 127–136.

119. N. C. Campanella, M. da Silva Demartini, C. Torres, E. T. de Almeida, and C. M. C. P. Gouvêa.; The cytotoxic and growth inhibitory effects of palladium(II) complexes on MDA-MB-435 cells. *Genetics Molecul. Biol.* **2012**, 35, 159–163.

120. M. Ž. Mijajlovic, M. V. Nikolic, V. V. Jevtic, Z. R. Ratkovic, B. S. Markovic et al. Cytotoxicity of palladium(II) complexes with some alkyl deri- vates of thiosalicylic acid. Crystal structure of the bis(S-butyl-thiosalicylate) palladium(II) complex, [Pd(S-bu-thiosal)2]. *Polyhedron*, **2015** , 90, 34–40.

121. A. Valentini, F. Conforti, A. Crispini, A. de Martino, R. Condello, C. Stellitano, G. Rotilio, M. Ghedini, G. Federici, S. Bernardini et al.; Synthesis, oxidant properties, and antitumoral effects of a heteroleptic palladium(II) complex of curcumin on human prostate cancer cells. *J. Med. Chem.* **2009**, 52, 484–491.

122. A. Garai, I. Pant, S. Banerjee, B. Banik, P. Kondaiah, A.R. Chakravarty.; Photorelease and cellular delivery of mitocurcumin from its cytotoxic Cobalt(III) complex in visible light. *Inorg. Chem.* **2016**, 55, 6027–6035.

123. S. Banerjee, I. Pant, I. Khan, P. Prasad, A. Hussain, P. Kondaiah, A.R. Chakravarty.; Remarkable enhancement in photocytotoxicity and hydrolytic stability of curcumin on binding to an oxovanadium(IV) moiety. *Dalton Trans.* **2015**, 44, 4108–4122.

124. S. Li, G. Xu, Y. Zhu, J. Zhao, S. Gou.; Bifunctional ruthenium(II) polypyridyl complexes of curcumin as potential anticancer agents. *Dalton Trans.* **2020**, 49, 9454–9463.

125. A. Castonguay, C. Doucet, M. Juhas, D. Maysinger.; New Ruthenium(II)-letrozole complexes as anticancer therapeutics. *J. Med. Chem.* **2012**, 55, 8799–8806.

126. L. Bonfili, R. Pettinari, M. Cuccioloni, V. Cecarini, M. Mozzicafreddo, M. Angeletti, G. Lupidi, F. Marchetti, C. Pettinari, A.M. Eleuteri.; Arene-RuII complexes of curcumin

exert antitumor activity via proteasome inhibition and apoptosis induction. *ChemMedChem.* **2012**, 7, 2010–2020.

127. F. Caruso, R. Pettinari, M. Rossi, E. Monti, M.B. Gariboldi, F. Marchetti, C. Pettinari, A. Caruso, M.V. Ramani, G.V. Subbaraju.; The in vitro antitumor activity of arene-ruthenium(II) curcuminoid complexes improves when decreasing curcumin polarity. *J. Inorg. Biochem.* **2016**, 162, 44–51.

128. A. C. D. Silva, P. D. D. F. Santos, J. T. D. P. Silva, F. V. Leimann, L. Bracht, et al. Impact of curcumin nanoformulation on its antimicrobial activity. *Trends Food Sci. Technol*. **2018**, 72, 74–82.

129. A. Shakeri, F. Khakdan, V. Soheili, A. Sahebkar, G. Rassam, et al. Chemical composition, antibacterial activity, and cytotoxicity of essential oil from Nepeta ucrainica L. spp. kopetdaghensis. *Indus. Crops Products*. **2014,** 58, 315–321.

130. M.J. Logan-Smith, P.J. Lockyer, J.M. East, and A.G. Lee.; Curcumin, a molecule that inhibits the Ca^{2+}-ATPase of sarcoplasmic reticulum but increases the rate of accumulation of Ca^{2+}. *Journal of Biological Chemistry*, **2001**. 276, 46905-46911.

131. D. Rai, J.K. Singh, N. Roy, and D. Panda.; Curcumin inhibits FtsZ assembly: an attractive mechanism for its antibacterial activity. *Biochemical Journal*, **2008**, 410, 147-155.

132. P. Tyagi, M. Singh, H. Kumari, A. Kumari, K. Mukhopadhyay.; Bactericidal activity of curcumin I is associated with damaging of bacterial membrane. *PloS one*, **2015** ,10, p.e0121313.

133. L. Pari, D. Tewas, and J. Eckel.; Role of curcumin in health and disease. *Archives of physiology and biochemistry*, **2008**. 114, 127-149.

134. P. Hu, P. Huang, and M.W. Chen, Curcumin reduces Streptococcus mutans biofilm formation by inhibiting sortase A activity. *Archives of oral biology*, **2013**, 58,1343-1348.

135. J. L. Hobman, and L. C. Crossman.; Bacterial antimicrobial metal ion resistance. *J. Med. Microbiol.* **2015**, 64, 471–497.

136. R. J. Turner.; Metal-based antimicrobial strategies. *J. Microbial. Bio-technol*. **2017**, 10, 1062–1065.

137. M. Subhan, K. Alam, M. Rahaman, M. Rahman, and M. Awal.; Synthesis and characterization of metal complexes containing curcumin ($C_{21}H_{20}O_6$) and study of their anti-microbial activities and DNA binding properties. *J. Sci. Res*., **2014**, 6, 97–109.

138. A. Kareem, M. Arshad, S.A.A. Nami, N. Nishat.; Herbo-mineral based schiff base ligand and its metal complexes: Synthesis, characterization, catalytic potential and biological applications. *J. Photochem. Photobiol. B Biol.* **2016**, 160, 163–171.

139. G. Chauhan, G. Rath, A.K. Goyal.; In-vitro antiviral screening and cytotoxicity evaluation of copper-curcumin complex. *Artif. Cells Nanomed. Biotechnol.* **2013**, 41, 276–281.

140. M. Gholami, H. Zeighami, R. Bikas, A. Heidari, F. Rafiee, F. Haghi.; Inhibitory activity of metal-curcumin complexes on quorum sensing related virulence factors of Pseudomonas Aeruginosa PAO1. *AMB Express* **2020**, 10, 111–120.

141. S. Hatamie, M. Nouri, S. K. Karandikar, A. Kulkarni, S. D. Dhole, et al. Complexes of cobalt nanoparticles and polyfunctional curcumin as antimicrobial agents. *Mater. Sci. Eng.* **2012**, 32, 92–97.

142. A. Papadimitriou, I. Ketikidis, M.E.K. Stathopoulou, C.N. Banti, C. Papachristodoulou, L. Zoumpoulakis, S. Agathopoulos, G.V. Vagenas, S.K. Hadjikakou.; Innovative material

containing the natural product curcumin, with enhanced antimicrobial properties for active packaging. *Mater. Sci. Eng. C.* **2018**, 84, 118–122.

143. A. Singh, P.K. Dutta.; Green synthesis, characterization and biological evaluation of chitin glucan based zinc oxide nanoparticles and its curcumin conjugation. *Int. J. Biol. Macromol.* **2020**, 156, 514–521.

144. P. Srivastava, M. Shukla, G. Kaul, S. Chopra, A.K. Patra.; Rationally designed curcumin based Ruthenium(II) antimicrobials effective against drug-resistant: Staphylococcus aureus. *Dalton Trans.* **2019**, 48, 11822–11828.

145. Y.M. Song, J.P. Xu, L. Ding, Q. Hou, J.W. Liu, Z.L. Zhu.; Syntheses, characterization and biological activities of rare earth metal complexes with curcumin and 1,10-phenanthroline-5,6-dione. *J. Inorg. Biochem.* **2009**, 103, 396–400.

146. G. Katsipis, V. Tsalouxidou, E. Halevas, E. Geromichalou, G. Geromichalos, A.A. Pantazaki.; In vitro and in silico evaluation of the inhibitory effect of a curcumin-based Oxovanadium (IV) complex on alkaline phosphatase activity and bacterial biofilm formation. *Appl. Microbiol. Biotechnol.* **2021**, 105, 147–168.

CHAPTER 4

Review on *in-silico* approaches in Inorganic Chemistry: DFT, Molecular Docking & Molecular Dynamics

Introduction

Inorganic complexes have emerged as a novel class of therapeutic agents having various advantages over conventional drugs that are largely organic by character.[1–4] These complexes, containing one or more transition metal ions like platinum, ruthenium or gold enfold a plethora of activities that includes DNA-binding, enzyme inhibition and various types of redox activity that serves as an important attribute in drug action.[4–6] The extraordinary versatility and efficacy of these metal complexes are due to their ability to access multiple coordination geometries, show different oxidation states and accommodate themselves into different ligand environments within the biological system. Therefore, they can have selective interactions with different biological targets.[7] Discovery and optimization of metal-based drugs require a comprehensive understanding of their electronic structures, binding affinities and behaviour within a biological environment.[7-10] Investigation of these aspects can be conducted efficiently through *in silico* approaches that could be Density Functional Theory (DFT), Molecular Docking and Molecular Dynamics (MD) simulation.[11]

In recent years, a major trend in chemistry research has been an explosive growth in Computational Chemistry, the journey of which started in the late 1920s. At that time positive impact on computational quantum chemistry was found in a book named "Introduction to quantum mechanics with application to chemistry" by Linus Pauling and Edgar Bright Wilson that was published in late 1940s.[12,13] Further in 1950s with the development of computer technology, semi-empirical atomic orbital calculations were performed including a major advancement by way of "The Linear Combination of Atomic Orbitals Molecular Orbitals" ("LCAO MO" approach).[13] Quantum mechanical calculations like *ab initio*, DFT and MD used in computational chemistry greatly improved. Today DFT is an indispensable theoretical tool for understanding electronic structures and reactivity of metal-based complexes. DFT study of complexes allowed for an accounting of metal-ligand binding, charge distribution and molecular orbitals that are

fundamental to rationalize pharmacological activity.[14] Through DFT calculations one can predict redox potentials,[15] ligand exchange kinetics[16] and activation barriers of metal complexes[17] which serve as important factors that determine their stability and bio-availability.[17] DFT aids in creating new metal-based pharmaceuticals by allowing theoretical evaluation of diverse structural alterations thereby directing the synthesis of innovative molecules with improved therapeutic characteristics.[14-17] On the other hand, molecular docking is an extremely useful technique in computational chemistry that is used to predict binding modes and affinities of metal-based complexes with biological macromolecules like DNA, protein or enzymes.[18,19] Researchers use this methodology to predict binding of biomacromolecules with metal complexes at the atomic level that is also able to guide us in predicting which residues are necessary for binding and also specificity of binding energy profiles.[20] Recently, extensive docking studies on platinum based pharmaceuticals especially cisplatin and its derivatives were carried out which provide insight into mode of actions of metal based drugs.[21,22] In addition, molecular docking was also adopted to screen novel binding sites present on biological targets and predict off-target activities supporting the rational design of metal-based drug candidates with high selectivity and low toxic side effects.[23,24]

Molecular Dynamics (MD) Simulations were used along with DFT and docking studies providing an alternate view to dynamical nature of metal based complexes in physiological surroundings. Using MD simulations, conformational flexibility, solvation effects and interaction dynamics of metal based drugs with biological targets could be accessible over time.[25,26] This methodology enriches one with a detailed knowledge of thermodynamic and kinetic stability of metal complex formation both in aqueous and in lipid milieu, as well as conformational changes that can be induced upon binding to DNA or to a protein or to mechanisms of drug resistance etc.[25-28] For instance, MD simulations have been employed to gain mechanistic views on dynamic binding between a class of ruthenium-based anticancer agents targeting DNA, aiding our

understanding of the mode of action and also providing guidelines on how these compounds could be modified to enhance their efficacy and reduce associated toxicities.[29,30]

The combination of DFT, molecular docking analysis and MD simulations can provide a useful framework for rational design and optimization of inorganic metal based-drugs.[15–28] These *in silico* tools allow for a deeper insight into the electronic, structural and dynamic characteristics of metal-based compounds that may be used to design productive and selective therapeutic agents. In the light of advancing computational tools and algorithms they form a more active network that aids new drug discovery processes for metal-based drugs with specific properties aimed towards superior clinical outcome.[15-31]

4.1 Quantum Chemical Calculations: Density Functional Theory

Density functional theory (DFT) may be said to be one of the most successful tools that have had an influence on modern-day quantum chemistry.[13-16] According to the famous Hohenberg and Kohn theorems,[32,33] DFT has built a solid foundation for information gathering techniques that can effectively provide information on energy, structure and properties of atoms and/or molecules. These methods are much more economical than those of *ab initio* wave functions.[13-16, 32, 33]

An excellent illustration was provided by Koch and Holthausen in their book, "Chemist's Guide to Density Functional Theory".[34] This book is a comprehensive review of the effectiveness of DFT in evaluating various molecular properties. Today, DFT has found wide application in the domain of organic chemistry, inorganic chemistry, materials science and biochemistry so that the target audience has broadened immensely in order to encompass an entire scientific community.[13-16] The Nobel Prize in Chemistry in 1998 was awarded to Professor J. A. Pople, a leading personality on wave function quantum chemistry and Professor Walter Kohn, considered the forefather of DFT.[35] This recognition acknowledges the enormous influence of quantum chemistry in present day chemical research and an indispensable role of DFT in chemical science.[13-16,35]

4.1.1 Some Theoretical Background of DFT:

4.1.1.1 The Fundamental Wave Equation in Quantum mechanics:

The Schrödinger equation undoubtedly serves as the basic equation in quantum mechanics (Eq.1). It describes the wave function (or state function) of a specific quantum-mechanical system.[36,37] The Schrödinger equation has had far-reaching impact in describing the electronic structure of matter. Eq.1 is a time independent Schrödinger Equation,

$$\hat{H}\,\Psi = E\,\Psi \tag{1}$$

$\hat{H}$ denotes the Hamiltonian operator and Ψ represents the wave function of the system, E signifies eigenvalue which corresponds to the energy of the system. The Hamiltonian operator is composed of potential energy and kinetic energy components.

$$\hat{H} = \frac{-\hbar^2}{2m}\nabla^2 + V_{PE} \tag{2}$$

$\hbar = h/2\pi$, mass is represented as m, potential energy is represented by V_{PE}, ∇ is the symbol of the Laplacian operator.[37-38]

$$\nabla^2 = \frac{\partial^2}{\partial x^2} + \frac{\partial^2}{\partial y^2} + \frac{\partial^2}{\partial z^2} \tag{3}$$

x, y and *z* are the positions of Cartesian coordinate in three-dimension. The Schrödinger equation can only be solved for extremely basic systems like the hydrogen atom and molecular H_2^+ ions due to complexity of all connected terms.[37-38] Various numerical techniques are combined with Schrödinger equation to handle complicated systems like many-body problems etc.

4.1.1.2 Time independent Schrödinger equation into Many-Body problem:

The many-body problem involves multiple interacting particles within a single microscopic system, necessitating the application of quantum mechanics.[39] In quantum chemical systems, particle interactions encompass electron-electron interactions, electron-nuclei interactions and various other interactions due to which an exact and precise calculation may not be achieved. For that Born–Oppenheimer approximation[40,41] was considered which simplifies the Schrödinger

equation by assuming that the nuclei remains static while electrons occupy the ground state due to significantly faster motion of electrons compared to nuclei at a given moment. The system may be considered as having a frozen nuclei with surrounding electrons in the ground state allowing for separation of the total Hamiltonian operator into two terms related to the nuclei and those related to electrons.[40-42]

$$\hat{\mathrm{H}} = \widehat{T_N}(R) + \widehat{T_e}(r) + \widehat{V_{Ne}}(r,R) + \widehat{V_{ee}}(r) + \widehat{V_{NN}}(R) \qquad (4)$$

In Eq. 4 $\widehat{T_N}(R)$ and $\widehat{T_e}(r)$ represent kinetic operators of nuclei and electrons respectively; $\widehat{V_{NN}}(R)$, $\widehat{V_{Ne}}(r,R)$ and $\widehat{V_{ee}}(r)$ represent the potential operators of Coulombic interaction of nuclei-nuclei, nuclei-electron and electron-electron. Neglecting relativistic effect and nuclear kinetic energy operator one can write the molecular Hamiltonian in atomic units as in Eq. 5 and 6

$$\hat{\mathrm{H}} = -\sum_{i=1}^{N}\frac{1}{2}\nabla_i^2 - \sum_{i=1}^{N}\sum_{A=1}^{M}\frac{Z_A}{|r_i - R_A|} + \frac{1}{2}\sum_{i=1}^{N}\sum_{\substack{j=1\\ j\neq i}}^{N}\frac{1}{|r_i - r_j|} + \frac{1}{2}\sum_{A=1}^{n}\sum_{\substack{B=1\\ A\neq B}}^{n}\frac{Z_A Z_B}{|R_A - R_B|} \qquad (5)$$

$$\hat{\mathrm{H}} \equiv \sum_i h(i) + \frac{1}{2}\sum_{i\neq j} g(i,j) + \widehat{V_{NN}}(R) \qquad (6)$$

where *i* and *j* denote summation over electrons located at places r_i and *A* and *B* represent summation over nuclei situated at positions *R* with nuclear charges *Z*. The expression $-\frac{1}{2}\nabla_i^2 = \frac{1}{2}p_i^2$ is the quantum mechanical formulation of the kinetic energy operator for the *i*th electron having momentum p_i. This Hamiltonian pertains to Born–Oppenheimer (BO) approximation, wherein kinetic energy of the nuclei is neglected and nuclear locations are treated as fixed parameters in the equations.[43] Utilizing Born–Oppenheimer approximation, Schrödinger equation may be partitioned into two components, that for the nuclei and for electrons as in Eq. 7

$$\Psi(\{r_i\},\{R_i\}) = \Psi_N(\{R_i\}) \times \Psi e(\{r_i, R_i\}) \qquad (7)$$

where $\Psi_N(\{R_i\})$ represents the wavefunction of the nuclei, dependent only on nuclei positions R_i; whereas $\Psi e\ (\{r_i, R_i\})$ denotes wavefunction of electrons depending on both nuclei positions R_i and electron positions r_i. The Schrödinger equation is similarly used to solve nuclear and electronic energies as shown in Eqs. 8 and 9

$$\widehat{\mathrm{H}_e}(\{r_i, R_i\})\ \Psi_e\ (\{r_i, R_i\}) = E_e\ \Psi_e\ (\{r_i, R_i\}) \quad (8)$$

$$\widehat{\mathrm{H}_N}(\{R_i\})\ \Psi_N\ (\{R_i\}) = E_N\ \Psi_N\ (\{R_i\}) \quad (9)$$

E_e represents electronic energy and E_N nuclei energy. Overall energy of the system can be expressed as the sum of the total electronic energy and nuclear-nuclear energy interactions by Eq.10

$$E_{Total} = E_{electronic} + E_{nucelar-nuclear} \quad (10)$$

4.1.1.3 Introduction of Hartree-Fock approximation:

One of the major use of Born–Oppenheimer approximation is to separate wave functions for the nucleus from that of the electrons and vice versa. But then, solving of Schrödinger equation remains challenging due to too many electrons in a system. In 1928, Hartree introduced a technique that he termed self-consistent field (SCF) approach to streamline representation of wavefunction and energy computation of atoms and ions.[44] In this method, electronic motions are considered approximately independent for a stable molecule or atom; each electron moves within the electronic field generated by the nucleus and other electrons. Each electronic state is characterized by a corresponding single-electron wavefunction and total electron states are derived by multiplying all single-electron wavefunctions together to obtain Eq. 11.

$$\Psi_{(r)} = \Psi_{(1)}(r_1).\ \Psi_{(2)}(r_2).\ \Psi_{(3)}(r_3) \ldots\ldots\ldots\ \Psi_{(n)}(r_n) \quad (11)$$

In 1930, Slater[45] and Fock[46] proposed a way to more accurately characterize the electronic wavefunction of a system, namely the Hartree-Fock method.[48] This technique treats electrons as fermions meaning no two electrons may occupy the same quantum state in accordance with Pauli

exclusion principle. Electron 1 occupies state Ψ_1 with spin α; electron 2 occupies state Ψ_1 with spin β and so on.[47] To concurrently fulfil the anti-symmetry principle Slater determinant was employed to express wavefunction of an N-electron system as follows [47-50]

$$\Psi_{HF} = \frac{1}{\sqrt{N!}} \begin{vmatrix} \Psi_{1,\alpha}(1) & \Psi_{1,\beta}(1) & \cdots & \cdots & \Psi_{N,\beta}(1) \\ \Psi_{1,\alpha}(2) & \Psi_{1,\beta}(2) & \cdots & \cdots & \Psi_{N,\beta}(2) \\ \vdots & \vdots & \ddots & \ddots & \vdots \\ \Psi_{1,\alpha}(N) & \Psi_{1,\beta}(N) & \cdots & \cdots & \Psi_{N,\alpha}(N) \end{vmatrix} \quad (12)$$

where rows correspond to electron coordinates and columns represent single wavefunctions.[47-50] By exchanging any two rows or columns the sign of Eq. 12 will alter in accordance with our understanding of mathematics ensuring anti-symmetry principle. Furthermore, since Eq. 12 has two equivalent rows or columns that result in the value of the determinant zero, it guarantees that no two distinct electrons will occupy the same electronic state.[47-50] In this approximation, electron correlation effect and all relativistic effects have been neglected. This significant approximation results in substantial deviations between experimental and calculated outcomes. The correlation effects are defined in Eq. 13:

$$E_{Correlation} = E_{exact} - E_{HF} \quad (13)$$

4.1.1.4 Foundation of DFT and Hohenberg-Kohn theorem:

In 1960s, DFT was established as a cost-effective alternative to Hartree-Fock technique by which total energy of a system could be calculated by considering exchange and correlation together. This approach ascertains the characteristics of a many-electron system by employing functionals of spatially dependent electron density in place of wavefunctions.[51] The basic standpoint of DFT is very much similar to Thomas-Fermi model (1927) that deals with a roughly uniform distribution of electrons within an atom.[52,53] Nonetheless, this model continues to exhibit inaccuracies in the exchange energy and disregards electron correlation. The density functional theory established a solid theoretical foundation with the publication of Hohenberg-Kohn theorems.[54] In 1964, they said that it was electronic density $\rho(r)$ and not electronic wave function

that determines the ground state electronic energy of a molecular system. According to their first theorem, both external potential $V_{ext}(r)$ and total energy E_{Total} are functional of the electron density $\rho(r)$. The existence of this functional is the subject of the first Hohenberg–Kohn theorem (1964). It is represented in Eq. 14 and Eq. 15 respectively.[54]

$$E_{Total} = E_{Total}\,[\rho(r)] \tag{14}$$

$$V_{ext}(r) = V_{ext}(r)\,[\rho(r)] \tag{15}$$

In their second theorem, they showed that through DFT molecular wave function cannot be calculated. Instead, ground state energy (E_0) and other features of a molecule may be calculated by directly analysing the electron density ρ_0(r) of the ground state, typically denoted as ρ_0(r) in DFT.[54] According to them, the energy of a system attains its minimum (E_0), indicating that all other energies with arbitrary densities inside the system exceed the energy corresponding to the ground-state density ρ_0(r).

$$E_0[\rho(r)] \geq E_0\left[\rho_0(r)\right] \tag{16}$$

In Eq. 16 the subscript '0' denotes ground state; $E_0[\rho(r)]$ represents the system energy computed using random density; whereas $E_0\left[\rho_0(r)\right]$ indicates minimum energy achieved when density state attains the ground state.

Nevertheless, Hohenberg-Kohn theorem, does not provide a method for calculating E_0 from ρ_0(r), nor does it offer guidance on obtaining $\rho_0(r)$, without already determining the wave function.[54-56] However, by knowing $\rho(r)$ which ultimately determines the energy of a system and all other ground state electronic properties one can solve electronic wave functions. On the other hand to obtain energy function (ground state), one can apply the Born-Oppenheimer approximation and thus Eq. 17 is obtained.

$$E\,[\rho(r)] = T_e[\rho(r)] + V_{ee}[\rho(r)] + V_{eN}[\rho(r)] \tag{17}$$

In Eq. 17, $T_e[\,\rho(r)\,]$ represents electronic kinetic energy functional, $V_{ee}[\,\rho(r)]$ represents electron-electron repulsion functional and $V_{eN}[\,\rho(r)]$ represents electron-nucleus repulsion functional.

Total energy can be expressed as a function of electron density when one isolates energy associated with interaction between electrons and an external potential as in Eq. 18

$$E\,[\,\rho(r)] = F_{HK}\,\rho(r) + \int \rho(r)\,V_{ext}(r)dr \qquad (18)$$

where, $F_{HK}\,\rho(r)$ is Hoenberg-Kohn functional, that includes electronic kinetic energy functional, $T_e[\,\rho(r)]$ and electron-electron repulsion functional $V_{ee}[\,\rho(r)]$. Therefore, Eq. 18 becomes

$$E\,[\,\rho(r)] = T_e[\rho(r)] + V_{ee}[\rho\,(r)] + \int \rho\,(r)\,V_{ext}(r)dr \qquad (19)$$ [54-56]

4.1.1.5 Introduction of Kohn-Sham Equations:

Kohn-Sham proposed a method in 1965 that utilizes one-electron Schrödinger equation to ascertain electron density $\rho(r)$, incorporating self-consistent equations that account for exchange and correlation effects.[56] The principal equation formulated by Kohn-Sham is expressed in Eq. 20.

$$\left[\frac{-\hbar^2}{2m}\nabla^2 + \upsilon_{KS}(r)\right]\varphi_i(r) = \varepsilon_i\varphi_i(r) \qquad (20)$$

Eq. 20 simplifies the complexity of many-electron wavefunctions to a single Slater determinant of one-electron wavefunctions where $\upsilon_{KS}(r)$ denotes Kohn-Sham potential signifying the effective external potential governing the motion of non-interacting particles. $\varphi_i(r)$ denotes Kohn-Sham orbital function while the value ε_i represents the eigenvalue of the corresponding Kohn-Sham orbital indicating the energy associated with that orbital.[56]

Now, electron density may be determined using the equation below:

$$\rho\,(r) = \sum_{i=1}^{N} |\varphi_i(r)| \qquad (21)$$

In Eq. 21, N represents number of electrons present in the system. Eq. 22 and Eq. 23 deals with Kohn-Sham potential $\upsilon_{KS}(r)$ which is the summation of external potential V_{ext} (nuclei generated potential), the Hartree term and exchange correlation potential in terms of position (r).[57-59]

$$\upsilon_{KS}(r) = V_{ext}(r) + V_{hatree}(r) + V_{xc}(r) \quad (22)$$

$$\upsilon_{KS}(r) = -\sum_{A} Z_A|r - R_A|^{-1} + \int \rho(r')|r - r'|^{-1}dr' + V_{xc}(r) \quad (23)$$

According to Kohn-Sham theory, total energy along with Kohn-Sham potential is expressed as in Eq. 24.[57-59]

$$E(\rho) = T(\rho) + E_{ee}(\rho) + \int \upsilon_{KS}(r)\,\rho(r)dr + V_{xc}(\rho) \quad (24)$$

In Eq. 24, $T(\rho)$ represents kinetic energy of non-interacting electrons; $E_{ee}(\rho)$ is the interaction energy among electrons; $\upsilon_{KS}(r)$ is the external potential as previously stated; and $V_{xc}(\rho)$ is the exchange-correlation potential represented by Eq. 25.[57-59]

$$V_{xc} = \frac{\delta E_{XC}(\rho)}{\delta \rho(r)} \quad (25)$$

$E_{XC}(\rho)$ is composed of four components: the Coulomb functional, the Exchange functional, the Correlation functional and the Kinetic functional. The introduction of approximation is unavoidable as certain component parts of DFT can never be precisely determined. An effective approximation of $E_{XC}(\rho)$ results in a precise and efficient approach, exemplified by Local (spin) Density Approximation (L(S)DA), Generalized Gradient Approximation (GGA) and hybrid functional all of which are widely recognized in contemporary DFT studies.[57-59]

4.1.1.6 Different Density Functionals:

Currently, no universal density functional is available in any algorithm to accurately characterize a specific electron density. Available DFs can be categorized into six groups like local density approximation (LDA), generalized gradient approximation (GGA), meta-GGA, hybrid DFs, double-hybrid DFs and range-separated DFs.[60-64]

4.1.1.6.1 Local Density Approximation or Local Spin Density approximation:

This approximation (L(S)DA) is a fundamental approximation yielding a reasonably accurate exchange-correlation function. This was introduced in Kohn-Sham's paper[57] and can be traced back to the Thomas-Fermi model.[52] The L(S)DA assumes that density is considered homogeneous throughout. The exchange-correlation energy using LSDA and LDA can be expressed in Eq. 26 and Eq. 27 respectively

$$E_{xc}^{LSDA}\big(\rho(r)\big) = \int \rho(r)\varepsilon_{xc}\left(\rho\left(r^{\alpha}, r^{\beta}\right)\right)dr \tag{26}$$

$$E_{xc}^{LDA}\big(\rho(r)\big) = \int \rho(r)\varepsilon_{xc}\big(\rho(r)\big)dr \tag{27}$$

Here, $\varepsilon_{xc}\big(\rho(r)\big)$) denotes the exchange-correlation energy associated with each particle. This approach effectively characterizes molecular geometries, dipole moments and vibration frequencies. However, it demonstrates significant limitations in predicting bonding energies. It is possible to divide it into two components which are exchange term (ε_x) and correlation term (ε_c), respectively, for the purpose of better understanding.[60,65]

$$\varepsilon_{xc} = \varepsilon_x + \varepsilon_c \tag{28}$$

Compared to ε_c, ε_x is a significantly simpler problem to solve. Examples of L(S)DA are S-VWN3, S-VWN5, S-PWL etc. They possess slater exchange functional and different correlation functional. For example S-VWN3 has VWN no 3 correlation functional.[60,65]

4.1.1.6.2 Generalised Gradient Approximation Density Functional:

Since homogeneous electron gas model is followed by LDA and L(S)DA hence it is applicable to a system where density is fluctuating slowly with position. As homogeneous density assumption applied on L(S)DA, so, correlation energy gets higher priority always over exchange energy in LDA or LSDA. To overcome this problem density gradient is provided to describe ε_x in Generalized Gradient Approximation (GGA) along with density. Eq. 28 represents the energy of the GGA functional.[61]

$$E_{xc}^{GGA}(\rho(r)) = \int \rho(r)\varepsilon_{xc}\left(\rho\left(r^{\alpha}, r^{\beta}\nabla_r^{\alpha}\nabla_r^{\beta}\right)\right)dr \qquad (29)$$

Some examples of GGA DFs are BPW91, BPBE, BLYP, PBE etc. For BLYP the exchange functional is B88 and correlation functional is LYP.[66]

4.1.1.6.3 Hybrid and Double Hybrid Density Functional:

In 1993, Becke proposed to mix GGA functionals with exact exchange resulting in a hybrid functional.[67] The hybrid DFs introduced by Becke were based on adiabatic connection fluctuation-dissipation theorem (ACFD).[67] Hybrid DFs are functionals that substitute part of the exchange functional with non-local exchange calculated by HF (Hartree Fock) theory. The double hybrid DFs are functionals that substitute part of the correlation energy with correlation energy calculated by *ab initio* methods (e.g. MP2).[61] Some examples are Becke one-parameter hybrid functional (B1B95), another most popular DF is Becke three-parameter, Lee-Yang-Parr functional (B3LYP). In this case, Becke's three parameter exchange functional combined with Lee-Yang-Parr correlation functional. Apart for that Minnesota 05-2X (M05-2X), Minnesota 06-2X (M06-2X) etc DFs are there.[67-70]

4.1.2 Application of DFT in Coordination Chemistry:

DFT, today is one of the most widely used methods in understanding coordination chemistry, providing chemists with valuable insights into the properties, reactivity and electronic structures of coordination compounds. Some of the major applications in coordination chemistry that includes (i) Geometry optimisation both in gas and solution phases, (ii) Spectroscopic properties, (iii) TD-DFT (iv) studies related to understanding of mechanism, (v) NBO calculations (vi) magnetic properties, (vii) Metal-ligand binding analysis (viii) catalysis (viii) non-covalent interactions, (ix) ELF and LOF analysis etc.[71-74]

DFT is also useful in calculating electronic structures of coordination compounds which provide a complete account of frontier molecular orbitals like HOMO-LUMO, electron density

distribution, and metal-ligand interactions. It helps in identifying oxidation states, spin states and electron configurations of metal centres in coordination compounds. Through DFT optimisation it is possible to predict structural properties of coordination compounds like bond lengths, bond angles, dihedral angles etc. It helps to visualize 3D structures.[71-74] It has also been possible to compare theoretically obtained geometries with that obtained from experimental data using X-ray crystallography.[75] With the advent of DFT studies interpretation of spectroscopy like UV-Vis absorption spectra, IR, Raman, EPR and NMR of coordination compounds has been possible helping in an understanding how ligands and metal centres interact and in identifying different coordination environments.[74,75]

To analyse spectroscopic features like UV-Vis absorption, molecules must be solubilized in a specific solvent that is associated with the relaxation of the structure of the original molecule to an extent that in turn facilitates increased charge separation. The solute will also induce electric polarization in the solution. To address this issue in solution phase, several solvent models were created in quantum chemistry. Predominant category among them is the implicit solvent model in quantum chemistry known as "continuum self-consistent reaction field solvation models (SCRF), sometimes also referred to as the "polarized continuum model" (PCMs).[76] The PCM family of solvation models comprising the conductor-like PCM (C-PCM), the dielectric PCM (D-PCM), the integral-equation-formalism PCM (IEF-PCM), isodensity PCM (IPCM) and self-consistent isodensity PCM (SCI-PCM) are models grounded in physical principles that are intricately integrated into the system's Hamiltonian enabling investigation of solvation effects on diverse chemical and physical properties. These encompass solution-phase geometries, vibrational frequencies (IR), electronic excitation energies and several other parameters.[76]

Excited state electronic structure simulations of transition metal complexes are an essential addition to spectroscopic methods. However, computational approaches for studying ground and excited state features of coordination compounds have challenges due to size, state degeneracies,

dynamical correlation and relativistic effects. The multi-configurational (MCSCF) formalism[77] with relativistic effects seem best for describing ground state and excited state properties of coordination compounds; however DFT methods are widely used to simulate the electronic spectra of transition metal complexes. Time-dependent DFT (TD-DFT) being most prevalent in this regard.[78]

Vİcek Jr. and Záliˇs reviewed DFT and TD-DFT applications in electronic spectroscopy and excited-state characteristics of d^6 transition metal complexes.[79] Accurate CT transition energies and excited states of low-valent d^6 metal complexes are best determined utilizing hybrid DFs and also estimating the molecule in the solvent. Garino and Salassa provided a comprehensive survey of photochemically active transition metal complexes examined by TD-DFT.[80] The optical characteristics of some Ir complexes were examined through TD-DFT utilizing the widely recognized B3LYP functional. Ortho-metalated iridium compounds demonstrate pronounced phosphorescence, utilized in organic light-emitting diodes (OLEDs) to surpass efficiency constraints dictated by the generation of triplet excitons. The excited state of Ir complexes is intricate, encompassing both triplet metal-to-ligand charge transfer (^{3}MLCT) as well as triplet ligand-to-ligand charge transfer (^{3}LLCT) concurrently.[81]

DFT is extensively employed to investigate reaction mechanisms of coordination compounds, especially those that play a crucial role in catalysis. This offers a profound understanding of transition states, intermediates and activation energies aiding chemists in comprehending reaction pathways and modulation of metal centre reactivity. DFT calculations that incorporate dispersion, thermochemical and continuum solvent effects have been utilized by Minenkov et al. to investigate metathesis of ethyl vinyl ether facilitated by ruthenium catalysts $L(PCy_3)(X)_2Ru$ = CHPh (where L represents PCy_3, IMes (1,3-dimesitylimidazol-2-ylidene), H_2IMes (1,3-dimesityl-4,5-dihydroimidazol-2-ylidene); and X denotes Cl, Br, I in toluene.[82] The computational technique has been evaluated against experimental data and produces adequate

accuracy even for weakly bound transition states of phosphine and olefin dissociation and association. In another study, mechanistic intricacies of the catalytic cycle for water oxidation facilitated by $[Ru^{II}(damp)(bpy)(H_2O)]^{2+}$ complex were investigated by experimental methods as well as by DFT (M06-L and CASSCF/CASPT2) computations.[83] Yang et al. studied the mechanism of co-catalyzed ligand controlled hydroarylation of styrenes through DFT calculations.[84] Mustard et al. used experiments and DFT calculations at B3LYP/def2-SVP level of theory to clarify the whole mechanism and source of diastereospecificity of a Cu(I)-catalyzed rearrangement of vinyloxiranes to dihydrofurans.[85]

In terms of population analysis, Mulliken population analysis (MPA) and Natural Bond Orbital (NBO) analysis are common population analysis approaches that depend on electron density partitioning. Weinhold and colleagues' NBO approach quantifies a molecule's electronic structure.[86] NBO computations yield natural atomic charges, Wiberg Bond Indices (WBIs), natural electron configurations and bond orbitals.[86]

Currently, DFT may consistently be utilized to design novel compounds and investigate uncharted bonding states in transition metal chemistry. To elucidate electronic structure and bonding characteristics of coordination compounds, several population analysis techniques, including charge decomposition analysis (CDA) and energy decomposition analysis (EDA), are utilized. Additional theoretical instruments for examining the electronic structure of a molecule include topological study of electron density distribution known as Atoms in Molecules (AIM) theory, Electron Localization Function (ELF) and Reduced Density Gradient (RDG) approaches. In bio-inorganic chemistry, DFT is utilized to investigate metalloenzymes and biomimetic systems. It aids in comprehending coordinating environment of metal centres in enzymes and their role in facilitating biological activities. DFT facilitates construction of coordination compounds that replicate active sites of metalloenzymes.[74, 87]

4.2 Molecular Docking Simulations

Molecular Docking represents a sophisticated computational modelling technique. This simulation technique strengthens experimental methods by predicting energy-minimized posture of two molecules linked together to produce a stable association.[88-93] It is quick and economical in comparison to trial-and-error approaches employed in experimental investigations. It might substitute or incite experimentation.[88-93] It elucidates and comprehends investigations establishing a correlation between theoretical and practical dimensions of molecular interaction.[88-93] It is not always possible to get the structure of a stable association of two different molecules docked together using experimental methods like solution NMR, X-ray diffraction, electron microscopy, solution scattering, and neutron diffraction. This could be because of the cost, the length of time needed for research and that there are too many parameters to control and that sometimes these materials are also not available.[88-94] In this scenario, utilizing an *in-silico* approach grounded in structural data enables the identification of optimal correspondence between two molecules to forecast their intermolecular attraction or repulsion.[90-94] It mainly evaluates the interaction between a molecule inside a binding pocket of another molecule emphasizing attainment of minimum binding energy. The engagement of an organic ligand or an inorganic metal complex (termed ligand here) with a biomolecule (designated as a macromolecule, receptor or target) is a prominent subject area in molecular docking investigations and can be analysed through a series of non-covalent contact mechanisms.[89-94] An accurate and reliable prediction of docking results between proteins and ligands is essential in modern structure-based drug design.[95] Interaction between biologically related macromolecules including DNA, RNA, proteins, carbohydrates, lipids, enzymes and small organic or inorganic molecules is essential for a variety of biological processes. These include regulation of gene expression, control of cell transport, signal transduction, enzyme inhibition, antibody-antigen recognition and assembly of multi-domain proteins.[88-95] Within a biological cell, their interactions facilitate the execution of specific biological functions. It is

essential to conduct a docking study in order to accurately predict interaction and alignment of biomolecules. Such interactions may occur between a variety of molecule pairs that might include DNA-ligand, RNA-ligand, protein–protein, protein-RNA, protein-DNA, protein-drug, protein-nanoparticle, enzyme–substrate, and enzyme-drug, among others.[90-95]

4.2.1 Some theoretical background of Docking:

In order to gain a more comprehensive understanding of docking, it is necessary to be familiar with few fundamental terms associated with it like dock pose, binding mode, dock score, ranking, pose prediction etc. As the objective of docking is to determine the optimal alignment of a ligand and its receptor binding site, therefore, there are a variety of configurations, conformations and orientations in which a ligand molecule can connect with a receptor simultaneously (Fig. 1). So each kind of docking mode is termed as dock pose in Molecular Docking. In addition to the conformation of ligand and receptor when bound together, binding mode also describes orientation of the ligand with respect to receptor.[88-95] Docking score is the evaluation of a specific pose and involves quantifying the favourable intermolecular interactions including hydrogen bonds and hydrophobic contacts.[88-95] To identify the most favourable pose energetically, each pose is assessed for its compatibility with the target with regard to shape and properties, including electrostatics resulting in a corresponding dock score. A favourable dock score for a specific ligand indicates its potential as an effective binder. Ranking is the process of determining which ligands are most likely to interact favourably with a specific receptor based on the predicted free energy of binding.[88-95] Consequently, all ligands are ranked according to their respective dock scores that are their predicted affinities following completion of docking. This rank-ordered list is subsequently utilized for additional synthesis and biological investigation exclusively for compounds that are anticipated to be most active. Pose prediction is the process of identifying the precise binding mode of a ligand through a series of trials and retaining poses that are energetically

optimal. Due to their adaptability, it necessitates determining appropriate orientation and conformation of the bound ligand.[90-95]

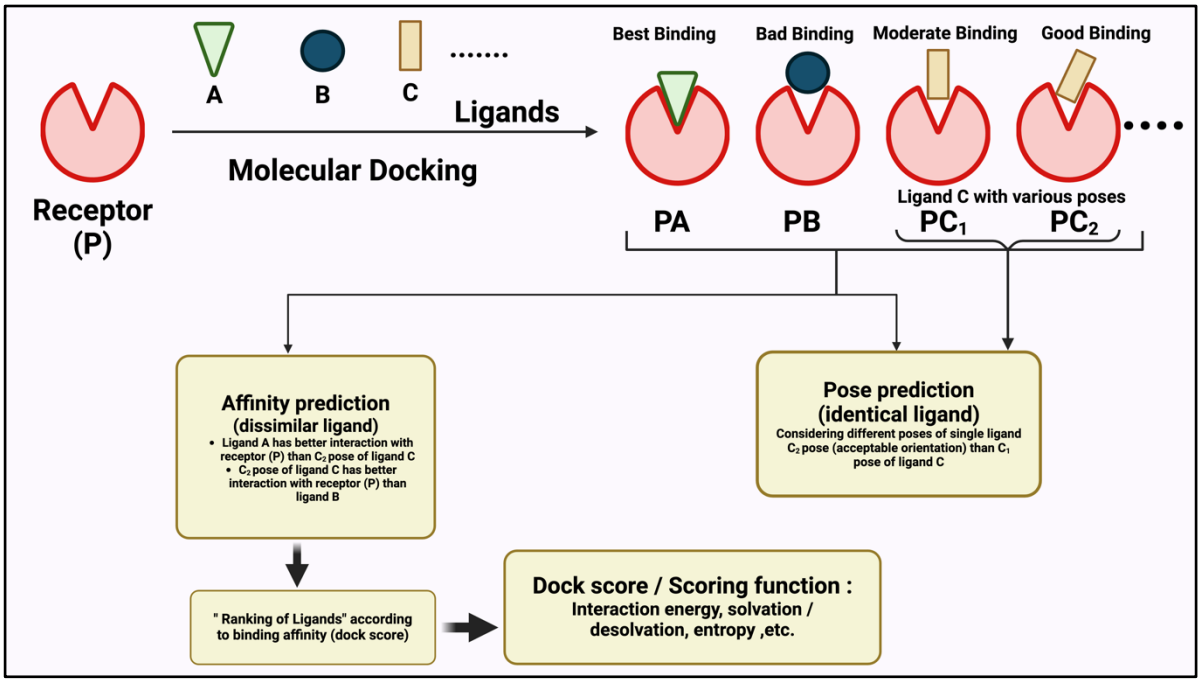


Figure 1: Model docked complex of Receptor-ligand

4.2.1.1 Mathematical viewpoint of Docking:

The primary objective of molecular docking is to predict the structure of the ligand-receptor complex through computational methods. Docking involves two interrelated steps: initially sampling ligand conformations within the protein's active site followed by ranking these conformations using a scoring function. Sampling algorithms should ideally reproduce the experimental binding mode with the scoring function ranking it highest among all generated conformations. This overview presents fundamental concepts of docking theory from two distinct perspectives.[94-96]

4.2.1.1.1. Sampling Algorithm:

The presence of six degrees of translational and rotational freedom with conformational degrees of freedom of both the ligand and the protein results in a vast array of potential binding mechanisms between the two molecules. Generating all potential conformations computationally

is too costly. That is why numerous sampling methods were created and extensively utilized in molecular docking software. Some of them are discussed below.[96]

Matching algorithms (MA) utilize molecular shape to map a ligand into a protein's active site focusing on shape features and chemical information.[97-99] Here, the protein and the ligand are depicted as pharmacophores. Chemical properties such as hydrogen-bond donors and acceptors were considered during the matching process. Matching algorithms offer rapid processing capabilities making them suitable for enrichment of active compounds from extensive libraries.[100] Ligand docking matching algorithms are implemented in the DOCK, FLOG, LibDock and SANDOCK programs.[101-104]

Incremental construction (IC) methods introduce the ligand into an active site through a fragmental and stepwise approach.[105-107] The ligand is segmented into multiple fragments by cleaving its rotatable bonds after which one fragment is chosen for initial docking into the active site. This anchor typically represents the largest fragment or the component that may play a crucial functional role or interact with the protein. The remaining fragments may be added incrementally. Various orientations are produced to accommodate the active site, demonstrating ligand's flexibility. The incremental construction method has been utilized in DOCK 4.0, FlexX, Hammerhead, SLIDE and eHiTS.[105,108-111]

Genetic algorithms (GA) represent a recognized category of stochastic methods.[112-114] The concept of GA originates from Darwin's theory of evolution. The ligand's degrees of freedom are represented as binary strings referred to as genes. These genes constitute the 'chromosome,' which represents the ligand's pose. Mutation and crossover represent two types of genetic operators utilized in genetic algorithms. Mutation introduces random alterations to genes while crossover facilitates exchange of genetic material between two chromosomes. The application of genetic operators to genes results in the formation of a novel ligand structure. New structures may be evaluated using a scoring function and those that surpass a specified threshold could be utilized

for subsequent generation. Genetic algorithms were applied in AutoDock, GOLD, DIVALI and DARWIN.[112,115-118]

Monte Carlo (MC) methods generate ligand pose via bond rotation, as well as rigid-body translation and rotation. The conformation achieved through this transformation is evaluated using an energy-based selection criterion. If it meets the criterion it would be preserved and subsequently altered to produce the next conformation. The primary advantage of MC is its capacity to facilitate significant changes enabling the ligand to traverse energy barriers on the potential energy surface a feat not readily accomplished by molecular dynamics simulation methods. Applications of Monte Carlo methods can be observed in earlier versions of AutoDock, ICM, QXP.[118-120]

4.2.1.1.2 Scoring functions:

Various types of non-covalent interaction forces facilitate binding of receptor and ligand, resulting in the formation of a stable receptor-ligand complex. The relevant interactions include torsional, hydrophilic, hydrophobic, van der Waals, electrostatic, hydrogen-bonding, and desolvation among others. The primary objective was to identify the most stable receptor-ligand complex characterized by optimized geometry and minimum binding energy. The energy score and binding pose energy terms are determined through application of scoring functions which is a mathematical tool employed to predict binding affinity or energy between a receptor and a ligand in their bound state. The scoring function evaluates and ranks predicted ligand conformations in the docking results. The ligand with the highest score is considered the optimal binder demonstrating the greatest binding affinity to the receptor. Scoring functions can be categorized into four types (i) force field-based, (ii) empirical-based, (iii) knowledge-based methods and (iv) machine learning.[121,122]

Force-field based scoring functions employ various non-covalent force fields to predict protein-ligand interactions. It typically utilize standard parameters derived from established force fields like AMBER.[123,124] These functions take into account both intramolecular energy of the

ligand and intermolecular energy of the protein-ligand complex.[125] The various non-covalent interactions including van der Waals (ΔE_{VDW}), electrostatic ($\Delta E_{\mathrm{electrostatic}}$), hydrogen bonding ($\Delta E_{\mathrm{H-bond}}$) and desolvation ($\Delta G_{\mathrm{desolvation}}$) play a significant role in determining the total binding energy in scoring functions. The generalized functional form of energy calculation commonly employed in this type of scoring function is presented as follows.[122]

$$\Delta G_{Bind} = \Delta E_{\mathrm{VDW}} + \Delta E_{\mathrm{electrostatic}} + \Delta E_{\mathrm{H-bond}} + \Delta G_{\mathrm{desolvation}} \quad (30)$$

Docking software that uses force-field based scoring functions are GoldScore, DOCK and earlier versions of Auto Dock. For example, DOCK software that employs this strategy uses Eq. 31[126-129]

$$\Delta G = \sum_i \sum_j \left(\frac{A_{ij}}{r_{ij}^{12}} - \frac{B_{ij}}{r_{ij}^{6}} + \frac{q_i q_j}{\varepsilon(r_{ij}) r_{ij}} \right) \quad (31)$$

Here r_{ij} represents the distance between protein atom *i* and ligand atom *j*, A_{ij} and B_{ij} represents van der Waals components (repulsive and attractive); q_i and q_j represents atomic charges and $\varepsilon(r_{ij})r_{ij}$ represents distance-dependent dielectric constant.

The AutoDock docking program calculates net free energy by combining several potentials such as van der Waals (ΔG_{vdW}), hydrogen bonding (ΔG_{H-Bond}), electrostatics (ΔG_{elect}), tortional (ΔG_{tor}) and desolvation (ΔG_{sol}) with the help of Eq. 32.[130]

$$\Delta G = \Delta G_{vdw} \sum_{ij} \left(\frac{A_{ij}}{r_{ij}^{12}} - \frac{B_{ij}}{r_{ij}^{6}} \right) + \Delta G_{H-bond} \sum_{ij} E(\theta) \left(\frac{C_{ij}}{r_{ij}^{12}} - \frac{D_{ij}}{r_{ij}^{10}} \right)$$

$$+ \Delta G_{elec} \sum_{ij} \frac{q_i q_j}{\varepsilon(r_{ij}) r_{ij}} + \Delta G_{sol} \sum_{ij} (S_i V_j + S_j V_i) e^{\left(\frac{-r_{ij}^2}{2\sigma^2} \right)} + \Delta G_{tor} N_{tor} \quad (32)$$

In Eq. 32 different ΔG are the coefficients of distinct potentials acquired from separate investigations of receptor-ligand complexes accompanied with known binding constants. The total

is computed for each pair of ligand atom (i) and receptor atom (j) as well as each pair of atoms in the ligand separated by three or more bonds.

The empirical or regression-based scoring function relies on a compilation of weighted scoring terms (ΔG_i) derived from various intermolecular interactions, including van der Waals forces, hydrogen bonding, hydrophobic effects, desolvation, electrostatics and the number of rotatable bonds (entropy) etc. which is very much identical to force-field-based scoring function. The corresponding equation is

$$\Delta G = \sum_i W_i \Delta G_i \qquad (33)$$

In Eq. 33 the weighted score parameters (W_i) are obtained using regression analysis of experimentally determined binding energy and three-dimensional structural data of established protein-ligand complexes with known 3D structures[131] which is similar to knowledge-based scoring function. Empirical-based scoring functions are used in ChemScore (employed in GOLD), GlideScore (implemented in Glide), Score, Fresno, AutodockVina, Lin_F9 etc.[132-137] Calculation of ChemScore is shown by Eq. 34

$$ChemScore = S_{H-bond} + S_{metal} + S_{lipophilic} + P_{rotor} + P_{strain} + P_{clash} + P_{covalent} + P_{constraint} \qquad (34)$$

Here S_{H-bond}, S_{metal} and $S_{lipophilic}$ represent scores for hydrogen bonding, coordinate bonding with metal ions and lipophilic contacts. On the other hand, the P_{rotor} , P_{strain} , P_{clash} , $P_{covalent}$ and $P_{constraint}$ represent penalties assigned for frozen rotatable bonds, ligand's internal strain energy, steric clashes between protein and ligand, covalent type docking and restrained docking.[132]

The knowledge-based or potential of mean force scoring function use statistical analyses of potentials derived from experimentally determined three-dimensional protein-ligand complexes to predict the potential of mean force via inverse Boltzmann distribution.[138-141] The concerned equation is as follows

$$A = \sum_i^{lig} \sum_j^{prot} w_{ij}(r) \qquad (35)$$

In Eq. 35 $w_{ij}(r)$ denotes the potential between any two atoms i and j at a distance r, determined by Boltzmann inversion as follows:

$$w_{ij}(r) = -k_B T ln\left[g_{ij}(r)\right] = -k_B T ln\left[\frac{\rho_{ij}(r)}{\rho_{ij}^{*}}\right] \quad (36)$$

In this context, $g_{ij}(r)$ represents the radial distribution function (RDF) of the atom pair *i–j* at a separation of r, k_B denotes Boltzmann constant, T signifies temperature, $\rho_{ij}(r)$ indicates the density of the atom pair *i–j* at a distance r, and ρ_{ij}^{*} refers to density of the atom pair *i–j* in a reference state where atomic interactions are considered negligible. Some examples of such scoring functions include AutoDock Vina, ITScore, KECSA, PMF and DrugScore of FlexX .[136,142-145]

Machine learning (ML) or descriptor-based scoring functions employ machine learning techniques. The functional version of binding affinity learns from previous existing data. Docking tools that use machine learning scoring functions produce more accurate docking results than traditional scoring function-based docking tools.[146] These ML scoring algorithms use ML approaches as deep neural networks (DNN), convolutional neural networks (CNN), graphical neural networks (GNN), support vector machines (SVM), random forests (RF), and extreme gradient boosting (XGB) .[146,147]

4.2.2 Types of Docking methodologies:

Based on flexibility we have three types of docking namely (Fig.2)

(i) Rigid receptor-ligand docking,

(ii) Rigid receptor – flexible ligand docking,

(iii) Flexible receptor -ligand docking,

On the other hand based on structural information in receptor's binding pocket we have two types of docking (Fig.3)

(i) Blind docking

(ii) Active site or Site specific docking

4.2.2.1 Rigid receptor-Rigid ligand docking:

When the ligand and receptor are regarded as rigid entities, the search space is significantly constrained, encompassing just three translational and three rotational degrees of freedom. Ligand flexibility may be managed by utilizing a pre-computed set of ligand conformations or by permitting a certain degree of atom–atom overlap between the protein and the ligand (Fig.2A). Software like DOCK, [101,107,108,148] FLOG [102] and certain protein-protein docking algorithms, like FTDOCK,[149] employed a methodology that maintained the rigidity of both the ligand and receptor throughout the docking procedure.

4.2.2.2 Rigid receptor-Flexible ligand docking:

In this methodology, first the ligand binds to the protein conformation with the least energy. Then the protein undergoes a conformational shift following a first contact. As a result, the interacting residues of protein molecules undertake conformational modifications to better fit together and reduce net binding energy. The results obtained using this model are the most accurate, indicating that molecules and atoms move physically in nature (Fig. 2B). The ligand initially binds to the receptor (in its original shape) before causing the receptor's structural modification to accept it. Without the ligand, the receptor's structurally altered state may not exist (Fig. 2B). Flexible docking using the induced-fit model allows for conformational changes while predicting the binding pose of proteins in interactions with other molecules such as ligands, proteins, or peptides.[150,151] Nearly all docking applications have embraced this concept, including AutoDock[126,127] and FlexX [152.]

AutoDock 3.0 employs Monte Carlo simulated annealing, evolutionary algorithms, genetic algorithms and Lamarckian genetic algorithms to simulate ligand flexibility while maintaining receptor rigidity.[153] The scoring function utilizes the AMBER force field, encompassing van der Waals forces, hydrogen bonding, electrostatic interactions, conformational entropy, and desolvation components. Each phrase is assigned a weight based on an empirical scaling factor derived from experimental data. AutoDock 4.0 can simulate receptor flexibility by permitting the movement of side chains. This version of AutoDock allows for evaluation of protein-protein docking interactions.[154,155] AutoDock Vina has just been launched as the most current version for molecular docking and virtual screening.[136] By redocking the 190 receptor-ligand complexes utilized as a training set for AutoDock 4, AutoDock Vina demonstrated an approximate two orders of magnitude enhancement in speed and a markedly improved accuracy in binding mode prediction. Moreover these are free softwares.

4.2.2.3 Flexible receptor-Flexible ligand docking:

It is a completely flexible docking approach in which both the ligand and the receptor are treated as flexible bodies, i.e., an evaluation of rotations of the molecules (both receptor and ligand) is performed to search for an optimal conformation and orientation of molecules to interact with one another. This approach produces high-accuracy predictions of docked conformations that closely mimic experimental data, although it may need extensive computer calculations and effort (Fig.2C). The induced-fit method may be applied to both semi-flexible and completely flexible docking methods and docking process becomes more complex when interacting molecule has a large number of conformational degrees of freedom.[156] For example, the LJ potential in GOLD and the smooth potential in AutoDock 3.0 fall into this category.

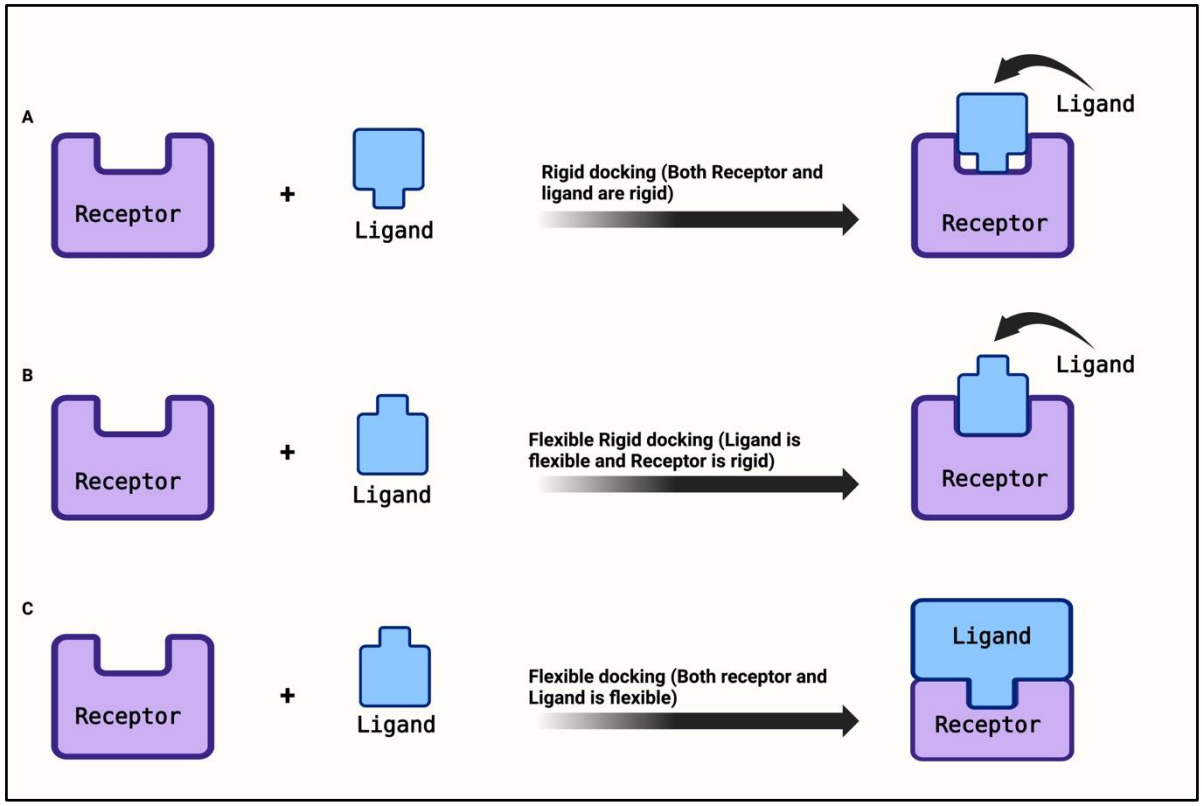


Figure 2: Different types of Docking based on flexibility parameter

4.2.2.4 Blind Docking:

Blind docking is docking that does not consider the structural information of the receptor molecule's binding or active site (where the ligand is expected to bind and interact with it). If the ligand under investigation does not interact with the receptor in its binding site (the receptor may have a binding pocket where it interacts with another partner ligand in nature), or if the location of the binding site is unknown, the entire surface of the receptor is searched for the binding pocket to accommodate the ligand (Fig.3A) If it is not possible to target the entire receptor molecule, pockets that can place the ligand can be identified. This sort of docking investigation is typically conducted to evaluate the potential interaction between a new protein and the ligand under consideration.[157]

4.2.2.5 Active site Docking:

Active site or site-specific docking refers to a docking study that uses receptor binding site information. Previous findings concerning the location of the binding pocket, active receptor residues and binding modes of known ligands in the binding site minimize the search region of interest, increasing the speed and efficacy of docking search (Fig.3B). For well-studied protein molecules, knowledge of the binding pocket information may be employed; if it is unknown, it can be obtained by mapping the protein to a family of well-known proteins with comparable structure and function and known active site information. In this docking mechanism, the ligand attaches solely to the active site and nothing else.[158]

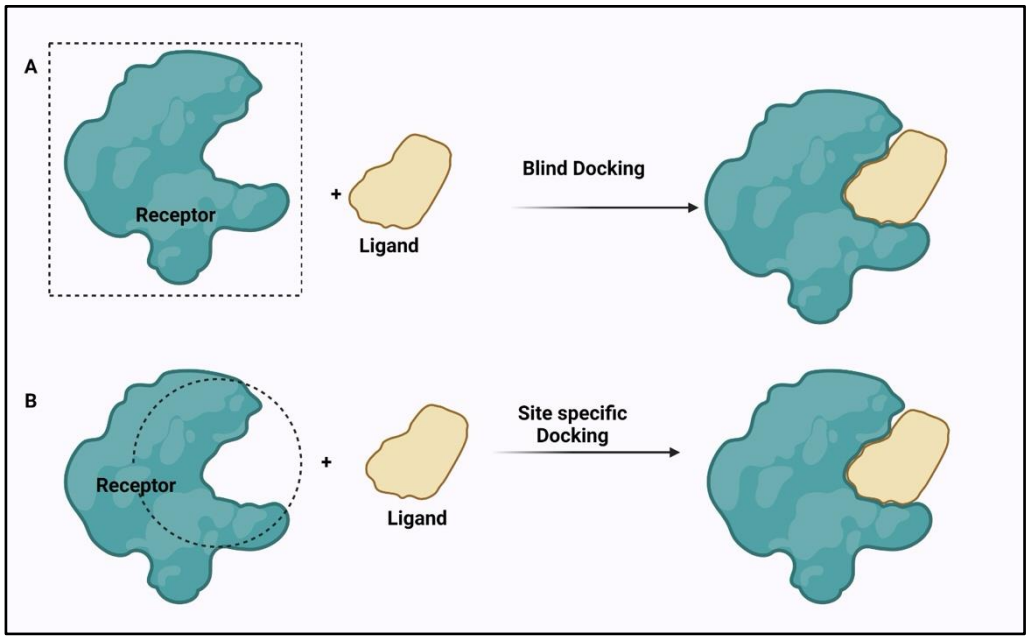


Figure 3: Different types of Docking based on receptor's binding pocket

4.2.3 Different models of Docking Study:

There are three models present to describe the binding of ligand molecule inside receptor cavity and they are –

(i) Lock and Key Models

(ii) Induced-Fit Models

(iii) Conformational fit model

The initial model for ligand-receptor binding mechanism is the lock-and-key theory proposed by Fischer,[159] wherein the ligand fits into the receptor analogous to a lock and key (Fig. 4A). The initial documented docking methods[101] were founded on this theory, treating both the ligand and receptor as rigid entities.

The "induced-fit" theory proposed by Koshland advances the lock-and-key model by asserting that the protein's active site is continuously modified through interactions with ligands during their binding process (Fig. 4B).[160,161] This theory assumes that both the ligand and receptor must be considered flexible in the docking process. Thus, it may characterize the binding events with greater precision than the rigid approach. Due to constraints in computational resources, docking has traditionally been conducted using a flexible ligand and a rigid receptor, and this approach continues to be the most widely utilized method.[112,113,162-165] Recent efforts have focused on addressing receptor flexibility.[166,167] Nonetheless, flexible receptor docking, particularly concerning backbone flexibility, remains a significant challenge for existing docking methods. This study proposes a Local Move Monte Carlo (LMMC) approach as a potential solution to flexible receptor docking issues.[168]

Monod, Wyman, and Changeux proposed the conformational selection model in 1975, which states that the unbound receptor exists in various conformational states based on relative free energy according to Gibbs distribution before binding to the ligand, and the ligand selects the best fit among them to form the final stable docked complex.[169] The difference between the induced-fit and conformation selection models is that in the induced-fit model, the ligand binds to the receptor before any structural change on the receptor, whereas in the conformation selection model a structural change occurs on the receptor before ligand binding.

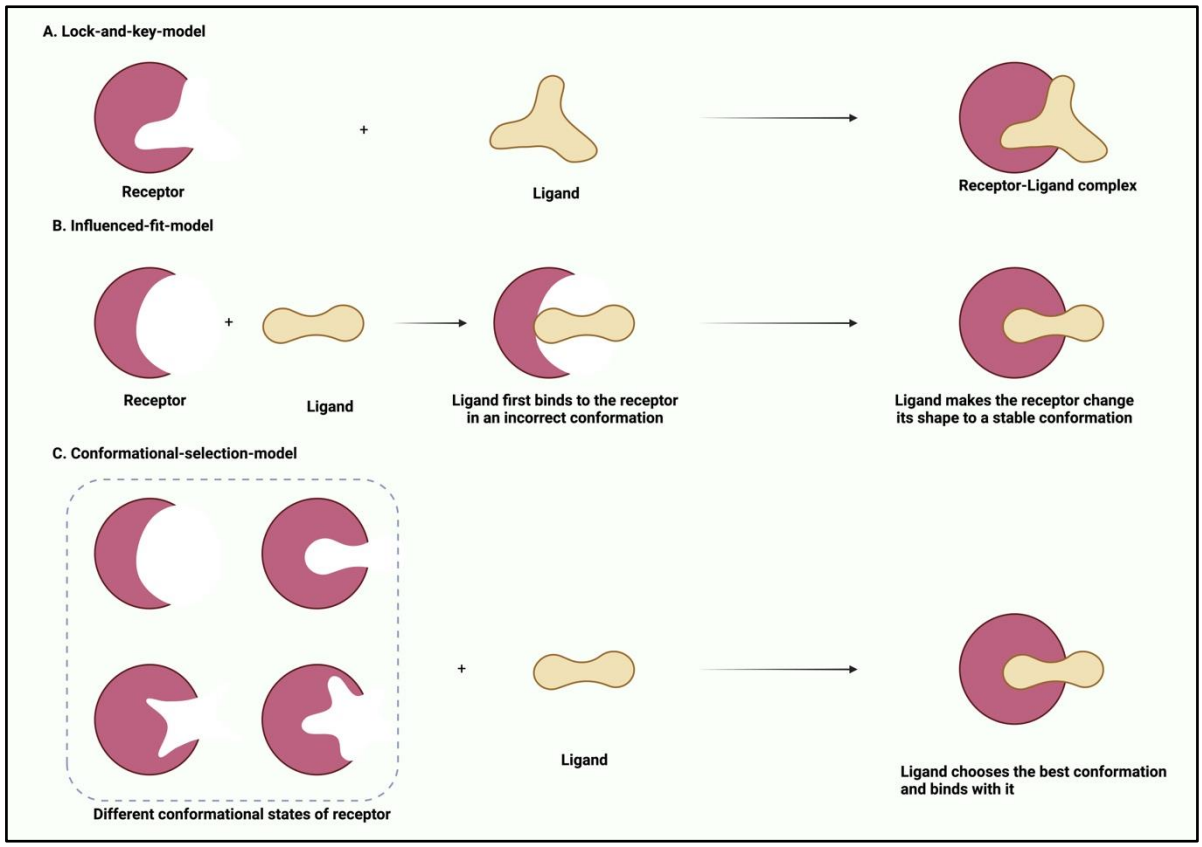


Figure 4: Different models of docking study

4.2.4 Basic steps involved in protein-ligand Docking Study:

Molecular docking consists of a six-step process, irrespective of the software or docking algorithms employed.[146,163] This procedure is

(i) Selection of protein

(ii) Preparation of the protein

(iii) Identification of hit / lead / ligand

(iv) Prediction of Active site

(v) Docking of protein -ligand

(vi) Post-docking analysis

Step 1 : The first stage in the docking process is to identify potential target proteins and ligands. Protein can be obtained from the Protein Data Bank (PDB) database (http://pdb.org) or Swiss

UniProt knowledge base (http://expasy.org/sprot). Homology modelling can also be done with Swiss model repository (http://swissmodel.expasy.org/repository/), modeller programs like I-TASSER, and other tools if the target protein is not in the database but similar sequences are present. By utilizing tools such as WHATCHECK[170] and Ramachandran plots [171] it is possible to verify the stereochemistry of the model by analyzing bond lengths, torsion angles, and rotational angles.

Step 2 : In this step a receptor has to be prepared completely for docking. Utilizing Chimera or PDF Fixer, selected receptor protein undergoes modifications to replace missing nucleotides or residues if any. Thereafter protein is subsequently put through energy minimization to loosen up the structure and get rid of any steric interference. The protonation states of ionizable residues are then established to provide proper electrostatic interactions during docking.[104-110] To further simplify the system, water molecules, and extraneous ligands are eliminated from the protein structure. To appropriately reflect the protein's behavior during docking simulations, proper force field parameters are supplied to it. Through these preparation steps, the protein structure is optimized and refined, providing a suitable starting point for successful molecular docking studies[172.]

Step 3 : In this step ligand is selected for docking by a variety of criteria, including their chemical diversity, their potential for drug development, or their known biological activity. Ligand structure is available from small molecule databases such as ZINC and PubChem.[173,174] These online databases allow for the collection of a large number of identified compounds for further virtual screening. If the 3D atomic coordinates of the ligand structure are not directly available, they may be obtained from experimental databases.[112-120] In such cases 2D structures of target molecule may be prepared using ChemSketch (Advanced Chemistry Development, Inc., Toronto, On, Canada, www.acdlabs.com, 2019), ChemDraw (PerkinElmer Informatics), and Avogadro.[175] Thereafter by

assigning charges, optimizing their geometry, and generating various conformers, the ligands are subsequently prepared for docking.[125-145]

Step 4 : It is possible to either specify the binding pockets at the beginning of the molecular docking process or to identify them after the docking process. Consequently, in order to validate the binding pocket of interest during the molecular docking process, two distinct techniques may be intended of, as will be (i) Blind docking and (ii) site-specific docking (*section 4.2.2.4 and section 4.2.2.5*)

Step 5 : The ligand is docked to the protein and interactions are examined. The scoring function assigns a score based on optimal docked ligand complex selected.[133-159] The docking procedure is structurally validated by removing the co-crystallized ligand from the receptor's active site and redocking it to confirm that it binds to the same active site and interacts with same amino acid residues as previously.[176]

Step 6 : Upon docking the ligands to the protein the data are evaluated to recognise the most promising candidates for subsequent investigation. The binding affinity of each ligand is determined by the expected interaction energy and the ligands are ordered according to their affinity scores. Docked structures are examined to discern critical interactions between ligands and protein including hydrogen bonds, hydrophobic interactions and electrostatic interactions. These can elucidate the mechanism of action of ligands and inform about further structural optimization.[172]

The fundamental steps are diagrammatically represented in Fig. 5.

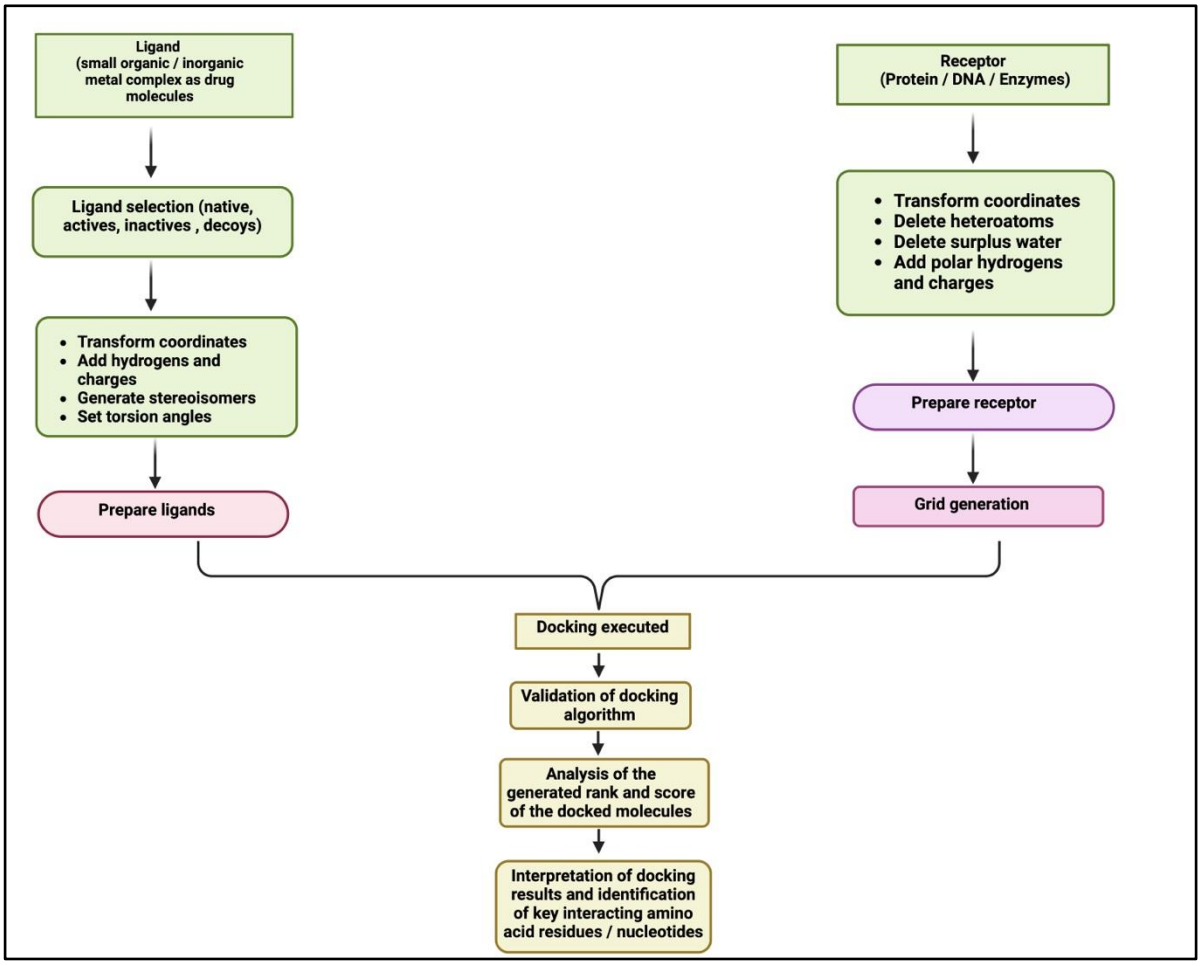


Figure 5 : Docking protocol

4.2.5 Application of Docking Study:

Molecular docking is extensively employed in hit detection during drug development. It assists in discovering prospective medication candidates by forecasting binding affinity of small compounds to a certain protein or receptor. Docking can be employed to evaluate an extensive database of small molecules to ascertain those that exhibit high-affinity binding to a target protein.[93-95]

Upon identification of a promising chemical, molecular docking can be employed to refine the lead compound's structure to enhance its binding affinity and selectivity. Docking may be utilized to build novel analogs by forecasting the binding configurations of changed structures.[126-139]

The field of bioremediation makes use of molecular docking in order to make predictions regarding binding affinity of small molecules to enzymes that are part of the process of degrading environmental contaminants. Through the use of docking it is possible to create inhibitors or activators of enzymes that can assist or improve efficacy of bioremediation.[177]

Docking can also be utilized to forecast Absorption, Distribution, Metabolism, Excretion, and Toxicity (ADMET) characteristics of small compounds. The anticipated ADMET attributes can be utilized to exclude compounds with undesirable characteristics at a very early stage of the drug development process.[178]

Molecular docking may be integrated with molecular dynamics simulations to investigate the dynamic behaviour of protein-ligand complexes. The simulations facilitate the comprehension of conformational alterations that transpire upon ligand binding and the stability of the complex.[25-27]

4.3 Molecular Dynamics simulations

Molecular dynamics (MD) simulations are among the most potent instruments in computational chemistry research, providing atomistic insights into the trajectory of molecular systems.[179] MD were initially developed in the theoretical physics community throughout 1950s with the first MD simulation conducted by Alder and Wainwright in 1957. Their groundbreaking research established the foundation for molecular dynamics as a computational instrument in physical sciences.[180] After the first macromolecular simulation of bovine pancreatic trypsin inhibitor (BPTI), performed in 1975 using a primitive molecule mechanics potential, lasted just 9.2 ps.[181] Since then, enhancements in algorithms, computer resources, and force field development have markedly increased the efficiency and precision of molecular dynamics simulations.[182-184] Molecular dynamics replicate the physical movements of atoms in the protein molecule in its natural environment.[179-187] In MD atoms are allowed to interact for a set amount of

time in order to calculate their trajectory within and around the protein molecule having a particular force field.[185-187] Simulation offers detailed information on the individual motion of atoms across time in a particular force field. Currently, molecular dynamics simulations find extensive application across various disciplines such as chemistry, physics, biology, and materials science, facilitating the design and advancement of novel drugs, materials, and nanodevices.[179-187] Recent developments in molecular dynamics methodologies, including coarse-grained simulations and enhanced sampling techniques, have significantly broadened the capacity to simulate larger and more complex systems.[179-187]

4.3.1 Theoretical aspects of Classical MD simulations:

Classical molecular dynamics simulation is a deterministic approach that adheres to the principles of classical mechanics to illustrate the temporal progression of the phase space of a collection of interacting atoms or molecules. This approach produces a set of coordinates and momenta (velocities) of the constituent particles of system over time by integrating Newton's equations of motion.[179]

In a basic atomic system, the force (F_i) acting on the system, according to Newton's second equation of motion, may be expressed as

$$F_i = m_i\, a = m_i\, \frac{d^2 r_i}{dt^2} \tag{37}$$

In Eq. 37 F_i is defined as the cumulative force acting on atom *i* in the direction *r*, m_i represents mass of atom *i*, and r_i denotes the position of atom *i*. If we assume the location and velocity of atom *i* at time t are known, then the position and velocity at time (t + dt), where dt is the time interval between two simulation snapshots. This may be approximated by solving Eq. 37 using an integration strategy.

The most common employed integration method is Verlet algorithm.[188-189] In this method the values for the current location $r(t)$; acceleration $a(t)$; and the position of the atom from the preceding step r(t – δdt) should be known. The position and velocities of atom *i* for the subsequent step may be determined using Eq. 38 and Eq. 39, respectively.

$$r\,(t+\,\delta t) = 2r(t) - r(t-\,\delta t) + \,a(t)\,\delta t^2 \qquad (38)$$

$$v\,(t) = \frac{r\,(t+\delta t) - r(t-\delta t)}{2\delta t} \qquad (39)$$

Eq. 38 and Eq. 39 provide the fundamental structure of the Verlet method and are susceptible to truncation errors on the order of δt^4 for positions and δt^2 for velocities. The estimation of velocities are crucial for calculating kinetic energy which is necessary for evaluating the conservation of total energy. This test is a critical stage in MD simulation, since it confirms the stability and accuracy of the simulation. To address the issue of truncation problems linked to the fundamental version of the Verlet method, other versions of the algorithm were created. The Velocity Verlet algorithm is one of the most prominent and often employed variations. The positions and velocities of the atoms are determined using a modified version of Verlet algorithm (Eq. 40 and 41)[188-189]

$$r\,(t+\,\delta t) = \,r(t) + v(t)\delta t\frac{1}{2}\delta t^2 a(t) \qquad (40)$$

$$v\,(t+\,\delta t) = v\left(1+\frac{\delta t}{2}\right) + \frac{1}{2}\,a\,(t+\,\delta t)\delta t \qquad (41)$$

4.3.1.1 Force Field in MD simulation:

A force field is a mathematical model that approximates the potential energy of a system of atoms or molecules.[190,191] Force field parameters are derived from experimental and quantum mechanical investigations of tiny molecules and is proposed that these parameters may be transferred to desired bigger molecules.[190-191] In molecular mechanics, the forces exerted on atom *i* can originate from both internal and external sources. The internal sources mostly refer to interaction forces between bound and non-bonded atoms. External sources may encompass

environmental stressors such as electric fields, heat, and pressure, which are applied to the system from outside.[190-192] To ascertain the forces, it is essential to calculate the potential energy of the system, which may be articulated as a summation of bonded, non-bonded, and cross-term interactions.[190-192] The derivatives of the potential energy function are referred to as force fields and that is why the force on each particle in a system may be estimated using the negative gradient of the total potential energy of system.[190-192]

$$F_i = -\frac{\partial U(r^N)}{\partial r_i} \qquad (42)$$

Here forces F_i acting on atoms and these are usually derived from a potential energy $U(r^N)$, where $r^N = (r_1, r_2, \ldots r_N)$ represents the complete set of 3N atomic coordinates.

The potential energy of a system, $U(r^N)$ may be determined using an empirical force field, based on atom positions in the simulation system supplied by the user. After defining an empirical force field, solving the above equations repeatedly yields the trajectory of the system, which is actually the location and velocity as a function of time. In a force field, bonded interactions include harmonic oscillator energy of bond lengths, bond angles and sometimes improper dihedrals (hard terms) and torsional dihedral angles (soft terms, sometimes including improper dihedrals), whereas non-bonded interactions include Van der Waals and electrostatic interactions described by Coulomb's law. It is noteworthy that Van der Waals interaction terms characterized by a Lennard-Jones potential function, encompass solely dispersion or London interactions among transient dipoles whereas Keesom interactions (involving permanent dipoles) and Debye (induced dipole) interactions are incorporated within the electrostatic (Coulomb) term, without explicit elaboration on charge distribution momenta.[192-194]

$$U(r^N) = \sum_{bonds} \frac{1}{2} k_b (r - r_0)^2 + \sum_{angle} \frac{1}{2} k_\theta (\theta - \theta_0)^2 + \sum_{\substack{improper \\ dihedrals}} \frac{1}{2} k_\xi (\xi - \xi_0)^2 +$$

$$\sum_{dihedrals} K_\phi [1 + \cos(n\phi - \delta)] + \sum_{\substack{atom \\ pairs\ i,j}} \frac{1}{4\pi\varepsilon_0} q_i q_j r_{ij}^{-1} + A_{ij} r_{ij}^{-12} - B_{ij} r_{ij}^{-6} \qquad (43)$$

In Eq. 43, potential energy $U(r^N)$ is a function of the Cartesian coordinate system R, which defines the locations of all atoms, from which the internal coordinates for bond lengths (r), bond angles (θ), dihedral angles (φ) and interparticle distances (r_{ij}) are derived. The precision of a molecular dynamics simulation is significantly influenced by the parameterization of the force field. The parameters employed in a force field are generally obtained from empirical data or quantum mechanical computations. Meticulous validation of these parameters is essential for guaranteeing the dependability of MD simulations.[190-194] In the process of validation, results of simulations are compared to experimental data, which includes thermodynamic properties, structural features and dynamic behaviours. Numerous force fields exist, and choosing the most suitable one for a particular application is crucial in simulation research. AMBER03, AMBER94, AMBER96, CHARMM27, OPLS-AA, GROMOS87 and GROMOS96 are examples of extensively utilized molecular force fields for the purpose of biomolecular simulations.[195-198]

4.3.1.2 Thermodynamic Ensembles:

A trajectory derived from the solution of the Newton equations of motion corresponds to the microcanonical or NVE ensemble. In this case, the system evolves with a fixed number of particles (N), volume (V) and energy (E). Apart from NVE ensemble in MD, NVT and NPT ensemble are also used. In NVT ensemble a thermostat is used to regulate the system's temperature. On the other hand, both thermostat and barostat are used to control temperature and pressure in NPT ensemble.[199] Various thermostats, including Berendsen temperature coupling, velocity rescaling and Nose-Hoover temperature coupling, are employed to regulate system temperature, while different barostats like Berendsen pressure coupling and the Parrinello-Rahman method are utilized to manage system pressure.[200-203] The use of such ensembles allows for more flexibility in the study of molecular systems under a variety of environmental circumstances, which is reflective of real-world environments.[199-203]

4.3.2 Methodology of MD Simulation:

There are multiple steps involved in MD simulation The essential steps involved are simulations of proteins or a protein ligand complex and

(i) Creation of simulation environment

(ii) Minimisation of energy

(iii) Heating and Equilibration

(iv) Production run

(v) Analysis of trajectory

(vi) Free energy of binding calculation in case of protein - ligand complex

4.3.2.1 Creation of simulation environment:

Protein and protein-ligand simulation is conducted to mimic experimental conditions, necessitating the consideration of many factors for differing physical variables, including pressure and temperature. Typically, the above type of simulations are conducted in the conventional ensemble (NVT) especially during the first equilibration phases or in isothermal-isobaric (NPT) ensemble.[199-203] For simulation, the protein or protein-ligand molecules must be contained within the unit cell and solvated with specified solvent. A wide array of explicit water models exist with the most prominent being TIP3P, TIP4P, TIP5P, SPC and SPC/E.[204] These are governed by quantum mechanics-based molecular mechanics and corroborated by experimental techniques. To prevent polarization of the simulation ensemble the system's overall charge must be maintained at zero by substituting certain solvent molecules with ions. To prevent interaction issues at the system boundary, constrained spherical boundary models for solute and solvent may be utilized, incorporating specific adjustments for density and polarization effects. The widely favoured method is cubic or rectangular periodic boundary conditions (PBC) which entails repetitions of the system across 26 adjacent unit cells.[205] When a molecule exits the system on one side, its corresponding counterpart arrives from the adjacent system on the other side, resulting in

conservation of mass and particle number. Molecules in imaging systems facilitate the computation of long-range non-bonded interactions with Ewald summation directly employed in typical solvated periodic boundary simulations of biomolecular systems to calculate the electrostatic interactions inside the system.[206]

4.3.2.2 Minimisation of Energy:

This stage entails identifying the global minimum energy about the positions of side chain atoms, which reflects the geometry of certain atomic configurations where the net attractive force on each atom is maximized. Numerous techniques exist for calculating minimal energy with the most prevalent being steepest descent and conjugate gradient approaches. The steepest descent method is a first-order iterative descent technique that use the gradient of the potential energy surface. This stage entails identifying the global minimum energy about the positions of side chain atoms which reflects the geometry of certain atomic configurations where the net attractive force on each atom is maximized. It pertains directly to the forces in the molecular mechanical characterization of molecular systems, facilitating a search trajectory toward the closest energy minimum.[207]

4.3.2.3 Heating the system and equilibration:

The heating phase involves numerically integrating Newton's equations of motion which depict the system's temporal development and assigning each atom in the system a starting velocity (at 0 K) during energy minimization. New velocities are assigned at short specified intervals, corresponding to slightly higher temperatures and the simulation is allowed to run until the target temperature is reached. Heating causes structural tensions to release progressively, removing force constraints on various subdomains of the simulation system. Thermalization is often carried out using Langevin dynamics at constant volume.[208]

4.3.2.4 Production run:

The final stage of the MD process to eliminate protein restrictions is the production phase. It generates a protein molecule's trajectory across an appropriate time scale in accordance with certain equilibrium criteria such as NVT, NPT and NVE. There is a range of several hundred picoseconds to microseconds or even longer for this timeframe.[209]

4.3.2.5 Analysis of MD trajectories:

This stage utilizes the recorded coordinates and velocities of the system for subsequent analysis. MD simulations facilitate the visualization and comprehension of conformational alterations at an atomic scale when integrated with visualization tools that can exhibit the relevant structural parameters in a time-dependent manner. MD simulations consistently compute the subsequent quantities.

1) Root mean square deviation (RMSD),

2) Root mean square fluctuation (RMSF),

3) Radius of gyration (ROG),

4) Solvent accessible surface area (SASA),

5) Total energy of the system in terms of MMGBSA or MMPBSA.[210]

The root mean square deviation (RMSD) value serves as a measure of the stability of the receptor-ligand complex.[211-214] Calculation of root mean square deviation (RMSD) facilitates the quantitative assessment of alterations in protein structure during the course of the simulation. The equation and terms that characterize RMSD are presented in Eq. 44

$$\text{RMSD} = \sqrt{\frac{1}{N}\sum_{i=1}^{N} ||x_i(t_2) - x_i(t_1)||^2} \qquad (44)$$

Where $x_i(t)$ denotes the location of atom i at time t and N represents the total number of atoms in the molecule. The initial frame of a trajectory (t_1) is frequently employed as a reference and RMSD values (t_1, t_2) are calculated for all subsequent frames $(t_2 > t_1)$.[211-214]

RMSD values are a widely used tool for MD simulation analysis.[211] These graphs often exhibit a steep slope in the initial nanoseconds and then fluctuate around a mean value for the remainder of the simulation. The simulation is either still equilibrating or there are persistent structural changes if RMSD time series do not achieve a steady state. Large loops and other extremely flexible areas are the cause of the problems in obtaining equilibration states. These can result in high RMSD values. Thus it could be helpful to calculate RMSD for each protein domain.[214]

The root mean square fluctuation (RMSF) accounts for variations of each residue, atom (such as alpha carbons), etc., in contrast to root mean square deviation (RMSD), which examines the mean of the total atom selection (such as the protein backbone, alpha carbons) over time. RMSF illustrates the structural behaviour of a single residue whereas RMSD explains the structural behaviour of the entire protein. The calculation of RMSF involves determining the difference between location of particle i and another reference point.[212,215]

$$\text{RMSF} = \sqrt{\frac{1}{T}\sum_{t_j=1}^{T}\left(X_i(t_j) - \bar{X}_i\right)^2} \qquad (45)$$

$X_i(t_j)$ represents the location of atom i at time t_j and is the reference position across time, where t is the time over which one desires to average. Since RMSF values quantify the variations of each residue in a protein, they are often compared to the crystallographic B-factors. RMSF, in general, is a measure of the flexibility of the backbone. These variations are more pronounced in the protein's looped or disorganized regions.[213,215]

When performing MD simulations, the radius of gyration (Rg) is a highly helpful tool for comparing various situations, particularly during folding and unfolding experiments.[216] Rg quantifies how compact a protein is; it is the distance from an axis at which one can reasonably

suppose that a body's mass is concentrated and at which the mass's moment of inertia about the axis would equal its real mass' moment of inertia.[216] Typically, while analyzing MD simulations, Rg is determined over time with the help of Eq. 46

$$\mathrm{ROG} = \sqrt{\frac{1}{N_i}\sum_i (r_i - r_{cm})^2} \qquad (46)$$

In this context, $(r_i - r_{cm})$ denotes the distance from atom *i* to the molecular center of mass.

Molecular Mechanics-Poisson Boltzmann Surface Area (MM-PBSA) uses MD simulations extensively to investigate dynamics, structure and thermodynamic characteristics of biological molecules and their complexes with ligands.[217] Apart for this technique using the combined Molecular Mechanical/Generalized Born Surface Area (MM-GBSA) technique is a more reliable method of estimating binding free energy of ligands to proteins.[218] The force-field based MM-GBSA approach uses the difference between free energies of protein, ligand and the complex in solution to calculate free energy of binding. The combination of electrostatic solvation energy (GB), non-electrostatic contribution to solvation energy (SA), and gas-phase molecular mechanics (MM) energy yields free energy. Since it can regard protein and ligand as flexible, allowing for structural reorganizations necessary for the induced-fit pose, it offers a more accurate prediction. MM-GBSA requires additional calculation for the same reason. Since they are less involved than traditional docking experiments, they are typically used after a finished docking research to assign new scores to certain ligands.[219]

Total binding energy ΔG_{bind} can be calculated using Eq. 47

$$\Delta G_{bind} = \mathrm{E}_{complex} - \mathrm{E}_{ligand} - \mathrm{E}_{receptor} \qquad (47)$$

here E_{ligand} and $\mathrm{E}_{receptor}$ represent optimized free ligand and receptor respectively, and $\mathrm{E}_{complex}$ represents the energy of the optimized complex.

There is another way to break down Eq. 47 as

$$\Delta G_{bind} = \Delta H - T\Delta S \qquad (48)$$

$$\Delta G_{bind} = \Delta E_{MM} + \Delta \mathrm{G}_{sol} - T\Delta S \qquad (49)$$

The ΔE_{MM} denotes changes in internal energy (ΔE_{int}), electrostatic energy (ΔE_{elec}) and vdW energy (ΔE_{vdw}) in gas-phase molecular mechanics (MM) system.

$$\Delta E_{MM} = \Delta E_{int} + \Delta E_{elec} + \Delta E_{vdw} \quad (50)$$

Eq. 51 defines ΔG_{sol} as total electrostatic solvation energy between solute and continuum solvent including polar contributions ($\Delta G_{PB/GB}$) and non-polar contributions (ΔG_{SA}).

$$\Delta G_{sol} = \Delta G_{PB/GB} + \Delta G_{SA} \quad (51)$$

$$\Delta G_{SA} = \gamma\, SASA + b \quad (52)$$

One may compute $\Delta G_{PB/GB}$ using the generalized Born (GB) model or Poisson-Boltzmann (PB) model. Using solvent-accessible surface area (SASA), one may estimate ΔG_{SA}, where b is a correction constant and γ the surface tension constant. Using normal-mode analysis, one may determine the change in conformational entropy ($-T\Delta S$).[217-219]

4.3.3 Application of Molecular Dynamics:

MD simulations are widely used to investigate protein folding mechanisms that are critical in understanding their function.[220] MD can simulate the dynamic behaviour of proteins, specifically how they adopt their natural forms offering vital insights into disorders caused by misfolded proteins like in Alzheimer's disease.[221] MD simulations are also an effective technique for investigating biomolecular interactions such as ligand binding, protein-protein interactions and membrane transport mechanisms.[222]

MD simulations are also used in drug development to explore interactions between small compounds (as potential medicines) and biological targets like proteins or nucleic acids. These simulations can aid the identification of prospective drug candidates by predicting how effectively a molecule binds to its target and understanding the dynamic behaviour of the protein-ligand complex.[27] Materials science commonly use MD simulations to investigate atomic characteristics of nanomaterials, polymers and crystals. They play an important role in investigating the

mechanical, thermal and electrical characteristics of materials as well as in designing novel materials with specified qualities.[223] MD simulations give information on phase transitions like melting, crystallization and glass transitions. By simulating how systems evolve at different temperatures and pressures MD can capture processes driving these transitions and assist in forecasting the characteristics of materials at particular stages.[224]

References

1. R. K. Sodhi, S. Paul; Metal Complexes in Medicine: An Overview and Update from Drug Design Perspective. *Canc Therapy & Oncol Int J.*, **2019**; 14, 555883.
2. J. Karges, R.W Stokes, S.M. Cohen; Metal Complexes for Therapeutic Applications. *Trends Chem.*, **2021**, 3, 523-534.
3. S. R. Inza, D. Plano, C. Sanmartín; Metal-based compounds containing selenium: An appealing approach towards novel therapeutic drugs with anticancer and antimicrobial effects, *European Journal of Medicinal Chemistry*, **2022**, 244,114834
4. T. C. Johnstone, K. Suntharalingam, & S. J. Lippard; The Next Generation of Platinum Drugs: Targeted Pt(II) Agents, Nanoparticle Delivery, and Pt(IV) Prodrugs. *Chemical Reviews*, **2016**,116, 3436-3486.
5. A. Jain; Multifunctional, heterometallic ruthenium-platinum complexes with medicinal applications, *Coordination Chemistry Reviews*, **2019**, 401, 213067.

6. M. Frezza, S. Hindo, D. Chen, A. Davenport, S. Schmitt, D. Tomco, QP. Dou; Novel metals and metal complexes as platforms for cancer therapy. *Curr Pharm Des*. **2010** 16, 1813-25.

7. M. Zaki, F. Arjmand, S. Tabassum; Current and future potential of metallo drugs: Revisiting DNA-binding of metal containing molecules and their diverse mechanism of action, *Inorganica Chimica Acta*, **2016**, 444, 1-22.

8. Y. Yu, Q. Xu, S. He, H. Xiong, Q. Zhang, W. Xu, V. Ricotta, L. Bai, Q. Zhang, Z. Yu, J. Ding, H. Xiao, D. Zhou; Recent advances in delivery of photosensitive metal-based drugs, *Coordination Chemistry Reviews*, **2019**, 387, 154-179.

9. Y. Chang, B.A. Hawkins, J. J. Du, P.W. Groundwater, D.E. Hibbs, F. Lai; A Guide to In Silico Drug Design. *Pharmaceutics.* **2022,** 15, 1-52.

10. E. Boros, P.J Dyson, G. Gasser; Classification of metal-based drugs according to their mechanisms of action. *Chem.* **2020** , 6, 41-60.

11. G. Tiwari, M. S. Chauhan and D. Sharma; "*In silico* study of inhibition activity of boceprevir drug against 2019-nCoV main protease" *Zeitschrift für Naturforschung C*, **2024**, 79, 1-12.

12. L. Pauling, P.D., Sc.D. and E. B. Wilson, Jr., Introduction to quantum mechanics, with applications to chemistry. . Journal of Chemical Technology and Biotechnology, 1936. 55(44): p. 861.

13. S.J. Smith, B.T. Sutcliffe; The development of Computational Chemistry in the United Kingdom. Reviews in Computational Chemistry., 1997. 10: p. 271-316.

14. K. Kaavin, D. Naresh, MR Yogeshkumar, M. K. Prakash, S. Janarthanan, M. M. Krishnan, M. Malathi; In-silico DFT studies and molecular docking evaluation of benzimidazo methoxy quinoline-2-one ligand and its Co, Ni, Cu and Zn complexes as

potential inhibitors of Bcl-2, Caspase-3, EGFR, mTOR, and PI3K, cancer-causing proteins, *Chemical Physics Impact*, **2024**, 8, 100418.

15. J. A. Pascual, I. S. Sanchez, P. Mauleón, M. Agirre, A. C. Lopes, O. Zugazua, E. S. Díez, J. R. A. Moreno, P. Ocón; DFT calculation, a practical tool to predict the electrochemical behaviour of organic electrolytes in aqueous redox flow batteries, *Journal of Power Sources*, **2023**, 564, 232817.

16. F. M. Alkhatib, H. M. Alsulami; Synthesis, characterization, DFT calculations and biological activity of new Schiff base complexes, *Heliyon*, **2023**, 9, e18988.

17. N. Ye, Z. Yang, Y. Liu; Applications of density functional theory in COVID-19 drug modeling. *Drug Discov Today*. **2022**, 27, 1411-1419.

18. X.Y Meng, H.X Zhang, M Mezei, M. Cui; Molecular docking: a powerful approach for structure-based drug discovery. *Curr Comput Aided Drug Des*. **2011**, 7, 146-57.

19. Zabiulla, S. Kouser, M. Joythi, A. B. Begum, M.S. Asha, F. H. Al-Ostoot, D.P. Lakshmeesha, R. Ramu, S. A. Khanum; Molecular docking, synthesis and antimicrobial evaluation of metal complexes with Schiff base, *Results in Chemistry*, **2023,** 5, 100650.

20. M.S Refat, A. Gaber, Y.S Althobaiti, H. Alyami W.F Alsanie, S. Shakya, A.M.A Adam, M.I Kobeasy, K.A. Asla; Spectroscopic and Molecular Docking Studies of Cu(II), Ni(II), Co(II), and Mn(II) Complexes with Anticonvulsant Therapeutic Agent Gabapentin. Molecules. **2022**, 27, 4311.

21. S. Razak, T. Afsar, N. Bibi, M. Abulmeaty, W. Qamar, A. Almajwal, A. Inam, D. A. Disi, M. Shabbir, M.A. Bhat; Molecular docking, pharmacokinetic studies, and in vivo pharmacological study of indole derivative 2-(5-methoxy-2-methyl-1H-indole-3-yl)-N'-[(E)-(3-nitrophenyl) methylidene] acetohydrazide as a promising chemoprotective agent against cisplatin induced organ damage. *Sci Rep*. **2021**, 11, 6245.

22. K. J. Al-Adilee, S. H. Jawad, H. A. K. Kyhoiesh, H. M. Hassan; Synthesis, characterization, biological applications, and molecular docking studies of some transition metal complexes with azo dye ligand derived from 5-methyl imidazole, *Journal of Molecular Structure*, **2024**, 1295, 136695.

23. J. Zhao, Y. Cao, L. Zhang; Exploring the computational methods for protein-ligand binding site prediction, *Computational and Structural Biotechnology Journal*, **2020**, 18, 417-426.

24. M. Sahadevan, M. Sundaram, K. Subramanian; Quantum mechanical approaches and molecular docking studies of metal based anticancer drugs cis-Diammine glycolato platinum and Diaminocyclohexane oxalatoplatinum structures, *Computational Biology and Chemistry*, **2023**, 106, 107940.

25. M. Karplus, & J. A. McCammon; Molecular Dynamics Simulations of Biomolecules. *Nature Structural Biology*, **2002**, 9, 646-652.

26. T. U. da Silva, E. T. da Silva, K. de C. Pougy, C. H. da S. Lima, S. de P. Machado; Molecular modeling of indazole-3-carboxylic acid and its metal complexes (Zn, Ni, Co, Fe and Mn) as NO synthase inhibitors: DFT calculations, docking studies and molecular dynamics simulations, *Inorganic Chemistry Communications*, **2022**, 135, 109120.

27. O.M.H. Salo-Ahen, I. Alanko, R. Bhadane, A.M.J.J. Bonvin, R.V. Honorato, S. Hossain, Juffer, A.H. Kabedev, A.; Lahtela-Kakkonen, M.; Larsen, A.S.; et al. Molecular Dynamics Simulations in Drug Discovery and Pharmaceutical Development. *Processes*, **2021**, 9, 71.

28. J. Aghajani, P. Farnia, P. Farnia, J. Ghanavi, A.A. Velayati; Molecular Dynamic Simulations and Molecular Docking as a Potential Way for Designed New Inhibitor Drug without Resistance. *Tanaffos.* **2022**, 21, 1-14.

29. C. Gossens, I. Tavernelli, and U. Rothlisberger; DNA Structural Distortions Induced by Ruthenium−Arene Anticancer Compounds. *Jour.Am.Chem.Soc* ., **2008** ,130 , 10921-10928.

30. S. M. Meier-Menches, C. Gerner, W. Berger, C. G. Hartinger, & B. K. Keppler; Structure–Activity Relationships for Ruthenium and Osmium Anticancer Agents – Towards Clinical Development. *Chemical Society Reviews*, **2018**, 47, 909-928.

31. S. F. Sousa, P. A. Fernandes, & M. J. Ramos.; Protein–ligand docking: Current status and future challenges. *Proteins:*, **2006**, 65, 15-26.

32. Y. Bai, L. Vogt-Maranto, M.E. Tuckerman, et al. Machine learning the Hohenberg-Kohn map for molecular excited states. *Nat Commun*, **2022,** 13, 7044.

33. V.Sahni.; The Hohenberg-Kohn Theorems and Kohn-Sham Density Functional Theory, *Quantal Density Functional Theory*, **2004**, ISBN : 978-3-642-07419-6

34. W. Koch, M.C. Holthausen.; A chemist guide to Density Functional Theory, *Wiley-VCH*, **2000**, ISBNs: 3-527-30372-3 (Softcover); 3-527-60004-3 (Electronic).

35. W. Kohn.; Nobel Lecture: Electronic structure of matter—wave functions and density functionals, *Rev. Mod. Phys.*, **1999**, 71, 1253.

36. D.J. Griffiths.; Introduction to Quantum Mechanics (2nd ed.). **2004**, New Jersey, U.S.: Prentice Hall.

37. E. Schrödinger.; An Undulatory Theory of the Mechanics of Atoms and Molecules. *Physical Review*, **1926**. 28,1049-1070.

38. C. L. Levada, H. Maceti, I. J. Lautenschleguer.; Review of the Schrödinger Wave Equation, *IOSR Journal of Applied Chemistry*, **2018**,11, 1-7.

39. Y. B. Band, Y. Avishai.; 14-Many-body theory, *Quantum Mechanics with Applications to Nanotechnology and Information Science*, *Academic Press*, **2013**, 825-870.

40. J.M. Combes.; The Born-Oppenheimer approximation. In The Schrödinger Equation: Proceedings of the International Symposium "50 Years Schrödinger Equation" in Vienna, Vienna: Springer Vienna. **1977**, 139-159.

41. C.D. Sherrill.; The born-oppenheimer approximation. School of Chemistry and Biochemistry, Georgia Institute of Technology. **2005**, 242.

42. B.T. Sutcliffe.; The Born-Oppenheimer Approximation. *In Methods in Computational Molecular Physics*, Boston, MA: Springer US. , **1992** ,19-46.

43. J. Rana, S. Liao.; On time independent Schrödinger equations in quantum mechanics by the homotopy analysis method. *Theoretical and Applied Mechanics Letters*. **2019** 9, 376-81.

44. D.R. Hartree.; The Wave Mechanics of an Atom with a Non-Coulomb Central Field. Part I. Theory and Methods. Mathematical Proceedings of the Cambridge Philosophical Society, **1928**. 24, 89-110.

45. J.C. Slater.; Note on Hartree's Method. *Physical Review*, **1930**. 35, 210-211.

46. V. Fock.; Näherungsmethode zur Lösung des quanten mechanischen Mehrkö problems *Zeitschrift für Physik*, **1930**, 61, 126-148.

47. P.O. Löwdin.; Quantum theory of many-particle systems. II. Study of the ordinary Hartree-Fock approximation. *Physical Review.* **1955**, 97, 1490.

48. P. Lykos, G.W. Pratt.; Discussion on the Hartree-Fock approximation. *Reviews of Modern Physics*. **1963** , 35, 496.

49. T.A Kaplan, W.H. Kleiner.; Hartree-Fock theory: Slater determinants of minimum energy. *Physical Review.* **1967** ,156, 1.

50. G. Moritz, M. Reiher.; Decomposition of density matrix renormalization group states into a Slater determinant basis. *The Journal of chemical physics*. **2007**, 126.

51. N. Argaman, G. Makov.; Density functional theory: An introduction. *American Journal of Physics*. **2000** , 68, 69-79.

52. L.H. Thomas.; The calculation of atomic fields. Mathematical Proceedings of the Cambridge Philosophical Society, **1927**, 23, 542-548.

53. E. Fermi.; Un Metodo Statistico per la Determinazione di alcune Prioprietà dell'Atomo. *Rend. Accad. Naz. Lincei*., **1927**. 6, 602-607.

54. P. Hohenberg, and W. Kohn.; Inhomogeneous Electron Gas. *Physical Review*, **1964**. 136, B864-B871.

55. S.T Epstein, C.M. Rosenthal.; The Hohenberg-Kohn theorem. *Journal of Chemical Physics*. **1976**, 64, 247-249.

56. P.E. Lammert.; In search of the Hohenberg-Kohn theorem. *Journal of Mathematical Physics*. **2018** , 59.

57. W. Kohn, and L.J. Sham, Self-Consistent Equations Including Exchange and Correlation Effects. *Physical Review*, **1965**. 140, A1133-A1138.

58. F.M. Bickelhaupt, E.J. Baerends.; Kohn-Sham density functional theory: predicting and understanding chemistry. *Reviews in computational chemistry*, **2000** ,1-86.

59. H.S Yu, S.L Li, D.G. Truhlar.; Perspective: Kohn-Sham density functional theory descending a staircase. *The Journal of chemical physics*, **2016** , 145.

60. F. Lechermann, F. Welsch, C. Elsässer, C. Ederer, M. Fähnle, J.M. Sanchez, B. Meyer.; Density-functional study of Fe_3Al: LSDA versus GGA. *Physical Review B.,* **2002** 65,132104.

61. S. Grimme.; Semiempirical GGA-type density functional constructed with a long-range dispersion correction. *Journal of computational chemistry*. **2006** ,27, 1787-99.

62. B.G. Janesko.; Replacing hybrid density functional theory: motivation and recent advances. *Chemical Society Reviews*. **2021**, 50, 8470-95.

63. J.M. Martin, G. Santra.; Empirical double-hybrid density functional theory: A 'third way'in between WFT and DFT. *Israel Journal of Chemistry*. **2020**, 60, 787-804.

64. J.H Skone, M. Govoni, G. Galli.; Nonempirical range-separated hybrid functionals for solids and molecules. *Physical Review B.* **2016** , 93, 235106.

65. B. Medasani, M. Haranczyk, A. Canning, M. Asta.; Vacancy formation energies in metals: A comparison of MetaGGA with LDA and GGA exchange–correlation functionals. *Computational Materials Science*. **2015**, 101, 96-107.

66. J.P. Finley.; Using the local density approximation and the LYP, BLYP and B3LYP functionals within reference-state one-particle density-matrix theory. *Molecular Physics.* **2004**,102, 627-39.

67. W. Kohn, A.D. Becke, R.G. Parr.; Density functional theory of electronic structure. *The journal of physical chemistry*. **1996**, 100, 12974-80.

68. J. T. Rives, W.L. Jorgensen.; Performance of B3LYP density functional methods for a large set of organic molecules. *Journal of chemical theory and computation***. 2008** 4, 297-306.

69. M.M Quintal, A. Karton, M.A Iron, A.D Boese, J.M. Martin.; Benchmark study of DFT functionals for late-transition-metal reactions. *The Journal of Physical Chemistry A*. **2006**, 110, 709-16.

70. E.I Musina, A.A Karasik, A.S. Balueva, I.D. Strelnik, T.I. Fesenko, A.B. Dobrynin, T.P. Gerasimova, S.A. Katsyuba, O.N. Kataeva, P. Lönnecke, E. Hey-Hawkins.; Synthesis and Stereoselective Interconversion of Chiral 1-Aza-3, 6-diphosphacycloheptanes. *European Journal of Inorganic Chemistry*. **2012**, 11, 1857-66.

71. H. Chermette.; Density functional theory: a powerful tool for theoretical studies in coordination chemistry. *Coordination chemistry reviews*. **1998** ,178, 699-721.

72. A.C. Tsipis.; DFT/TDDFT insights into the chemistry, biochemistry and photophysics of copper coordination compounds. *RSC advances*. **2014**, 4, 32504-29.

73. I. Ciofini, C.A. Daul.; DFT calculations of molecular magnetic properties of coordination compounds. *Coordination Chemistry Reviews*. **2003** , 238, 187-209.

74. R. Bhavani, S. Elangovan, G. Suresh, S. Sankar, N. Kanagathara, P. Revathi.; Molecular structure, optical, first-order hyper polarizability, electronic properties, reactivity (ELF and LOL)computational analysis using DFT and Multiwfn for 2, 3-diaminopyridinium selenate. *Inorganic Chemistry Communications*. **2024** , 165, 112584.

75. E.J. Klinker, J. Kaizer, W.W. Brennessel, N.L. Woodrum, C.J. Cramer, L. Que.; Structures of nonheme oxoiron (IV) complexes from X-ray crystallography, NMR spectroscopy, and DFT calculations. *Angewandte Chemie-International Edition*. **2005** 44, 3690-3693.

76. J. Tomasi, B. Mennucci, R. Cammi.; Quantum mechanical continuum solvation models. *Chemical reviews*. **2005**,105, 2999-3094.

77. BO. Roos.; The multiconfigurational (MC) self-consistent field (SCF) theory. In Lecture notes in quantum chemistry: *European summer school in quantum chemistry* **1992**,177-254, Berlin, Heidelberg: Springer Berlin Heidelberg.

78. E.J. Baerends, G. Ricciardi, A Rosa, SJ. Van Gisbergen.; A DFT/TDDFT interpretation of the ground and excited states of porphyrin and porphyrazine complexes. *Coordination chemistry reviews*. **2002**, 230, 5-27.

79. A Vlček Jr, S. Záliš.; Modeling of charge-transfer transitions and excited states in d^6 transition metal complexes by DFT techniques. *Coordination chemistry reviews*. **2007** 251, 258-87.

80. C. Garino, L. Salassa.; The photochemistry of transition metal complexes using density functional theory. *Philosophical Transactions of the Royal Society A: Mathematical, Physical and Engineering Sciences.* **2013**, 371, 20120134.

81. D. Ramlot, M. Rebarz, L. Volker, M. Ovaere, D. Beljonne, W. Dehaen, L. Van Meervelt, C. Moucheron, A. Kirsch-De Mesmaeker.; An experimental and theoretical approach to the photophysical properties of some Rh and Ir complexes incorporating the dipyrromethene ligand. *European Journal of Inorganic Chemistry*. **2013**, 12, 2031-40.

82. Y. Minenkov, G. Occhipinti, V.R. Jensen.; Complete reaction pathway of ruthenium-catalyzed olefin metathesis of ethyl vinyl ether: Kinetics and mechanistic insight from DFT. *Organometallics.* **2013**, 32, 2099-111.

83. L. Vigara, M.Z Ertem, N. Planas, F. Bozoglian, N. Leidel, H. Dau, M. Haumann, L. Gagliardi, C.J. Cramer, t A. Llobe.; Experimental and quantum chemical characterization of the water oxidation cycle catalysed by $[Ru^{II}(damp)(bpy)(H_2O)]^{2+}$. *Chemical science*. **2012**, 3,2576-86.

84. Z. Yang, H. Yu, Y. Fu.; Mechanistic study on ligand-controlled cobalt-catalyzed regioselectivity-switchable hydroarylation of styrenes. *Chemistry–A European Journal*. **2013** ,19,12093-12103.

85. T.J Mustard, D.J Mack, J.T. Njardarson, P.H. Cheong.; Mechanism and the origins of stereospecificity in copper-catalyzed ring expansion of vinyl oxiranes: a traceless dual transition-metal-mediated process. *Journal of the American Chemical Society*. **2013** 135, 1471-5.

86. A.E. Reed, L.A. Curtiss, F. Weinhold.; Intermolecular interactions from a natural bond orbital, donor-acceptor viewpoint. *Chemical Reviews*. **1988**, 88, 899-926.

87. K. Arulaabaranam, S. Muthu, G. Mani, A.B. Geoffrey.; Speculative assessment, molecular composition, PDOS, topology exploration (ELF, LOL, RDG), ligand-protein interactions, on 5-bromo-3-nitropyridine-2-carbonitrile. *Heliyon*. **2021**, 7.

88. M. Gupta, R. Sharma, A. Kumar.; Docking techniques in pharmacology: How much promising?. *Computational biology and chemistry*. **2018**, 76, 210-217.

89. G.M Morris, M. Lim-Wilby.; Molecular docking. *Methods Mol Biol*. **2008**, 443, 365-82.

90. J. Fan, A. Fu, L. Zhang.; Progress in molecular docking. *Quantitative Biology*. **2019**,7, 83-9.

91. N.S. Pagadala, K. Syed, J. Tuszynski.; Software for molecular docking: a review. *Biophysical reviews*. **2017**, 9, 91-102.

92. S. Agarwal, R.J. Mehrotra.; An overview of molecular docking. *JSM chem*. **2016**, 4,1024-8.

93. X.Y. Meng, H.X. Zhang, M. Mezei, M. Cui.; Molecular docking: a powerful approach for structure-based drug discovery. *Current computer-aided drug design*. **2011** , 7, 146-57.

94. D.A. Gschwend, A.C. Good, I.D. Kuntz.; Molecular docking towards drug discovery. *Journal of Molecular Recognition: An Interdisciplinary Journal*. **1996**, 9,175-86.

95. S.J. Macalino, V. Gosu, S. Hong, S. Choi.; Role of computer-aided drug design in modern drug discovery. *Archives of pharmacal research*. **2015**, 38,1686-1701.

96. K.M. Elokely, R.J. Doerksen.; Docking challenge: protein sampling and molecular docking performance. *Journal of chemical information and modeling*. **2013**, 53, 1934-1945.

97. A.T. Brint, P. Willett.; Algorithms for the Identification of Three-Dimensional Maximal Common Substructures. *J. Chem. Inf. Comput. Sci.* **1987**, 27,152–158.

98. D. Fischer, R. Norel, H. Wolfson, R. Nussinov.; Surface motifs by a computer vision technique: searches, detection, and implications for protein-ligand recognition. *Proteins.* **1993**, 16, 278– 292.

99. R. Norel, D. Fischer, H. J. Wolfson, R. Nussinov.; Molecular surface recognition by a computer vision-based technique. *Protein Eng.* **1994**, 7, 39–46.

100. N. Moitessier, P. Englebienne, D. Lee, J. Lawandi, C.R. Corbeil.; Towards the development of universal, fast and highly accurate docking/scoring methods: a long way to go. *Br J Pharmacol*. **2008**; 153, S7–26.

101. I.D. Kuntz, J.M. Blaney, S.J. Oatley, R. Langridge, T.E. Ferrin.; A geometric approach to macromolecule-ligand interactions. *J Mol Biol*. **1982**; 161, 269–288.

102. M.D. Miller, S.K. Kearsley, D.J. Underwood, R.P. Sheridan.; FLOG: a system to select 'quasi-flexible' ligands complementary to a receptor of known three-dimensional structure. *J Comput Aided Mol Des.* **1994**, 8, 153–174.

103. D.J. Diller, K.M. Merz Jr. High throughput docking for library design and library prioritization. *Proteins.* **2001**, 43, 113–124.

104. P. Burkhard, P. Taylor, M.D. Walkinshaw.; An example of a protein ligand found by database mining: description of the docking method and its verification by a 2.3 A X-ray structure of a thrombin-ligand complex. *J Mol Biol*. **1998**, 277, 449–466.

105. M. Rarey, B. Kramer, T. Lengauer, G. Klebe.; A fast flexible docking method using an incremental construction algorithm. *J Mol Biol*. **1996**, 261, 470–489.

106. R.L. DesJarlais, R.P. Sheridan, J.S. Dixon, I.D. Kuntz, R. Venkataraghavan.; Docking flexible ligands to macromolecular receptors by molecular shape. *J Med Chem*. **1986**, 29, 2149–2153.

107. I.D. Kuntz, A.R. Leach.; Conformational analysis of flexible ligands in macromolecular receptor sites. *J. Comput. Chem*. **1992**, 13, 730–748.

108. T.J. Ewing, S. Makino, A.G. Skillman, I.D. Kuntz.; DOCK 4.0: search strategies for automated molecular docking of flexible molecule databases. *J Comput Aided Mol Des.* **2001**, 15, 411– 428.

109. W. Welch, J. Ruppert, A.N. Jain Hammerhead: fast, fully automated docking of flexible ligands to protein binding sites. *Chem Biol*. **1996**, 3, 449–462.

110. V. Schnecke, L.A. Kuhn.; Virtual Screening with Solvation and Ligand-Induced Complementarity. *Perspectives in Drug Discovery and Design*. **2000**, 20,171–190.

111. Z. Zsoldos, D. Reid, A. Simon, B.S. Sadjad, A.P. Johnson.; eHiTS: an innovative approach to the docking and scoring function problems. *Curr Protein Pept Sci***. 2006**, 7,421–435.

112. Morris GM, Goodsell DS, Halliday RS, Huey R, Hart WE, Belew RK, Olson AJ. Automated docking using a Lamarckian genetic algorithm and an empirical binding free energy function. *Journal of Computational Chemistry*. **1998**, 19, 1639–1662.

113. Jones G, Willett P, Glen RC, Leach AR, Taylor R. Development and validation of a genetic algorithm for flexible docking. *J Mol Biol*. **1997**, 267, 727–748.

114. C.M. Oshiro, I.D. Kuntz, J.S. Dixon.; Flexible ligand docking using a genetic algorithm. *J Comput Aided Mol Des*. **1995**, 9, 113–130.

115. M.L. Verdonk, J.C. Cole, M.J. Hartshorn, C.W. Murray, R.D. Taylor.; Improved protein-ligand docking using GOLD. *Proteins*. **2003**, 52, 609–623.

116. K.P. Clark Ajay, Flexible ligand docking without parameter adjustment across four ligand- receptor complexes. *J Comput Chem*. **1995**, 16,1210–1226.

117. J.S. Taylor, R.M. Burnett., DARWIN: a program for docking flexible molecules. *Proteins*. **2000**, 41,173–191.

118. D.S. Goodsell, A.J. Olson.; Automated docking of substrates to proteins by simulated annealing. *Proteins*. **1990**, 8, 195–202

119. R. Abagyan, M. Totrov, D. Kuznetsov.; ICM-A new method for protein modeling and design: Applications to docking and structure prediction from the distorted native conformation. *J. Comput. Chem*. **1994**, 15, 488–506

120. C. McMartin, R.S. Bohacek.; QXP: powerful, rapid computer algorithms for structure-based drug design. *J Comput Aided Mol Des*. **1997**, 11, 333–344.

121. C. Yang, E.A. Chen, Y. Zhang.; Protein–ligand docking in the machine-learning era. *Molecules.* **2022**, 27, 4568.

122. J. Liu, R. Wang.; Classification of current scoring functions. *Journal of chemical information and modeling.*, **2015**, 55, 475-82.

123. ,E.C. Meng, B.K. Shoichet, I.D. Kuntz.; Automated docking with grid based energy evaluation. *J.Comput.Chem.***1992**,13,505–524.

124. J. Wang, R.M. Wolf, J.W. Caldwell, P.A. Kollman, D.A. Case.; Development and testing of a general amber force field. *Journal of computational chemistry*. **2004** 25, 1157-1174.

125. N.Huang, C.Kalyanaraman, K.Bernacki, M.P.Jacobson.; Molecular mechanics methods for predicting protein–ligand binding. *Phys. Chem. Chem. Phys.* **2006**, 8, 5166–5177.

126. G.M. Morris, R. Huey, A.J. Olson Using autodock for ligand-receptor docking. *Current protocols in bioinformatics*. **2008** , 24, 8-14.

127. G.M. Morris, D.S. Goodsell, R. Huey, A.J. Olson.; Distributed automated docking of flexible ligands to proteins: parallel applications of AutoDock 2.4. *Journal of computer-aided molecular design*. **1996** ,10, 293-304.

128. S.J.Weiner, P.A.Kollman, D.A. Case, U.C. Singh, C. Ghio,; G. Alagona, S. Profeta, P. Weiner.; A new forcefield for molecular mechanical simulation of nucleic acids and proteins. *J. Am. Chem. Soc.* **1984**, 106, 765–784.

129. S.J. Weiner, P.A. Kollman, D.T. Nguyen, D.A. Case.; An all atom force field for simulations of proteins and nucleic acids. *J. Comput. Chem.* **1986**, 7, 230–252.

130. G.M. Morris, D.S. Goodsell, R.S. Halliday, R. Huey, W.E. Hart, R.K. Belew, A.J. Olson.; Automated docking using a Lamarckian genetic algorithm and an empirical binding free energy function. *Journal of computational chemistry*. **1998** ,19,1639-1662.

131. R.A. Friesner, J.L. Banks, R.B. Murphy, T.A. Halgren, J.J. Klicic, D.T. Mainz, M.P. Repasky, E.H. Knoll, M. Shelley, J.K. Perry.; Glide: A new approach for rapid, accurate docking and scoring. 1. Method and assessment of docking accuracy. *J. Med. Chem.* **2004**, 47, 1739–1749.

132. M.L. Verdonk, J.C. Cole, M.J. Hartshorn, C.W. Murray, R.D. Taylor.; Improved protein–ligand docking using GOLD. *Proteins: Structure, Function, and Bioinformatics*. **2003** , 52, 609-23.

133. R.A. Friesner, J.L. Banks, R.B. Murphy, T.A. Halgren, J.J. Klicic, D.T. Mainz, M.P. Repasky, E.H. Knoll, M. Shelley, J.K. Perry, D.E. Shaw Glide: a new approach for rapid, accurate docking and scoring. 1. Method and assessment of docking accuracy. *Journal of medicinal chemistry*. **2004** ,47,1739-49.

134. R. Wang, Y. Lu, S. Wang.; Comparative evaluation of 11 scoring functions for molecular docking. *Journal of medicinal chemistry*. **2003** , 46, 2287-2303.

135. D.B. Kitchen, H. Decornez, J.R. Furr, J. Bajorath.; Docking and scoring in virtual screening for drug discovery: methods and applications. *Nature reviews Drug discovery*. **2004** 3, 935-49.

136. O. Trott, A.J. Olson.; AutoDock Vina: improving the speed and accuracy of docking with a new scoring function, efficient optimization, and multithreading. *Journal of computational chemistry*. **2010** , 31, 455-461.

137. C. Yang, Y. Zhang.; Lin_F9: A Linear Empirical Scoring Function for Protein-Ligand Docking. *J Chem Inf Model*. **2021** , 61, 4630-4644.

138. I. Muegge, Y.C. Martin.; A general and fast scoring function for protein-ligand interactions: a simplified potential approach. *J Med Chem*. **1999**; 42, 791–804.

139. J.B.O. Mitchell, R.A. Laskowski, A. Alex, J.M. Thornton.; Bleep-potential of mean force describing protein-ligand interactions: I. generating potential. *J. Comput. Chem*. **1999**; 20, 1165–1176.

140. A.V. Ishchenko, E.I. Shakhnovich.; SMall Molecule Growth 2001 (SMoG2001): an improved knowledge-based scoring function for protein-ligand interactions. *J Med Chem.* **2002**, 45, 2770–2780.

141. M. Feher, E. Deretey, S. Roy.; BHB: a simple knowledge-based scoring function to improve the efficiency of database screening. *J Chem Inf Comput Sci*. **2003**; 43, 1316–1327.

142. H.F.G. Velec, H. Gohlke, G. Klebe.; DrugScore(CSD)-knowledge-based scoring function derived from small molecule crystal data with superior recognition rate of near-native ligand poses and better affinity prediction. *J. Med. Chem.* **2005**, 48, 6296–6303.

143. I. Muegge.; PMF scoring revisited. *J. Med. Chem.* **2006**, 49, 5895–5902

144. H, Gohlke, M. Hendlich, G. Klebe.; Knowledge-based scoring function to predict protein-ligand interactions. *Journal of molecular biology*. **2000** ,295, 337-356.

145. R.S. DeWitte, E.I. Shakhnovich.; SMoG: de novo design method based on simple, fast, and accurate free energy estimates. 1. Methodology and supporting evidence. *Journal of the American Chemical Society*. **1996** ,118, 11733-44.

146. , P.J. Ballester, J.B.O. Mitchell.; A machine learning approach to predicting protein–ligand binding affinity with applications to molecular docking. *Bioinformatics* **2010**, 26, 1169–1175

147. J.D. Durrant, J.A. McCammon.; NNScore: A neural-network-based scoring function for the characterization of protein-ligand complexes. *J. Chem. Inf. Model.* **2010**, 50, 1865–1871

148. B.K. Shoichet, R.M. Stroud, D.V. Santi, I.D. Kuntz, K.M. Perry.; Structure-based discovery of inhibitors of thymidylate synthase. *Science*. **1993**, 259,1445–1450.

149. H.A. Gabb, R.M. Jackson, M.J. Sternberg.; Modelling protein docking using shape complementarity, electrostatics and biochemical information. *J Mol Biol*. **1997**, 272,106–120.

150. S.B. Nabuurs, M. Wagener, J. De Vlieg.; A flexible approach to induced fit docking. *Journal of medicinal chemistry*. **2007** , 50, 6507-6518.

151. M.Y. Mizutani, Y. Takamatsu, T. Ichinose, K. Nakamura, A. Itai.; Effective handling of induced-fit motion in flexible docking. Proteins: Structure, Function, and *Bioinformatics.* **2006** , 63, 878-91.

152. M. Rarey, B. Kramer, T. Lengauer, G. Klebe.; A fast flexible docking method using an incremental construction algorithm. *J. Mol. Biol.* **1996**, 261, 470–489.

153. G. M. Morris, D. S. Goodsell,, R.S. Halliday,, R. Huey, W. E. Hart,, R. K. Belew, and A. J. Olson.; Automated Docking Using a Lamarckian Genetic Algorithm and and Empirical Binding Free Energy Function. *J. Computational Chemistry*, **1998,** 19, 1639-1662. "

154. R. Huey, G. M. Morris, A. J. Olson, and D. S. Goodsell.; A semiempirical free energy force field with charge-based desolvation. *J. Comput. Chem*. **2007** , 28, 1145- 1152.

155. R. Huey, D. S. Goodsell, G. M. Morris and A. J. Olson.; Grid-based hydrogen bond potentials with improved directionality. *Letters in Drug Design and Discovery*, **2004** 1, 178-183.

156. S.L. Vankayala, L.C. Warrensford, A.R. Pittman, B.C. Pollard, F.L. Kearns, J.D. Larkin, H.L. Woodcock CIFDock: A novel CHARMM-based flexible receptor–flexible ligand docking protocol. *Journal of computational chemistry*. **2022** 43, 84-95.

157. C. Hetényi, D. van der Spoel.; Blind docking of drug-sized compounds to proteins with up to a thousand residues. *FEBS letters*. **2006** , 580, 1447-50.

158. T. Singh, D. Biswas, B. Jayaram.; AADS-An automated active site identification, docking, and scoring protocol for protein targets based on physicochemical descriptors. *Journal of chemical information and modeling*. **2011**, 51, 2515-2527.

159. E.Fischer.;Einflussder Configuration auf die Wirkung der Enzyme .*Ber.DerDtsch.Chem.Ges.* **1894**,27,2985–2993

160. DE Jr. Koshland.; Correlation of Structure and Function in Enzyme Action. *Science*. **1963**, 142,1533–1541.

161. G.G. Hammes.; Multiple conformational changes in enzyme catalysis. *Biochemistry*. **2002**, 41, 8221–8228.

162. M. Rarey, B. Kramer, T. Lengauer, G. Klebe A fast flexible docking method using an incremental construction algorithm. *J Mol Biol*. **1996**, 261, 470–489.

163. R.A. Friesner, J.L. Banks, R.B. Murphy, T.A. Halgren, J.J. Klicic, D.T. Mainz, M.P. Repasky, E.H. Knoll, M. Shelley, J. K. Perry, D.E. Shaw, P. Francis, P.S. Shenkin.; Glide: a new approach for rapid, accurate docking and scoring. 1 Method and assessment of docking accuracy. *J Med Chem.* **2004**, 47,1739–1749.

164. M.R. McGann, H.R. Almond, A. Nicholls, J.A. Grant, F.K. Brown.; Gaussian docking functions. *Biopolymers*. **2003**, 68, 76–90.

165. E Perola, W.P. Walters, P.S. Charifson.; A detailed comparison of current docking and scoring methods on systems of pharmaceutical relevance. *Proteins.* **2004**, 56, 235–249.

166. H. Claussen, C. Buning, M. Rarey, T. Lengauer. FlexE: efficient molecular docking considering protein structure variations. *J Mol Biol*. **2001**, 308, 377–395.

167. J. Subramanian, S. Sharma, C BR. Modeling and selection of flexible proteins for structure-based drug design: backbone and side chain movements in p38 MAPK. *ChemMedChem*. **2008**, 3, 336–344.

168. M. Cui, M. Mezei, R. Osman.; Prediction of protein loop structures using a local move Monte Carlo approach and a grid-based force field. *Protein Engineering, Design & Selection*. **2008**, 21, 729-735 .

169. J. Monod, J. Wyman, Jp. Changeux.; On The Nature Of Allosteric Transitions: A Plausible Model. *J Mol Biol*. **1965** ,12, 88-118.

170. R.W. Hooft, G. Vriend, C. Sander, E.E. Abola, Errors in protein structures. *Nature* **1996**, 381, 272.

171. G.T. Ramachandran, V. Sasisekharan.; Conformation of polypeptides and proteins. In *Advances in Protein Chemistry*; Elsevier: Amsterdam, The Netherlands, **1968**; 23, 283–437.

172. K. K. Chaudhary, & N. Mishra, A review on molecular docking: Novel tool for drug discovery. *JSM Chem.* **2016**, 4, 1029.

173. J.J. Irwin, B.K. Shoichet.; ZINC- a free database of commercially available compounds for virtual screening. *Journal of chemical information and modeling*. **2005** 45, 177-82.

174. S. Kim, J. Chen, T. Cheng, A. Gindulyte, J. He, S. He, Q. Li, B.A. Shoemaker, P.A. Thiessen, B. Yu, L. Zaslavsky.; PubChem 2019 update: improved access to chemical data. *Nucleic acids research*. **2019** , 47, D1102-9.

175. M.D. Hanwell, D.E. Curtis, D.C. Lonie, T. Vandermeersch, E. Zurek, G.R. Hutchison.; Avogadro: an advanced semantic chemical editor, visualization, and analysis platform. *Journal of cheminformatics*. **2012** , 4,1-7.

176. S. Mukherjee, T.E. Balius, R.C. Rizzo.; Docking validation resources: protein family and ligand flexibility experiments. *Journal of chemical information and modeling*. **2010** , 50, 1986-2000.

177. P. S. Suresh, A. Kumar, R. Kumar & V. P. Singh.; An in silico approach to bioremediation: Laccase as a case study. *J. Mol. Graph Model.* , **2008**, 26, 845.9 .

178. C.M. Nisha, A. Kumar, P. Nair, N. Gupta, C. Silakari, T. Tripathi, A. Kumar.; Molecular Docking and In Silico ADMET Study Reveals Acylguanidine 7a as a Potential Inhibitor of β-Secretase. *Advances in bioinformatics*. **2016**,9258578.

179. M.E. Tuckerman, G.J. Martyna.; Understanding modern molecular dynamics: Techniques and applications. *The Journal of Physical Chemistry B.,* **2000** ,104,159-78.

180. B.J. Alder, T.E. Wainwright.; Phase transition for a hard sphere system. *The Journal of chemical physics*. **1957** , 27,1208-1209.

181. P.J. Artymiuk, C.C. Blake, D.E Grace, S.J. Oatley, D.C. Phillips, et al. Crystallographic studies of the dynamic properties of lysozyme. *Nature*., **1979**, 280, 563-568

182. J.D. Durrant, J.A. McCammon Molecular dynamics simulations and drug discovery. *BMC biology*. **2011**, 9, 1-9.

183. S.A. Hollingsworth, R.O. Dror.; Molecular dynamics simulation for all. *Neuron.*, **2018** 99,1129-43.

184. M. Karplus, G.A. Petsko.; Molecular dynamics simulations in biology. *Nature***. 1990** 347, 631-639.

185. B. Leimkuhler, C. Matthews.; Molecular dynamics. *Interdisciplinary applied mathematics*. **2015,** 39.

186. E.R. Lindahl.; Molecular dynamics simulations. *Molecular modeling of proteins*. **2008**, 3-23.

187. A.C. Wright.; The comparison of molecular dynamics simulations with diffraction experiments. *Journal of Non-Crystalline Solids*. **1993** , 159, 264-268.

188. H. Grubmüller, H. Heller, A. Windemuth, K. Schulten.; Generalized Verlet algorithm for efficient molecular dynamics simulations with long-range interactions. *Molecular Simulation*. **1991** , 6, 121-42.

189. Q. Spreiter, M. Walter.; Classical molecular dynamics simulation with the Velocity Verlet algorithm at strong external magnetic fields. *Journal of Computational Physics*. **1999** , 152, 102-19.

190. M.A. González.; Force fields and molecular dynamics simulations. *École thématique de la Société Française de la Neutronique*. **2011**,12,169-200.

191. O. Borodin .; Polarizable force field development and molecular dynamics simulations of ionic liquids. *The Journal of Physical Chemistry B.* **2009** 113, 11463-11478.

192. J. Henriques, C. Cragnell, M. Skepo.; Molecular dynamics simulations of intrinsically disordered proteins: force field evaluation and comparison with experiment. *Journal of chemical theory and computation*. **2015** ,11, 3420-3431.

193. L.T. Kong, C. Denniston, M.H. Müser, Y. Qi.; Non-bonded force field for the interaction between metals and organic molecules: a case study of olefins on aluminum. *Physical Chemistry Chemical Physics*. **2009**, 11, 10195-10203.

194. M.J. Field, P.A. Bash, M. Karplus.; A combined quantum mechanical and molecular mechanical potential for molecular dynamics simulations. *Journal of computational chemistry*. **1990** ,11, 700-733.

195. J. Wang, R.M. Wolf, J.W. Caldwell, P.A. Kollman, D.A. Case.; Development and testing of a general amber force field. *Journal of computational chemistry*. **2004** 25,1157-1174.

196. K. Vanommeslaeghe, E. Hatcher, C. Acharya, S. Kundu, S. Zhong, J. Shim, E. Darian, O. Guvench, P. Lopes, I. Vorobyov, Jr AD. Mackerell.; CHARMM general force field:

A force field for drug-like molecules compatible with the CHARMM all-atom additive biological force fields. *Journal of computational chemistry*. **2010**, 31,671-690.

197. G.A. Kaminski, R.A. Friesner, J. Tirado-Rives, W.L. Jorgensen. Evaluation and reparametrization of the OPLS-AA force field for proteins via comparison with accurate quantum chemical calculations on peptides. *The Journal of Physical Chemistry B.* **2001**, 105, 6474-6487.

198. N. Schmid, A.P. Eichenberger, A. Choutko, S. Riniker, M. Winger, A.E. Mark, W.F. Van Gunsteren.; Definition and testing of the GROMOS force-field versions 54A7 and 54B7. *European biophysics journal***. 2011** ,40, 843-856.

199. W.W. Wood, J.J. Erpenbeck, Jr GA Baker, JD. Johnson.; Molecular dynamics ensemble, equation of state, and ergodicity. *Physical Review E.*, **2000** ,63, 011106.

200. A. Mudi, C. Chakravarty.; Effect of the Berendsen thermostat on the dynamical properties of water. *Molecular Physics*. **2004** ,102, 681-685.

201. C. Braga, K.P. Travis.; A configurational temperature Nosé-Hoover thermostat. *The Journal of chemical physics*. **2005** , 123.

202. Y. Lin, D. Pan, J. Li, L. Zhang, X. Shao ; Application of Berendsen barostat in dissipative particle dynamics for nonequilibrium dynamic simulation. *The Journal of Chemical Physics*. **2017**, 146.

203. H. Saito, H. Nagao, K. Nishikawa, K. Kinugawa; Molecular collective dynamics in solid para-hydrogen and ortho-deuterium: The Parrinello–Rahman-type path integral centroid molecular dynamics approach. *The Journal of chemical physics*. **2003,** 119, 953-963.

204. P. Mark, L. Nilsson.; Structure and dynamics of the TIP3P, SPC, and SPC/E water models at 298 K. *The Journal of Physical Chemistry A***. 2001**, 105, 9954-9960.

205. I.C. Yeh, G. Hummer.; System-size dependence of diffusion coefficients and viscosities from molecular dynamics simulations with periodic boundary conditions. *The Journal of Physical Chemistry B*. **2004** ,108, 15873-15879.

206. T.E. Cheatham, J.H. Miller, T. Fox, P.A. Darden, P.A. Kollman.; Molecular Dynamics Simulations on Solvated Biomolecular Systems: The Particle Mesh Ewald Method Leads to Stable Trajectories of DNA, RNA, and Proteins. *J Am Chem Soc*. **1995** ,117, 4193-4194.

207. V. Daggett ;Protein folding-simulation. *Chem Rev*., 2006 , 106, 1898-191.

208. G. Bussi, M. Parrinello.; Accurate sampling using Langevin dynamics. *Physical Review E—Statistical, Nonlinear, and Soft Matter Physics*. **2007**, 75, 056707.

209. E.R. Lindahl.; Molecular dynamics simulations. *Molecular modeling of proteins*. **2008**, 3-23.

210. N. Michaud-Agrawal, E.J. Denning, T.B. Woolf, O. Beckstein.; MD Analysis: a toolkit for the analysis of molecular dynamics simulations. *Journal of computational chemistry*. **2011**, 32, 2319-2327.

211. A. Grossfield, D.M. Zuckerman, Quantifying uncertainty and sampling quality in biomolecular simulations. *Annu. Rep. Comput. Chem.*, **2009**, 5, 23-48.

212. P.V. Klimovich, M.R. Shirts, D.L. Mobley.; Guidelines for the analysis of free energy calculations. *J. Comput. Aided. Mol. Des.*, **2015**, 29, 397-411.

213. M. Vincenzi, S. Costantini, S. Scala, D. Tesauro, A. Accar- do, M. Leone, G. Colonna J. Guillon, L. Portella, A.M. Trotta, L. Ronga, F. Rossi.; Conformational ensembles explored dynamically from disordered peptides targeting chemokine receptor CXCR4. *Int. J. Mol. Sci.*, **2015**, 16, 12159-12173.

214. K. Sargsyan, C. Grauffel, C. Lim.; How molecular size impacts RMSD applications in molecular dynamics simulations. *Journal of chemical theory and computation*. **2017** ,13,1518-1524.

215. N.C. Benson, V. Daggett.; A comparison of multiscale methods for the analysis of molecular dynamics simulations. *The Journal of Physical Chemistry B*. **2012**, 116, 8722-8731.

216. E. Yamamoto, T. Akimoto, A. Mitsutake, R. Metzler.; Universal relation between instantaneous diffusivity and radius of gyration of proteins in aqueous solution. *Physical review letters*. **2021**, 126, 128101.

217. S. Genheden, U. Ryde.; The MM/PBSA and MM/GBSA methods to estimate ligand-binding affinities. *Expert. Opin. Drug. Discov.,* **2015**, 10, 449-461.

218. P. A. Kollman, I. Massova, C. Reyes,; B. Kuhn,; S. Huo,; L. Chong,; M. Lee,; T. Lee,; Y. Duan,; W. Wang.; Calculating structures and free energies of complex molecules: Combining molecular mechanics and continuum models. *Acc. Chem. Res.* **2000**, 33, 889–897.

219. G. Rastelli, A.D. Rio, G. Degliesposti, M. Sgobba.; Fast and accurate predictions of binding free energies using MM-PBSA and MM-GBSA. *Journal of computational chemistry*. 2010, 31, 797-810.

220. V. Daggett.; Protein folding−simulation. *Chemical reviews*. **2006**, 106, 1898-1916.

221. N.V. Buchete, R. Tycko, G. Hummer.; Molecular dynamics simulations of Alzheimer's β-amyloid protofilaments. *Journal of molecular biology*. **2005**, 353, 804-821.

222. F. Khalili-Araghi, J. Gumbart, P.C. Wen, M. Sotomayor, E. Tajkhorshid, K. Schulten.; Molecular dynamics simulations of membrane channels and transporters. *Current opinion in structural biology*. **2009**, 19, 128-137.

223. C. Massobrio, J. Du, M. Bernasconi, P.S. Salmon.; Molecular dynamics simulations of disordered materials. *Heidelberg: Springer*; **2015**.

224. S.L. Duncan, I.S. Dalal, R.G. Larson.; Molecular dynamics simulation of phase transitions in model lung surfactant monolayers. *Biochimica et Biophysica Acta (BBA)-Biomembranes.* **2011**, 1808, 2450-2465.

CHAPTER 5

Genesis and Scope

The rapid rise in antibiotic-resistant bacteria has created a pressing issue in contemporary healthcare,[1-6] necessitating the development of innovative therapeutic agents with distinct mechanisms, for combating bacterial pathogens.[7-12] Plant-derived bio-active compounds (phytochemicals) have attracted considerable attention owing to their potential as antibacterial agents.[13-16] Curcumin, the main active ingredient of Curcuma longa (turmeric), has shown remarkable biological activities, including antibacterial, antioxidant and anti-inflammatory effects.[17-27] The compound has been used for centuries for its medicinal properties in traditional healing practices.[17-28] Structurally it is a polyphenol with a diketone configuration that enables it to interact with various biomolecules through hydrogen bonding, hydrophobic interactions and metal-ion chelation.[29-32] This structural flexibility allows Curcumin to influence multiple biological pathways which makes it an intriguing candidate for antibacterial applications.[17-28] However, its effectiveness under physiological conditions is limited by poor bio-availability and chemical instability.[26,33-36] *Chapter 2* explores the various aspects related to the stability of Curcumin and its diverse medicinal properties including its potential as an antibacterial agent.

Recent developments in the synthesis of metal complexes of Curcumin have shown the potential for enhancing their antibacterial efficacy.[37-40] Curcumin forms stable complexes with various transition and non-transition metal ions.[37-45] These metal complexes exhibit improved stability, solubility and bioavailability which can amplify antibacterial effects of Curcumin.[37-42] Research has demonstrated that Curcumin metal complexes are more effective against bacterial strains than Curcumin alone, particularly in resistant strains in which conventional antibiotics are ineffective.[46,47] *Chapter 3* discusses some of the aspects on the use of Curcumin and its metal complexes for antibacterial therapeutics.

Analysis of the molecular structure of Curcumin[26] and its metal complexes[37-40] is crucial for evaluating their chemical attributes and durability. Application of Density Functional Theory

(DFT) optimization enables the measurement of molecular geometry, including bond length, bond angle as well as electronic properties like the HOMO-LUMO energy levels etc.[48-50] This approach has allowed scientists to determine the most energetically favourable conformations and electronic configurations providing an insight on binding and durability of Curcumin-metal complexes.[38-42,48-50] These electronic characteristics aid in assessing the stability, predict reactivity and examine potential interactions between Curcumin and its biological targets. [38-42,48-52] In conjunction with DFT, molecular docking serves as an initial screening method to examine how Curcumin and its metal complexes interact with bacterial proteins.[48-52] This approach predicts the binding strength, spatial arrangement and the mechanisms of interaction between Curcumin, its metal complexes and biological macromolecules like DNA and protein.[48-53] Combining Molecular Docking with Molecular Dynamics (MD) simulation provides a time-based view of how Curcumin-metal complexes might interact with bacterial targets.[54,55] This approach goes beyond the static picture offered by docking alone, allowing researchers to observe the flexibility and durability of ligand-protein binding processes. The stability of these structures can be assessed using RMSD and RMSF measurements obtained from MD simulations[55-57] which indicate that Curcumin and its metal complexes remain bound under physiological conditions. *Chapter 4* highlights basic principles of some of these theoretical investigations. These computational methods also reveal important details about binding site interactions such as hydrogen bonding patterns and hydrophobic contacts that are crucial for understanding the mechanism of action of Curcumin and its metal complexes.

With a view to realize some of the above mentioned facts, during the course of the research work three complexes of Curcumin were synthesized using Mn(II), Cu(II) and Zn(II) as metal ions. These were analysed using experimental methods and theoretical computations and have been discussed elaborately in *Chapters 8, 9 and 10* respectively. This approach aided in forecasting structural characteristics that could be related to bioactivity.

The chapters also emphasize on model DNA-binding experiments since interaction with DNA is a crucial mechanism through which Curcumin and its metal complexes exhibit antibacterial effects. The compounds interfere with essential cellular processes by attaching to bacterial DNA, resulting in cell cycle arrest or programmed cell death. Examination of DNA-binding capabilities of Curcumin and its complexes offers valuable insights into their molecular-level mechanism of action. Techniques like UV-Vis spectroscopy and fluorescence spectroscopy can reveal binding affinity, mode of interaction (e.g. intercalation, groove binding or electrostatic interaction) and specificity of these complexes towards bacterial DNA. Understanding these interactions is essential for assessing their potential as antibacterial agents and enhancing structures for targeted DNA interactions. Furthermore, studying DNA-binding interactions of Curcumin-metal complexes sheds light on aspects whether complexes interact differently in comparison to free Curcumin and if a difference in interaction has some positive manifestation on biological activity. Inclusion of metal ions could improve binding affinity and this might promote intercalative or groove-binding modes, potentially increasing specificity towards bacterial DNA than that of the host. Computational techniques, including molecular docking and molecular dynamics (MD) simulations have emerged as crucial tools for examining how Curcumin and its metal complexes interact with DNA. These *in silico* approaches offer valuable insights into binding mechanisms, interaction energies and structural stability of curcumin-DNA complexes enhancing molecular-level understanding of the mode of action. Docking analyses forecast initial binding locations and configurations, enabling scientists to assess binding strength and interaction patterns between DNA and Curcumin-metal complexes. Subsequently, MD simulations provided a dynamic view revealing conformational shifts, stability and solvation effects over time in a physiologically relevant setting. These factors being essential for the

functioning of any compound as an antibacterial agent was therefore elaborately discussed in *Chapter 11*.

FtsZ, a protein essential for bacterial cell division is a prime target of antibacterial agents.[59-62] This highly conserved protein in prokaryotes plays a crucial role in cell division by forming a Z ring at its site of division.[59-63] Interference with FtsZ function halts cell division leading to bacterial death.[59-63] Thus, FtsZ has been identified as a validated target for antibacterial drugs, especially against resistant strains.[64-67] Research has demonstrated Curcumin interacts with FtsZ, hindering its polymerization and GTPase activity that are essential for cell division.[64-67] By targeting FtsZ, Curcumin and its derivatives not only impede bacterial growth, but also induce cell death, making them effective antibacterial compounds.[68-69] However, the efficacy of Curcumin is limited, prompting scientists to investigate its metal complexes as potent FtsZ inhibitors. Computational techniques, including molecular docking and MD simulations, are crucial for understanding the interactions between the Curcumin-metal complexes and FtsZ. The methods allow visualization of FtsZ binding sites and an assessment of binding affinities of curcumin and its metal complexes, which has been discussed thoroughly in *Chapter 12*.

Researchers have assessed the antibacterial capabilities of Curcumin and its metal-based derivatives using various *in vitro* tests.[70] These evaluations typically employ techniques such as disk diffusion, minimum inhibitory concentration (MIC) measurements, various killing assays and membrane permeabilization. During investigations, bacterial species *Escherichia coli* and *Staphylococcus aureus* were treated with Curcumin and metal complexes to evaluate their efficacy in suppressing bacterial proliferation. The results of laboratory experiments consistently demonstrate Curcumin-metal complexes display enhanced antibacterial properties over that of Curcumin suggesting increased potency in their favour.

Curcumin and its metal complexes demonstrate a potential as antibacterial agents, not only in traditional *in vitro* settings but also as possible treatments for bacteria that are resistant to multiple drugs. The integration of *in vitro* experiments and computational studies provide a solid basis for elucidating how these compounds combat bacteria. Additionally, targeting the FtsZ protein is a unique approach that could be effective against various bacterial pathogens, including those unresponsive to conventional antibiotics. These compounds might offer a promising solution for the challenge posed by antibiotic resistance which is why they were investigated. An improved antibacterial efficacy if observed under both laboratory and computer-based (*in silico*) approaches might then highlight the ability of metal complexes to address limitations of Curcumin. By focusing on FtsZ, complexes could provide targeted and efficient methods for halting bacterial growth, potentially leading to new forms of antibacterial treatment. To fully understand their therapeutic potential, additional studies also became necessary as the work progresses so as to refine the complexes and evaluate their effectiveness in living organisms.

References:

1. S. Sagar, S. Kaistha, A.J. Das, and R. Kumar; Antibiotic resistant bacteria: a challenge to modern medicine. *Springer Singapore*. **2019**.

2. N.A. Church, J.L. McKillip; Antibiotic resistance crisis: challenges and imperatives. *Biologia*, **2021**, 76, 1535-1550.

3. D. Chinemerem Nwobodo, M.C. Ugwu, C. Oliseloke Anie, M.T. Al-Ouqaili, J. Chinedu Ikem, U. Victor Chigozie, M. Saki; Antibiotic resistance: The challenges and some emerging strategies for tackling a global menace. *Journal of clinical laboratory analysis*, **2022**, 36, e24655.

4. O.O. Komolafe; Antibiotic resistance in bacteria-an emerging public health problem. *Malawi medical journal*, **2003**, 15, 63-67.

5. F. Akram, M. Imtiaz, I. ul Haq; Emergent crisis of antibiotic resistance: A silent pandemic threat to 21st century. *Microbial pathogenesis*, **2023**, 174,105923.

6. L. Serwecińska; Antimicrobials and antibiotic-resistant bacteria: a risk to the environment and to public health. *Water*, **2020**, 12, 3313.

7. G. Muteeb, M.T. Rehman, M. Shahwan, M. Aatif; Origin of antibiotics and antibiotic resistance, and their impacts on drug development: A narrative review. *Pharmaceuticals*, **2023,** 16, 1615.

8. P.K. Mantravadi, K.A. Kalesh, R.C. Dobson, A.O. Hudson, A. Parthasarathy; The quest for novel antimicrobial compounds: emerging trends in research, development, and technologies. *Antibiotics*, **2019**, 8, 8.

9. J.M.V. Makabenta, A. Nabawy, C.H. Li, S. Schmidt-Malan, R. Patel, V.M. Rotello; Nanomaterial-based therapeutics for antibiotic-resistant bacterial infections. *Nature Reviews Microbiology*, **2021**, 19, 23-36.

10. M. Gopikrishnan, S. Haryini; Emerging strategies and therapeutic innovations for combating drug resistance in Staphylococcus aureus strains: A comprehensive review. *Journal of Basic Microbiology*, **2024**, 64, 2300579.

11. T.M. Belete; Novel targets to develop new antibacterial agents and novel alternatives to antibacterial agents. *Human Microbiome Journal*, **2019**, 11, 100052.

12. K.M. O'Connell, J.T. Hodgkinson, H.F. Sore, M. Welch, G.P. Salmond, D.R. Spring; Combating multidrug-resistant bacteria: current strategies for the discovery of novel antibacterials. *Angewandte Chemie International Edition*, **2013**, 52, 10706-10733.

13. N. Chaachouay, L. Zidane; Plant-derived natural products: a source for drug discovery and development. *Drugs and Drug Candidates*, **2024**, 3, 184-207.

14. T.L. Nguyen, A. Ora, S.T. Häkkinen, A. Ritala, R. Räisänen, M. Kallioinen-Mänttäri, K. Melin; Innovative extraction technologies of bioactive compounds from plant by-products for textile colorants and antimicrobial agents. *Biomass conversion and biorefinery*, **2024**, 14, 24973-25002.

15. N. Nasim, I.S. Sandeep, S. Mohanty; Plant-derived natural products for drug discovery: current approaches and prospects. *The Nucleus*, **2022**, 65, 399-411.

16. D.M. Jo, N. Tabassum, D.K. Oh, S.C. Ko, K.W. Kim, D. Yang, J.Y. Kim, G.W. Oh, G. Choi, D.S. Lee, S.K. Park; Green Medicine: Advancing Antimicrobial Solutions with Diverse Terrestrial and Marine Plant-Derived Compounds. *Processes*, **2024**, 12, 2316.

17. B. Kocaadam , N. Sanlier. ; Curcumin, an active component of turmeric (curcuma longa), and its effects on health. Crit. *Rev. Food Sci. Nutr.,* **2017**, 57, 2889–2895.

18. B. B. Aggarwal, C. Sundaram , N. Malani , H. Ichikawa.; Curcumin: The Indian solid gold., *Adv. Exp. Med. Biol.*, **2007**, 595, 1 – 75.

19. N. K. Pandeya.; Old wives' tales: Modern miracles-Turmeric as traditional medicines in India, *Trees for Life Journal.*,**2005**,1:3.

20. J. Tilak, M. Banerjee, H. Mohan, T. P. A. Devasagayam.; Antioxidant availability of turmeric in relation to its medicinal and culinary uses. *Phytother. Res.*, **2004**,18, 798 – 804.

21. B.B. Aggarwal, A. Kumar, A. C. Bharti; Anticancer potential of Curcumin: Preclinical and clinical studies. *Anticancer Res.,* **2003**, 23, 363–398.

22. R.Wilken, S.M. Veena, M.B. Wang, E.S. Srivatsan; Curcumin: A review of anticancer properties and therapeutic activity in head and neck squamous cell carcinoma. *Mol. Cancer.,* **2011,** 10, 1–19.

23. G. Grykiewicz, P. Silfirski; Curucmin and Curcuminoids in quest for medicinal status. *Acta Biochim. Pol.,* **2012**, 59, 201–212.

24. T. Esatbeyoglu, P. Huebbe, M.A. Insa, E. DawnChin, A.E. Wagner, G. Rimbach; Curcumin—From Molecule to Biological Function. *Angew. Chem. Int. Ed*., **2012**, 51, 5308–5332.

25. S. Gupta, S. Prasad, H. K. Ji, S. Patchva, L. J. Webb, K. I. Priyadarsini, B. B. Aggarwal; Multitargeting by Curcumin as revealed by molecular interaction studies. *Nat. Prod. Rep.,* **2011**, 28, 1937–1955.

26. K.I. Priyadarsini; Chemical and structural features influencing the biological activity of Curcumin. *Curr. Pharm. Des.*, **2013**, 19, 2093–2100.

27. O.P. Sharma; Antioxidant activity of Curcumin and related compounds. *Biochem. Pharmacol*., **1976**, 25, 1811–1812.

28. Z. Ma, N.Wang, H. He, X. Tang; Pharmaceutical strategies of improving oral systemic bioavailability of Curcumin for clinical application. *J. Control. Release.*, **2019**, 316, 359–380.

29. H. H. Tonnesen, J. Karlsen, A. Mostad; Structural studies of Curcuminoids I. The crystal structure of Curcumin. Acta Chemica Scabdinavica B, 1982,36, 475-479. P.P. Sahoo, Y.V. Ramshankar, S. Suresh, T.N. Guru Row; Redetermination of Curcumin : (1E, 4Z,6E-5-hydroxy-3-methoxy-phenyl- hepta-1,4,6-triene-3-one). *Acta Crystal*., **2007**, 63, 860–862.

30. J. Emsley; The composition, structure and hydrogen bonding of the β-diketones, *Springer-Verlag*, **1984**,148-191.

31. J.S. Wright; Predicting the antioxidant activity of Curcumin and Curcuminoids. *J Mol Stru (Theochem)*, **2002**, 591,207-217.

32. T.M. Kolev, E.A. Velcheva, B.A. Stamboliyska, M. Spiteller; DFT and Experimental studies of the structure and vibrational spectra of Curcumin. *Int. Jour. Quant Chem*, **2005**,102, 1069-1079.

33. Y. J. Wang, M. H. Pan, A.L. Cheng, L.I. Lin, Y.S. Ho, C.Y. Hsieh, J.K. Lin; Stability of Curcumin in buffer solutions and characterization of its degradation products. *Jour. Pharm. Biomed. Anal.* **1997,** 15, 1867−1876.

34. O. N. Gordon, C. Schneider; Vanillin and ferulic acid: Not the major degradation products of Curcumin. *Trends Mol. Med.*, **2012,** 18, 361−363.

35. C. Schneider, O. N. Gordon, R. L. Edwards, P. B. Luis; Degradation of Curcumin: From mechanism to biological implications. *Jour. Agric. Food Chem.*, **2015,** 63, 7606−7614.

36. A. Khurana, C. T. Ho; High-performance liquid-chromatographic analysis of Curcuminoids and their photo-oxidative decomposition compounds in Curcuma longa l. *Jour. Liq. Chromatogr.*, **1988,** 11, 2295−2304.

37. S. Prasad, D. DuBourdieu, A. Srivastava, P. Kumar, R. Lall; Metal-Curcumin Complexes in Therapeutics: An Approach to Enhance Pharmacological Effects of Curcumin. *Int J Mol Sci*. **2021**, 22, 7094.

38. T. Sarakar, S. Banerjee, A. Hussain; Remarkable visible light-triggered cytotoxicity of mitochondria targeting mixed-ligand cobalt(III) complexes of curcumin and phenanthroline bases binding to human serum albumin, *RSC Advances*, **2015**, 22.

39. R. Sareen, N. Jain, and K. L. Dhar; Curcumin-Zn(II) complex for enhanced solubility and stability: an approach for improved delivery and pharmacodynamic effects. *Pharm. Dev. Technol.*, **2016,** 21, 630–635.

40. R. Pallikkavil, M. B. Ummathur, S. Sreedharan, and K. Krishnankutty; Synthesis, characterization and antimicrobial studies of Cd (II), Hg (II), Pb (II), Sn (II) and Ca (II) complexes of curcumin. *Main Group Metal Chem.*, **2013**, 36, 123–127.

41. M. Subhan, K. Alam, M. Rahaman, M. Awal; Synthesis and characterization of metal complexes containing curcumin ($C_{21}H_{20}O_6$) and study of their anti-microbial activities and DNA binding properties. *J. Sci. Res.* **2014**, 6, 97–109.

42. K. Mitra, S. Gautam, P. Kondaiah, and A. R. Chakravarty; Platinum (II) complexes of curcumin showing photocytotoxicity in visible light. *Eur. J. Inorg. Chem.,* **2017**, 1753–1763.

43. M. R. Hayes, and J. Metcalfe. ;The boron-curcumin complex in the determination of trace amounts of boron. *Analyst*., **1962**, 87.1041, 956-969.

44. F. Ahmadi, A. A. Alizadeh, N. Shahabadi and M. R. Nasrabadi.; Study binding of Al–curcumin complex to ds-DNA, monitoring by multispectroscopic and voltammetric techniques, *Spectrochim. Acta, Part A*, **2011**, 79, 1466–1474.

45. M. Asti, E. Ferrari, S. Croci, G. Atti, S. Rubagotti, M. Iori, P. C. Capponi, A. Zerbini, M. Saladini and A. Versari; Synthesis and characterization of (68)Ga-labeled curcumin and curcuminoid complexes as potential radiotracers for imaging of cancer and Alzheimer's disease. *Inorg. Chem.*, **2014**, 53, 4922–4933.

46. Y. Lyu, M. Yu, Q. Liu, Q. Zhang, Z. Liu, Y. Tian, D. Li, M. Changdao.; Synthesis of silver nanoparticles using oxidized amylose and combination with curcumin for enhanced antibacterial activity. *Carbohydr. Polym.*, **2020**, 230, 115573.

47. S. Shome, A.D. Talukdar, and H. Upadhyaya; Antibacterial activity of curcumin and its essential nanoformulations against some clinically important bacterial pathogens: A comprehensive review. *Biotechnology and Applied Biochemistry*, **2022**, 69, 2357-2386.

48. C.P.V. Mary, S. Vijayakumar, R. Shankar; Metal chelating ability and antioxidant properties of Curcumin-metal complexes–A DFT approach. *Journal of Molecular Graphics and Modelling*, **2018**, 79, 1-14.

49. R.L.G.Q. Corrêa, M.M.F. de Moraes, K.T. de Oliveira, Y.A. Aoto, M.D. Coutinho-Neto, P. Homem-de-Mello; Diving into the optoelectronic properties of Cu (II) and Zn

(II) curcumin complexes: a DFT and wavefunction benchmark. *Journal of Molecular Modeling*, **2023**, 29, 166.

50. A. Khireddine, M. Boukelkoul, Y. Atalay, Ö. Tamer, D. Avcı, L. Merzoud, H. Chermette; Structural, Electronic, Thermodynamic, Optical and Nonlinear Optical Properties of Curcumin Complexes with Transition Metals: DFT and TD-DFT Study. *ChemistrySelect*, **2022**, 7, e202104442.

51. A. Kumar, V. Kumar, K. Kumari, P. Jain, N.K. Kaushik, P. Singh; Promising iron (II) complexes of curcumins: designing, density functional theory, and molecular docking. *Journal of Physical Organic Chemistry*, **2021**, 34, e4196.

52. R. Kushwaha, R. Rai, V. Gawande, V. Singh, A.K. Yadav, B. Koch, P. Dhar, S. Banerjee; Antibacterial Photodynamic Therapy by Zn(II)-Curcumin Complex: Synthesis, Characterization, DFT Calculation, Antibacterial Activity, and Molecular Docking. *ChemBioChem*, **2024**, 25, p.e202300652.

53. P. Jeyaraman, A. Alagarraj, R. Natarajan; In silico and in vitro studies of transition metal complexes derived from curcumin–isoniazid Schiff base. *Journal of Biomolecular Structure and Dynamics*, **2020**, 488-499.

54. M. Liu, M. Yuan, M. Luo, X. Bu, H.B. Luo, X. Hu; Binding of curcumin with glyoxalase I: Molecular docking, molecular dynamics simulations, and kinetics analysis. *Biophysical chemistry*, **2010**, 147, 28-34.

55. G. Sabarees, V. Velmurugan, V.R. Solomon; Molecular docking and molecular dynamics simulations discover curcumin analogs as potential wound healing agents. *Chemical Physics Impact*, **2024**, 8, 100441.

56. P.P. Rao, T. Mohamed, K. Teckwani, G. Tin; Curcumin binding to beta amyloid: a computational study. *Chemical biology & drug design*, **2015**, 86, 813-820.

57. R. Suravajhala, A. Parashar, G. Choudhir, A. Kumar, B. Malik, V.A. Nagaraj, G. Padmanaban, R. Polavarapu, P. Suravajhala, P.K. Kishor; Molecular docking and dynamics studies of curcumin with COVID-19 proteins. *Network Modeling Analysis in Health Informatics and Bioinformatics*, **2021**, 10, 44.

58. K.A. Hurley, T.M. Santos, G.M. Nepomuceno, V. Huynh, J.T. Shaw , D.B. Weibel, Targeting the bacterial division protein FtsZ. *Journal of medicinal chemistry*, **2016**, 59, 6975-6998.

59. J. Löwe, L.A. Amos; Crystal structure of the bacterial cell-division protein FtsZ. *Nature*, **1998**. 391, 203-206.

60. X. Wang, J. Lutkenhaus; The FtsZ protein of Bacillus subtilis is localized at the division site and has GTPase activity that is dependent upon FtsZ concentration. *Molecular microbiology*, **1993**, 9, 435-442.

61. D. Bramhill , C.M. Thompson; GTP-dependent polymerization of Escherichia coli FtsZ protein to form tubules. *Proceedings of the National Academy of Sciences*, **1994**, , 91, 5813-5817.

62. P. De Boer, R. Crossley, and L. Rothfield; The essential bacterial cell-division protein FtsZ is a GTPase. *Nature*, **1992**, 359, 254-256.

63. N.L. Elsen, J. Lu, G. Parthasarathy, J.C. Reid, S. Sharma, S.M. Soisson, K.J. Lumb; Mechanism of action of the cell-division inhibitor PC190723: modulation of FtsZ assembly cooperativity. *Journal of the American Chemical Society*, **2012**, 134, 12342-12345.

64. R.C. Mishra, R. Kumari, S. Yadav, and J.P. Yadav; Target based virtual screening of new leads inhibitor against bacterial cell division protein FtsZ for the discovery of antibacterial agents. *Medicinal Chemistry*, **2020,** 16,169-175.

65. P. Domadia, S. Swarup, A. Bhunia, J. Sivaraman, D. Dasgupta; Inhibition of bacterial cell division protein FtsZ by cinnamaldehyde. *Biochemical pharmacology*, **2007,** 74, 831-840.

66. H.P. Erickson; Atomic structures of tubulin and FtsZ. *Trends Cell Biol*,. **1998** 8,133-137.

67. I.E. Vishnyakov, S.N. Borchsenius; FtsZ and bacterial cell division. *Cell and Tissue Biology*, **2007.** 1, 206-214.

68. D. Rai, Singh, J.K., Roy, N. and Panda, D., 2008. Curcumin inhibits FtsZ assembly: an attractive mechanism for its antibacterial activity. *Biochemical Journal*, *410*(1), pp.147-155.

69. S. Kaur, N.H. Modi, D. Panda, N. Roy; Probing the binding site of curcumin in Escherichia coli and Bacillus subtilis FtsZ–a structural insight to unveil antibacterial activity of curcumin. *European journal of medicinal chemistry*, **2010**, 45, 4209-4214.

70. S. Prasad, D. DuBourdieu, A. Srivastava, P. Kumar, R. Lall; Metal–curcumin complexes in therapeutics: an approach to enhance pharmacological effects of curcumin. *International journal of molecular sciences*, **2021**, 22, 7094.

CHAPTER 6

Experimental: Materials and Methods

Introduction

This chapter makes a mention of the materials acquired or synthesized for various experiments, along with experimental techniques employed to characterize compounds and investigate their biophysical interactions which fall under a broader category of research methodology. It also includes the instruments used in these processes. Different aspects of computational chemistry that includes density functional theory (DFT), molecular docking, molecular dynamics which are essential for solving structures and for understanding interactions with biological macromolecules, are addressed. Equations that were utilized for the purpose of assessing various biophysical interactions of compounds used have been mentioned in detail in this chapter. Some biophysical assays as well as some computer software programs that were utilized for analyzing and fitting the experimental data have also been highlighted in this chapter.

6.1 Materials used

Curcumin (HCur) was obtained from Sigma-Aldrich and stored at −5°C. Before an experiment, stock solutions were prepared in ethanol and DMSO and stored in a dark environment. Manganese(II) dichloride tetrahydrate, Copper(II) acetate monohydrate, Zinc(II) acetate, sodium nitrate (AR), sodium dihydrogen phosphate and disodium hydrogen phosphate were procured from Merck, India. All types of solutions were prepared using millipore water. Millipore water was used to prepare phosphate buffer by dissolving sodium dihydrogen phosphate and disodium hydrogen phosphate to arrive at the desired pH for that experiment. Sodium nitrate (AR) was employed to regulate ionic strength of the medium. Calf thymus DNA acquired from Sisco Research Laboratories, India was dissolved in millipore water to produce a solution containing 120 mM NaCl, 35 mM KCl, and 5 mM $CaCl_2$. It was allowed to stand for at least twenty-four hours before the same was used. The absorbance of the DNA solutions was

measured at 260 and 280 nm, and the A_{260}/A_{280} ratio was calculated. The ratio of 1.8 to 1.9 signifies that the DNA was sufficiently pure and did not require further purification. The DNA was evaluated by an assessment of its circular dichroism (CD) spectra at 260 nm utilizing a CD spectropolarimeter (J815, JASCO, Japan). The concentrations of these DNA solutions were ascertained from the nucleotide content utilizing a molar extinction value of 6,600 M^{-1} cm^{-1} at 260 nm. Products associated with the breakdown of Curcumin in aqueous media, specifically vanillin, vanillic acid and ferulic acid, were acquired from Sisco Research Laboratories, India. Nitrobluetetrazolium dichloride (NBT^{2+}) was acquired from Sigma-Aldrich.

6.2 Experimental

6.2.1 Determination of stoichiometry of metal complexes of Curcumin:

6.2.1.1 By mole-ratio method:

To determine stoichiometry of complex formation, equimolar amounts of Mn^{II}, Cu^{II}, and Zn^{II} were mixed with HCur. The mole ratio method employed[1,2] two approaches: one in which the metal ion concentration was varied for a fixed concentration of HCur, and the other, in which, HCur concentration was changed for a fixed metal ion concentration. The formation of Mn^{II} and Zn^{II} complexes with HCur was monitored at 430 nm, whereas complex formation due to Cu^{II} was observed at 428 nm. Each experiment yielded two linear plots, and their point of intersection was used to ascertain the stoichiometry of complex formation in solution.[1,2]

6.2.1.2 Job's method of continuous variation:

In this approach, stoichiometry was investigated by altering the concentrations of both ligand and metal ions. The Mn^{II} and Zn^{II} complexes displayed a peak at 430 nm while Cu^{II} complex showed a peak at 428 nm.[1,2]

6.2.2 Determination of pK_a of Curcumin in the absence and presence of metal ions:

The pH-metric titration of HCur was conducted over a pH range of 4.75 to 12.00, both with and without the presence of metal ions (Mn^{II}, Cu^{II}, and Zn^{II}). For titrations involving metal ions, the ratio of metal ions to HCur was determined using the data from stoichiometry determination experiments. In the absence of metal ions, the dissociation of the enolic-OH group was determined by monitoring the changes in absorbance at 467 nm. Further dissociation was attributed to the phenolic -OH groups. Equations describing the dissociation of the three protons from HCur without metal ions are provided below

$$LH_2H^* \rightleftharpoons LH_2^- + H^{*+} \qquad K_1 = \frac{[H^{*+}][LH_2^-]}{[LH_2H^*]} \qquad (1)$$

$$LH_2^- \rightleftharpoons LH^{2-} + H^+ \quad K_2 = \frac{[L^{3-}][H^+]^2}{[LH_2^-]} \qquad (2)$$

$$LH^{2-} \rightleftharpoons L^{3-} + H^+ \qquad K_3 = \frac{[LH^{2-}][H^+]}{[LH^{2-}]} \qquad (3)$$

pK_a of HCur could be evaluated with the help of Eq. 4.

$$A_{obs} = \frac{A_1}{(1 + 10^{pH - pKa1} + 10^{pH - pKa2} + 10^{pH - pKa3})} + \frac{A_2}{(1 + 10^{pKa1 - pH} + 10^{pH - pKa2}) + 10^{pH - pKa3}} +$$

$$\frac{A_3}{(1 + 10^{pKa1 - pH} + 10^{pKa2 - pH} + 10^{pH - pKa3})} + \frac{A_4}{(1 + 10^{pKa1 - pH} + 10^{pKa2 - pH} + 10^{pKa3 - pH})} \qquad (4)$$

where A_1, A_2, A_3 and A_4 refer to absorbance due to LH_2H^*, LH_2^-, $LH^{2-}$and L^{3-}respectively while pK_{a1}, pK_{a2}, pK_{a3} are the pK_a values for the dissociation of three protons on HCur.

Dissociation of a proton of HCur in the presence of a metal ion was determined in ethanol (10%) – aqueous (90%) solutions at 32°C and a fixed ionic strength of the medium that was maintained with 0.1 M $NaNO_3$. Absorbance of HCur was followed at 430 nm in the presence of Mn^{II} and Zn^{II}, while it was followed at 428 nm for Cu^{II}. For Mn^{II} and Cu^{II} data were subsequently fitted to Eq. 5 and stability constants β^* & β for the Mn^{II} complex of Curcumin were determined using Eqs. 6-10.[1-4]

$$A_{obs} = \frac{A_1}{(1 + 10^{pH - pKa1} + 10^{pH - pKa2})} + \frac{A_2}{(1 + 10^{pKa1 - pH} + 10^{pH - pKa2})} + \frac{A_3}{(1 + 10^{pKa1 - pH} + 10^{pKa2 - pH})} \quad (5)$$

$$Mn^{2+} + 3LH_2H^* \rightleftharpoons [Mn(LH_2)_3]^- + 3H^{*+} \quad (6)$$

$$\beta^* = \frac{[Mn(LH_2)_3][H^{*+}]^3}{[Mn^{2+}][LH_2H^*]^3} \quad (7)$$

$$\text{or,} \quad Mn^{2+} + 3LH_2^- \rightleftharpoons [Mn(LH_2)_3]^- \quad (8)$$

$$\beta = \frac{[Mn(LH_2)_3]}{[Mn^{2+}][LH_2^-]^3} \quad (9)$$

$$\beta = \frac{\beta^*}{K_1^3} \quad (10)$$

Stability constants β^* and β for Cu^{II} complex of Curcumin were determined using Eqs. 11-15.[1-4]

$$Cu^{2+} + 2LH_2H^* \rightleftharpoons [Cu(LH_2)_2]^- + 2H^{*+} \quad (11)$$

$$\beta^* = \frac{[Cu(LH_2)_2][H^{*+}]^2}{[Cu^{2+}][LH_2H^*]^2} \quad (12)$$

$$\text{or,} \quad Cu^{2+} + 2LH_2^- \rightleftharpoons [Cu(LH_2)_2] \quad (13)$$

$$\beta = \frac{[Cu(LH_2)_2]}{[Cu^{2+}][LH_2^-]^2} \quad (14)$$

$$\beta = \frac{\beta^*}{K_1^2} \quad (15)$$

Dissociation of a proton of HCur in the presence of Zn^{II} was determined in ethanol (10%) – aqueous (90%) solutions at 32°C at a fixed ionic strength maintained by 0.1 M $NaNO_3$.

Absorbance of HCur was followed at 430 nm in presence of Zn^{II} and fitted to Eq.16 that can determine the dissociation of one proton. pK_a (= 7.38) was obtained.

$$A_{obs} = \frac{A_1}{(1 + 10^{pH - pKa1})} + \frac{A_2}{(1 + 10^{pKa1 - pH})} \quad (16)$$

A_1 and A_2 are absorbances due to LH_2H^* and LH_2^- respectively in the presence of Zn^{II}. LH_2H^* represents Curcumin; K_1 is the dissociation constant of the enolic-OH proton of Curcumin when titrated in the absence of Zn^{II}. Stability constants β^* and β were determined using Eqs. 17-21.[1-4]

$$Zn^{2+} + LH_2H^* \rightleftharpoons [Zn(LH_2)]^+ + H^{*+} \quad (17)$$

$$\beta^* = \frac{[Zn(LH_2)^+][H^{*+}]}{[Zn^{2+}]\,[LH_2H^*]} \quad (18)$$

or, $$Zn^{2+} + LH_2^- \rightleftharpoons [Zn(LH_2)]^+ \quad (19)$$

$$\beta = \frac{[Zn(LH_2)]}{[Zn^{2+}]\,[LH_2^-]} \quad (20)$$

$$\beta = \frac{\beta^*}{K_1} \quad (21)$$

6.2.3 Synthesis of transition metal complexes of Curcumin (HCur):

6.2.3.1 Synthesis of the Mn^{II} complex of HCur:

HCur (0.2762 g, 0.75 mmol) was dissolved in a 15 mL deaerated mixture of acetonitrile and ethanol (1:3). Triethylamine (0.104 mL, 0.75 mmole) was used to neutralize the solution. Subsequently, a solution of $MnCl_2.4H_2O$ (0.0495 g, 0.25 mmole) in 10 mL of deaerated ethanol-water (1:1) was added. To ensure an inert environment, Ar gas was continuously bubbled through the mixture. The preparation was stirred for a 24-hour period. The resulting greenish-brown precipitate was isolated and washed sequentially with chloroform, diethyl ether, ethanol, THF, and acetonitrile. The choice of washing solvent was based on the solubility of HCur, which

facilitated the removal of undesired impurities. This process resulted in the formation of a purified complex. The final product was then dried in a vacuum desiccator.

6.2.3.2 Synthesis of a Cu^{II} complex of Curcumin:

In 15 mL deaerated acetonitrile-ethanol mixture (1:2) 0.76 mmole (0.2799 gm) Curcumin was dissolved followed by the neutralization by introducing 0.75 mmole (0.104 mL) of triethylamine. Following this a 0.38 mmole (0.0758 gm) $Cu(OCOCH_3)_2.H_2O$ dissolved in 15 mL deaerated ethanol-water mixture (1:1) was added. To create an inert atmosphere pure argon gas was passed through the reaction mixture. The whole set up was stirred for 2 hours and subsequently refluxed for a further 3 hours under inert conditions. A greenish-black precipitate was isolated. It was washed with chloroform, diethyl ether, ethanol, THF and acetonitrile in that sequence depending upon the solubility of Curcumin in each of these solvents. The product was dried in a vacuum dessicator.

6.2.3.3 Synthesis of a Zn^{II} complex of Curcumin:

In 50 mL de-aerated mixture of acetonitrile and methanol (1:3 ratio), 0.74 g (2 mmole) of HCur was dissolved. The solution was neutralized with triethylamine (0.277 mL, 2 mmol). Subsequently, 0.37 g (2 mmole) of $Zn(CH_3COO)_2$, dissolved in 30 mL of a de-aerated methanol-water mixture (1:1 ratio) was added to the above solution. To maintain an inert environment, Ar gas was bubbled through the mixture. The mixture (solution) was then stirred under heat (approximately 60°C) for one hour, followed by refluxing for an additional two hours in an inert atmosphere. The resulting orange-brown precipitate was collected and washed sequentially with chloroform, diethyl ether, ethanol, tetrahydrofuran (THF), and acetonitrile. The choice of

solvents was based on the solubility of HCur, which allowed for the removal of unwanted impurities. Finally, the product was dried using a vacuum desiccator.

6.2.4 Instrument used for different experiments:

6.2.4.1 Instrument used for characterization of the complexes:

UV-Vis spectra of the complexes were recorded on a JASCO V-630 spectrophotometer. IR spectra of Curcumin (HCur) and those of their complexes were recorded on Perkin Elmer Spectrum Two FTIR spectrophotometer. Mass spectrum was recorded on Micromass Q-Tofmicro^{TM}, Waters Corporation while TGA were recorded on Mettler Toledo TGA/SDTA 851^{e}. Elemental analysis was carried out on Perkin Elmer 2400 Series-II CHN analyzer. Magnetic susceptibility measurement of powdered samples at room temperature (298 K) were recorded by the Gouy method using Magway MSB MK1, Sherwood Scientific Ltd.

6.2.4.2 Instrument used *for in silico* experiments of the metal complexes and HCur:

All the in silico experiments were performed on a Linux operating system supported with GPU-NVIDIA RTX 3060 Ti and an Intel i7 9700kF processor.

6.2.5 Qunatum Chemical Calculations for the structure determination of the metal complexes:

All computations were carried out using DFT method; Gaussian 09 program[5] was used for a study with regard to the Cu^{II} and Zn^{II} complexes while Gaussian 16 program was used for the Mn^{II} complex.[6] For C, H and O we used standard 6-31G+(d,p) basis set coupled with Becke three parameter hybrid functional and Lee-Yang-gradient Parr's corrected correlation functional (B3LYP).[7] For Mn^{II} and Zn^{II} metal ion, LanL2DZ basis set[8] was used but for Cu^{II} SDD basis set was used.[9] To account for long-range dispersion impact, Becke-Johnson damping (GD3BJ) and

Grimmes' third order correction for dispersion were used. In both gaseous and DMSO solvent environments, ground state (S_0) geometries were fully optimised utilizing the program's extremely strict convergence criteria. In order to guarantee the stationary points' global minima, frequencies were calculated on optimized geometries where all vibrational frequencies were found to be positive. All simulations regarding solution phase were performed in DMSO as solvent using the integral equation formalism variant (IEFPCM) of polarizable continuum model.[10] TDDFT in DMSO solvent was carried out to establish the geometry of the Cu^{II} and Zn^{II} complex.[11,12] Frontier MO composition analysis was performed with gauss sum programme[13] and investigations of MO orbital and molecular electrostatic potential (MEP) surface[14] were done with GaussView 6.1.[15] In addition, frontier molecular orbital energies were used to calculate quantum mechanical descriptors, like MOs gap (E), ionisation potential (IP), electron affinity (EA), electronegativity (χ), chemical hardness (η), mean energy (M), chemical potential (μ), chemical softness (σ) and electrophilicity index (ω). These computations were performed using the following formulae.[14,16,17]

$$\Delta E = E_{LUMO} - E_{HOMO} \quad (22) \; ; \quad IP = -E_{HOMO} \quad (23)$$

$$EA = -E_{LUMO} \quad (24) \; ; \quad \chi = -\mu = (IP+EA)/2 \quad (25)$$

$$\eta = \Delta E/2 \quad (26) \; ; \quad \sigma = 1/2\eta \quad (27)$$

$$\omega = \chi^2/2\eta \quad (28) \; ; \quad M = -\chi \quad (29)$$

6.2.5.1 Non-covalent interaction (NCI) and bond critical point analysis:

This study aimed to analyze the interactions present within molecular systems, specifically focusing on attractive and repulsive forces. By mapping these interactions as iso-surfaces over the molecular system, we were able to observe the non-covalent interactions.[18,19] One can distinguish between favorable and unfavorable interactions by examining the plot of

reduced density gradient (RDG) versus the sign of the product of the second Hessian eigenvalue and electron density [sign (λ_2) ρ in a.u.]. The color scheme of red, green, and blue illustrates the varying strengths of interactions. The blue iso-surface represents strong attractive interactions, the red iso-surface represents strong repulsive interactions, and the green iso-surface represents weak attractive interactions. As anticipated, the representation of covalent and coordination bonds is denoted by the color blue.[18-19] Calculations were performed using Multiwfn version 3.8.[20] The NCI spike and iso-surface plots were visualized using the VMD 1.9.2 program.[21] Furthermore, for Zn^{II} curcumin complex the strength of hydrogen bonds was characterized using the DAMQT-2.1.0 package, which analyzes electron density at bond critical points.[22]

6.2.5.2 Analysis of ELF and LOL:

Studies through ELF (Electron Localization Function) and LOL (localized Orbital Locator) primarily focus on analyzing topological surfaces. Using the Multiwfn software package[20], it could be shown that there is a strong likelihood of detecting an electron pair on the surface of a molecule, as indicated by the ELF and LOL measurements. The relief map of ELF and LOL displays variations in peak area, revealing electron density surrounding each atom, signifying either a high or low electron density. ELF and LOL have a consistent chemical composition due to their dependence on kinetic energy density. Understanding the distribution of electron pairs is a key aspect of the ELF theory,[23] while the LOL theory focuses on the overlapping of localized orbitals caused by orbital gradients.[24]

6.2.6 Analysis of chemical stability of Curcumin and its metal complexes in physiological buffer conditions:

6.2.6.1 Using UV-Vis spectroscopy:

Studying the stability of metal complexes and Curcumin was done under physiological conditions (phosphate buffer saline: 10 mM sodium phosphate, 150 mM NaCl, pH 7.4) as well as in various media used for bacterial growth (MHB, BHI, and DMEM). For this experiment, the absorption spectra were scanned in the range of 250 nm – 600 nm using a UV-2450 spectrophotometer by Shimadzu.[25] Stock solutions with a concentration of 10 mM were prepared by dissolving the complexes and curcumin in DMSO. Adding a small volume (2 μL) from stock solutions to 1 mL PBS and 1 mL microbiological medium resulted in a final concentration of 20 μM in each condition. Subsequent absorption spectra were recorded over a period of 30 minutes, with measurements taken every 5 minutes. As part of the experiment, the stability of complexes was tested under reducing conditions by conducting the same procedure with the addition of 10 μM DTT, a reducing agent followed by the recording of its absorption spectra as before.

6.2.6.2 Using HPLC

Further the stability of Curcumin and its only Cu^{II} complex in phosphate buffer was facilitated through the use of HPLC and for that both the Curcumin and its Cu^{II} complex were incubated at 30°C in a 0.1 M phosphate buffer with a pH of 7.2. Standards such as vanillin, vanillic acid, and ferulic acid were utilized and the analysis of these compounds was conducted using HPLC using a C18 column (C18 column: 250 × 4.6 mm, 5 lam particle size, Shimadzu) For the mobile phase, a combination of different solvents was used, including 12% THF, 5% acetonitrile, 2% acetic acid, and water. This mixture was run isocratically, meaning that the composition remained constant throughout the analysis. The flow rate of the mobile phase was

set at 1 ml per minute. Detection was accomplished at a wavelength of 254 nm, with injection volumes of 20 µL. Identification of chromatographic peaks from incubation samples was achieved through comparison with authentic standards. One can determine the amount of Curcumin that has not been altered.

6.2.7 Biophysical interactions of metal complexes with calf thymus DNA:

6.2.7.1 Titration of metal complexes of Curcumin with calf thymus DNA:

Owing to instability of HCur dissolved in phosphate buffer (pH = 7.4), any attempt to study DNA binding using UV-Vis spectroscopy and fluorescence spectroscopy was avoided. Nevertheless, the complexes were subjected to titration due to its lack of significant absorbance change in the same pH 7.4 medium over a specific period of time. Complexes were dissolved in phosphate buffer medium (pH = 7.4), containing 120 mM NaCl, 35 mM KCl and 5 mM $CaCl_2$. Such aqueous solutions of with or without calf thymus DNA was prepared each time in a manner that the final volume of the solution in the cuvette was 2000 µL but having an incremental presence of DNA. This was subsequently transferred to a quartz cuvette and absorbance and/or fluorescence was measured. Calf thymus DNA was taken from a standard stock solution of specific strength until saturation was reached. Concentration of the complex was kept constant each time. When studying the complexes, any observed change in absorbance of the solution after adding calf thymus DNA could be attributed to an interaction between the complex and DNA. The analysis was conducted using a JASCO V-630 spectrophotometer and the binding with calf thymus DNA was studied considering the following equilibrium (Eq. 30)

$$\mathrm{L} + \mathrm{DNA} \rightleftharpoons \mathrm{L-DNA} \qquad \mathrm{K_d} = \frac{[\mathrm{L}][\mathrm{DNA}]}{[\mathrm{L-DNA}]} \qquad (30)$$

L represents the complex and K_d the dissociation constant whose reciprocal provides a value for the apparent binding constant (K_{app}).[26-30] Eq. 30 considered in the reverse direction yields a double reciprocal Eq. 31.

$$\frac{1}{\Delta A} = \frac{1}{\Delta A_{max}} + \frac{K_d}{\Delta A_{max}(C_D - C_L)} \qquad (31)$$

ΔA denotes the change in absorbance of the complex at a definite pH at which binding experiments were done. For each titration curve, ΔA_{max} indicates the maximum change in absorbance following interaction of complexes with calf thymus DNA. Change in absorbance was followed at the λ_{max} of compounds. Here, reciprocal of the change in absorbance ($1/\Delta A$) was plotted against reciprocal of ($C_D - C_L$). C_D refers to concentration of calf thymus DNA and C_L to the complex. Using Eq. 31, ΔA_{max} and K_{app} (= K_d^{-1}) may be determined from the intercept and slope respectively. [26-30]

A plot of $\Delta A/\Delta A_{max}$ against concentration of DNA was fitted using non-linear square fit analysis (Eq. 32 & 33), that also yielded K_d. The apparent binding constant (K_{app}) was found as the inverse of K_d ; $K_{app} = K_d^{-1}$.[26-30]

$$K_d = \frac{\left[C_L - \left(\frac{\Delta A}{\Delta A_{max}}\right)C_L\right]\left[C_D - \left(\frac{\Delta A}{\Delta A_{max}}\right)C_L\right]}{\left(\frac{\Delta A}{\Delta A_{max}}\right)C_L} \qquad (32)$$

$$C_L\left(\frac{\Delta A}{\Delta A_{max}}\right)^2 - (C_L + C_D + K_d)\left(\frac{\Delta A}{\Delta A_{max}}\right) + C_D = 0 \qquad (33)$$

Eq. 34 is another form of a double reciprocal plot that has an intercept on the y-axis = 1, providing values for apparent binding constants.[26-30]

$$\frac{1}{(C_b/C_L)} = 1 + \frac{1}{[K]\,[C_D]} \qquad (34)$$

The plot of $\Delta A/\Delta A_{max}$ against [DNA]/[complex] provides a value for " n_b " which denotes the site size of interaction. Overall binding constant (K*) was obtained by multiplying K_{app} (obtained using Eq. 31 and Eqs. 32 & 33) with "n_b".[26-30]

A modified form of the original Scatchard equation (Eq. 35) was also used to analyze results.[31] Overall binding constant (K*) and binding stoichiometry "n" (= n_b^{-1}) were obtained directly.[26-31]

$$r/C_f = K^*(n - r) \qquad (35)$$

$r = C_b/C_D$ where C_b" is the concentration of bound compound and "C_D" concentration of calf thymus DNA. "C_f" refers to the concentration of the free compound in solution. K* is the intrinsic or overall binding constant of the complex binding to a substrate. "n" is the binding stoichiometry in terms of the number of bound compound per nucleotide while "n_b" reciprocal of "n" denotes binding site size in terms of the number of nucleotide bound to each compound.[26-31]

6.2.7.2 Titration of Cu^{II} complex of Curcumin with DNA at different temperatures and evaluation of thermodynamic parameters

At four distinct temperatures, the complex was titrated with calf thymus DNA while maintaining a consistent pH of around 7.4 and ionic strength of the medium ([NaCl] = 150 mM). The temperature was regulated using a peltier TCC controller from Shimadzu, which was connected to a UV 1800 Shimadzu UV spectrophotometer Model TCC-240A from Japan. As a consequence of performing DNA binding studies corresponding to a variation in temperature, thermodynamic parameters, including the van't Hoff enthalpy (ΔH), entropy (ΔS), and free energy (ΔG), were calculated using Eqs. 36 - 38.

$$\ln K^* = \frac{-\Delta H}{RT} + \frac{\Delta S}{R} \qquad (36)$$

$$\Delta G^0 = -RT \ln K^* \quad (37)$$

$$\Delta G = \Delta H - T\Delta S \quad (38)$$

R represents the universal gas constant, while T denotes absolute temperature. The apparent binding constant (K_{app}) and overall binding constant (K*) obtained at each temperature were plotted using Eq. 36. The values for ΔH and ΔS were obtained by calculating the slope and intercept, respectively. Afterwards, ΔG was calculated using Eq. 38.[32] Unfortunately, being unable to access an Isothermal Titration Calorimeter (ITC) restricted the chance to determine thermodynamic parameters in a model-independent manner.

6.2.8 Superoxide dismutase activity of the Mn^{II} complex of Curcumin:

An enzyme assay using hypoxanthine-xanthine oxidase was used to generate superoxide, with some modifications to a previously described method.[33,34] The reactions involved are listed below.

$$\text{Hypoxanthine} + H_2O + O_{2\cdot} \rightarrow \text{Xanthine} + H_2O_2 \quad (39)$$

$$\text{Xanthine} + H_2O + O_2 \rightarrow \text{Uric acid} + H_2O_2 \quad (40)$$

$$\text{Xanthine} + H_2O + 2\,O_2 \rightarrow \text{Uric acid} + 2\,O_2^- + 2\,H^+ \quad (41)$$

A mixture containing 50 μM hypoxanthine, 300 μM NBT^{2+}, 0.04 unit/ml xanthine oxidase, and 50 μM Mn^{II} complex of curcumin was dissolved in a solution of 10% DMSO and 20 mM phosphate buffer (pH 7.4). The mixture was then incubated at 25°C for 10 minutes. The NBT^+ formed was measured using a spectrophotometer at 524 nm. The percentage inhibition of NBT^+ formation was calculated using Eq. 42.

$$\% \text{ inhibition} = (A_0 - A_s) \times 100/A_0 \quad (42)$$

A_0 and A_s are the absorbance due to NBT^+ at 524 nm in the absence and presence of Mn^{II} complex respectively. Percentage inhibition was plotted as a function of Mn^{II} complex.

Experiments with the native SOD enzyme were conducted again. Comparison was made between the percentage inhibition caused by the Mn^{II} complex and the SOD, both recorded under identical conditions. This experiment was conducted specifically for the Mn^{II} complex of Curcumin.

6.2.9 *In silico* molecular modeling of Curcumin (HCur) and its metal complexes with selected DNA and bacterial FtsZ protein model:

6.2.9.1 Molecular Docking:

6.2.9.1.1 Molecular Docking of selected molecules with DNA models:

Molecular docking studies were performed using Autodock software (version 4.2.6) which is an interactive molecular graphics program from where binding energy was obtained.[35] Additionally, command-line tool Autodock Vina (version 1.2.3; http://vina.scripps.edu)[36,37] was used from that binding affinity could be obtained. Both binding energy and binding affinity, output of programs used and regarded as docking score were generated using different scoring functions.[37,38] For docking studies for DNA, we used two separate DNA models, to establish the priority of interaction modes of prepared molecules. Selected PDB ID: 3FT6 model indicates intercalation,[39,40] and PDB ID: 101D model indicates groove binding.[41-43] Both models were downloaded from the protein data bank (http://www.rcsb.org./pdb) having resolution of 1.12 Å and 2.25 Å, respectively. Both have A and B strands with a sequence 5'-D(CGATCG)-3' for 3FT6 and 5'-D(CGCGAATTCGCG)-3' for 101D.[39-43] Before docking studies, chosen DNA models were checked for missing nitrogenous base pairs using UCSF Chimera (version 1.15; https://www.rbvi.ucsf.edu/chimera).[44,45] Then their energy were minimized using steepest descent and conjugate gradient techniques where the AMBER ff1 4SB force field [46,47] was applied and saved in PDB format. On the other hand, DFT optimized HCur and its metal

complexes with crystalized ligands Proflavin (PRL) for 3FT6 model and Netropsin (NT) for 101D model were further underwent for addition of hydrogen and Gasteiger charges using UCSF Chimera and saved as PDB format.[48] Thereafter, using Autodock tools (version 1.5.7) the saved PDB files of DNA models (3FT6 and 101D) and chosen molecules were opened and after merging non-polar hydrogens on both receptor and target molecules they were saved in PDBQT format.[48,49] Grid boxes were created with 38 Å × 32 Å × 32 Å at 0.35 Å spacing for 3FT6 model and 46 Å × 48 Å × 50 Å at 0.35 Å spacing for 101D model . Although in 3FT6 model there were two symmetrical binding side so one binding site was selected for docking study that reduced the computational cost. Docking studies of all forms of HCur and its metal complexes with, PRL and NT co-cystallised ligands for 3FT6 and 101D were carried out using Lamarckian Genetic Algorithm (LGA) to achieve lowest free energy of binding (G). Three replicates of the above experiment, each with a total number of 10 solutions, showing an energy minima with a population size of 150 and number of evaluations ~2500000 were obtained;[48,49] Following docking experiments, RMSD cluster maps were obtained with a cluster tolerance of 2.0 Å each for all the selected molecules. 2D and 3D interactions of different nucleotides with all docked molecules were visualized with BIOVIA Discovery Studio (version 2021) and PyMOL software (DeLano, 2002).[50,51]

6.2.9.1.2 Molecular Docking of selected molecules with FtsZ protein models:

For showing FtsZ inhibition activity on both *E.Coli* and *S.aureus* bacteria docking study was performed. The structure of *E.Coli* FtsZ protein (PDB ID : 6UNX) and *S.aureus* FtsZ protein (PDB ID : 4DXD) was downloaded from RCSB protein data bank having a resolution of 1.40 Å for 6UNX and 2.01 Å for 4DXD.[52-54] Before performing molecular docking studies like that for DNA both protein models were checked for missing amino acid residues using UCSF

Chimera (version 1.15; https://www.rbvi.ucsf.edu/chimera)[44,45] then their energy was minimized using steepest descent and conjugate gradient techniques where the AMBER ff1 4SB force field[46,47] was applied and saved in PDB format. Subsequent to this, molecular interaction experiments were performed. On the other hand, DFT optimized HCur and its metal complexes with crystalized ligands 3-[(6-chloro[1,3]thiazolo[5,4-b]pyridin-2-yl)methoxy]-2,6-difluorobenzamide (9PC) for 4DXD model and Guanosine-5-triphosphate (GTP) for 6UNX model were further underwent for addition of hydrogen and Gasteiger charges using UCSF Chimera and saved as PDB format.[48] Thereafter, using Autodock tools (version 1.5.7) the saved PDB files of FtsZ models (4DXD and 6UNX) and chosen molecules were opened and after merging non-polar hydrogens on both receptor and target molecules they were saved in PDBQT format.[48,49] Grid boxes were created with 44 Å × 54 Å × 40 Å at 0.35 Å at spacing for 6UNX protein model and 56 Å × 60 Å × 62 Å at 0.35 Å at spacing for 4DXD protein model. All docking studies were carried out using Lamarckian Genetic Algorithm (LGA) to achieve lowest free energy of binding (G). For molecular docking studies, three replicates were performed; for each a total number of 10 solutions were computed, each showing an energy minima having a population size of 150 and number of evaluations ~2500000; the maximum number of generations being 27000.[48,49] After docking, RMSD cluster maps were obtained with a cluster tolerance of 2.0 Å each for HCur and metal complexes. The BIOVIA Discovery Studio (version 2021) and PyMOL software (DeLano, 2002) were used for visualisation of 2D and 3D interactions of different amino acid residues with docked molecules at the binding side of proteins models that could be responsible for inhibition of FtsZ acitivity.[50,51]

6.2.9.2 Molecular Dynamics simulations:

MD simulation studies were carried out for apo DNA models (PDB ID: 3FT6 and 101D), apo *E. coli* FtsZ protein (PDB ID: 6UNX), apo *S. aureus* FtsZ protein (PDB ID: 4DXD) and docked HCur and metal complexes of HCur to investigate their stability and physical movements under physiological simulation environment. Desmond (version 2020.1)[55,56] was used to run molecular dynamics simulation, a GPU-accelerated program running on the Linux operating system integrated with an NVIDIA RTX 3060 Ti GPU and Intel i7 9700kF processor. In order to prepare the systems, the OPLS-2005 force field[57] and explicit solvent model with SPC water molecules were employed.[58] Energy of all systems were then reduced by using an orthorhombic boundary solvation box having a dimension 10Å × 10Å × 10Å for DNA and cubic boundary solvation box having a dimension 10Å × 10Å × 10Å for protein models. The correct quantity of Na^+ or Cl^- ions was introduced to each system to neutralize it. Each system received an additional 0.15 M NaCl solution to replicate the physiological environment. The Desmond default relaxation approach was used to relax the prepared systems. An NVT ensemble was initially used to equilibrate the entire system for 500 ps at 10 K. Following the preceding phase, an NPT ensemble was used to complete a quick run of equilibration and minimization for 100 ns at 300 K and 1.01325 bar pressure. The Nose-How over chain coupling approach was used to set up the NPT ensemble.[59] Temperature was set at 300 K, relaxation period was set at 1.0 ps and pressure was maintained at 1 bar throughout all simulations. A time step of 2 fs was applied. With a relaxation duration of 2 ps, the Martyna-Tobias-Klein chain coupling scheme barostat method was employed to control pressure.[60] Long-range electrostatic interactions were calculated using the particle mesh Ewald approach[61] with a fixed coulomb interaction radius of

9.0Å. With each trajectory, bonded forces were calculated using RESPA integrator for a time step of 2 fs.

6.2.9.2.1 Trajectory analysis through various interaction diagrams:

Maestro, a Desmond GUI application, was used to study simulation interaction diagrams including root-mean square deviation (RMSD), root mean square fluctuation (RMSF), solvent accessible surface area (SASA), number of H-bonds and radius of gyration.[62,63]

Root mean square deviation (RMSD) is a commonly employed metric in molecular dynamics (MD) simulations to assess the structural alterations of molecules over time. It calculates the average distance between corresponding atoms in a system (typically macromolecules such as proteins or nucleic acids) compared to a reference structure, such as the initial or experimentally determined configuration.[62-65]

RMSD serves as a valuable indicator of structural deviation throughout a simulation, making it an essential tool for evaluating the stability, flexibility, and conformational changes in molecular systems. A low RMSD indicates relatively stable structures, whereas higher RMSD values suggest significant conformational shifts. RMSD analysis plays a crucial role in examining processes such as protein folding, ligand binding, and structural fluctuations, offering insights into molecular stability and dynamic behavior at the atomic scale.[62-65]

In MD simulations, root mean square fluctuation (RMSF) is a critical indicator for assessing protein flexibility. This measure calculates a typical deviation of atoms or residues from their average positions over time, highlighting areas of high and low mobility. By providing insights into protein dynamics, RMSF can help researchers identify flexible loops, disordered regions and stable structural components. Such information is essential for understanding protein / DNA function, ligand interactions and conformational shifts. Applications of RMSF extend to

various fields that includes drug development, protein engineering and structural biology research.[62-68]

Radius of gyration is a key parameter used in molecular dynamics (MD) analysis to characterize compactness and overall size of a molecular system. This is particularly useful for studying conformational changes in proteins, polymers and other macromolecules during simulation. Rg helps to track the compactness of a protein structure during folding simulations, indicating transitions between ~~the~~ unfolded, intermediate and folded states. Changes in Rg over time can reveal large-scale structural rearrangements of macromolecules. A stable Rg value over time suggests a stable conformation whereas fluctuations indicate structural instability or flexibility. Decrease in Rg typically indicates compaction or folding while an increase in Rg suggests expansion or unfolding. Sudden changes in Rg may indicate conformational transitions or domain movement.[62-68]

In molecular dynamics simulations, solvent-accessible surface area (SASA) is a fundamental concept that quantifies the area of a molecule's surface that is accessible to solvent molecules (typically water). SASA analysis has numerous applications in molecular dynamics, including elucidating protein-folding mechanisms, identifying protein-protein interaction regions and revealing potential binding sites for ligands. This also facilitates our understanding of the relationship between hydrophobicity and protein structure, as folded proteins typically exhibit hydrophobic residues with lower SASA values. During simulations, researchers can monitor SASA values over time to observe conformational change. Further, SASA is frequently employed to approximate solvation free energies in implicit solvent models. Additionally, SASA values can be utilized to estimate the entropy change associated with protein-ligand binding, contributing to more accurate predictions of binding affinity in drug discovery.[62-68]

Hydrogen bonds are essential for shaping the structure, activity, and movement of biological molecules and materials. These noncovalent interactions are particularly significant in proteins, nucleic acids, and other biomolecules, influencing their three-dimensional shapes and interactions between molecules. In molecular dynamics simulations, the quantity of hydrogen bonds serves as a crucial indicator for understanding molecular stability, flexibility, and reactivity. By monitoring the formation and breakdown of hydrogen bonds over time, one can obtain insights into various phenomena such as protein folding, ligand binding, and the structural integrity of biomolecules under diverse environmental conditions. The measurement of hydrogen bonds in molecular dynamics simulations typically involves establishing geometric criteria, such as distances and angles between donors and acceptors, to identify and enumerate these interactions throughout the trajectory of the simulation.[62-68]

6.2.9.2.2 Binding free energy analysis by MDS:

Molecular dynamics (MD) simulations are crucial for studying atomic-level interactions in biological systems. These simulations are vital for calculating the binding free energies between protein and ligand or DNA-ligand, which is essential for drug discovery and development. The Molecular Mechanics Generalized Born Surface Area (MM-GBSA) method is popular for this purpose, owing to its balance of computational efficiency and accuracy.[69,70]

MM-GBSA, an endpoint approach, combines molecular mechanics energy calculations with implicit solvent models to estimate receptor-ligand binding free energies. This method was applied to representative snapshots from an MD trajectory, accounting for conformational flexibility and entropic contributions in the binding process.[69,70]

The generalized Born surface area (MM-GBSA) method and molecular mechanics were utilized to calculate binding free energies of all simulated systems. The simulation trajectory's last 10

frames out of 1000 with a 1-step sampling size and OPLS-2005 force field coupled with python script thermal_mmgbsa.py were used to determine MM-GBSA binding free energy.[69,70] The principle of additivity was used to estimate binding free energy of MD trajectory using MM-GBSA (kcal/mol), in which individual energy modules such as columbic, covalent, hydrogen bond, van der Waals, self-contact, lipophilic, solvation and stacking of ligand and DNA or protein were obtained. Equation 43 was used to calculate $\Delta G_{binding}$

$$\Delta G_{binding} = \Delta G_{MM} + \Delta G_{Solv} - \Delta G_{SA} \quad (43)$$

where $\Delta G_{binding}$ designates binding free energy of binding, ΔG_{MM} designates difference between free energies of protein-ligand or DNA-ligand complexes and total energy of protein or DNA and ligand in isolated state, ΔG_{solv} designates the difference in solvation energies of DNA-ligand or protein-ligand complex and sum of solvation energies of DNA and ligand in the unbound state, ΔG_{SA} designates difference in surface area energies for protein/DNA and ligand.

References:

1. P. Das, C. K. Jain, S. Roychoudhury, H. K. Majumder, S. Das; Design, synthesis and *invitro*anticancer activity of a Cu(II) complex of Carminic acid: A novel small molecule inhibitor of human DNA topoisomerase I and topoisomerase II. *Chemistry Select*, **2016**, 1, 6623-6631.
2. S. Mukherjee-Chatterjee, C. K. Jain, S. Singha, P. Das, S. Roychoudhury, H. K. Majumder, S. Das; Activity of Co^{II}-Quinalizarin: A novel analogue of anthracycline-based anticancer agents targets human DNA topoisomerase, whereas quinalizarin itself acts via formation of semiquinone on acute lymphoblastic leukemia MOLT-4 and HCT 116 cells. *ACS Omega*, **2018**, 3, 10255-10266.
3. M. Saha, S. Singha, M. Chakraborty, S. Mazumdar, S. Kumar, P. Karmakar, S. Das.; Characterization of a MnII complex of Alizarin suggests attributes explaining a superior anticancer activity: A comparison with anthracycline drugs. *Polyhedron*, **2019**, 173, 114104.
4. B. Mandal, S. Singha, S. K. Dey, S. Mazumdar, S. Kumar, P. Karmakar , S. Das; CuII complex of emodin with improved anticancer activity as demonstrated by its performance on HeLa and Hep G2 cells. *RSC Adv.*, **2017**, 7, 41403.
5. M. J. Frisch, G. W. Trucks, H. B. Schlegel, G. E. Scuseria, M. A. Robb, J. R. Cheeseman, G. Scalmani, V. Barone, G. A. Petersson, H. Nakatsuji, X. Li, M. Caricato, A. Marenich, J. Bloino, B. G. Janesko, R. Gomperts, B. Mennucci, H. P. Hratchian, J. V. Ortiz, A. F. Izmaylov, J. L. Sonnenberg, D. Williams-Young, F. Ding, F. Lipparini, F. Egidi, J. Goings, B. Peng, A. Petrone, T. Henderson, D. Ranasinghe, V. G. Zakrzewski, J. Gao, N. Rega, G. Zheng, W. Liang, M. Hada, M. Ehara, K.

Toyota, R. Fukuda, J. Hasegawa, M. Ishida, T. Nakajima, Y. Honda, O. Kitao, H. Nakai, T. Vreven, K. Throssell, J. A. Montgomery, Jr., J. E. Peralta, F. Ogliaro, M. Bearpark, J. J. Heyd, E. Brothers, K. N. Kudin, V. N. Staroverov, T. Keith, R. Kobayashi, J. Normand, K. Raghavachari, A. Rendell, J. C. Burant, S. S. Iyengar, J. Tomasi, M. Cossi, J. M. Millam, M. Klene, C. Adamo, R. Cammi, J. W. Ochterski, R. L. Martin, K. Morokuma, O. Farkas, J. B. Foresman, and D. J. Fox.; **2016**, Gaussian 09, Revision D.01, Gaussian, Inc., Wallingford CT.

6. M. J. Frisch, G. W. Trucks, H. B. Schlegel, G. E. Scuseria, M. A. Robb, J. R. Cheeseman, G. Scalmani, V. Barone, G. A. Petersson, H. Nakatsuji, X. Li, M. Caricato, A. V. Marenich, J. Bloino, B. G. Janesko, R. Gomperts, B. Mennucci, H. P. Hratchian, J. V. Ortiz, A. F. Izmaylov, J. L. Sonnenberg, D. Williams-Young, F. Ding, F. Lipparini, F. Egidi, J. Goings, B. Peng, A. Petrone, T. Henderson, D. Ranasinghe, V. G. Zakrzewski, J. Gao, N. Rega, G. Zheng, W. Liang, M. Hada, M. Ehara, K. Toyota, R. Fukuda, J. Hasegawa, M. Ishida, T. Nakajima, Y. Honda, O. Kitao, H. Nakai, T. Vreven, K. Throssell, J. A. Montgomery, Jr., J. E. Peralta, F. Ogliaro, M. J. Bearpark, J. J. Heyd, E. N. Brothers, K. N. Kudin, V. N. Staroverov, T. A. Keith, R. Kobayashi, J. Normand, K. Raghavachari, A. P. Rendell, J. C. Burant, S. S. Iyengar, J. Tomasi, M. Cossi, J. M. Millam, M. Klene, C. Adamo, R. Cammi, J. W. Ochterski, R. L. Martin, K. Morokuma, O. Farkas, J. B. Foresman, and D. J. Fox, **2016**, Gaussian 16, Revision C.01, Gaussian, Inc., Wallingford CT.

7. (a) A. D. Becke; Density-functional thermochemistry. III. The role of exact exchange, *J. Chem. Phys*. **1993**, 98, 5648e5652; (b) C. T. Lee, W. T. Yang, R. G. Parr;

Development of the Colle-Salvetti correlation-energy formula into a functional of the electron density, *Phys. Rev. B.* **1988**, 37, 785e789.

8. S. Chiodo, N. Russo, E. Sicilia; LANL2DZ basis sets recontracted in the framework of density functional theory, *Jour. Chem. Phys*. **2006**, 125, 104107.
9. T. H. Dunning Jr. and P. J. Hay; Gaussian Basis Sets for Molecular Calculations, In: Methods of Electronic Structure Theory, **1977**, Schaefer H. F. III, Ed., Vol. 2 Plenum Press, New York, 1-27.
10. M. A.-González, N. F.-Holguín, M. Gallo, E. O.-Borunda, D. G.-Mitnik; TD-DFT/IEFPCM determination of the absorption and emission spectra of DABCYL. *Journal of Molecular Structure: THEOCHEM*, **2010**, 945, 101-103.
11. M. Cossi, V. Barone, Time-dependent density functional theory for molecules in liquid solutions, *Chem. Phys*. **2001**, 115, 4708e4717.
12. E. K. U. Gross, and W. Kohn; Time-dependent density functional theory in, *Adv. Quant*. *Chem*., **1990**, 21, 255e291.
13. N. M. O'Boyle, A. L. Tenderholt and K. M. Langner. *J. Comp. Chem*., **2008**, 29, 839-845.
14. Z. Akbari, C. Stagno, N. Iraci, T. Efferth, E. A. Omer, A. Piperno M. Montazerozohori M.F. Dehnayebi , N. Micale; Biological evaluation, DFT, MEP, HOMO-LUMO analysis and ensemble docking studies of Zn(II) complexes of bidentate and tetradentate Schiff base ligands as antileukemia agents. *Journal of Molecular Structure*, **2024**,1301,137400.
15. R. Dennington, T. A. Keith, and J. M. Millam, Semichem Inc., Shawnee Mission, KS, **2016**. GaussView, Version 6.1.

16. V. K. Choudhary, A. K. Bhatt, D. Dash, N. Sharma.; DFT calculations on molecular structures, HOMO-LUMO study, reactivity descriptors and spectral analyses of newly synthesized diorganotin(IV) 2-chloridophenylacetohydroxamate complexes, *Jour. Comp. Chem.* **2019**, 1-10.

17. N. Sepay, R. Mondal, M. K. Al-Muhanna, D. Saha; Identification of natural flavonoids as novel EGFR inhibitors using DFT, molecular docking, and molecular dynamics, *New Journal of Chemistry,* **2022**, 20

18. E.R. Johnson, S. Keinan, P. Mori-Sánchez, J. Contreras-García, A.J. Cohen, W. Yang.; Revealing Noncovalent Interactions. *J. Am.Chem. Soc*., **2010**, 132, 6498–6506.

19. F. Akman , A. Demirpolat , A. S. Kazachenko , Anna S. Kazachenko, N. Issaoui and O.A.Dossary; Molecular Structure, Electronic Properties, Reactivity (ELF, LOL, and Fukui), and NCI-RDG Studies of the Binary Mixture of Water and Essential Oil of Phlomis bruguieri. *Molecules*, **2023**,28,2684.

20. T. Lu, F. Chen; Multiwfn: A multifunctional wavefunction analyzer. *Jour. Comput. Chem.,* **2012**, 33, 580-592.

21. W. Humphrey, A. Dalke, and K. Schulten; "VMD - Visual Molecular Dynamics", *J. Molec. Graphics*, **1996**, 14, 33-38.

22. A. Kumar, S. D. Yeole, S. R. Gadre, R. Lopez, J.F. Rico, G. Ramirez, I. Ema, D. Zorrilla; DAMQT 2.1.0: A new version of the DAMQT package enabled with the topographical analysis of electron density and electrostatic potential in molecules. *Jour. Comput. Chem.*. **2015**, 36, 2350-2359.

23. B. Fathima Rizwana, J. C. Prasana, S.Muthu, C.S.Abraham.; Molecular docking studies, charge transfer excitation and wave function analyses(ESP,ELF,LOL) on valacyclovir:A potential anti viral drug. *Comput,Biol.Chem*., **2019**,78, 9–17.

24. Heiko Jacobsen.; Localized-orbital locator (LOL) profiles of chemical bonding. *Can. J.Chem*. **2008,**86(7) 695–702.

25. P. Kumar, S.K. Kandi, S. Manohar, K. Mukhopadhyay, D.S. Rawat; Monocarbonyl curcuminoids with improved stability as antibacterial agents against Staphylococcus aureus and their mechanistic studies, *ACS Omega*, **2019**, 4 675-687.

26. P. Das, D. Bhattacharya, P. Karmakar, S. Das; Influence of ionic strength on the interaction of THA and its Cu(II) complex with DNA helps to explain studies on various breast cancer cells. *RSC Adv*.**2015**, 5,73099-73111.

27. P. S. Guin, P. C. Mandal, S. Das; The binding of a hydroxy-9,10-anthraquinone Cu^{II} complex to calf thymus DNA: Electrochemistry and UV/Vis spectroscopy, *ChemPlusChem*, **2012**,77, 361-369.

28. P. Das, C. K. Jain, S. K. Dey, R. Saha, A. D. Chowdhury, S. Roychoudhury, S. Kumar, H. K. Majumder, S. Das; Synthesis, crystal structure, DNA interaction and *in vitro* anticancer activity of a Cu(II) complex of purpurin: dual poison for human DNA topoisomerase I and II. *RSC Adv*.**2014**, 4,59344-59357.

29. B. Mandal, S. Singha, S.K. Dey, S. Mazumdar, T. K. Mondal, P. Karmakar, S. Kumar, S. Das; Synthesis, crystal structure from PXRD of a $Mn^{II}(purp)_2$ complex, interaction with DNA at different temperatures and pH and lack of stimulated ROS formation by the complex. *RSCAdv*. **2016**, 6, 51520–51532.

30. M. Saha, P. Nandy, M. Chakraborty, P. Das, S. Das; The importance of pK_a in an analysis of the interaction of compounds with DNA. *Biophys. Chem*. **2018**,236, 15-21.

31. G. Scatchard.; The attractions of proteins for small molecules and ions, *Ann. N. Y. Acad. Sci*.**1949**,51, 660–672.

32. G. W. Castellan; In: Physical Chemistry, third ed., *Addison-Wesley/Narosa Publishing House, New Delhi*, (Indian Student Edition), **1989**, p. 799.

33. J. Robak, R.J.Gryglewski; Flavonoids are scavengers of superoxide anions. *Bio chem Pharmacol*. **1988**, 37, 837-841.

34. B. Mishra, K. I. Priyadarsini, M. S. Kumar, M. K. Unnikrishnan, H. Mohan; Effect of O-glycosilation on the antioxidant activity and free radical reactions of a plant flavonoid, chrysoeriol. *Biorg. Med. Chem*. **2003**,11, 2677-2685.

35. G. M. Morris,, R. Huey, W. Lindstrom, M. F. Sanner, R. K. Belew, D. S. Goodsell, A. J. Olson; Auto dock4 and Auto dock tools 4: Automated docking with selective receptor flexiblity. *Jour. Comput. Chem.*, **2009**, 16**,** 2785-2791.

36. J. Eberhardt, D. Santos-Martins, A.F. Tillack, S. Forli; AutoDock Vina 1.2.0: New docking methods, expanded force field, and python bindings. *Jour. Chem. Inf. Model.* **2021**, 61, 8, 3891–3898.

37. O. Trott, and A. J. Olson; Auto Dock Vina: Improving the speed and accuracy of docking with a new scoring function, efficient optimization, and multithreading. *Jour. Comp. Chem*., **2010**, 31, 455-461.

38. R. Huey, G. M. Morris, A. J. Olson, D. S. Goodsell; A semiempirical free energy force field with charge-based desolvation. *Jour. Comp. Chem.*, **2007**, 28**,** 1145-1152.

39. A. Soni, P. Khurana, T. Singh, B. Jayaram; A DNA intercalation methodology for an efficient prediction of ligand binding pose and energetics. *Bioinformatics*, **2017**, 33, 1488-1496.

40. Y. Ren, H.Z. Zhang, S.L. Zhang, Y.L. Luo, L. Zhang, C.H. Zhou, R.X. Geng; Synthesis and bioactive evaluations of novel benzotriazole compounds as potential antimicrobial agents and the interaction with calf thymus DNA. *Journal of Chemical Sciences*, **2015**, 127, 2251-2260.

41. K.D. Goodwin, E.C. Long, M.M. Georgiadis; A host–guest approach for determining drug–DNA interactions: an example using netropsin. *Nucleic acids research*, **2005**, 33, 4106-4116.

42. A. Lauria, P. Diana, P. Barraja, A. Montalbano, G. Cirrincione, G. Dattolo, A.M. Almerico, MADoSPRO: a new approach to molecular modelling studies on a series of DNA minor groove binders. *QSAR & Combinatorial Science*, **2006**, 25, 252-262.

43. K. Bielawski, A. Bielawska, D. Bartulewicz, A. Różański; Molecular modelling of the interaction of carbocyclic analogues of netropsin and distamycin with d (CGCGAATTCGCG) 2. *Acta Biochimica Polonica*, **2000**, 47, 855-866.

44. E.F. Pettersen, T.D. Goddard, C.C. Huang, G.S. Couch, D.M. Greenblatt, E.C. Meng, T.E. Ferrin; UCSF Chimera—a visualization system for exploratory research and analysis. *Journal of computational chemistry*, **2004**, 25, 1605-1612.

45. E.C. Meng, E.F. Pettersen, G.S. Couch, C.C. Huang, T.E. Ferrin; Tools for integrated sequence-structure analysis with UCSF Chimera. *BMC bioinformatics*, **2006**, 7, 1-10.

46. L. Wu, L. Zhou, M. Mo, Y. Li, J. Han, J. Li, Y. Yang, X. Zhang, C. Gong, K. Lu, L. Gong; The effect of the multiple mutations in Omicron RBD on its binding to human ACE2 receptor and immune evasion: an investigation of molecular dynamics simulations. **2021**.

47. J. A. Maier, C. Martinez, K. Kasavajhala, L. Wickstrom, K. E. Hauser, C. Simmerling; ff14SB: Improving the accuracy of protein side chain and backbone parameters from ff99SB, *Jour. Chem Theor. Comp*. **2015**,11, 3696-3713

48. A. Ghosh, N. Mukerjee, B. Sharma, A. Pant, K. Y. Mohanta, R. D. Jawarkar; Target specific inhibition of protein tyrosine kinase in conjunction with cancer and SARS-COV-2 by olive nutraceuticals, *Fronts. Pharmacol.*, **2022**, 12.

49. D. Patra, S. Paul, N. Sepay, R. Kundu, T. Ghosh; Structure-activity relationship on DNA binding and anticancer activities of a family of mixed ligand oxidovanadium (V) hydrazone complexes, *Jour. Biomol. Struct. Dyn*., **2017**, 36, 4143-4155.

50. S. Sharma, A. Sharma, U. Gupta; Molecular Docking studies on the Anti-fungal activity of Allium sativum (Garlic) against Mucormycosis (black fungus) by BIOVIA discovery studio visualizer 21.1. 0.0. *Annals of Antivirals and Antiretrovirals*, **2021**, 5, 028-032.

51. S. Yuan, H.S. Chan, Z. Hu; Using PyMOL as a platform for computational drug design. *Wiley Interdisciplinary Reviews: Computational Molecular Science*, **2017**, 7, e1298.

52. K. AbouAitah, R.A. Geioushy, S.A. Nour, M.T. Emam, M.A. Zakaria, O.A. Fouad, Y.M. Shaker, B.S. Kim; A Combined Phyto-and Photodynamic Delivery Nanoplatform Enhances Antimicrobial Therapy: Design, Preparation, In Vitro Evaluation, and Molecular Docking. *ACS Applied Bio Materials*, **2024**, 7, 6873-6889.

53. M. A. Schumacher, T. Ohashi, L. Corbin, H. P. Erickson; High-resolution crystal structures of Escherichia coli FtsZ bound to GDP and GTP. *Acta Cryst*., **2020**, F76, 94â102.

54. Y. Qiu, L. Zhou, Y. Hu, Y. Bao; Discovery of promising FtsZ inhibitors by E-pharmacophore, 3D-QSAR, molecular docking study, and molecular dynamics simulation. *Journal of Receptors and Signal Transduction*, **2019**, 39, 154-166.

55. R.O. Dror, R.M. Dirks, J.P. Grossman, H. Xu, D.E. Shaw; Biomolecular simulation: a computational microscope for molecular biology. *Annual review of biophysics*, **2012**, 41, 429-452.

56. D.E. Shaw, P. Maragakis, K. Lindorff-Larsen, S. Piana, R.O. Dror, M.P. Eastwood, J.A. Bank, J.M. Jumper, J.K. Salmon, Y. Shan, and W. Wriggers, Atomic-level characterization of the structural dynamics of proteins. *Science*, **2010**, 330, 341-346.

57. D. Shivakumar, J. Williams, Y. Wu, W. Damm, J Shelley, W. Sherman; Prediction of absolute solvation free energies using Molecular Dynamics free energy perturbation and the OPLS force field, *Journal of Chemical theory and computation*, **2010**, 65, 1509-1519.

58. W. L. Jorgensen, J. Chandrasekhar, D. Madura, D. Comparison of simple potential functions for simulating liquid water, *J.Chem.Phys*, **1983**, 79, 926.

59. G. J. Martyna, M. L. Klein, Nose-Hoover chains: The canonical ensemble via continuous dynamics. *Jour. Chem. Phys*, **1992**, 97, 2635-2643.

60. G. J. Martyna, D. J. Tobias, M. L. Klein, Constant pressure molecular dynamics algorithms. *Jour. Chem. Phys*, **1994**, 101, 4177-4189.

61. A. Y. Toukmaji, J. A. Board, Ewald summation techniques in perspective: a survey, *Computer physics communications*, **1996**, 95, 2-3, 73-92.

62. M. E. A. Zaki, S. A. Al-Hussain, V. H. Masand, S. Akasapu, S. O. Bajaj, N. N. E. El-Sayed, A. Ghosh, I. Lewaa, Identification of anti-SARS-CoV-2 compounds from food

using QSAR-based virtual screening, molecular docking, and molecular dynamics simulation analysis. *Pharmaceuticals*, **2021**, 14, 357; doi: 10.3390/ph14040357.

63. N. Michaud-Agrawal, E.J. Denning, T.B. Woolf, and O. Beckstein; MD Analysis: a toolkit for the analysis of molecular dynamics simulations. *Journal of computational chemistry*, **2011**, 32, 2319-2327.
64. K. Sargsyan, C. Grauffel, C. Lim; How molecular size impacts RMSD applications in molecular dynamics simulations. *Journal of chemical theory and computation*, **2017,** 13, 1518-1524.
65. N.C. Benson, V. Daggett; A comparison of multiscale methods for the analysis of molecular dynamics simulations. *The Journal of Physical Chemistry B*, **2012,** 116, 8722-8731.
66. M.Y. Lobanov, N.S. Bogatyreva, O.V. Galzitskaya; Radius of gyration as an indicator of protein structure compactness. *Molecular Biology*, **2008**, 42, 623-628.
67. A.R. Bizzarri, C.X. Wang, W.Z. Chen, S. Cannistraro; Hydrogen bond analysis by MD simulation of copper plastocyanin at different hydration levels. *Chemical physics*, **1995**, 201, 463-472.
68. A.M. da Fonseca,, B.J. Caluaco, J.M.C. Madureira, S.Q. Cabongo, E.M. Gaieta, F. Djata, R.P. Colares, M.M. Neto, C.F.C. Fernandes, G.S. Marinho, H.S. Dos Santos; Screening of potential inhibitors targeting the main protease structure of SARS-CoV-2 via molecular docking, and approach with molecular dynamics, RMSD, RMSF, H-bond, SASA and MMGBSA. *Molecular Biotechnology*, **2024**, 66, 1919-1933.
69. S. Genheden , U. Ryde ; The MM/PBSA and MM/GBSA methods to estimate ligand-binding affinities. *Expert opinion on drug discovery*, **2015**, 10, 449-461.

70. A. Rajan, P.L. Freddolino, K. Schulten, Going beyond clustering in MD trajectory analysis: an application to villin headpiece folding. *PLoS One*, **2010**. 5, p.e9890.

CHAPTER 7

Characterization of Curcumin through different spectroscopy and Quantum Chemical calculations

Introduction

The lipophilic poly-phenol curcumin has been extensively studied in recent decades and shows promising potential.[1-10] Despite its pharmacological effectiveness, the molecule has encountered several challenges that hindered its ability to reach its maximum potential.[1-10] Numerous studies have demonstrated its pharmacological and therapeutic effects on a wide range of diseases.[1,2 4-9, 11] Even with dose being as high as 12g/day over 3 months, *in vivo* and clinical experiments have consistently demonstrated its safety and minimal toxicity.[7] Despite promising pharmacological results, the molecule's low water solubility and fragile physiological stability have hindered its potential.[12-16] Under physiological conditions, Curcumin (HCur) breaks down to multiple smaller molecules in solution, exacerbating the problem.[17] It is challenging to ascertain whether pharmacological findings related to HCur are linked to a single unit of Curcumin in solution or to all of its fragments. Researchers investigating the molecule's pharmacological and/or medicinal properties have not been able to address this crucial matter to the extent it should have been addressed; however, a report from a group with a broader focus revealed that under normal conditions, the molecule degrades into multiple smaller compounds which they very successfully identified using HPLC.[17] Reviews on the performance of HCur in different solutions raise the question whether fragments derived from Curcumin could be utilized in right proportions to achieve similar effectiveness in aqueous solution.[1,2,4,6-12,17] Based on the findings of the work on HPLC-separated degradation products of Curcumin, it has been observed that it cannot exist as a standalone entity in aqueous solutions or in cellular environments.[17] It was discovered that the absorbance of HCur gradually decreases in aqueous buffer or in cellular media (Fig. 10). The degraded products of HCur are colourless and do not disrupt its absorbance in solution in any way in the wavelength range 400 nm to 450 nm. Decrease in absorbance in

aqueous buffer or in cellular media suggests a breakdown of Curcumin that in turn puts a question mark on its efficacy either as a standalone entity or a mixture of degraded products.

7.1 Determination of pK_a of Curcumin

Dissociation of protons on HCur was determined with the help of a pH-metric titration (Eqs. 1 to 3, *Chapter 6,Experimental*) carried out in ethanol (10%) – aqueous (90%) solutions at 32°C and an ionic strength of the medium of 0.1 M $NaNO_3$. pH was recorded using a pH meter (Equip-Tronics EQ-610, India); pH values were suitably corrected and reported as they would be in a purely aqueous solution. The change in absorbance of HCur was followed at 467 nm. Dissociation of protons on HCur was evaluated using Eq.4, (*Chapter 6, Experimental*). pK_{a1}= 7.17 ± 0.31; pK_{a2} = 10.5 ± 0.16; pK_{a3} = 11.44 ± 0.17 (Fig.1). Our values are in accordance with those that were determined earlier.[18-20]

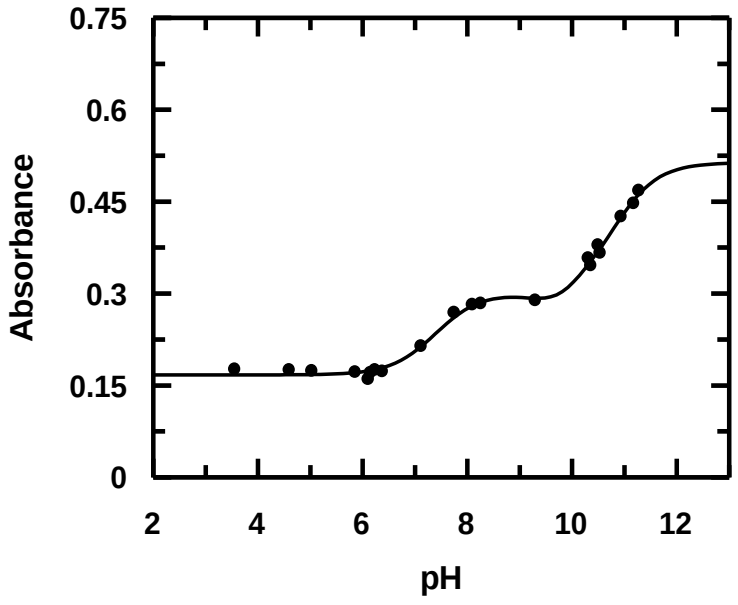


Figure 1: Spectrophotometric titration of HCur as shown by a variation in absorbance at 467 nm; [HCur] = 5 µM, [$NaNO_3$] = 0.1 M, Temperature =305K.

7.2 Characterization of Curcumin

7.2.1 By UV-Vis spectroscopy:

UV-Vis spectrum of HCur was recorded in DMSO solvent and λ_{max} was obtained at 430 nm (Fig.2)

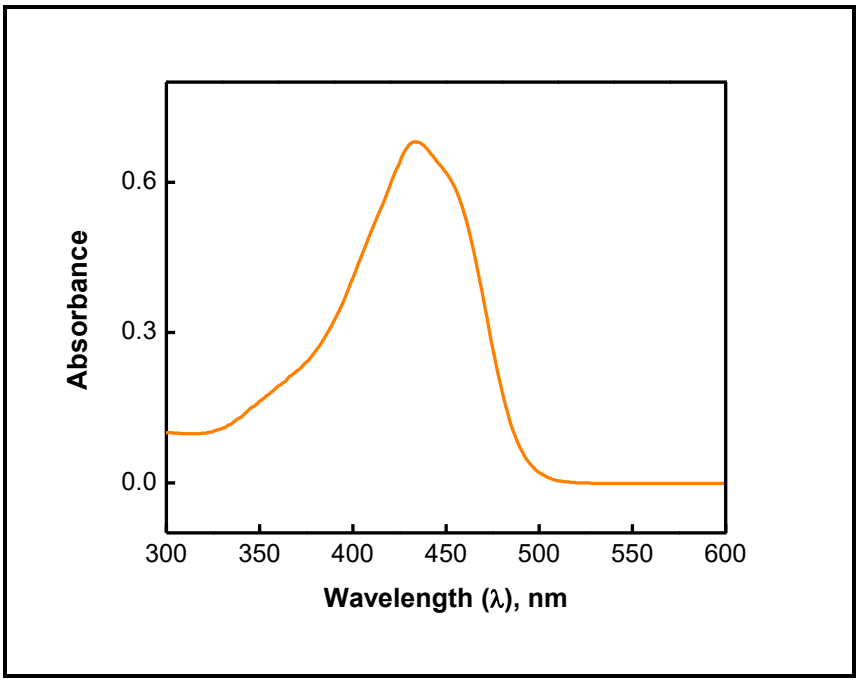


Figure 2: Absorption spectra of Curcumin (HCur) in DMSO solvent

7.2.2 IR spectra of Curcumin:

FTIR spectrum of HCur (Fig. 3), recorded on a Perkin Elmer Spectrometer (Spectrum Two) by use of the ATR technique indicates a peak at 3516 cm^{-1}owing to –OH stretching. Sharp peaks at 1627 cm^{-1} and 1604 cm^{-1}were attributed to C=O stretching vibrations in HCur. Peaks at 1506 cm^{-1} and 1429 cm^{-1} indicates C=C stretching and C=O bending vibrations respectively.

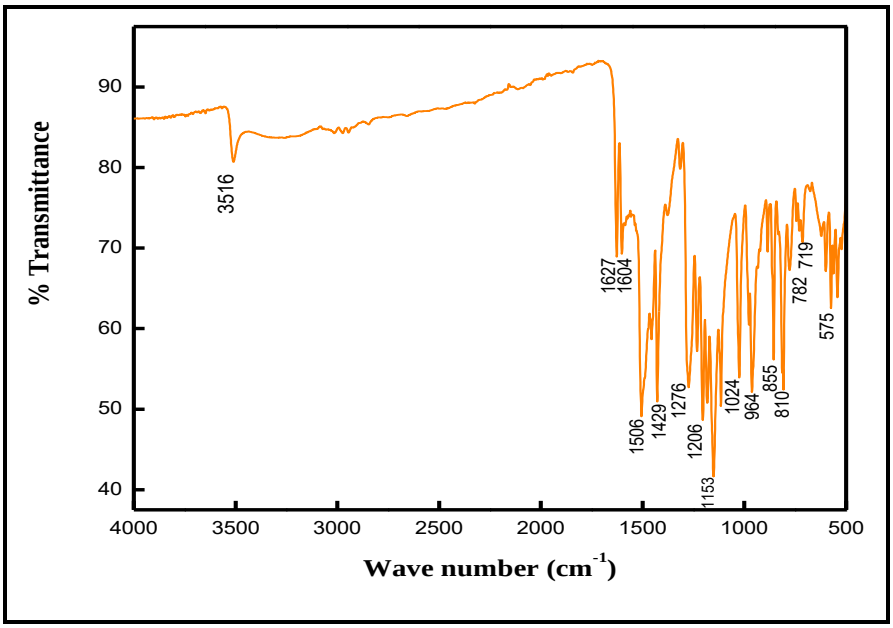


Figure 3: FTIR spectrum of Curcumin (HCur)

7.3 Quantum Chemical calculations based on spectroscopic evidence

DFT was employed using the 6-31G+(d,p) basis set at the restricted B3LYP level[21] in Gaussian 09 software package[22] to optimize the structure of HCur. Since it exists in two different conformers, keto and enol, hence optimization was done in both forms. Both optimized structures are shown in Fig. 4. After optimization, energy of the keto form was found to be –34373.60 eV whereas that of the enol form was –34373.96 eV. Dipole moment and polarizability of the keto form of the molecule was -5.973 Debye and 286.8493 a.u respectively. On the other hand, dipole moment and polarizability of the enol form was 2.9934 Debye and 356.7234 a.u respectively. Since the energy of the enol form was low, hence all computational work was done by taking the optimized enol form of Curcumin.

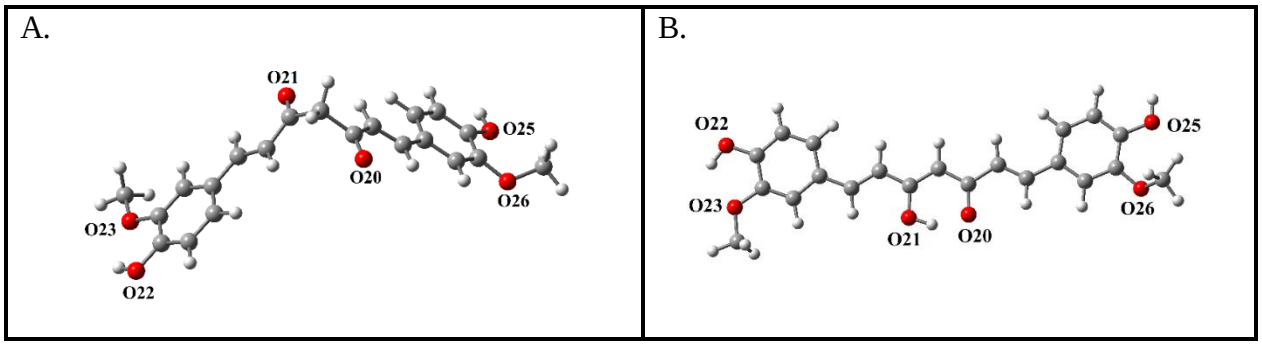


Figure 4: Ground state optimized geometries of HCur (A) keto form and (B) enol form

7.3.1 Frontier molecular orbitals:

Utilization of frontier molecular orbitals enable the formulation of accurate qualitative forecasts about excitation characteristics and electron transport capacities.[23,24] The phenomenon of electronic absorption is often defined as the migration of a single electron from the highest occupied molecular orbital (HOMO) to the lowest unoccupied molecular orbital (LUMO) representing a transition from the ground state to the first excited state.[23,24] The highest occupied molecular orbital (HOMO) functions as an electron-donating entity and lowest unoccupied molecular orbital (LUMO) as an electron-accepting entity. The energy levels of the highest occupied molecular orbital (HOMO) and lowest unoccupied molecular orbital (LUMO), along with the energy gap between them serve as markers of chemical reactivity of molecules.[23,24] The energies of a few HOMOs and LUMOs (Fig.5) of Curcumin in its enol form in DMSO is shown in Table 1. The HOMO-LUMO gap of Curcumin in DMSO considering the enol form was found to be 3.30 eV.

Table 1: HOMO-LUMO values of Curcumin (Enol Form)

Serial No	Molecular Orbital	Energy (eV)
102	LUMO+4	0.30367
101	LUMO+3	-0.0663
100	LUMO+2	-0.1823
99	LUMO+1	-1.1260
98	LUMO	-2.2710
97	HOMO	-5.4705
96	HOMO-1	-5.8539
95	HOMO-2	-6.3944
94	HOMO-3	-6.5919
93	HOMO-4	-6.7097

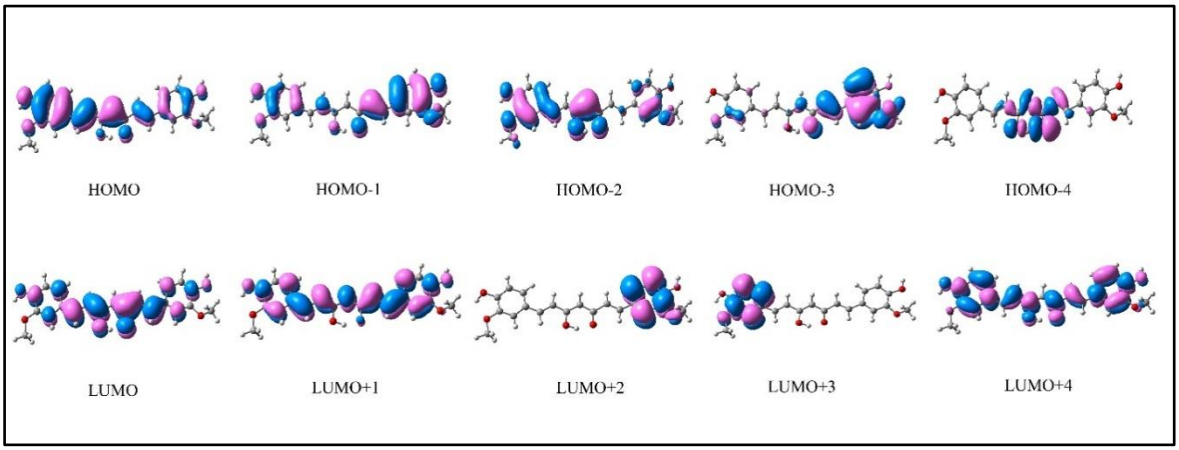


Figure 5: The frontier molecular orbital of the optimized HCur in solution phase

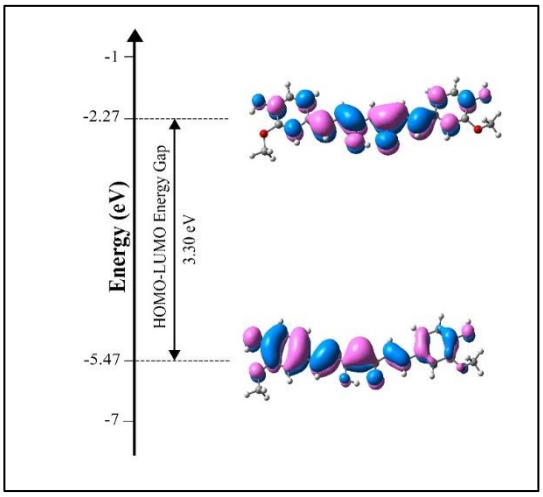


Figure 6: HOMO-LUMO gap of HCur in solution phase (DMSO)

7.3.2 Molecular electrostatic potential surface analysis:

The molecular electrostatic potential (MEP) is a parameter closely linked to distribution of electronic density inside a molecule. It serves as a valuable tool for identifying specific locations within a molecule that are favourable for electrophilic and nucleophilic processes and also for facilitating hydrogen-bonding interactions. The molecular electrostatic potential (MEP) has been utilized to predict locations where electrophilic and/or nucleophilic assault may occur in a molecule that is under investigation.[25,26] Fig. 7 illustrates the charge distribution of the molecule in three-dimensional representation. The diagram illustrates the distinct values of electrostatic potential at the surface, employing a colour scheme to represent these values. Specifically, regions with largest electronegative potential are displayed in red, regions with highest positive potential are depicted in blue while regions with zero potential are depicted in green. The potential increase is expected to occur in the following sequence: red < orange < yellow < green < blue. The maps shown exhibit a color-coded scheme ranging from the darkest shade of red (-2394.77 kj/mol) to deepest shade of blue (2750.02 kj/mol). In this scheme, blue signifies the highest level of attraction while red signifies highest level of repulsion. The presence of a lone pair of electronegative atoms is commonly associated with areas of negative potential.[24-26] The areas of negative charge inside the molecule under investigation were shown to be situated proximal to oxygen atoms comprising of a hydroxy group or a carbonyl group, as evidenced by molecular electrostatic potential (MEP) map of molecules.[24] Nevertheless, areas with highest positive charge are situated on hydrogen atoms of the phenolic O-H groups. These regions might be considered as prospective locations for nucleophilic attack, with a maximum charge value of +2750.02 kJ/mol.

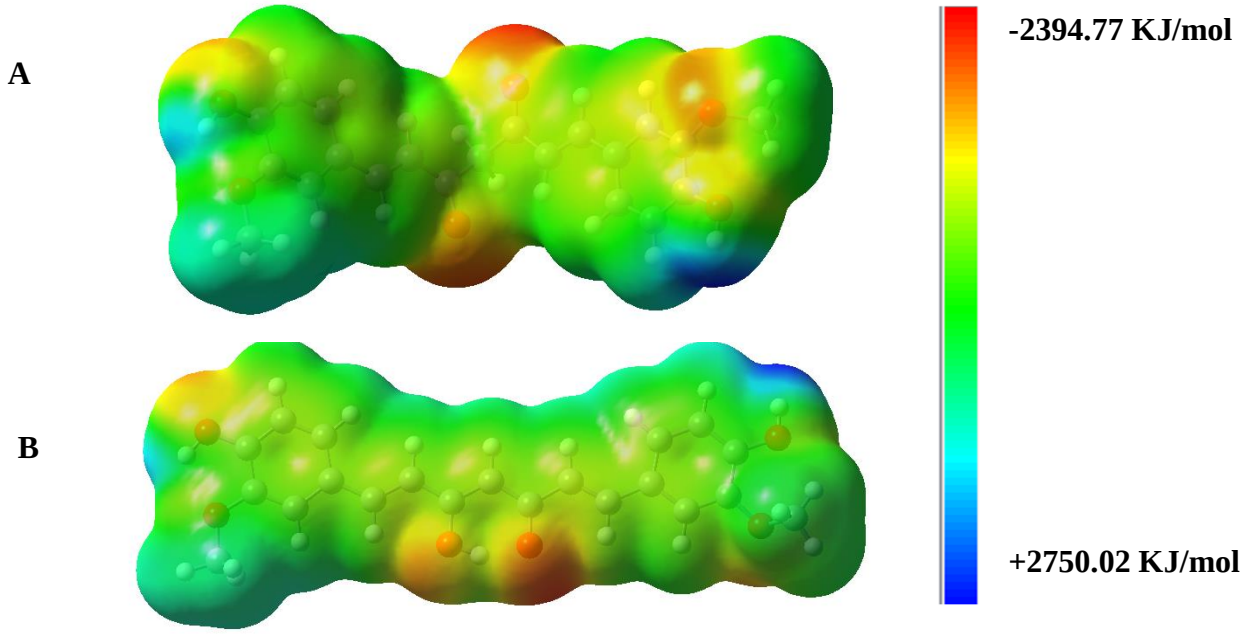


Figure 7: Molecular electrostatic potential surface of HCur (A) Keto form (B) Enol form

7.3.3 Quantum descriptor analysis:

The HOMO and LUMO exert influence over the kinetic stability, electrical conductivity and chemical reactivity of a molecule. Soft molecules often exhibit a relatively narrow HOMO-LUMO energy gap and have a higher degree of biological and chemical reactivity.[25,26] Molecules characterised by a significant disparity in energy levels between their highest occupied molecular orbital (HOMO) and lowest unoccupied molecular orbital (LUMO) exhibit limited biological reactivity, enhanced stability and reduced susceptibility to interactions with other substances. In the context of small HOMO-LUMO energy gaps, occurrence of intramolecular charge transfer (ICT) between an electron-donor group and an electron-acceptor group is viable. In contrast to molecular systems with strong electron-donating properties, molecular systems with high electron-accepting capabilities, exhibit lower energy levels for their highest occupied molecular

orbital (E_{HOMO}) and lowest unoccupied molecular orbital (E_{LUMO}).[25,26] The quantum descriptor of all molecules following the process of geometry optimisation is presented in Table 2. A reduced HOMO-LUMO gap promotes the facilitation of electron donation (IP) and acceptance (EA). Due to its elevated electron affinity, the molecule has a propensity to readily engage with biomolecules through the process of electron density redistribution towards its own structure. Such molecules have a soft nature as seen by its lower η value, described in Eq.26 (*Chapter 6, Experimental*). A high electronophilicity index (ω) is indicative of a strong propensity for electron-rich substances.

Table 2: Quantum descriptors for Curcumin in electron volts (eV) with the RB3LYP-631G+ (d,p) functional

Compound	HOMO (eV)	LUMO (eV)	ΔE	IP	EA	χ	η	M	σ	ω
Curcumin (HCur)	-5.47	-2.27	3.20	5.47	2.27	3.87	1.60	-3.87	0.31	4.68

7.3.4 NCI-RDG Analysis:

RDG (Reduced density gradient) is a highly effective technique to analyze non-covalent interactions in real space, utilizing electron density and its derivatives.[27,28] This approach has demonstrated an ability to differentiate between different types of interactions in small molecules and molecular complexes. In order to calculate RDG values we utilized the following equation: [27,28]

$$\text{RDG (r)} = \frac{1}{2(3\pi^2)^{1/3}} \frac{|\nabla\rho(r)|}{\rho(r)^{4/3}}$$

Through analysis of low and high density gradient values, one can realize the presence of weak and strong interactions. Graphs showing relationship between RDG and low-gradient peak density (ρ) values can provide insights into the intensity of an interaction. A proposed tool for distinguishing a wide range of interaction types involves the product of electron density and sign of the second eigenvalues. The sign λ_2 is an important parameter that helps to differentiate between bound ($\lambda_2 < 0$) and non-coupling ($\lambda_2 > 0$) interactions. Based on certain principles, interactions can be classified into three distinct types. The first is a type of attraction, which is characterized by negative sign (λ_2). The second hypothesis suggests a strong repulsion type of nonbinding interaction, which is supported by the presence of large and positive values of the sign (λ_2). The third type, known as weak interactions (van der Waals interactions), is typically characterized by values that are very close to zero.[27,28] Fig. 8 displays the projected RDG plots for Curcumin. Different types of colour schemes were used to describe interactions between hydrogen, oxygen and carbon present in the molecule. The red colour observed suggests a significant level of repulsion within the system. The green—illustrates van der Waals interactions. Blue correspond to strong hydrogen bond interaction present with in the molecular system.

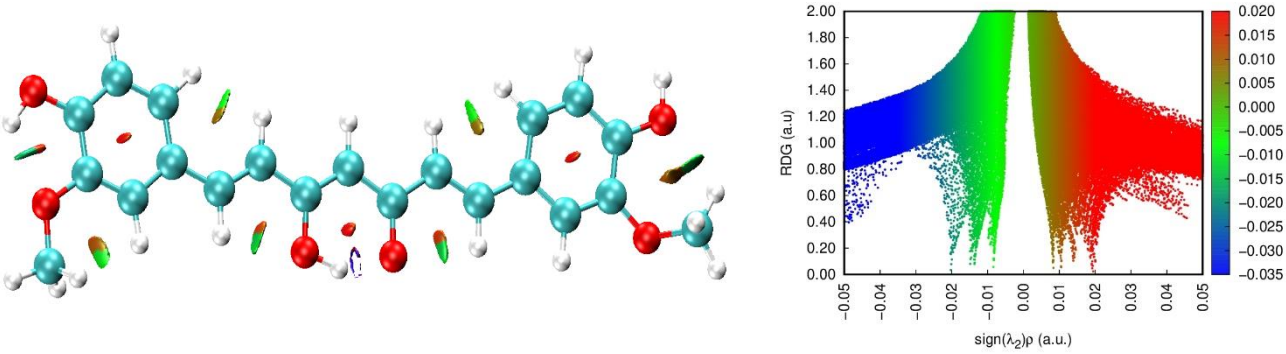


Figure 8: NCI (right) and RDG (left) plot of optimized Curcumin molecule in solution phase

7.3.5 ELF and LOL analysis:

The studies ELF (Electron Localization Function) and LOL (localized Orbital Locator) primarily focus on the analysis of topological surfaces. Research conducted using the Multiwfn software package[29] has shown a significant likelihood of locating an electron pair on the surface of a molecule, as indicated by ELF and LOL. In Fig. 9, the colour shaded and relief map of ELF and LOL has been shown. The relief map highlights the electron environment around each atom, with variations in peak area indicating either a large or contracted electron density. The chemical content of ELF and LOL is homogenous due to their dependence on kinetic energy density. The ELF theory explains the distribution of electron pairs, while LOL describes the overlapping of localized orbitals caused by gradient of orbitals.[30] The ELF map is designed to cover a range from 0.0 to 1.0. Interestingly, the region below 0.5 displays a delocalized electronic region[31] while the LOL reaches significant values above 0.5 in areas where electron density is primarily influenced by electron localization.[32] The different shades of colour on ELF and LOL maps provide evidence of the presence of bonding and nonbonding electrons. In particular, the red colour surrounding hydrogen atoms indicate the presence of these electrons. The presence of a red-yellow colour around oxygen atoms (e.g. O20) indicates a strong concentration of electrons, which can be attributed to factors such as covalent bond formation, a lone pair of electrons, or a nuclear shell in that particular region. The blue colour surrounding the carbon atoms indicate the presence of a delocalized electron cloud. The central region of a hydrogen atom in the LOL appears white due to the electron density surpassing the upper limit of the colour scale.

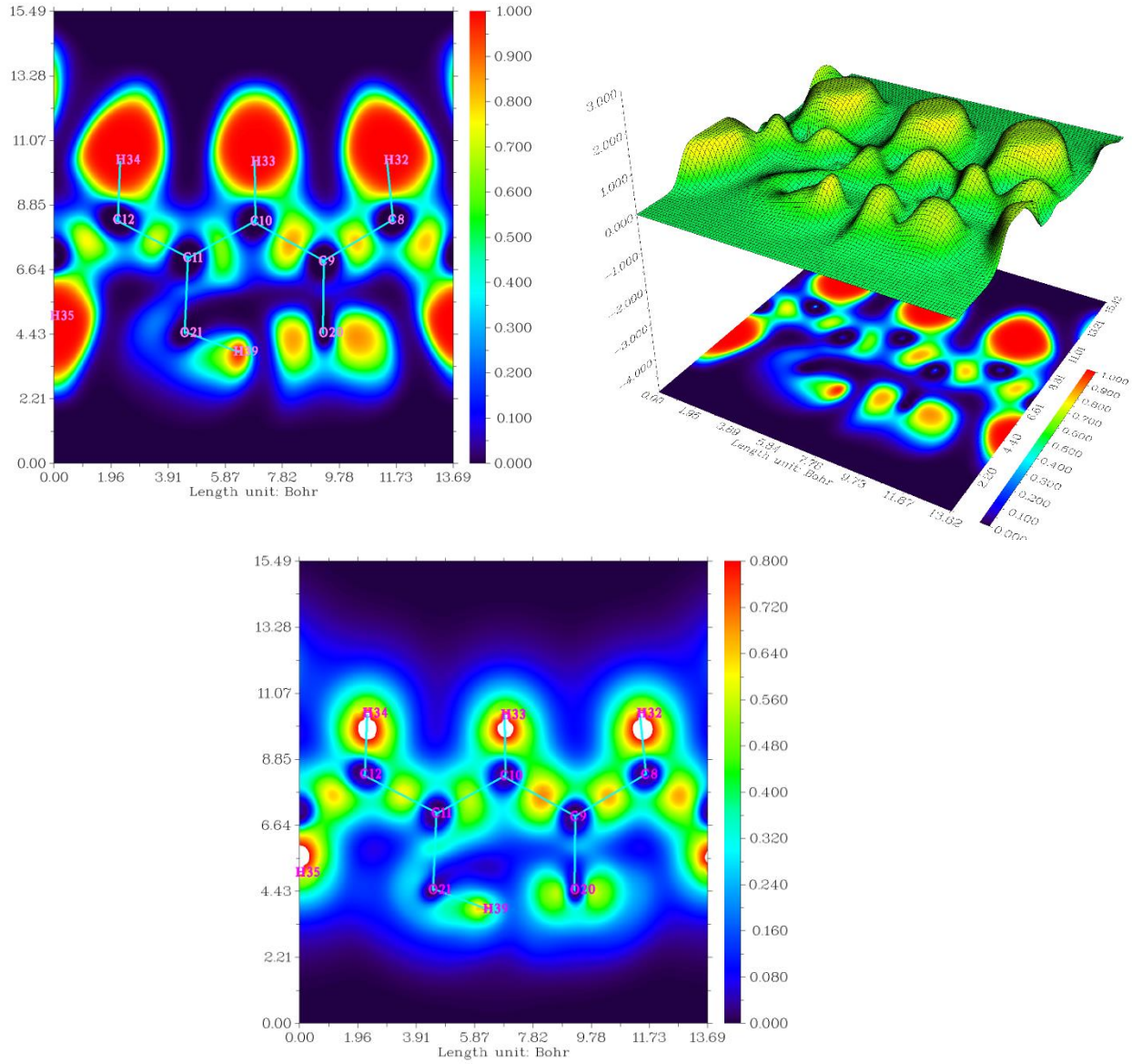


Figure 9: Electron localization function (ELF) maps (Top) and localized orbital locator (LOL) maps (Bottom) of Curcumin in enol form

7.4 Stability of Curcumin under physiological buffer system

7.4.1 Followed by UV-Vis spectroscopy:

Given the known information about the instability of HCur[33], we conducted a study to assess its stability in various biological environments (Figs. 10). From various UV-Vis absorption figures, it is evident that HCur exhibited instability in PBS buffer, DTT (Dithiothreitol), BHI (Brain heart infusion), MHB (Mueller-Hinton agar), DMEM (Dulbecco's Modified Eagle Medium) etc. biological medium. From Fig. 10 B it is clear that HCur experienced a significant decrease in absorption intensity after just 5 minutes of co-incubation with DTT which is a potent reducing agent.[34-35]

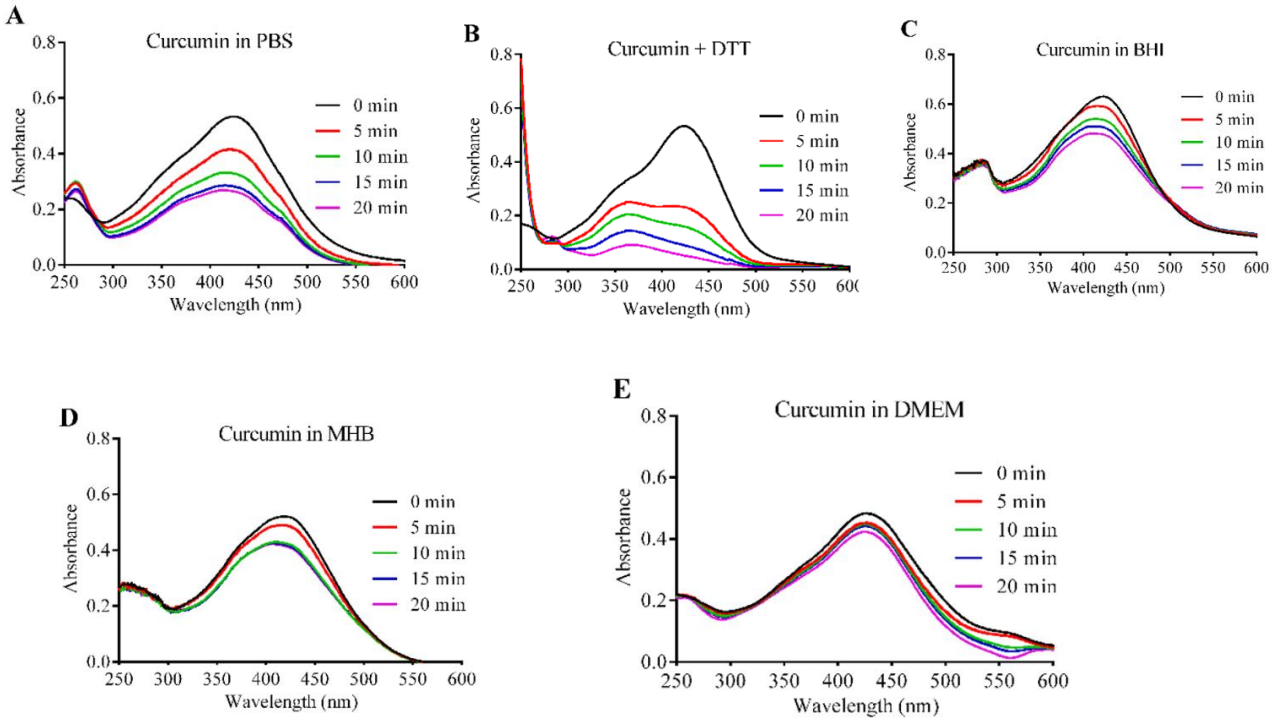


Figure 10: UV-Visible spectra of Curcumin (A) PBS buffer, (B) in presence of 10 μM DTT (C) BHI (D) MHB and (E) DMEM media

7.4.2 Followed by High pressure Liquid Chromatography:

The stability of curcumin in PBS was also examined using HPLC. Previous research in this regard show that Curcumin can produce various degradation products, like trans-6-(4'-hydroxy-3'-methoxyphenyl)-2,4-dioxo-5-hexenal, vanillin, vanilic acid, ferulic acid, and feruloyl methane.[17,36] In this research experiment, Curcumin and its various degraded compounds were dissolved in a phosphate buffer and conducted HPLC at different time intervals following dissolution. The HPLC was carried out using a C18 column and a mobile phase with a previously mentioned composition. An ongoing degradation was observed in case of Curcumin with increasing time as indicated by a decrease in peak height, as previously reported[17] (Fig.11). From the HPLC plots it is clear that there are significant amounts of degraded products of curcumin was forming with increasing time. So, after this study one may conclude that after 24 hr. incubation in phosphate buffer all most all the degraded product such as vanillin, vanilic acid, and ferulic acid must be present in solution, alongside curcumin (Fig. 12)

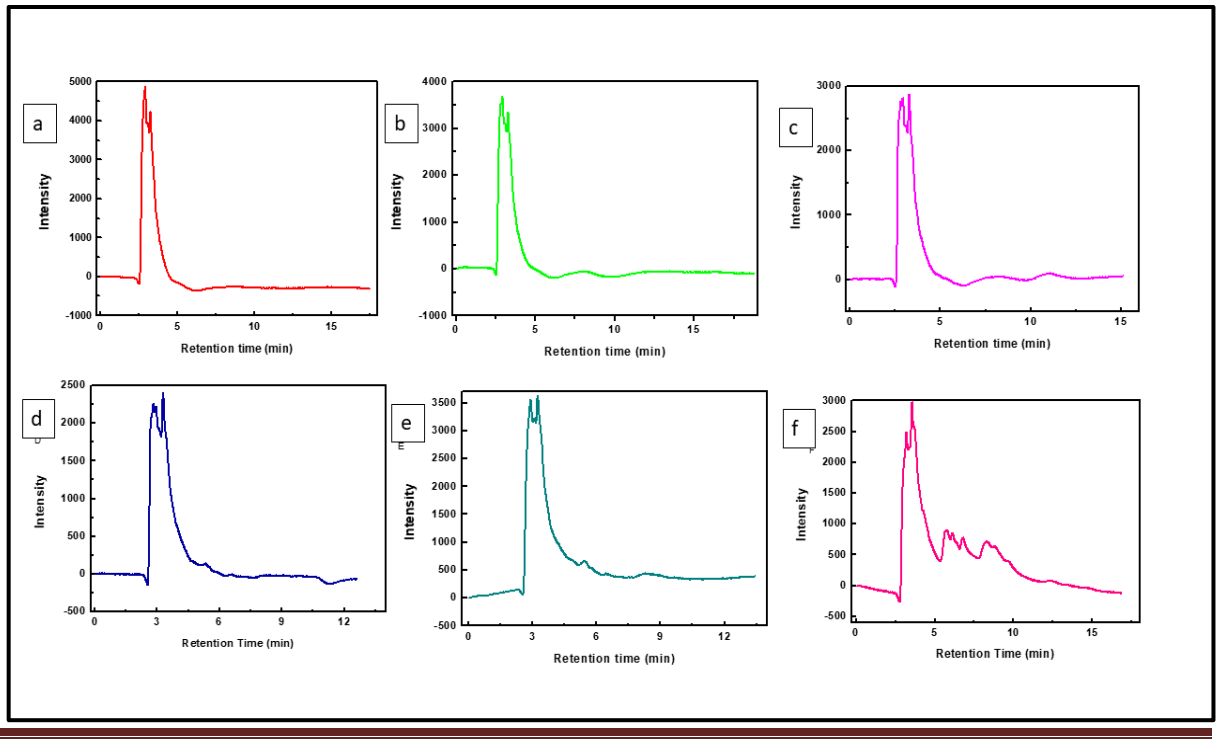


Figure 11: Chromatograms obtained following HPLC of Cur (100 µM); (a) immediately, (b) after 20 minutes, (c) after 75 minutes, (d) after 2 hours, (e) after 3 hours thirty minutes and (f) after 24 hours from the time of dissolution (incubation) of it in 0.1 M phosphate buffer. Column: C-18, Eluent: 12% THF, 5% CH_3CN, 2% acetic acid in water.

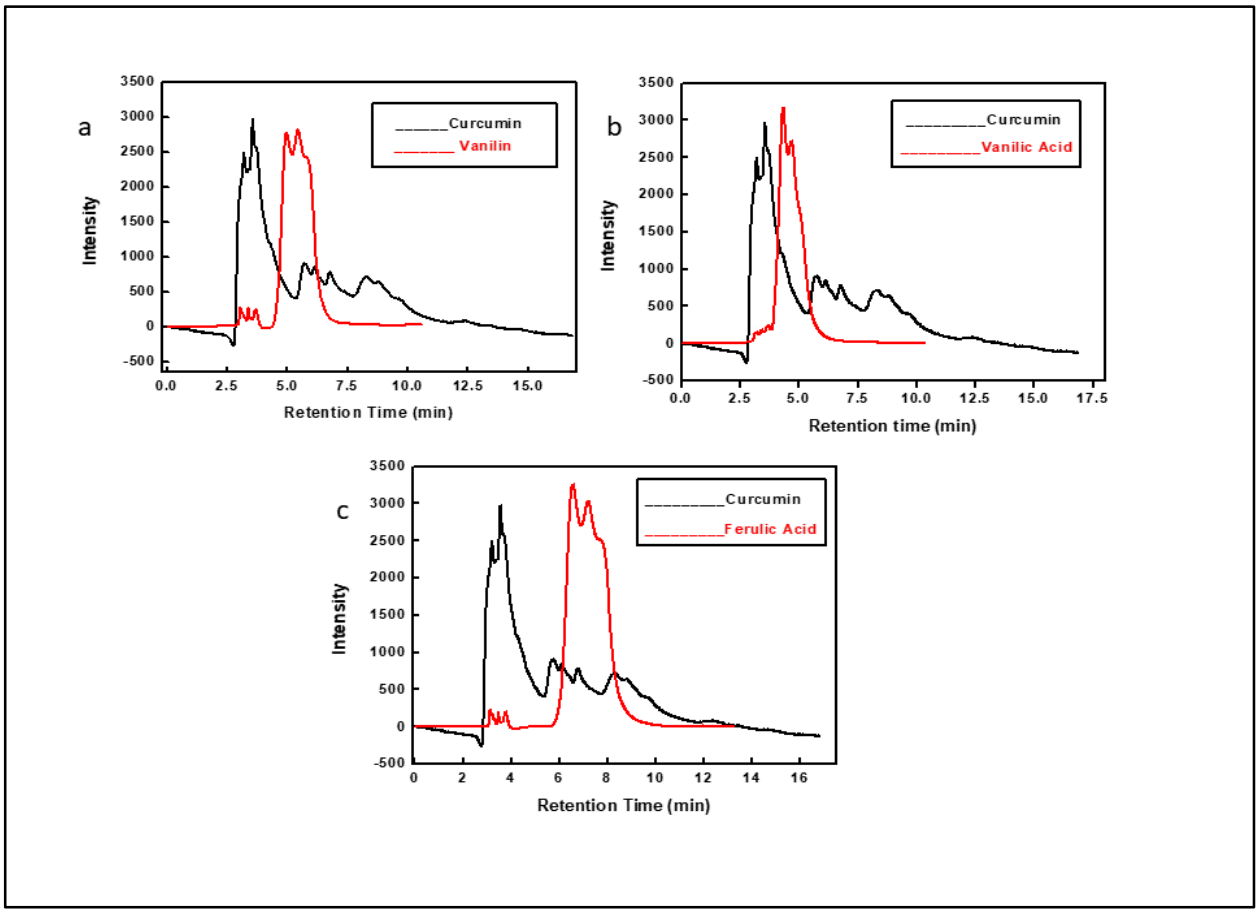


Figure 12 : Chromatograms (—) obtained following HPLC of Cur at 2 hours from the dissolution of curcumin (100 µM) in 0.1 M phosphate buffer. (a) denotes an overlay of chromatograms of curcumin and vanillin (6.67 µM), (b) overlay of chromatograms of curcumin and vanilic acid (2.0 µM), and (c) overlay of chromatograms of curcumin and ferulic acid (5.9 µM),. Column: C-18, Eluent: 12% THF, 5% CH_3CN, 2% acetic acid in water.

References

1. B. B. Aggarwal, C. Sundaram, N. Malani, H. Ichikawa.; Curcumin: the Indian solid gold. In: *The molecular targets and therapeutic uses of curcumin in health and disease*. **2007**, (pp. 1-75). Springer, Boston, MA.
2. J. S. Jurenka.; Anti-inflammatory properties of curcumin, a major constituent of Curcuma longa: a review of preclinical and clinical research. *Alternative Medicine Review*. **2009**, 14, 141-153.
3. T. Ak, and İ. Gülçin.; Antioxidant and radical scavenging properties of curcumin. *Chemico-biological Interactions*. **2008**, 174, 27-37.
4. R. Wilken, M. S. Veena, M. B. Wang, and E. S. Srivatsan.; Curcumin: A review of anti-cancer properties and therapeutic activity in head and neck squamous cell carcinoma. *Mol. Cancer*. **2011,** 10:12. doi: 10.1186/1476-4598-10-12.
5. S. Wanninger, V. Lorenz, A. Subhan, and F. T. Edelmann.; Metal complexes of curcumin–synthetic strategies, structures and medicinal applications. *Chem. Soc. Rev.***2015**, 44, 4986-5002.
6. S. Y. Teow, K. Liew, S. A. Ali, A. S. B. Khoo, and S. C. Peh.; Antibacterial action of curcumin against Staphylococcus aureus: a brief review. *Journal of Tropical Medicine*, **2016**, Article ID : 2853054, 1-10
7. A. Goel, A. B. Kunnumakkara, and B. B. Aggarwal.; Curcumin as "Curecumin": from kitchen to clinic. *Biochem. Pharmacol*. **2008**,75, 787-809.
8. K. Neelofar, S. Shreaz, B. Rimple, S. Muralidhar, M. Nikhat, & L. A. Khan.; Curcumin as a promising anticandidal of clinical interest. *Can. Jour.Microbiol.* **2011**, 57, 204-210.

9. P. Tyagi, M. Singh, H. Kumari, A. Kumari, and K. Mukhopadhyay.; Bactericidal activity of Curcumin I is associated with damaging of bacterial membrane. *PloS one*,**2015**, *10(3)*.1-15.

10. R. A. Sharma, W. P. Steward, and A.J. Gescher.; Pharmacokinetics and pharmacodynamics of Curcumin. *Adv. Exp. Med. Biol*. **2007**,595, 453-470.

11. R. Banerjee.; Inhibitory effect of Curcumin-Cu(II) and Curcumin-Zn(II) complexes on amyloid-beta peptide fibrillation, *Bioinorg. Chem. Appl*. **2014**, 325873 (2014).

12. S. Banerjee, P. Prasad, A. Hussain, I. Khan, P. Kondaiah, A. R. Chakravarty.; Remarkable photocytotoxicity of curcumin in HeLa cells in visible and arresting its degradation on oxovanadium (IV) complex formation. *Chem. Comm*. **2012,** 48, 7702-7704.

13. K. I. Priyadarsini.; The chemistry of Curcumin: From extraction to therapeutic agent. *Molecules*, **2014**,19, 20091-20112.

14. M. D. Cas and R. Ghidoni.; Dietary Curcumin: Correlation between bioavailability and health potential, *Nutrients*. **2019**, 11(9), 2147,1-14.

15. S. B. de Souza Ferreira and M. L. Bruschi.; Improving the bioavailability of curcumin: is micro/nanoencapsulation the key?, *Ther Deliv*. **2019**, 10(2), 83-86.

16. P. Anand, A. B. Kunnumakkara, R. A. Newman, B. B. Aggarwal.; Bioavailability of Curcumin: Problems and promises, *Mol. Pharmaceutics.* **2007**, 4, 807–818.

17. Y.-J. Wang, M-H. Pan, A-Li. Cheng, L.-I. Lin, Y-S. Ho, Chang-Yao Hsieh, Jen-Kun Lin.; Stability of curcumin in buffer solutions and characterization of its degradation products. *J. Pharma. Biomed. Anal*. **1997**,15, 1867-1876.

18. H. H. Tønnesen, M. Másson, T. Loftsson.; Studies of curcumin and curcuminoids. XXVII. Cyclodextrincomplexation: solubility, chemical and photochemical stability. *Int J Pharm.*, **2002**, 244,127-135.

19. M. B.-Pineda; M. T. Ramírez-Silva, M. Romero-Romo, E. González-Vergara, A. Rojas-Hernández.; Determination of acidity constants of curcumin in aqueous solution and apparent rate constant of its decomposition. *Spectrochim. Acta A Mol. Biomol. Spectrosc.***2004**, 60,1091-1097.

20. K. I. Priyadarsini.; The Chemistry of Curcumin: From Extraction to Therapeutic Agent. *Molecules*, **2014**, 19, 20091-20112.

21. (a) A. D. Becke.; Density-functional thermochemistry. III. The role of exact exchange, *J. Chem. Phys*. **1993**, 98, 5648e5652; (b) C. T. Lee, W. T. Yang, R. G. Parr.; Development of the Colle-Salvetti correlation-energy formula into a functional of the electron density, *Phys. Rev. B.* **1988**, 37, 785e789.

22. M. J. Frisch, G. W. Trucks, H. B. Schlegel, G. E. Scuseria, M. A. Robb, J. R. Cheeseman, G. Scalmani, V. Barone, G. A. Petersson, H. Nakatsuji, X. Li, M. Caricato, A. Marenich, J. Bloino, B. G. Janesko, R. Gomperts, B. Mennucci, H. P. Hratchian, J. V. Ortiz, A. F. Izmaylov, J. L. Sonnenberg, D. Williams-Young, F. Ding, F. Lipparini, F. Egidi, J. Goings, B. Peng, A. Petrone, T. Henderson, D. Ranasinghe, V. G. Zakrzewski, J. Gao, N. Rega, G. Zheng, W. Liang, M. Hada, M. Ehara, K. Toyota, R. Fukuda, J. Hasegawa, M. Ishida, T. Nakajima, Y. Honda, O. Kitao, H. Nakai, T. Vreven, K. Throssell, J. A. Montgomery, Jr., J. E. Peralta, F. Ogliaro, M. Bearpark, J. J. Heyd, E. Brothers, K. N. Kudin, V. N. Staroverov, T. Keith, R. Kobayashi, J. Normand, K. Raghavachari, A. Rendell, J. C. Burant, S. S. Iyengar, J.

Tomasi, M. Cossi, J. M. Millam, M. Klene, C. Adamo, R. Cammi, J. W. Ochterski, R. L. Martin, K. Morokuma, O. Farkas, J. B. Foresman, and D. J. Fox.; **2016**, Gaussian 09, Revision D.01, Gaussian, Inc., Wallingford CT.

23. V. K. Choudhary, A. K. Bhatt, D. Dash, N. Sharma.; DFT calculations on molecular structures, HOMO-LUMO study, reactivity descriptors and spectral analyses of newly synthesized diorganotin(IV) 2-chloridophenylacetohydroxamate complexes, *Jour. Comp. Chem.* **2019**, 1-10.

24. Z. Akbari, C. Stagno, N. Iraci, T. Efferth, E. A. Omer, A. Piperno M. Montazerozohori M.F. Dehnayebi , N. Micale.; Biological evaluation, DFT, MEP, HOMO-LUMO analysis and ensemble docking studies of Zn(II) complexes of bidentate and tetradentate Schiff base ligands as antileukemia agents. *Journal of Molecular Structure*, **2024**,1301,137400.

25. A. Kumar, G. Gatto, F. Delogu L.Pilia.; DFT study of [Pt(Cl)2L] complex (L = rubeanic acid) and its derived compounds with DNA purine bases. *Chemical Physics*, **2020,** 530, 110646.

26. N. Sepay, R. Mondal, M. K. Al-Muhanna, D. Saha.; Identification of natural flavonoids as novel EGFR inhibitors using DFT, molecular docking, and molecular dynamics, *New Journal of Chemistry*, **2022**, 20

27. E.R. Johnson, S. Keinan, P. Mori-Sánchez, J. Contreras-García, A.J. Cohen, W. Yang.; Revealing Noncovalent Interactions. *J. Am.Chem. Soc*., **2010**, 132, 6498–6506.

28. F. Akman , A. Demirpolat , A. S. Kazachenko , Anna S. Kazachenko, N. Issaoui and O.A.Dossary.; Molecular Structure, Electronic Properties, Reactivity (ELF, LOL, and

Fukui), and NCI-RDG Studies of the Binary Mixture of Water and Essential Oil of Phlomis bruguieri. *Molecules,* **2023**,28,2684.

29. T. Lu, F. Chen.; Multiwfn: A multifunctional wavefunction analyzer. *Jour. Comput. Chem.***2012**, 33, 580-592.

30. B.Silvi, A.Savin.; Classification of chemical bonds based on topological analysis of electron localization functions. *Nature,* **1994**, 371(6499), 683–686.

31. B. Fathima Rizwana, J. C. Prasana, S.Muthu, C.S.Abraham.; Molecular docking studies, charge transfer excitation and wave function analyses(ESP,ELF,LOL) on valacyclovir:A potential anti viral drug. *Comput,Biol.Chem*., **2019**,78, 9–17.

32. Heiko Jacobsen.; Localized-orbital locator (LOL) profiles of chemical bonding. *Can. J.Chem*. **2008,**86(7) 695–702.

33. P. Kumar, S.K. Kandi, S. Manohar, K. Mukhopadhyay.; D.S. Rawat, Monocarbonyl curcuminoids with improved stability as antibacterial agents against Staphylococcus aureus and their mechanistic studies. *ACS Omega*, **2019**, 4, 675-687.

34. Y.M. Go, D.P. Jones, Redox compartmentalization in eukaryotic cells, *Biochimica et biophysica acta*. **2008**, 1780, 1273-1290.

35. S. Chakraborti, G. Dhar, V. Dwivedi, A. Das, A. Poddar, G. Chakraborti, G. Basu, P. Chakrabarti, A. Surolia, B. Bhattacharyya.; Stable and potent analogues derived from the modification of the dicarbonyl moiety of curcumin. *Biochemistry*, **2013**, 52, 7449-7460.

36. P. Galer, B. Sket.; Photodegradation of methoxy substituted curcuminiods. *Acta Chim. Slov*. **2015**, 62, 346-353.

CHAPTER 8

Synthesis, characterization, structural analysis through quantum chemical computations of a Mn^{II}-Curcumin complex and an investigation of superoxide dismutase like activity & DNA binding

Introduction

Owing to the hydrolytic instability of Curcumin in cellular media, attributed to its β-diketone moiety that leads to limited bio-availability, it becomes essential to find out ways to prevent such instability and make it more available biologically.[1-8] To deal with the problem of instability that is widely regarded as a significant drawback for HCur, a complex using Mn^{II} was synthesized, keeping in mind the fact metal complexes of HCur have been reported to prevent its degradation.[2, 8-11] Several complications could arise owing to the presence of phenolic –OH in HCur that are potential centers of activity, however, with careful precautions, such coordination complexes of HCur could exhibit unique biological properties that can be utilized for the benefit of mankind.[2, 8-19] Manganese was selected for complex formation since the human body needs it as it has several roles that include the production and activation of many enzymes (oxidoreductases, transferases, hydrolases, lyases, isomerases, and ligases), control of glucose and lipid metabolism, enhancement of protein synthesis, formation of vitamins B and C, promotion of blood cell formation and hormonal regulation and immunity.[20-22] In addition, arginase, glutamine synthetase, phosphoenolpyruvate decarboxylase and manganese superoxide dismutase (Mn-SOD) play a role in metabolic processes and serve as participants to counter the stress of free radicals.[22,23]

In this chapter, the formation of a complex of Mn^{II} with HCur has been discussed with particular emphasis on elemental analysis and spectroscopic techniques. The structure was determined through DFT calculations and several non-covalent interactions examined by the NCI-RDG plots.[24]

The hydrolytic stability of the coordination compound in different biological media was checked to determine whether presence of Mn^{II} was able to stabilize Curcumin by preventing its bio-degradability. The study also focuses on the SOD-like activity of the complex that leads to the production of reactive intermediates and their subsequent interaction with DNA. Since Gram-

positive (*S. aureus*) and Gram-negative (*E. coli*) bacteria are widely observed in nature and are quite frequently known to cause infections, effectiveness of a prepared coordination compound against such clinically relevant Gram-positive (*S. aureus*) and Gram-negative (*E. coli*) bacteria were investigated.[25-27]

Result and discussion

8.1 Stoichiometry of complex formation for Mn^{II} and HCur by mole ratio and Job's method of continuous variation

This was ascertained by mixing different volumes of equimolar Mn^{II} and HCur.[28, 29] In the mole ratio method, in one set of experiments the concentration of HCur was kept constant while Mn^{II} was varied and in another set of experiments the concentration of Mn^{II} was kept constant while HCur was varied.[28,29] For the situation when HCur was kept constant, the absorbance recorded at 430 nm at different time intervals from mixing was plotted against $(T_M/T_L)_{TL}$ (Fig. 1A, 1B, 1C). T_M and T_L represent concentrations of Mn^{II} and HCur respectively in the experimental solutions. Two straight lines were obtained for all three plots having an intersection at 0.3, thus suggesting that the ratio in which HCur binds to Mn^{II} is 3:1. When Mn^{II} was kept constant and HCur varied, absorbance was again recorded at 430 nm at different time intervals and plotted against $(T_L/T_M)_{TM}$ (Fig. 2A, 2B). When recorded immediately data points indicated two intersections suggesting the possibility of two species (1:2 and 1:3). However, when recorded after 24 hours the plot clearly indicated the formation of a species where one Mn^{II} was bound to three HCur.

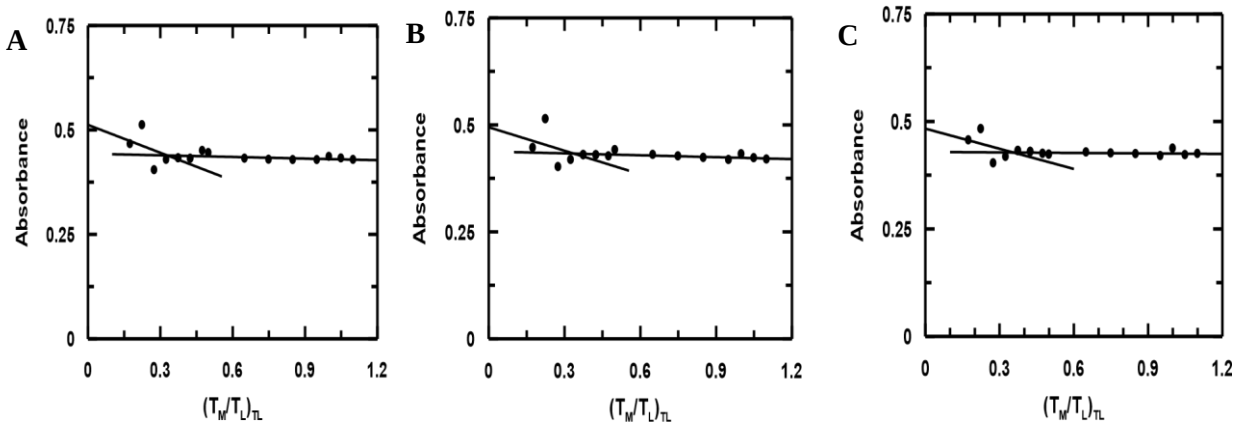


Figure 1: Mole-ratio plots showing variation in absorbance at 430 nm for a change in concentration of Mn^{II} for a fixed concentration of HCur = 10 µM; (A) immediately after HCur and Mn(II) were mixed; (B) after 6 hours from the time HCur and Mn^{II} were mixed; (C) after 24 hours from the time HCur and Mn^{II} were mixed; pH of the medium: ~7.4, [$NaNO_3$] = 0.01 M, Temperature = 303 K.

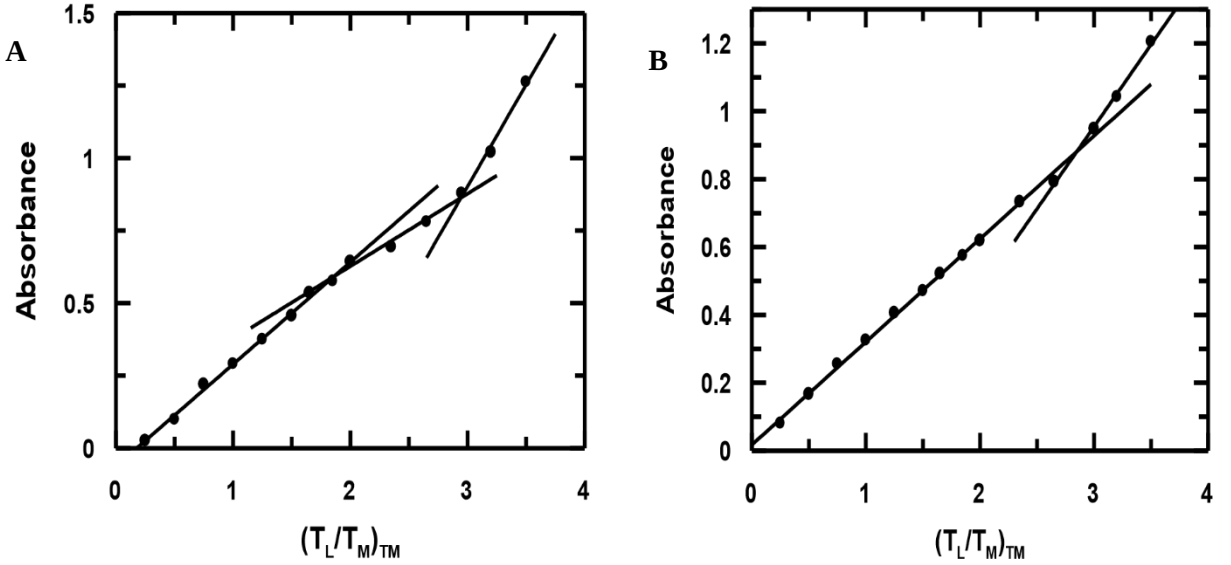


Figure 2 : Mole-ratio plots showing variation in absorbance at 430 nm for a change in concentration of HCur for a fixed concentration of Mn^{II} = 10 µM; (A) immediately after HCur and Mn^{II} were mixed; (B) after 24 hours from the time HCur and Mn^{II} were mixed; pH of the medium: ~7.4, [$NaNO_3$] = 0.01 M, Temperature = 303 K.

In experiments for Job's method of continuous variation appropriate amounts of HCur was mixed with Mn^{II} in 10 mL volumetric flasks and after shaking the solution for a constant time (3 minutes), absorbance was recorded at 430 nm. Plots of three different experiments (Fig. 3A, 3B, 3C) indicate the formation of a 1:2 and 1:3 species in solution.

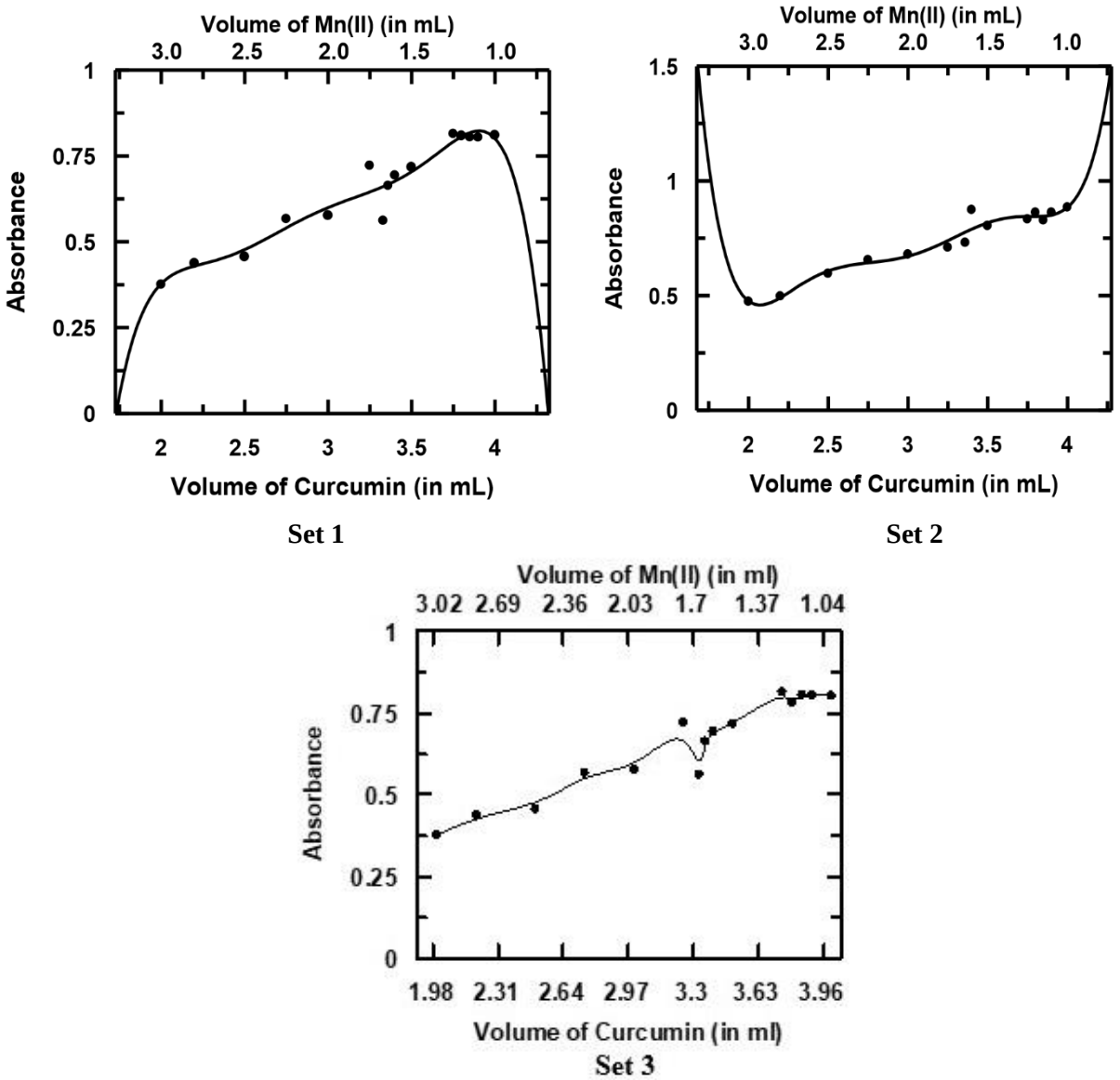


Figure 3: Plot showing a variation in absorbance at 430 nm for a continuous variation of HCur and Mn^{II} for three different experiments, Set 1, Set 2 and Set 3 at pH (~7.4). Strength of stock solutions of Mn^{II} and HCur were 100 µM; [$NaNO_3$] = 0.01 M, Temperature for Set 1 = 300 K; Temperature for Set 1 = 305 K; Temperature for Set 1 = 303 K.

If we consider the metal ion to be M and ligand L, then, formation of a metal-ligand complex, may be thought to follow the following sequence of reactions (Eqs 1-3)

$$M + L \rightleftharpoons ML \qquad (1)$$

$$ML + L \rightleftharpoons ML_2 \qquad (2)$$

$$ML_2 + L \rightleftharpoons ML_3 \qquad (3)$$

Since each step is an equilibrium step and only 3 minutes was allowed as interaction time before absorbance was recorded using a spectrophotometer it is only likely that for each solution having a certain composition, all species (ML, ML_2 and ML_3) would be present simultaneously. If attainment of equilibrium (1) is fast and the other two relatively slow, we should see responses for ML_2 and ML_3. However, if equilibrium (1) is slow we would see responses for ML and ML_2. Sometimes in such cases, we may not see an exclusive response for ML_3 in the time-frame of the analysis but rather existence of two species say ML_2 and ML_3. However, if one refluxes M and L, taking L in excess, for say 4 to 5 hours, which was actually done to prepare the complex there would be a strong possibility to get ML_3 exclusively.

Something like this probably happened for Mn^{II}-Curcumin where both from mole-ratio and Job's plots for species in between 1:2 and 1:3 (but tending to 1:3) responses were obtained. Had equilibrium for reaction 3 been fast , would have got a response for ML_3 only, but probably that was not the case. All figures pertaining to the discussion above have been provided (Figs. 1,2 & 3).

8.2 Determination of stability constant of Mn^{II}-Curcumin in solution

Dissociation of a proton of HCur in the presence of Mn^{II} was determined in ethanol (10%) –aqueous (90%) solution at 32°C and a fixed ionic strength of the medium (0.1 M $NaNO_3$). Absorbance of HCur was followed at 430 nm in the presence of Mn^{II} and fitted to Eq. 5 (*Chapter 6, Experimental)*. pK_{a1} (= 5.89 ± 0.43) and pK_{a2} (= 8.83 ± 0.20) were determined (Fig. 4). The

titration data was also fitted to Eq. 4 (*Chapter 6, Experimental)* able to determine the dissociation of three protons. However, when the data was fitted to Eq. 4 (*Chapter 6, Experimental)* values for pK_{a1} and pK_{a2} remained same as that obtained from Eq. 5, (*Chapter 6, Experimental*) but that of pK_{a3} was 12.44 ± 23.07 which was absurd. Hence, it was concluded that in presence of Mn^{II}, both phenolic–OH protons present on HCur dissociate simultaneously as determined from Eq. 5 (*Chapter 6, Experimental)*. Stability constants β^* and β were determined using Eq.6-10 (*Chapter 6, Experimental*) and found to be 2.52×10^{18} ($\log \beta = 18.4$).

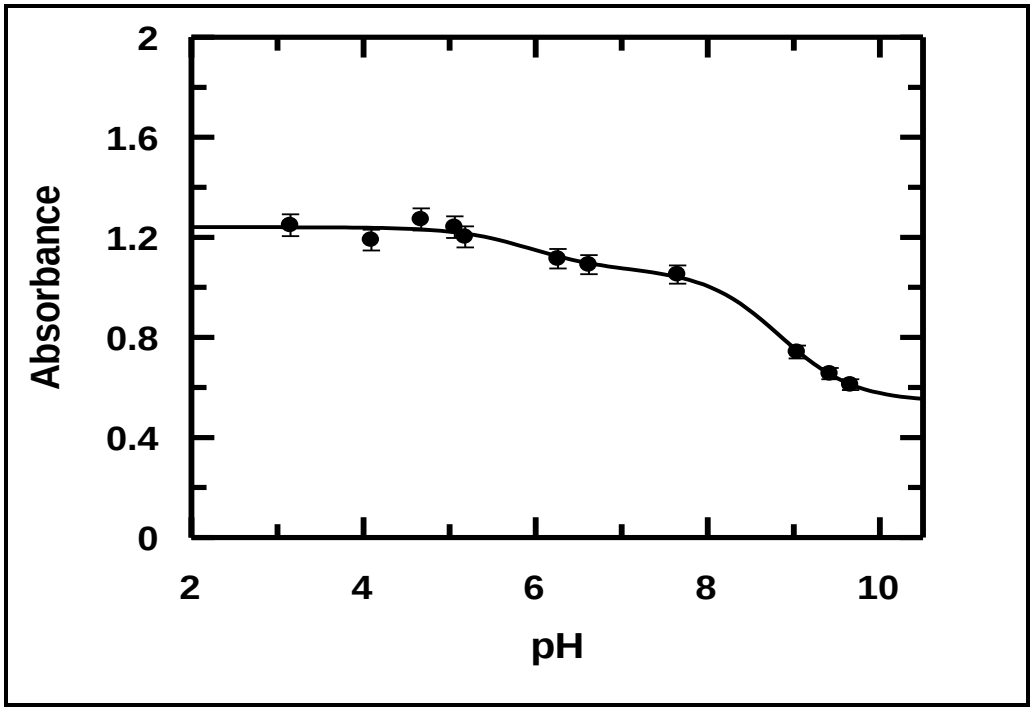


Figure 4: Titration of HCur performed in the presence of Mn^{II}, as shown by a variation in absorbance at 430 nm;[HCur] =30 µM, [Mn^{II}] = 10 µM, [$NaNO_3$] = 0.01 M, Temperature = 305 K.

8.3 Characterization of the complex

8.3.1 Analysis of Mass spectrum:

Mass spectrum was recorded on Micromass Q-Tof micro^{TM}, Waters Corporation. Considering the complex to be a 1:3 species, analysis of its mass spectrum was done (Fig. 5). The molecular ion peak was obtained in a cluster of peaks having m/z 1157.4994, 1156.4755 and 1155.3969 [m/z (theo) = 1158.0467]. From the molecular ion, departure of one ligand has Mn^{II} bound to two HCur with an expected m/z value of 789.6771. Peaks obtained at m/z = 790.6039, 789.5612 and 787.5536 support the formation of such a fragment. Again, if two ligands depart, the fragment remaining has m/z = 422.3076. A peak at m/z = 421.7341 confirms formation of such a species. Peaks at m/z = 364.7516 and 368.8801 indicate free HCur. Therefore, mass spectrum of the complex provides good evidence in favour of complex formation where Mn^{II} is bound to HCur in the ratio 1:3

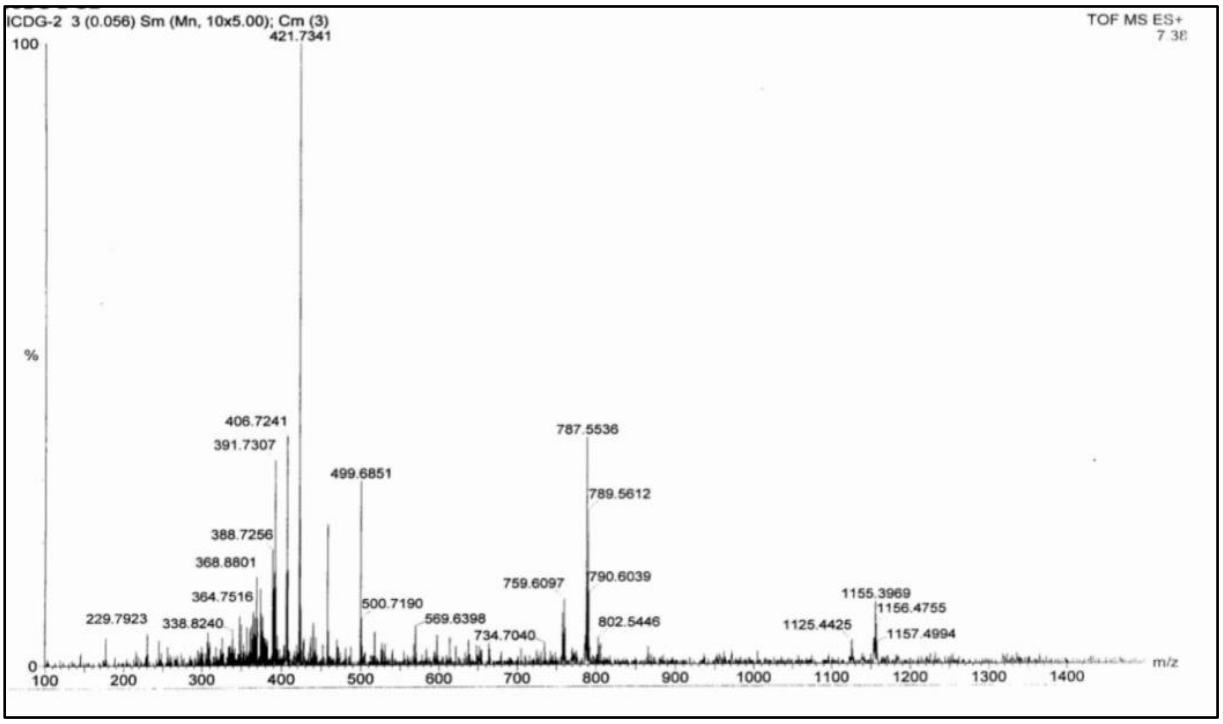


Figure 5: Mass spectra of the Mn^{II}complex of HCur

8.3.2 Thermo-gravimetric analysis of the complex:

Thermo-gravimetric analysis was done on Mettler Toledo TGA/SDTA 851 (Fig. 6). It showed that upto 100°C there was no appreciable loss in weight. Considering the initial weight at 28°C to be 15.4364 mg, weight recorded at ~ 196°C was 14.2364 mg. Hence, loss in weight was 1.2 mg. Percentage loss in weight (7.774 %) corresponds to the loss of three -OCH_3 groups from the complex, probably one from each ligand (theoretical loss = 7.772 %). At 280°C, the weight recorded was 13.0463 mg. Hence, loss in weight and percentage loss were 2.3901 mg and 15.483 % respectively. This loss in weight corresponds to the loss of six -OCH_3 groups from the complex i.e. two from each ligand (theoretical loss = 15.543 %). Hence, TGA data also suggests formation of a 1:3 complex.

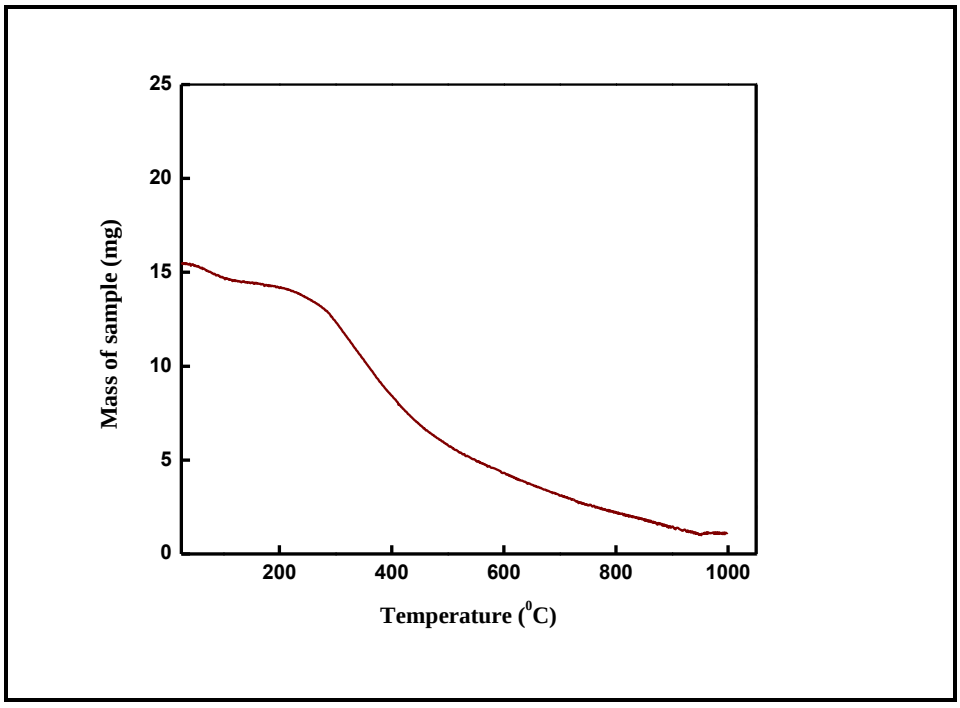


Figure 6: TGA of the Mn^{II} complex of HCur

8.3.3 Molar conductance of the complex:

Molar conductance of the complex was determined on a conductivity meter EUTECH CON 700, Thermo Scientific, Eutech Instruments in pure DMSO and found to be 15.2 S m^2mol^{-1} suggesting it to be a non-electrolyte in solution.[30] Furthermore, this observation suggests that the chemical formula of the compound may be $[Mn^{II}(Cur)_2(HCur)]$, as this particular combination necessitates the presence of a non-electrolyte character in the complex.

8.3.4 Magnetic susceptibility measurements:

Such measurement of powdered samples at room temperature (298 K) were according to Gouy method on Magway MSB MK1, Sherwood Scientific Ltd. μ_{eff} was found to be 6.06 B.M

8.3.5 UV-Vis spectra of Curcumin and its Mn^{II} complex in DMSO:

Owing to poor solubility in water, spectrum of the complex was recorded in DMSO (Fig. 7). λ_{max} obtained at 400 nm has a molar extinction coefficient (ε) = 2.85×10^4 M^{-1} cm^{-1}. This was comparable to the spectrum recorded during physicochemical experiments where Mn^{II} and HCur were allowed to interact with each other showing a peak at 430 nm in aqueous-ethanol medium (Fig. 7).

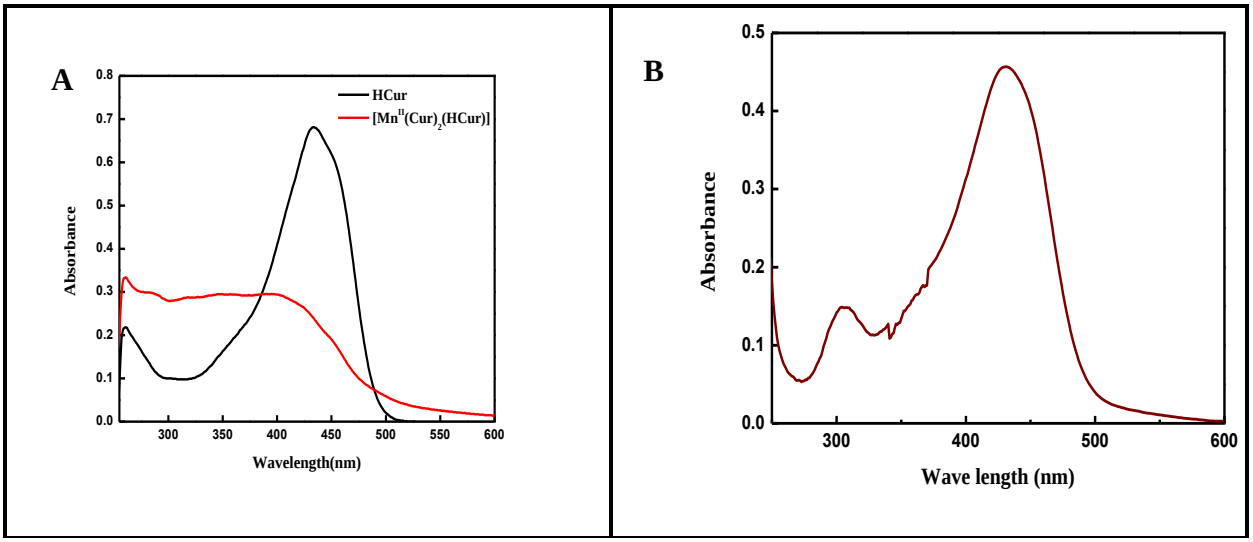


Figure 7: (A) Absorption spectra for HCur and $[Mn^{II}(Cur)_2(HCur)]$ in DMSO, (B) Absorption spectrum of Mn^{II} interacting with HCur in ethanol-water during determination of stoichiometry

8.3.6 Analysis of IR spectra:

The FTIR spectrum of HCur (*Fig. 3, Chapter 7*) recorded on a Perkin Elmer Spectrometer (Spectrum Two) by ATR technique indicates a peak at 3516 cm^{-1} owing to –OH stretching which in case of the complex was observed as a broad band at 3403 cm^{-1} (Fig. 8).[31] Sharp peaks at 1627 cm^{-1} and 1604 cm^{-1}, attributed to C=O stretching vibrations in HCur (*Fig. 3, Chapter 7*) were shifted to lower wavenumbers (1581 cm^{-1} and 1516 cm^{-1}respectively) in the complex, having low intensities. This suggests involvement of the carbonyl group in binding Mn^{II}. Peaks at 1506 cm^{-1} and 1429 cm^{-1} due to C=C stretching and C=O bending vibrations in the IR spectrum of HCur (*Fig. 3, Chapter 7*) also showed significant changes in the complex.[31]

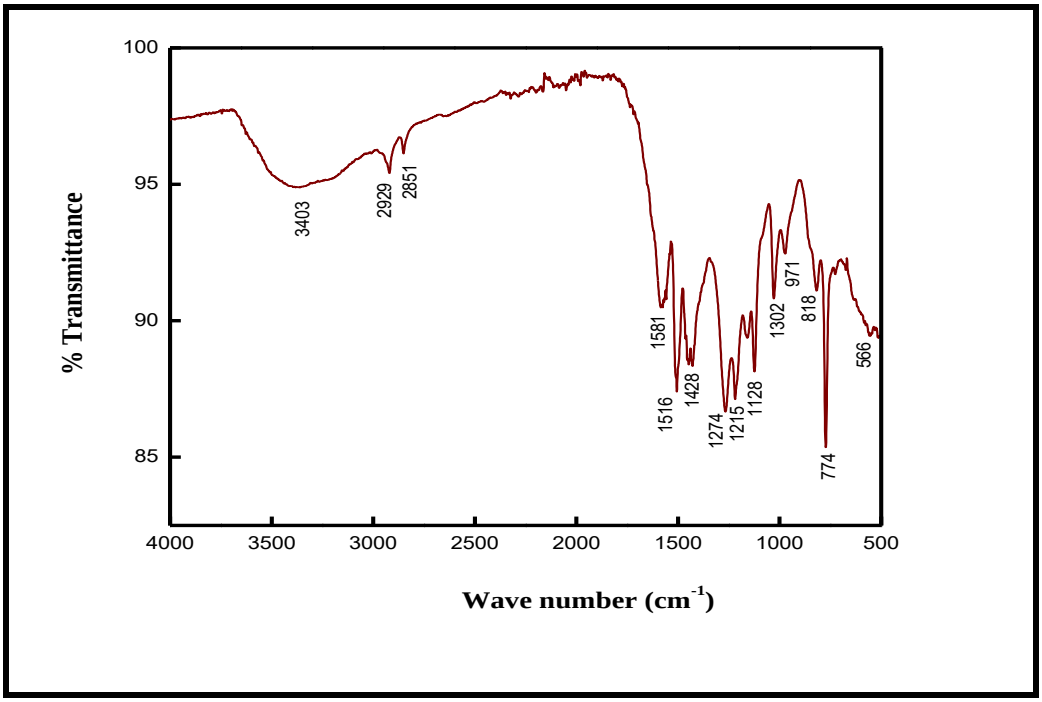


Figure 8: FTIR spectrum for $[Mn^{II}(Cur)_2(HCur)]$

From the above mentioned experimental evidences, it could be concluded that the structure of the complex could be $[Mn^{II}(Cur)_2(HCur)]$ where two Curcumin moieties are present as anions and one in neutral form. This structure was considered for geometry optimization through DFT calculations.

8.4 Quantum Chemical calculations based on experimental evidence

Although single crystals of the prepared complex were attempted since they were not obtained, the structure was established from DFT calculations based on experimental evidence. The 6-31G+(d,p) basis set in conjunction with LanL2Dz were used at restricted B3LYP level[32] in Gaussian 16 software package[33] to optimize the structure of the Mn^{II} complex of Curcumin. The obtained structure has a good correlation with experimental data. Ground state optimized geometries of the complex in gaseous state and in DMSO (as medium) was depicted in Fig. 9 with a numbering scheme for the coordination environment. Important parameters concerning coordination

geometry are arranged in Table 1. The optimized coordinates for these configurations are provided in Table 2. Final optimized structures of the ground state configuration show an octahedral coordination environment both in gas phase and in solution (DMSO). The energy (EUB3LYP) of the Mn^{II} complex of Curcumin in gas phase was found to be -105919.65 eV and has a dipole moment of 10.98 Debye, with a polarizability of 1349.45 a.u. The energy (UB3LYP) of the complex in solution phase was -105921.82 eV with dipole moment and polarizability being 18.61 Debye and 2066.87 a.u. respectively.

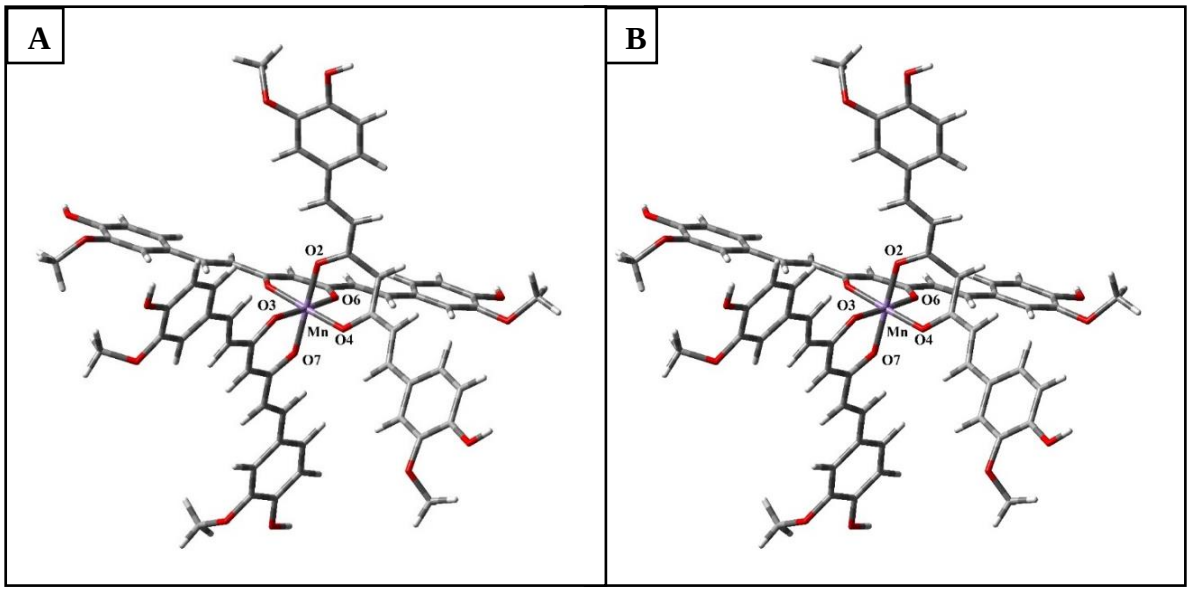


Figure 9: Ground state optimized geometries of the complex (A) Gas Phase, (B) Solution Phase

Table 1: Coordinated bond distances (in Å) and bond angles (in °) of the complex Mn(II)-Curcumin.

Bond	Gas phase	In DMSO	Angle	Gas phase	In DMSO
Mn–O2	1.987	2.012	O4–Mn–O6	92.02	92.20
Mn–O3	1.933	1.947	O3–Mn–O5	88.70	88.12
Mn–O4	1.942	1.950	O4–Mn–O3	89.61	89.97
Mn–O5	1.923	1.932	O6–Mn–O5	89.66	89.68
Mn–O6	1.932	1.913	O2–Mn–O6	93.40	92.30

Mn–O7	1.936	1.941	O2–Mn–O3	86.68	87.05
			O2–Mn–O5	91.98	91.04
			O2–Mn–O4	86.24	86.68
			O3–Mn–O7	91.42	91.81
			O5–Mn–O7	90.28	90.47
			O4–Mn–O7	91.44	91.81
			O6–Mn–O7	88.57	88.89

Table 2: Optimized coordinates of [$Mn^{II}(Cur)_2(HCur)$]in ground state geometry

	Gaseous phase				In DMSO solvent		
Atom	**x**	**y**	**z**	**Atom**	**x**	**y**	**z**
Mn1	-0.577	0.095	-0.415	Mn1	-0.354	-0.015	-0.530
O2	0.476	-1.131	-1.463	O2	0.762	-1.319	-1.529
O3	0.819	0.064	0.859	O3	1.054	0.004	0.794
O4	-1.363	-1.390	0.473	O4	-1.138	-1.548	0.345
O5	0.331	1.491	-1.263	O5	0.499	1.477	-1.393
O6	-1.930	0.078	-1.722	O6	-1.744	0.010	-1.884
O7	-1.562	1.326	0.616	O7	-1.429	1.200	0.527
C8	-1.156	2.029	1.644	C8	-1.064	1.870	1.593
C9	0.093	1.866	2.256	C9	0.183	1.724	2.225
H10	0.341	2.498	3.098	H10	0.381	2.328	3.102
C11	1.021	0.899	1.848	C11	1.173	0.809	1.823
C12	0.137	1.975	-2.465	C12	0.061	2.246	-2.357
C13	-0.948	1.612	-3.279	C13	-1.156	2.029	-3.029
H14	-1.035	2.072	-4.254	H14	-1.445	2.731	-3.801
C15	-1.940	0.716	-2.877	C15	-2.005	0.941	-2.772
C16	0.186	-2.381	-1.705	C16	0.429	-2.531	-1.835
C17	-1.471	-2.612	0.045	C17	-1.289	-2.751	-0.131
C18	-1.225	-2.869	-1.433	C18	-1.008	-2.960	-1.610
H19	-1.334	-3.925	-1.678	H19	-1.162	-4.002	-1.900
H20	-1.929	-2.263	-2.015	H20	-1.672	-2.315	-2.197
C21	2.282	0.776	2.578	C21	2.414	0.722	2.596
H22	2.422	1.451	3.414	H22	2.489	1.381	3.457
C23	3.217	-0.128	2.223	C23	3.415	-0.125	2.260
H24	2.984	-0.759	1.369	H24	3.246	-0.746	1.382

C25	-2.084	3.022	2.185	C25	-2.035	2.811	2.159
H26	-1.730	3.595	3.035	H26	-1.707	3.367	3.033
C27	-3.310	3.207	1.659	C27	-3.274	2.975	1.639
H28	-3.577	2.577	0.814	H28	-3.519	2.365	0.772
C29	-4.328	4.156	2.101	C29	-4.326	3.872	2.112
C30	-5.569	4.182	1.440	C30	-5.578	3.854	1.465
C31	-4.128	5.064	3.154	C31	-4.153	4.771	3.186
C32	-6.558	5.070	1.845	C32	-6.615	4.686	1.887
H33	-5.754	3.500	0.619	H33	-5.738	3.177	0.632
C34	-5.108	5.962	3.569	C34	-5.180	5.608	3.614
H35	-3.190	5.101	3.690	H35	-3.212	4.838	3.719
C36	-6.355	5.954	2.904	C36	-6.431	5.557	2.964
H37	-7.518	5.070	1.337	H37	-7.579	4.652	1.384
C38	4.512	-0.356	2.856	C38	4.698	-0.302	2.934
C39	5.362	-1.347	2.333	C39	5.611	-1.247	2.422
C40	4.968	0.381	3.963	C40	5.085	0.438	4.072
C41	6.599	-1.587	2.917	C41	6.849	-1.450	3.031
H42	5.044	-1.928	1.475	H42	5.343	-1.825	1.544
C43	6.206	0.154	4.556	C43	6.319	0.246	4.687
H44	4.364	1.164	4.401	H44	4.430	1.181	4.511
C45	7.033	-0.861	4.027	C45	7.208	-0.718	4.167
H46	7.241	-2.363	2.512	H46	7.538	-2.188	2.628
O47	-7.354	6.821	3.340	O47	-7.447	6.385	3.437
H48	-8.155	6.720	2.763	H48	-8.281	6.232	2.953
O49	-4.756	6.761	4.645	O49	-4.932	6.405	4.731
O50	8.255	-1.118	4.644	O50	8.422	-0.908	4.824
H51	8.734	-1.828	4.145	H51	8.941	-1.622	4.406
O52	6.490	0.942	5.661	O52	6.576	0.973	5.848
C53	7.875	1.332	5.969	C53	7.825	1.739	5.932
H54	7.773	2.067	6.769	H54	7.746	2.296	6.865
H55	8.469	0.481	6.296	H55	8.690	1.075	5.951
H56	8.358	1.794	5.101	H56	7.903	2.436	5.089
C57	-5.353	8.091	4.838	C57	-5.210	7.843	4.643
H58	-6.404	8.026	5.111	H58	-6.279	8.028	4.535
H59	-4.767	8.529	5.648	H59	-4.840	8.254	5.582
H60	-5.255	8.705	3.937	H60	-4.663	8.287	3.802
C61	1.096	2.959	-2.958	C61	0.900	3.381	-2.750
H62	0.903	3.355	-3.949	H62	0.511	4.005	-3.550
C63	2.160	3.351	-2.228	C63	2.089	3.643	-2.159

H64	2.275	2.895	-1.248	H64	2.399	2.961	-1.370
C65	-3.070	0.460	-3.766	C65	-3.248	0.814	-3.540
H66	-3.033	0.951	-4.733	H66	-3.392	1.548	-4.328
C67	1.180	-3.292	-2.148	C67	1.408	-3.470	-2.306
H68	0.865	-4.316	-2.311	H68	1.052	-4.474	-2.517
C69	-1.734	-3.694	0.926	C69	-1.640	-3.846	0.713
H70	-1.785	-4.680	0.480	H70	-1.722	-4.816	0.231
C71	-1.943	-3.509	2.267	C71	-1.896	-3.703	2.056
H72	-1.867	-2.489	2.635	H72	-1.787	-2.702	2.466
C73	2.472	-2.898	-2.381	C73	2.719	-3.127	-2.498
H74	2.701	-1.854	-2.183	H74	2.991	-2.104	-2.248
C75	-4.107	-0.323	-3.406	C75	-4.180	-0.131	-3.278
H76	-4.075	-0.751	-2.408	H76	-3.972	-0.804	-2.449
C77	-5.285	-0.648	-4.208	C77	-5.449	-0.344	-3.972
C78	-6.285	-1.457	-3.644	C78	-6.327	-1.336	-3.490
C79	-5.471	-0.205	-5.532	C79	-5.844	0.385	-5.114
C80	-7.444	-1.817	-4.333	C80	-7.558	-1.595	-4.094
H81	-6.183	-1.834	-2.634	H81	-6.066	-1.924	-2.617
C82	-6.620	-0.553	-6.226	C82	-7.071	0.136	-5.725
H83	-4.722	0.409	-6.014	H83	-5.194	1.146	-5.530
C84	-7.616	-1.345	-5.647	C84	-7.939	-0.840	-5.219
H85	-6.764	-0.192	-7.240	H85	-7.367	0.709	-6.601
C86	3.180	4.323	-2.610	C86	3.009	4.738	-2.460
C87	4.223	4.598	-1.711	C87	4.212	4.831	-1.728
C88	3.171	5.019	-3.835	C88	2.757	5.723	-3.439
C89	5.242	5.509	-1.989	C89	5.140	5.846	-1.955
H90	4.267	4.097	-0.752	H90	4.447	4.099	-0.964
C91	4.180	5.925	-4.125	C91	3.678	6.740	-3.675
H92	2.383	4.848	-4.556	H92	1.842	5.695	-4.020
C93	5.223	6.177	-3.229	C93	4.874	6.807	-2.949
H94	4.172	6.448	-5.077	H94	3.476	7.489	-4.437
O95	-8.793	-1.667	-6.327	O95	-9.185	-1.093	-5.788
H96	-8.697	-1.428	-7.285	H96	-9.364	-0.490	-6.535
O97	-8.349	-2.590	-3.626	O97	-8.378	-2.542	-3.487
O98	6.256	7.062	-3.531	O98	5.830	7.794	-3.179
H99	6.081	7.488	-4.409	H99	5.564	8.381	-3.912
O100	6.212	5.638	-1.009	O100	6.329	5.801	-1.230
C101	6.947	6.901	-0.845	C101	6.758	7.005	-0.509
H102	7.523	6.757	0.069	H102	7.635	6.691	0.056

H103	7.602	7.098	-1.692	H103	7.013	7.806	-1.203
H104	6.260	7.746	-0.721	H104	5.972	7.338	0.179
C105	-9.224	-3.535	-4.336	C105	-8.957	-3.608	-4.313
H106	-9.721	-4.090	-3.539	H106	-9.449	-4.272	-3.602
H107	-9.946	-3.016	-4.963	H107	-9.676	-3.204	-5.026
H108	-8.640	-4.224	-4.958	H108	-8.166	-4.153	-4.843
C109	-2.258	-4.527	3.247	C109	-2.300	-4.739	2.986
C110	-2.413	-5.893	2.929	C110	-2.517	-6.088	2.615
C111	-2.433	-4.149	4.593	C111	-2.503	-4.396	4.344
C112	-2.709	-6.809	3.927	C112	-2.900	-7.033	3.562
H113	-2.300	-6.234	1.908	H113	-2.385	-6.399	1.585
C114	-2.731	-5.061	5.604	C114	-2.886	-5.335	5.298
H115	-2.335	-3.112	4.887	H115	-2.353	-3.375	4.679
C116	-2.863	-6.423	5.262	C116	-3.078	-6.674	4.905
H117	-2.816	-7.860	3.674	H117	-3.056	-8.067	3.263
C118	3.564	-3.718	-2.862	C118	3.790	-3.974	-2.992
C119	4.835	-3.131	-3.030	C119	5.097	-3.440	-3.077
C120	3.434	-5.088	-3.180	C120	3.603	-5.315	-3.402
C121	5.946	-3.844	-3.474	C121	6.178	-4.194	-3.526
H122	4.984	-2.081	-2.814	H122	5.290	-2.415	-2.780
C123	4.535	-5.805	-3.623	C123	4.677	-6.075	-3.854
H124	2.479	-5.586	-3.077	H124	2.617	-5.765	-3.367
C125	5.793	-5.213	-3.769	C125	5.968	-5.533	-3.911
H126	4.427	-6.861	-3.855	H126	4.520	-7.107	-4.160
O127	6.909	-5.938	-4.187	O127	7.070	-6.274	-4.330
H128	6.636	-6.865	-4.408	H128	6.821	-7.196	-4.532
O129	-3.131	-7.349	6.268	O129	-3.434	-7.601	5.883
H130	-3.244	-8.249	5.867	H130	-3.494	-8.502	5.510
O131	-2.838	-4.518	6.873	O131	-2.982	-4.906	6.621
O132	7.124	-3.121	-3.554	O132	7.436	-3.597	-3.492
C133	8.216	-3.557	-4.434	C133	8.250	-3.608	-4.714
H134	8.937	-2.740	-4.385	H134	9.122	-3.002	-4.471
H135	8.662	-4.490	-4.092	H135	8.547	-4.625	-4.975
H136	7.870	-3.686	-5.465	H136	7.698	-3.151	-5.543
C137	-3.591	-5.197	7.936	C137	-4.220	-5.182	7.357
H138	-4.615	-5.421	7.619	H138	-5.083	-4.768	6.822
H139	-3.107	-6.121	8.247	H139	-4.353	-6.254	7.510
H140	-3.606	-4.473	8.752	H140	-4.097	-4.669	8.311

From Table 1, the model geometry is seen to possess a distorted octahedral arrangement around the Mn^{II} centre. Calculated Mn–O distances were found in the expected range of 1.869-1.926 Å.[34] Hence, DFT calculations unequivocally support formation of an octahedral complex. If we consider the coordination environment around the metal ion (Figure 9A & 9B), O5 and O6 belong to one ligand, O3 and O7 to a second ligand while O2 and O4 to a third ligand. Interestingly, Mn–O bond lengths (Table 1) suggest Mn–O2 and Mn–O4 are slightly longer than other four Mn–O bond distances (Mn–O3, Mn–O7, Mn–O5, Mn–O6) indicating coordination by oxygen donor sites from two ligands to be of one type while that due to the third ligand being slightly different. In reality, these are supported by charge balance and evidence from conductance measurements (reported in *section 8.3.3*) that suggest binding of one Curcumin to Mn^{II} is different from the other two. Using the data in Table 1, it can be said that those oxygen coordinations that result in a slightly larger Mn–O bond length coordinate Mn^{II} where Curcumin is in the diketo (neutral) form denoted as HCur. The other four oxygen coordinations of Mn^{II} showing an almost similar Mn–O bond length has Curcumin coordinating Mn^{II} as an enolate anion (denoted as Cur^{-}). Further to this, we also found from the DFT calculated structure that in case of Curcumin coordinating Mn^{II} in diketo form, carbon-oxygen bond distances are slightly shorter (as expected) than the other four carbon-oxygen bonds where it coordinates as enolate anion. When coordination occurs as enolate anion, resonating C=O and C—O^{-} forms are involved; hence, carbon-oxygen bond distances are likely to be slightly larger than when it is a purely diketo coordination (Fig. 10). This was actually found for the complex suggesting that Curcumin coordinating through O2 and O4 positions coordinate Mn^{II} in diketo form following which their corresponding carbon-oxygen bond distances (C16-O2 and C17-O4) are slightly shorter (Table 3).

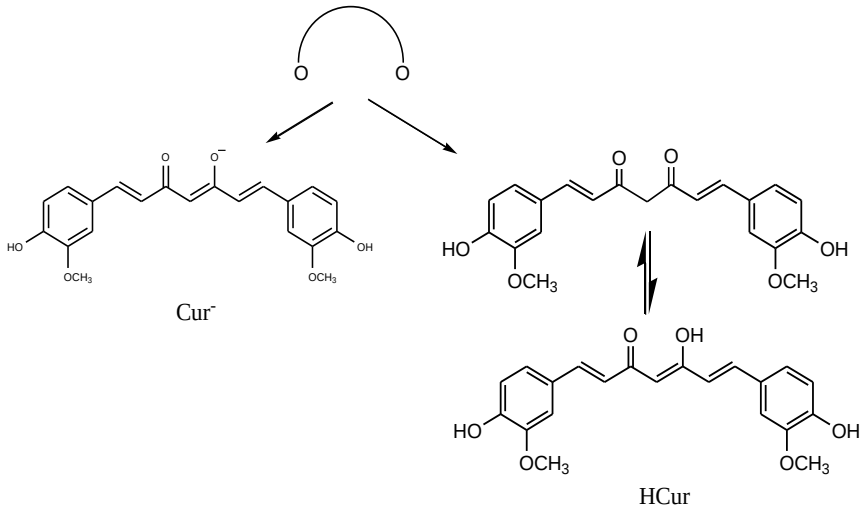


Figure 10: Structures of Curcumin as diketo and enolate anion

Table 3. Optimized bond lengths for carbon-oxygen bonds of Curcumin involved in coordination of Mn^{II}.

Bond Type	Bond Length (Å)	
	Gas Phase	Solution (DMSO) phase
C16-O2	1.293	1.289
C17-O4	1.302	1.305
C15-O6	1.312	1.315
C12-O5	1.308	1.317
C11-O3	1.311	1.316
C8-O7	1.311	1.318

8.4.1 MO composition analysis:

The frontier orbital of $[Mn^{II}(Cur)_2(HCur)]$ optimized in gas and solution phases are shown in Fig. 11 and Fig. 12 respectively. Description of both occupied and virtual MOs were made, based on their atomic composition and visual inspection of a three-dimensional representation. The $[Mn^{II}(Cur)_2(HCur)]$ moiety was assumed to be composed of four fragments, Mn, $(Cur)_1$, $(Cur)_2$ and (HCur). Their compositions are described in Table 4.

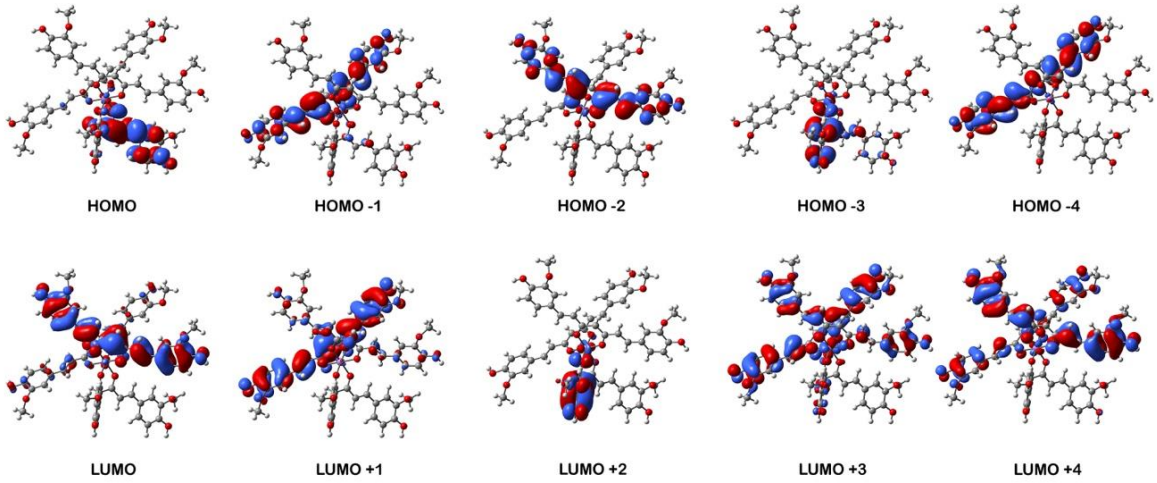


Figure 11: The frontier orbital of the optimized $[Mn^{II}(Cur)_2(HCur)]$ in gas phase

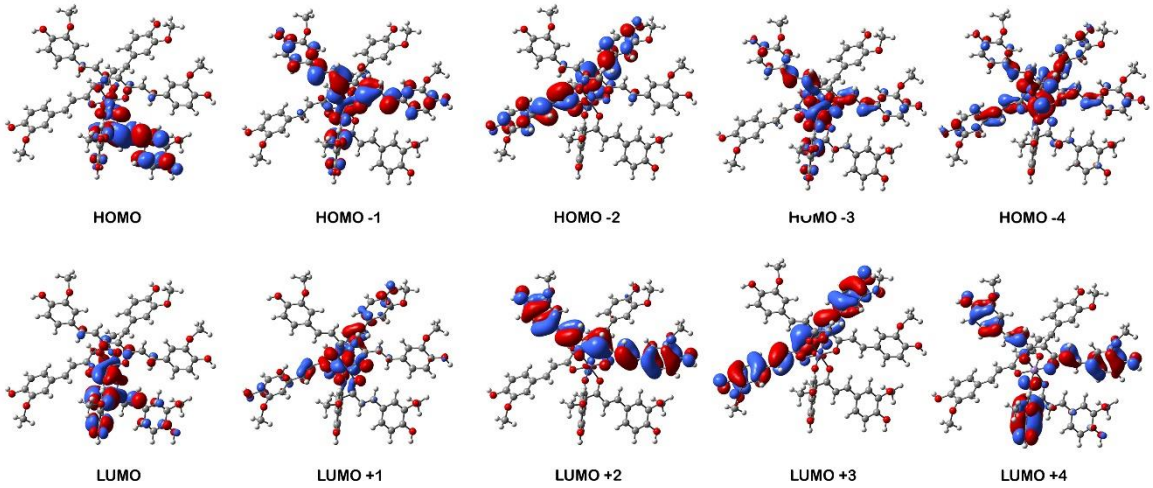


Figure 12: The frontier orbital of the optimized $[Mn^{II}(Cur)_2(HCur)]$in solution (DMSO) phase

Table 4: Some of selected MOs of $[Mn^{II}(Cur)_2(HCur)]$in ground state geometry along with their energies and percentage compositions.

Gaseous phase optimized structure:

Orbital	**MO**	**Energy (eV)**	**% Composition**			
			Mn	(Cur)1	(Cur)2	(HCur)
303	L+4	-1.09	0	100	0	0
302	L+3	-1.70	2	0	97	1
301	L+2	-1.94	1	0	2	97
300	L+1	-2.04	1	2	97	0
299	LUMO	-2.18	1	97	2	0
298	HOMO	-5.24	1	2	0	97
297	H-1	-5.48	2	96	0	2
296	H-2	-5.64	5	1	89	5
295	H-3	-5.68	4	2	9	85
294	H-4	-5.78	17	44	19	20

Solution phase optimized structure:

Orbital	**MO**	**Energy (eV)**	**% Composition**			
			Mn	$(Cur)_1$	$(Cur)_2$	(HCur)
303	L+4	-1.09	1	99	0	0
302	L+3	-1.70	1	0	98	1
301	L+2	-1.94	0	1	2	97
300	L+1	-2.04	1	2	97	0
299	LUMO	-2.14	1	97	2	0
298	HOMO	-5.16	1	2	0	97
297	H-1	-5.48	1	96	0	2
296	H-2	-5.64	5	2	88	5

295	H-3	-5.68	4	2	9	85
294	H-4	-5.78	17	43	20	20

We observed both for gas and solution phases optimized geometries, HOMO-1 to LUMO+4 have negligible contribution from the metal; i.e. contributions only from curcumins. According to calculations, the HOMO-LUMO energy gap for $[Mn^{II}(Cur)_2(HCur)]$ in gas and solution phases were 3.053 eV and 3.012 eV respectively and they are shown in Fig. 13.

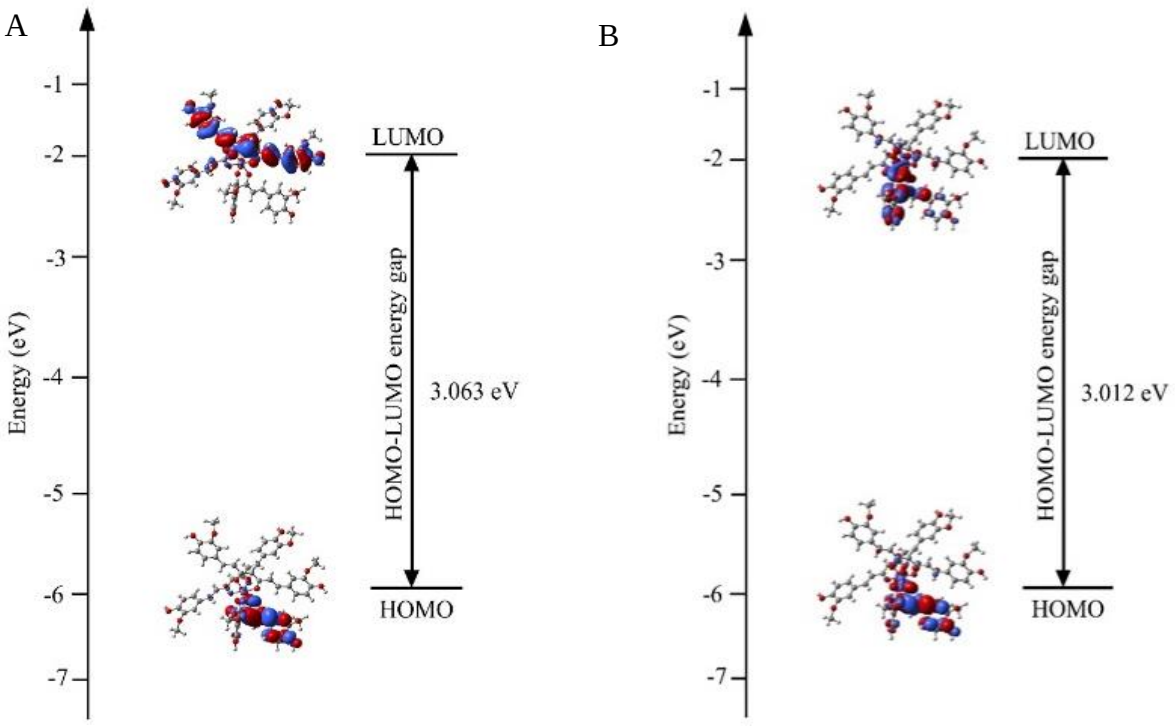


Figure 13: HOMO-LUMO gap of $[Mn^{II}(Cur)_2(HCur)]$ (A) Gas phase (B) Solution phase

The highest occupied molecular orbital (HOMO) and lowest unoccupied molecular orbital (LUMO) are ligand-centric in each phase with almost entire contribution coming from HCur.

8.4.2 Quantum descriptor analysis:

Understanding the impact of frontier molecular orbitals on a molecule's kinetic stability, electrical conductivity and chemical reactivity is crucial. Soft molecules are characterized by a narrow HOMO-LUMO energy gap.[35,36] These would demonstrate heightened biological and chemical reactivity. When molecules possess a significant HOMO-LUMO energy gap, they exhibit diminished biological response, exceptional stability and reduced reactivity towards other compounds.[35,36] Intramolecular charge transfer (ICT) could occur when there is a small energy gap between electron-donor and electron-acceptor groups allowing transfer of charges within the molecule. Effective electron acceptor molecular systems typically have a lower energy level of the lowest unoccupied molecular orbital (E_{LUMO}) compared to effective electron donor molecular systems, which tend to have a higher energy level of the highest occupied molecular orbital (E_{HOMO}).[35,36] In Table 5, we present a comparison of the quantum descriptor of HCur and $[Mn^{II}(Cur)_2(HCur)]$ after conducting geometry optimization. Electron donation and electron acceptance are made possible by a small HOMO-LUMO gap. The electron affinity of $[Mn^{II}(Cur)_2(HCur)]$ is slightly lower than that of HCur suggesting that the complex can interact with nucleotides or amino acid residues from DNA or protein by attracting electron density towards itself. Alternately, a soft molecule is characterized by a lower η value (Eq. 26, *Chapter 6, Experimental*).[35,36] When Mn^{II} binds to HCur, it undergoes a transformation, becoming more flexible and allowing for increased electron delocalization. This, in turn promotes a greater number of non-covalent interactions.

Table 5: Quantum descriptor for HCur and [$Mn^{II}(Cur)_2(HCur)$] in eV with B3LYP-6-31G+(d,p) functional for C,H,O and LanL2dZ functional for Mn^{II}

Compound	HOMO	LUMO	ΔE	IP	EA	χ	η	M	σ	ω
HCur	-5.47	-2.27	3.20	5.47	2.27	3.87	1.60	-3.87	0.31	4.68
Mn(Cur)	-5.16	-2.14	3.01	5.16	2.14	3.65	1.51	-3.65	0.33	4.41

8.4.3 Molecular electrostatic potential surface analysis:

The molecular electrostatic potential has been depicted in Fig. 14 generated by Gauss view 6 software. Calculations were performed using DFT/B3LYP functional and 6-31G+(d,p) in conjunction with LanL2Dz (For Mn^{II}) as basis sets. The Molecular Electrostatic Potential (MEP) is a crucial parameter for studying and establishing a connection between the molecular structure and physiochemical properties of many compounds that includes biomolecules and drugs. An understanding of charge distribution may be utilized to determine how molecules interact with each other and to find locations for both intra and inter-molecular interactions.[37] The MESP map is a visualization of electronic density which is commonly employed to identify areas with negative and positive electrostatic potentials, that are eventually useful in detecting electrophilic and nucleophilic regions.[38] The MESP maps may be utilized to determine mode of binding between a substrate and receptor and display the following colours that represent different electron charges; red (electron rich), orange (partial negative charge), yellow (slightly electron-rich location), blue (positive charge), and green (neutral).[37,38]

According to Fig. 14, the negative sites on the Mn^{II}-Curcumin complex are mostly concentrated at the carbonyl metal centre. As a result, these sites become well-suited for an electrophilic attack. The complex exhibits pale blue patches on methoxy hydrogen and phenolic hydrogen indicating weak interactions like that of hydrogen bonding between phenolic –OH and

–OCH_3 groups etc. The parts highlighted in green indicate regions with no potential and are neutral like hydrogen atoms of phenyl rings. The electrostatic potential values range from -320.25 KJ/mol (red) to +320.25 KJ/mol (blue) to indicate the presence of nucleophilic and electrophilic regions suggesting that the molecule in question can participate in biological and chemical processes making it applicable in the field of medicinal chemistry.

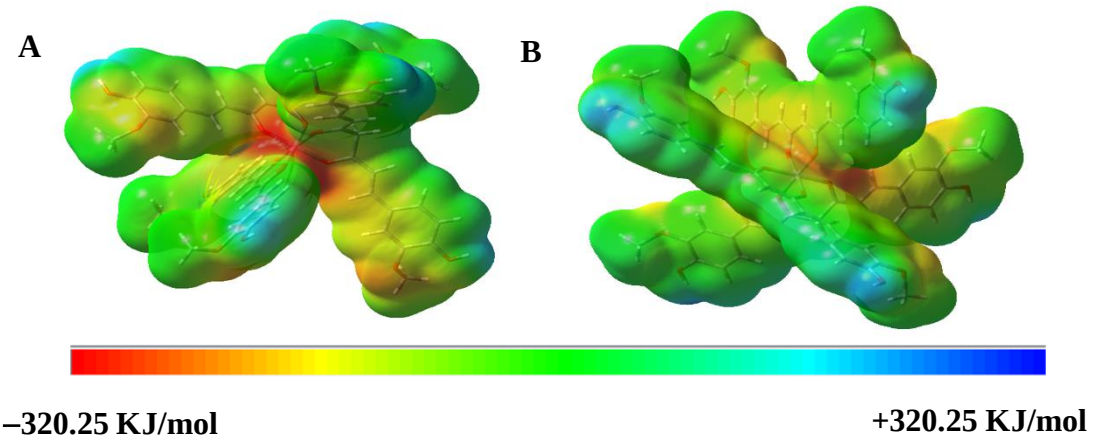


Figure 14: Molecular electrostatic Potential surface of $[Mn^{II}(Cur)_2(HCur)]$ in (A) Gas phase and (B) solution phase

8.4.4 Non-covalent interactions (NCI) & Reduced density gradient (RDG) analysis:

RDG is a powerful technique for examining non-covalent interactions in real space, making use of electron density and its derivatives. This approach has proven its capability to distinguish between various types of interactions in small molecules and metal complexes. The equation that is used for RDG calculation is [39,40]

$$RDG(r) = \frac{1}{2(3\pi^2)^{1/3}} \frac{|\nabla\rho(r)|}{\rho(r)^{4/3}}$$

By examining values for low-density and high-density gradient, one can confirm the presence of weak and strong interactions respectively. Graphs that illustrate the correlation between RDG and low-gradient peak density (ρ) values can offer valuable insights into the strength of an interaction.

One potential method for differentiating between various types of interactions is by utilizing the electron density and the sign of the second eigenvalues. The sign λ_2 is an important parameter that helps to differentiate between bound ($\lambda_2 < 0$) and non-coupling ($\lambda_2 > 0$) interactions. Based on certain principles, interactions can be classified into three distinct types. The first is a type of attraction, which is characterized by negative sign (λ_2). The second hypothesis suggests a strong repulsion type of nonbonding interaction supported by the presence of large and positive values of the sign (λ_2). The third type, known as weak interactions (van der Waals interactions), is typically characterized by values of sign (λ_2) that are very close to zero.[39,40] Fig.15 shows projected RDG plots for Mn^{II} Curcumin complex. Various types of interactions were identified by visual inspection of the same. Based on the observed red colour, it appears that there is a notable level of repulsion in the system. More red region was found near the metal ligand binding site. This is because more oxygen atoms were present near the binding site which cause inter electronic repulsion. Here the green colour represents hydrogen bonded interaction within the molecular system. More hydrogen bond interaction was found between phenolic oxygen and methoxy hydrogen. Blue indicates a significant van der Waals interactions or coordinate bond interaction within the molecular system.

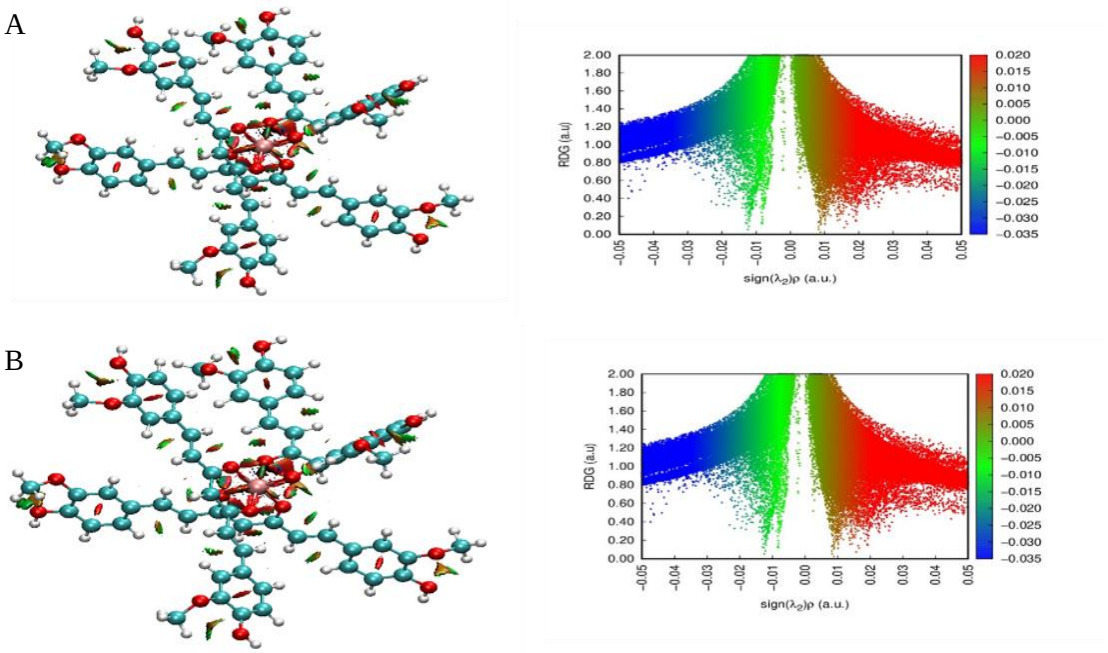


Figure 15: NCI (left) and RDG (right) plot of optimized [$Mn^{II}(Cur)_2(HCur)$] molecule in (A) gas Phase, (B) solution phase

8.4.5 Analysis of ELF and LOL:

Topology assessments like electron localized function (ELF) and localized orbital locator (LOL) are commonly employed to uncover the atomic shell structure, classify chemical bonding, and verify charge-shift bonds on the molecular surface. ELF and LOL calculations were conducted for the Mn^{II} complex of Curcumin using Multiwfn program.[41] Understanding the electron localized function is crucial for accurately assessing Pauli's repulsion, which is primarily influenced by the kinetic energy of an electron. In addition, the ELF is based on the analysis of electron pair density,[42] while LOL identifies the maximum number of localized orbitals that overlap because of orbital gradient.[43,44] When the ELF value is large, it suggests that electrons are more localized. This could mean there is a covalent bond, inner shells or a lone pair of electrons.[42-44] On the other hand, smaller ELF values (< 0.5 Bohr) indicate regions where electrons are expected to be delocalized. The color shade maps for optimized [$Mn^{II}(Cur)_2(HCur)$] molecule can be seen in Fig 16. The color shades of ELF and LOL maps provide evidence of the presence of bonding and non-bonding

electrons.[43,44] Within the complex molecule, yellow, green and slight orange region surrounding the oxygen atoms, O2, O4, O7 and O5 (with an ELF value more than 0.5) signifies the existence of high electron density. On the other hand, blue regions encircling the carbon atoms (e.g. C69) in Curcumin and manganese ion indicate the presence of a dispersed electron cloud. The electron depletion regions between valence and inner shell are illustrated by the small blue circles surrounding the Mn^{II}. The covalent bond is primarily concentrated around carbon–carbon atoms, with a smaller portion present around the carbon–oxygen atom and existence of coordinate bond was found between Mn^{II} and oxygen atoms (O2, O4, O7 and O5) indicated by its distinct orange-yellow colour.

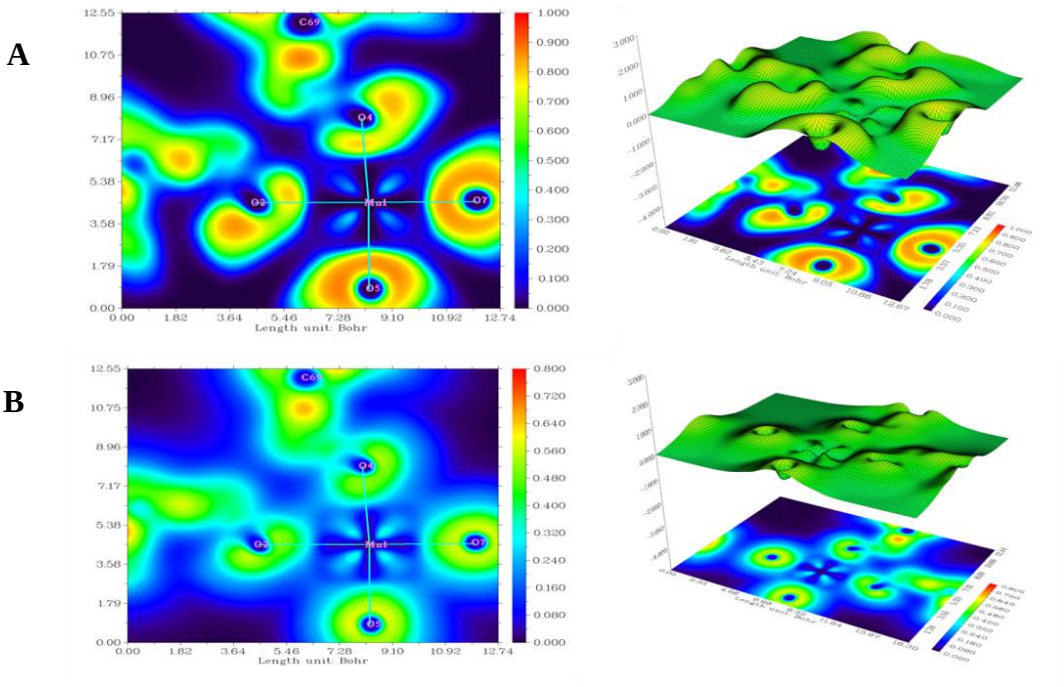


Figure 16: (A)Electron localization function (ELF) maps (Top) and (B) localized orbital locator (LOL) maps (Bottom) of optimized $[Mn^{II}(Cur)_2(HCur)]$ molecule

8.5 Analysis of stability of $[Mn^{II}(Cur)_2(HCur)]$ in different biological media

Considering the instability of HCur in different biological milieu, the stability of $[Mn^{II}(Cur)_2(HCur)]$ was checked in them (Figs. 17 and 18).[45] Fig. 17 & 18 indicate unlike HCur there were no changes in the absorbance of the complex in biological buffer and/or microbiological media. Worth noting here is the fact that HCur is more stable in microbiological media (Fig 17 & 18) compared to that in PBS buffer. Since the environment for most cellular compartments is reducing in nature hence stability of HCur and $[Mn^{II}(Cur)_2(HCur)]$ was checked in presence of DTT (dithiothreitol), a strong reducing agent.[45] HCur lost 50% of its absorption intensity within 5 minutes of co-incubation with DTT whereas no change was observed in the spectrum of $[Mn^{II}(Cur)_2(HCur)]$ even after 20 minutes of incubation. As evident from Fig.17 and 18, the complex is stable in physiological buffer media even under reducing conditions

.

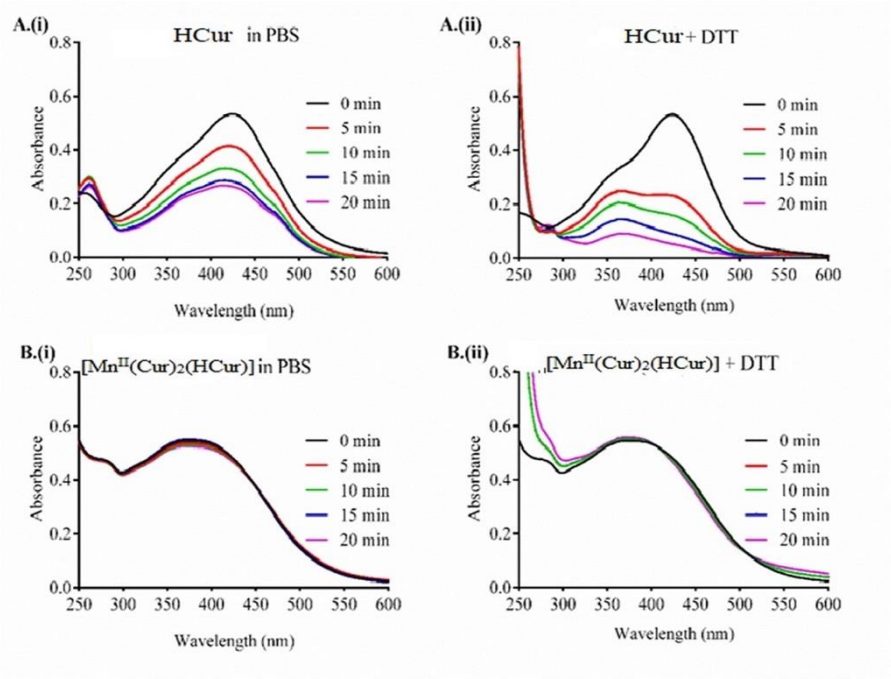


Figure 17: UV-visible spectra of (A) HCur and (B) $[Mn^{II}(Cur)_2(HCur)]$ in presence of (i) only PBS buffer (pH 7.4) and (ii) PBS buffer with 10 μM DTT.

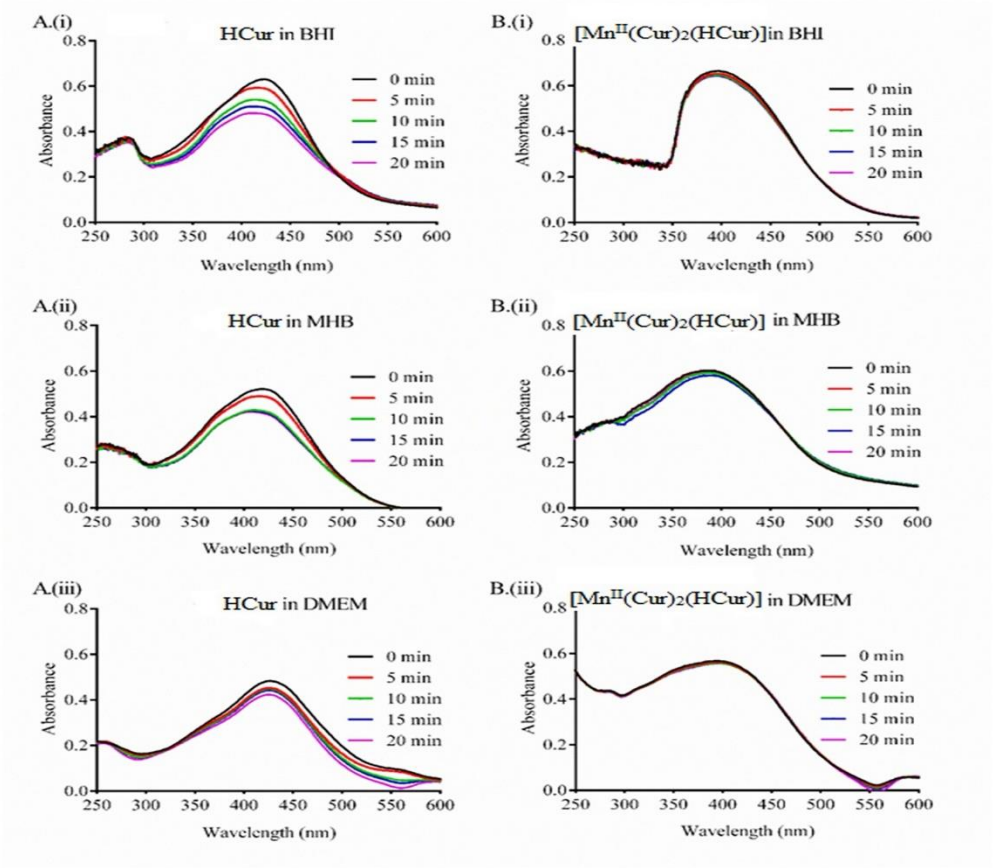


Figure 18 : UV-visible absorption spectra of (A) HCur and (B) [$Mn^{II}(Cur)_2(HCur)$] in different bacterial growth medium (i) BHI, (ii) MHB, and (iii) DMEM.

8.6 Interaction of [$Mn^{II}(Cur)_2(HCur)$] with calf thymus DNA

[$Mn^{II}(Cur)_2(HCur)$] was titrated with calf thymus DNA at constant pH (=7.4) and constant ionic strength of the medium (0.15 mM).[46-48] Titrations showed a gradual decrease in absorbance at 367 nm which was used to follow the interaction (Fig. 19). Fig. 20 A is a plot of $1/\Delta A$ versus $1/[C_D\text{-}C_L]$ (Eq. 31, *Chapter 6, Experimental*) that provides a value for apparent binding constant [K_{app} (= K_d^{-1})]. Titrations were repeated thrice. Values were obtained in the range 2.73×10^4 M^{-1} to 5.47×10^4 M^{-1}.[46,48-52]

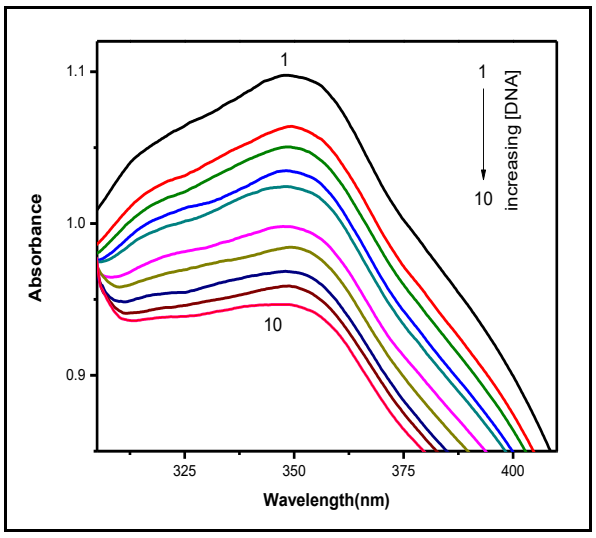


Figure 19: Absorption spectra of $[Mn^{II}(Cur)_2(HCur)]$ in the absence (1) and presence of different concentrations of calf thymus DNA (2) 62.65 μM, (3) 124.69 μM, (4) 246.94 μM, (5) 307.16 μM, (6) 599.69 μM, (7) 851.32 μM, (8) 1092.60μM, (9) 1248.02 μM and (10) 1399.30 μM.

Fig. 20 B is a plot of $\Delta A/\Delta A_{max}$ versus concentration of calf thymus DNA. Non-linear curve fitting was applied (Eqs. 32 and 33, *Chapter 6, Experimental*) for three separate titrations and average apparent binding constant (K_{app}= 6.87 × 10^4 M^{-1}) was evaluated.[46-52] Inset of Fig. 20 B provides a value for n_b (= 8.0), the number of nucleotides bound to the complex following interaction with calf thymus DNA. Titration data was also fitted to Eq. 34 (*Chapter 6, Experimental*) that plots inverse of fraction of complex bound to calf thymus DNA to the inverse of concentration of calf thymus DNA used in the experiment.[48-52] The inverse of the slope of the plot (Fig. 21) provides yet another value of apparent binding constant. An average of K_{app} from Eq. 34 (*Chapter 6, Experimental*) obtained from three separate titrations was 2.10 × 10^4 M^{-1}.

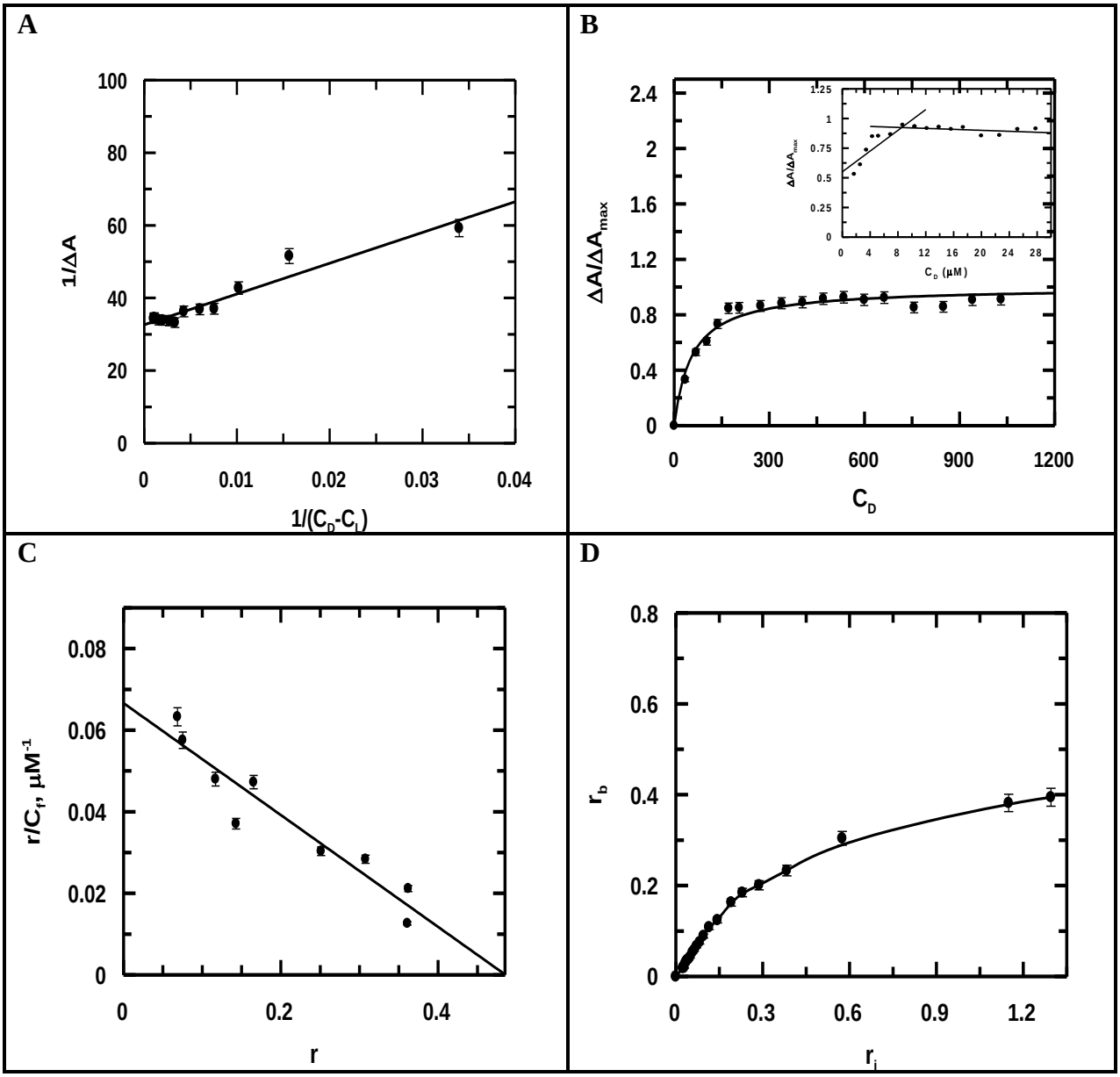


Figure 20 : (A) A double reciprocal plot for the interaction of $[Mn^{II}(Cur)_2(HCur)]$ with calf thymus DNA leading to the determination of apparent binding constant (K_{app}) at pH 7.4 (30 mM phosphate buffer) and ionic strength 0.15 M; $[Mn^{II}(Cur)_2(HCur)]$ = 40μM, pH = 7.4; Temperature = 298 K.(B) Binding isotherm for $[Mn^{II}(Cur)_2(HCur)]$ interacting with calf thymus DNA when $\Delta A/\Delta A_{max}$ was plotted against concentration of DNA; the dark line indicates the fitted data obeying Eq.32 (*Chapter 6, Experimental*). Inset: Plot of normalized increase in absorbance as a function of mole-ratio of calf thymus DNA to $[Mn^{II}(Cur)_2(HCur)]$. (C) A modified Scatchard plot for the interaction of $[Mn^{II}(Cur)_2(HCur)]$ with calf thymus DNA; (D) Plot of input $[Mn^{II}(Cur)_2(HCur)]$/DNA ratio (r_i) to bound $[Mn^{II}(Cur)_2(HCur)]$/DNA ratio (r_b) as

calculated from the decrease in absorbance following interaction of $[Mn^{II}(Cur)_2(HCur)]$ with calf thymus DNA; $[Mn^{II}(Cur)_2(HCur)]$ = 40 μM, [NaCl] = 150 mM, pH = 7.4, Temp.= 298K.

Apparent binding constants obtained from three different approaches (Eqs. 31-34; *Chapter 6, Experimental*) when multiplied with n_b provides overall binding constant (K′) (Table 6). Data from the titration was also fitted to a modified form of the Scatchard equation (Fig. 20C)[53] and K′ and n (= n_b^{-1}) were obtained. "n" denotes number of complex molecules bound to a nucleotide. Fig. 20D relates the ratio of input drug/DNA (r_i) to ratio of bound drug/DNA (r_b) as derived from Scatchard calculations.[53] For such a plot, a 45° line passing through initial points indicate that the entire compound was eventually bound to DNA.[53]

Table 6: Binding constant values for interaction of the complex with calf thymus DNA

Apparent binding constants $K_{app}\times 10^{-4}$ (M^{-1})			Site size (n_b) from mole ratio plot	Overall binding constant ($K' \times 10^{-5} M^{-1}$) $K' = K_{app}\times n_b$			Overall binding constant $K'\times10^{-5}$ (M^{-1}) from Scatchard plot, Eq. 35 (Chapter 6: Expt.)
From double reciprocal plot Eq. 31 (Chapter 6: Expt.)	From non-linear fit Eq. 33 (Chapter 6: Expt.)	From double reciprocal plot with y-intercept = 1 Eq. 34 (Chapter 6: Expt.)		Using K_{app} from Eq. 31 (Chapter 6: Expt.)	Using K_{app} fromEq. 33 (Chapter 6: Expt.)	Using K_{app} fromEq. 34 (Chapter 6: Expt.)	
4.10	6.87	2.10	8.0	3.28	5.50	1.68	1.26

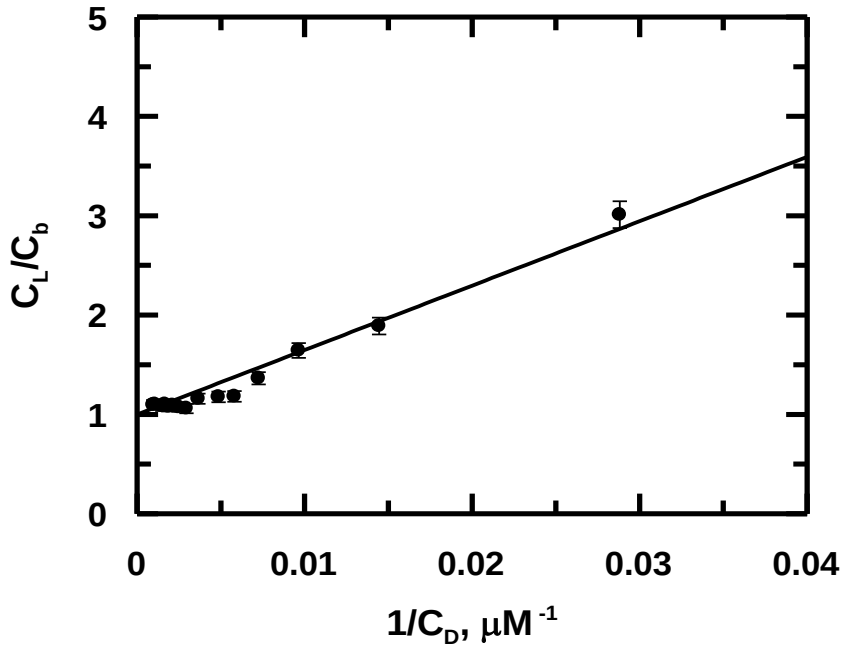


Figure 21: Double reciprocal plot for a UV-Vis titration of 40 μM $[Mn^{II}(Cur)_2(HCur)]$ by calf thymus DNA using phosphate buffer (~pH 7.4) at 298 K.

8.7 Hypoxanthine to xanthine, xanthine oxidase-inhibiting activity of $[Mn^{II}(Cur)_2(HCur)]$

Xanthine oxidase is an enzyme that generates reactive oxygen species by catalyzing the oxidation of hypoxanthine to xanthine and then of xanthine to uric acid.[54,55] Since xanthine oxidase is a superoxide producing enzyme its use was made in an assay where depletion of superoxide was followed by the reduction of nitro-bluetetrazolium dichloride (NBT^{2+}) that has an affinity for it. The assay indicates $[Mn^{II}(Cur)_2(HCur)]$ has superoxide dismutase (SOD) like activity and assists in disproportionation of superoxide radical anion to molecular oxygen and hydrogen peroxide (Fig. 22). Such formation of H_2O_2 in the system where $[Mn^{II}(Cur)_2(HCur)]$ is present is important since either on its own or through the generation of the hydroxyl radical (HO·), known for its ability to cause oxidative stress, provides yet another reason as to why the complex shows improved anti-bacterial activity (reported in the following section).[56-59]

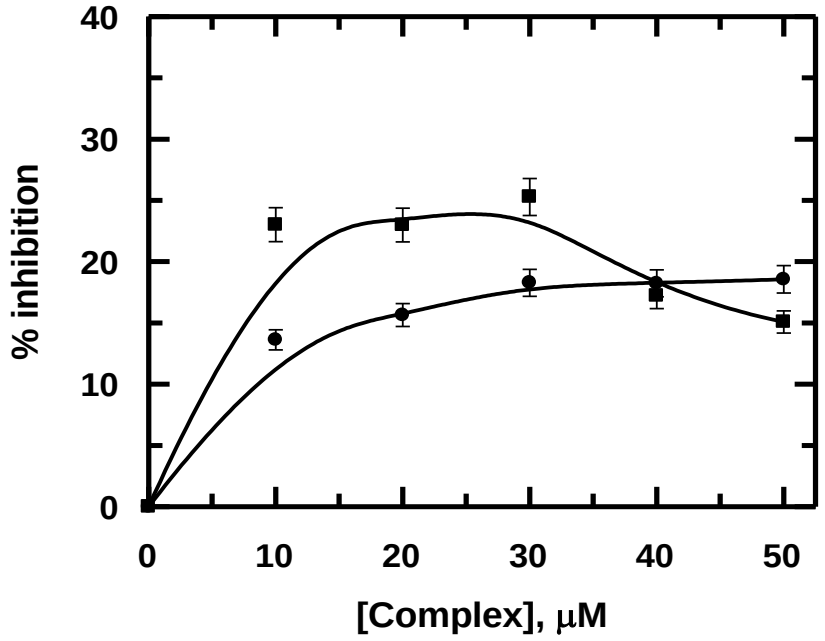


Figure 22: Percentage inhibition of superoxide radical anion formed due to hypoxanthine/xanthine oxidase enzyme assayed by NBT^{+} absorption at 524 nm in the presence of $[Mn^{II}(Cur)_2(HCur)]$ (■) and SOD (•); 50 μM hypoxanthine, 0.04 unit of xanthine oxidase, 300 μM NBT^{2+} and 10% DMSO.

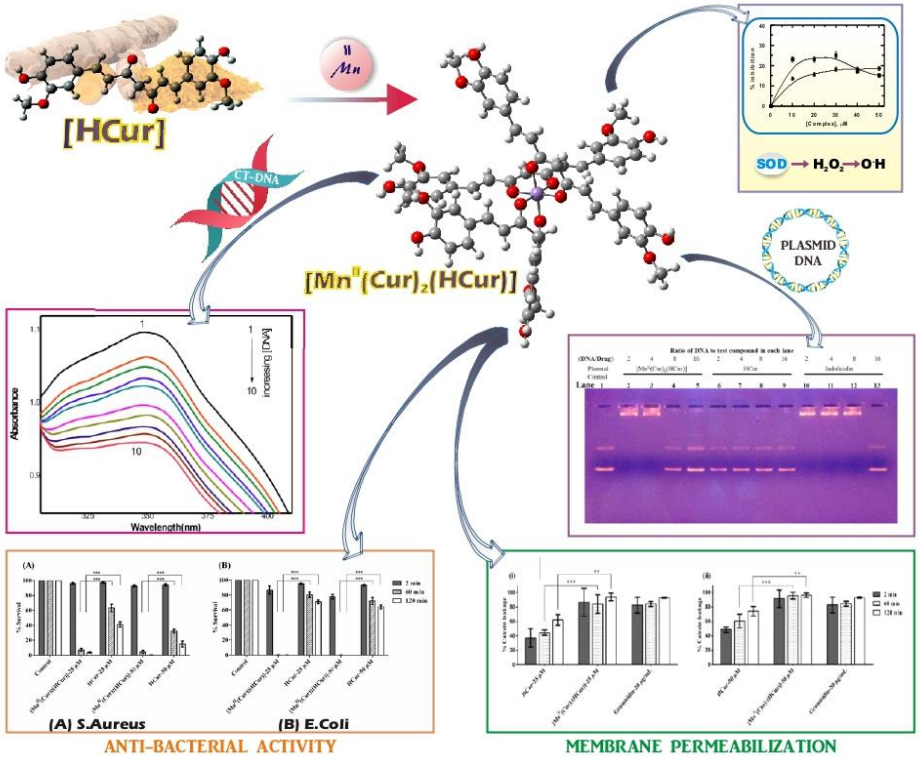
8.8 Biological applications of the prepared $[Mn^{II}(Cur)_2(HCur)]$ complex

Biological attributes of complex formation for the compound $[Mn^{II}(Cur)_2(HCur)]$ that was prepared by me (Mr. Tanmoy Saha) during the course of my research work was put to investigation through a collaboration in the laboratory of Prof. Kasturi Mukhopadhyay at the School of Environmental Sciences, Jawaharlal Nehru University, New Delhi. There, studies were performed with regard to antibacterial activity on *S. aureus* and *E. coli strains,* a study was done to realize the mechanism of antibacterial action due to HCur and Mn(II) complex exploring membrane permeabilization of *S. aureus* as understood by calcein leakage assay, binding affinity of the Mn(II) complex with LPS, evaluation of membrane damage in *S. aureus* using fluorescence microscopy, morphological changes of the cell membrane in *S. aureus* induced *by* HCur, the Mn(II) complex and gramicidin D as observed by scanning electron microscope (SEM), ultrastructural changes in

S. aureus induced *by* HCur, the Mn(II) complex and gramicidin D as observed by transmission electron microscope (TEM), a comparative DNA binding study using plasmid DNA with HCur and $[Mn^{II}(Cur)_2(HCur)]$, a non-hemolytic and non-toxic activity of $[Mn^{II}(Cur)_2(HCur)]$ on mammalian cells. The outcome of several such studies are very encouraging and suggest the possibility of further investigations with this complex.

All aspects mentioned above is showcased in our publication mentioned below:

Saha, T., Kumar, P., Sepay, N., Ganguly, D., Tiwari, K., Mukhopadhyay, K. and Das, S., 2020. Multitargeting antibacterial activity of a synthesized Mn^{2+} complex of curcumin on gram-positive and gram-negative bacterial strains. ACS omega, 5(27), pp.16342-16357.



References:

1. R. A. Sharma, W. P. Steward, A. J. Gescher; Pharmacokinetics and pharmacodynamics of curcumin. *Adv. Exp. Med. Biol*., **2007**, 595, 453-470.
2. S. Banerjee, P. Prasad, I. Khan, A. Hussain, P. Kondaiah, A. R. Chakravarty; Mitochondria targeting photocytotoxic oxidovanadium(IV) complexes of curcumin and (acridinyl) dipyridophenazine in visible light. *Z. Anorg. Allg. Chem*., **2014**,640, 1195-1204.
3. Y. J. Wang, M. H. Pan, A. L. Cheng, L. I. Lin, Y. S. Ho, C. Y. Hsieh, J. K. Lin; Stability of curcumin in buffer solutions and characterization of its degradation products. *J PharmBiomed. Anal.*, **1997**, 15**,** 1867-1876.
4. M. Kharat, Z. Du, G. Zhang, D. J. McClements; Physical and chemical stability of curcumin in aqueous solutions and emulsions: Impact of pH, temperature, and molecular environment. *J Agric Food Chem*., **2017**,65, 1525-1532.
5. H. H. Tønnesen, M. Másson, T. Loftsson; Studies of curcumin and curcuminoids. XXVII. Cyclodextrin complexation: solubility, chemical and photochemical stability. *Int J Pharm.*, **2002**, 244,127-135.
6. M. Bernabé-Pineda, M. T. Ramírez-Silva, M. Romero-Romo, E. González-Vergara, A. Rojas-Hernández; Determination of acidity constants of curcumin in aqueous solution and apparent rate constant of its decomposition. *Spectrochim. ActaA Mol. Biomol. Spectrosc.*, **2004**, 60,1091-1097.
7. K. I. Priyadarsini; Determination of acidity constants of curcumin in aqueous solution and apparent rate constant of its decomposition. *Molecules*, **2014**, 19, 20091-20112.
8. M. S. Refat; Synthesis and characterization of ligational behavior of curcumin drug towards some transition metal ions: chelation effect on their thermal stability and biological activity.

Spectrochimica Acta Part A: Molecular and Biomolecular Spectroscopy, **2013**, 105, 326-337.

9. O. Vajragupta, P. Boonchoong, H. Watanabe, M. Tohda, N. Kummasud, Y. Sumanont; Manganese complexes of curcumin and its derivatives: evaluation for the radical scavenging ability and neuroprotective activity. *Free Rad. Biol. Med*., **2003**, 35, 1632–1644.
10. Y. Sumanont, Y. Murakami, M. Tohda, O. Vajragupta, H. Watanabe, K. Matsumoto; Effects of Manganese complexes of Curcumin and diacetylcurcumin on Kainic acid-induced neurotoxic responses in the rat hippocampus, *Biol. Pharm. Bull*., **2007**, 30, 1732-1739.
11. S. Wanninger, V. Lorenz, A. Subhan, F. T. Edelmann; Metal complexes of curcumin – synthetic strategies, structures and medicinal applications. *Chem. Soc. Rev*., **2015**, 44, 4986-5002.
12. N. Bicer, E. Yildiz, A. A. Yegani, F. Aksu; Synthesis of curcumin complexes with iron(III) and manganese(II), and effects of curcumin–iron(III) on Alzheimer's disease**.** *New J. Chem.*, **2018**, 42, 8098-8104.
13. A. Goel, A. B. Kunnumakkara, B. B. Aggarwal; Curcumin as "Curecumin": from kitchen to clinic.*Biochem. Pharmacol.*, **2008**, 75,787-809.
14. K. Neelofar, S. Shreaz, B. Rimple, S. Muralidhar, M. Nikhat, L. A. Khan; Curcumin as a promising anticandidal of clinical interest.*Can. J. Microbiol*., **2011**, 57, 204-210.
15. P. Tyagi, M. Singh, H. Kumari, A. Kumari, K. Mukhopadhya; Bactericidal activity of curcumin I is associated with damaging of bacterial membrane. *PloS one*, **2015**, 10, e0121313.

16. M. K. Mishra, P. Sanphui, U. Ramamurthy, G. R. Desiraju; Solubility-hardness correlation in molecular crystals: Curcumin and sulfathiazole polymorphs. *CrystalGrowth and Design*, **2014**, 14,3054-3061.

17. F. Caruso, M. Rossi, A. Benson, ; C. Opazo, D. Freedman, E. Monti, M. B. Gariboldi, J.; Marchetti, F. Shaulky, R. Pettinari, C. Pettinari; Ruthenium–arene complexes of curcumin: X-ray and density functional theory structure, synthesis, and spectroscopic characterization, in vitro antitumor activity, and DNA docking studies of (*p*-cymene) Ru(curcuminato)chloro*J Med.Chem*., **2012**, 55, 1072–1081.

18. M. H. M. Leung, T. Harada, T. W. Kee; Delivery of curcumin and medicinal effects of the copper(II)-curcumin complexes,*Curr.Pharm.Des.***2013**, 19, 2070-2083.

19. M. Pröhl, U. S. Schubert, W. Weigand, M. Gottschaldt; Metal complexes of curcumin and curcumin derivatives for molecular imaging and anticancer therapy. *Coord. Chem. Rev*. **2016**, 307,32-41.

20. P. Chen, J. Bornhorst , M.A. Aschner; Manganese metabolism in humans, **2018**.

21. K.M. Erikson, M. Aschner; Manganese: its role in disease and health. *Met. Ions Life Sci*, **2019,** 19, 253-266.

22. G.D.Lawrence, D.T. Sawyer; The chemistry of biological manganese. *Coordination Chemistry Reviews*, **1978**. 27, 173-193.

23. Y. Sheng, I.A. Abreu, D.E. Cabelli, M.J. Maroney, A.F. Miller, M. Teixeira, J.S. Valentine, Superoxide dismutases and superoxide reductases. *Chemical reviews*, **2014**. 114, 3854-3918.

24. F. Akman , A. Demirpolat , A. S. Kazachenko , Anna S. Kazachenko, N. Issaoui and O.A.Dossary ; Molecular Structure, Electronic Properties, Reactivity (ELF, LOL, and

Fukui), and NCI-RDG Studies of the Binary Mixture of Water and Essential Oil of Phlomis bruguieri. *Molecules*, **2023**,28,2684.

25. J. L. Raygada, D. P. Levine; Methicillin-resistant *Staphylococcus aureus:* A growing risk in the hospital and in the community. *Am Health Drug Benefits.* **2009**,2, 86-95.
26. S. Bakthavatsalam, S. D. Sharma, M. Sonawane, V. Thirumalai, A. Datta; A zebrafish model of manganism reveals reversible and treatable symptoms that are independent of neurotoxicity, *Disease models &*mechanisms, **2014**, 7, 1239-1251.
27. A. Hochkoeppler, F. Borsetti, F. D. Piaz, F. D'Alessio, A. Stefan, R. Brandimarti, A. Sarkar, A. Datta, A. M. Silva, T. den Blaauwen, M. Alberto, E. Spisni.; Manganese is a Deinococcus radiodurans growth limiting factor in rich culture medium, *Microbiology*, **2018**, 164.
28. P. Das, C. K. Jain, S. Roychoudhury, H. K. Majumder, S. Das; Design, synthesis and invitroanticancer activity of a Cu(II) complex of Carminic acid: A novel small molecule inhibitor of human DNA topoisomerase I and topoisomerase II, *Chemistry Select* , **2016**, 1, 6623-6631.
29. S. Mukherjee-Chatterjee, C. K. Jain, S. Singha, P. Das, S. Roychoudhury, H. K. Majumder, S. Das.; Activity of Co^{II}-Quinalizarin: A novel analogue of anthracycline-based anticancer agents targets human DNA topoisomerase, whereas quinalizarin itself acts via formation of semiquinone on acute lymphoblastic leukemia MOLT-4 and HCT 116 cells. *ACS Omega*, **2018**, 3, 10255-10266.
30. I. Ali, W.A. Wani, K. Saleem, Empirical formulae to molecular structures of metal complexes by molar conductance. *Synthesis and reactivity in inorganic, metal-organic, and nano-metal chemistry,* **2013**, 43, 1162-1170.

31. K. Nakamoto; Infrared and Raman spectra of inorganic and coordination compounds, 3rd edition, *Wiley-Interscience*, New York, **1978**.

32. (a) A. D. Becke.; Density-functional thermochemistry. III. The role of exact exchange, J. Chem. Phys., **1993**, 98, 5648e5652; (b) C. T. Lee, W. T. Yang, R. G. Parr.; Development of the Colle-Salvetti correlation-energy formula into a functional of the electron density, Phys. Rev. B., **1988**, 37, 785e789.

33. M. J. Frisch, G. W. Trucks, H. B. Schlegel, G. E. Scuseria, M. A. Robb, J. R. Cheeseman, G. Scalmani, V. Barone, G. A. Petersson, H. Nakatsuji, X. Li, M. Caricato, A. V. Marenich, J. Bloino, B. G. Janesko, R. Gomperts, B. Mennucci, H. P. Hratchian, J. V. Ortiz, A. F. Izmaylov, J. L. Sonnenberg, D. Williams-Young, F. Ding, F. Lipparini, F. Egidi, J. Goings, B. Peng, A. Petrone, T. Henderson, D. Ranasinghe, V. G. Zakrzewski, J. Gao, N. Rega, G. Zheng, W. Liang, M. Hada, M. Ehara, K. Toyota, R. Fukuda, J. Hasegawa, M. Ishida, T. Nakajima, Y. Honda, O. Kitao, H. Nakai, T. Vreven, K. Throssell, J. A. Montgomery, Jr., J. E. Peralta, F. Ogliaro, M. J. Bearpark, J. J. Heyd, E. N. Brothers, K. N. Kudin, V. N. Staroverov, T. A. Keith, R. Kobayashi, J. Normand, K. Raghavachari, A. P. Rendell, J. C. Burant, S. S. Iyengar, J. Tomasi, M. Cossi, J. M. Millam, M. Klene, C. Adamo, R. Cammi, J. W. Ochterski, R. L. Martin, K. Morokuma, O. Farkas, J. B. Foresman, and D. J. Fox, **2016**, Gaussian 16, Revision C.01, Gaussian, Inc., Wallingford CT.

34. P. Deb, M. Ghose, N. Sepay, S. Maity, K. K. Mukherjea; Synthesis, characterization, theoretical simulation, and DNA-nuclease activity of a newly synthesized Mn–oximato complex, *J. Coord. Chem.*,**2018**,71, 3250-3265.

35. V. K. Choudhary, A. K. Bhatt, D. Dash, N. Sharma; DFT calculations on molecular structures, HOMO-LUMO study, reactivity descriptors and spectral analyses of newly

synthesized diorganotin(IV) 2-chloridophenylacetohydroxamate complexes, *Jour. Comp. Chem.*, **2019**, 1-10.

36. Z. Akbari, C. Stagno, N. Iraci, T. Efferth, E. A. Omer, A. Piperno M. Montazerozohori M.F. Dehnayebi , N. Micale.; Biological evaluation, DFT, MEP, HOMO-LUMO analysis and ensemble docking studies of Zn(II) complexes of bidentate and tetradentate Schiff base ligands as antileukemia agents. *Journal of Molecular Structure*, **2024**,1301,137400.
37. J.S.Al-Otaibi; Detailed quantum mechanical studies on bioactive benzodiazepine derivatives and their adsorption over graphene sheets. *Spectrochimica Acta Part A: Molecular and Biomolecular spectroscopy*, **2020**, 235, 118333.
38. J.S.Murray, K.Sen; Molecular Electrostatic Potentials concepts and applications, Theoretical and computational chemistry,*Elsevier*,**1996**,1-137.
39. E.R. Johnson, S. Keinan, P. Mori-Sánchez, J. Contreras-García, A.J. Cohen, W. Yang; Revealing Noncovalent Interactions. *J. Am.Chem. Soc.*, **2010**, 132, 6498–6506.
40. F. Akman, A. Demirpolat , A. S. Kazachenko , Anna S. Kazachenko, N. Issaoui and O.A.Dossary; Molecular Structure, Electronic Properties, Reactivity (ELF, LOL, and Fukui), and NCI-RDG Studies of the Binary Mixture of Water and Essential Oil of Phlomis bruguieri. *Molecules*, **2023**,28,2684.
41. T. Lu, F. Chen; Multiwfn: A multifunctional wavefunction analyzer. *Jour. Comput. Chem.***2012**, 33, 580-592.
42. B.Silvi, A.Savin; Classification of chemical bonds based on topological analysis of electron localization functions. *Nature*, **1994**, 371(6499), 683–686.
43. B. Fathima Rizwana, J. C. Prasana, S.Muthu, C.S.Abraham; Molecular docking studies, charge transfer excitation and wave function analyses(ESP,ELF,LOL) on valacyclovir:A potential anti viral drug. *Comput,Biol.Chem.*, **2019**,78, 9–17.

44. Heiko Jacobsen; Localized-orbital locator (LOL) profiles of chemical bonding. *Can. J. Chem*., **2008**, 86, 695–702.

45. D.G. Westbrook, A.K. Bhunia; Dithiothreitol enhances Listeria monocytogenes mediated cell cytotoxicity. Microbiology and immunology, **2000**, 44, 431-438.

46. P. Das, D. Bhattacharya, P. Karmakar, S. Das, Influence of ionic strength on the interaction of THA and its Cu(II) complex with DNA helps to explain studies on various breast cancer cells. *RSC Adv.,* **2015**, 5,73099-73111.

47. S. Ghosh, P. Kundu, B. K. Paul; N. Chattopadhyay; Binding of an anionic fluorescent probe with calf thymus DNA and effect of salt on the probe–DNA binding: A spectroscopic and molecular docking investigation. *RSC Adv.***, 2014**,4, 63549-63558.

48. M. Saha, S. Singha, M. Chakraborty, S. Mazumdar, S. Kumar, P. Karmakar, S. Das; Characterization of a Mn^{II} complex of alizarin suggests attributes explaining a superior anticancer activity: A comparison with anthracycline drugs, *Polyhedron*, **2019**,173, 114104.

49. P. S. Guin, P. C. Mandal, S. Das; The binding of a hydroxy-9,10-anthraquinone Cu^{II} complex to calf thymus DNA: Electrochemistry and UV/Vis spectroscopy, *Chem Plus Chem*, **2012**,77, 361-369.

50. P. Das, C. K. Jain, S. K. Dey, R. Saha, A. D. Chowdhury, S. Roychoudhury, S. Kumar, H. K. Majumder, S. Das; Synthesis, crystal structure, DNA interaction and *in vitro* anticancer activity of a Cu (II) complex of purpurin: dual poison for human DNA topoisomerase I and II. *RSC Adv.*,**2014**, 4,59344-59357.

51. B. Mandal, S. Singha, S.K. Dey, S. Mazumdar, T. K. Mondal, P. Karmakar, S. Kumar, S. Das; Synthesis, crystal structure from PXRD of a $Mn^{II}(purp)_2$ complex, interaction with DNA at

different temperatures and pH and lack of stimulated ROS formation by the complex. *RSCAdv*. **2016**, 6, 51520–51532.

52. M. Saha, P. Nandy, M. Chakraborty, P. Das, S. Das; The importance of pK_a in an analysis of the interaction of compounds with DNA. *Biophys. Chem.* **2018**,236, 15-21.
53. G. Scatchard; The attractions of proteins for small molecules and ions, *Ann. N. Y. Acad. Sci*.**1949**,51, 660–672.
54. C. H. Huang, S. Mong, S. T. Crooke; Interactions of a new antitumor antibiotic BBM-928A with deoxyribonucleic acid. Bifunctional intercalative binding studied by fluorometry and viscometry. *Biochemistry*, **1980**,19, 5537-5542.
55. T. Ardan, J. Kovaceva, J. Cejková.; Comparative histochemical and immune histochemical study on xanthine oxidoreductase/xanthine oxidase in mammalian corneal epithelium. *ActaHistochemica.*, **2004**, 106, 69–75.
56. R. Hille, J. Hall, P. Basu.; The mononuclear molybdenum enzymes. *Chem. Rev.*, **2014**, 114, 3963–4038.
57. G. Lyngsie, L Krumina, A. Tunlid, P. Persson.; Generation of hydroxyl radicals from reactions between a dimethoxyhydroquinone and iron oxide nanoparticles. *ScientificReports,***2018**, 8, Article number: 10834.
58. S. Gligorovski, R. Strekowski, S. Barbati, D. Vione.; Environmental implications of hydroxyl radicals (˙OH). *Chem. Rev.***2015**,115, 13051–13092.
59. C. Thomas, M. M. Mackey, A. A. Diaz, D. P. Cox.; Hydroxyl radical is produced via the Fenton reaction in submitochondrial particles under oxidative stress: Implications for diseases associated with iron accumulation, *Redox Report,* **2009**, 14, 102-108.

CHAPTER 9

Synthesis, characterization, structural elucidation using Quantum Chemical calculations and temperature-dependent DNA binding studies of a Cu^{II}–Curcumin complex

Introduction

To understand various aspects related to the chemistry of Curcumin in the biological system, it is crucial to ensure that it remains intact in solution as a "single entity". This means that before it interacts with a biological target its degradation must be prevented. Only then can its bio-availability be increased.[1-10] One possible way to do this is through the formation of metal ion complexes.[5] Curcumin bound to a metal centre stays as a "single-unit".[11,12] Moreover, the presence of a metal ion helps in cellular absorption as well as the fact that it addresses concerns related to its solubility.[11,18-21] In the light of all these considerations, a Cu^{II}-Curcumin complex was prepared, thoroughly characterized and investigated for its biological attributes. More importantly it was seen that the complex did not degrade either in in aqueous buffer or in biological cellular medium suggesting that it could maintain Curcumin as a "single unit".[11-21]

The selection of copper ion was made as it plays a crucial role in cellular physiology, serving both as an essential component and a potential toxin. Cu^{2+}/Cu^{+} function as cofactors for several enzymes enabling vital cellular processes during processes like respiration, neural transmission, tissue maturation, oxidative stress defense and iron metabolism.[22-24] Maintaining an adequate intracellular copper level is therefore necessary to support some of these important functions. Deficiency of copper ions can impair the activity of several enzymes like cytochrome c oxidase, lysyl oxidase, dopamine-b-hydroxylase, superoxide dismutase and ceruloplasmin that regulate crucial processes in the biosystem.[22-25] The significance of proper intracellular copper ion balance is evident in human X-linked Menkes disease.[26] Redox chemistry of copper ions underlies their essential nature in living organisms. However, the same redox activity also leads to toxicity, particularly when the ions are present in excess.[22-26] Wilson disease for example, a human genetic disorder, results from harmful effects of excess copper ion accumulation in the liver causing hepatic cirrhosis and neuronal degeneration.[27,28]

In the light of antibacterial action shown by Curcumin, subsequent investigations have tried to identify the advantages of complex formation.[11-21] Antibacterial activity on Staphylococcus aureus (*S. aureus*) and Escherichia coli (*E. coli*) were checked as part of studies with the complex. Since pathogens like Staphylococcus aureus (*S. aureus*) and Escherichia coli (*E. coli*) are responsible for a wide range of severe illnesses they were used as primary biological targets during investigations.[29-30] Patients with compromised immune systems, particularly those weakened by viral infections, like those affected during the COVID-19 crisis are at high risk of contracting infections due to these pathogens. Clinical strains of these pathogens are progressively becoming resistant to a wide range of antibiotics worldwide displaying a significant extent of multi-drug resistance.[31-33] Hence, one is left with only a few viable treatment alternatives to combat diseases caused by such bacteria that are continually adapting to a changing environment.[34,35] Therefore, it was decided that investigations look for other options; preferably from a natural source to replace existing antibiotics. Exploration of the vast potential of medicinal plants led scientists to identify a plethora of active chemicals having outstanding antibacterial properties. One such is Curcumin whose potential as an active metabolite has garnered a lot of interest in the last few decades.[1-3] In addition to its numerous therapeutic benefits, it was found to have a wide range of antimicrobial properties, effectively combating fungi, viruses and bacteria.[36-38] With the help of a series of fluorescence and microscopy-based experiments, investigations reveal how Curcumin and its Cu^{II} complex exert antibacterial effects.

Result and discussion

9.1 Physicochemical studies on the formation of a Cu^{II} complex of Curcumin

Stoichiometry of complex formation between Cu^{II} and HCur was determined using mole ratio method where Cu^{II} was kept constant while the concentration of Curcumin was varied. The same was also attempted using Job's method of continuous variation.

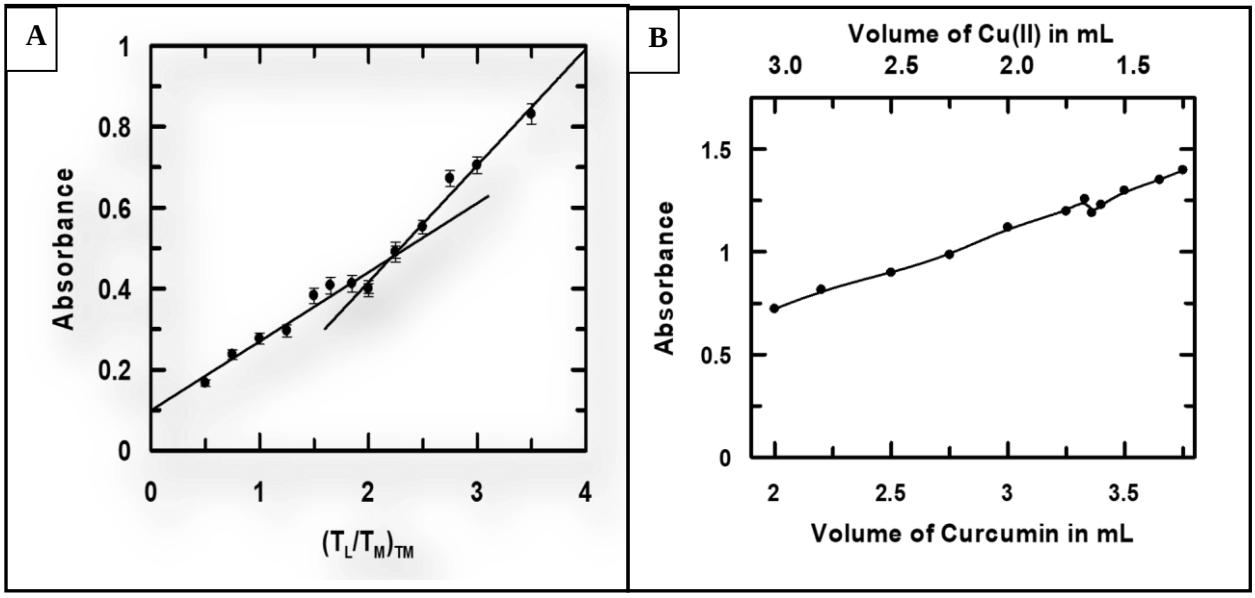


Figure 1: (A) A mole-ratio plot showing interaction of Cu^{II} with Curcumin in solution at pH ~7.4; (B) Job's plot of continuous variation showing interaction of Cu^{II} with Curcumin at pH~7.4. [$NaNO_3$] = 0.01M, Temperature = 298 K.

In mole-ratio method, absorbance was measured at 428 nm and plotted against ratio of Curcumin to Cu^{II} [Fig. 1(A)]. Straight lines were obtained; intersection of which helped to determine stoichiometry of complex formation in solution. Stoichiometry was also determined by continuously varying the concentration of Curcumin and Cu^{II} as shown in Fig. 1(B). Both methods suggest the formation of a 1:2 metal-ligand complex at pH ~7.4.

9.2 Characterization of the Cu^{II} complex of Curcumin

Although physicochemical investigations performed with regard to mole ratio and Job's method of continuous variation suggests formation of a 1:2::metal:ligand complex in aqueous solution, several attempted preparation of the complex by mixing 1 part by mole of Cu^{II}acetate with 2 parts by mole of HCur always resulted in a 1:1 species where besides HCur, an acetate and a molecule of water were the other ligands (*Chapter 6, Experimental*). In fact, this very compound has been prepared earlier, where researchers had taken Cu^{II}acetate and Curcumin in 1:1 molar ratio.[39] The prepared compound was anlaysed thoroughly by different techniques.

9.2.1 Analysis of the mass spectrum:

Mass spectrum of the complex showed a molecular ion peak at m/z = 507.3225 (Fig. 2); m/z_{theo} being 507.39 considering ^{63}Cu and 509.39 considering ^{65}Cu established the fact that a 1:1 complex was formed; hence the formula of the complex would be $[Cu^{II}(Cur)(OCOCH_3)(OH_2)]$.

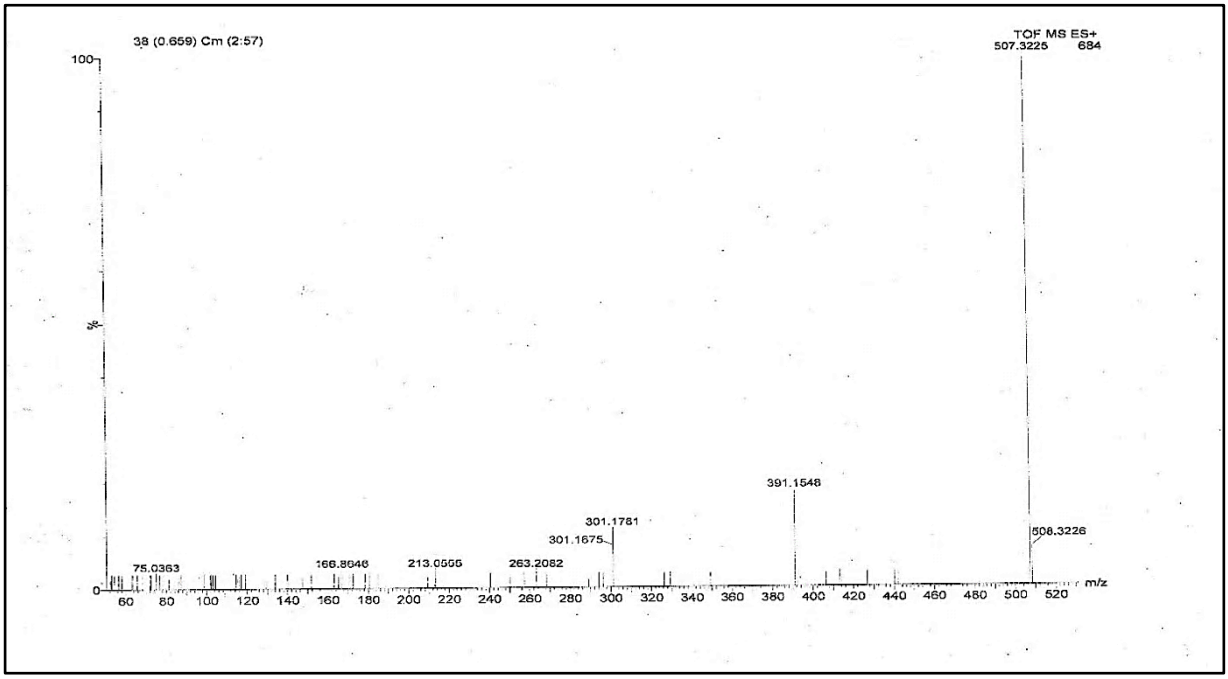


Figure 2: Mass spectra of the Cu^{II} complex of Curcumin

9.2.2 Thermo-gravimetric analysis:

Such an analysis of the complex (Fig. 3) indicates up to 200°C there is not much loss in weight from an initial weight of 19.5742 mg recorded at 46.82°C. At ~ 237.5°C, weight recorded was 18.2162 mg. Hence, the loss in weight and percentage loss were 1.358 mg and 6.93% respectively that correspond to loss of one –OH from HCur, an H_2O from the coordination site, that corresponds to a theoretical loss of 6.90%. At 357.2°C, weight of the compound was 15.2641 mg. The loss in weight and percentage loss were 4.3101 mg and 22.01% respectively. This decrease in weight corresponds to the loss of two -OH groups from Curcumin, a molecule of H_2O and an acetate from the coordination site, showing a theoretical loss of 21.89%. At 467 ^{0}C, the weight was 11.9583 mg; loss in weight and percentage loss were 7.6159 mg and 38.90% respectively. This corresponds to loss of two -OH, two –OCH_3 from HCur and H_2O, acetate from the coordination site; theoretical loss in weight being 38.86 %.

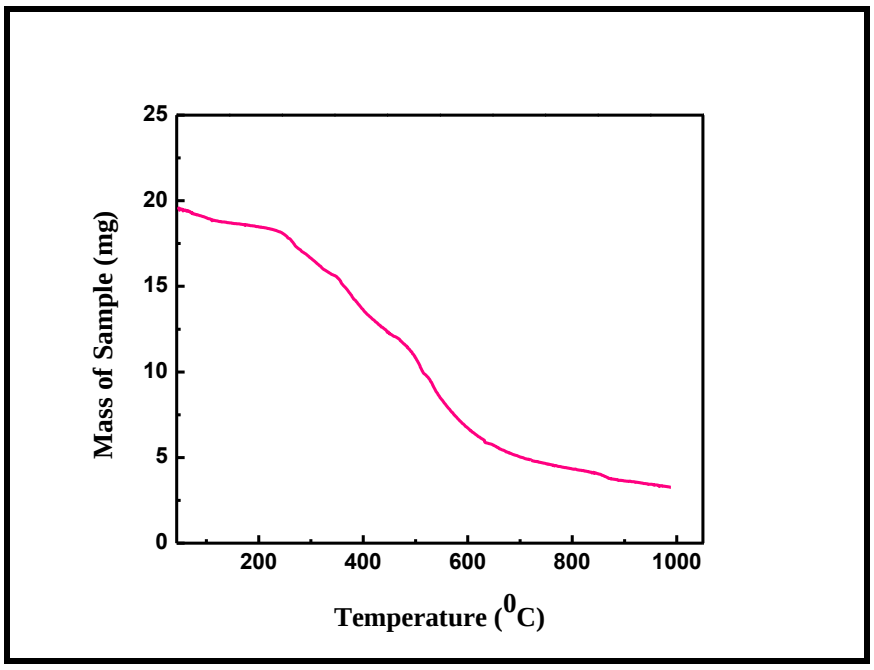


Figure 3: TGA of [Cu^{II}(Cur)($OCOCH_3$)(OH_2)]

9.2.3 UV-Vis spectra of Curcumin and its Cu^{II} complex in DMSO:

Curcumin and its Cu^{II} complex were dissolved in DMSO. λ_{max} of Curcumin appeared at 428 nm while that for the complex was at 426 nm (Fig.4)

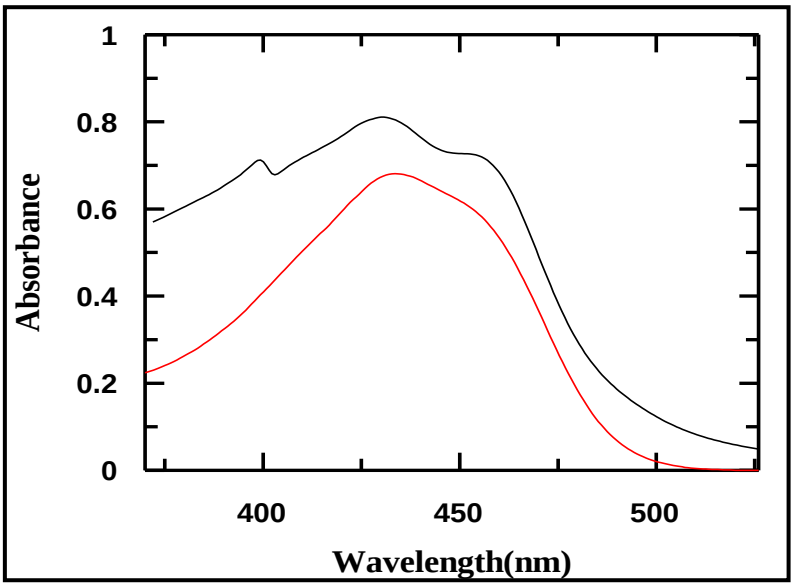


Figure 4: Absorption spectra of Curcumin (10 μM —) and [Cu^{II}(Cur)] (18 μM —) in DMSO.

9.2.4 Analysis of IR spectra:

IR spectrum of HCur shows a peak at 3516 cm^{-1} attributed to –OH stretching (*Fig. 3, Chapter 7*). Peaks at 1627 cm^{-1} and 1608 cm^{-1} were due to C=O stretching vibrations while those at 1506 cm^{-1} and 1429 cm^{-1} were for C=C stretching and C=O bending.[40] Peaks in the range 1276 cm^{-1} to 1153 cm^{-1} were due to phenolic –OH bending, –C–O stretching, alkoxy C–O bending etc. while that at 964 cm^{-1}, 855 cm^{-1} and 810 cm^{-1} were due to alkene C_{sp2}–H bending. The sharp peak for –OH stretching in HCur (*Fig. 3, Chapter 7*) appeared as a broad band around 2931 cm^{-1} in the complex (Fig. 5). Response for carbonyl stretching vibrations got shifted to lower wavenumbers (1615 cm^{-1} & 1590 cm^{-1}) for the complex; also having a relatively low intensity indicating an involvement of the carbonyl group in HCur in binding Cu^{II} (Fig. 5).[40]

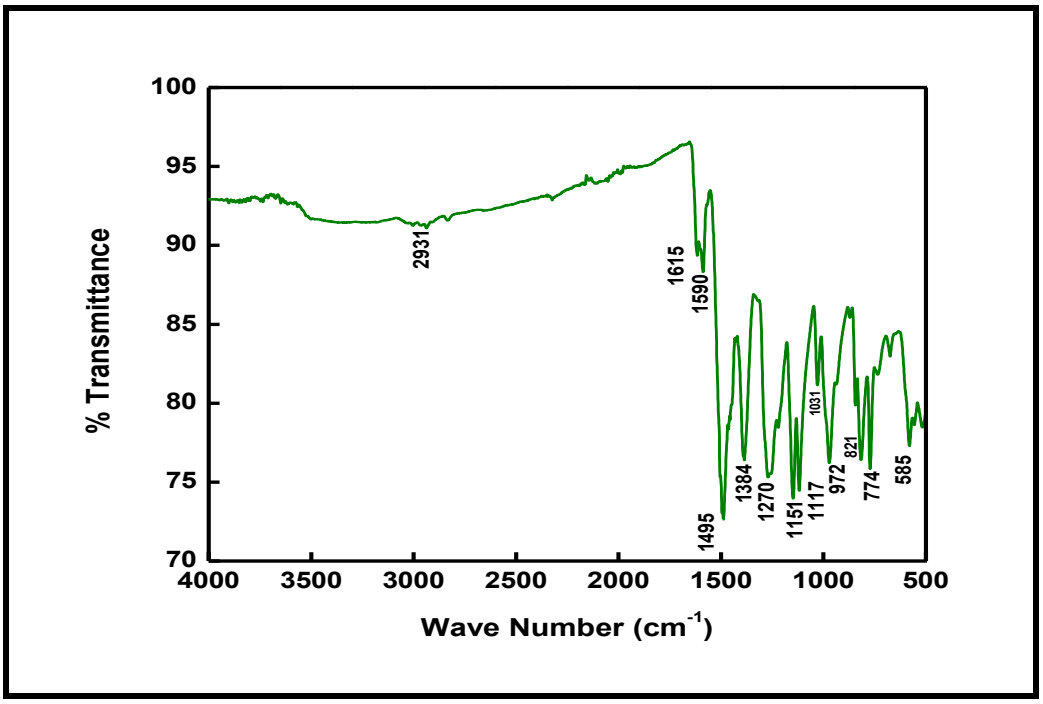


Figure 5: FTIR spectrum for $[Cu^{II}(Cur)(OCOCH_3)(H_2O)]$

Peaks in the region 1495 cm^{-1} to 1117 cm^{-1} in the IR spectrum of the complex showed distinct changes attributed to bonds that are close to the zone of co-ordination with the metal centre (viz. –OH, –CH, –C–C bending modes).[40]

9.3 Determination of stability constant of [Cu(Cur)] in solution

pH-metric titration of HCur in the presence of Cu^{II} was performed by taking HCur and Cu^{II} in 1:1 molar ratio in the pH range 4.75 to 10.50. Change in absorbance was followed at 428 nm (Fig. 6).

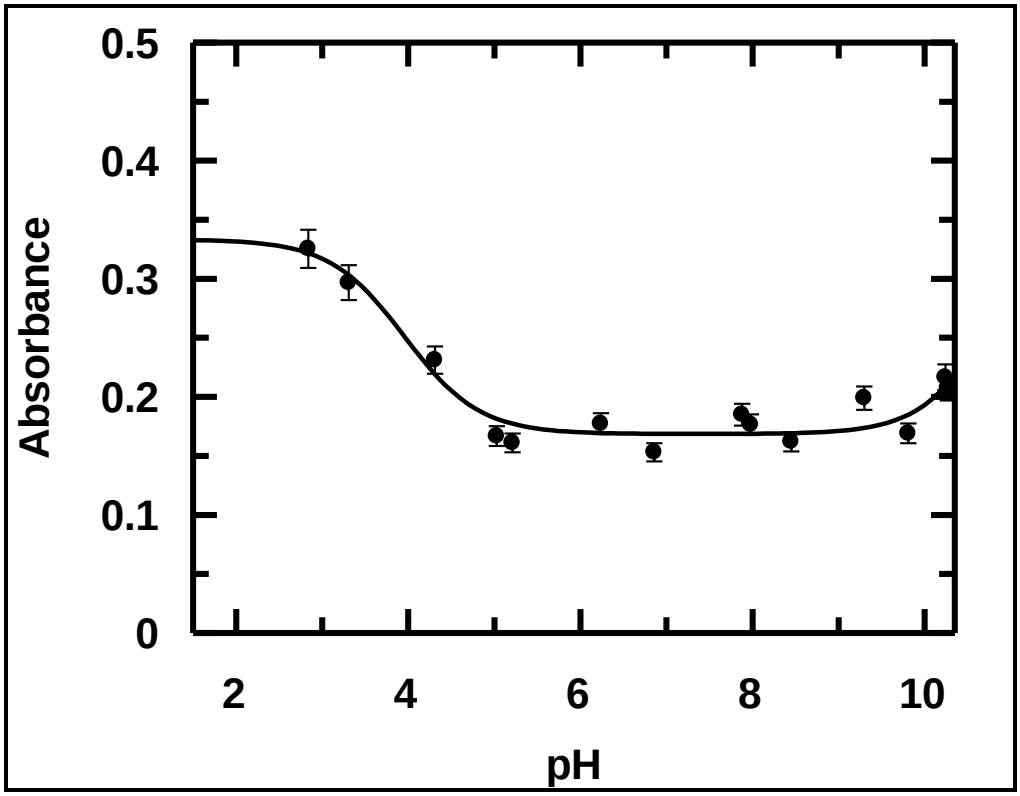


Figure 6: Fitted plot of Curcumin in aqueous solution in presence of Cu^{II} at different pH. [Curcumin] = 10 μM, $[Cu(OAc)_2]$ = 10 μM, $[NaNO_3]$ = 0.01 M, Temperature = 300 K. The solid line is the fitted data according to Eq. 5.

The titration data was fitted to Eq. 5 (*Chapter 6: Experimental*). pK_{a1}(= 3.95 ± 0.43) and pK_{a2} (= 11.07 ± 0.20) was determined. Hence, it was identified that in presence of Cu^{II} the enolic –OH of HCur dissociates much earlier than when HCur is present alone. Stability constants β^* and β were determined using Eqs. 11-15 (*Chapter 6: Experimental*) and found to be 3.31×10^8 (log β = 8.52).

9.4 DFT calculations based on spectroscopic evidence

By performing DFT calculations using Gaussian 09 software[41] at B3LYP functional[42] and 6-31G+ (d,p) as basis set for C, H and O atoms[42] and SDD as the basis set for Cu^{II},[43] ground states of optimized molecular structure of $[Cu^{II}(Cur)(OCOCH_3)(OH_2)]$ in gas and solution phases were obtained as doublets. Ground state optimized geometries of the complex both in gaseous state and in DMSO (solution state) are depicted in Fig. 7 with a numbering scheme for the coordination environment. Important parameters regarding coordination geometry are arranged in Table 1. Optimized coordinates for these configurations are provided in Table 2. Final optimized structures of the ground state configuration show a planar coordination environment both for gas and solution phase calculations. The two oxygens of Curcumin, the oxygen of a molecule of water and acetyl oxygen are connected to Cu^{II} in syn-anti fashion forming the basal plane (Fig. 7).

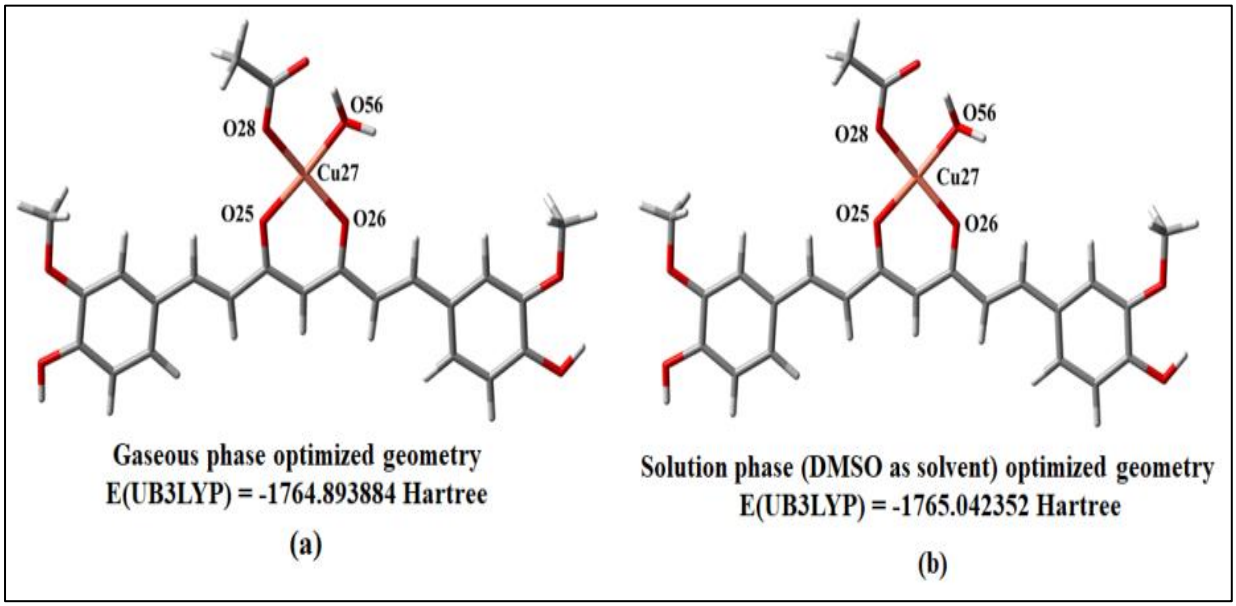


Figure 7: Ground state optimized geometries of the $[Cu^{II}(Cur)(OCOCH_3)(OH_2)]$ (a) Gas phase, (b) Solution Phase

Table 1: Coordinated bond distances (in Å) and bond angles (in °) of the complex Cu(II)-Curcumin.

Bond	Gas phase	In DMSO	Angle	Gas phase	In DMSO
Cu27–O25	1.917	1.916	O25–Cu27–O26	80.16	93.46
Cu27–O26	1.934	1.919	O25–Cu27–O28	101.57	89.32
Cu27–O28	1.966	1.966	O26–Cu27–O56	99.07	87.54
Cu27–O56	1.940	1.954	O28–Cu27–O56	79.54	90.83
			Dihedral angle		
			O25–O26–O28–O56	12.53	11.34

Table 2: Optimized coordinates of [Cu(Cur)($OCOCH_3$)(OH_2)]in ground state geometry

Gaseous phase				In DMSO solvent			
Atom	**x**	**y**	**z**	**Atom**	**x**	**y**	**z**
C1	7.3408	-2.9137	-0.0162	C1	-7.3120	-2.9320	0.0415
C2	7.2790	-1.5031	0.0332	C2	-7.2758	-1.5226	-0.0440
C3	6.0358	-0.8766	0.0451	C3	-6.0465	-0.8709	-0.0638
C4	4.8296	-1.6180	0.0093	C4	-4.8304	-1.5922	-0.0013
C5	4.9140	-3.0225	-0.0397	C5	-4.8872	-2.9971	0.0830
C6	6.1571	-3.6554	-0.0520	C6	-6.1166	-3.6535	0.1039
O7	8.5967	-3.4943	-0.0264	O7	-8.5574	-3.5344	0.0596
O8	8.4964	-0.8452	0.0666	O8	-8.5050	-0.8841	-0.1032
C9	3.5691	-0.8851	0.0255	C9	-3.5829	-0.8432	-0.0270
C10	2.3133	-1.3938	-0.0015	C10	-2.3242	-1.3462	0.0071
C11	1.1276	-0.5384	0.0204	C11	-1.1386	-0.4988	-0.0224
C12	-0.1445	-1.1426	-0.0171	C12	0.1247	-1.1123	0.0151
C13	-1.3656	-0.4510	0.0027	C13	1.3549	-0.4373	-0.0129
C14	-2.6072	-1.2232	-0.0381	C14	2.5839	-1.2181	0.0305
C15	-3.8333	-0.6484	-0.0058	C15	3.8134	-0.6466	-0.0024
C16	-5.1315	-1.3124	-0.0397	C16	5.1012	-1.3224	0.0344
C17	-6.2977	-0.5094	0.0273	C17	6.2738	-0.5290	-0.0321
C18	-7.5557	-1.0945	2×E-4	C18	7.5244	-1.1281	-0.0026

C19	-7.6918	-2.4938	-0.0955	C19	7.6407	-2.5294	0.0948
C20	-6.5535	-3.2961	-0.1634	C20	6.4956	-3.3216	0.1622
C21	-5.2876	-2.7119	-0.1357	C21	5.2360	-2.7239	0.1322
O22	-8.9465	-3.0658	-0.1223	O22	8.8934	-3.1104	0.1230
O23	-8.7813	-0.4255	0.0599	O23	8.7521	-0.4768	-0.0613
C24	-8.7856	1.0227	0.1648	C24	8.7665	0.9780	-0.1700
O25	1.3234	0.7606	0.0729	O25	-1.3248	0.8089	-0.0810
O26	-1.4636	0.8648	0.0594	O26	1.4668	0.8792	-0.0809
Cu27	-0.0094	2.1384	0.1173	Cu27	0.0360	2.1572	-0.1271
O28	1.3824	3.5027	-0.1380	O28	-1.3518	3.5323	0.0929
C29	1.2468	4.8001	-0.2255	C29	-1.2115	4.8263	0.2451
O30	0.1330	5.4206	-0.0898	O30	-0.0882	5.4370	0.1696
C31	2.5036	5.5872	-0.5011	C31	-2.4715	5.6036	0.5247
H32	5.9746	0.2044	0.0828	H32	-6.0053	0.2089	-0.1290
H33	4.0141	-3.6258	-0.0682	H33	-3.9775	-3.5826	0.1340
H34	6.2124	-4.7403	-0.0899	H34	-6.1525	-4.7362	0.1690
H35	8.5353	-4.4686	-0.0609	H35	-8.4852	-4.5074	0.1203
H36	3.6466	0.1999	0.0634	H36	-3.6803	0.2388	-0.0800
H37	2.1309	-2.4635	-0.0406	H37	-2.1426	-2.4146	0.0571
H38	-0.1826	-2.2245	-0.0622	H38	0.1514	-2.1936	0.0671
H39	-2.4905	-2.3013	-0.0931	H39	2.4600	-2.2942	0.0888
H40	-3.8575	0.4378	0.0550	H40	3.8503	0.4388	-0.0651
H41	-6.1903	0.5668	0.1013	H41	6.1781	0.5473	-0.1072
H42	-6.6813	-4.3693	-0.2373	H42	6.6069	-4.3964	0.2374
H43	-4.4143	-3.3514	-0.1907	H43	4.3559	-3.3530	0.1865
H44	-9.6246	-2.3589	-0.0655	H44	9.5764	-2.4065	0.0667
H45	-9.8363	1.3077	0.1972	H45	9.8184	1.2539	-0.2028
H46	-8.3026	1.4786	-0.7067	H46	8.2845	1.4326	0.7008
H47	-8.2825	1.3490	1.0819	H47	8.2636	1.2990	-1.0871
H48	2.2743	6.6498	-0.5834	H48	-2.2535	6.6678	0.6142
H49	2.9684	5.2305	-1.4260	H49	-2.9303	5.2431	1.4514
H50	3.2233	5.4242	0.3083	H50	-3.1939	5.4416	-0.2817

C51	8.4986	0.6058	0.1197	C51	-8.5168	0.5717	-0.1949
H52	8.0162	1.0374	-0.7653	H52	-8.0421	1.0231	0.6823
H53	8.0013	0.9717	1.0258	H53	-8.0123	0.9105	-1.1055
H54	9.5513	0.8843	0.1387	H54	-9.5697	0.8453	-0.2295
H55	-2.2567	3.3495	0.2910	H55	2.2953	3.3389	-0.1659
O56	-1.3192	3.5286	0.4565	O56	1.3864	3.5315	-0.4515
H57	-0.8942	4.4722	0.2302	H57	0.9800	4.4474	-0.1799

9.4.1 FMO composition analysis:

Frontier molecular orbitals (FMOs) of the complex optimized in gas and solution phase are shown in Fig. 8 and Fig. 9. Assignment of the type of each MO was made on the basis of its composition and by visual inspection of its three-dimensional representation. Since spin-α and spin-β components of each molecular orbital are localized on different parts of the molecule, hence MO composition analysis was seen to have contributions from four segments namely Cu, HCur, water and acetate. For some frontier MOs, orbital energies and contribution from each fragment in terms of atomic orbital contribution to frontier molecular orbital (FMO) are listed in Table 3. These were calculated using the GaussSum programme.[44] The MO gap of spin-α and spin-β components of each molecular orbital in gas and solution phases are shown in Fig.10.

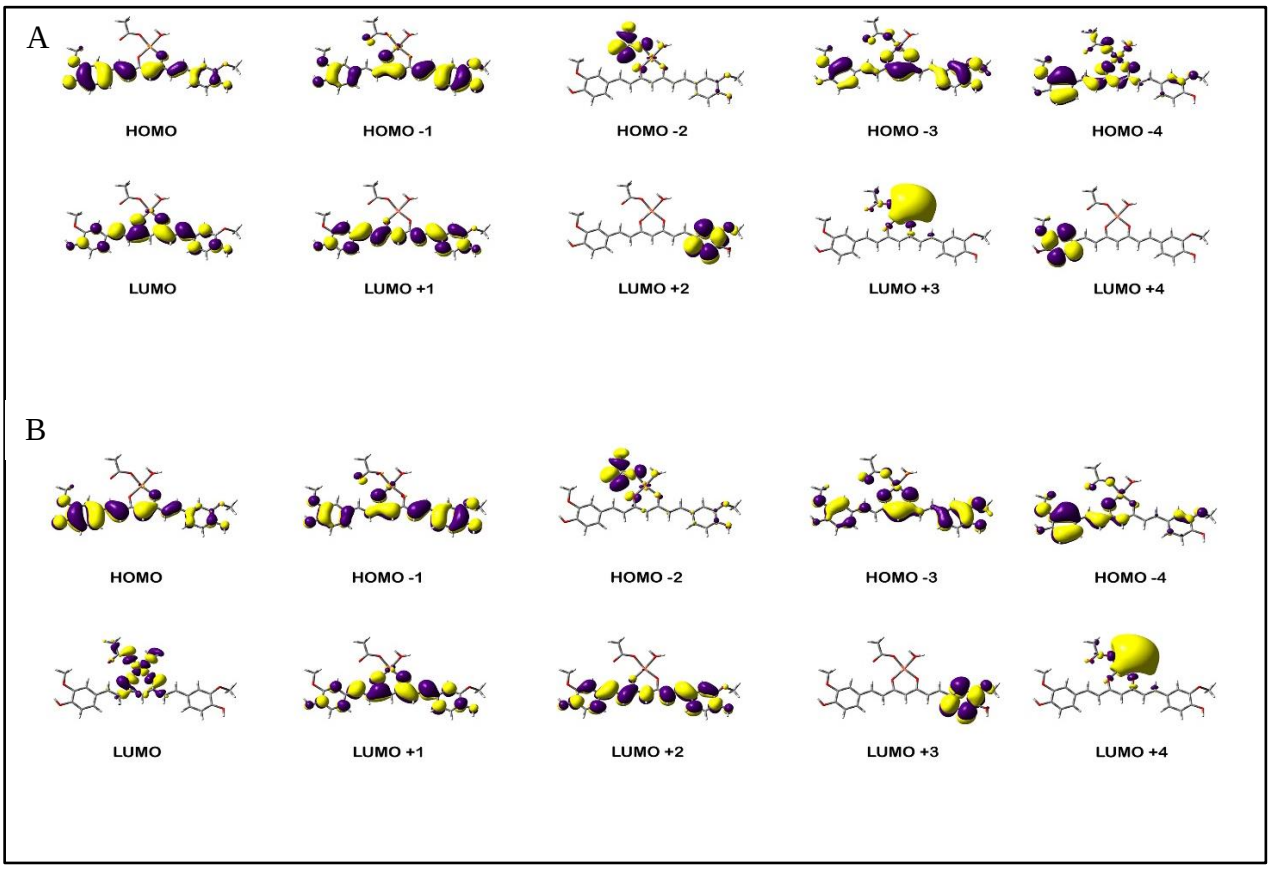


Figure 8: FMOs of [Cu^{II}(Cur)($OCOCH_3$)(OH_2)] in Gas Phase (A) α-FMOs , (B) β-FMOs

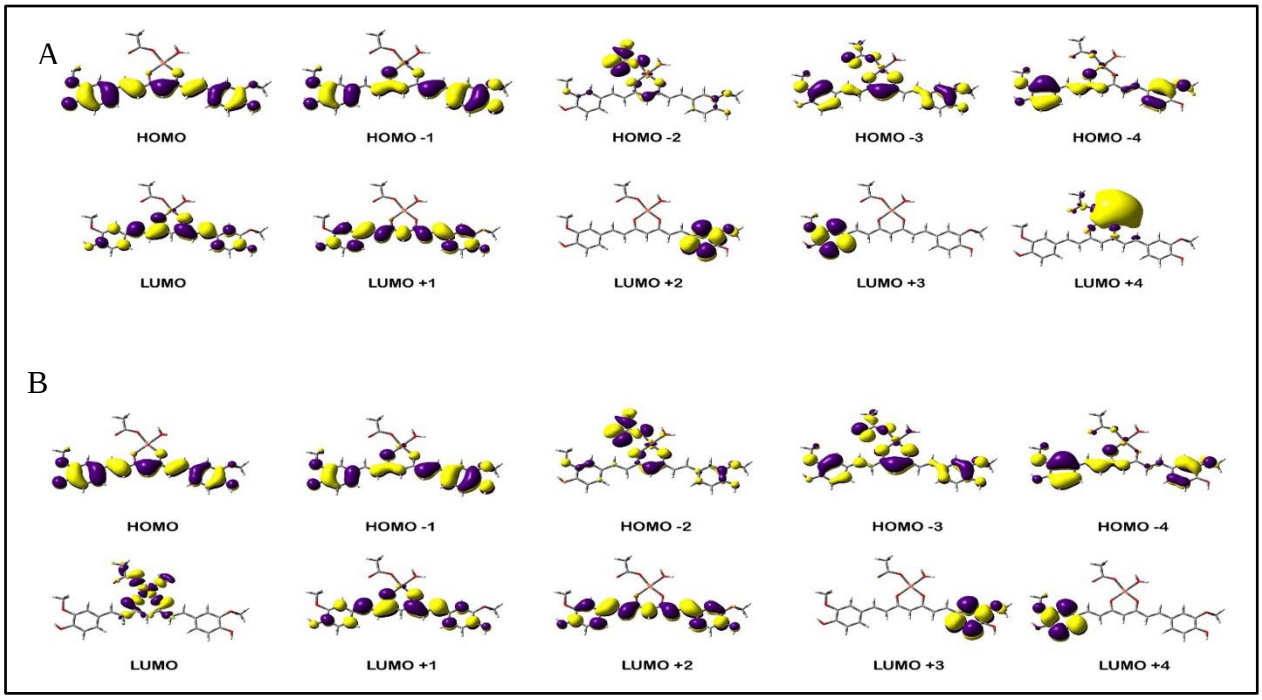


Figure 9: FMOs of [Cu^{II}(Cur)($OCOCH_3$)(OH_2)] in Solution Phase (A) α-FMOs , (B) β-FMOs

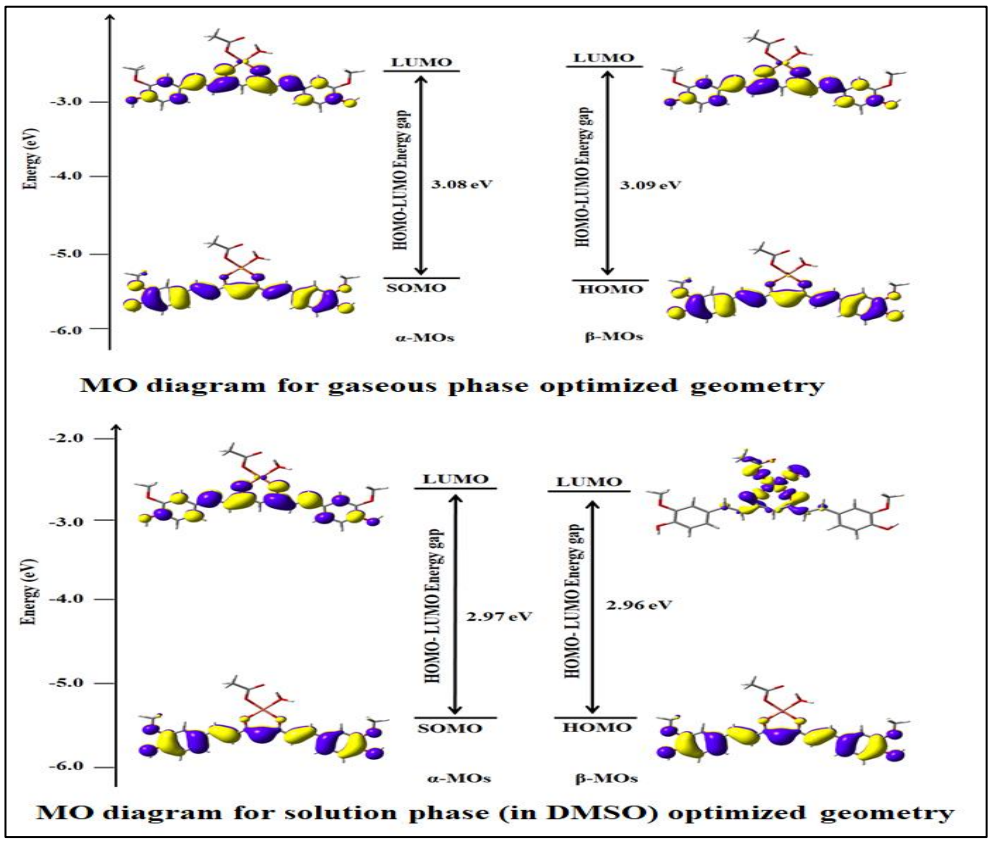


Figure 10: Frontier molecular orbitals (FMOs) of optimized geometries of $[Cu^{II}(Cur)(OCOCH_3)(OH_2)]$

Table 3: Some selected MOs of $[Cu^{II}(Cur)(OCOCH_3)(OH_2)]$ in ground state geometry along with their energies and percentage composition.

The Gas phase optimized structure:

For α-electrons:

Orbital	MO	Energy (eV)	% Composition			
			Cu	Curcumin	Water	Acetate
132	L+4	-0.03	0	100	0	0
131	L+3	-0.15	0	100	0	0
130	L+2	-0.24	89	3	6	2
129	L+1	-1.16	1	99	0	0
128	LUMO	-2.39	1	99	0	0
127	HOMO	-5.47	0	100	0	0

126	H-1	-5.81	0	100	0	0
125	H-2	-6.36	2	97	0	1
124	H-3	-6.55	16	58	5	21
123	H-4	-6.69	1	97	1	1

For β-electrons:

Orbital	**MO**	**Energy (eV)**	**% Composition**			
			Cu	Curcumin	Water	Acetate
131	L+4	-0.15	0	100	0	0
130	L+3	-0.23	89	3	6	2
129	L+2	-1.15	1	99	0	0
128	L+1	-2.29	70	18	6	7
127	LUMO	-2.37	1	99	0	0
126	HOMO	-5.40	6	0	100	0
125	H-1	-5.79	1	99	0	0
124	H-2	-6.32	3	95	1	1
123	H-3	-6.66	2	96	0	1
122	H-4	-6.88	1	96	0	3

The Solution phase (DMSO) optimized structure:

For α-electrons:

Orbital	**MO**	**Energy (eV)**	**% Composition**			
			Cu	Curcumin	Water	Acetate
132	L+4	-0.09	0	99	0	0
131	L+3	-0.12	0	100	0	0
130	L+2	-0.43	92	2	4	2
129	L+1	-1.27	1	99	0	0
128	LUMO	-2.60	1	99	0	0
127	HOMO	-5.57	0	100	0	0
126	H-1	-5.90	0	100	0	0
125	H-2	-6.51	1	98	0	0

124	H-3	-6.79	0	100	0	0
123	H-4	-6.88	17	63	5	15

For β-electrons:

Orbital	**MO**	**Energy (eV)**	**% Composition**			
			Cu	Curcumin	Water	Acetate
131	L+4	-0.12	0	100	0	0
130	L+3	-0.41	92	2	4	2
129	L+2	-1.27	1	99	0	0
128	L+1	-2.58	3	96	0	0
127	LUMO	-2.61	67	22	5	6
126	HOMO	-5.57	0	100	0	0
125	H-1	-5.89	0	100	0	0
124	H-2	-6.49	2	97	0	1
123	H-3	-6.78	1	99	0	0
122	H-4	-6.91	3	95	0	2

The gas phase optimized configuration shows that the highest singly occupied molecular orbital (SOMO) and LUMO of both spin-α and spin-β components are ligand centric (i.e. almost entire contribution comes from HCur forming the SOMO in each case) with practically negligible contribution from metal AOs (~ 1% contribution from Cu to form LUMO in both cases). Solution phase optimized geometry shows a similar trend i.e. a ligand (HCur) centric contribution (almost 100%) while forming SOMO for both spin-α and spin-β components.

While for spin-α, LUMO is totally from ligand moieties with practically no participation from metal AOs, for spin-β, LUMO is distributed over the ligand framework with an appreciable contribution from metal ion (67% Cu and 22% Curcumin). Introducing the complex to a dielectric medium reduces HOMO–LUMO energy gap both for spin-α and spin-β orbitals (Fig. 10**)**. These FMOs are handy in explaining the electronic structure and optoelectronic properties of the complex. For molecular crystals, HOMO–LUMO energy gap could be corroborated with optical

energy band gap as derived from UV-Vis absorption spectrum (Fig. 11). The optical energy band gap (E_g) derived from the equation $E_g = \frac{1240}{\lambda_{max}}$ eV, where λ_{max} is the wavelength corresponding to maximum absorption was found to be 2.877 eV, comparable to an average HOMO–LUMO energy gap of 2.965 eV for the complex in DMSO.

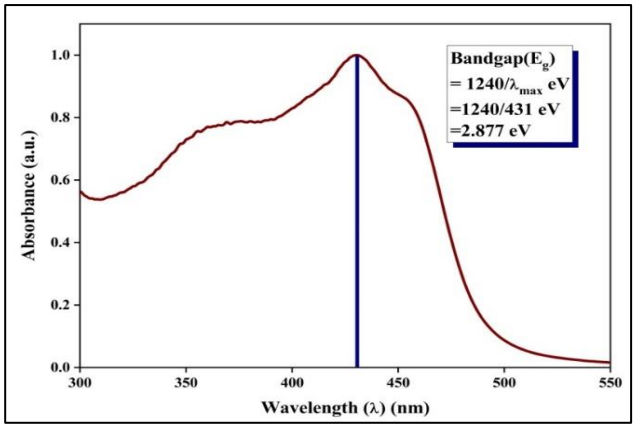


Figure 11: Experimental UV-vis absorption maximum with corresponding optical bandgap

9.4.2 Opto-electronic absorption property:

Opto-electronic property is useful for identifying the exact molecular geometry since excitation from a ground state to next excited state in a dielectric medium (DMSO) would produce similar absorption behavior as that measured experimentally in the same solvent. In case of DMSO, since there is a cut off wavelength for absorption (~ 268 nm) hence absorption spectrum of the complex shows dispersion below 300 nm. For this reason, experimental pattern below 350 nm was not considered instead spectrum was recorded up to 600 nm and compared with the calculated one (Fig. 12). The calculated electronic absorption spectrum in DMSO consists of multiple peaks supporting a multiple transition nature for the complex.

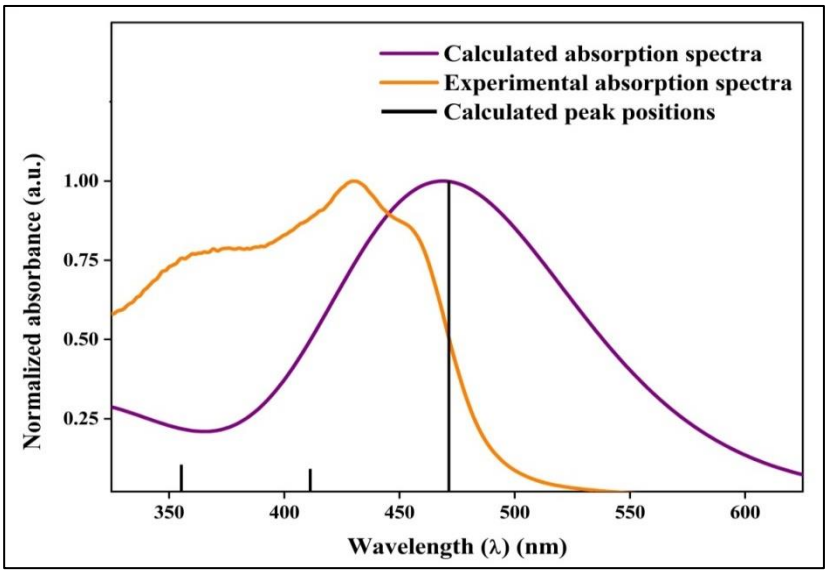


Figure 12: Comparison of experimental and theoretical UV-vis absorption spectra showing most feasible peak positions

Peaks in the experimental spectrum were assigned visually. The most probable transitions having maximum intensities ($f \geq 0.10$) close to experimental absorption peaks with corresponding excitation wavelengths, energy, oscillator strengths (f), character and C I coefficients are listed in Table 4 in ascending order of energy in which they appear in the spectrum. Charge-transfer transitions among different moieties of the complex viz. water molecule, acetate and HCur with varying amounts of metal to ligand contribution gives rise to excitation peaks, although intra-ligand charge transfer within HCur were seen to be mainly responsible. Time Dependent Density Functional Theory (TDDFT) calculation[45,46] of the ground state doublet geometry produces excited states showing slight spin contamination with fractional values of 0.004 to 0.017 (Table 4).

Table 4: A list of experimental UV-Vis transitions for [Cu(Cur)($OCOCH_3$)(OH_2)] in DMSO with corresponding theoretically calculated UV-Vis transitions with vertical excitation energies (E_{ex}), oscillator strengths (f) as obtained from TDDFT method in DMSO.

Experimental excitation values (nm)	Calculated excitation values (nm)	Excitation energy (eV)	Excited state involved	$<S^2>$/ Fractional diffrn. with ideal for the exct. state	Osc. strength (f)	Key transition involved	CI expansion coefficient
454/431	471.458	2.6298	D_8	0.754/0.004	1.5853	HOMO(A)→LUMO(A)(49%) HOMO(B)→L+1(B) (49%)	0.70209 0.69712
410	411.279	3.0146	D_{11}	0.760/0.010	0.1451	H-1(A)→LUMO(A) (51%) H-1(B)→L+1(B) (44%)	0.71509 0.66366
356	355.327	3.4893	D_{17}	0.767/0.017	0.1665	H-2(A)→LUMO(A) (43%) H-2(B)→L+1(B) (47%) H-2(B)→LUMO(B) (2%)	0.65917 0.68596 0.15045

9.4.3 Natural transition orbital analysis:

Excited state computation results were interpreted using natural transition orbital (NTO) analyses based on calculated transition density matrices.[47] Virtual/unoccupied and occupied NTOs are referred to as "electron/particle" and "hole" transition orbitals respectively. This allowed us to identify and visualize electronic transitions that were considered in terms of excitation from a hole-NTO to an electron-NTO for both spin-α and spin-β components with a weight average that this occupied-virtual pair contributes to excitation. NTOs for most relevant peaks are depicted in Fig.13.

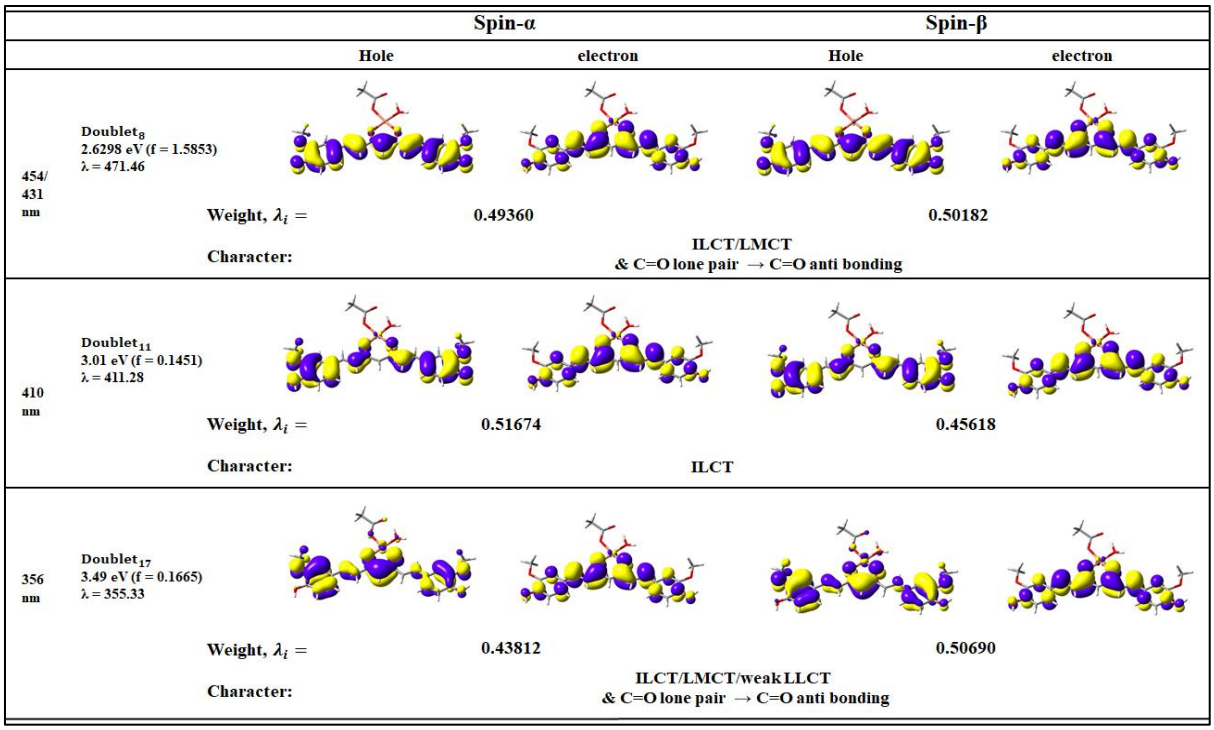


Figure 13: NTO analysis describing calculated UV-vis peak positions

While explaining excitation, the lowest energy transitions that were experimentally observed near 454 nm and 431 nm were found at 471.5 nm (2.63 eV, f = 1.5853) being the most prominent calculated peak. This transition is ascribed to π(HCur) → d_{xz} + π*(HCur) ILCT in association with some LMCT character together with lone pair (O) → antibonding (O) transition. The net electron transfer between ligand to metal fragments and within ligand fragments are 0.03076e and 0.95795e respectively. The next higher energy transition obtained experimentally at around 410 nm was computed and found at 411.28 nm (3.01 eV, f = 0.1451); attributed to π(HCur) → π*(HCur) ILCT. Net electron transfer within ligand fragments is 0.95108e. UV excitation near the experimentally observed peak of 356 nm was found at 355.33 nm (3.489 eV, f = 0.1665) and attributed to d_{yz}(Cu) + π(HCur + Acetate + water) → d_{xy}(Cu) + π*(HCur) ILCT together with slight LMCT nature and a very weak LLCT, where intra-ligand and ligand to ligand net electron transfers were 0.89872e and 0.04376e respectively.

9.4.4 Quantum descriptor analysis:

It is important to comprehend the influence of frontier molecular orbitals on a molecule's kinetic stability, electrical conductivity and chemical reactivity. Soft molecules exhibit a limited difference in energy between their highest occupied molecular orbital (HOMO) and lowest unoccupied molecular orbital (LUMO). They exhibit increased biological and chemical reactivity. Molecules with substantial HOMO-LUMO energy gap demonstrate decreased biological response, remarkable stability and decreased reactivity towards other substances. Intramolecular charge transfer (ICT) is possible when there is a narrow energy difference between electron-donor and electron-acceptor groups, enabling movement of charge in the molecule. Molecular systems that effectively take electrons often have a lower energy level in their lowest unoccupied molecular orbital (E_{LUMO}), while molecular systems that effectively donate electrons tend to have a higher energy level in their highest occupied molecular orbital (E_{HOMO}). Table 5 displays a comparison of quantum descriptor of HCur and $[Cu^{II}(Cur)(OCOCH_3)(OH_2)]$ following completion of geometry optimization. The small HOMO-LUMO gap enables electron donation and electron uptake. Electron affinity of $[Cu^{II}(Cur)(OCOCH_3)(OH_2)]$ is markedly greater than HCur, indicating that the complex should exhibit a pronounced inclination to interact with nucleotides or amino acid residues in DNA and/or protein by attracting electron density towards itself. On the other hand, a soft molecule is defined by a reduced η value,[48,49] as stated in *Eq. 26 of Chapter 6*, Experimental. Upon binding to Cu^{II}, HCur undergoes metamorphosis resulting in enhanced flexibility and facilitating more electron delocalization and permitting higher quantity of non-covalent interactions. A high value of ω, the electrophilicity index implies a significant affinity for electron-rich compounds.[48,49] The Cu^{II} complex demonstrates higher affinity towards biological macromolecules in comparison to HCur.

Table 5: Quantum descriptor for optimised HCur and [Cu(Cur)] in eV with B3LYP functional coupled with 6-31G+(d,p) for C,H,O and SDD basis set for Cu^{II}

Compound	HOMO	LUMO	ΔE	IP	EA	χ	η	M	σ	ω
HCur	-5.47	-2.27	3.20	5.47	2.27	3.87	1.60	-3.87	0.31	4.68
[Cu(Cur)]	-5.60	-2.52	3.08	5.60	2.52	4.06	1.54	-4.06	0.32	5.35

9.4.5 MEP surface analysis:

Fig. 14 displays the molecular electrostatic potential surface of $[Cu^{II}(Cur)(OCOCH_3)(OH_2)]$ which was calculated using Gauss view 6 software.[50] Calculations were conducted with DFT/B3LYP functional and 6-31G+(d,p) as basis set in conjunction with SDD (for Cu^{II}). Molecular Electrostatic Potential (MEP) is an essential tool for examining and establishing a relationship between molecular structure and physiochemical characteristics of various compounds that includes biomolecules and pharmaceuticals. Knowledge of charge distribution can be employed to ascertain the manner in which molecules interact and to identify sites for both intra and inter-molecular interactions.[51] The MESP map is a graphical representation of the distribution of electron density. It is widely used to identify regions with negative and positive electrostatic potentials that can be useful in recognizing areas susceptible to electrophilic and nucleophilic attack.[52] The MESP maps can be used to ascertain the binding mode between a substrate and receptor. The MESP maps utilize a color scheme to depict distinct electron charges: red, indicates abundance of electrons, orange, represents partial negative charge, yellow, indicates somewhat electron-rich region, blue, represents positive charge and green, indicates neutral regions.[51,52] From Fig. 14 it is seen that the most negative region is located on an acetate oxygen making it most susceptible to electrophilic attack. The complex had faint blue areas on methoxy and phenolic hydrogen indicating weak interactions like hydrogen bonding between

phenolic –OH and –OCH_3 groups. The green area represents regions of zero potential that are neutral sites located on hydrogen atoms found in phenyl rings. The electrostatic potential values span from -956.86 KJ/mol (red) to 278.25 KJ/mol (blue) to denote existence of both nucleophilic and electrophilic regions. This implies the molecule can participate in biological and chemical reactions making it suitable for its use in medicinal chemistry.

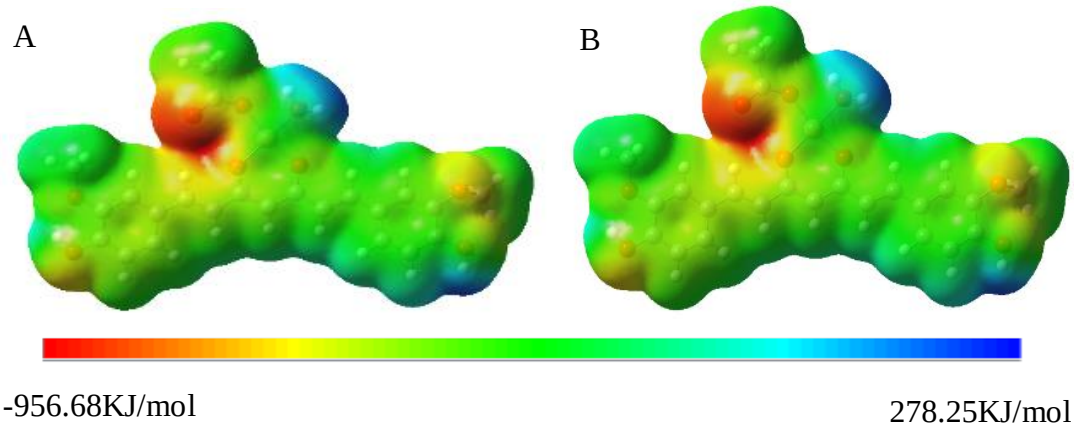


Figure 14: Molecular electrostatic potential surface of [Cu^{II}(Cur)($OCOCH_3$)(OH_2)] in (A) Gas phase and (B) solution phase

9.4.6 Non-covalent interactions (NCI) & Reduced density gradient (RDG) analysis:

Reduced density gradient (RDG) is a robust method for investigating non-covalent interactions by analyzing distribution of electrons and their derivatives.[53,54] This technique has demonstrated the capacity to differentiate between different types of non-covalent interactions present in small organic molecules that act as ligands and their corresponding metal complexes. The equation utilized for calculating RDG is [53,54]

$$RDG = \frac{1}{2(3\pi^2)^{1/3}} \frac{|\nabla\rho|}{\rho^{4/3}}$$

Through a careful analysis of values of low and high-density gradients, one can establish the existence of both weak and strong interactions. Graphs that depict the relationship between RDG

and low-gradient peak density (ρ) provide valuable insights into the intensity of an interaction. One possible way to distinguish between different types of interactions is by using electron density and sign of second eigenvalues. The sign of the parameter λ_2 is crucial in distinguishing between bonded interactions ($\lambda_2 < 0$) and non-coupling interactions ($\lambda_2 > 0$). Three different types of interactions can be categorized based on specific principles. Attraction is indicated by negative sign of values (λ_2). Another hypothesis suggests the presence of a strong repulsion-like interaction, supported by significant and positive values of the sign (λ_2). Weak interactions also referred to as van der Waals interactions are typically characterized by values very close to zero. Fig.15 shows projected RDG plots for [Cu^{II}(Cur)($OCOCH_3$)(OH_2)]. Several types of interactions were used to explain the relationship between hydrogen, oxygen, metal ion and carbon within the molecule. From the observed red color, it seems there is repulsion in the system; more precisely in the vicinity of two carbonyl oxygens close to the binding site on the metal. Van der Waals interactions are represented by a green color. Blue indicates a noteworthy hydrogen bond interaction in the system.

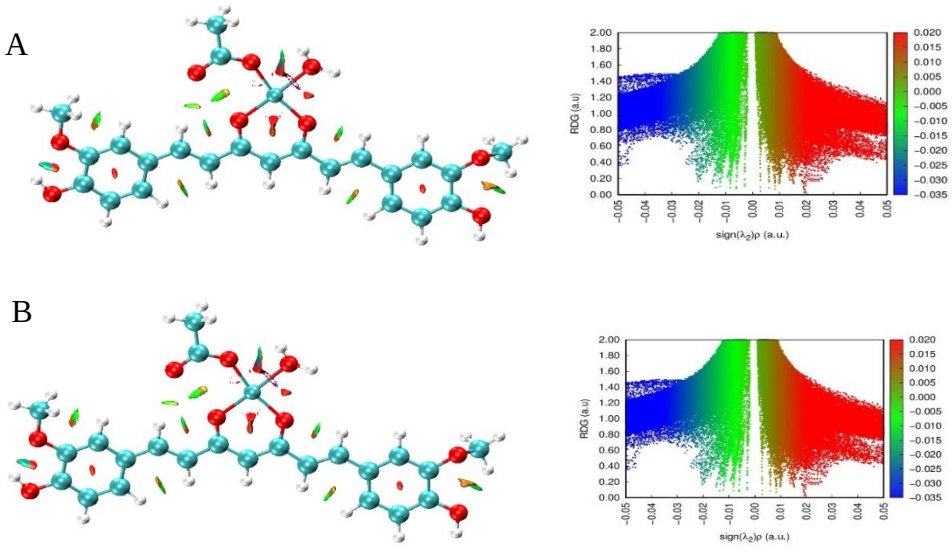


Figure 15: NCI (right) and RDG (left) plot of optimized [Cu^{II}(Cur)($OCOCH_3$)(OH_2)] molecule in (A) Gas Phase , (B) Solution (DMSO) phase

9.4.7 ELF and LOL analysis :

The studies ELF (Electron Localization Function) and LOL (localized Orbital Locator) primarily focus on analysis of topological surfaces. Research conducted using Multiwfn software package[55] has shown a significant likelihood of locating an electron pair on the surface of a molecule as indicated by ELF and LOL. In Fig. 16, the colour shades and relief map of ELF and LOL is shown. The relief map highlights electron environment around each atom; variations in peak area indicate either a large or contracted electron density. The chemical content of ELF and LOL is homogenous due to their dependence on kinetic energy density. The ELF theory explains the distribution of electron pairs, while LOL describes overlapping of localized orbitals caused by gradient of orbitals.[56] The ELF map is designed to cover a range from 0.0 to 1.0. Interestingly, the region below 0.5 displays a delocalized electronic region[57] while LOL reaches significant values above 0.5 in areas where electron density is primarily influenced by electron localization.[58] The different shades of colour on ELF and LOL maps provide evidence of the presence of bonding and non-bonding electrons. In particular, the red colour surrounding hydrogen atoms indicate the presence of these electrons. The presence of a green-yellow colour around oxygen atoms (e.g. O20, O21, O29, O30) indicates a strong concentration of electrons that may be attributed to factors such as covalent bond formation, a lone pair of electrons or a nuclear shell in that particular region. The blue colour surrounding the carbon and oxygen atoms indicate the presence of a delocalized electron cloud. The central region of a hydrogen atom in LOL appears white due to electron density surpassing the upper limit of the colour scale.[58]

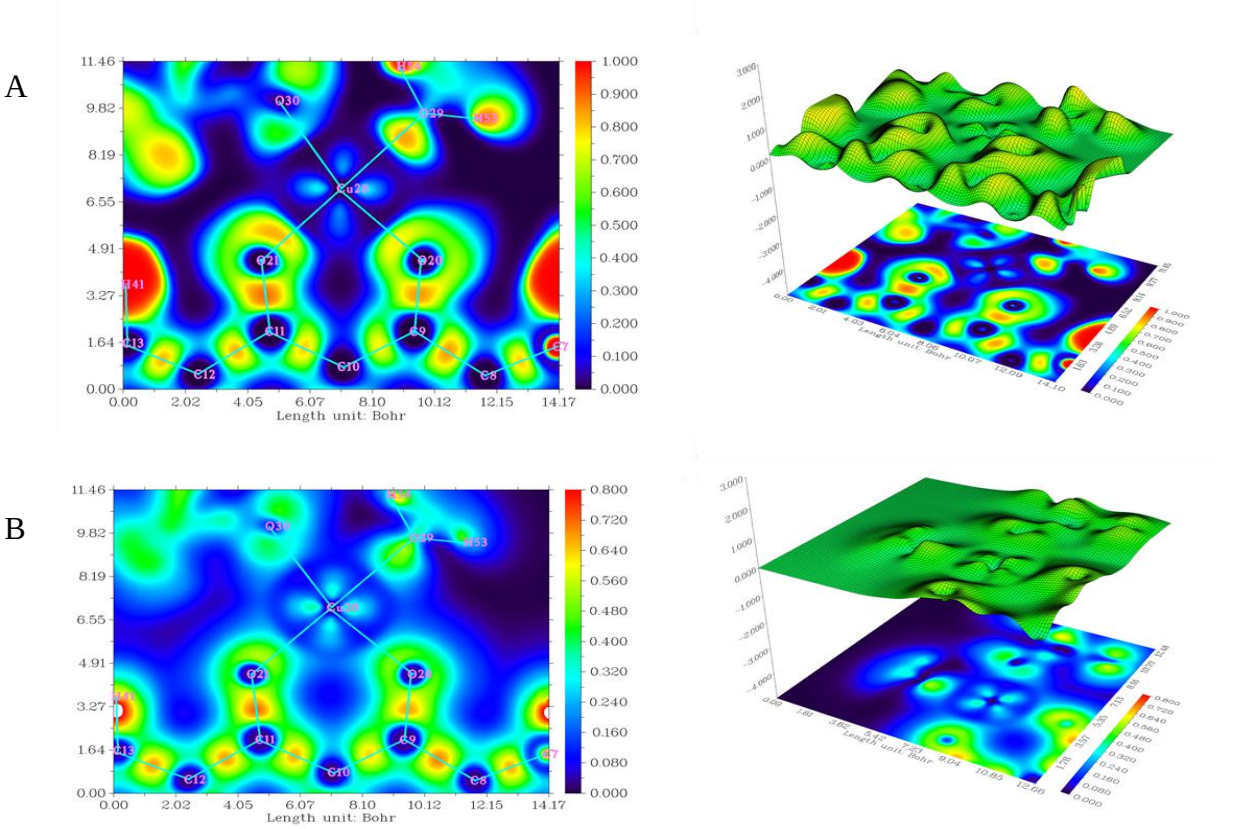


Figure 16: Electron localization function (ELF) maps (A) and localized orbital locator (LOL) maps (B) of optimized [Cu^{II}(Cur)($OCOCH_3$)(OH_2)] molecule

9.5 Comparative stability analysis of the Cu^{II} complex under physiological conditions

9.5.1 Followed by UV-Vis spectroscopy:

Considering the chemical instability of HCur in different media, a study was carried out to ascertain if complex formation of HCur with Cu^{II} could help in stabilizing it under physiological conditions. To answer this question the stability of Cu(Cur) in different biological milieu was examined and compared with that of HCur. As reported earlier[59] intensity of the absorption spectrum of HCur decreased significantly over time in buffer solutions; more than 50% of its original intensity was lost in the first 20 minutes of incubation in PBS. In contrast, absorption spectrum of Cu(Cur) did not decrease (Fig. 17) but remained stable over time in PBS. Such results

indicate the complex is reasonably stable in physiological buffer and in different microbiological media. Since cytosolic environment is reducing, the stability of Cu(Cur) and Curcumin was studied in the presence of a common reducing agent, dithiothreitol (DTT).[60,61] In line with previous findings in this regard,[59,61] it was observed that a much faster rate of degradation of Curcumin was observed in the presence of DTT; Curcumin being lost to an extent that was more than 50% of its absorption intensity in the first 5 minutes of incubation. On the other hand, Cu(Cur) was stable as absorption intensity did not decrease even after 20 minutes of incubation in presence of DTT (Fig. 17). Hence, as evident from Fig. 17, complex formation of Curcumin results in enhanced stability in biological medium even under reducing conditions and at physiological pH, unlike that observed for Curcumin, when present alone.

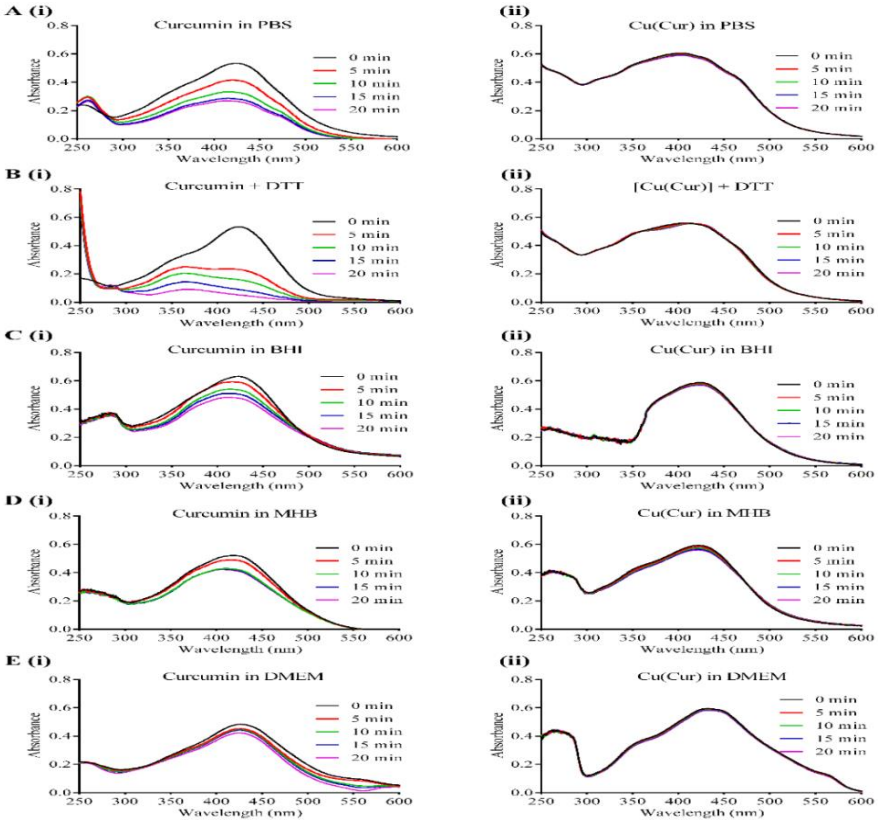


Figure 17: UV-Visible spectra of Curcumin and Cu(Cur) in (A) PBS buffer, (B) in presence of 10 μM DTT (C) BHI (D) MHB and (E) DMEM media

9.5.2 Followed by HPLC:

HCur and Cu(Cur) were dissolved in phosphate buffer and from the time of dissolution of the compounds, HPLC was performed at different time intervals on a C_{18} column with 12% THF, 5% CH_3CN, 2% acetic acid in water as mobile phase.[17] In case of HCur, a steady degradation identified by a decrease in peak height for it was observed (*Fig. 11, Chapter 7*).[17] Fig. 18 show chromatograms recorded for Cu(Cur) at different time intervals following dissolution in phosphate buffer. For the complex, degradation was a lot restricted. An overlay of chromatograms obtained for HCur and the Cu^{II} complex clearly demonstrates this (Fig. 19). It is seen from chromatograms in Figure 19 (b) recorded after two hours and Figure 19 (c) recorded after 24 hours from the time of dissolution of the compounds that while there is a progressive degradation in case of HCur with a simultaneous formation of different degraded products, in case of the complex this was not observed. Fig. 19 is also clearly indicative of the fact that degradation of HCur is a lot restricted following its complex formation with Cu^{II}. Thus for the complex, there is a high possibility of HCur remaining as "one unit" and not being degraded into different products. Showing this is an important aspect of the performed work, one of the main intentions of forming a metal complex with Curcumin. Thus it is apparent that degraded products of HCur like vanillin, vanilic acid and ferulic acid are present in solution to a considerable extent alongside HCur when it is present alone in a medium (*Fig. 12 Chapter 7*) but when HCur is bound to a metal centre, even after a similar time has elapsed after its dissolution in phosphate buffer no degraded products were identified by HPLC indicating HCur bound to Cu^{II} in a complex does not degrade (Fig. 18).

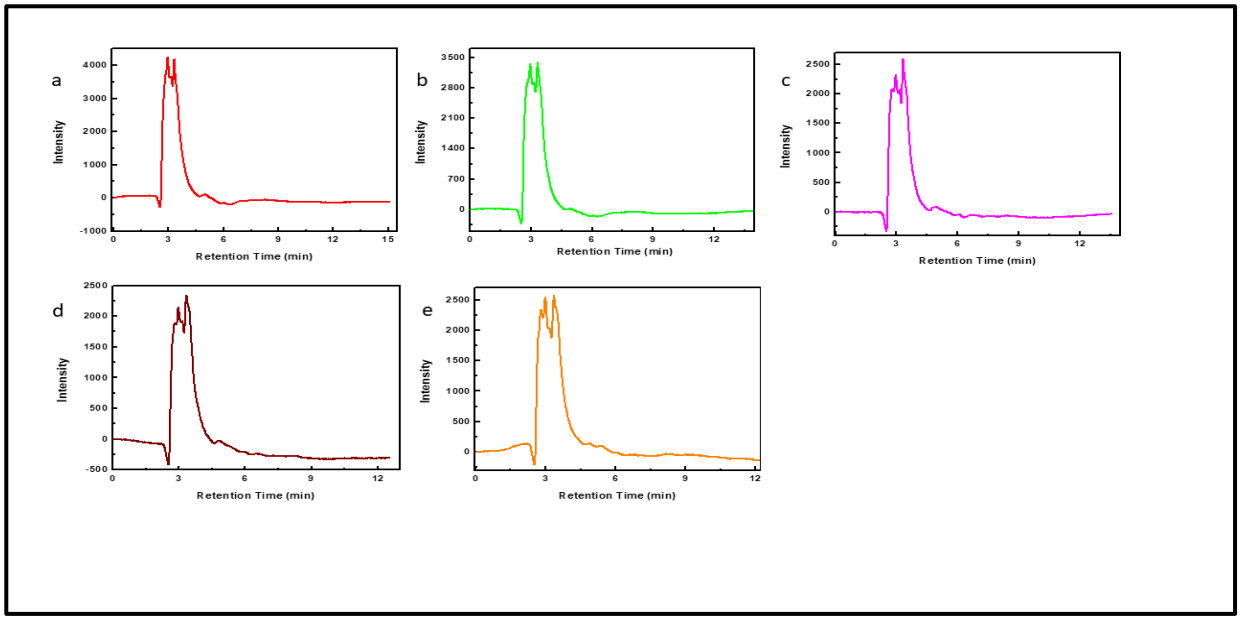


Figure 18: Chromatograms obtained for Cu(Cur) (100 µM) by HPLC after it was injected (a) immediately, (b) after 20 minutes, (c) after 75 minutes, (d) after 2 hours and (e) after 24 hours from the time of its dissolution in 0.1 M phosphate buffer. Column: C-18, Eluent: 12% THF, 5% CH_3CN, 2% acetic acid in water.

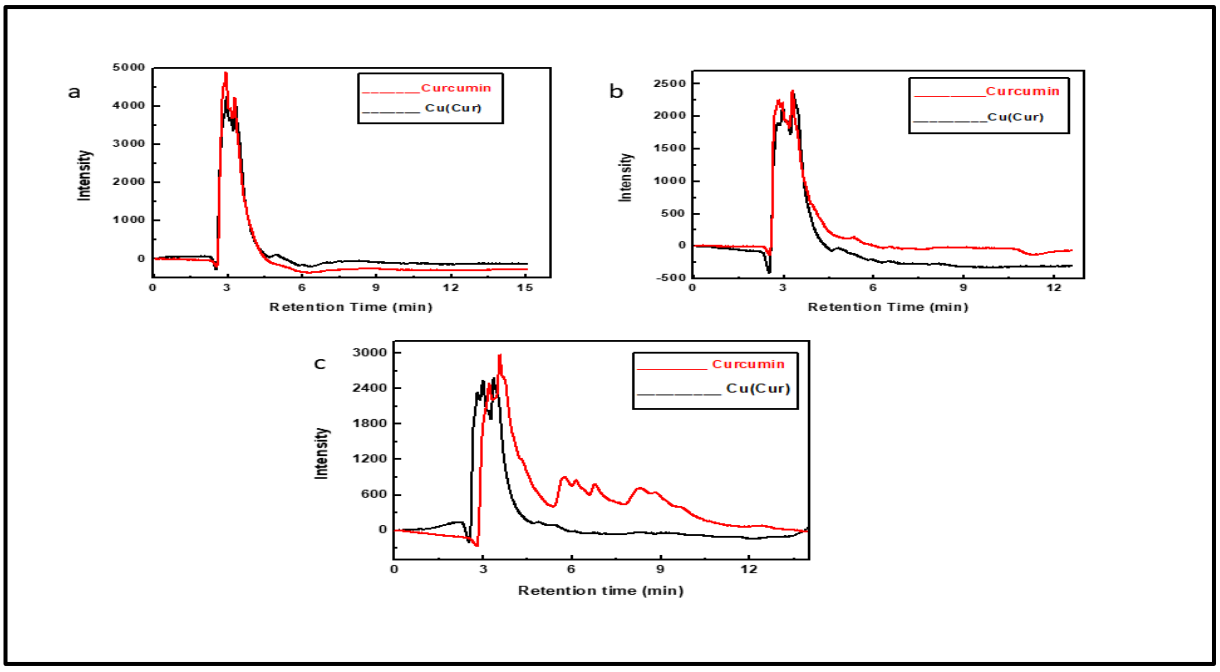


Figure 19: Chromatograms obtained following HPLC of curcumin (—) and Cu(Cur) (—) at (a) immediately, (b) at 2 hours and (c) at 24 hours from the time of dissolution of the compounds in PBS. Column: C-18, Eluent: 12% THF, 5% CH_3CN, 2% acetic acid in water.

9.6 Interaction of $[Cu^{II}(Cur)(OCOCH_3)(OH_2)]$ with calf thymus DNA

The complex was titrated with calf thymus DNA at constant pH (~ 7.4) and ionic strength (~ 0.15 mM) of the medium. A gradual decrease in absorbance at 430 nm helped to evaluate interaction between the complex and DNA (Fig. 20).

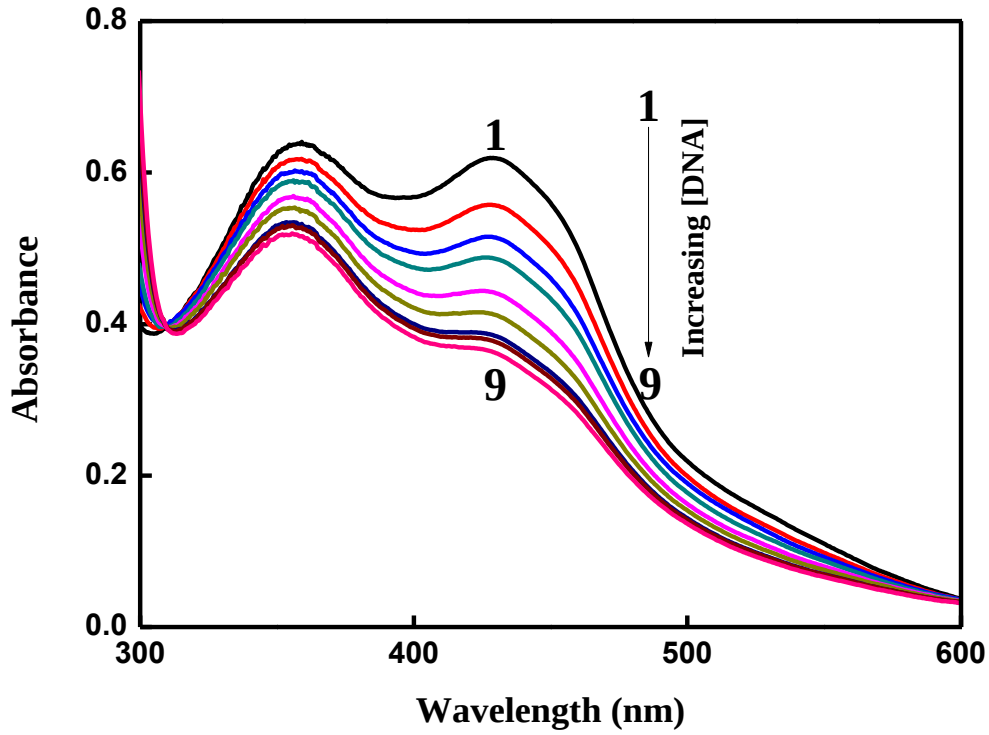


Figure 20: Absorption spectra of 21 μM $[Cu(Cur)(OCOCH_3)(OH_2)]$ in the absence (1) and presence of different concentrations of calf thymus DNA (2) 85.55 μM, (3) 169.85 μM, (4) 280.32 μM, (5) 494.91 μM, (6),701.450 μM (7) 948.96 μM, (8) 1044.82 μM, (9) 1231.39 μM;[NaCl] = 150 mM, pH = 7.4,Temp. = 298K.

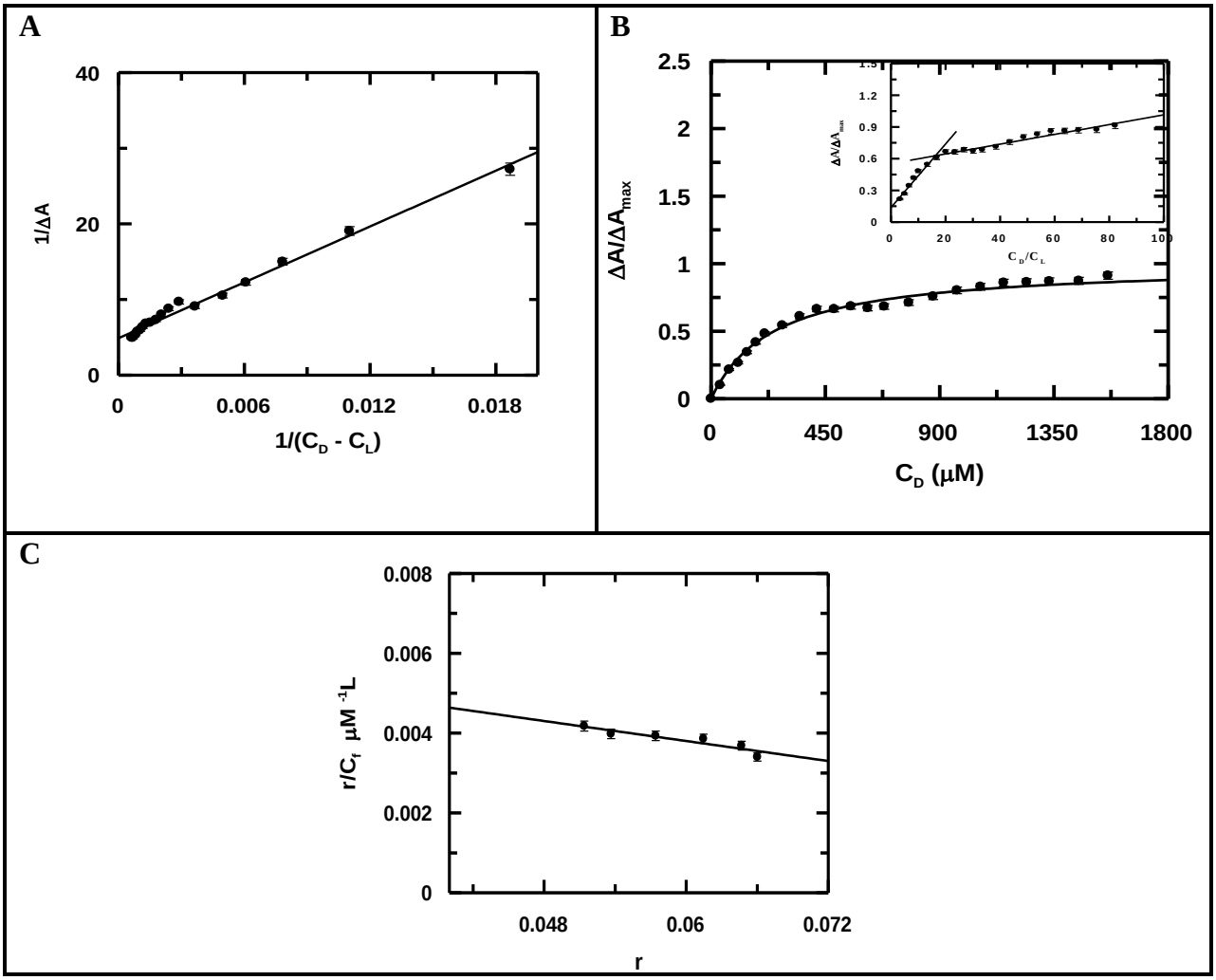


Figure 21 :(A) Double reciprocal plot for the interaction of [Cu(Cur)] with calf-thymus DNA to evaluate apparent binding constant (K_{app}) of the complex to DNA, (B) binding isotherm for [Cu(Cur)] interacting with calf thymus DNA when $\Delta A/\Delta A_{max}$ was plotted against concentration of DNA; the dark line is the fitted data obeying Eq.33(*Chapter 6, Experimental*). Inset: Plot of normalized increase in absorbance as a function of mole-ratio of calf thymus DNA to [Cu(Cur)]. (C) A modified Scatchard plot for interaction of [Cu(Cur)] with calf thymus DNA; [Cu(Cur)] = 21.0 μM, [NaCl] = 150 mM, pH = 7.4 (30 mM phosphate buffer), Temp.= 308K.

Fig. 21 (A) is a plot of $1/\Delta A$ versus $1/[C_D\text{-}C_L]$ [Eq. 31, *Chapter 6, Experimental*] that provide values for K_{app} (= K_d^{-1}) from three independent titrations.[62-66] Average of these values was 3.98×10^3 M^{-1}. Fig. 21 (B) is a plot of $\Delta A/\Delta A_{max}$ versus concentration of calf thymus DNA to which non-linear curve fitting was applied (Eqs. 32 & 33, *Chapter 6, Experimental*). Three independent titrations provide an average apparent binding constant of 4.03×10^3 M^{-1} at 298 K. Inset of Fig. 21 (B) is a plot that provides a value for n_b (= 18.0), number of nucleotides bound to the complex following interaction with DNA.[62-66] The titration data was also fitted to a modified form of the Scatchard equation (Eq. 35, *Chapter 6, Experimental*, Fig. 21 C) yielding values for K* and n (= n_b^{-1}).[67] Values obtained from the Scatchard equation were close to that obtained from other methods of analyses (Eq. 31-33, *Chapter 6, Experimental*), thus justifying methods that calculate them. Titration of the complex with DNA is important for a number of reasons. Since a titration of HCur when present alone is not possible with DNA owing to its physiological instability etc. in solution, a monomeric complex of Cu^{II} with HCur, in which HCur does not undergo degradation makes it a good representative to realize HCur's ability to bind to DNA.[17] However, while considering the data, it should be kept in mind that for the complex there would be an influence due to the metal centre as well.[63, 64, 68,69] Hence, from this data one may realize with necessary conditions mentioned above what would have happened had HCur remained as a "single unit" in solution and interacted with DNA. An idea to this effect on the binding of HCur to DNA is important. Had HCur been able to bind DNA alone the value would then be close to that realized for the complex or may be somewhat less depending on the contribution of Cu^{II} in the binding process.[63,64,68,69] Nevertheless, an idea on HCur's binding to DNA was obtained where no data was earlier available. From an estimate of the binding constant, it would be possible to explain the role of HCur in biological media, whose manifestation is often reported to be beneficial.[11-13]

9.6.1 Interaction of $[Cu^{II}(Cur)(OCOCH_3)(OH_2)]$ with calf thymus DNA at different temperatures

Titration of the complex with DNA performed at different temperatures was plotted according to Eqs. 31-35 (*Chapter 6, Experimental*). The results are shown in Table 6. Analysis of the data indicates that with an increase in temperature there is a slight increase in the affinity of the complex to bind to DNA manifested by increasing values for binding constants. Hence, plots of $\ln K_{app}$ or $\ln K^*$ for the complex against 1/T were obtained as straight lines with negative slopes (Eq. 37, *Chapter 6, Experimental*) (Fig 22). Change in enthalpy (ΔH) and entropy (ΔS) were determined from the slope and intercept of such van't Hoff plots. The change in free energy (ΔG) being negative indicates binding is favoured (Fig.22)

Table 6: Binding parameters of $[Cu^{II}(Cur)(OCOCH_3)(OH_2)]$ with calf thymus DNA at different temperatures studied using UV-Vis spectroscopy

Temp (K)	Apparent binding constants $K_{app}\times10^{-3}(M^{-1})$		Site size (n_b) from mole ratio plot	Overall binding constant $K^*\times10^{-4}$ (M^{-1}) [$K^*=K_{app}\times n_b$] Eq. 31 *(Chapter 6: Expt.)*	Overall binding constant $K'\times10^{-4}$ (M^{-1}) (From Scatchard plot) Eq. 35 *(Chapter 6: Expt.)*	Site size (n_b) from Scatchard plot
	From double reciprocal plot Eq. 31 *(Chapter 6: Expt.)*	From non-linear fit Eq. 33 *(Chapter 6: Expt.)*				
293	3.70	3.75	10.0	3.73	4.10	9.09
298	3.98	4.03	18.0	7.21	4.81	10.0
303	4.37	4.39	17.0	7.45	3.33	16.0
308	4.64	4.69	18.0	8.40	5.19	20.8

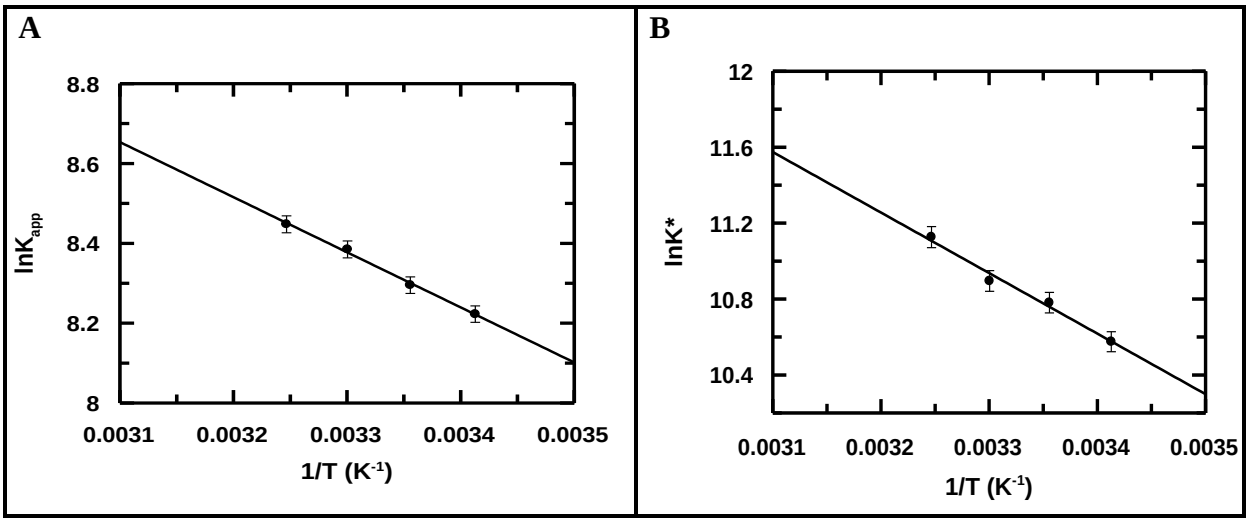


Figure 22: (A)Van't Hoff plots for binding of [Cu^{II}(Cur)($OCOCH_3$)(OH_2)] with calf thymus DNA considering apparent binding constants at different temperatures. (B) Van't Hoff plots for the binding of [Cu^{II}(Cur)($OCOCH_3$)(OH_2)] with calf thymus DNA considering overall binding constants at different temperatures.

Since, interaction of [Cu^{II}(Cur)($OCOCH_3$)(OH_2)] with calf thymus DNA results in positive values for binding enthalpy and binding entropy (Fig. 22, Table 6) it clearly demonstrates binding is entropically driven. For entropy driven molecule-DNA interactions, solvent molecules and counter ions are expelled from bound surfaces of both participating substances as they bind to each other, for which there is a gain in entropy. Such coming together of reactants is reported to release bound water from the hydration zone of the minor groove and release counter ions from bound surfaces of interacting partners; being the cause for increase in entropy.[63-65] This is counterbalanced by some enthalpy related unfavourable effects that occur simultaneously, like breaking of hydrogen bonds and non-covalent interactions due to solvent molecules and counter ions existing either in unbound form of DNA or in the substance which is to bind to the DNA (here the Cu^{II} complex). In some cases, binding site is characterized by a widening of the minor

groove to accommodate the molecule.[70-72] All of these show up as a positive value for the change in enthalpy. In such entropically driven molecule-DNA interactions, hydrophobic interactions have a major role.[73,74] In case of neutral DNA intercalators for example, intercalation occurs via entropically driven interactions.[75] In our case, since Curcumin is also sparingly soluble in water, it is likely that interaction of the complex with DNA could be stabilized by hydrophobic interactions. Again, absence of a net charge on the complex permits a comparison with some neutral DNA intercalators.[76] The fact that binding could be stabilized by hydrophobic interactions is also reflected in the corresponding ΔH and ΔS values obtained.

Previous reports indicate that the two common binding modes for small molecules to bind to DNA are intercalation and groove-binding.[76-78] While intercalation is mostly favoured for planar and aromatic substances that insert between DNA base pairs leading to unwinding and lengthening of the double helix, groove binding does not disturb the duplex structure but fits nicely into the minor groove with only a slight distortion to the structure. Calorimetric studies have determined enthalpic and entropic contributions to DNA binding for different compounds enriching the literature and revealing distinctive thermodynamic signatures that allow one to either identify or differentiate groove-binders from intercalators.[73-79] Such data reveal groove-binding interactions are those that provide a favorable entropy contribution to free energy, while intercalators are those that have an unfavorable entropy contribution but a favorable enthalpy contribution. Predominantly, groove-binding is entropy driven while intercalation is enthalpy driven. Although the molecular basis of such contrasting thermodynamic signatures for the two binding modes cannot be generalized for all molecules that interact with DNA, however they do provide a good idea that enables one to categorize new DNA binding agents into different binding types, considering aspects like structure of the participating substance, changes in ΔH and ΔS.

Table 7: Thermodynamic parameters for interaction of [Cu^{II}(Cur)($OCOCH_3$)(OH_2)] with calf thymus DNA in 30mM phosphate buffer (pH ~7.4), ionic strength = 0.15 M

	ΔG(Kcal/mole)	ΔH(Kcal/mole)	ΔS(e.u)
Considering lnK_{app}versus 1/T	-4.897	2.732	25.60
Considering lnK^*versus 1/T	-6.348	6.314	42.49

From the discussion above and considering existing literature in this regard,[73-79] it may be said [Cu^{II}(Cur)($OCOCH_3$)(OH_2)] interacts with calf thymus DNA as a groove binding agent.

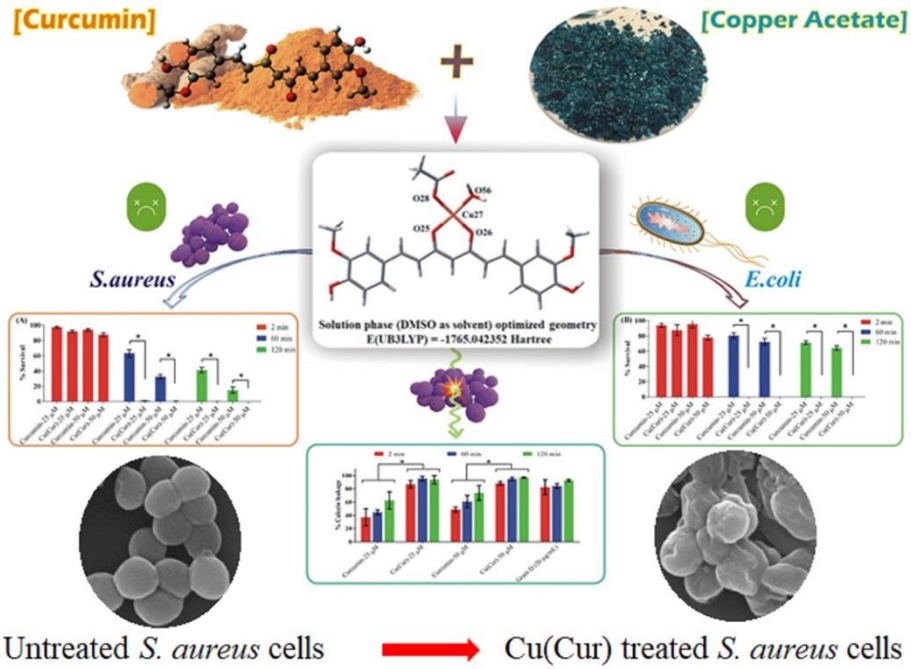
9.7 Biological applications of the prepared [Cu^{II}(Cur)($OCOCH_3$)(OH_2)] complex

Biological attributes of complex formation for the compound [Cu^{II}(Cur)($OCOCH_3$)(OH_2)] prepared by me (Mr. Tanmoy Saha) during my research work was subjected to several investigations through a collaboration in the laboratory of Prof. Kasturi Mukhopadhyay at the School of Environmental Sciences, Jawaharlal Nehru University, New Delhi. There, studies were performed with regard to antibacterial activity on *S. aureus* and *E. coli strains,* a study was done to realize the mechanism of antibacterial action due to HCur and the Cu(II) complex exploring membrane permeabilization of *S. aureus* as realized from calcein leakage assay, assessment of membrane integrity in *S. aureus* due to HCur and the Cu(II) complex by fluorescence microscopy, evaluation of membrane damage in *S. aureus* using fluorescence microscopy, morphological changes of the cell membrane in *S. aureus* induced *by* HCur, its Cu(II) complex and gramicidin D as realized through the use of a scanning electron microscope (SEM), that of ultrastructural changes in *S. aureus* induced *by* HCur, the Cu(II) complex and gramicidin D as recorded using a transmission electron microscope (TEM), potential toxicity studies of Cu(Cur) on mammalian cells

viz. a non-hemolytic and non-toxic activity study and that of cytotoxic potential on RBCs and 3T3 fibroblast cells. In addition to the hemolytic assay, MTT assay was also carried out to further rule out any potential cytotoxicity on mammalian cells. The outcome of several studies mentioned above is encouraging and suggests a requirement for further investigations with the prepared Cu(II) complex of Curcumin.

All of that mentioned above is showcased in our publication mentioned below:

Kumar, P., Saha,T., Behera, S., Gupta, S., Das, S., Mukhopadhyay, K., *2021.* Enhanced efficacy of a Cu^{2+} complex of curcumin against Gram-positive and Gram-negative bacteria: Attributes of complex formation *Jour. Inorg. Biochem., 222, 111494.*



References:

1. B. B. Aggarwal, C. Sundaram, N. Malani, and H. Ichikawa; Curcumin: the Indian solid gold. In: The molecular targets and therapeutic uses of curcumin in health and disease. *Springer, Boston, MA.*, **2007**, 595, 1-75.
2. J. S. Jurenka; Anti-inflammatory properties of curcumin, a major constituent of Curcuma longa: a review of preclinical and clinical research. *Alternative Medicine Review.*, **2009**,14, 141-153.
3. T. Ak, İ.Gülçin; Antioxidant and radical scavenging properties of curcumin. *Chemico-bi*Ak, *ological Interactions.*, **2008**,174, 27-37.
4. R. Wilken, M. S. Veena, M. B. Wang, E. S. Srivatsan; Curcumin: A review of anti-cancer properties and therapeutic activity in head and neck squamous cell carcinoma. *Mol. Cancer*., **2011**, 10:12.
5. S. Wanninger, V. Lorenz, A. Subhan, F. T. Edelmann; Metal complexes of curcumin–synthetic strategies, structures and medicinal applications. *Chem. Soc. Rev.*, **2015**, 44, 4986-5002.
6. S. Y. Teow, K. Liew, S. A. Ali, A. S. B. Khoo, S. C. Peh; Antibacterial action of curcumin against Staphylococcus aureus: a brief review. *Journal of Tropical Medicine*., **2016**, 2853045.
7. A. Goel, A. B. Kunnumakkara, B. B. Aggarwal; Curcumin as "Curecumin": from kitchen to clinic. *Biochem. Pharmacol*., **2008**, 75, 787-809.
8. K. Neelofar, S. Shreaz, B. Rimple, S. Muralidhar, M. Nikhat, & L. A. Khan; Curcumin as a promising anticandidal of clinical interest. *Can. Jour.Microbiol.*, **2011**, 57, 204-210.

9. P. Tyagi, M. Singh, H. Kumari, A. Kumari and K. Mukhopadhyay; Bactericidal activity of Curcumin I is associated with damaging of bacterial membrane. *PloS one 10*., **2015**, e0121313.

10. R. A. Sharma, W. P. Steward, A.J. Gescher; Pharmacokinetics and pharmacodynamics of Curcumin. *Adv. Exp. Med. Biol*., **2007**, 595, 453-470.

11. R. Banerjee; Inhibitory effect of Curcumin-Cu(II) and Curcumin-Zn(II) complexes on amyloid-beta peptide fibrillation, *Bioinorg. Chem. Appl*., **2014**, 325873.

12. S. Banerjee, P. Prasad, A. Hussain, I. Khan, P. Kondaiah, A. R. Chakravarty; Remarkable photocytotoxicity of curcumin in HeLa cells in visible and arresting its degradation on oxovanadium (IV) complex formation. *Chem. Comm*., **2012**, 48, 7702-7704.

13. K. I. Priyadarsini; The chemistry of Curcumin: From extraction to therapeutic agent. *Molecules*., **2014**, 19, 20091-20112.

14. M. D. Cas and, R. Ghidoni; Dietary Curcumin: Correlation between bioavailability and health potential, *Nutrients*., **2019**; 11(9), 2147.

15. S. B. de Souza Ferreira and M. L. Bruschi; Improving the bioavailability of curcumin: is micro/nanoencapsulation the key?, *Ther Deliv*.,**2019**, 10, 83-86.

16. P. Anand, A. B. Kunnumakkara, R. A. Newman, B. B. Aggarwal; Bioavailability of Curcumin: Problems and promises, *Mol. Pharmaceutics.*, **2007**, 4, 807–818.

17. Y. J. Wang, M. H. Pan, A. L. Cheng, L. I. Lin, Y. S. Ho, C. Y. Hsieh, J. K. Lin; Stability of curcumin in buffer solutions and characterization of its degradation products. *J PharmBiomed. Anal.*, **1997**, 15**,** 1867-1876.

18. K. Mitra, S. Gautam, P. Kondaiah, A. R. Chakravarty; Platinum(II) complexes of Curcumin showing photocytotoxicity in visible light. *Eur. J. Inorg. Chem*. **2017**, 1753-1763.

19. S. Wanninger, V. Lorenz, A. Subhan , F. T. Edelmann.; Metal complexes of curcumin – synthetic strategies, structures and medicinal applications. *Chem. Soc. Rev.*, **2015**, 44, 4986-5002.

20. F. Caruso, M. Rossi, A. Benson, C. Opazo, D. Freedman, E. Monti, M. B. Gariboldi, J. Shaulky, F. Marchetti, R. Pettinari , C. Pettinari; Ruthenium–Arene complexes of Curcumin: X-Ray and density functional theory structure, synthesis, and spectroscopic characterization, *in vitro* antitumor activity, and DNA docking studies of (*p*-Cymene)Ru(curcuminato)chloro. *J. Med. Chem.*, **2012**, 55, 1072–1081.

21. H. M. Leung, M. Harada, W. Takaaki, T. Kee; Delivery of Curcumin and medicinal effects of the Copper(II)-Curcumin complexes. *Current Pharmaceutical Design*.,**2013**,19, 2070-2083.

22. T. Tsang, C.I. Davis, D.C. Brady; Copper biology. *Current Biology*, **2021**, 31, R421-R427.

23. M.C. Linder, M. Hazegh-Azam; Copper biochemistry and molecular biology. *The American journal of clinical nutrition*, **1996**, 63, 797S-811S.

24. R.A. Festa, D.J. Thiele; Copper: an essential metal in biology. *Current Biology*, **2011**, 21, R877-R883.

25. D.L. Watts; The nutritional relationships of copper. *Journal of Orthomolecular Medicine*, **1989**, 4, 99-108.

26. N. Horn, T. Tønnesen, and Z. Türner, Menkes disease: an X-linked neurological disorder of the copper metabolism. *Brain Pathology*, **1992**, 2, 351-362.

27. M.E Aliaga, C. López-Alarcón, R. Bridi, H. Speisky; Redox-implications associated with the formation of complexes between copper ions and reduced or oxidized glutathione. *Journal of inorganic biochemistry*, **2016**, 154, 78-88.

28. A. Członkowska, T. Litwin, P. Dusek, P. Ferenci, S. Lutsenko, V. Medici, J.K. Rybakowski, K.H. Weiss, M.L. Schilsky; Wilson disease. *Nature reviews Disease primers*, **2018**. 4, p.21.

29. H.F. Wertheim, D.C. Melles, M.C. Vos, W. van Leeuwen, A. van Belkum, H.A. Verbrugh, J.L. Nouwen; The role of nasal carriage in *Staphylococcus aureus* infections. *The Lancet infectious diseases*., **2005**, 5, 751-762.

30. E.F. Kong, J.K. Johnson; Community-Associated Methicillin-Resistant *Staphylococcus aureus*: *An Enemy amidst Us.*, **2016**,12, e1005837.

31. K. Hiramatsu, Y. Katayama, M. Matsuo, T. Sasaki, Y. Morimoto, A. Sekiguchi, T. Baba; Multi-drug-resistant *Staphylococcus aureus* and future chemotherapy. *Journal of infection and chemotherapy: official journal of the Japan Society of Chemotherapy.*, **2014,** 20 593-601.

32. V. Niranjan, A. Malini; Antimicrobial resistance pattern in *Escherichia coli* causing urinary tract infection among inpatients. *Indian J Med Res.*, **2014**,139 945-948.

33. F.Y. Ramírez-Castillo, A.C. Moreno-Flores, F.J. Avelar-González, F. Márquez-Díaz, J. Harel, A.L. Guerrero-Barrera; An evaluation of multidrug-resistant *Escherichia coli* isolates in urinary tract infections from Aguascalientes, Mexico: cross-sectional study. *Ann Clin Microbiol Antimicrob.*, **2018**,17, 34-34.

34. P.M. Hawkey, R.E. Warren, D.M. Livermore, C.A.M. McNulty, D.A. Enoch, J.A. Otter, A.P.R. Wilson; Treatment of infections caused by multidrug-resistant Gram-negative bacteria: report of the British Society for Antimicrobial Chemotherapy/Healthcare

Infection Society/British Infection Association Joint Working Party†. *Journal of Antimicrobial Chemotherapy*, **2018**, 73, iii2-iii78.

35. N.G. El Chakhtoura, E. Saade, A. Iovleva, M. Yasmin, B. Wilson, F. Perez, R.A. Bonomo; Therapies for multidrug resistant and extensively drug-resistant non-fermenting gram-negative bacteria causing nosocomial infections: a perilous journey toward 'molecularly targeted' therapy. *Expert review of anti-infective therapy*, **2018**,16, 89-110.
36. K. Neelofar, S. Shreaz, B. Rimple, S. Muralidhar, M. Nikhat, L.A. Khan; Curcumin as a promising anticandidal of clinical interest. *Can J Microbiol*., **2011**, 57, 204-210.
37. B.C. Mounce, T. Cesaro, L. Carrau, T. Vallet, M. Vignuzzi; Curcumin inhibits Zika and chikungunya virus infection by inhibiting cell binding. *Antiviral Research*, **2017**, 142, 148-157.
38. J. Wang, X. Zhou, W. Li, X. Deng, Y. Deng, X. Niu; Curcumin protects mice from *Staphylococcus aureus* pneumonia by interfering with the self-assembly process of α-hemolysin. *Sci Rep.*, **2016**, 6 , 28254-28254.
39. A. Barik, B. Mishra, L. Shen, H. Mohan, R M Kadam, S Dutta, H. Y Zhang, K. I Priyadarsini; Evaluation of a new copper(II)-curcumin complex as superoxide dismutase mimic and its free radical reactions. *Free Radic Biol Med*., **2005**, 15, 39(6), 811-22.
40. K. Nakamoto.; Infrared and Raman spectra of inorganic and coordination compounds, 3rd edition, *Wiley-Interscience*, New York, **1978**.
41. M. J. Frisch, G. W. Trucks, H. B. Schlegel, G. E. Scuseria, M. A. Robb, J. R. Cheeseman, G. Scalmani, V. Barone, G. A. Petersson, H. Nakatsuji, X. Li, M. Caricato, A. Marenich, J. Bloino, B. G. Janesko, R. Gomperts, B. Mennucci, H. P. Hratchian, J. V. Ortiz, A. F. Izmaylov, J. L. Sonnenberg, D. Williams-Young, F. Ding, F. Lipparini, F. Egidi, J.

Goings, B. Peng, A. Petrone, T. Henderson, D. Ranasinghe, V. G. Zakrzewski, J. Gao, N. Rega, G. Zheng, W. Liang, M. Hada, M. Ehara, K. Toyota, R. Fukuda, J. Hasegawa, M. Ishida, T. Nakajima, Y. Honda, O. Kitao, H. Nakai, T. Vreven, K. Throssell, J. A. Montgomery, Jr., J. E. Peralta, F. Ogliaro, M. Bearpark, J. J. Heyd, E. Brothers, K. N. Kudin, V. N. Staroverov, T. Keith, R. Kobayashi, J. Normand, K. Raghavachari, A. Rendell, J. C. Burant, S. S. Iyengar, J. Tomasi, M. Cossi, J. M. Millam, M. Klene, C. Adamo, R. Cammi, J. W. Ochterski, R. L. Martin, K. Morokuma, O. Farkas, J. B. Foresman, and D. J. Fox.; **2016**, Gaussian 09, Revision D.01, Gaussian, Inc., Wallingford CT.

42. (a) A. D. Becke; Density-functional thermochemistry. III. The role of exact exchange, J. Chem. Phys. 1993, 98, 5648e5652; (b) C. T. Lee, W. T. Yang, R. G. Parr.; Development of the Colle-Salvetti correlation-energy formula into a functional of the electron density, Phys. Rev. B. 1988, 37, 785e789.
43. H. Li, L. Zhang, Y. Wang, X. Fan; Theoretical studies on the photoisomerization mechanism of osmium(II) sulfoxide complexes. *RSC Advances*, **2015**,72,1-15.
44. N. M. O'Boyle, A. L. Tenderholt, K. M. Langner; Cclib: a library for package independent computational chemistry algorithms, *J. Comput. Chem*. **2008**, 29, 839-845.
45. M. Cossi, J. V. Barone; Time-dependent density functional theory for molecules in liquid solutions, *Chem. Phys*. **2001**, 115, 4708e4717.
46. E. K. U. Gross, W. Kohn; Time-dependent density functional theory in, *Adv. Quant. Chem*. **1990**, 21, 255e291.
47. R. L. Martin; Natural transition orbitals. *J. Chem. Phys*., **2003**, 118, 4775−4777.
48. V. K. Choudhary, A. K. Bhatt, D. Dash, N. Sharma; DFT calculations on molecular structures, HOMO-LUMO study, reactivity descriptors and spectral analyses of newly

synthesized diorganotin(IV) 2-chloridophenylacetohydroxamate complexes, *Jour. Comp. Chem.* **2019**, 1-10.

49. Z. Akbari, C. Stagno, N. Iraci, T. Efferth, E. A. Omer, A. Piperno M. Montazerozohori M.F. Dehnayebi , N. Micale; Biological evaluation, DFT, MEP, HOMO-LUMO analysis and ensemble docking studies of Zn(II) complexes of bidentate and tetradentate Schiff base ligands as antileukemia agents. *Jour. of Mol. Struc.*, **2024**,1301,137400.
50. Roy Dennington, Todd A. Keith, and John M. Millam.; GaussView version 6.0.16., Semichem Inc., *Shawnee Mission, KS,* **2016**.
51. J. S. Al-Otaibi; Detailed quantum mechanical studies on bioactive benzodiazepine derivatives and their adsorption over graphene sheets. *Spectrochimica Acta Part A: Molecular and Biomolecular spectroscopy*, **2020**, 235, 118333.
52. J. S. Murray, K. Sen; Molecular Electrostatic Potentials concepts and applications, Theoretical and computational chemistry, *Elsevier*, **1996**,1-137.
53. E.R. Johnson, S. Keinan, P. Mori-Sánchez, J. Contreras-García, A.J. Cohen, W. Yang; Revealing Noncovalent Interactions. *J. Am. Chem. Soc.*, **2010**, 132, 6498–6506.
54. F. Akman, A. Demirpolat , A. S. Kazachenko , Anna S. Kazachenko, N. Issaoui and O.A.Dossary; Molecular Structure, Electronic Properties, Reactivity (ELF, LOL, and Fukui), and NCI-RDG Studies of the Binary Mixture of Water and Essential Oil of Phlomis bruguieri. *Molecules*, **2023**, 28, 2684.
55. T. Lu, F. Chen; Multiwfn: A multifunctional wavefunction analyzer. *Jour. Comput. Chem*.**2012**, 33, 580-592.
56. B.Silvi, A.Savin; Classification of chemical bonds based on topological analysis of electron localization functions. *Nature*, **1994**, 371(6499), 683–686.

57. B. Fathima Rizwana, J. C. Prasana, S.Muthu, C.S.Abraham; Molecular docking studies, charge transfer excitation and wave function analyses (ESP,ELF,LOL) on valacyclovir:A potential anti viral drug. *Comput,Biol.Chem*., **2019**,78, 9–17.

58. Heiko Jacobsen.; Localized-orbital locator (LOL) profiles of chemical bonding. *Can. J. Chem*. **2008**,86(7), 695–702.

59. P. Kumar, S.K. Kandi, S. Manohar, K. Mukhopadhyay, D.S. Rawat; Monocarbonyl curcuminoids with improved stability as antibacterial agents against Staphylococcus aureus and their mechanistic studies, *ACS Omega*, **2019** , 4 , 675-687.

60. Y.M. Go, D.P. Jones; Redox compartmentalization in eukaryotic cells, *Biochimica et biophysica acta*, **2008,** 1780, 1273-1290.

61. S. Chakraborti, G. Dhar, V. Dwivedi, A. Das, A. Poddar, G. Chakraborti, G. Basu, P. Chakrabarti, A. Surolia, B. Bhattacharyya; Stable and potent analogues derived from the modification of the dicarbonyl moiety of curcumin, *Biochemistry*, **2013**, 52 , 7449-7460.

62. T. Deb, D. Choudhury, P. S. Guin, M. B. Saha, G. Chakrabarti, S. Das; A complex of Co(II) with 2-hydroxyphenyl-azo-2′-naphthol (HPAN) is far less cytotoxic than the parent compound on A549-lung carcinoma and peripheral blood mononuclear cells: Reasons for reduction in cytotoxicity, *Chem-Biol. Inter.*, **2011**, 189, 206-214.

63. P. S. Guin, P. C. Mandal, and S. Das; The binding of a hydroxy-9,10-anthraquinone Cu^{II} complex to calf thymus DNA: Electrochemistry and UV/Vis spectroscopy, *ChemPlusChem*., **2012,** 77, 361-369.

64. P. Das, C. K. Jain, S. K. Dey, R. Saha, A. D. Chowdhury, S. Roychoudhury, S. Kumar, H. K. Majumder, S. Das; Synthesis, crystal structure, DNA interaction and *in vitro* anticancer activity of a Cu(II) complex of purpurin: dual poison for human DNA topoisomerase I and II. *RSC Adv.*, **2014,** 4, 59344-59357.

65. B. Mandal, S. Singha, S. K. Dey, S. Mazumdar, T. K. Mondal, P. Karmakar, S. Kumar, S. Das, Synthesis, crystal structure from PXRD of a $Mn^{II}(purp)_2$ complex, interaction with DNA at different temperatures and pH and lack of stimulated ROS formation by the complex, *RSC Adv*., **2016,** 6, 51520–51532.

66. S. Mukherjee-Chatterjee, C. K. Jain, S. Singha, P. Das, S. Roychoudhury, H. K. Majumder, S. Das; Activity of Co^{II}-Quinalizarin: A novel analogue of anthracycline-based anticancer agents targets human DNA topoisomerase, whereas quinalizarin itself acts via formation of semiquinone on acute lymphoblastic leukemia MOLT-4 and HCT 116 cells. *ACS Omega.*, **2018**, 3, 10255-10266.

67. G. Scatchard.; The attractions of proteins for small molecules and ions, *Ann. N. Y. Acad. Sci*., **1949**,51, 660–672.

68. P. Das, C. K. Jain, S. Roychoudhury, H. K. Majumder, S. Das; Design, synthesis and *in vitro* anticancer activity of a Cu(II) complex of Carminic Acid: A novel small molecule inhibitor of human DNA topoisomerase I and topoisomerase II. *ChemistrySelect* 1., **2016**, 6623-6631.

69. D. Ganguly, C. K. Jain, R. C. Santra, S. Roychoudhury, H. K. Majumder, T. K. Mondal, S. Das; Anticancer activity of a complex of Cu^{II} with 2-(2-hydroxyphenylazo)-indole-3′-acetic acid on three different cancer cell lines: A novel feature for azo complexes *ChemistrySelect,***2017**, 2, 2044-2054.

70. S. Majee, R. Sen, S. Guha, D. Bhattacharya, D. Dasgupta; Differential interactions of the Mg^{2+} complexes of Chromomycin A_3 and Mithramycin with poly(dG-dC)·poly(dC-dG) and poly(dG)·poly(dC). *Biochemistry,* **1997**, 36, 2291-2299.

71. S. Das , D. Dasgupta; Binding of $(MTR)_2Zn^{2+}$ complex to chromatin: a comparison with $(MTR)_2Mg^{2+}$ complex. *J. Inorg. Biochem.,* **2005**, 99, 707-715.

72. S. Roy, R. Banerjee, and M. Sarkar; Interaction of a common painkiller Piroxicam and Copper-piroxicam with chromatin causes structural alterations accompanied by modulation at the epigenomic/genomic level. *J. Inorg. Biochem*., **2006**, 100, 1320-1331.

73. J. B. Chaires; Drug—DNA interactions. *Current Opinion in Structural Biology*, **1998** , 8, 314-320

74. I. Haq; Thermodynamics of drug–DNA interactions. *Arch. Biochem. Biophys.*, **2002**, 403, 1-15.

75. V. A. Bloomfield, D. M. Crothers, and I. Tinoco; In: Nucleic Acid: Structures, Properties and functions, University Science Books, Sausalito, CA, **1999**.p. 56.

76. F. Leng, J. B. Chaires and M. J. Warring; Energetics of echinomycin binding to DNA. *Nucl. Acid Res.*, **2003**, 31, 6191-6197.

77. S. Kashanian, and J. E. N. Dolatabadi; *In vitro* studies on calf thymus DNA interaction and 2-*tert*-butyl-4-methylphenol food additive. *Eur. Food Res. Technol*., **2010**, 230, 821–825.

78. J. B. Chaires; A thermodynamic signature for drug–DNA binding mode. *Arch. Biochem. Biophys.*, **2006**, 453, 26–31.

79. N. Shahabadi, S. Kashanian, and F. Darabi., *In vitro* study of DNA interaction with a water-soluble dinitrogen Schiff base. *DNA Cell Biol*., **2009**, 28, 589-596.

CHAPTER 10

Synthesis, characterization, establishment of structure through Quantum Chemical calculations of a Zn^{II} Complex of Curcumin and its efficacy as a DNA binding agent

Introduction

The clinical application of Curcumin faces significant hurdles due to its poor bioavailability, rapid metabolism, and low water solubility.[1-7] Despite its potent therapeutic properties, Curcumin's clinical efficacy is significantly limited by its poor pharmacokinetics.[1-7] Curcumin is poorly absorbed from the gastrointestinal tract, rapidly metabolized in the liver and intestinal mucosa to various metabolites, such as Curcumin glucuronide and Curcumin sulfate, which have reduced therapeutic activity compared to the parent compound, and quickly eliminated from the body.[8-10] This results in low bioavailability, which is a major obstacle to its clinical application.[9] These factors collectively contribute to the low systemic availability of Curcumin, necessitating the development of strategies to enhance bioavailability.[11,12] One promising strategy to overcome limitations of Curcumin is through formation of metal complexes that can influence its physicochemical properties like stability, solubility and bioavailability.[13-17] Not only are the metal-Curcumin complexes more resistant to hydrolysis and oxidative degradation that extends the half-life of Curcumin in biological systems.[13-17] Keeping these in mind, a Zn^{II}-Curcumin complex was synthesized and its biological properties carefully examined. Notably, it was observed that after complex formation the stability of Curcumin increased, preventing its rapid degradation and metabolism. Subsequently, experiments were conducted to determine the benefits of complex formation considering its antibacterial impact.

In the human body, zinc stands out as a highly abundant micronutrient and is ubiquitous, being used for the maintenance of regulatory, structural and catalytic roles in about 3000 proteins, including small and large proteins, enzymes and transcription factors.[18-20] Further, it has recently been shown that Zn is important for intracellular and intercellular communication as a regulatory and signalling component.[21,22] Therefore, it is not surprising that it has an essential role in cellular biology.[18-22] An approximately 10% of human proteins are related to Zn ions,

involved in the control of gene expression, DNA processes, chromatin organization, cell growth and development, apoptosis, immune response and antioxidant defense.[23-25] Due to the vast functional significance of Zn, its cellular levels are strictly controlled to maintain them at narrow physiological concentrations.[26] However, the uptake, intracellular distribution, storage, and elimination of zinc are strictly controlled, safeguarding the organism against zinc accumulation beyond necessary physiological concentrations.[18-26], which cannot be feasible for other elements such as iron, copper, and mercury are known to accumulate excessively beyond physiological levels.[18-26]

The prepared Zn^{II}-Curcumin complex was tried for antibacterial activity on *Staphylococcus aureus* (*S. aureus*) and *Escherichia coli* (*E. coli*). An alarming rise in antibiotic-resistant bacterial infections poses a critical threat to global public health, necessitating an urgent development of novel antibacterial agents.[27-30] Amongst most notorious pathogens contributing to this crisis are *Staphylococcus aureus* (*S. aureus*) and *Escherichia coli* (*E. coli*), both implicated in various infections.[27-33] *S. aureus*, a Gram-positive bacterium is known to cause skin infections, pneumonia, endocarditis and sepsis while *E. coli*, a Gram-negative bacterium, is involved in urinary tract infections, gastroenteritis and neo-natal meningitis.[27-33] The increasing prevalence of methicillin-resistant *Staphylococcus aureus* (MRSA) and extended-spectrum beta-lactamase (ESBL)-producing *E. coli* has severely limited the effectiveness of existing antibiotics, highlighting a need for alternative therapeutic strategies.[34,35] Natural products with diverse chemical structures and bio-active properties have historically played a pivotal role in drug discovery and development.[36,37] One such promising natural compound is Curcumin, that has been studied extensively for its wide range of pharmacological activities.[38-43] This chapter focuses on the potential of Curcumin and its Zn^{II} complex as a basis for developing new

antibacterial agents, particularly for treating various resistant strains through various biological modeling and *invitro* studies.

Result and discussion

10.1 Physicochemical studies on the formation of a Zn^{II} complex with Curcumin

The mole ratio method[44] was employed to determine the stoichiometry of complex formation between Zn^{II} and Curcumin (HCur). In this approach, the concentration of HCur remained constant while that of Zn^{II} was altered. Additionally, the Job's method of continuous variation[44] was utilized to investigate the same phenomenon.

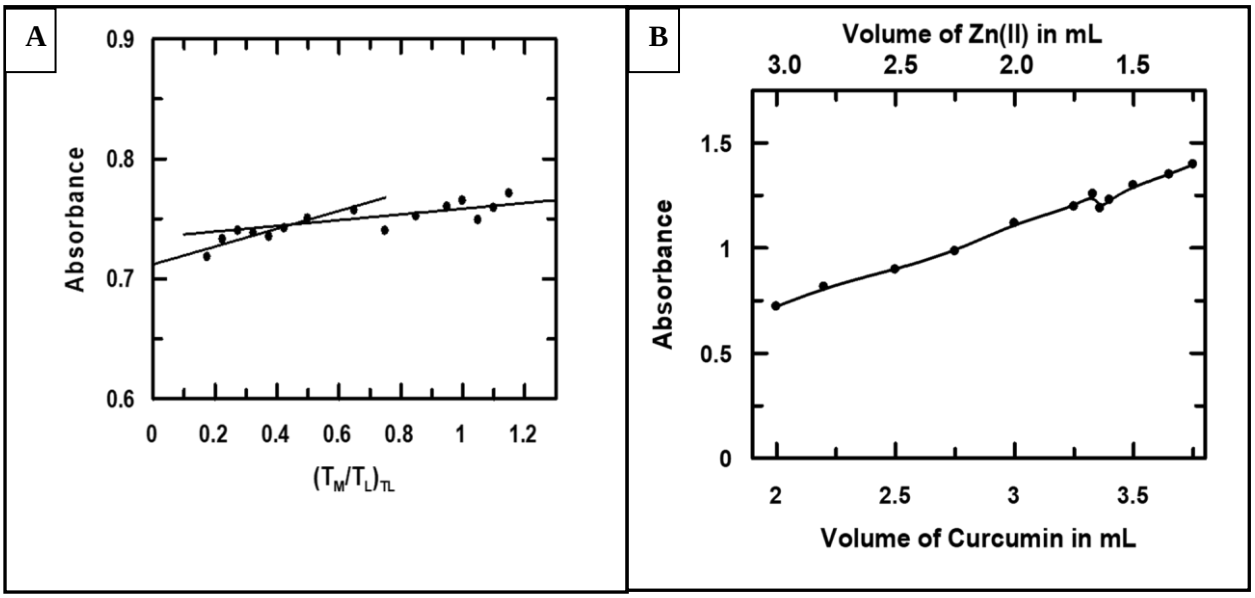


Figure 1: (A) Mole-ratio plot of Zn^{II} with Curcumin in solution at pH ~7.4; (B) Job's plot of continuous variation showing interaction of Zn^{II} with Curcumin at pH~7.4. [$NaNO_3$] = 0.01M, Temperature = 298 K.

In case of mole-ratio method, absorbance was measured at 430 nm and plotted against ratio of Curcumin to Zn^{II} [Fig. 1(A)]. Straight lines were obtained the intersection of which helped to determine stoichiometry of complex formation in solution. Stoichiometry was also determined by

continuously varying the concentration of Curcumin and Zn^{II} as shown in Fig. 1(B). Both methods suggest the formation of a 1:2 metal-ligand complex at pH ~7.4.

10.2 Characterization of Zn^{II} -Curcumin complex

Although physicochemical investigations performed with regard to mole ratio and Job's method of continuous variation suggests formation of a 1:2::metal:ligand complex in aqueous solution several attempts at preparing the complex by mixing 1 part by mole of Zn^{II}acetate with 2 parts by mole of HCur always resulted in a 1:1 species.

10.2.1 Analysis of mass spectrum:

The mass spectrum of the complex reveals molecular ion peaks at m/z = 508.4731, 510.5261, and 512.2132, corresponding to the three most abundant Zn isotopes (theoretical m/z values: 508.38 for ^{64}Zn, 510.38 for ^{66}Zn, and 512.38 for ^{68}Zn) (Fig. 2). After the loss of a water molecule from the molecular ion, peaks appear at m/z values 490.7648, 492, and 494 with theoretical m/z values of 490.38 for ^{64}Zn, 492.38 for ^{66}Zn, and 494.38 for ^{68}Zn (Fig. 2). The loss of both water and an acetate molecule from the molecular ion produces peaks with m/z values 449.2687, 451.4157, and 453.1284 where theoretical m/z values are 449.38 for ^{64}Zn, 451.38 for ^{66}Zn, and 453.38 for ^{68}Zn (Fig. 2). The experimental results in the mass spectrum align exceptionally well with the theoretically predicted fragments. Moreover, they closely match the expected pattern for any fragment, considering the relative abundance of Zn isotopes [five stable isotopes: ^{64}Zn (48.63%), ^{66}Zn (27.90%), ^{67}Zn (4.10%), ^{68}Zn (18.75%), and ^{70}Zn (0.62%); the three most abundant were identified in the mass spectrum]. Consequently, the mass spectrum provides strong evidence supporting the presence of $[Zn^{II}(Cur)(OCOCH_3)(OH_2)]$

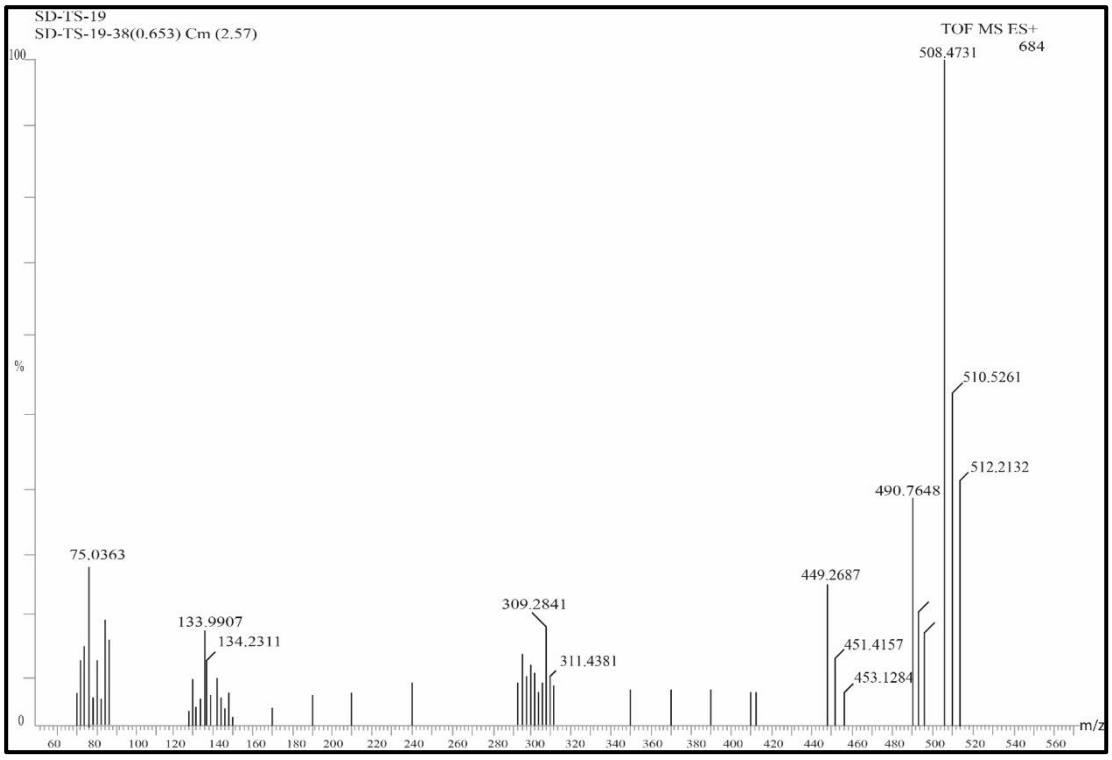


Figure 2: Mass spectra of $[Zn^{II}(Cur)(OCOCH_3)(OH_2)]$

10.2.2 Thermo-gravimetric analysis:

The TGA plot of the complex (Fig. 3) shows two steps. The first corresponds to a mass loss of 6.21 % at 140°C and the second corresponds to a mass loss of 80.68% at 500°C. Considering the complex to be containing one Curcumin, one acetate and water and having the formula $[Zn^{II}(Cur)(OCOCH_3)(OH_2)]$ the mass loss of 5.68% may be explained due to the loss of $-OCH_3$ group from Curcumin moiety.

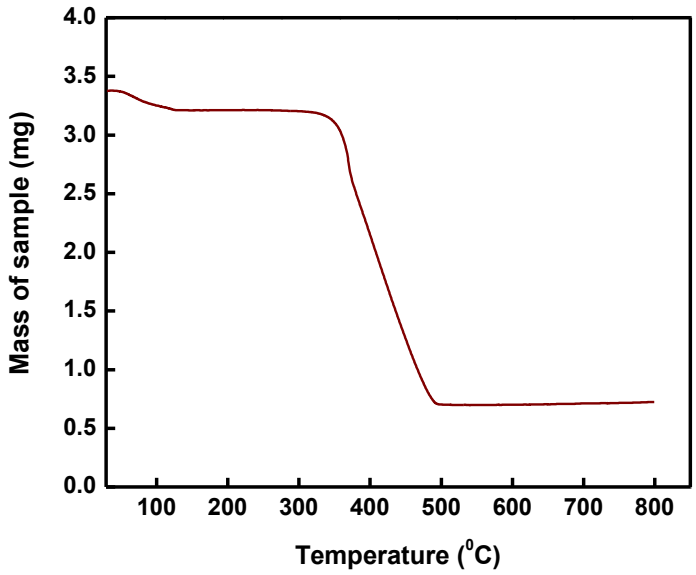


Figure 3: TGA of $[Zn^{II}(Cur)(OCOCH_3)(OH_2)]$

10.2.3 UV-Vis spectra of Curcumin and $[Zn^{II}(Cur)(OCOCH_3)(OH_2)]$ in DMSO:

λ_{max} of HCur was found at 432 nm. In case of $[Zn^{II}(Cur)(OCOCH_3)(OH_2)]$ λ_{max} was at 426 nm in DMSO indicating a blue shift in wavelength following complex formation.

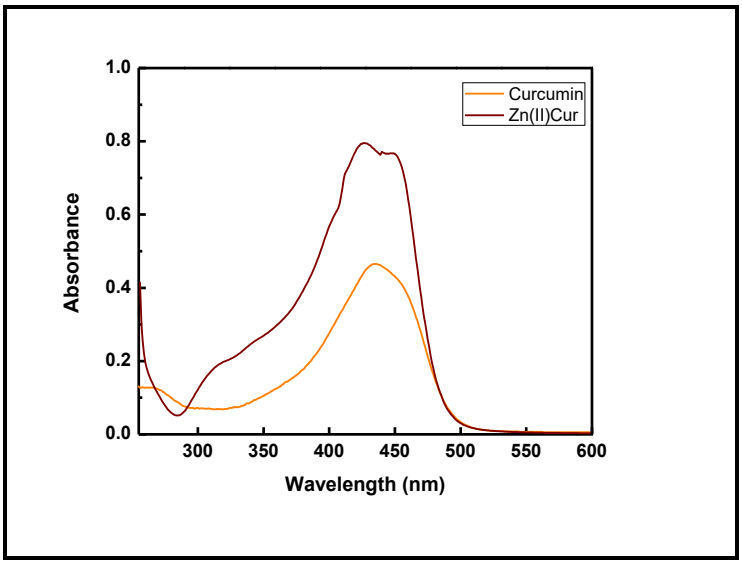


Figure 4: Absorption spectra of Curcumin (—10 μM) and Zn(Cur)(—10μM) in DMSO λ_{max} for Curcumin = 432 nm , λ_{max} for Zn(Cur) = 426 nm

10.2.4 Analysis of IR spectra:

IR spectrum of pure HCur has a peak at 3516 cm^{-1} attributed to –OH stretching (*Fig. 3, Chapter 7*). Peaks at 1627 cm^{-1} and 1608 cm^{-1} were due to C=O stretching vibrations while those at 1506 cm^{-1} and 1429 cm^{-1} due to C=C stretching and C=O bending vibrations.[45] Responses from 1276 cm^{-1} to 1153 cm^{-1} are due to phenolic –OH bending, –C–O stretching, alkoxy C–O bending etc. Peaks at 964 cm^{-1}, 855 cm^{-1} and 810 cm^{-1} are due to alkene C_{sp2}–H bending. The sharp peak for –OH stretching in HCur (*Fig. 3, Chapter 7*) appeared as a broad band at around 2931 cm^{-1} for the complex, (Fig.5). Responses for carbonyl stretching vibrations for HCur at 1608 cm^{-1} (*Fig. 3, Chapter 7*) got shifted to lower wavenumbers (1599 cm^{-1}) having relatively low intensity indicating an involvement of the carbonyl of HCur in binding Zn^{II} (Fig.5). Peaks in the region 1475 cm^{-1} to 842 cm^{-1} in the IR spectrum of the complex showed distinct changes attributed to a change in bonds close to the zone of co-ordination for Zn^{II} (viz. –OH, –CH, –C–C bending modes).[45] Peaks at 476 cm^{-1} corresponds to Zn-O stretching frequency.

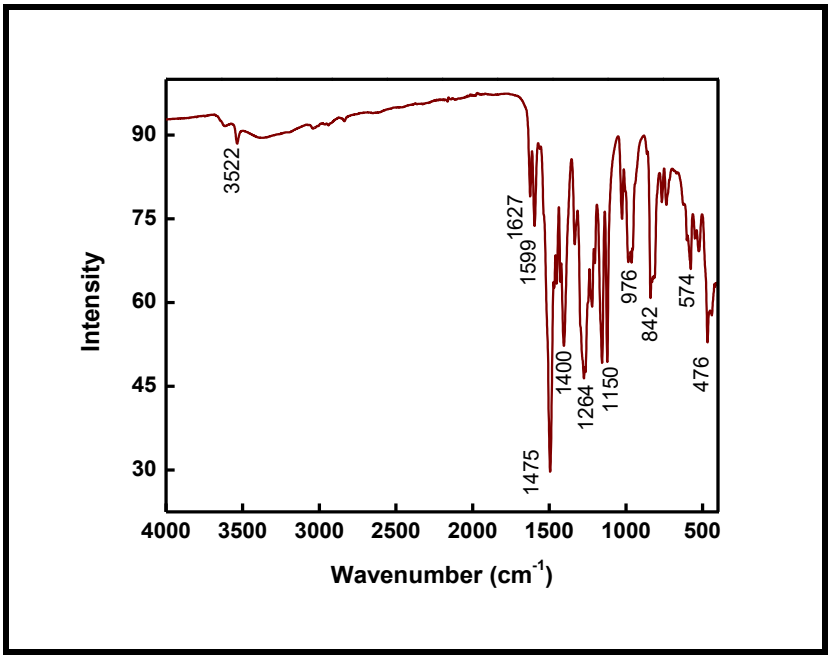


Figure 5: FTIR spectrum for $[Zn^{II}(Cur)(OCOCH_3)(OH_2)]$

10.3 Stability constant determination of Zn^{II}-Curcumin complex in solution

The pH-metric titration of HCur was conducted in the pH range 4.75 to 12.22 in the absence and presence of Zn^{II}. For titrations performed in presence of Zn^{II}, metal ion and HCur were taken in the ratio 1:1. Change in absorbance at 467 nm for HCur alone (*Fig. 1, Chapter 7*) and that at 430 nm in presence of Zn^{II} (Fig. 6) was fitted to Eq. 4 and Eq.16 (*Chapter 6,: Experimental*).

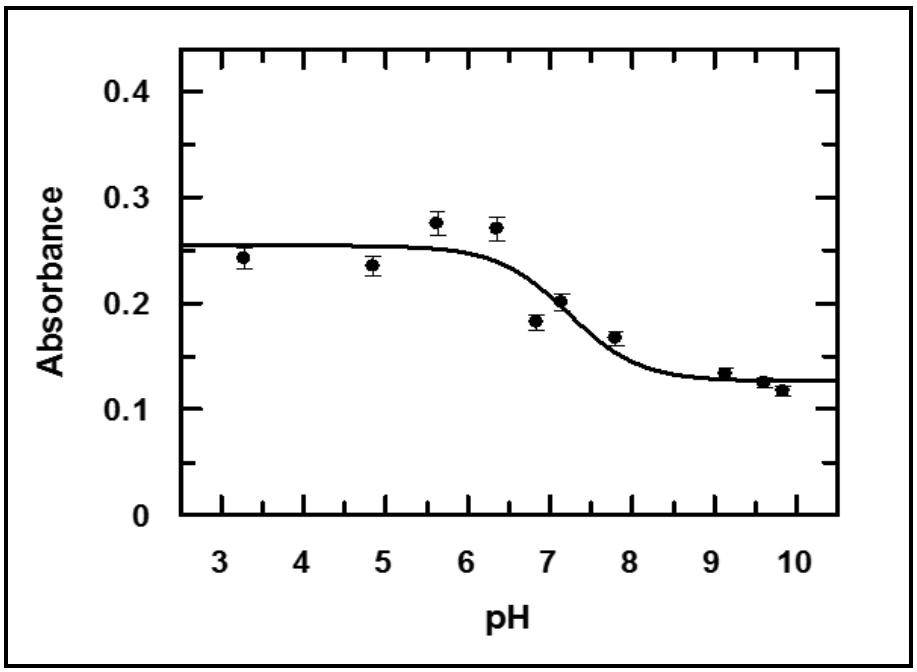


Figure 6: Fitted plot of Curcumin in aqueous solution in the presence of Zn^{II} at different pH. [Curcumin] = 10 µM, $[Zn^{II}(OAc)_2]$ = 5 µM, $[NaNO_3]$ = 0.01 M, Temperature = 300 K. Black solid line is the fitted data according to Eq.16 of *Chapter 6: Experimental*

Here, spectrophotometric titration was performed taking HCur and Zn^{II} in the ratio 1:1 in the pH range 4.75 to 12.22. The change in absorbance at 430 nm for a change in pH was fitted to Eq. 16 (*Chapter 6: Experimental*) that helped to determine the stability constant of the complex in solution. Considering HCur as LH_2H^*, A_1, A_2, A_3 and A_4 represent absorbance due to LH_2H^*, LH_2^-, LH^{2-} and L^{3-} respectively. Fitting the data according to Eq. 4 (*Chapter 6: Experimental*),

pK_1, pK_2 and pK_3 were 7.17 ± 0.31, 10.50 ± 0.16 and 11.47 ± 0.17 respectively (*Fig. 1, Chapter 7*) when HCur was titrated alone. Absorbance of HCur was followed at 430 nm in the presence of Zn^{II} and fitted to Eq. 16. pK_{a1} (=7.08 ± 0.43) was determined. Stability constants β^* and β were determined using Eqs. 17-21, (*Chapter 6: Experimental*) and found to be 2.45×10^5 ($\log \beta$ = 5.39).

10.4 Quantum chemical calculations for $[Zn^{II}(Cur)(OCOCH_3)(OH_2)]$

Fig. 7 illustrates the DFT optimized ground state geometries of Zn (in gas phase and DMSO) with a numbering scheme for the coordination environment. The optimized molecular structures were found to have singlet ground states. Gaussian 09 software[46] was employed for DFT calculations using B3LYP functional[47] and 6-31G+(d,p) basis sets for C, H, and O atoms[47], while LanL2DZ basis set[48] was used for Zn^{II}. Table 1 presents key parameters related to coordination geometry. The calculated Zn-O bond lengths (Table 1) show good correlation with those reported for [Zn(Cur)(bipy)(acetate)][49], whose structure was determined through single crystal X-ray diffraction analysis.

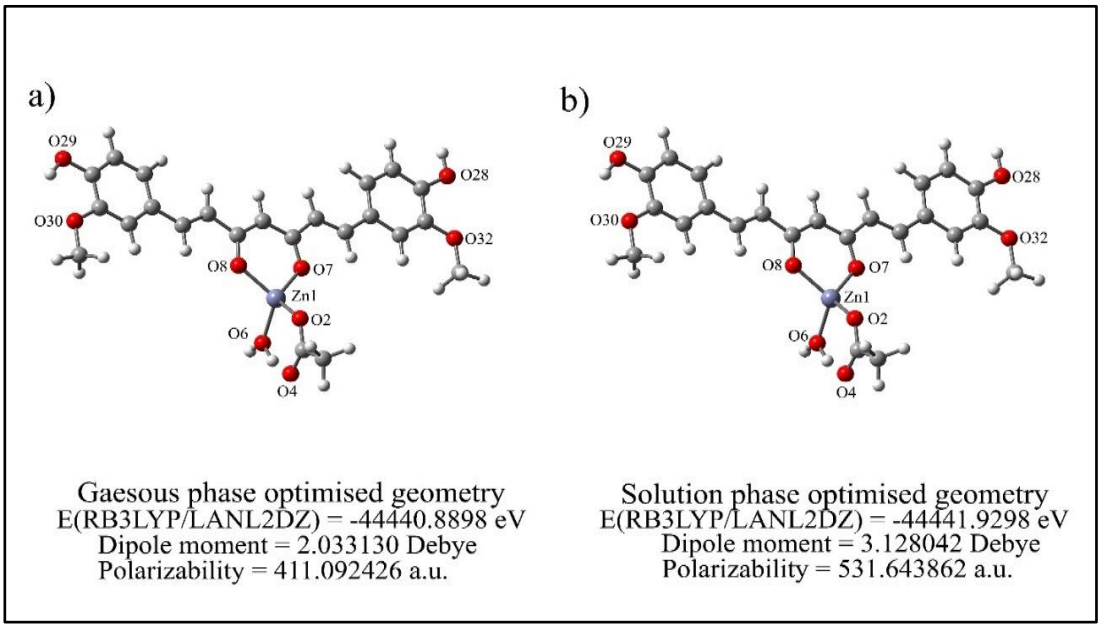


Figure 7: Ground state optimized geometries of the [Zn (Cur)](a) Gas phase (b) Solution phase

The final optimized structures of ground state configurations exhibit tetrahedral coordination in both gaseous and solution (DMSO) phases (Fig.7). Optimized coordinates for both gas and solution phases are provided in Table 2.

Table 1: Coordinated bond distances (in Å) and bond angles (in °) of [Zn(Cur)

Bond	Gaseous phase	In DMSO	Angle	Gaseous phase	In DMSO
Zn1–O2	1.976	2.006	O2–Zn1–O6	92.08	90.55
Zn1–O7	1.967	1.987	O2–Zn1–O7	120.43	106.36
Zn1–O6	1.993	2.008	O6–Zn1–O8	117.50	107.79
Zn1–O8	1.968	1.989	O7–Zn1–O8	91.66	90.77

Table 2: Optimized coordinates of [Zn^{II}(Cur)($OCOCH_3$)(OH_2)]in ground state geometry.

	Gaseous phase			In DMSO solvent		
Atom	**x**	**y**	**z**	**x**	**y**	**z**
Zn1	-0.027898	2.128519	0.325552	-0.004670	2.180313	-0.318790
O2	0.033618	3.649987	-0.934913	0.003218	3.689327	0.971033
C3	0.125871	4.921342	-0.652651	0.003755	4.968277	0.707904
O4	0.415291	5.361471	0.553258	0.001402	5.450266	-0.480505
C5	-0.035822	5.890735	-1.806151	0.006377	5.905951	1.888337
O6	-0.253407	3.344115	1.904894	-0.009317	3.417030	-1.896387
O7	1.408664	0.765856	0.231228	-1.438100	0.822442	-0.234719
O8	-1.414066	0.755488	0.231239	1.427783	0.820773	-0.240152
C9	1.258324	-0.527508	0.104657	-1.265766	-0.474540	-0.099143
C10	-1.252729	-0.539033	0.104358	1.254548	-0.476076	-0.103613
C11	0.000687	-1.180560	0.043724	-0.005957	-1.106808	-0.036473
C12	-2.470253	-1.364155	0.020995	2.452015	-1.314885	-0.016719
C13	-3.698193	-0.796606	0.054379	3.700793	-0.792095	-0.060106
C14	-4.993354	-1.481671	-0.020339	4.971962	-1.502768	0.019600
C15	2.470410	-1.361053	0.022301	-2.464072	-1.312193	-0.008998
C16	3.702386	-0.802839	0.055550	-3.712728	-0.789608	-0.050668

C17	4.991829	-1.500012	-0.017093	-4.983391	-1.502481	0.030619
C18	-5.118312	-2.882097	-0.109373	5.074446	-2.903989	0.154134
C19	-6.377025	-3.489475	-0.180697	6.317263	-3.532462	0.228856
C20	-7.528728	-2.702040	-0.164061	7.485274	-2.773305	0.170847
C21	-7.418301	-1.299574	-0.073513	7.402564	-1.373274	0.035643
C22	-6.167990	-0.692866	-0.001731	6.167902	-0.744200	-0.039152
C23	6.174062	-0.723908	-0.002009	-6.181302	-0.750209	-0.036422
C24	7.437068	-1.317054	-0.069899	-7.431761	-1.358750	0.034519
C25	7.532763	-2.724869	-0.153946	-7.509813	-2.761871	0.177460
C26	6.367225	-3.499139	-0.167178	-6.334542	-3.514185	0.244893
C27	5.105448	-2.897409	-0.099729	-5.084186	-2.899299	0.173081
O28	8.804154	-3.270222	-0.220138	-8.772592	-3.324919	0.243703
O29	-8.775315	-3.291528	-0.236099	8.718214	-3.388621	0.245429
O30	-8.652330	-0.647441	-0.067426	8.653094	-0.749777	-0.008461
C31	-8.660185	0.796212	0.026379	8.710866	0.695003	-0.141944
O32	8.632993	-0.624486	-0.061768	-8.641899	-0.688447	-0.024773
C33	8.578859	0.817544	0.023786	-8.627819	0.755733	-0.170958
H34	-0.146232	6.915394	-1.440046	0.014328	6.942910	1.552377
H35	-0.892991	5.605820	-2.422997	0.883620	5.707981	2.513162
H36	0.867953	5.823222	-2.429421	-0.878488	5.720389	2.506388
H37	0.716415	4.236783	1.544382	-0.005703	4.309267	-1.524925
H38	-0.446980	3.211145	2.862077	-0.025406	3.316886	-2.857531
H39	0.006953	-2.259137	-0.063298	-0.006322	-2.185006	0.076721
H40	-2.325935	-2.436814	-0.072599	2.285001	-2.382634	0.089254
H41	-3.719696	0.289680	0.143419	3.761854	0.289670	-0.164515
H42	2.318116	-2.432811	-0.070292	-2.297208	-2.380104	0.096636
H43	3.733386	0.283295	0.142961	-3.775739	0.291824	-0.156172
H44	-4.231718	-3.506681	-0.121443	4.176741	-3.509552	0.201426
H45	-6.489406	-4.565186	-0.249118	6.404086	-4.607291	0.332683
H46	-6.077411	0.387337	0.066517	6.100326	0.332886	-0.141605
H47	6.083536	0.356168	0.061509	-6.108837	0.325339	-0.144892
H48	6.450604	-4.581695	-0.230313	-6.401837	-4.593592	0.355019

H49	4.219021	-3.521827	-0.109572	-4.191101	-3.510764	0.228984
H50	8.792849	-4.244746	-0.273390	-8.721003	-4.295361	0.342592
H51	-9.481431	-2.612123	-0.215254	9.421487	-2.706544	0.191361
H52	-9.708434	1.090015	0.015698	9.771429	0.942840	-0.152156
H53	-8.140146	1.242138	-0.829042	8.221332	1.185481	0.706811
H54	-8.191259	1.124798	0.960937	8.242986	1.019447	-1.078125
H55	9.616310	1.146771	0.015674	-9.677274	1.045843	-0.194339
H56	8.094826	1.139106	0.954201	-8.138626	1.056718	-1.105034
H57	8.047526	1.244069	-0.835884	-8.128553	1.237590	0.678086

10.4.1 Frontier molecular orbital analysis:

Fig. 8 displays the frontier orbitals of [Zn(Cur)] optimized in both gas and solution phases. The analysis of occupied and virtual molecular orbitals (MOs) were conducted based on their atomic compositions and visual inspection of the three-dimensional representations. The [Zn(Cur)] complex consisted of four components: Zn, HCur, water, and acetate. Table 3 outlines their compositions. Optimized geometries were determined for both the gas and solution phases. The orbitals from HOMO-1 to LUMO+4 showed no contribution from Zn^{II}, with contributions solely from HCur. However, Zn^{II} contributes to the orbitals from HOMO-2 to HOMO-4.

Calculations revealed that the HOMO-LUMO energy gap for [Zn(Cur)] was 3.09 eV in the gas phase and 2.63 eV in the solution phase. In contrast, the HOMO-LUMO energy gap for HCur in the solution phase was 3.30 eV (*Fig. 6, Chapter 7*). Fig. 9 shown the HOMO-LUMO gaps for [Zn(Cur)] in both gas and solution phases. Almost all the HOMO and LUMO were predominantly located on HCur in each phase, with being the main contributor.

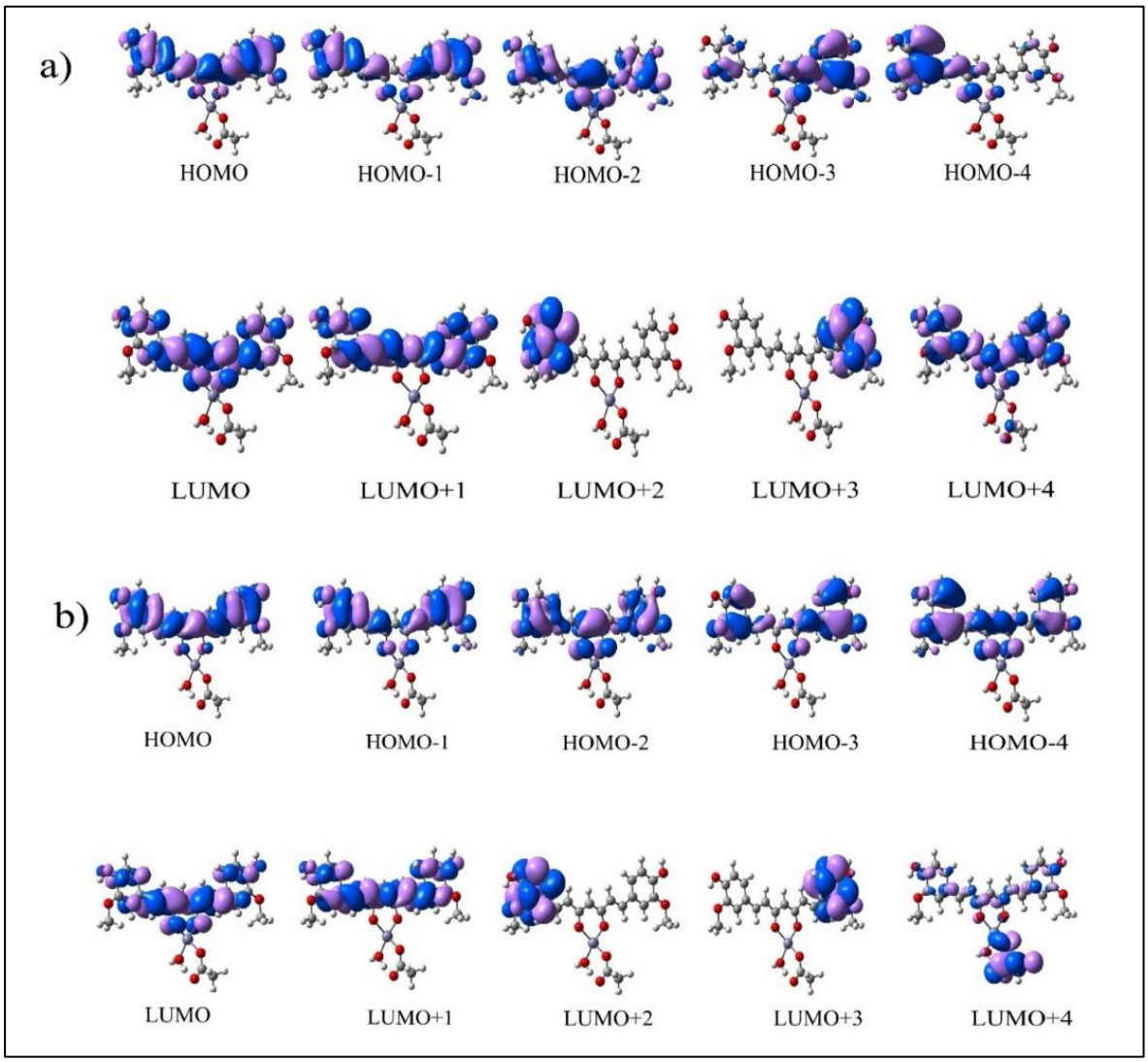


Figure 8: Frontier orbitals of the optimized [Zn(Cur)] (a) Gaseous Phase (b) Solution Phase

Table 3: Some of selected MOs of [Zn(Cur)($OCOCH_3$)(OH_2)]in ground state geometry along with their energies and percentage compositions.

Gaseous phase optimized structure:

Orbital	MO	Energy (eV)	% Composition			
			Zn	Curcumin	Acetate	Water
128	L+4	0.08	0	99	1	0
127	L+3	-0.32	0	100	0	0
126	L+2	-0.34	0	100	0	0
125	L+1	-1.27	0	100	0	0
124	LUMO	-2.47	0	100	0	0

123	HOMO	-5.56	0	100	0	0
122	H-1	-5.90	0	100	0	0
121	H-2	-6.43	1	99	0	0
120	H-3	-6.83	1	99	0	0
119	H-4	-6.96	1	99	0	0

Solution phase optimized structure:

Orbital	**MO**	**Energy (eV)**	**% Composition**			
			Zn	Curcumin	Acetate	Water
128	L+4	-0.07	0	100	0	0
127	L+3	-0.33	0	100	0	0
126	L+2	-0.35	0	100	0	0
125	L+1	-1.28	0	100	0	0
124	LUMO	-2.49	0	100	0	0
123	HOMO	-5.57	0	100	0	0
122	H-1	-5.91	0	100	0	0
121	H-2	-6.45	1	99	0	0
120	H-3	-6.84	1	99	0	0
119	H-4	-6.97	0	99	1	0

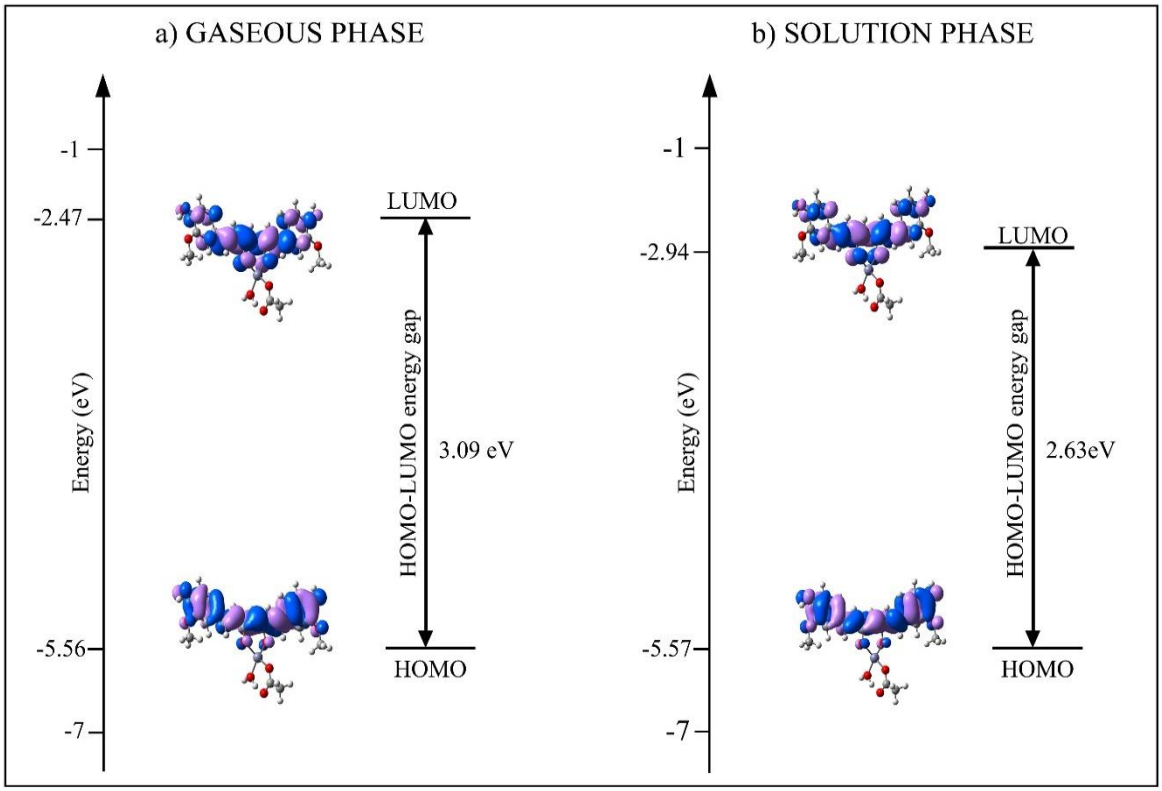


Figure 9: HOMO-LUMO energy gap of [Zn(Cur)] (a) Gas phase (b) Solution phase

For molecules in the crystalline form, the HOMO-LUMO energy gap can be confirmed using the optical energy band gap obtained from UV-Vis absorption (Fig. 9). The optical energy bandgap (Eg) was calculated to be 2.91 eV (Fig.10) using the formula $E_g = 1240/\lambda_{max}$ eV. This result is in close agreement with the theoretical HOMO-LUMO energy gap of 2.63 eV for [Zn(Cur)] in DMSO.

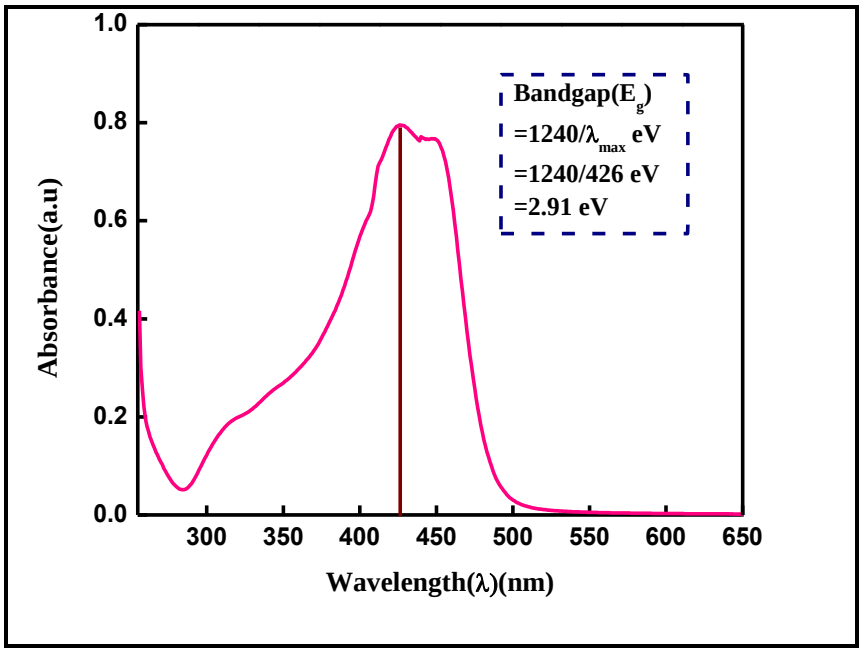


Figure 10: Experimental UV-vis absorption with associated optical bandgap

10.4.2 Opto-electronic absorption analysis:

Optoelectronic properties proved valuable in determining precise molecular geometry, as excitation from the ground state to an excited state in a dielectric medium (DMSO) would produce an absorption identical to that observed experimentally in the same solvent. The absorption cutoff wavelength of DMSO is approximately 268 nm and [Zn(Cur)] absorption spectrum shows dispersion below 300 nm, so to compare the observed patterns with the calculated ones, the spectrum was recorded up to 650 nm instead of below 300 nm (Fig. 11). The computed electronic absorption spectrum in DMSO, featuring multiple peaks, supports the multiple-transition nature of [Zn(Cur)]. The peaks in the experimental spectra were visually assigned. Table 4 presents the most probable transitions in order of increasing energy as they appear in the spectrum with maximum intensity ($f \geq 0.10$), corresponding to the experimental absorption peaks and associated excitation wavelengths, energy, oscillator strengths (f), character, and CI coefficients. Charge-transfer transitions within the HCur moiety were primarily

responsible for the excitation peaks. For TDDFT calculations, nearly all states were considered singlet.[50,51]

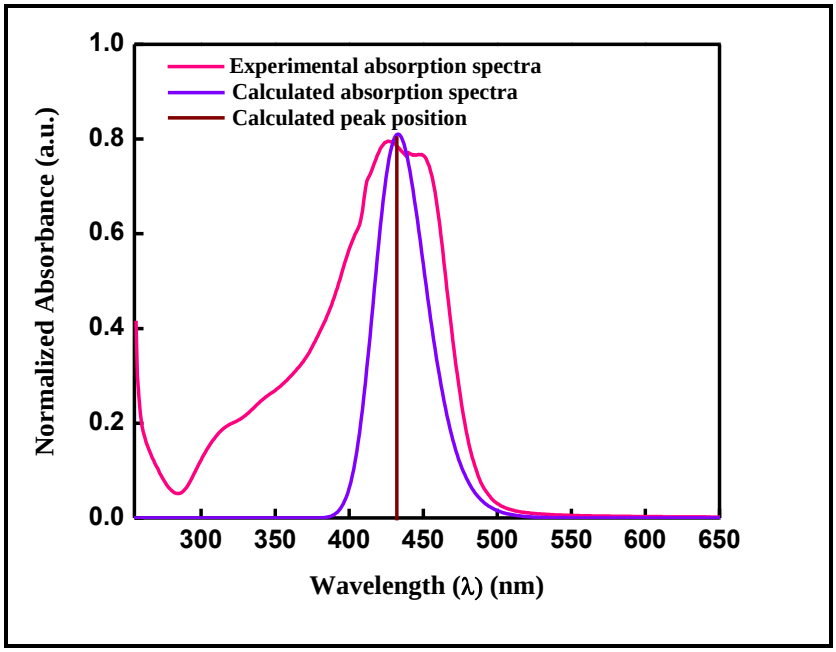


Figure 11: Comparison of experimental and theoretical UV-vis absorption spectra showing the most feasible peak positions

Table 4: A list of experimental UV-Vis transitions for Zn(II)-Curcumin in the solvent DMSO with the corresponding theoretically calculated UV-Vis transitions with various excitation energies (E_{ex}), oscillator strengths (f) as obtained from TDDFT method in DMSO

Experimental excitation values (nm)	Calculated excitation values (nm)	Excitation energy (eV)	Electronic Transitions	Osc. strength (f)	Key transitions involved	CI expansion coefficient	Character
426	431 nm	2.7313 eV	$S_0 \rightarrow S_3$	1.6121	HOMO → LUMO(100%)	0.70657	ILCT
410	394.88 nm	3.1398 eV	$S_0 \rightarrow S_5$	0.1080	HOMO-1 → LUMO (97%)	0.69608	ILCT
350	351.07 nm	3.5316 eV	$S_0 \rightarrow S_6$	0.0001	HOMO-5 → LUMO (98%)	0.69877	ILCT/ LLCT

10.4.3 Natural transition orbital (NTO) analysis:

The analysis relied on the calculated transition density matrices to elucidate the findings of the excited-state calculations. The concepts of "electron/particle" and "hole" transition orbitals were employed to characterize virtual/unoccupied and occupied NTOs, respectively.[52] By examining the relative importance of transition density matrices and occupied-virtual pair contributions to excitation, it became feasible to identify and illustrate the electronic transitions under investigation as excitations from a hole-NTO to an electron-NTO in the solution phase excited geometry.[52] NTOs for the most prominent peaks are displayed in Fig. 12.

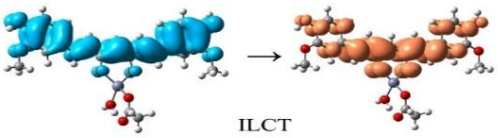
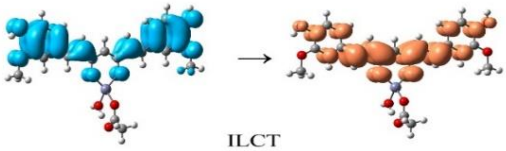
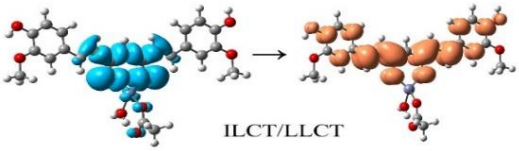
Experimental Excitation (nm)	Calculated Excitation (nm)	Excitation Energy (eV)	Excited state involved	Osc. Strength (f)	λi	ELECTRON → HOLE
426	453.94	2.7313	S3	1.6121	1	 ILCT
410	394.88	3.1398	S5	0.1080	0.97	 ILCT
350	351.07	3.5316	S6	0.0001	0.98	 ILCT/LLCT

Figure 12: NTO analysis describing the calculated UV-Vis peak positions

The most significant calculated peak was identified at 431 nm (2.7313 eV, f = 1.6121), corresponding to the lowest energy transition observed experimentally near 426 nm. This transition was categorized as an ILCT. The subsequent higher energy UV transition, estimated at 394.88 nm (3.13 eV, f = 0.180), was also attributed to ILCT and that was experimentally

observed at 410 nm. The UV excitation at 351.07 nm (3.5316 eV, f = 0.0001), detected close to the experimental peak at 350 nm, may be classified as ILCT or an extremely weak LLCT.

10.4.4 Analysis of quantum descriptor:

Frontier molecular orbitals (HOMOs and LUMOs) affect the kinetic stability, electrical conductivity and chemical reactivity of molecules. Soft molecules must have a narrow HOMO-LUMO energy gap and show enhanced biological and chemical reactivity. The opposite situation occurs: molecules with a broad HOMO–LUMO energy gap show low biological response, high stability, and low reactivity toward other molecules. In addition, small HOMO-LUMO energy gaps allow for intra-molecular charge transfer (ICT) of electrons from an electron donor to an electron acceptor. Notably, effective electron acceptor systems exhibit lower E_{LUMO} values than efficient electron donor systems, which are characterized by higher E_{HOMO} values.

Geometry optimization of HCur and [Zn(Cur)] is carried out and the resulting quantum descriptors are computed and compared in Table 5. IP and EA are facilitated by a small HOMO-LUMO gap. Electron affinity of [Zn(Cur)] is quite high compared to HCur which indicates that the complex might easily interact with biomolecules (like DNA or protein) by withdrawing electron density towards itself. On the other hand the lower η value (*Eq. 26, chapter 6, Experimental*) [53,54] of [Zn(Cur)] compared to HCur indicates that upon complex formation with Zn^{II}, HCur becomes soft and shows greater electron delocalization that facilitates more non-covalent interaction. A high value of ω (electrophilicity index) for [Zn(Cur)] represents high affinity towards electron rich species compared to HCur.

Table 5: Quantum descriptor for HCur and [Zn(Cur)] in eV with B3LYP-6-31G+(d,p) functional

Compound	HOMO	LUMO	ΔE	IP	EA	χ	η	M	σ	ω
HCur	-5.47	-2.27	3.20	5.47	2.27	3.87	1.60	-3.87	0.31	4.68
[Zn(Cur)]	-5.57	-2.94	2.63	5.57	2.94	4.62	1.32	-4.26	0.75	6.87

10.4.5 Analysis of MEP surface:

The "molecular electrostatic potential surface (MEP)" for the optimized geometries of Zn(Cur) was computed both in gas and solution phase (Fig. 13). The iso-value of the envelope was set to be 0.02 a.u, and the reverse rainbow color scheme was applied uniformly. Negative potential is represented in red, and positive potential in blue.[54–57] The hydrogen atoms on the phenolic O-H groups showed positive charges, whereas those on the CH_3 groups were only slightly positive. Similarly, the H atoms in H_2O were identified as mild positive. The most negative potential regions were observed adjacent to carbonyl O atoms and O atoms of acetate. Inferring that there is a strong likelihood that molecules would create hydrogen bonding connections between H of water and carbonyl O of an acetate that could eventually stabilize the system.

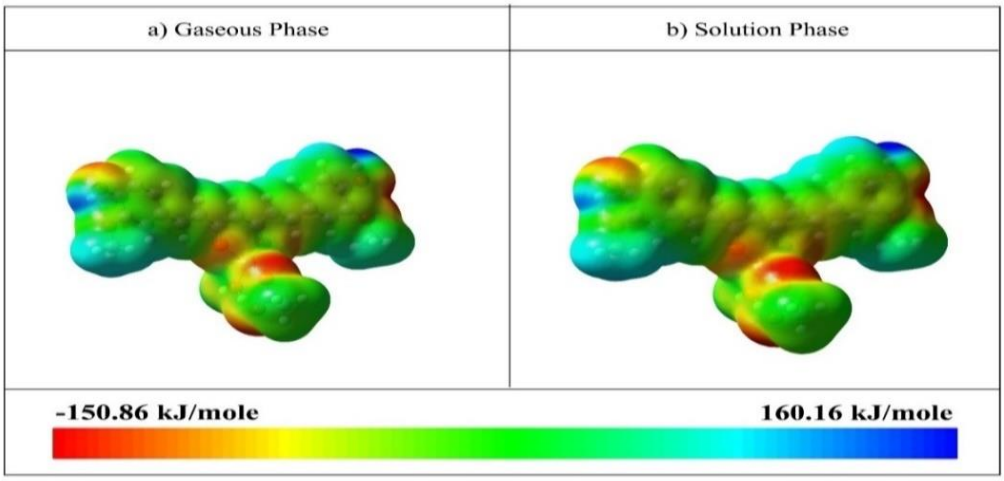


Figure 13: Molecular electrostatic Potential surface of [Zn(Cur)] in (a) Gas phase and (b) solution phase

10.4.6 Non-covalent interactions (NCI) and bond Critical Point Analysis:

Reduced density gradient (RDG) is a robust method for investigating non-covalent interactions by analyzing distribution of electrons and their derivatives.[58,59] This technique has demonstrated the capacity to differentiate between different types of non-covalent interactions present in small organic molecules that act as ligands and for the same compounds when present in a metal complexes. The equation utilized for calculating RDG being[58,59]

$$RDG = \frac{1}{2(3\pi^2)^{1/3}} \frac{|\nabla\rho|}{\rho^{4/3}}$$

Through careful analysis of the values of low and high-density gradients, one can establish the existence of both weak and strong interactions. Graphs that depict the relationship between RDG and low-gradient peak density (ρ) provide valuable insights into the intensity of an interaction. One possible way to distinguish between different types of interactions is by using electron density and sign of second eigenvalues. The sign of the parameter λ_2 is crucial in distinguishing between bonded interactions ($\lambda_2 < 0$) and non-coupling interactions ($\lambda_2 > 0$). Three different types of interactions can be categorized based on specific principles. Attraction is indicated by negative sign of values (λ_2). Another hypothesis suggests the presence of a strong repulsion-like interaction, supported by significant and positive values of the sign (λ_2). Weak interactions, also referred to as van der Waals interactions are typically characterized by values close to zero. Fig.14 shows the projected RDG plots for $[Zn^{II}(Cur)(OCOCH_3)(OH_2)]$. Several types of interactions were used to explain the relationship between hydrogen, oxygen, Zn^{II} and carbon within the molecule. An observed red color suggests there is repulsion in the system. More precisely in the vicinity of two carbonyl oxygens close to the binding site of the metal. Van der Waals interactions are represented by a green color. Blue is a clear indication for a noteworthy hydrogen bond interaction ~~with~~in the system. From NCI analysis (Fig. 14), it was observed

carbonyl-O of acetate in [Zn(Cur)] and H of O-H in water form strong intra-molecular hydrogen bond; displayed as a blue iso-surface.

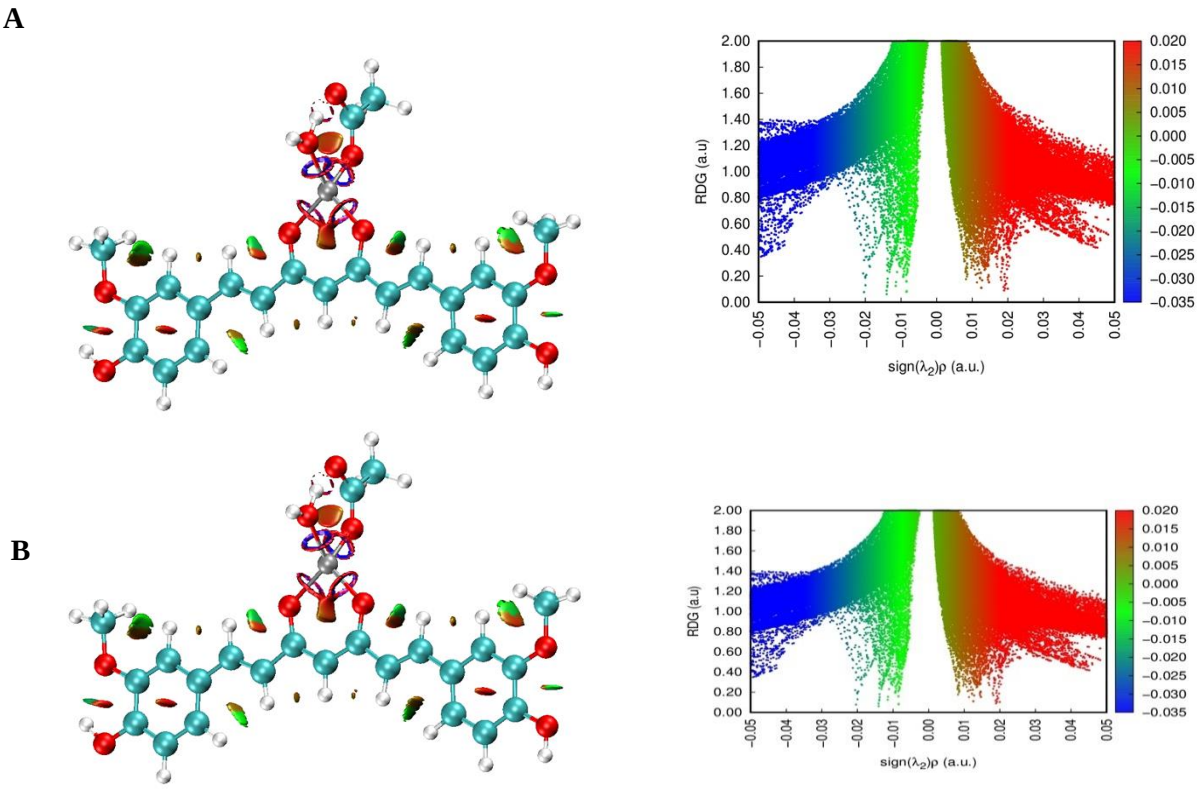


Figure 14: NCI (right) and RDG (left) plot of optimized [Zn^{II}(Cur)($OCOCH_3$)(OH_2)] molecule in (A) Gas Phase , (B) Solution (DMSO) phase

The bond strength of [Zn(Cur)] was estimated by critical point analysis with Quantum theory of atoms-in-molecules (QTAIM) descriptors.[60] Surprisingly, there is a strong hydrogen bond obtained between water and the acetate ion. Using critical point analysis, we observed threefold enhancement in strength of the formed hydrogen bond over that of a normal hydrogen bond. It may be noticed from Table 6 that for normal hydrogen bonds (NHB)\ρ = 0.02 e/bohr^3 and for strong hydrogen bonds (SHB)\ρ = 0.062 e/bohr^3. In fact, strength of an SHB is equivalent to that of a coordinate covalent bond but less than a covalent bond which is usually 0.2 e/bohr^3.

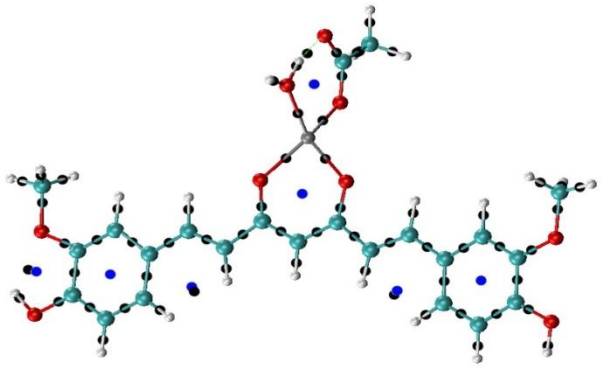


Figure 15: DFT optimized geometry of [Zn(Cur)] showing hydrogen bond critical points (CP) indicated by blue and black spheres; black spheres represent bond critical points (3, -1) in which one of them represents hydrogen bond critical point; blue spheres represent ring critical point.

Table 6: Intramolecular Bond Critical Points in [ZnCur] . The electron densities at the CPs are in (ρ in e/bohr^3)

Critical Point type (z)	CP Index	x	y	z	ρ in e/bohr^3
(3,-1)	63	-0.1257635E+01	0.3000844E+01	-0.6239480E+00	0.6537932E-01 (Zn--O)
(3,-1)	64	0.1237809E+01	0.2999654E+01	-0.6295046E+00	0.6531302E-01 (Zn--O)
(3,-1)	65	-0.9208475E-02	0.9118020E+01	-0.2079456E+01	**0.6192872E-01 (SHB)**
(3,-1)	66	-0.8315368E-02	0.5611219E+01	0.4626012E+00	0.6161470E-01 (Zn--O)
(3,-1)	67	-0.1002158E-01	0.5429999E+01	-0.2089363E+01	0.6161335E-01 (Zn--O)
(3,-1)	68	0.1700016E+02	-0.3904205E+01	0.2067873E+00	**0.2045178E-01 (NHB)**

10.4.7 ELF and LOL Analysis:

The studies ELF (Electron Localization Function) and LOL (localized Orbital Locator) primarily focus on analysis of topological surfaces. Research conducted using Multiwfn software package[61] has shown a significant likelihood of locating an electron pair on the surface of a molecule, indicated by ELF and LOL. In Fig. 16, the colour shades and relief map of ELF and LOL is shown. The relief map highlights electron environment around each atom; variations in peak area indicate either a large or contracted electron density. The chemical content of ELF and LOL is homogenous due to their dependence on kinetic energy density. The ELF theory explains the distribution of electron pairs while LOL describes overlap of localized orbitals caused by gradient of orbitals.[49] The ELF map is designed to cover a range from 0.0 to 1.0. Interestingly, the region below 0.5 displays a delocalized electronic region[62] while LOL reaches significant values above 0.5 in areas where electron density is primarily influenced by electron localization.[63] The different shades of colour on ELF and LOL maps provide evidence of the presence of bonding and non-bonding electrons. In particular, the red colour surrounding hydrogen atoms indicate the presence of these electrons. The presence of a green colour around oxygen atoms (e.g. O7, O8 Fig.16 B) indicates a strong concentration of electrons that may be attributed to factors such as covalent bond formation, a lone pair of electrons or a nuclear shell in that particular region. The blue colour surrounding carbon and oxygen atoms indicate the presence of a delocalized electron cloud. The central region of a hydrogen atom in LOL appears white due to electron density surpassing the upper limit of the colour scale.[64]

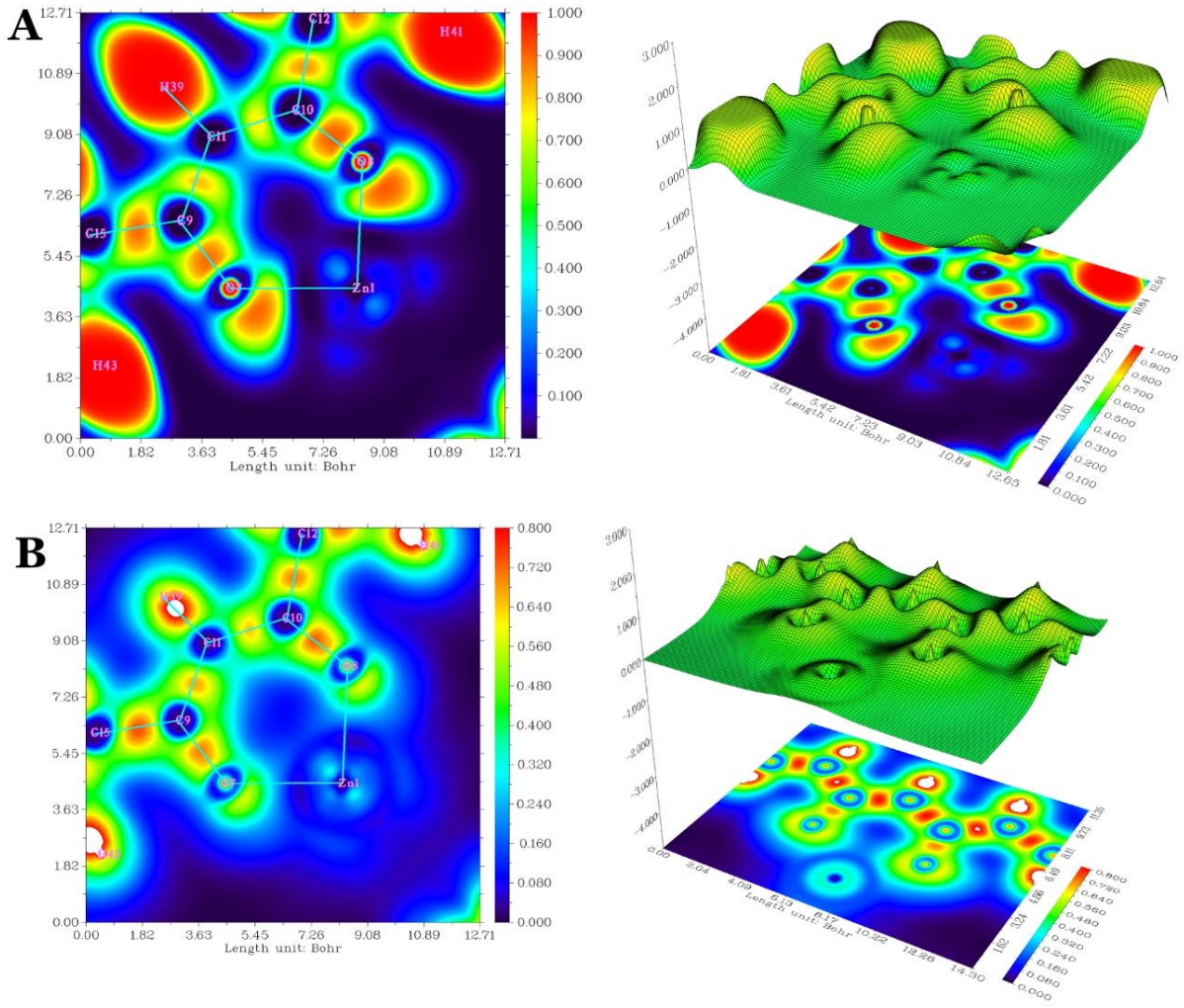


Figure 16: (A)Electron localization function (ELF) maps and (B)localized orbital locator (LOL) maps of optimized [Zn^{II}(Cur)($OCOCH_3$)(OH_2)] molecule

10.5 A comparative stability analysis of [Zn^{II}(Cur)($OCOCH_3$)(OH_2)] under physiological conditions

10.5.1 Followed by UV-Vis spectroscopy:

Considering the chemical instability of HCur, we started this study with the question, that is, does complex formation of HCur with Zn^{II} help in stabilizing it under physiological conditions? To be able to answer this question the stability of Zn(Cur) in different biological milieu were compared and examined and. As reported earlier[65] intensity of absorption spectra of

HCur decreased significantly over time in buffer solutions; indeed, more than 50% of its original intensity was lost within the first 20 minutes of incubation in PBS. In contrast, absorption spectra of Zn(Cur) did not decrease but remained stable over time in PBS. These results suggest the complex to be reasonably stable in physiological buffer medium and in different microbiological media. There was no noticeable decrease in absorbance intensity for the complex (Fig.17).

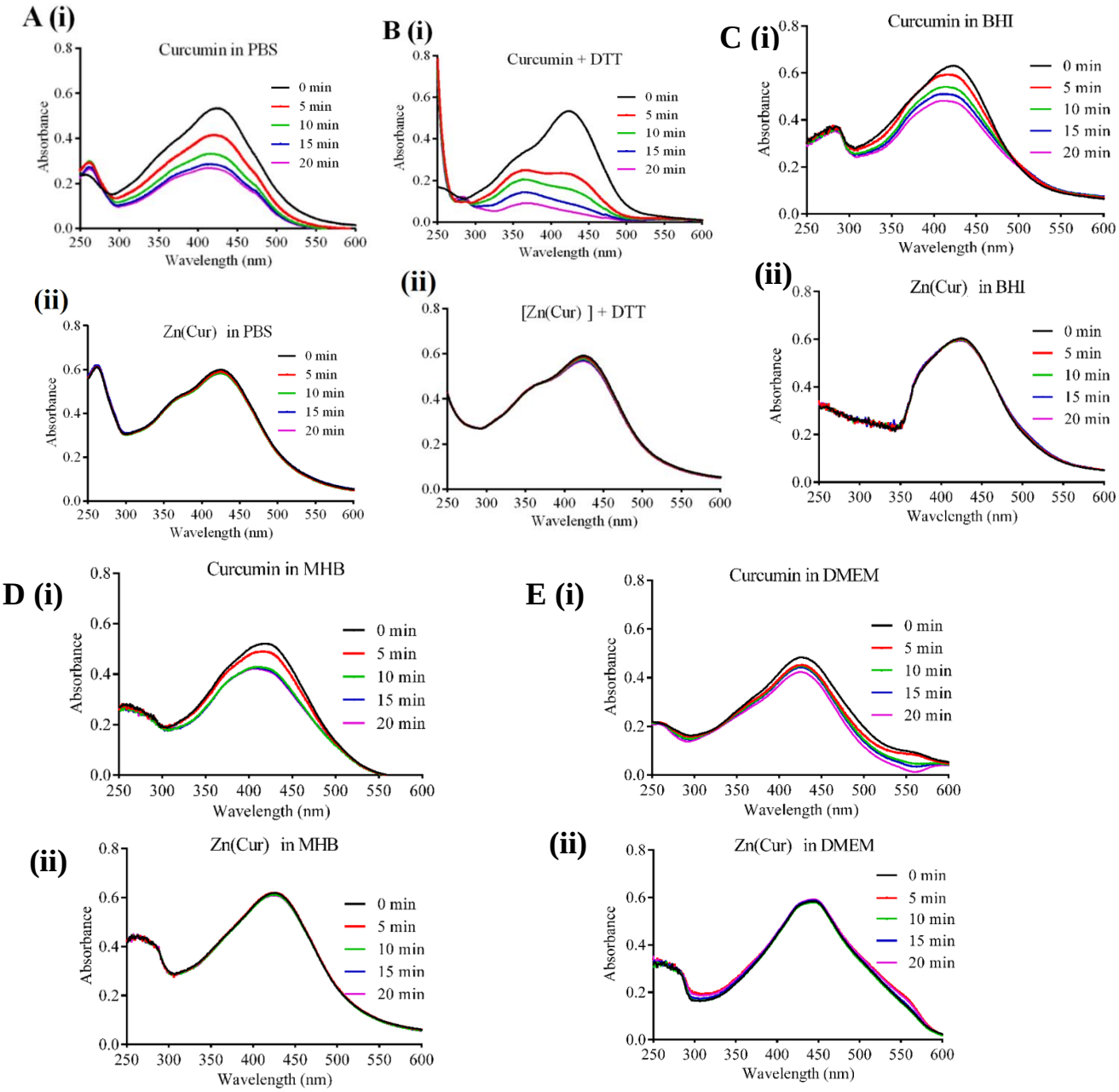


Figure 17: UV-Visible spectra of Curcumin and Zn(Cur) in (A) PBS buffer, (B) in presence of 10 µM DTT (C) BHI (D) MHB and (E) DMEM media

Since the cytosolic environment is reducing, stability of Zn(Cur) and HCur was also studied in presence of a common reducing agent, dithiothreitol (DTT). In line with previous findings we observed a much faster degradation of HCur in the presence of DTT. HCur lost more than 50% of its absorption intensity within the first 5 minutes of incubation. On the other hand, Zn(Cur) was found to be exceptionally stable since its absorption intensity did not decrease even after 20 min of incubation with DTT (Fig. 17).

Overall, as evident from Fig. 17, complex formation of HCur results in increased stability of Zn(Cur), at physiological pH even under reducing conditions, unlike that observed for HCur alone. This improved stability is attributed to complex formation, i.e. to the binding of Zn^{II} to the hydrolysis prone β-diketone moiety preventing a degradation of the complex under aqueous physiological conditions.

10.6 Interaction of $[Zn^{II}(Cur)(OCOCH_3)(OH_2)]$ with calf thymus DNA

[Zn(Cur)] was titrated with calf thymus DNA at constant pH (= 7.4) and constant ionic strength (0.15 mM) of the medium. A gradual decrease in absorbance at 430 nm or a gradual increase in fluorescence at 570 nm helped in evaluating the interaction occurring between [Zn(Cur)] and calf thymus DNA (Fig. 18).

Fig. 19 (A) is a double reciprocal plot of $1/\Delta A$ versus $1/[C_D\text{-}C_L]$ [*Eq. 31, Chapter 6, Experimental*] that provides values for K_{app} (= K_d^{-1}) from two independent titrations.[66-70] An average of their values was $2.23 \times 10^3\ M^{-1}$.

Fig. 19 (B) is a plot of $\Delta A/\Delta A_{max}$ versus concentration of calf thymus DNA to which non-linear curve fit was applied (*Eqs. 32 & 33,* chapter 6, *Experimental*). Two independent titrations provide an average apparent binding constant of $2.25 \times 10^3\ M^{-1}$ at 298 K. Inset of Fig. 19 (B)

provides a value of n_b as 10.0, i.e. number of nucleotides bound to [Zn(Cur)] following interaction with calf thymus DNA.[66-70]

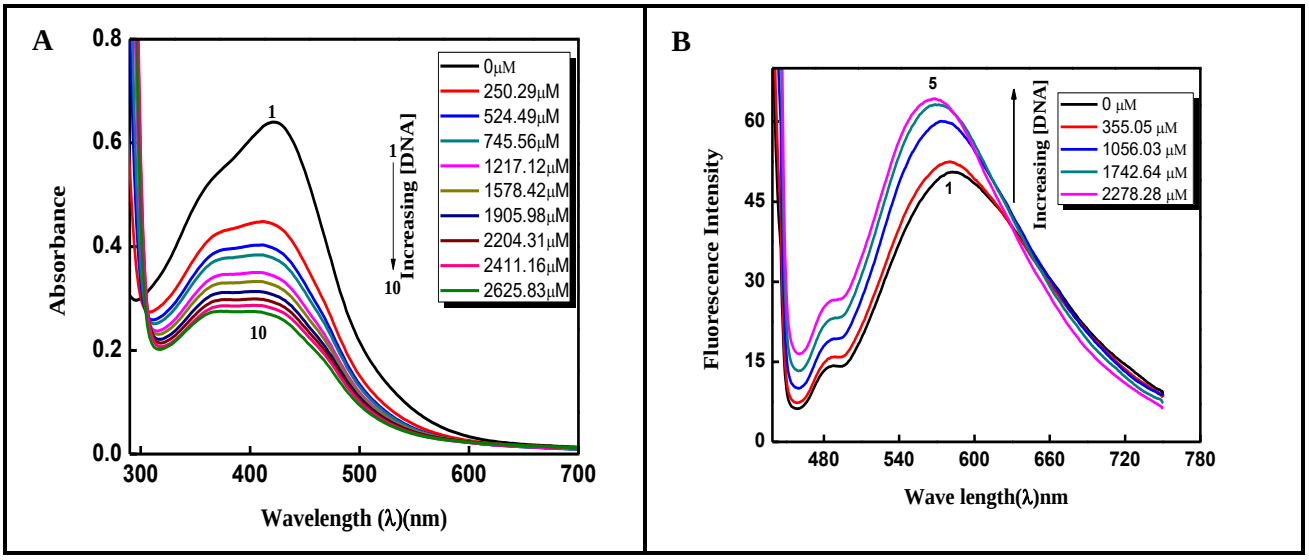


Figure 18: (A) Absorption spectra of [Zn(Cur)] in the absence (1) and presence of different concentrations of calf thymus DNA (2) 250.29 μM, (3) 524.49 μM, (4) 745.56 μM, (5) 1217.12 μM, (6) 1578.42 μM, (7) 1905.98 μM, (8) 2204.31 μM, (9) 2411.16 μM and (10) 2625.83 μM; [NaCl] = 150 mM, pH = 7.4; Temp. = 298 K. (B) Fluorescence intensity of [Zn(Cur)] in the absence (1) and presence of different concentrations of calf-thymus DNA (2) 355.05 μM, (3) 1056.03 μM, (4) 1742.64 μM, (5) 2278.28 μM;;[NaCl] = 150 mM, pH = 7.4, Temp. = 298 K.

The titration data was also fitted to a modified form of the Scatchard equation (*Eq. 35*, Chapter 6, *Experimental)* Fig.19 (C).[71] K* and n (= n_b^{-1}) was obtained. Values obtained from *Eq. 34*, *Chapter 6, Experimental* were close to that obtained from other methods of analyses (*Eq. 31-33*, *Chapter 6, Experimental*) justifying the techniques that calculate them.

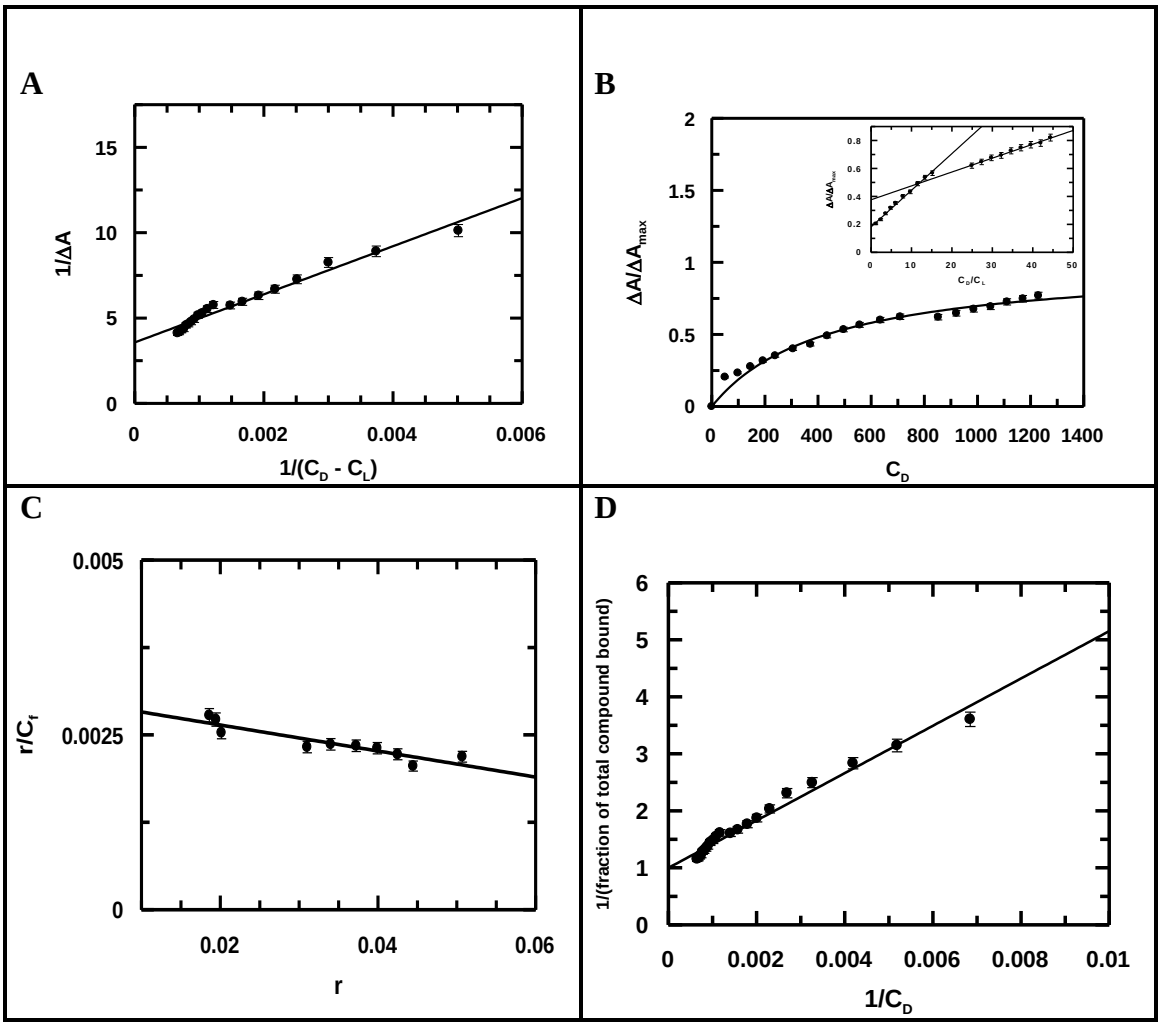


Figure 19: (A) Double reciprocal plot for the interaction of [Zn(Cur)] with calf-thymus DNA to evaluate apparent binding constant (K_{app}) of the complex to DNA, (B) binding isotherm for [Zn(Cur)] interacting with calf thymus DNA when $\Delta A/\Delta A_{max}$ was plotted against concentration of DNA; the dark line is the fitted data obeying Eq.33(*Chapter 6, Experimental*). Inset: Plot of normalized increase in absorbance as a function of mole-ratio of calf thymus DNA to [Zn(Cur)]. (C) A modified Scatchard plot for interaction of [Zn(Cur)] with calf thymus DNA; (D) a plot showing 1/fraction of total compound bound vs 1/concentration of calf thymus DNA taken ; [Zn(Cur)] = 41.2 μM, [NaCl] = 150 mM, pH = 7.4 (30 mM phosphate buffer), Temp.= 298K.

Table 7: Binding parameters for interaction of [Zn(Cur)] with calf thymus DNA at pH = 7.4.

DNA binding methods	No. of Expt.	Apparent binding constant K_{app} (M^{-1})			Site size from mole-ratio plot	Overall binding Constant $K^*(M^{-1})$ $K^* = K_{app} \times n_b$			Overall binding Constant from Scatchard $\times 10^{-4}$	Site size from Scatchard plot
		Double reciprocal plot $\times 10^{-3}$	Non-linear plot $\times 10^{-3}$	Double reciprocal plot, y-intercept =1 $\times 10^{-3}$		Double reciprocal $\times 10^{-4}$	Non-linear $\times 10^{-4}$	Double reciprocal plot, y-intercept =1 $\times 10^{-4}$		
	1	2.54	2.51	2.41	10.0	2.54	2.51	2.41	1.86	6.0
Absorbance	2	1.91	1.99	1.89	11.0	2.10	2.19	2.08	2.04	8.0
Fluorescence	1	2.08	1.77	1.42	5.0	1.04	0.90	0.71	1.49	6.0
	2	0.96	0.92	0.72	8.0	0.58	0.55	0.57	0.70	7.0

Titration of this complex with DNA is important for a number of reasons. First, since titration of HCur with DNA has not been possible owing to reasons mentioned earlier, the monomeric complex of Zn^{II} with HCur, where HCur shows no degradation, makes it a model, that in a way represents the binding of HCur to DNA.

However, while considering the data, one has to remember that for [Zn(Cur)] there would be an influence of Zn^{II} to the process of binding.[66-69] Therefore, being able to maintain HCur as a single unit in solution, and that there would be no extra influence due to the complex owing to lack of redox behavior on the part of Zn^{II}, the binding constant value of the complex could well represent HCur. Hence, with HCur connected to a metal centre, one can now have an idea of its binding to DNA, that was not possible experimentally. Second, from an estimate of binding constant values obtained for [Zn(Cur)] it might become possible to explain some of the mechanisms that are involved during an interaction of HCur with DNA (considering HCur as one unit in the coordination compound) and its consequences thereof, during biological interactions, where besides various fragmented forms generated in solution, a substantial portion does remain

as one unit.[14] Hence, together (that is fragmented products of HCur and "HCur as one unit") it might become possible to explain a lot of the beneficial activities of HCur.[14]

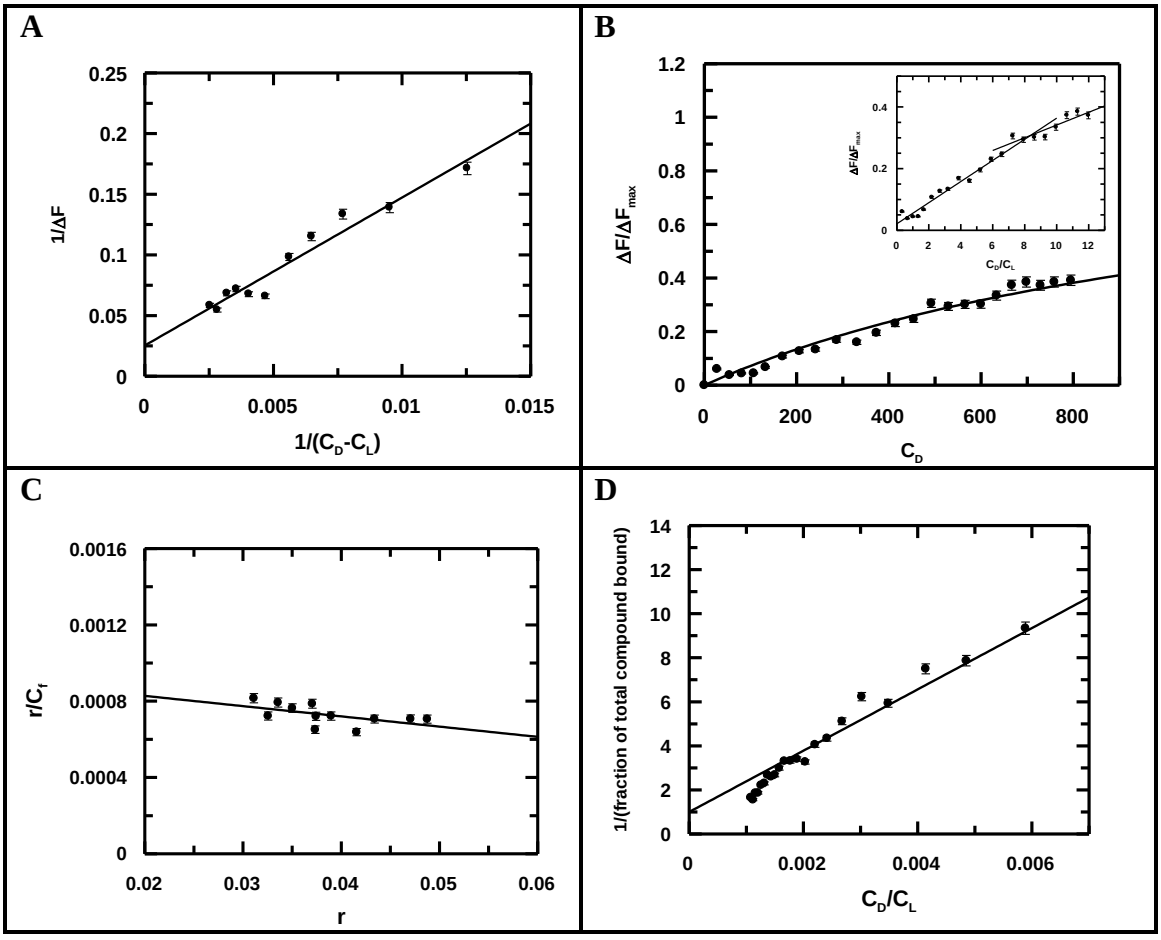


Figure 20 : (A) Double reciprocal plot for the interaction of [Zn(Cur)] with calf-thymus DNA to evaluate apparent binding constant (K_{app}), (B) Binding isotherm for [Zn(Cur)] interacting with calf thymus DNA when $\Delta F/\Delta F_{max}$ was plotted against concentration of DNA; the dark line indicates fitted data obeying Eq. 33(*Chapter 6, Experimental*). Inset: Plot of normalized increase in absorbance as a function of mole-ratio of calf thymus DNA to [Zn(Cur)]. (C) A modified Scatchard plot for interaction of [Zn(Cur)] with calf thymus DNA; (D) A plot showing 1/fraction of total compound bound vs 1/conc. of calf thymus DNA; [Zn(Cur)] = 82.4 μM, [NaCl] = 150 mM, pH = 7.4 (30 mM phosphate buffer), Temp.= 298K.

10.7 Biological applications of the prepared [Zn^{II}(Cur)($OCOCH_3$)(OH_2)] complex

Biological attributes of the complex [Zn^{II}(Cur)($OCOCH_3$)(OH_2)] that was prepared by me (Mr. Tanmoy Saha) during my research work was subjected to several investigations through a collaboration in the laboratory of Prof. Kasturi Mukhopadhyay at the School of Environmental Sciences, Jawaharlal Nehru University, New Delhi. Studies were performed on antibacterial activity on *S. aureus* and *E. coli strains*. A study investigated the mechanism of antibacterial action due to the Zn(II) complex by exploring membrane permeabilization of *S. aureus* as realized from the calcein leakage assay. Calcein leakage due to Zn(Cur) was nearly comparable to that of gramicidin D, a well-known pore-forming peptide suggesting that the complex was efficient in permeabilizing bacterial membrane. Overall, Zn(Cur) showed better and statistically significant increase in membrane permeabilization compared to Curcumin. To ascertain membrane-directed mechanism of the complex, membrane integrity was assessed by a fluorescence-based dual staining procedure using DNA binding dyes SYTO 9 and P I. SYTO 9 can penetrate all cell membranes (intact or damaged) freely and label cells green. In contrast, P I can only penetrate cells with damaged membranes. When both dye are present, P I with stronger binding affinity for DNA, replaces SYTO 9 resulting in red fluorescence for dead cells. Such fluorescently-labeled cells were visualized by fluorescence microscopy.

The color of Zn(Cur) treated cells was predominantly red suggesting that most were dead with compromised membrane. This membrane damaging property of the Zn^{II} complex was in line with findings of calcein leakage assay. In case of HCur-treated cells, mixed population of red, green and yellow stained cells were observed. Yellow fluorescent cells retained both red and green dyes thus indicating only a minor damage to the membrane that allowed only some P I to enter the cell, but not high enough to be able to replace all the SYTO 9 bound to DNA.

Morphological changes in treated samples were compared with untreated ones and with gramicidin D-treated samples. Experiments realized through the use of scanning electron microscope (SEM), revealed *S. aureus* of the untreated control group maintained a smooth surface with uniform morphology. However, surface perturbation and release of intracellular content as debris were evident for cells that had underwent treatment with Zn(Cur) or HCur. These treated cells appeared to be seriously wrinkled, holed with multiple dents on the surface. Changes in surface morphology following treatment with Zn^{II} complex was comparable to that of gramicidin D-treated samples indicating the complex should be further explored in this regard. Ultrastructural changes in *S. aureus* following treatment of 50 μM HCur and Zn(Cur) were visualized using transmission electron microscope and compared to untreated as well as gramicidin D- treated cells. It was evident that untreated control sample had regular cocci morphology with intact cell envelope. After treatment with compounds, several distinguished signs of damaged cell envelop were apparent. Most cells had shredded cell wall that led to a distorted and irregular shape. Many cells lacked cytoplasmic content; intracellular content were also seen oozing out from a few cells. These ultrastructural changes that resulted from the treatment of Zn(Cur) were comparable to that observed in case of gramicidin D-treated samples. Alterations in bacterial surface realized by SEM and TEM confirmed bacterial membrane to be a primary target for the complex indicating membrane perturbation to be a key mechanism for antibacterial activity in *S. aureus* cells.

Toxicity studies were performed using Zn(Cur) on mammalian cells to see if complex formation imparted any form of toxicity on normal cells. Hemolytic and cytotoxic potential studies of Zn(Cur) on RBCs and 3T3 fibroblast cells respectively were carried out. Results of hemolytic assay confirmed that Zn(Cur), like curcumin, was nearly non-hemolytic up to 500 μM. It caused only 2.19 ± 1.19 % hemolysis at 250 μM and 6.96 ± 2.30 % hemolysis at 500 μM.

Further to hemolytic assay, MTT assay was done to rule out any potential cytotoxicity on mammalian cells. Studies revealed that Zn(Cur) did not impart any cytotoxic effect on 3T3 murine fibroblast cells up to 500 μM. The complex caused only 7.81 ± 1.06% cytotoxicity at 250 μM and 14.88 ± 2.27% cytotoxicity at 500 μM. 2.0% Triton X-100 was used as the positive control which imparted 87.86 ± 2.82% cytotoxicity relative to untreated growth control.

Hence, both toxicity assays indicated that the Zn^{II} complex was non-toxic exhibiting negligible toxicity on mammalian cells up to 500 μg/mL, well above the dose required for antibacterial activity, suggesting it to be a safe antibacterial agent.

References:

1. R. A. Sharma, W. P. Steward, A. J. Gescher; Pharmacokinetics and pharmacodynamics of curcumin. *Adv. Exp. Med. Biol*., **2007**, 595, 453-470.
2. B. B. Aggarwal, C. Sundaram, N. Malani, and H. Ichikawa; Curcumin: the Indian solid gold. In: The molecular targets and therapeutic uses of curcumin in health and disease. *Springer, Boston, MA.*, **2007**, 595, 1-75.
3. J. S. Jurenka; Anti-inflammatory properties of curcumin, a major constituent of Curcuma longa: a review of preclinical and clinical research. *Alternative Medicine Review.*, **2009**,14, 141-153.
4. T. Ak, and İ.Gülçin; Antioxidant and radical scavenging properties of curcumin. *Chemico-bi*Ak, *ological Interactions*., **2008**,174, 27-37.
5. R. Wilken, M. S. Veena, M. B. Wang, E. S. Srivatsan; Curcumin: A review of anti-cancer properties and therapeutic activity in head and neck squamous cell carcinoma. *Mol. Cancer*., **2011**, 10:12.

6. A. Goel, A. B. Kunnumakkara, B. B. Aggarwal; Curcumin as "Curcumin": from kitchen to clinic. *Biochem. Pharmacol.*, **2008**, 75, 787-809.

7. K. Neelofar, S. Shreaz, B. Rimple, S. Muralidhar, M. Nikhat, & L. A. Khan; Curcumin as a promising anticandidal of clinical interest. *Can. Jour.Microbiol.,* **2011**, 57, 204-210.

8. M. Metzler, E. Pfeiffer, S.I. Schulz, J.S. Dempe; Curcumin uptake and metabolism. *Biofactors,* **2013**, 39, 14-20.

9. P. Anand, A. B. Kunnumakkara, R. A. Newman, B. B. Aggarwal; Bioavailability of Curcumin: Problems and promises, *Mol. Pharmaceutics.*, **2007**, 4, 807–818.

10. Y. J. Wang, M. H. Pan, A. L. Cheng, L. I. Lin, Y. S. Ho, C. Y. Hsieh, J. K. Lin; Stability of curcumin in buffer solutions and characterization of its degradation products. *J PharmBiomed. Anal.,* **1997**, 15**,** 1867-1876.

11. M. Kharat, Z. Du, G. Zhang, D. J. McClements; Physical and chemical stability of curcumin in aqueous solutions and emulsions: Impact of pH, temperature, and molecular environment. *J Agric Food Chem.,* **2017**,65, 1525-1532.

12. H. H. Tønnesen, M. Másson, T. Loftsson; Studies of curcumin and curcuminoids. XXVII. Cyclodextrin complexation: solubility, chemical and photochemical stability. *Int J Pharm.*, **2002**, 244,127-135.

13. S. Wanninger, V. Lorenz, A. Subhan and F. T. Edelmann; Metal complexes of curcumin–synthetic strategies, structures and medicinal applications. *Chem. Soc. Rev.*, **2015**, 44, 4986-5002.

14. K. Mitra, S. Gautam, P. Kondaiah, A. R. Chakravarty; Platinum(II) complexes of Curcumin showing photocytotoxicity in visible light. *Eur. J. Inorg. Chem*. **2017**, 1753-1763.

15. M. S. Refat; Synthesis and characterization of ligational behavior of curcumin drug towards some transition metal ions: chelation effect on their thermal stability and biological activity. *Spectrochimica Acta Part A: Molecular and Biomolecular Spectroscopy*,**2013**, 105, 326-337.

16. F. Caruso, M. Rossi, A. Benson, C. Opazo, D. Freedman, E. Monti, M. B. Gariboldi, J. Shaulky, F. Marchetti, R. Pettinari and C. Pettinari; Ruthenium–Arene complexes of Curcumin: X-Ray and density functional theory structure, synthesis, and spectroscopic characterization, *in vitro* antitumor activity, and DNA docking studies of (*p*-Cymene)Ru(curcuminato)chloro. *J. Med. Chem.*, **2012**, 55, 1072–1081.

17. H. M. Leung, M. Harada, W. Takaaki, T. Kee; Delivery of Curcumin and medicinal effects of the Copper(II)-Curcumin complexes. *Current Pharmaceutical Design*.,**2013**,19, 2070-2083.

18. D.P. Kiouri, C.T. Chasapis, T. Mavromoustakos, C.A. Spiliopoulou, M.E. Stefanidou; Zinc and its binding proteins: essential roles and therapeutic potential. *Archives of Toxicology*, **2024**. 1-19.

19. N.Karunasinghe; Zinc in Prostate Health and Disease: A Mini Review. *Biomedicines*, **2022**, 10, 3206.

20. M. Maywald, L. Rink; Zinc in human health and infectious diseases. *Biomolecules*, **2022,** 12, 1748.

21. T. Fukada, S. Yamasaki, K. Nishida, M. Murakami, T. Hirano; Zinc homeostasis and signaling in health and diseases: Zinc signaling. *Journal of Biological Inorganic Chemistry*, **2011**, 16, 1123-1134.

22. H. Sharir, M. Hershfinkel; The extracellular zinc-sensing receptor mediates intercellular communication by inducing ATP release. *Biochemical and biophysical research communications*, **2005**, 332, 845-852.

23. A. Formigari, P. Irato, A. Santon; Zinc, antioxidant systems and metallothionein in metal mediated-apoptosis: biochemical and cytochemical aspects. *Comparative Biochemistry and Physiology Part C: Toxicology & Pharmacology*, **2007**, 146, 443-459.

24. K. Subramanian Vignesh, G.S. Deepe Jr; Metallothioneins: emerging modulators in immunity and infection. *International journal of molecular sciences*, **2017**, 18, 2197.

25. A. Álvarez-Barrios, L. Álvarez, M. García, E. Artime, R. Pereiro, H. González-Iglesias; Antioxidant defenses in the human eye: A focus on metallothioneins. *Antioxidants*, **2021**,10, 89.

26. M.P. Cuajungco, M.S. Ramirez, M.E. Tolmasky; Zinc: Multidimensional effects on living organisms. *Biomedicines*, **2021**, 9, 208.

27. H.F. Wertheim, D.C. Melles, M.C. Vos, W. van Leeuwen, A. van Belkum, H.A. Verbrugh, J.L. Nouwen; The role of nasal carriage in *Staphylococcus aureus* infections. *The Lancet infectious diseases*, **2005**, 5, 751-762.

28. E.F. Kong, J.K. Johnson; Community-Associated Methicillin-Resistant *Staphylococcus aureus*: *An Enemy amidst Us.*, **2016**,12, e1005837.

29. K. Hiramatsu, Y. Katayama, M. Matsuo, T. Sasaki, Y. Morimoto, A. Sekiguchi, T. Baba; Multi-drug-resistant *Staphylococcus aureus* and future chemotherapy. *Journal of infection and chemotherapy: official journal of the Japan Society of Chemotherapy*, **2014,** 20 593-601.

30. V. Niranjan, A. Malini; Antimicrobial resistance pattern in *Escherichia coli* causing urinary tract infection among inpatients. *Indian J Med Res*, **2014**,139, 945-948.

31. F.Y. Ramírez-Castillo, A.C. Moreno-Flores, F.J. Avelar-González, F. Márquez-Díaz, J. Harel, A.L. Guerrero-Barrera; An evaluation of multidrug-resistant *Escherichia coli* isolates in urinary tract infections from Aguascalientes, Mexico: cross-sectional study. *Ann Clin Microbiol Antimicrob*, **2018**,17, 34-34.

32. P.M. Hawkey, R.E. Warren, D.M. Livermore, C.A.M. McNulty, D.A. Enoch, J.A. Otter, A.P.R. Wilson; Treatment of infections caused by multidrug-resistant Gram-negative bacteria: report of the British Society for Antimicrobial Chemotherapy/Healthcare Infection Society/British Infection Association Joint Working Party†. *Journal of Antimicrobial Chemotherapy*, **2018**, 73, iii2-iii78.

33. N.G. El Chakhtoura, E. Saade, A. Iovleva, M. Yasmin, B. Wilson, F. Perez, R.A. Bonomo; Therapies for multidrug resistant and extensively drug-resistant non-fermenting gram-negative bacteria causing nosocomial infections: a perilous journey toward 'molecularly targeted' therapy. *Expert review of anti-infective therapy*, **2018**,16, 89-110.

34. F.D. Lowy; Staphylococcus aureus infections. *New England journal of medicine*, **1998**, 339, 520-532.

35. J.D. Pitout, K.B. Laupland; Extended-spectrum β-lactamase-producing Enterobacteriaceae: an emerging public-health concern. *The Lancet infectious diseases*, **2008,** 8, 159-166.

36. N. Chaachouay, L. Zidane; Plant-derived natural products: a source for drug discovery and development. *Drugs and Drug Candidates*, **2024**, 3, 184-207.

37. V. Prachayasittikul, A. Worachartcheewan, W. Shoombuatong, N. Songtawee, S. Simeon, V. Prachayasittikul, C. Nantasenamat; Computer-aided drug design of bioactive natural products. *Current Topics in Medicinal Chemistry*, **2015**, 15, 1780-1800.

38. K. Neelofar, S. Shreaz, B. Rimple, S. Muralidhar, M. Nikhat, L.A. Khan.; Curcumin as a promising anticandidal of clinical interest. *Can J Microbiol*., **2011**, 57, 204-210.

39. B.C. Mounce, T. Cesaro, L. Carrau, T. Vallet, M. Vignuzzi; Curcumin inhibits Zika and chikungunya virus infection by inhibiting cell binding. *Antiviral Research*, **2017**, 142, 148-157.

40. S. Y. Teow, K. Liew, S. A. Ali, A. S. B. Khoo and S. C. Peh; Antibacterial action of curcumin against Staphylococcus aureus: a brief review. *Journal of Tropical Medicine*, **2016**, 2853045.

41. P. Tyagi, M. Singh, H. Kumari, A. Kumari and K. Mukhopadhyay; Bactericidal activity of Curcumin I is associated with damaging of bacterial membrane. *PloS one 10*., **2015**, e0121313.

42. S. Banerjee, P. Prasad, I. Khan, A. Hussain, P. Kondaiah, A. R. Chakravarty; Mitochondria targeting photocytotoxic oxidovanadium(IV) complexes of curcumin and (acridinyl) dipyridophenazine in visible light. *Z. Anorg. Allg. Chem*., **2014**,640, 1195-1204.

43. M. Bernabé-Pineda, M. T. Ramírez-Silva, M. Romero-Romo, E. González-Vergara, A. Rojas-Hernández; Determination of acidity constants of curcumin in aqueous solution and apparent rate constant of its decomposition. *Spectrochim. ActaA Mol. Biomol. Spectrosc.*, **2004**, 60,1091-1097.

44. P. Das, C. K. Jain, S. Roychoudhury, H. K. Majumder, S. Das; Design, synthesis and invitroanticancer activity of a Cu(II) complex of Carminic acid: A novel small molecule inhibitor of human DNA topoisomerase I and topoisomerase II, *ChemistrySelect* , **2016**, 1, 6623-6631.

45. K. Nakamoto; Infrared and Raman spectra of inorganic and coordination compounds, 3rd edition, Wiley-Interscience, New York, **1978**.

46. M. J. Frisch, G. W. Trucks, H. B. Schlegel, G. E. Scuseria, M. A. Robb, J. R. Cheeseman, G. Scalmani, V. Barone, G. A. Petersson, H. Nakatsuji, X. Li, M. Caricato, A. Marenich, J. Bloino, B. G. Janesko, R. Gomperts, B. Mennucci, H. P. Hratchian, J. V. Ortiz, A. F. Izmaylov, J. L. Sonnenberg, D. Williams-Young, F. Ding, F. Lipparini, F. Egidi, J. Goings, B. Peng, A. Petrone, T. Henderson, D. Ranasinghe, V. G. Zakrzewski, J. Gao, N. Rega, G. Zheng, W. Liang, M. Hada, M. Ehara, K. Toyota, R. Fukuda, J. Hasegawa, M. Ishida, T. Nakajima, Y. Honda, O. Kitao, H. Nakai, T. Vreven, K. Throssell, J. A. Montgomery, Jr., J. E. Peralta, F. Ogliaro, M. Bearpark, J. J. Heyd, E. Brothers, K. N. Kudin, V. N. Staroverov, T. Keith, R. Kobayashi, J. Normand, K. Raghavachari, A. Rendell, J. C. Burant, S. S. Iyengar, J. Tomasi, M. Cossi, J. M. Millam, M. Klene, C. Adamo, R. Cammi, J. W. Ochterski, R. L. Martin, K. Morokuma, O. Farkas, J. B. Foresman, and D. J. Fox.; **2016**, Gaussian 09, Revision D.01, *Gaussian, Inc.*, Wallingford CT.

47. (a) A. D. Becke; Density-functional thermochemistry. III. The role of exact exchange, J. Chem. Phys. 1993, 98, 5648e5652; (b) C. T. Lee, W. T. Yang, R. G. Parr.; Development of the Colle-Salvetti correlation-energy formula into a functional of the electron density, Phys. Rev. B. 1988, 37, 785e789.

48. C.E. Check, T.O. Faust, J.M. Bailey, B.J. Wright, T.M. Gilbert, L.S. Sunderlin; Addition of polarization and diffuse functions to the LANL2DZ basis set for p-block elements, *The Journal of Physical Chemistry A*, **2001**, 105, 8111-8116.

49. S.Grabner, B.Modec; Zn (II) curcuminate complexes with 2,2′-bipyridine and carboxylates. Molecules, **2019**, 24, 2540.

50. M. Cossi, J. V. Barone; Time-dependent density functional theory for molecules in liquid solutions, *Chem. Phys*. **2001**, 115, 4708e4717.

51. E. K. U. Gross, W. Kohn; Time-dependent density functional theory in, *Adv. Quant. Chem*. **1990**, 21, 255e291.

52. R. L. Martin; Natural transition orbitals. *J. Chem. Phys*., **2003**, 118, 4775−4777.

53. V. K. Choudhary, A. K. Bhatt, D. Dash, N. Sharma; DFT calculations on molecular structures, HOMO-LUMO study, reactivity descriptors and spectral analyses of newly synthesized diorganotin(IV) 2-chloridophenylacetohydroxamate complexes, *Jour. Comp. Chem.* **2019**, 1-10.

54. Z. Akbari, C. Stagno, N. Iraci, T. Efferth, E. A. Omer, A. Piperno M. Montazerozohori M.F. Dehnayebi , N. Micale; Biological evaluation, DFT, MEP, HOMO-LUMO analysis and ensemble docking studies of Zn(II) complexes of bidentate and tetradentate Schiff base ligands as antileukemia agents. *Jour. of Mol. Struc.*, **2024**,1301,137400.

55. Roy Dennington, Todd A. Keith, and John M. Millam.; GaussView version 6.0.16., Semichem Inc., *Shawnee Mission, KS,* **2016**.

56. J. S. Al-Otaibi; Detailed quantum mechanical studies on bioactive benzodiazepine derivatives and their adsorption over graphene sheets. *Spectrochimica Acta Part A: Molecular and Biomolecular spectroscopy*, **2020**, 235, 118333.

57. J. S. Murray, K. Sen; Molecular Electrostatic Potentials concepts and applications, Theoretical and computational chemistry, *Elsevier,* **1996**,1-137.

58. E.R. Johnson, S. Keinan, P. Mori-Sánchez, J. Contreras-García, A.J. Cohen, W. Yang; Revealing Noncovalent Interactions. *J. Am. Chem. Soc.*, **2010**, 132, 6498–6506.

59. F. Akman, A. Demirpolat , A. S. Kazachenko , Anna S. Kazachenko, N. Issaoui and O.A.Dossary; Molecular Structure, Electronic Properties, Reactivity (ELF, LOL, and

Fukui), and NCI-RDG Studies of the Binary Mixture of Water and Essential Oil of Phlomis bruguieri. *Molecules*, **2023**, 28, 2684.

60. F. Weinhold; Natural bond critical point analysis: Quantitative relationships between natural bond orbital-based and QTAIM-based topological descriptors of chemical bonding. *Journal of computational chemistry*, **2012**, 33, 2440-2449.

61. **T. Lu, F. Chen;** Multiwfn: A multifunctional wavefunction analyzer. *Jour. Comput. Chem*.**2012**, 33, 580-592.

62. B.Silvi, A.Savin; Classification of chemical bonds based on topological analysis of electron localization functions. *Nature*, **1994**, 371(6499), 683–686.

63. B. Fathima Rizwana, J. C. Prasana, S.Muthu, C.S.Abraham; Molecular docking studies, charge transfer excitation and wave function analyses (ESP,ELF,LOL) on valacyclovir:A potential anti viral drug. *Comput,Biol.Chem*., **2019**,78, 9–17.

64. Heiko Jacobsen.; Localized-orbital locator (LOL) profiles of chemical bonding. *Can. J. Chem*. **2008**,86(7), 695–702.

65. P. Kumar, S.K. Kandi, S. Manohar, K. Mukhopadhyay, D.S. Rawat; Monocarbonyl curcuminoids with improved stability as antibacterial agents against Staphylococcus aureus and their mechanistic studies, *ACS Omega*, **2019**, 4, 675-687.

66. T. Deb, D. Choudhury, P. S. Guin, M. B. Saha, G. Chakrabarti, S. Das; A complex of Co(II) with 2-hydroxyphenyl-azo-2′-naphthol (HPAN) is far less cytotoxic than the parent compound on A549-lung carcinoma and peripheral blood mononuclear cells: Reasons for reduction in cytotoxicity, *Chem-Biol. Inter*., **2011**, 189, 206-214.

67. P. S. Guin, P. C. Mandal, and S. Das; The binding of a hydroxy-9,10-anthraquinone Cu^{II} complex to calf thymus DNA: Electrochemistry and UV/Vis spectroscopy, *ChemPlusChem.*, **2012**, 77, 361-369.

68. P. Das, C. K. Jain, S. K. Dey, R. Saha, A. D. Chowdhury, S. Roychoudhury, S. Kumar, H. K. Majumder, S. Das; Synthesis, crystal structure, DNA interaction and *in vitro* anticancer activity of a Cu(II) complex of purpurin: dual poison for human DNA topoisomerase I and II. *RSC Adv*., **2014**, 4, 59344-59357.

69. B. Mandal, S. Singha, S. K. Dey, S. Mazumdar, T. K. Mondal, P. Karmakar, S. Kumar, S. Das, Synthesis, crystal structure from PXRD of a $Mn^{II}(purp)_2$ complex, interaction with DNA at different temperatures and pH and lack of stimulated ROS formation by the complex, *RSC Adv.*, **2016**, 6, 51520–51532.

70. S. Mukherjee-Chatterjee, C. K. Jain, S. Singha, P. Das, S. Roychoudhury, H. K. Majumder, S. Das; Activity of Co^{II}-Quinalizarin: A novel analogue of anthracycline-based anticancer agents targets human DNA topoisomerase, whereas quinalizarin itself acts via formation of semiquinone on acute lymphoblastic leukemia MOLT-4 and HCT 116 cells. *ACS Omega*., **2018**, 3, 10255-10266.

71. G. Scatchard.; The attractions of proteins for small molecules and ions, Ann. N. Y. Acad. Sci., 1949,51, 660–672.

CHAPTER 11

In silico molecular modeling experiments to elucidate the DNA binding modes of Curcumin and its metal complexes

Introduction

DNA binding interactions are crucial for understanding how small molecules interact with DNA to exert their biological effects. DNA binding interactions are not simple and are mediated through a number of different processes that includes intercalation, groove binding and electrostatic interactions.[1-5] Intercalation is a non-covalent interaction where planar aromatic molecules are actually sandwiched between two base pairs of the DNA double helix, anchoring the DNA-ligand complex by a π–π stacking with base pairs of the DNA and of the aromatic rings of the ligand.[3,6-9] Many compounds that bind to DNA in an intercalative mode induce changes in the structure of the DNA, either causing DNA unwinding and/or elongation which prevents processes that are linked to a preservation of a correct three dimensional structure like for example, replication and transcription.[3,6-9] Ethidium bromide is a member of this category; a molecule capable of showing strong fluorescence upon intercalation and is widely used in molecular biology to stain DNA.[10-12] Intercalation of ethidium bromide affects DNA polymerase activity, thereby inhibiting replication and transcription, making it capable of initiating mutations.[13-17] Another category of interactions between DNA and any ligand is groove binding, where the molecule attaches to the minor or major groove of the DNA helix.[18-22] This form of binding is often sequence-dependent with the ligands identifying the sequence site and then bind to such specific DNA sequences through a connect with functional groups on base pairs.[18-25] In most cases, groove-binding molecules are long and curved, and do not disrupt the DNA double helix structure.[18,23-25] These ligands can also form hydrogen bonds, develop van der Waals and hydrophobic interactions with DNA.[18-25] Distamycin is a well-characterized minor groove-binding molecule that has been widely used in DNA-binding assays.[26-28] This molecule fits into the minor groove, particularly when there are many Adenine (A) and Thymine(T) units that interact with it via hydrogen bonding.[26-29] A similar minor groove binder is Netropsin, also capable of binding to AT-rich regions of the DNA through formation of hydrogen bonds.[30-32]

These groove binders can modulate gene expression by preventing the interaction of transcription factors and other regulatory proteins with DNA. Hence, functions of specific genes can be turned off.[33-36] Electrostatic interactions also have an important role in DNA binding owing to the presence of a negatively charged phosphate backbone.[37-39] The basis of many electrostatic DNA-binding interactions lies in positively charged molecules being attracted to the negatively charged backbone of DNA.[37-39] Such interactions are less specific than that of intercalation or groove binding, but is of extreme importance in molecules containing charged functional groups for the stabilization of the initial DNA-ligand interaction which precedes secondary interactions such as intercalation or groove binding.[37-40] Natural examples of molecules that interact with DNA through electrostatic interactions are polyamines such as spermidine or spermine.[41-43] These small, positively charged molecules neutralize the negative charge on the DNA that help to stabilize it in the helical form allowing the DNA to pack itself inside the cell. Although polyamines do not have a high specificity, they are essential regulators of gene expression through changes in DNA conformation and binding to other regulatory proteins.[44-46] It has been seen that some molecules may interact with DNA both by intercalation and groove binding which enhance their affinity and selectivity.[47,48] Notable examples are Doxorubicin and Actinomycin D which insert themselves between base pairs and also interact at the minor groove via their sugar unit, forming a stable DNA-ligand complex.[47-54] This dual mode of binding allows for stronger and more enduring doxorubicin-DNA interaction, thereby improving doxorubicin's effectiveness as a chemotherapeutic agent in disrupting replication and transcription.[49-53] Molecules with such dual-binding demonstrate how intercalative and groove binding modes can work together to create an exceptionally stable DNA-ligand complex.[55,56] By utilizing both binding mechanisms, these compounds increase their specificity and affinity for DNA, making them excellent candidates for therapeutical applications and in research.[47-56] In this connection, molecular docking and molecular dynamics along with other computational

chemistry tools, have helped in an understanding of atomistic level investigation of DNA–ligand interactions and identify key nucleotides.[57-60] Researchers can now use these techniques to explore and visualize how ligands bind to DNA, to estimate affinity of binding, to assess the stability of the DNA–ligand complex and to predict preferred binding mode of a molecule *i.e.* whether it intercalates or binds in grooves or there is an electrostatic interaction.[57-61] On the other hand, molecular dynamics simulations allow us to characterize the dynamics of these interactions, showing how a compound and DNA continuously change their conformations in a time frame to optimize binding.[61]

Results and Discussion

11.1 Molecular docking interaction of DNA models with Curcumin & its metal complexes to examine binding mechanism

Two DNA models were employed to investigate the binding modes of HCur and its metal complexes. For intercalation mode, the PDB ID 3FT6 model was selected, which includes coligand proflavine (PRL), a known intercalator and bacteriostatic disinfectant.[62,63] PDB ID 101D model containing the crystallized ligand netropsin (NT), an antibiotic and a recognized groove binder, was used to study groove binding (Fig 1).[64-66] Redocking experiments were done using the native co-crystal ligands PRL and NT. Findings reveal that in both instances the redocked and co-crystal ligands overlap and interact with nearly identical nucleotides at their respective binding sites (Fig. 2). The root mean square deviation (RMSD) between co-crystal and redocked ligand poses was calculated to be 1.92 Å at the PRL binding site and 1.25 Å at the NT binding site. It is known today that an RMSD below 2 Å indicates a valid molecular docking protocol and results of this study demonstrate accuracy of the molecular docking protocol used.[67] These results suggest that the docking algorithm effectively replicate the experimentally

observed binding modes for both PRL and NT binding sites. This validation lends credibility to the reliability of subsequent docking simulations and predictions made using this protocol.

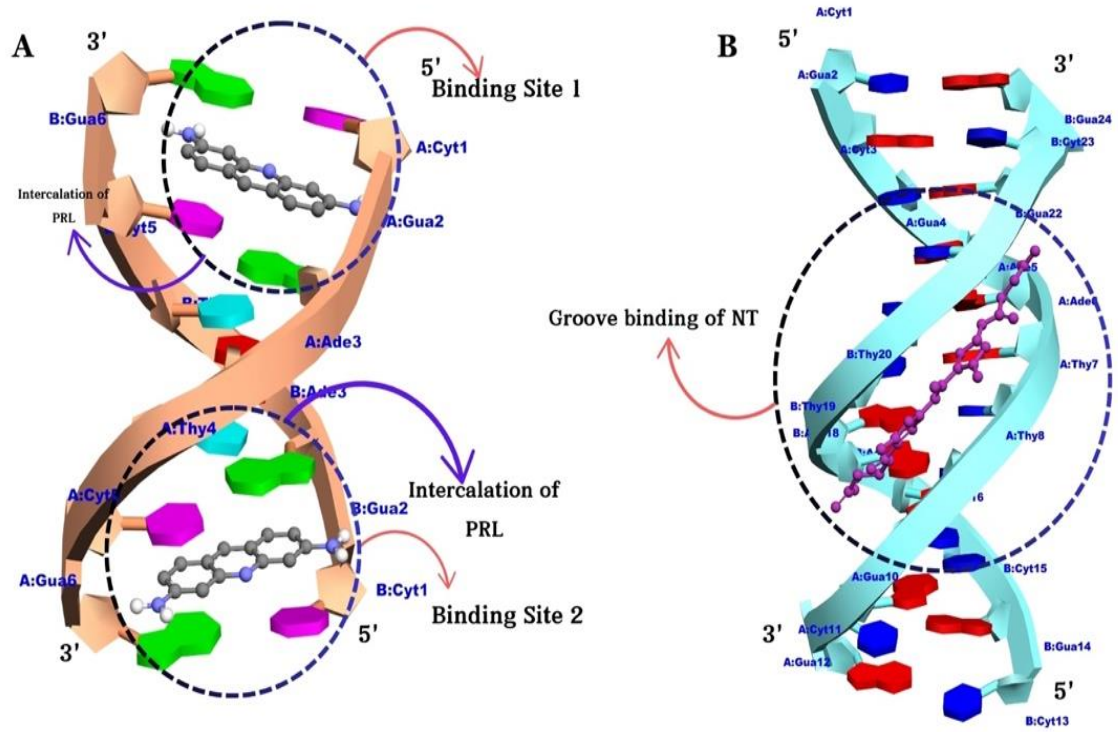


Figure 1: (A) Crystal structure of DNA of intercalation model (PDB ID : 3FT6) , (B) Crystal structure of DNA of groove binding model (PDB ID : 101D)

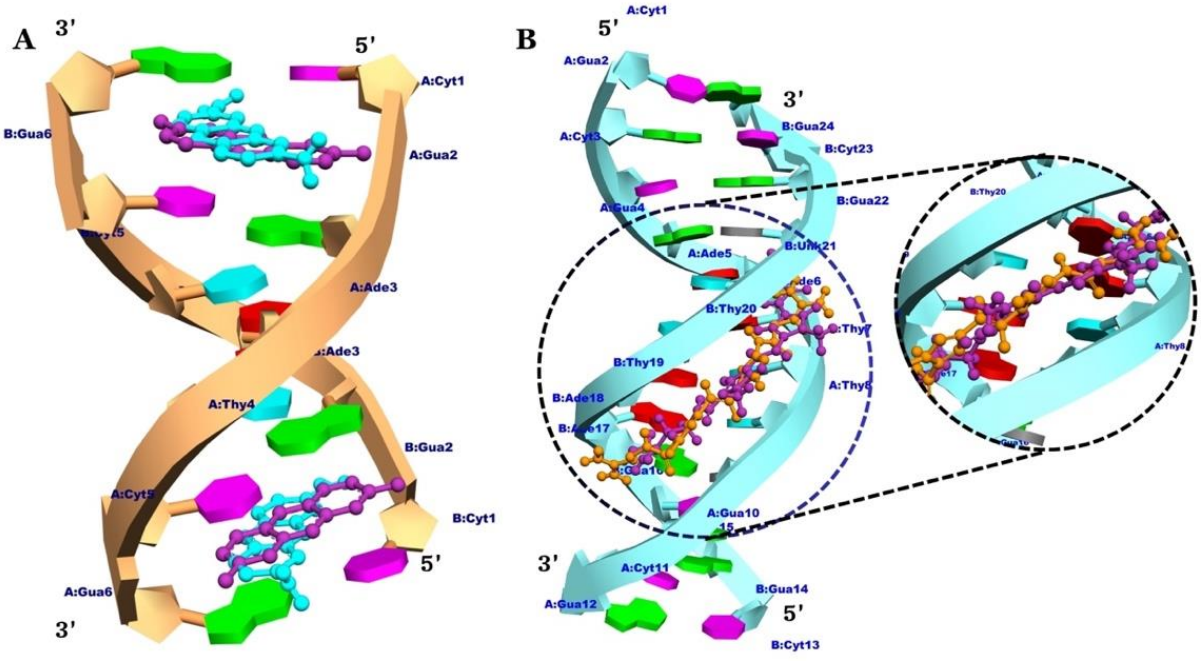


Figure 2 : (A) Redocking of native co-crystal ligand PRL into the binding site 1 and 2 of DNA intercalator model (PDB ID: 3FT6). Here magenta ligand represent native co-crystal ligand poses and cyan ligands represent redocked poses at the PRL binding site, (B) Redocking of native co-crystal ligand NT into the binding site of DNA crystal structure of groove binder model (PDB ID: 101D). Here magenta ligand represent native co-crystal ligand (NT) pose and yellow coloured ligand represent redocked pose at the NT binding site.

To investigate the binding patterns in both scenario, rigid molecular docking techniques were employed. Flexibility was incorporated into PRL (co-ligand in case of 3FT6 DNA model) and NT (in case of 101D DNA model), HCur, Mn(Cur), Cu(Cur), and Zn(Cur) to create ten conformations. This method was employed to forecast DNA-ligand interactions and determine the most energetically advantageous docked positions. Analysis following docking for the intercalator DNA model (PDB ID: 3FT6) indicated that the co-crystallized ligand PRL having an inhibitory concentration of 58.13 μM demonstrated docking scores of -6.37 Kcal/mole in Autodockvina (version 1.2.5) and -6.21 Kcal/mole in Autodock 4.2.6. (Table1, Fig. 3).[68-70] 2D and 3D interaction diagrams (Fig. 3) revealed that PRL established two hydrogen bonds, one with Gua-6 of strand B and another with Gua-2 of strand A in 3FT6 model. A comprehensive list of additional interaction modes, including π-π stacking, is provided in Table 1. Only binding site 1 was selected for this docking study.

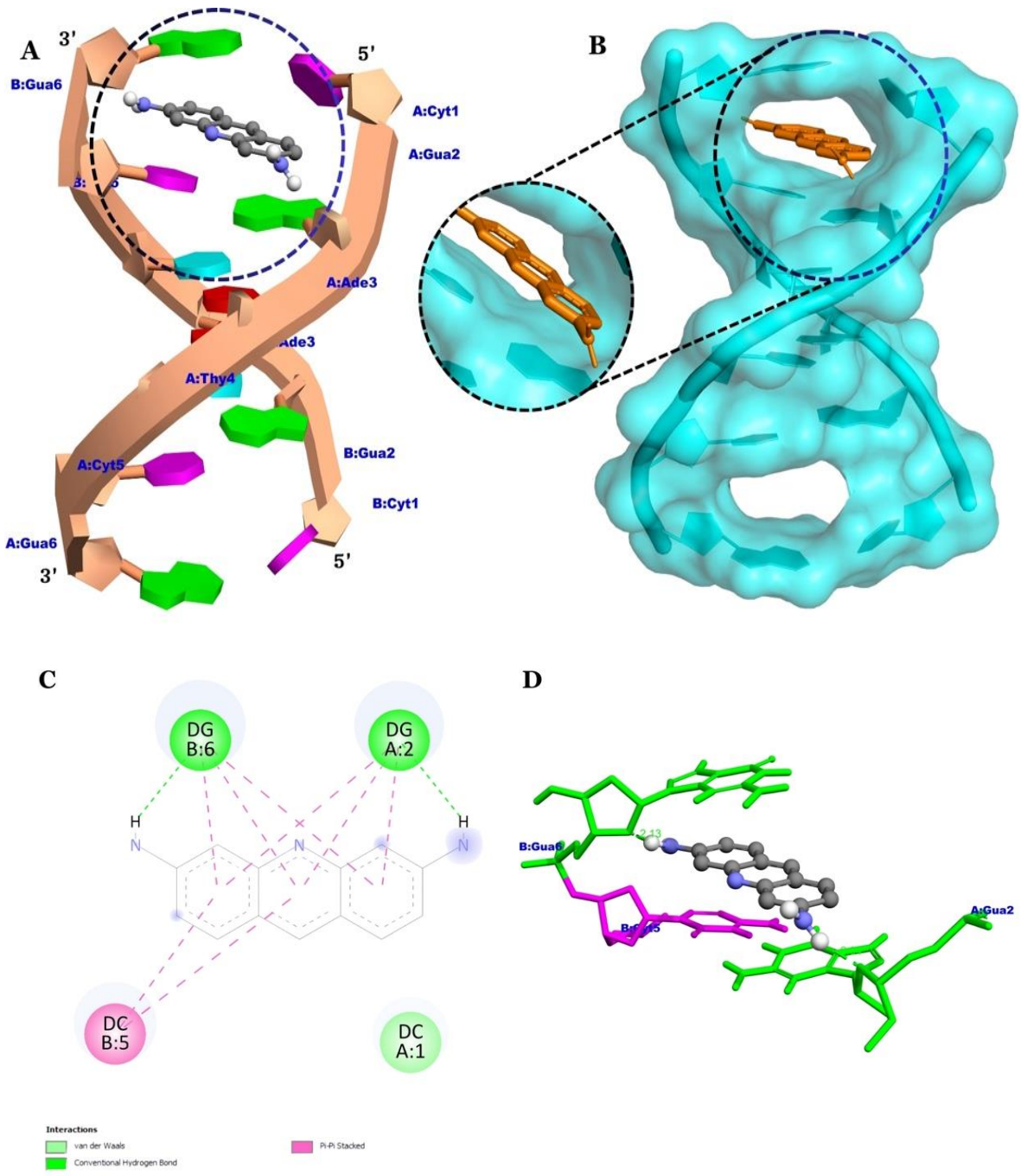


Figure 3 :(A) Ribbon representation of Docked PRL ligand into DNA (PDB ID : 3FT6), (B) Surface view of docked PRL into DNA (PDB ID : 3FT6), (C) 2D interactions of PRL ligand with DNA , (D) 3D interactions of PRL ligand with DNA (PDB ID : 3FT6)

In contrast, HCur established a single hydrogen bond with Gua-6 of strand B (PDB ID: 3FT6). The docking scores were -6.03 Kcal/mol using Autodock vina v 1.2.5 and -6.15 Kcal/mol with AutoDock v 4.2.6 resulting in an inhibition constant of 36.66 μM (Table 1). In this case, hydrogen bond lengths between HCur and nucleic acid bases were ≤ 3.00 Å (Fig.4)

.

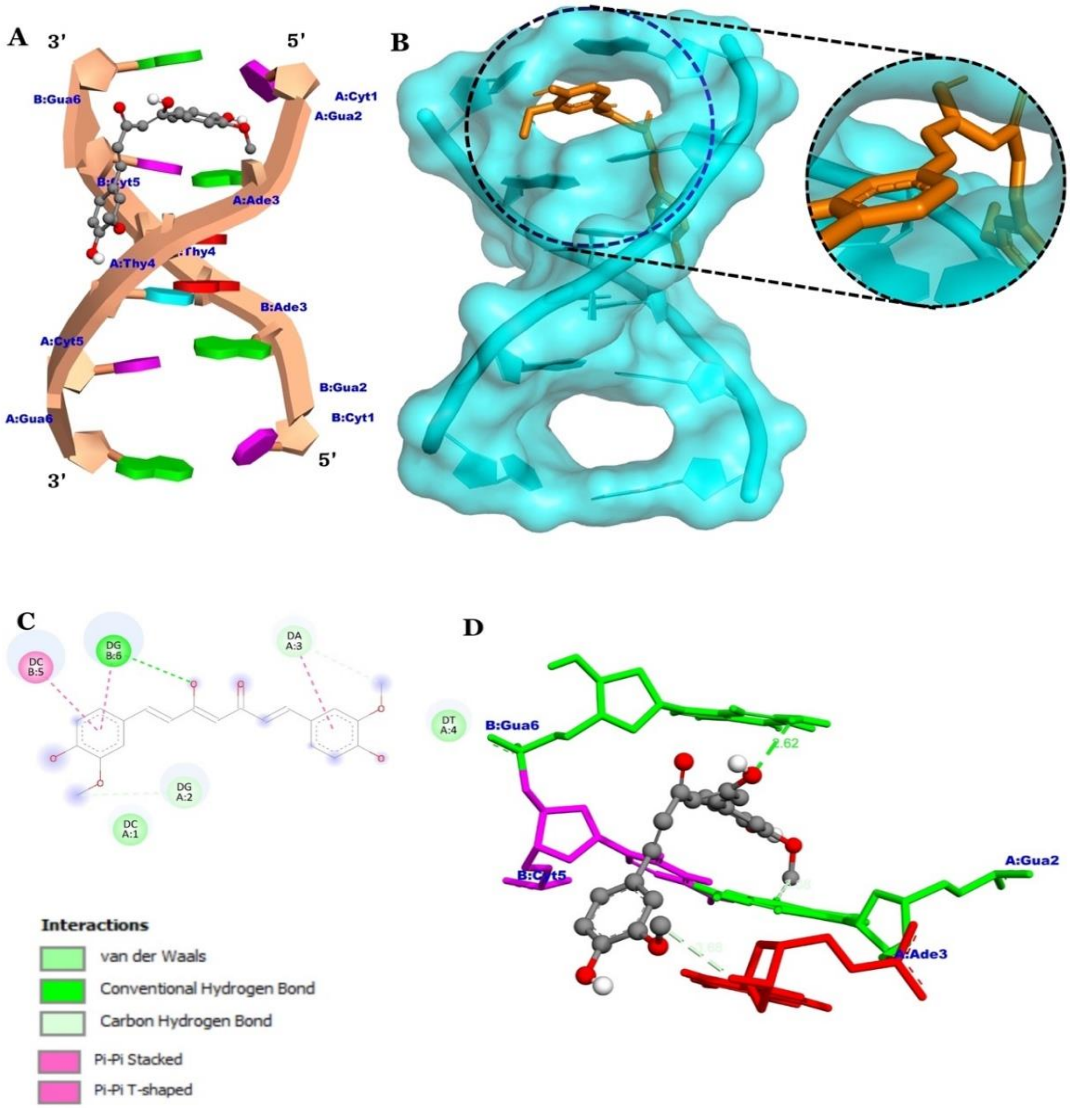
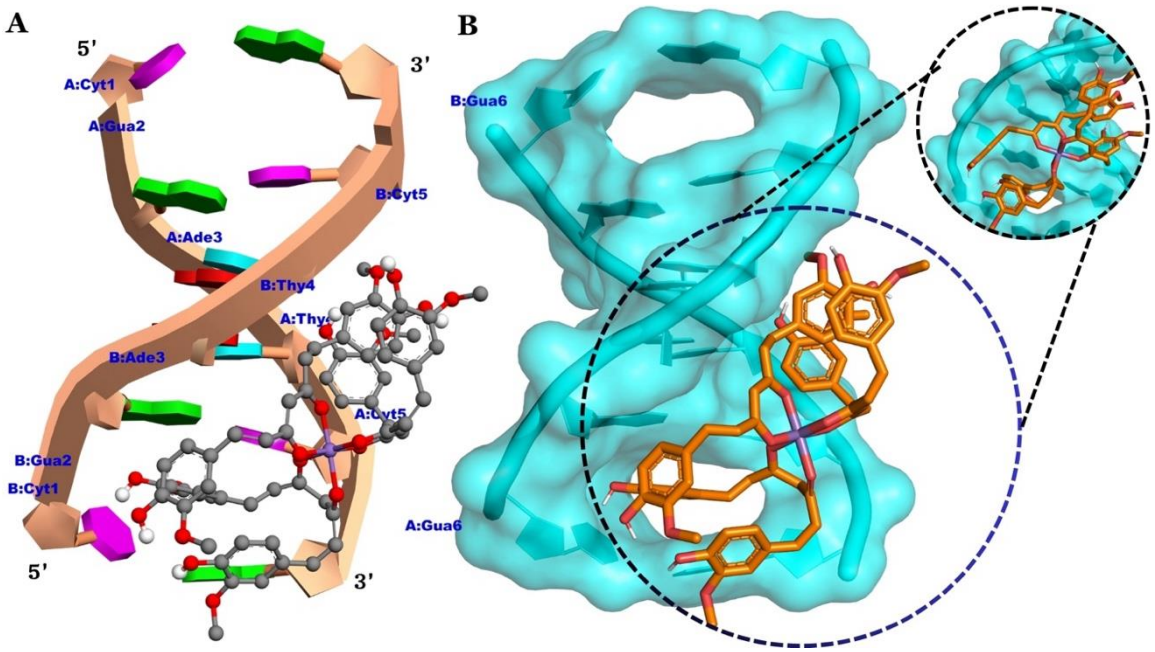


Figure 4 :(A) Ribbon representation of Docked HCur ligand into DNA (PDB ID : 3FT6), (B) Surface view of docked HCur into DNA (PDB ID : 3FT6), (C) 2D interactions of HCur ligand with DNA , (D) 3D interactions of HCur ligand with DNA (PDB ID : 3FT6)

Mn(Cur) formed three hydrogen bonds with Gua-6 on strand A and with Thy-4 and Cyt-5 on strand B (PDB ID: 3FT6). A docking score of -4.25 Kcal/mol was calculated by Autodock vina v 1.2.5 and -3.81 Kcal/mol by AutoDock v 4.2.6, yielding an inhibition constant of 117.58 μM (Table 1). From Fig.4 it is very clear that Mn(Cur) does not intercalate DNA; moreover due to bulky size it is unlikely to intercalate DNA. The very low binding affinity and energy values also argue against intercalation. The minimum binding energy and affinity indicate other mechanisms of interaction with DNA were operative that might be groove binding or electrostatic interactions.



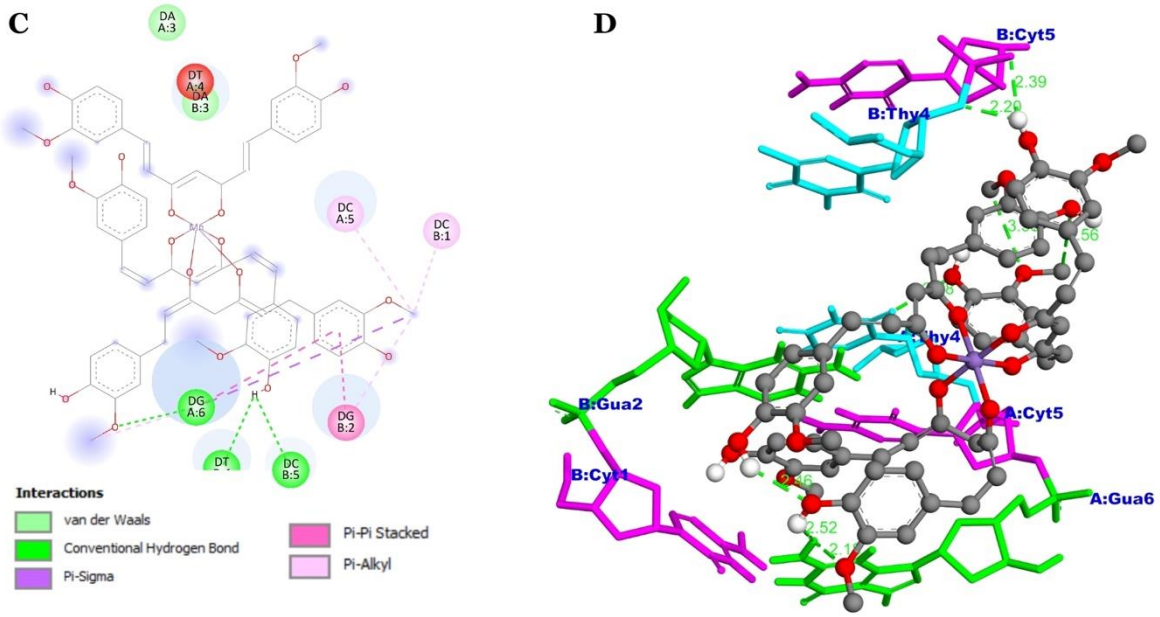


Figure 5 :(A) Ribbon representation of Docked Mn(Cur) ligand into DNA (PDB ID : 3FT6), (B) Surface view of docked Mn(Cur) into DNA (PDB ID : 3FT6), (C) 2D interactions of Mn(Cur) ligand with DNA , (D) 3D interactions of Mn(Cur) ligand with DNA (PDB ID : 3FT6)

Cu(Cur) forms three hydrogen bonds with Gua-2 on strand A and Gua-6 on strand B (PDB ID: 3FT6) (Fig. 6). The docking score calculated by Autodock vina v 1.2.5 was -7.60 Kcal/mol, while AutoDock v 4.2.6 produced a score of -7.49 Kcal/mol leading to an inhibition constant of 7.78 μM (Table 1). Several π-alkyl interactions were identified which contribute to stabilization of the intercalated metal complex within the DNA structure (Table 1). These interactions are essential for determining overall binding affinity between Cu(Cur) and DNA. π-alkyl interactions provide additional stability, improving the ability of the complex to intercalate between base pairs of DNA.

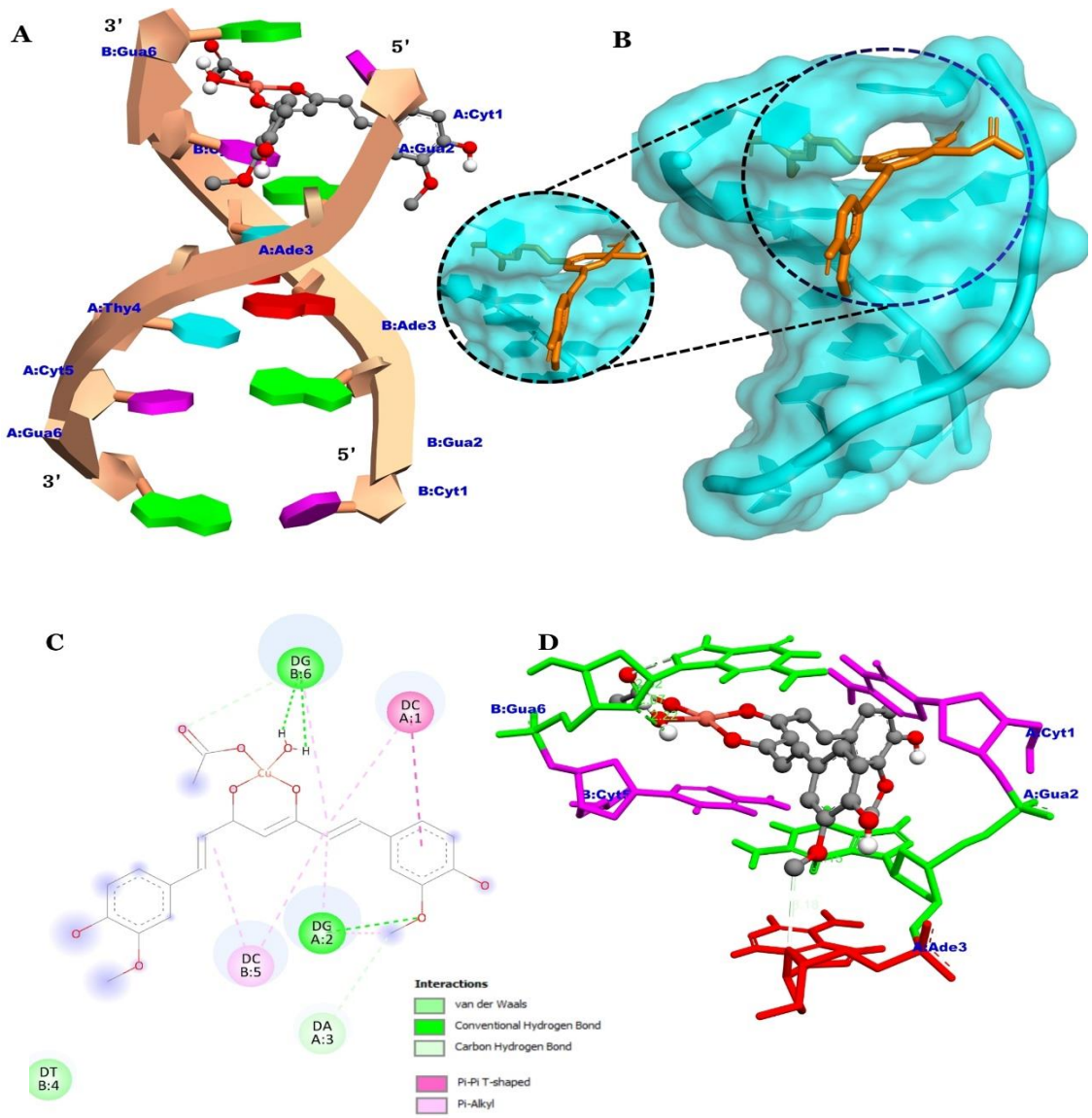


Figure 6 :(A) Ribbon representation of docked Cu(Cur) ligand into DNA (PDB ID:3FT6), (B) surface view of docked Cu(Cur) into DNA (PDB ID:3FT6), (C) 2D interactions of Cu(Cur) ligand with DNA, (D) 3D interactions of Cu(Cur) ligand with DNA (PDB ID:3FT6)

Zn(Cur) complex established three hydrogen bonds with Gua-6 on strand B and Gua-2 on strand A (PDB ID:3FT6) (Fig. 7). Docking scores -6.98 Kcal/mol calculated by Autodock vina v 1.2.5, and -7.09 Kcal/mol derived from AutoDock v 4.2.6 correspond to an inhibition constant of 8.27 μM (Table 1). In particular, it was observed that multiple π-π stacking interactions contributed some stabilizing factor to the intercalated metal complex in the DNA structure (Table 1). This

has a significant influence on overall Zn(Cur)-DNA binding affinity. These interactions can significantly affect the orientation and positioning of the complex in the DNA groove.

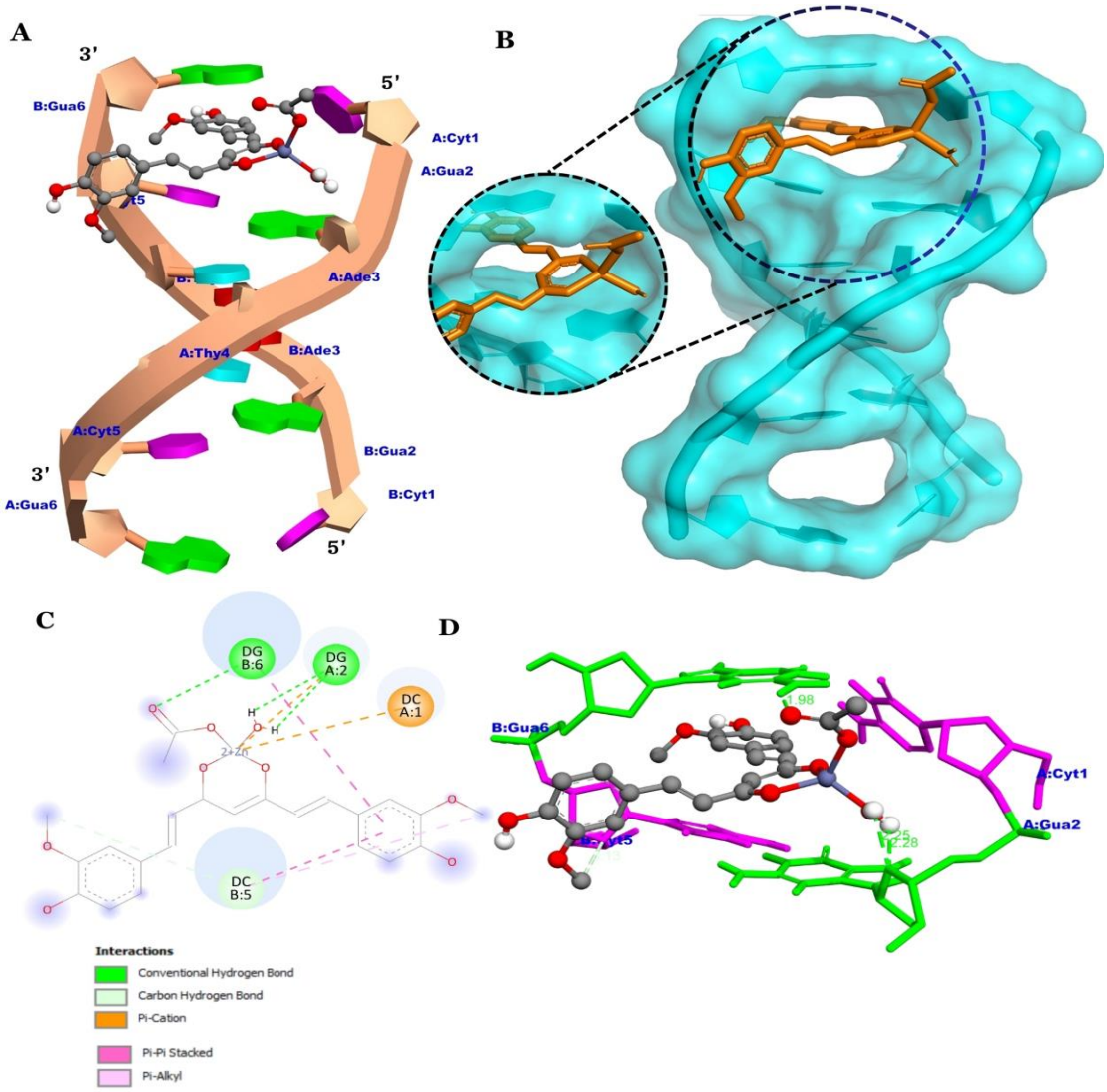


Figure 7 : (A) Ribbon representation of Docked Zn(Cur) ligand into DNA (PDB ID : 3FT6), (B) Surface view of docked Zn(Cur) into DNA (PDB ID : 3FT6), (C) 2D interactions of Zn(Cur) ligand with DNA , (D) 3D interactions of Zn(Cur) ligand with DNA (PDB ID : 3FT6)

Table 1: Docking ligands, docking Score, interacting nucleotides of DNA intercalator model (PDB ID: 3FT6)

Name of the ligands	Autodock Vina_1.2.5	Autodock 4.2.6		Active site Interacting amino acids residues and type of interactions (Å)
	Binding Affinity (Kcal/mol)	Binding Energy (Kcal/mol)	Inhibition Constant Ki (µM)	
PRL	-6.37	-6.21	58.13	**H-bonding:** Gua-6(B) (2.13Å), Gua-2(A) (2.04Å) **Π – Π Staking:** Gua-2(A) (3.92Å, 5.11 Å, 5.54 Å, 3.57 Å, 3.96 Å), Cyt-5(B) (3.66 Å, 5.07 Å), Gua-6 (B) (3.57 Å,5.01 Å,3.675 Å.564.04 Å)
HCur	-6.03	-6.15	36.66	**H-bonding:** Gua-6(B) (2.62Å) **Π – Π Staking:** Gua-6(B) (4.78Å, 4.79 Å), Cyt-5(B) (4.13 Å), Ade-3(A) (4.92 Å)
Mn(Cur)	-4.25	-3.81	117.58	**H-bonding:** Gua-6(A) (2.17Å), Thy-4(B) (2.19 Å), Cyt-5(B) (2.38 Å) **Π–Π Staking:** Gua-6(A) (4.83Å), Gua-2(B) (4.94 Å, 4.05 Å) **Π-alkyl:**Cyt-5(A)(4.25Å),Gua-6(A)(4.54 Å, 5.30 Å) Cyt-1(B)(4.86 Å), Gua-2(4.68 Å)
Cu(Cur)	-7.60	-7.49	7.78	**H-bonding:** Gua-2(A) (2.14Å), Gua-6(B) (2.06Å, 2.22 Å) **Π – Π Staking:** Cyt-1(A) (5.23 Å) **Π-alkyl:** Cyt-1(A) (4.68Å), Gua-2(A) (5.13Å, 3.96Å, 5.41 Å) Ade-3(A) (4.87 Å), Cyt-5(B) (4.91 Å, 4.96 Å), Gua-6(B) (4.96 Å, 4.05 Å)
Zn(Cur)	-6.98	-7.09	8.27	**H-bonding:** Gua-6(B) (1.98Å), Gua-2(A) (2.27 Å), Gua-2(A) (2.24 Å) **Π–Π Staking:** Gua-6(B) (4.86Å, 5.55 Å), Cyt-5(B) (4.53 Å)

To forecast DNA-ligand interactions and determine the most energetically advantageous docking position for the groove binder DNA model (PDB ID:101D), 10 different conformations were generated by allowing flexibility in NT (the co-ligand) and with HCur, Mn(Cur), Cu(Cur) and Zn(Cur). The docking analysis of the groove binder DNA model (PDB ID:101D) showed that co-crystallized ligand NT having an inhibitory concentration of 4.82 µM, displayed docking scores of -10.26 Kcal/mole in Autodockvina (version 1.2.5) and -9.25 Kcal/mole in Autodock

4.2.6. (Table 2, Fig. 8). Hydrogen bonds between a molecule and a nucleic acid base are considered significant when their length is ≤ 3.00Å.

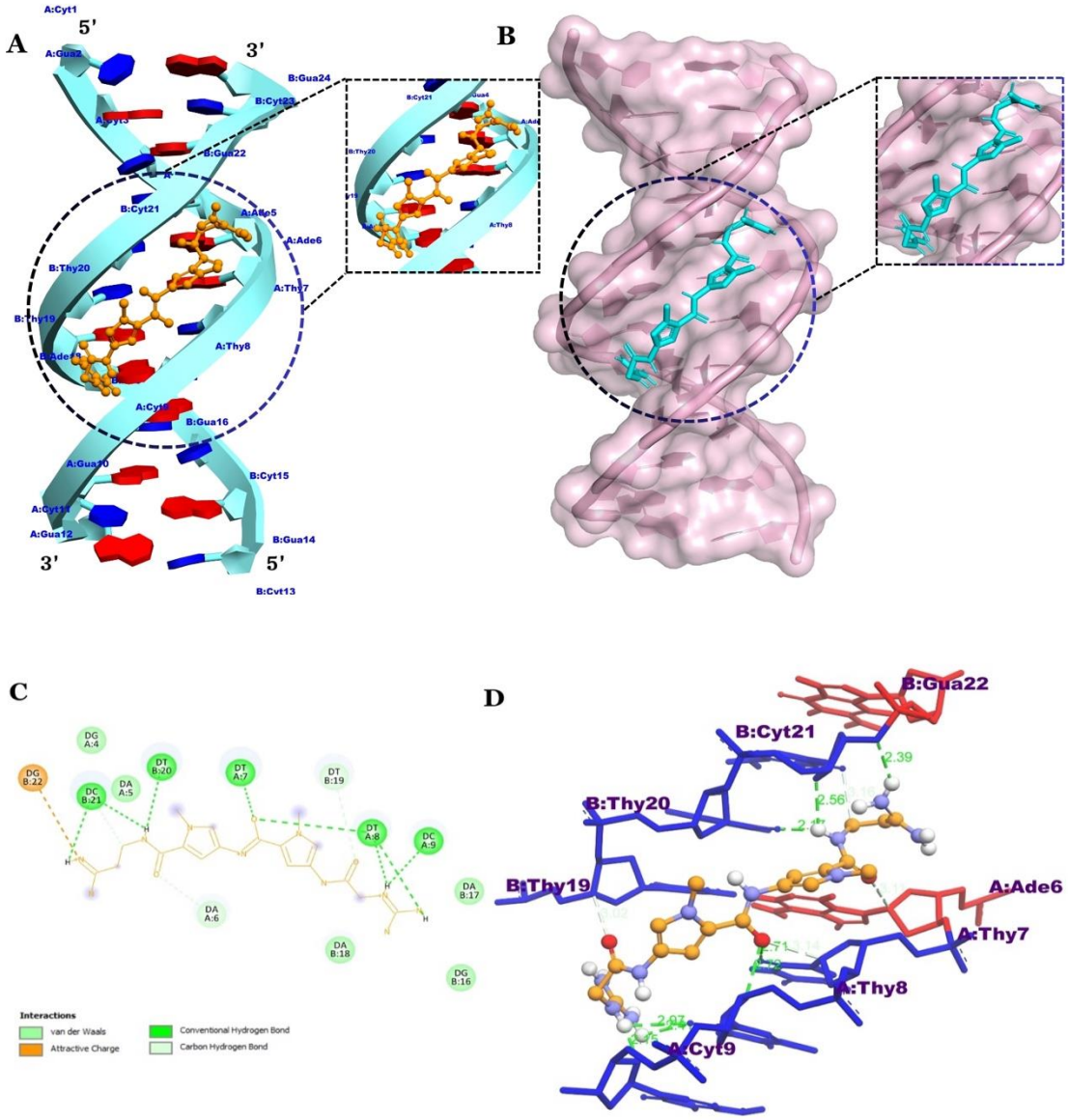
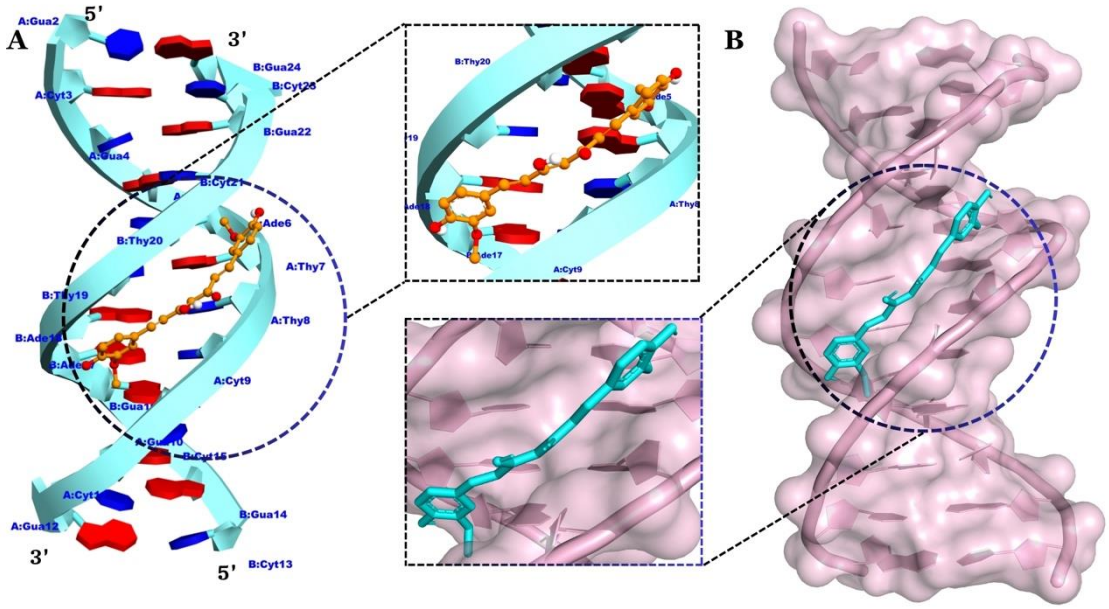


Figure 8 : (A) Ribbon representation of Docked NT ligand into DNA (PDB ID : 101D), (B) Surface view of docked NT into DNA (PDB ID : 101D), (C) 2D interactions of NT ligand with DNA , (D) 3D interactions of NT ligand with DNA (PDB ID : 101D)

2D and 3D interaction diagrams (Fig. 8C & D) indicate NT establishes eight hydrogen bonds with nucleotides Thy-7 of strand A, Thy-8 of strand A, Cyt-9 of strand A, Thy-20 of strand B, and Cyt-21 of strand B. Additional interaction modes are presented in Table 2. The hydrogen bonds between NT and specific nucleotides of strands A and B in the 101D DNA model are essential for stabilizing the ligand-DNA complex. Further examination of the supplementary interaction modes outlined in Table 2 may offer insights into overall binding mechanism and the potential functional implications of this molecular interaction.

HCur formed three hydrogen bonds with DNA bases having length ≤ 3.00 Å: Ade-6 on strand A, Ade-8 on strand B and Thy-17 on strand B (PDB ID: 101D) (Fig. 9). Docking scores were -8.15 Kcal/mol (Autodock vina v 1.2.5) and -7.23 Kcal/mol (AutoDock v 4.2.6) resulting in an inhibition constant of 27.17 μM (Table 1). Additionally, numerous hydrophobic interactions were observed, including C-H bond and π-alkyl interactions (Table 2). The complex network of hydrogen bonds and hydrophobic interactions significantly enhances the stability of DNA-HCur complex. These interactions work together to secure HCur within the DNA structure. The intensity and specificity of these molecular interactions are crucial in determining binding affinity and potential biological activity of the complex.



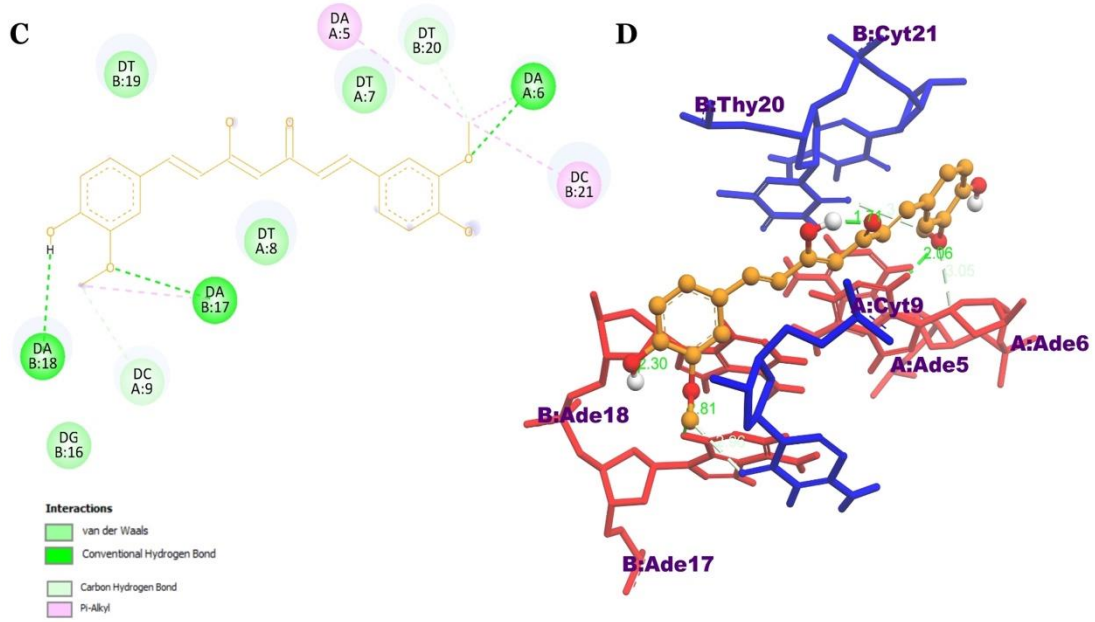


Figure 9 :(A) Ribbon representation of docked HCur ligand into DNA (PDB ID : 101D), (B) Surface view of docked HCur into DNA (PDB ID : 101D), (C) 2D interactions of HCur ligand with DNA , (D) 3D interactions of HCur ligand with DNA (PDB ID : 101D)

In contrast, Mn(Cur) forms a single hydrogen bond with the DNA base Thy-8 on strand A (PDB ID:101D) (Fig. 10). Two methods were employed to calculate docking scores; Autodock vina v 1.2.5 produced a score of -7.34 Kcal/mol while AutoDock v 4.2.6 yielded -6.81 Kcal/mol resulting in an inhibition constant of 77.58 μM (Table 1). Furthermore, various hydrophobic interactions, including C-H bond and π–alkyl interactions were identified (Table 2). These interactions play a crucial role in determining overall binding affinity and specificity of the Mn(Cur) complex for DNA. The groove-binding mechanism enables the complex to fit tightly within DNA potentially affecting its conformation and function.

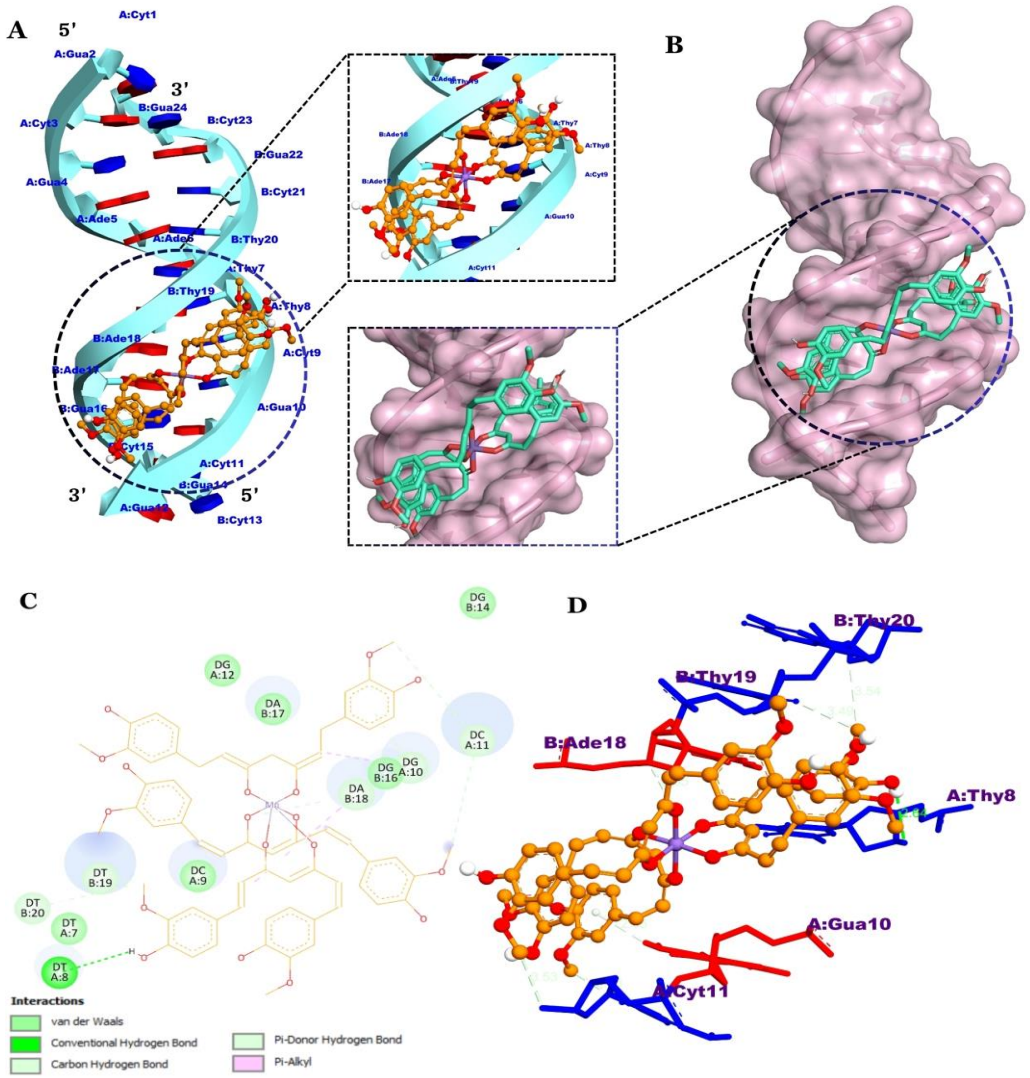


Figure 10 :(A) Ribbon representation of docked Mn(Cur) ligand into DNA (PDB ID:101D), (B) surface view of docked Mn(Cur) into DNA (PDB ID:101D), (C) 2D interactions of Mn(Cur) ligand with DNA , (D) 3D interactions of Mn(Cur) ligand with DNA (PDB ID:101D)

Cu(Cur) establishes three hydrogen bonds with DNA bases, specifically Gua-4 on strand A, Ade-17 on strand B, and Ade-6 on strand A (PDB ID:101D) (Fig. 11). Two different approaches were used to determine docking scores: Autodock vina v 1.2.5 generated a score of -8.41 Kcal/mol while AutoDock v 4.2.6 produced -8.13 Kcal/mol, corresponding to an inhibition constant of 6.25 μM (Table 2). Additionally, several hydrophobic interactions, including C-H bonds and π–

alkyl interactions were observed (Table 2). A combination of hydrogen bonds and hydrophobic interactions significantly enhance the stability of the DNA-Cu(Cur) complex as a groove binder. Analysis of these interactions is important for overall binding affinity and specificity of Cu(Cur) to DNA. The groove-binding mechanism in a way permits the complex to sit snugly in the DNA structure, which may affect its conformation and function.

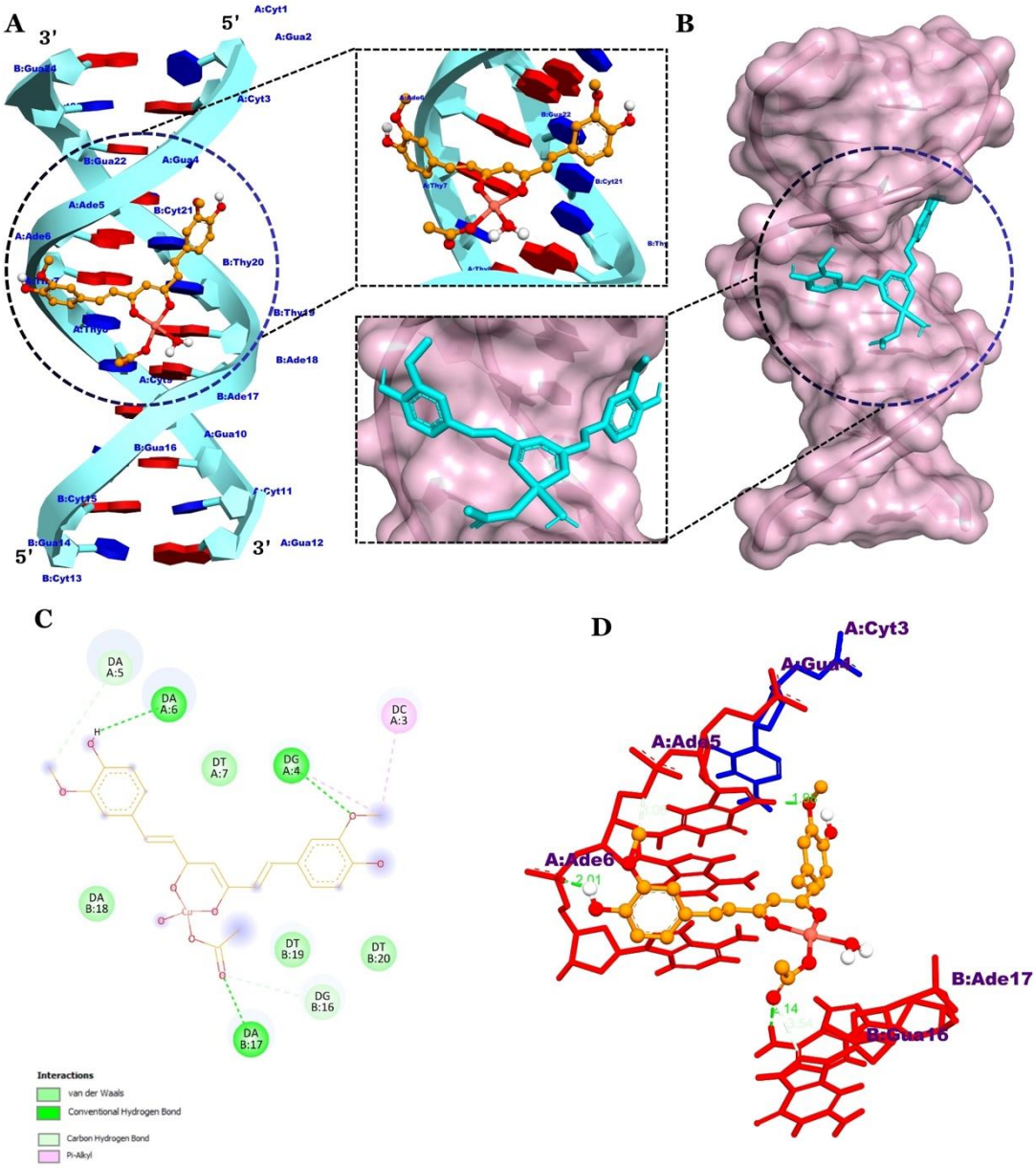


Figure 11 :(A) Ribbon representation of docked Cu(Cur) ligand into DNA (PDB ID:101D), (B) surface view of docked Cu(Cur) into DNA (PDB ID:101D), (C) 2D interactions of Cu(Cur) ligand with DNA, (D) 3D interactions of Cu(Cur) ligand with DNA (PDB ID:101D)

Zn(Cur) forms four hydrogen bonds with DNA bases, interacting specifically with Ade-5 on strand A, Thy-19 on strand B, and Gua-16 on strand B (PDB ID:101D) (Fig.12). Docking scores were -7.84 Kcal/mol (Autodock vina v 1.2.5) and -7.31 Kcal/mol (AutoDock v 4.2.6), with an inhibition constant of 22.49 μM (Table 2). Multiple hydrophobic interactions including C-H bonds and π–alkyl interactions were also observed (Table 2). Binding of Zn(Cur) to the DNA groove could allow it to be tucked into the DNA structure for stable packing, potentially altering the shape and function of DNA.

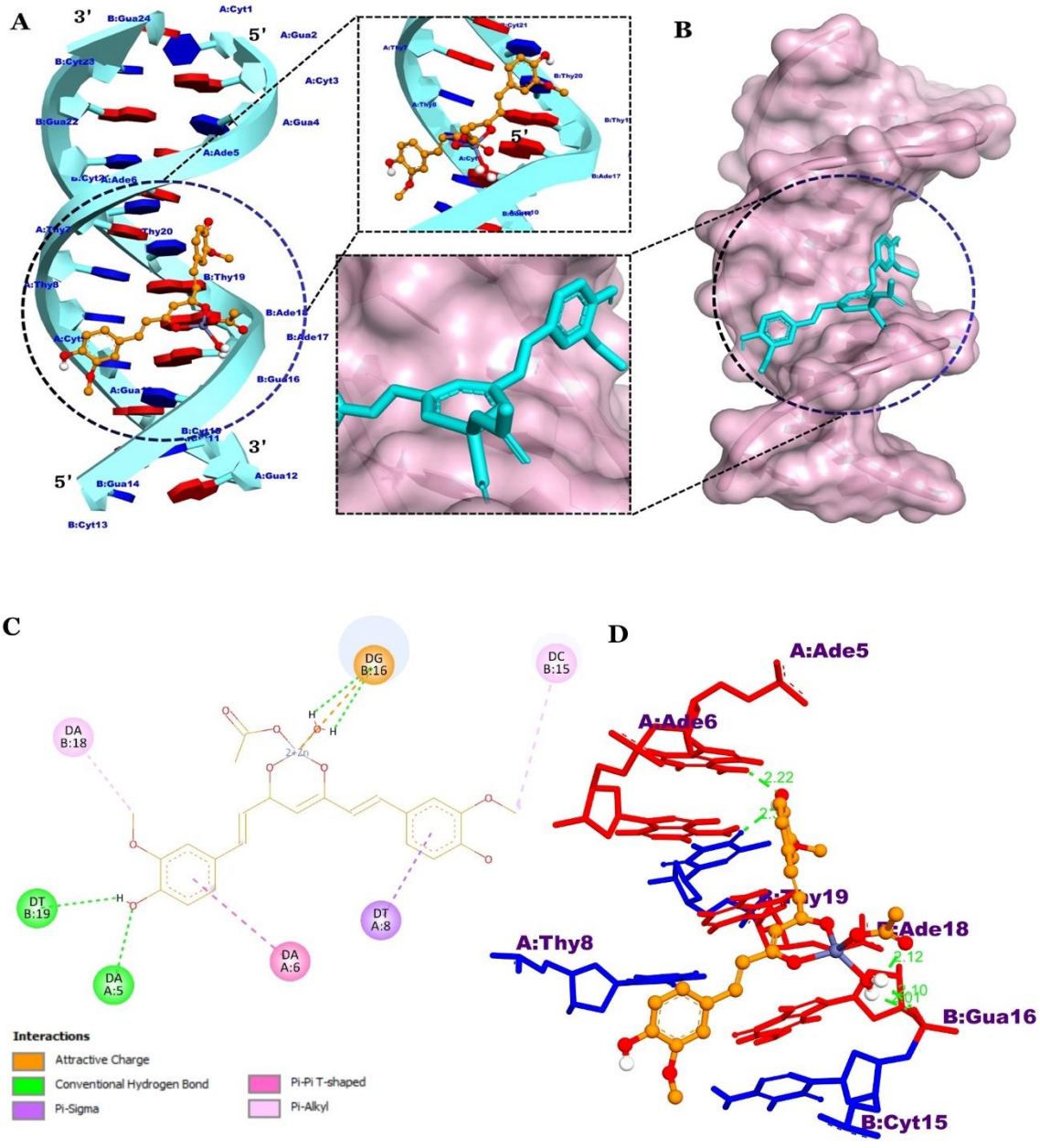


Figure 12 :(A) Ribbon representation of docked Zn(Cur) ligand into DNA (PDB ID : 101D), (B) surface view of docked Zn(Cur) into DNA (PDB ID : 101D), (C) 2D interactions of Zn(Cur) ligand with DNA , (D) 3D interactions of Zn(Cur) ligand with DNA (PDB ID:101D)

Table 2: Docking ligands, docking Score, interacting nucleotides of DNA groovebinder model (PDB ID: 101D)

Name of the ligands	Autodock Vina_1.2.5	Autodock 4.2.6		Active site Interacting amino acids residues and type of interactions (Å)
	Binding Affinity (Kcal/mol)	Binding Energy (Kcal/mol)	Inhibition Constant Ki (µM)	
NT	-10.26	-9.25	4.82	**H-bonding**: Thy-7(A) (2.70Å), Thy-8(A) (2.71Å, 2.40Å, 2.97 Å), Cyt-9(A) (2.14Å), Thy-20 (B) (2.17Å), Cyt-21(B) (2.55 Å, 2.39 Å) **C-H Bonding**: Ade-6(A) (3.10 Å), Thy-7(A) (3.13 Å), Thy-19(B) (3.02 Å) Cyt-21(B) (3.16 Å)
HCur	-8.15	-7.23	27.17	**H-bonding:** Ade-6(A) (2.06Å), Thy-17(B) (2.81 Å), Ade-8(B) (2.29 Å) **C-H Bonding**: Ade-6(A) (3.05 Å), Thy-20(B) (3.70 Å), Cyt-9(A) (2.96 Å) **Π – alkyl:** Ade-5(A) (4.31Å), Ade-6(A) (4.52 Å, 4.20 Å), Cyt-9(A) (5.00 Å), Ade-17(B) (4.68 Å), Cyt-21(B) (5.32 Å)
Mn(Cur)	-7.34	-6.81	77.58	**H-bonding:** Thy-8(A) (2.63Å) **C-H Bonding**: Ade-18(B) (3.65 Å), Thy-19(B) (3.48 Å), Thy-20(B) (3.54 Å),Cyt-11(A)(3.53 Å, 3.46 Å) **Π-alkyl:** Gua-10(A)(5.23Å,4.80 Å),Ade-18(B)(5.46 Å,) Ade-18(B)(5.03 Å)
Cu(Cur)	-8.41	-8.13	6.25	**H-bonding:** Gua-4(A) (1.98Å), Ade-17(B) (2.14Å), Ade-6(A)(2.00 Å) **C-H Bonding:** Gua-16(B) (3.54 Å), Ade-5(A) (3.06 Å) **Π-alkyl:** Cyt-3(A) (4.66Å), Gua-4(A) (4.58Å)
Zn(Cur)	-7.84	-7.31	22.49	**H-bonding:** Ade-5(A) (2.21Å), Thy-19(B) (2.33 Å), Gua-16(B) (2.01 Å, 2.09 Å) **C-H Bonding:** Thy-8(A) (3.74 Å) **Π-alkyl:** Cyt-15(B) (5.25Å), Ade-18(A) (4.28Å)

Hence, molecular docking analysis indicates HCur, Cu(Cur) and Zn(Cur) interact with DNA through two mechanisms: intercalation and groove binding. In contrast, Mn(Cur) engages solely in groove binding. Despite efforts to dock Mn(Cur) via intercalation, it exclusively exhibits groove binding, which corresponds to its substantial molecular size. The structural analysis of these curcumin complexes shows an importance of the choice of the metal ion in determining interaction with DNA. Differences in binding mechanisms might result in different biological functions and therefore different applications during treatment.

11.2 Analysis of Molecular Dynamics trajectories by examining the mode of DNA interaction with Curcumin and its metal complexes

Standard trajectory analysis of molecular dynamics (MD) simulations involves several calculations to evaluate various aspects of a system. These include computing the root mean square deviation (RMSD) to evaluate structural stability, determining the root mean square fluctuation (RMSF) to examine atomic flexibility, assessing the radius of gyration (ROG) to measure structural compactness and performing hydrogen bond analysis to investigate interaction patterns.[71-74] These analytical methods offer valuable insights into the dynamics, molecular interactions and overall behaviour of the system, helping to gain a deeper understanding of biological processes, material characteristics and chemical phenomena at the atomic scale.

11.2.1 Analysis of RMSD:

This study evaluated the binding mechanism and pattern of DNA bound to the respective co-ligands, PRL and NT. These were then compared with HCur and metal complexes Mn(Cur), Cu(Cur) and Zn(Cur) that were docked to the binding site of the selected DNA model. Calculations were performed over 100 ns time scale for two different DNA models. All MD

systems were prepared using an SPC water solvent model with appropriate charges and a 0.15 (M) NaCl electrolyte environment (Fig.13 and 14). (*Chapter 6, experimental*)

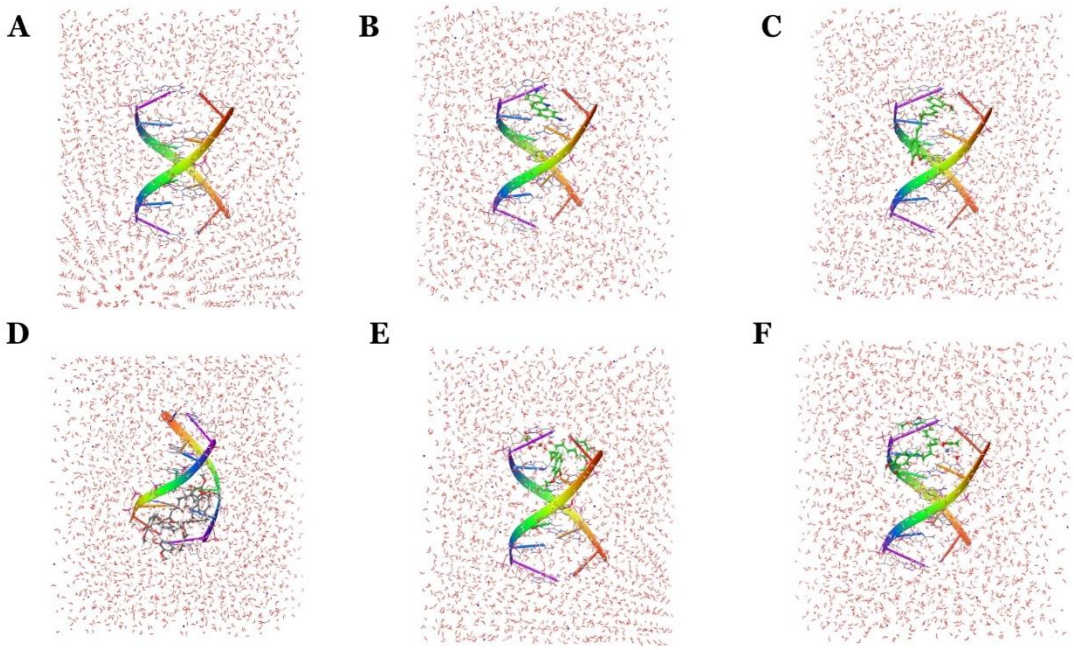


Figure 13 : (A) 3FT6 DNA model inside orthorhombic boundary box and surrounded by SPC water model (B) PRL docked 3FT6 DNA model inside orthorhombic boundary box and surrounded by SPC water model, (C) HCur docked 3FT6 DNA model inside orthorhombic boundary box and surrounded by SPC water model, (D) Mn(Cur) docked 3FT6 DNA model inside orthorhombic boundary box and surrounded by SPC water model, (E) Cu(Cur) docked 3FT6 DNA model inside orthorhombic boundary box and surrounded by SPC water model, (F) Zn(Cur) docked 3FT6 DNA model inside orthorhombic boundary box and surrounded by SPC water model

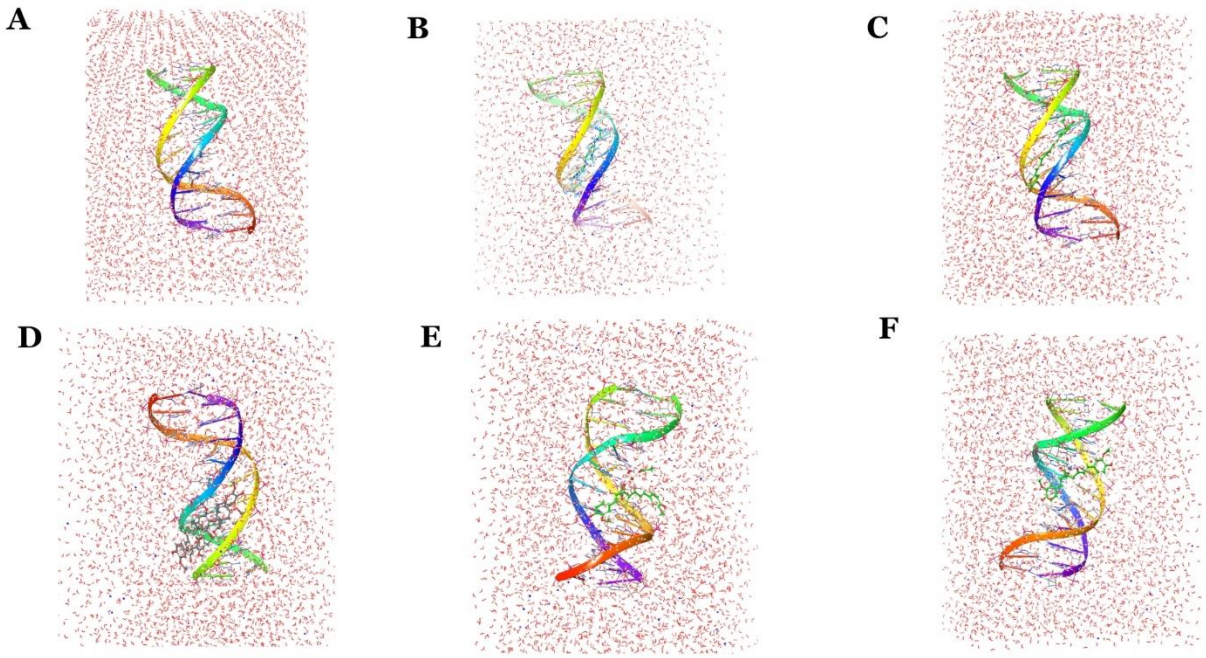


Figure 14 : (A) 101D DNA model inside orthorhombic boundary box and surrounded by SPC water model (B) NT docked 101D DNA model inside orthorhombic boundary box and surrounded by SPC water model, (C) HCur docked 101D DNA model inside orthorhombic boundary box and surrounded by SPC water model, (D) Mn(Cur) docked 101D DNA model inside orthorhombic boundary box and surrounded by SPC water model, (E) Cu(Cur) docked 101D DNA model inside orthorhombic boundary box and surrounded by SPC water model, (F) Zn(Cur) docked 101D DNA model inside orthorhombic boundary box and surrounded by SPC water model

Reduction in RMSD of the phosphate backbone of the intercalator model DNA (PDB ID:3FT6) and groove binder DNA model (PDB ID: 101D) was observed when complexed with target molecules like HCur, Mn(Cur), Cu(Cur) and Zn(Cur), suggesting stable complexation in a biological environment.

RMSD trends was compared over 100 ns simulations for 3FT6 docked HCur and its metal complexes with docked co-ligand PRL. All prepared metal complexes of HCur and of the co-

crystallized ligand PRL docked to the DNA (PDB ID:3FT6) demonstrated stable conformations. PRL, HCur, Mn(Cur), Cu(Cur) and Zn(Cur) exhibited steady binding, as reflected by their RMSD values. The average RMSD of apo-3FT6 is 5.96 ± 0.82 Å, while for 3FT6 attached to PRL and HCur, the values are 4.04 ± 0.83 Å and 3.46 ± 0.87 Å, respectively. When 3FT6 is complexed with Mn(Cur), Cu(Cur), and Zn(Cur), the RMSD values become 3.62 ± 0.38 Å, 2.70 ± 0.39 Å, and 2.38 ± 0.48 Å respectively. Unbound 3FT6, with a higher RMSD, undergoes more significant conformational changes in both strands A and B. Reduction in RMSD when HCur and Zn(Cur) were bound to 3FT6 indicated the formation of stable adducts that could withstand further conformational changes. The lower RMSD of Zn(Cur) with 3FT6 suggests that this complex is more stable than other congeners (Fig. 15A).

In case of groove binder DNA model 101D the average RMSD was found 8.91 ± 0.73 Å (Fig.15B). When this model complexed with co-ligand NT then its average RMSD became 7.23 ± 1.18 Å. In contrast, for HCur, average RMSD of the 101D model was 6.49 ± 0.97 Å. For Mn (Cur), Cu(Cur) and Zn(Cur) average RMSD were 6.15 ± 0.77 Å, 5.33 ± 0.64 Å, 5.63 ± 0.68 Å respectively.

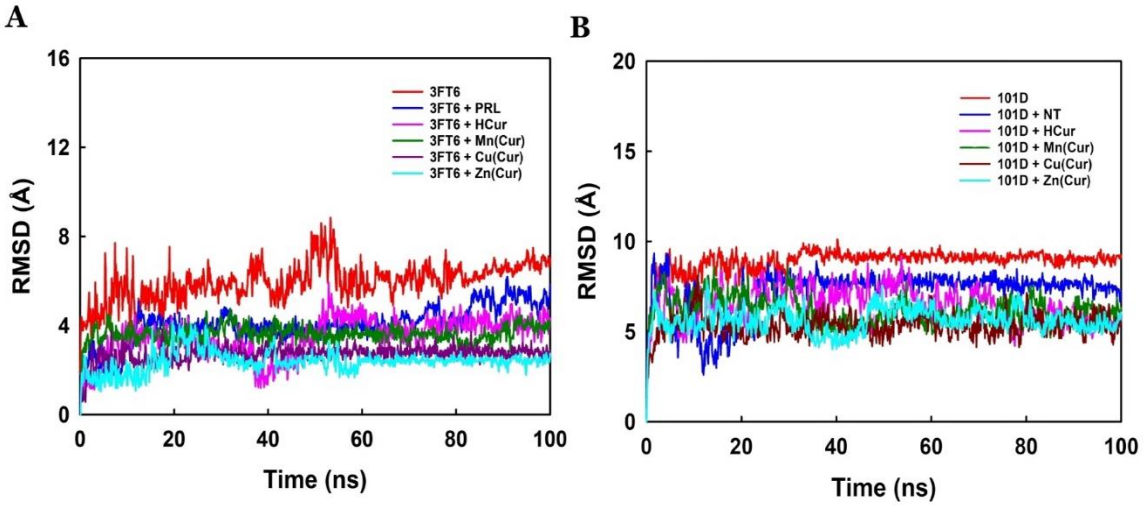


Figure 15: (A) RMSD values of phosphate backbone of 3FT6 DNA model and with docked PRL, HCur, Mn(Cur), Cu(Cur) and Zn(Cur) (B) RMSD values of phosphate backbone of 101D DNA model and with docked NT, HCur, Mn(Cur), Cu(Cur) and Zn(Cur)

11.2.2 Analysis of RMSF:

The RMSF of the apo-DNA model 3FT6 (intercalator model) was 9.01 Å ± 1.82. When it was complexed with PRL, the value became 7.85 Å ± 2.27. HCur, had a value of 6.77 Å ± 2.01. But when metal complexes of HCur were used, average RMSF goes down drastically to 6.20 Å ± 1.40 for Mn(Cur), 6.07 Å ± 1.38 for Cu(Cur) and 6.05 Å ± 1.35 for Zn(Cur). The observed decrease in average RMSF for metal complexes of HCur suggests a potential stabilizing effect on 3FT6 DNA structure. (Fig. 16 A)

Conversely, RMSF of groove binder DNA model (PDB ID:101D) measured 13.82 Å ± 4.91, which decreased to 9.51 Å ± 3.71 when bound to its co-crystallized ligand, NT. HCur, exhibited an RMSF of 9.88 Å ± 3.65 Notably, introduction of metal-Curcumin complexes led to a significant reduction in average RMSF values: 10.96 Å ± 4.23 for Mn(Cur), 10.72 Å ± 3.92 for Cu(Cur), and 10.12 Å ± 3.67 for Zn(Cur) (Fig.16 B). This substantial decrease in average RMSF for metal-Curcumin complexes indicates a possible stabilizing effect on DNA structure (PDB:101D). Such stabilization may result from the formation of more robust or numerous interactions between metal-Curcumin complexes and DNA.

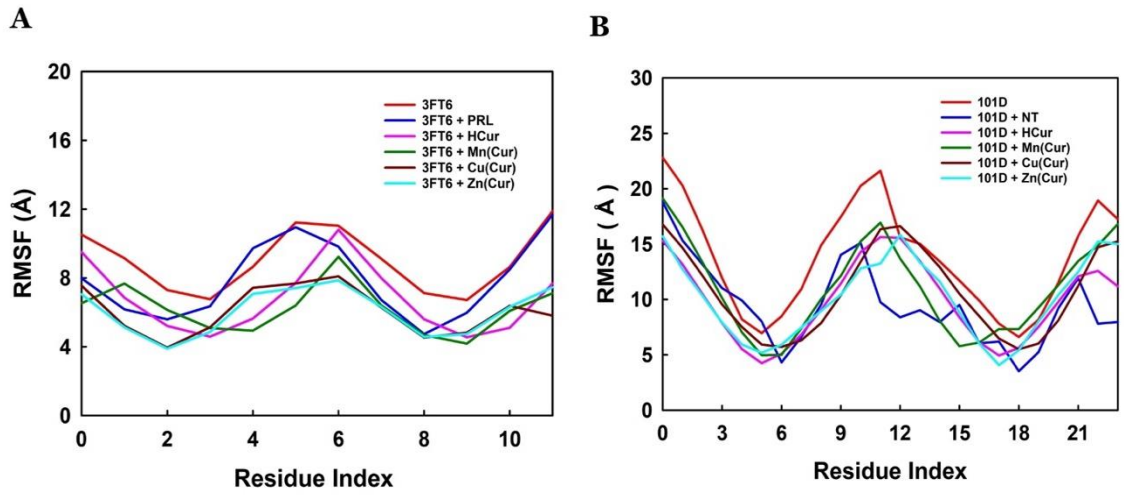


Figure 16: (A) RMSF plot of 3FT6 DNA model and with docked PRL, HCur, Mn(Cur), Cu(Cur) and Zn(Cur), (B) RMSF plot of 101D DNA model and with docked NT, HCur, Mn(Cur), Cu(Cur) and Zn(Cur)

11.2.3 Analysis of Radius of gyration (Rg):

For the 3FT6 model, the average Rg of the apo DNA was 8.63 Å ± 0.55. It decreased when it formed a complex with the co-crystallized ligand PRL by 8.03 Å ± 0.44. For HCur it was 7.97 Å ± 0.20, for Mn(Cur) 7.85 Å ± 0.23, for Cu(Cur) 7.36 Å ± 0.25 and for Zn(Cur) 7.68 Å ± 0.38 . The observed reduction in average radius of gyration (Rg) upon ligand binding suggests that the DNA undergoes a conformational change, becoming more compact in the presence of various ligands. This trend was consistent across all tested complexes, with the Cu(Cur) complex showing the most significant decrease in Rg compared with the apo DNA. Similar Rg values for metal-HCur complexes indicate that they may induce comparable structural changes in the DNA (Fig.17A).

The 101D model exhibited an average Rg of 16.40 Å ± 1.92 for the apo protein. This decreased to 12.10 Å ± 0.91 when the DNA formed a complex with co-crystallized NT ligand. The Rg values for various compounds were: HCur, 10.93 Å ± 1.22, Mn(Cur), 9.85 Å ± 1.10, Cu(Cur), 9.99 Å ± 1.0, and Zn(Cur), 9.08 Å ± 0.96 (Fig. 17B). Reduction in Rg values suggests that the DNA undergoes conformational changes upon ligand binding with metal-HCur complexes having varying effects on protein compactness. Among metal-curcumin complexes, Zn(Cur) appeared to induce the most significant reduction in Rg, potentially indicating a tighter DNA conformation. These findings imply different metal-HCur complexes may interact with the DNA in distinct ways, possibly influencing its structural stability and function.

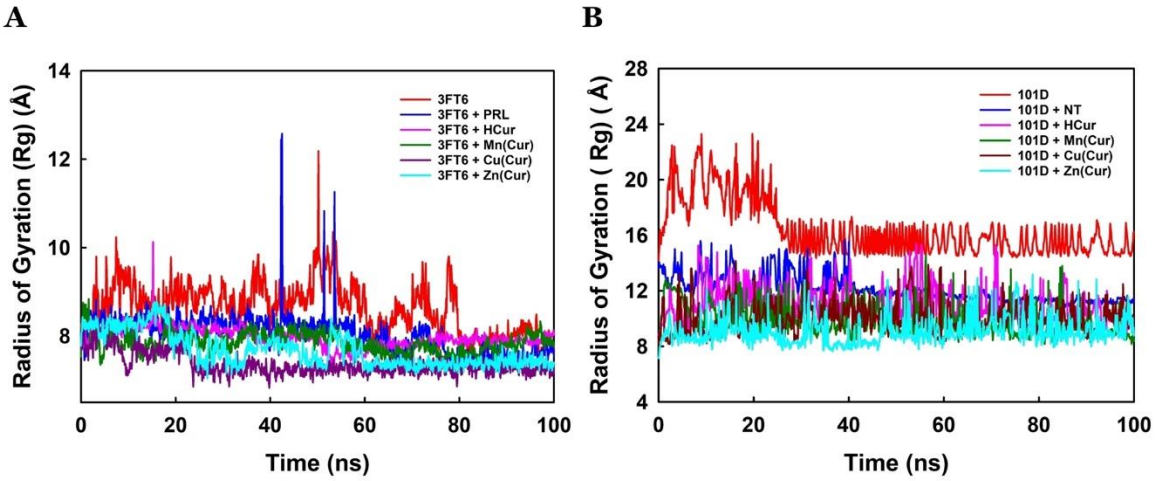


Figure 17: (A) Radius of gyration plot of 3FT6 DNA model and with docked PRL, HCur, Mn(Cur), Cu(Cur) and Zn(Cur), (B) Radius of gyration plot of 101D DNA model and with docked NT, HCur, Mn(Cur), Cu(Cur) and Zn(Cur)

11.2.4 Analysis of Solvent accessible surface area (SASA):

SASA was evaluated for intercalator and groove binder DNA model (PDB IDs: 3FT6 and 101D) in complex with their respective co-crystallized ligands, the standard inhibitor HCur, and its metal complexes over a 100 ns simulation period. Unbound 3FT6 model exhibited an average SASA value of 1341.38 $Å^2$ ± 0.61. When bound to PRL, the value decreased to 591.61 $Å^2$ ± 0.95. Average SASA for HCur was 438.96 $Å^2$ ± 0.69 whereas for Mn(Cur), Cu(Cur), and Zn(Cur) values were 728.66 $Å^2$ ± 0.45, 408.40 $Å^2$ ± 0.18, and 413.95 $Å^2$ ± 0.54 respectively (Fig. 18A). Observed variations in SASA values across different ligand-bound states suggest that metal complexes of HCur may interact differently with DNA (PDB: 3FT6) than HCur. These differences in SASA could indicate changes in DNA conformation or accessibility upon binding. The significantly lower SASA value for all selected compound bound 3FT6 compared to unbound form suggests a substantial conformational change or a tighter binding interaction for that particular compound.

The unbound-101D model exhibited an average SASA of 774.14 $Å^2$ ± 0.38. When complexed with NT, the 101D model showed an average SASA of 469.78 $Å^2$ ± 0.67. The average SASA values for 101D complexed with HCur, Mn(Cur), Cu(Cur), and Zn(Cur) were 395.11 $Å^2$ ± 0.86, 407.24 $Å^2$ ± 0.74, 421.13 $Å^2$ ± 0.24 and 366.58 $Å^2$ ± 0.43 respectively (Fig 17 B). SASA measurements offer valuable information on how the conformation of a DNA changes when it binds to various compounds. A notable reduction in SASA for different compound bound state of 101D model indicated a more condensed structure compared to unbound form. Notably, complexes formed with metal-Curcumin compounds exhibit diverse levels of surface accessibility, which may suggest different binding mechanisms or structural modifications.

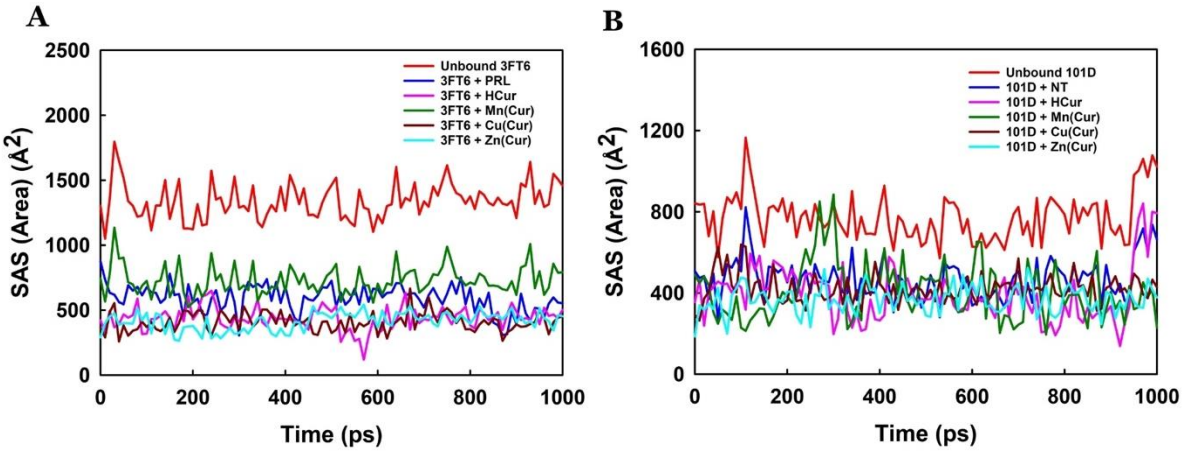


Figure 18: (A) SASA plot of unbound 3FT6 DNA model and with docked PRL, HCur, Mn(Cur), Cu(Cur) and Zn(Cur), (B) SASA plot of unbound 101D protein model and with docked NT, HCur, Mn(Cur), Cu(Cur) and Zn(Cur)

11.2.5 Analysis of Hydrogen bond during MD simulation:

The study examined hydrogen bond interactions during a 100 ns simulation of intercalator DNA model (PDB ID: 3FT6) and groove binder DNA model (PDB ID: 101D), along with their respective co-crystallized ligands (PRL for 3FT6 and NT for 101D), as well as HCur, Mn(Cur), Cu(Cur), and Zn(Cur) at the active sites. The geometric criteria considered for all hydrogen bonds were a hydrogen donor-acceptor distance of less than 3.0 Å and an angle of less

than 3^0. Results showed that in the 3FT6 DNA model, the average number of hydrogen bonds formed was 1.27 ± 0.63 for PRL, 1.09 ± 0.49 for HCur, 2.00 ± 0.88 for Mn(Cur), 1.06 ± 0.29 for Cu(Cur), and 2.14 ± 0.58 for Zn(Cur) (Fig 19 A).

Conversely, in the 101D DNA model, average number of hydrogen bonds formed were 5.84 ± 1.30 for NT, 1.99 ± 0.55 for HCur, 0.49 ± 0.12 for Mn(Cur), 1.98 ± 0.51 for Cu(Cur), and 3.09 ± 0.29 for Zn(Cur) (Fig. 19 B). These results suggest that although hydrogen bonding patterns differed between the two DNA models Zn(Cur) appeared to form more hydrogen bonds in groove binder model than in intercalator model.

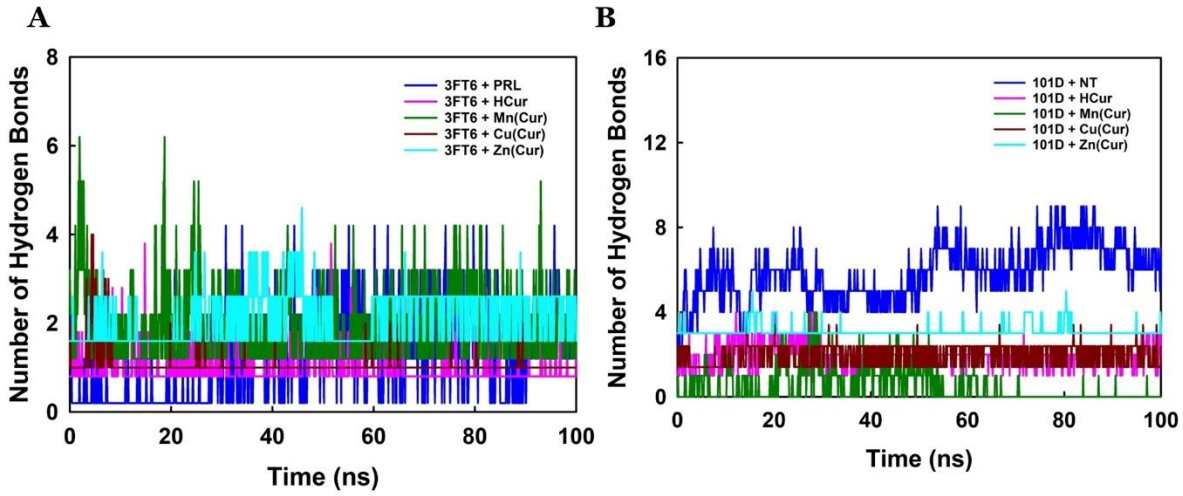


Figure 19: (A) H-Bond plot of 3FT6 DNA model docked with PRL, HCur, Mn(Cur), Cu(Cur) and Zn(Cur), (B) H-Bond plot of 101D DNA model docked with NT, HCur, Mn(Cur), Cu(Cur) and Zn(Cur)

11.2.6 Calculations of Molecular Mechanics Generalized Born Surface Area (MM-GBSA)

The binding energies of various ligands (HCur, Mn(Cur), Cu(Cur), and Zn(Cur)) at the binding sites of the 3FT6 and 101D DNA models were evaluated using the MM-GBSA method.[75,76] This assessment utilized the final 10 ns of the 100 ns molecular dynamics simulation trajectories (Table 3). The binding energy of PRL with the intercalator model DNA (PDB ID: 3FT6) was -23.62 Kcal/mol ± 1.52, lower than HCur's binding energy of -36.38 Kcal/mol ± 2.77

at the same site. This discrepancy may be attributed to larger RMSD of PRL than that of HCur. The binding energies of Mn(Cur), Cu(Cur), and Zn(Cur) were -11.15 Kcal/mol ± 9.10, -27.47 Kcal/mol ± 3.83, and -22.06 Kcal/mol ± 5.56, respectively. These values suggest that Cu(Cur) forms the strongest interaction with the target molecule, followed by HCur, Zn(Cur), and Mn(Cur). The differences in binding energies between these complexes can be explained by variations in their molecular structures and specific interactions with the binding site.

For the groove binder DNA model (PDB ID: 101D), the binding energy with NT was -53.14 Kcal/mol ± 3.02 which was lower than HCur (-64.46 Kcal/mol ± 6.38). This difference may be due to slightly larger RMSD of NT than that of HCur. The metal-Curcumin complexes Mn(Cur), Cu(Cur), and Zn(Cur) showed binding energies of -32.58 Kcal/mol ± 10.07, -68.92 Kcal/mol ± 4.57, and -53.07 Kcal/mol ± 3.93, respectively. These higher binding energies indicate stronger interactions between the DNA and HCur and its metal-complexes compared with HCur alone. This enhanced binding affinity could potentially improve the therapeutic effectiveness of HCur when combined with other metal ions. The observed variations in binding energies among the metal-Curcumin complexes suggest that the chosen metal ions significantly affect the overall binding properties of the Curcumin-based compounds. Further investigation into the structural and electronic characteristics of these metal-Curcumin complexes may provide valuable insights for optimizing their design, leading to improved DNA binding and pharmacological outcomes.

Table 3 shows that ΔG_{bind}-Coulomb, ΔG_{bind}-van der Waals, and ΔG_{bind}-lipophilic were the main contributors to $\Delta G_{binding}$ for the stability of the simulated complexes. In contrast, ΔG_{bind}-covalent and ΔG_{bind}-solvationGB promoted the instability of these complexes. These findings indicate that electrostatic interactions, van der Waals forces, and hydrophobic effects play crucial roles in stabilizing DNA-ligand complexes. The destabilizing effects of covalent bonding and

solvation energies underscore the intricate interplay of the forces governing molecular interactions in these systems.

Table 3. Binding free energy components for the apo 3FT6 and docked PRL, HCur, Mn(Cur), Cu(Cur), Zn(Cur) along with apo 101D and docked with NT, HCur, Mn(Cur), Cu(Cur), Zn(Cur) complexes calculated by MM-GBSA.

Compound code	MM-GBSA (kcal/mol)					
	ΔG_{bind}	**ΔG_{bind}Lipo**	**ΔG_{bind}vdW**	**ΔG_{bind}Coulomb**	**ΔG_{bind}SolvGB**	**ΔG_{bind}Covalent**
3FT6-PRL	-23.62 ± 1.52	-1.89± 0.20	-21.28 ± 1.27	-230.47 ± 17.47	25.51 ± 2.58	3.42 ± 0.57
3FT6-HCur	-36.38 ± 2.77	-9.76 ± 1.13	-37.95 ± 3.16	-204.05 ± 13.84	14.22 ± 2.41	1.21 ± 1.27
3FT6-Mn(Cur)	-11.15± 9.10	-14.38 ± 2.36	-56.42 ± 4.50	-31.22 ± 10.93	59.15± 12.75	1.74 ± 1.31
3FT6-Cu(Cur)	-27.47± 3.83	-8.95 ± 0.62	-13.13 ± 26.54	-285.12 ± 14.75	13.12 ± 1.88	2.64 ± 1.06
3FT6-Zn(Cur)	-22.06 ± 5.56	-9.32 ± 0.65	-49.51 ± 2.53	-235.52 ± 11.84	26.84 ± 2.74	1.45 ± 1.57
101D-NT	-53.14 ± 3.02	-8.11 ± 0.34	-58.19 ± 2.53	-246.58 ± 20.14	55.04 ± 8.24	4.70 ± 1.30
101D-HCur	-64.64 ± 6.38	-11.28 ± 1.40	-44.03 ± 6.90	-212.08 ± 15.33	24.25 ± 3.10	2.51 ± 0.14
101D-Mn(Cur)	-32.58 ± 10.07	-5.14 ± 3.14	-26.72 ± 3.99	-131.98± 13.28	58.56 ± 7.38	2.69 ± 1.56
101D-Cu(Cur)	-68.92± 4.57	-12.34 ± 0.72	-51.14 ± 1.88	-349.57 ± 18.87	33.19 ± 6.72	3.18 ± 0.83
101D-Zn(Cur)	-53.07 ± 3.93	-10.37 ± 0.80	-44.97 ± 2.80	-263.49 ± 12.99	49.53 ± 4.77	2.97 ± 1.29

(G_{bind}) total free energy of binding; (G_{bind}Lipo) lipophilic energy; (G_{bind}vdW) van der Waals interaction energy; (G_{bind}Coulomb) prime coulomb energy; (G_{bind}SolvGB) solvation energy generalized born; (G_{bind}Covalent) covalent binding energy

11.2.7 Trajectory snapshots analysis during MD simulation:

Molecular dynamics (MD) simulations spanning 100 ns were conducted to examine the stability of unbound DNA and DNA-ligand complexes. Images were captured during the 50 ns period for both the intercalator (3FT6) and groove binder (101D) models. The analysis revealed that the DNA double helix structure and ligands at their respective binding sites generally maintained stability and integrity throughout the 100 ns MD simulation for all dynamic systems, with the exception of DNA-Mn(Cur). The structural changes observed in DNA-Mn(Cur) may be linked to a higher root mean square deviation (RMSD) value of Mn(Cur) at the DNA binding sites in both the 3FT6 and 101D models. Cu(Cur) and Zn(Cur) demonstrated effective binding to both DNA models through intercalation or groove-binding mechanisms, sustaining this interaction throughout the MD simulation in a manner comparable to the standard molecules PRL or NT (Fig.20 & 21).

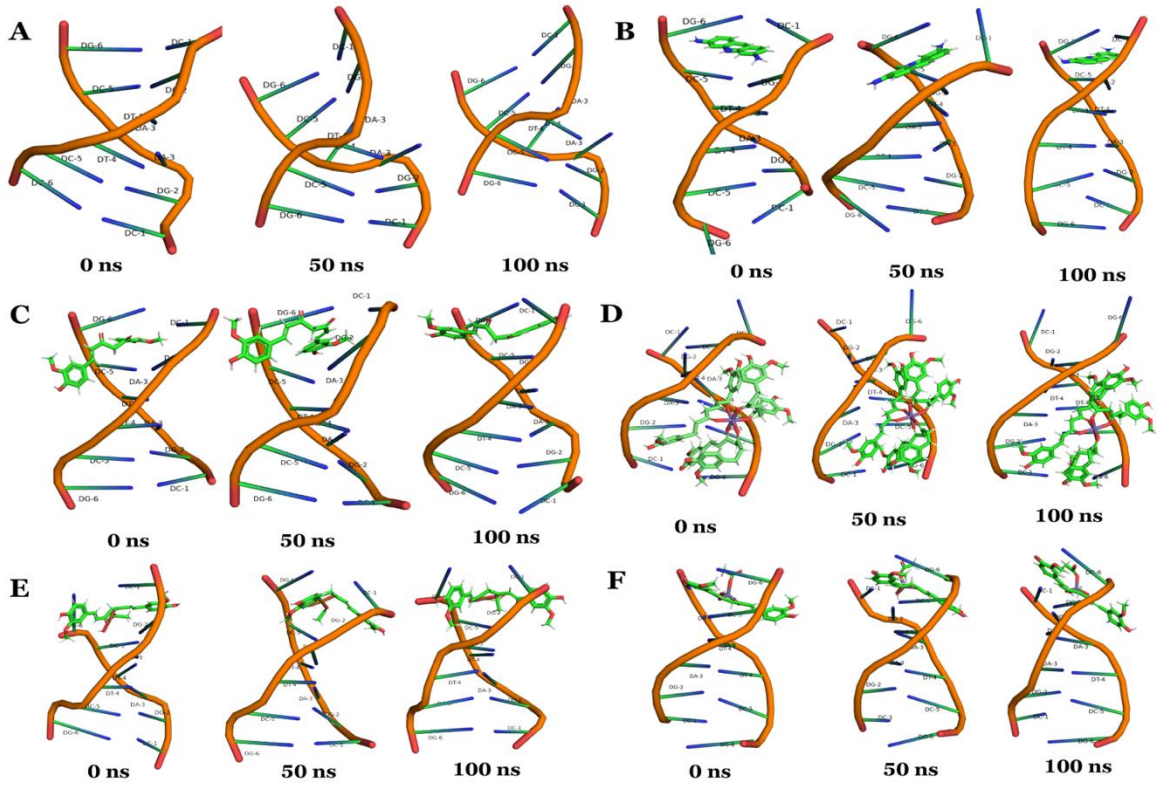


Figure 20 : Snapshots from 100 ns MD trajectories with 50 ns interval (A) Free DNA (3FT6) , (B) DNA-PRL , (C) DNA-HCur, (D) DNA-Mn(Cur) , (E) DNA-Cu(Cur), (F) DNA-Zn(Cur)

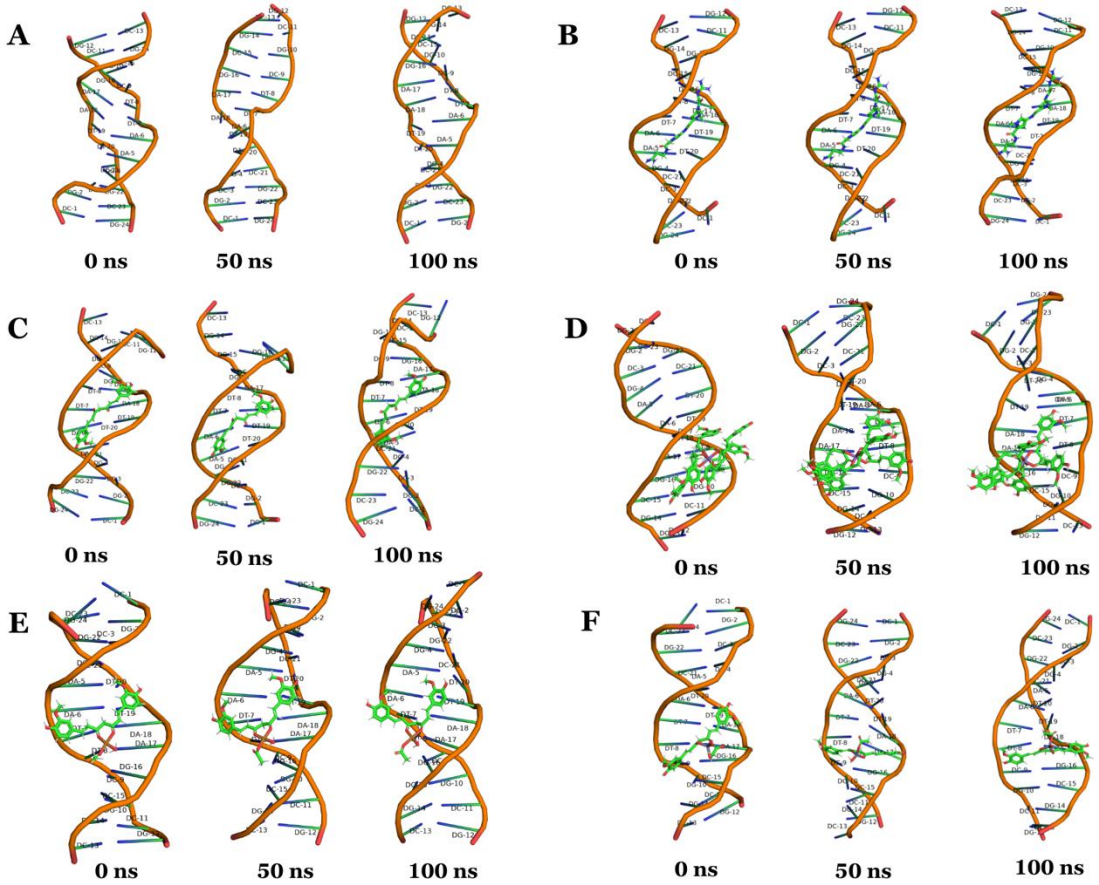


Figure 21 : Snapshots from 100 ns MD trajectories with 50 ns interval (A) Free DNA (101D) , (B) DNA-NT , (C) DNA-HCur, (D) DNA-Mn(Cur) , (E) DNA-Cu(Cur), (F) DNA-Zn(Cur)

References

1. A. Paul, S. Bhattacharya; Chemistry and biology of DNA-binding small molecules. *Current science*, **2012**, 212-231.
2. C. Selvaraj, S.K. Singh; Computational and experimental binding mechanism of DNA-drug interactions. *Current Pharmaceutical Design*, **2018**, 24, 3739-3757.
3. A. Rescifina, C. Zagni, M.G. Varrica, V. Pistarà, A. Corsaro; Recent advances in small organic molecules as DNA intercalating agents: Synthesis, activity, and modeling. *European journal of medicinal chemistry*, **2014**, 74, 95-115.
4. V. Brabec, J. Kasparkova; Ruthenium coordination compounds of biological and biomedical significance. DNA binding agents. *Coordination chemistry reviews*, **2018**, 376, 75-94.
5. I. Haq; Thermodynamics of drug–DNA interactions. *Archives of biochemistry and biophysics*, **2002**, 403, 1-15.
6. A. Mukherjee, W.D. Sasikala; Drug–DNA intercalation: From discovery to the molecular mechanism. *Advances in protein chemistry and structural biology*, **2013**, 92, 1-62.
7. W.J. Pigram, W. Fuller, L.D. Hamilton; Stereochemistry of intercalation: interaction of daunomycin with DNA. *Nature New Biology*, **1972**, 235, 17-19.
8. A. Mukherjee, R. Lavery, B. Bagchi, J.T. Hynes; On the molecular mechanism of drug intercalation into DNA: a simulation study of the intercalation pathway, free energy, and DNA structural changes. *Journal of the American Chemical Society*, **2008**, 130, 9747-9755.
9. W.D. Wilson, A.N. Gough, J.J. Doyle, M.W. Davidson; Coralyne. Intercalation with DNA as a possible mechanism of antileukemic action. *Journal of Medicinal Chemistry*, **1976**,19, 1261-1263.

10. S. Nafisi, A.A. Saboury, N. Keramat, J.F. Neault, H.A. Tajmir-Riahi; Stability and structural features of DNA intercalation with ethidium bromide, acridine orange and methylene blue. *Journal of Molecular Structure*, **2007**, 827, 35-43.

11. P.V. Scaria, R.H. Shafer; Binding of ethidium bromide to a DNA triple helix. Evidence for intercalation. *Journal of Biological Chemistry*, **1991**, 266, 5417-5423.

12. D.P. Heller, C.L. Greenstock; Fluorescence lifetime analysis of DNA intercalated ethidium bromide and quenching by free dye. *Biophysical chemistry*, **1994**, 50, 305-312.

13. K. Nath, J.W. Sarosy, J. Hahn, C.J. Di Como; Effects of ethidium bromide and SYBR® Green I on different polymerase chain reaction systems. *Journal of biochemical and biophysical methods*, **2000**, 42, 15-29.

14. H. Yoshikawa, N. Ogasawara, M. Seiki; Initiation of DNA replication in Bacillus subtilis: IV. The effect of an intercalating dye, ethidium bromide. *Molecular and General Genetics MGG*, **1980**, 179, 265-272.

15. S.Z. Hirschman, E. Garfinkel; Inhibition of hepatitis B DNA polymerase by intercalating agents. *Nature*, **1978**, 271, 681-683.

16. X.P. Sun, F. Wang; The DNA intercalator, ethidium bromide, alters the pattern of DNAse I hypersensitive sites of the βA-globin gene in chicken erythrocytes. *Biochimica et Biophysica Acta (BBA)-Gene Structure and Expression*, **1991**, 1089, 158-166.

17. J. Huang, Z. Wang, J.K. Kim, X. Su, Z. Li; Detecting arbitrary DNA mutations using graphene oxide and ethidium bromide. *Analytical chemistry*, **2015**, 87, 12254-12261.

18. S.M. Nelson, L.R. Ferguson, W.A. Denny; Non-covalent ligand/DNA interactions: minor groove binding agents. *Mutation Research/Fundamental and Molecular Mechanisms of Mutagenesis*, **2007**, 623, 24-40.

19. G.S. Khan, A. Shah, D. Barker; Chemistry of DNA minor groove binding agents. *Journal of photochemistry and photobiology B: Biology*, **2012**, 115, 105-118.

20. B.P. Reddy, S.M. Sondhi, J.W. Lown; Synthetic DNA minor groove-binding drugs. *Pharmacology & therapeutics,* **1999**, 84, 1-111.

21. P.L. Hamilton, D.P. Arya; Natural product DNA major groove binders. *Natural product reports*, **2012**, 29, 134-143.

22. L. Strekowski, B. Wilson; Noncovalent interactions with DNA: an overview. *Mutation Research/Fundamental and Molecular Mechanisms of Mutagenesis,* **2007**, 623, 3-13.

23. U. Heinemann, C. Alings, M. Bansal; Double helix conformation, groove dimensions and ligand binding potential of a G/C stretch in B-DNA. *The EMBO Journal*, **1992**, 11, 1931-1939.

24. S. Neidle; DNA minor-groove recognition by small molecules. *Natural product reports,* **2001**,18, 291-309.

25. A. Lauria, A. Montalbano, P. Barraja, G. Dattolo, A.M. Almerico; DNA minor groove binders: an overview on molecular modeling and QSAR approaches. *Current medicinal chemistry*, **2007**, 14, 2136-2160.

26. S. Marchini, M. Broggini, C. Sessa, M. D'Incalci; Development of distamycin-related DNA binding anticancer drugs. *Expert opinion on investigational drugs*, **2001**, 10 , 1703-1714.

27. H. Loskotová, V. Brabec; DNA interactions of cisplatin tethered to the DNA minor groove binder distamycin. *European journal of biochemistry*, **1999**, 266, 392-402.

28. P. Majumder, D. Dasgupta; Effect of DNA groove binder distamycin A upon chromatin structure. *PLoS One*, **2011**, 6, e26486.

29. D.L. Boger, B.E. Fink, M.P. Hedrick; Total synthesis of distamycin A and 2640 analogues: a solution-phase combinatorial approach to the discovery of new, bioactive DNA binding agents and development of a rapid, high-throughput screen for determining

relative DNA binding affinity or DNA binding sequence selectivity. *Journal of the American Chemical Society*, **2000**, 122, 6382-6394.

30. C. Zimmer; Effects of the antibiotics netropsin and distamycin A on the structure and function of nucleic acids. *Progress in nucleic acid research and molecular biology*, **1975**, 15, 285-318.

31. M.L. Kopka, C. Yoon, D. Goodsell, P. Pjura, R.E. Dickerson; The molecular origin of DNA-drug specificity in netropsin and distamycin. *Proceedings of the National Academy of Sciences*, **1985**, 82, 1376-1380.

32. R.M. Wartell, J.E. Larson, R.D. Wells; Netropsin: a specific probe for AT regions of duplex deoxyribonucleic acid. *Journal of Biological Chemistry*, **1974**, 249, 6719-6731.

33. M. Amine Bouhlel, M. Lambert, M.H. David-Cordonnier; Targeting transcription factor binding to DNA by competing with DNA binders as an approach for controlling gene expression. *Current topics in medicinal chemistry*, **2015**, 15, 1323-1358.

34. M. Gniazdowski, W.A. Denny, S.M. Nelson, M. Czyz; Transcription factors as targets for DNA-interacting drugs. *Current medicinal chemistry*, **2003**, 10, 909-924.

35. J.J. Welch, F.J. Rauscher 3rd, T.A. Beerman; Targeting DNA-binding drugs to sequence-specific transcription factor. DNA complexes. Differential effects of intercalating and minor groove binding drugs. *Journal of Biological Chemistry*, **1994**, 269, 31051-31058.

36. P.B. Dervan, A.T. Poulin-Kerstien, E.J. Fechter, B.S. Edelson; Regulation of gene expression by synthetic DNA-binding ligands, *Springer Berlin Heidelberg* , **2005**,1-31.

37. V. K. Misra, B. Honig; On the magnitude of the electrostatic contribution to ligand-DNA interactions. *Proceedings of the National Academy of Sciences*, **1995**, 92, 4691-4695.

38. L.D. Williams, L.J. Maher III; Electrostatic mechanisms of DNA deformation. *Annual review of biophysics and biomolecular structure*, **2000**, 29, 497-521.

39. J.A. Subirana, M. Soler-Lopez; Cations as hydrogen bond donors: a view of electrostatic interactions in DNA. *Annual review of biophysics and biomolecular structure*, **2003**, 32, 27-45.

40. V.V. Kostjukov, N.M. Khomytova, D.B. Davies; M.P. Evstigneev; Electrostatic contribution to the energy of binding of aromatic ligands with DNA. *Biopolymers: Original Research on Biomolecules*, **2008**, 89, 680-690.

41. B.G. Feuerstein, N. Pattabiraman, L. J. Marton; Spermine-DNA interactions: a theoretical study. *Proceedings of the National Academy of Sciences*, **1986**, 83, 5948-5952.

42. B.G. Feuerstein, N. Pattabiraman, L.J. Marton; Molecular mechanics of the interactions of spermine with DNA: DNA bending as a result of ligand binding. *Nucleic acids research*, **1990**, 18, 1271-1282.

43. P.M. Vertino, R.J. Bergeron, P.F. Cavanaugh Jr, C.W. Porter; Structural determinants of spermidine–DNA interactions. *Biopolymers: Original Research on Biomolecules*, **1987**, 26, 691-703.

44. A.C. Childs, D.J. Mehta, E.W. Gerner; Polyamine-dependent gene expression. *Cellular and Molecular Life Sciences CMLS*, **2003**, 60, 1394-1406.

45. K. Igarashi, K. Kashiwagi; Modulation of cellular function by polyamines. *The international journal of biochemistry & cell biology*, **2010**, 42, 39-51.

46. L. Miller-Fleming, V. Olin-Sandoval, K. Campbell, M. Ralser; Remaining mysteries of molecular biology: the role of polyamines in the cell. *Journal of molecular biology*, **2015,** 427, 3389-3406.

47. C. Bailly, J. P. Henichart; DNA recognition by intercalator-minor-groove binder hybrid molecules. *Bioconjugate Chemistry*, **1991**, 2, 379-393.

48. G. Bischoff, S. Hoffmann; DNA-binding of drugs used in medicinal therapies. *Current medicinal chemistry*, **2002**, 9, 321-348.

49. C. Pérez-Arnaiz, N. Busto, J.M. Leal, B. García; New insights into the mechanism of the DNA/doxorubicin interaction. *The Journal of Physical Chemistry B*, **2014**, 118, 1288-1295.

50. S.R. Byrn, G.D. Dolch; Analysis of binding of daunorubicin and doxorubicin to DNA using computerized curve-fitting procedures. *Journal of pharmaceutical sciences*, **1978**, 67, 688-693.

51. E.F. Silva, R.F. Bazoni, E.B. Ramos, M.S. Rocha; DNA-doxorubicin interaction: New insights and peculiarities. *Biopolymers*, **2017**, 107, e22998.

52. Y.J. Schneider, R. Baurain, A. Zenebergh, and A. Trouet; DNA-binding parameters of daunorubicin and doxorubicin in the conditions used for studying the interaction of anthracycline-DNA complexes with cells in vitro. *Cancer Chemotherapy and Pharmacology*, **1979**, 2, 7-10.

53. R.M. Wadkins, T.M. Jovin; Actinomycin D and 7-aminoactinomycin D binding to single-stranded DNA. *Biochemistry*, **1991**, 30, 9469-9478.

54. J. Kleeff, M. Kornmann, H Sawhney M. Korc; Actinomycin D induces apoptosis and inhibits growth of pancreatic cancer cells. *International journal of cancer*, **2000**, 86, 399-407.

55. H. Baruah; DNA interactions of a hybrid anticancer agent: A biophysical and high-resolution structural study, *Wake Forest University*, **2005**.

56. S. Bhaduri, N. Ranjan, D.P. Arya; An overview of recent advances in duplex DNA recognition by small molecules. *Beilstein journal of organic chemistry*, **2018**, 14, 1051-1086.

57. L. Ozalp, S.S. Erdem, B. Yüce-Dursun, Ö. Mutlu, M. Özbil; Computational insight into the phthalocyanine-DNA binding via docking and molecular dynamics simulations. *Computational biology and chemistry*, **2018**, 77, 87-96.

58. P. Vijayalakshmi, C. Selvaraj, S.K. Singh, J. Nisha, K. Saipriya, P. Daisy; Exploration of the binding of DNA binding ligands to Staphylococcal DNA through QM/MM docking and molecular dynamics simulation. *Journal of Biomolecular Structure and Dynamics*, **2013**, 31, 561-571.

59. F. Jafari, S. Moradi, A. Nowroozi, K. Sadrjavadi, L. Hosseinzadeh, M. Shahlaei; Exploring the binding mechanism of paraquat to DNA by a combination of spectroscopic, cellular uptake, molecular docking and molecular dynamics simulation methods. *New Journal of Chemistry*, **2017**, 41, 14188-14198.

60. R. Rohs, I. Bloch, H. Sklenar, Z. Shakked; Molecular flexibility in ab initio drug docking to DNA: binding-site and binding-mode transitions in all-atom Monte Carlo simulations. *Nucleic acids research*, **2005**, 33, 7048-7057.

61. T.A. de Oliveira, L.R. Medaglia, E.H.B. Maia, L.C. Assis, P.B. de Carvalho, A.M. da Silva, A.G. Taranto; Evaluation of docking machine learning and molecular dynamics methodologies for DNA-ligand systems. *Pharmaceuticals*, **2022**, 15, 132.

62. A. Soni, P. Khurana, T. Singh, B. Jayaram; A DNA intercalation methodology for an efficient prediction of ligand binding pose and energetics. *Bioinformatics*, **2017**, 33, 1488-1496.

63. Y. Ren, H.Z. Zhang, S.L. Zhang, Y.L. Luo, L. Zhang, C.H. Zhou, R.X. Geng; Synthesis and bioactive evaluations of novel benzotriazole compounds as potential antimicrobial agents and the interaction with calf thymus DNA. *Journal of Chemical Sciences*, **2015**, 127, 2251-2260.

64. K.D. Goodwin, E.C. Long, M.M. Georgiadis; A host–guest approach for determining drug–DNA interactions: an example using netropsin. *Nucleic acids research*, **2005**, 33, 4106-4116.

65. A. Lauria, P. Diana, P. Barraja, A. Montalbano, G. Cirrincione, G. Dattolo, A.M. Almerico; MADoSPRO: a new approach to molecular modelling studies on a series of DNA minor groove binders. *QSAR & Combinatorial Science*, **2006**, 25, 252-262.

66. K. Bielawski, A. Bielawska, D. Bartulewicz, A. Różański; Molecular modelling of the interaction of carbocyclic analogues of netropsin and distamycin with d (CGCGAATTCGCG) 2. *Acta Biochimica Polonica*, **2000**, 47, 855-866.

67. D. Yusuf, A.M. Davis, G.J. Kleywegt, S. Schmitt; An alternative method for the evaluation of docking performance: RSR vs RMSD. *Journal of chemical information and modeling*, **2008**, 48, 1411-1422.

68. G. M. Morris, R. Huey, W. Lindstrom, M. F. Sanner, R. K. Belew, D. S. Goodsell, A. J. Olson; Autodock4 and AutoDockTools4: automated docking with selective receptor flexiblity. *Jour. Comp. Chem.*, **2009**, 16, 2785-91.

69. J. Eberhardt, D. Santos-Martins, A.F. Tillack, S. Forli; AutoDock Vina 1.2.0: New Docking Methods, Expanded Force Field, and Python Bindings. *Journal of Chemical Information and Modeling*, **2021**.

70. O. Trott, A. J. Olson; AutoDock Vina: improving the speed and accuracy of docking with a new scoring function, efficient optimization, and multithreading. *Journal of computational chemistry*, **2010**, 31, 455-461.

71. N. Michaud-Agrawal, E.J. Denning, T.B. Woolf, and O. Beckstein; MD Analysis: a toolkit for the analysis of molecular dynamics simulations. Journal of computational chemistry, 2011, 32, 2319-2327.K. Sargsyan, C. Grauffel, C. Lim; How molecular size impacts RMSD applications in molecular dynamics simulations. *Journal of chemical theory and computation*, **2017**, 13, 1518-1524.

72. N.C. Benson, V. Daggett; A comparison of multiscale methods for the analysis of molecular dynamics simulations. *The Journal of Physical Chemistry B,* **2012**, 116, 8722-8731.

73. M.Y. Lobanov, N.S. Bogatyreva, O.V. Galzitskaya; Radius of gyration as an indicator of protein structure compactness. *Molecular Biology*, **2008,** 42, 623-628.

74. A.R. Bizzarri, C.X. Wang, W.Z. Chen, S. Cannistraro; Hydrogen bond analysis by MD simulation of copper plastocyanin at different hydration levels. *Chemical physics*, **1995**, 201, 463-472.

75. X. Wang, H. Zhang, W. Li; DNA-binding mechanisms of human and mouse cGAS: a comparative MD and MM/GBSA study. *Physical Chemistry Chemical Physics*, **2020**, 22, 26390-26401.

76. U. Issar, T. Kumari, R. Kakkar; Assessment of molecular binding of Hoechst 33258 analogues into DNA using docking and MM/GBSA approach. *Journal of Computational Science*, **2015**, 10, 166-177.

CHAPTER 12

In silico molecular modeling investigations for the establishment of antibacterial properties of Curcumin and its metal complexes through FtsZ inhibition

Introduction

One of the most important issues being faced with regard to the application of modern medicine is the growing threat of resistance to antibiotics.[1-4] Hence, there is an urgent need for new antibacterial drugs because with the emergence of multidrug-resistant (MDR) bacteria many of the current antibiotics have been rendered useless.[5-7] An effective method that has surfaced in the hunt for novel targets and approaches for the development of antibacterial drugs is the suppression of the bacterial cell cycle.[8,9] FtsZ (Filamenting temperature-sensitive mutant Z) is one of the proteins involved in this crucial process that has attracted a lot of interest as a possible target for antibacterial drugs.[9-12] The role of FtsZ in bacterial cell division and its absence in eukaryotic cells makes it an attractive target for selective antibacterial drug design.[9-12] Moreover, targeting FtsZ offers an opportunity to overcome some of the challenges associated with current antibiotics that target the bacterial cell wall synthesis or protein synthesis as these pathways are commonly exploited by existing drugs thus contributing to resistance.[9-13]

FtsZ is fundamental to the process of bacterial cytokinesis, establishing itself as an essential protein for the survival and proliferation of bacteria. Inhibiting FtsZ leads to a disruption in cell division, thereby offering a strategy to impede bacterial growth and its reproduction.[9-13] FtsZ is a remarkably conserved protein similar to tubulin, which establishes the dynamic Z-ring at the site of bacterial cell division.[12-14] The Z-ring serves as a structural framework for the assembly of additional division proteins and is crucial for the development of the septum, that ultimately divides daughter cells.[10-14] Considering its significant importance, the inhibition of FtsZ has been acknowledged as an effective approach to address bacterial infections, especially those resulting from antibiotic-resistant strains.[9,10,12-14]

Computational chemistry, which includes molecular docking, virtual screening, and molecular dynamics simulations has played an instrumental role in advancing our understanding of FtsZ inhibition and identifying potential inhibitors.[15-20] Through these techniques, researchers can explore molecular interactions between FtsZ and small-molecule inhibitors, assess their binding affinities and optimize the design of novel compounds.[15-20]

12.1 Structure and function of FtsZ

With 40% to 50% sequence identity, FtsZ is structurally and functionally similar to the majority of bacteria, a large number of archaea, a small number of chloroplasts and very few primitive mitochondria.[21] Some FtsZ bacteria have a three-dimensional structure that resembles α- and β-tubulin.[21] Eukaryotic microtubules rely on tubulin as its central component. There is evidence that the proteins tubulin and FtsZ work together to maintain the structure and form of live cells and facilitate cell division.[21-23] FtsZ can take up two forms in bacterial cells; monomers and higher-order polymers. The form it would take depends on whether it is attached to a guanosine 5'-triphosphate (GTP) or a guanosine 5'-diphosphate (GDP).[24] The FtsZ protein contains two enzymatic domains with diverse folds; an N-terminal domain connected to a C-terminal domain with various extensions and a C-terminal tail.[25,26] A core H7 helix divides the enzymatic domain into two globular subdomains; one at the N-terminus and the other at C-terminus. There is a nucleotide-binding pocket in the N-terminal enzymatic domain and a GTPase-activating site in the C-terminal subdomain (Fig. 1). Furthermore, an H5 helix connects the N-terminal enzymatic domain to the lengthy C-terminal domain.[27, 28] The C-terminal domain is important in the development of the protofilament.[25-28] The active site of GTPase is located between two monomers. The extended C-terminal tail is not well-structured and interacts with multiple accessory proteins.[29,30] The C-terminal peptide is not involved in assembly formation

but is required for interactions with other membrane-associated cell division proteins like FtsZ inducers, FtsA and ZipA to maintain Z ring stability.[31,32] Rupture of the C-terminal peptide affects FtsZ function most likely by inhibiting its contact with both cell division proteins.[33-35]

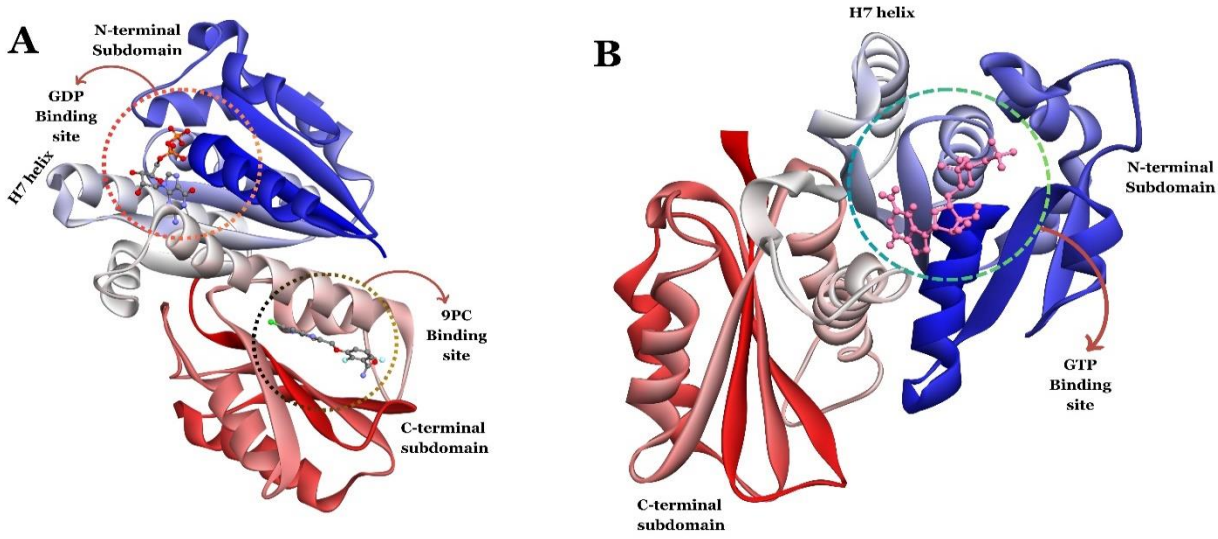


Figure 1: (A) Crystal structure of FtsZ in *S.aureus* organism (PDB ID : 4DXD) , (B) Crystal structure of FtsZ in *E.Coli* organism (PDB ID : 6UNX)

The fundamental architecture of FtsZ is characterized by an N-terminal nucleotide-binding domain (NBD) and a C-terminal GTPase activation domain (GAD) interconnected by elongated central helix H7. To date, various FtsZ inhibitors have been identified that interact either with (i) the nucleotide-binding pocket within the N-terminal subdomain, including polyphenolic derivatives UCM05 and UCM44,[36,37] the marine natural product chrysophaentin A and synthetic hemi-chrysophaentin.[38,39] A significant number of anti-FtsZ drugs work by inhibiting significant sites for GTP binding or interactions between FtsZ subunits which in turn disrupts FtsZ polymerization.

(ii) the cleft situated between the H7 helix and the C-terminal subdomain, exemplified by the benzamide PC190723;[40,41] and (iii) C-terminal subdomain, represented by the peptide MciZ (mother cell inhibitor of FtsZ).[42]

Focusing on FtsZ, for advancement of antibacterial candidates presents numerous benefits. First, it is crucial for the proliferation and sustainability of nearly all prokaryotic organisms. Furthermore, it exhibits a remarkable degree of conservation across bacterial species. Further, it exhibits notable distinctions from its eukaryotic counterpart tubulin thereby presenting a potential to create FtsZ-targeting agents that could minimize toxicity towards eukaryotic cells.[43]

Results and Discussion

12.2 Molecular docking interaction of FtsZ with Curcumin & its metal complexes

Investigating the inhibition of FtsZ protein, can provide insights into novel antibacterial strategies. This study focuses on the possibility as to how HCur and its metal complexes might interact with *S. aureus* and *E. coli* by specifically targeting the FtsZ protein. This was achieved through the molecular docking and molecular dynamics approach. To understand interactions at a molecular level, two FtsZ protein models were selected: one representing *S.aureus* (PDB ID: 4DXD) notable for its dual binding sites (GDP binding site and 9PC, binding site Fig 1 A) and *E. coli* (PDB ID: 6UNX) distinguished by its singular GTP-binding site in the N-terminal subdomain (Fig.1 B). The selection of protein models using the Ramachandran plot (Fig. 2) ensures structural integrity, which is again a crucial step before conducting further studies. The selection of these specific protein models provides a comprehensive basis for comparing the FtsZ proteins across different bacterial species. Further analysis of the structural differences between *S. aureus* and *E. coli* FtsZ proteins could reveal insights into their functional divergence and also

species-specific adaptations. Additionally, examining the conservation and variability of GDP, GTP and 9PC binding sites may shed light on potential targets for novel antibacterial compounds.

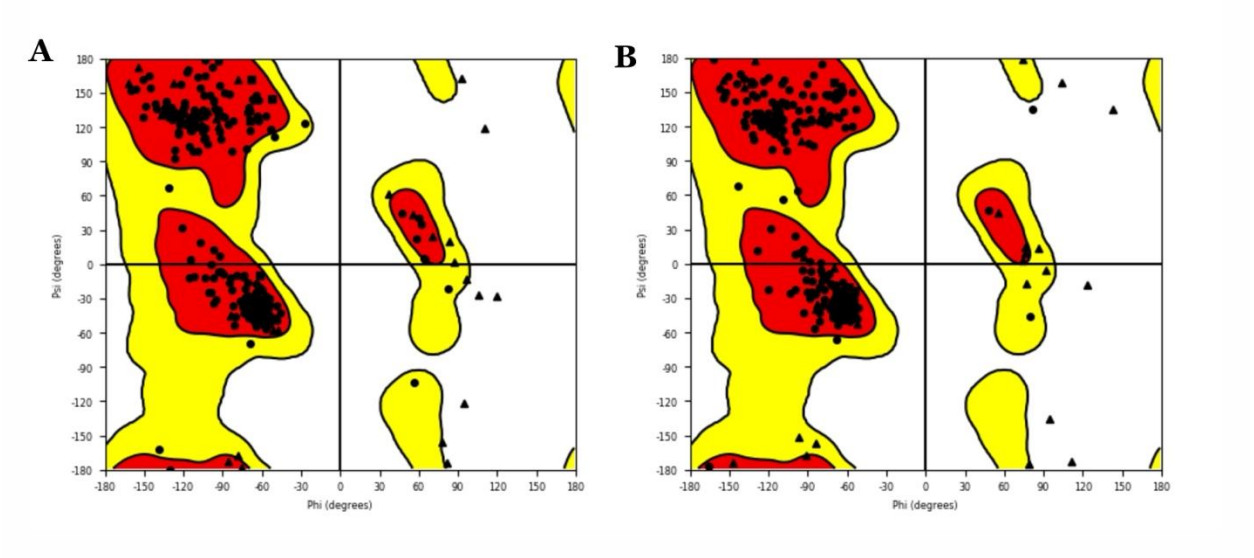


Figure 2 : (A) Ramachandran plot of FtsZ protein for the *S.aureus* model (PDB ID : 4DXD), (B) Ramachandran plot of FtsZ protein for the *E.coli* model (PDB ID : 6UNX)

Inhibition effects were shown for HCur and its prepared metal complexes that effectively binds with FtsZ protein at the 9PC binding site for *S.aureus* (PDB ID : 4DXD) and GTP-binding site for *E.Coli* (PDB ID : 6UNX). Redocking experiments of native co-crystal ligand 9PC for *S.aureus* (PDB ID: 4DXD) and GTP for *E.Coli* (PDB ID: 6UNX) were done. It was found that in both cases redocked and co-crystal ligands superimpose each other and interact with almost identical amino acids residues at their respective binding sites (Fig. 3). The root mean square deviation (RMSD) values between co-crystal and redocked ligand pose is 1.77 Å at the 9PC binding site and 1.98 Å at the GTP binding site for *E.Coli* FtsZ protein (PDB ID : 6UNX). Generally, RMSD < 2 Å is considered a valid molecular docking protocol.[44]

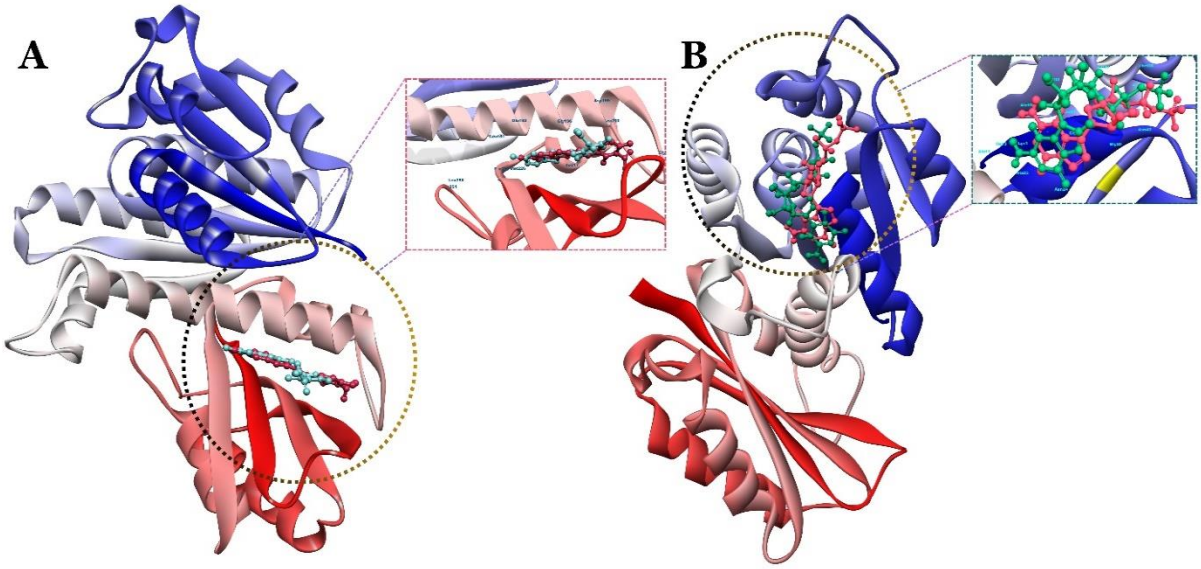


Figure 3:(A) Redocking of native co-crystal ligands into binding site of FtsZ crystal structure of *S.aureus* (PDB ID: 4DXD). Here, the colour magenta represents native co-crystal ligand poses and cyan represents redocked poses at the 9PC binding site, (B) Redocking of native co-crystal ligand (GTP) into the binding site of FtsZ crystal structure of *E.Coli* (PDB ID: 6UNX). Here the colour green represents native co-crystal ligand (GTP) pose and pink colour represents redocked pose at the GTP binding site.

To determine binding pattern, rigid molecular docking was performed in both cases. For *S.aureus* FtsZ protein (PDB ID:4DXD) the 9PC (co-ligand), HCur, Mn(Cur), Cu(Cur) and Zn(Cur) were made flexible to obtain 10 conformations to predict the receptor-ligand interaction and examine the most energetically favorable docked position. Active site residue of 4DXD was also determined using an online tool CASTp (Computer Atlas of Surface Topography of Proteins).[45] After docking it was found that for *S.aureus* (PDB ID : 4DXD), the co-crystallized ligand 9PC with an inhibitory concentration of 0.17 μM showed a docking score of -9.04 Kcal/mole in Autodockvina (version 1.2.5) and -9.21 Kcal/mole in Autodock 4.2.6. (Table 1, Fig. 4). The 9PC made 5 hydrogen bonds with amino acid Asn-263, Val-207, Asn-208, Gly-227,

Val-310 of chain A of 4DXD, as revealed by the 2D and 3D interaction diagrams (Fig. 4). A list of other interaction modes is provided in Table 1.

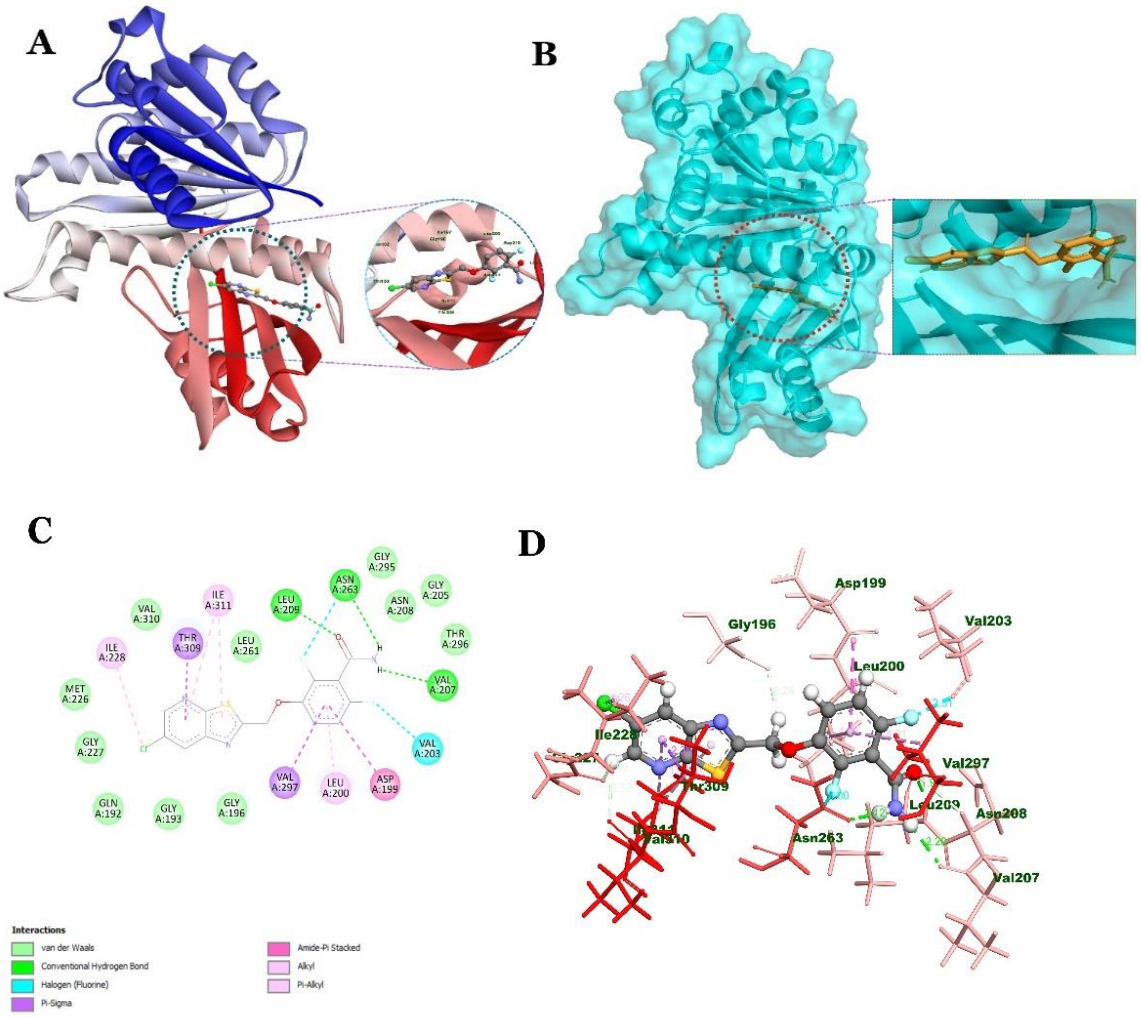


Figure 4 :(A) Ribbon representation of docked 9PC ligand into C-terminal subdomain, (B) surface view of docked 9PC into FtsZ protein of *S.aureus* (PDB ID : 4DXD), (C) 2D interaction of 9PC ligand with 4DXD molel of FtsZ protein, (D) 3D interaction of 9PC ligand with 4DXD model of FtsZ protein.

On the other hand, HCur forms five hydrogen bonds with FtsZ protein (PDB ID : 4DXD) with Gly-205, Thr-265, Val-310, Leu-209, Val-207 of chain A. Docking scores were -7.64 Kcal/mol in Autodock vina v 1.2.5 and -7.60 Kcal/mol in AutoDock v 4.2.6 with an inhibition concentration of 2.69 µM (Table 1). All hydrogen bonds mentioned above, between HCur and amino acid bases, had bond lengths less than 3.00 Å (Fig.5).

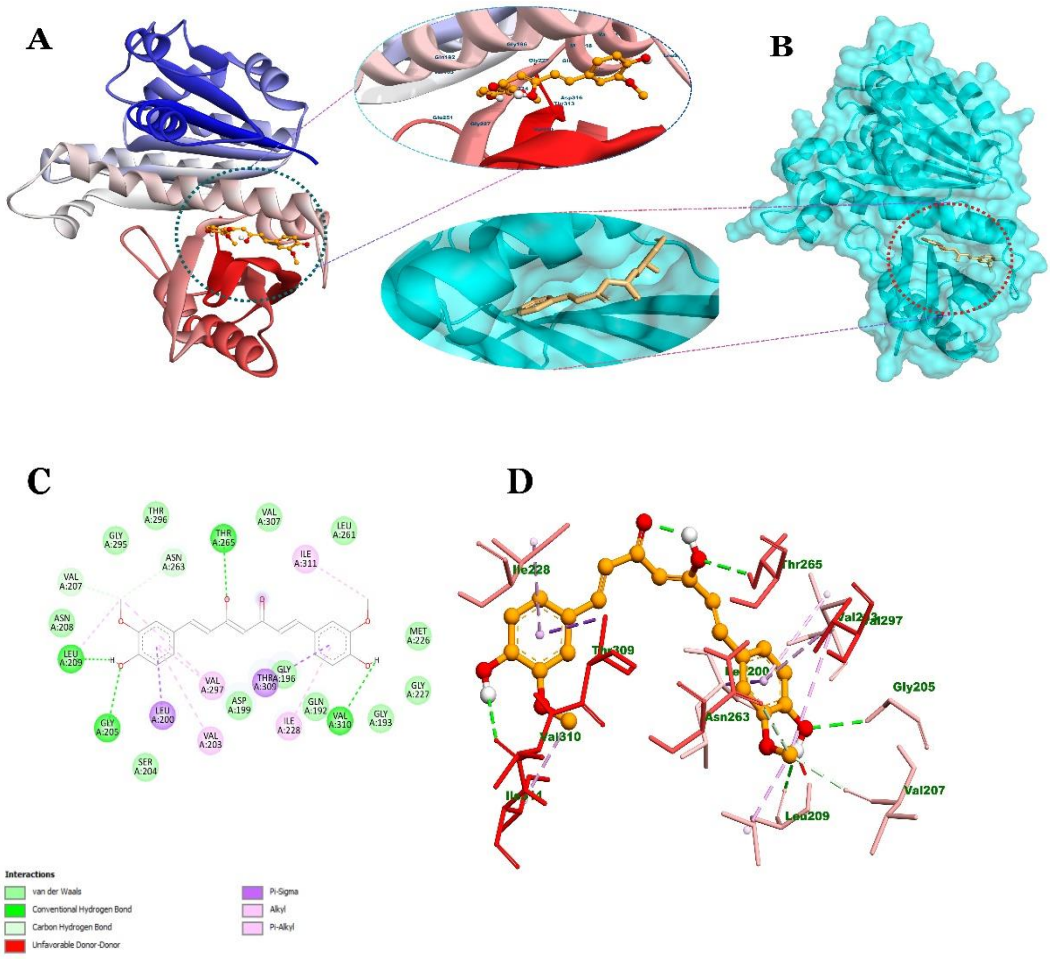


Figure 5: (A) Docked poses of HCur at 9PC binding sites of FtsZ protein model 4DXD. (B) surface view of docked pose of HCur at 9PC binding sites of FtsZ protein model 4DXD (C) 2D interactions of HCur with 4DXD model of FtsZ protein and (D) 3D interactions of HCur with 4DXD molel of FtsZ protein

In case of Mn(Cur), Autodockvina v 1.2.5 and Autodock v 4.2.6 yielded docking scores of -7.85 Kcal/mole and -7.81 Kcal/mole respectively and exhibited an inhibitory concentration of 3.58 μM. The formation of hydrogen bonds involved interactions with amino acids Asn-299, Thr-309 and Asn-37 of chain A. These were derived from the analysis of 2D and 3D interaction diagrams, as illustrated in Fig.6.

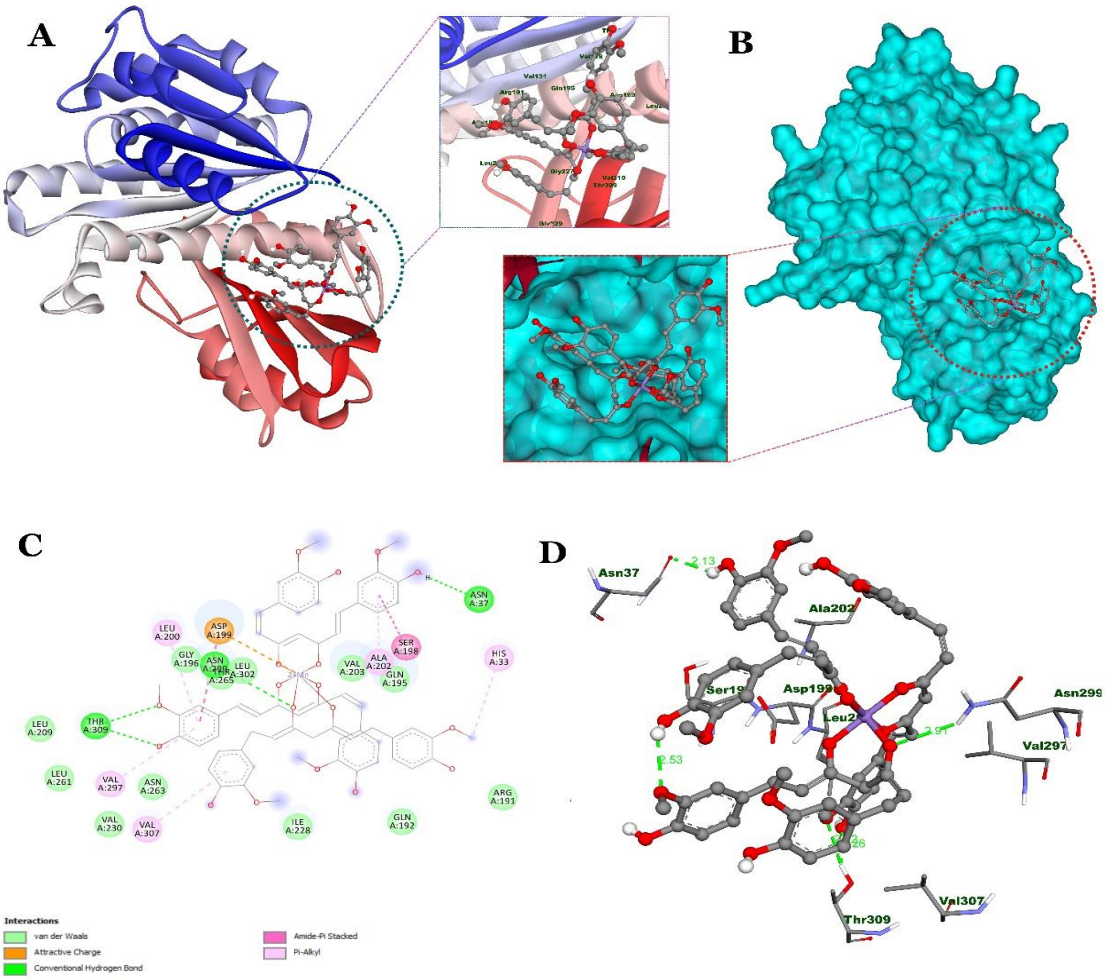


Figure 6: (A) Docked poses of Mn(Cur) at 9PC binding sites of FtsZ protein model 4DXD, (B) surface view of docked pose Mn(Cur) at 9PC binding sites of FtsZ protein model 4DXD (C) 2D interactions and (D) 3D interactions of docked structure Mn(Cur) with 4DXD molel of FtsZ protein

Docking scores for Cu(Cur) as determined by Autodockvina v 1.2.5 and Autodock v 4.2.6, were -8.21 Kcal/mole and -8.74 Kcal/mole respectively with an inhibitory concentration of 0.39 μM. Analysis revealed that H-bonds were formed through interactions between amino acids Leu-209 and Ile-298. This was obtained by examining the 2D and 3D interaction diagrams (Fig.7).

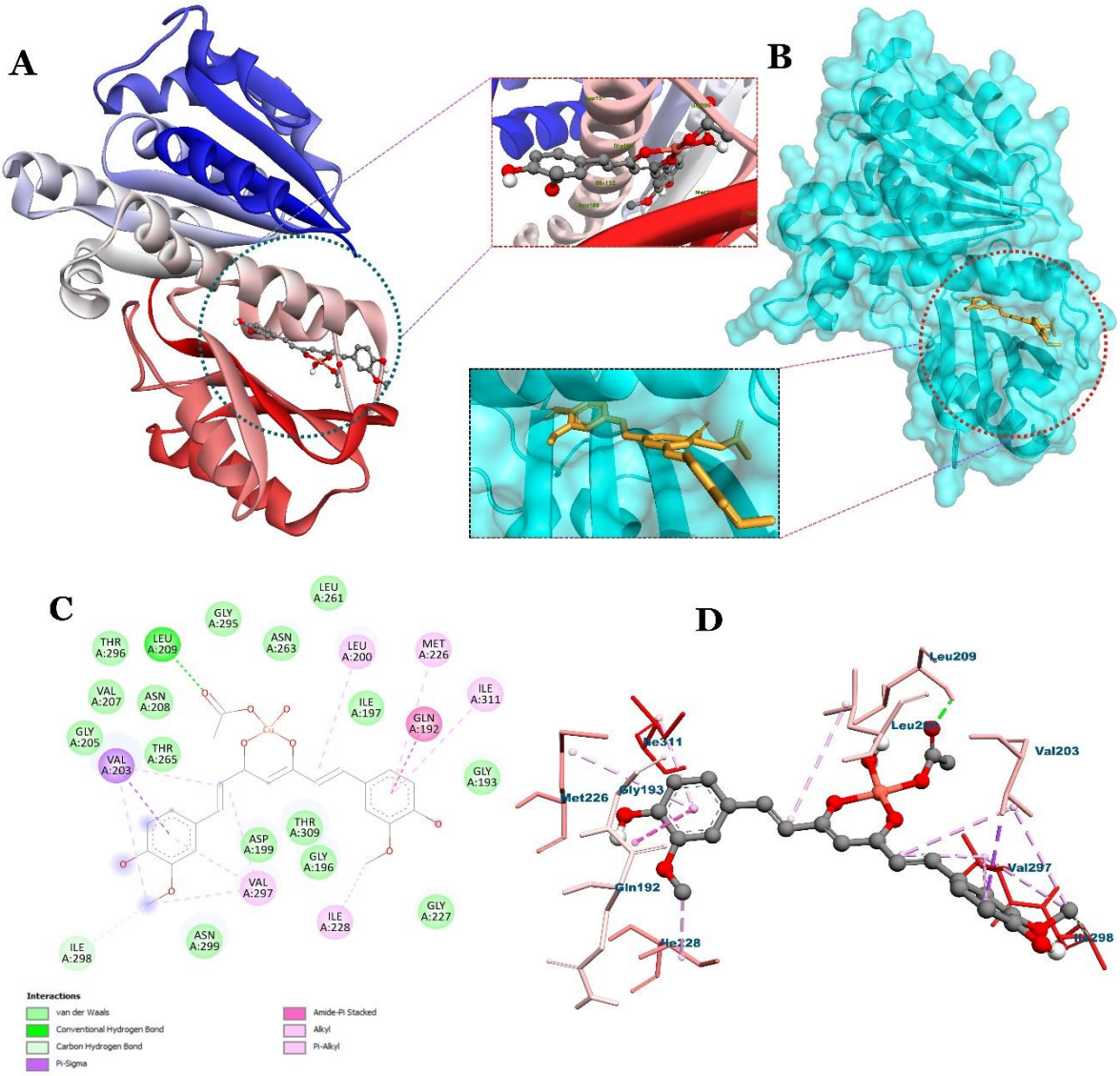


Figure 7: (A) Docked poses of Cu(Cur) at 9PC binding sites of FtsZ protein model 4DXD, (B) surface view of docked pose of Cu(Cur) at 9PC binding site of FtsZ protein model 4DXD. (C) 2D interactions and (D) 3D interactions of docked structure Cu(Cur) ligand with 4DXD molel of FtsZ protein

According to Autodockvina v 1.2.5 and Autodock v 4.2.6, Zn(Cur) had a docking score of -9.15 Kcal/mole and -9.57 Kcal/mole respectively with an inhibitory concentration of 0.09 μM. We found that amino acids Gly-205, Leu-209, Gly-227, Asn-208, Gly-193, Gln-192 interact to create H-bonds. 2D and 3D interaction diagrams provided this information (Fig.8).

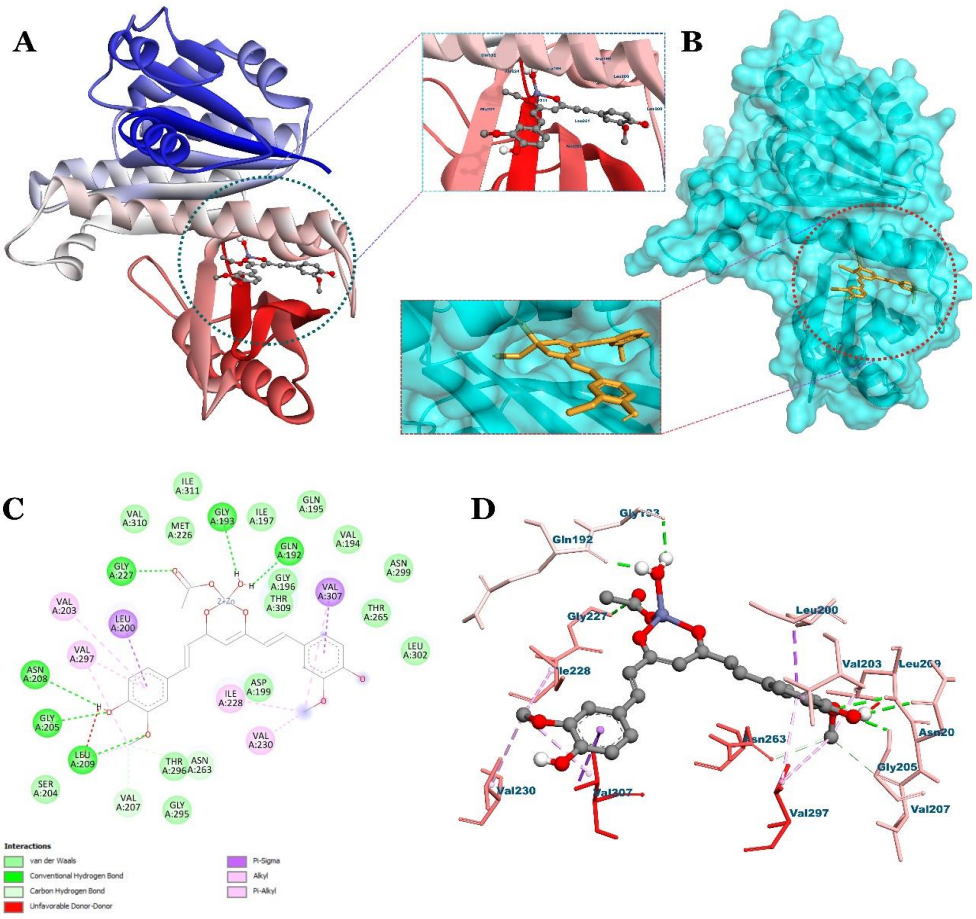


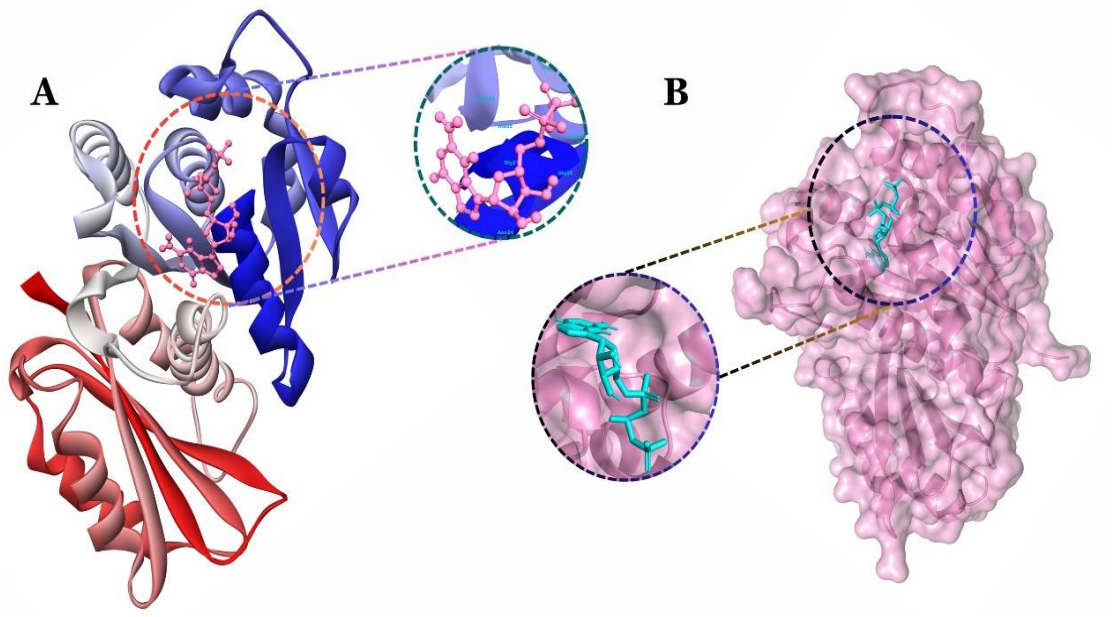
Figure 8: (A) Docked poses of Zn(Cur) at 9PC binding sites of FtsZ protein model 4DXD, (B) surface view of docked pose Zn(Cur) at 9PC binding site of FtsZ protein model 4DXD. (C) 2D interactions and (D) 3D interactions of docked structure of Zn(Cur) with 4DXD molel of FtsZ protein

Table 1: Docking ligands, docking score, interacting amino acid residues of *S.aureus* FtsZ protein (PDB ID: 4DXD)

Name of the ligands	Autodock Vina_1.2.5	Autodock 4.2.6		Active site Interacting amino acids residues and type of interactions (Å)
	Binding Affinity (Kcal/mol)	Binding Energy (Kcal/mol)	Inhibition Constant Ki (μM)	
9PC	-9.04	-9.21	0.17	**H-bonding:** Asn-263_A (2.11Å), Val-207_A (2.19Å), Asn-208_A (2.74 Å), Gly-227_A (2.93 Å), Val-310_A(2.52 Å) **Π – σ bonding:** Thr-309_A (2.39Å), **Π-Alkyl:** Leu-200_A (4.16Å), Val-297_A(4.81 Å), Ile-311_A (5.44 Å, 5.16 Å)
HCur	-7.64	-7.60	2.69	**H-bonding:** Gly-205_A(2.73Å), Thr-265_A (2.61Å), Val-310_A (2.67Å), Leu-209_A (2.50 Å), Val-207_A (2.89 Å) **Π – σ bonding:** Thr-309_A (3.80Å), Leu-200_A (3.42 Å), **Π-Alkyl:** Ile-228_A (4.62 Å), Val-203_A (5.25 Å), Val-297_A (4.41 Å)
Mn(Cur)	-7.85	-7.81	3.58	**H-bonding:** Asn-299_A (2.91Å), Thr-309_A (2.82Å, 2.25 Å), Asn-37_A (2.13 Å) **Π-Alkyl:** Leu-200_A(4.76Å), Val-297_A(5.49 Å), Ala-202_A (3.60 Å), Val-307_A (5.12 Å)
Cu(Cur)	-8.21	-8.74	0.39	**H-bonding:** Leu-209_A (2.03Å), Ile-298_A (2.45 Å) **Π—sigma bonding:** Val-203_A (3.61Å) **Π-Alkyl:** Met-226_A (5.47Å), Ile-311_A (5.22 Å), Val-297_A (5.41Å)
Zn(Cur)	-9.15	-9.57	0.09	**H-bonding:** Gly-205_A (2.10Å), Leu-209_A (2.23Å), Gly-227_A (2.54Å), Asn-208_A (2.48 Å), Gly-193_A (2.18 Å), Gln-192_A (1.78 Å) **Π—sigma bonding:** Leu-200_A (3.46Å), Val-307_A (3.63Å,3.81 Å) **Π-Alkyl:** Val-203_A (5.24Å) Val-297_A (4.41 Å)

To predict receptor-ligand interactions and identify the most energetically favorable docked position for the *E. coli* FtsZ protein (PDB ID: 6UNX), 10 conformations were generated by making the co-ligand GTP, HCur, Mn(Cur), Cu(Cur) and Zn(Cur) flexible. The active site residue of 6UNX was also determined using the online tool Computer Atlas of Surface Topography of Proteins (CASTp).[45]

Docking results for *E. coli* (PDB ID: 6UNX) revealed that the co-crystallized ligand GTP, with inhibitory concentration 53.82 μM exhibited docking scores of -7.26 Kcal/mole in Autodockvina (version 1.2.5) and -7.67 Kcal/mole in Autodock 4.2.6. (Table 2, Fig. 9). 2D and 3D interaction diagrams (Fig. 9 C & D) showed that GTP forms six hydrogen bonds with amino acids Gly-21, Gly-107, Thr-108, Gly-109, and Arg-142 of chain A of 4DXD. Additional interaction modes are presented in Table 2. The hydrogen bonds formed between GTP and specific amino acids in chain A of 4DXD play a crucial role in stabilizing ligand-protein complex. Further analysis of additional interaction modes listed in Table 2 could provide insights into the overall binding mechanism and potential functional implications of this molecular interaction.



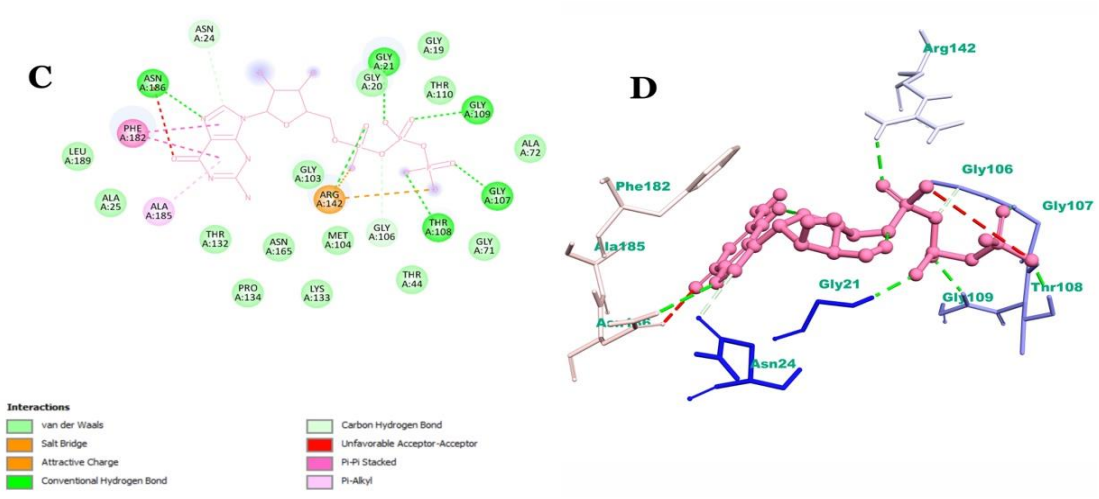


Figure 9: (A) Representation of docked GTP ligand into N-terminal subdomain in FtsZ protein of *E.coli* (PDB ID : 6UNX), (B) surface view of docked pose GTP at active sites of FtsZ protein model 6UNX. (C) 2D interactions and (D) 3D interactions of docked structure GTP ligand with 6UNX molel of FtsZ protein

Conversely, HCur forms five hydrogen bonds with FtsZ protein (PDB ID: 6UNX) involving Thr-108, Asn-165, Asn-186, Asn-24 and Gly-71 of chain A. The docking score was determined to be -7.68 Kcal/mol in Autodock vina v 1.2.5 and -7.49 Kcal/mol in AutoDock v 4.2.6 with an inhibition constant of 2.59 μM (Table 2). All hydrogen bond lengths between HCur and the amino acid residues were ≤ 3.00 Å. (Fig.10)

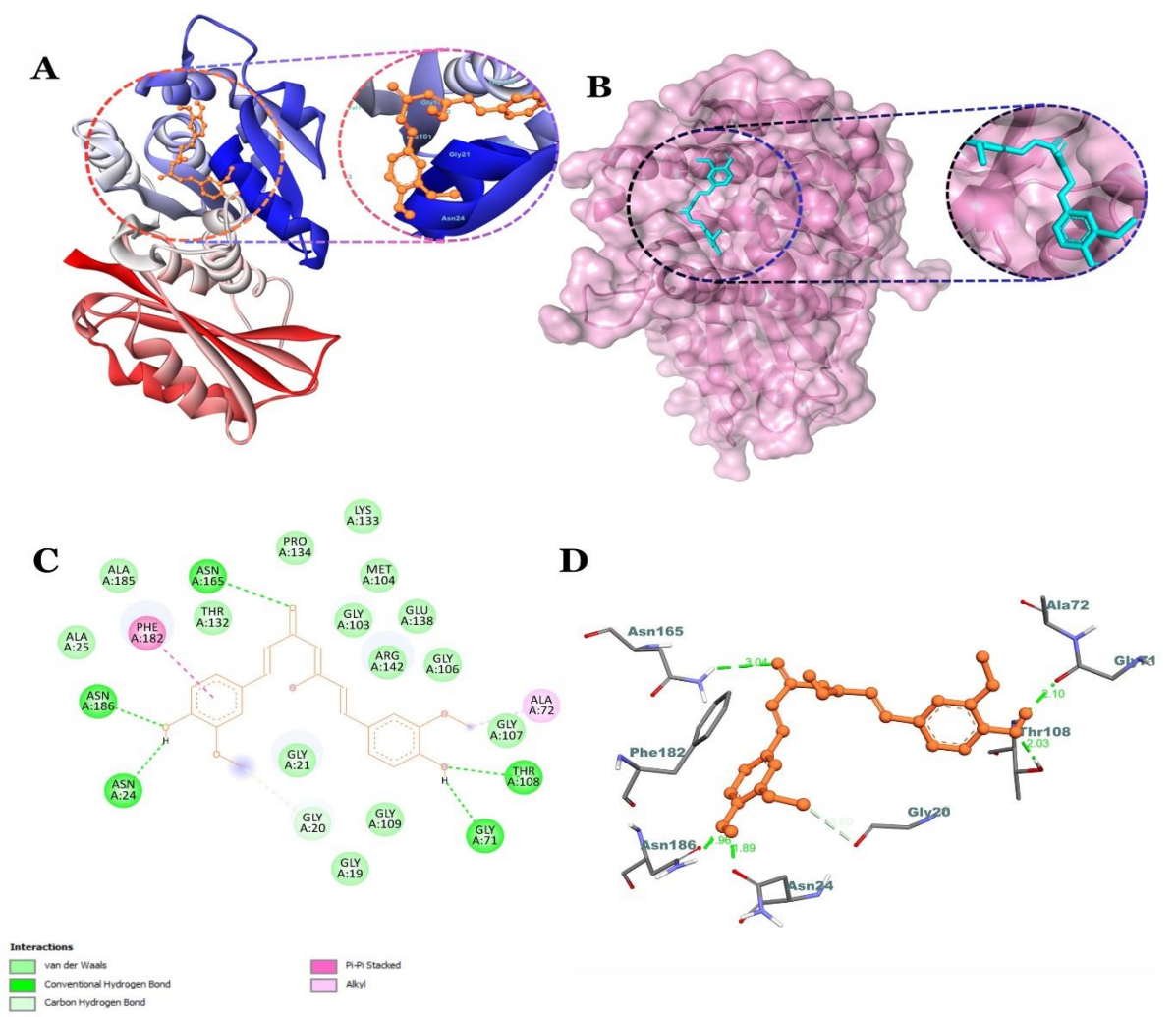


Figure 10: (A) Representation of docked pose of HCur into N-terminal subdomain in FtsZ protein of *E.coli* (PDB ID : 6UNX), (B) surface view of docked pose HCur at active sites of the FtsZ protein model 6UNX. (C) 2D interactions and (D) 3D interactions of docked structure of HCur with 6UNX molel of FtsZ protein

For Mn(Cur), docking scores were -8.41 Kcal/mole and -7.96 Kcal/mole using Autodockvina v 1.2.5 and Autodock v 4.2.6, respectively with inhibitory concentration 5.83 μM. Analysis of 2D and 3D interaction diagrams (Fig.11) revealed H-bond interactions involving Asn-24, Thr-108, and Leu-179 on chain A. The H-bond interactions with these specific residues suggest a strong binding affinity between the compound and target protein. Additionally, hydrophobic

interactions and van der Waals forces likely contribute to overall stability of ligand-protein complex.

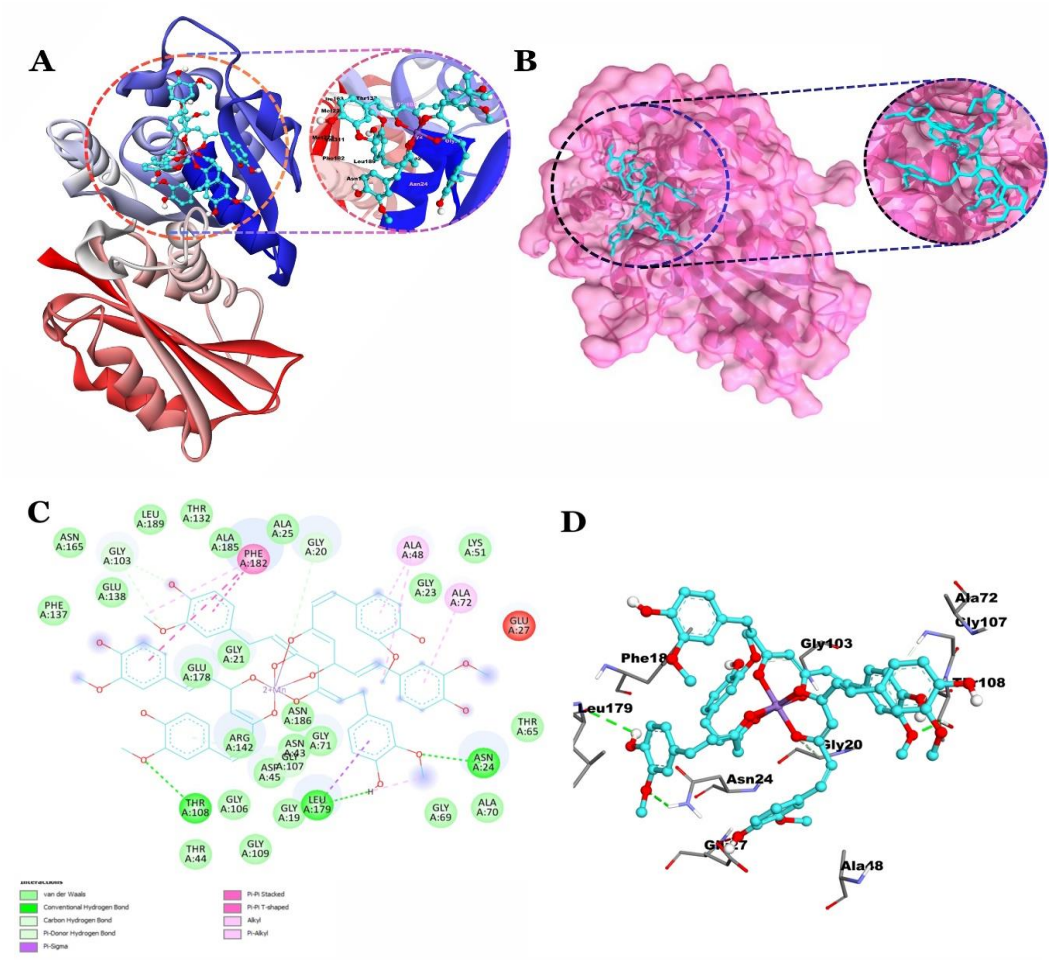


Figure 11: (A) Representation of docked pose of Mn(Cur) into N-terminal subdomain in FtsZ protein of *E.coli* (PDB ID : 6UNX), (B) surface view of docked pose HCur at active sites of FtsZ protein model 6UNX. (C) 2D interactions and (D) 3D interactions of docked structure Mn(Cur) with 6UNX model of FtsZ protein

Cu(Cur) exhibited docking scores of -7.85 Kcal/mole (Autodockvina v 1.2.5) and -7.59 Kcal/mole (Autodock v 4.2.6), with inhibitory concentration 2.72 μM. The corresponding interaction diagrams (Fig. 12) showed H-bonds were formed by Met-104, Gly-107, Thr-108, Gly-71 and Thr-132 on chain A.

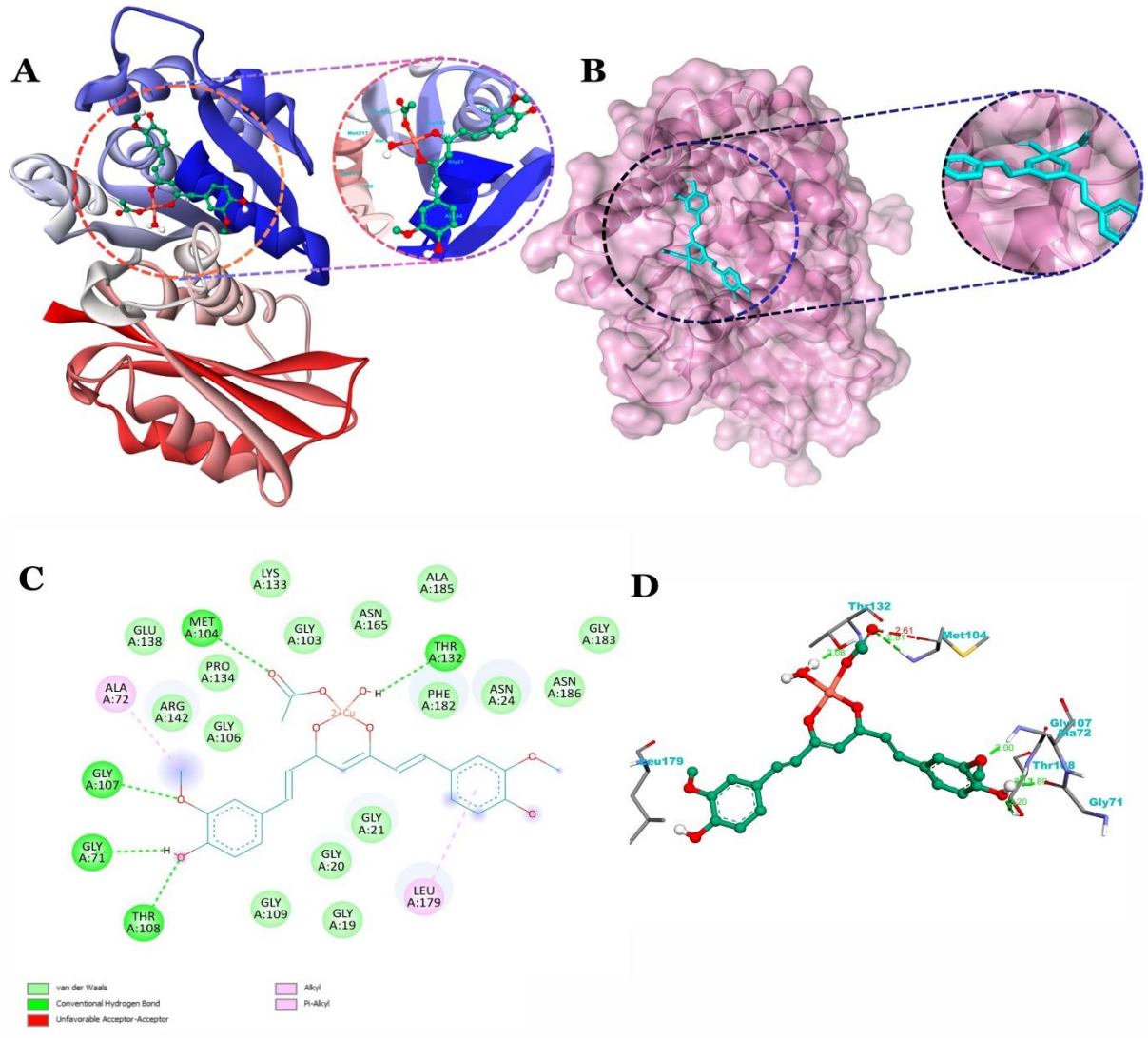


Figure 12: (A) Representation of docked pose of Cu(Cur) into N-terminal subdomain in FtsZ protein of *E.coli* (PDB ID : 6UNX), (B) surface view of docked pose HCur at active sites of FtsZ protein model 6UNX. (C) 2D interactions and (D) 3D interactions of docked structure Cu(Cur) with 6UNX molel of FtsZ protein

Docking scores for Zn(Cur), as determined by Autodockvina v 1.2.5 and Autodock v 4.2.6, were -7.75 Kcal/mole and -7.10 Kcal/mole respectively with inhibitory concentration 7.53 µM. Examination of 2D and 3D interaction diagrams (Fig. 13) helped in identification of H-bond formation involving amino acids Thr-108, Phe-135, Asn-165, Gly-71 and Gln-192 on chain A.

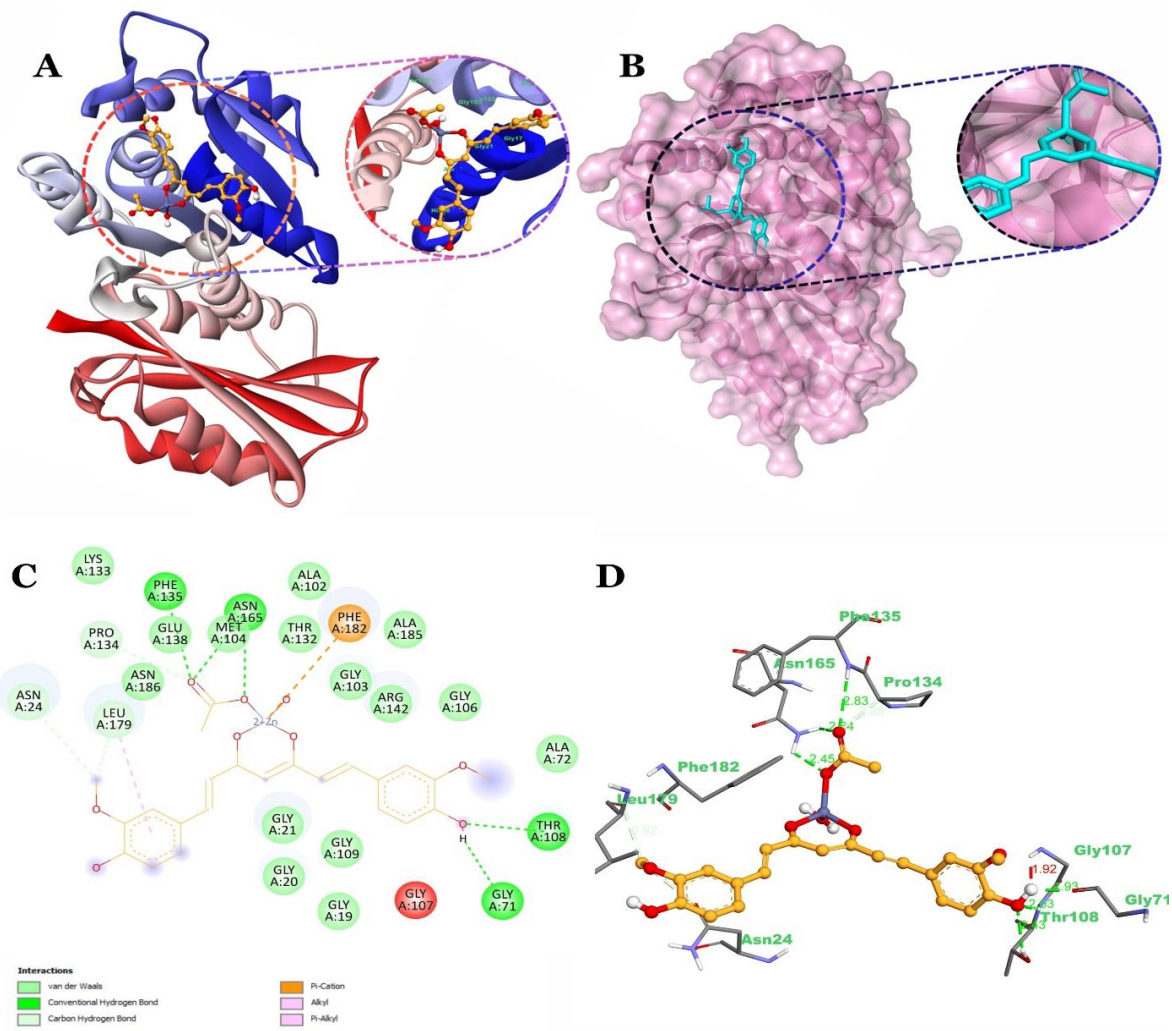


Figure 13: (A) Representation of docked pose of Zn(Cur) into N-terminal subdomain in FtsZ protein of *E.coli* (PDB ID : 6UNX), (B) surface view of docked pose HCur at active sites of FtsZ protein model 6UNX. (C) 2D interactions and (D) 3D interactions of docked structure Zn(Cur) with 6UNX molel of FtsZ protein

Table 2: Docking ligands, docking Score, interacting amino acids residues of *E.Coli* FtsZ protein (PDB ID: 6UNX)

Name of the ligands	Autodock Vina_1.2.5	Autodock 4.2.6		Active site Interacting amino acids residues and type of interactions (Å)
	Binding Affinity (Kcal/mol)	Binding Energy (Kcal/mol)	Inhibition Constant Ki (µM)	
GTP	-7.26	-7.67	53.82	**H-bonding:** Gly-21_A (2.14Å), Gly-107_A (1.90Å), Thr-108_A (1.92 Å, 2.40 Å), Gly-109_A (2.23 Å), Arg-142_A(2.25 Å) **Π – Π staked:** Phe-182_A (4.00 Å ,4.10Å), **Π-Alkyl:** Ala-185_A (5.042Å)
HCur	-7.68	-7.49	2.59	**H-bonding:** Thr-108_A(2.02Å), Asn-165_A (2.61Å), Asn-186_A (1.95Å), Asn-24_A (1.88 Å), Gly-71_A (2.10 Å) **Π – Π staked:** Phe-182_A (3.97Å) **Π-Alkyl:** Ala-72_A (3.74 Å)
Mn(Cur)	-8.41	-7.96	5.83	**H-bonding:** Asn-24_A (2.39Å), Thr-108_A (2.06Å), Leu-179_A (2.96 Å) **Π-Alkyl:** Phe-182_A(4.17Å), Ala-72_A(5.25 Å), Ala-48_A (4.05 Å).
Cu(Cur)	-7.85	-7.59	2.72	**H-bonding:** Met-104_A (2.80Å), Gly-107_A (1.99 Å), Thr-108_A (2.13Å, 2.20 Å), Gly-71_A (1.88 Å), Thr-132_A (2.08Å), **Π—sigma bonding:** Ala-72_A (4.28Å) **Π-Alkyl:** Leu-179_A (4.84Å)
Zn(Cur)	-7.75	-7.10	7.53	**H-bonding:** Thr-108_A (2.03Å, 2.42 Å), Phe-135_A (2.82Å), Asn-165_A (2.44Å, 2.64Å), Gly-71_A (1.92 Å), Gln-192_A (1.78 Å) **Π—sigma bonding:** Pro-134_A (2.84Å), Asn-24_A (3.31Å), Leu-179_A (2.92 Å) **Π-Alkyl:** Leu-179_A (4.99 Å)

12.3 Analysis of molecular dynamics trajectories examining FtsZ's interactions with Curcumin and its metal complexes

Trajectory analysis in molecular dynamics (MD) simulation is the process of extracting meaningful insights from time-resolved positions and velocities of particles in a simulated system. The trajectory file generated during MD run records atomic or molecular movements over time. Analyzing these trajectories allows one to study key properties like structural changes, conformational stability, molecular interactions and time-dependent behavior. Common trajectory analysis techniques include calculating root mean square deviation (RMSD) to assess structural stability, root mean square fluctuation (RMSF) to understand atomic flexibility, radius of gyration (ROG) for structural compactness and hydrogen bond analysis for interaction patterns.[46-50] These provide critical information about the system's dynamics, molecular interactions and overall behavior helping to uncover insights into biological processes, material properties and chemical phenomena at the atomic level.

12.3.1 Analysis of RMSD:

In this study, molecular dynamics (MD) simulations were conducted to evaluate the stability and inhibiting properties of the FtsZ protein bound to its coligand (9PC) and HCur. These were then compared with prepared metal complexes of HCur, such as Mn(Cur), Cu(Cur), and Zn(Cur), docked to the active site of the selected FtsZ protein models. Calculations were performed for two different protein models, *S. aureus* (PDB ID: 4DXD) and *E. Coli* (PDB ID: 6UNX), over 100 ns. The MD systems were prepared using an SPC water solvent model with appropriate charges and a 0.15 (M) NaCl electrolyte environment (Fig.14 and 15). (*Chapter 6, experimental*)

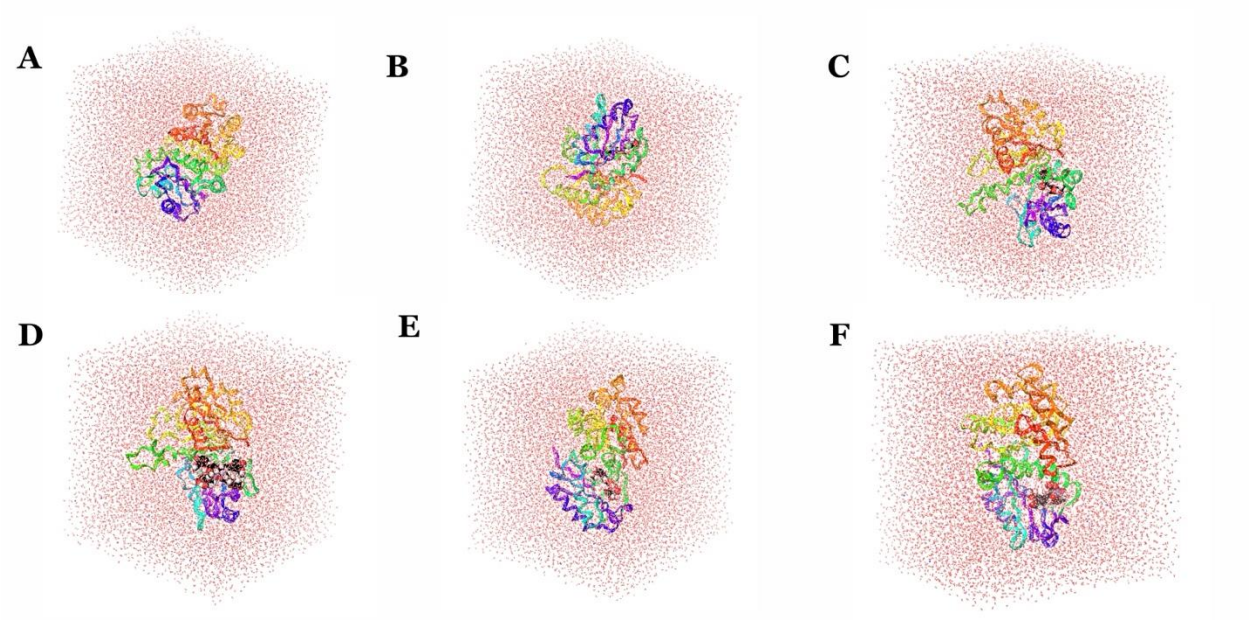


Figure 14 : (A) 4DXD protein model inside cubic boundary box and surrounded by SPC water model (B) 9PC docked 4DXD protein model inside cubic boundary box and surrounded by SPC water model, (C) HCur docked 4DXD protein model inside cubic boundary box and surrounded by SPC water model, (D) Mn(Cur) docked 4DXD protein model inside cubic boundary box and surrounded by SPC water model, (E) Cu(Cur) docked 4DXD protein model inside cubic boundary box and surrounded by SPC water model, (F) Zn(Cur) docked 4DXD protein model inside cubic boundary box and surrounded by SPC water model

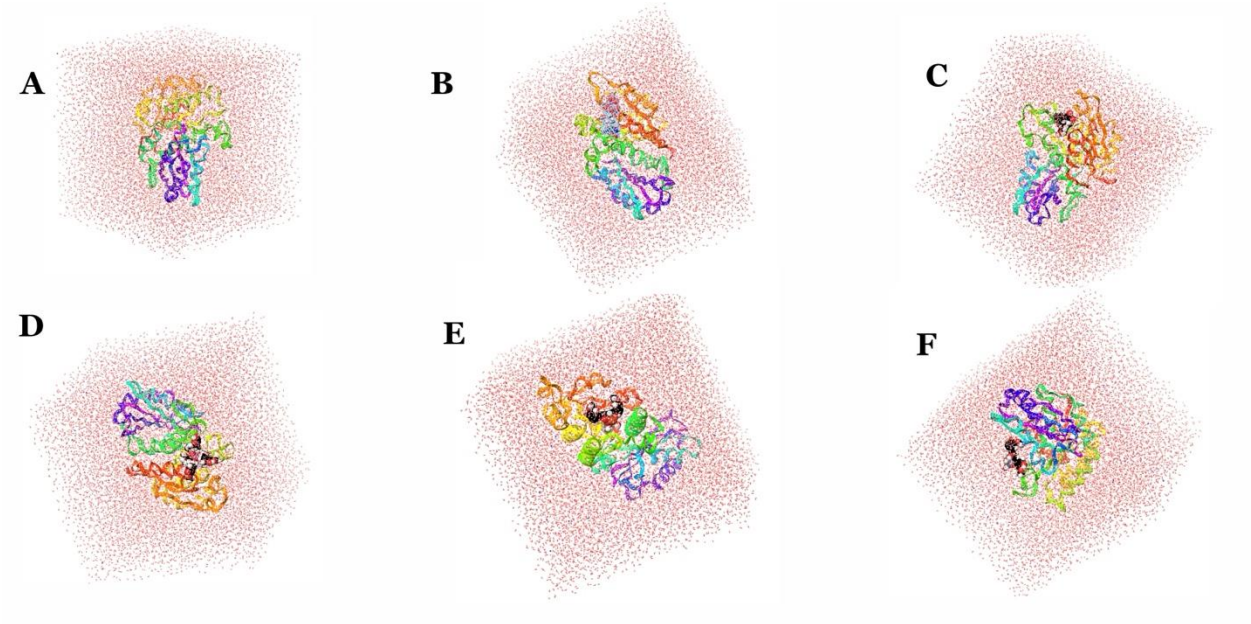


Figure 15 : (A) 6UNX protein model inside cubic boundary box and surrounded by SPC water model (B) GTP docked 6UNX protein model inside cubic boundary box and surrounded by SPC water model, (C) HCur docked 6UNX protein model inside cubic boundary box and surrounded by SPC water model, (D) Mn(Cur) docked 6UNX protein model inside cubic boundary box and surrounded by SPC water model, (E) Cu(Cur) docked 6UNX protein model inside cubic boundary box and surrounded by SPC water model, (F) Zn(Cur) docked 6UNX protein model inside cubic boundary box and surrounded by SPC water model

A reduction in RMSD of C-alpha backbone of *S. aureus* (PDB ID: 4DXD) and *E. coli* (PDB ID: 6UNX) protein models was observed when complexed with target molecules like HCur, Mn(Cur), Cu(Cur) and Zn(Cur), suggesting stable complexation in a biological environment. RMSD trends were compared over 100 ns simulations for 4DXD docked HCur and its metal complexes with standard docked inhibitor 9PC. All prepared metal complexes of HCur and co-crystallized inhibitor 9PC docked to FtsZ protein of *S. aureus* (4DXD) demonstrated stable conformations. Although initial RMSD values were higher for 4DXD-Cu(Cur) than for 4DXD alone, the interaction trends changed over time. RMSD decreased after 40 ns of simulation time

indicating that Cu(Cur) required time to adjust as evidenced by the observed fluctuations in C-alpha backbone of 4DXD (Fig. 16A). Conversely, 9PC, HCur, Mn(Cur) and Zn(Cur) exhibited steady binding, reflected by their RMSD values. The average RMSD of apo-4DXD was 3.58 ± 0.72 Å, while for 4DXD attached to 9PC and HCur, values were 3.03 ± 0.28 Å and 2.98 ± 0.32 Å respectively. When 4DXD was complexed with Mn(Cur), Cu(Cur) and Zn(Cur) the RMSD values became 3.07 ± 0.42 Å, 3.41 ± 0.46 Å, and 2.89 ± 0.22 Å, respectively. Unbound 4DXD with a higher RMSD undergoes more significant conformational changes in chain A. Reduction in RMSD when HCur and Zn(Cur) were bound to 4DXD indicated formation of stable adducts that could withstand further conformational changes. A lower RMSD of Zn(Cur) with 4DXD suggests that this complex was more stable than other congeners.(Fig. 16A)

In case of the *E.Coli* representative FtsZ protein model (PDB ID :6UNX), average RMSD was found to be 2.64 ± 0.23 Å (Fig. 16B). When this model docked with its coligand GTP then its average RMSD becomes 2.38 ± 0.21 Å. In contrast, for HCur, the average RMSD of the 4DXD model was 2.24 ± 0.19 Å. For Mn (Cur), Cu(Cur) and Zn(Cur) average RMSD becomes 2.14 ± 0.24 Å, 2.10 ± 0.16 Å, 1.90 ± 0.21 Å respectively. RMSD values suggest that metal-Curcumin complexes generally demonstrate reduced structural deviations in comparison to unbound Curcumin. Among the metal complexes analyzed, Zn(Cur) exhibited the lowest average RMSD, indicating the possibility of a more stable structure or a closer alignment with the reference model. The observed variations in RMSD values across different metal-Curcumin complexes may be attributed to specific interactions between metal ions and Curcumin, potentially influencing the overall molecular conformation. Lower RMSD values observed with Zn(Cur) suggest a tighter binding and potentially more significant conformational stability of the

complex. This could imply a stronger inhibitory effect on the FtsZ protein highlighting the importance of the choice of the metal ion in designing Curcumin-based inhibitors.

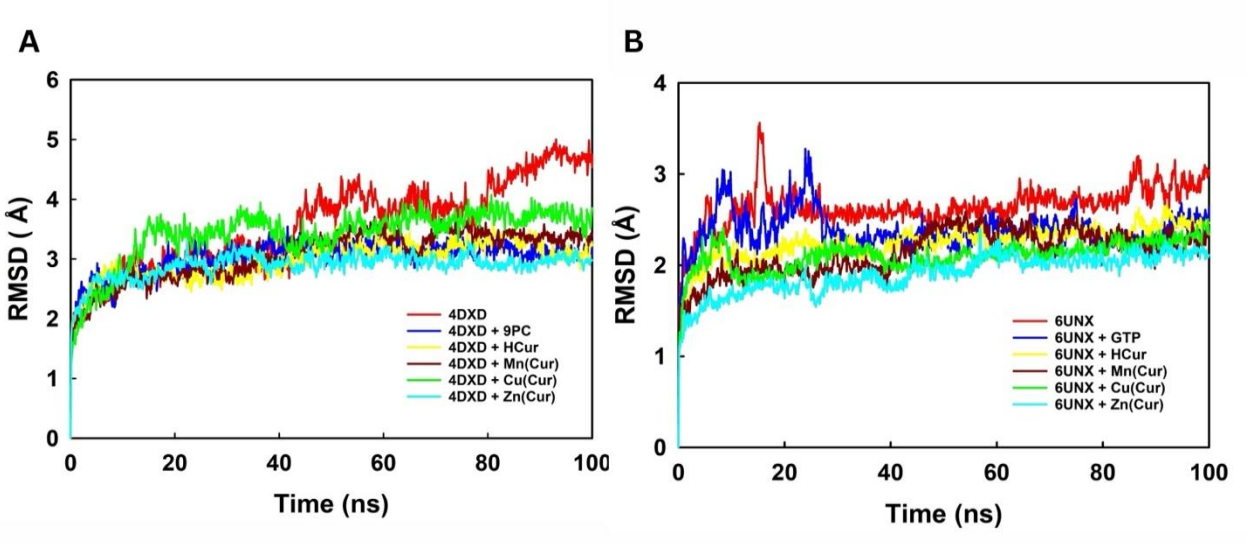


Figure 16: (A) RMSD values of C-alpha backbone of 4DXD protein model and with docked 9PC, HCur, Mn(Cur), Cu(Cur) and Zn(Cur) (B) RMSD values of C-alpha backbone of 6UNX protein model and with docked GTP, HCur, Mn(Cur), Cu(Cur) and Zn(Cur)

12.3.2 Analysis of RMSF:

RMSF of the apo FtsZ protein model of *S. aureus* (PDB ID: 4DXD) was 1.80 Å ± 0.41 and when it was complexed with 9PC the value became 1.27 Å ± 0.13. HCur had a value 1.39 Å ± 0.69. When metal complexes of HCur were used average RMSF drastically decreased to values 1.44 Å ± 0.61 for Mn(Cur), 1.58 Å ± 0.80 for Cu(Cur) and 1.41 Å ± 0.57 for Zn(Cur). This decrease in average RMSF for metal complexes of HCur suggests a potential stabilizing effect on the 4DXD protein structure. (Fig. 17 A) Conversely, RMSF of the *E.Coli* representative apo FtsZ protein model (PDB ID: 6UNX) measured 1.25 Å ±0.66 which decreases to 1.12 Å ± 0.71 when bound to its co-crystallized ligand, GTP. HCur, exhibited RMSF of 0.85 Å ± 0.44. Notably, the introduction of metal-Curcumin complexes led to a significant reduction in average RMSF

values to 0.72 Å ± 0.42 for Mn(Cur), 0.81 Å ± 0.37 for Cu(Cur) and 0.76 Å ± 0.46 for Zn(Cur) (Fig.17 B). This substantial decrease in average RMSF for metal-Curcumin complexes indicates a significant stabilizing effect on the *E. coli* representative protein structure (PDB: 6UNX). Such stabilization may result from the formation of more robust or numerous interactions between the metal-Curcumin complexes and the protein. The varying RMSF values for different metal complexes (Mn, Cu, and Zn) indicate that the choice of metal ion influences the extent of protein stabilization, possibly because of differences in coordination geometry or binding affinity.

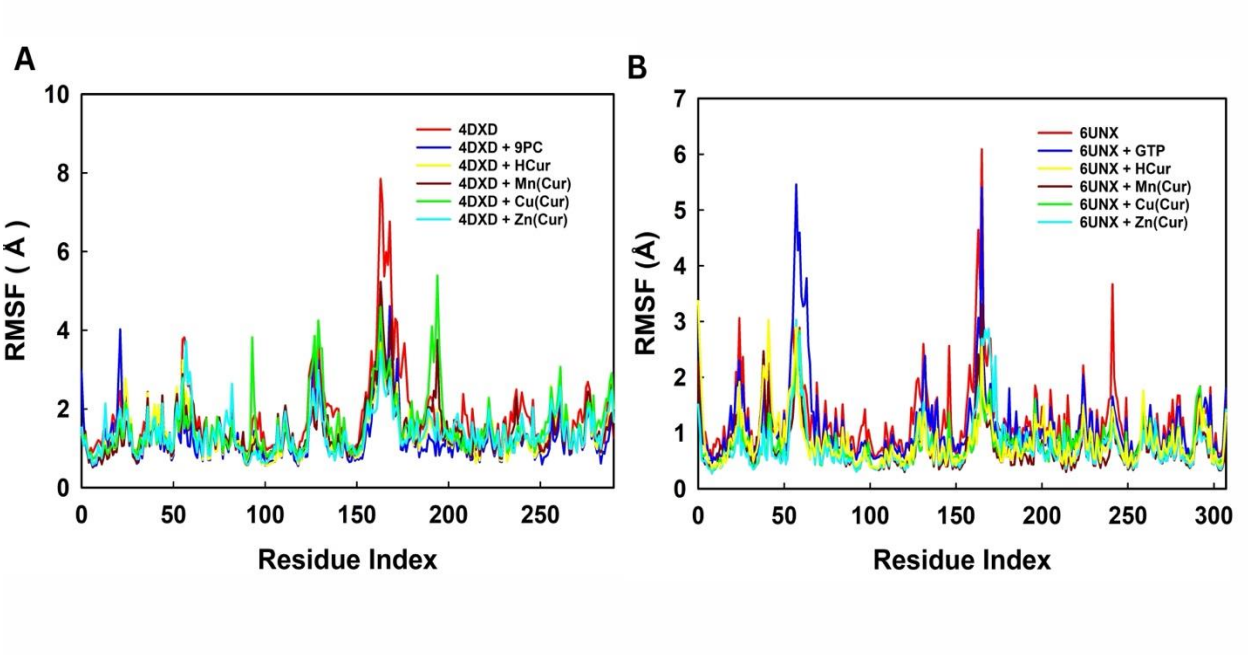


Figure 17: (A) RMSF plots of 4DXD protein model and docked 9PC, HCur, Mn(Cur), Cu(Cur) and Zn(Cur), (B) RMSF plots of 6UNX protein model and docked GTP, HCur, Mn(Cur), Cu(Cur) and Zn(Cur).

12.3.3 Analysis of Radius of gyration (Rg):

In this study, Rg variation was observed for FtsZ protein models of *S. aureus* and *E. coli* with the docked co-crystallized inhibitor ligand 9PC for *S. aureus* (PDB ID: 4DXD) and GTP for *E. coli* (PDB ID: 6UNX). In addition, inhibition effect was compared with that of HCur and the prepared metal complexes of HCur i. e. Mn(Cur), Cu(Cur) and Zn(Cur).

For the 4DXD model, average Rg of the apo protein was 19.83 Å ± 0.16. It was reduced when it formed a complex with the co-crystallized ligand 9PC to a value 19.54 Å ± 0.08. For HCur this was 19.56 Å ± 0.11 while for Mn(Cur) it was 19.55 Å ± 0.16. For Cu(Cur) the values was 19.44 Å ± 0.18 and for Zn(Cur) it was 19.46 Å ± 0.17 . This observed reduction in the average radius of gyration (Rg) upon ligand binding suggests that the protein undergoes a conformational change becoming more compact in the presence of various ligands. This trend was consistent for all tested complexes, with Cu(Cur) showing the most significant decrease in Rg compared to the apo protein. A similarity in Rg values for metal-HCur complexes indicate they may induce comparable structural changes in the protein (Fig. 18A).

The 6UNX model exhibited an average Rg of 19.50 Å ± 0.09 for the apo protein. This decreased to 19.15 Å ± 0.13 when the protein formed a complex with co-crystallized GTP ligand. Rg values for various compounds were as follows: HCur: 19.08 Å ± 0.12, Mn(Cur): 18.92 Å ± 0.12, Cu(Cur): 19.25 Å ± 0.11 and Zn(Cur): 19.11 Å ± 0.13 (Fig. 18B). This reduction in Rg values suggests that the protein undergoes conformational changes upon binding to a ligand, with metal-HCur complexes having varying effects on protein compactness. Amongst metal-Curcumin complexes, Mn(Cur) appeared to induce the most significant reduction in Rg, indicating a tighter protein conformation during its interaction. These findings imply different

metal-HCur complexes may interact with the protein in distinct ways possibly influencing its structural stability and function.

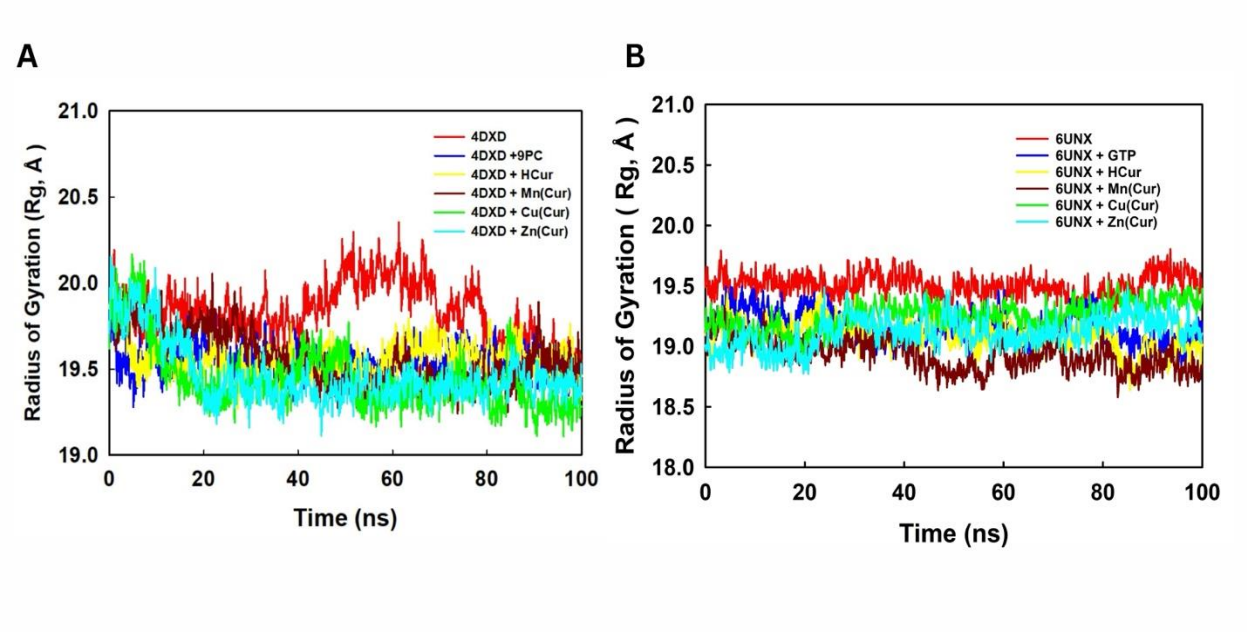


Figure 18: (A) Radius of gyration plot of 4DXD protein model and with docked 9PC, HCur, Mn(Cur), Cu(Cur) and Zn(Cur), (B) Radius of gyration plot of 6UNX protein model and with docked GTP, HCur, Mn(Cur), Cu(Cur) and Zn(Cur)

12.3.4 Analysis of Solvent accessible surface area (SASA):

SASA was evaluated for protein models of *S. aureus* and *E. coli*, i.e. PDB IDs: 4DXD and 6UNX respectively in bound state with their respective co-crystallized ligands, the HCur and its metal complexes over a 100 ns simulation period. The unbound 4DXD model exhibited an average SASA value of 1159.91 $Å^2$ ± 0.96. When bound to 9PC, the value decreased to 171.96 $Å^2$ ± 0.29. The average SASA for HCur was 175.55 $Å^2$ ± 0.89, whereas for Mn(Cur), Cu(Cur) and Zn(Cur) values were 494.24 $Å^2$ ± 0.54, 337.31 $Å^2$ ± 0.46 and 344.65 $Å^2$ ± 0.78 respectively (Fig. 19A). The observed variations in SASA values across different ligand-bound states suggest that metal complexes of HCur may interact differently with *S.aureus* protein (PDB: 4DXD) than

HCur. These differences in SASA could indicate changes in protein conformation or accessibility upon binding of different ligands. The significantly lower SASA value for all selected ligands bound 4DXD compared to the unbound form suggests a substantial conformational change or a tighter binding interaction for that particular ligand.

The unbound-6UNX model exhibited an average SASA of 948.43 $Å^2$ ± 0.45. When complexed with GTP, the 6UNX model showed an average SASA of 299.22 $Å^2$ ± 0.92. The average SASA values for 6UNX complexed with HCur, Mn(Cur), Cu(Cur) and Zn(Cur) were 330.03 $Å^2$ ± 0.21, 411.55 $Å^2$ ± 0.17, 238.64 $Å^2$ ± 0.72 and 348.26 $Å^2$ ± 0.94 respectively (Fig 19B). SASA measurements offer valuable information on how the conformation of a protein changes when it binds to various ligands. A notable reduction in SASA for different ligands in the bound state of 6UNX model indicated a more condensed structure compared to the unbound form. Notably, complexes formed with metal-Curcumin compounds exhibit diverse levels of surface accessibility, which may suggest different binding mechanisms or structural modifications.

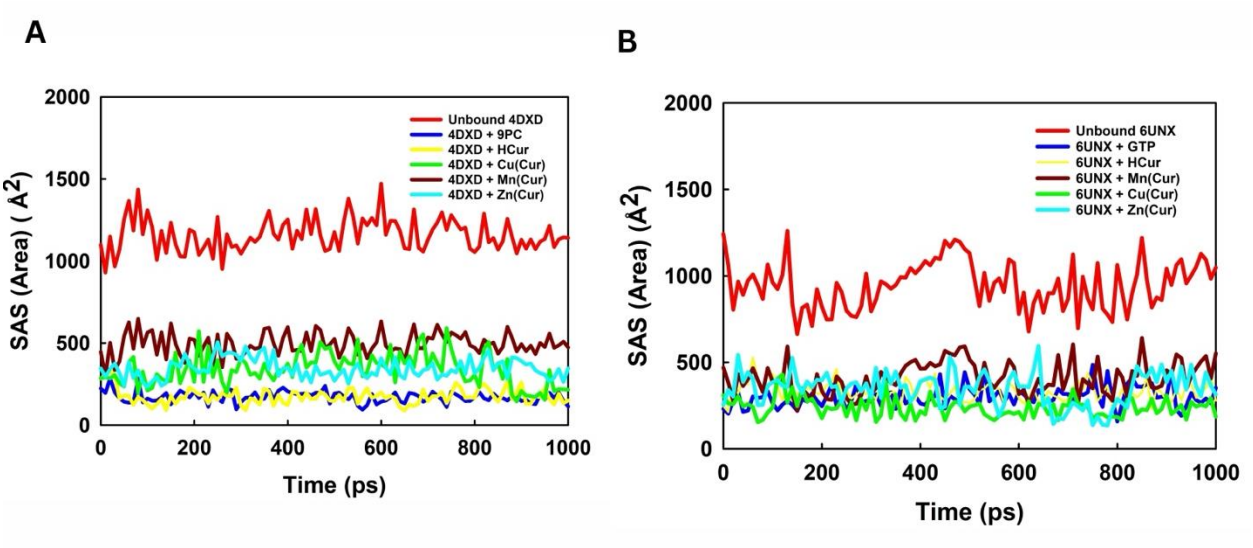


Figure 19: (A) SASA plot of unbound 4DXD protein model and with docked 9PC, HCur, Mn(Cur), Cu(Cur) and Zn(Cur), (B) SASA plot of unbound 6UNX protein model and with docked GTP, HCur, Mn(Cur), Cu(Cur) and Zn(Cur)

12.3.5 Analysis of Hydrogen bond during MD simulation:

The study examined hydrogen bond interactions during a 100 ns simulation of FtsZ proteins from *S. aureus* (PDB ID: 4DXD) and *E. coli* (PDB ID: 6UNX), along with their respective co-crystallized ligands (9PC for 4DXD and GTP for 6UNX), as well as HCur, Mn(Cur), Cu(Cur), and Zn(Cur) at the active sites. The geometric criteria considered for all hydrogen bonds were a hydrogen donor-acceptor distance of less than 3.5 Å and an angle of less than 3^0. Results showed that in the 4DXD protein model, the average number of hydrogen bonds formed was 3.23 ± 0.63 for 9PC, 2.85 ± 0.76 for HCur , 2.41 ± 0.91 for Mn(Cur), 0.81 ± 0.55 Cu(Cur), and 3.54 ± 0.81 for Zn(Cur) (Fig 20 A). Conversely, in the 6UNX protein model, the average number of hydrogen bonds formed were 5.03 ± 0.91 for GTP, 3.04 ± 0.55 for HCur, 2.19 ± 0.96 for Mn(Cur), 4.39 ± 0.62 for Cu(Cur), and 3.95 ± 0.66 for Zn(Cur) (Fig. 20 B)

These results suggested that the hydrogen bonding patterns differed between the two protein models. The HCur ligand appears to form more hydrogen bonds in the first model than in the 6UNX model, whereas GTP showed a relatively high number of hydrogen bonds in the 6UNX model. The metal-HCur complexes (Mn, Cu, and Zn) also exhibited varying hydrogen bonding behaviors between the two models, potentially indicating differences in their interactions with the protein structures.

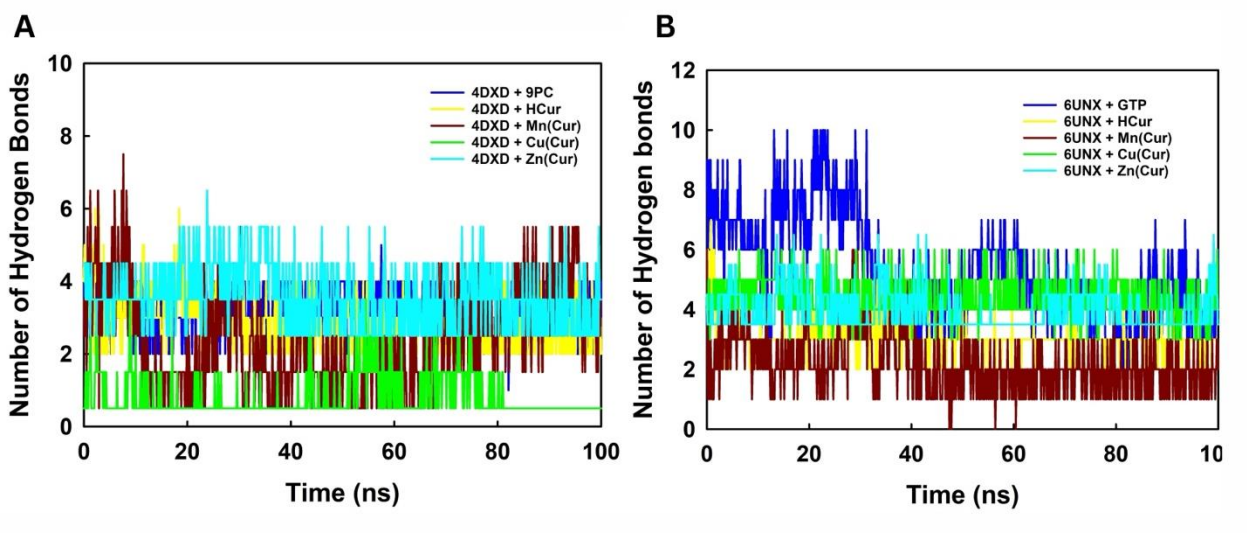


Figure 20: (A) H-Bond plot of 4DXD protein model docked with 9PC, HCur, Mn(Cur), Cu(Cur) and Zn(Cur), (B) H-Bond plot of 6UNX protein docked with GTP, HCur, Mn(Cur), Cu(Cur) and Zn(Cur)

12.3.6 Calculations of Molecular Mechanics Generalized Born Surface Area (MM-GBSA)

The MM-GBSA method[51,52] was employed to assess the binding energies of various ligands (HCur, Mn(Cur), Cu(Cur), and Zn(Cur)) at the binding sites of *S. aureus* and *E. coli* protein models (4DXD and 6UNX). This evaluation utilized the final 10 ns of molecular dynamics simulation trajectories, which spanned a total of 100 ns (Table 3).

The binding energy of the 9PC molecule with 4DXD model of *S. aureus* protein is -75.95 Kcal/mol ± 2.28, which is less than that of HCur when it binds to the same site on 4DXD. HCur exhibited a binding energy of -85.73 Kcal/mol ± 5.13. This difference might be attributed to the larger RMSD of 9PC than that of HCur. In contrast, the binding energies of Mn(Cur), Cu(Cur), and Zn(Cur) are -70.23 Kcal/mol ± 5.17, -65.21 Kcal/mol ± 3.02, and -95.89 Kcal/mol ± 3.43, respectively. These values indicate that Zn(Cur) formed the strongest interaction with the target molecule, followed by HCur, Mn(Cur), and Cu(Cur). The variations in binding energies among these complexes may be explained by differences in their molecular structures and the specific interactions they establish with the binding site.

The binding energy of the GTP molecule with 6UNX model of *E. coli* protein (-42.52 Kcal/mol ± 8.57) was lower than that of HCur (-49.26 Kcal/mol ± 1.26) when binding to the same active site. This disparity may be due to slightly larger RMSD of GTP than HCur. In comparison, the metal-Curcumin complexes Mn(Cur), Cu(Cur) and Zn(Cur) demonstrated binding energies of -58.62 Kcal/mol ± 8.23, -55.28 Kcal/mol ± 3.61 and 69.19 Kcal/mol ± 3.37, respectively. These higher binding energies indicate stronger interactions between HCur complexes and the target protein than with HCur alone. Such enhanced binding affinity could potentially improve the therapeutic effectiveness of HCur when combined with these metal ions. The observed differences in binding energies among the various metal-Curcumin complexes suggest that the selected metal ions significantly affect the overall binding properties of the Curcumin-based compounds. Additional research into the structural and electronic characteristics of these metal-Curcumin complexes may offer valuable insights for optimizing their design, leading to enhanced protein binding and improved pharmacological results.

The findings presented in Table 3 indicate that the primary contributors to $\Delta G_{binding}$ for the stability of the simulated complexes were ΔG_{bind}-Coulomb, ΔG_{bind}-van der Waals, and ΔG_{bind}-lipophilic. Conversely, ΔG_{bind}-covalent and ΔG_{bind}-solvationGB promoted instability in these complexes. These results suggest that electrostatic interactions, van der Waals forces, and hydrophobic effects play crucial roles in stabilizing protein-ligand complexes. The destabilizing effects of covalent bonding and solvation energies highlight the complex' interplay of the forces governing molecular interactions in these systems.

Table 3. Binding free energy components for the apo 4DXD and docked 9PC, HCur, Mn(Cur), Cu(Cur), along with apo 6UNX and docked with 9PC, HCur, Mn(Cur), Cu(Cur) complexes calculated by MM-GBSA.

Compound code	MM-GBSA (kcal/mol)					
	ΔG_{bind}	**ΔG_{bind}Lipo**	**ΔG_{bind}vdW**	**ΔG_{bind}Coulomb**	**ΔG_{bind}SolvGB**	**ΔG_{bind}Covalent**
4DXD-9PC	-75.95 ± 2.28	-18.15± 0.41	-56.09 ± 1.32	-14.94 ± 1.34	14.10 ± 0.88	3.58 ± 0.47
4DXD-HCur	-85.73 ± 5.13	-27.30 ± 1.50	-62.10 ± 2.84	-6.73 ± 2.02	22.03 ± 1.80	3.75 ± 1.60
4DXD-Mn(Cur)	-70.23± 5.17	-22.63 ± 5.17	-62.12 ± 7.55	-29.46 ± 2.50	92.65± 3.96	9.40 ± 6.32
4DXD-Cu(Cur)	-65.21± 3.02	-17.90 ± 2.86	-42.12 ± 6.89	-23.21 ± 4.75	20.49 ± 9.88	0.22 ± 0.70
4DXD-Zn(Cur)	-95.89 ± 3.43	-16.99 ± 0.59	-52.55 ± 2.87	-15.99 ± 2.21	43.32 ±9.63	2.19 ± 0.64
6UNX-GTP	-42.52 ± 8.57	-5.80 ± 0.57	-35.97 ± 5.54	-55.08 ± 42.66	58.92 ± 34.62	1.77 ± 1.86
6UNX-HCur	-49.26 ± 1.26	-15.09 ± 1.32	-44.25 ± 2.74	-6.99 ± 3.09	17.54 ± 2.27	1.23 ± 2.46
6UNX-Mn(Cur)	-58.62 ± 8.23	-22.03 ± 4.26	-68.06 ± 6.52	-196.98± 46.40	236.54 ± 49.39	5.10 ± 3.86
6UNX-Cu(Cur)	-55.28± 3.61	-13.24 ± 0.71	-47.49 ± 3.18	-128.27 ± 13.59	181.43 ± 9.99	3.71 ± 0.99
6UNX-Zn(Cur)	-69.19 ± 3.37	-9.10 ± 1.60	-31.10 ± 4.19	-80.35 ± 14.56	97.84 ± 16.08	4.36 ± 3.11

(G_{bind}) total free energy of binding; (G_{bind}Lipo) lipophilic energy; (G_{bind}vdW) van der Waals interaction energy; (G_{bind}Coulomb) prime coulomb energy; (G_{bind}SolvGB) solvation energy generalized born; (G_{bind}Covalent) covalent binding energy

12.3.7 Trajectory snapshots analysis during MD simulation:

In molecular dynamics (MD) simulations, analyzing secondary structures plays a vital role, as it offers insights into the local configuration and behavior of biomolecules, particularly proteins. This analysis involves identifying specific local structural elements, such as alpha helices, beta sheets, and turns within the biomolecule. By examining the content and variations in secondary structures, researchers can forecast the conformational dynamics of biomolecules, which may influence their functionality and interactions with other biomolecules.[53]

A comprehensive investigation was conducted to examine the changes in the secondary structures of *S.aureus* (PDB ID : 4DXD) and *E.coli* (PDB ID : 6UNX) proteins during a 100 ns MD simulation. By visual inspection of trajectories revealed that the protein in all dynamic systems maintained its overall secondary structure, showing minimal deviation from its initial state (Fig 21 and 22). Furthermore, all ligands remained attached to the binding site throughout the simulation period, with a very small deviation that reflected in the RMSD values. These observations suggest that the ligand-protein complexes exhibit stability and maintain their structural integrity throughout the simulation. The consistency in the secondary structure and persistent binding of ligands indicate that the interactions between the proteins and their respective ligands are robust and potentially biologically relevant.

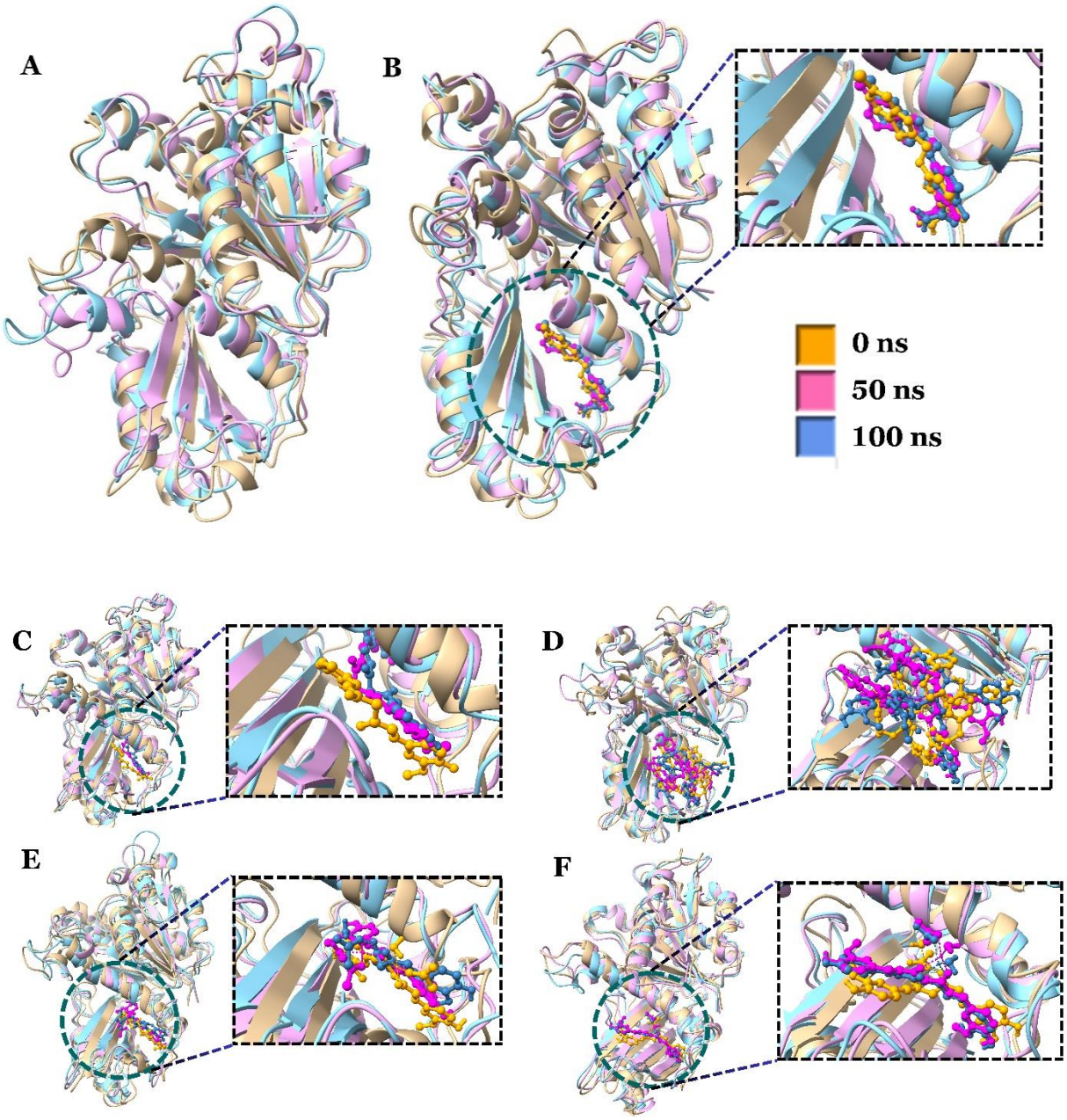


Figure 21 : Secondary structural analysis of 4DXD (with/without ligand). (A) Apo, (B) 9PC, (C) HCur, (D) Mn(Cur), (E) Cu(Cur) (F) Zn(Cur). The snapshots (3D) were taken from the 100 ns M.D. trajectory of each biomolecular system with an interval of 100 ns (0 ns: Gold, 100 ns: Cyan, and 200 ns: Pink)

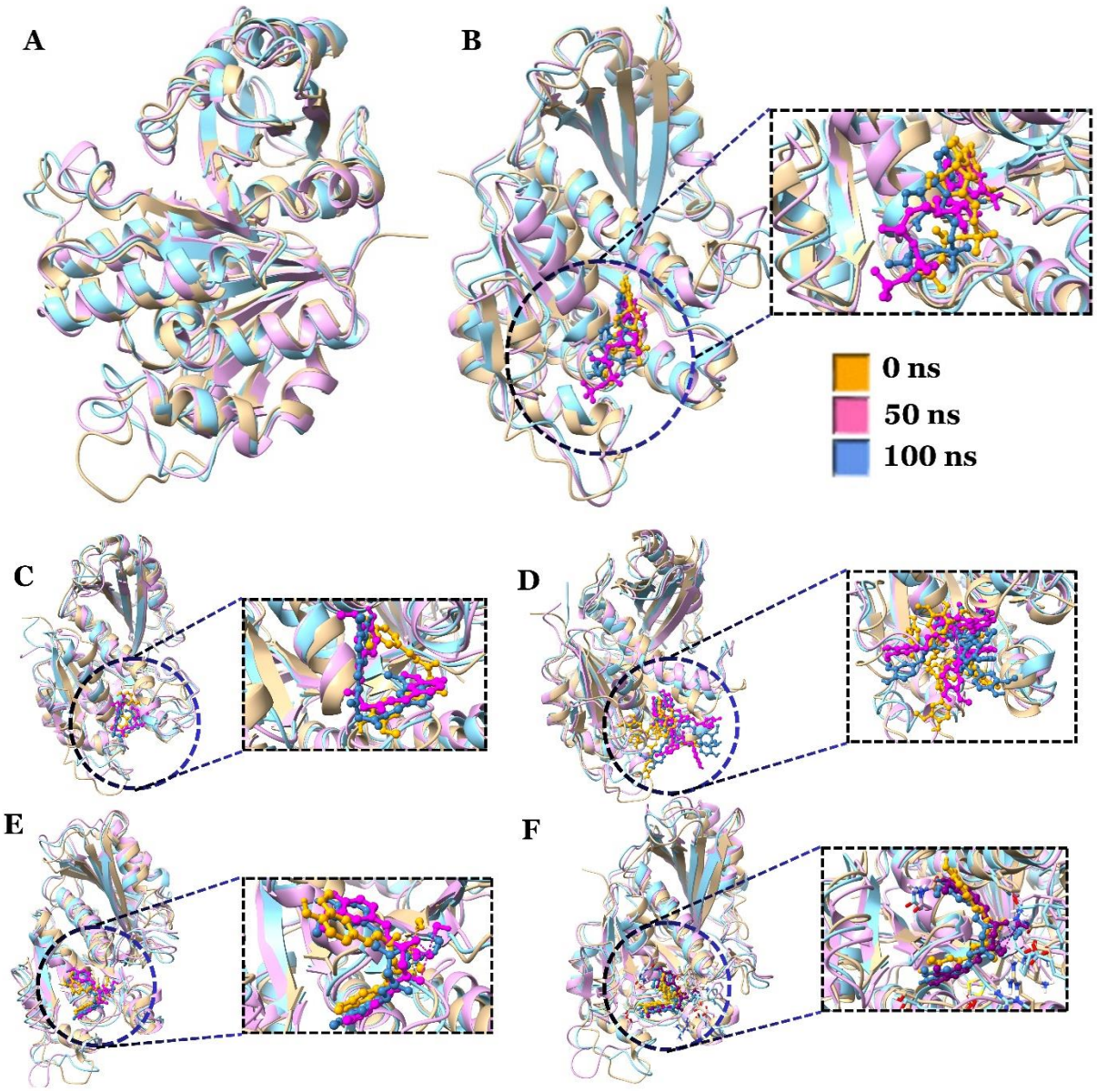


Figure 22: Secondary structural analysis of 6UNX (with/without ligand). (A) Apo, (B) GTP, (C) HCur, (D) Mn(Cur), (E) Cu(Cur) (F) Zn(Cur). The snapshots (3D) were taken from the 100 ns M.D. trajectory of each biomolecular system with an interval of 100 ns (0 ns: Gold, 100 ns: Cyan, and 200 ns: Pink)

References

1. C.A. Nadgir, D.A. Biswas; Antibiotic resistance and its impact on disease management. *Cureus*, **2023**, 15, 4.
2. A. MacGowan, and E. Macnaughton; Antibiotic resistance. *Medicine*, **2017**, 45, 622-628.
3. A. Kapil; The challenge of antibiotic resistance: need to contemplate. *Indian Journal of Medical Research*, **2005**, 121, 83.
4. N. Rosenblatt-Farrell; The landscape of antibiotic resistance. **2009**.
5. J. Tanwar, S. Das, Z. Fatima, S. Hameed; Multidrug resistance: an emerging crisis. *Interdisciplinary perspectives on infectious diseases*, **2014**, 1, 541340.
6. E. Medina, D.H. Pieper; Tackling threats and future problems of multidrug-resistant bacteria. *How to overcome the antibiotic crisis: facts, challenges, technologies and future perspectives*, **2016**, 3-33.
7. K.M. O'Connell, J.T. Hodgkinson, H.F. Sore, M. Welch, G.P. Salmond, D.R. Spring; Combating multidrug-resistant bacteria: current strategies for the discovery of novel antibacterials. *Angewandte Chemie International Edition*, **2013**. 52, 10706-10733.
8. P.E.T.E.R. Gilbert, P.J. Collier, M.R. Brown; Influence of growth rate on susceptibility to antimicrobial agents: biofilms, cell cycle, dormancy, and stringent response. *Antimicrobial agents and chemotherapy*, **1990**. 34, 1865-1868.
9. K.A. Hurley, T.M. Santos, G.M. Nepomuceno, V. Huynh, J.T. Shaw , D.B. Weibel, Targeting the bacterial division protein FtsZ. *Journal of medicinal chemistry*, **2016**, 59, 6975-6998.
10. J. Löwe, and L.A. Amos; Crystal structure of the bacterial cell-division protein FtsZ. *Nature*, **1998**. 391, 203-206.
11. X. Wang, J. Lutkenhaus; The FtsZ protein of Bacillus subtilis is localized at the division site and has GTPase activity that is dependent upon FtsZ concentration. *Molecular microbiology*, **1993**, 9, 435-442.

12. D. Bramhill , C.M. Thompson; GTP-dependent polymerization of Escherichia coli FtsZ protein to form tubules. *Proceedings of the National Academy of Sciences*, **1994**, , 91, 5813-5817.

13. P. De Boer, R. Crossley, and L. Rothfield; The essential bacterial cell-division protein FtsZ is a GTPase. *Nature*, **1992**, 359, 254-256.

14. N.L. Elsen, J. Lu, G. Parthasarathy, J.C. Reid, S. Sharma, S.M. Soisson, K.J. Lumb; Mechanism of action of the cell-division inhibitor PC190723: modulation of FtsZ assembly cooperativity. *Journal of the American Chemical Society*, **2012**, 134, 12342-12345.

15. K.I. Ramachandran, G. Deepa, K. Namboori, *Computational chemistry and molecular modeling: principles and applications*. Springer Science & Business Media. **2008**.

16. C.N. Cavasotto, M.G. Aucar, N.S. Adler; Computational chemistry in drug lead discovery and design. *International Journal of Quantum Chemistry*, **2019**, 119, 25678.

17. S. Ballu, R. Itteboina, S.K. Sivan, V. Manga; Structural insights of Staphylococcus aureus FtsZ inhibitors through molecular docking, 3D-QSAR and molecular dynamics simulations. *Journal of Receptors and Signal Transduction*, **2018**, 38, 61-70.

18. G.P.V. Sangeeta, K.P. Nagasree, J.R. Namratha, M.M.K. Kumar; Synthesis, screening and docking analysis of novel benzimidazolium compounds as potent anti microbial agents targeting FtsZ protein. *Microbial pathogenesis*, **2018,** 124, 258-265.

19. R.C. Mishra, R. Kumari, S. Yadav, and J.P. Yadav; Target based virtual screening of new leads inhibitor against bacterial cell division protein FtsZ for the discovery of antibacterial agents. *Medicinal Chemistry*, **2020,** 16,169-175.

20. P. Domadia, S. Swarup, A. Bhunia, J. Sivaraman, D. Dasgupta; Inhibition of bacterial cell division protein FtsZ by cinnamaldehyde. *Biochemical pharmacology*, **2007,** 74, 831-840.

21. H.P. Erickson; Atomic structures of tubulin and FtsZ. *Trends Cell Biol*,. **1998** 8,133-137.

22. I.E. Vishnyakov, S.N. Borchsenius; FtsZ and bacterial cell division. *Cell and Tissue Biology*, **2007.** 1, 206-214.

23. M.A. Oliva, S.C. Cordell, J. Löwe; Structural insights into FtsZ protofilament formation. *Nature structural & molecular biology*, **2004,** 11, 1243-1250.

24. S. Tripathy, S.K. Sahu; FtsZ inhibitors as a new genera of antibacterial agents. *Bioorganic chemistry*, **2019,** 91, 103169.

25. H.P. Erickson, D.E. Anderson, M. Osawa; FtsZ in bacterial cytokinesis: cytoskeleton and force generator all in one. *Microbiology and molecular biology reviews*, **2010**, 74, 504-528.

26. J. Mingorance, G. Rivas, M. Velez, P. Gomez-Puertas, M. Vicente; Strong FtsZ is with the force: mechanisms to constrict bacteria. *Trends in microbiology*, **2010,** 18, 348-356.

27. J. Löwe, F. van den Ent, L.A. Amos; Molecules of the bacterial cytoskeleton. *Annu. Rev. Biophys. Biomol. Struct.*, **2004**, 33 ,177-198.

28. K.A. Michie, J. Löwe; Dynamic filaments of the bacterial cytoskeleton. *Annu. Rev. Biochem.*, **2006** , 75, 467-492.

29. L. Mosyak, Y. Zhang, E. Glasfeld, S. Haney, M. Stahl, J. Seehra, W.S. Somers; The bacterial cell-division protein ZipA and its interaction with an FtsZ fragment revealed by X-ray crystallography. *The EMBO journal*. **2000**.

30. K. Yan, K.H. Pearce, D.J. Payne; A conserved residue at the extreme C-terminus of FtsZ is critical for the FtsA-FtsZ interaction in Staphylococcus aureus. *Biochemical and biophysical research communications*, **2000** , 270, 387-392.

31. M. Krupka, M. Sobrinos-Sanguino, M. Jiménez, G. Rivas, W. Margolin; Escherichia coli ZipA organizes FtsZ polymers into dynamic ring-like protofilament structures. *MBio.*, **2018**, 9, 10-1128.

32. C. Ortiz, P. Natale, L. Cueto, M. Vicente; The keepers of the ring: regulators of FtsZ assembly. *FEMS microbiology reviews*, **2016**, 40, 57-67.

33. E. Harry, L. Monahan, L. Thompson; Bacterial cell division: the mechanism and its precison. *International review of cytology*, **2006**, 253, 27-94.

34. P. Mateos-Gil, P. Tarazona, and M. Vélez; Bacterial cell division: modeling FtsZ assembly and force generation from single filament experimental data. *FEMS microbiology reviews*, **2019** , 43, 73-87.

35. L. Romberg, P.A. Levin; Assembly dynamics of the bacterial cell division protein FtsZ: poised at the edge of stability. *Annual Reviews in Microbiology*, **2003**, 57, 125-154.

36. L.B. Ruiz-Avila, S. Huecas, M. Artola, A. Vergoñós, E. Ramírez-Aportela, E. Cercenado, I. Barasoain, H. Vázquez-Villa, M. Martín-Fontecha, P. Chacón, M.L. López-Rodríguez; Synthetic inhibitors of bacterial cell division targeting the GTP-binding site of FtsZ. *ACS chemical biology*, **2013**, 8, 2072-2083.

37. M. Artola, L.B. Ruiz-Avila, A. Vergoñós, S. Huecas, L. Araujo-Bazán, M. Martín-Fontecha, H. Vázquez-Villa, C. Turrado, E. Ramírez-Aportela, A. Hoegl, M. Nodwell; Effective GTP-replacing FtsZ inhibitors and antibacterial mechanism of action. *ACS Chemical Biology*, **2015 ,** 10, 834-843.

38. J.L. Keffer, S. Huecas, J.T. Hammill, P. Wipf, J.M. Andreu, C.A. Bewley; Chrysophaentins are competitive inhibitors of FtsZ and inhibit Z-ring formation in live bacteria. *Bioorganic & medicinal chemistry*, **2013**, 21, 5673-5678.

39. A. Plaza, J.L. Keffer, G. Bifulco, J.R. Lloyd, C.A. Bewley; Chrysophaentins A− H, antibacterial bisdiarylbutene macrocycles that inhibit the bacterial cell division protein FtsZ. *Journal of the American Chemical Society*, **2010**, 132, 9069-9077.

40. N.L. Elsen,, J. Lu, G. Parthasarathy, J.C. Reid, S. Sharma, S.M. Soisson, K.J. Lumb; Mechanism of action of the cell-division inhibitor PC190723: modulation of FtsZ assembly cooperativity. *Journal of the American Chemical Society*, **2012**,.134, 12342-12345.

41. J.M. Andreu,, C. Schaffner-Barbero,, S. Huecas, D. Alonso, M.L. Lopez-Rodriguez, L.B. Ruiz-Avila, R. Núñez-Ramírez, O. Llorca, A.J. Martín-Galiano; The antibacterial cell division inhibitor PC190723 is an FtsZ polymer-stabilizing agent that induces filament assembly and condensation. *Journal of Biological Chemistry*, **2010,** 285, 14239-14246.

42. L. Araújo-Bazán, S. Huecas, J. Valle, D. Andreu, J.M. Andreu; Synthetic developmental regulator MciZ targets FtsZ across Bacillus species and inhibits bacterial division. *Molecular microbiology*, **2019**, 111, 965-980.

43. A. Casiraghi, L. Suigo, E. Valoti, V. Straniero; Targeting bacterial cell division: A binding site-centered approach to the most promising inhibitors of the essential protein FtsZ. *Antibiotics*, **2020**, 9, 69.

44. A. Bordogna, A. Pandini, L. Bonati; Predicting the accuracy of protein–ligand docking on homology models. *Journal of computational chemistry*, **2011** , 32, 81-98.

45. W. Tian, C. Chen, X. Lei, J. Zhao, J. Liang; CASTp 3.0: computed atlas of surface topography of proteins. *Nucleic acids research*, **2018**, 46, 363-367.

46. N. Michaud-Agrawal, E.J. Denning, T.B. Woolf, and O. Beckstein; MD Analysis: a toolkit for the analysis of molecular dynamics simulations. *Journal of computational chemistry*, **2011**, 32, 2319-2327.

47. K. Sargsyan, C. Grauffel, C. Lim; How molecular size impacts RMSD applications in molecular dynamics simulations. *Journal of chemical theory and computation*, **2017,** 13, 1518-1524.

48. N.C. Benson, V. Daggett; A comparison of multiscale methods for the analysis of molecular dynamics simulations. *The Journal of Physical Chemistry B*, **2012,** 116, 8722-8731.

49. M.Y. Lobanov, N.S. Bogatyreva, O.V. Galzitskaya; Radius of gyration as an indicator of protein structure compactness. *Molecular Biology*, **2008**, 42, 623-628.

50. A.R. Bizzarri, C.X. Wang, W.Z. Chen, S. Cannistraro; Hydrogen bond analysis by MD simulation of copper plastocyanin at different hydration levels. *Chemical physics*, **1995**, 201, 463-472.

51. A.M. da Fonseca,, B.J. Caluaco, J.M.C. Madureira, S.Q. Cabongo, E.M. Gaieta, F. Djata, R.P. Colares, M.M. Neto, C.F.C. Fernandes, G.S. Marinho, H.S. Dos Santos; Screening of potential inhibitors targeting the main protease structure of SARS-CoV-2 via molecular docking, and

approach with molecular dynamics, RMSD, RMSF, H-bond, SASA and MMGBSA. *Molecular Biotechnology*, **2024**, 66, 1919-1933.

52. S. Genheden , U. Ryde ; The MM/PBSA and MM/GBSA methods to estimate ligand-binding affinities. *Expert opinion on drug discovery*, **2015**, 10, 449-461.

53. A. Rajan, P.L. Freddolino, K. Schulten, Going beyond clustering in MD trajectory analysis: an application to villin headpiece folding. *PLoS One*, **2010**. 5, p.e9890.

CHAPTER 13

Summary & Conclusion

This thesis on Curcumin and its metal complexes looked at several aspects of complex formation using different metal ions that are biologically useful. It tried to highlight how both from a chemical point of view and a biochemical point of view, complex formation was actually advantageous. Studies that were performed showed several attributes of complex formation that either addressed some of the limitations of Curcumin and turned them into an advantage or provided an improvement of already existing properties related to the molecule.

A major problem of Curcumin is its hydrolytic instability and bio-availability that prevents it from showing its full therapeutic potential on any biological target. Besides, owing to hydrolytic instability, it cannot be said with certainty, if an observed biological activity reported to be of Curcumin is actually due to it or is a combination of its hydrolysed products as well. Since hydrolysis of Curcumin has been shown to be time dependent, the biological activity would also be different for different concentrations and different times of interaction making realization of biological activity a real challenging task. To a considerable extent, complex formation of Curcumin with Mn^{II}, Cu^{II} and Zn^{II} as metal ions could address many such discrepancies mentioned above by being able to maintain Curcumin as a "single unit". Both spectrophotometric studies as well as HPLC that were performed as a part of this study clearly demonstrated the hydrolytic instability of Curcumin and a lack of it in the complexes in aqueous solution and in biological milieu for a considerable length of time.

Through complex formation, manifestations of Curcumin as a "single unit", bound to a metal centre could be realized as having an importance in biology. This was possible through a comparison of the role of degraded products in the observed efficacy of Curcumin, allowing for a realization of the extent to which each degraded product contributes towards biological activity. Although some work was done in this regard, it is not a part of this thesis. Since Curcumin has a good number of pharmacological properties, whose mechanism of

action is still not very clear, with a major reason being hydrolytic instability, these could be addressed through complex formation.

Physicochemical investigations were conducted on the formation of each complex prior to determining their stability constants in aqueous solution. Various spectroscopic techniques, mass spectrometry and thermogravimetric analysis etc. were employed to characterize the three complexes. Density functional theory was used to elucidate the structures of all three complexes based on spectroscopic data. The HOMO-LUMO energy gaps of the complexes confirmed their suitability for intramolecular charge transfer. As molecules with narrow HOMO-LUMO energy gaps are considered soft, so all the synthesized compounds fall into this category. These soft molecules demonstrate enhanced biological and chemical reactivity owing to electron donation. Quantum descriptor analysis further supported their soft nature and high electron-withdrawing capacity, suggesting potential interactions with proteins or DNA through electron polarization. The low HOMO-LUMO gap facilitated both electron donation (IP) and acceptance (EA). The complexes exhibited significantly higher electron affinity compared to Curcumin, indicating their ability to interact with nucleotides or amino acid residues of DNA or proteins by attracting electron density. Upon complex formation with selected metal ions, Curcumin was found to be softer displaying greater electron delocalization and promoting more non-covalent interactions. Spectroscopic and computational analyses provided crucial information regarding the electronic properties of the complexes. Results indicate that complexes may engage in interesting interaction with biological macromolecules.

Coming to mechanism of action of molecules in general, most are known to show biological efficacy by targeting cellular DNA in different ways, one of which could be through binding to DNA thus affecting its correct three dimensional structure, a pre-requisite for efficient biological activity. DNA binding studies are not known for Curcumin owing to

its instability in aqueous solution and in biological milieu. However, since all three complexes of Curcumin were reasonably stable in aqueous solution, the possibility of their binding to DNA was investigated. Hence, as a part of the present study, interaction of $[Mn^{II}(Cur)_2(HCur)]$, $[Cu^{II}(Cur)(CH_3COO)(H_2O)]$ and $[Zn^{II}(Cur)(CH_3COO)(H_2O)]$ were undertaken with calf thymus DNA. Binding constant values were [3.28 to 5.50] $\times 10^5$ M^{-1} for the Mn^{II} complex, [3.73 to 4.10] $\times 10^4$ M^{-1} for the Cu^{II} complex and [0.6 to 2.54] $\times 10^4$ M^{-1} for the Zn^{II} complex. For the Cu^{II} complex, titrations were even performed at four different temperatures, enabling a determination of thermodynamic parameters ΔH and ΔS that helped to predict the binding type for the Cu^{II}–Curcumin species to DNA and throw light on the interaction of Curcumin with DNA as well. In fact, binding of complexes to DNA helped to realize to a considerable extent how Curcumin might have interacted with DNA if it's binding could be followed in aqueous solution containing an electrolyte. Information obtained for the complexes was used to speculate and predict a probable mechanism of action for Curcumin (wherever it was thought that action might be related to interaction with DNA). Thus interaction of monomeric complexes with DNA has a lot of bearing on how Curcumin might interact with DNA when present as a "single unit", a situation that would otherwise never be possible to realize in aqueous buffer or in the presence of electrolytes. Hence, information obtained from binding of the complexes of Curcumin with DNA serve as an important starting point for the evaluation of binding parameters and identify the binding type in theoretical evaluations for the interaction of Curcumin with DNA.

This was actually attempted and achieved through *in silico* molecular docking and dynamics studies of Curcumin and its metal complexes with selected DNA models obtained from the protein data bank that showed an unique dual binding nature towards DNA. The study suggests their capacities to bind to DNA both by intercalative and groove binding mechanisms resulting in a better understanding of their binding dynamics. Molecular

Dynamics studies further confirmed the stability and time sustainability of the complexes within binding regions over the time scale of the experiments performed. Moreover, docking simulations showed different 2D and 3D interactions with nucleotides of the DNA. The present study suggests that Molecular Dynamics simulation and binding free energy calculations were in good agreement with docking studies and that they exhibit properties of higher binding and probable inhibition of DNA in its functional role in the bio-system. Theoretical studies corroborate experimental DNA binding studies that were done using calf thymus DNA. Hence, such compounds may be considered as potential drug candidates against DNA since they target the DNA moiety and inhibit activities like replication and transcription that play crucial roles for stopping growth of cells.

The results also highlight not only the versatility of Curcumin and its metal complexes as DNA binding agents but also the ligand's structural features that could determine binding affinity and specificity. Identification and elucidation of such dual binding behaviour is essential for understanding the molecular basis of their biological activity, including their role in therapeutic applications both as anticancer agents and antimicrobial agents. These findings are to be validated through future experimental and computational studies that would explore the potential of metal complexes of Curcumin in bio-medicine.

To decipher the mechanism for antibacterial efficacy of Curcumin and its metal complexes, inhibition of FtsZ protein, a crucial bacterial cytoskeletal protein for cell division was done by *in silico* molecular docking and molecular dynamics approach. Computational studies showed that Curcumin and its metal complexes bind strongly to the active site of FtsZ protein models both in *S.aureus* and *E.Coli* with high binding energy involving critical residues needed for both FtsZ polymerization and GTPase activity. Additional molecular dynamics simulations then assured that these complexes were stable within the FtsZ binding pocket and that they were capable of disrupting FtsZ dynamics. Results from the study

provide useful information on antibacterial mechanism of Curcumin and their metal complexes. FtsZ represents a potential target for bacterial cell division and in turn, bacterial growth inhibition. Therefore compounds targeting FtsZ may show effects on bacterial cell division. The results of this study support the development of Curcumin based metal complexes as potential antibacterial agents and provide a framework for future experimental validation and optimization of their therapeutic potential.

The Mn-Curcumin complex exhibited notable superoxide dismutase (SOD) mimetic activity, resulting in production of reactive oxygen species (ROS) which is only likely to contribute to bacterial killing. This ROS generation could potentially compromise the integrity of bacterial cell membranes, enhance their permeability to ultimately cause cell death. The capacity of the complex to imitate SOD activity indicates its possible broader use under conditions related to oxidative stress. Additional research into the mechanism of action and potential synergistic effects with other antimicrobial agents may uncover promising therapeutic approaches.

By targeting a critical component of the bacterial cell division i.e. by inhibiting the FtsZ protein [Zn^{II}(Cur)(CH_3COO)(H_2O)] could be included into the family of such inhibitors as it is seen to offer a novel mechanism of action that may be harnessed to combat multi-drug resistant bacteria, enhance efficacy of existing antibiotics and further one's understanding of bacterial cell biology.

From the above said experimental and computational modeling findings, evaluation of the *in vitro* antibacterial effectiveness of Curcumin and its metal complexes against *E. coli* and *S. aureus* strains were conducted in the *laboratory of Prof. Kasturi Mukhopadhyay at Jawaharlal Nehru University (JNU) in New Delhi*. The bacterial killing assay revealed that exposing targets to 25 μM metal complexes for 60 min resulted in around 97-98% killing of

bacterial cells whereas Curcumin at the same concentration and duration killed around 36-37%. Increasing the concentration to 50 μM allowed the complexes to kill approximately 99% of cells in 60 minutes while Curcumin at this concentration killed around 66-67% in the same time frame. All complexes demonstrated notably enhanced antibacterial activity compared to Curcumin. A calcein leakage assay also performed in collaboration with *Prof. Kasturi Mukhopadhyay's laboratory at JNU New Delhi*, showed that complexes induced rapid membrane permeabilization in *S. aureus*. The bacterial membrane disruptive mechanism was confirmed by confocal microscopy and visualized by SEM and TEM study. All such findings were published in joint publications (*Appendix-I, Related to thesis, 1 and 3)*. The exceptional potency of these complexes was further supported by their favourable toxicological profile exhibiting neither hemolytic nor cytotoxic effects on mammalian cells. The safety profile suggested that complexes are suitable candidates for future *in vivo* studies.

Overall, the present study was an attempt to develop Curcumin-based antibacterial compounds where the multitargeting mode of action of the complexes, being non-toxic at much higher concentration and stability at physiological conditions advocates its potential as an alternative to the antibiotic; also making it an excellent candidate for further *ex vivo* and *in vivo* investigations for its therapeutic applications.

APPENDIX-I

List of Publications

List of Publications

Related to thesis

1) **Tanmoy Saha**, Prince Kumar, Nayim Sepay, Durba Ganguly, Kanchan Tiwari, Kasturi Mukhopadhyay, Saurabh Das; "Multitargeting antibacterial activity of a synthesized Mn^{2+} complex of Curcumin on gram-positive and gram-negative bacterial strains". ***ACS Omega***, **2020**, 5, 16342-16357.
2) **Tanmoy Saha**, Soumen Singha, Sanjay Kumar, Saurabh Das, "Spectroscopy driven DFT computation for a structure of the monomeric Cu^{2+}-Curcumin complex and thermodynamics driven evaluation of its binding to DNA: Pseudo-binding of Curcumin to DNA." ***Journal of Molecular Structure***, **2020,** 1221, p.128732.
3) Prince Kumar, **Tanmoy Saha**, Swastik Behera, Shalini Gupta, Saurabh Das, Kasturi Mukhopadhyay, "Enhanced efficacy of a Cu^{2+} complex of curcumin against Gram-positive and Gram-negative bacteria: Attributes of complex formation." ***Journal of Inorganic Biochemistry***, **2021**, 222, p.111494.
4) **Tanmoy Saha**, Subrahmanyam Sappati, Saurabh Das, "An insight into the mixed quantum mechanical-molecular dynamics simulation of a Zn^{II}-Curcumin complex with a chosen DNA sequence that supports experimental DNA binding investigations." ***International Journal of Biological Macromolecules***, **2023**., 245, p.125305.

Not Related to thesis

5) Sayantani Chatterjee, Chetan Kumar Jain, **Tanmoy Saha**, Susanta Roychoudhury, Hemanta.Kumar Majumder, Saurabh Das, "Utilizing coordination chemistry through formation of a Cu^{II}-quinalizarin complex to manipulate cell biology: an *in vitro*, *in silico* approach." ***Journal of Inorganic Biochemistry*, 2023**, 249, p.112369.

6) Birendra Nath Patra, Asit Kumar Das, Samiran Misra, Partha Pratim. Jana, Paula Brandao, Mohd Afzal, Abdullah Alarifi, **Tanmoy Saha**, Debabrata Bera, Satyajit. Haldar, Dasarath Mal, Nayim Sepay, "Hydrothermal syntheses of d^{10}-based Zn(II) and Cd(II) metal–organic frameworks for the catalysis of the Knoevenagel condensation." ***Journal of Molecular Structure***, **2024** 1300, p.137229.

7) Vishnu Raja Vijayakumar, Priyanka Jayam Rajendran, M. Poornimaa, K. Ramanathan, **Tanmoy Saha**, Saurabh Das, Dhanasekaran Dharumadurai, "Structural geometry, electronic properties and pre-clinical evaluation of antibacterial compounds from lichen-associated Streptomyces mobaraensis DRM1 and Nocardiopsis synnemataformans DRM2." ***Journal of Molecular Structure***, **2024**, 1312, p.138561.

Probable Publications from the work reported in the thesis

1) **Tanmoy Saha**, Prince Kumar, Kasturi Mukhopadhyay, Saurabh Das, "Bacterial cell permeabilization and FtsZ inhibiting attributes of a Zn^{II}Curcumin complex as realized through *in vitro* experiments and molecular docking-dynamics approach respectively"

Probable Publications from work not related to the thesis

2) **Tanmoy Saha**, Sayantani Chatterjee, Saurabh Das, "An *in silico* DNA binding investigation that uses DFT, molecular docking and molecular dynamic simulations on mono and tetra acetylated derivatives of quinalizarin to compare experimental DNA binding information"

3) Somenath Banerjee, **Tanmoy Saha**, Dhanasekaran Dharymadurai, Saurabh Das, Rartha Sarathi Guin, " Electrochemical behavior, interaction with SDS micelles, *in silico caspase-3* activation and permeation into A549 human lung carcinoma cells by a Cu^{II} complex of sodium 3-amino-2-hydroxy-9,10-anthraquinone-1-sulphonate"

4) Tusar Kanti Mondal, **Tanmoy Saha**, Sougata Ghosh Chowdhury, Parimal Karmakar, Saurabh Das; "Exploring free radical induced activity due to Carminic acid, its Co^{II} complex as realized through *in situ* electrochemical generation of semiquinone: Correlation with studies on A549 lung carcinoma cells."

APPENDIX-II

List Of Conference proceedings

ORAL PRESENTATION IN CONFERENCE PROCEEDINGS

2024 **Oral Presentation: Tanmoy Saha**, Saurabh Das, "**Investigation and comparison of *in vitro* and *in silico* methods shed light on antimicrobial properties exhibited by Curcumin and its transition metal complexes**" (SABIC2024/OL/36) at the **6th Symposium on Advanced Biological Inorganic Chemistry (6th SABIC) 7th-11th January 2024**, organised by Indian Association for the Cultivation of Science, Kolkata and Tata Institute of Fundamental Research, Mumbai, at Altair Boutique Hotel , Salt Lake, Kolkata.

2021 **Oral Presentation & *Recipient of Indian Chemical Society Research Excellence Award*: Tanmoy Saha**, Price Kumar, Kasturi Mukhopadhyay, Saurabh Das **"Enhanced stability of Curcumin in presence of Zn(II) ion : *In silico* observations explain *in vitro* experiments on bacterial targets"** at the **58th Annual Convention of Chemists & International Conference on Recent Trends in Chemical Sciences (ACC-RTCS-2021) 21st-24th December 2021**, organised by Indian Chemical Society, Kolkata.

2020 **Oral Presentation: Tanmoy Saha**, Mouli Saha, Promita Nandy Price Kumar, Kasturi Mukhopadhyay, Saurabh Das **"Enhanced stability of Curcumin in presence of Cu^{2+}ion: A HPLC study and its biological attributes on bacterial strain** at the **57th Annual Convention of Chemists & International Conference on Recent Trends in Chemical Sciences (ACC-RTCS-2020) 26th-29th December 2020**, organised by Indian Chemical Society, Kolkata.

PUBLICATION OF ABSTRACT IN CONFERENCE PROCEEDINGS

2024 **Poster: Tanmoy Saha**, Saurabh Das, **"Investigation and comparison of *in vitro* and *in silico* methods shed light on antimicrobial properties exhibited by Curcumin and its transition metal complexes"** (SABIC2024/PR/11) at the **6th Symposium on Advanced Biological Inorganic Chemistry (6th SABIC) 7th-11th January 2024**, organised by Indian Association for the Cultivation of Science, Kolkata and Tata Institute of Fundamental Research, Mumbai, at Altair Boutique Hotel, Salt Lake, Kolkata.

2023 **Poster: Tanmoy Saha**, Sayantani Chatterjee, Saurabh Das, **"*In silico* DNA binding investigations of mono and tetra acetylated derivatives of quinalizarin to compare experimental DNA binding results"** (P-61) at the **P.C. Ray Memorial International Conference on "Contemporary Ideas, Innovations & Initiatives in Chemical Sciences (CI3CS-2023) 23rd & 24th August 2023**, organised by Department of Chemistry, Presidency University, at Presidency University, Kolkata.

2020 **Poster: Tanmoy Saha**, Prince Kumar, Nayim Sepay, Durba Ganguly, Kasturi Mukhopadhyay, Saurabh Das **"An Mn(II) complex of Curcumin shows antibacterial activity against gram positive and gram negative bacterial cell"** at the **National seminar on Emerging trends in Chemical Sciences under Centre for Advanced Studies II Program 7th January 2020**, organised by Department of Chemistry, Jadavpur University at Jadavpur University, Kolkata.

APPENDIX-III

List Of Workshop & Online trainings

ONLINE TRAINING & WORKSHOP

2020 **"Online training workshop on Computational Density Functional Theory"** 4th and 5th July 2020, organised by Thanthai Periyar Goverrnment Polytechnic College, Vellore-632002 , Tamil Nadu, India

2020 **"Online training session on Quantum Computational NBO calculations"** 12th July 2020, organised by Thanthai Periyar Goverrnment Polytechnic College, Vellore-632002 , Tamil Nadu, India

2021 . **Online training : " Advanced Molecular Dynamics Simulation -A Summer school -2021"** organised by Department of Physics, Kathmandu University, Nepal and Department of Chemistry, IISER Pune, India and Green Club of Thoughts, Kathmandu University, Nepal held during 5th July to 16th July 2021.

2021 **Online training : " Advanced Molecular Dynamics Simulation -A Winter school -2021"** organised by The International School of Photonics, Cochin University of Science and Technology (CUSAT), India, Department of Physics, Kathmandu University, Nepal and Department of Chemistry, IISER Pune, India and Green Club of Thoughts, Kathmandu University, Nepal and Scidart Academy held during 6th to 17th September 2021

APPENDIX-IV

Reprint of Publications Included in the Thesis

This is an open access article published under an ACS AuthorChoice License, which permits copying and redistribution of the article or any adaptations for non-commercial purposes.

ACS OMEGA

http://pubs.acs.org/journal/acsodf

Article

Multitargeting Antibacterial Activity of a Synthesized Mn^{2+} Complex of Curcumin on Gram-Positive and Gram-Negative Bacterial Strains

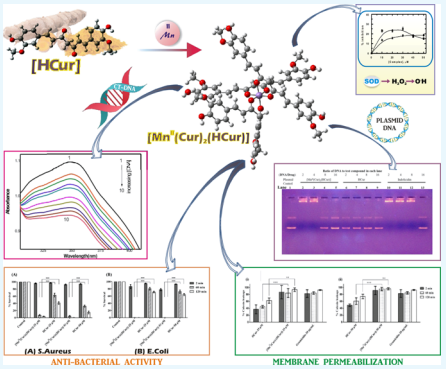
Tanmoy Saha,[‖] Prince Kumar,[‖] Nayim Sepay, Durba Ganguly, Kanchan Tiwari, Kasturi Mukhopadhyay,* and Saurabh Das*

Cite This: *ACS Omega* 2020, 5, 16342−16357

Read Online

ACCESS | Metrics & More | Article Recommendations | Supporting Information

ABSTRACT: Curcumin is an important molecule with a plethora of pharmacological activities and therapeutic potentials. Despite its efficacy, it remained a potential drug candidate owing to hydrolytic instability and poor aqueous solubility. To overcome the limitations related to low solubility, low bioavailability, and the fact that curcumin is never present in solution as a "single unit", its complex was prepared with Mn^{II} with the idea that binding to a metal ion might help to resolve these issues. The complex was characterized by elemental and spectral analysis. The structure of the complex was determined by density functional theory calculations. The complex was stable at physiological buffer conditions, unlike curcumin. It did not have any detrimental effect on mammalian cells. There was a significant enhancement in the antibacterial activity of the complex compared to curcumin against both Gram-positive (*Staphylococcus aureus*) and Gram-negative (*Escherichia coli*) bacteria. It showed a strong affinity for deoxyribonucleic acid (DNA) evident from a high binding constant value with calf thymus DNA and also from the retarded electrophoretic mobility of bacterial plasmid DNA. The complex showed "superoxide dismutase-like" activity leading to the generation of reactive oxygen species (ROS). The complex caused bacterial membrane perturbation evident from calcein leakage assay, which was further corroborated by scanning and transmission electron microscopic experiments. Overall, the present study shows improved stability and antibacterial potency of a nontoxic complex over curcumin. Its multitargeting mode of action such as ROS-production, effective binding with DNA, and permeabilization of bacterial membrane together allows it to be an effective antibacterial agent that could be taken further for therapeutic use against bacterial infections.



1. INTRODUCTION

Curcumin (HCur) [1,7-bis(4-hydroxy-3-methoxyphenyl)-hepta-1,6-dienne-3,5-dione], the yellow pigment extracted from turmeric (*Curcuma longa* Linn), is a well-known lipophilic polyphenolic compound.[1−4] Besides its traditional use as a cooking ingredient in many Asian communities, it has been an integral component of Ayurveda and used in wound healing, common cold, fever, inflammation, arthritis, and so forth.[1−5] Although known for a long time, it gained considerable attention in the last few decades when numerous studies established that HCur possesses many pharmacological properties that include antitumor, anti-inflammatory, antioxidant, and antiviral applications in neuro-degenerative diseases.[2−9] Moreover, the excellent potency of HCur is associated with its safe toxicity profile, as clinical trials have shown it to be safe even at high oral doses of 12 g per day.[10] In addition to its plethora of pharmacological properties, HCur also possesses antimicrobial activity against a wide range of micro-organisms.[11] Earlier, we have reported that HCur is highly effective against both Gram-positive and Gram-negative bacterial strains under *in vitro* conditions.[12] However, its full potential as a therapeutic agent could not be achieved owing to poor physiological stability and low aqueous solubility, resulting in poor bioavailability.[13−15]

HCur is a symmetrical molecule showing a dynamic keto−enol tautomerism because of the β-diketone moiety. The presence of β-diketone is probably a reason for its hydrolytic instability in cellular medium, resulting in poor bioavailability.[13,16] In fact, HCur undergoes rapid degradation in different physiological buffers as well as in different cell culture media, although in the latter, it is slightly more stable because of the presence of serum proteins.[17,18] Therefore, to address the issue of stability, considered a serious disadvantage, a complex was prepared with Mn^{II}.[19] Complexes of Mn^{II} with HCur were prepared earlier, but the one which we prepared was different in terms of composition.[19−21] Phenolic −OH groups that are centers of potential activity often lead to

Received: November 30, 2019
Accepted: June 16, 2020
Published: July 6, 2020

Downloaded via 202.78.234.147 on August 12, 2021 at 14:16:56 (UTC).
See https://pubs.acs.org/sharingguidelines for options on how to legitimately share published articles.

© 2020 American Chemical Society

https://dx.doi.org/10.1021/acsomega.9b04079
ACS Omega 2020, 5, 16342−16357

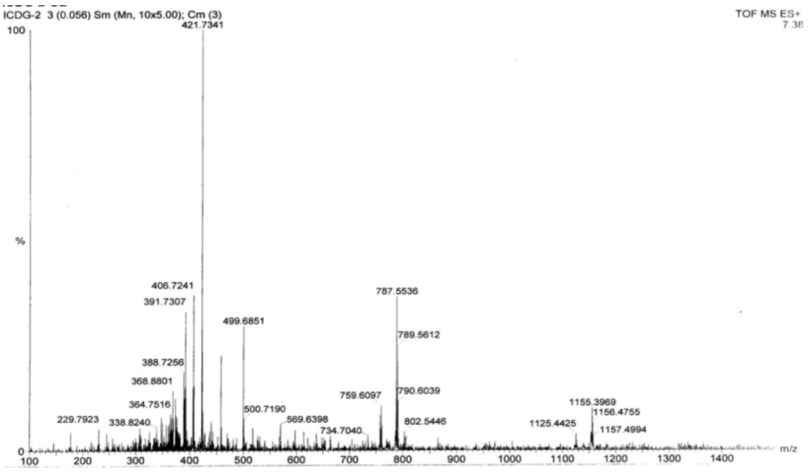


Figure 1. Mass spectra of the Mn^{II} complex of HCur.

complications during complex formation, forming insoluble polymeric species.[7,9,14−16,19,22] However, when prepared with precaution, coordination complexes of HCur possess different biological attributes that can be used to an advantage.[16,23−25] In the present investigation, a Mn^{II}−HCur complex was prepared and characterized by elemental and spectral analysis and its electronic structure was established by density functional theory (DFT) calculations. We then investigated the hydrolytic stability of the complex in different biological milieu to find out if complex formation with Mn^{II} improves stability. It was studied for its superoxide dismutase (SOD)-like activity, resulting in the generation of reactive intermediates and interaction with deoxyribonucleic acid (DNA). Further, its antibacterial activity was investigated against clinically significant Gram-positive (*Staphylococcus aureus*) and Gram-negative (*Escherichia coli*) bacteria. These are among the most prevalent and most common causes of hospital- and community-acquired infections. *S. aureus* is an opportunistic pathogen causing several life-threatening diseases such as osteomyelitis, endocarditis, and toxic shock syndrome.[26] According to the Broad Institute, *E. coli* accounts for 17.3% of clinical infections requiring hospitalization and happens to be the second most common source of infection behind *S. aureus* (18.8%). In Gram-negative bacteria, there is an additional layer of protection of the outer membrane of lipopolysaccharides (LPSs), allowing them to resist most of the traditional antibiotics and making Gram-negative bacteria more dangerous in hospital settings.

Next, to decipher the mechanism behind the superior antibacterial activity of the complex over HCur, we assessed the ability to permeabilize the cytoplasmic membrane of the bacteria using the fluorescence-based calcein leakage assay. We also examined the affinity of the complex toward LPSs of *E. coli* using BODIPY-TR-cadaverine displacement assay. These membrane-targeting modes of action were further confirmed by microscopic visualization. Further, to rationalize the therapeutic potential of the complex, its toxic effects on mammalian cells were evaluated.[27,28]

2. RESULTS AND DISCUSSION

2.1. Characterization of the Complex. Owing to poor solubility in water, the spectrum of the complex was recorded in dimethyl sulfoxide (DMSO) (Figure S1, Supporting Information). λ_{max} obtained at 400 nm in DMSO (molar extinction coefficient ε = 2.85 × 10^4 M^{-1} cm^{-1}) was comparable to the spectrum recorded during physicochemical experiments where Mn^{II} and HCur were allowed to interact with each other, showing peaks at 430 nm in aqueous−ethanol medium (Figure S2, Supporting Information). The Fourier transform infrared (FTIR) spectrum of HCur (Figure S3, Supporting Information), recorded on a PerkinElmer spectrometer (Spectrum Two) with samples by use of the attenuated total reflection technique, indicates a peak at 3516 cm^{-1} owing to −OH stretching, which for the complex was observed as a broad band at 3403 cm^{-1} (Figure S4, Supporting Information).[29] Sharp peaks at 1627 and 1604 cm^{-1}, attributed to C═O stretching vibrations in HCur, got shifted to lower wavenumbers (1581 and 1516 cm^{-1}, respectively) in the complex having low intensities, suggesting involvement of the carbonyl group in binding Mn^{II}. Peaks at 1506 and 1429 cm^{-1} due to C═C stretching and C═O bending vibrations in the IR spectrum of HCur also showed significant changes in the complex.[29]

The mass spectrum was recorded on a Micromass Q-TOF Micro, Waters Corporation. Analysis of mass spectrometry data was done considering a 1:3 complex formed between Mn^{II} and HCur (Figure 1). The molecular ion peak was obtained in a cluster of peaks having m/z 1157.4994, 1156.4755, and 1155.3969 [m/z (theo) = 1157.3004]. From the molecular ion, loss of one ligand has Mn^{II} bound to two curcumins. Both curcumins could be bound as enolate (expected m/z = 789.1743) or one could be bound in the enolate form and the other as a diketone (expected m/z = 790.1822). Hence, peaks obtained at m/z = 790.6039, 789.5612, and 787.5536 (expected m/z −2H) support formation of such fragments.

Loss of two ligands from the molecular ion should form a 1:1 metal/ligand fragment with expected peaks at m/z = 422.0562 (if enolate) and 423.0640 (if diketo). Appearance of a peak at m/z = 421.7341 indicates formation of this fragment. Peaks at m/z = 364.7516 and 368.8801 indicate free HCur released by the complex during analysis. Therefore, the mass spectrum of the complex provides good evidence in favor of a 1:3 metal to ligand stoichiometry.

Thermogravimetric analysis (TGA) of the complex performed on a Mettler Toledo TGA/SDTA 851 (Figure S5, Supporting Information) shows up to 100 °C; there is no appreciable loss in weight. Considering the initial weight at 28 °C to be 15.4364 mg, the weight recorded at ∼196 °C was

https://dx.doi.org/10.1021/acsomega.9b04079
ACS Omega 2020, 5, 16342−16357

14.2364 mg. Hence, loss in weight was 1.2 mg. Percentage loss in weight (7.774%) corresponds to the loss of three $-OCH_3$ groups from the complex, probably one from each ligand (theoretical loss = 7.772%). At 280 °C, the weight recorded was 13.0463 mg. Hence, loss in weight and percentage loss were 2.3901 mg and 15.483%, respectively. This loss in weight corresponds to the loss of six $-OCH_3$ groups from the complex, that is, two from each ligand (theoretical loss = 15.543%). Hence, TGA data also suggest the formation of a 1:3 complex. The molar conductance of the complex in pure DMSO was determined on a conductivity meter EUTECH CON 700, Thermo Scientific, Eutech Instruments and found to be 15.2 S m^2 mol^{-1}, suggesting it to be a nonelectrolyte in solution. We tried to obtain single crystals of the prepared complex but were not successful. Hence, we tried to obtain a structure from DFT based on spectroscopic evidence. The obtained structure has good correlation with experimental data. Magnetic susceptibility measurements of powdered samples at room temperature (298 K) were done by the Gouy method on Magway MSB MK1, Sherwood Scientific Ltd. The μ_{eff} was found to be 6.06 BM.

2.2. Optimization of Molecular Geometry and Electronic Structure. The geometries of both the ligand and the complex were optimized using DFT. What transpired from the DFT study is that Mn^{II} forms an octahedral complex with curcumin with two molecules of it coordinating the metal center as enolate anion (Cur) and one coordinating it in the diketo form (HCur). The ground-state optimized geometry of the ligand and its Mn^{II} complex are shown in Figure 2.

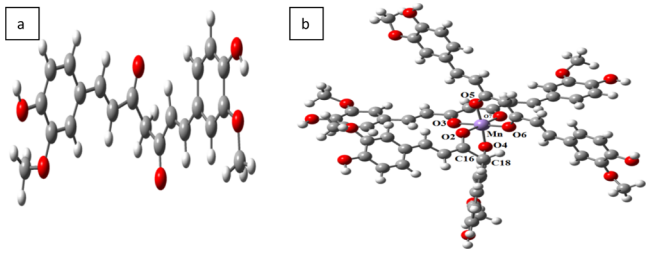


Figure 2. Optimized geometry of (a) HCur and (b) $[Mn^{II}(Cur)_2(HCur)]$.

Optimized geometrical parameters of the complex are listed in Table 1. The model geometry possesses a distorted octahedral arrangement around Mn^{II}. Calculated Mn−O distances were found in the expected range of 1.869−1.926 Å.[30] Hence, DFT calculations unequivocally support the formation of an octahedral Mn^{II} complex. If we consider the coordination environment around Mn^{II} (Figure 2b), O5 and O6 belong to one ligand, O3 and O7 to a second ligand, and O2 and O4 are from a third ligand. Interestingly, Mn−O bond lengths (Table 1) suggest that Mn−O2 and Mn−O4 are slightly longer than the other four (i.e., Mn−O3, Mn−O7, Mn−O5, Mn−O6), indicating that coordination by oxygen donor sites from two ligands are of one type and that from the third ligand is slightly different.

This fact is supported experimentally by the conductance measurement data (reported in Section 2.1) that had suggested the complex to be a nonelectrolyte. In other words, the calculated Mn−O bond distance data suggesting binding of two curcumins to Mn^{II} as enolate anions and one as diketone explain the formation of a neutral complex that correlated with

Table 1. Selected Optimized Geometrical Parameters for a Complex in Ground State Calculated at LANL2DZ Levels for the Metal and 6-31G Levels for the Atoms C, H, and O

bond type	bond length (Å)
Mn−O2	1.926
Mn−O3	1.889
Mn−O4	1.900
Mn−O5	1.869
Mn−O6	1.882
Mn−O7	1.884
bond angle	value (deg)
O2−Mn−O3	87.30
O2−Mn−O4	89.01
O2−Mn−O5	87.90
O2−Mn−O6	90.53
O2−Mn−O7	178.34
O3−Mn−O4	88.74
O3−Mn−O5	87.67
O3−Mn−O6	177.84
O3−Mn−O7	91.59
O4−Mn−O5	175.37
O4−Mn−O6	91.16
O4−Mn−O7	92.21
O5−Mn−O6	92.33
O5−Mn−O7	90.81
O6−Mn−O7	90.58
C16−C18−C17	105.69

the experimental data (obtained from conductance) as one of a nonelectrolyte.

From the data in Table 1, it can be said that those oxygen coordinations with a slightly larger Mn−O bond length have curcumin coordinating Mn^{II} in the diketo (neutral) form, denoted as HCur in the formula. The other four oxygen coordinations of Mn^{II} showing an almost similar Mn−O bond length have curcumin coordinating the metal center as enolate anions (denoted in the formula as Cur). Further, we also found from the DFT calculated structure that in case of curcumin while coordinating Mn^{II} in the diketo form, carbon−oxygen bond distances are slightly shorter (as expected) than the other four carbon−oxygen bond distances where they coordinate as enolate anions. When coordination occurs because of resonating C═O and $C-O^-$ forms as for any enolate anion, carbon−oxygen bond distances are likely to be slightly larger than when it is a diketo coordination (Figure S6, Supporting Information). This was actually found for this complex, suggesting that curcumin coordinating Mn^{II} through O2 and O4 does so as diketo, following which their corresponding carbon−oxygen bond distances (C16−O2 and C17−O4) were slightly shorter (Table S1, Supporting Information). Our values may be compared with a 1:1 Mn^{II}/curcumin complex reported earlier where the structure was also arrived at with DFT calculations.[31]

For HCur in its ground state, the electron densities of the highest occupied molecular orbitals (HOMO) and the lowest unoccupied molecular orbitals (LUMO) reside mainly over the benzene ring. The energy difference between HOMO and LUMO was found to be 3.55 eV (Figure 3). This assignment is supported by time-dependent DFT (TD-DFT) calculations. For the complex, the LUMO, LUMO + 1, and HOMO originate from symmetry orbitals of ligands with contribution from Mn d orbitals. The energy difference between HOMO

https://dx.doi.org/10.1021/acsomega.9b04079
ACS Omega 2020, 5, 16342−16357

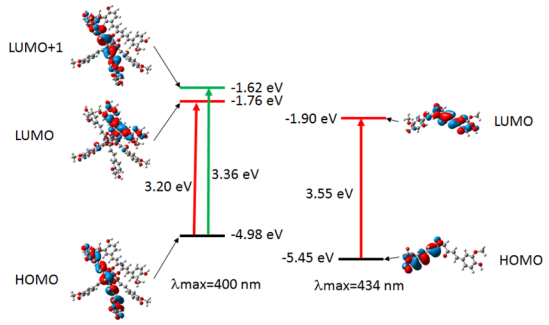


Figure 3. Frontier molecular orbitals involved in the UV−vis absorption of the ligand and the metal complex.

and LUMO in the complex was found to be 3.36 and 3.20 eV, respectively.

2.3. Analysis for Stability of the Complex in Different Media by UV−Visible Spectroscopy. Considering the facts that are known pertaining to the instability of HCur, we examined the stability of $[Mn^{II}(Cur)_2(HCur)]$ in different biological milieu (Figures S7 and S8, Supporting Information).[18] As seen from different figures, in contrast to HCur, there were no changes in the absorbance intensity of the complex (Figures S7 and S8, Supporting Information) in a biological buffer and microbiological media. Worth noting is the fact that HCur is more stable in microbiological media (Figure S8, Supporting Information) compared to phosphate-buffered saline (PBS) buffer. As the environment for most cellular compartments is reducing in nature, the stability of HCur and $[Mn^{II}(Cur)_2(HCur)]$ was investigated in the presence of dithiothreitol (DTT), a strong reducing agent.[32] HCur lost 50% of its absorption intensity within 5 min of coincubation with DTT, whereas no change was observed in the spectrum of $[Mn^{II}(Cur)_2(HCur)]$ even after 20 min of incubation. As evident from Figures S7 and S8, Supporting Information, the complex is stable in physiological buffer and media even under reducing conditions.

2.4. Interaction of $[Mn^{II}(Cur)_2(HCur)]$ with Calf Thymus DNA. The complex was titrated with calf thymus DNA at constant pH (=7.4) and constant ionic strength of the

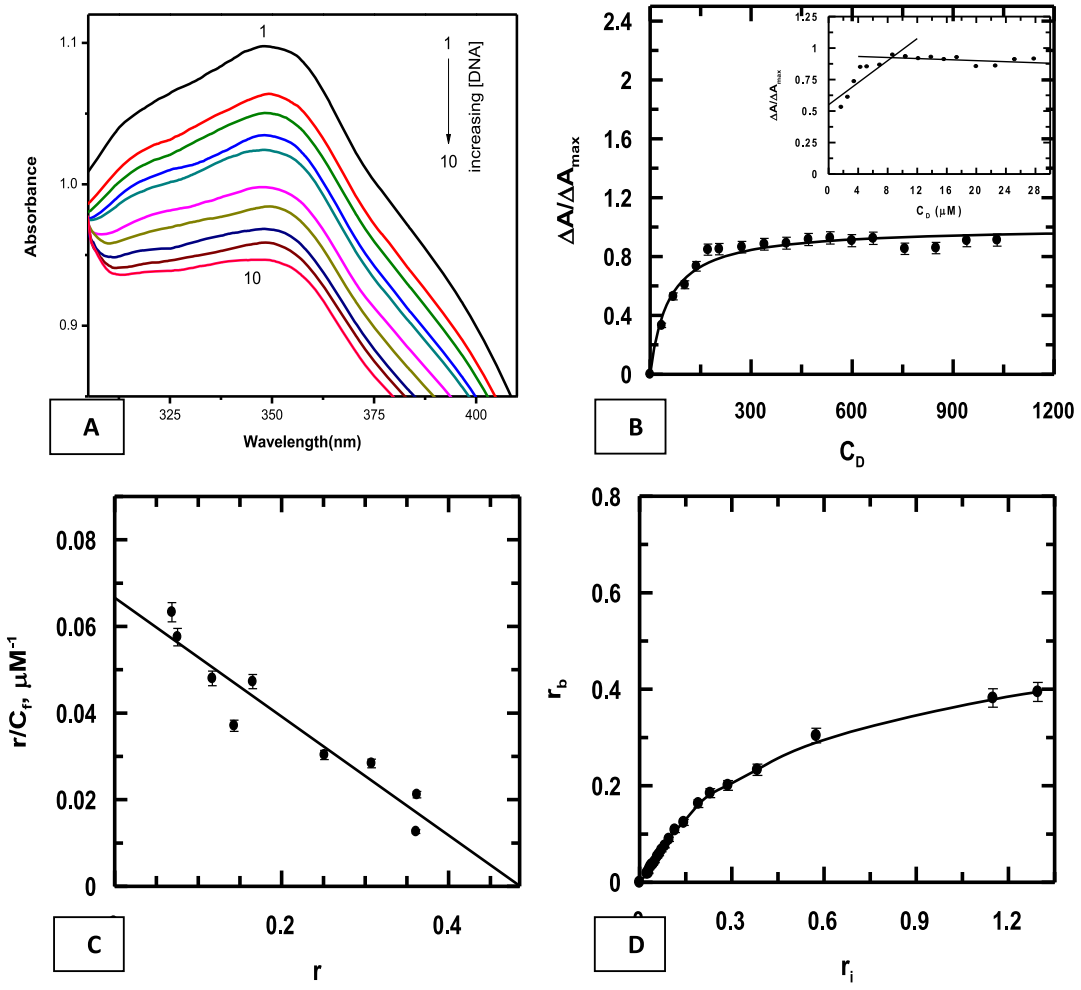


Figure 4. (A) Absorption spectra of $[Mn^{II}(Cur)_2(HCur)]$ in the absence (1) and presence of different concentrations of calf thymus DNA (2) 62.65, (3) 124.69, (4) 246.94, (5) 307.16, (6) 599.69, (7) 851.32, (8) 1092.60, (9) 1248.02, and (10) 1399.30 μM; (B) binding isotherm for $[Mn^{II}(Cur)_2(HCur)]$ interacting with calf thymus DNA when $\Delta A/\Delta A_{max}$ was plotted against the concentration of DNA; the dark line indicates the fitted data obeying eq 4. Inset: Plot of normalized increase in absorbance as a function of mole-ratio of calf thymus DNA to $[Mn^{II}(Cur)_2(HCur)]$; (C) modified Scatchard plot for the interaction of $[Mn^{II}(Cur)_2(HCur)]$ with calf thymus DNA; (D) plot of input $[Mn^{II}(Cur)_2(HCur)]$/DNA ratio (r_i) to bound $[Mn^{II}(Cur)_2(HCur)]$/DNA ratio (r_b) as calculated from the decrease in absorbance following interaction of $[Mn^{II}(Cur)_2(HCur)]$ with calf thymus DNA; $[Mn^{II}(Cur)_2(HCur)]$ = 40 μM, [NaCl] = 150 mM, pH = 7.4, temp. = 298 K.

https://dx.doi.org/10.1021/acsomega.9b04079
ACS Omega 2020, 5, 16342−16357

Table 2. Binding Constant Values for Interaction of the Complex with the Calf Thymus DNA

apparent binding constants $K_{app} \times 10^{-4}$ (M^{-1})				overall binding constant ($K' \times 10^{-5}$ M^{-1}) $K' = K_{app} \times n_b$			
from double reciprocal plot eq 2	from nonlinear fit eq 4	from double reciprocal plot with y-intercept = 1 eq 5	site size (n_b) from mole ratio plot	using K_{app} from eq 2	using K_{app} from eq 4	using K_{app} from eq 5	overall binding constant $K' \times 10^{-5}$ (M^{-1}) (by the Scatchard plot, eq 6)
4.10	6.87	2.10	8.0	3.28	5.50	1.68	1.26

medium (0.15 mM).[33−35] Titrations showed a gradual decrease in absorbance at 367 nm, which was used to follow the interaction of $[Mn^{II}(Cur)_2(HCur)]$ with calf thymus DNA (Figure 4A). Figure S9, Supporting Information, is a plot of $1/\Delta A$ versus $1/[C_D - C_L]$ (eq 2) that provides a value for apparent binding constant [K_{app} ($=K_d^{-1}$)]. Titrations were repeated thrice. The values obtained were in the range of 2.73×10^4 to 5.47×10^4 M^{-1}.[33,35−39] Figure 4B is a plot of $\Delta A/\Delta A_{max}$ versus concentration of calf thymus DNA. Nonlinear curve fitting was applied (eqs 3 and 4) on three separate titrations and an average apparent binding constant ($K_{app} = 6.87 \times 10^4$ M^{-1}) were evaluated.[33,35−39] The inset of Figure 4B provides a value for n_b (=8.0), the number of nucleotides bound to the complex following its interaction with calf thymus DNA.

The titration data were also fitted to eq 5 that plots the inverse of the fraction of the complex bound to the calf thymus DNA to the inverse of the concentration of the calf thymus DNA used in the experiment.[33,36−39] The inverse of the slope of the plot (Figure S10, Supporting Information) provides yet another value of apparent binding constant. An average of K_{app} from eq 5 obtained from three separate titrations was 2.10×10^4 M^{-1}. Apparent binding constants obtained from three different approaches (eqs 2−5) when multiplied with n_b provide the overall binding constant (K') [Table 2]. Data from the titration were also fitted to a modified form of the Scatchard equation (Figure 4C).[40] K' and n ($=n_b^{-1}$) were obtained. "n" denotes the number of complex molecules bound to a nucleotide. Figure 4D relates the ratio of the input drug/DNA (r_i) to the ratio of the bound drug/DNA (r_b) as derived from Scatchard calculations.[41] For such a plot, a 45° line passing through the initial points indicates that the entire compound was eventually bound to the DNA.[41]

2.5. Hypoxanthine to Xanthine/Xanthine Oxidase-Inhibiting Activity of $[Mn^{II}(Cur)_2(HCur)]$. Xanthine oxidase is an enzyme that generates reactive oxygen species (ROS) by catalyzing the oxidation of hypoxanthine to xanthine and then of xanthine to uric acid.[42,43] As xanthine oxidase is a superoxide-producing enzyme, it was used in an assay where depletion of superoxide was followed by reduction of nitro-blue tetrazolium dichloride (NBT^{2+}) having an affinity for it. The assay indicates that $[Mn^{II}(Cur)_2(HCur)]$ has SOD-like activity, that is, it assists in disproportionation of a superoxide radical anion to molecular oxygen and hydrogen peroxide (Figure 5).

Thus, such formation of H_2O_2 in the system where $[Mn^{II}(Cur)_2(HCur)]$ is present is important as it leads to the generation of a hydroxyl radical ($HO^•$) known for its ability to cause oxidative stress. Therefore, this provides another reason why the complex shows improved antibacterial activity reported and discussed in the following sections.[44−46] In this regard, it should however be mentioned (as correctly pointed out by one reviewer while reviewing this manuscript) that although we consider formation of the hydroxyl radical ($HO^•$) as logically formed from H_2O_2 and use it to explain the better performance of the complex in comparison to curcumin, it would have been nice had we shown its actual formation by the deoxyribose assay, which, for more than one reason, could not be included in our study.[47,48]

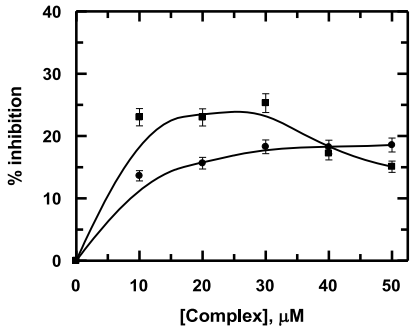


Figure 5. Percentage inhibition of a superoxide radical anion formed because of the hypoxanthine/xanthine oxidase enzyme assayed by NBT^+ absorption at 524 nm in the presence of $[Mn^{II}(Cur)_2(HCur)]$ (■) and SOD (●); 50 μM hypoxanthine, 0.04 unit of xanthine oxidase, 300 μM NBT^{2+} and 10% DMSO.

2.6. Antibacterial Activity of $[Mn^{II}(Cur)_2(HCur)]$ on *S. aureus* and *E. coli*. The antibacterial efficacy of $[Mn^{II}(Cur)_2(HCur)]$ was compared to that of HCur against *S. aureus* ATCC 29213 and *E. coli* ATCC 25922 with the help of a killing assay, exposing cells (10^6 cfu/mL) to two different concentrations (25 and 50 μM) and plating aliquots on a brain heart infusion (BHI) agar plate at selected time intervals. The percentage survival of $[Mn^{II}(Cur)_2(HCur)]$- and HCur-treated bacterial cells was calculated after comparing with untreated control (Figure 6A,B). Bacterial survival is also presented in the logarithmic scale as $\log_{10}$ cfu/mL in the Supporting Information (Figure S11, Supporting Information). The complex $[Mn^{II}(Cur)_2(HCur)]$ showed a significant (p-value ≤ 0.001) improvement in antibacterial activity compared to HCur against both *S. aureus* and *E. coli*. As seen from the killing assay of *S. aureus* in Figure 6A, exposure of 25 μM $[Mn^{II}(Cur)_2(HCur)]$ for 60 min caused 92.90 ± 1.87% killing, whereas a similar exposure of HCur could kill only 36.68 ± 5.13% cells. Upon increasing the concentration to 50 μM, $[Mn^{II}(Cur)_2(HCur)]$ caused 95.58 ± 2.08% killing, whereas a similar increase for HCur killed 67.48 ± 2.77% in 60 min.

Exposure of 50 μM $[Mn^{II}(Cur)_2(HCur)]$ for 120 min showed 99.68 ± 0.12% killing, whereas 85.04 ± 3.94% killing was observed with HCur (Figure 6A). In the log-scale representation, exposure of 50 μM $[Mn^{II}(Cur)_2(HCur)]$ for 120 min caused 2.52 ± 0.15 $\log_{10}$ cfu/mL reduction, whereas a similar concentration of HCur caused only 0.78 ± 0.13 $\log_{10}$ cfu/mL reduction in an initial cell count of 5.76 ± 0.02 $\log_{10}$ cfu/mL cells (Figure S11, Supporting Information). Further, a killing assay on *E. coli*, presented in Figure 6B, showed a much more prominent antibacterial effect by the complex than HCur. Exposure of 25 μM of $[Mn^{II}(Cur)_2(HCur)]$ for 60 min showed 99.72 ± 0.05% cell killing, whereas a similar exposure

https://dx.doi.org/10.1021/acsomega.9b04079
ACS Omega 2020, 5, 16342−16357

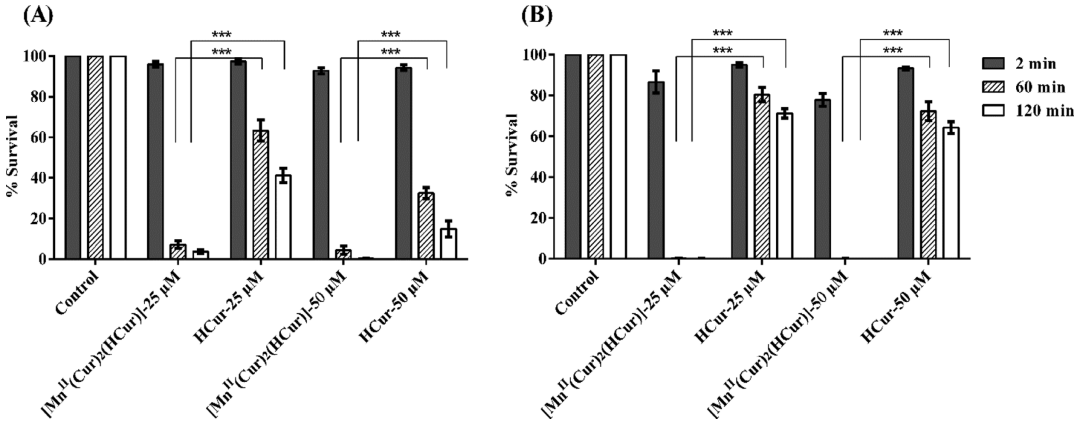


Figure 6. Antibacterial efficacy of 25 and 50 μM of $[Mn^{II}(Cur)_2(HCur)]$ and HCur in PBS buffer against (A) *S. aureus* and (B) *E. coli* cells ($\sim 10^6$ cfu/mL). Gray columns, columns with stripes, and white columns denote the time of exposure (2, 60, and 120 min, respectively) to the compounds. The data represent mean ±SD)of three independent experiments (***$p \leq 0.001$).

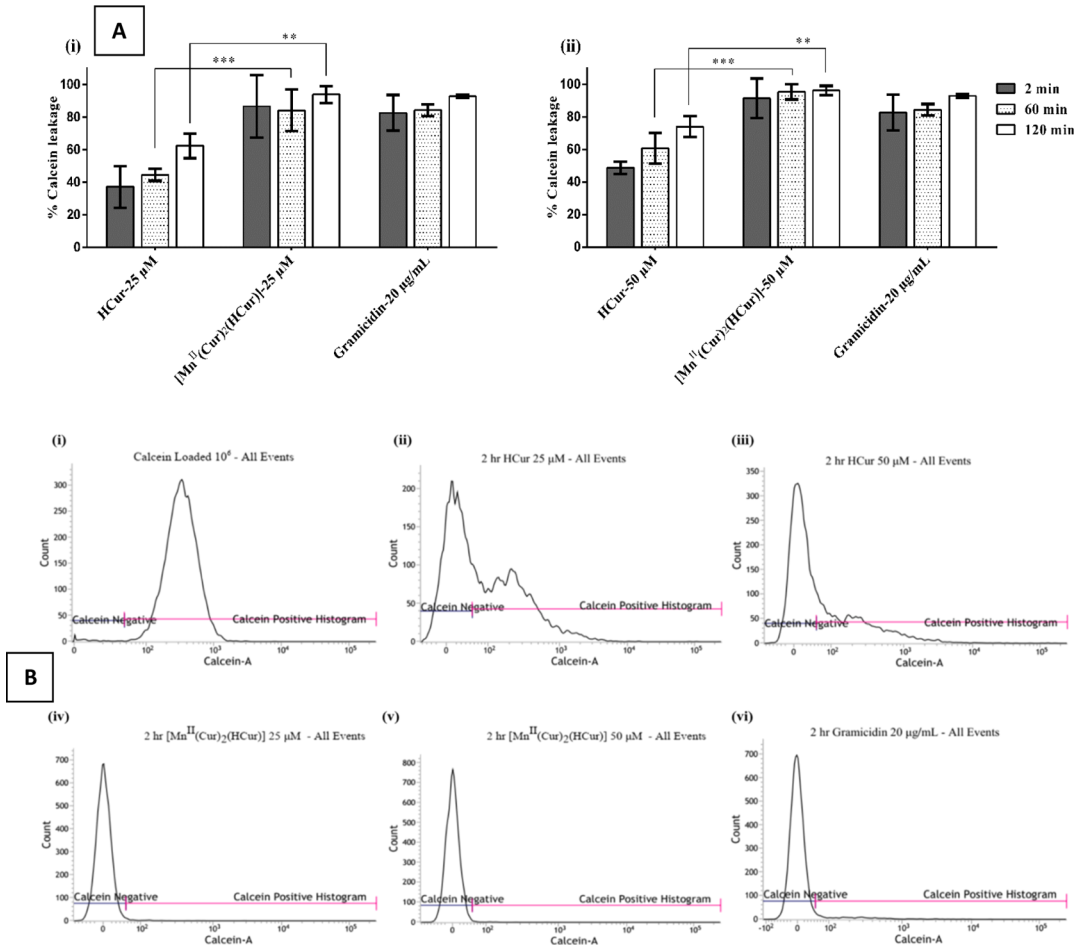


Figure 7. (A) Percentage of calcein leakage from bacterial cells caused by 25 and 50 μM $[Mn^{II}(Cur)_2(HCur)]$ and HCur upon exposure of 2, 60, and 120 min of incubation. (B) Representative histograms of calcein-loaded cells incubated with 25 and 50 μM $[Mn^{II}(Cur)_2(HCur)]$ and HCur for 120 min. A total of 10,000 cells were acquired for each flow cytometry analysis. The data represent the mean ±SD of three independent experiments (**$p \leq 0.01$, ***$p < 0.001$).

of HCur killed only 19.59 ± 3.63% cells. Even after increasing the concentration and exposure time to 50 μM and 2 h, respectively, HCur could kill only 35.69 ± 2.82% cells, whereas under similar conditions, $[Mn^{II}(Cur)_2(HCur)]$ caused 100% killing. In the log scale, there was no observable reduction in $\log_{10}$ cfu/mL compared to the control even after increasing the concentration and exposure time to 50 μM and 120 min for HCur. However, under similar conditions, the complex caused 4.02 ± 0.67 $\log_{10}$ cfu/mL in an initial cell count of 5.49 ± 0.24 $\log_{10}$ cfu/mL (Figure S11, Supporting Information).

Overall, the killing efficacy of the complex $[Mn^{II}(Cur)_2(HCur)]$ was found to be significantly (p-value

https://dx.doi.org/10.1021/acsomega.9b04079
ACS Omega 2020, 5, 16342−16357

$\leq$ 0.001) better than HCur in both *S. aureus* and *E. coli* in all tested conditions.

2.7. Mechanism of Antibacterial Action Due to the Complex. *2.7.1. Membrane Permeabilization of S. aureus by Calcein Leakage.* Toward deciphering the mechanism behind the antibacterial activity of $[Mn^{II}(Cur)_2(HCur)]$, its ability to permeabilize bacterial membranes was studied by calcein leakage assay using flow cytometry.[12,49,50] Bacterial cells were exposed to two different concentrations of HCur and $[Mn^{II}(Cur)_2(HCur)]$, that is, 25 and 50 μM, respectively. The results presented in Figure 7A(i) show 25 μM $[Mn^{II}(Cur)_2(HCur)]$ caused 86.71 $\pm$ 19.19% dye leakage for a 2 min incubation as compared to HCur causing only 37.22 $\pm$ 12.81%. Incubation of 50 μM HCur for 120 min showed 73.93 $\pm$ 11.16% dye leakage, whereas exposure to the same time and a similar concentration of $[Mn^{II}(Cur)_2(HCur)]$ caused a dye leakage of 96.19 $\pm$ 4.95%, comparable to 20 μg/mL gramicidin-D (92.8 $\pm$ 1.78%) [Figure 7A(ii)]. Overall, the complex showed a better membrane permeabilization activity than HCur. In fact, the extent of permeabilization by the complex was almost equal to that of the well-known pore-forming peptide gramicidin-D. Figure 7B shows histograms of calcein-loaded cells incubated with 25 and 50 μM HCur and $[Mn^{II}(Cur)_2(HCur)]$ for 120 min. The loss in calcein fluorescence as a result of membrane permeabilization for $[Mn^{II}(Cur)_2(HCur)]$-treated samples was found to be statistically significant compared to HCur at time intervals of 60 min (p-value < 0.001) and 120 min (p-value < 0.01) of incubation, respectively.

2.7.2. Binding Affinity of the Complex with LPS. As LPS is the major constituent of the outer membrane of Gram-negative bacteria, we examined the ability of the complex to bind to LPS, using a fluorescence-based displacement assay with BODIPY-TR-cadaverine.[51] As shown in Figure 8, there was a

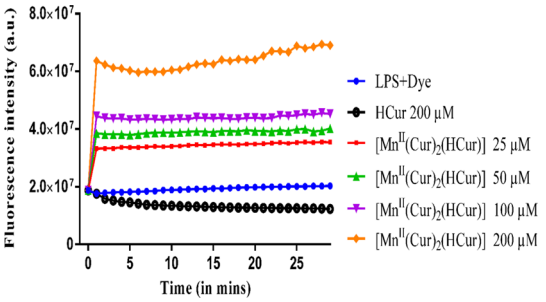


Figure 8. Binding affinity of compounds to LPSs determined by the BODIPY-cadaverine displacement method. Representative data of LPS binding of the complex (25, 50, 100, and 200 μM) and 200 μM of HCur for 30 min are presented here.

rapid increase in fluorescence intensity in a dose-dependent manner. Increase of dye fluorescence reflected its dequenching because of its displacement by the complex from LPS, suggesting that the complex has a marked affinity toward LPSs, whereas the parent molecule (HCur) does not bind to LPSs even at the highest tested concentration of 200 μM. Therefore, LPS binding and calcein leakage assay collectively suggested that the complex first binds to LPSs, which leads to disruption of the *E. coli* outer membrane and then it induced permeabilization of the inner membrane.

2.7.3. Evaluation of Membrane Damage in S. aureus Using Fluorescence Microscopy. To assess the membrane integrity and bacterial cell viability, a mixture of two DNA-binding fluorescent probes SYTO 9 and propidium iodide (PI) were used. SYTO 9 is a green fluorescent stain that generally labels all bacterial cells. In contrast, PI is a red fluorescent stain with stronger binding affinity for DNA compared to SYTO 9 and penetrates only those cells having a damaged membrane. When both dyes are present, it is possible to replace SYTO 9 from DNA, causing a decrease in SYTO 9 (green) fluorescence.[12,52]

A fluorescein isothiocyanate (FITC) filter (green) corresponding to SYTO 9 and a PI filter (red) were followed by a bright field under 60× objective and used to visualize the samples treated with 50 μM $[Mn^{II}(Cur)_2(HCur)]$ and HCur, which were subsequently compared with untreated cells taken as control. The representative merged image of both channels (FITC + PI) is presented in Figure 9. As clearly evident from Figure 9A, untreated control cells appeared predominantly green, indicating that cells are viable and the membrane intact. However, $[Mn^{II}(Cur)_2(HCur)]$-treated cells appeared predominantly red, indicating a loss in membrane integrity and viability of cells (Figure 9B). Cells treated with HCur appeared to be having a mixed population of green, red, and yellow (where both red and green dyes were retained) (Figure 9C). This might be due to minor damages in the membrane allowing only some PI to enter the cells, which is not sufficient to replace all SYTO 9 from DNA. Thus, such cells appear green and yellow.

2.7.4. Morphological Changes in S. aureus Observed by a Scanning Electron Microscope. To further assess if $[Mn^{II}(Cur)_2(HCur)]$ is able to perturb the surface integrity of *S. aureus* ATCC 29213, the cells were visualized by scanning electron microscopy (SEM) following treatment. As shown in Figure S12A, Supporting Information, untreated cells looked bright, smooth, and having an intact surface with round morphology. However, in cells that were treated with 50 μM $[Mn^{II}(Cur)_2(HCur)]$ and HCur, surface perturbation was evident. These cells had an irregular shape with a dent or depression on the surface, along with the appearance of blebs with a rough surface (Figure S12B,C, Supporting Information). Loss of surface morphology and release of intracellular content as debris for complex-treated cells was comparable to cells treated with 20 μg/mL gramicidin D (Figure S12D, Supporting Information).

2.7.5. Ultrastructural Changes in S. aureus Observed by a Transmission Electron Microscope. Further, ultrastructural changes in the cell wall and membrane of *S. aureus* ATCC 29213 cells were examined by transmission electron microscopy (TEM) after 2 h of exposure with 50 μM $[Mn^{II}(Cur)_2(HCur)]$ and HCur. As evident from Figure 10A, untreated control cells had an intact surface with intact cell wall and membrane. However, following treatment with $[Mn^{II}(Cur)_2(HCur)]$, the membrane architecture and surface integrity were severely compromised, with most cells being irregularly shaped. Many cells (ghost cells) lacked cytoplasmic content and were devoid of a cell wall, whereas few of the cells had shredded cell walls and a membrane through which intracellular content oozed out (Figure 10B,C). The results are comparable to those of the well-known pore-forming polypeptide gramicidin D (20 μg/mL) treated cells (Figure 10D). Overall, observations obtained with the help of TEM lend support to the calcein leakage assay that confirms membrane perturbation as the mode of action because of $[Mn^{II}(Cur)_2(HCur)]$.

https://dx.doi.org/10.1021/acsomega.9b04079
ACS Omega 2020, 5, 16342−16357

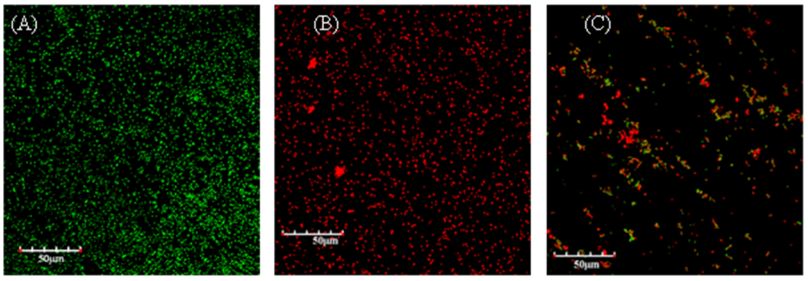


Figure 9. Fluorescence microscopy assay for viability of *S. aureus* ATCC 29213 treated with 50 μM HCur and $[Mn^{II}(Cur)_2(HCur)]$ for 2 h after staining with fluorescent probes SYTO 9 and PI. Representative merged image of both (FITC + PI) channels of (A) untreated control cells, (B) $[Mn^{II}(Cur)_2(HCur)]$, and (C) HCur. Green indicates live bacteria and red indicates dead and membrane-damaged bacterial cells.

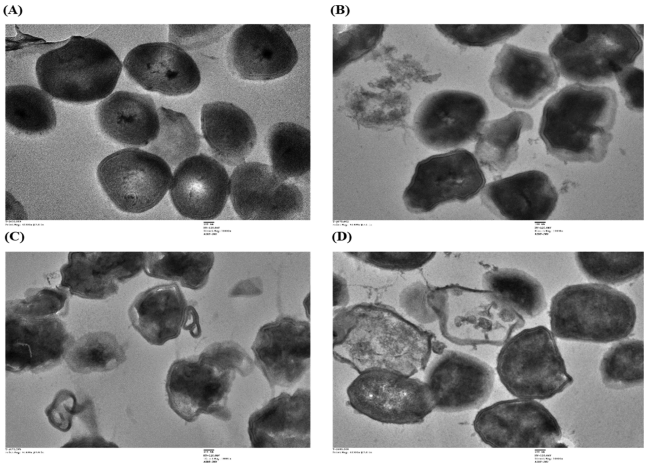


Figure 10. TEM images of *S. aureus* ATCC 29213 treated with 50 μM of HCur, $[Mn^{II}(Cur)_2(HCur)]$, and 20 μg/mL gramicidin D for 2 h. (A) Untreated control cells, (B) HCur, (C) $[Mn^{II}(Cur)_2(HCur)]$, and (D) gramicidin D-treated cells.

2.7.6. Comparative DNA Binding Ability of $[Mn^{II}(Cur)_2(HCur)]$. Although membrane permeabilization occurred within 2 min of incubation of $[Mn^{II}(Cur)_2(HCur)]$ (Figure 7A), no effective killing was observed in that time scale (Figure 6). This suggests that there might be some intracellular targets as well. To explore further on possible intracellular targets, the DNA-binding ability of $[Mn^{II}(Cur)_2(HCur)]$ was compared with HCur using the gel retardation assay or electrophoretic mobility shift assay, which is a common electrophoresis technique to study the affinity of test compounds toward DNA. Figure 11 shows evidence for binding of $[Mn^{II}(Cur)_2(HCur)]$ with DNA (100 ng) at 25 and 50 μM, respectively, reflected by retardation in electrophoretic mobility of plasmid DNA. When compared with $[Mn^{II}(Cur)_2(HCur)]$, HCur did not show effective DNA binding, that is, it did not retard the mobility of plasmid DNA under similar conditions (Figure 11). Indolicidin was used as the control for DNA-binding studies, showing that the concentration required was 12.5 μM. Such DNA-binding studies reveal a high affinity of $[Mn^{II}(Cur)_2(HCur)]$ for plasmid DNA against that observed with HCur, suggesting it to be the cause of intracellular plasmid DNA targeting that could be another mode for antibacterial activity due to $[Mn^{II}(Cur)_2(HCur)]$.

Based on the studies mentioned above, it could now be said that $[Mn^{II}(Cur)_2(HCur)]$ targets bacterial cell membranes as well as the DNA of *S. aureus*. There are several reports suggesting that membrane permeabilization alone is not

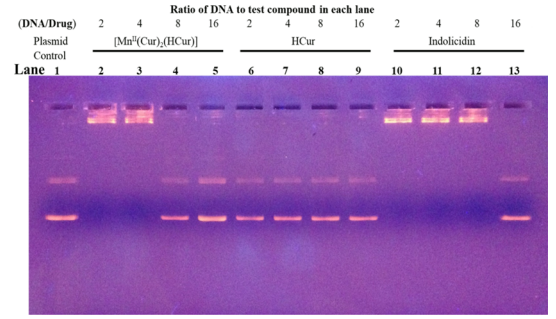


Figure 11. Plasmid DNA-binding ability of $[Mn^{II}(Cur)_2(HCur)]$, HCur, and indolicidin compared using 1.0% agarose gel electrophoresis. Lane 1 denotes plasmid DNA alone; lanes 2−5 denote plasmid DNA in the presence of 50, 25, 12.5, 6.25 μM $[Mn^{II}(Cur)_2(HCur)]$; lanes 6−9 denote plasmid DNA in the presence of 50, 25, 12.5, 6.25 μM HCur; lanes 10−13 denote plasmid DNA in the presence of 50, 25, 12.5, 6.25 μM indolicidin.

sufficient to kill bacterial cells and that intracellular targets such as DNA have an important role in bactericidal action.[53,54] In fact, our results with HCur and $[Mn^{II}(Cur)_2(HCur)]$ hint in that direction. We feel that the cytoplasmic membrane may not be the primary target and that there are probably roles of intracellular targets such as DNA as well, which get modified following interaction with compounds. Hence, a combination of both aspects could probably be the reason for the complex's potential staphylocidal action.

2.8. $[Mn^{II}(Cur)_2(HCur)]$ Was Nonhemolytic and Nontoxic toward Mammalian Cells. As HCur does not possess any toxicity, it becomes essential to know if following complex formation, any toxicity is developed in mammalian cells. Hence, the toxicity of $[Mn^{II}(Cur)_2(HCur)]$ was evaluated by studying its hemolytic and cytotoxic activity against mouse red blood cells (RBCs) and the 3T3 murine fibroblast cell line, respectively. For this purpose, much higher concentrations (250 and 500 μM) were used, which are well above the dose required for antibacterial activity. As evident from Figure 12A, similar to HCur, $[Mn^{II}(Cur)_2(HCur)]$ was nearly nonhemolytic. It was 2.60 ± 1.60% hemolytic at 250 μM and 9.68 ± 0.93% at 500 μM; 0.1% Triton X-100 was used as the positive control in the experiment.

To further rule out any potential toxicity, cytotoxicity of $[Mn^{II}(Cur)_2(HCur)]$ was also determined on the 3T3 murine fibroblast cell line using the 3-(4,5-dimethylthiazol-2-yl)-2,5-diphenyltetrazolium bromide (MTT) assay and the result was compared to that of HCur. As shown in Figure 12B, $[Mn^{II}(Cur)_2(HCur)]$ showed cytotoxicity of 6.74 ± 2.91% (at 250 μM) and 11.26 ± 5.02% (at 500 μM), which was in

https://dx.doi.org/10.1021/acsomega.9b04079
ACS Omega 2020, 5, 16342−16357

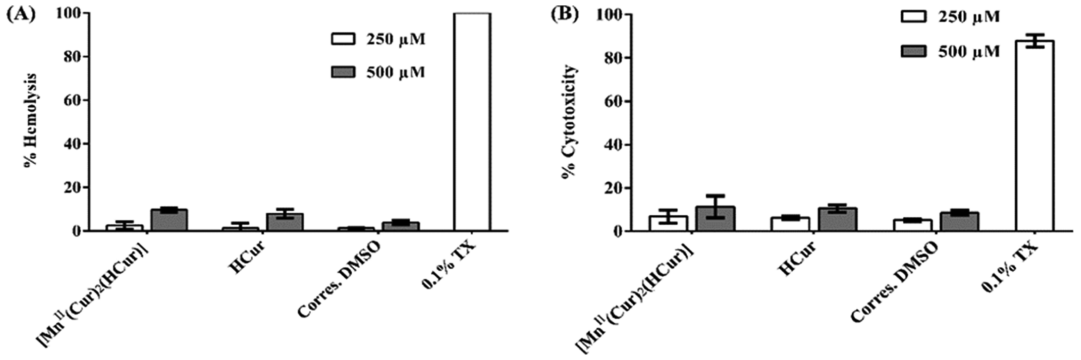


Figure 12. (A) Hemolytic activity of $[Mn^{II}(Cur)_2(HCur)]$ and HCur on mouse RBC. For the experiment, 0.1% Triton X-100 was used as the positive control (considering 100% hemolysis). The experiment was performed in duplicate on two different days; each data point represents mean ± SD; (B) cytotoxicity of $[Mn^{II}(Cur)_2(HCur)]$ and HCur on the 3T3 murine fibroblast cell line. Percentage viability of cells relative to the untreated control was measured using an MTT assay; % cytotoxicity is presented. The experiment was performed in triplicate on three different days; each data point represents mean ± SD.

the same range of toxicity observed for HCur. A 2.0% Triton X-100 was used as the positive control, showing 83.60 ± 5.38% cytotoxicity relative to an untreated growth as the control. Hence, altogether, it is evident that the studied complex exhibited little or no toxicity on mammalian RBCs and the fibroblast cell line even at concentrations much higher than one would use as a dose for antibacterial activity.

3. CONCLUSIONS

In the present study, a complex of Mn^{II} with curcumin $[Mn^{II}(Cur)_2(HCur)]$ was prepared and characterized. Although the reported complex did not show a significant improvement in aqueous solubility, it was however found to be stable in different biological milieu as compared to HCur. The complex showed a significant enhancement in antibacterial activity against clinically relevant pathogens like *S. aureus* and *E. coli* when compared with HCur. The complex first binds to LPSs of the outer leaflet of the outer membrane of *E. coli*. This binding probably leads to disruption of the outer membrane, which then induces permeabilization in the cytoplasmic membrane of bacteria as evident from the LPS-binding assay. For *S. aureus*, the calcein leakage assay clearly established the bacterial membrane disruption by the complex. This membrane-targeting mode of action was further corroborated by SEM and TEM techniques, showing remarkable morphological changes on the *S. aureus* cell surface. Apart from membrane disruption, it also targets intracellular DNA as it shows reasonably good binding for DNA, as evident from the gel retardation assay using bacterial plasmid DNA. The complex showed a significant SOD-like activity leading to generation of ROS, which might contribute toward bacterial cell killing. H_2O_2 formed as a consequence probably interacts with bacterial cells showing enhanced antibacterial activity compared to HCur. The metal ion in the complex being Mn^{II}, capable of reaching a higher oxidation state in the presence of peroxide might also show oxidative stress.[55] The multitargeting mode of activity of the complex not only boosts its antibacterial potency but also makes it difficult for bacteria to generate a resistance against it. Moreover, $[Mn^{II}(Cur)_2(HCur)]$ showed almost no detrimental effect on mammalian cells. Therefore, the complex could become an excellent candidate for therapeutic use. The study provides valuable information for further research for a therapeutic application of the complex at a time of increasing resistance to almost all conventional antibiotics.

4. EXPERIMENTAL SECTION

4.1. Materials. HCur was purchased from Sigma-Aldrich and carefully stored at −5 °C. Stock solutions were prepared in ethanol/DMSO before an experiment and if required stored in the dark. $MnCl_2{\cdot}4H_2O$ was purchased from E. Merck, India. Phosphate buffer was prepared in Millipore water. Sodium nitrate (AR) was used to maintain the ionic strength of the medium. Calf thymus DNA purchased from Sisco Research Laboratories, India, was dissolved in Millipore water containing 120 mM NaCl, 35 mM KCl, and 5 mM $CaCl_2$. Absorbance of the DNA solution was recorded at 260 and 280 nm, respectively, and A_{260}/A_{280} was noted. The ratio found in the range 1.8−1.9 suggests the DNA to be sufficiently free from protein, requiring no further purification. The DNA was also characterized by measuring its circular dichroism (CD) spectra at 260 nm on a CD spectropolarimeter (J815, JASCO, Japan). Plasmid DNA was purchased from Agilent Technologies and used without further purification. The concentration of DNA was determined in terms of nucleotide, considering the molar extinction coefficient at 260 nm to be 6600 M^{-1} cm^{-1}. Nitroblue tetrazolium dichloride (NBT^{2+}), MTT, calcein-acetoxy methyl ester (calcein-AM), LPS *E. coli* (055:B5), and gramicidin D were purchased from Sigma-Aldrich. LIVE/DEAD BacLight Bacterial Viability Kit (L7007) and BODIPY-TR-cadaverine dye were procured from Invitrogen. Agar powder, Luria-Bertani (LB) broth, and Brain Heart Infusion (BHI) medium were purchased from HiMedia Laboratories. Mueller−Hinton broth (MHB) and Dulbecco's modified Eagle's medium (DMEM) were procured from Difco and HiMedia, respectively

4.1.1. Bacterial Strain Used. *S. aureus* (ATCC 29213) and *E. coli* (ATCC 25922) were used in the study. Bacterial strains were stored as frozen stock in 15% (v/v) glycerol at −80 °C till subcultured at 37 °C on BHI and LB agar plates for further studies.

4.2. Methods. *4.2.1. Determination of pK_a of Curcumin.* Dissociation of protons on HCur was determined with the help of pH-metric titrations (eqs S1 and S2) carried out in ethanol (10%)−aqueous (90%) solution at 32 °C and an ionic strength due to 0.1 M $NaNO_3$. pH was recorded using a pH meter (Equip-Tronics EQ-610, India); pH values were suitably

https://dx.doi.org/10.1021/acsomega.9b04079
ACS Omega 2020, 5, 16342−16357

corrected and reported as would be in a pure aqueous solution. Change in absorbance of HCur was followed at 467 nm. Dissociation of protons on HCur was evaluated using eq S3, Supporting Information. pK_{a1} = 7.17 ± 0.31; pK_{a2} = 10.5 ± 0.16; pK_{a3} = 11.44 ± 0.17 [Figure S13, Supporting Information]. Our values were in accordance with those determined earlier.[56−58]

4.2.2. Determination of Stoichiometry of Complex Formation between Mn^{II} and HCur by the Mole Ratio and Job's Method of Continuous Variation. The stoichiometry of complex formation was ascertained by mixing different volumes of equimolar Mn^{II} and HCur.[59,60] In the mole ratio method, in one set of experiments, the concentration of HCur was maintained constant and the concentration of Mn^{II} was varied, whereas in another, the concentration of Mn^{II} was constant and that of HCur was varied.[59,60] The absorbance recorded at 430 nm was plotted against $(T_M/T_L)_{TL}$ and $(T_L/T_M)_{TM}$ (Figure S14A,B). T_M and T_L are the concentrations of Mn^{II} and HCur in experimental solutions, respectively. Straight lines were obtained, the intersection of which indicates the ratio in which HCur binds to Mn^{II}. In Job's method of continuous variation (Figure S14C), absorbance was recorded at 430 nm and plotted against volumes of HCur and Mn^{II}.[59,60] The stoichiometry of Mn^{II} to HCur was found in the range 1:2 to 1:3, gradually tending to 1:3.

4.2.3. Determination of pK_a of HCur in the Presence of Mn^{II}. Dissociation of a proton of HCur in the presence of Mn^{II} was determined in ethanol (10%)−aqueous (90%) solution at 32 °C and a fixed ionic strength of the medium because of 0.1 M $NaNO_3$. Absorbance of HCur was followed at 430 nm in the presence of Mn^{II} and fitted to eq S4, Supporting Information. pK_{a1} (=5.89 ± 0.43) and pK_{a2} (=8.83 ± 0.20) were determined (Figure S15, Supporting Information). Titration data were also fitted to eq S3, Supporting Information, able to determine dissociations of three protons. However, when the data were fitted to eq S3, Supporting Information values for pK_{a1} and pK_{a2} remained the same as that obtained from eq S4, Supporting Information, but the value for pK_{a3} was 12.44 ± 23.07, which is absurd. Hence, we concluded that in the presence of Mn^{II}, the two phenolic −OH protons present on HCur dissociate simultaneously as determined from eq S3, Supporting Information. Stability constants β^* and β were determined using eqs S5−S9, Supporting Information, and found to be 2.52×10^{18} ($\log \beta$ = 18.4).

4.2.4. Preparation of the Complex. HCur (0.2762 g, 0.75 mmol) was dissolved in 15 mL of deaerated acetonitrile−ethanol mixture (1:3). The solution was neutralized with triethylamine (0.104 mL, 0.75 mmol), followed by the addition of $MnCl_2 \cdot 4H_2O$ (0.0495 g, 0.25 mmol) dissolved in 10 mL of deaerated ethanol−water mixture (1:1). Argon was passed through the mixture to maintain an inert atmosphere. The whole setup was stirred for 24 h. A greenish brown precipitate was recovered and washed with chloroform, diethyl ether, ethanol, tetrahydrofuran, and acetonitrile separately depending on the solubility of HCur in these solvents to wash away undesired impurities. A pure complex was obtained. Percentage yield: ∼60%. Elemental analysis was done on a PerkinElmer 2400 Series-II CHN analyzer. Anal. Calcd (%) for $C_{63}H_{58}O_{18}Mn$: C, 65.32; H, 5.052. Found: C, 65.12; H, 5.16. The complex was not soluble in common solvents such as methanol, ethanol, acetonitrile, dichloromethane. It was soluble partly in dimethyl formamide and reasonably well in DMSO.

4.2.5. DFT Calculations. DFT is an important tool to study the geometry, electronic structure, and optical properties of a compound. It is very useful in situations where the structure of the compound cannot be obtained experimentally. In such cases, an attempt for a structure is made with the help of DFT calculations that are performed based on experimental (e.g., spectroscopic) evidence. The TD-DFT approach has also been demonstrated to be reliable for calculating spectral properties of many transition-metal complexes.[61] In our case, in the absence of a crystal structure, we optimized the molecular geometry of HCur and the complex formed with Mn^{II} by DFT using the Gaussian 09 package.[62] The ligand (HCur) geometry was optimized with Becke3 parameter hybrid exchange functional and Lee−Yang−Parr correlation functional (B3LYP)[63] with the 6-31+G(d,p) basis set. Optimization of the complex was done using unrestricted hybrid DFT by Becke's three-parameter exchange functional[63,64] with the nonlocal Lee−Yang−Parr electron correlation functional (UB3LYP model).[63,64] The basis set chosen for Mn was LANL2DZ (ECP)[65] and this was used jointly with the 6-31G(d,p) basis set for other atoms, namely, C, H, and O, using Gaussian 09.[62] TD-DFT was performed considering optimized geometry using the CAM-B3LYP[63,66,67] function in combination with LANL2DZ (ECP) for the Mn atom[65] and 6-31G(d,p) for other atoms (C, H, and O) to calculate spectral properties of the complex. The geometry of the ligand and the complex was fully optimized without any symmetry constraints. The Gauss Sum 2.1 program[68] was used for calculating molecular orbital contributions from atoms or groups.

4.2.6. Comparative Analysis of Stability of HCur and the Complex in Physiological Buffer and Various Cell Media. To evaluate the stability of HCur and $[Mn^{II}(Cur)_2(HCur)]$ under physiological buffer conditions (PBS pH = 7.4) and in different bacterial growth media [BHI, MHB, and Dulbecco's modified Eagle's medium (DMEM)], absorption spectra were recorded with the help of a UV−vis spectrophotometer. HCur and the complex were dissolved in DMSO. From a stock of concentration 20 mM, 1 μL was taken and added to 1 mL of PBS buffer (10 mM sodium phosphate, 150 mM NaCl, pH 7.4) or to 1 mL of growth medium to achieve a final concentration of 25 μM. The absorption spectrum of the mixture was recorded for 20 min at an interval of 5 min. As the environment of most cellular compartments is reducing in nature, we investigated the stability of HCur and $[Mn^{II}(Cur)_2(HCur)]$ in the presence of 10 μM DTT, a strong reducing agent.[32] DTT is one of the most commonly used reducing agents in biological buffers, and previous reports suggest that HCur loses its biological activity when treated with DTT as it accelerates degradation of HCur.[69]

4.2.7. Interaction of $[Mn^{II}(Cur)_2(HCur)]$ with Calf Thymus DNA. As HCur dissolved in phosphate buffer (pH = 7.4) is prone to changes, realized from a change in absorbance, DNA-binding studies using UV−vis spectroscopy were not attempted. However, titration of the complex was carried out as it did not show any appreciable change in absorbance in the same medium (pH 7.4) when followed for a certain length of time. In case of the complex, a change in absorbance of the solution observed upon addition of calf thymus DNA could then be attributed to an interaction of the complex with DNA. This was followed on a JASCO V-630 spectrophotometer and analyzed according to eqs 1−6.

https://dx.doi.org/10.1021/acsomega.9b04079
ACS Omega 2020, 5, 16342−16357

$$L + DNA \rightleftharpoons L - DNA \qquad K_d = \frac{[L][DNA]}{[L - DNA]} \tag{1}$$

L represents the complex and K_d the dissociation constant whose reciprocal provides a value for the apparent binding constant (K_{app}).[33,36−39] Equation 2 is generated from eq 1 where the reciprocal of the change in absorbance was plotted against the reciprocal of ($C_D - C_0$). C_D refers to concentration of calf thymus DNA and C_0 to complex. Using eq 2, ΔA_{max} and K_{app} ($=K_d^{-1}$) may be determined from the intercept and slope, respectively.

$$\frac{1}{\Delta A} = \frac{1}{\Delta A_{max}} + \frac{K_d}{\Delta A_{max}(C_D - C_0)} \tag{2}$$

ΔA denotes the change in absorbance of the complex at a definite pH at which binding experiments were done. For each titration curve, ΔA_{max} indicates the maximum change in absorbance.

$$K_d = \frac{\left[C_0 - \left(\frac{\Delta A}{\Delta A_{max}}\right)C_0\right]\left[C_D - \left(\frac{\Delta A}{\Delta A_{max}}\right)C_0\right]}{\left(\frac{\Delta A}{\Delta A_{max}}\right)C_0} \tag{3}$$

$$C_0\left(\frac{\Delta A}{\Delta A_{max}}\right)^2 - (C_0 + C_D + K_d)\left(\frac{\Delta A}{\Delta A_{max}}\right) + C_D = 0 \tag{4}$$

Equations 3 and 4 were used to fit the data by nonlinear square fit analysis and eq 5 to another form of a double reciprocal plot that has an intercept on y-axis = 1, providing values for apparent binding constants.[33,36−39] The plot of $\Delta A/\Delta A_{max}$ versus ratio of the concentration of calf thymus DNA to the complex provides two straight lines whose intersection gives us n_b, the site size of interaction, indicating the number of nucleotides bound to the complex. Apparent binding constants, when multiplied with n_b, provide the overall binding constant (K').

$$\frac{1}{(C_b/C_L)} = 1 + \frac{1}{[K][C_D]} \tag{5}$$

The titration data were also analyzed by a modified form of the original Scatchard equation [eq 6] and the overall binding constant (K') and site size ($n = n_b^{-1}$) were determined.[40]

$$r/C_f = K'(n - r) \tag{6}$$

$r = C_b/C_D$; C_b is the concentration of the bound form of the complex and C_f, the free form. "n" provides binding stoichiometry in terms of bound complex per nucleotide and is the reciprocal of "n_b".

4.2.8. SOD Activity of the Complex. Superoxide was generated by an enzyme assay using hypoxanthine/xanthine oxidase with some modifications of a method described earlier.[70,71] The reactions involved are mentioned below

$$\text{hypoxanthine} + H_2O + O_2 \rightarrow \text{xanthine} + H_2O_2 \tag{7}$$

$$\text{xanthine} + H_2O + O_2 \rightarrow \text{uric acid} + H_2O_2 \tag{8}$$

$$\text{xanthine} + H_2O + 2O_2 \rightarrow \text{uric acid} + 2O_2^- + 2H^+ \tag{9}$$

A mixture of 50 μM hypoxanthine, 300 μM NBT^{2+}, 0.04 unit/mL xanthine oxidase, and 0−50 μM $[Mn^{II}(Cur)_2(HCur)]$ dissolved in 10% DMSO and 20 mM phosphate buffer (pH 7.4) was incubated at 25 °C for 10 min. The NBT^+ formed was measured using a spectrophotometer at 524 nm. Percentage inhibition of NBT^+ formation was calculated using eq 10.

$$\%\ \text{inhibition} = (A_0 - A_s) \times 100/A_0 \tag{10}$$

A_0 and A_s are the absorbance because of NBT^+ at 524 nm in the absence and presence of $[Mn^{II}(Cur)_2(HCur)]$, respectively. Percentage inhibition was plotted as a function of $[Mn^{II}(Cur)_2(HCur)]$. Similar experiments were repeated with the native SOD enzyme. Percentage inhibition due to $[Mn^{II}(Cur)_2(HCur)]$ was compared to SOD recorded under identical conditions.

4.2.9. Killing Assay. The killing assay was performed according to procedures mentioned in the literature.[12,72] Bacterial cells were grown in BHI broth to a mid-logarithmic phase. Cells were then centrifuged, washed, and resuspended in PBS buffer (10 mM sodium phosphate, 150 mM NaCl, pH 7.4). Resuspended cells were adjusted to an OD_{600} of 0.5 spectrophotometrically (~10^8 cfu/mL). A final inoculum of 10^5 cfu/mL was exposed to various concentrations of $[Mn^{II}(Cur)_2(HCur)]$ and HCur in PBS buffer. At selected time points (2, 60, and 120 min), aliquots were plated on a BHI agar plate in triplicate and incubated overnight at 37 °C. Bacterial colonies were counted the following day and bacterial survival expressed as mean percentage versus nontreated control (set as 100% survival). Each experiment was repeated independently on three separate days.

4.2.10. Bacterial Membrane Permeabilization Assay. Bacterial membrane permeabilization due to $[Mn^{II}(Cur)_2(HCur)]$ and HCur exposure was quantified by calcein leakage assay using flow cytometry, as described earlier.[12,49,74] Calcein-AM is a membrane-permeating, nonfluorescent derivative of calcein. After entering cells, calcein-AM is cleaved by cytoplasmic esterases, releasing fluorescent calcein, which is membrane-impermeable. Therefore, calcein can leak out of cells only if the membrane is damaged. Briefly, *S. aureus* ATCC 29213 cells were grown to mid-logarithmic phase in BHI medium and adjusted to OD_{600} of 1.0 (~10^9 cfu/mL) in PBS buffer as previously mentioned. Mid-log cells (10^8 cfu/mL) were loaded with 2 μg/mL of calcein-AM by incubating them in the dark at 37 °C for 2 h. Calcein-loaded cells were diluted to 10^6 cfu/mL and treated with 25 or 50 μM $[Mn^{II}(Cur)_2(HCur)]$ and HCur for 2 h at 37 °C. Afterward, the fluorescence of cell-entrapped calcein was quantified using a flow cytometer (BD FACSVerse, San Jose, CA) with excitation and emission wavelengths of 490 and 517 nm, respectively. A total of 10,000 cells were acquired for each flow cytometer analysis. Cells showing <10 fluorescence units (FL units) were inferred to have lost calcein because of drug-induced permeabilization and cells showing >10 FL units were interpreted to have retained calcein, indicative of an intact membrane. Untreated calcein-loaded cells were considered as the negative control and 20 μg/mL gramicidin D, a well-known pore-forming antimicrobial peptide-treated cells as the positive control. Release of calcein from treated samples was measured on three different days.

4.2.11. LPS-Binding Assay. The binding affinity of the complex to LPS was quantified by a fluorescence-based displacement assay using BODIPY-TR-cadaverine, as previously described.[51] Fluorescence of this dye is quenched upon binding to LPS, and displacement of the dye by the test

https://dx.doi.org/10.1021/acsomega.9b04079
ACS Omega 2020, 5, 16342−16357

compound results in dequenching of BODIPY-TR-cadaverine fluorescence. For this displacement assay, a stock solution of BODIPY-TR-cadaverine and LPS was diluted in 50 mM Tris buffer (pH 7.4) to yield a final concentration of 5 μg/mL BODIPY-TR-cadaverine and 50 μg/mL of LPS. The background fluorescence of this mixture was recorded with SpectraMax iD5 Multi-Mode Microplate Reader (excitation wavelength was 580 nm; emission wavelength was 620 nm). The change in fluorescence with different concentrations of the complex and HCur was recorded up to 30 min.

4.2.12. Fluorescence Microscopy. Bacterial viability was analyzed using a LIVE/DEAD BacLight Bacterial Viability Kit according to the manufacturer's protocol. Briefly, a dye mixture was prepared containing an equal volume of SYTO 9 and PI.[12,52] The bacterial suspension (10^9 cfu/mL) treated with 50 μM HCur and $[Mn^{II}(Cur)_2(HCur)]$ for 2 h was incubated with 3 μL of dye mixture for each milliliter of bacterial suspension for 15 min in the dark. A 5 μL aliquot of the stained bacterial suspension was trapped between a glass slide and a coverslip. The slide was observed under a confocal fluorescence microscope (Olympus Fluoview FV 1000) using 60× objective with FITC (corresponding to SYTO 9) and PI filters. The excitation/emission maxima were 480/500 nm for SYTO 9 and 490/635 nm for PI, respectively.

4.2.13. Scanning Electron Microscopy. Bacterial samples for SEM measurements were prepared as described earlier.[12,52] Briefly, mid-logarithmic phase cells of *S. aureus* ATCC 29213 (10^9 cfu/mL) were treated with 50 μM HCur and $[Mn^{II}(Cur)_2(HCur)]$ for 2 h at 37 °C with shaking. Gramicidin D (20 μg/mL)-treated cells and untreated bacterial cells were used as the control. After incubation, the cells were washed thrice with 10 mM phosphate buffer (NaH_2PO_4/Na_2HPO_4, pH 7.4) and then fixed with 2.5% glutaraldehyde overnight at 4 °C. The following day, the cells were again washed thrice with the same buffer and dehydrated sequentially with 30−100% ethanol for 10 min each. They were then dried on a coverslip under vacuum in a desiccator. Finally, the cells were coated with gold and viewed via a scanning electron microscope (EVO 40, Carl Zeiss, Germany) available at AIRF, JNU. The experiment was performed twice independently on two separate days. Similar images were obtained.

4.2.14. Transmission Electron Microscopy. For TEM, bacterial samples were prepared according to a protocol described earlier.[12,52] Samples were prepared as described for SEM until overnight fixation with 2.5% glutaraldehyde at 4 °C. Further, 1% osmium tetroxide was used to postfix cells and then sequentially dehydrated by 50−100% acetone. Each sample was embedded in epoxy resin, and ultrathin sections were prepared using a microtome. The sections were placed on a copper grid and stained with uranyl acetate, followed by lead citrate. The samples were then washed twice in Milli-Q water and dried under vacuum in a desiccator. The grid was viewed via a transmission electron microscope (Zeol-JEM 2100, Japan) available at AIRF, JNU.

4.2.15. DNA Gel Retardation Assay. Shift in mobility of plasmid DNA upon interaction with HCur and $[Mn^{II}(Cur)_2(HCur)]$ was determined using a gel retardation assay, which is a common electrophoresis technique used to study the interaction of a test compound with DNA. This experiment was performed using a protocol described earlier.[49] In brief, 100 ng of plasmid DNA was incubated with different concentrations of $[Mn^{II}(Cur)_2(HCur)]$ and HCur for 1 h at room temperature in binding buffer (5% glycerol, 10 mM Tris-HCl (pH 8.0), 1 mM ethylenediaminetetraacetic acid (EDTA), 1 mM DTT, 20 mM KCl, and 50 μg/mL bovine serum albumin). Afterward, 4 μL of a native loading buffer (10% Ficoll 400, 10 mM Tris-HCl, pH 7.5, 50 mM EDTA, 0.25% bromophenol blue, and 0.25% xylene cyanol) was added. The reaction mixture was loaded onto 1% agarose gel with ethidium bromide using 0.5 times Tris borate−EDTA buffer (45 mM Tris-borate and 1 mM EDTA, pH 8.0). In this assay, a well-known DNA-binding peptide indolicidin was used as control.[73] The experiment was repeated on three different days. Similar results were obtained.

4.2.16. Hemolytic Assay. The ability of $[Mn^{II}(Cur)_2(HCur)]$ and HCur to induce hemolysis was assessed according to a protocol described earlier.[50,74] Briefly, fresh mice blood was collected and centrifuged at 1500 rpm for 10 min to remove blood plasma. The pellets of RBCs were washed thrice in 35 mM PBS buffer and resuspended in 4% v/v of the same buffer. In a 96-well plate, the compounds were serially diluted to a final volume of 100 μL in each well. Next, 100 μL of RBC suspension was added to each well and incubated at 37 °C for 1 h. The accompanying DMSO used to dissolve $[Mn^{II}(Cur)_2(HCur)]$ was also tested under identical conditions. After incubation, the plates were centrifuged at 1500 rpm for 10 min. The supernatant (20 μL) was added to 80 μL of PBS in a fresh 96-well plate. Hemoglobin release was measured at 414 nm using a Thermo Scientific Varioskan Flash Multiplate reader. For positive control, 0.1% Triton X-100 was used, and for negative control, RBC in PBS buffer was used. Percentage hemolysis was determined using eq 11.

$$\%\ \text{hemolysis} = [(\text{OD of sample} - \text{OD of PBS}) / (\text{OD of 0.1\% Triton X} - \text{OD of PBS})] \times 100 \quad (11)$$

The experiment was performed in accordance with the guidelines of CPCSEA (Committee for the Purpose of Control and Supervision of Experiments on Animals) and Institutional Animal Ethics Committee (IAEC-23/2018) of Jawaharlal Nehru University, New Delhi, India.

4.2.17. Cytotoxicity Assay. The cytotoxicities of HCur and $[Mn^{II}(Cur)_2(HCur)]$ on mouse fibroblast 3T3 cells were determined by an MTT assay.[50,74] Briefly, 3T3 cells were seeded in DMEM supplemented with 10% fetal bovine serum (FBS) and antibiotics (1× anti−anti) until they reached over 75% confluency. Cells were added to each well of a 24-well plate to a final count of 0.2×10^5 cells/well and incubated for 24 h at 37 °C in a 5% CO_2 incubator. After 24 h, the medium was removed. The cells were suspended in fresh media with 10% FBS and treated with 250 and 500 μM each of HCur and $[Mn^{II}(Cur)_2(HCur)]$ that were dissolved in DMSO. The final DMSO concentration in the reaction mixture was less than 0.5%. The DMSO concentration accompanying the compounds was tested under similar conditions. After 4 h of incubation in a 5% CO_2 atmosphere, the medium was carefully aspirated, and 1 mL of the MTT solution (0.1 mg/mL) was added to each well. The plate was incubated for 2 h at 37 °C in the dark in a 5% CO_2 atmosphere. Later, the plate was centrifuged at 1000 rpm for 5 min, and the supernatant was removed. Subsequently, 100 μL of DMSO was added to solubilize the formazan crystals formed by reduction of the tetrazolium salt. OD was measured at 570 nm, and the

https://dx.doi.org/10.1021/acsomega.9b04079
ACS Omega 2020, 5, 16342−16357

percentage survival was determined using eq 12. The assay was repeated on three separate days.

$$\text{Cell viability (\%)} = [(\text{OD}_{570} \text{ of sample}) / (\text{OD}_{570} \text{ of untreated control})] \times 100 \quad (12)$$

■ ASSOCIATED CONTENT

Supporting Information

The Supporting Information is available free of charge at https://pubs.acs.org/doi/10.1021/acsomega.9b04079.

Absorption spectra of curcumin and the Mn^{II} complex in DMSO; absorption spectra of Mn^{II} interacting with curcumin during determination of stoichiometry of complex formation; IR spectrum of curcumin; IR spectrum of $[Mn^{II}(Cur)_2(HCur)]$; TGA of $[Mn^{II}(Cur)_2(HCur)]$; keto−enol tautomerism of curcumin; optimized bond lengths for carbon−oxygen bonds of curcumin involved in coordination of Mn^{II}; behavior of curcumin and its Mn^{II} complex realized from a change in absorbance on being taken in PBS buffer or in PBS buffer with 10 μM DTT; behavior of curcumin and the Mn^{II} complex realized from a change in absorbance when taken in different bacterial growth mediums; double reciprocal plot for interaction of $[Mn^{II}(Cur)_2(HCur)]$ with calf thymus DNA; double reciprocal plot with y intercept = 1 for interaction of $[Mn^{II}(Cur)_2(HCur)]$ with calf thymus DNA; bacterial survival in logarithmic scale, indicating the antibacterial efficacy of $[Mn^{II}(Cur)_2(HCur)]$ and curcumin on *S. aureus* and *E. coli* cells; SEM images of *S. aureus* ATCC 29213 treated with either no compound or with curcumin, $[Mn^{II}(Cur)_2(HCur)]$, and gramicidin D to realize membrane permeabilization by the calcein leakage assay; equations related to dissociation of the three protons on curcumin; spectrophotometric titration of curcumin; mole ratio and Job's plots of continuous variation for curcumin with Mn^{II}; spectrophotometric titration of curcumin in the presence of Mn^{II}; and evaluation of the stability constant of the complex formed in solution (PDF)

■ AUTHOR INFORMATION

Corresponding Authors

Saurabh Das − *Department of Chemistry, Jadavpur University, Kolkata 700032, India;* orcid.org/0000-0002-0455-8760; Phone: +91 33 24572148; Email: dasrsv@yahoo.in; Fax: +91 33 24146223

Kasturi Mukhopadhyay − *School of Environmental Sciences, Jawaharlal Nehru University, New Delhi 110067, India;* orcid.org/0000-0002-6886-1080; Email: kasturim@mail.jnu.ac.in, kasturi26@hotmail.com

Authors

Tanmoy Saha − *Department of Chemistry, Jadavpur University, Kolkata 700032, India*

Prince Kumar − *School of Environmental Sciences, Jawaharlal Nehru University, New Delhi 110067, India;* orcid.org/0000-0002-8326-1382

Nayim Sepay − *Department of Chemistry, Jadavpur University, Kolkata 700032, India;* orcid.org/0000-0001-7702-3989

Durba Ganguly − *Department of Inorganic Chemistry, Indian Association for the Cultivation of Science, Kolkata 700032, India*

Kanchan Tiwari − *School of Environmental Sciences, Jawaharlal Nehru University, New Delhi 110067, India*

Complete contact information is available at: https://pubs.acs.org/10.1021/acsomega.9b04079

Author Contributions

‖T.S. and P.K. have equal contributions.

Notes

The authors declare no competing financial interest.

■ ACKNOWLEDGMENTS

P.K. and K.T. acknowledge UGC for an SRF and a non-NET fellowship, respectively. T.S. is grateful to the "Governing body" of Sri Aurobindo Institute of Education, Salt Lake, Kolkata for permission to pursue research leading to a Ph D degree. S.D. wishes to thank the RUSA 2.0 program of the Government of India, operating at Jadavpur University under which he received a "Research Support to Faculty Members" in the Research Thrust Area "Research in Sustainable Development", Sanction ref. no. R-11/438/19 dated 30.05.2019. Besides, S.D. is grateful to the DST-PURSE program of the Government of India for financial support to the Department of Chemistry, Jadavpur University, from where funds were used for this study (for purchase of chemicals). He acknowledges the support received from UGC, New Delhi, through funding of the research program on "Advanced Materials" as part of UPE II to Jadavpur University and also acknowledges the UGC-CAS II program operating at the Department of Chemistry, Jadavpur University, for financial support to purchase "Chemicals and Glassware". This work was also supported by financial grants to K.M. from DST-SERB (EMR/2016/001708) and DBT (BT/PR27737/MED/29/1265/2018). K.M. is also grateful for receiving funds from DST-PURSE (Phase-II) and UGC (UPE-II: ID 59), which came to Jawaharlal Nehru University. The authors wish to thank Dr. Partha Ray, Department of Chemistry, JU, for kindly providing the IR data of the complex, Dr. Shouvik Chattopadhyay, Department of Chemistry, JU, for some useful discussions on the structure of the complex, Ashok Sahu, Dr. Ruchita Pal, and Manu Vashistha, AIRF, JNU, for their help in acquisition of confocal microscopy, SEM, and TEM images, respectively. The authors are grateful to the three reviewers who reviewed the manuscript with extreme care and provided suggestions for its improvement.

■ ABBREVIATIONS

HCur, curcumin; Cur^-, monoanionic Curcumin; *S. aureus*, *Staphylococcus aureus*; *E. coli*, *Escherichia coli*

■ REFERENCES

(1) Aggarwal, B. B.; Sundaram, C.; Malani, N.; Ichikawa, H. Curcumin: the Indian solid gold. *The molecular Targets and Therapeutic Uses of Curcumin in Health and Disease*; Springer, Boston, MA, 2007; pp 1−75.

(2) Jurenka, J. S. Anti-inflammatory properties of curcumin, a major constituent of *Curcuma longa*: a review of preclinical and clinical research. *Altern. Med. Rev.* **2009**, *14*, 141−153.

(3) Ak, T.; Gülçin, İ. Antioxidant and radical scavenging properties of curcumin. *Chem.-Biol. Interact.* **2008**, *174*, 27−37.

(4) Prasad, S.; Aggarwal, B. B. Turmeric, the Golden Spice, From Traditional Medicine to Modern Medicine. In *Herbal Medicine: Biomolecular and Clinical Aspects*, 2nd ed.; Benzie, I. F. F., Wachtel-Galor, S., Eds.; CRC Press/Taylor & Francis: Boca Raton (FL), USA, 2011; Chapter 13.
(5) Sato, H.; Chuang, V. T. G.; Yamasaki, K.; Yamaotsu, N.; Watanabe, H.; Nagumo, K.; Anraku, M.; Kadowaki, D.; Ishima, Y.; Hirono, S.; Otagiri, M.; Maruyama, T. Differential effects of methoxy group on the interaction of curcuminoids with two major ligand binding sites of human serum albumin. *PLoS One* **2014**, *9*, No. e87919.
(6) Wilken, R.; Veena, M. S.; Wang, M. B.; Srivatsan, E. S. Curcumin: A review of anti-cancer properties and therapeutic activity in head and neck squamous cell carcinoma. *Mol. Cancer* **2011**, *10*, 12.
(7) Wanninger, S.; Lorenz, V.; Subhan, A.; Edelmann, F. T. Metal complexes of curcumin - synthetic strategies, structures and medicinal applications. *Chem. Soc. Rev.* **2015**, *44*, 4986−5002.
(8) Teow, S.-Y.; Liew, K.; Ali, S. A.; Khoo, A. S.-B.; Peh, S.-C. Antibacterial action of curcumin against *Staphylococcus aureus*: A Brief Review. *J. Trop. Med.* **2016**, *2016*, 1−10.
(9) Bicer, N.; Yildiz, E.; Yegani, A. A.; Aksu, F. Synthesis of curcumin complexes with iron(III) and manganese(II), and effects of curcumin-iron(III) on Alzheimer's disease. *New J. Chem.* **2018**, *42*, 8098−8104.
(10) Goel, A.; Kunnumakkara, A. B.; Aggarwal, B. B. Curcumin as "Curecumin": From kitchen to clinic. *Biochem. Pharmacol.* **2008**, *75*, 787−809.
(11) Neelofar, K.; Shreaz, S.; Rimple, B.; Muralidhar, S.; Nikhat, M.; Khan, L. A. Curcumin as a promising anticandidal of clinical interest. *Can. J. Microbiol.* **2011**, *57*, 204−210.
(12) Tyagi, P.; Singh, M.; Kumari, H.; Kumari, A.; Mukhopadhyay, K. Bactericidal activity of curcumin I is associated with damaging of bacterial membrane. *PLoS One* **2015**, *10*, No. e0121313.
(13) Sharma, R. A.; Steward, W. P.; Gescher, A. J. Pharmacokinetics and pharmacodynamics of curcumin. *Adv. Exp. Med. Biol.* **2007**, *595*, 453−470.
(14) Banerjee, S.; Prasad, P.; Hussain, A.; Khan, I.; Kondaiah, P.; Chakravarty, A. R. Remarkable photocytotoxicity of curcumin in HeLa cells in visible light and arresting its degradation on oxovanadium (IV) complex formation. *Chem. Commun.* **2012**, *48*, 7702−7704.
(15) Mitra, K.; Gautam, S.; Kondaiah, P.; Chakravarty, A. R. Platinum(II) Complexes of Curcumin Showing Photocytotoxicity in Visible Light. *Eur. J. Inorg. Chem.* **2017**, 1753−1763.
(16) Banerjee, S.; Prasad, P.; Khan, I.; Hussain, A.; Kondaiah, P.; Chakravarty, A. R. Mitochondria targeting Photocytotoxic Oxidovanadium(IV) Complexes of Curcumin and (Acridinyl)-dipyridophenazine in Visible Light. *Z. Anorg. Allg. Chem.* **2014**, *640*, 1195−1204.
(17) Wang, Y.-J.; Pan, M.-H.; Cheng, A.-L.; Lin, L.-I.; Ho, Y.-S.; Hsieh, C.-Y.; Lin, J.-K. Stability of curcumin in buffer solutions and characterization of its degradation products. *J. Pharm. Biomed. Anal.* **1997**, *15*, 1867−1876.
(18) Kharat, M.; Du, Z.; Zhang, G.; McClements, D. J. Physical and chemical stability of curcumin in aqueous solutions and emulsions: Impact of pH, temperature, and molecular environment. *J. Agric. Food Chem.* **2017**, *65*, 1525−1532.
(19) Refat, M. S. Synthesis and characterization of ligational behavior of curcumin drug towards some transition metal ions: chelation effect on their thermal stability and biological activity. *Spectrochim. Acta, Part A* **2013**, *105*, 326−337.
(20) Vajragupta, O.; Boonchoong, P.; Watanabe, H.; Tohda, M.; Kummasud, N.; Sumanont, Y. Manganese complexes of curcumin and its derivatives: evaluation for the radical scavenging ability and neuroprotective activity. *Free Radical Biol. Med.* **2003**, *35*, 1632−1644.
(21) Sumanont, Y.; Murakami, Y.; Tohda, M.; Vajragupta, O.; Watanabe, H.; Matsumoto, K. Effects of Manganese complexes of Curcumin and diacetylcurcumin on Kainic acid-induced neurotoxic responses in the rat hippocampus. *Biol. Pharm. Bull.* **2007**, *30*, 1732−1739.
(22) Mishra, M. K.; Sanphui, P.; Ramamurty, U.; Desiraju, G. R. Solubility-hardness correlation in molecular crystals: Curcumin and sulfathiazole polymorphs. *Cryst. Growth Des.* **2014**, *14*, 3054−3061.
(23) Caruso, F.; Rossi, M.; Benson, A.; Opazo, C.; Freedman, D.; Monti, E.; Gariboldi, M. B.; Shaulky, J.; Marchetti, F.; Pettinari, R.; Pettinari, C. Ruthenium−arene complexes of curcumin: X-ray and density functional theory structure, synthesis, and spectroscopic characterization, *in vitro* antitumor activity, and DNA docking studies of (*p*-cymene) Ru(curcuminato)chloro. *J. Med. Chem.* **2012**, *55*, 1072−1081.
(24) Leung, M. H. M.; Harada, T.; Kee, T. W. Delivery of curcumin and medicinal effects of the copper(II)-curcumin complexes. *Curr. Pharm. Des.* **2013**, *19*, 2070−2083.
(25) Pröhl, M.; Schubert, U. S.; Weigand, W.; Gottschaldt, M. Metal complexes of curcumin and curcumin derivatives for molecular imaging and anticancer therapy. *Coord. Chem. Rev.* **2016**, *307*, 32−41.
(26) Raygada, J. L.; Levine, D. P. Methicillin-resistant *Staphylococcus aureus*: A growing risk in the hospital and in the community. *Am. Health Drug Benefits* **2009**, *2*, 86−95.
(27) Bakthavatsalam, S.; Das Sharma, S.; Sonawane, M.; Thirumalai, V.; Datta, A. A zebrafish model of manganism reveals reversible and treatable symptoms that are independent of neurotoxicity. *Dis. Models Mech.* **2014**, *7*, 1239−1251.
(28) Borsetti, F.; Dal Piaz, F.; D'Alessio, F.; Stefan, A.; Brandimarti, R.; Sarkar, A.; Datta, A.; Montón Silva, A.; den Blaauwen, T.; Alberto, M.; Spisni, E.; Hochkoeppler, A. Manganese is a *Deinococcus radiodurans* growth limiting factor in rich culture medium. *Microbiology* **2018**, *164*, 1266−1275.
(29) Nakamoto, K. *Infrared and Raman spectra of inorganic and coordination compounds, Part A: Theory and Applications in Inorganic Chemistry*, 6th ed.; Wiley-Interscience: New York, 2009.
(30) Deb, P.; Ghose, M.; Sepay, N.; Maiti, S.; Mukherjea, K. K. Synthesis, characterization, theoretical simulation, and DNA-nuclease activity of a newly synthesized Mn−oximato complex. *J. Coord. Chem.* **2018**, *71*, 3250−3265.
(31) Mary, C. P. V.; Vijayakumar, S.; Shankar, R. Metal chelating ability and antioxidant properties of Curcumin-metal complexes - A DFT approach. *J. Mol. Graphics Modell.* **2018**, *79*, 1−14.
(32) Go, Y.-M.; Jones, D. P. Redox Compartmentalization in eukaryotic cells. *Biochim. Biophys. Acta* **2008**, *1780*, 1273−1290.
(33) Das, P.; Bhattacharya, D.; Karmakar, P.; Das, S. Influence of ionic strength on the interaction of THA and its Cu(II) complex with DNA helps to explain studies on various breast cancer cells. *RSC Adv.* **2015**, *5*, 73099−73111.
(34) Ghosh, S.; Kundu, P.; Paul, B. K.; Chattopadhyay, N. Binding of an anionic fluorescent probe with calf thymus DNA and effect of salt on the probe-DNA binding: a spectroscopic and molecular docking investigation. *RSC Adv.* **2014**, *4*, 63549−63558.
(35) Saha, M.; Singha, S.; Chakraborty, M.; Mazumdar, S.; Kumar, S.; Karmakar, P.; Das, S. Characterization of a MnII complex of alizarin suggests attributes explaining a superior anticancer activity: A comparison with anthracycline drugs. *Polyhedron* **2019**, *173*, 114104.
(36) Guin, P. S.; Mandal, P. C.; Das, S. The binding of a hydroxy-9,10-anthraquinone Cu^{II} complex to calf thymus DNA: Electrochemistry and UV/Vis spectroscopy. *ChemPlusChem* **2012**, *77*, 361−369.
(37) Das, P.; Jain, C. K.; Dey, S. K.; Saha, R.; Chowdhury, A. D.; Roychoudhury, S.; Kumar, S.; Majumder, H. K.; Das, S. Synthesis, crystal structure, DNA interaction and *in vitro* anticancer activity of a Cu(II) complex of purpurin: dual poison for human DNA topoisomerase I and II. *RSC Adv.* **2014**, *4*, 59344−59357.
(38) Mandal, B.; Singha, S.; Dey, S. K.; Mazumdar, S.; Mondal, T. K.; Karmakar, P.; Kumar, S.; Das, S. Synthesis, crystal structure from PXRD of a $Mn^{II}(purp)_2$ complex, interaction with DNA at different temperatures and pH and lack of stimulated ROS formation by the complex. *RSC Adv.* **2016**, *6*, 51520−51532.

https://dx.doi.org/10.1021/acsomega.9b04079
ACS Omega 2020, 5, 16342−16357

(39) Saha, M.; Nandy, P.; Chakraborty, M.; Das, P.; Das, S. The importance of pK_a in an analysis of the interaction of compounds with DNA. *Biophys. Chem.* **2018**, *236*, 15−21.
(40) Scatchard, G. The attractions of proteins for small molecules and ions. *Ann. N.Y. Acad. Sci.* **1949**, *51*, 660−672.
(41) Huang, C.-H.; Mong, S.; Crooke, S. T. Interactions of a new antitumor antibiotic BBM-928A with deoxyribonucleic acid. Bifunctional intercalative binding studied by fluorometry and viscometry. *Biochemistry* **1980**, *19*, 5537−5542.
(42) Ardan, T.; Kovačeva, J.; Čejková, J. Comparative histochemical and immunohistochemical study on xanthine oxidoreductase/xanthine oxidase in mammalian corneal epithelium. *Acta Histochem.* **2004**, *106*, 69−75.
(43) Hille, R.; Hall, J.; Basu, P. The mononuclear molybdenum enzymes. *Chem. Rev.* **2014**, *114*, 3963−4038.
(44) Lyngsie, G.; Krumina, L.; Tunlid, A.; Persson, P. Generation of hydroxyl radicals from reactions between a dimethoxyhydroquinone and iron oxide nanoparticles. *Sci. Rep.* **2018**, *8*, 10834.
(45) Gligorovski, S.; Strekowski, R.; Barbati, S.; Vione, D. Environmental implications of hydroxyl radicals ($^{\bullet}OH$). *Chem. Rev.* **2015**, *115*, 13051−13092.
(46) Thomas, C.; Mackey, M. M.; Diaz, A. A.; Cox, D. P. Hydroxyl radical is produced via the Fenton reaction in submitochondrial particles under oxidative stress: Implications for diseases associated with iron accumulation. *Redox Rep.* **2009**, *14*, 102−108.
(47) Gutteridge, J. M. C.; Halliwell, B. The deoxyribose assay: an assay both for 'free' hydroxyl radical and for site-specific hydroxyl radical production. *Biochem. J.* **1988**, *253*, 932−933.
(48) Luqman, S.; Kumar, R. Importance of deoxyribose degradation assay for evaluating hydroxyl radical scavenging activity of punica extract. *Int. J. Food Prop.* **2012**, *15*, 942−948.
(49) Joshi, S.; Mumtaz, S.; Singh, J.; Pasha, S.; Mukhopadhyay, K. Novel miniature membrane active lipopeptidomimetics against planktonic and biofilm embedded methicillin-resistant *Staphylococcus aureus*. *Sci. Rep.* **2018**, *8*, 1021.
(50) Singh, M.; Mukhopadhyay, K. C-Terminal amino acids of alpha-melanocyte-stimulating hormone are requisite for its antibacterial activity against *Staphylococcus aureus*. *Antimicrob. Agents Chemother.* **2011**, *55*, 1920−1929.
(51) Ouberai, M.; El Garch, F.; Bussiere, A.; Riou, M.; Alsteens, D.; Lins, L.; Baussanne, I.; Dufrêne, Y. F.; Brasseur, R.; Decout, J.-L.; Mingeot-Leclercq, M.-P. The *Pseudomonas aeruginosa* membranes: A target for a new amphiphilic aminoglycoside derivative? *Biochim. Biophys. Acta, Biomembr.* **2011**, *1808*, 1716−1727.
(52) Kumar, P.; Kandi, S. K.; Manohar, S.; Mukhopadhyay, K.; Rawat, D. S. Monocarbonyl Curcuminoids with Improved Stability as Antibacterial Agents against *Staphylococcus aureus* and Their Mechanistic Studies. *ACS Omega* **2019**, *4*, 675−687.
(53) Koo, S.-P.; Bayer, A. S.; Yeaman, M. R. Diversity in Anti staphylococcal Mechanisms among Membrane-Targeting Antimicrobial Peptides. *Infect. Immun.* **2001**, *69*, 4916−4922.
(54) Xiong, Y.-Q.; Yeaman, M. R.; Bayer, A. S. *In Vitro* Antibacterial Activities of Platelet Microbicidal Protein and Neutrophil Defensin against *Staphylococcus aureus* Are Influenced by Antibiotics Differing in Mechanism of Action. *Antimicrob. Agents Chemother.* **1999**, *43*, 1111−1117.
(55) Glenn, J. K.; Akileswaran, L.; Gold, M. H. Mn(II) oxidation is the principal function of the extracellular Mn-peroxidase from phanerochaete chrysosporium. *Arch. Biochem. Biophys.* **1986**, *251*, 688−696.
(56) Tønnesen, H. H.; Másson, M.; Loftsson, T. Studies of curcumin and curcuminoids. XXVII. Cyclodextrin complexation: solubility, chemical and photochemical stability. *Int. J. Pharm.* **2002**, *244*, 127−135.
(57) Bernabé-Pineda, M.; Ramírez-Silva, M. T.; Romero-Romo, M.; González-Vergara, E.; Rojas-Hernández, A. Determination of acidity constants of curcumin in aqueous solution and apparent rate constant of its decomposition. *Spectrochim. Acta, Part A* **2004**, *60*, 1091−1097.
(58) Priyadarsini, K. The Chemistry of Curcumin: From Extraction to Therapeutic Agent. *Molecules* **2014**, *19*, 20091−20112.
(59) Das, P.; Jain, C. K.; Roychoudhury, S.; Majumder, H. K.; Das, S. Design, Synthesis and *in vitro* Anticancer Activity of a Cu(II) Complex of Carminic Acid: A Novel Small Molecule Inhibitor of Human DNA Topoisomerase I and Topoisomerase II. *ChemistrySelect* **2016**, *1*, 6623−6631.
(60) Mukherjee Chatterjee, S.; Jain, C. K.; Singha, S.; Das, P.; Roychoudhury, S.; Majumder, H. K.; Das, S. Activity of Co^{II}-Quinalizarin: A novel analogue of anthracycline-based anticancer agents targets human DNA topoisomerase, whereas quinalizarin itself acts via formation of semiquinone on acute lymphoblastic leukemia MOLT-4 and HCT 116 cells. *ACS Omega* **2018**, *3*, 10255−10266.
(61) (a) Liu, T.; Zhang, H.-X.; Xia, B.-H. Theoretical studies on structures and spectroscopic properties of a series of novel cationic [trans-(C/N)2Ir(PH3)2]+ (C/N = ppy, bzq, ppz, dfppy). *J. Phys. Chem. A* **2007**, *111*, 8724−8730. (b) Zhou, X.; Zhang, H.-X.; Pan, Q.-J.; Xia, B.-H.; Tang, A.-C. Theoretical Studies of the Spectroscopic Properties of [Pt(trpy)C⋮CR]+(trpy = 2,2′,6′,2″-Terpyridine; R = H, CH2OH, and C6H5). *J. Phys. Chem. A* **2005**, *109*, 8809−8818. (c) Zhou, X.; Ren, A.-M.; Feng, J.-K. Theoretical studies on the ground states in (M=Fe, Ru, Os) and excited states in using density functional theory. *J. Organomet. Chem.* **2005**, *690*, 338−347.
(62) Frisch, M. J.; Trucks, G. W.; Schlegel, H. B.; Scuseria, G. E.; Robb, M. A.; Cheeseman, J. R.; Scalmani, G.; Barone, V.; Mennucci, B.; Petersson, G. A.; Nakatsuji, H.; Caricato, M.; Li, X.; Hratchian, H. P.; Izmaylov, A. F.; Bloino, J.; Zheng, G.; Sonnenberg, J. L.; Hada, M.; Ehara, M.; Toyota, K.; Fukuda, R.; Hasegawa, J.; Ishida, M.; Nakajima, T.; Honda, Y.; Kitao, O.; Nakai, H.; Vreven, T.; Montgomery, J. A., Jr.; Peralta, J. E.; Ogliaro, F.; Bearpark, M.; Heyd, J. J.; Brothers, E.; Kudin, K. N.; Staroverov, V. N.; Kobayashi, R.; Normand, J.; Raghavachari, K.; Rendell, A.; Burant, J. C.; Iyengar, S. S.; Tomasi, J.; Cossi, M.; Rega, N.; Millam, J. M.; Klene, M.; Knox, J. E.; Cross, J. B.; Bakken, V.; Adamo, C.; Jaramillo, J.; Gomperts, R.; Stratmann, R. E.; Yazyev, O.; Austin, A. J.; Cammi, R.; Pomelli, C.; Ochterski, J. W.; Martin, R. L.; Morokuma, K.; Zakrzewski, V. G.; Voth, G. A.; Salvador, P.; Dannenberg, J. J.; Dapprich, S.; Daniels, A. D.; Farkas, Ö.; Foresman, J. B.; Ortiz, J. V.; Cioslowski, J.; Fox, D. J. *Gaussian 09*, Revision A.1; Gaussian, Inc.; Wallingford, CT, 2009.
(63) Becke, A. D. Density-functional exchange-energy approximation with correct asymptotic behavior. *Phys. Rev. A: At., Mol., Opt. Phys.* **1988**, *38*, 3098.
(64) Leung, K.; Rempe, S. B.; Schultz, P. A.; Sproviero, E. M.; Batista, V. S.; Chandross, M. E.; Medforth, C. J. Density functional theory and DFT+U study of transition metal porphines adsorbed on Au(111) surfaces and effects of applied electric fields. *J. Am. Chem. Soc.* **2006**, *128*, 3659−3668.
(65) Lee, C.; Yang, W.; Parr, R. G. Development of the Colle-Salvetti correlation-energy formula into a functional of the electron density. *Phys. Rev. B: Condens. Matter Mater. Phys.* **1988**, *37*, 785−789.
(66) (a) Hay, P. J.; Wadt, W. R. *Ab initio* effective core potentials for molecular calculations. Potentials for the transition metal atoms Sc to Hg. *J. Chem. Phys.* **1985**, *82*, 270−283. (b) Handy, N. C.; Schaefer, H. F. On the evaluation of analytic energy derivatives for correlated wave functions. *J. Chem. Phys.* **1984**, *81*, 5031−5033. (c) Nicklass, A.; Dolg, M.; Stoll, H.; Preuss, H. *Ab initio* energy-adjusted pseudopotentials for the noble gases Ne through Xe: Calculation of atomic dipole and quadrupolepolarizabilities. *J. Chem. Phys.* **1995**, *102*, 8942−8952.
(67) Yanai, T.; Tew, D. P.; Handy, N. C. A new hybrid exchange-correlation functional using the coulomb-attenuating method (CAM-B3LYP). *Chem. Phys. Lett.* **2004**, *393*, 51−57.
(68) O'boyle, N. M.; Tenderholt, A. L.; Langner, K. M. Cclib: A library for package-independent computational chemistry algorithms. *J. Comput. Chem.* **2008**, *29*, 839−845.
(69) Aggarwal, S.; Ichikawa, H.; Takada, Y.; Sandur, S. K.; Shishodia, S.; Aggarwal, B. B. Curcumin (Diferuloylmethane) Down-Regulates Expression of Cell Proliferation and Antiapoptotic and Metastatic Gene Products through Suppression of IκBα Kinase and Akt Activation. *Mol. Pharmacol.* **2006**, *69*, 195−206.

https://dx.doi.org/10.1021/acsomega.9b04079
ACS Omega 2020, 5, 16342−16357

(70) Robak, J.; Gryglewski, R. J. Flavonoids are scavengers of superoxide anions. *Biochem. Pharmacol.* **1988**, *37*, 837−841.
(71) Mishra, B.; Priyadarsini, K. I.; Kumar, M. S.; Unnikrishnan, M. K.; Mohan, H. Effect of O-glycosilation on the antioxidant activity and free radical reactions of a plant flavonoid, chrysoeriol. *Bioorg. Med. Chem.* **2003**, *11*, 2677−2685.
(72) Singh, M.; Gadepalli, R.; Dhawan, B.; Mukhopadhyay, K. Combination of alpha-melanocyte stimulating hormone with conventional antibiotics against methicillin resistant *Staphylococcus aureus*. *PLoS One* **2013**, *8*, No. e73815.
(73) Hsu, C.-H.; Chen, C.; Jou, M. L.; Lee, A. Y. L.; Lin, Y. C.; Yu, Y. P.; Wu, S. H. Structural and DNA-binding studies on the bovine antimicrobial peptide, indolicidin: Evidence for multiple conformations involved in binding to membranes and DNA. *Nucleic Acids Res.* **2005**, *33*, 4053−4064.
(74) Singh, J.; Joshi, S.; Mumtaz, S.; Maurya, N.; Ghosh, I.; Khanna, S.; Natarajan, V. T.; Mukhopadhyay, K. Enhanced Cationic Charge is a Key Factor in Promoting Staphylocidal Activity of α-Melanocyte Stimulating Hormone via Selective Lipid Affinity. *Sci. Rep.* **2016**, *6*, 31492.

https://dx.doi.org/10.1021/acsomega.9b04079
ACS Omega 2020, 5, 16342−16357

Journal of Molecular Structure 1221 (2020) 128732

Contents lists available at ScienceDirect

Journal of Molecular Structure

journal homepage: http://www.elsevier.com/locate/molstruc

Spectroscopy driven DFT computation for a structure of the monomeric Cu^{2+}-Curcumin complex and thermodynamics driven evaluation of its binding to DNA: Pseudo-binding of Curcumin to DNA

Tanmoy Saha [a], Soumen Singha [b], Sanjay Kumar [b], Saurabh Das [a, *]

[a] Department of Chemistry (Inorganic Section), Jadavpur University, Kolkata, 700032, India
[b] Department of Physics, Jadavpur University, Kolkata, 700032, India

ARTICLE INFO

Article history:
Received 25 March 2020
Received in revised form
17 June 2020
Accepted 18 June 2020
Available online 25 June 2020

Keywords:
Curcumin
Cu^{II}
DFT
DNA binding
ΔH
ΔS
ΔG

ABSTRACT

In an attempt to overcome limitations of Curcumin from being an important molecule in biology and medicine, a monomeric complex of Cu^{II} [Cu(Cur)($OCOCH_3$)(H_2O)] was prepared. Physico-chemical studies in solution using copper acetate and Curcumin indicate formation of a 1:2 Cu^{II}:Curcumin species. However, attempts to prepare it always led to the formation of a 1:1 Cu^{II}:Curcumin species, if Cu^{II}-acetate was used as the starting material. In the absence of a single crystal or an appropriate powder X ray diffraction data that would allow solving of the structure, it was arrived at by spectroscopy guided DFT calculations. Unlike Curcumin, the prepared complex was stable under physiological conditions, an advance achieved through complex formation. Effective binding of the complex to DNA with an ability to enhance cellular uptake owing to the presence of Cu^{II} are other benefits of complex formation that might increase its cytotoxic potential. The complex has a reasonably strong affinity for DNA realized from binding constant values obtained with calf thymus DNA at different temperatures in the range 25 °C −35 °C. This enabled an evaluation of thermodynamic parameters (ΔH, ΔS and ΔG), that helped in determining the mode of binding between the complex and DNA as realized from a correlation of thermodynamic signatures to binding types. The study may be considered a case of pseudo-binding of Curcumin to DNA since the complex containing a Curcumin bound the metal ion does not dissociate in solution under physiological conditions, i.e. remains as one unit. Hence binding of the complex to DNA is also the binding of Curcumin to it present as one "single unit", a major advancement based on a bio-physical approach. Besides, aspects like stability of the complex in solution, prevention of degradation of Curcumin in aqueous buffer or biological milieu, binding with mammalian DNA are other aspects that are significant for use of the complex on biological targets.

© 2020 Elsevier B.V. All rights reserved.

1. Introduction

Curcumin, that has been comprehensively studied in the last few decades is a well-known lipophilic poly-phenol compound having a lot of potential [1–10]. However, the molecule suffers from several problems that has held it back from occupying the position it should have, given its pharmacological performance [1–10]. Various studies have shown its pharmacological properties and therapeutic utilities on different diseased conditions [1,2,4–9,11]. *In vivo* studies and clinical trials have indicated its safety, being well-tolerated having minimal toxicity even at doses as high as 12g/day over a period of 3 months [7]. However, in spite of such excellent pharmacological reports, the molecule has not been able to show its full potential owing to low aqueous solubility and poor physiological stability (being prone to degradation in physiological buffer under reducing conditions) [12–16]. The problem is further aggravated by the fact that under physiological conditions Curcumin does not remain a single molecule; it forms several smaller fragments in solution [17]. Therefore, whatever pharmacological reports are available on Curcumin, it would be extremely difficult to say whether these are due to Curcumin present in solution as "one unit" or they are a cumulative effect of all fragments formed from it. While most researchers concentrating on the pharmacological or medicinal aspects of the molecule have remained silent on this very important issue, a report by a group whose focus we thought was

* Corresponding author.
E-mail address: dasrsv@yahoo.in (S. Das).

https://doi.org/10.1016/j.molstruc.2020.128732
0022-2860/© 2020 Elsevier B.V. All rights reserved.

not only pharmacology, categorically showed that under physiological conditions the molecule breaks down to result in the formation of a number of small compounds which they identified using HPLC [17]. Reading their report and other reports on the performance of Curcumin in aqueous solution or in biological media, one wonders if these fragments or at least some of them, that are formed from Curcumin, be added in the correct proportion in which they are obtained in solution upon degradation (due to hydrolysis or otherwise), would it show the same efficacy as that of Curcumin taken in aqueous solution [1,2,4,6–12,17]. If the paper on the identification of degraded products of Curcumin separated by HPLC were to be believed then Curcumin cannot be present as a "single-unit" either in aqueous solution or in cellular medium [17]. In fact, we too have data showing there is a gradual decrease in the absorbance of Curcumin when dissolved in aqueous buffer or in cellular media (Fig. S1, S I). Since degradation products of Curcumin are colourless, there is no interference to the absorbance of Curcumin from any of the formed products in solution followed over the wavelength range 400 nm–450 nm. A decreasing trend in its absorbance when dissolved in aqueous buffer or cellular media clearly indicates its breaksdown. Therefore, complications like low solubility, low bio-availability and the fact that the molecule is never present in solution as a "single-unit" raises questions whether it is Curcumin or its degradation products that do the work in biology [1–4,6–10]. Some of these questions remain unanswered, requiring attention. Hence, to understand things better it is important in the first place to have Curcumin in solution as a "single-unit", i. e. preventing its degradation before it interacts with a biological target and then to think of gradually improving its bioavailability. This may be achieved through complex formation. Metal bound Curcumin remains a "single-unit" and the presence of a metal ion should assist in cellular uptake, also taking care of issues like solubility etc. [11,18–22] With these thoughts in mind we ventured to prepare a complex of Cu^{II} with Curcumin. Our physicochemical experiments using Cu^{II}-acetate and Curcumin suggested formation of a 1:2 complex but when we tried preparing it we always obtained a 1:1 species which some researchers reported earlier [11,23]. We performed certain studies with it since we realized that such a complex would actually resemble Curcumin enabling us to compare with it; the 1:2 species having two Curcumins would not be a correct comparison since there are no reports showing Curcumin dimerizes in biological media. The prepared complex was stable in aqueous solution or in biological cellular media suggesting Curcumin remains a "single-unit" bound to Cu^{II} which is very significantly important (Fig. S1, S I).

2. Experimental

2.1. Materials

2.1.1. Chemicals

Curcumin [≥ 94% (curcuminoid content), ≥ 80% (Curcumin)] procured from Sigma-Aldrich was recrystallized and further purified. It was then dissolved in methanol and stored very carefully in the dark. Calf thymus DNA, purchased from Sisco Research Laboratories, India was dissolved in millipore water containing 120 mM NaCl, 35 mM KCl and 5 mM $CaCl_2$. Its concentration was determined by measuring its absorbance at 260 nm considering molar extinction coefficient at that wavelength to be 6600 M^{-1} cm^{-1}. From the ratio of the values of absorbance of calf thymus DNA at 260 and 280 nm it was decided that the DNA was sufficiently free of protein, requiring no further purification. The calf thymus DNA was also characterized by recording its CD spectrum at 260 nm using a CD spectropolarimeter (J815, JASCO, Japan). Copper^{II}-acetate monohydrate, sodium nitrate (AR), sodium dihydrogen phosphate (AR) and disodium hydrogen phosphate (AR) were purchased from Merck, India. Millipore water was used for preparing all solutions.

2.2. Methods

2.2.1. Determination of stoichiometry of complex formation by the mole ratio method

Stoichiometry of complex formation was ascertained by mixing different volumes of equimolar concentrations of copper^{II}-acetate and Curcumin. In the mole ratio method, concentration of Cu^{II} was kept constant while Curcumin was varied. Absorbance recorded at 428 nm was plotted against $(T_L/T_M)_{TM}$ (Fig. 1) where T_M and T_L are concentrations of Cu^{II} and Curcumin respectively in each experimental solution. Two straight lines were obtained whose intersection provides the ratio in which Curcumin binds to Cu^{II}.

2.2.2. Preparation of [Cu(Cur)($OCOCH_3$)(H_2O)]

Going by the information obtained from the stoichiometry study, 0.76 mmol (0.2799 gm) Curcumin was dissolved in 15 mL deaerated acetonitrile-ethanol mixture (1:2). The solution was neutralized by adding 0.75 mmol (0.104 mL) triethylamine followed by addition of 0.38 mmol (0.0758 gm) $Cu(OCOCH_3)_2.H_2O$ in 15 mL deaerated ethanol-water mixture (1:1). Pure argon gas was passed through the reaction mixture to create an inert atmosphere. The whole set up was stirred for 2 h and subsequently refluxed for a further 3 h under inert conditions. A greenish-black precipitate was isolated. It was washed with chloroform, diethyl ether, ethanol, THF and acetonitrile in that sequence depending upon the solubility of Curcumin in each of the solvents used. Mass spectrum of the product reveals a molecular ion peak at $m/z = 507.3225$, suggesting the formula to be [Cu(Cur)($OCOCH_3$)(H_2O)]. Hence, although a 1:2 Cu^{II}-Curcumin complex was predicted from physico-chemical experiments, an attempted preparation of the complex with Cu^{II} taken as copper acetate and Curcumin in the ratio 1:2, always resulted in a 1:1 species. The other two ligands being acetate and water. Since physico-chemical studies predict formation of a 1:2 complex, we attempted the preparation several times but each time a 1:1 Cu^{II}-Curcumin species was obtained if copper acetate was used as the source of Cu^{II} in the preparation. λ_{max} for the complex was detected at 426 nm in DMSO which tallied appreciably with a

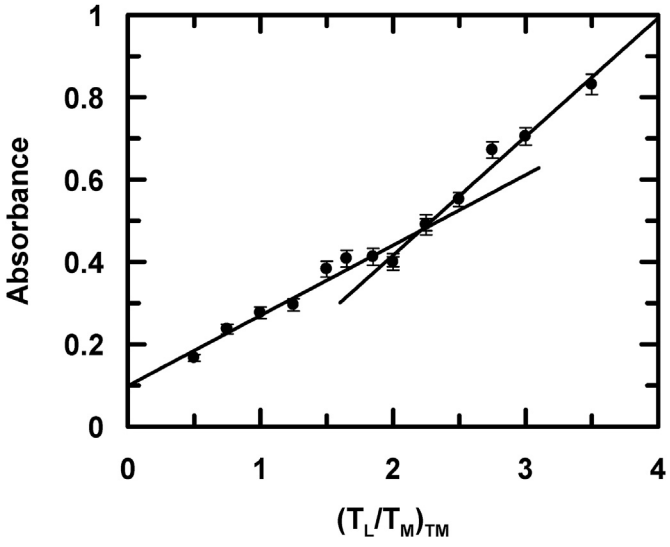


Fig. 1. Plot showing a gradual variation in absorbance at 428 nm for change in concentration of Curcumin for a fixed concentration of Cu^{II} (= 10 μM) at pH ~7.4; [$NaNO_3$] = 0.01 M, Temperature = 298 K.

report of 1:1 Cu^{II}-Curcumin in the literature [23]. We then attempted preparing the complex by mixing the starting materials [Cu^{II} acetate and Curcumin] in the ratio 1:1 taking 0.75 mmol (0.2762 gm) Curcumin in 15 mL deaerated acetonitrile-ethanol mixture (1:2), neutralizing it with 0.75 mmol (0.104 mL) triethylamine and subsequently adding 0.75 mmol (0.1497 gm) $Cu(O\text{-}COCH_3)_2.H_2O$ in 15 mL deaerated ethanol-water mixture (1:1). Argon gas was passed through the mixture to create an inert atmosphere. As earlier, the reaction mixture was stirred for 2 h and refluxed for a further 3 h. An identical precipitate was isolated. It was washed in the order of solvents as was done earlier (mentioned above). Mass spectrum and UV–Vis spectrum were recorded and found to be same as that obtained when Cu^{II} acetate and Curcumin were mixed in the ratio 1:2.

2.2.3. Quantum chemical calculation

2.2.3.1. Perspective. Since, inspite of our best efforts we could not isolate single crystals of the prepared complex, a structure suggesting its coordination environment was not possible. The product being slightly amorphous prevented solving of the structure from powder X ray diffraction data that we had obtained of it. Hence, a model for the coordination environment around Cu^{II} was visualized from spectroscopic and mass spectrometric measurements. Later, refinement of the model was done by simulating an UV–vis absorption spectrum theoretically and comparing it with an experimental one.

2.2.3.2. Computational methodology. Computational analysis of a proposed structure was performed on the basis of a model structure optimized in ground state geometry in gaseous state and in DMSO. All quantum-chemical calculations were performed using Gaussian 09 [24]. The system being an open-shell one (having odd number of electrons), the unrestricted B3LYP level of theory (UB3LYP) [25] with standard 6-311+G basis set for C, H and O atoms in conjunction with SDD effective core potential basis set [26] for the Cu atom were used. Zero imaginary vibration frequency confirms stability of the optimized geometry. To correctly describe the interaction of the biologically important chemical species with the Cu^{2+} ion in solvent medium long range dispersion correction was added by Grimmes dispersion correction with Becke –Jhonson Damping (GD3BJ) [27].

Again, the half-and-half functional BHandHLYP [28] is found to yield a comparatively better result for treating the open shell Cu^{2+} complexes with biological moities [29,30]. The theoretical thermochemical parameters related to interaction of Cu^{2+} with Curcumin i. e. the interaction energies ΔH and ΔG were estimated from Eq. (1) referring to the simplified atomic level representation of the reaction scheme:

$$Cu(acetate)_2 + Curcumin + H_2O \rightarrow Cu^{II} - complex + acetic\ acid. \quad (1)$$

$$\Delta H \text{ or } \Delta G = [P_{Et}] - [R_{Et}]$$

where, P_{Et} and R_{Et} are the sum of the ZPE corrected electronic energies or free energies of products and reactants respectively. For these calculations each of the reaction species were treated with both B3LYP-GD3BJ and BHandHLYP functionals in conjuction with the above mentioned split basis set for the elements in solvent DMSO medium. The optimized geometries at the true minima were confirmed from the non-negative frequency values obtained from frequency calculations. Also the zero point vibrational energy corrections (ZPVE) to the electronic energies were obtained from the frequency calculations.

Time-dependent density functional theory (TDDFT) was employed to compute electronic (UV–vis) absorption of the complex [31] on the basis of ground-state geometry optimized in DMSO (media) using conductor-like polarizable continuum (CPCM) model [32]. Frontier Molecular Orbital analysis was carried out using Gauss View and MO composition analysis was done with GaussSum program [33].

2.2.4. Interaction of[Cu(Cur)(OCOCH$_3$)(H$_2$O)] with calf thymus DNA

Since Curcumin dissolved in phosphate buffer shows a change in absorbance (Fig. S1, S I) observed by monitoring it with time, DNA binding study with Curcumin was not performed as one would not be sure whether Curcumin or any of its degraded products were binding to DNA. Besides, with a continuously changing absorbance for Curcumin itself, any change in absorbance due to the addition of DNA cannot be correctly attributed to that of binding with DNA. However, when the complex was dissolved in 150 mM NaCl, 35 mM KCl, 5 mM $CaCl_2$ in phosphate buffer (pH 7.4) and the solution monitored for the next 3 h, unlike Curcumin, it was found to be stable (Fig. S1, S I). Hence, titration of the complex with calf thymus DNA was possible. The change in absorbance following the addition of calf thymus was followed on JASCO V-630 spectrophotometer, Japan.

$$L + DNA \rightleftharpoons L - DNA \qquad K_d = \frac{[L][DNA]}{[L - DNA]} \quad (2)$$

Eq. (2) is an equilibrium showing interaction of the complex with DNA; L representing the complex. Reciprocal of K_d provides the apparent binding constant (K_{app}) [34–38]. Eq. (3) is generated from Eq. (2) where reciprocal of the change in absorbance was plotted against reciprocal of ($C_D - C_0$). C_D refers to concentration of calf thymus DNA and C_0, the concentration of the complex. Using Eq. (3), ΔA_{max} and K_{app} ($= K_d^{-1}$) were determined from the intercept and slope respectively.

$$\frac{1}{\Delta A} = \frac{1}{\Delta A_{max}} + \frac{K_d}{\Delta A_{max}(C_D - C_0)} \quad (3)$$

ΔA denotes change in absorbance of the complex at pH = 7.4. For each titration, ΔA_{max} indicates the maximum possible change in absorbance.

$$K_d = \frac{\left[C_0 - \left(\frac{\Delta A}{\Delta A_{max}}\right)C_0\right]\left[C_D - \left(\frac{\Delta A}{\Delta A_{max}}\right)C_0\right]}{\left(\frac{\Delta A}{\Delta A_{max}}\right)C_0} \quad (4)$$

$$C_0\left(\frac{\Delta A}{\Delta A_{max}}\right)^2 - (C_0 + C_D + K_d)\left(\frac{\Delta A}{\Delta A_{max}}\right) + C_D = 0 \quad (5)$$

$\Delta A/\Delta A_{max}$ was subsequently plotted against C_D. Eqs. (4) and (5) were used to fit the data by non-linear square fit analysis providing another value for the apparent binding constant [34–38]. A plot of $\Delta A/\Delta A_{max}$ against ratio of concentration of calf thymus DNA to complex provides two straight lines, the intersection of which provides n_b (number of nucleotides bound to the complex). Evaluated apparent binding constants (K_{app}) when multiplied with n_b provide overall binding constants (K*). The data obtained from a titration of the complex with calf thymus DNA was also analyzed by a modified form of the Scatchard equation [Eq. (6)] [39]. The overall binding constant (K*) and site size n ($= n_b^{-1}$ = number of bound complex per nucleotide) was determined.

$$r/C_f = K'(n - r) \quad (6)$$

$r = C_b/C_D$; C_b denotes concentration of the bound form of the complex while C_f denotes the free form.

2.2.4.1. Titration of [Cu(Cur)(OCOCH$_3$)(H$_2$O)] with calf thymus DNA at different temperatures and evaluation of thermodynamic parameters. The complex was titrated with calf thymus DNA at four different temperatures at constant pH (~7.4) and constant ionic strength ([NaCl] = 150 mM) of the medium. The temperature was controlled using peltier TCC controller (Shimadzu) connected to a UV 1800 Shimadzu UV spectrophotometer Model TCC-240A, Japan. Thermodynamic parameters, ΔH (van't Hoff enthalpy), ΔS (entropy) and ΔG (free energy) were determined using Eqs. (7)–(9).

$$\ln K^* = \frac{-\Delta H}{RT} + \frac{\Delta S}{R} \quad (7)$$

$$\Delta G^0 = -RT\ln K^* \quad (8)$$

$$\Delta G = \Delta H - T\Delta S \quad (9)$$

R is the universal gas constant and T absolute temperature. Both apparent (K_{app}) and overall (K*) binding constants determined at each temperature were plotted according to Eq. (7). ΔH and ΔS were determined from the slope and the intercept respectively. Subsequently, ΔG was obtained with the help of Eq. (9) [40]. In this regard, we wish to mention since we did not have access to an Isothermal Titration Calorimeter (ITC) this prevented us from model independent determination of thermodynamic parameters.

3. Results and discussions

3.1. Characterization of [Cu(Cur)(OCOCH$_3$)(H$_2$O)]

3.1.1. Characterization of the complex by different instrumental techniques

Owing to low solubility in water, spectrum of the complex was recorded in DMSO (Fig. S2, S I). λ_{max} was obtained at 430 nm. IR spectrum of the complex was compared with that of Curcumin (Fig. S3 and S4, S I respectively) [41]. The mass spectrum of the complex showed a molecular ion peak at $m/z = 507.3225$ (Fig. 2; $m/z_{theo} = 507.39$ considering ^{63}Cu). A thermogravimetric analysis (TGA) was also done (Fig. S5, S I). From mass and TGA the formula was decided to be as mentioned above. Magnetic susceptibility measured according to Gouy method provided μ_{eff} as 1.738 BM without diamagnetic correction and 1.63 BM with it.

3.1.2. DFT calculations based on spectroscopic evidence

Ground states of optimized molecular structures were found as doublets. Both ground state optimized geometries of the complex with B3LYP-GD3BJ functional (in gaseous state and in DMSO as medium) are depicted in Fig. 3 with a numbering scheme for the coordination environment. The optimized coordinates for these configurations are provided in Table S1a, S I. Important parameters concerning these coordination geometries are arranged in Table 1. The final optimized structure of the ground state configuration show a square planar coordination environment for both gaseous and solution (in DMSO) state calculations. The two oxygens of Curcumin, the oxygen of a molecule of water and the acetylic oxygen are connected to the central Cu^{II} in syn-anti fashion forming the basal plane (Fig. 3). In addition, the optimized geometries of Curcumin in DMSO as solvent at both B3LYP-GD3BJ and BHandHLYP level and its copper(II)-complex (in DMSO) with BHandHLYP functional is presented in Fig. S6. Optimized coordinates are listed in Tables S1b and S1c respectively. The solvated complex shows similar square planar geometry as calculated with B3LYP level with dispersion correction. The changes in dimension of the binding site of the ligand due to complex formation in DMSO medium have also been depicted in Fig. S6.

3.1.2.1. MO composition analysis. The frontier molecular orbitals (FMOs) of the complex optimized with B3LYP functional in gas and solution phases are shown in Fig. 4. Again, FMOs for Curcumin and its Cu(II) complex at BHandHLYP level is presented in Fig. S7. Assignment of the type of each MO was made on the basis of its composition and by visual inspection of its three-dimensional representation. Since spin-α and spin-β components of each molecular orbital is localized on different parts of the molecule, for MO composition analysis, contributions from four segments namely Cu, Curcumin, water and acetate were considered. For B3LYP optimized geometries of complex some of the frontier MOs, orbital energies and contribution from each fragment in terms of atomic orbital contribution to frontier molecular orbital (MO) are listed in Table S2, S I.

The gas phase optimized configuration shows that the highest singly occupied molecular orbital (SOMO) and LUMO of both spin-α and spin-β components are ligand centric (i. e. almost the entire contribution is from Curcumin forming the SOMO in each case) with practically negligible contribution from metal AOs (~1% contribution from Cu to form LUMO in both cases). The solution phase optimized geometry shows a similar trend i.e. the ligand (Curcumin) centric contribution is almost 100% while forming SOMO for both spin-α and spin-β components.

While for spin-α, LUMO is totally from ligand moieties with practically no participation from metal AOs, in case of spin-β, LUMO is distributed over the ligand framework with appreciable contribution from the metal ion (67% Cu and 22% Curcumin). Introducing the complex to a dielectric medium reduces the HOMO–LUMO energy gap for both spin-α and spin-β orbitals (Fig. 4). These FMOs are handy in explaining the electronic structure and optoelectronic properties of complexes. For molecular crystals, the HOMO–LUMO energy gap could be corroborated with optical energy bandgap as derived from UV–vis absorption spectrum (Fig. 5). The optical energy band gap (E_g) derived from the equation, $E_g = \frac{1240}{\lambda_{max}}$eV, where λ_{max} is the wavelength corresponding to maximum absorption intensity, was found to be 2.877 eV, comparable to the average HOMO–LUMO energy gap of 2.965 eV of the complex in DMSO, In solvent medium the B3LYP level calculated HOMO-LUMO energy gap of the complex is lower than the solo Curcumin molecule establishing the stability of the complex. In contrary for the BHandHLYP functional, which is found to describe correctly open shell Cu(II) systems, the HOMO-LUMO enegy gaps of the complex show comparable values with HOMO-LUMO energy gap of solo Curcumin calculated at the same level as shown in Fig. S7.

3.1.2.2. Thermochemical parameters. Thermochemical parameters defining the interaction between biologically significant Curcumin with a lewis acidic Cu(II) ion were estimated from the optimized geometries of the solvated complex in DMSO by frequency calculation that in turn produces the zero-point-vibrational energy corrected electronic energies ($\boldsymbol{\epsilon_0 + E_{ZPVE}}$), enthalpy and free energy corrected electronic energies i.e., ($\boldsymbol{\epsilon_0 + H_c}$and $\boldsymbol{\epsilon_0 + G_c}$) respectively.

The values of the parameters calculated with dispersion corrected B3LYP-D3BJ and BHandHLYP methods in combination with the 6-311+G basis set are enlisted in Table S3. The solvent phase

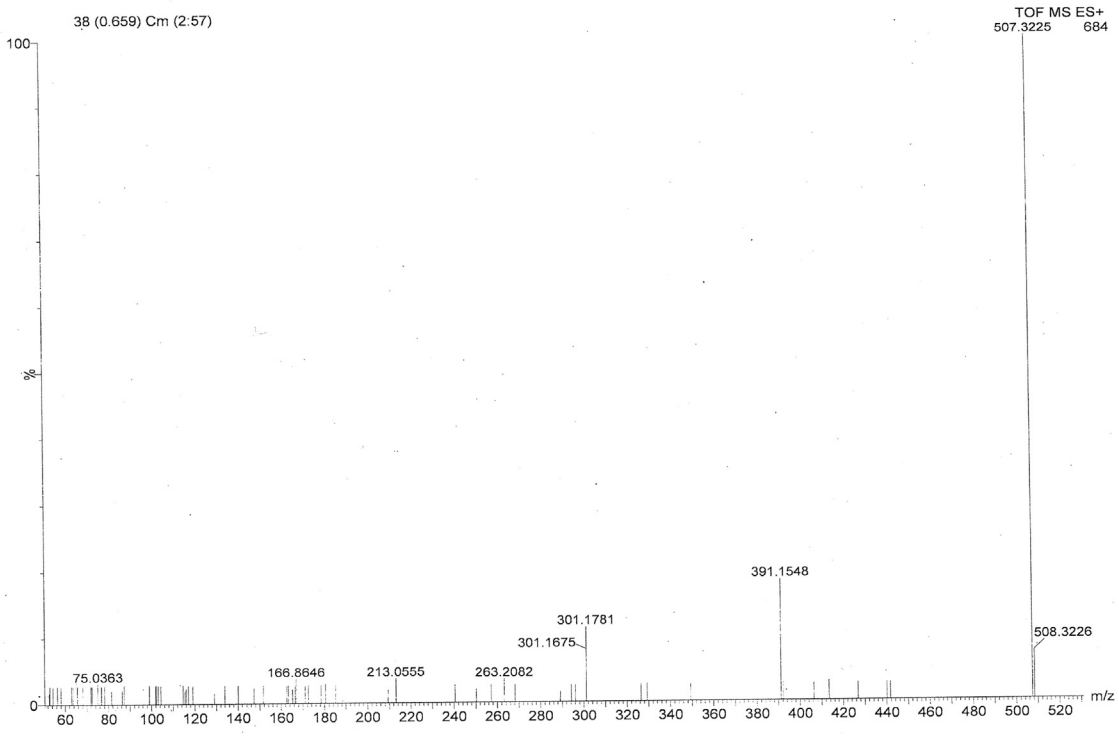


Fig. 2. Mass spectra of the Cu^{II} complex of Curcumin.

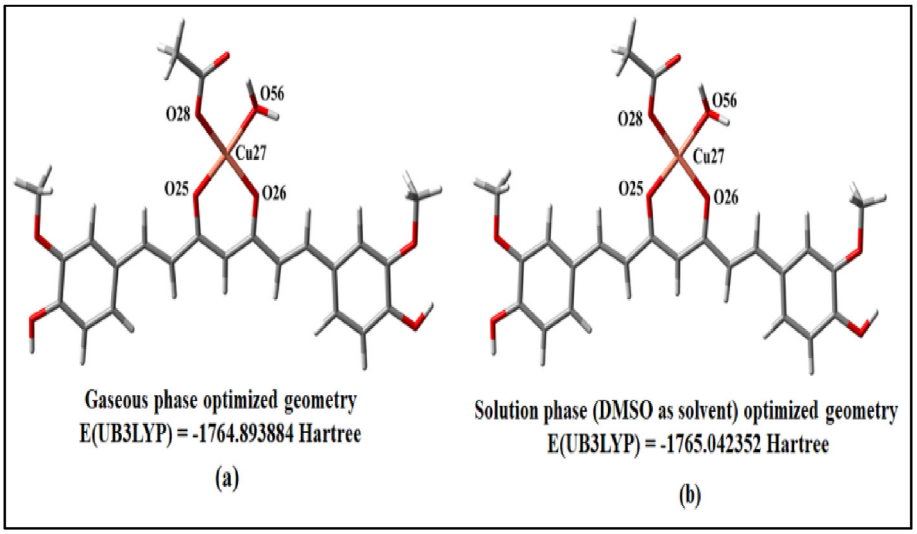


Fig. 3. Ground state optimized geometries of the complex.

Table 1
Coordinated bond distances (in Á) and bond angles (in °) of the complex Cu(II)-Curcumin.

Bond	Gaseous phase	In DMSO	Angle	Gaseous phase	In DMSO
Cu27–O25	1.917	1.916	O25–Cu27–O26	80.16	93.46
Cu27–O26	1.934	1.919	O25–Cu27–O28	101.57	89.32
Cu27–O28	1.966	1.966	O26–Cu27–O56	99.07	87.54
Cu27–O56	1.940	1.954	O28–Cu27–O56	79.54	90.83
Dihedral angle					
			O25–O26–O28–O56	12.53	11.34

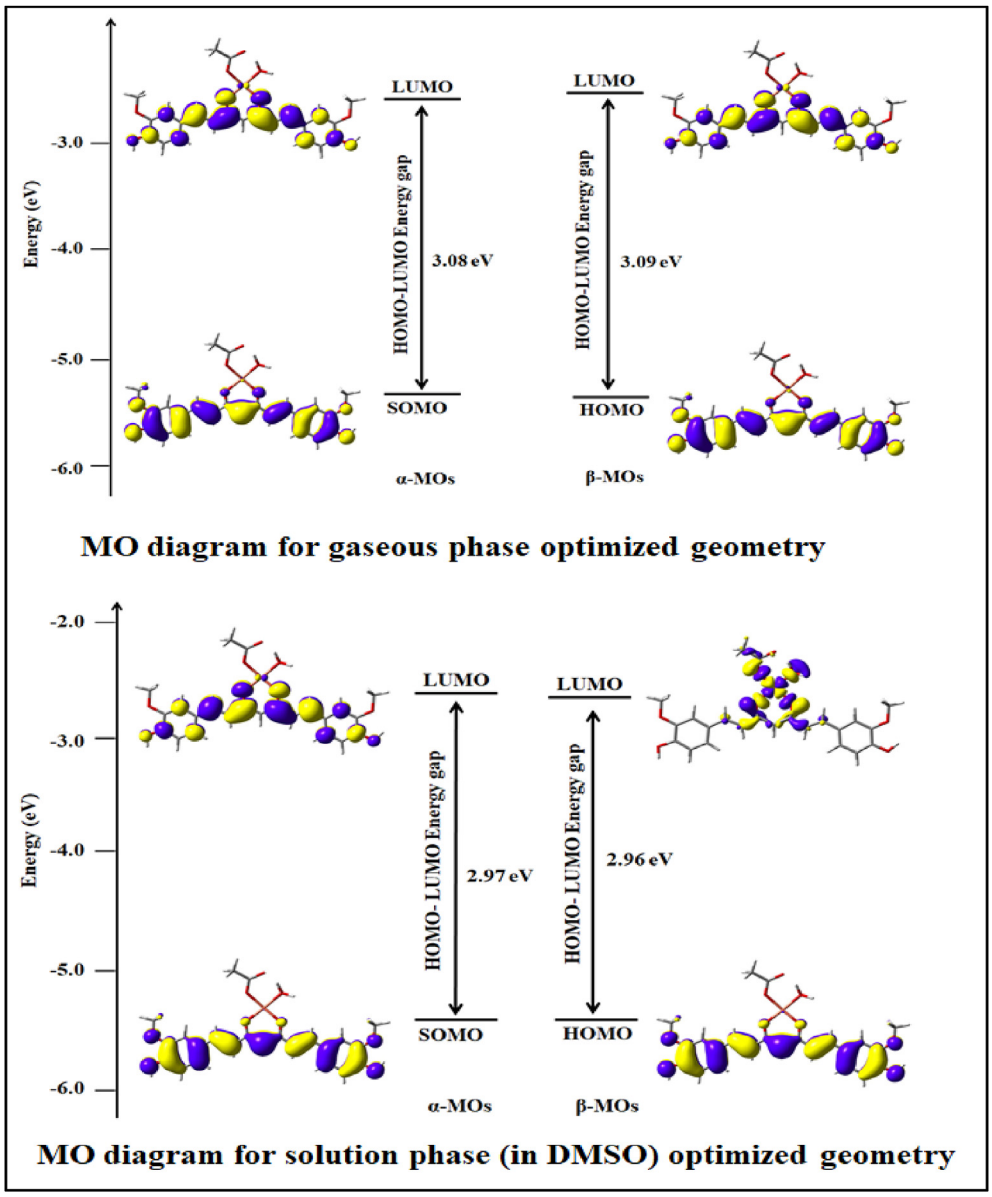


Fig. 4. The frontier molecular orbitals (FMOs) of the optimized geometries of Cu(II)-Curcumin.

data of reaction enthalpies ($\Delta_r H^0$) and free energies ($\Delta_r G^0$) of the reaction are assembled in Table 2. These values corroborate interaction enthalpy and free energy of interaction. Now, predicted values of $\Delta_r H^0$ and $\Delta_r G^0$ being −36.09 kcal/mol and −17.80 kcal/mol respectively for the complex in DMSO medium at room temperature (298.15 K) at B3LYP level indicate interaction of Cu(II) with Curcumin lowers the electronic energies of the metal complex and also point to a spontaneous nature of formation of the complex as well as its thermodynamic stability. Again the half and half functional BHandHLYP which can effectively describe spin delocalization of open shell Cu(II) systems [29,30] predict interaction enthalpy and free energy to be −156.93 eV and −143.58 eV that outperforms the B3LYP model for a quantative estimation of the binding affinity of Cu(II) with Curcumin. In addition, both dispersion corrected B3LYP and BHandHLY level of calculations yield comparable values for the magnetic moment (μ) of the complex (4.74 D and 4.48 D respectively), large enough to have good polar character and affinity towards polar solvent media.

3.1.2.3. Opto-electronic absorption property. The opto-electronic property is useful in identifying the exact molecular geometry since excitation from ground state to the next excited state in a dielectric medium (DMSO) would produce similar absorption behavior as that measured in the same solvent experimentally. Since there is a cut off wavelength for absorption in case of DMSO (~268 nm), absorption spectrum of the complex shows dispersion below 300 nm. Hence, experimental pattern below 350 nm was not considered, instead the spectrum was recorded up to 600 nm and compared with the calculated one (Fig. 6). The calculated electronic absorption spectrum in DMSO consists of multiple peaks supporting a multiple transition nature for the complex.

Peaks in the experimental spectrum were assigned visually. The most probable transitions having maximum intensities ($f \geq 0.10$) close to experimental absorption peaks with corresponding excitation wavelengths, energy, oscillator strengths (f), character and C I coefficients are listed in Table S4, S I in ascending order of energy in which they appear in the spectrum. Charge-transfer transitions

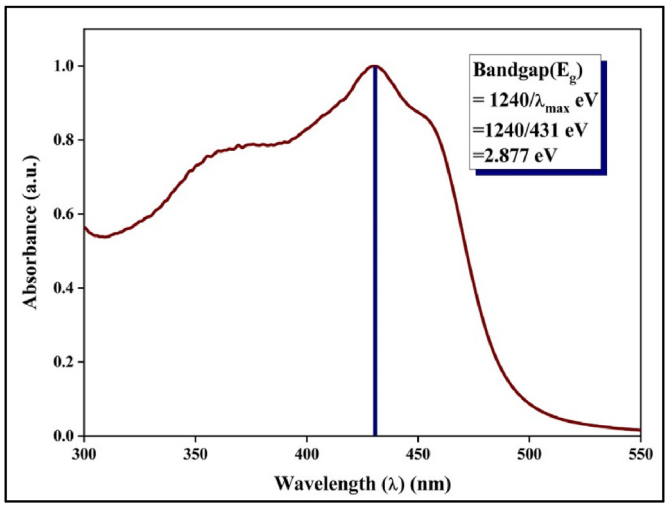


Fig. 5. Experimental UV–vis absorption maximum with the corresponding optical bandgap.

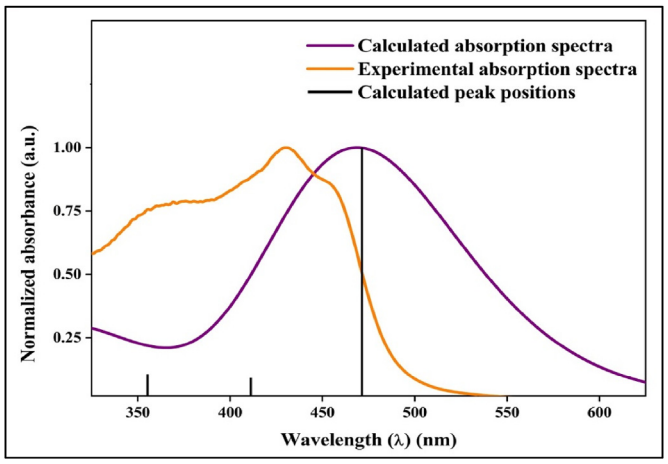


Fig. 6. Comparison of experimental and theoretical UV–vis absorption spectra showing the most feasible peak positions.

among different moieties of the complex viz. water molecule, acetate and Curcumin with varying amounts of metal to ligand contribution gives rise to excitation peaks, although intra-ligand charge transfer within Curcumin moieties were seen to be mainly responsible. TDDFT calculation of the ground state doublet geometry produces excited states showing slight spin contamination with fractional values of 0.004–0.017 (Table S4, S I). All states were approximately considered as doublets.

Excited state computational results were interpreted using natural transition orbital (NTO) analyses based on calculated transition density matrices [42]. The virtual/unoccupied and occupied NTOs were referred to as "electron/particle" and "hole" transition orbitals respectively. This allowed us to identify and visualize electronic transitions that were being considered in terms of excitation from a hole-NTO to an electron-NTO for both spin-α and spin-β components with weights with which this occupied-virtual pair contributes to excitation. NTOs for the most relevant peaks are depicted in Fig. 7.

While explaining excitations, lowest energy transitions that were experimentally observed near 454 nm and 431 nm was found at 471.5 nm (2.63 eV, f = 1.5853) being the most prominent calculated peak. This transition is ascribed to π (Curcumin) → d_{xz} + π* (Curcumin) ILCT in association with some LMCT character together with lone pair (O) → antibonding (O) transition. Net electron transfers from ligand to metal fragments and within ligand fragments are 0.03076e and 0.95795e respectively [43]. The next higher energy UV transition around 410 nm was computed at 411.28 nm (3.01 eV, f = 0.1451) and attributed to π (Curcumin) → π* (Curcumin) ILCT. The net electron transfer within ligand fragments is 0.95108e. The UV excitation near the experimentally observed peak of 356 nm was found at 355.33 nm (3.489 eV, f = 0.1665) and attributed to d_{yz}(Cu) + π (Curcumin + Acetate + water) → d_{xy}(Cu) + π*(Curcumin) ILCT together with slight LMCT nature and very weak LLCT where intra-ligand and ligand to ligand net electron transfers were 0.89872e and 0.04376e respectively.

3.2. Interaction of [Cu(Cur)(OCOCH$_3$)(OH$_2$)] with calf thymus DNA

The complex was titrated with calf thymus DNA at constant pH (= 7.4) and ionic strength (0.15 mM) of the medium. The gradual decrease in absorbance at 430 nm helped in evaluating the interaction between the complex and DNA (Fig. 8). Fig. 9 is a plot of 1/ΔA versus 1/[C_D-C_L] [Eq. (3)] that provides values for K_{app} (= K_d^{-1}) from three independent titrations [34–38]. The average of these values was 3.98 × 10^3 M^{-1}.

Fig. 10 is a plot of ΔA/ΔA_{max} versus concentration of calf thymus DNA to which the non-linear curve fitting analysis was applied (Eqs. (4) and (5)). Three independent titrations provided an average apparent binding constant value of 4.03 × 10^3 M^{-1} at 298 K. Inset of Fig. 10 provides a value for n_b (= 18.0), i. e. the number of nucleotides bound to the complex following interaction with calf thymus DNA [34–38].

The titration data was also fitted to a modified form of the Scatchard equation (Eq. (6), Fig. 11) [39]. K* and n (= n_b^{-1}) were obtained. Values obtained from Eq. (6) were close to that obtained from other methods of analyses (Eqs. (3)–(5), Figs. 9 and 10), hence they justify the methods that calculate them.

Titration of the complex with DNA is important for a number of reasons. First, since a titration of Curcumin with DNA is not possible owing to its physiological instability in solution (mentioned earlier), a monomeric complex of Cu(II) with one Curcumin bound to it, showing no signs of degradation really makes it a model that represents Curcumin's binding to DNA. While considering the data, one has to keep in mind that in case of the complex there might be an influence of Cu(II) on the observed binding as well [35,36,44,45]. Hence, if Curcumin were to be present in "one-piece" in solution, its

Table 2
Summary of the thermodynamic parameters (interaction enthalpies $\Delta_r H^0$ and free energies $\Delta_r G^0$ of reaction for the reaction species under investigation) and electronic properties (homo-lumo energy gaps E_g^{HL} and dipole moments μ) of the complex calculated in DMSO medium.

System	Method	$\Delta_r H^0$ (kcal/mol)	$\Delta_r G^0$(kcal/mol)	E_g^{HL} (eV)		M (Debye)
				α	β	
Cu(Cur)	B3LYP-D3BJ	−36.09	−27.80	2.967	2.956	4.738981
(OCOCH$_3$)(H$_2$O)	BHandHLYP	−156.93	−143.58	4.967	4.978	4.4796517

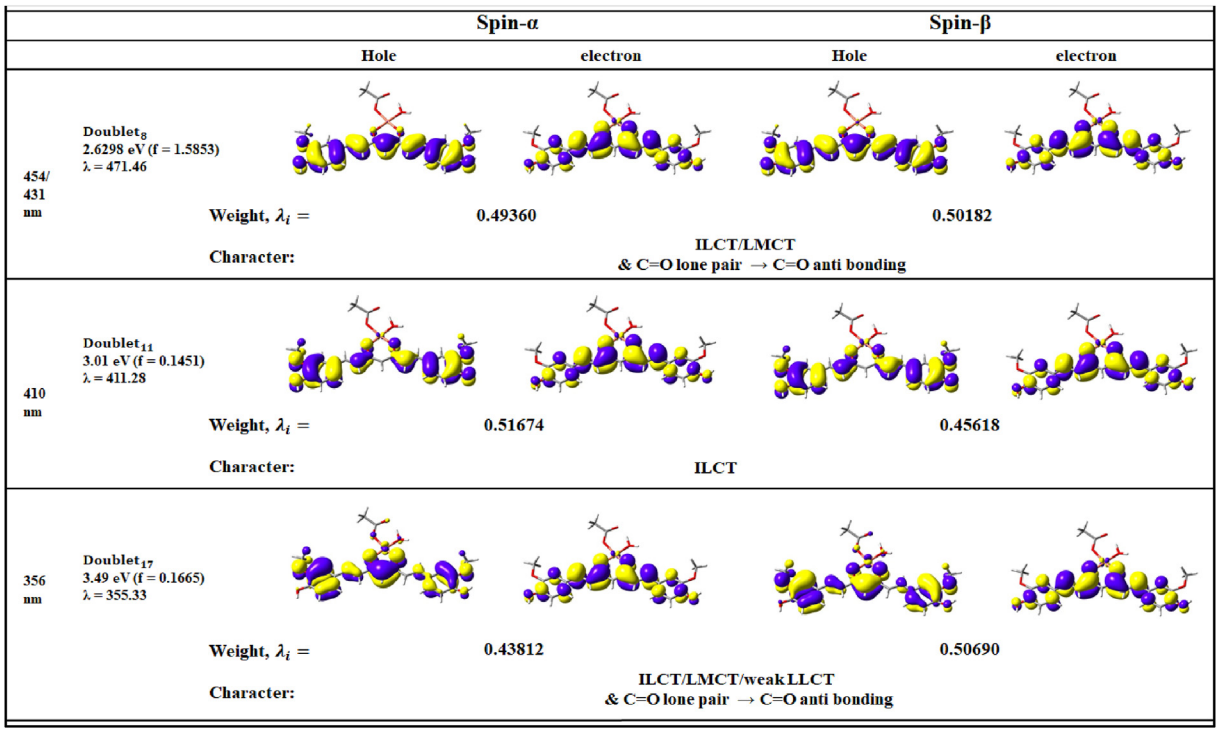


Fig. 7. NTO analysis describing the calculated UV–vis peak positions.

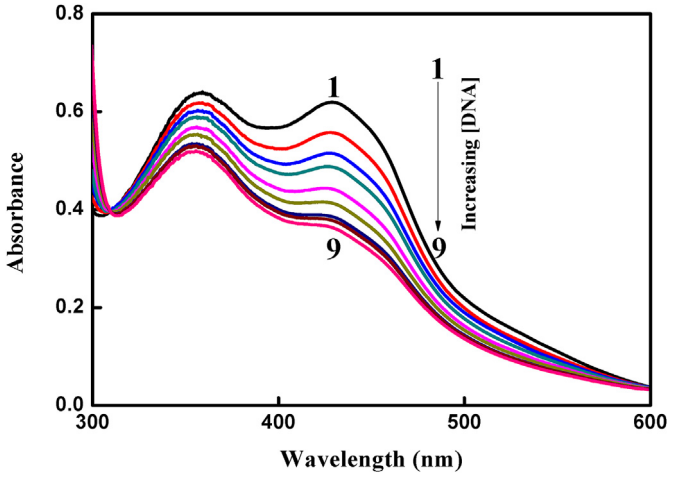


Fig. 8. Absorption spectra of 21 μM [Cu(Cur)(OCOCH$_3$)(OH$_2$)] in the absence (1) and presence of different concentrations of calf thymus DNA (2) 85.55 μM, (3) 169.85 μM, (4) 280.32 μM, (5) 494.91 μM, (6),701.450 μM (7) 948.96 μM, (8) 1044.82 μM, (9) 1231.39 μM; [NaCl] = 150 mM, pH = 7.4,Temp. = 298K.

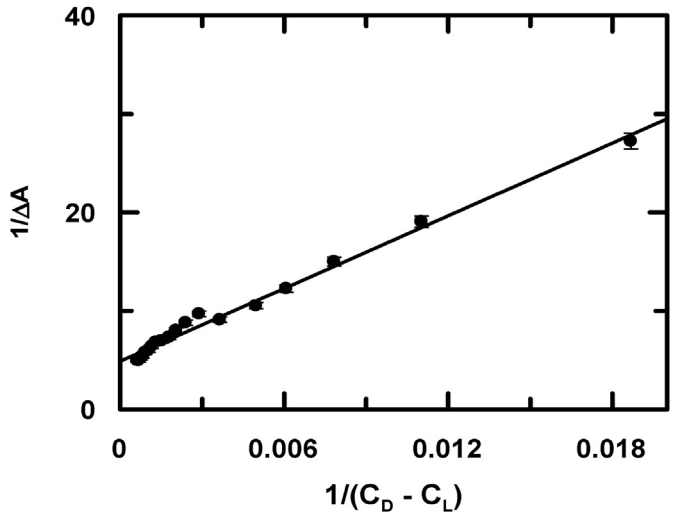


Fig. 9. Double reciprocal plot for the interaction of [Cu(Cur)(OCOCH$_3$)(OH$_2$)] with calf thymus DNA to evaluate apparent binding constant (K_{app}) of the complex to DNA at pH 7.4 (30 mM phosphate buffer) and ionic strength (0.15 M); [Cu(Cur)(OCOCH$_3$)(OH$_2$)] = 21 μM, pH = 7.4; Temperature = 298 K.

value for binding could either be close to that of the complex or slightly less (as realized from similar Cu^{II} complexes) [35,36,44,45]. Nevertheless, an idea on Curcumin's binding to DNA may be obtained where there was none. Since when Curcumin is present alone, it degrades under physiological conditions much before it interacts with DNA [17]. Secondly, from an estimate of binding constant values obtained for the complex it may now be possible to explain mechanisms that involve interaction of Curcumin with DNA in a biological process whose manifestation is reported as beneficial.

3.2.1. Interaction of the Cu(II) complex of Curcumin with calf thymus DNA at different temperatures

Titrations of the complex with calf thymus DNA performed at different temperatures were plotted according to Eqs. (3)–(6); results are shown in Table 3. Analysis of the data indicates with increase in temperature there is a slight increase in the affinity of the complex to bind to DNA, reflected by increasing values of binding constants. Hence, plots of log of either K_{app} or K* (i.e. lnK_{app} or lnK*) for the complex against 1/T were obtained as straight lines with

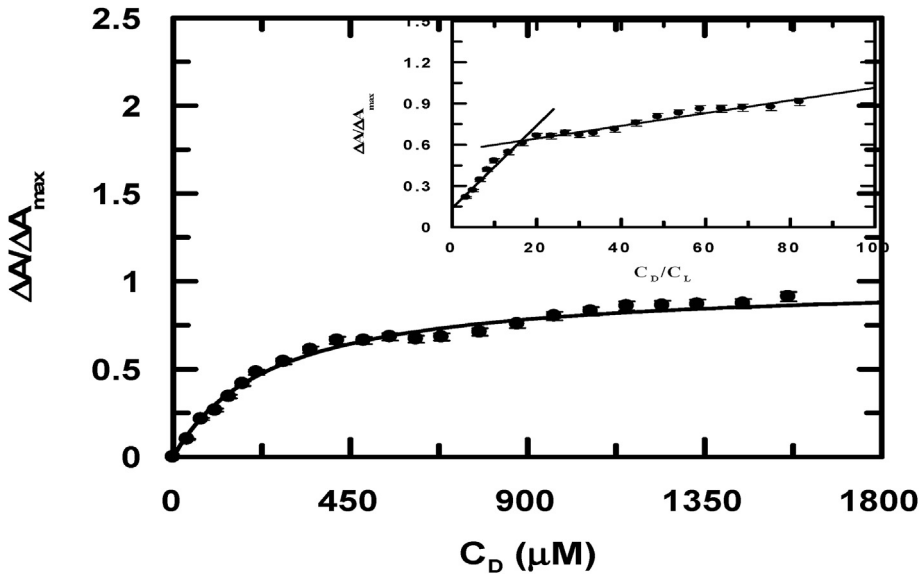


Fig. 10. Binding isotherm for the interaction of [Cu(Cur)($OCOCH_3$)(OH_2)] with calf thymus DNA where $\Delta A/\Delta A_{max}$ was plotted against concentration of DNA. The dark line shows the fitted data obeying Eq. (4); [complex] = 21 μM, pH = 7.4; Temperature = 300K. Inset: Plot of normalized increase in absorbance as a function of mole-ratio of calf thymus DNA to the complex.

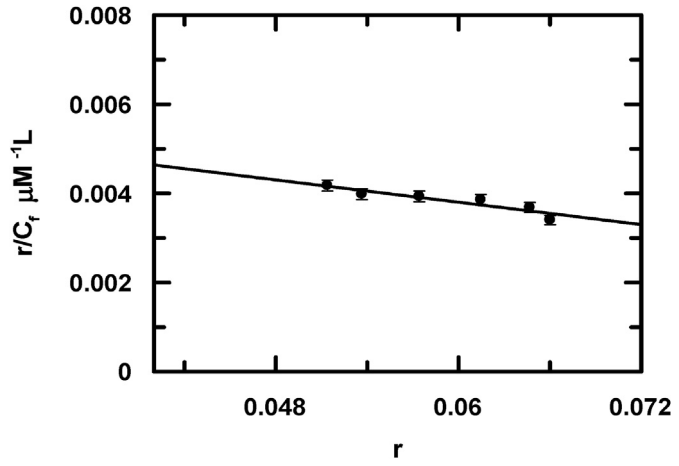


Fig. 11. Scatchard plot for the interaction of [Cu(Cur)($OCOCH_3$)(OH_2)] with calf thymus DNA; [complex] = 21 μM, pH = 7.4, Temperature = 308 K.

negative slopes (Eq. (6)). Change in enthalpy (ΔH) and entropy (ΔS) were determined from the slope and intercept of the van't Hoff plots. The change in free energy (ΔG) being negative indicates binding is favoured.

Since, interaction of [Cu(Cur)($OCOCH_3$)(OH_2)] with calf thymus DNA results in positive values for binding enthalpy and entropy (Fig. S8, S I & Fig. 12, Table 4) it clearly indicates binding is entropically driven. For entropy driven molecule-DNA interactions, solvent molecules and counter ions are actually expelled from bound surfaces of both the participating substances as they bind to each other leading to gain in entropy. Such coming together of reactants is reported to release bound water from the hydration zone of the minor groove as well as release counter ions from bound surfaces of interacting partners; being the cause for an increase in entropy [46–48]. This is counter balanced by some enthalpically unfavorable effects that occur simultaneously like the breaking of hydrogen bonds and non-covalent interactions of solvent molecules and counter ions that existed either in the unbound form of DNA or in the substance binding to DNA (here the complex). In some cases, the binding site is characterized by a widening of the minor groove in order to accommodate the molecule [46–48]. All these show up by a positive value of change in enthalpy. In such entropically driven molecule-DNA interactions, hydrophobic interactions have a major role to play [49,50]. In case of neutral DNA intercalators for example, intercalation occurs via entropically driven interactions [51]. In our case, since Curcumin is sparingly soluble in water, it is most likely that interaction of the complex with DNA could be stabilized by hydrophobic interactions. Again the absence of a net charge on the complex allows for a comparison of the case quite favourably with some neutral DNA intercalators [52]. The fact that binding could be stabilized by hydrophobic interactions is also reflected in ΔH and ΔS values obtained following an interaction of the complex with DNA.

Table 3
Binding parameters of [Cu(Cur)($OCOCH_3$)(OH_2)] with calf thymus DNA at different temperatures studied using UV–Vis spectroscopy.

Temp (K)	Apparent binding constants $K_{app} \times 10^{-3}(M^{-1})$		Site size (n_b) from mole ratio plot	Overall binding constant $K^* \times 10^{-4}$ (M^{-1}) [$K^* = K_{app} \times n_b$]	Overall binding constant $K^{/} \times 10^{-4}(M^{-1})$ (From Scatchard plot)	Site size (n_b) from Scatchard plot
	From double reciprocal plot	From non linear – fit				
293	3.70	3.75	10.0	3.73	4.10	9.09
298	3.98	4.03	18.0	7.21	4.81	10.0
303	4.37	4.39	17.0	7.45	3.33	16.0
308	4.64	4.69	18.0	8.40	5.19	20.8

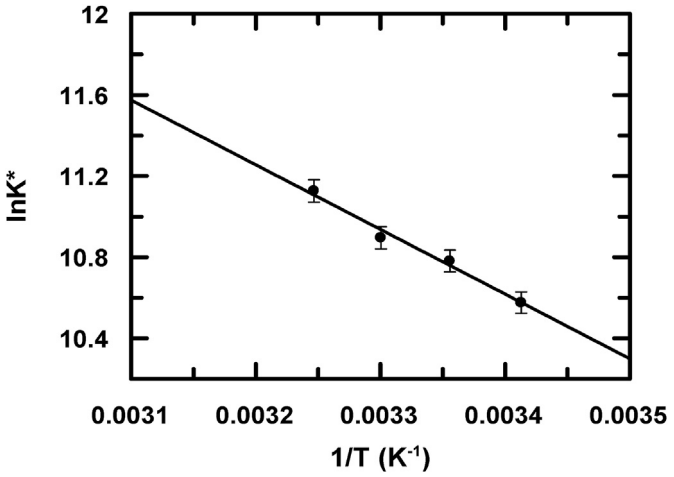


Fig. 12. van't Hoff plots of binding of [Cu(Cur)($OCOCH_3$)(OH_2)] with calf thymus DNA considering apparent binding constants at different temperatures.

Table 4
Thermodynamic parameters for the interaction of [Cu(Cur)($OCOCH_3$)(OH_2)] with calf thymus DNA in 30 mM phosphate buffer (pH ~ 7.4) and ionic strength of 0.15 M

	Δ***G***(Kcal/mole)	Δ***H***(Kcal/mole)	Δ***S***(e.u)
Considering lnK_{app}versus 1/T	−4.897	2.732	25.60
Considering lnK*versus 1/T	−6.348	6.314	42.49

Previous reports indicate the two common binding modes for small molecules to bind to DNA are intercalation and groove-binding [53–55]. While intercalation is mostly favoured for planar and aromatic substances that inserts between DNA base pairs leading to unwinding and lengthening of the double helix, groove binding does not disturb the duplex structure but fits nicely into the minor groove with only a very slight distortion to the structure. Calorimetric studies that have determined enthalpic and entropic contributions to DNA binding for different compounds have enriched the literature revealing distinctive thermodynamic signatures that today allow one to either identify or differentiate groove-binders from intercalators [49–53]. Such data reveal groove-binding interactions are those that provide a favorable entropy contribution to free energy, while intercalators are those that have an unfavorable entropy contribution but favorable enthalpy contribution. Predominantly, groove-binding is entropy driven while intercalation is enthalpy driven. Although the molecular basis of such contrasting thermodynamic signatures for the two binding modes cannot be generalized for all molecules that interact with DNA, they however do provide a good idea that enable one to categorize new DNA binding agents into binding types, taking into consideration aspects like the structure of the participating substance and changes in ΔH and ΔS.

From the discussion above and existing literature support in this regard [49–55], it may be said for the complex [Cu(Cur)($OCOCH_3$)(OH_2)] that groove binding is probably the major mode of binding to calf thymus DNA.

4. Conclusion

A Cu(II) complex of Curcumin was prepared with an intention of improving upon aspects like low solubility, low bio-availability and instability under physiological conditions or in different cellular media which seems achieved. The prepared complex was characterized with the help of different techniques and a structure obtained by DFT calculations. Since Curcumin has a number of pharmacological properties whose mechanism of action is not clearly known owing to its instability in aqueous solution and different biological milieu, we tried to see if in the form of a Cu^{II} complex with one Curcumin bound to it, a resemblance to Curcumin "as one unit" be realized. This can be useful to explain the mechanism of action of Curcumin if it is based on an interaction with DNA. Therefore, how the monomeric complex interacts with DNA has a lot of bearing on how Curcumin may interact with DNA if present "as one unit", a situation not possible to realize by taking Curcumin alone in aqueous buffer in presence of other electrolytes (for reasons mentioned earlier). Since titrations were performed at four different temperatures it enabled us to calculate thermodynamic parameters like ΔH and ΔS that helped to predict the binding type of this monomeric Cu^{II} Curcumin species with DNA which could throw some light on the interaction of Curcumin with DNA as well. This is not only useful to us but for all other researchers who have noted some biological utility regarding Curcumin and its complexes, that would allow them to enumerate upon pathways that involve a DNA interaction. More importantly a representative complex like this one, allows one to derive the effects of Curcumin remaining in "one piece" i.e. as a "single unit" bound to Cu^{II} against fragmented products in solution when present alone either in physiological buffer or biological milieu for which a DNA titration of it is not possible.

CRediT authorship contribution statement

Tanmoy Saha: Data curation, Formal analysis, Investigation, Visualization, Writing - review & editing. **Soumen Singha:** Data curation, Formal analysis, Investigation, Methodology, Software, Visualization, Writing - original draft, Writing - review & editing. **Sanjay Kumar:** Conceptualization, Data curation, Formal analysis, Investigation, Methodology, Software, Supervision, Visualization, Writing - original draft, Writing - review & editing. **Saurabh Das:** Conceptualization, Data curation, Formal analysis, Funding acquisition, Project administration, Resources, Investigation, Methodology, Supervision, Validation, Visualization, Writing - original draft, Writing - review & editing.

Declaration of competing interest

The authors declare that they have no known competing financial interests or personal relationships that could have appeared to influence the work reported in this paper.

5. Acknowledgments

SS wish to thank Department of Science & Technology, New Delhi for a DST-INSPIRE Senior Research Fellowship. TS is grateful to the "Governing body" of Sri Aurobindo Institute of Education, Salt Lake, Kolkata for permission to pursue research leading to a Ph D degree. SD wish to thank the "RUSA 2.0" program of the Government of India operating at Jadavpur University under which he received a "Research Support to Faculty Members" grant in the thrust area "Research in Sustainable Development" (Sanction Ref. no. R-11/438/19 dated 30.05.2019). He is grateful to DST-PURSE, Government of India for financial support to Jadavpur University and also UGC, New Delhi for funding the research program on 'Advanced Materials' as part of UPE II to Jadavpur University from where funds were used to purchase chemicals and laboratory accessories. He acknowledges the financial support received from the UGC-CAS II program of the Department of Chemistry, Jadavpur University for purchase of chemicals, consumables and glassware.

Appendix A. Supplementary data

Supplementary data to this article can be found online at https://doi.org/10.1016/j.molstruc.2020.128732.

References

[1] B.B. Aggarwal, C. Sundaram, N. Malani, H. Ichikawa, Curcumin: the Indian solid gold. The Molecular Targets and Therapeutic Uses of Curcumin in Health and Disease, Springer, Boston, MA, 2007, pp. 1–75.

[2] J.S. Jurenka, Anti-inflammatory properties of curcumin, a major constituent of Curcuma longa: a review of preclinical and clinical research, Alternative Med. Rev. 14 (2009) 141–153.

[3] T. Ak, İ. Gülçin, Antioxidant and radical scavenging properties of curcumin, Chem. Biol. Interact. 174 (2008) 27–37.

[4] R. Wilken, M.S. Veena, M.B. Wang, E.S. Srivatsan, Curcumin: a review of anti-cancer properties and therapeutic activity in head and neck squamous cell carcinoma, Mol. Canc. 10 (2011) 12, https://doi.org/10.1186/1476-4598-10-12.

[5] S. Wanninger, V. Lorenz, A. Subhan, F.T. Edelmann, Metal complexes of curcumin–synthetic strategies, structures and medicinal applications, Chem. Soc. Rev. 44 (2015) 4986–5002.

[6] S.Y. Teow, K. Liew, S.A. Ali, A.S.B. Khoo, S.C. Peh, Antibacterial action of curcumin against Staphylococcus aureus: a brief review, J. Trop. Med. (2016) 10, https://doi.org/10.1155/2016/2853045. Article ID 2853045.

[7] A. Goel, A.B. Kunnumakkara, B.B. Aggarwal, Curcumin as "Curecumin": from kitchen to clinic, Biochem. Pharmacol. 75 (2008) 787–809.

[8] K. Neelofar, S. Shreaz, B. Rimple, S. Muralidhar, M. Nikhat, L.A. Khan, Curcumin as a promising anticandidal of clinical interest, Can. Jour.Microbiol. 57 (2011) 204–210.

[9] P. Tyagi, M. Singh, H. Kumari, A. Kumari, K. Mukhopadhyay, Bactericidal activity of Curcumin I is associated with damaging of bacterial membrane, PloS One 10 (2015), e0121313.

[10] R.A. Sharma, W.P. Steward, A.J. Gescher, Pharmacokinetics and pharmacodynamics of curcumin, Adv. Exp. Med. Biol. 595 (2007) 453–470.

[11] R. Banerjee, Inhibitory effect of Curcumin-Cu(II) and Curcumin-Zn(II) complexes on amyloid-beta peptide fibrillation, Bioinorgan. Chem. Appl. 2014 (2014) 325873.

[12] S. Banerjee, P. Prasad, A. Hussain, I. Khan, P. Kondaiah, A.R. Chakravarty, Remarkable photocytotoxicity of curcumin in HeLa cells in visible and arresting its degradation on oxovanadium (IV) complex formation, Chem. Commun. (J. Chem. Soc. Sect. D) 48 (2012) 7702–7704.

[13] K.I. Priyadarsini, The chemistry of Curcumin: from extraction to therapeutic agent, Molecules 19 (2014) 20091–20112.

[14] M.D. Cas, R. Ghidoni, Dietary Curcumin: correlation between bioavailability and health potential, Nutrients 11 (9) (2019) 2147, https://doi.org/10.3390/nu11092147.

[15] S.B. de Souza Ferreira, M.L. Bruschi, Improving the bioavailability of curcumin: is micro/nanoencapsulation the key? Ther. Deliv. 10 (2019) 83–86, https://doi.org/10.4155/tde-2018-0075.

[16] P. Anand, A.B. Kunnumakkara, R.A. Newman, B.B. Aggarwal, Bioavailability of curcumin: problems and promises, Mol. Pharm. 4 (2007) 807–818.

[17] Y.-J. Wang, M.-H. Pan, A-Li Cheng, L.-I. Lin, Y.-S. Ho, Chang-Yao Hsieh, Jen-Kun Lin Stability of curcumin in buffer solutions and characterization of its degradation products, J. Pharmaceut. Biomed. Anal. 15 (1997) 1867–1876.

[18] K. Mitra, S. Gautam, P. Kondaiah, A.R. Chakravarty, Platinum(II) complexes of Curcumin showing photocytotoxicity in visible light, Eur. J. Inorg. Chem. (2017) (2017) 1753–1763, https://doi.org/10.1002/ejic.201601078.

[19] S. Wanninger, V. Lorenz, A. Subhan, F.T. Edelmann, Metal complexes of curcumin – synthetic strategies, structures and medicinal applications, Chem. Soc. Rev. 44 (2015) 4986–5002.

[20] F. Caruso, M. Rossi, A. Benson, C. Opazo, D. Freedman, E. Monti, M.B. Gariboldi, J. Shaulky, F. Marchetti, R. Pettinari, C. Pettinari, Ruthenium–Arene complexes of Curcumin: X-Ray and density functional theory structure, synthesis, and spectroscopic characterization, *in vitro* antitumor activity, and DNA docking studies of (p-Cymene)Ru(curcuminato)chloro, J. Med. Chem. 55 (2012) 1072–1081.

[21] H.M. Leung, M. Harada, W. Takaaki, T. Kee, Delivery of Curcumin and medicinal effects of the Copper(II)-Curcumin complexes, Curr. Pharmaceut. Des. 19 (2013) 2070–2083.

[22] T. Deb, P.K. Gopal, D. Ganguly, P. Das, M. Paul, M.B. Saha, S. Paul, S. Das, Enhancement of anti-leukemic potential of 2-hydroxyphenyl-azo-2′-naphthol (HPAN) on MOLT-4 cells through conjugation with Cu(ii), RSC Adv. 4 (2014) 18419–18430.

[23] A. Barik, B. Mishra, L. Shen, H. Mohan, R.M. Kadam, S. Dutta, H.-Y. Zhang, K.I. Priyadarsini, Evaluation of a new copper(II)-curcumin complex as superoxide dismutase mimic and its free radical reactions, Free Rad. Biol. Med. 39 (2005) 811–822.

[24] M.J. Frisch, G.W. Trucks, H.B. Schlegel, G.E. Scuseria, M.A. Robb, J.R. Cheeseman, G. Scalmani, V. Barone, G.A. Petersson, H. Nakatsuji, X. Li, M. Caricato, A.V. Marenich, J. Bloino, B.G. Janesko, R. Gomperts, B. Mennucci, H.P. Hratchian, J.V. Ortiz, A.F. Izmaylov, J.L. Sonnenberg, D. Williams-Young, F. Ding, F. Lipparini, F. Egidi, J. Goings, B. Peng, A. Petrone, T. Henderson, D. Ranasinghe, V.G. Zakrzewski, J. Gao, N. Rega, G. Zheng, W. Liang, M. Hada, M. Ehara, K. Toyota, R. Fukuda, J. Hasegawa, M. Ishida, T. Nakajima, Y. Honda, O. Kitao, H. Nakai, T. Vreven, K. Throssell, J.A. Montgomery Jr., J.E. Peralta, F. Ogliaro, M.J. Bearpark, J.J. Heyd, E.N. Brothers, K.N. Kudin, V.N. Staroverov, T.A. Keith, R. Kobayashi, J. Normand, K. Raghavachari, A.P. Rendell, J.C. Burant, S.S. Iyengar, J. Tomasi, M. Cossi, J.M. Millam, M. Klene, C. Adamo, R. Cammi, J.W. Ochterski, R.L. Martin, K. Morokuma, O. Farkas, J.B. Foresman, D.J. Fox, Gaussian 09, Revision D.01, Gaussian, Inc., Wallingford CT, 2016.

[25] (a) A.D. Becke, Density-functional thermochemistry. III. The role of exact exchange, J. Chem. Phys. 98 (1993) 5648–5652;
(b) C.T. Lee, W.T. Yang, R.G. Parr, Development of the Colle-Salvetti correlation-energy formula into a functional of the electron density, Phys. Rev. B 37 (1988) 785–789.

[26] T.H. Dunning Jr., P.J. Hay, Gaussian basis sets for molecular calculations, in: H.F. Schaefer III (Ed.), Methods of Electronic Structure Theory vol. 2, Plenum Press, New York, 1977, pp. 1–27.

[27] S. Grimme, S. Ehrlich, S.L. Goerigk, Effect of the damping function in dispersion corrected density functional theory, J. Comput. Chem. 32 (2011) 1456–1465.

[28] A.D. Becke, A new mixing of Hartree-Fock and local density functional theories, J. Chem. Phys. 98 (1993) 1372–1377.[Note that these are the half-and-half functionals implemented in Gaussian 09 (ref 25) which are not the same as the ones proposed in this reference, i. e. no. 28].

[29] S. Mandal, G. Das, H. Askari, Experimental and quantum chemical modeling studies of the interactions of L-phenylalanine with divalent transition metal cations, J. Chem. Inf. Model. 54 (9) (2014) 2524–2535.

[30] S. Mandal, G. Das, H. Askari, Amino acid-type interactions of L-3,4-dihydroxyphenylalanine with transition metal ions: an experimental and theoretical investigation, J. Mol. Struct. 1100 (2015) 162–173.

[31] E.K.U. Gross, W. Kohn, Time-dependent density functional theory in, Adv. Quant. Chem. 21 (1990) 255–291.

[32] M. Cossi, V.J. Barone, Time-dependent density functional theory for molecules in liquid solutions, Chem. Phys. 115 (2001) 4708–4717.

[33] N.M. O'Boyle, A.L. Tenderholt, K.M. Langner, cclib: a library for package-independent computational chemistry algorithms, J. Comput. Chem. 29 (2008) 839–845.

[34] T. Deb, D. Choudhury, P.S. Guin, M.B. Saha, G. Chakrabarti, S. Das, A complex of Co(II) with 2-hydroxyphenyl-azo-2′-naphthol (HPAN) is far less cytotoxic than the parent compound on A549-lung carcinoma and peripheral blood mononuclear cells: reasons for reduction in cytotoxicity, Chem-Biol. Inter. 189 (2011) 206–214.

[35] P.S. Guin, P.C. Mandal, S. Das, The binding of a hydroxy-9,10-anthraquinone Cu^{II} complex to calf thymus DNA: electrochemistry and UV/Vis spectroscopy, ChemPlusChem 77 (2012) 361–369, https://doi.org/10.1002/cplu.201100046.

[36] P. Das, C.K. Jain, S.K. Dey, R. Saha, A.D. Chowdhury, S. Roychoudhury, S. Kumar, H.K. Majumder, S. Das, Synthesis, crystal structure, DNA interaction and in vitro anticancer activity of a Cu(II) complex of purpurin: dual poison for human DNA topoisomerase I and II, RSC Adv. 4 (2014) 59344–59357.

[37] B. Mandal, S. Singha, S.K. Dey, S. Mazumdar, T.K. Mondal, P. Karmakar, S. Kumar, S. Das, Synthesis, crystal structure from PXRD of a $Mn^{II}(purp)_2$ complex, interaction with DNA at different temperatures and pH and lack of stimulated ROS formation by the complex, RSC Adv. 6 (2016) 51520–51532.

[38] S. Mukherjee-Chatterjee, C.K. Jain, S. Singha, P. Das, S. Roychoudhury, H.K. Majumder, S. Das, Activity of Co^{II}-Quinalizarin: a novel analogue of anthracycline-based anticancer agents targets human DNA topoisomerase, whereas quinalizarin itself acts via formation of semiquinone on acute lymphoblastic leukemia MOLT-4 and HCT 116 cells, ACS Omega 3 (2018) 10255–10266.

[39] G. Scatchard, The attractions of proteins for small molecules and ions, Ann. N. Y. Acad. Sci. 51 (1949) 660–672.

[40] G.W. Castellan, Physical Chemistry, third ed., Addison-Wesley/Narosa Publishing House, New Delhi, 1989, p. 799. Indian Student Edition.

[41] K. Nakamoto, Infrared and Raman Spectra of Inorganic and Coordination Compounds, third ed., Wiley-Interscience, New York, 1978.

[42] R.L. Martin, Natural transition orbitals, J. Chem. Phys. 118 (2003) 4775–4777.

[43] (a) T. Lu, F. Chen, Quantitative analysis of molecular surface based on improved Marching Tetrahedra algorithm, J. Mol. Graph. Model. 38 (2012) 314–323;
(b) T. Lu, F. Multiwfn Chen, A multifunctional wavefunction analyzer, J. Comput. Chem. 33 (2012) 580–592.

[44] P. Das, C.K. Jain, S. Roychoudhury, H.K. Majumder, S. Das, Design, synthesis and in vitro anticancer activity of a Cu(II) complex of Carminic Acid: a novel small molecule inhibitor of human DNA topoisomerase I and topoisomerase II, ChemistrySelect 1 (2016) 6623–6631.

[45] D. Ganguly, C.K. Jain, R.C. Santra, S. Roychoudhury, H.K. Majumder, T.K. Mondal, S. Das, Anticancer activity of a complex of CuII with 2-(2-hydroxyphenylazo)-indole-3/-acetic acid on three different cancer cell lines: a novel feature for azo complexes, ChemistrySelect 2 (2017) 2044–2054.

[46] S. Majee, R. Sen, S. Guha, D. Bhattacharya, D. Dasgupta, Differential interactions of the Mg2+ complexes of Chromomycin A3 and Mithramycin with poly(dG-dC)·poly(dC-dG) and poly(dG)·poly(dC), Biochemistry 36 (1997) 2291–2299.

[47] S. Das, D. Dasgupta, Binding of $(MTR)_2Zn^{2+}$ complex to chromatin: a comparison with $(MTR)_2Mg^{2+}$ complex, J. Inorg. Biochem. 99 (2005) 707–715.

[48] S. Roy, R. Banerjee, M. Sarkar, Interaction of a common painkiller Piroxicam

and Copper-piroxicam with chromatin causes structural alterations accompanied by modulation at the epigenomic/genomic level, J. Inorg. Biochem. 100 (2006) 1320–1331.
[49] J.B. Chaires, Drug—DNA interactions, Curr. Opin. Struct. Biol. 8 (1998) 314–320.
[50] I. Haq, Thermodynamics of drug–DNA interactions, Arch. Biochem. Biophys. 403 (2002) 1–15.
[51] V.A. Bloomfield, D.M. Crothers, I. Tinoco, in: Nucleic Acid: Structures, Properties and Functions, University Science Books, Sausalito, CA, 1999, p. 56.
[52] F. Leng, J.B. Chaires, M.J. Warring, Energetics of echinomycin binding to DNA, Nucleic Acids Res. 31 (2003) 6191–6197.
[53] S. Kashanian, J.E.N. Dolatabadi, *In vitro* studies on calf thymus DNA interaction and 2-tert-butyl-4-methylphenol food additive, Eur. Food Res. Technol. 230 (2010) 821–825.
[54] J.B. Chaires, A thermodynamic signature for drug–DNA binding mode, Arch. Biochem. Biophys. 453 (2006) 26–31.
[55] N. Shahabadi, S. Kashanian, F. Darabi, *In vitro* study of DNA interaction with a water-soluble dinitrogen Schiff base, DNA Cell Biol. 28 (2009) 589–596.

Journal of Inorganic Biochemistry 222 (2021) 111494

Contents lists available at ScienceDirect

Journal of Inorganic Biochemistry

journal homepage: www.elsevier.com/locate/jinorgbio

Enhanced efficacy of a Cu^{2+} complex of curcumin against Gram-positive and Gram-negative bacteria: Attributes of complex formation

Prince Kumar [a,1], Tanmoy Saha [b], Swastik Behera [a], Shalini Gupta [c], Saurabh Das [b], Kasturi Mukhopadhyay [a,*]

[a] Antimicrobial Research Laboratory, School of Environmental Sciences, Jawaharlal Nehru University, New Delhi 110 067, India
[b] Department of Chemistry (Inorganic Section), Jadavpur University, Kolkata 700 032, India
[c] Molecular Biology Laboratory, School of Biotechnology, Jawaharlal Nehru University, New Delhi 110 067, India

ARTICLE INFO

Keywords:
Curcumin
Copper-curcumin metal complex
S. aureus
E. coli
Membrane-permeabilization
Antibacterial activity

ABSTRACT

Curcumin is a tantalizing molecule with multifaceted therapeutic potentials. However, its therapeutic applications are severely hampered because of poor bioavailability, attributed to its instability and aqueous insolubility. In an attempt to overcome this inherent limitation and develop curcumin-based antibacterials, we had earlier synthesized and characterized a metal complex of Cu(II) with curcumin, having the formula [Cu(Curcumin)$(OCOCH_3)(H_2O)$], hereafter referred to as Cu(Cur). In this study, the complex, i.e., Cu(Cur), was investigated for its stability and antibacterial activity along with its possible mechanism of action in comparison to the parent molecule, curcumin. Complex formation resulted in improved stability as Cu(Cur) was found to be highly stable under different physiological conditions. Such improved stability was verified with the help of UV–Vis spectroscopy and HPLC. With improved stability, Cu(Cur) exhibited potent and significantly enhanced activity over curcumin against both *E. coli* and *S. aureus*. *Calcein leakage assay* revealed that the complex triggered immediate membrane permeabilization in *S. aureus*. This membrane disruptive mode of action was further corroborated by microscopic visualization. The excellent potency of the complex was augmented by its safe toxicological profile as it was non-hemolytic and non-cytotoxic towards mammalian cells, making it a suitable candidate for in vivo investigations. Altogether, this investigation is a critical appraisal that advocates the antibacterial potential of this stable, membrane-targeting and non-toxic complex, thereby presenting new perspectives for its therapeutic application against bacterial infections.

1. Introduction

Since time immemorial, plants have been a treasure trove of medicines and that continues even today. Despite technological advances in drug discovery, plants have been the source of about one-quarter of all FDA-approved drugs [1,2]. However, the use of plant-derived compounds as antibacterial agents has been virtually non-existent. After the advent of antibiotics, we have solely relied on microbes as their source, with 97% antibacterial drugs derived from them [1]. Antibiotics were nothing short of a miraculous cure to otherwise fatal infections and changed the therapeutic paradigm by saving millions of lives. However, their prolonged irrational use has fostered bacterial resistance, which poses one of the biggest threats to global public health. To raise the alarm on the current situation, the Centers for Disease Control and Prevention (CDC) has released a report titled "Antibiotic Resistance Threats in the United States, 2019." According to this report, the burden of resistant pathogens is unacceptably high, with more than 2.8 million infections resulting in at least 35,000 deaths each year in the US alone [3]. Antibiotic resistance causes an estimated 700,000 deaths each year worldwide and is every bit as deadly as COVID-19, or even worse lurking behind the current outbreak. The irrational use of antibiotics has increased manifold during the current COVID-19 pandemic, despite warnings by the World Health Organization (WHO) and CDC [4–6], which may have further exacerbate the resistance crisis.

In the current pandemic, *Staphylococcus aureus* (*S. aureus*) and *Escherichia coli* (*E. coli*) are perhaps the pathogens of greatest concern because of their ability to cause a diverse array of life-threatening infections [7,8]. These are the two most common and prevalent causes of hospital- and community-acquired infections, and patients with

* Corresponding author.
E-mail address: kasturim@mail.jnu.ac.in (K. Mukhopadhyay).
[1] Present address: Department of Botany, T. S. College, Hisua, Nawada, Magadh University, Bodhgaya 824 234, India.

https://doi.org/10.1016/j.jinorgbio.2021.111494
Received 6 August 2020; Received in revised form 14 May 2021; Accepted 24 May 2021
Available online 27 May 2021
0162-0134/© 2021 Published by Elsevier Inc.

Abbreviations

S. aureus	*Staphylococcus aureus*
E. coli	*Escherichia coli*
DTT	dithiothreitol
DMEM	Dulbecco's modified Eagle's medium
MHB	Mueller Hinton broth
BHI	brain heart infusion

weakened immune systems are at higher risk of developing infections from these opportunistic pathogens. The clinical isolates of these pathogens are gradually losing susceptibility to multiple classes of antibiotics and exhibiting multidrug resistance [9–11]. Inevitably, we are left with fewer effective treatment options against infections of such constantly adapting bacteria [12,13]. This therapeutic crisis not only demands an empirical use of the remaining effective antibiotics but also desires a search for alternative options urgently. In this quest, underutilized medicinal plants might serve as prospective reservoirs, and in recent times, many plant-based active compounds have been extracted with a broad spectrum of antimicrobial activity. Among such active metabolites, curcumin is one of the most promising polyphenolic compounds that received enormous attention in the last few decades [14–16].

Curcumin, chemically known as diferuloylmethane, is a tantalizing lipophilic molecule obtained from the dietary spice turmeric (*Curcuma longa*) that has long been known for its multiple health benefits. The appealing medicinal properties of turmeric have been attributed mainly to its primary active component, curcumin that has been extensively studied for its antioxidant [15], anti-inflammatory [16], anti-cancer [17], and therapeutic utilities in neurodegenerative disorders [18]. Many in vivo studies and clinical trials have highlighted the safety of curcumin as it is non-toxic and well-tolerated in humans, even at a dose as high as 12 g/day for over three months and therefore "generally regarded as safe (GRAS)" by the US FDA [19–21]. Besides its various therapeutic properties, curcumin was reported to possess a broad spectrum of antimicrobial properties against fungi, viruses, and bacteria [22–25]. We have also reported its antibacterial activity against Gram-positive and Gram-negative bacteria under in vitro conditions [26,27]. Despite its excellent pharmacological potentials, curcumin's therapeutic applications are severely hindered owing to its aqueous insolubility and poor chemical stability under physiological conditions [28,29]. These shortcomings consequently result in very poor bioavailability [30,31], which is a major obstacle in its development as a drug [32]. A promising approach to circumvent the limitations mentioned above could be the complex formation of curcumin with a metal ion.

Curcumin is a symmetrical molecule that exhibits keto-enol tautomerism due to intermolecular hydrogen transfer at the central β-diketone moiety (Fig. S1, SI). This β-diketone in curcumin is considered to be its hydrolytic center, where degradation takes place, resulting in several products like feruloylmethane, ferulic acid, and vanillin, under aqueous conditions [28,33]. However, this hydrolysis prone moiety is capable of acting as a chelating ligand towards different metal ions. Hence, if this moiety is made to engage with a metal ion, it would form a stable complex of curcumin [34–36]. Reports have suggested improved biological activity of curcumin after complexation with bio-friendly cations that address issues like chemical stability and solubility under physiological conditions [27,36–38]. This has opened up new avenues, and several metallocurcumin complexes have been reported, exploring various biological activities. The presence of a metal ion is reported to improve upon such aspects as cellular uptake, binding of the complex to DNA or other cell organelles, or even its ability to either alter or introduce a redox-active pathway through the generation of free radicals [27,35,36,39–44]. Most of these studies of the complexes have been directed towards exploring their antioxidant, anti-inflammatory, and anti-HIV activities as well as their effect against neurodegenerative diseases [38,45]. However, limited but promising results have also been reported for their antibacterial activity [46–50]. But most of these studies were limited to understanding their antibacterial potential only via determining their zone of inhibition; none of them explored the mechanistic aspects. Clearly, there remains a requisite to fill up the void by systematically investigating the antibacterial activity and exploring the mechanism.

Since copper salts have been repeatedly reported to exhibit antibacterial properties [51–53], we thought of using them to stabilize the β-diketone moiety of curcumin. Keeping this in mind, we synthesized and characterized a complex of curcumin with Cu(II) [39]. In the present study, we tried finding out whether complex formation with Cu(II) can stabilize curcumin under physiological conditions. Then, we tried to investigate some of the positive attributes of complex formation in terms of antibacterial activity studied against the two most clinically significant bacteria *S. aureus* and *E. coli*. Next, efforts were made to decipher the mechanism behind the antibacterial activity of the complex through different fluorescence and microscope-based assays. Finally, to assess any potential toxicity of the complex against mammalian cells, hemolytic and cytotoxicity assays were performed.

2. Experimental section

2.1. Materials

2.1.1. Chemicals

Curcumin was purchased from Sigma-Aldrich. Copper (II) acetate monohydrate and sodium nitrate were procured from Merck, India. Dithiothreitol (DTT), 3-(4,5-dimethylthiazol-2-yl)-2,5-diphenyltetrazolium bromide (MTT), calcein-acetoxy methyl ester (calcein-AM), and gramicidin D were purchased from Sigma-Aldrich. Dulbecco's modified Eagle's medium (DMEM), brain heart infusion (BHI), Luria-Bertani (LB) medium, Mueller Hinton broth (MHB), and agar powder were purchased from Himedia Laboratories. LIVE/DEAD *Bac*Light Bacterial Viability Kit (L7007) was procured from Invitrogen. Sodium dihydrogen phosphate and disodium hydrogen phosphate required to prepare buffer solutions for physiological pH were acquired from Merck, India.

2.1.2. Bacterial strains used

Gram-positive *S. aureus* (ATCC 29213) and Gram-negative *E. coli* (ATCC 25922) bacterial strains were used in the study. The exponential phase bacterial cells were stored at −80 °C in 15% (*v*/v) glycerol stock till sub-cultured on nutrient agar plate for further use.

2.2. Methods

2.2.1. Preparation of the complex [Cu(Curcumin)($OCOCH_3$)(H_2O)]

The preparation and characterization of the complex were recently published [39]. Briefly, curcumin was dissolved in a deaerated acetonitrile-ethanol mixture and neutralized with triethylamine followed by the addition of $Cu(OCOCH_3)_2.H_2O$ in deaerated ethanol-water solution. Next, to create an inert atmosphere, argon gas was passed through the reaction mixture, and it was stirred for 2 h. The solution was then refluxed for an additional 3 h. Subsequently, a greenish-black precipitate was extracted. It was washed with different solvents like chloroform, diethyl ether, ethanol, tetrahydrofuran (THF), and acetonitrile. A 1:1 Cu(II)-curcumin complex [Cu(Curcumin)($OCOCH_3$)(H_2O)] was obtained, which was hereafter referred to as Cu(Cur) [13]. Structures of curcumin and Cu(Cur) are provided in Fig. S1, SI [39]. Fig. S2, SI shows the existence of both diketo and enolate forms of curcumin in solution. λ_{max} for the complex was obtained at 426 nm in DMSO (Fig. S3, SI), which is largely consistent with reports in the literature [54].

2.2.2. Chemical stability analysis of the complex in physiological buffer conditions

2.2.2.1. Using UV–Vis spectroscopy. The comparative stability of Cu(Cur) and curcumin was studied under physiological conditions [phosphate buffered saline (PBS): 10 mM sodium phosphate, 150 mM NaCl, pH 7.4] and in different media (MHB, BHI, and DMEM) used for bacterial growth purposes. For this, absorption spectra were scanned in the range from 250 nm to 600 nm using a UV-2450 spectrophotometer, Shimadzu [55]. Stock solutions of 10 mM were prepared by dissolving the complex and curcumin in dimethyl sulfoxide (DMSO). A small volume (2 μL) from stock solutions was added to 1 mL PBS and 1 mL microbiological medium to obtain a final concentration of 20 μM in each condition. Absorption spectra were subsequently recorded for the next 30 min at intervals of 5 min. The stability of the complex under reducing conditions was also checked by repeating the same experiment in the presence of 10 μM DTT, a reducing agent. Absorption spectra were recorded as earlier.

2.2.2.2. Using HPLC. The filtrate of curcumin and its Cu(II) complex incubated at 30 °C in 0.1 M phosphate buffer, pH 7.2, were analyzed using HPLC for stability studies. Vanillin, vanillic acid, ferulic acid were used as standards. Separations were performed on a C18 column. The mobile phase was 12% tetrahydrofuran (THF), 5% acetonitrile, 2% acetic acid in water run isocratically at a flow rate of 1 mL per min (C18 column: 250 × 4.6 mm, 5 lam particle size, Shimadzu). Sample detection was achieved at 254 nm; injection volumes were 20 μL. Chromatographic peaks from incubation samples were identified by comparison with authentic standards. The amount of unaltered curcumin remaining behind was realized.

2.2.3. Killing assay

The experiment was carried out as previously described with slight modifications [26,27]. Briefly, target cells of *S. aureus* and *E. coli* were grown till mid-logarithmic phase in the requisite broth medium (BHI and LB). Cells were centrifuged at 4000 rpm for 10 min, washed in 10 mM PBS (pH 7.4), and then adjusted spectrophotometrically to an $OD_{600} = 0.5$ ($\sim 10^8$ CFU/mL) in the same buffer. Bacterial suspensions of $\sim 10^6$ CFU/mL were treated with different concentrations (25 and 50 μM) of Cu(Cur) and curcumin in PBS at 37 °C. Afterwards, aliquots were withdrawn at regular intervals (2, 60, and 120 min) and plated in triplicate on BHI agar plates after suitable dilutions in PBS buffer followed by overnight incubation at 37 °C. The following day, the mean of the bacterial colony-forming unit per mL (CFU/mL) was calculated, and bacterial survival was expressed compared to a non-treated control (considered as 100% survival).

2.2.4. Membrane permeabilization assay

The permeabilization of bacterial cells was quantified using a flow cytometer using the calcein leakage assay, as previously described [55,56]. Briefly, *S. aureus* cells adjusted to $\sim 10^9$ CFU/mL ($OD_{600} = 1.0$) in PBS, were labeled with calcein-AM (2 μg/mL) in the presence of 10% MHB for 2 h at 37 °C in the dark. Calcein-loaded cells were washed with PBS to remove the excess dye, and then diluted samples of the dye-loaded cells ($\sim 10^6$ CFU/mL) were incubated with 25 and 50 μM of Cu (Cur) and curcumin. For control experiments, untreated and 20 μg/mL gramicidin D-treated labeled cells were incubated under similar conditions. Following incubation, calcein leakage was quantified by measuring the fluorescence of cell-entrapped calcein at an excitation wavelength of 490 nm and emission wavelength of 517 nm using a flow cytometer (BD FACS Verse, San Jose, CA). For each cytometry analysis, a total of 10,000 events were acquired, and cells having <10 fluorescence units were considered to have lost calcein as a result of drug-induced permeabilization.

2.2.5. Fluorescence microscopy

A *Bac*Light Bacterial Viability Kit (L7007) composed of two fluorophores, SYTO 9 and propidium iodide (PI), was employed to detect the integrity of the bacterial membrane as per the manufacturer's protocol [26,55]. Briefly, bacterial suspensions, pre-treated with 50 μM Cu(Cur) and curcumin for 2 h, were stained with SYTO 9 and PI in the dark for 15 min. After incubation, 5 μL of the stained sample was confined between a glass slide and coverslip. The samples were examined under a fluorescence microscope (Olympus Fluoview FV 1000 model) with PI and FITC (corresponding to SYTO 9) filters.

2.2.6. Sample preparation for scanning electron microscopy (SEM)

Morphological changes in bacteria induced by the compounds were examined via SEM, for which samples were prepared and processed as previously described [55,57]. Briefly, $\sim 10^9$ CFU/mL log phase *S. aureus* cells were treated with Cu(Cur), curcumin and gramicidin D (control) for 2 h at 37 °C. After treatment, cells were harvested, washed twice with buffer, and then fixed overnight in 2.5% glutaraldehyde. After fixation, cells were washed thrice with buffer to remove glutaraldehyde and then dehydrated for 10 min each with an increasing ethanol concentration (30% to 100%). Finally, dehydrated and dried samples were coated with gold using a sputter coater (Polaron OM-SC7640) and immediately viewed under a Scanning electron microscope (EVO 40, Carl Zeiss) available at AIRF, JNU, New Delhi, India.

2.2.7. Sample preparation for transmission electron microscopy (TEM)

Samples for TEM were prepared as reported earlier [55,57]. Briefly, bacterial cells ($\sim 10^9$ CFU/mL), untreated control, and test drug-treated were centrifuged, washed, and fixed in 2.5% glutaraldehyde as described for sample preparation for SEM. Samples were then postfixed with osmium tetroxide (1%) before dehydrating with graded acetone series. Next, samples were embedded in epoxy resin and fine sectioned with a microtome. These ultrathin sections were collected on copper grids and stained with uranyl acetate. After several washings in Milli-Q water, each grid was again stained with lead citrate. Samples were rinsed and dried before viewing in a Transmission electron microscope (JEOL-JEM 2100, Japan) at AIRF, JNU, New Delhi, India.

2.2.8. Hemolytic assay

The potential hemolytic activity of Cu(Cur) and curcumin was evaluated as described previously with some modifications [55,57,58]. In brief, blood samples were collected from mice (in accordance with ethical guidelines of the Institutional Animal Ethics Committee of JNU, New Delhi, India; IAEC number- 23/2018). Red blood cells (RBCs) were isolated via centrifugation at 1500 rpm for 10 min, then washed in buffer (35 mM sodium phosphate, 150 mM NaCl, pH 7.4) and resuspended to 4% v/v in the same buffer. Subsequently, 100 μL of different concentrations of compounds (two-fold serial dilutions) were mixed with 100 μL of 4% RBCs suspensions in a microtiter plate and incubated for 1 h at 37 °C. For control experiments, RBCs suspension in buffer and 0.1% Triton X-100 were incubated under similar conditions. Following incubation, samples were centrifuged, and 20 μL of supernatant from each well was transferred into a fresh microtiter plate containing 80 μL buffer. The extent of hemolysis was determined by reading the absorbance of hemoglobin at 414 nm using a microplate reader (Verioskan Flash Multiplate reader, Thermo Scientific). Percentage hemolysis was evaluated using Eq. (1).

$$\%\text{hemolysis} = [(\text{OD of sample–OD of PBS})/(\text{OD of 0.1\%Triton X–OD of PBS})] \times 100 \quad (1)$$

2.2.9. Cytotoxicity assay

2.2.9.1. Cytotoxicity against mouse fibroblast cells. Cytotoxicity due to the complex was investigated against 3 T3 mouse fibroblast cells using a standard MTT assay [55,57,58]. Briefly, fibroblast cells were cultured in DMEM supplemented with 10% serum and ~0.2 × 10^5 3 T3 cells were seeded in each well of a 24-well plate. After 24 h of incubation, the medium was aspirated, and fresh medium containing 250 and 500 μM of curcumin and Cu(Cur) was added to each well in triplicate. It was then incubated for 4 h. Control samples (untreated cells, 2% Triton X-100-, and corresponding 0.5% DMSO-treated cells) were also incubated in parallel sets. Following incubation, the medium was removed and then MTT solution (1 mL, final concentration 0.1 mg/mL in DMEM) was added to each well and the plate was further incubated for 2 h in the dark. Next, DMSO was added to each well to dissolve precipitated MTT formazan crystals after discarding the supernatant. Absorbance was measured at 570 nm. Compared to the untreated control (100% cell viability), the % cytotoxicity of the treated samples was calculated using Eq. (2).

$$\%\text{Cytotoxicity} = [(\text{OD of control}–\text{OD of sample})/(\text{OD of control})] \times 100 \quad (2)$$

2.2.9.2. Cytotoxicity against human embryonic kidney cells. The cytotoxicity of the complex was further explored against human embryonic kidney epithelial cells (HEK293) using MTT assay as described earlier with some modifications [59,60]. Briefly, HEK293 cells were cultured in DMEM medium supplemented with 10% FBS and 1% Pen-Strep antibiotic. Around 5 × 10^3 cells were seeded into each well of a 96-well plate. After 16–18 h of incubation, the medium was aspirated and fresh medium containing 250 and 500 μM of Cu(Cur) was added to each well in triplicate. The control set included untreated cells, corresponding DMSO treated cells, and 2% Triton X-100 treated cells in triplicates. The samples were incubated for 24 h, following which 15 μL of MTT solution (final concentration of 0.2 mg/mL) was added to each well and was incubated for another 2.5 h. Next, the supernatant was discarded, and 100 μL of DMSO was added to each well to dissolve precipitated MTT formazan crystals. Parallel to this, HEK293 cells with similar experimental parameters were exposed to the complex for 4 h and then incubated for another 72 h in fresh medium. Again, cytotoxicity was calculated using Eq. (2) compared to untreated control (100% cell viability).

3. Results and discussion

3.1. A comparative stability analysis of the complex under physiological conditions

3.1.1. Using UV–Vis spectroscopy

Considering the chemical instability of curcumin, we started this study with the question, does the complexation of curcumin with Cu(II) help in stabilizing it under physiological conditions? To answer it, we examined and compared the stability of Cu(Cur) in different biological milieu. As previously reported [55], the intensity of absorption spectra of curcumin decreased significantly over time in buffer solutions; indeed, more than 50% of its initial intensity was lost within the first 20 min of incubation in PBS. In contrast, absorption spectra of Cu(Cur) did not decrease and remained stable over time in PBS. The results indicate the complex to be reasonably stable in physiological buffer and also in different microbiological media, as there was no noticeable decrease in absorbance for the complex (Fig. S4, SI).

Since the cytosolic environment is reducing, the stability of Cu(Cur) and curcumin was also studied in the presence of a commonly used reducing agent DTT [61,62]. In line with previous findings [27,55,62], we observed a much faster degradation of curcumin in the presence of DTT, as curcumin lost more than 50% of its absorption intensity within the first 5 min of incubation. On the other hand, Cu(Cur) was found to be exceptionally stable since its absorption intensity did not decrease even after 20 min of incubation with DTT (Fig. S4, SI).

Overall, as evident from Fig. S4, SI, complex formation of curcumin resulted in increased stability of Cu(Cur) at physiological pH even under reducing conditions, unlike that observed for curcumin. This improved stability is attributed to complex formation, i.e., to binding of Cu(II) to the hydrolysis prone β-diketone moiety, thus preventing degradation of the complex under aqueous physiological conditions.

3.1.2. Using HPLC

The instability of curcumin was also investigated in an aqueous buffer (PBS) using HPLC. Some earlier studies performed in this regard indicate the formation of degradation products from curcumin like vanillin, vanillic acid, ferulic acid, feruloyl methane, etc. [28,63]. In our case, we dissolved curcumin and Cu(Cur) in phosphate buffer, and at different time intervals from the time of dissolution (incubation) of the compounds, HPLC was performed using a C18 column and a mobile phase whose composition has been mentioned earlier. In case of curcumin, a steady degradation identified by a decrease in peak height was observed, as reported earlier [28] (Fig. S5, SI). For the complex, the degradation of curcumin was a lot restricted. An overlay of chromatograms obtained for curcumin and its Cu(II) complex clearly demonstrates this (Fig. 1). It can be seen from Fig. 1 (b), which represents HPLC performed after 2 h and Fig. 1 (c) performed after 24 h from the time of dissolution of the compounds that while there is progressively an increased degradation of curcumin and formation of various degraded products, in case of the complex no such behavior was observed. Fig. 1 is clearly indicative of the fact that degradation of curcumin is remarkably checked following complex formation with Cu(II) and that in the case of the complex, there is a high possibility of curcumin remaining as "one unit" and not being degraded into different fragmented products. Achieving this, in fact, was one of the main intentions of forming a complex with curcumin. Fig. S5, SI and Fig. S6, SI show chromatograms recorded for curcumin and Cu(Cur), respectively, at different time intervals following their dissolution in phosphate buffer. Curcumin shows a steady degradation in phosphate buffer as the time from its dissolution and recording of HPLC gradually increases. On the contrary, for the complex, degradation is significantly less. It becomes more and more apparent that degraded products of curcumin like vanillin, vanillic acid,

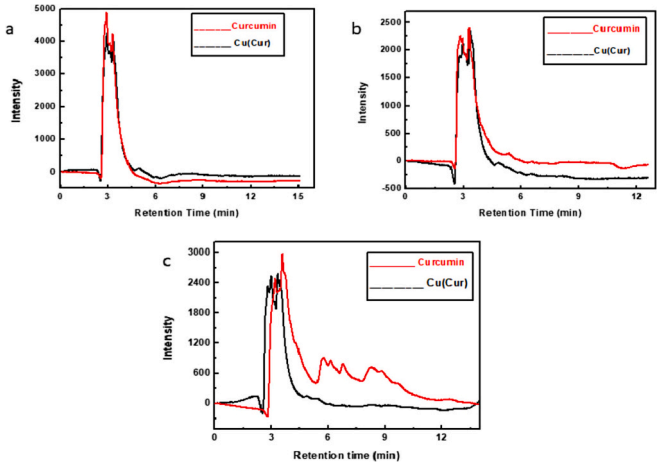


Fig. 1. Chromatograms obtained following HPLC of curcumin (—) and Cu(Cur) (—) at (a) immediately, (b) at 2 h and (c) at 24 h from the time of dissolution of the compounds in 0.1 M phosphate buffer. Column: C-18, Eluent: 12% THF, 5% CH_3CN, 2% acetic acid in water.

and ferulic acid are present in solution to a considerable extent along with curcumin (Fig. S7, SI). Even after a similar time was allowed for the dissolution of Cu(Cur) in phosphate buffer, no such degraded products were identified following HPLC of the complex, indicating that negligible degradation of the curcumin bound to the metal ion in the complex had occurred as compared to the HPLC performed immediately after the dissolution of the complex in phosphate buffer (Fig. 1).

3.2. Antibacterial efficacy of cu(cur) against S. aureus and E. coli

Antibacterial activity of Cu(Cur) was determined against the two most clinically relevant bacteria *S. aureus* and *E. coli*, and its efficacy was compared with the parent molecule curcumin. For this assay, bacterial cells (~10^6 CFU/mL) were exposed to different concentrations (25 and 50 μM) of the complex and curcumin up to 120 min. The killing efficacy was determined by comparing the percentage survival of curcumin- and Cu(Cur)- treated bacterial cells with untreated control (considered as 100%) and presented in Fig. 2A and B. Of note, as reported earlier, free Cu (II), i.e., $Cu(OAc)_2.H_2O$ did not show any antibacterial activity till 162 μM [41,42,64].

As shown in Fig. 2A, the killing assay exhibited that 60 min of exposure to 25 μM of Cu(Cur) caused 98.97 ± 0.28% killing, while for the same concentration and exposure time, curcumin killed only 36.73 ± 5.02% of cells. When the concentration was increased to 50 μM, the complex was able to kill 99.63 ± 0.23% bacterial cells, while a similar concentration of curcumin caused the killing of 67.41 ± 2.77% cells in 60 min (Fig. 2A). After increasing exposure time to 120 min, 50 μM of Cu (Cur) was able to cause complete eradication of approximately 10^6 CFU/mL, i.e., 100% killing was possible; in contrast, 84.94 ± 3.92% of killing was achieved with curcumin. Hence compared to curcumin, Cu(Cur) showed significant ($p \leq 0.001$) improvement in antibacterial efficacy against *S. aureus* at both time points and both concentrations.

In general, Gram-negative bacteria are innately resistant to many antibiotics, that are otherwise highly effective on Gram-positive bacteria, due to their outer membrane [65]. Hence, we evaluated any differential antibacterial efficacy of the complex against *E. coli* and found that the complex could completely eradicate *E. coli* cells as well. The killing assay of *E. coli* highlighted that 60 min of exposure to 25 μM of Cu (Cur) resulted in 100% killing of bacterial cells, while at the same concentration, curcumin could kill only 19.59 ± 3.63% cells (Fig. 2B). Even when concentration was increased to 50 μM and exposure time to 120 min, still curcumin could only kill 35.69 ± 2.82% of cells. Such enhancement in killing efficacy of Cu(Cur), compared to curcumin, was statistically significant ($p \leq 0.001$) at both time points of 60 and 120 min, also at both concentrations.

3.3. Mechanistic insights into the antibacterial activity of cu(cur)

3.3.1. Bacterial membrane permeabilization by calcein leakage assay

Towards deciphering the mechanism of action of the complex, we examined its membrane permeabilizing ability by the calcein leakage assay [55,56]. Calcein-AM is a non-fluorescent derivative of calcein, which is hydrophobic in nature, so it can easily cross the cell membrane. Once inside the cells, its acetoxymethyl ester is hydrolyzed by cytoplasmic esterases, and the non-fluorescent calcein-AM gets converted to a green-fluorescent calcein, which cannot cross the membrane unless it gets damaged [66].

Calcein-loaded bacterial cells were treated with two different concentrations (25 and 50 μM) of curcumin and Cu(Cur) and for three different time points (2, 60, and 120 min), presented in Fig. 3. The results showed that 25 μM of Cu(Cur) after only 2 min of exposure caused 86.95 ± 5.88% calcein leakage (Fig. 3). In comparison, at the same concentration and exposure time, curcumin caused only 37.22 ± 12.81% dye leakage. Even when the concentration was further increased

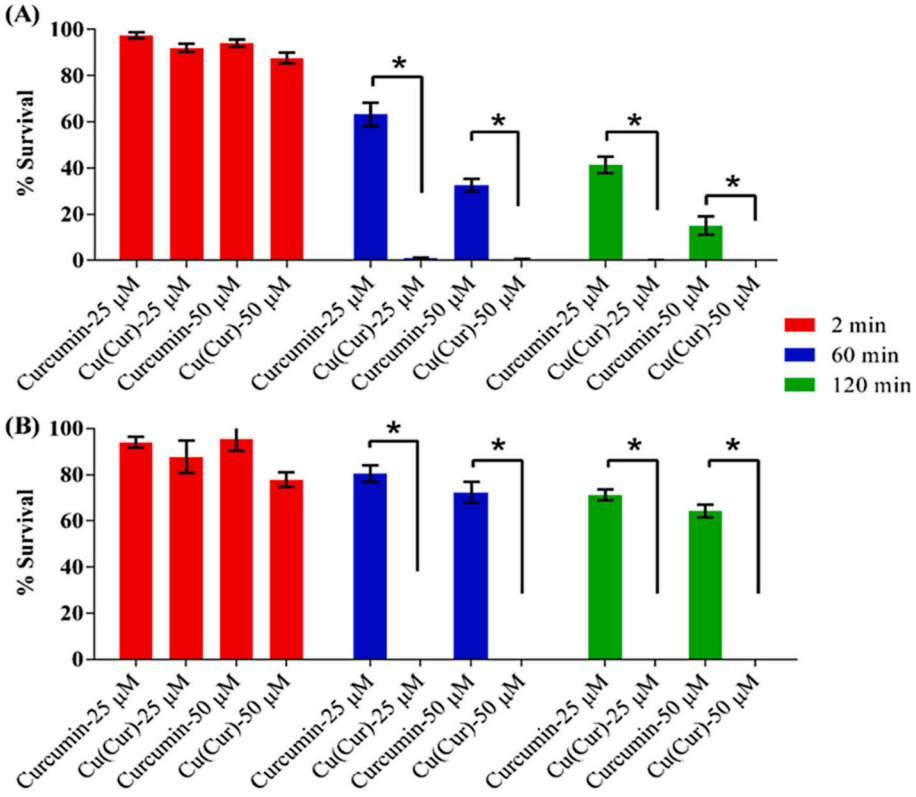


Fig. 2. Bacterial killing kinetics of curcumin and Cu(Cur) against 10^6 CFU/mL of (A) *S. aureus* and (B) *E. coli* cells at 25 and 50 μM in PBS buffer. Red, blue, and green blocks represent 2 min, 60 min, and 120 min exposure of compounds, respectively. The experiment was performed on three independent days, and each bar represents mean ± SD (*$p \leq 0.001$). (For interpretation of the references to colour in this figure legend, the reader is referred to the web version of this article.)

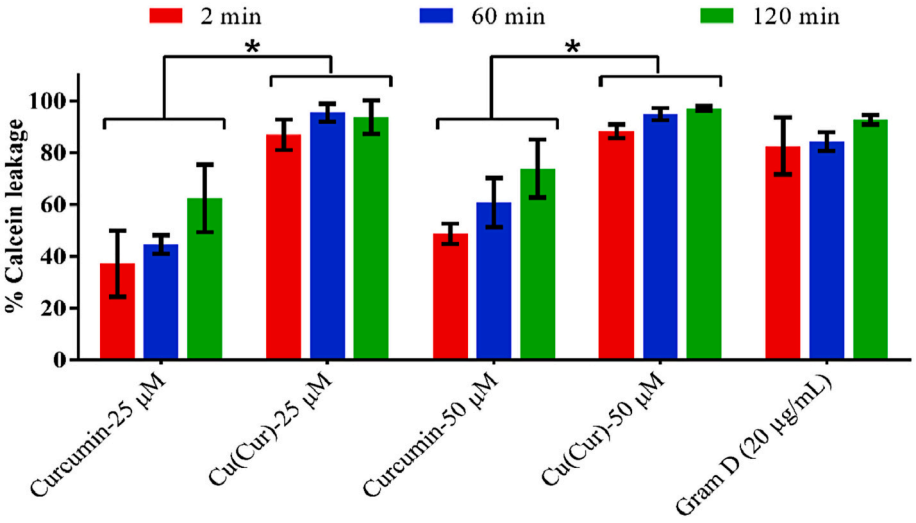


Fig. 3. Membrane permeabilization induced by curcumin and Cu(Cur) in *S. aureus* detected by calcein leakage assay. The percentage leakage caused by 25 and 50 μM of curcumin, Cu(Cur), and 20 μg/mL gramicidin D (Gram D) upon exposure of 2 min, 60 min, and 120 min. The experiment was repeated thrice, and the error bar represent mean ± SD (*$p \leq 0.01$). A total of 10,000 events were acquired with a low flow rate for each flow cytometry analysis.

to 50 μM, curcumin caused only 48.69 ± 3.92% leakage. The calcein leakage of Cu(Cur) was comparable with that of gramicidin D, a well-known pore-forming peptide that caused 82.68 ± 10.93% leakage at 20 μg/mL (Fig. 3), suggesting, the complex was very efficient in permeabilizing the bacterial membrane.

Further, our time-dependent membrane permeabilization study presented in Fig. 3 showed that at 25 μM, the complex caused 95.47 ± 3.49% permeabilization after 60 min of incubation; in comparison, curcumin caused only 44.59 ± 3.66% permeabilization. Overall, Cu(Cur) showed a better and statistically significant increase in membrane permeabilization compared to curcumin at both concentrations and at every time interval, i.e., 2 min, 60 min, and 120 min (p-value ≤ 0.01). Indeed, the extent of permeabilization due to Cu(Cur) was almost equal or even better than 20 μg/mL gramicidin D. Histograms of the calcein-loaded *S. aureus* cells incubated with the complex and curcumin for 2, 60, and 120 min are presented in Figs. 4, 5, and 6, respectively.

3.3.2. *Assessment of membrane integrity of S. aureus cells by fluorescence microscopy*

Calcein leakage assay indicated membrane permeabilization as a possible mode of action of Cu(Cur). To further ascertain the membrane-directed mechanism of the complex, the integrity of the bacterial membrane was assessed by a fluorescence-based dual staining procedure using DNA binding dyes SYTO 9 and PI. SYTO 9 can penetrate all cell membranes (intact and damaged) freely and labels the cells green. In contrast, PI can only penetrate cells with damaged membranes. When both dyes are present, PI, having a stronger binding affinity for DNA, replaces SYTO 9 from DNA, resulting in red fluorescence for the dead cells [67]. The fluorescently-labeled cells were visualized with fluorescence microscopy and representative merged images of both FITC and PI filters are presented in Fig. 7.

The untreated control cells appeared as a green lawn (Fig. 7 A), suggesting the intact membrane and viability of these cells, whereas the colour of Cu(Cur)-treated cells was predominantly red (Fig. 7 B), suggesting mostly dead cells with the compromised membrane. This membrane damaging property of the complex was in line with the findings of the calcein leakage assay. As for curcumin-treated cells, a mixed population of red, green, and yellow stained cells was observed (Fig. 7 C). The yellow fluorescent cells retained both red and green dyes; this indicated minor damage to the membrane that allows only some of PI to enter the cell, which is not high enough to replace all SYTO 9 bound to DNA; therefore, it appeared yellow and green [67,68].

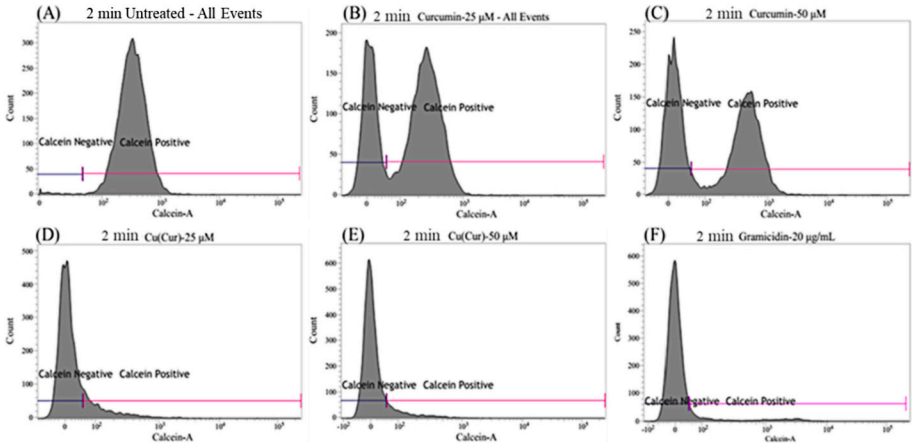


Fig. 4. Representative flow cytometry histograms of calcein leakage assay. Calcein-loaded cells were incubated with curcumin, Cu(Cur), and gramicidin D for 2 min. (A) Untreated control, (B) 25 μM of curcumin, (C) 50 μM of curcumin, (D) 25 μM of Cu(Cur), (E) 50 μM of Cu(Cur), and (F) 20 μg/mL gramicidin D.

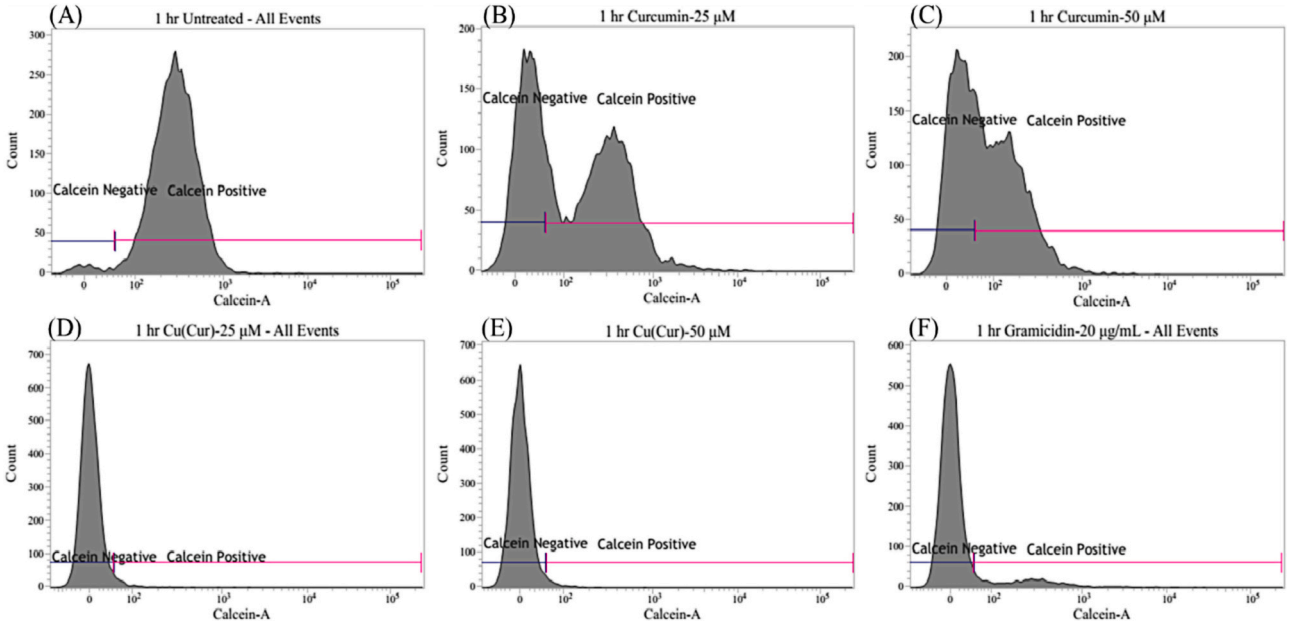


Fig. 5. Representative flow cytometry histograms of calcein leakage assay. Calcein-loaded cells were incubated with curcumin, Cu(Cur), and gramicidin D for 60 min. (A) Untreated control, (B) 25 µM of curcumin, (C) 50 µM of curcumin, (D) 25 µM of Cu(Cur), (E) 50 µM of Cu(Cur), and (F) 20 µg/mL gramicidin D.

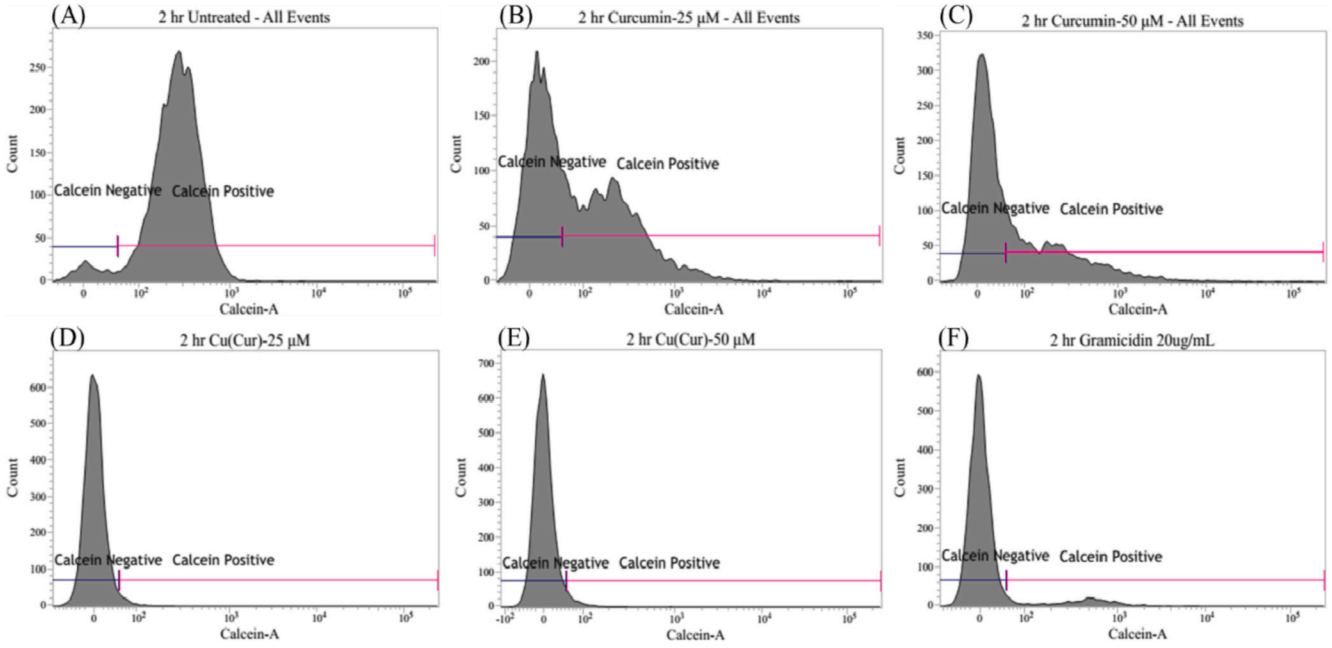


Fig. 6. Representative flow cytometry histograms of calcein leakage assay. Calcein-loaded cells were incubated with curcumin, Cu(Cur), and gramicidin D for 120 min. (A) Untreated control, (B) 25 µM of curcumin, (C) 50 µM of curcumin, (D) 25 µM of Cu(Cur), (E) 50 µM of Cu(Cur), and (F) 20 µg/mL gramicidin D.

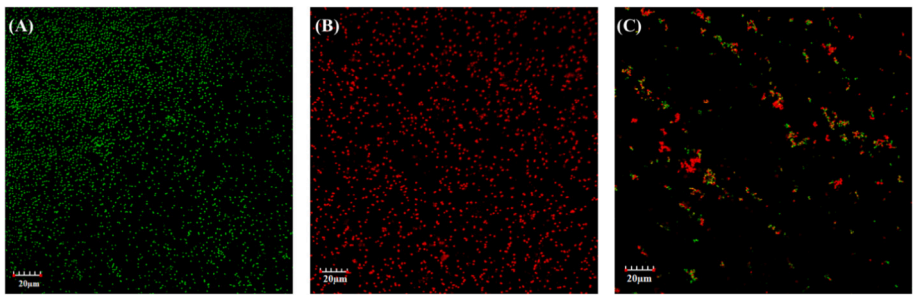


Fig. 7. Confocal microscopy images of *S. aureus* treated with 50 µM Cu(Cur) and curcumin for 2 h after staining with fluorescent probes SYTO 9 and PI. Representative merged images of both (FITC + PI) channels of (A) untreated control cells, (B) Cu(Cur)-, and (C) curcumin-treated cells. Green indicates live bacteria, while red indicates dead and membrane-damaged bacterial cells. (For interpretation of the references to colour in this figure legend, the reader is referred to the web version of this article.)

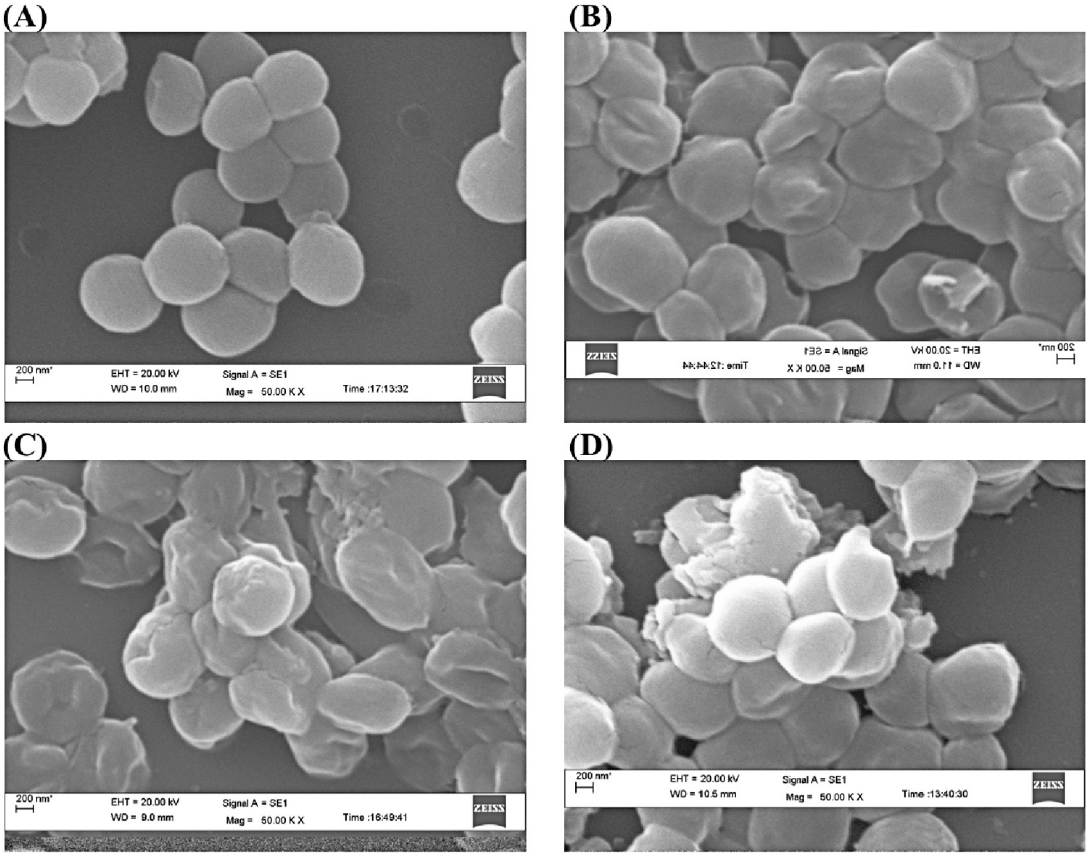


Fig. 8. Scanning electron micrographs of *S. aureus* treated for 2 h with 50 μM of curcumin and Cu(Cur), and 20 μg/mL gramicidin D. (A) Untreated control cells, (B) curcumin, (C) Cu(Cur), and (D) gramicidin D-treated cells at 50,000× magnification.

3.3.3. Investigation of morphological changes in S. aureus using scanning electron microscope

The membrane-disruptive mechanism of action of Cu(Cur) was further validated by visualizing the surface perturbations in *S. aureus* cell membrane, using SEM, following 2 h of incubation with 50 μM curcumin and Cu(Cur). Morphological changes in treated samples were

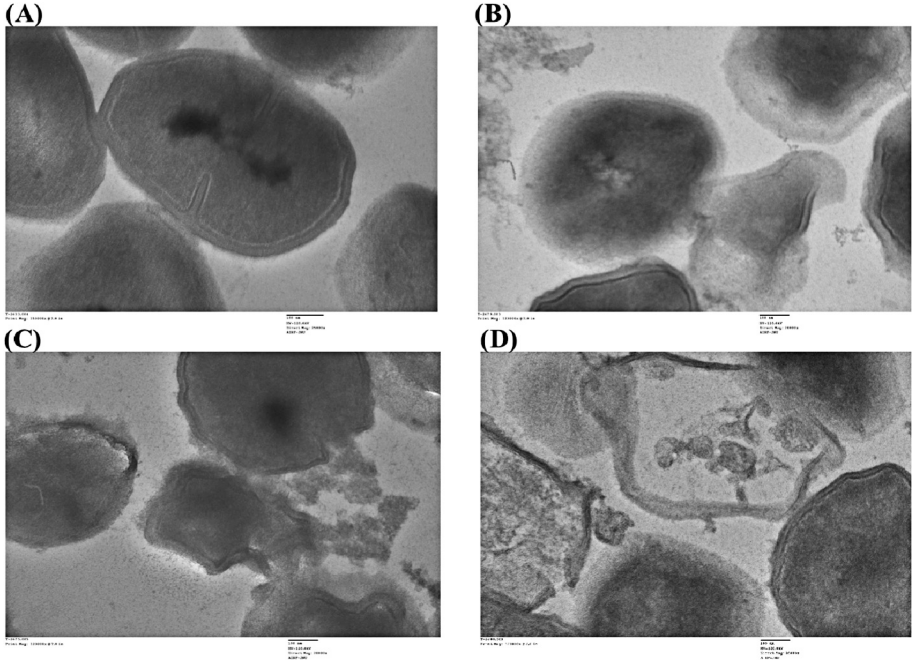


Fig. 9. Transmission electron micrographs of *S. aureus* treated with 50 μM each of curcumin and Cu(Cur) and 20 μg/mL gramicidin D for 2 h. (A) Untreated control cells, (B) curcumin, (C) Cu(Cur) and (D) gramicidin D (20 μg/mL) treated cells at 20,000× magnification.

compared to untreated ones and gramicidin D-treated samples (positive control). As evident from Fig. 8 A, *S. aureus* cells of the untreated control group maintained a smooth surface and uniform size with round morphology. However, surface perturbation and release of intracellular content as debris were evident for cells that had undergone treatment with Cu(Cur) and curcumin. These treated cells appeared to be highly wrinkled, with holes and multiple dents on the surface (Fig. 8 B–C). Changes in surface morphology following treatment with the complex were comparable to that of gramicidin D-treated samples (Fig. 8 D).

3.3.4. Investigation of ultrastructural changes in S. aureus using transmission electron microscope

Additionally, ultrastructural changes in *S. aureus* cells after treatment of 50 μM curcumin and Cu(Cur) were visualized using TEM and compared to untreated and gramicidin D-treated cells. From Fig. 9 A, it is evident that the untreated control sample had regular cocci morphology with an intact cell envelope. After treatment, several distinguished signs of damaged cell envelop were apparent. Most of the cells had a shredded cell wall which led to a distorted and irregular shape. Many cells lacked cytoplasmic content; intracellular contents were also oozing out from a few cells (Fig. 9 B–C). These ultrastructural changes that resulted from the treatment of Cu(Cur) were comparable to that of gramicidin D-treated samples (Fig. 9 D).

Overall, these alterations in bacterial surface visualized by microscopic images of both SEM and TEM indicate membrane perturbation to be the key mechanism for antibacterial activity of the complex, at least for *S. aureus* cells.

3.4. Potential toxicity studies of Cu(Cur) towards mammalian cells

Since curcumin is well tolerated and does not impart any toxicity, it was paramount to test whether complex formation introduces any toxicity in mammalian cells. Therefore, first, we investigated the hemolytic activity of Cu(Cur) on mouse RBCs. Next, we studied the cytotoxic potential of Cu(Cur) against mouse embryo fibroblast cells (3T3) and then human embryonic kidney epithelial cells (HEK293) with different exposure times. For this, we selected two concentrations of the complex, i.e., 250 and 500 μM, which were many-fold higher than its antibacterial dose.

Results of the hemolytic assay (Fig. 10 A) confirmed that Cu(Cur), like curcumin, was nearly non-hemolytic up to 500 μM. It caused only 2.19 ± 1.19% hemolysis at 250 μM and 6.96 ± 2.30% hemolysis at 500 μM. In this experiment, cell lysis by 0.1% Triton X-100 was used as the positive control.

In addition to hemolytic assay, MTT assay was also carried out to further rule out any potential cytotoxicity on mammalian cells. This assay assesses cellular metabolic activity as a proxy for cell viability in terms of the ability of viable cells to reduce the MTT reagent to formazan crystals by mitochondrial dehydrogenases [69]. As evident from Fig. 10 B, Cu(Cur) had a negligible cytotoxic effect on 3 T3 murine fibroblast cells up to 500 μM. The complex caused only 7.81 ± 1.06% cytotoxicity at 250 μM and 14.88 ± 2.27% cytotoxicity at 500 μM. 2.0% Triton X-100 was used as a positive control, which caused 87.86 ± 2.82% cytotoxicity relative to untreated growth control.

The MTT assay was further extended to human cell lines for a longer time to provide additional insights into the safety profile of the complex. As evident from Fig. 11 A, continuous exposure of Cu(Cur) for 24 h against HEK293 cells resulted in 8.72 ± 4.61%, and 22.34 ± 10.27% cytotoxicity at 250 and 500 μM, respectively, whereas 2% Triton X-100 (positive control) caused 95.72 ± 1.09% cytotoxicity relative to untreated control.

In addition, to ensure the non-toxic effect of Cu(Cur), human HEK293 cell lines were incubated for an additional 72 h in a fresh medium after 4 h of exposure to the complex. As seen from Fig. 11 B, exposing HEK293 cells to the complex for 4 h, followed by incubation for 72 h resulted in 22.75 ± 5.86%, and 28.18 ± 4.15% cytotoxicity at 250 μM and 500 μM concentration of Cu(Cur), respectively, while 2% Triton X-100 exhibited 95.22 ± 0.65% cytotoxicity relative to untreated control. Moreover, cytotoxicity studies against human cell lines suggest that the continuous exposure of 24 h of Cu(Cur) imparts little to negligible cytotoxic effect, while brief exposure (4 h) followed by a more extended incubation period exhibited a slightly higher cytotoxic effect at the tested concentrations. The latter may have resulted due to the declining nutrients in the medium, which was replenished only once during the entire 72 h duration.

Collectively, the toxicity assays indicate that the complex was non-toxic as it exhibited negligible to low toxicity in mammalian cells up to 500 μM, which was well above the dose required for antibacterial activity, which substantiates its therapeutic potential as a safe antibacterial agent.

4. Conclusion

In this study, a synthesized Cu(II) complex of curcumin, Cu(Cur), was studied for its stability and antibacterial activity, and the results were compared with curcumin in parallel experiments. The complex showed significantly improved stability under different physiological conditions than curcumin, which is a positive attribute of complex formation. However, the complex formation could not improve aqueous solubility as these complexes were still sparingly soluble in water. However, the complex showed significant enhancement in antibacterial activity over curcumin against both Gram-positive and Gram-negative bacterial cells. Of note, as previously reported by us [41,42,64], free Cu(II) salt did not show any antibacterial activity up to 162 μM. The calcein leakage assay revealed that Cu(Cur) triggered immediate membrane permeabilization in *S. aureus*. Confocal microscopy also confirmed the membrane perturbation mode of action as highlighted by predominantly red fluorescence of PI in complex-treated *S. aureus*. The membrane targeting mode of action was further substantiated through electron microscopy. SEM and TEM images showcased the noteworthy morphological and ultrastructural changes in cell surface following treatment with the complex. All these studies confirmed that the complex targets bacterial

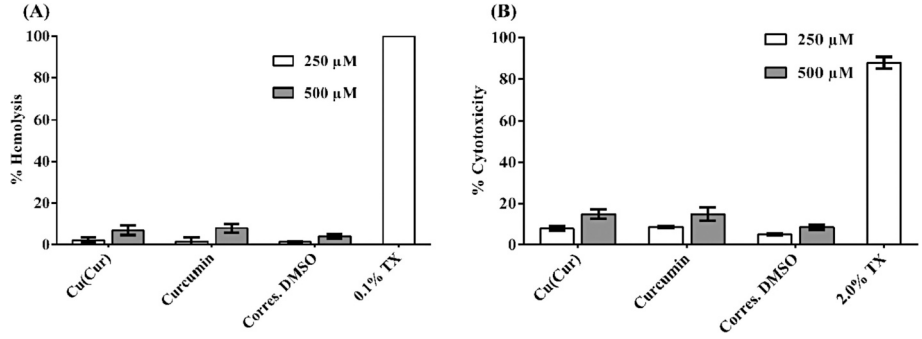


Fig. 10. (A) Hemolytic activity of Cu(Cur) and curcumin on mouse RBCs. In this assay, 0.1% Triton X-100 (TX) was used as a positive control (considered 100% hemolysis). Each bar represents mean ± SD from a single assay performed in triplicate. (B) Cytotoxicity of Cu(Cur) and curcumin on 3T3 murine fibroblast cell line. The percentage viability of cells relative to the untreated control was measured using the MTT assay. The experiment was repeated thrice in duplicate independently, and each data point represents mean ± SD.

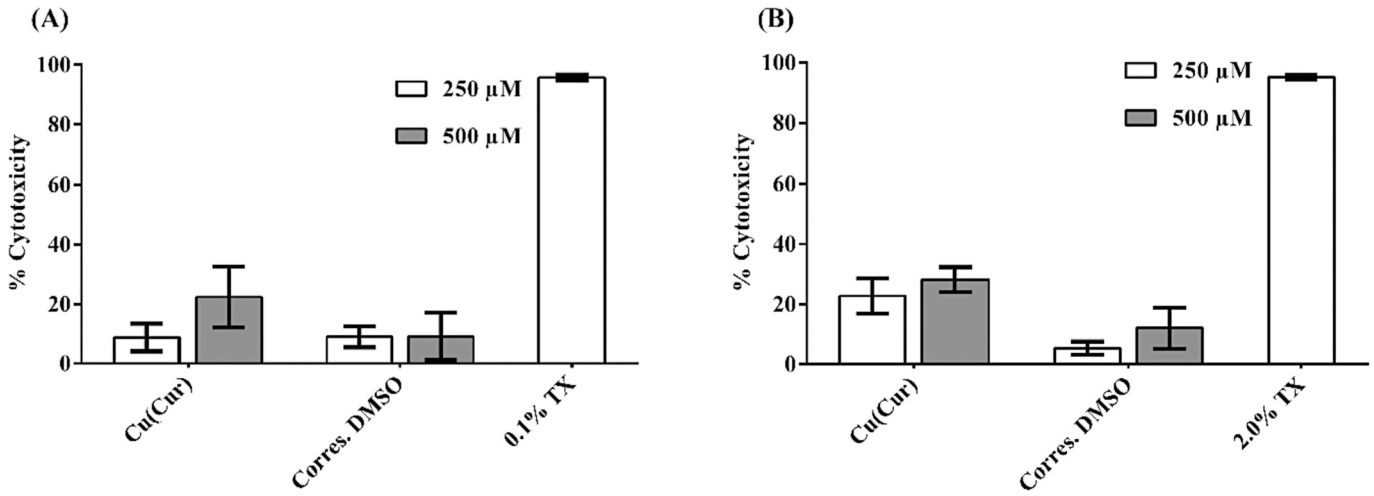


Fig. 11. Cytotoxicity of Cu(Cur) against human embryonic kidney epithelial (HEK293) cells. (A) Continuous exposure of the complex for 24 h, (B) exposure of complex for 4 h followed by further incubation of 72 h in fresh medium. The experiment was repeated twice in triplicates, and each data point represents mean ± SD.

membrane and that membrane perturbation is a key mechanism for the antibacterial activity of the complex. Moreover, the excellent potency of the complex was further strengthened by its minimal toxicity towards mammalian cells, as it was nearly non-hemolytic and non-cytotoxic, even at much higher concentrations than that required for its antibacterial activity.

In this context, it is worth mentioning that, to the best of our knowledge, there is a recent report on a Cu-curcumin metal complex possessing antibacterial activity against *S. aureus* and *E. Coli* [70], where ligands involved are entirely different. Their curcumin was used as a starting material, but it has been heavily modified by allowing it to combine with nicotinamide, where the NH_2 group of each nicotinamide forms a Schiff base adduct with two carbonyls of curcumin. Thus, the core of curcumin itself is changed. Although this study is important from a synthetic chemistry point of view, so far as biology is concerned, it would be far from reality as such ligands would not be readily available in nature. On the other hand, ours is a complex where curcumin is in its native form, a form that can be readily available from food, and if that is in the immediate vicinity of Cu(II) ions, then a combination of the two leading to complex formation can be a more realistic alternative.

Overall, the present study, aimed to develop a curcumin-based antibacterial compound, advocates the potential of this physiologically stable, membrane targeting, non-toxic complex, making it an excellent candidate for further ex vivo and in vivo investigations (potential inhibition of bacterial cell growth internalized/associated with mammalian cells) for its therapeutic applications [71,72].

Declaration of Competing Interest

The authors declare no conflict of interest.

Acknowledgments

KM is grateful to University Grants Commission (UGC-UPE-II: ID-59) and DST-PURSE (Phase-II) for receiving grants that came to JNU, New Delhi. She is also thankful for the financial grants from Department of Biotechnology (DBT-BT/PR27737/MED/29/1265/2018) and Department of Science and Technology (DST-SERB-EMR/2016/001708). SD wishes to thank Jadavpur University, Kolkata for financial support in the form of a major research project under RUSA 2.0 on the thrust area "Research in Sustainable Development" [Sanction Ref. no. R-11/438/19 dated 30.05.2019]. He acknowledges financial support from DST-PURSE, UGC (funding for research program on "Advanced Materials", as part of UPE II to Jadavpur University) and UGC–CAS II Program that operated at the Department of Chemistry, Jadavpur University for the last five years. PK is grateful to UGC for Research Fellowship. TS is thankful to the Governing body of Sri Aurobindo Institute of Education, Salt Lake, Kolkata for permission to pursue research leading to a Ph.D. degree. SB and SG are thankful to CSIR and UGC for their fellowships, respectively. Authors acknowledge Ashok Sahu, Manu Vashistha, and Dr. Ruchita Pal of AIRF, JNU for their help in acquisition of confocal and electron microscopy images. We also thank Dr. Swati Tiwari (SBT, JNU) and Prof. Rupesh Chaturvedi (SBT, JNU) for providing mammalian cell cultures and biosafety level-II (BSL-2) facilities.

Appendix A. Supplementary data

Supplementary data to this article can be found online at https://doi.org/10.1016/j.jinorgbio.2021.111494.

References

[1] E. Patridge, P. Gareiss, M.S. Kinch, D. Hoyer, An analysis of FDA-approved drugs: natural products and their derivatives, Drug Discov. Today 21 (2016) 204–207.
[2] N.E. Thomford, D.A. Senthebane, A. Rowe, D. Munro, P. Seele, A. Maroyi, K. Dzobo, Natural products for drug discovery in the 21st century: innovations for novel drug discovery, Int. J. Mol. Sci. 19 (2018) 1578.
[3] S.S. Kadri, Key takeaways from the U.S. CDC's 2019 antibiotic resistance threats report for frontline providers, Crit. Care Med. 48 (2020) 939–945.
[4] T.M. Rawson, D. Ming, R. Ahmad, L.S.P. Moore, A.H. Holmes, Antimicrobial use, drug-resistant infections and COVID-19, Nat. Rev. Microbiol. 18 (2020) 409–410.
[5] J. Hsu, How COVID-19 is accelerating the threat of antimicrobial resistance, Br. Med. J. 369 (2020) m1983.
[6] T.M. Rawson, L.S.P. Moore, N. Zhu, N. Ranganathan, K. Skolimowska, M. Gilchrist, G. Satta, G. Cooke, A. Holmes, Bacterial and fungal co-infection in individuals with coronavirus: a rapid review to support COVID-19 antimicrobial prescribing, Clin. Infect. Dis. 71 (2020) 2459–2468.
[7] H.F. Wertheim, D.C. Melles, M.C. Vos, W. van Leeuwen, A. van Belkum, H. A. Verbrugh, J.L. Nouwen, The role of nasal carriage in *Staphylococcus aureus* infections, Lancet Infect. Dis. 5 (2005) 751–762.
[8] E.F. Kong, J.K. Johnson, Community-associated methicillin-resistant *Staphylococcus aureus*: an enemy amidst us, PLoS Pathog. 12 (2016), e1005837.
[9] K. Hiramatsu, Y. Katayama, M. Matsuo, T. Sasaki, Y. Morimoto, A. Sekiguchi, T. Baba, Multi-drug-resistant *Staphylococcus aureus* and future chemotherapy, J. Infect. Chemother. 20 (2014) 593–601.
[10] V. Niranjan, A. Malini, Antimicrobial resistance pattern in *Escherichia coli* causing urinary tract infection among inpatients, Indian J. Med. Res. 139 (2014) 945–948.
[11] F.Y. Ramírez-Castillo, A.C. Moreno-Flores, F.J. Avelar-González, F. Márquez-Díaz, J. Harel, A.L. Guerrero-Barrera, An evaluation of multidrug-resistant *Escherichia coli* isolates in urinary tract infections from Aguascalientes, Mexico: cross-sectional study, Ann. Clin. Microbiol. Antimicrob. 17 (2018), 34.
[12] P.M. Hawkey, R.E. Warren, D.M. Livermore, C.A.M. McNulty, D.A. Enoch, J. A. Otter, A.P.R. Wilson, Treatment of infections caused by multidrug-resistant Gram-negative bacteria: report of the British Society for Antimicrobial Chemotherapy/Healthcare Infection Society/British Infection Association Joint Working Party, J. Antimicrob. Chemother. 73 (2018) iii2–iii78.

[13] N.G. El Chakhtoura, E. Saade, A. Iovleva, M. Yasmin, B. Wilson, F. Perez, R. A. Bonomo, Therapies for multidrug resistant and extensively drug-resistant non-fermenting gram-negative bacteria causing nosocomial infections: a perilous journey toward 'molecularly targeted' therapy, Expert Rev. Anti-Infect. Ther. 16 (2018) 89–110.

[14] B.B. Aggarwal, C. Sundaram, N. Malani, H. Ichikawa, Curcumin: the Indian solid gold, Adv. Exp. Med. Biol. 595 (2007) 1–75.

[15] T. Ak, I. Gülçin, Antioxidant and radical scavenging properties of curcumin, Chem. Biol. Interact. 174 (2008) 27–37.

[16] J.S. Jurenka, Anti-inflammatory properties of curcumin, a major constituent of *Curcuma longa*: a review of preclinical and clinical research, Altern. Med. Rev. 14 (2009) 141–153.

[17] M.A. Tomeh, R. Hadianamrei, X. Zhao, A review of curcumin and its derivatives as anticancer agents, Int. J. Mol. Sci. 20 (2019) 1033.

[18] M. Mutsuga, J.K. Chambers, K. Uchida, M. Tei, T. Makibuchi, T. Mizorogi, A. Takashima, H. Nakayama, Binding of curcumin to senile plaques and cerebral amyloid angiopathy in the aged brain of various animals and to neurofibrillary tangles in Alzheimer's brain, J. Vet. Med. Sci. 74 (2012) 51–57.

[19] A. Goel, A.B. Kunnumakkara, B.B. Aggarwal, Curcumin as "Curecumin": from kitchen to clinic, Biochem. Pharmacol. 75 (2008) 787–809.

[20] K.M. Nelson, J.L. Dahlin, J. Bisson, J. Graham, G.F. Pauli, M.A. Walters, The essential medicinal chemistry of curcumin, J. Med. Chem. 60 (2017) 1620–1637.

[21] C.D. Lao, M.T.T. Ruffin, D. Normolle, D.D. Heath, S.I. Murray, J.M. Bailey, M. E. Boggs, J. Crowell, C.L. Rock, D.E. Brenner, Dose escalation of a curcuminoid formulation, BMC Complement. Altern. Med. 6 (2006) 10.

[22] K. Neelofar, S. Shreaz, B. Rimple, S. Muralidhar, M. Nikhat, L.A. Khan, Curcumin as a promising anticandidal of clinical interest, Can. J. Microbiol. 57 (2011) 204–210.

[23] S.Y. Teow, K. Liew, S.A. Ali, A.S. Khoo, S.C. Peh, Antibacterial action of curcumin against *Staphylococcus aureus*: a brief review, J. Trop. Med. 2016 (2016) 2853045.

[24] B.C. Mounce, T. Cesaro, L. Carrau, T. Vallet, M. Vignuzzi, Curcumin inhibits Zika and chikungunya virus infection by inhibiting cell binding, Antivir. Res. 142 (2017) 148–157.

[25] J. Wang, X. Zhou, W. Li, X. Deng, Y. Deng, X. Niu, Curcumin protects mice from *Staphylococcus aureus* pneumonia by interfering with the self-assembly process of α-hemolysin, Sci. Rep. 6 (2016), 28254.

[26] P. Tyagi, M. Singh, H. Kumari, A. Kumari, K. Mukhopadhyay, Bactericidal activity of curcumin I is associated with damaging of bacterial membrane, PLoS One 10 (2015), e0121313.

[27] T. Saha, P. Kumar, N. Sepay, D. Ganguly, K. Tiwari, K. Mukhopadhyay, S. Das, Multitargeting antibacterial activity of a synthesized Mn^{2+} complex of curcumin on Gram-positive and Gram-negative bacterial strains, ACS Omega 5 (2020) 16342–16357.

[28] Y.J. Wang, M.H. Pan, A.L. Cheng, L.I. Lin, Y.S. Ho, C.Y. Hsieh, J.K. Lin, Stability of curcumin in buffer solutions and characterization of its degradation products, J. Pharm. Biomed. Anal. 15 (1997) 1867–1876.

[29] H.H. Tønnesen, J. Karlsen, Studies on curcumin and curcuminoids, Z. Lebensm. Unters. Forsch. 180 (1985) 402–404.

[30] R.A. Sharma, W.P. Steward, A.J. Gescher, Pharmacokinetics and pharmacodynamics of curcumin, Adv. Exp. Med. Biol. 595 (2007) 453–470.

[31] S.B. de Souza Ferreira, M.L. Bruschi, Improving the bioavailability of curcumin: is micro/nanoencapsulation the key? Ther. Deliv. 10 (2019) 83–86.

[32] P. Anand, A.B. Kunnumakkara, R.A. Newman, B.B. Aggarwal, Bioavailability of curcumin: problems and promises, Mol. Pharm. 4 (2007) 807–818.

[33] W.-H. Lee, C.-Y. Loo, M. Bebawy, F. Luk, R.S. Mason, R. Rohanizadeh, Curcumin and its derivatives: their application in neuropharmacology and neuroscience in the 21st century, Curr. Neuropharmacol. 11 (2013) 338–378.

[34] I. Priyadarsini, The chemistry of curcumin: from extraction to therapeutic agent, Molecules 19 (2014) 20091–20112.

[35] S. Banerjee, P. Prasad, A. Hussain, I. Khan, P. Kondaiah, A.R. Chakravarty, Remarkable photocytotoxicity of curcumin in HeLa cells in visible light and arresting its degradation on oxovanadium(IV) complex formation, Chem. Commun. 48 (2012) 7702–7704.

[36] M.H. Leung, T. Harada, T.W. Kee, Delivery of curcumin and medicinal effects of the copper(II)-curcumin complexes, Curr. Pharm. Des. 19 (2013) 2070–2083.

[37] D. Pucci, A. Crispini, B. Sanz Mendiguchía, S. Pirillo, M. Ghedini, S. Morelli, L. De Bartolo, Improving the bioactivity of Zn(II)-curcumin based complexes, Dalton Trans. 42 (2013) 9679–9687.

[38] S. Wanninger, V. Lorenz, A. Subhan, F.T. Edelmann, Metal complexes of curcumin – synthetic strategies, structures and medicinal applications, Chem. Soc. Rev. 44 (2015) 4986–5002.

[39] T. Saha, S. Singha, S. Kumar, S. Das, Spectroscopy driven DFT computation for a structure of the monomeric Cu^{2+}-curcumin complex and thermodynamics driven evaluation of its binding to DNA: pseudo-binding of curcumin to DNA, J. Mol. Struct. 128732 (2020).

[40] T. Deb, P. Gopal, D. Ganguly, D.P. Das, M. Paul, M. Saha, S. Paul, S. Das, Enhancement of anti-leukemic potential of 2-hydroxyphenyl-azo-2′-naphthol (HPAN) on MOLT-4 cells through conjugation with Cu(II), RSC Adv. 4 (2014) 18419–18430.

[41] R.C. Santra, D. Ganguly, S. Jana, N. Banyal, J. Singh, A. Saha, S. Chattopadhyay, K. Mukhopadhyay, S. Das, Synthesizing a Cu(II) complex of tinidazole to tune the generation of the nitro radical anion in order to strike a balance between efficacy and toxic side effects, New J. Chem. 41 (2017) 4879–4886.

[42] R.C. Santra, D. Ganguly, J. Singh, K. Mukhopadhyay, S. Das, A study on the formation of the nitro radical anion by ornidazole and its significant decrease in a structurally characterized binuclear Cu(II)-complex: impact in biology, Dalton Trans. 44 (2015) 1992–2000.

[43] K. Mitra, S. Gautam, P. Kondaiah, A.R. Chakravarty, Platinum(II) complexes of curcumin showing photocytotoxicity in visible light, Eur. J. Inorg. Chem. 2017 (2017) 1753–1763.

[44] T. Deb, D. Choudhury, P.S. Guin, M.B. Saha, G. Chakrabarti, S. Das, A complex of Co(II) with 2-hydroxyphenyl-azo-2′-naphthol (HPAN) is far less cytotoxic than the parent compound on A549-lung carcinoma and peripheral blood mononuclear cells: reasons for reduction in cytotoxicity, Chem. Biol. Interact. 189 (2011) 206–214.

[45] A. Shakeri, Y. Panahi, T.P. Johnston, A. Sahebkar, Biological properties of metal complexes of curcumin, BioFactors 45 (2019) 304–317.

[46] M.S. Refat, Synthesis and characterization of ligational behavior of curcumin drug towards some transition metal ions: chelation effect on their thermal stability and biological activity, Spectrochim. Acta A Mol. Biomol. Spectrosc. 105 (2013) 326–337.

[47] Y.M. Song, J.P. Xu, L. Ding, Q. Hou, J.W. Liu, Z.L. Zhu, Syntheses, characterization and biological activities of rare earth metal complexes with curcumin and 1,10-phenanthroline-5,6-dione, J. Inorg. Biochem. 103 (2009) 396–400.

[48] Y. Lyu, M. Yu, Q. Liu, Q. Zhang, Z. Liu, Y. Tian, D. Li, M. Changdao, Synthesis of silver nanoparticles using oxidized amylose and combination with curcumin for enhanced antibacterial activity, Carbohydr. Polym. 230 (2020) 115573.

[49] P. Jahangoshaei, L. Hassani, F. Mohammadi, A. Hamidi, K. Mohammadi, Investigating the effect of gallium curcumin and gallium diacetylcurcumin complexes on the structure, function and oxidative stability of the peroxidase enzyme and their anticancer and antibacterial activities, J. Biol. Inorg. Chem. 20 (2015) 1135–1146.

[50] P. Srivastava, M. Shukla, G. Kaul, S. Chopra, A.K. Patra, Rationally designed curcumin based ruthenium(II) antimicrobials effective against drug-resistant *Staphylococcus aureus*, Dalton Trans. 48 (2019) 11822–11828.

[51] A. Ananth, S. Dharaneedharan, M.-S. Heo, Y.S. Mok, Copper oxide nanomaterials: synthesis, characterization and structure-specific antibacterial performance, Chem. Eng. J. 262 (2015) 179–188.

[52] N. Febré, V. Silva, A. Báez, H. Palza, K. Delgado, I. Aburto, V. Silva, Antibacterial activity of copper salts against microorganisms isolated from chronic infected wounds, Rev. Med. Chil. 144 (2016) 1523–1530.

[53] J. Sheikh, H. Juneja, V. Ingle, P. Ali, T.B. Hadda, Synthesis and in vitro biology of Co(II), Ni(II), Cu(II) and Zinc(II) complexes of functionalized beta-diketone bearing energy buried potential antibacterial and antiviral O, O pharmacophore sites, J. Saudi Chem. Soc. 17 (2013) 269–276.

[54] A. Barik, B. Mishra, L. Shen, H. Mohan, R.M. Kadam, S. Dutta, H.Y. Zhang, K. I. Priyadarsini, Evaluation of a new copper(II)-curcumin complex as superoxide dismutase mimic and its free radical reactions, Free Radic. Biol. Med. 39 (2005) 811–822.

[55] P. Kumar, S.K. Kandi, S. Manohar, K. Mukhopadhyay, D.S. Rawat, Monocarbonyl curcuminoids with improved stability as antibacterial agents against *Staphylococcus aureus* and their mechanistic studies, ACS Omega 4 (2019) 675–687.

[56] P. Kumar, S.K. Kandi, K. Mukhopadhyay, D.S. Rawat, Synthesis of novel monocarbonyl curcuminoids, evaluation of their efficacy against MRSA, including ex vivo infection model and their mechanistic studies, Eur. J. Med. Chem. 112276 (2020).

[57] J. Singh, S. Joshi, S. Mumtaz, N. Maurya, I. Ghosh, S. Khanna, V. Natarajan, K. Mukhopadhyay, Enhanced cationic charge is a key factor in promoting staphylocidal activity of α-melanocyte stimulating hormone via selective lipid affinity, Sci. Rep. 6 (2016) 31492.

[58] S. Joshi, S. Mumtaz, J. Singh, S. Pasha, K. Mukhopadhyay, Novel miniature membrane active lipopeptidomimetics against planktonic and biofilm embedded methicillin-resistant *Staphylococcus aureus*, Sci. Rep. (2018) 1021.

[59] N. Kannan, S. Shanmuga Sundar, S. Balaji, A. Amuthan, N. Anil Kumar, N. Balasubramanian, Physiochemical characterization and cytotoxicity evaluation of mercury-based formulation for the development of anticancer therapeuticals, PLoS One 13 (2018), e0200035.

[60] S.A.S. Shandiz, F. Sharifian, S. Behboodi, F. Ghodratpour, F. Baghbani-Arani, Evaluation of metastasis suppressor genes expression and in vitro anti-cancer effects of zinc oxide nanoparticles in human breast cancer cell lines MCF-7 and T47D, Avicenna J. Med. Biotechnol. 13 (2021) 9–14.

[61] Y.M. Go, D.P. Jones, Redox compartmentalization in eukaryotic cells, Biochim. Biophys. Acta 1780 (2008) 1273–1290.

[62] S. Chakraborti, G. Dhar, V. Dwivedi, A. Das, A. Poddar, G. Chakraborti, G. Basu, P. Chakrabarti, A. Surolia, B. Bhattacharyya, Stable and potent analogues derived from the modification of the dicarbonyl moiety of curcumin, Biochemistry 52 (2013) 7449–7460.

[63] P. Galer, B. Šket, Photodegradation of methoxy substituted curcuminoids, Acta Chim. Slov. 62 (2015) 346–353.

[64] R.C. Santra, K. Sengupta, R. Dey, T. Shireen, P. Das, P.S. Guin, K. Mukhopadhyay, S. Das, X-ray crystal structure of a Cu(II) complex with the antiparasitic drug tinidazole, interaction with calf thymus DNA and evidence for antibacterial activity, J. Coord. Chem. 67 (2014) 265–285.

[65] A.H. Delcour, Outer membrane permeability and antibiotic resistance, Biochim. Biophys. Acta 1794 (2009) 808–816.

[66] S.P. Koo, A.S. Bayer, M.R. Yeaman, Diversity in antistaphylococcal mechanisms among membrane-targeting antimicrobial peptides, Infect. Immun. 69 (2001) 4916–4922.

[67] L. Boulos, M. Prévost, B. Barbeau, J. Coallier, R. Desjardins, LIVE/DEAD BacLight: application of a new rapid staining method for direct enumeration of viable and total bacteria in drinking water, J. Microbiol. Methods 37 (1999) 77–86.

[68] M.S. Gião, S.A. Wilks, N.F. Azevedo, M.J. Vieira, C.W. Keevil, Validation of SYTO 9/propidium iodide uptake for rapid detection of viable but noncultivable *Legionella pneumophila*, Microb. Ecol. 58 (2009) 56–62.
[69] T. Mosmann, Rapid colorimetric assay for cellular growth and survival: application to proliferation and cytotoxicity assays, J. Immunol. Methods 65 (1983) 55–63.
[70] A. Kareem, M. Arshad, S.A. Nami, N. Nishat, Herbo-mineral based Schiff base ligand and its metal complexes: synthesis, characterization, catalytic potential and biological applications, J. Photochem. Photobiol. B Biol. 160 (2016) 163–171.
[71] R. Kotcherlakota, A.K. Barui, S. Prashar, M. Fajardo, D. Briones, A. Rodríguez-Diéguez, C.R. Patra, S. Gómez-Ruiz, Curcumin loaded mesoporous silica: an effective drug delivery system for cancer treatment, Biomater. Sci. 4 (2016) 448–459.
[72] V.S. Bollu, A.K. Barui, S.K. Mondal, S. Prashar, M. Fajardo, D. Briones, A. Rodriguez-Dieguez, C.R. Patra, S. Gómez-Ruiz, Curcumin-loaded silica-based mesoporous materials: synthesis, characterization and cytotoxic properties against cancer cells, Mater. Sci. Eng. C 63 (2016) 393–410.

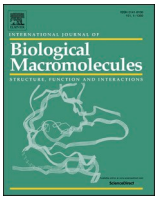
International Journal of Biological Macromolecules 245 (2023) 125305



Contents lists available at ScienceDirect

International Journal of Biological Macromolecules

journal homepage: www.elsevier.com/locate/ijbiomac





An insight into the mixed quantum mechanical-molecular dynamics simulation of a Zn^{II}-Curcumin complex with a chosen DNA sequence that supports experimental DNA binding investigations

Tanmoy Saha [a], Subrahmanyam Sappati [b,c], Saurabh Das [a,*]

[a] Department of Chemistry (Inorganic Section), Jadavpur University, Kolkata 700 032, India
[b] Department of Physical Chemistry, Gdańsk University of Technology, Gdańsk 80-233, Poland
[c] Department of Pharmaceutical Technology and Biochemistry, Gdańsk University of Technology, Gdańsk 80-233, Poland

ARTICLE INFO

Keywords:
Curcumin
Zn^{II}
DFT
Molecular docking
Molecular dynamic simulation
RMSD
RMSF
Radius of gyration
SASA
Hydrogen bonds

ABSTRACT

An important aspect of research pertaining to Curcumin (HCur) is the need to arrest its degradation in aqueous solution and in biological milieu. This may be achieved through complex formation with metal ions. For this reason, a complex of HCur was prepared with Zn^{II}, that is not likely to be active in redox pathways, minimizing further complications. The complex is monomeric, tetrahedral, with one HCur, an acetate and a molecule of water bound to Zn^{II}. It arrests degradation of HCur to a considerable extent that was realized by taking it in phosphate buffer and in biological milieu. The structure was obtained by DFT calculations. Stable adduct formation was identified between optimized structures of HCur and [Zn(Cur)] with DNA (PDB ID: 1BNA) through experiments validated with multiscale modeling approach. Molecular docking studies provide 2D and 3D representations of binding of HCur and [Zn(Cur)] through different non-covalent interactions with the nucleotides of the chosen DNA. Through molecular dynamics simulation, a detailed understanding of binding pattern and key structural characteristics of the generated DNA-complex was obtained following analysis by RMSD, RMSF, radius of gyration, SASA and aspects like formation of hydrogen bonds. Experimental studies provide binding constants for [Zn(Cur)] with calf thymus DNA at 25 °C that effectively helps one to realize its high affinity towards DNA. In the absence of an experimental binding study of HCur with DNA, owing to its tendency to degrade in solution, a theoretical analysis of the binding of HCur to DNA is extremely helpful. Besides, both experimental and simulated binding of [Zn(Cur)] to DNA may be considered as a case of pseudo-binding of HCur to DNA. In a way, such studies on interaction with DNA helps one to identify HCur's affinity for cellular target DNA, not realized through experiments. The entire investigation is an understanding of experimental and theoretical approaches that has been compared continuously, being particularly useful when a molecule's interaction with a biological target cannot be realized experimentally.

1. Introduction

Curcumin (HCur) is a lipophilic poly-phenol having a lot of potential that has promoted investigations on it in recent years [1–10]. Given its pharmacological effectiveness, there are a number of issues that prevent it from assuming the position it rightly deserves [1–10]. Research has demonstrated several medicinal benefits of HCur that are useful in treating various medical conditions and pharmacological issues [1,2,4–9,11,12]. Clinical trials and in vivo investigations demonstrate safety, low toxicity even at dose as high as 12 g/day for a period of three months [7]. However, the molecule fails to achieve its full potential in spite of outstanding pharmacological reports owing to poor solubility in aqueous media. It is prone to degradation in physiological buffer under reducing conditions [13–18]. The situation gets further complicated because it breaks down into smaller molecules in solution under pathophysiological conditions making it difficult to assign observed pharmacological actions to curcumin itself. Evidence suggests curcumin does not remain in solution as a single unit [12,18–20]. Consequently, it becomes difficult to say if the findings of pharmacological studies on curcumin are a result of curcumin itself or an outcome of the combined

Abbreviations: HCur, Curcumin; [Zn(Cur)], Zn^{II} complex of Curcumin.

* Corresponding author.
E-mail address: saurabh.das@jadavpuruniversity.in (S. Das).

https://doi.org/10.1016/j.ijbiomac.2023.125305
Received 28 February 2023; Received in revised form 24 May 2023; Accepted 30 May 2023
Available online 13 June 2023
0141-8130/© 2023 Elsevier B.V. All rights reserved.

effects of fragments produced in solution following hydrolysis. There is of course the likelihood of curcumin being present in solution as one unit in some proportion, depending upon the extent of hydrolysis in a certain medium. Like that of others, our observations too demonstrate when HCur is dissolved in aqueous buffer or in cellular media its absorbance decreases gradually [12,18]. There is however, no interference to the absorbance of HCur from any of the species generated from it (as all are colourless). Therefore, breakdown of curcumin is clearly evident as a gradual decline in absorbance when dissolved either in aqueous buffer or in cellular media [12,18]. Hence, to better comprehend situations and interpret pharmacological properties, it is important to have curcumin in solution as a "single unit" that entails preventing its degradation before interaction with a biological target. Formation of a coordination compound with it can accomplish this [12,13,18,20]. Metal-bound curcumin exists as a "single-unit" [12,13,18,20]. Inclusion of a metal ion should aid cellular uptake and take care of aspects related to solubility [21].

We synthesized a coordination complex (Zn^{II}-HCur) keeping these facts in mind. The complex was found to be stable in aqueous solution and in biological cellular media indicating HCur bound to Zn^{II} remains a "single-unit". By observing changes in absorption and emission spectra pertaining to Zn^{II}-HCur, interaction with calf-thymus DNA was experimentally explored, something that is not possible with HCur for reasons mentioned earlier (Fig. S1, SI). A comprehensive in silico analysis was performed to realize the nature of binding of HCur with DNA and to confirm and support what could have been achieved experimentally had HCur not degraded in solution [12,13,18,20]. To this end, molecular docking and molecular dynamics simulation techniques were used [22,23]. Molecular docking provides three-dimensional structures of compounds bound to DNA [24–27]. It generates a reasonably good understanding between experimental and theoretical approaches. Using molecular dynamics simulation we were able to gain an in-depth understanding of the binding pattern and in the process pin point key structural characteristics of the generated "DNA-compound" adducts [24–31].

2. Experimental

2.1. Materials

2.1.1. Chemicals

HCur was purchased from Sigma-Aldrich and stored in the dark following its dissolution in methanol. DNA extracted from the thymus of a calf was bought from Sisco Research Laboratories, India and dissolved in millipore water containing 120 mM NaCl, 35 mM KCl and 5 mM $CaCl_2$. By measuring the absorbance at 260 nm and considering molar extinction coefficient for DNA as 6600 M^{-1} cm^{-1}, its concentration was ascertained. Absorption at 260 and 280 nm respectively, helped in determining whether the DNA was adequately free of protein, to decide if it required further purification. In order to further analyze calf thymus DNA that would be used, a CD spectropolarimeter was employed to procure a CD spectrum at 260 nm (J815, JASCO, Japan). Zinc(II)-acetate was bought from Sigma-Aldrich. Sodium nitrate (AR), sodium dihydrogen phosphate and disodium hydrogen phosphate were obtained from E Merck, India. All solutions were prepared in millipore water.

2.2. Instruments used

All spectroscopy related experiments were performed on a JASCO V-630 spectrophotometer, Japan. Temperature was controlled using a circulating thermo-stated water bath. Fluorescence measurements were made on Duetta, Horiba Scientific. CD was recorded on J815 Spectropolarimeter, JASCO, Japan. IR of solid samples were recorded on Spectrum Two, FTIR spectrophotometer, Perkin Elmer in the range 4000–400 cm^{-1}. TGA was done on Mettler Toledo TGA/SDTA 851 thermal analyzer. Micromass Q-T of micro™, Waters Corporation was used to record a mass spectrum. pH of solutions were recorded on a pH meter (LI 613, Elico, India). DFT, molecular docking and molecular dynamics simulation were performed on a Linux operating system supported with GPU-NVIDIA RTX 3060 Ti and Intel i7 9700kF processor.

2.3. Methods

2.3.1. Preparation of Zn^{II} Curcumin [Zn(Cur)]

HCur (0.74 g, 2 mmole) was dissolved in 50 mL de-aerated acetonitrile-methanol mixture (1:3). The solution was neutralized with triethylamine (0.277 mL, 2 mmole) followed by addition of $Zn(CH_3COO)_2$ (0.37 g, 2 mmole) dissolved in 30 mL de-aerated methanol-water mixture (1:1). Argon gas was passed through the mixture to maintain an inert atmosphere. The mixture was stirred under heat (~60 °C) for an hour. It was then refluxed for another 2 h under inert atmosphere. An orange brown precipitate was obtained. This was recovered and washed with chloroform, diethyl ether, ethanol, THF and acetonitrile separately, depending on the solubility of HCur in these solvents to wash away undesired impurities. A pure coordination compound was thus obtained which was not soluble in common solvents like methanol, ethanol, acetonitrile or dichloromethane. However, it was partly soluble in dimethylformamide (DMF) and to a reasonably good extent in dimethyl sulphoxide (DMSO).

2.3.2. Quantum chemical calculations

2.3.2.1. Perspective. Despite our best efforts, since we were unable to procure single crystals of [Zn(Cur)], a structure indicating its coordination environment eluded us. Again, due to its amorphous nature we were unable to solve its structure using powder X-ray diffraction data that we had collected. Hence, we were compelled to rely on data obtained from spectroscopic measurements that enabled us to create a model for the coordination environment around Zn^{II}. Subsequently, this model was improved by theoretically calculating its UV–vis absorption spectrum and comparing it with that obtained experimentally.

2.3.2.2. Computational methodology. All computations were carried out using DFT method and Gaussian 09 programme [32]. For C, H and O we used standard 6-31G+(d,p) basis set coupled with Becke three parameter hybrid functional and Lee-Yang-gradient Parr's corrected correlation functional (B3LYP) [33]. For Zn, the LanL2DZ basis set was used [34]. To account for long-range dispersion impact, Becke-Johnson damping (GD3BJ) and Grimmes' third order correction for dispersion were used. In both gaseous and DMSO solvent environments, ground state (S_0) geometries were fully optimized utilizing the program's extremely strict convergence criteria. In order to guarantee the stationary points' global minima, frequencies were calculated on optimized geometries where all vibrational frequencies were found to be positive. All simulations regarding the solution phase were performed in DMSO as solvent using integral equation formalism variant (IEFPCM) of polarizable continuum model [35]. Excited state calculation (TDDFT) in DMSO solvent was carried out to establish the geometry of the coordination compound [36]. Frontier MO composition analysis was performed with Gauss Sum programme [37] and investigations of MO orbital and molecular electrostatic potential (MEP) surface were done with GaussView. In addition, frontier molecular orbital energies were used to calculate quantum mechanical descriptors like MO gap (E), ionization potential (IP), electron affinity (EA), electronegativity (χ), chemical hardness (η), mean energy (M), chemical potential (μ), chemical softness (σ) and electrophilicity index (ω). These computations were performed using the following formulae [38].

$$\Delta E = E_{LUMO} - E_{HOMO} \quad (1)$$

$$IP = -E_{HOMO} \quad (2)$$

$$EA = -E_{LUMO} \quad (3)$$

$$\chi = -\mu = (IP + EA)/2 \quad (4)$$

$$\eta = \Delta E/2 \quad (5)$$

$$\sigma = 1/2\eta \quad (6)$$

$$\omega = \chi^2/2\eta \quad (7)$$

$$M = -\chi \quad (8)$$

2.3.2.3. Non-covalent interaction (NCI) and bond critical point analysis. This study was carried out to separate attractive and repulsive interactions present in molecular systems allowing us to observe non-covalent interactions by mapping them as isosurfaces over the molecular system [39]. It is possible to differentiate between attractive/stabilizing (favorable) and repulsive (unfavorable) interactions using the plot of reduced density gradient (RDG) versus sign of the product of second Hessian eigenvalue and electron density [sign (λ_2) ρin a.u.]. The color scheme of red, green and blue depicts strength of interactions; blue isosurface denote strong attractive interactions, red isosurface, strong repulsive interactions and green isosurface, weak attractive interactions. As expected, covalent and coordination bonds are represented by blue. NCI calculations were done on Multiwfn version 3.8 [40]. The RDG-based NCI spike and isosurface plot of [Zn(Cur)] in gaseous and solution phase were visualized using VMD 1.9.2 program. In addition to electron density, at bond critical points, it helps us to characterize the strength of hydrogen bonds by DAMQT-2.1.0 package [41].

2.3.3. Interaction of [Zn(Cur)] with calf thymus DNA

As already mentioned, HCur dissolved in phosphate buffer shows a gradual decrease in absorbance (Fig. S1, SI) that was realized by monitoring it with time [12,18]. For this reason, DNA binding studies could not be performed with it as the compound degrades in solution. For this reason, an attempt was made to follow the interaction theoretically to realize what could have happened if HCur were present as one unit and were to interact with DNA. On the other hand, [Zn(Cur)] dissolved in 150 mM NaCl, 35 mM KCl and 5 mM $CaCl_2$, in phosphate buffer (pH 7.4) or in biological milieu is stable and does not degrade (Fig. S1, S I). Hence, titration of [Zn(Cur)] with calf thymus DNA has been possible. A change in absorbance or fluorescence following the addition of calf thymus was monitored. The following equilibrium (Eq. (9)) depicts binding of [Zn(Cur)] with calf thymus DNA.

$$L + DNA \rightleftharpoons L\text{-}DNA \qquad K_d = \frac{[L][DNA]}{[L\text{-}DNA]} \quad (9)$$

L represents [Zn(Cur)]. Reciprocal of K_d provides the apparent binding constant (K_{app}) [42–46].

2.3.3.1. By UV–vis spectroscopy. Eq. (10) may be generated from Eq. (9) where reciprocal of the change in absorbance was plotted against reciprocal of ($C_D - C_0$). C_D denotes total concentration of calf thymus DNA while C_0, denotes concentration of [Zn(Cur)]. Using Eq. (10), ΔA_{max} and K_{app} ($= K_d^{-1}$) was determined from the intercept and slope respectively.

$$\frac{1}{\Delta A} = \frac{1}{\Delta A_{max}} + \frac{K_d}{\Delta A_{max}(C_D - C_0)} \quad (10)$$

ΔA denotes change in absorbance of [Zn(Cur)] at pH = 7.4. ΔA_{max} indicates the maximum possible change in absorbance.

$$K_d = \frac{\left[C_0 - \left(\frac{\Delta A}{\Delta A_{max}}\right)C_0\right]\left[C_D - \left(\frac{\Delta A}{\Delta A_{max}}\right)C_0\right]}{\left(\frac{\Delta A}{\Delta A_{max}}\right)C_0} \quad (11)$$

$$C_0\left(\frac{\Delta A}{\Delta A_{max}}\right)^2 - (C_0 + C_D + K_d)\left(\frac{\Delta A}{\Delta A_{max}}\right) + C_D = 0 \quad (12)$$

Subsequently, $\Delta A/\Delta A_{max}$ was plotted against C_D. Eqs. (11) & (12) were used to fit the experimental data by non-linear square fit analysis that provides a value for apparent binding constant for the interaction of [Zn(Cur)] with calf thymus DNA [42–46]. A plot of $\Delta A/\Delta A_{max}$ against ratio of concentration of calf thymus DNA to [Zn(Cur)] provides two straight lines, the intersection of which provides n_b (number of nucleotides bound to [Zn(Cur)]). Apparent binding constants (K_{app}) obtained from Eqs. (10) & (12) when multiplied with n_b provides the overall binding constant (K*). The titrimetric data of [Zn(Cur)] with calf thymus DNA was also analyzed according to a modified form of the Scatchard equation [Eq. (13)] [47]. Overall binding constant (K*) and site size n ($= n_b^{-1}$ = number of bound complex per nucleotide) was determined.

$$r/C_f = K^{'}(n - r) \quad (13)$$

$r = C_b/C_D$; C_b denotes concentration of bound form of [Zn(Cur)] while C_f denotes free form.

2.3.3.2. By fluorescence spectroscopy. Binding of [Zn(Cur)] with calf thymus DNA was also followed using fluorescence spectroscopy. [Zn(Cur)] was excited at 436 nm while emission was followed over the wavelength range 436 to 700 nm. Emission maxima appeared at 584 nm. Upon addition of calf thymus DNA, fluorescence increased which was followed after allowing for suitable corrections owing to dilution; thus ΔF was obtained. Like that for monitoring by UV–Vis spectroscopy, standard equations (Eqs. (10)–(13)) were used where change in fluorescence (ΔF) was considered instead of change in absorbance (ΔA) and plotted against the change in concentration due to DNA and [Zn(Cur)]. Hence, using fluorescence spectroscopy, apparent binding constant (K_{app}), overall binding constant (K*) and site size of interaction (either n_b or n) were determined.

2.3.4. Molecular modeling

2.3.4.1. Molecular docking. Molecular docking studies were performed using the Autodock software (version 4.2.6) which is an interactive molecular graphics program using which binding energy could be obtained [48]. Additionally, the command-line tool Autodock Vina (version 1.2.3; http://vina.scripps.edu) [48,49] was used from where binding affinity values were obtained. Both binding energy and binding affinity, output of programs used and regarded as docking score were generated using different scoring functions [50,51]. The crystal structure of DNA (PDB ID: 1BNA) [52] was downloaded from the protein data bank (http://www.rcsb.org./pdb) having resolution of 1.90 Å. The downloaded DNA has A and B chains having the sequence 5′-D (CGCGAATTCGCG)-3′. Before performing molecular interaction studies, the DNA was checked for missing nitrogenous base pairs using UCSF Chimera (version 1.15; https://www.rbvi.ucsf.edu/chimera) and its energy was minimized using steepest descent and conjugate gradient techniques. It was then saved in PDB format. Subsequently, molecular interaction experiments were performed. Optimized HCur and [Zn(Cur)] were saved as two separate mol2 files and were further converted to PDB using the openbabel software. Thereafter, using Autodock tools (version 1.5.6) saved PDB files of DNA and chosen molecules were opened. After merging non-polar hydrogens on both receptor and target molecules they were saved in PDBQT format [53]. Grid boxes were created with specific dimensions at a spacing of 0.35 Å. Docking studies of 1BNA-HCur and 1BNA-[Zn(Cur)] were carried out using Lamarckian Genetic Algorithm (LGA) to achieve the lowest free energy of binding (G). For molecular docking studies, three replicates were performed; for each a total number of 10 solutions were computed, each showing an energy minima having a population size of 150 and number of evaluations ~2,500,000; the maximum number of generations being 27,000

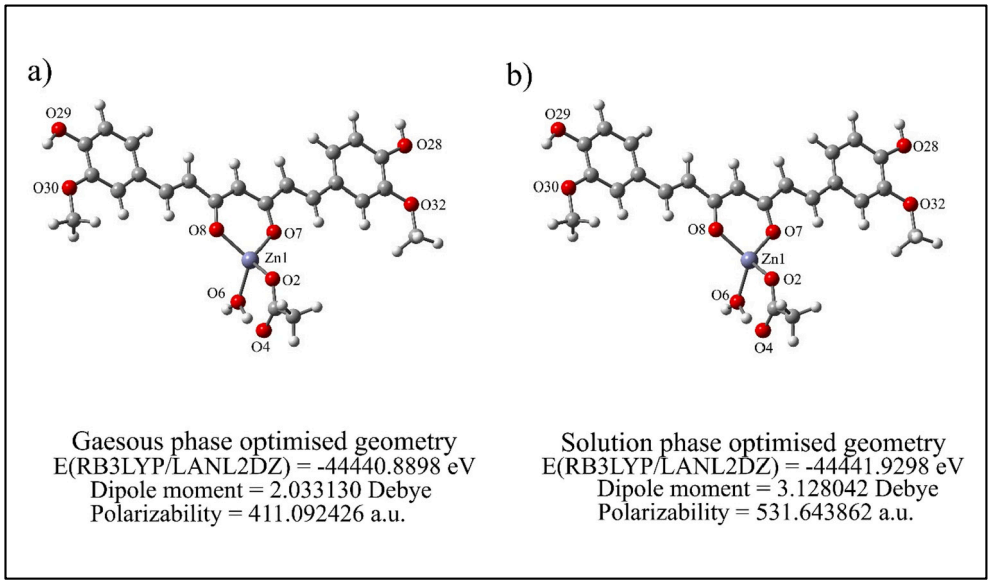


Fig. 1A. Ground state optimized geometries of the [Zn(Cur)] (a) Gaseous phase (b) Solution phase.

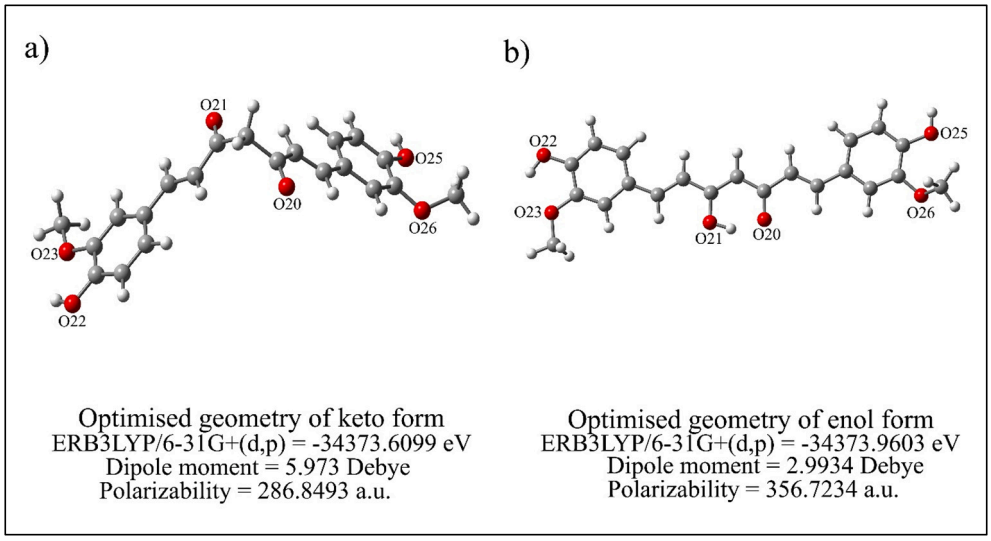


Fig. 1B. Ground state optimized geometries of the HCur (a) keto form (b) enol form.

Table 1
Coordinated bond distances (in Á) and bond angles (in °) of [Zn(Cur)].

Bond	Gaseous phase	In DMSO	Angle	Gaseous phase	In DMSO
Zn1–O2	1.976	2.006	O2–Zn1–O6	92.08	90.55
Zn1–O7	1.967	1.987	O2–Zn1–O7	120.43	106.36
Zn1–O6	1.993	2.008	O6–Zn1–O8	117.50	107.79
Zn1–O8	1.968	1.989	O7–Zn1–O8	91.66	90.77

[53,54]. After docking, RMSD cluster maps were obtained with cluster tolerance of 2.0 Å, each for HCur and [Zn(Cur)]. The BIOVIA Discovery Studio (version 2021) and PyMOL software (DeLano, 2002) were used for visualisation of 2D and 3D interactions of different nucleotides with HCur and [Zn(Cur)], to visualize the best possible geometry of compounds inside DNA.

2.3.4.2. Molecular dynamics. MD simulation studies were carried out on free DNA (PDBID: 1BNA), HCur docked DNA and [Zn(Cur)] docked DNA complex to investigate stability and physical movements. Desmond (version 2020.1) [55] was used to run molecular dynamics simulation which is a GPU-accelerated program running on the Linux operating system integrated with an NVIDIA RTX 3060 Ti GPU and Intel i7 9700kF processor. In order to prepare the systems, the OPLS-2005 force field [56] and explicit solvent model with SPC water molecules were employed [57]. Energy of all systems were then reduced by using an orthorhombic boundary solvation box having dimension 10 Å × 10 Å × 10 Å. Then, the correct quantity of Na^+ or Cl^- ions was introduced to each system to neutralize it. Each system received an additional 0.15 M NaCl solution to replicate the physiological environment. The Desmond default relaxation approach was used to relax the prepared systems. An NVT ensemble was initially used to equilibrate the entire system for 500 ps at 10 K. Following the preceding phase, an NPT ensemble was used to complete a quick run of equilibration and minimization for 100 ns at 300 K and 1.01325 bar pressure. The Nose-How over chain coupling approach was used to set up NPT ensemble [58]. Temperature was set to 300 K, relaxation period was set at 1.0 ps and pressure was maintained at 1 bar throughout simulations. A time step of 2 fs was applied. With a

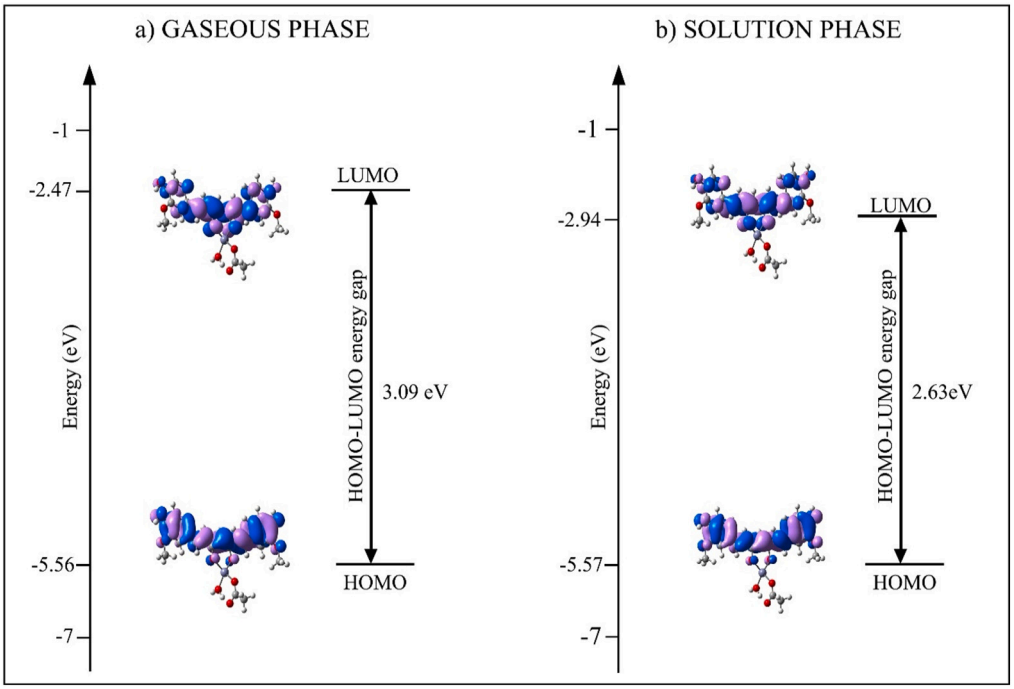


Fig. 2. HOMO-LUMO gap of [Zn(Cur)] (a) Gas phase (b) Solution phase.

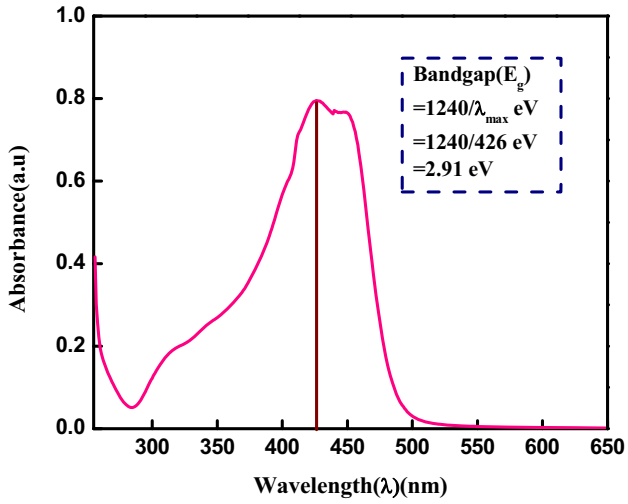


Fig. 3. Experimental UV–Vis absorption maxima with corresponding optical bandgap.

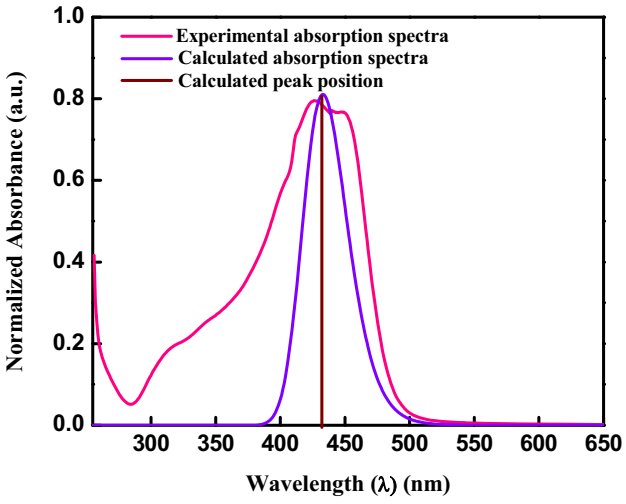


Fig. 4. Comparison of experimental and theoretical UV–Vis absorption spectra showing most feasible peak positions.

relaxation duration of 2 ps, the Martyna-Tobias-Klein chain coupling scheme barostat method was employed to control pressure [59]. Long-range electrostatic interactions were calculated using the particle mesh Ewald approach [60] with a fixed coulomb interaction radius of 9.0 Å. With each trajectory, bonded forces were calculated using RESPA integrator for a time step of 2 fs. Maestro, a Desmond GUI application, was used to study simulation interaction diagrams. One can also forecast stability of DNA and DNA-ligand compounds using simulation-derived parameters including root-mean square deviation (RMSD), root mean square fluctuation (RMSF), number of H-bonds and radius of gyration [61].

2.3.4.3. Binding free energy analysis by MDS. The generalized Born surface area (MM-GBSA) method and molecular mechanics were utilized to calculate binding free energies of DNA-ligand complexes. The simulation trajectory's last 10 frames out of 1000 with a 1-step sampling size and OPLS-2005 force field coupled with python script thermal_mmgbsa.py were used to determine MM-GBSA binding free energy [62,63]. The principle of additivity was used to estimate binding free energy of MD trajectory using MM-GBSA (kcal/mol), in which individual energy modules like columbic, covalent, hydrogen bond, van der Waals, self-contact, lipophilic, solvation and stacking of ligand and DNA were obtained. Eq. (14) was used to calculate $\Delta G_{binding}$

$$\Delta G_{binding} = \Delta G_{MM} + \Delta G_{Solv} - \Delta G_{SA} \quad (14)$$

where $\Delta G_{binding}$ designates binding free energy, ΔG_{MM} designates difference between free energies of DNA-ligand complexes and total energy of DNA and ligand in an isolated state, ΔG_{solv} denotes difference in solvation energies of the DNA-ligand adduct and sum of solvation energies of DNA and ligand in unbound state, ΔG_{SA} designates difference

Experimental Excitation (nm)	Calculated Excitation (nm)	Excitation Energy (eV)	Excited state involved	Osc. Strength (f)	λi	ELECTRON → HOLE
426	453.94	2.7313	S3	1.6121	1	ILCT
410	394.88	3.1398	S5	0.1080	0.97	ILCT
350	351.07	3.5316	S6	0.0001	0.98	ILCT/LLCT

Fig. 5. NTO analysis describing the calculated UV–Vis peak positions.

Table 2
Quantum descriptor for HCur and [Zn(Cur)] in eV with B3LYP-6-31G+(d,p) functional.

Compound	HOMO	LUMO	ΔE	IP	EA	X	η	M	σ	ω
HCur	−5.57	−2.27	3.30	5.57	2.27	3.92	1.65	−3.92	0.60	4.65
[Zn(Cur)]	−5.57	−2.94	2.63	5.57	2.94	4.26	1.32	−4.26	0.75	6.87

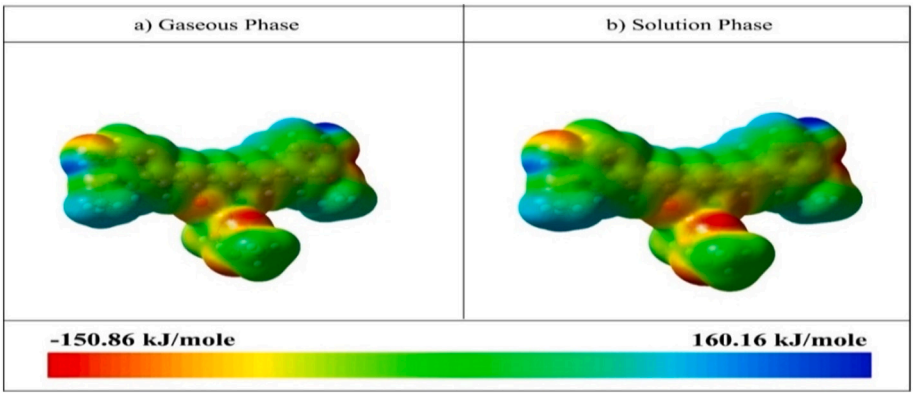


Fig. 6. Molecular electrostatic Potential surface of [Zn(Cur)] in (a) Gas phase and (b) solution phase.

in surface area energies for DNA and ligand.

3. Results and discussions

3.1. Characterization of the Zn^{II}-Curcumin complex

3.1.1. Using different instrumental techniques

Owing to poor solubility in water, spectrum of [Zn(Cur)] was recorded in DMSO (Fig. S2, SI). λ_{max} was detected at 426 nm. IR spectrum of [Zn(Cur)] was compared with that of HCur (Figs. S3 and S4, S I respectively). Mass spectrum of [Zn(Cur)] shows molecular ion peaks at m/z = 508.4731, 510.5261, 512.2132 owing to three relatively abundant isotopes of Zn (m/z_{theo} being 508.38 for ^{64}Zn; 510.38 for ^{66}Zn; 512.38 for ^{68}Zn) (Fig. S5, SI). Following the loss of a molecule of water from the molecular ion, peaks with m/z values 490.7648, 492 and 494 were obtained, Fig. S5, SI; m/z_{theo} for these fragments being 490.38 for ^{64}Zn; 492.38 for ^{66}Zn; 494.38 for ^{68}Zn. Loss of a molecule of water and acetate from the molecular ion, results in peaks with m/z values 449.2687, 451.4157 and 453.1284; Fig. S5, SI; m/z_{theo} being 449.38 for ^{64}Zn; 451.38 for ^{66}Zn; 453.38 for ^{68}Zn. Experimental responses in mass spectrum were in excellent agreement with those of the theoretically expected fragments. In fact, they were also in extremely good agreement

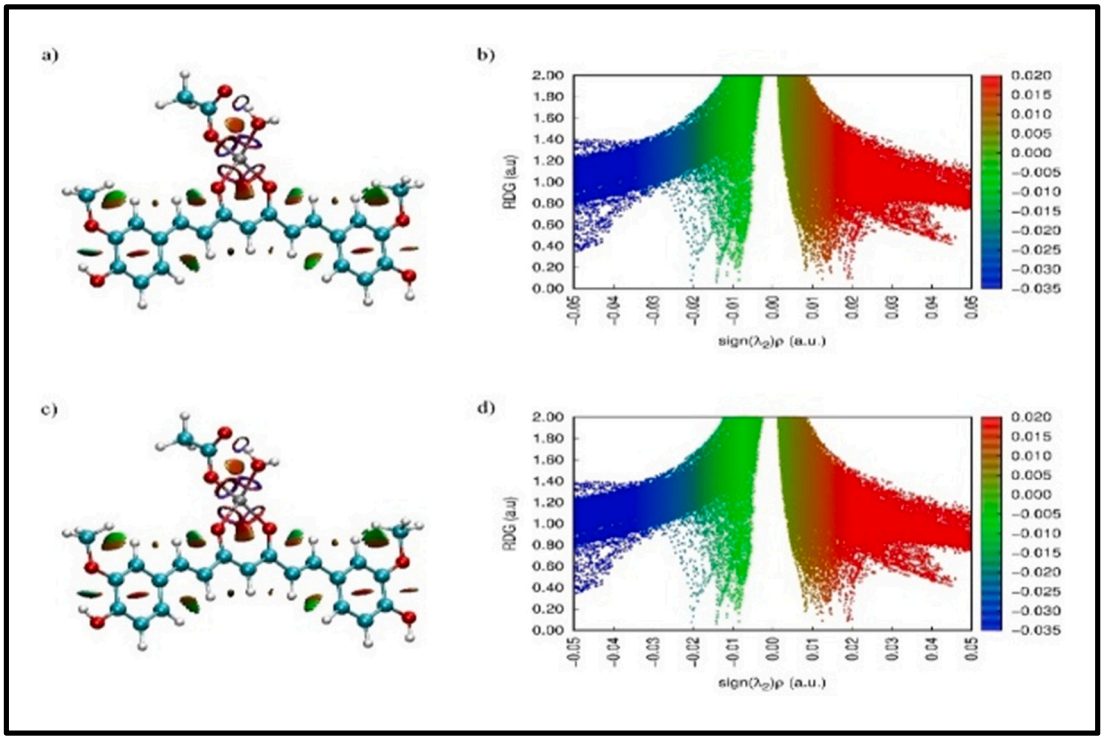


Fig. 7. NCI plots of [Zn(Cur)] (I) Gas phase (a, b), (II) Solution Phase (c, d).

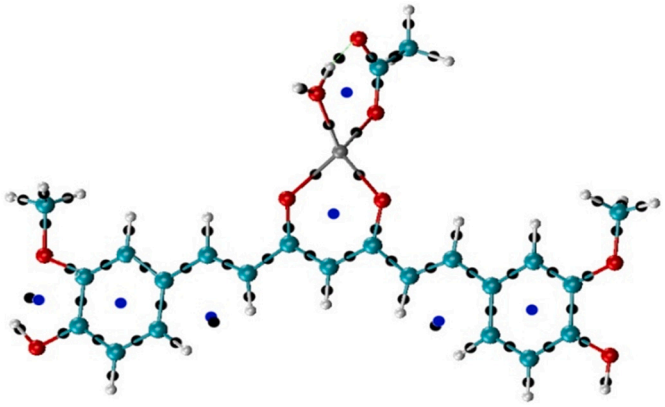


Fig. 8. DFT optimized geometry of [Zn(Cur)] showing hydrogen bond critical points (CP) indicated by blue and black spheres; black spheres represent bond critical points (3,−1) in which one of them represents hydrogen bond critical point; blue spheres represent ring critical point.

pertaining to what would be expected of a fragment considering relative abundance of the isotopes of Zn [the five stable isotopes being [^{64}Zn (48.63 %), ^{66}Zn (27.90 %), ^{67}Zn (4.10 %), ^{68}Zn (18.75 %), and ^{70}Zn (0.62 %); the three most abundant of the five were identified in our mass spectrum]. Hence, mass spectrum provides clean evidence in favor of [Zn(Cur)(CH_3COO)H_2O]. TGA (Fig. S6, SI) also indicates that the formula of our coordination compound should be [Zn(Cur)(CH_3COO)H_2O].

3.1.2. DFT calculations based on spectroscopic evidence

Ground states of optimized molecular structures were singlet. The ground state optimized geometries of [Zn(Cur)] (in gaseous state and in DMSO) and of HCur in keto and enol forms are depicted in Figs. 1A and 1B respectively, with a numbering scheme for the coordination environment. The optimized coordinates of these configurations [Zn(Cur)] are provided in Table S1, SI. Important parameters concerning the coordination geometry are arranged in Table 1. Calculated bond lengths (Table 1) for Zn-O are in good agreement with those that are reported for [Zn(Cur)(bipy)(acetate)] [64], whose structure was established from single crystal X ray diffraction studies. Final optimized structures of ground state configurations show tetrahedral coordination both in gas and solution (DMSO) phases (Fig. 1A).

3.1.2.1. MO composition analysis. The frontier orbital of [Zn(Cur)] optimized in gas and solution phases and HCur in solution phase are shown in Figs. S6 and S7, SI, respectively. Description of both occupied and virtual MOs were made based on their atomic composition and visual inspection of a three-dimensional representation. [Zn(Cur)] moiety was assumed to be composed of four fragments, Zn, Curcumin, water and acetate. Their compositions are described in Table S2, SI. We observed both for gas and solution phases optimized geometries, HOMO-1 to LUMO+4 have no contribution from the metal; i. e. contributions only from curcumin. For HOMO-2 to HOMO-4 there was some contribution from the metal. According to calculations, the HOMO-LUMO energy gap for [Zn(Cur)] in gas and solution phases were 3.09 eV and 2.63 eV respectively. On the other hand, HOMO-LUMO energy gap for HCur in solution phase was 3.30 eV (shown in Fig. S8, SI). The HOMO-LUMO gap in gas and solution phases of [Zn(Cur)] are shown in Fig. 2.

The highest occupied molecular orbital (HOMO) and lowest unoccupied molecular orbital (LUMO) are ligand-centric in each phase with almost entire contribution coming from HCur. For molecular crystals, optical energy band gap resulting from UV–Vis absorption could be used to confirm the HOMO-LUMO energy gap (Fig. 2). The optical energy band gap (Eg) calculated using $Eg = 1240/\lambda_{max}$ eV was found to be 2.91 eV equivalent to theoretical HOMO-LUMO energy gap of [Zn(Cur)] in DMSO (2.63 eV) (Fig. 3).

3.1.2.2. Opto-electronic absorption property. Since excitation from ground state to an excited state in a dielectric medium (DMSO) would result in identical absorption as that recorded experimentally in the same solvent, opto-electronic property was helpful in pin pointing a

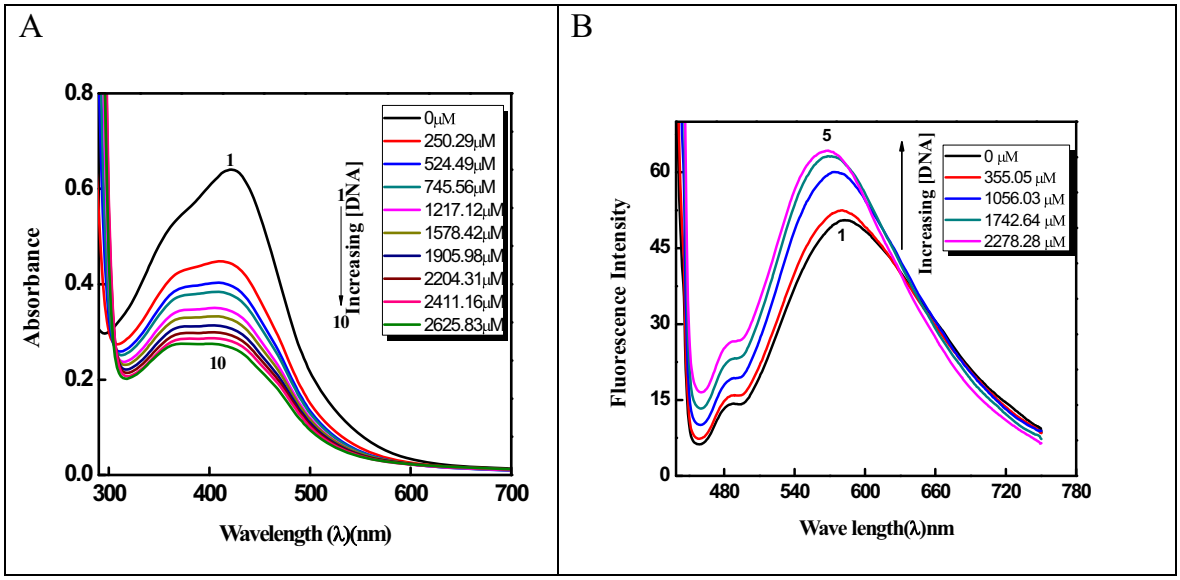


Fig. 9. (A) Absorption spectra of [Zn(Cur)] in the absence (1) and presence of different concentrations of calf thymus DNA (2) 250.29 μM, (3) 524.49 μM, (4) 745.56 μM, (5) 1217.12 μM, (6) 1578.42 μM, (7) 1905.98 μM, (8) 2204.31 μM, (9) 2411.16 μM and (10) 2625.83 μM; [NaCl] = 150 mM, pH = 7.4; Temp. = 298 K. (B) Fluorescence intensity of [Zn(Cur)] in the absence (1) and presence of different concentrations of calf-thymus DNA (2) 355.05 μM, (3) 1056.03 μM, (4) 1742.64 μM, (5) 2278.28 μM; [NaCl] = 150 mM, pH = 7.4, Temp. = 298 K.

precise molecular geometry. DMSO has a cut off wavelength for absorption at ~268 nm. Since the absorption spectrum of [Zn(Cur)] exhibits dispersion below 300 nm, therefore to compare observed patterns with calculated ones, the spectrum was recorded up to 650 nm rather than going below 300 nm (Fig. 4). A multiple transition nature for [Zn (Cur)] is supported by computed electronic absorption spectrum in DMSO having several peaks. The experimental spectrum's peaks were visually assigned. In Table S3, SI, most likely transitions are presented in increasing order of energy in which they appear in the spectrum with maximum intensity ($f \geq 0.10$) corresponding to experimental absorption peaks and related excitation wavelengths, energy, oscillator strengths (f), character and CI coefficients. Excitation peaks were mainly due to charge-transfer transitions within HCur. Almost all states were regarded as singlet that were used for TDDFT calculations.

Natural transition orbital (NTO) analysis based on computed transition density matrices were used to explain results of excited state computation. The terms "electron/particle" and "hole" transition orbitals were used to describe virtual/unoccupied and occupied NTOs respectively. From a relative weightage of transition density matrices and occupied-virtual pair contributions to excitation, we were able to recognize and depict electronic transitions that were being studied in terms of excitation from a hole-NTO to an electron-NTO for solution phase excited geometry. Fig. 5 shows NTOs for the most significant peaks.

The most significant computed peak was at 431 nm (2.7313 eV, f = 1.6121), which was the lowest energy transition observed experimentally, close to 426 nm. This transition is due to ILCT. The next higher energy UV transition estimated at 394.88 nm (3.13 eV, f = 0.180) is also attributed to ILCT and was experimentally found at 410 nm. The UV excitation at 351.07 nm (3.5316 eV, f = 0.0001) detected close to the experimental peak at 350 nm may be attributed to ILCT or an extremely weak LLCT.

3.1.2.3. Quantum descriptor analysis. Frontier molecular orbitals affect a molecule's kinetic stability, electrical conductivity and chemical reactivity (HOMOs and LUMOs). Soft molecules are those that have narrow HOMO-LUMO energy gap. These exhibit greater biological and chemical reactivity. Molecules having large HOMO-LUMO energy gap have low biological response, are extremely stable and are less reactive towards other compounds. Intra-molecular charge transfer (ICT) from an electron-donor group to an electron-acceptor group is possible in small HOMO-LUMO energy gaps. Good electron acceptor molecular systems have lower E_{LUMO} than good electron donor molecular systems with higher E_{HOMO}. In Table 2, we compare the quantum descriptor of HCur with that of [Zn(Cur)] that was obtained after geometry optimisation. Electron donation (IP) and electron acceptance (EA) is faciliated due to low HOMO-LUMO gap. Electron affinity of [Zn(Cur)] is quite high compared to HCur which indicates that the complex might easily interact with nucleotides from DNA by dragging the electron density towards itself. On the other hand, a soft molecule is defined as one having lower η value (Eq. (5)) [65,66]. Upon complex formation with Zn^{II}, HCur becomes soft and shows greater electron delocalization that facilitates more non-covalent interaction. A high value of ω (electrophilicity index) represents high affinity towards electron rich species. [Zn(Cur)] has a higher affinity compared to HCur.

3.1.2.4. MEP surface analysis. Fig. 6 displays "molecular electrostatic potential surface" computed over optimal geometries in both gas and solvent phases. The envelope's isovalue was selected to be 0.02 a.u. and the reverse rainbow color scheme was used throughout [67]. Areas with negative potential are denoted in red, while areas with positive potential are in blue. It is evident hydrogen atoms on phenolic O—H are positively charged, whereas hydrogen on CH_3 are just marginally positive. H—atoms in H_2O are likewise identified to be somewhat positive. The most negative potential regions were next to carbonyl O atoms, along with O-atoms of acetate, while the ring of HCur was found to have greater MEP values than carbonyl oxygens. Inferring that there is a strong likelihood that molecules would create hydrogen bonding connections between H of water and carbonyl O of an acetate that could eventually stabilize the system, we compared MEP of keto and enol forms of HCur only and found carbonyl oxygens are electron rich (red in color, Fig. S9, SI) along with phenolic OH.

3.2. Non-covalent interactions (NCI) and bond critical point analysis

From NCI analysis (Fig. 7), it was observed carbonyl-O of acetate in [Zn(Cur)] and H of H—O—H in water form strong intra-molecular hydrogen bond; displayed as the blue isosurface.

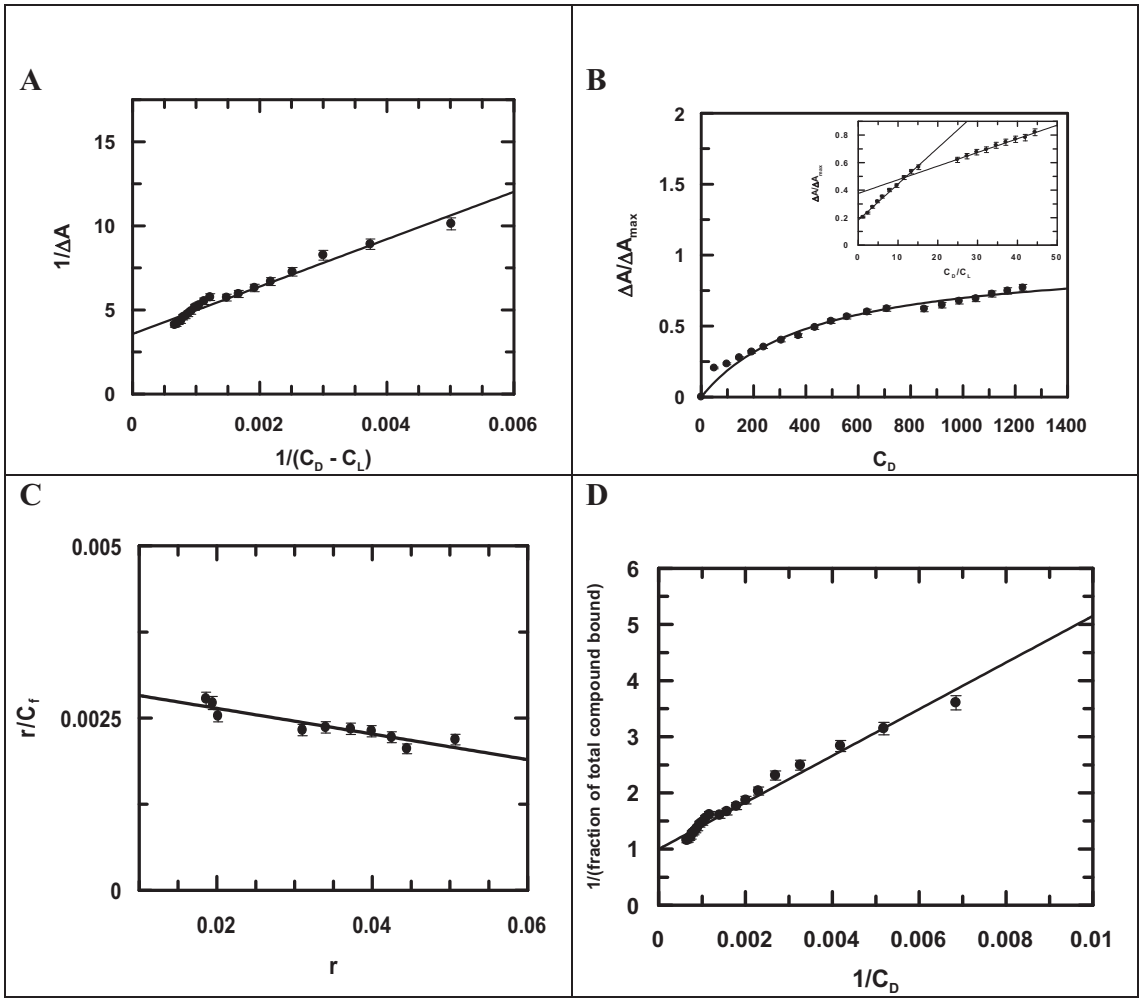


Fig. 10. (A) Double reciprocal plot for the interaction of [Zn(Cur)] with calf-thymus DNA to evaluate apparent binding constant (K_{app}) of the complex to DNA, (B) binding isotherm for [Zn(Cur)] interacting with calf thymus DNA when $\Delta A/\Delta A_{max}$ was plotted against concentration of DNA; the dark line is the fitted data obeying Eq. (12). Inset: Plot of normalized increase in absorbance as a function of mole-ratio of calf thymus DNA to [Zn(Cur)]. (C) A modified Scatchard plot for interaction of [Zn(Cur)] with calf thymus DNA; (D) a plot showing 1/fraction of total compound bound vs 1/concentration of calf thymus DNA taken; [Zn(Cur)] = 41.2 μM, [NaCl] = 150 mM, pH = 7.4 (30 mM phosphate buffer), Temp. = 298 K.

Table 3
Binding parameters for interaction of [Zn(Cur)] with calf thymus DNA at pH = 7.4.

DNA binding methods	No. of expt.	Apparent binding constant K_{app} (M^{-1})			Site size from mole-ratio plot	Overall binding constant $K^*(M^{-1})$ $K^* = K_{app} \times n_b$			Overall binding constant from Scatchard $\times 10^{-4}$	Site size from Scatchard plot
		Double reciprocal plot $\times 10^{-3}$	Non-linear plot $\times 10^{-3}$	Double reciprocal plot, y-intercept =1 $\times 10^{-3}$		Double reciprocal $\times 10^{-4}$	Non-linear $\times 10^{-4}$	Double reciprocal plot, y-intercept =1 $\times 10^{-4}$		
	1	2.54	2.51	2.41	10.0	2.54	2.51	2.41	1.86	6.0
Absorbance	2	1.91	1.99	1.89	11.0	2.10	2.19	2.08	2.04	8.0
Fluorescence	1	2.08	1.77	1.42	5.0	1.04	0.90	0.71	1.49	6.0
	2	0.96	0.92	0.72	8.0	0.58	0.55	0.57	0.70	7.0

The bond strength of [Zn(Cur)] was estimated by critical point analysis with Quantum theory of atoms-in-molecules (QTAIM) descriptors. Surprisingly, there is a strong hydrogen bond obtained between water and acetate ion. Using critical point analysis, we observed threefold enhancement in strength of the formed hydrogen bond over that of normal hydrogen bond. It may be noticed from Table S4, SI that for normal hydrogen bonds (NHB)\ρ = 0.02 e/bohr^3 and for strong hydrogen bonds it is (SHB)\ρ = 0.062 e/bohr^3. In fact, strength of an SHB is equivalent to that of a coordinate covalent bond, but less than a covalent bond which is usually 0.2 e/bohr^3 (Fig. 8).

3.2.1. *Experimental binding of [Zn(Cur)] with calf thymus DNA*

[Zn(Cur)] was titrated with calf thymus DNA at a constant pH (= 7.4) and a constant ionic strength (0.15 mM) of the medium. A gradual decrease in absorbance at 430 nm or a gradual increase in fluorescence at 570 nm helped in evaluating the interaction occurring between [Zn(Cur)] and calf thymus DNA (Fig. 7).

Fig. 9 is a double reciprocal plot of 1/ΔA versus 1/[C_D-C_L] [Eq. (10)]

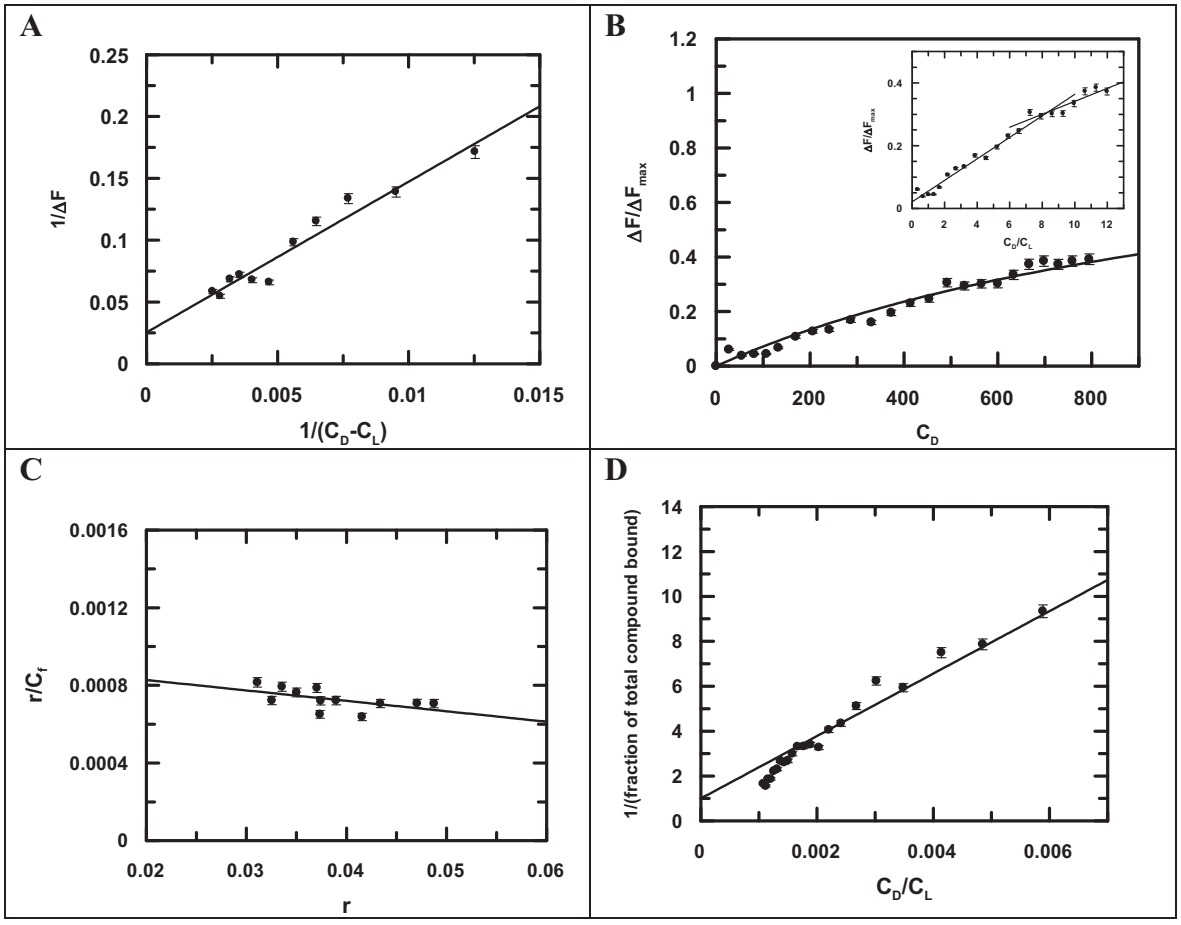


Fig. 11. (A) Double reciprocal plot for the interaction of [Zn(Cur)] with calf-thymus DNA to evaluate apparent binding constant (K_{app}), (B) Binding isotherm for [Zn (Cur)] interacting with calf thymus DNA when $\Delta F/\Delta F_{max}$ was plotted against concentration of DNA; the dark line indicates fitted data obeying Eq. (12). Inset: Plot of normalized increase in absorbance as a function of mole-ratio of calf thymus DNA to [Zn(Cur)]. (C) A modified Scatchard plot for interaction of [Zn(Cur)] with calf thymus DNA; (D) A plot showing 1/fraction of total compound bound vs 1/conc. of calf thymus DNA; [Zn(Cur)] = 82.4 μM, [NaCl] = 150 mM, pH = 7.4 (30 mM phosphate buffer), Temp. = 298 K.

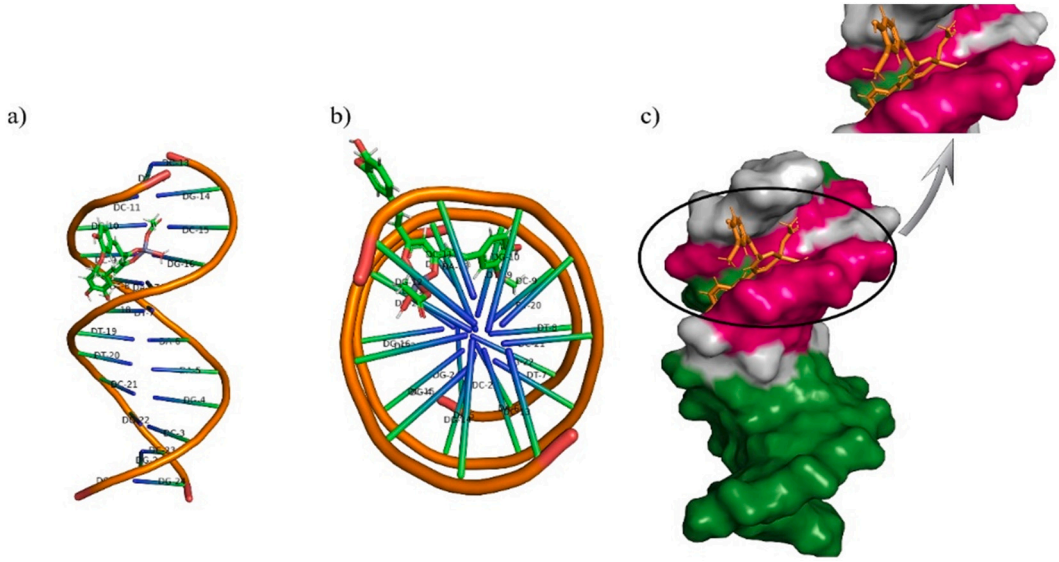


Fig. 12. Docked position of [Zn(Cur)] in enol form with DNA (PDB ID:1BNA) (a) side view (b) top view (c) surface view.

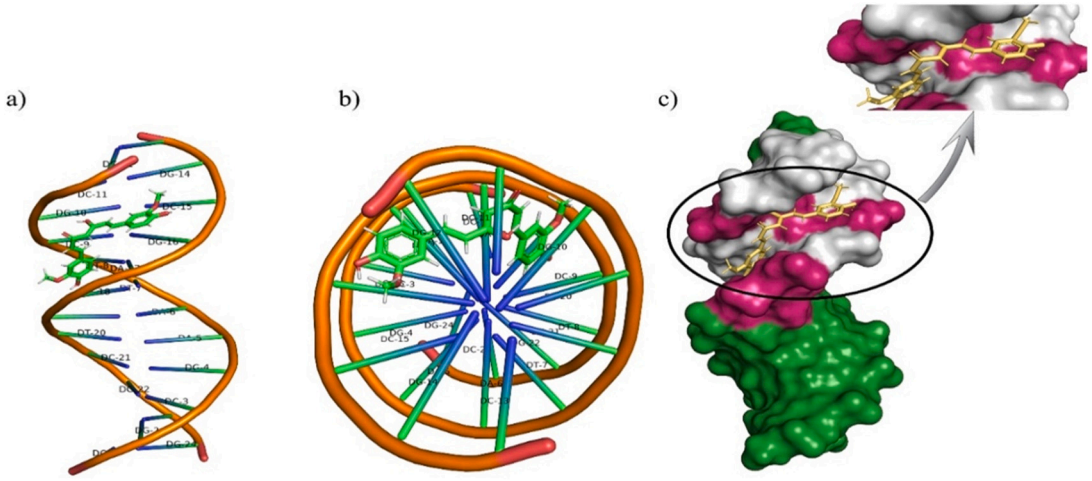


Fig. 13. Docked position of HCur with DNA (PDB ID:1BNA) (a) side view (b) top view (c) surface view.

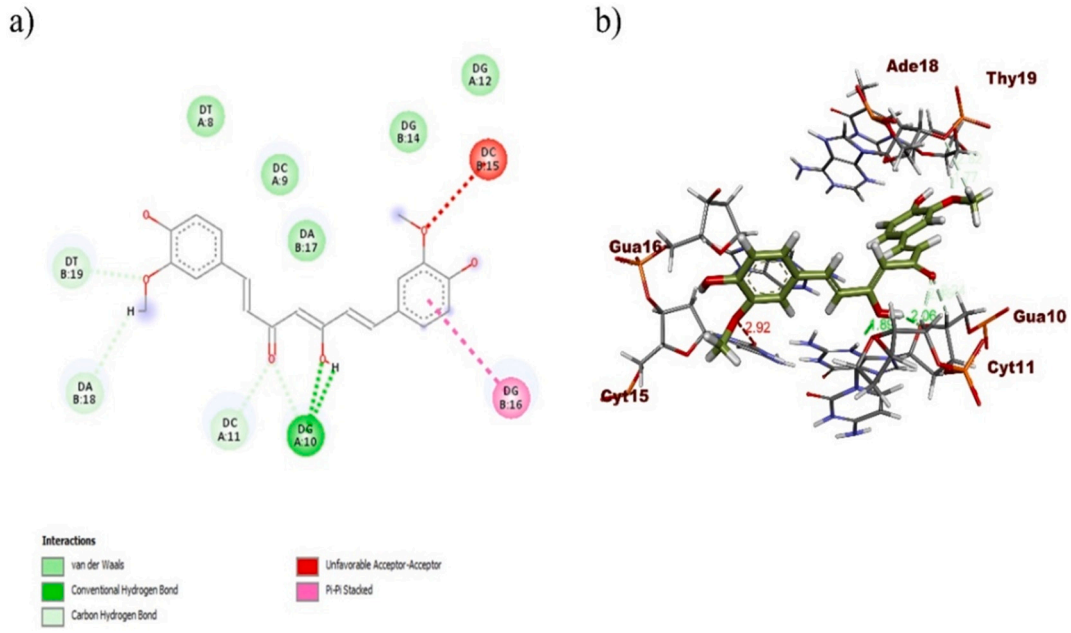


Fig. 14. Docked position of HCur with DNA (PDB ID: 1BNA) (a) 2D representation of interactions (b) 3D representation of interactions.

that provides values for K_{app} ($= K_d^{-1}$) from two independent titrations [42–46]. An average of their values was $2.23 \times 10^3\ M^{-1}$.

Fig. 10B is a plot of $\Delta A/\Delta A_{max}$ versus concentration of calf thymus DNA to which non-linear curve fit was applied (Eqs. (11) & (12)). Two independent titrations provide an average apparent binding constant of $2.25 \times 10^3\ M^{-1}$ at 298 K. Inset of Fig. 10 provides a value of n_b as 10.0, i.e. number of nucleotides bound to [Zn(Cur)] following interaction with calf thymus DNA [42–46].

The titration data was also fitted to a modified Scatchard equation (Eq. (5), Fig. 10) [47]. K* and n ($= n_b^{-1}$) were obtained. Values obtained from Eq. (13) were close to that obtained from other methods of analyses (Eqs. (9)–(12), Figs. 9 & 10) justifying techniques that calculate them (Table 3).

Titration of this complex with DNA is important for a number of reasons. First, since titration of HCur with DNA has not been possible owing to reasons mentioned earlier, the monomeric complex of Zn^{II} with HCur, where HCur shows no degradation, makes it a model study that in a way represents the binding of HCur to DNA.

However, while considering the data, one has to remember that for [Zn(Cur)] there would be an influence of Zn^{II} to the binding process [20,42–45]. Therefore, being able to maintain HCur as a single unit in solution, and that, there would be no extra influence due to a coordination compound being considered, owing to lack of any redox behavior (since Zn^{II}), the obtained binding constant value of the coordination compound could well represent that for HCur [20]. Hence, with HCur connected to a metal centre, one can have an idea of its binding to DNA, that was not possible earlier. Secondly, from an estimate of binding constant values obtained for [Zn(Cur)] it might now become possible to explain some of the mechanisms involved during interaction of HCur with DNA (considering the fact that HCur remains as one unit in this coordination compound) and its consequences thereof, during biological interactions, where besides the various fragmented forms that are generated in solution for HCur, a substantial portion of HCur does remain as one unit [12,13,18–20]. Hence, altogether (that is fragmented products of HCur and "HCur as one unit") it might now become possible to explain many beneficial activities of HCur [12,13,18–20] (Fig. 11).

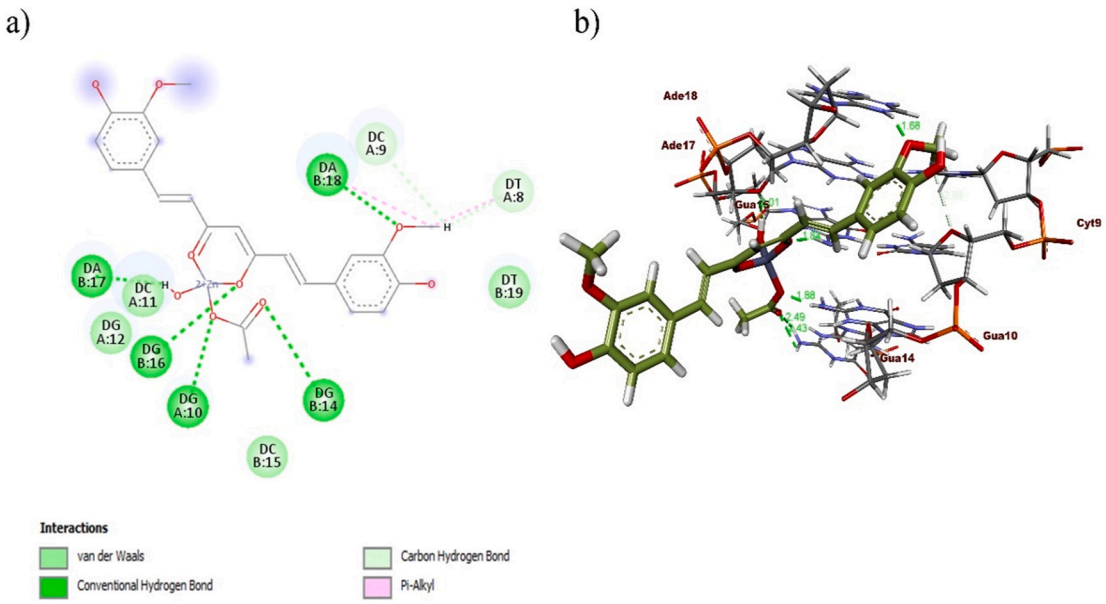


Fig. 15. Docked position of [Zn(Cur)] with DNA (PDB ID: 1BNA) (a) 2D representation of interactions (b) 3D representation of interactions.

3.2.2. *Computational DNA binding studies*

3.2.2.1. Molecular docking studies. Binding modes of [Zn(Cur)] and HCur with the desired regions of DNA were established using in silico molecular docking. This is a compelling framework for comprehending interactions between compounds and DNA in any rational drug design and for understanding structural characteristics of ligand-receptor complexes, binding energy and affinity of a ligand with its receptors that supports experimental findings. Both molecules were successfully docked with PDB ID: 1BNA having the sequence $d(CGCGAATTCGCG)_2$ to undergo extensive molecular mechanics for estimating binding energy or binding affinity of [Zn(Cur)] and HCur with the chosen DNA (PDB ID: 1BNA) (Figs. 12 and 13 respectively). Rigid molecular docking was used to determine the binding pattern. To forecast optimum molecule-DNA fit and analyze most energetically advantageous docked position, the molecule was made flexible to achieve several conformations. Autodockvina (version 1.2.3) and Autodock 4.2.6 predicted docking scores of −8.29 Kcal/mol and −7.67 Kcal/mol respectively for HCur with an inhibitory concentration of 2.41 μM. As shown by 2D and 3D interaction diagrams (Figs. 14 and 15), the nucleotide Gua-10 chain A of DNA formed hydrogen bonds (H-bonds) with HCur's enolic oxygen and hydrogen, measuring 2.06 Å and 1.89 Å respectively. Table S5, SI includes a list of additional interaction modes. It is evident from Fig. 14 (a) that HCur interacts with the chosen DNA.

Docking scores of −8.56 Kcal/mol and −8.36 Kcal/mol respectively were obtained for [Zn(Cur)] anticipated by Autodock vina v1.2.3 and Autodock v4.2.6 with inhibitory concentration 0.7298 μM. We realized that interacting nucleotides Gua-14(B) (2.43 Å, 2.49 Å), Gua-10(A) (1.88 Å), Gua-16(B) (1.84 Å), Ade-17(B) (2.01 Å) and Ade-18(B) (1.68 Å) form H-bonds. This was obtained from the 2D and 3D interaction diagrams (Fig. 15). Therefore, from binding energy and affinity values (S4, SI) it could be concluded that [Zn(Cur)] interacts with the chosen DNA via intercalation and has greater binding energy of interaction than HCur [Figs. 12(b) and 13(b)]. In Figs. 12(c) and 13(c) magenta indicates all types of polar interactions, green indicates the normal state of the nucleic acid base while white indicates all other weakly interacting regions.

3.2.2.2. Molecular dynamics. An understanding of the stability of apo-DNA, DNA-HCur and DNA-[Zn(Cur)] guided by root mean square deviation (RMSD) of DNA during the 100 ns simulation provides stability to DNA in an otherwise identical solvent, charge, electrolyte environment. A decrease in RMSD value of DNA is an indication of the extent to which the same DNA is stable in a similar environment. Comparing RMSD trends for simulations followed over 100 ns, both HCur and [Zn(Cur)] docked DNA show stable conformations. Although initially RMSD values are similar for DNA-[Zn(Cur)], DNA-HCur and DNA itself but as time progressed, tendencies of interactions become different and the one due to DNA-[Zn(Cur)] and DNA-HCur move significantly lower than the red line that denotes RMSD values for DNA itself. This could indicate the Zn compound in its interaction with DNA is very steady on aspects concerning stability; on the other hand, HCur takes time to adjust, manifested by its observed fluctuations. However, once it has suitably bound itself it also remains steady, so as to match the trend-line for DNA-[Zn(Cur)]. The average RMSD of apo-DNA is 10.67 Å, while for DNA attached to HCur and [Zn(Cur)] they are 9.39 Å and 9.29 Å (Fig. 16A) respectively. Unbound DNA with a higher RMSD has therefore undergone more conformational change in its two chains, A and B. The fact that RMSD reduces when HCur and [Zn(Cur)] are bound to DNA indicates they form stable adducts with DNA that can withstand further conformational changes within the DNA. A lower RMSD of [Zn(Cur)] with DNA suggests higher stability of the complex than that of HCur-DNA.

In our case, the Root Mean Square Fluctuation (RMSF) would be a measure of the motion of a nucleobase around its mean position along the trajectory of MD simulation. It should indicate flexibility of some portions of the chosen DNA (1BNA). RMSF of the bound form of HCur with 1BNA is similar to that of 1BNA itself, particularly in the region of residue index 10–15, while that of [Zn(Cur)] bound 1BNA shows significantly lower fluctuation in the same region (Fig. 16B). The RMSF plot of [Zn(Cur)] exhibit a significantly lower nature than that for HCur, clearly indicating positional fluctuations of nucleobases were more in the other two states as compared to [Zn(Cur)] derived bound state.

In molecular dynamics simulation, radius of gyration (Rg) measures how compact the receptor is upon binding to a ligand. Lower Rg values imply the ligand is more compact inside the receptor cavity, thus stabilizing the adduct. In this investigation, DNA linked to [Zn(Cur)] initially showed somewhat increased displacements between 17 and 20 ns, but thereafter, it became stable (Fig. 16C). Contrarily, HCur bound to DNA exhibits variability between 20 and 80 ns that denote less efficient binding. Significantly stable gyration (Rg) of [Zn(Cur)] with DNA suggests that the DNA is oriented in a highly compact manner when

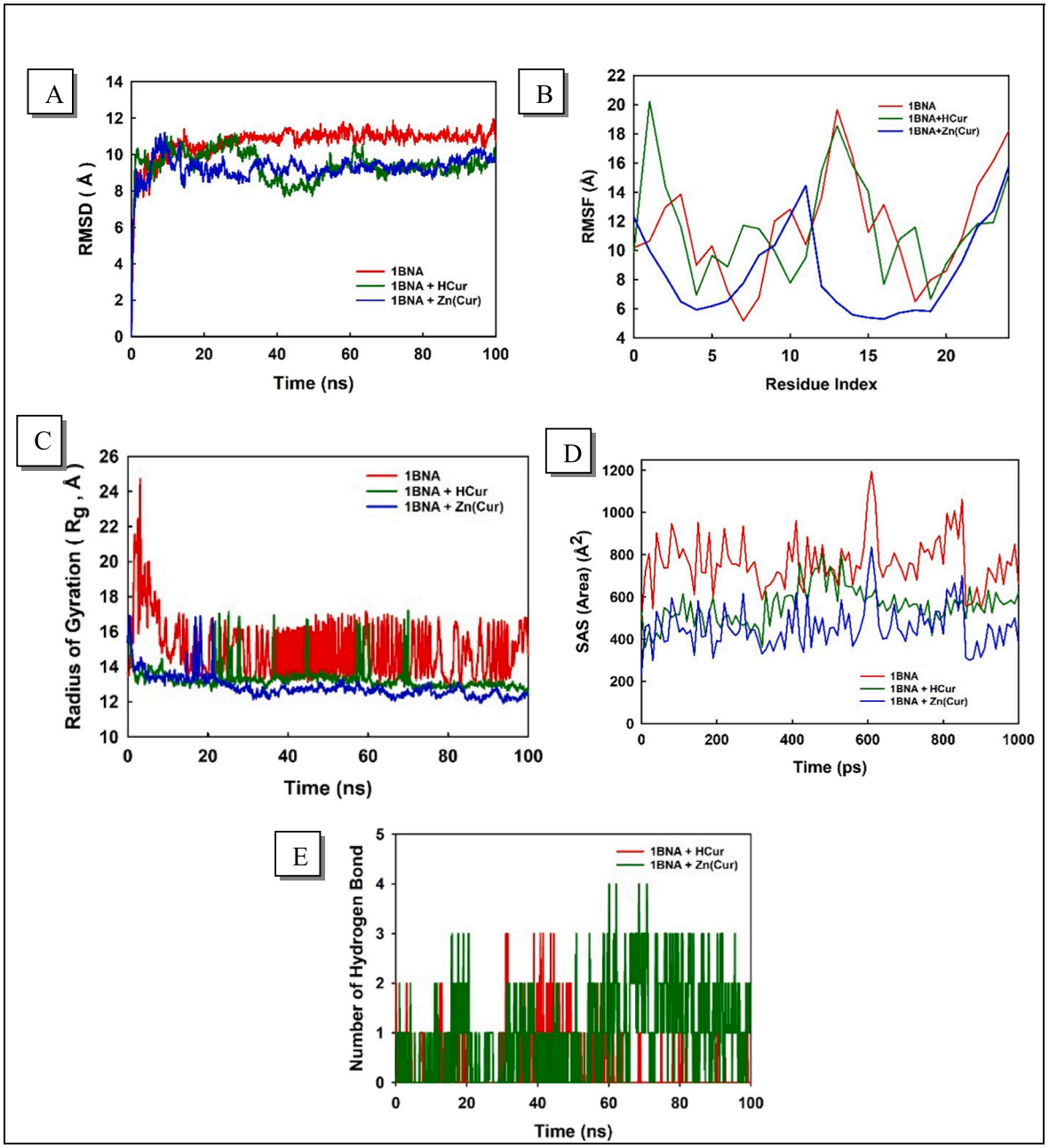


Fig. 16. (A) RMSD plot of free DNA (PDB ID: 1BNA), DNA with HCur and DNA with [Zn(Cur)], (B) RMSF plot of free DNA (PDB ID: 1BNA), DNA with HCur and DNA with [Zn(Cur)], (C) Radius of gyration plot of free DNA (PDB ID: 1BNA), DNA with HCur and DNA with [Zn(Cur)], (D) SASA and (E) Hydrogen bonding plots of HCur and [Zn(Cur)] formed with DNA during simulation.

attached to [Zn(Cur)].

SASA was determined using the entire atom's 100 ns molecular dynamics journey and plotted against time (Fig. 16D). An understanding of the ligand's location within the binding pocket could be had through an analysis of SASA parameters. One might think of ligand binding to a receptor cavity as that of a solvent replacement effect. A lower SASA value compared to apo-DNA suggest that the ligand is present in the binding pocket.

When HCur was bound to DNA, the average SASA value was 558.613 $Å^2$, while when [Zn(Cur)] was attached, the average SASA value was 455.654 $Å^2$. These values are significantly lower than when compounds were not bound to DNA (896.270 $Å^2$). Again, it may be noted that decrease in average SASA value was significantly lower in case of [Zn(Cur)] than in case of HCur. Based on our findings mentioned above, it may be concluded [Zn(Cur)] has a higher affinity for DNA and that it intercalates after 100 ps simulation (Fig. 16D).

Number of hydrogen bonds between DNA and HCur or [Zn(Cur)] shows adducts (i. e. complexes) have significant interaction and that they are stable. As simulation continued for 100 ns, there were considerable number of hydrogen bonds between DNA and HCur or [Zn(Cur)] (Fig. 16E). In Fig. 16E, an average of three hydrogen bonds were seen forming between DNA and [Zn(Cur)] over the course of 100 ns simulation detecting molecules achieving stable associated species. In contrast, only one hydrogen bond was formed between DNA and HCur in the same time scale of simulation.

This suggests associated structures formed by [Zn(Cur)] are more stable than that formed by HCur with the same DNA background (PDB ID-1BNA). The interaction of [Zn(Cur)] with 1BNA at the first frame (0

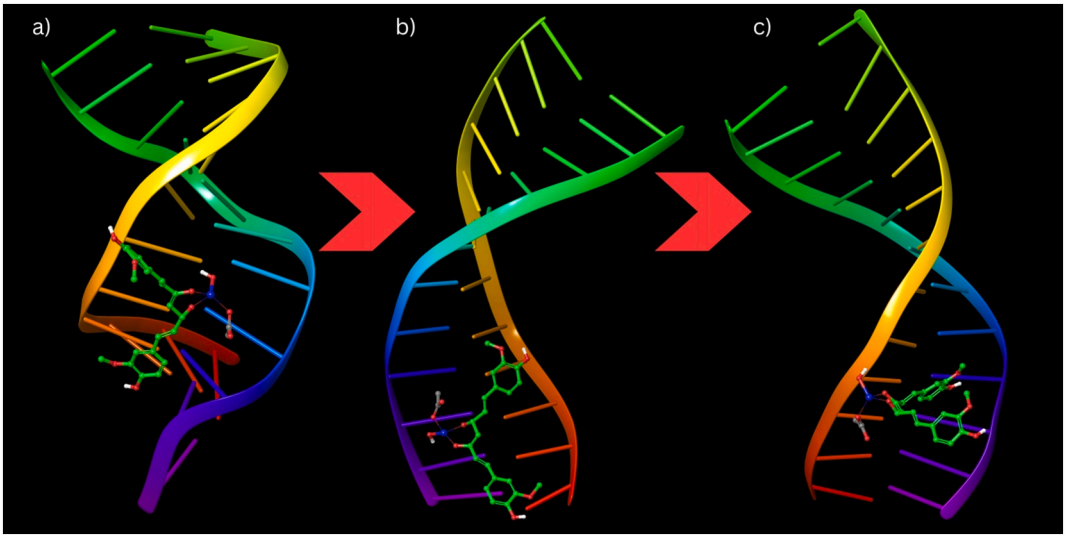


Fig. 17. Structural superimposition of (a) first frame (0 ns); (b) an intermediate frame (50 ns) and (c) last frame (100 ns) of [Zn(Cur)] bound with 1BNA after simulation.

Table 4
Binding free energy components for the DNA-Hcur and DNA-[Zn(Cur)] complexes calculated by MM-GBSA.

Compound code	MM-GBSA (kcal/mol)					
	ΔG_{bind}	ΔG_{bind}Lipo	ΔG_{bind}vdW	ΔG_{bind}Coulomb	ΔG_{bind}SolvGB	ΔG_{bind}Covalent
DNA-HCur	−46.50 ± 6.35	−17.13 ± 1.23	−47.29 ± 2.17	−0.3151 ± 5.54	35.97 ± 2.78	2.76 ± 1.90
DNA-[Zn(Cur)]	−50.89 ± 2.28	−21.53 ± 3.54	−51.28 ± 1.25	−0.5164 ± 4.20	46.58 ± 3.24	1.75 ± 2.50

(G_{bind}) total free energy of binding; (G_{bind}Lipo) lipophilic energy; (G_{bind}vdW) van der Waals interaction energy; (G_{bind}Coulomb) prime coulomb energy; (G_{bind}SolvGB) solvation energy generalized born; (G_{bind}Covalent) covalent binding energy.

ns), an intermediate frame (50 ns) and last frame (100 ns) is provided in Fig. 17. From the three figures, it is clearly evident that [Zn(Cur)] binding is one of intercalation as the compound tries to position itself between the strands of DNA. This signifies [Zn(Cur)] is well docked at a site of 1BNA that has been further confirmed by MM-GBSA calculations (Table 4).

3.2.2.3. Molecular mechanics generalized born surface area (MM-GBSA) calculations. Utilizing the molecular dynamic simulation trajectory, binding free energy along with other contributing energies in the form of MM-GBSA were determined for DNA-HCur and DNA-[Zn(Cur)] systems. Results in Table 4 suggest that maximum contribution to $\Delta G_{binding}$ for stability of the simulated compounds were due to ΔG_{bind}-coulomb, ΔG_{bind}-van der waals and ΔG_{bind}-lipophilic while ΔG_{bind}-covalent and ΔG_{bind}-solvation contribute to instability. $\Delta G_{binding}$ for the DNA-[Zn(Cur)] adduct was comparatively more negative in terms of free energy than DNA-HCur. These results support the potential of [Zn(Cur)] over HCur in binding DNA and showed efficiency of binding to the selected DNA as well as an ability to form stable DNA-ligand complexes.

4. Conclusion

The present study suggests MD simulation and binding free energy calculations are in good agreement with docking studies and that they exhibit properties of higher binding and probable inhibition of DNA in its functional role in the bio-system. Theoretical studies corroborate an experimental DNA binding study that was performed using calf thymus DNA. Hence, such compounds may be considered as potential drug candidates against DNA since they target the DNA moiety and inhibit activities like replication and transcription that play crucial roles for stopping growth of cells.

CRediT authorship contribution statement

The following is an author statement outlining all authors' individual contributions using relevant CRediT roles for manuscript having Manuscript Number: IJBIOMAC-D-23-02305.

Tanmoy Saha: Conceived and designed the experiments; performed them; analyzed and interpreted the data.

Subrahmanyam Sappati: Conceived and designed the experiments; analyzed and interpreted the data; helped in writing the paper.

Saurabh Das: Conceived and designed experiments; analyzed and interpreted the data; wrote the paper.

Declaration of competing interest

The authors declare that they have no known competing financial interests or personal relationships that could have appeared to influence the work reported in this paper.

Acknowledgments

SD wish to thank "RUSA 2.0" program of Government of India, operating at Jadavpur University through which he received a grant "Research Support to Faculty Members" in the thrust area "Research in Sustainable Development" (Sanction Ref. no. R-11/438/19 dated 30.05.2019). SS wishes to gratefully acknowledge Gdańsk University of Technology for Nobelium (No. 16/2021/IDUB/I.1) grant under "The Excellence Initiative – Research University" (IDUB) program. TS gratefully acknowledge Dr. Soumen Singha of the Department of Physics, Jadavpur University for his help and cooperation with regard to DFT calculations. He wishes to thank the "Governing Body" of Sri Aurobindo Institute of Education, Salt Lake, Kolkata for their support in his research endeavours.

Appendix A. Supplementary data

Supplementary data to this article can be found online at https://doi.org/10.1016/j.ijbiomac.2023.125305.

References

[1] B.B. Aggarwal, C. Sundaram, N. Malani, H. Curcumin Ichikawa, The Indian solid gold, in: The Molecular Targets and Therapeutic Uses of Curcumin in Health and Disease, Springer, Boston, MA, 2007, pp. 1–75.

[2] J.S. Jurenka, Anti-inflammatory properties of curcumin, a major constituent of *Curcuma longa*: a review of preclinical and clinical research, Altern. Med. Rev. 14 (2009) 141–153.

[3] T. Ak, İ. Gülçin, Antioxidant and radical scavenging properties of curcumin, Chem. Int. 174 (2008) 27–37.

[4] R. Wilken, M.S. Veena, M.B. Wang, E.S. Srivatsan, Curcumin: A review of anti-cancer properties and therapeutic activity in head and neck squamous cell carcinoma, Mol. Cancer 10 (2011) 12, https://doi.org/10.1186/1476-4598-10-12.

[5] S. Wanninger, V. Lorenz, A. Subhan, F.T. Edelmann, Metal complexes of curcumin–synthetic strategies, structures and medicinal applications, Chem. Soc. Rev. 44 (2015) 4986–5002.

[6] S.Y. Teow, K. Liew, S.A. Ali, A.S.B. Khoo, S.C. Peh, Antibacterial action of curcumin against *Staphylococcus aureus*: a brief review, J. Trop. Med. 2016 (2016), 2853045, https://doi.org/10.1155/2016/2853045 (10 pp.).

[7] A. Goel, A.B. Kunnumakkara, B.B. Aggarwal, Curcumin as "Curecumin": from kitchen to clinic, Biochem. Pharmacol. 75 (2008) 787–809.

[8] K. Neelofar, S. Shreaz, B. Rimple, S. Muralidhar, M. Nikhat, L.A. Khan, Curcumin as a promising anticandidal of clinical interest, Can. J. Microbiol. 57 (2011) 204–210.

[9] P. Tyagi, M. Singh, H. Kumari, A. Kumari, K. Mukhopadhyay, Bactericidal activity of Curcumin I is associated with damaging of bacterial membrane, PLoS One 10 (2015), e0121313.

[10] R.A. Sharma, W.P. Steward, A.J. Gescher, Pharmacokinetics and pharmacodynamics of Curcumin, Adv. Exp. Med. Biol. 595 (2007) 453–470.

[11] R. Banerjee, Inhibitory effect of Curcumin-Cu(II) and Curcumin-Zn(II) complexes on amyloid-beta peptide fibrillation, Bioinorg. Chem. Appl. 2014 (2014), 325873.

[12] T. Saha, P. Kumar, N. Sepay, D. Ganguly, K. Tiwari, K. Mukhopadhyay, S. Das, Multitargeting antibacterial activity of a synthesized Mn^{2+} complex of Curcumin on gram-positive and gram-negative bacterial strains, ACS Omega 5 (27) (2020) 16342–16357.

[13] S. Banerjee, P. Prasad, A. Hussain, I. Khan, P. Kondaiah, A.R. Chakravarty, Remarkable photocytotoxicity of curcumin in HeLa cells in visible and arresting its degradation on oxovanadium (IV) complex formation, Chem. Commun. 48 (2012) 7702–7704.

[14] K.I. Priyadarsini, The chemistry of Curcumin: from extraction to therapeutic agent, Molecules 19 (2014) 20091–20112.

[15] M.D. Cas, R. Ghidoni, Dietary Curcumin: correlation between bioavailability and health potential, Nutrients. 11 (9) (2019) 2147, https://doi.org/10.3390/nu11092147.

[16] Ferreira S.B. de Souza, M.L. Bruschi, Improving the bioavailability of curcumin: is micro/nanoencapsulation the key? Ther. Deliv. 10 (2019) 83–86, https://doi.org/10.4155/tde-2018-0075.

[17] P. Anand, A.B. Kunnumakkara, R.A. Newman, B.B. Aggarwal, Bioavailability of Curcumin: problems and promises, Mol. Pharm. 4 (2007) 807–818.

[18] P. Kumar, T. Saha, S. Behera, S. Gupta, S. Das, K. Mukhopadhyay, Enhanced efficacy of a Cu^{2+} complex of curcumin against gram positive and gram-negative bacteria: attributes of complex formation, J. Inorg. Biochem. 222 (2021), 111494.

[19] Y.-J. Wang, M.-H. Pan, A-Li Cheng, L.-I. Lin, Y.-S. Ho, Chang-Yao Hsieh, Jen-Kun Lin, Stability of curcumin in buffer solutions and characterization of its degradation products, J. Pharm. Biomed. Anal. 15 (1997) 1867–1876.

[20] T. Saha, S. Singha, S. Kumar, S. Das, Spectroscopy driven DFT computation for a structure of the monomeric Cu^{2+}-Curcumin complex and thermodynamics driven evaluation of its binding to DNA: Pseudo-binding of Curcumin to DNA, J. Mol. Struct. 1221 (2020), 128732.

[21] Enhancement of anti-leukemic potential of 2-hydroxyphenyl-azo-2′-naphthol (HPAN) on MOLT-4 cells through conjugation with Cu(II), RSC Adv. 4 (2014) 18419–18430.

[22] K.S. Moghadam, E.S. Toroghi, K.M. Vatanparast, P. Jouyaeian, P. Mokaberi, H. Yazdyani, A.Z. Tehranizadeh, R.M. Saberi, J. Chamani, Novel perspective into the interaction behavior study of the cyanidin with human serum albumin-holo transferrin complex: spectroscopic, calorimetric and molecular modeling approaches, J. Mol. Liq. 356 (2022), 119042.

[23] A.R. Darban, B. Shareghi, A. Asoodeh, J. Chamani, Multi-spectroscopic and molecular modeling studies of interaction between two different angiotensin I converting enzyme inhibitory peptides from gluten hydrolysate and human serum albumin, J. Biomol. Struct. Dyn. 35 (16) (2017) 3648–3662.

[24] C.J. Dhanaraj, I.U. Hassan, J. Johnson, J. Joseph, R.S. Joseyphus, Synthesis, spectral characterization, DNA interaction, anticancer and molecular docking studies on some transition metal complexes with bidentate ligand, J. Photochem. Photobiol. B Biol. 162 (2016) 115–124.

[25] N. Marjani, M. Dareini, M. Asadzade-Lotfabad, M. Pejhan, P. Mokaberi, Z. Amiri-Tehranizadeh, M.R. Saberi, J. Chamani, Evaluation of the binding effect and cytotoxicity assay of 2-Ethyl-5-(4-methylphenyl) pyramido pyrazole ophthalazine trione on calf thymus DNA: spectroscopic, calorimetric, and molecular dynamics approaches, Luminescence 37 (2) (2022) 310–322.

[26] Z.N. Feizabadi, A.Z. Tehranizadeh, S.A. Rad, P. Mokaberi, N. Nosrati, F. Hashemzadeh, R.H. Rahimi, R.M. Saberi, J. Chamani, Determining the interaction behavior of calf thymus DNA with anastrozole in the presence of histone H1: spectroscopies and cell viability of MCF-7 cell line investigations, DNA Cell Biol. 40 (8) (2021) 1039–1051.

[27] H. Maheri, F. Hashemzadeh, N. Shakibapour, E. Kamelniya, M.B. Nikouei, P. Mokaberi, P. Chamani, Glucokinase activity enhancement by cellulose nanocrystals isolated from jujube seed: a novel perspective for type II diabetes mellitus treatment (in vitro), J. Mol. Struct. 1269 (2022), 133803.

[28] A. Spinello, A. Terenzi, G. Barone, Metal complex-DNA binding: insights from molecular dynamics and DFT/MM calculations, J. Inorg. Biochem. 124 (2013) 63–69.

[29] J.C. Masztafiak, et al., Direct determination of metal complexes's interaction with DNA by atomic telemetry and multiscale molecular dynamics, J. Phys. Chem. Lett. 8 (2017) 805–811.

[30] Characterization of the structural changes of human serum albumin upon interaction with single-walled and multi-walled carbon nanotubes: spectroscopic and molecular modeling approaches, Res. Chem. Intermed. 45 (2019) 401–423.

[31] J. Chamani, G.H. Moosavi-Movahedi, A.A. Hakimelahi, Structural changes in β-lactoglobulin by conjugation with three different kinds of carboxymethyl cyclodextrins, Thermochim. Acta 432 (2005) 106–111.

[32] M.J. Frisch, G.W. Trucks, H.B. Schlegel, G.E. Scuseria, M.A. Robb, J.R. Cheeseman, G. Scalmani, V. Barone, G.A. Petersson, H. Nakatsuji, X. Li, M. Caricato, A. V. Marenich, J. Bloino, B.G. Janesko, R. Gomperts, B. Mennucci, H.P. Hratchian, J. V. Ortiz, A.F. Izmaylov, J.L. Sonnenberg, D. Williams-Young, F. Ding, F. Lipparini, F. Egidi, J. Goings, B. Peng, A. Petrone, T. Henderson, D. Ranasinghe, V. G. Zakrzewski, J. Gao, N. Rega, G. Zheng, W. Liang, M. Hada, M. Ehara, K. Toyota, R. Fukuda, J. Hasegawa, M. Ishida, T. Nakajima, Y. Honda, O. Kitao, H. Nakai, T. Vreven, K. Throssell, J.A. Montgomery Jr., J.E. Peralta, F. Ogliaro, M. J. Bearpark, J.J. Heyd, E.N. Brothers, K.N. Kudin, V.N. Staroverov, T.A. Keith, R. Kobayashi, J. Normand, K. Raghavachari, A.P. Rendell, J.C. Burant, S.S. Iyengar, J. Tomasi, M. Cossi, J.M. Millam, M. Klene, C. Adamo, R. Cammi, J.W. Ochterski, R.L. Martin, K. Morokuma, O. Farkas, J.B. Foresman, D.J. Fox, Gaussian 09, Revision D.01, Gaussian, Inc., Wallingford CT, 2016.

[33] (a) A.D. Becke, Density-functional thermochemistry. III. The role of exact exchange, J. Chem. Phys. 98 (1993), 5648e5652;
(b) C.T. Lee, W.T. Yang, R.G. Parr, Development of the Colle-Salvetti correlation-energy formula into a functional of the electron density, Phys. Rev. B 37 (1988), 785e789.

[34] S. Chiodo, N. Russo, E. Sicilia, LANL2DZ basis sets recontracted in the framework of density functional theory, J. Chem. Phys. 125 (2006), 104107.

[35] M. Cossi, J.V. Barone, Time-dependent density functional theory for molecules in liquid solutions, Chem. Phys. 115 (2001), 4708e4717.

[36] E.K.U. Gross, W. Kohn, Time-dependent density functional theory in, Adv. Quantum Chem. 21 (1990), 255e291.

[37] N.M. O'Boyle, A.L. Tenderholt, K.M. Langner, Cclib: a library for package independent computational chemistry algorithms, J. Comput. Chem. 29 (2008) 839–845.

[38] V.K. Choudhary, A.K. Bhatt, D. Dash, N. Sharma, DFT calculations on molecular structures, HOMO-LUMO study, reactivity descriptors and spectral analyses of newly synthesized diorganotin(IV) 2-chloridophenylacetohydroxamate complexes, J. Comp. Chem. (2019) 1–10.

[39] A. Otero-de-la-Roza, E.R. Johnson, J. Contreras-García, Revealing non-covalent interactions in solids: NCI plots revisited, Phys. Chem. Chem. Phys. (2012) 35.

[40] T. Lu, F. Chen, Multiwfn: a multifunctional wavefunction analyzer, J. Comput. Chem. 33 (2012) 580–592.

[41] A. Kumar, S.D. Yeole, S.R. Gadre, R. Lopez, J.F. Rico, G. Ramirez, I. Ema, D. Zorrilla, DAMQT 2.1.0: a new version of the DAMQT package enabled with the topographical analysis of electron density and electrostatic potential in molecules, J. Comput. Chem. 36 (2015) 2350–2359.

[42] T. Deb, D. Choudhury, P.S. Guin, M.B. Saha, G. Chakrabarti, S. Das, A complex of Co(II) with 2-hydroxyphenyl-azo-2′-naphthol (HPAN) is far less cytotoxic than the parent compound on A549-lung carcinoma and peripheral blood mononuclear cells: reasons for reduction in cytotoxicity, Chem.-Biol. Inter. 189 (2011) 206–214.

[43] P.S. Guin, P.C. Mandal, S. Das, The binding of a hydroxy-9,10-anthraquinone Cu^{II} complex to calf thymus DNA: electrochemistry and UV/Vis spectroscopy, ChemPlusChem 77 (2012) 361–369, https://doi.org/10.1002/cplu.201100046.

[44] P. Das, C.K. Jain, S.K. Dey, R. Saha, A.D. Chowdhury, S. Roychoudhury, S. Kumar, H.K. Majumder, S. Das, Synthesis, crystal structure, DNA interaction and *in vitro* anticancer activity of a Cu(II) complex of purpurin: dual poison for human DNA topoisomerase I and II, RSC Adv. 4 (2014) 59344–59357.

[45] B. Mandal, S. Singha, S.K. Dey, S. Mazumdar, T.K. Mondal, P. Karmakar, S. Kumar, S. Das, Synthesis, crystal structure from PXRD of a $Mn^{II}(purp)_2$ complex, interaction with DNA at different temperatures and pH and lack of stimulated ROS formation by the complex, RSC Adv. 6 (2016) 51520–51532.

[46] S. Mukherjee-Chatterjee, C.K. Jain, S. Singha, P. Das, S. Roychoudhury, H. K. Majumder, S. Das, Activity of Co^{II}-Quinalizarin: a novel analogue of anthracycline-based anticancer agents targets human DNA topoisomerase, whereas quinalizarin itself acts via formation of semiquinone on acute lymphoblastic leukemia MOLT-4 and HCT 116 cells, ACS Omega 3 (2018) 10255–10266.

[47] G. Scatchard, The attractions of proteins for small molecules and ions, Ann. N. Y. Acad. Sci. 51 (1949) 660–672.

[48] G.M. Morris, R. Huey, W. Lindstrom, M.F. Sanner, R.K. Belew, D.S. Goodsell, A. J. Olson, Auto dock4 and Auto dock tools 4: automated docking with selective receptor flexiblity, J. Comput. Chem. 16 (2009) 2785–2791.

[49] J. Eberhardt, D. Santos-Martins, A.F. Tillack, S. Forli, AutoDock Vina 1.2.0: new docking methods, expanded force field, and python bindings, J. Chem. Inf. Model. 61 (8) (2021) 3891–3898.
[50] O. Trott, A.J. Olson, Auto Dock Vina: improving the speed and accuracy of docking with a new scoring function, efficient optimization, and multithreading, J. Comp. Chem. 31 (2010) 455–461.
[51] R. Huey, G.M. Morris, A.J. Olson, D.S. Goodsell, A semiempirical free energy force field with charge-based desolvation, J. Comp. Chem. 28 (2007) 1145–1152.
[52] H.R. Drew, R.M. Wing, T. Takano, C. Broka, S. Tanaka, K. Itakura, R.E. Dickerson, Structure of a B-DNA dodecamer: conformation and dynamics, Proc. Natl. Acad. Sci. U. S. A. 78 (1981) 2179–2183.
[53] A. Ghosh, N. Mukerjee, B. Sharma, A. Pant, K.Y. Mohanta, R.D. Jawarkar, Target specific inhibition of protein tyrosine kinase in conjunction with cancer and SARS-COV-2 by olive nutraceuticals, Front. Pharmacol. (2022) 12.
[54] D. Patra, S. Paul, N. Sepay, R. Kundu, T. Ghosh, Structure-activity relationship on DNA binding and anticancer activities of a family of mixed ligand oxidovanadium (V) hydrazone complexes, J. Biomol. Struct. Dyn. 36 (2017) 4143–4155.
[55] D.E. Shaw, Research Desmond. www.deshawresearch.com. https://www.deshawresearch.com/downloads/download_desmond.cgi/.
[56] D. Shivakumar, J. Williams, Y. Wu, W. Damm, J. Shelley, W. Sherman, Prediction of absolute solvation free energies using molecular dynamics free energy perturbation and the OPLS force field, J. Chem. Theory Comput. 65 (2010) 1509–1519.
[57] W.L. Jorgensen, J. Chandrasekhar, D. Madura, Comparison of simple potential functions for simulating liquid water, J.Chem.Phys 79 (1983) 926.
[58] G.J. Martyna, M.L. Klein, Nose-Hoover chains: the canonical ensemble via continuous dynamics, J. Chem. Phys. 97 (1992) 2635–2643.
[59] G.J. Martyna, D.J. Tobias, M.L. Klein, Constant pressure molecular dynamics algorithms, J. Chem. Phys. 101 (1994) 4177–4189.
[60] A.Y. Toukmaji, J.A. Board, Ewald summation techniques in perspective: a survey, Comput. Phys. Commun. 95 (2–3) (1996) 73–92.
[61] M.E.A. Zaki, S.A. Al-Hussain, V.H. Masand, S. Akasapu, S.O. Bajaj, N.N.E. El-Sayed, A. Ghosh, I. Lewaa, Identification of anti-SARS-CoV-2 compounds from food using QSAR-based virtual screening, molecular docking, and molecular dynamics simulation analysis, Pharmaceuticals 14 (2021) 357, https://doi.org/10.3390/ph14040357.
[62] S. Genheden, U. Ryde, The MM/PBSA and MM/GBSA methods to estimate ligand-binding affinities, Expert Opin. Drug Discovery 5 (2015) 449–461.
[63] M.I. Choudhary, M. Shaikh, A. Tul-Wahab, A. Ur-Rahman, *In silico* identification of potential inhibitors of key SARS-CoV-2 3CL hydrolase (Mpro) via molecular docking, MMGBSA predictive binding energy calculations, and molecular dynamics simulation, PLoS One 15 (7) (2020), e0235030.
[64] S. Grabner, B. Modec, Zn(II) Curcuminate complexes with 2, 2′-bipyridine and carboxylates molecules, Molecules 24 (2019) 2540, https://doi.org/10.3390/molecules24142540.
[65] P.K. Chattaraj, S. Giri, Electrophilicity index within a conceptual DFT framework, Annu. Reports Sect. 'C' Phys. Chem. 105 (2009) 13–39.
[66] P.K. Chattaraj, U. Sarkar, D.R. Roy, Electrophilicity index, Chem. Rev. 106 (2006) 2065–2091.
[67] M. Ghosh, N. Sepay, C. Rizzoli, C.K. Ghosh, A. Banerjee, S. Saha, Mononuclear copper (II) schiff base complex: synthesis, structure, electrical analysis and protein binding study, New J. Chem. 45 (2021) 2995–3006.

Journal of Inorganic Biochemistry 249 (2023) 112369

Contents lists available at ScienceDirect

Journal of Inorganic Biochemistry

journal homepage: www.elsevier.com/locate/jinorgbio

Utilizing coordination chemistry through formation of a Cu^{II}-quinalizarin complex to manipulate cell biology: An *in vitro*, *in silico* approach

Sayantani Chatterjee [a,b], Chetan Kumar Jain [c,d,1], Tanmoy Saha [a], Susanta Roychoudhury [c,2], Hemanta Kumar Majumder [d], Saurabh Das [a,*]

[a] Department of Chemistry (Inorganic Section), Jadavpur University, Kolkata 700 032, India
[b] Department of Chemistry, Vijaygarh Jyotish Ray College, Kolkata 700 032, India
[c] Cancer Biology & Inflammatory Disorder Division, Indian Institute of Chemical Biology, Kolkata 700 032, India
[d] Infectious Diseases and Immunology Division, Indian Institute of Chemical Biology, Kolkata 700 032, India

ARTICLE INFO

Keywords:
Anthracyclines
Cu^{II}-quinalizarin
Calf thymus DNA
DFT
Topoisomerase
Molecular docking

ABSTRACT

Quinalizarin, an analogue of anthracycline anticancer agents, is an anticancer agent itself. A Cu^{II} complex was prepared and characterized by elemental analysis, UV-Vis & IR spectroscopy, mass spectrometry, EPR and DFT. The intention behind the preparation of the complex was to increase cellular uptake, compare its binding with DNA against that of quinalizarin, modulation of semiquinone formation, realization of human DNA topoisomerase I & human DNA topoisomerase II inhibition and observation of anticancer activity. While the first two attributes of complex formation lead to increased efficacy, decrease in semiquinone generation could results in a compromise with efficacy. Inhibition of human DNA topoisomerase makes up this envisaged compromise in free radical activity since the complex shows remarkable ability to disrupt activities of human DNA topoisomerase I and II. The complex unlike quinalizarin, does not catalyze flow of electrons from NADH to O_2 to the extent known for quinalizarin. Hence, decrease in semiquinone or superoxide radical anion could make modified quinalizarin [as Cu^{II} complex] less efficient in free radical pathway. However, it would be less cardiotoxic and that would be advantageous to qualify it as a better anticancer agent. Although binding to calf thymus DNA was comparable to quinalizarin, it was weaker than anthracyclines. Low cost of quinalizarin could justify consideration as a substitute for anthracyclines but the study revealed IC_{50} of quinalizarin/Cu^{II}-quinalizarin was much higher than anthracyclines or their complexes. Even then, there is a possibility that Cu^{II}-quinalizarin could be an improved and less costly form of quinalizarin as anticancer agent.

1. Introduction

Inorganic compounds (more specifically coordination compounds) in varied forms are a subject of discussion today for diverse biological functions; be it naturally present in the environment or incorporated synthetically into a biological system [1–3]. Their varied role in biosystems are well realized [1–3]. What transpired in majority of cases is that a transition metal ion upon binding an organic moiety became the center of activity in that coordination environment, permitting the execution of desired biological functions; most often such environments have more than one role [4–12]. While a major reason to prepare metal complexes has been to gain easy passage into biological systems, several other attributes of complex formation also exist [5–12]. A good amount of research on anticancer activity by inorganic complexes is found in literature today; *cis* platin, being a forerunner, either used alone or in combination with others [11–13]. A major reason why metal complexes like *cis* platin are successful in cancer chemotherapy is in their ability to interact with DNA leading to its distortion; depriving cells from performing their function [13–15]. An important class of anticancer agents are anthracyclines, whose efficacy is severely compromised by

Abbreviation: THAQ, 1, 2, 5, 8-tetrahydroxy-9,10-antharquinone; Cu Q, $[Cu^{II}(THAQ)_2(H_2O)_2]$.

* Corresponding author.
E-mail address: saurabh.das@jadavpuruniversity.in (S. Das).

[1] Present address for Chetan Jain: Department of Biotechnology, Sun Pharmaceutical Industries Limited, Tandalja, Vadodara- 390,020, INDIA

[2] Present address for Susanta Roychoudhury: Chief, Basic Research, Saroj Gupta Cancer Centre and Research Institute, Mahatma Gandhi Road, Thakurpukur, Kolkata – 700,063, INDIA.

https://doi.org/10.1016/j.jinorgbio.2023.112369
Received 17 February 2023; Received in revised form 6 September 2023; Accepted 8 September 2023
Available online 21 September 2023
0162-0134/© 2023 Published by Elsevier Inc.

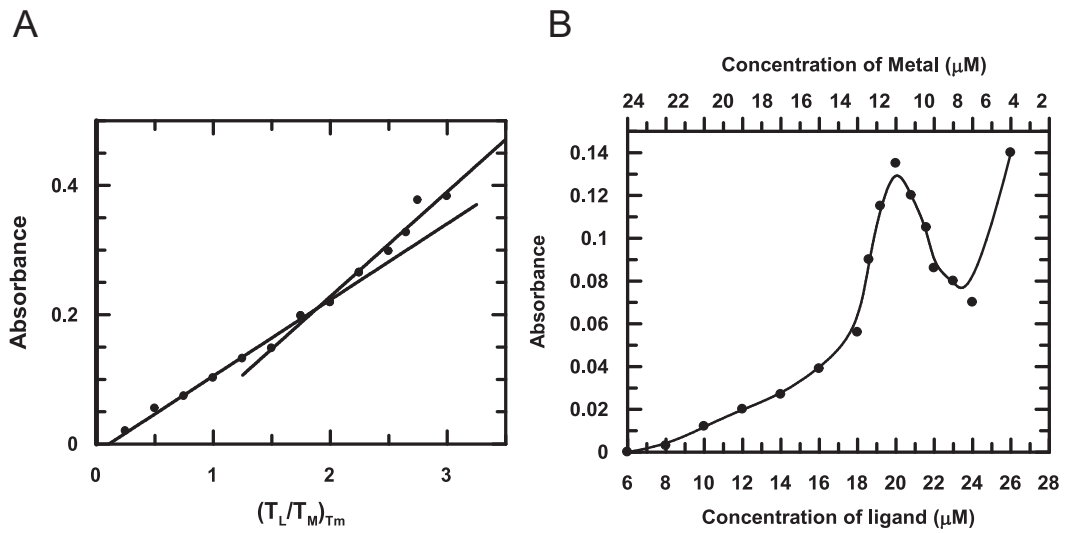


Fig. 1. Plots show a gradual variation in absorbance at 554 nm for (A) change in [THAQ]:[Cu^{II}] at a fixed concentration of Cu^{II} and (B) continuous variation of THAQ and Cu^{II} at physiological pH (~7.4); [Cu^{II}] = 10 μM. For (B), strength of stock solutions were Cu^{II} = THAQ = 100 μM; each solution was diluted in 10 mL volumetric flasks. [NaCl] =10 mM, Temperature = 298 K.

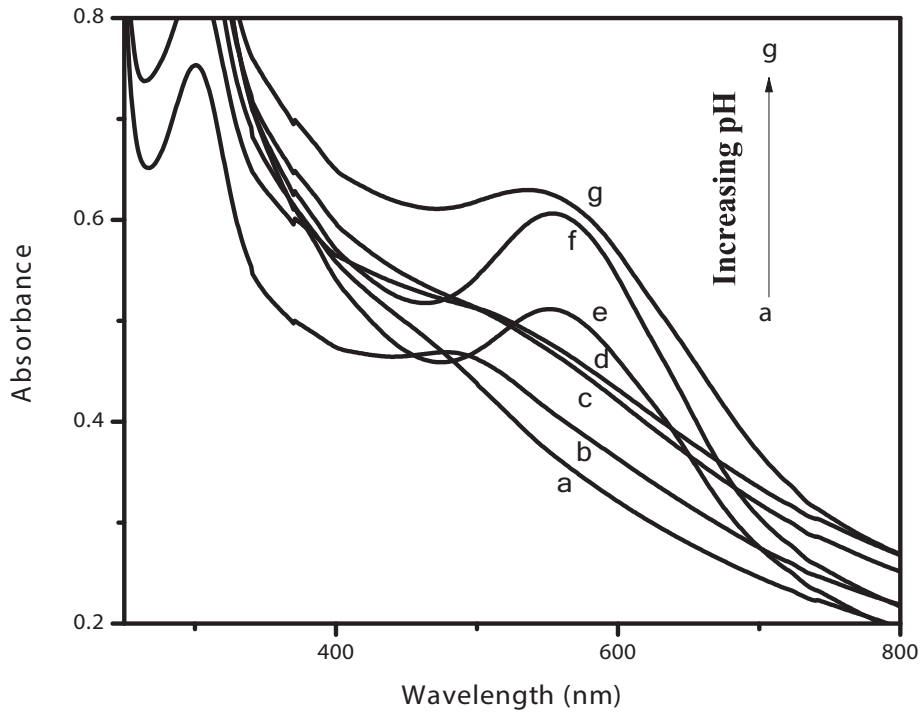


Fig. 2. Absorption spectra of THAQ in presence of Cu^{II} in aqueous solution at different pH; (a) 3.21; (b) 4.57; (c) 5.21; (d) 6.05; (e) 7.05; (f) 8.16; (g) 10.5 [THAQ] = 20 μM, [Cu^{II}] = 10 μM, [$NaNO_3$] =10 mM, T = 301 K.

cardiotoxic side effects [16–20]. Hence, effort to strike a balance between efficacy and adverse effects has become important. Metal complexes of anthracyclines or analogues have showed varied response in this regard. Although mechanism of action, is still being investigated several contradictions have already been identified [19–26]. However, the progress made with regard to metal complexes of anthracyclines or their analogues is worth mentioning [22–28]. What got revealed through studies on metal complexes of anthracyclines and/or their analogues is that these complexes display an ability to distort DNA preventing important biological functions from occurring. They help to release a drug close to a target, generate free radicals that are useful for efficacy, target various support systems (enzymes) that help DNA carry out essential activities like replication and/or transcription [19–27]. An important aspect related to anthracyclines, their metal complexes or by analogues and their metal complexes is the inhibition of human DNA topoisomerase I and human DNA topoisomerase II, whose destabilization is considered important for targeting cancer cells [24–26,29–35].

Here, we report the potential of a Cu^{II} complex of quinalizarin (1,2,5,8-tetrahydroxy-9,10-anthraquinone (THAQ); a simpler analogue of anthracyclines, on ALL MOLT-4 cells against that of quinalizarin itself [26,36–39]. Quinalizarin exerts anti-tumor effect on different types of cancer [36–39]. However, the underlying mechanism and signaling pathways are not clear [36–39]. Several studies discuss effects of quinalizarin on proliferation, apoptosis and generation of reactive oxygen

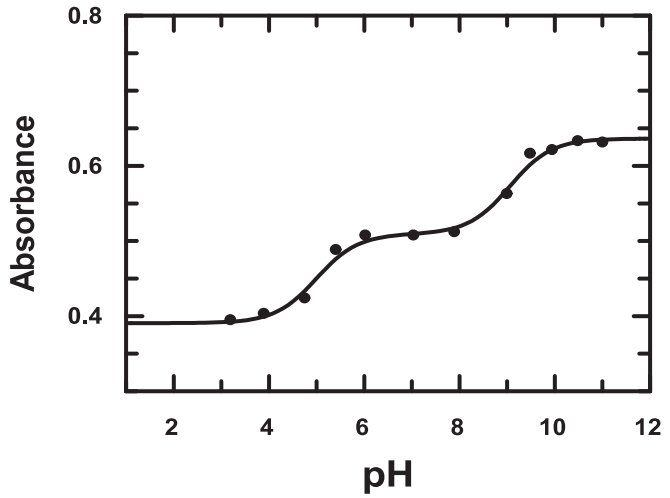


Fig. 3. A spectrophotometric titration of THAQ in the presence of Cu^{II}, shown by variation in absorbance at 550 nm; [THAQ] = 20 μM, [Cu^{II}] = 10 μM, [$NaNO_3$] =10 mM, T = 301 K.

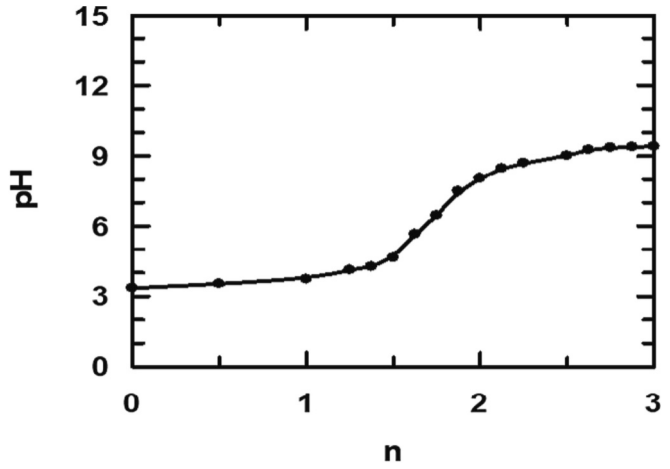


Fig. 4. A titration curve for THAQ determined in presence of Cu^{II}; n corresponds to number of base equivalents added per molecule of THAQ. Samples contained an excess of strong acid; when it is neutralized $n = 0$.

species (ROS) [26,36–39]. Studies suggest quinalizarin exhibit significant cytotoxic effect on human breast cancer cells and human lung cancer cells in a dose-dependent manner; that it activates p38 kinase, inhibits extracellular signal-regulated kinase, is a signal transducer and activator of transcription 3 (STAT3) and NF-κB signaling pathways, *etc.* [26,36–39] Cu(II) was chosen owing to certain established attributes pertaining to it [24,30,39–42]. Different experiments were performed to investigate and correlate possible roles the complex might have in biology that could explain findings on ALL MOLT-4 cells [6–9,24–26,30,35–42]. Performance of the complex was compared with anthracyclines and their analogues, with metal ion complexes that were prepared earlier, both in free radical pathway and as inhibitor of human DNA topoisomerase [21–27,31]. Interaction of THAQ and its Cu(II) complex was also investigated through *in silico* molecular docking studies that substantiated our experimental findings.

2. Experimental

2.1. Materials and preparation of solutions

Quinalizarin (THAQ) was procured from BDH, England and purified by recrystallization from alcohol-water mixture. Stock solutions were prepared in methanol having concentration ~ 10^{-4} M. Since solutions of hydroxy-9,10-anthraquinones are sensitive to light and oxygen, stock solutions were prepared just before use and if required stored in dark bottles under de-aerated conditions. $Cu(ClO_4)_2.6H_2O$ [Merck, India] was dissolved in water to prepare an aqueous solution having concentration of 10^{-4} M. This was used for physico-chemical experiments. All solutions were prepared using de-ionized triple-distilled water. $Cu(ClO_4)_2.6H_2O$ was handled with care.

Calf thymus DNA was purchased from Sisco Research Laboratories, India and dissolved in phosphate buffer for a minimum of 6 h. Concentration of calf thymus DNA was determined considering a molar extinction coefficient of 6600 M^{-1} cm^{-1} at 260 nm. Absorbance at 260 nm and 280 nm were noted for calculating A_{260}/A_{280}. Values being >1.8 but <1.9 suggest DNA to be free from protein. The quality of calf thymus DNA was also checked by its characteristic circular dichroism band at 260 nm recorded on J815 Spectropolarimeter, JASCO, Japan. Phosphate buffer used to maintain pH and ionic strength in physiological range (6.8 to 8.2) contained 150 mM NaCl, 35 mM KCl, 3.5 mM $CaCl_2$ and 0.5 mM $MgCl_2$.

2.2. Instruments used

Absorption spectroscopy was performed on JASCO V-630 spectrophotometer, Japan using a 10 mm × 10 mm quartz cuvette. Temperature was controlled with a circulating thermo-stated water bath. Fluorescence measurements were made on Duetta, Horiba Scientific where 10 mm × 10 mm fluorescence cuvette was used. Circular dichroism was done on J815 Spectropolarimeter, JASCO, Japan. Infra-red spectroscopy of solid samples was recorded on Spectrum Two, FTIR spectrophotometer, Perkin Elmer. TGA was performed on Mettler Toledo TGA/SDTA 851 thermal analyzer. Micromass Q-T of micro™, Waters Corporation was used for recording mass spectrum of the complex; the ESI-MS technique was used. pH of solutions were recorded with on a pH meter (LI 613, Elico, India). DFT, molecular docking and molecular dynamics simulation were performed on a Linux operating system supported with GPU-NVIDIA RTX 3060 Ti and Intel i7 9700kF processor.

2.3. Methods

2.3.1. Determination of stoichiometry of complex formation in 90% aqueous-10% methanol solution

Stoichiometry of interaction leading to complex formation was determined by mole ratio and Job's method of continuous variation. In the mole ratio method, a series of solutions were prepared keeping concentration of Cu^{II} fixed, while THAQ was varied. Absorbance at 554 nm was plotted against $(T_L/T_M)_{Tm}$; T_L and T_M refer to concentrations of THAQ and Cu^{II} respectively. Intersection of two straight lines indicates a ligand to metal ratio for complex formation in solution. In Job's method of continuous variation, complimentary mixtures were prepared in 10 mL volumetric flasks and absorbance was recorded at 554 nm. The major peak in the Job's plot indicates stoichiometry of complex formation.

2.3.2. Spectrophotometric titration of THAQ in the presence of Cu(II) and determination of stability constant of the complex in solution

Complex formation and subsequently its stability was ascertained using absorption spectroscopy. Cu^{II} and THAQ were taken in the ratio 1:2, as identified in "stoichiometry determination" experiments. Concentration of THAQ in experiments where a spectrophotometric titration was performed was 2 × 10^{-5} mol dm^{-3}. Absorption of THAQ in the presence of Cu^{II} was recorded at different pH. pK_a for dissociation of protons of THAQ in presence of Cu^{II} was determined by a spectrophotometric titration; the data was fitted to Eq. (1). Initially, metal to ligand mixture (1:2) was acidified to pH ~3.00. Solutions were slowly titrated

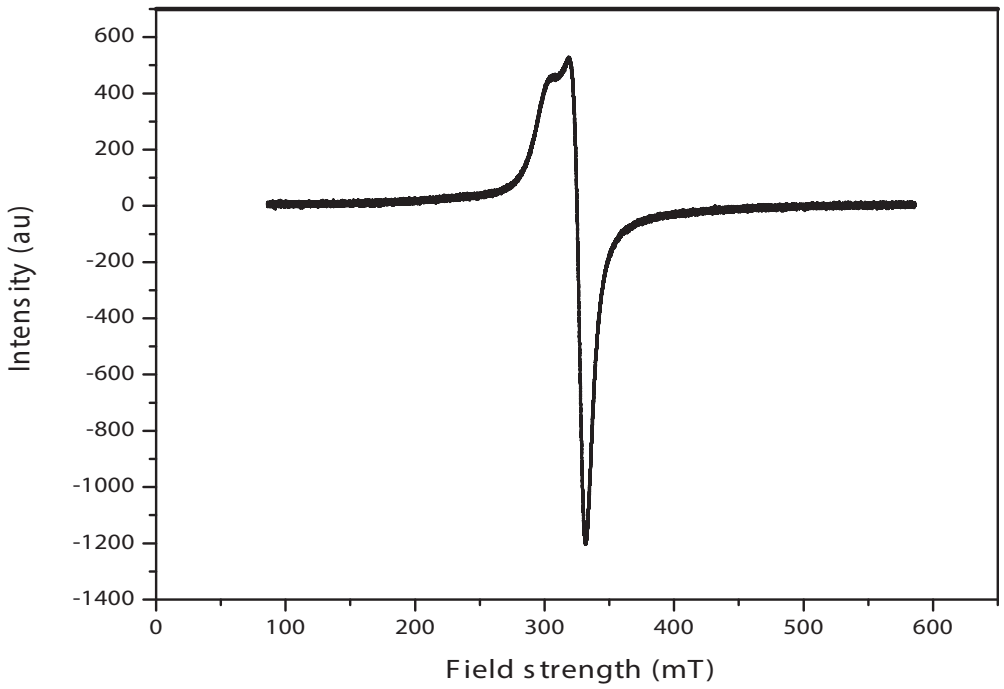


Fig. 5. Room temperature (298 K) solid state EPR spectrum of $Cu^{II}(THAQ)_2(H_2O)_2$.

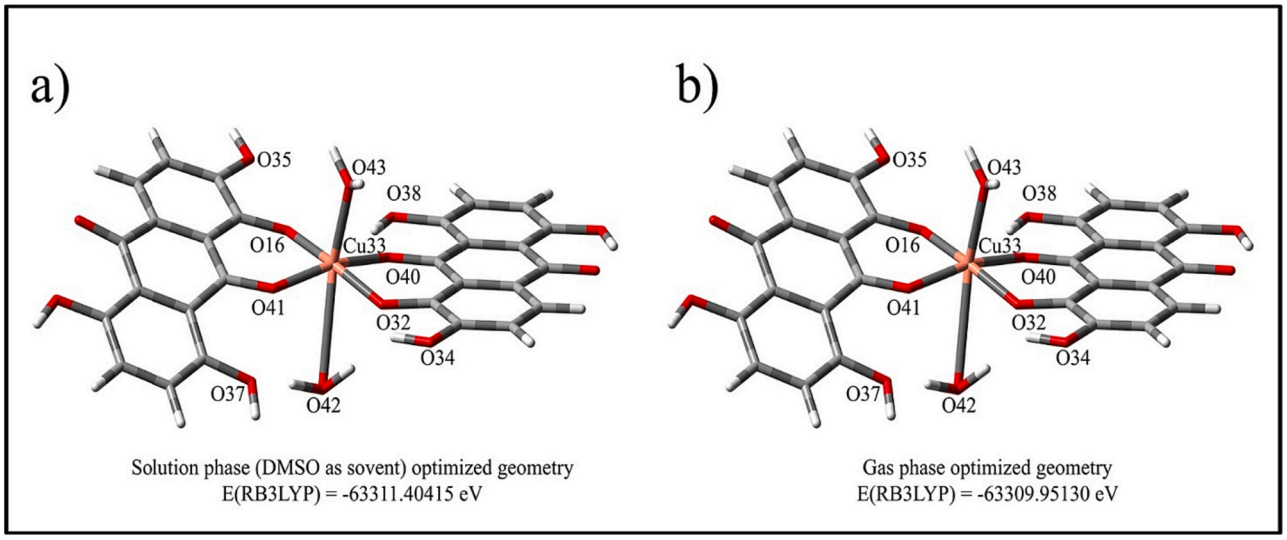


Fig. 6. Ground state optimized geometries of $Cu^{II}(THAQ)_2(H_2O)_2$ (a) Solution phase (b) gaseous phase.

using 0.01 mol dm^{-3} NaOH keeping metal to ligand ratio constant. Absorption spectra recorded at different pH enabled determination of a change in absorbance of THAQ in presence of Cu^{II} that helped to determine pK_a of THAQ in presence of Cu^{II}.

$$A_{obs} = A_1/\left(1+10^{pH-pK}\right) + A_2/\left(1+10^{pK-pH}\right) \quad (1)$$

Formation constants β* and β for 1:2 complex is described through Eqs. (2)–(6) [22–27]:

$$Cu^{2+} + 2LH_3H^{*} \rightleftharpoons Cu(LH_2H^{*})_2 + 2H^{+} \quad (2)$$

$$\beta^{*} = \frac{\left[Cu(LH_2H^{*})_2\right][H^{+}]^2}{\left[Cu^{2+}\right][LH_3H^{*}]^2} \quad (3)$$

$$Cu^{2+} + 2\,LH_2H^{*-} \rightleftharpoons Cu(LH_2\,H^{*})_2 \quad (4)$$

$$\beta = \frac{\left[Cu(LH_2H^{*})_2\right]}{\left[Cu^{2+}\right][LH_2H^{*-}]^2} \quad (5)$$

$$\beta = \frac{\beta^{*}}{K_2{}^2} \quad (6)$$

K_2 denotes dissociation constant of phenolic-OH of THAQ engaged in intra-molecular hydrogen bonding with quinone oxygen.

2.3.3. Potentiometric studies leading to evaluation of number of base equivalents per THAQ

Potentiometric titrations were carried out for THAQ in presence of Cu^{II} using a LMPH-10, LABMAN pH meter. Concentration of THAQ in solution was 2×10^{-4} mol dm^{-3}. Ratio of THAQ to Cu(II) was 2:1. Titration curves were treated quantitatively. Constancy in pH meter

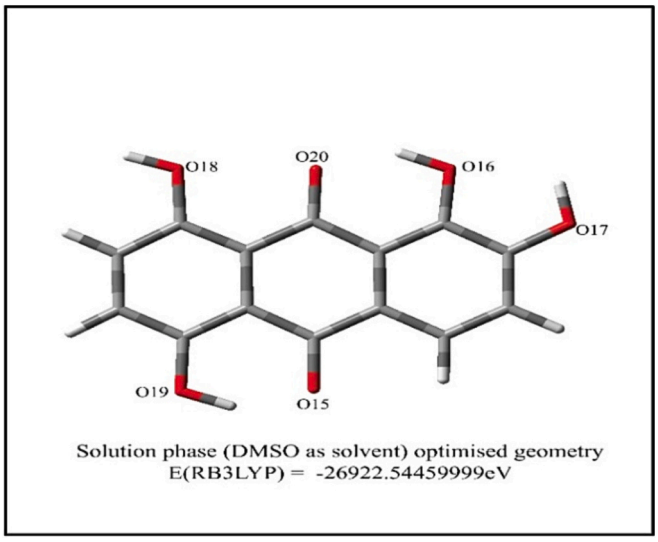


Fig. 7. Ground state optimized geometry of THAQ in solution phase.

Table 1
Coordinated bond distances (in Å) and bond angles (in °) of $Cu^{II}(THAQ)_2(H_2O)_2$.

Bond	Gaseous phase	In DMSO	Angle	Gaseous phase	In DMSO
Cu33–O16	1.937	1.919	O16–Cu33–O41	88.25	88.47
Cu33–O41	1.997	1.990	O32–Cu33–O40	88.22	87.38
Cu33–O32	1.954	1.963	O32–Cu33–O41	96.24	94.39
Cu33–O40	1.999	2.000	O16–Cu33–O40	88.49	87.89
Cu33−O43	2.366	2.223	O40−Cu33−O43	87.58	96.91
Cu33−O42	2.676	3.065			

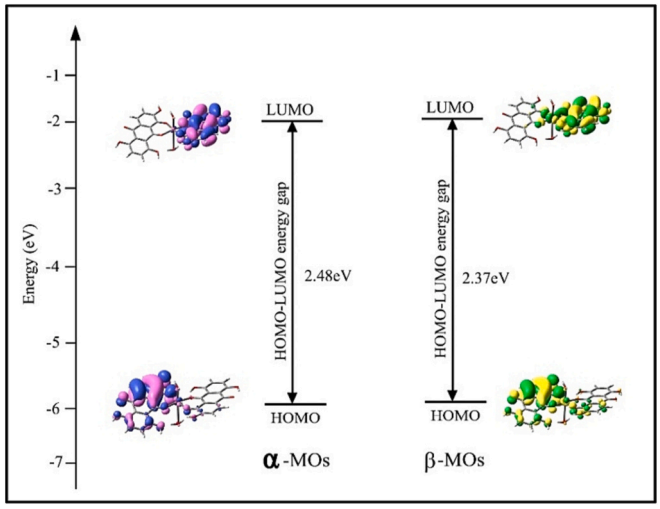


Fig. 8. HOMO-LUMO energy gap of $Cu^{II}(THAQ)_2(H_2O)_2$ in α and β MOs.

reading was achieved in reasonable time (5–7 min). Titrations were repeated with samples of THAQ at 1:2 metal to ligand ratio and reproducibility was almost always within 0.02 pH unit. Experiments were performed at 298 K with ionic strength maintained at 0.01 mol dm^{-3} using $NaNO_3$. To convert pH meter readings to hydrogen-ion concentration, electrode was calibrated after Irving et al. [43,44]

2.3.4. Preparation of the complex

THAQ in ethanol (2.75×10^{-3} g in 100 mL) was mixed with an aqueous solution of Cu^{II}, taken in the form of copper(II) perchlorate (1.85×10^{-3} g in 50 mL) in a round bottom flask at pH ~ 5.0 to 5.5. It was heated to 60 °C using a reflux condenser for 4 h. The obtained precipitate was recovered through filtration and washed with ethanol. The compound not being very soluble in common solvents like methanol, ethanol or acetonitrile, DMSO was used to prepare working solutions. Although attempt was made to obtain single crystals using a combination of solvents, we were not successful in getting one. Hence, the structure was determined using computational methods based on spectroscopic evidence.

The complex was characterized using UV-Vis spectroscopy, infra-red spectroscopy, elemental analysis, mass spectrometry, magnetic susceptibility measurements and thermo-gravimetric studies.

Anal. Calc. (%) for $C_{28}H_{18}O_{14}Cu$: C, 52.36; H, 2.83; Found: C, 52.09; H, 2.89. A solution of the complex (~1×10^{-4} M) was prepared by dissolving the solid in DMSO. Thereafter, experimental solutions were prepared by an exact dilution of the stock solution using a calibrated micropipette (Pipetman-M23866E, Gilson, France).

2.3.5. Computational methodology

Gaussian 09 program and DFT approach were applied to calculations undertaken [45]. We used a standard 6-31G+(d,p) basis set, Becke three parameter hybrid functional and Lee-Yang-gradient Parr's corrected correlation functional (B3LYP) for elements C, H and O [46]. For Cu the LanL2DZ basis set was used [47]. The Grimmes third order correction for dispersion and Becke-Johnson damping (GD3BJ) were used to account for long-range dispersion impact. Geometry of the ground state (S_0) for gaseous state was fully optimized using the program's extremely stringent convergence criteria. Structure optimization in DMSO (solvent) was done by using integral equation formalism variant (IEFPCM) of polarizable continuum model [48]. Frequencies were determined on optimized geometries where all vibrational frequencies were considered positive to ensure global minima of stationary points. Investigating MO orbitals and molecular electrostatic potential (MEP) surface were done using GaussView [49]. MO composition was calculated using Gausssum program. In addition, frontier molecular orbital energies were used to calculate quantum mechanical descriptors like MO gap (E), ionisation potential (IP), electron affinity (EA), electronegativity (χ), chemical hardness (η), mean energy (M), chemical potential (μ), chemical softness (σ) and electrophilicity index (ω). These were performed using following formulae [50].

$$\Delta E = E_{LUMO} - E_{HOMO} \quad (7)$$

$$IP = -E_{HOMO} \quad (8)$$

$$EA = -E_{LUMO} \quad (9)$$

$$\chi = -\mu = (IP + EA)/2 \quad (10)$$

$$\eta = \Delta E/2 \quad (11)$$

$$\sigma = 1/2\eta \quad (12)$$

Table 2
Quantum descriptor for THAQ and $Cu^{II}(THAQ)_2(H_2O)_2$ in eV with B3LYP-6-31G+(d, p) functional.

Compound	HOMO	LUMO	ΔE	IP	EA	X	η	M	σ	ω
THAQ	−5.57	−2.61	2.96	5.57	2.61	4.09	1.48	−4.09	0.33	5.65
$Cu^{II}(THAQ)_2(H_2O)_2$	−5.93	−3.45	2.48	5.93	3.45	4.69	1.24	−4.69	0.40	8.86

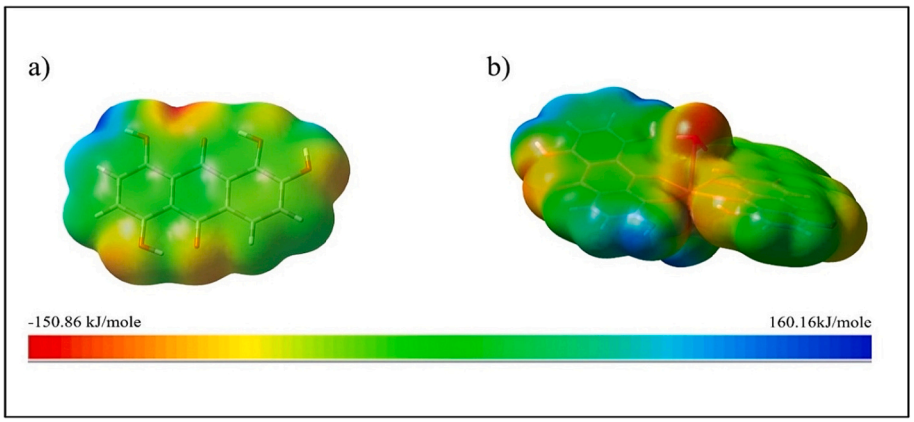


Fig. 9. Molecular electrostatic potential surface of a) THAQ b) $Cu^{II}(THAQ)_2(H_2O)_2$.

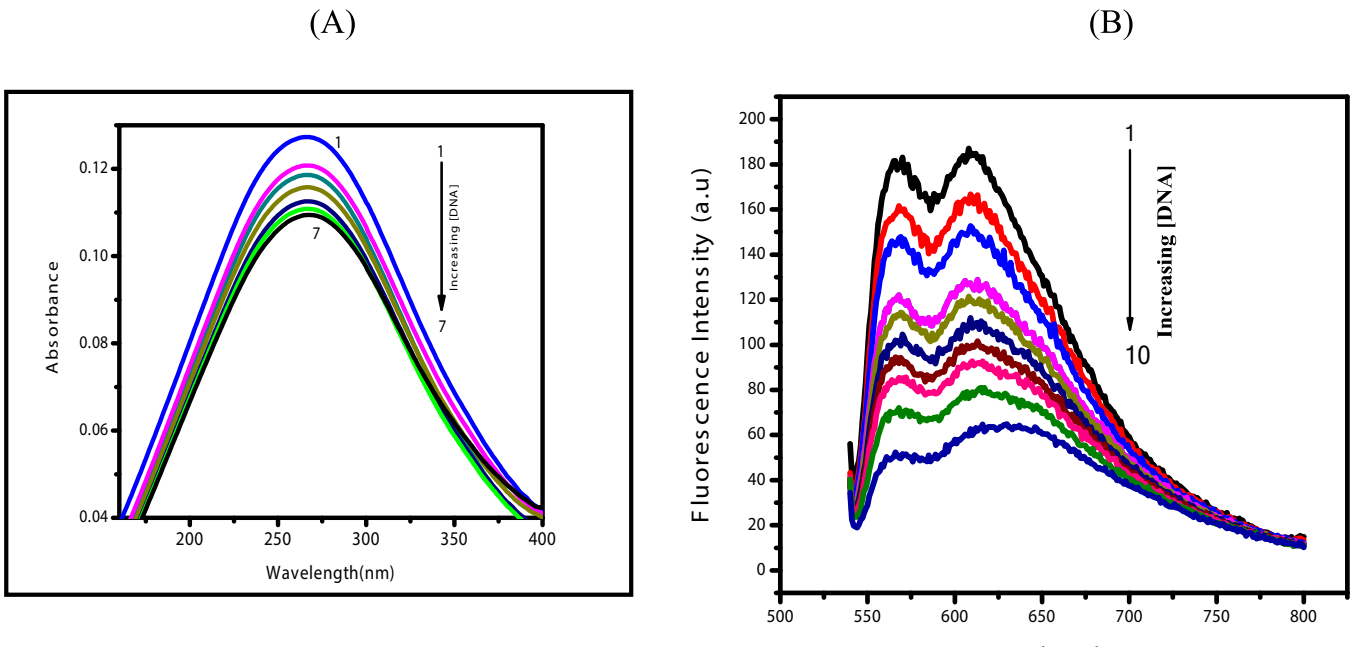


Fig. 10. (A) Absorption spectra of 100 μM $Cu^{II}(THAQ)_2(H_2O)_2$ in absence (1) and presence of different concentrations of calf thymus DNA (2) 156.05 μM (3) 308.29 μM (4) 601.90 μM (5) 715.47 μM (6) 936.30 μM (7) 1149.10 μM, (B) Fluorescence spectra of 50 μm $Cu^{II}(THAQ)_2(H_2O)_2$ in absence (1) and presence of different concentrations of calf thymus DNA (2) 105.36 μM (3) 209.69 μM (4) 415.27 μM (5) 516.56 μM (6) 666.65 μM (7) 814.58 μM (8) 960.38 μM (9) 1104.11 μM (10) 1292.61 μM; [NaCl] = 120 mM, pH = 7.4, Temperature = 298 K.

$$\omega = \chi^2/2\eta \tag{13}$$

$$M = -\chi \tag{14}$$

2.3.6. *Interaction of the complex with calf thymus DNA*

Binding with DNA was followed by UV-Vis spectroscopy. DNA binding was also followed by fluorescence spectroscopy. Keeping the concentration of the complex constant, solutions were gradually titrated with increasing amounts of calf thymus DNA. Interaction was followed by recording changes in absorbance and/or fluorescence that were subsequently used to evaluate binding parameters. The equilibrium shown in Eq. (15) was considered for interaction.

$$L + DNA \rightleftharpoons L\text{—}DNA \qquad K_d = \frac{[L][DNA]}{[L-DNA]} \tag{15}$$

L denotes the complex and K_d the dissociation constant [24–28,51,52] The interaction was realized in a direction reverse to that shown in Eq. (15). Data obtained from the titration was analyzed by several independent fitting methods like double reciprocal plot, non-linear square fit analysis and the modified form of Scatchard equation [24–28,51–53]. Eq. (16) is a typical double reciprocal equation where reciprocal of change in absorbance was plotted against reciprocal of (C_D – C_0). C_D refers to concentration of calf thymus DNA in solution and C_0, of THAQ. From Eq. (16), ΔA_{max} and K_{app} ($1/K_d$) were determined as the intercept and slope respectively [24–28,51,52].

$$\frac{1}{\Delta A} = \frac{1}{\Delta A_{max}} + \frac{K_d}{\Delta A_{max}(C_D - C_L)} \tag{16}$$

ΔA represents a change in absorbance observed following interaction of the complex with DNA at a particular wavelength and pH. For each titration curve, ΔA_{max} provides the maximum change in absorbance at that wavelength and pH. The value of ΔA_{max} (from Eq. (16)) was used to calculate $\Delta A/\Delta A_{max}$ for all titration curves. Using Eqs. (15), (17) and (18) were obtained.

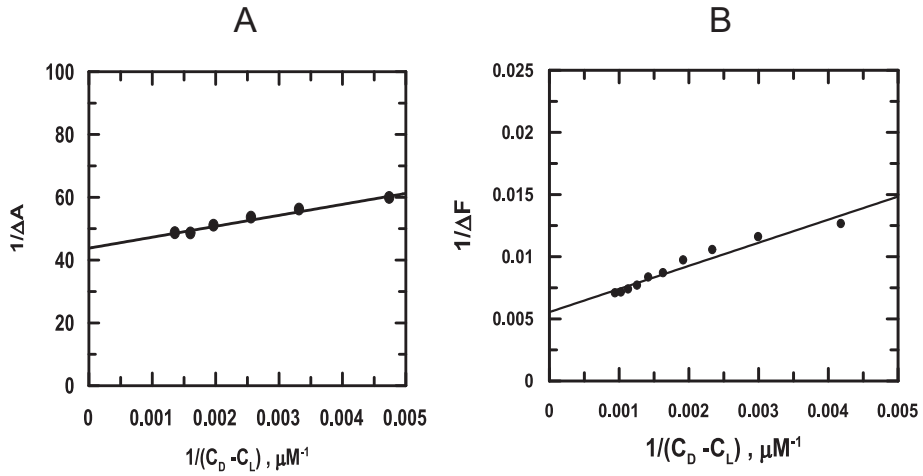


Fig. 11. Double reciprocal plots show reciprocal of change in absorbance (A) or fluorescence (B) against reciprocal of difference in concentration of calf thymus DNA and $Cu^{II}(THAQ)_2(H_2O)_2$ at pH = 7.4 following interaction with calf thymus DNA. $[Cu^{II}(THAQ)_2(H_2O)_2]$ = 100 μM (for UV-VIS spectroscopy) and 50 μM (for fluorescence spectroscopy), [NaCl] = 120 mM; Temperature = 301 K.

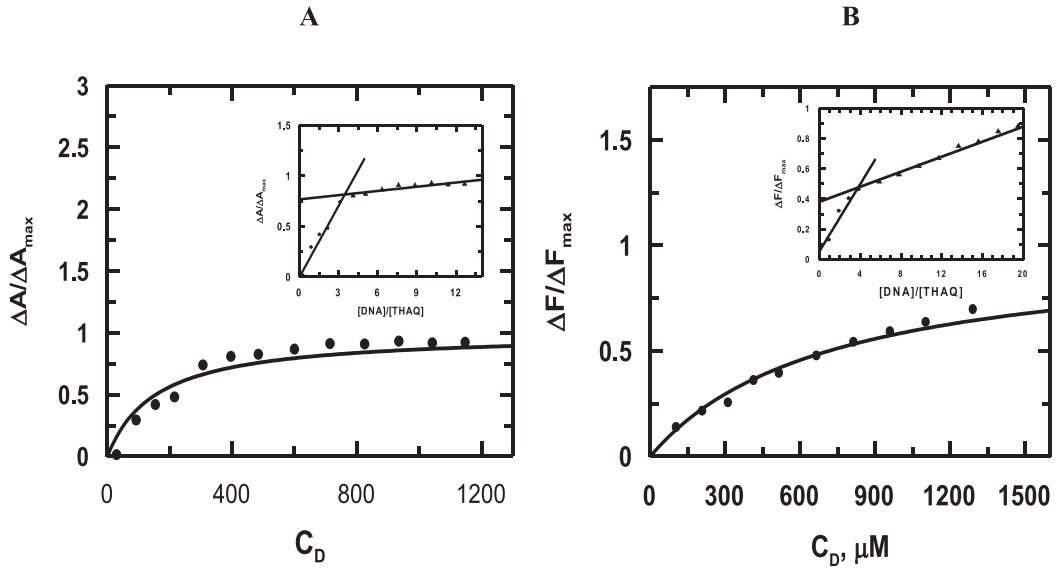


Fig. 12. Binding isotherm for interaction of $Cu^{II}(THAQ)_2(H_2O)_2$ with calf thymus DNA when $\Delta A/\Delta A_{max}$ (A) or $(\Delta F/\Delta F_{max})$ (B) were plotted against concentration of calf thymus DNA. $[Cu^{II}(THAQ)_2(H_2O)_2]$ = 100 μM for titration followed by UV-VIS spectroscopy and 50 μM for titration followed by fluorescence spectroscopy; [NaCl] = 120 mM; pH = 7.4; Temp. = 301 K. Inset: Plot of normalized increase of absorbance (A) and fluorescence (B) as a function of mole-ratio of calf thymus DNA to $Cu^{II}(THAQ)_2(H_2O)_2$.

Table 3
Binding parameters for interaction of $Cu^{II}(THAQ)_2(H_2O)_2$ with calf thymus DNA at pH 7.4.

Experiment	$K_{app} \times 10^{-4}(M^{-1})$ from double-reciprocal plot	$K_{app} \times 10^{-4}$ (M^{-1}) from non-linear curve fitting	$K_{app} \times 10^{-4}$ (M^{-1}) from double-reciprocal plot with intercept = 1	Site size (n_b) from inset of Fig. 9	$K' \times 10^{-5}(M^{-1})$ ($K' = K_{app} \times n_b$)	$K' \times 10^{-5}(M^{-1})$ Scatchard plot	n_b Scatchard plot
Fluorescence Spectroscopy	(0.55–0.80)	(0.65–0.76)	(0.64–1.00)	4	(0.25–0.34)	(0.26–0.39)	3.89–4.25
UV-Vis Spectroscopy	(0.86–1.25)	(0.72–1.68)	(0.83–1.18)	4	(0.34–0.55)	(0.33–0.43)	3.80–3.90

$$K_d = \frac{\left[C_L - \left(\frac{\Delta A}{\Delta A_{max}}\right)C_L\right]\left[C_D - \left(\frac{\Delta A}{\Delta A_{max}}\right)C_L\right]}{\left(\frac{\Delta A}{\Delta A_{max}}\right)C_L} \quad (17)$$

$$C_L\left(\frac{\Delta A}{\Delta A_{max}}\right)^2 - (C_L + C_D + K_d)\left(\frac{\Delta A}{\Delta A_{max}}\right) + C_D = 0 \quad (18)$$

$\Delta A/\Delta A_{max}$ was subsequently plotted against C_D. Eqs. (17) & (18) provide non-linear square fit analysis from where apparent binding constant (K_{app}) could be evaluated and compared with that obtained from Eq. (16). The data obtained from a titration of the complex with calf thymus DNA was also analyzed using a modified form of Scatchard equation [Eq. (19)] [53] from where intrinsic or overall binding constant (K′) and site size (n) were determined.

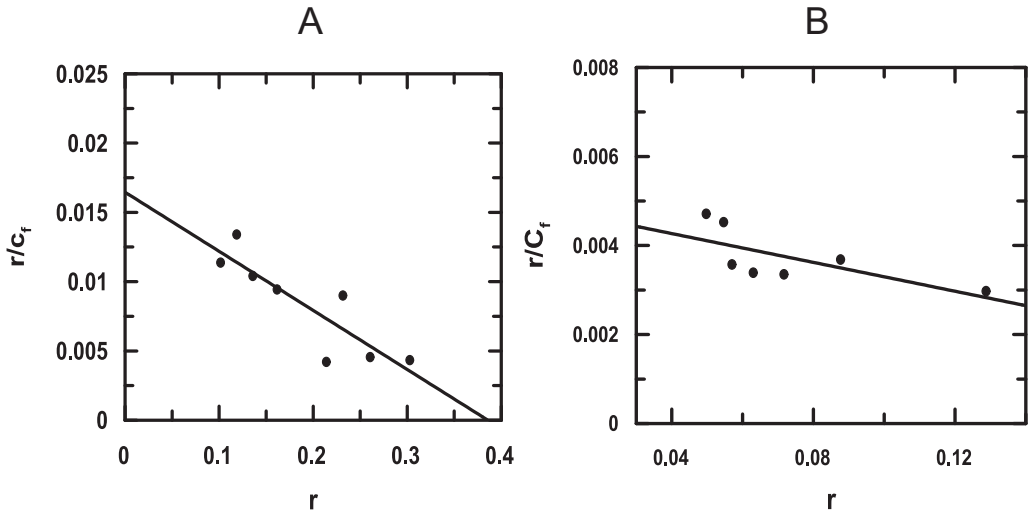


Fig. 13. Scatchard plots for the interaction of $Cu^{II}(THAQ)_2(H_2O)_2$ with calf thymus DNA, $[Cu^{II}(THAQ)_2(H_2O)_2]$ = 100 μM (for UV-Vis spectroscopy) and 50 μM (for fluorescence spectroscopy); [NaCl] = 120 mM, pH = 7.4, Temperature = 301 K.

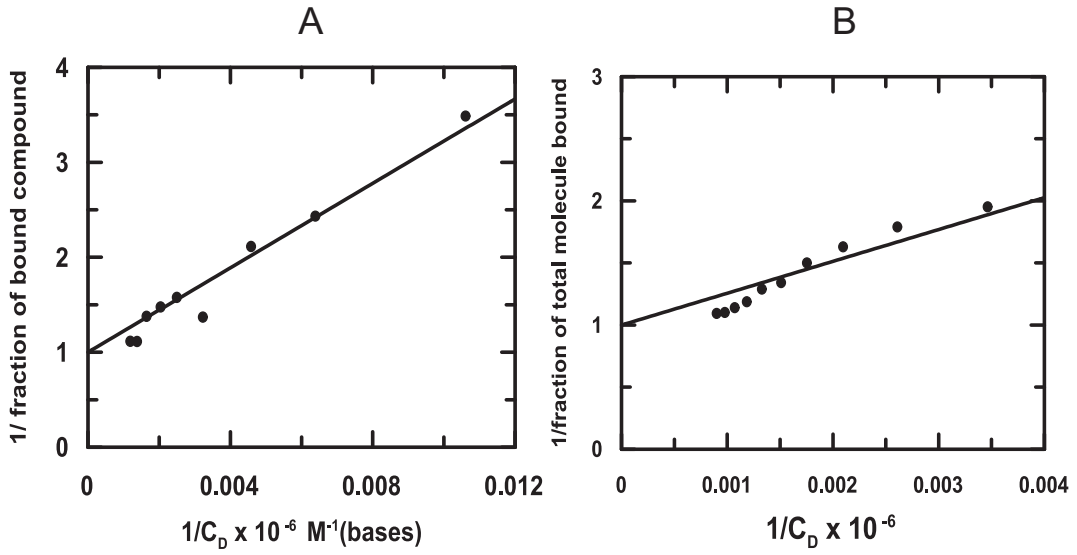


Fig. 14. Double reciprocal plots with y intercept = 1 for a titration of $Cu^{II}(THAQ)_2(H_2O)_2$ with calf thymus DNA at pH 7.4. $[Cu^{II}(THAQ)_2(H_2O)_2]$ = 100 μM (for UV-Vis experiments) and 50 μM (for fluorescence experiments); [NaCl] =120 mM, pH = 7.4, Temperature = 301 K.

$$\frac{r}{C_f} = K^{*}\,(n–r) \tag{19}$$

$r = C_b/C_D$ where, "C_b" denotes concentration of bound complex, "C_f", that of free complex, "K′" the overall binding constant. "n" denotes binding stoichiometry in terms of number of bound complex per nucleotide while "n_b", reciprocal of "n", denotes binding site size in terms of number of nucleotides bound to a complex.

When concentration of free calf thymus DNA is in much excess over that of the bound form, apparent binding constant (K_{app}) might be determined using another double–reciprocal equation considering Eq. (15). The equilibrium constant shown in Eq. (15) may be written as

$$K = \frac{[C_b]}{[C_f]\,[C_D]} \tag{20}$$

If the concentration of the complex is C_0, then at any point of the titration, we may write $C_0 = C_b + C_f$. Considering this one arrives at Eq. (21)

$$\frac{1}{[C_D][K]} + 1 = \frac{[C_0]}{[C_b]} \tag{21}$$

Upon rearrangement, Eq. (21) yields $\frac{1}{(C_b/C_0)} = 1 + \frac{1}{[K]\,[C_D]}$. K is determined from a double reciprocal plot of $\frac{1}{\text{fraction of total compound bound}}$ *vs* $\frac{1}{[C_D]}$ with y-intercept = 1 as inverse of the slope [24–28,51,52]. This binding constant (K) upon multiplication with n_b yields overall binding constant (K′).

2.3.7. Formation of superoxide in an enzyme assay that uses NADH dehydrogenase

Enzyme assay was performed at 298 K where cytochrome *c* acts as electron acceptor [24–28,51,52,54]. THAQ and the complex participates in the assay where NADH-cytochrome *c* reductase activity was followed by reduction of cytochrome *c* at 550 nm. The assay was performed at pH 7.4 using 0.05 M Hepes buffer. The test solution contained 80.5 μM cytochrome *c*, 157.5 μM NADH and 3 UL^{-1} NADH dehydrogenase and compounds under investigation. Concentration of compounds were varied from 0 to 50.0 μM. Activity of NADH dehydrogenase

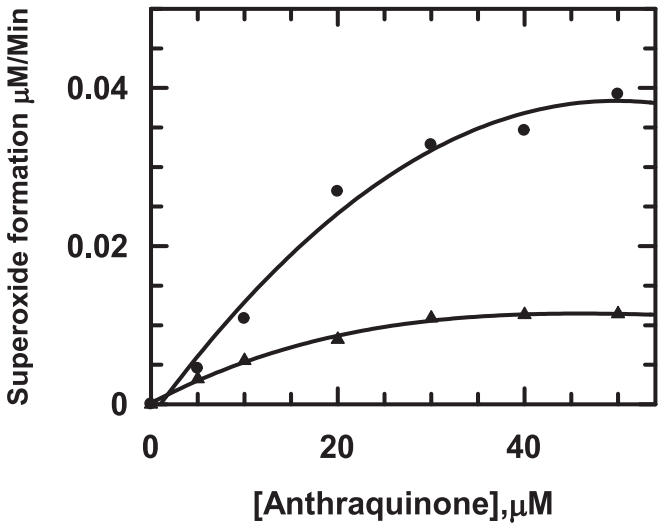


Fig. 15. Effect of THAQ and $Cu^{II}(THAQ)_2(H_2O)_2$ on superoxide formation in presence of NADH dehydrogenase. Superoxide formation was determined spectrophotometrically by rate of superoxide dismutase-inhibitable cytochrome *c* reduction. The reaction mixture contained 100 mM Hepes buffer (pH 7.2), 80.0 μM cytochrome *c*, 160.0 μM NADH, 10 UI^{-1} NADH dehydrogenase, 0 or 40.0 μg ml^{-1} SOD and indicated amount of compounds; ●THAQ; ▲ $Cu^{II}(THAQ)_2(H_2O)_2$.

was expressed in units, where one unit of activity reduces 1.0 μ mole oxidized cytochrome *c* per minute at pH 7.4 at 298 K. Formation of superoxide radical anion catalyzed by compounds was measured from reduction of cytochrome *c* inhibited by SOD in presence of NADH and NADH dehydrogenase. Enzyme assay was followed by kinetics software of JASCO V-630 spectrophotometer, Japan.

2.3.8. DNA relaxation assay for topoisomerase I and topoisomerase II

DNA relaxation assay for recombinant human DNA topoisomerase I and human DNA topoisomerase II were performed in the absence and presence of THAQ and its Cu^{II} complex by briefly incubating 100 fmol supercoiled pBS SK (+) DNA with 50 fmol enzyme in buffer (that was provided with enzymes). The reaction buffer contained 5 mM dithiothreitol as reducing agent. DMSO concentration was maintained at 0.5% (vehicle control). Reactions were incubated at 37 °C for 30 min and loaded on 1% agarose gel. It was thereafter electrophoresed overnight at 20 V. On completion of electrophoresis, gels were stained with 0.5 μg mL^{-1} ethidium bromide and viewed by Gel Doc 2000 (BioRad) under UV illumination. Relaxation was realized by monitoring decreased electrophoretic mobility of relaxed topoisomers of pBS SK (+) DNA [24–26].

2.3.9. Molecular docking

Molecular docking studies were performed using Autodock software (version 4.2.6), an interactive molecular graphics program from where binding energy was obtained and regarded as the docking score [55]. Human DNA topoisomerase II alpha (PDB ID: 4fm9) and beta (PDB ID: 3QX3) were retrieved from a protein data bank (http://www.rcsb.org./pdb) having a resolution of 2.90 Å and 2.16 Å (http://www.rcsb.org/pdb/) respectively [56]. Before performing molecular interaction studies both proteins were checked for any missing amino acid residues using UCSF Chimera (version 1.15; https://www.rbvi.ucsf.edu/chimera) and its energy was minimized using steepest descent and conjugate gradient techniques. It was then saved in PDB format. Subsequently molecular interaction experiments were performed. Optimized THAQ and $Cu^{II}(THAQ)_2(H_2O)_2$ were saved as two separate mol2 files that were converted to PDB using openbabel software. Thereafter, using Autodock tools (version 1.5.6) the saved PDB files of proteins and chosen molecules were opened and after merging non-polar hydrogen on both receptor and target molecules they were saved in PDBQT format [57]. Grid boxes were created with specific dimensions at 0.35 Å spacing. All docking studies were carried out using Lamarckian Genetic Algorithm (LGA) to achieve lowest free energy of binding (G) [58]. In case of molecular docking, three replicates were performed and for each a total of 10 solutions were computed, each showing an energy minima having a population size 150 and number of evaluations ~2,500,000; the maximum number of generations being 27,000. After docking, RMSD cluster maps were obtained with cluster tolerance of 2.0 Å. BIOVIA Discovery Studio (version 2021) and PyMOL software (DeLano, 2002) were used for visualisation of 2D and 3D interactions.

2.3.10. Cell culture

Since anthracyclines are used to treat acute lymphoblastic leukemia (ALL), we used a cell line of ALL origin (MOLT-4 cell line). Cells were cultured in RPMI-1640 media (GIBCO, Invitrogen, Carlsbad, CA, USA). Media were supplemented with 10% fetal bovine serum (GIBCO), antibiotic mixture 1 × penicillin–streptomycin–neomycin (GIBCO) and gentamicin reagent solution (GIBCO). Cells were incubated in a humidified CO_2 incubator at 37 °C [24–29].

2.3.11. Cell viability assay

Cells were seeded on a 96-well plate a day prior to addition of compounds. Experimental data obtained was the outcome of a single experiment but for each concentration of a compound three wells were used. Therefore, all results are in triplicate. Cells were treated with compounds dissolved in DMSO. Concentration of DMSO in cells was <0.5%. After 48 h incubation, cells were washed with 1 × phosphate-buffer saline and treated with MTT for 4 h at 37 °C. Precipitates were dissolved in DMSO and plates were analyzed on a Thermo MULTISKAN EX plate reader at 595 nm to determine IC_{50} [24–26]; IC_{50} being the concentration required to kill 50% of cell population.

3. Results and discussion

3.1. Physico-chemical studies on the interaction of Cu^{II} with THAQ

3.1.1. Determination of stoichiometry

Composition of the complex in solution was ascertained by taking equimolar solutions of Cu^{II} and THAQ. Thereafter we proceeded to determine stoichiometry of complex formation according to mole ratio method (Fig. 1A) and Job's method of continuous variation (Fig. 1B). From both methods, stoichiometry of the complex was found to be 1:2 for Cu^{II}: THAQ.

3.1.2. Dissociation of protons from THAQ in presence of Cu^{2+}

3.1.2.1. Using spectrophotometry. THAQ and Cu^{II} were taken in the ratio determined from stoichiometry studies. Thereafter, a spectrophotometric titration was performed over the pH range 3.0 to 11.0 (Fig. 2) considering an appropriate correction for pH in case of solvent used [43,44]. At pH 3.21, the absorption spectrum showed two peaks, one at 300 nm and another as a relatively weak shoulder at 480 nm. As pH increased (to 4.57), the UV peak at 300 nm decreased while the other one, underwent a red shift to be at 500 nm. With further increase in pH, till 7.05, the peak at 300 nm increased while that at 500 nm increased only slightly, accompanied by a slight red shift to be at 525 nm.

At pH 7.05, a distinct, well defined peak formed around 550 nm. With further increase in pH, intensity of this peak gradually increased. Change in absorbance of THAQ in the presence of Cu^{II} at 550 nm was fitted to Eq. (1) (Fig. 3). Two dissociations (pK_1 and pK_2, 4.99 ± 0.05 and 9.05 ± 0.03 respectively) were obtained. Stability constants β* and β for complex formation were determined considering pK_1 of THAQ that was determined in the presence of Cu^{II} and pK_2 of THAQ, determined in absence of Cu^{II}. Using Eqs. (2)–(6), value of formation constant (β) was

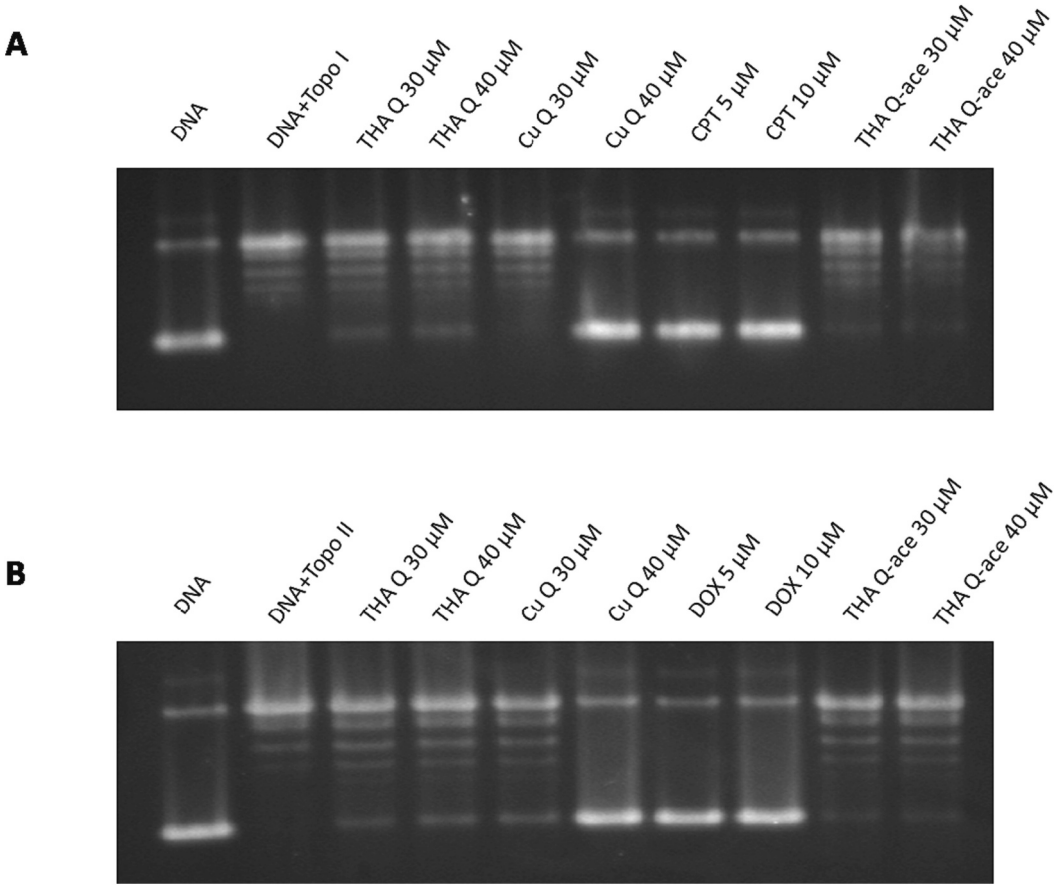


Fig. 16. DNA topoisomerase relaxation assays. a) DNA topo I relaxation assay. Lane 1 is 100 fmol supercoiled pBS (SK^+) DNA; Lane 2 is 100 fmol supercoiled pBS (SK^+) DNA with 50 fmol topoisomerase I enzyme; Lane 3 is same as Lane 2 but with 30 μM THAQ; Lane 4 is same as Lane 2 but with 40 μM THAQ; Lane 5 is same as Lane 2 but with 30 μMCu^{II}-$(THAQ)_2$; Lane 6 is same as Lane 2 but with 40 μM Cu^{II}-$(THAQ)_2$; Lane 7 is same as Lane 2 but with 5 μM CPT; Lane 8 is same as Lane 2 but with 10 μM CPT. Lane 9 is same as Lane 2 but with 30 μM THAQ-ace; Lane 10 is same as Lane 2 but with 40 μM THAQ-ace. All reactions were incubated at 37 °C for 30 min and analyzed by agarose gel electrophoresis. b) DNA topo II relaxation assay. Lane 1 is 100 fmol supercoiled pBS (SK^+) DNA; Lane 2 is 100 fmol supercoiled pBS (SK^+) DNA with 50 fmol topoisomerase II enzyme; Lane 3 is same as Lane 2 but with 30 μM THAQ; Lane 4 is same as Lane 2 but with 40 μM THAQ; Lane 5 is same as Lane 2 but with 30 μMCu^{II}-$(THAQ)_2$; Lane 6 is same as Lane 2 but with 40 μMCu^{II}-$(THAQ)_2$; Lane 7 is same as Lane 2 but with 5 μM DOX; Lane 8 is same as Lane 2 but with 10 μM DOX; Lane 9 is same as Lane 2 but with 30 μM THAQ-ace; Lane 10 is same as Lane 2 but with 40 μM THAQ-ace.All reactions were incubated at 37 °C for 30 min and analyzed by agarose gel electrophoresis.

found to be 9.12×10^{18} (log β = 18.96), comparable to stability constants reported earlier for similar Cu^{II} complexes of anthracyclines and of hydroxy-9,10-anthraquinones [24–28].

3.1.2.2. Potentiometric study. THAQ has four dissociable protons in the pH range studied; all being phenolic-OH. Owing to a possible overlap in their dissociation, pH metrically determined macro-constants are composite and cannot be directly assigned to individual acidic groups. Previous experience in this regard suggest owing to poorly conditioned systems, least square evaluation method could result in large uncertainties in calculated parameters; particularly owing to light and oxygen sensitivities of THAQ, that could lead to large differences in reported constants. At a higher concentration of THAQ, self-association would be significant. This could affect macroscopic dissociation constants determined pH metrically at high concentration. However, this is likely to be lot less in presence of a metal ion. Cu^{II} and THAQ were taken in 10 mL volumetric flasks in the ratio 1:2 and titration was performed using 0.005 M NaOH.

The titration curve obtained for Cu^{II}-THAQ clearly indicates complex formation starts at pH > 4.0 and after a rather flat portion there is a rise in pH in the titration curve corresponding to dissociation of two protons per metal ion, that was found independent of ligand (THAQ) excess (not shown here). This suggests formation of a 1:2 complex in the pH range 5–6.5 (Fig. 4). Titration was continued. The second proton from each THAQ starts dissociating at a pH slightly >8 and is complete by pH = 9.0.

3.2. Characterization of the Cu^{II} complex of THAQ

3.2.1. UV-Vis spectra of THAQ and the complex

Absorption spectra of THAQ in water and Cu^{II} complex in DMSO were recorded (Fig. S1). The spectrum of the complex dissolved in DMSO was similar to that obtained during pH-metric titration of THAQ performed in presence of Cu^{II} in the ratio 2:1, indicating species formed during physico-chemical investigations and that present following complex formation were identical.

3.2.2. IR of THAQ and complex

FTIR of solid samples were recorded as KBr pellets on a Perkin Elmer RX-I spectrophotometer in the range 4000 cm^{-1} - 400 cm^{-1}. Analysis of IR spectra of THAQ and complex revealed the sharp peak obtained due to stretching of phenolic-OH at 3379 cm^{-1} for THAQ (Fig. S2) was found as a broad band at 3448 cm^{-1} for the complex (Fig. S3) [59]. Broadening indicates OH groups on THAQ are involved in binding Cu^{II}. Response for phenolic -OH did not disappear completely for the complex since there were other –OH groups on THAQ that remained undissociated. Distinct peaks for carbonyl stretching at 1615 cm^{-1} and 1581 cm^{-1} for THAQ

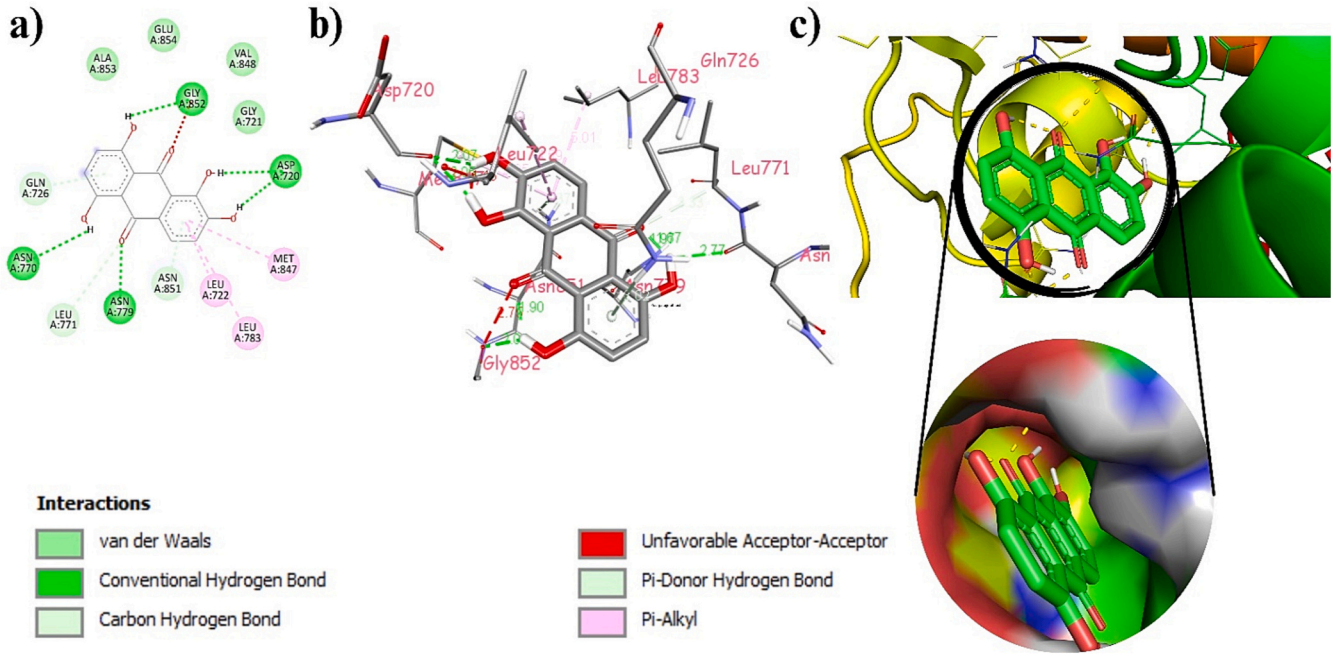


Fig. 17. Molecular docking interaction of THAQ inside the active site of DNA topoisomerase II alpha (PDB ID: 4fm9) (a) 2D representation of interaction, (b) 3D representation of interaction and (c) without and with the molecular surface (yellow dotted lines indicate hydrogen bonds). (For interpretation of the references to colour in this figure legend, the reader is referred to the web version of this article.)

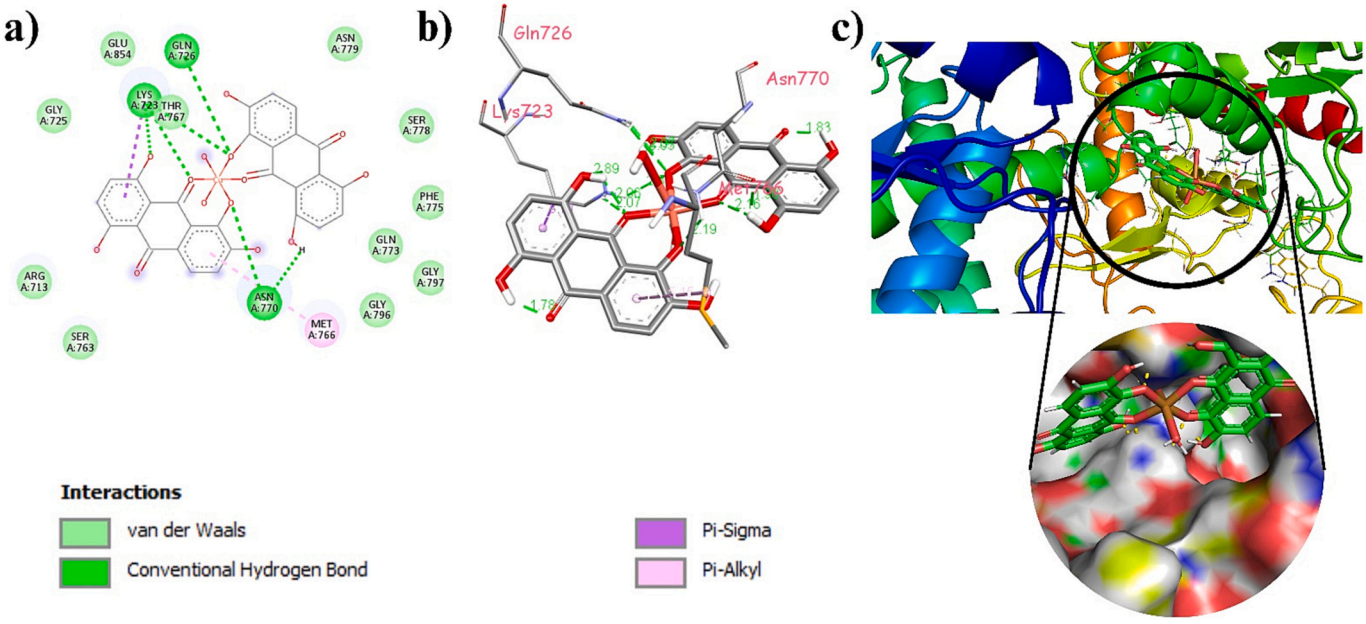


Fig. 18. Molecular docking interaction of $Cu^{II}(THAQ)_2(H_2O)_2$ inside the active site of DNA topoisomerase II alpha (PDB ID: 4fm9) (a) 2D representation of interaction, (b) 3D representation of interaction and (c) without and with the molecular surface (yellow dotted lines indicate hydrogen bonds). (For interpretation of the references to colour in this figure legend, the reader is referred to the web version of this article.)

became weak in the complex (detected at 1636 cm^{-1} and 1509 cm^{-1} respectively) suggesting one carbonyl on each THAQ was bound to the metal ion.

3.2.3. *Mass spectrometry*

Considering Cu^{II}-THAQ to be a 1:2 species as realized from physicochemical experiments, an analysis of fragments obtained in mass spectrometry were done (Fig. S4A, SI). Molecular ion peaks with two molecules of water and an atom of sodium appeared at $m/z = 663.33$ and 664.34 respectively. Loss of two molecules of water and sodium generated a species having m/z = 603.4190 (expected at m/z = 605.0 and 607.0 for ^{63}Cu and ^{65}Cu respectively). Simulated mass spectrum showing all possible fragments that might form from the molecular ion with isotopic distribution of Cu are shown in Fig. S4B/(A), using Chemfinfo.org online tools with SMILES, and in Fig. S4B/(B), S4B/(C) respectively, using https://www.sisweb.com/mstools/isotope.htm.

3.2.4. *Magnetic moment of $[Cu^{II}(THAQ)_2(H_2O)_2]$*

Magnetic susceptibility measurements were made at room temperature using Gouy method. It provided a magnetic moment of 1.45 BM

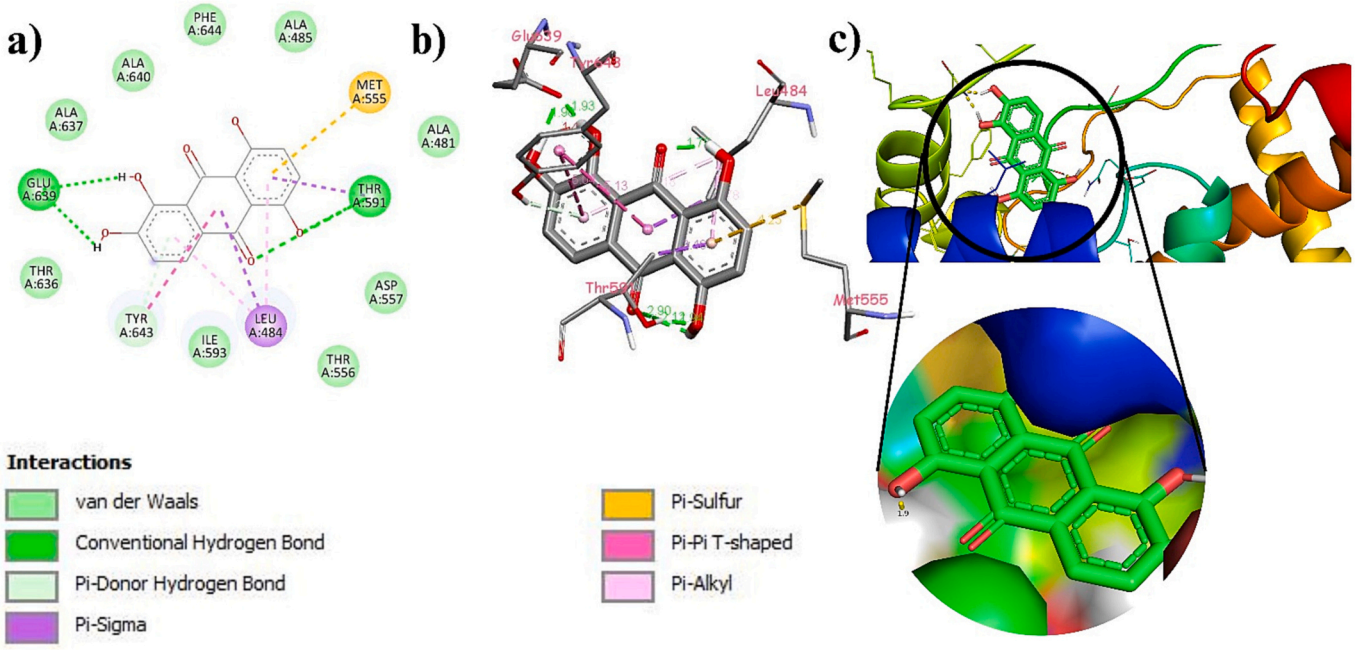


Fig. 19. Molecular docking interaction of THAQ inside active site of DNA topoisomerase II beta (PDB ID: 3QX3) (a) 2D representation of interaction, (b) 3D representation of interaction and (c) without and with the molecular surface (yellow dotted lines indicate hydrogen bonds). (For interpretation of the references to colour in this figure legend, the reader is referred to the web version of this article.)

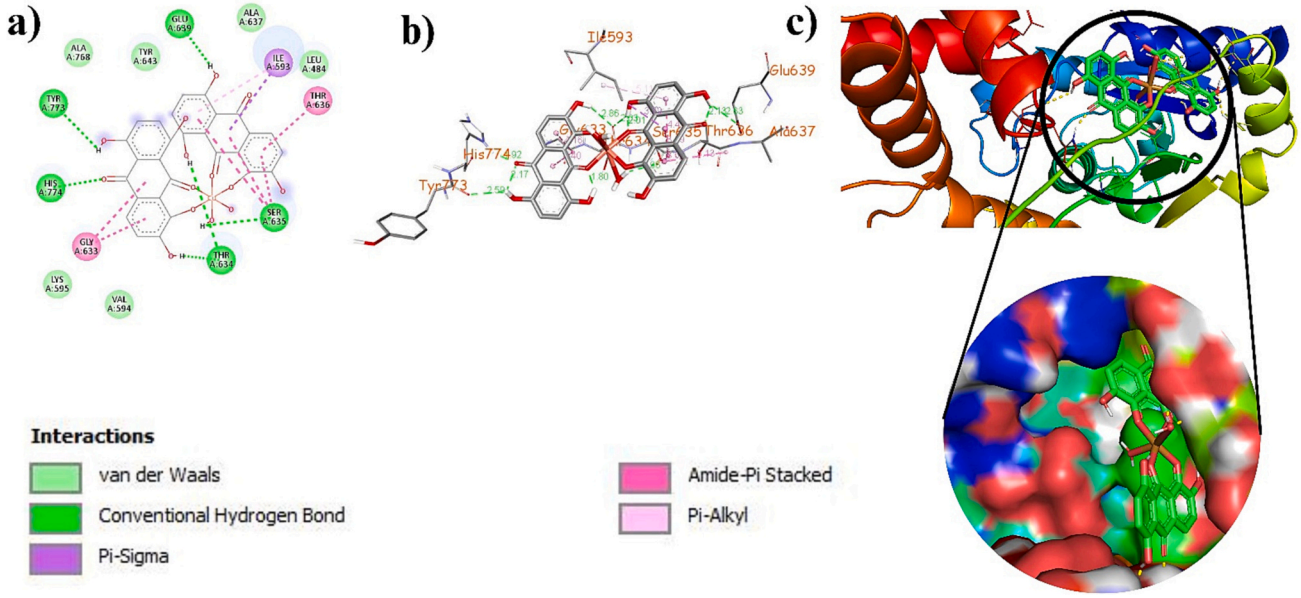


Fig. 20. Molecular docking interaction of $Cu^{II}(THAQ)_2(H_2O)_2$ inside the active site of DNA topoisomerase II beta (PDB ID: 3QX3) (a) 2D representation of interaction, (b) 3D representation of interaction and (c) without and with the molecular surface (yellow dotted lines indicate hydrogen bonds). (For interpretation of the references to colour in this figure legend, the reader is referred to the web version of this article.)

suggesting presence of one unpaired electron. However, magnetic moment of the complex was somewhat lower than that expected from spin only value for mononuclear Cu^{II}.

3.2.5. Thermo-gravimetric analysis

Thermo-gravimetric analysis of the complex shows loss of two water molecules in the temperature range 95 °C to 102 °C (Fig. S5, SI). An experimental loss of 5.61% was in accordance with that expected theoretically (5.83%). Hence, results obtained from mass spectrometry have a good correlation with TGA.

3.2.6. EPR spectroscopy

Room temperature EPR spectrum of powdered $[Cu^{II}(THAQ)_2(H_2O)_2]$ (Fig. 5) showed resonance field at 325 mT having g value = 2.075. This was as expected for an unpaired electron present on a mono-nuclear Cu^{II} species [60,61].

3.2.7. DFT calculations based on experimental evidence related to complex formation

Ground state optimized geometries of $Cu^{II}(THAQ)_2(H_2O)_2$ (in DMSO and in gaseous state) and of THAQ are shown in Figs. 6(a and b) and 7 by

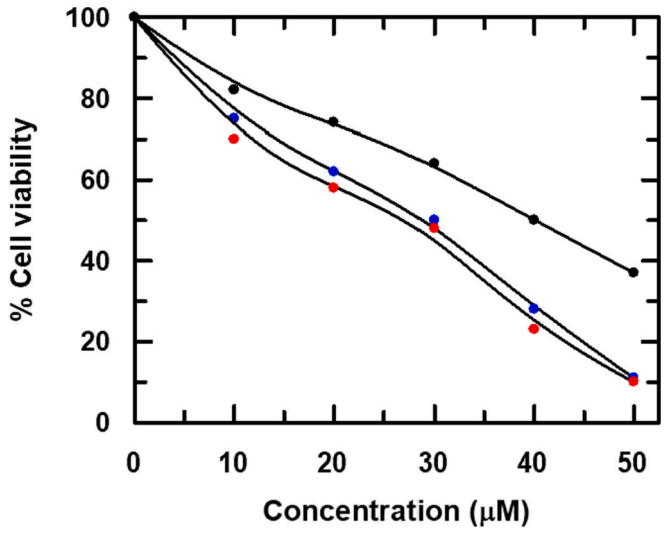


Fig. 21. Plot showing dose response curve for the effect of THAQ (•—•), THAQ-ace (•—•) and $Cu^{II}(THAQ)_2(H_2O)_2$ (•—•) on ALL MOLT-4 cells treated with each compound for 72 h and MTT assay performed.

a numbering system for the coordination environment. Table S1, SI contains coordinates of optimized $Cu^{II}(THAQ)_2(H_2O)_2$. Table 1 lists significant coordination geometry factors including computed bond lengths that tally favorably with aqua copper complexes [62]. Optimized structures for $Cu^{II}(THAQ)_2(H_2O)_2$ exhibit octahedral coordination in gas and solution (DMSO) phases (Fig. 6a and b).

3.2.7.1. Frontier molecular orbital analysis. Frontier orbital of optimized $Cu^{II}(THAQ)_2(H_2O)_2$ in solution phase is shown in Figs. S6 & S7, SI. Description of occupied and virtual MOs is based on atomic composition and visual inspection of their three-dimensional representation [63]. $Cu^{II}(THAQ)_2(H_2O)_2$ is considered to be made of five components Cu, $(H_2O)_a$ $(H_2O)_b$, $(C_{14}H_7O_6)_a$ and $(C_{14}H_7O_6)_b$. These are shown in Tables S2 and S3, SI.

According to calculations, HOMO-LUMO energy gap in α-MO is 2.48 eV and in β-MO it is 2.37 eV. The HOMO-LUMO gap is shown in Fig. 8. In Fig. S8, SI FMOs of THAQ are shown. In Fig. S9, SI HOMO-LUMO gap of free THAQ is seen to be 2.96 eV.

3.2.7.2. Quantum descriptor analysis. Kinetic stability, electrical conductivity and chemical reactivity of a molecule are influenced by HOMO and LUMO frontier molecular orbitals [64]. HOMO-LUMO energy gap is narrow in soft molecules. These are more reactive biologically and/or chemically. Molecules with large HOMO-LUMO energy gap have low biological response, are incredibly stable and less reactive towards other substances [65]. In case of narrow HOMO-LUMO energy gap, intramolecular charge transfer (ICT) from electron-donor group to electron-acceptor group becomes feasible [65]. Good electron acceptor molecules have smaller E_{LUMO} than good electron donor molecules that possess larger E_{HOMO}. Table 2 compares THAQ quantum descriptor with that of $Cu^{II}(THAQ)_2(H_2O)_2$ produced following geometry optimization.

Electron donation (IP) and electron acceptance (EA) is faciliated due to low HOMO-LUMO gap. Electron affinity of $Cu^{II}(THAQ)_2(H_2O)_2$ is high compared to THAQ indicating the complex might easily interact with nucleotides of DNA withdrawing electron density towards itself. On the other hand, a soft molecule is defined as one having lower η value (Eq. (11)). Upon complex formation with Cu^{II}, THAQ becomes soft allowing greater electron delocalization and facilitating more non-covalent interactions. A high value for ω (electrophilicity index) represents high affinity towards electron rich species [57]. The complex is seen to possess higher affinity than THAQ.

3.2.7.3. MEP surface analysis. Fig. 9 displays "molecular electrostatic potential surface" computed over optimal geometries in solvent phase. The envelope's isovalue was selected to be 0.02 a.u. and reverse rainbow colour scheme was used throughout [66]. Areas with negative potential are in red, those with positive potential in blue while green indicates hydrobic regions in a molecule. Analysis reveals hydrogen atoms on phenolic O—H and on aromatic rings are positive. The complex has a substantially negative region on z-axis around one water molecule while not so negative a region around oxygen of the other water molecule oriented exactly opposite to it. This suggests a likelihood of the molecule to form hydrogen bonds through such regions that might stabilize interactions of one molecule with another. MEP of THAQ also reveals a carbonyl oxygen and phenolic OH are electron rich (red in colour, Fig. 10) suggesting regions of coordination with Cu(II). MEP of $Cu^{II}(THAQ)_2(H_2O)_2$ suggests regions where water molecules are present to be electron rich, and that positively charged regions have increased following complex formation suggesting better targeting of biomolecules like DNA.

3.3. Interaction of $Cu^{II}(THAQ)_2(H_2O)_2$ with calf thymus DNA followed by UV-Vis and fluorescence spectroscopy

To understand the role of $Cu^{II}(THAQ)_2(H_2O)_2$ as an anticancer agent, it would be important to know various ways by which it might show anticancer activity. Since interaction with DNA is an important aspect this was pursued using calf thymus DNA. Titrations were performed at pH 7.4 and followed with UV-Vis and fluorescence spectroscopy (Fig. 10A & B). 100 μM $Cu^{II}(THAQ)_2(H_2O)_2$ was used for the titration that was followed by UV-Vis spectroscopy. Decrease in absorbance at 554 nm was observed following the addition of calf thymus DNA which was used to measure binding parameters. For titrations followed by fluorescence spectroscopy, 50 μM complex was excited at 540 nm and emission was measured at 567 nm. Free THAQ shows fluorescence emission at 710 nm upon excitation at 573 nm (Fig. S10, SI). In case of monitoring by fluorescence, a gradual decrease in response upon addition of calf thymus DNA served as an indication for an interaction of $Cu^{II}(THAQ)_2(H_2O)_2$ with it.

In either case, the bound form did not have any spectroscopic response at the wavelength where the interaction was monitored. Hence, following addition of calf thymus DNA both for the monitoring by UV-Vis spectroscopy and by fluorescence spectroscopy, response was due to free $Cu^{II}(THAQ)_2(H_2O)_2$ that gradually decreased. Binding parameters were analyzed using Eqs. (15)–(21) [25–29]. Inverse of the dissociation constant (K_d) for interaction with calf thymus DNA provides values for apparent binding constant (K_{app}). K_d was obtained from a double reciprocal plot where the reciprocal of change in absorbance

Table 4
A comparison and correlation of findings of $O_2^{\bullet-}$ generation, topoisomerase inhibition with experimentally obtained IC_{50} values for THAQ, THAQ-ace and $Cu^{II}(THAQ)_2(H_2O)_2$ on ALL MOLT-4 cells.

Compounds	Generation of $O_2^{\bullet-}$ in NADH dehydrogenase assay experiment (Fig. 11)	MIC for human DNA topoisomerase I inhibition (Fig. 12)	MIC for human DNA topoisomerase II inhibition (Fig. 12)	IC_{50} for ALL MOLT – 4 cells (Fig. 13)
THAQ	Substantial	> 40.0 μM	> 40.0 μM	27.2 μM
THAQ-ace [62]	Substantial	> 40.0 μM	> 40.0 μM	25.1 μM
$Cu^{II}(THAQ)_2(H_2O)_2$	Significant decrease was recorded	40.0 μM	40.0 μM	38.1 μM

[Fig. 11A] or fluorescence [Fig. 11B] were plotted against reciprocal of ($C_D - C_0$) [25–29]. C_D refers to concentration of calf thymus DNA and C_0 to concentration of $Cu^{II}(THAQ)_2(H_2O)_2$.

Such double reciprocal plots (Fig. 11A & B) yield values for ΔA_{max} and ΔF_{max} respectively following a change in absorbance or fluorescence due to interaction of $Cu^{II}(THAQ)_2(H_2O)_2$ with DNA. ΔA indicates change in absorbance of $Cu^{II}(THAQ)_2(H_2O)_2$ at 554 nm [pH = 7.4] and ΔF, change in fluorescence at 567 nm. Values for ΔA_{max} or ΔF_{max} were used to calculate $\Delta A/\Delta A_{max}$ and/or $\Delta F/\Delta F_{max}$ respectively. These were plotted against concentration of calf thymus DNA (C_D). Using Eqs. (17) and (18), plots of $\Delta A/\Delta A_{max}$ or $\Delta F/\Delta F_{max}$ *versus* C_D were fitted according to non-linear square fit analysis (Fig. 12A & B) [24–28] that provide values for $K_d = (1/K_{app})$.

K_{app} obtained from non-linear square fit analysis was then compared with values obtained from double reciprocal plots (Fig. 11 and Table 3). Spectrophotometric and fluorimetric titration of $Cu^{II}(THAQ)_2(H_2O)_2$ with calf thymus DNA was further analyzed by a modified form of the original Scatchard equation (Fig. 13A & B) [53]. Overall binding constant (K′) and site size (n) were determined. n_b was found to be ~4.0, exactly double that obtained for THAQ or THAQ-ace [67,68]. Therefore, if we consider mode of interaction of THAQ, THAQ-ace and $Cu^{II}(THAQ)_2(H_2O)_2$ to be similar with calf thymus DNA, which most likely would be intercalation (going by nature of spectral changes obtained) [67,68], then $Cu^{II}(THAQ)_2(H_2O)_2$ during interaction with calf thymus DNA either assumes a planar orientation by losing two molecules of water or maintaining two water molecules on an axis perpendicular to the plane containing two THAQ binds to the metal centre. Therefore, the DNA binding study also identifies that two THAQ molecules are bound to Cu^{II} in the complex as obtained from physico-chemical experiments. Hence, stoichiometry of complex formation may be ascertained for a coordination compound from titration with DNA if the mode of interaction of the ligand and the coordination compound prepared using the same ligand, are similar with DNA [24–29,52,67–69].

Titrimetric data for interaction of $Cu^{II}(THAQ)_2(H_2O)_2$ with calf thymus DNA was also analyzed with another form of a double reciprocal plot where y-intercept = 1 (Eq. (21)) [Fig. 14A & B]. Analysis provides K_{app} and K′ from absorbance and fluorescence measurements (Table 3). It was found that values obtained from different methods of analysis were not only comparable but they were quite close to each other considering they were obtained from different techniques (Table 3). It is worth mentioning here that binding constant values for the complex with calf thymus DNA were comparable to that found for THAQ. Hence, considering only the aspect of binding of compounds with DNA, the complex is not likely to score much over THAQ.

3.4. NADH dehydrogenase assay

Formation of superoxide radical anion in an enzyme assisted reaction occurs when semiquinone is oxidized by molecular oxygen. In $Cu^{II}(THAQ)_2(H_2O)_2$, a carbonyl of each THAQ is coordinated to Cu^{II}. Hence, only one of the two carbonyls of each THAQ may form semiquinone. Hence, with decrease in probability of formation of semiquinone, formation of superoxide radical anion also decreases which was seen through experiments for $Cu^{II}(THAQ)_2(H_2O)_2$ [23–28,54].

The semiquinone formed at a free carbonyl of THAQ in the complex can transfer an electron to a Cu^{II} centre on an adjacent complex in an inter-molecular pathway [70]. Therefore, probability that a semiquinone formed on $Cu^{II}(THAQ)_2(H_2O)_2$ would react with molecular oxygen decreases considerably [22–27,69,70]. Hence, a significant decrease in superoxide formation is expected owing to complex formation against that for THAQ under similar conditions [Fig. 15]. Since a combination of semiquinone and superoxide radical anion is believed to be responsible for cardiotoxicity induced by anthracyclines and/or anthraquinones, formation of a metal complex is beneficial [20,21]. Our findings through model experiments and its consequences thereof suggest $Cu^{II}(THAQ)_2(H_2O)_2$ could be less cardiotoxic than THAQ [23–28,69,70]. On the other hand, decrease in superoxide radical anion or other forms of ROS implies a decrease in cytotoxic efficacy as these same radicals are responsible for targeting cancer cells.

3.5. In-vitro activity of THAQ and $Cu^{II}(THAQ)_2(H_2O)_2$ on human DNA topoisomerase

Interaction of THAQ and $Cu^{II}(THAQ)_2(H_2O)_2$ were studied for DNA relaxation assays on recombinant human DNA topoisomerase I and human DNA topoisomerase II. If there is inhibition of the enzyme, bands for relaxed topoisomers do not appear on the gel. In our case, at 40 μM concentration, $Cu^{II}(THAQ)_2(H_2O)_2$ begins to show inhibition of relaxation activities on human DNA topoisomerase I and human DNA topoisomerase II. At 40 μM THAQ has no effect (Fig. 16A and B). Inhibitory effects were checked for migration of substrate DNA using standard compounds [CPT (camptothecin) for inhibition of topoisomerase I and DOX (doxorubicin) for inhibition of topoisomerase II) at two different concentrations, that serve as control (Fig. 16A & B). No migration of DNA indicates complete inhibition of topoisomerase. Results suggest $Cu^{II}(THAQ)_2(H_2O)_2$ is a dual inhibitor of human DNA topoisomerase I and human DNA topoisomerase II *in-vitro*, similar to CPT (control for topoisomerase I) and DOX (control for topoisomerase II); only that our inhibitory concentrations are higher.

Another modified form of THAQ, a tetra-acetylated derivative (THAQ-ace) [68] was also considered during DNA relaxation assay on recombinant human DNA topoisomerase I and human DNA topoisomerase II [68]. This was done to find out the type of modification necessary for a hydroxy-9,10-anthraquinone to form the right kind of derivative that would be able to bring about enzyme inhibition. Results reveal modification of THAQ by acetylation was not able to cause any significant difference to behavior of relaxed topoisomers regarding inhibition of human DNA topoisomerase I and human DNA topoisomerase II from that observed for THAQ. In fact, response for THAQ and its acetylated product (THAQ-ace) at concentrations 30 μM or 40 μM were similar with regard to bands obtained for relaxed topoisomers on the gel.

A comparison of results of Fig. 16 for a study on the interaction of compounds with human DNA topoisomerase reveals modification achieved through complex formation is able to inhibit the action of human DNA topoisomerase I and human DNA topoisomerase II. Neither THAQ nor THAQ-ace showed any sign of inhibition. Hence, a synthetic modification of THAQ, like acetylation of its –OH groups do not provide an answer to effective inhibition of DNA topoisomerase. Hence, this study clearly demonstrates the importance of the presence of a metal ion in an attempted modification of THAQ and highlights that it is crucial for such inhibition to occur.

3.6. In-silico modelling of THAQ and $Cu^{II}(THAQ)_2(H_2O)_2$ on human DNA topoisomerase

Binding modes of THAQ and $Cu^{II}(THAQ)_2(H_2O)_2$ with desired regions of human DNA topoisomerase II alpha (PDB ID: 4fm9) and human DNA topoisomerase II beta (PDB ID: 3qx3) were established through *in silico* molecular docking. This being a compelling framework helps one to comprehend interactions between compounds and proteins in any rational drug design and understand structural characteristics of compound-receptor complexes; binding energy for interaction of compounds with receptors support our experimental findings. Both compounds got docked successfully with topoisomerase II alpha (PDB ID: 4fm9) and topoisomerase II beta (PDB ID: 3qx3) to undergo extensive molecular mechanics. Rigid molecular docking was used to determine binding pattern. To forecast an optimum compound-protein fit and analyze the most energetically advantageous docked position, compounds were made flexible to achieve several conformations. Table S4, SI, includes a list of modes of interaction. It is evident from Figs. 17 to 20 that both THAQ and $Cu^{II}(THAQ)_2(H_2O)_2$ interact with chosen human DNA topoisomerase II alpha (PDB ID: 4fm9) and human DNA

topoisomerase II beta (PDB ID: 3qx3) models.

Results of molecular docking simulation indicates THAQ interacts with human DNA topoisomerase II alpha (PDBID: 4fm9) at ASN 770, ASN 779, ASP 720 and GLY 852 where there are seven interactions in all of which four are conventional hydrogen bond interactions (Fig. 17, Table S4, SI). For THAQ with PDBID: 4fm9, interaction between HD22….of ASN 779 and O15 of THAQ has a length of 1.97 Å. The binding energy obtained after docking was −6.66 kcal/mol with inhibitory concentration of 13.76 μM. For the same human DNA topoisomerase II alpha (PDBID: 4fm9), $Cu^{II}(THAQ)_2(H_2O)_2$ showed more negative binding energy (−7.31 kcal/mol) attributed to 6 hydrogen bond interactions at the active site of enzyme; the interacting residues being LYS 723, GLN 726, ASN 770 and SER 778. For example, HZ1 of LYS 723 and O32 of the complex create a hydrogen bond of length 2.86 Å. Other interactions of $Cu^{II}(THAQ)_2(H_2O)_2$ with PDBID: 4fm9 are provided in Table S4, SI. In case of human DNA topoisomerase II beta (PDBID: 3qx3), only two amino acid residues interact with THAQ at the active site making three hydrogen bonds. HG1 of THR 591 makes a hydrogen bond with O15 of THAQ corresponding to a length of 2.90 Å. Binding energy in this case was found to be −5.82 kcal/mol with inhibitory concentration of 54.03 μM (Fig. 19, Table S4, SI). For $Cu^{II}(THAQ)_2(H_2O)_2$ interacting with human DNA topoisomerase II beta (PDBID: 3qx3), there are fourteen interactions in all of which six are conventional hydrogen bond interactions. Amino acid residues involved are HIS 774, SER 635, THR 634, TYR 773, GLU 639. For example, OE2 of GLU 639, makes a hydrogen bond with H57 of the complex with length of interaction being 2.62 Å. Binding energy was found to be −7.59 kcal/mol with an inhibitory concentration of 2.73 μM (Fig. 20, Table S4, SI). Therefore, considering four results, it turns out that interaction of $Cu^{II}(THAQ)_2(H_2O)_2$ with human DNA topoisomerase II beta (PDBID: 3qx3) was most efficient, since it has a binding energy value of −7.59 kcal/mol and also lowest value for inhibitory concentration (2.73 μM). Overall, *in silico* studies, like DNA relaxation assays on recombinant human DNA topoisomerase I and human DNA topoisomerase II keeps $Cu^{II}(THAQ)_2(H_2O)_2$ well ahead of THAQ as an inhibitor of human DNA topoisomerase.

3.7. Effect of THAQ, its synthetically modified form THAQ-ace and $Cu^{II}(THAQ)_2$ on ALL MOLT-4 cells

An MTT assay was performed using THAQ, its tetra-acetylated derivative (THAQ-ace) [63] and $Cu^{II}(THAQ)_2(H_2O)_2$ on acute lymphoblastic leukemia (ALL) MOLT-4 cells. Results suggest both THAQ and THAQ-ace were better than $Cu^{II}(THAQ)_2(H_2O)_2$ in cell killing (Fig. 21). IC_{50} for THAQ was 27.2 μM, for THAQ-ace 25.1 μM and for $Cu^{II}(THAQ)_2(H_2O)_2$ 38.1 μM (Table 4). It is generally accepted that anthracyclines are cytotoxic to cells owing to their ability to generate semiquinone that in turn generate superoxide radical anion. From the results of this study it appears while THAQ or THAQ-ace are quite effective in generating semiquinone and superoxide radical anion, the complex is not. Again, with regard to human DNA topoisomerase I and human DNA topoisomerase II, the complex was seen to be at an advantage while THAQ and/or THAQ-ace were not that effective, at least in the concentration range in which our experiments were performed.

Since the study on ALL MOLT-4 cells indicate THAQ and/or THAQ-ace has a comparatively lower IC_{50} value than $Cu^{II}(THAQ)_2(H_2O)_2$, it demonstrates yet again that the mechanism by which cell death is achieved could largely be due to radical generation. Although other factors like topoisomerase inhibition, DNA binding contribute to cell cytotoxicity they were probably secondary to free radical induced damage.

For this reason, the complex inspite of being a superior inhibitor of human DNA topoisomerase I and human DNA topoisomerase II was unable to show a better performance than THAQ or THAQ-ace on ALL MOLT-4 cells. This study suggests while $Cu^{II}(THAQ)_2(H_2O)_2$ exerts its action on cells by inhibiting human DNA topoisomerase and by interacting with DNA, THAQ and/or THAQ-ace does it through generation of semiquinone and interaction with DNA and that the latter combination turns out to be more effective.

4. Conclusion

The prepared Cu^{II} complex of quinalizarin was studied with an intention to realize and/or identify possible improvement in biological efficacy owing to complex formation of quinalizarin with Cu^{II} through various model studies to project it as a less costly alternative to anthracyclines. The Cu^{II} complex binds to DNA and that was comparable to quinalizarin. The complex leads to substantial decrease in semiquinone/superoxide radical anion formation and was also identified as an efficient inhibitor of human DNA topoisomerase I and human DNA topoisomerase II. Less formation of semiquinone probably affects biological activity in the free radical pathway making it less effective on ALL MOLT-4 cells than quinalizarin, inspite of the fact that it was found to be a better inhibitor of human DNA topoisomerase I and human DNA topoisomerase II. As part of investigations undertaken, *in silico* molecular docking simulations were performed to investigate topoisomerase II as a potential target for THAQ and $Cu^{II}(THAQ)_2(H_2O)_2$. Human topoisomerase II a and b have a strong affinity for $Cu^{II}(THAQ)_2(H_2O)_2$ than for THAQ. A significant number of molecular contacts between $Cu^{II}(THAQ)_2(H_2O)_2$ and topoisomerase II were identified at the active site of the enzyme which could prevent the enzyme from doing its job and hence in the process prevent growth of cells. The study also suggests that the free radical pathway is probably superior in inducing cytotoxicity on ALL MOLT-4 cells than that which involves “inhibition of topoisomerase”. Since the complex generates less semiquinone and hence less superoxide radical anion, it might improve upon aspects related to “cardiotoxic side effects” that are reported as a disadvantage for this class of compounds (anthracyclines and their analogues) and considered a major problem for this class of drugs.

Author statement

Sayantani Chatterjee, Chetan Jain, Tanmoy Saha: Data curation, formal analysis, investigation, methodology, software, visualization, writing - original draft.

Hemanta Kumar Majumder: Conceptualization, Funding acquisition, methodology, project administration, resources, supervision, validation, visualization, writing - review & editing.

Susanta Roychoudhury: Conceptualization, Funding acquisition, methodology, project administration, resources, supervision, validation, visualization.

Saurabh Das: Conceptualization, Funding acquisition, methodology, project administration, resources, supervision, validation, visualization, writing - original draft.

Declaration of Competing Interest

The authors declare that they have no known competing financial interests or personal relationships that could have appeared to influence the work reported in this paper.

Data availability

Data will be made available on request.

Acknowledgement

SD gratefully acknowledges UGC-DAE-CSR Collaborative Research Scheme for a project having sanction number UGC-DAE-CSR-KC/CRS/l9/RC11/0985. He expresses his gratitude towards RUSA 2.0 program of the Government of India operating at Jadavpur University for a

project having Sanction Ref. no. R-11/438/19 dated 30.05.2019 under "Research Support to Faculty Members" on the thrust area "Research in Sustainable Development". SC wishes to thank the Principal, Vijaygarh Jyotish Ray College, Kolkata for her support and encouragement to pursue her research work. TS gratefully acknowledge the "Governing Body" of Sri Aurobindo Institute of Education, Salt Lake, Kolkata for supporting him for his research leading to a Ph D degree.

Appendix A. Supplementary data

Supplementary data to this article can be found online at https://doi.org/10.1016/j.jinorgbio.2023.112369.

References

[1] H.B. Gray, Proc. Natl. Acad. Sci. U. S. A. 100 (2003) 3563–3568.
[2] P. Chellan, P.J. Sadler, Chem. Eur. J. 26 (2020) 8676–8688.
[3] H. Sigel, A. Sigel, J. Indian Chem. Soc. 77 (2000) 501–509.
[4] K.L. Haasand, K.J. Franz, Chem. Rev. 109 (2009) 4921–4960.
[5] R.H. Holm, P. Kennepohl, E.I. Solomon, Chem. Rev. 96 (1996) 2239–2314.
[6] C.A. Puckett, R.J. Ernst, J.K. Barton, Dalton Trans. 39 (2010) 1159–1170.
[7] T. Deb, P.K. Gopal, D. Ganguly, P. Das, M. Paul, M.B. Saha, S. Paul, S. Das, RSC Adv. 4 (2014) 18419–18430.
[8] E. Urso, M. Maffia, J. Vasc. Res. 52 (2015) 172–196.
[9] C. Santini, M. Pellei, V. Gandin, M. Porchia, F. Tisato, C. Marzano, Chem. Rev. 114 (2014) 815–862.
[10] C. Marzano, M. Pellei, F. Tisato, C. Santini, Med. Chem. 9 (2009) 185–211.
[11] S. Gomez-Ruiz, D. Maksimovic-Ivanic, S. Mijatovic, G.N. Kaluderovic, Bioinorg. Chem. Appl. 2012 (2012) 14. Article ID 140284.
[12] S. Dasari, P.B. Tchounwou, Eur. J. Pharmacol. 740 (2014) 364–378.
[13] N. Farrell, Metal complexes as drugs and chemotherapeutic agents, in: Comprehensive Coordination Chemistry II 9, 2003, pp. 809–840.
[14] S.G. Castorena, A.M. Avalos, A.M. Betancourt, G.G. Avendaño, M.Z. Apata-Tarrés, A. Medina-Sansón, Pediatr. Hematol. Oncol. 24 (2007) 403–408.
[15] G. Lenglet, M.-H. David-Cordonnier, J. Nucleic Acids 2010 (2010) 290935.
[16] J. Wang, W.H. Konigsberg, Front. Mol. Biosci. 9 (2022) 824794.
[17] K. Shan, A.M. Lincoff, J.B. Young, Ann. Intern. Med. 125 (1996) 47–58.
[18] K. Leger, T. Slone, M. Lemler, D. Leonard, C. Cochran, W.P. Bowman, L. Bashore, N. Winick, Pediatr. Blood Cancer 62 (2015) 123–127.
[19] D.H. Kleiner, H. Ardehali, R. Fischmeister, P. Burridge, E. Hirsch, A.R. Lyon, Eur. Heart J. 40 (2019) 798–800.
[20] M.M.L. Fiallo, A. Garnier-Suillerot, Inorg. Chim. Acta 137 (1987) 119–121.
[21] E. Monti, L. Paracchini, F. Piccinini, et al., Cancer Chemother. Pharmacol. 25 (1990) 333–336.
[22] J. de Jong, B.C.P. Hüsken, B. Beekman, W.J.F. van der Vijgh, A. Bast, Eur. J. Pharm. Sci. 2 (1994) 229–237.
[23] M.M.L. Fiallo, A. Garnier-Suillerot, B. Matzanke, H. Kozlowski, J. Inorg. Biochem. 75 (1999) 105–115.
[24] P. Das, C.K. Jain, S.K. Dey, R. Saha, A.D. Chowdhury, S. Roychoudhury, S. Kumar, H.K. Majumder, S. Das, RSC Adv. 4 (2014) 59344–59357.
[25] P. Das, C.K. Jain, S. Roychoudhury, H.K. Majumder, S. Das, ChemistrySelect 1 (2016) 6623–6631.
[26] S.M. Chatterjee, C.K. Jain, S. Singha, P. Das, S. Roychoudhury, H.K. Majumder, S. Das, ACS Omega 3 (2018) 10255–10266.
[27] P.S. Guin, P.C. Mandal, S. Das, J. Coord. Chem. 65 (2012) 705–721.
[28] B. Mandal, S. Singha, S.K. Dey, S. Mazumdar, T.K. Mondal, P. Karmakar, S. Kumar, S. Das, RSC Adv. 6 (2016) 51520–51532.
[29] J. Wang, W.H. Konigsberg, Front. Mol. Biosci. 9 (2022) 824794.
[30] C. Molinaro, A. Martoriati, L. Pelinski, K. Cailliau, Cancers 12 (2020) 2863.
[31] J.C. Wang, Nat. Rev. Mol. Cell Biol. 3 (2002) 430–440.
[32] D.A. Koster, A. Crut, S. Shuman, M. Bjornsti, N.H. Dekker, Cell 142 (2010) 519–530.
[33] Y. Pommier, Chem. Rev. 109 (2009) 2894–2902.
[34] Y. Pommier, E. Leo, H.L. Zhang, C. Marchand, Chem. Biol. 17 (2010) 421–433.
[35] S. Salerno, F. Da Settimo, S. Taliani, F. Simorini, C. La Motta, G. Fornaciari, A. M. Marini, Curr. Med. Chem. 17 (2010) 4270–4290.
[36] G. Cozza, M. Mazzorana, E. Papinutto, J. Bain, M. Elliott, G. di Maira, A. Gianoncelli, M.A. Pagano, S. Sarno, M. Ruzzene, R. Battistutta, F. Meggio, S. Moro, G. Zagotto, L.A. Pinna, Biochem. J. 421 (2009) 387–395.
[37] L.-Q. Meng, C. Liu, Y.-H. Luo, X.-J. Piao, Y. Wang, Y. Zhang, J.-R. Wang, H. Wang, W.-T. Xu, Y. Liu, Y.-Q. Wu, H.-N. Sun, Y.-H. Han, M.-H. Jin, G.-N. Shen, Y.-Q. Zang, J. Li, N.-Z. Fang, Y.-D. Cui, C.-H. Jin, Mol. Med. Rep. 17 (2018) 2626–2634.
[38] Y.-Q. Zang, Y.-Q. Zhai, Y.-Y. Feng, X.-Y. Ju, F. Zuo, Environ. Toxicol. 36 (2021) 276–286.
[39] S.I. Erdagi, F.A. Ngwabebhoh, U. Yildiz, Mater. Sci. Eng. C 109 (2020) 110621.
[40] L. Finney, S. Mandava, L. Ursos, S.W. Zhang, D. Rodi, S. Vogt, D. Legnini, J. Maser, F. Ikpatt, O.I. Olopade, D. Glesne, Proc. Natl. Acad. Sci. U. S. A. 104 (2007) 2247–2252.
[41] S. Puig, J. Lee, M. Lau, D.J. Thiele, J. Biol. Chem. 277 (2002) 26021–26030.
[42] S.T. Puig, D.J. Thiele, Curr. Opin. Chem. Biol. 6 (2002) 171–180.
[43] H. Sigel, A.D. Zuberbühler, O. Yamauchi, Anal. Chim. Acta 255 (1991) 63–72.
[44] H.M. Irving, M.G. Miles, L.D. Pettit, Anal. Chim. Acta 38 (1967) 475–488.
[45] M.J. Frisch, G.W. Trucks, H.B. Schlegel, G.E. Scuseria, M.A. Robb, J.R. Cheeseman, G. Scalmani, V. Barone, G.A. Petersson, H. Nakatsuji, X. Li, M. Caricato, A. V. Marenich, J. Bloino, B.G. Janesko, R. Gomperts, B. Mennucci, H.P. Hratchian, J. V. Ortiz, A.F. Izmaylov, J.L. Sonnenberg, D. Williams-Young, F. Ding, F. Lipparini, F. Egidi, J. Goings, B. Peng, A. Petrone, T. Henderson, D. Ranasinghe, V. G. Zakrzewski, J. Gao, N. Rega, G. Zheng, W. Liang, M. Hada, M. Ehara, K. Toyota, R. Fukuda, J. Hasegawa, M. Ishida, T. Nakajima, Y. Honda, O. Kitao, H. Nakai, T. Vreven, K. Throssell, J.A. Montgomery Jr., J.E. Peralta, F. Ogliaro, M. J. Bearpark, J.J. Heyd, E.N. Brothers, K.N. Kudin, V.N. Staroverov, T.A. Keith, R. Kobayashi, J. Normand, K. Raghavachari, A.P. Rendell, J.C. Burant, S.S. Iyengar, J. Tomasi, M. Cossi, J.M. Millam, M. Klene, C. Adamo, R. Cammi, J.W. Ochterski, R.L. Martin, K. Morokuma, O. Farkas, J.B. Foresman, D.J. Fox, Gaussian 09, Revision D.01, Gaussian, Inc., Wallingford CT, 2016.
[46] (a) A.D. Becke, J. Chem. Phys. 98 (1993), 5648e5652;
(b) C.T. Lee, W.T. Yang, R.G. Parr, Phys. Rev. B 37 (1988), 785e789.
[47] S. Chiodo, N. Russo, E. Sicilia, J. Chem. Phys. 125 (2006) 104107.
[48] M. Cossi, J.V. Barone, Chem. Phys. 115 (2001), 4708e4717.
[49] N.M. O'Boyle, A.L. Tenderholt, K.M. Langner, J. Comput. Chem. 29 (2008) 839–845.
[50] V.K. Choudhary, A.K. Bhatt, D. Dash, N. Sharma, J. Comput. Chem. (2019) 1–10.
[51] S. Roy, R. Banerjee, M. Sarkar, J. Inorg. Biochem. 100 (2006) 1320–1331.
[52] P.S. Guin, P.C. Mandal, S. Das, Electrochemistry and UV/Vis spectroscopy, ChemPlusChem 77 (2012) 361–369.
[53] G. Scatchard, Ann. N. Y. Acad. Sci. 51 (1949) 660–672.
[54] H.R. Mahler, Methods in Enzymology 11, Academic Press, New York, USA, 1955, pp. 668–672.
[55] G.M. Morris, R. Huey, W. Lindstrom, M.F. Sanner, R.K. Belew, D.S. Goodsell, A. J. Olson, Auto dock4 and Auto dock tools 4: automated docking with selective receptor flexiblity, J. Comput. Chem. 16 (2009) 2785–2791.
[56] D.M. Khaled, M.E. Elshakre, M.A. Noamann, H. Butt, M.M.A. Fattah, D.A. Gaber, Int. J. Mol. Sci. 23 (2022) 11799.
[57] T. Saha, S. Sappati, S. Das, Int. J. Biol. Macromol. 245 (2023) 125305.
[58] A. Ghosh, N. Mukerjee, B. Sharma, A. Pant, Y.K. Mohanta, R.D. Jawarkar, R. L. Bakal, E.M. Terefe, G.E.S. Batiha, G.M. Hedeab, N.K.A. Albezrah, A. Dey, D. Baishya, Front. Pharmacol. 12 (2022), 812565.
[59] K. Nakamoto, Infrared and Raman Spectra of Inorganic and Coordination Compounds, 3rd ed., Wiley-Interscience, New York, 1978.
[60] C.J. Winscom, W. Lubitz, M. Baumgarten, Appl. Magn. Reson. 20 (2001) 35–70.
[61] M. Tachibana, M. Iwaizumi, S. Tero-Kubota, J. Inorg. Biochem. 30 (1987) 133–140.
[62] K.J. de Almeida, N.A. Murugan, Z. Rinkevicius, H.W. Hugosson, O. Vahtras, H. Agren, A. Cesar, Phys. Chem. Chem. Phys. 11 (2009) 508–519.
[63] T. Saha, S. Singha, S. Kumar, S. Das, J. Mol. Struct. 1221 (2020) 128732.
[64] P.K. Chattaraj, S. Giri, Annu. Rep. Sect. C Phys. Chem. 105 (2009) 13–39.
[65] P.K. Chattaraj, U. Sarkar, D.R. Roy, Chem. Rev. 106 (2006) 2065–2091.
[66] M. Ghosh, N. Sepay, C. Rizzoli, C.K. Ghosh, A. Banerjee, S. Saha, New J. Chem. 45 (2021) 2995–3006.
[67] S. Mukherjee, P. Das, S. Das, J. Phys. Org. Chem. 25 (2012) 385–393.
[68] S. Mukherjee, P.K. Gopal, S. Paul, S. Das, J. Anal. Oncol. 3 (2014) 122–129.
[69] P.S. Guin, S. Das, P.C. Mandal, J. Inorg. Biochem. 103 (2009) 1702–1710.
[70] S. Das, A. Bhattacharya, P.C. Mandal, M.C. Rath, T. Mukherjee, Radiat. Phys. Chem. 65 (2002) 93–100.

Journal of Molecular Structure xxx (xxxx) 137229

Contents lists available at ScienceDirect

Journal of Molecular Structure

journal homepage: www.elsevier.com/locate/molstruc

Hydrothermal syntheses of d10-based Zn(II) and Cd(II) metal–organic frameworks for the catalysis of the Knoevenagel condensation

Birendra Nath Patra [a], Asit Kumar Das [b, *], Samiran Misra [c], Partha Pratim Jana [c], Paula Brandao [d], Mohd Afzal [e], Abdullah Alarifi [e], Tanmoy Saha [f], Debabrata Bera [g], Satyajit Haldar [h, *], Dasarath Mal [a, *], Nayim Sepay [i, *]

[a] Department of Chemistry, VijaygahrJyotish Ray College, Kolkata 700032, India
[b] Department of Chemistry, Krishnath College, Murshidabad 742101, West Bengal, India
[c] Department of Chemistry, Indian Institute of Technology Kharagpur, West Bengal 721302, India
[d] Department of Chemistry, CICECO, University of Aveiro, 3810-193 Aveiro, Portugal
[e] Department of Chemistry, College of Science, King Saud University, Riyadh 11451, Saudi Arabia
[f] Department of Chemistry, Jadavpur University, Kolkata 700032, India
[g] Department of Food Technology and Biochemical Engineering, Jadavpur University, Kolkata 700032, India
[h] Department of Chemistry, Bangabasi Evening College Kolkata, West Bengal 700009, India
[i] Department of Chemistry, Lady Brabourne College, Kolkata 700017, India

ARTICLE INFO

Article history:
Received 27 August 2023
Received in revised form 17 November 2023
Accepted 29 November 2023

Keywords:
MOF
Zn- and Cd-MOF
Catalysis
Knoevenagel condensation

ABSTRACT

Metal–organic frameworks (MOFs) are compounds that feature metal clusters coordinated with organic ligands, forming impressive structures and properties. In this study, two MOFs of Zn(II) and Cd(II) were synthesized using the organic compound 5-hydroxy-2-pyrazinecarboxylic acid, forming **Zn-MOF** and **Cd-MOF**. To better understand the intricate structures of these MOFs, single-crystal X-ray crystallography was used to characterize their respective structures. The results showed that both MOFs have complex three-dimensional supramolecular structures that are highly symmetric and contain water molecules. Additionally, topological analysis of the MOFs indicated that they have a zeolite-like structure. The Hirshfeld surfaces analysis revealed that both crystal structures could preferentially interact with other molecules through hydrogen bonds. The MOFs were found to have a direct band gap, with the energy observed to be 2.44 and 2.71 eV for the **Zn-MOF** and **Cd-MOF** systems, respectively. The hydrogen bond formation ability of the MOFs, in combination with their low band gap energy, make them highly suitable for use in the cross-aldol reaction in water. Overall, the results of this study provide important insights into the unique properties and potential applications of MOFs in diverse fields.

© 20XX

1. Introduction

The fields of chemical and material sciences are experiencing remarkable growth, particularly in the area of Metal–organic frameworks (MOFs) [1,2]. MOFs are gaining popularity due to their exceptional structural topologies and potential applications as functional materials [3]. Their potential use in gas storage, purification, molecular sensing, drug delivery, biomedicine, photoluminescence, molecular-based magnetism, and photocatalysis is currently under rigorous investigation [4].

The scientific community is currently exploring the use of metal-containing molecules as catalysts [5], with particular attention being paid to noble metals such as platinum (Pt), (Re), ruthenium (Ru), and iridium (Ir) due to their high effectiveness [6–10]. However, common metal or polyoxometalate catalysts have also shown promising potential in various catalytic applications. [11] Despite molecular catalysts' advantages, they may face challenges in homogeneous catalysis due to their low stability and small surface area under catalytic conditions [12]. Additionally, their high solubility in polar solvents can pose issues when recovering and reusing them, further complicating their separation from the resulting products [13].

The production of MOFs is aimed at creating durable and permeable materials for catalysis [14]. In order to determine whether a particular MOF structure is suitable for use as a catalyst, it is crucial to examine its stability and porosity under varying reaction conditions [15]. Various external factors, such as magnetic or electric stirring, solvent, temperature, time, pH, and environment (including inert gas and vacuum conditions), can all impact the catalyst's stability [16]. While specific catalysts may undergo structural changes or even collapse during catalytic

* Corresponding authors.
E-mail addresses: akd.knc@gmail.com (A.K. Das), satyajithaldar@gmail.com (S. Haldar), dasarathmal@vjrc.ac.in (D. Mal), nayimsepay@yahoo.com (N. Sepay).

https://doi.org/10.1016/j.molstruc.2023.137229
0022-2860/© 20XX

CORRECTED PROOF

Note: Low-resolution images were used to create this PDF. The original images will be used in the final composition.

reactions, they can often be restored to their original form by applying specific methods [16].

Porous hybrid organic–inorganic crystalline solids, more commonly known as MOFs, have garnered considerable attention and popularity for their exceptional catalytic properties over the years [17]. These materials are created by combining metallic ions or clusters with polydentate organic linkers, resulting in a modular porosity that is highly useful in various applications [18]. MOFs are known for their chemical functionalization versatility, stability, and recyclability, making them highly sought after by researchers and industry professionals [19]. Additionally, their highly ordered and crystalline structures make them ideal for computational and theoretical approaches, further adding to their appeal. Overall, MOFs are an up-and-coming class of materials that continue to attract significant interest and research efforts in the scientific community [19].

Our study involved creating and customizing two **Zn-MOF** and **Cd-MOF**, using Zn(II) and Cd(II) metals, respectively. The MOFs were formed by combining the corresponding metal ions with 5-hydroxy-2-pyrazinecarboxylic acid. The structure of the MOFs was analyzed using single-crystal X-ray crystallography, which enabled us to determine their topology, non-covalent interactions, and band structure. These findings were used to explore the potential applications of MOFs. Our research revealed that the MOFs were effective catalysts for Knoevenagel condensation reaction in ethanol. Specifically, they exhibited acid-base catalytic properties, making them well-suited. Overall, our study provides valuable insights into the potential uses of **Zn-MOF** and **Cd-MOF** in various industrial and scientific applications.

2. Results and discussions

2.1. Synthesis and characterization of MOFs

Under hydrothermal conditions, 5-Hydroxy-2-pyrazinecarboxylic acid was reacted individually with Zn(II) and Cd(II) salts, resulting in the creation of high-purity and high-yield corresponding MOFs, as depicted in Scheme 1. Here, a mixture of Milli-Q water, Dimethylacetamide, and ethanol (4:2:1) was used as the reaction medium. The solubility of acid in this solvent system was enhanced by making the medium slightly alkaline. To achieve this, a NaOH solution was added to the medium where the compound was kept, adjusting the pH to 8. Upon adding an aqueous solution of metal nitrate salt to the mixture, the desired products (pale pink block for **Zn-MOF** and pink block crystals for **Cd-MOF**) were produced after heating at 130 °C for three days.

To characterize the MOFs, IR, powder x-ray crystallography, and thermogravimetric analysis (TGA) were initially performed. The Zn-MOF shows 3482 (for coordinating water OH), 1605 (aromatic carboxylate C═O after coordination with Zn^{2+}), 1377 (asymmetric starching of aromatic carboxylate C═O after coordination with Zn^{2+}) cm^{-1} peaks whereas, for **Cd-MOF**, these peaks were appeared at 3456, 1620, and 1385 cm^{-1} peaks, respectively (Fig. S1).

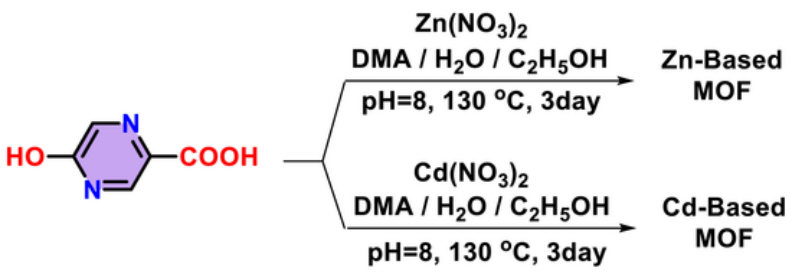
The powder X-ray crystallographic pattern of both MOFs fit well with the simulated powder X-ray pattern obtained from a single crystal X-ray structure. It indicates the phase purity of both the MOFs (Fig. S2).

The thermal stability of **Zn-MOF** and **Cd-MOF** was investigated using thermogravimetric analysis (TGA) (Fig. S3). In Fig. S3, TGA shows mass loss of MOFs starting at 206 °C and continuing to 341 °C. In this temperature region, there is a slow mass loss of approximately 6.13 % owing to the loss of one coordinated water molecule from the complex, which concurs well with the theoretical mass loss of 6.7 % (For **Cd-MOF**, fragment loss, m/z = 18; expected molecular formula after fragment of four coordinated water molecules = $C_5H_4N_2O_4Cd$; expected molecular weight 268.50). Second water loss starts when the temperature reaches 345 °C and continues up to 469 °C. During this temperature range, a slow loss of mass of 6.8% occurs at a temperature of 345 °C. A very similar TGA was observed for **Zn-MOF**. Therefore, the MOFs are stable enough at high temperatures. Therefore, the MOFs can act as very good catalysts due to their thermal stability.

2.2. Crystal structure of MOFs

Zinc (Zn) and Cadmium (Cd) are metallic elements in the periodic table's third and fourth rows, respectively. Both elements occupy group twelve. Notably, the bivalent metal cations of Zn and Cd exhibit similar behavior to 5-Hydroxy-2-pyrazinecarboxylic acid, producing very similar Metal–organic frameworks (MOFs). The structures of these MOFs were determined using single-crystal X-ray diffraction, revealing that Zn and Cd ions crystallize in a monoclinic crystal system with a $P2_1/n$ space group (Table S1, see supporting information file). The ligands in the distorted octahedral crystal structure of the MOFs consist of four oxygen atoms and two nitrogen atoms in a *cis* configuration with respect to the metal ions, as illustrated in Fig. 1. In both MOFs, all coordinating atoms except one oxygen from water originate from ligands. Each hexa-coordinated metal(II) ion is linked to two nitrogen centers from two pyrazine rings, one oxygen of the carboxylate, one oxygen from phenoxide, and the last one from one water, forming a molecular fragment. The pentadented L^{2-} coordinates with metal(II) ions to create a molecular fragment that is further linked to construct a complex 3D network. Notwithstanding the presence of several electron-rich sites within the molecule, they do not participate in the H-bonds. The asymmetrical unit of both MOFs consists of four Metal(II) ions, one L^{2-} (with the deprotonated carboxylic acids and phenol), and one water. The MOFs' pentadented L^{2-} coordinates with metal(II) ions to create a molecular fragment that further links to construct a complex 3D network. The structures' similarities suggest that the coordination geometries of Zn and Cd ions play a crucial role in the MOF's formation. It is quite intriguing to note that upon extrapolation of the 3D network of both MOFs, significant surface grooves are observed. This unique feature presents an ideal space for accommodating a variety of small molecules and additionally forms an H-bond with them. These MOFs can, therefore, act as catalysts through H-bond donation and acceptance, adding to their exceptional catalytic properties.

The **Zn-MOF** and **Cd-MOF** possess a complex three-dimensional network that results in a twenty-membered 'chair-like' ring structure. This structure is fused with eight-membered rings, and many systems share their arms to produce the intricate supramolecular architecture of the MOFs. The twenty-membered rings contain two water molecules at



Scheme 1. Synthesis of **Zn**- and **Cd**-MOFs under hydrothermal conditions.

CORRECTED PROOF

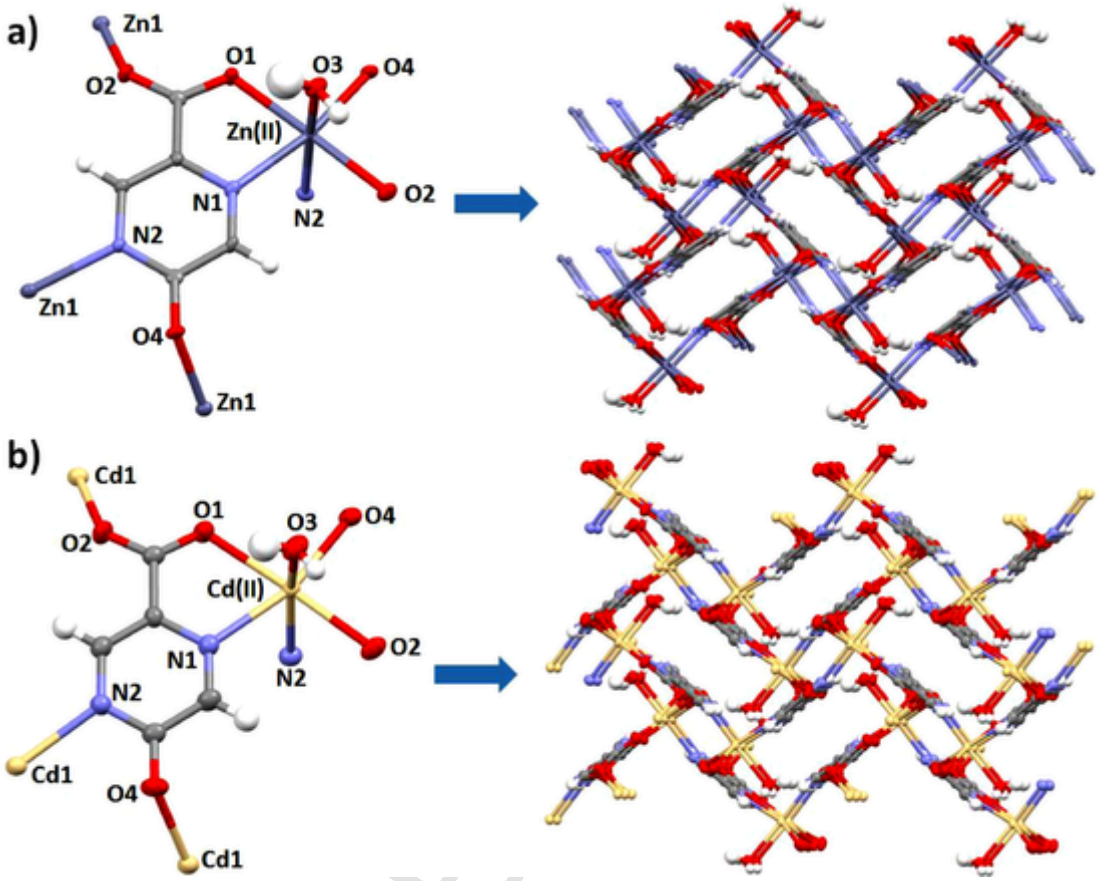


Fig. 1. The asymmetric unit and 2 × 2 × 2 packing of (a) **Zn-MOF** (CCDC 2291047) and (b) **Cd-MOF** (CCDC 229148).

each end facing the inner side of the ring. The large rings' opposite sides are 8.414 and 3.09 Å apart for **Zn-MOF** and 8.808 and 3.017 Å apart for **Cd-MOF** (Fig. S4, see supporting information file). Consequently, **Zn-MOF** has less space in the ring compared to **Cd-MOF**. This difference in the cavity volume may be attributed to the metal-chelating ligand bond distances. In the case of **Zn-MOF**, the Zn1- O1, Zn1-O2, Zn1-O3, Zn1-O4, Zn1-N1, and Zn1-N2 bond distances are 2.108(2), 2.148 (2), 2.158(3), 2.032(2), 2.196(3), and 2.153(3) Å, respectively. However, for **Cd-MOF**, the Cd1-O1, Cd1-O2, Cd1-O3, Cd1-O4, Cd1-N1, and Cd1-N2 bond distances were found to be 2.338(3), 2.314(3), 2.350(3), 2.219(3), 2.347(3), and 2.309(3) Å, respectively (Table S2).

2.3. Topology study

When metal is combined with organic ligands, it creates highly complex molecular structures through self-assembly. These structures can extend into three dimensions, thus forming a metal–organic framework (MOF). MOFs are known for their fascinating properties influenced by various factors, such as the framework's topology, the functional groups in the organic ligands, and the type of metal ions used. It is important to note that topology plays a crucial role in the development of new MOFs with specific properties. Therefore, carefully considering this aspect is necessary to create MOFs with desired characteristics.

Upon analyzing the **Zn-MOF** and **Cd-MOF**, it has been determined that the coordination bonds between the metal and ligand play a pivotal role in creating a remarkable supramolecular structure. The standard representation of both MOFs demonstrates a simple **sra** topological chain (Fig. 2), which is also evident in zeolite structures (ABW). The crystal packing reveals a 4/4/o1 net topology, and the Cambridge Crystallographic Database houses various MOFs with this topology, including QURTII, RUCHEF, USUWUC, and FUTZAX. From this, we can infer that the synthesized MOFs possess a zeolite structure and may exhibit catalytic properties akin to zeolite. However, further inquiry into their potential as a catalyst necessitates an examination of their ability to engage in non-covalent interactions with other molecules.

2.4. Hirshfeld surfaces analysis

One of the most effective means for identifying molecular interactions is using Hirshfeld surfaces (HS) when examining crystal structures. Specifically, the molecular Hirshfeld surfaces of both **Zn-MOF** and **Cd-MOF** compounds have been analyzed through this method. To generate these surfaces, a standard surface resolution of high quality was employed along with a scale of –0.15 (red) to +1.5 (blue) Å. The dnorm surface provides invaluable insight into the distance between two atoms across the surface in relation to the atomic radius of the atoms. The de and di surfaces also display the distances to the closest nuclei outside and inside the Hirschfeld surface, respectively. These methods are practical tools for the comprehensive analysis of molecular structures.

Bright red spots have emerged on the metal ion, pyrazine nitrogens, carboxylate oxygen, and water hydrogens of **Zn-MOF** and **Cd-MOF** on the dnorm surface (Fig. 3a and b). The first three red spots mentioned above were formed due to coordination bonds, while the spots on the water hydrogens indicate the potential for hydrogen bond formation. This observation is reinforced by the presence of red spots on the hydrogens of the water region exclusively on the de surface (as shown in Fig. 3c and d). The triangular-shaped red spots in the middle of the pyrazine ring on the shape index surface signify that both MOFs can form π-staking interactions (as demonstrated in Fig. 3e and f). It is noteworthy that the curvedness surface of **Zn-MOF** lacks sharp edges, which can be seen on the **Cd-MOF** (as illustrated in Fig. 3g and h).

CORRECTED

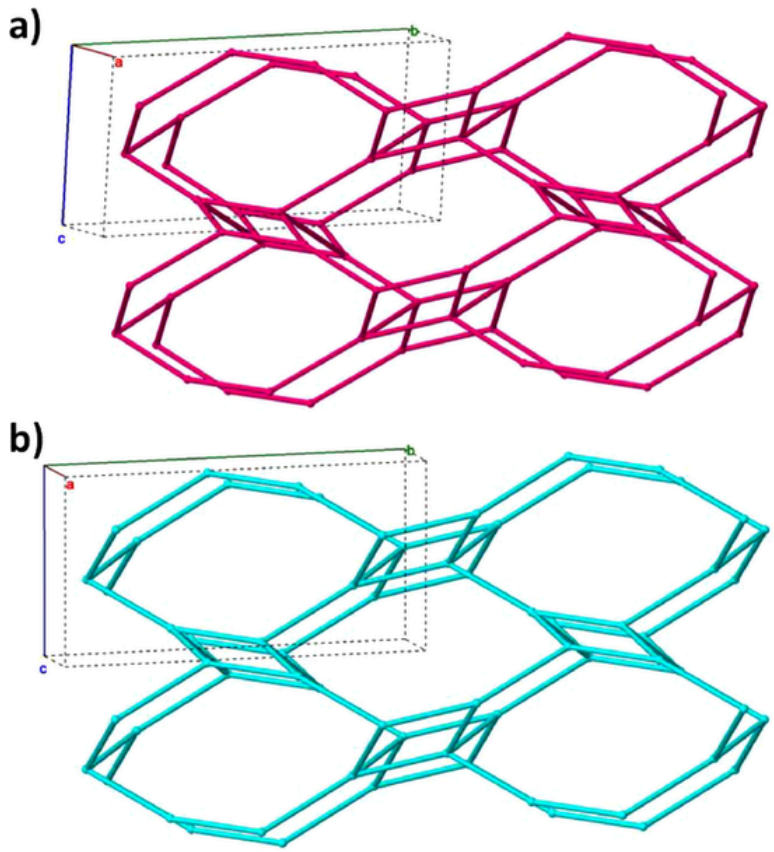


Fig. 2. Underlying 4/4/o1 net with ABW topological type for molecular packing of (a) $C_5H_4N_2O_4Zn$ (**Zn-MOF**) and (b) $C_5H_4N_2O_4Cd$ (**Cd-MOF**) structure.

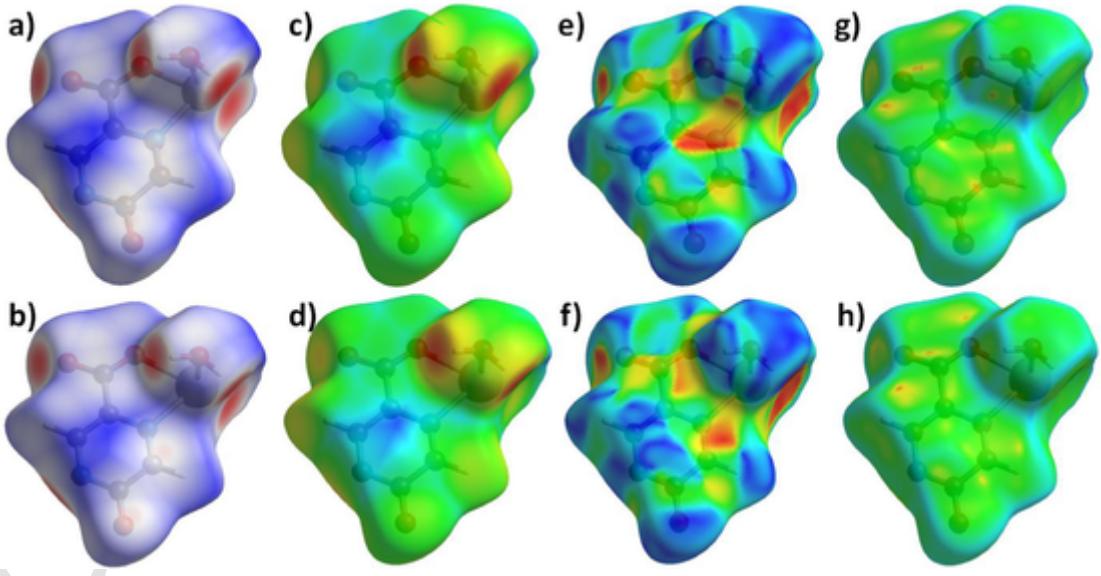


Fig. 3. The Hirshfeld surface mapped over d_{norm} for (a) **Zn-MOF** and (b) **Cd-MOF**, d_i for (c) **Zn-MOF** and (d) **Cd-MOF**, shape index for (e) **Zn-MOF** and (f) **Cd-MOF**, and curvedness for (g) **Zn-MOF** and (h) **Cd-MOF**.

After mapping the Hirshfeld surface, Fig. 4 provides the percentage contribution to the HS calculation of **Zn-MOF** and **Cd-MOF**. Further analysis is done through two-dimensional fingerprint plots based on de and di, which provide information related to the types of intermolecular interactions. The HS analysis shows that both MOFs are very similar in terms of interaction in the crystal. Upon analyzing the MOFs, it has been found that N···H, O···H, H···H, C···H, and O···C contacts significantly contribute to the total interactions. The O···H hydrogen bond contributes maximum in the total interactions, which is interesting. Notably, the N···H hydrogen bonding is relatively lower than O···H. The lower H···H and C···H contacts indicate less preference for van der Waals interactions. Therefore, the synthesized MOFs prefer to interact with other molecules through hydrogen bonding interactions. The analysis shows that the synthesized MOFs prefer hydrogen bonding

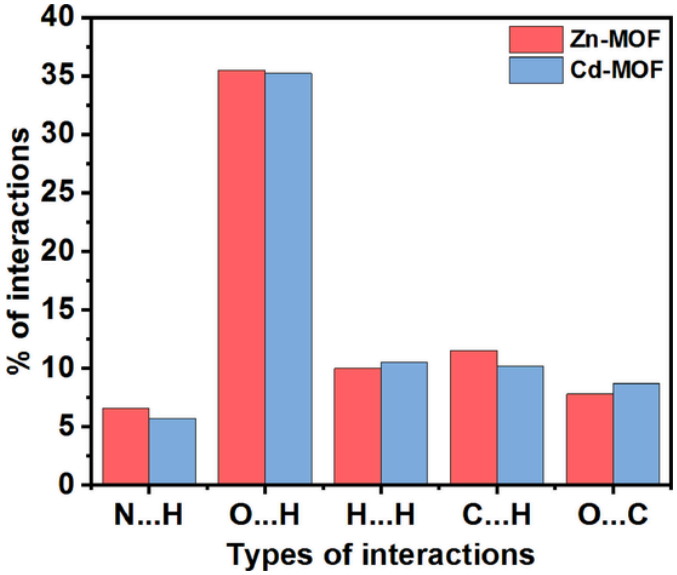


Fig. 4. Quantitative values of different non-covalent interactions involved in the crystal of MOFs.

over van der Waals interactions. The Hirshfeld surface mapping and two-dimensional fingerprint plots provide significant insight into the types of intermolecular interactions in the MOFs.

2.5. Band structure

The energy eigenvalues and corresponding eigenfunctions of a solid are fundamental in determining the placement of electrons in the material. By analyzing the energetic and spatial perspectives, we understand the cohesive behavior of atoms in the solid. Additionally, the band structure of a solid is beneficial in several other ways. For instance, it can offer insights into how electrons react to external changes, such as absorption or emission of light. This reaction is directly linked to the solid's optical and electrical properties, crucial in several applications. Moreover, the band structure plays a critical role in creating excitons-bound pairs of electrons and holes. This phenomenon is instrumental in determining the solid's optical and electrical properties. The band structure can also help determine the total energy of the solid, from which we can calculate a wide range of thermodynamic and mechanical properties. Therefore, the band structure is a crucial tool in materials science, not only for understanding the electronic structure but also for predicting the behavior of materials under different external conditions.

The unique band gap that arises from symmetrical molecular combinations in solid form yields intriguing physical properties. [20] The characteristics of materials' electrical properties are determined by the difference in energy between the valence band and the conduction band, known as the band gap. Molecules are categorized according to their band structure into two groups: direct band gap and indirect band gap. Direct band gap materials exhibit no momentum difference between the highest energy state in the valence band and the lowest energy state in the conduction band, enabling efficient electron transitions between these states with the aid of photons, rendering them useful in a broad range of applications. [21]

The synthesized MOFs underwent scrutiny to determine their band structure and band gap. The direct band gap energies of the **Zn-MOF** and **Cd-MOF** systems were established at 2.44 and 2.71 eV, respectively (Fig. 5 and S5). The Fermi energy, identified by a black dashed line, was located at 0.033 (Fig. 5a) and 0.027 eV (Fig. 5b) for the **Zn-MOF** and **Cd-MOF** systems, respectively. For **Zn-MOF**, the valence band maxima and conduction band minima were situated at the D and G points. Therefore, **Zn-MOF** is a silicon-type semiconductor having an indirect bandgap. Thus, the transition of electrons from the valence band maxima to the conduction band minima is difficult for this MOF. However, the valence band maxima and conduction band minima were situated at the D point, indicating that the **Cd-MOF** possesses a direct band gap and is thus an effective electron-transferring agent. It was initially thought that the metal ions in the MOFs had limited reactivity and would remain inert due to their stability and low tendency to release electrons from the metal center. However, further analysis of the valence band maxima (VBM) and direct band gap energy of both MOFs revealed positive values and a capacity for electron donation, indicating that they are indeed reactive. Additionally, the MOFs' conduction band minima (VBM) are lower in energy, which means they can accept electrons from other molecules. Due to these characteristics, the MOFs can serve as catalysts, making them a valuable tool in chemical reactions, and Cd-MOF may perform better.

2.6. Catalysis

The presence of water in MOFs contributes to their ability to form hydrogen bonding. At the same time, their crystal structure analysis reveals a porous surface, making them ideal candidates for acid-base catalysts. Given these properties, we are considering using MOFs in Knoevenagel condensation reactions between barbituric acid (**1a**) and aromatic aldehydes (**2a**). The performance of two Metal–Organic Frameworks (MOFs), **Zn-MOF** and **Cd-MOF**, was tested using a model reaction. The results showed that **Cd-MOF** performed more efficiently than **Zn-MOF**, with a yield of 79 % for product **3a**, while **Zn-MOF** only managed a yield of 71 %. The structure of **3a** was assigned using ^{1H}NMR

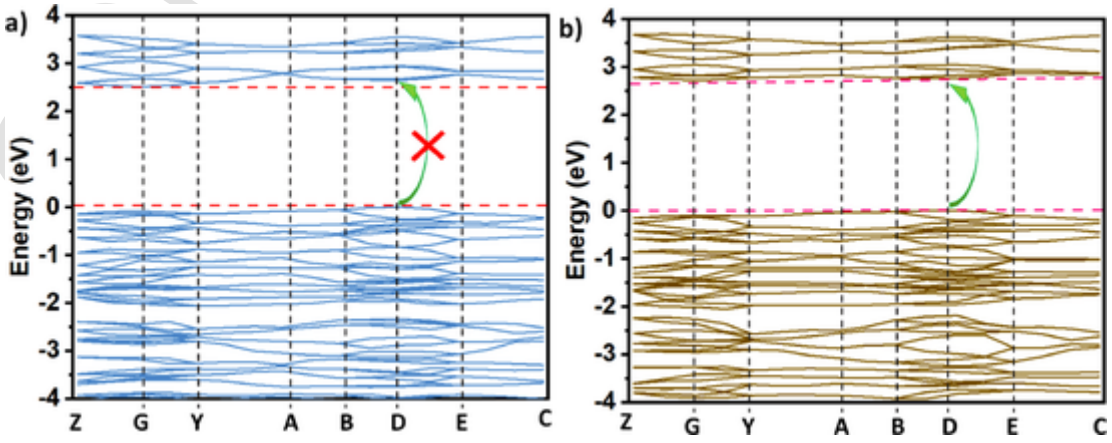


Fig. 5. Combined band structure and density of state of (a) **Zn-MOF** and (b) **Cd-MOF**.

CORRECTED PROOF

(Fig. S6) and ^{13C}NMR (Fig. S7) spectroscopy. The higher efficiency of **Cd-MOF** can be attributed to the crystal structure of the MOFs. Analysis of their crystal structures revealed that both MOFs have a similar shape with grooves on their surface that contain water molecules (as shown in Fig. 1). Both MOFs have similar H-bond forming ability, but **Cd-MOF** has larger grooves than **Zn-MOF** (see supporting information file, Fig. S4). This means that **Cd-MOF** can accommodate barbituric acid and 4-methoxybenzaldehyde more efficiently than **Zn-MOF**, leading to a higher yield of **3a** (Table 1).

As a part of the ongoing research program, the catalytic efficiency of **Cd-MOF** was investigated in the Knoevenagel condensation reaction between barbituric acid **1a** (1 mmol) and 4-methoxybenzaldehyde **2a** (1 mmol) in the presence of various solvents at different temperature with the variation of catalyst loading and reaction time to obtain the corresponding condensation products **3a** (Scheme 2). The detailed results are presented in Table 1.

From the results shown in Table 1, the Knoevenagel condensation reaction did not occur in the absence of any catalyst in EtOH (entry 1) and H_2O (entry 2) even under reflux conditions, where the unreacted substrates were isolated intact in all the cases. The conversion was dramatically improved when the reaction was performed in the presence of a catalyst (15 mg) in an EtOH medium with a 68 % yield (entry 3). Looking for better conversion, the amount of catalyst was increased (entries 4–7). The best result was obtained using 30 mg of catalyst, where the yield was increased to 92 % in less time (entry 6). Excess catalysts beyond this proportion (30 mg) are needed to afford better substrate conversion and increment of the yield (entry 7). Hence, the optimized condition for further studies has been chosen according to entry 6. The use of water as a solvent in place of ethanol led to the lesser yield of the desired product (entry 8). Moderate results were observed when MeOH was used in place of EtOH under the present reaction conditions (entry 9). Other solvents such as DCM, DMSO, DMF, and CH3CN were found to be not at all suitable as the reaction medium in this present protocol (entries 10–13).

Table 1
MOFs catalyzed optimization of the reaction conditions[a].

Entry	Catalyst loading (mg)	Solvent (mL)	Temperature (°C)	Time (h)	Yield (%)[b]	
					Zn-MOF	Cd-MOF
1	–	EtOH	Reflux	6.0	–	–
2	–	H_2O	Reflux	6.0	–	–
3	15	EtOH	Reflux	4.0	66	68
4	20	EtOH	Reflux	4.0	75	79
5	25	EtOH	Reflux	4.0	82	85
6	30	EtOH	Reflux	3.0	88	92
7	35	EtOH	Reflux	3.0	89	95
8	30	H_2O	Reflux	4.0	55	57
9	30	MeOH	Reflux	4.0	62	66
10	30	DCM	Reflux	4.0	–	
11	30	DMSO	100 °C	4.0	–	
12	30	DMF	100 °C	4.0	–	
13	30	CH_3CN	100 °C	4.0	Trace	Trace

[a] Reaction conditions: **1a** (1.0 mmol), **2a** (1.0 mmol), solvent (3 mL), catalyst, and temperature (as indicated).
[b] Isolated yield.

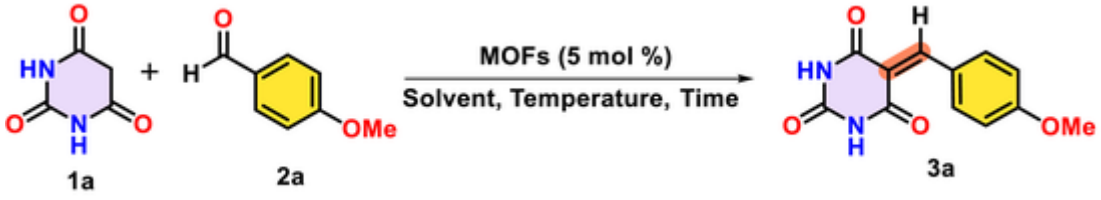
The scope of this present protocol was further extended to the synthesis of a series of Knoevenagel Condensation products through the reaction of barbituric acid (**1a**) with a variety of different aromatic aldehydes having polar, electron-rich, electron-deficient, neutral, and hydrophobic functional groups. In this reaction between barbituric acid and aromatic aldehydes, the corresponding 5-(substitutedbenzylidene) pyrimidine-2,4,6(1H,3H,5H)-trione compounds (**3a-3i**) were obtained good to excellent yield (Table 2).

The **Cd-MOF** catalyst works well with several aldehydes having different polarities, substituents, and electronic features. Compound **3a** was obtained in excellent yield (92 %) from polar as well as less reactive aldehyde (because of conjugation of methoxy group to the aldehyde). However, less polar and hydrophobic aldehyde **2b** performs very well as it produces a good yield (88 %) of **3b**. The slight drop in yield in this reaction may be due to the hydrophobic nature of the aldehyde because the catalytic site is polar. For benzaldehyde (**2c**), the yield of the product **3c** is comparable with **3b**. It indicates that polar molecules are better for this catalytic reaction. For this reason, halogenated aldehydes (**2d-e**) have been chosen for the reaction and found expected better results. For the nitro group containing aldehydes (**2g-i**), further improvement in the yield of the products (**3g-i**) was observed, which indicates the catalytic site is polar and prefers polar aldehydes for the reaction. The formation of all the compounds was characterized by melting point through matching with the reported melting point of the same compounds. Knoevenagel condensation reaction between barbituric acid (**1a**) and aromatic aldehydes (**2a-i**) has been performed for the first time with the help of any MOF as a catalyst. However, the performance of the catalytic activity of **Cd-MOF** with other reported MOFs was listed in Table S4 (See supporting information file). In this case, the reported MOFs have been used as catalysts in the Knoevenagel reaction between malononitrile and aromatic aldehydes. The results indicate that **Cd-MOF** can produce condensation products in good yield in a short time, polar solvent, and low temperature.

In the surface and core of **Cd-MOF**, the catalytic site has two water molecules. In this catalytic site, **1** and **2a** can form hydrogen bonds (Fig. 6). In this way, in system **4**, two reactants can stay in close proximity with proper orientation. The hydrogen bond formation will enhance the enol formation of **1** on the active side, whereas the electrophilicity of aldehyde carbon will increase for the same reason in **4**. Now, the enol will be involved in a nucleophilic attack on the reactive hydrogen-bonded aldehyde group inside the active site (**5**). In this way, C—C bond formation occurs. The water molecules in the active site may play a vital role in the water elimination step in the reaction. Here (**6**), the water molecule in the catalytic site can abstract the last enolizable proton from barbituric acid moiety, which endorses water elimination reaction from the system **6**. In this way, formed two molecules cannot fit at site **7**, and it helps to free the catalytic site for the next cycle.

2.7. Recycling study of Cd-MOF

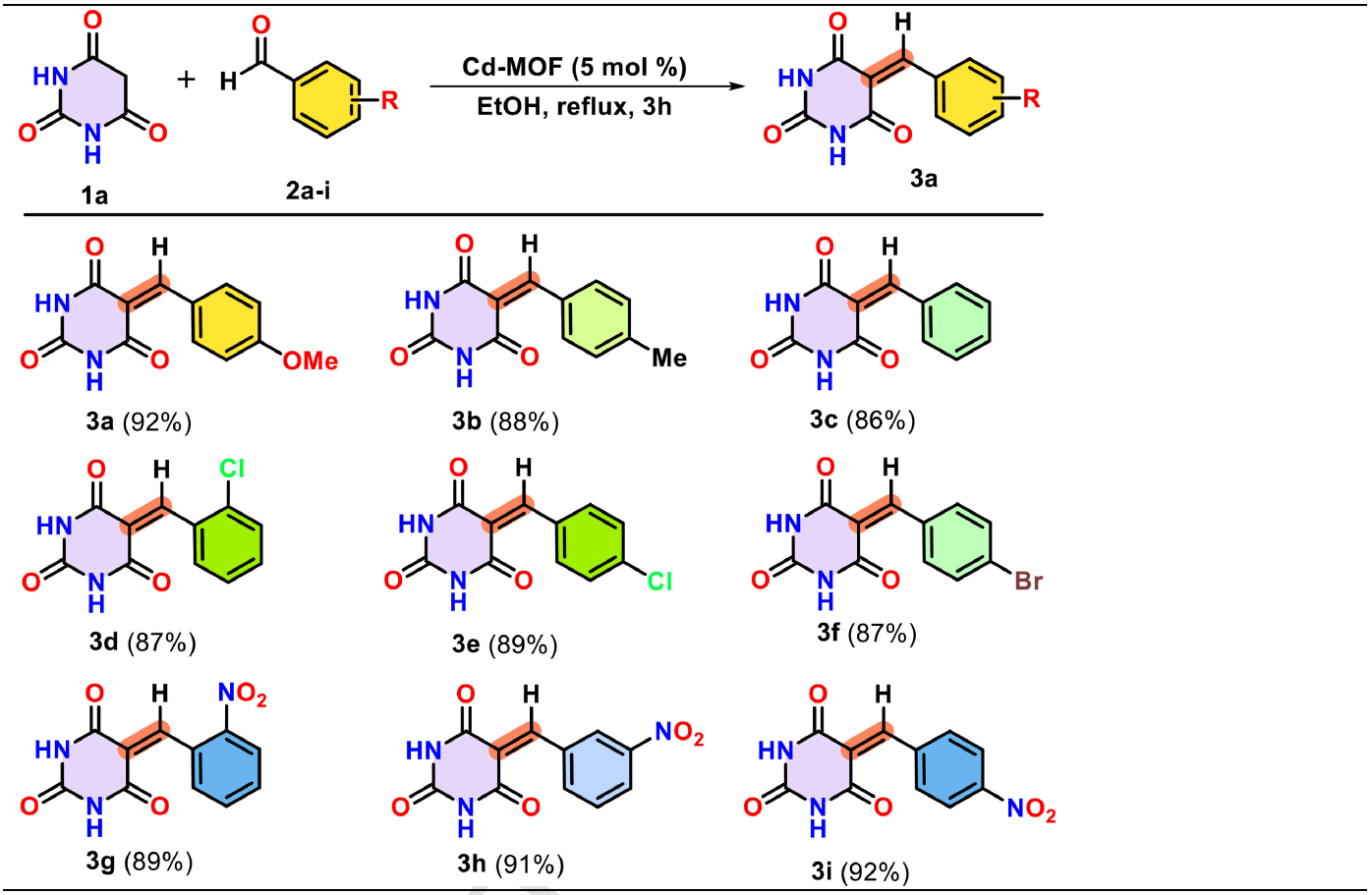
From the standpoint of 'Green Chemistry,' the recovery and recyclability of the catalyst are very essential. [22–24] Therefore, the recycling experiment was carried out using barbituric acid **1a** (1 mmol), 4-methoxybenzaldehyde **2a** (1 mmol), **Cd-MOF** (30 mg) in EtOH (3 mL) under reflux conditions. After the completion of the reaction (as moni-



Scheme 2. MOFs catalyzed **the** Knoevenagel Condensation reaction between barbituric acid (**1a**) and *p*-methoxybenzaldehyde (**2a**).

CORRECTED PROOF

Table 2
shows the scope of Knoevenagel condensation products using **Cd-MOF** as the heterogeneous catalyst.



tored by TLC), the crude product was extracted with ethyl acetate, and the catalyst was separated by filtration. Then, the recovered catalyst was washed repeatedly with EtOH and dried at 100 °C for 2 h. It was reused directly throughout four successive reactions with slight variation in yield (Fig. 7). PXRD and IR measurements of the catalyst before and after the catalytic cycle have been performed to demonstrate the structural integrity and crystallinity of the catalyst after the reaction (Figs. S2 and S3). There are slight changes in the IR and powder X-ray diffraction patterns between fresh and recycled catalysts. The results indicate that the Cd-MOF is sufficiently stable under Knoevenagel condensation reaction conditions. The changes in the patterns can be attributed to the etching of the surface structure of the catalyst. The catalyst retains its structural integrity and crystallinity after the reaction, suggesting that it can be used multiple times for reaction.

3. Experimental

3.1. Synthesis of MOFs

Zinc-based Metal–Organic Framework (**Zn-MOF**) was synthesized using a hydrothermal method. The initial reaction mixture was prepared by dissolving 5-Hydroxy-2-pyrazinecarboxylic acid (0.140 g, 1 mmol) in 5 mL of Milli-Q water. The pH of the solution was adjusted to 8 by adding a dilute solution of NaOH to a solution of $Zn(NO_3)_2{\cdot}6H_2O$ (1 mmol, 0.297 g). The resultant mixture was stirred for 30 min, after which **Zn-MOF** (chemical formula $C_5H_4ZnN_2O_4$) was obtained as white crystals in a 20 mL capacity Teflon-lined acid digestion bomb. The synthesis process was carried out at 140 °C for 3 days, followed by slow cooling at 5 °C /h to room temperature. The crystals formed were collected and dried in the air. Yield was ca. 70 % based on the metal. Anal. Calc. for $C_5H_4ZnN_2O_4$: C, 27.09; H, 1.81; N, 12.64. Found: C, 27.06; H, 1.79; N, 12.61 %.

Cd-MOF (chemical formula $C_5H_4CdN_2O_4$) was prepared hydrothermally like **1,** $Cd(NO_3)_2{\cdot}6H_2O$ was used instead of $Zn(NO_3)_2{\cdot}6H_2O$. After 3 days, pale pink block-shaped crystals were obtained. Crystals thus formed were collected and dried in the air. Yield was ca. 68% based on the metal Anal. Calc. for $C_5H_4CdN_2O_4$: C, 22.35; H, 1.49; N, 10.43 Found: C, 22.29; H, 1.46; N, 10.39.

3.2. Crystal structure of MOFs

The data collected at the X-ray diffraction beam Line (XRD1) of the Elettra Synchrotron of Trieste (Italy) with a Pilatus2M image plate detector shows some exciting features. A dataset was collected at 100 K (nitrogen stream supplied through an Oxford Cryostream 700) with a monochromatic wavelength of 0.700 Å with the rotating crystal method. It seems that the diffraction data were indexed, integrated, and scaled using XDS software [25]. The structure appears to have been solved by direct methods using Sir2014 [26] and refined with full-matrix least-squares based on F^2 with SHELXL-2018/3 [27]. It seems that all non-hydrogen atoms were refined anisotropically. It seems that all the relevant crystallographic data and details of the structure refinement are summarized in Table S1.

Crystallographic data of **Cd-MOF**: $C_5H_4N_2O_4Cd$, M = 268.50, monoclinic, space group $P2_1/n$, a = 6.9164(11), b = 10.3808(18), c = 9.3913(15) Å, β = 98.750(13)°, V = 666.43(19) Å^3, Z = 4, ρ_c = 2.676 g/cm^3, μ(Mo-K_α) = 0.7107 mm^{-1}, F(000) = 512.0, θ range = 6.844 to 57.68° Final R_1 [$I > 2\sigma(I)$] = 0.0291, wR_2 = 0.0414, S = 1.061 for 117 parameters and 1562 reflections,

CORRECT

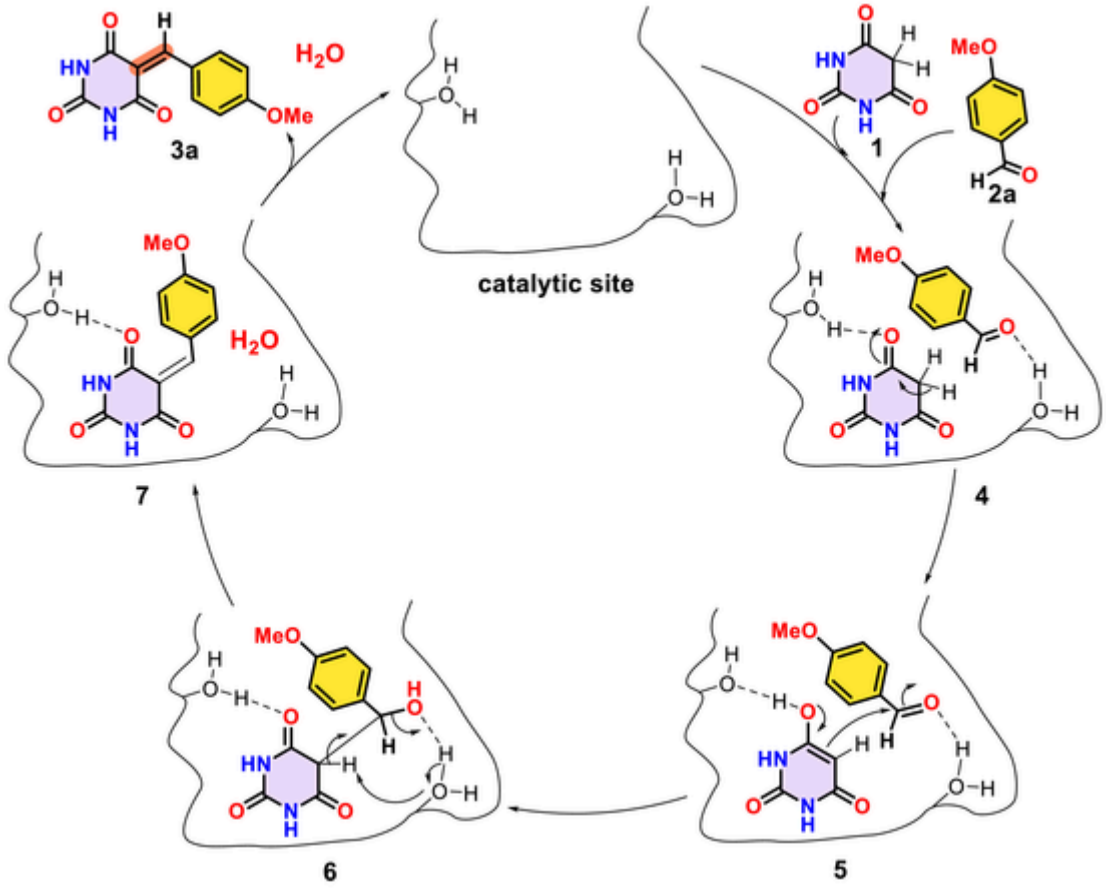


Fig. 6. Plausible Knoevenagel Condensation reaction mechanism with **Cd-MOF**.

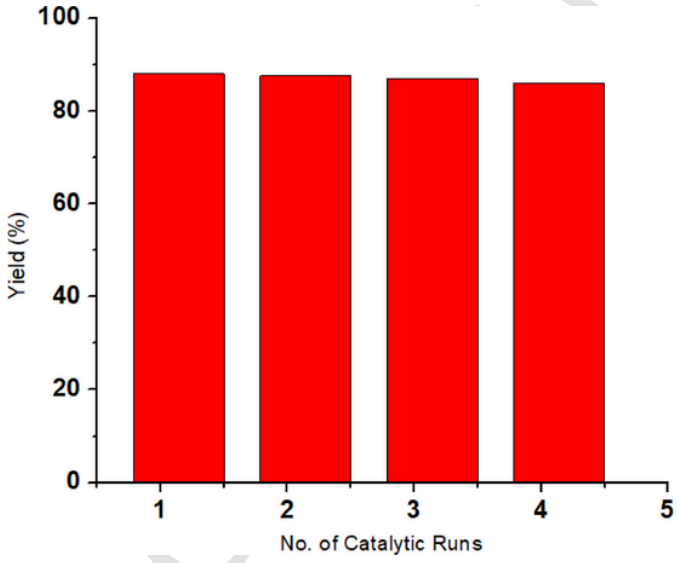


Fig. 7. Recycling study of **Cd-MOF** (up to four catalytic runs).

1562 unique [R_{int} = 0.0365], of which 1562 with $I > 2\sigma(I)$, max positive and negative peaks in the difference Fourier map 0.54, - 0.54 e Å^{-3}.

Crystallographic data of **Zn-MOF**: $C_5H_4N_2O_4Zn$, M = 221.47, monoclinic, space group $P2_1/n$, a = 6.7523(5), b = 10.0277(9), c = 9.1099(9) Å, β = 99.809(7)°, V = 607.81(9) Å^3, Z = 4, ρ_c = 2.420 g/cm^3, μ(Mo-K$_\alpha$) = 0.7107 mm^{-1}, F(000) = 440.0, θ range = 6.092 to 58.154°. Final R_1 [$I > 2\sigma(I)$] = 0.0384, wR_2 = 0.0684, S = 1.078 for 117 parameters and 1407 reflections, 1407 unique [R_{int} = 0.042], of which 1407 with $I > 2\sigma(I)$, max positive and negative peaks in the difference Fourier map 0.54, - 0.55 e Å^{-3}.

3.3. Topology study

The analysis of the periodic network topologies was done using the ToposPro program package and the TTD collection [28]. The RCSR three-letter codes were utilized to represent the network topologies [29]. In cases where the nets were not present in the RCSR, the Topos NDn nomenclature was used [30]. This nomenclature uses N to represent a sequence of coordination numbers of all non-equivalent nodes of the net. D is the periodicity of the net, which could be M, C, L, or T for 0-,1-,2-, and 3-periodic nets. Lastly, n represents the ordinal number of the net in the set of all non-isomorphic nets with the given ND sequence.

3.4. Hirshfeld surfaces study

The computation of Hirshfeld surfaces and 2D fingerprint plots from crystal structure files (CIF) was done using Crystal Explorer 3.1 [31,32]. To further enhance the accuracy of the analysis, a Normalized Hirshfeld surface, d_{norm}, was mapped over the Hirshfeld surface, enabling the derivation of shape indices and the decomposition of fingerprint plots by the function of d_e versus d_i. This approach ensures a thorough and meticulous study of the crystal structures. The d_{norm}, expressed as

$$d_{norm} = \left(d_i - r_i^{vdw}\right)/r_i^{vdw} + \left(d_e - -r_e^{vdw}\right)/r_e^{vdw}$$

When analyzing atoms, it is essential to consider their van der Waals radii, specifically r_i^{vdw} and r_e^{vdw}. These radii play a crucial role in identifying the areas where intermolecular interactions can occur. To better

understand molecular structures, exploring their three-dimensional shapes and the various types of close contact they exhibit is useful. The surface map was generated by Crystal Explorer and TONTO, using the parameters B3LYP/6-311G(d,p) ± 0.03 a.u.

3.5. Band structure

The band properties, density of states, and band structure of the complex structure were computed using CASTEP codes employing the Density Functional Theory (DFT) methodology [33]. The Perdew–Burke–Ernzerhof function was approximated using the Generalized Gradient Approximation (GGA) [34]. The molecular geometry was optimized utilizing the Broyden-Fletcher-Goldfarb-Shannon (BFGS) algorithm, resulting in a force of 40.001 eV A^{-1} that converged on a definitive value, as per the Hellmann-Feynman method. The relativistic analysis problem was addressed by employing Koelling-Harmon's method. New convergence criteria were established for the total energy and interionic displacement, which were set at approximately 1×10^{-5} energy per atom and 0.001 energy per atom, respectively. The basis set was constructed utilizing the ultrafine plane-wave cut-off energy combined with the ultrasoft pseudopotential scheme.

3.6. Catalysis

To a suspension of barbituric acid (**1a**, 1.0 mmol) and 4-methoxybenzaldehyde (**2a**, 1.0 mmol) in EtOH (3 mL), the catalyst (30 mg) was added and the mixture was refluxed. The progress of the reaction was monitored with thin-layer chromatography (TLC). After completion of the reaction, the reaction mixture was cooled to room temperature, ethyl acetate (15 mL) was added to the reaction mixture, and the catalyst was separated by filtration for reuse. The residual catalyst was repeatedly washed with ethyl acetate (3 × 5 mL). The combined organic layer was separated and dried with anhydrous sodium sulfate. The solvent was removed under reduced pressure to furnish the crude product **3a**, which was further purified by recrystallization from ethanol.

4. Conclusions

In summary, in this work, two MOFs of zinc and cadmium were prepared with the help of the hydrothermal method. The structure of the MOFs was characterized using single-crystal X-ray crystallography. They are crystallized in a monoclinic system and have complex supramolecular structures with fused 28- and 8-membered ring fusions. Each large ring contained two water molecules attached to the metal ions. The topological analysis was performed for simplification, and it was observed that the MOFs have zeolite-like *ABW* topology. Hirshfeld surface analysis indicates that the MOFs have the highest hydrogen bond-forming ability among all other types of interactions that they can offer. The direct band gap energies of the **Zn-MOF** and **Cd-MOF** systems were established at 2.44 and 2.71 eV, respectively. All these features of the MOFs help to choose them as an acid-base catalyst. Due to the large cavity size of **Cd-MOF**, it behaved as a better catalyst in the Knoevenagel condensation reaction. It was used to synthesize diverse barbiturates.

CRediT authorship contribution statement

Birendra Nath Patra: Writing – original draft. **Asit Kumar Das:** Writing – original draft. **Samiran Misra:** Resources. **Partha Pratim Jana:** Resources. **Paula Brandao:** Resources. **Mohd Afzal:** Formal analysis. **Abdullah Alarifi:** Formal analysis. **Tanmoy Saha:** Methodology. **Debabrata Bera:** Formal analysis. **Satyajit Haldar:** Resources. **Dasarath Mal:** Formal analysis, Supervision. **Nayim Sepay:** Conceptualization, Writing – review & editing, Formal analysis, Methodology, Supervision.

Declaration of Competing Interest

The authors declare that they have no known competing financial interests or personal relationships that could have appeared to influence the work reported in this paper.

Acknowledgment

DM gratefully acknowledges the Department of Science & Technology and Biotechnology, Government of West Bengal, for a financial grant (Grant No. 28(sanc)-ST/P/S&T/15G-4/2018). The authors gratefully acknowledge Prof. Sven Lidin for allowing the authors to single crystal X-ray data collection. Financial support from UGC by a grant (PSW-035/14-15 (ERO)) is gratefully acknowledged by SH. Dr. Mohd. Afzal extends his appreciation to Researchers Supporting Project number (RSPD2023R979), King Saud University, for financial assistance. NS gratefully acknowledges the Department of Chemistry, Lady Brabourne College, for its research facilities.

Supplementary materials

Supplementary material associated with this article can be found, in the online version, at doi:10.1016/j.molstruc.2023.137229.

References

[1] V.F. Yusuf, N.I. Malek, S.K. Kailasa, Review on metal–organic framework classification, synthetic approaches, and influencing factors: applications in energy, drug delivery, and wastewater treatment, ACS Omega 7 (2022) 44507–44531, https://doi.org/10.1021/acsomega.2c05310.
[2] Q.-L. Zhu, Q. Xu, Metal–organic framework composites, Chem. Soc. Rev. 43 (2014) 5468–5512, https://doi.org/10.1039/C3CS60472A.
[3] R.E. Sikma, K.P. Balto, J.S. Figueroa, S.M. Cohen, Metal–organic frameworks with low-valent metal nodes, Angew. Chem. Int. Ed. 61 (2022), https://doi.org/10.1002/anie.202206353.
[4] D. Bradshaw, A. Garai, J. Huo, Metal–organic framework growth at functional interfaces: thin films and composites for diverse applications, Chem. Soc. Rev. 41 (2012) 2344–2381, https://doi.org/10.1039/C1CS15276A.
[5] B.C. Gates, A. Katz, J. Liu, Nested metal catalysts: metal atoms and clusters stabilized by confinement with accessibility on supports, Precis. Chem. 1 (2023) 3–13, https://doi.org/10.1021/prechem.2c00011.
[6] J. Takaya, Catalysis using transition metal complexes featuring main group metal and metalloid compounds as supporting ligands, Chem. Sci. 12 (2021) 1964–1981, https://doi.org/10.1039/D0SC04238B.
[7] G. Pan, C. Hu, S. Hong, H. Li, D. Yu, C. Cui, Q. Li, N. Liang, Y. Jiang, L. Zheng, L. Jiang, Y. Liu, Biomimetic caged platinum catalyst for hydrosilylation reaction with high site selectivity, Nat. Commun. 12 (2021) 64, https://doi.org/10.1038/s41467-020-20233-w.
[8] N. Suárez, M.A. Arribas, A. Moreno, A. Martínez, High-performing Ir- and Pt-containing catalysts based on mesoporous beta zeolite for the selective ring opening of decalin, Catal. Sci. Technol. 10 (2020) 1073–1085, https://doi.org/10.1039/C9CY01812C.
[9] J. Hafeez, M. Bilal, N. Rasool, U. Hafeez, S. Adnan Ali Shah, S. Imran, Z. Amiruddin Zakaria, Synthesis of ruthenium complexes and their catalytic applications: a review, Arab. J. Chem. 15 (2022) 104165, https://doi.org/10.1016/j.arabjc.2022.104165.
[10] R. Bacchiocchi, J. De Maron, T. Tabanelli, D. Bianchi, F. Cavani, Supported rhenium catalysts for the hydrogenation of levulinic acid derivatives: limits and potential, Sustain. Energy Fuels 7 (2023) 671–681, https://doi.org/10.1039/D2SE01583H.
[11] X. Li, C. Xue, X. Zhou, Y. Wei, Y. Yu, Y. Fu, W. Liu, Y. Lan, Polyoxometalate-derived bimetallic catalysts for the nitrogen reduction reaction, Mater. Chem. Front. 7 (2023) 720–727, https://doi.org/10.1039/D2QM01131J.
[12] M.C. Román-Martínez, C. Salinas-Martínez de Lecea, Heterogenization of homogeneous catalysts on carbon materials. New Fut. Dev. Catal., 2013, pp. 55–78, https://doi.org/10.1016/B978-0-444-53876-5.00003-9.
[13] A.Z. Fadhel, P. Pollet, C.L. Liotta, C.A. Eckert, Combining the benefits of homogeneous and heterogeneous catalysis with tunable solvents and nearcritical water, Molecules 15 (2010) 8400–8424, https://doi.org/10.3390/molecules15118400.
[14] L. Chen, Q. Xu, Metal-organic framework composites for catalysis, Matter 1 (2019) 57–89, https://doi.org/10.1016/j.matt.2019.05.018.
[15] V. Pascanu, G. González Miera, A.K. Inge, B. Martín-Matute, Metal–organic frameworks as catalysts for organic synthesis: a critical perspective, J. Am. Chem.

CORRECTED PROOF

Soc. 141 (2019) 7223–7234, https://doi.org/10.1021/jacs.9b00733.
[16] J. Liu, L. Chen, H. Cui, J. Zhang, L. Zhang, C.-Y. Su, Applications of metal–organic frameworks in heterogeneous supramolecular catalysis, Chem. Soc. Rev. 43 (2014) 6011–6061, https://doi.org/10.1039/C4CS00094C.
[17] K. Berijani, A. Morsali, The role of metal–organic porous frameworks in dual catalysis, Inorg. Chem. Front. 8 (2021) 3618–3658, https://doi.org/10.1039/D1QI00394A.
[18] H. Furukawa, K.E. Cordova, M. O'Keeffe, O.M. Yaghi, The chemistry and applications of metal-organic frameworks, Science 341 (2013), https://doi.org/10.1126/science.1230444.
[19] L. Chen, X. Zhang, X. Cheng, Z. Xie, Q. Kuang, L. Zheng, The function of metal–organic frameworks in the application of MOF-based composites, Nanoscale Adv. 2 (2020) 2628–2647, https://doi.org/10.1039/D0NA00184H.
[20] G. Vasseur, Y. Fagot-Revurat, B. Kierren, M. Sicot, D. Malterre, Effect of symmetry breaking on electronic band structure: gap opening at the high symmetry points, Symmetry (Basel) 5 (2013) 344–354, https://doi.org/10.3390/sym5040344.
[21] P.A. Cox, The Electronic Structure and Chemistry of Solids, Oxford University Press, Oxford, 1987.
[22] A.K. Das, N. Sepay, S. Nandy, A. Ghatak, S. Bhar, Catalytic efficiency of β-cyclodextrin hydrate-chemoselective reaction of indoles with aldehydes in aqueous medium, Tetrahedron Lett. 61 (2020) 152231, https://doi.org/10.1016/j.tetlet.2020.152231.
[23] A.K. Das, S. Nandy, S. Bhar, Chemoselective and ligand-free aerobic oxidation of benzylic alcohols to carbonyl compounds using alumina-supported mesoporous nickel nanoparticle as an efficient recyclable heterogeneous catalyst, Appl. Organomet. Chem. 35 (2021), https://doi.org/10.1002/aoc.6282.
[24] S. Nandy, A.K. Das, S. Bhar, Chemoselective formation of C–N bond in wet acetonitrile using amberlyst ® -15(H) as a recyclable catalyst, Synth. Commun. 50 (2020) 3326–3336, https://doi.org/10.1080/00397911.2020.1801745.
[25] W. Kabsch, XDS, Acta Crystallogr. Sect. D Biol. 66 (2010) 125–132, https://doi.org/10.1107/S0907444909047337.
[26] M.C. Burla, R. Caliandro, B. Carrozzini, G.L. Cascarano, C. Cuocci, C. Giacovazzo, M. Mallamo, A. Mazzone, G. Polidori, Crystal structure determination and refinement via SIR2014, J. Appl. Crystallogr. 48 (2015) 306–309, https://doi.org/10.1107/S1600576715001132.
[27] G.M. Sheldrick, A short history of SHELX, Acta Crystallogr. Sect. A Found. Crystallogr. 64 (2008) 112–122, https://doi.org/10.1107/S0108767307043930.
[28] V.A. Blatov, A.P. Shevchenko, D.M. Proserpio, Applied Topological analysis of crystal structures with the program package ToposPro, Cryst. Growth Des. 14 (2014) 3576–3586, https://doi.org/10.1021/cg500498k.
[29] M. O'Keeffe, M.A. Peskov, S.J. Ramsden, O.M. Yaghi, The reticular chemistry structure resource (RCSR) database of, and symbols for, crystal nets, Acc. Chem. Res. 41 (2008) 1782–1789, https://doi.org/10.1021/ar800124u.
[30] E.V. Alexandrov, V.A. Blatov, A.V. Kochetkov, D.M. Proserpio, Underlying nets in three-periodic coordination polymers: topology, taxonomy and prediction from a computer-aided analysis of the Cambridge structural database, CrystEngComm 13 (2011) 3947, https://doi.org/10.1039/c0ce00636j.
[31] M.A. Spackman, D. Jayatilaka, Hirshfeld surface analysis, CrystEngComm 11 (2009) 19–32, https://doi.org/10.1039/B818330A.
[32] S.K. Seth, D. Sarkar, A. Roy, T. Kar, Insight into supramolecular self-assembly directed by weak interactions in acetophenone derivatives: crystal structures and Hirshfeld surface analyses, CrystEngComm 13 (2011) 6728, https://doi.org/10.1039/c1ce05670k.
[33] S.J. Clark, M.D. Segall, C.J. Pickard, P.J. Hasnip, M.I.J. Probert, K. Refson, M.C. Payne, First principles methods using CASTEP, Z. Krist. - Cryst. Mater. 220 (2005) 567–570, https://doi.org/10.1524/zkri.220.5.567.65075.
[34] J.P. Perdew, Y. Wang, Accurate and simple analytic representation of the electron-gas correlation energy, Phys. Rev. B 45 (1992) 13244–13249, https://doi.org/10.1103/PhysRevB.45.13244.

CORRECTED PROOF

Journal of Molecular Structure xxx (xxxx) 138561

Contents lists available at ScienceDirect

Journal of Molecular Structure

journal homepage: www.elsevier.com/locate/molstruc

Structural geometry, electronic properties and pre-clinical evaluation of antibacterial compounds from lichen-associated *Streptomyces mobaraensis* DRM1 and *Nocardiopsis synnemataformans* DRM2

Vishnu Raja Vijayakumar [a], Priyanka Jayam Rajendran [a], Poornimaa M. [b], Ramanathan K. [b], Tanmoy Saha [c], Saurabh Das [c], Dhanasekaran Dharumadurai [a, *]

[a] *Department of Microbiology, School of Life Sciences, Bharathidasan University, Tiruchirappalli – 620 024, Tamil Nadu, India*
[b] *Department of Biotechnology, School of Bio Sciences and Technology (SBST), Vellore Institute of Technology, Vellore 632 014 Tamil Nadu, India*
[c] *Department of Chemistry (Inorganic Chemistry), Jadavpur University, Kolkata 700 032 West Bengal, India*

ARTICLE INFO

Keywords:
Phenol
2,4-bis(1,1-dimethylethyl)
Lupeol
Lichen
Actinobiont
NBO analysis
Molecular dynamic simulation

ABSTRACT

Antibacterial compounds Phenol, 2,4-bis(1,1-dimethylethyl) and Lupeol obtained from lichen-associated *Streptomyces mobaraensis* DRM1 and *Nocardiopsis synnemataformans* DRM2 respectively. The geometry, electronic properties and binding affinities of antibacterial compound Phenol, 2,4-bis(1,1-dimethylethyl) and Lupeol was determined. The *in silico* molecular mechanics of bacterial growth inhibition by Phenol, 2,4-bis(1,1-dimethylethyl) and Lupeol was established in *Pseudomonas aeroginosa* and *Salmonella typhi* by molecular docking, molecular simulation approach. The bacterial growth is inhibited by inactivating the vital enzyme PqsA and actin in bacterial system of *Pseudomonas* and *Salmonella*. The antibacterial compound produced by lichen associated actinobiont are adhere to Lipinski rule 5 and established criteria for drug likeness with the acceptable ADME properties and expand our understanding of their pharmacological approach. Further it also revels the adaptation and survival lichen in adverse climatic condition through the antimicrobials in lichen-associated actinobiont.

1. Introduction

The research delves into lichens, distinctive symbiotic associations between fungi and algae or cyanobacteria that are renowned for thriving in extreme environments worldwide. Current inquiries in the field of medicinal chemistry have concentrated on the analysis of natural compounds derived from various biological sources, including lichens. Phenolic-type compounds found in lichens, such as depsides, depsidones, depsones, lactones, dibenzofurans, anthraquinones, pulvinic acid derivatives, and xanthones, have demonstrated a diverse array of bioactivities. These encompass antioxidant, anti-inflammatory, anticancer, antimutagenic, and antifungal properties [1].

The discovery of these bioactive compounds within lichens emphasizes their potential as promising contenders for the creation of novel therapeutic agents in medicine. This underscores the significance of exploring natural products derived from diverse biological sources. Lichens produce distinctive compounds crucial for identification, yet computational studies on these compounds are limited [2]. Therefore, the present research planned to explore lichen antibacterial compounds by systematically investigating molecular properties using computational methods like density functional theory (DFT), including optimized geometry, frontier molecular orbital, molecular electrostatic potential, NBO analysis, ADME properties, molecular docking, and molecular dynamic simulation. DFT proves versatile for electronic structure calculations [3], making it a valuable tool in understanding molecular systems efficiently [4]. Frontier molecular orbital (FMO) analysis examines a molecule's electron-donating and -accepting potential, influencing reactivity. Molecular electrostatic potential (MEP) visualizes electric charge distribution, aiding predictions of chemical reactivity. Natural bond orbital (NBO) analysis provides insights into chemical bonding, offering details about electron delocalization and interactions study [5]. ADME properties (Absorption, Distribution, Metabolism, Excretion) are critical in drug development, influencing effectiveness and safety [6].

The *in silico* exploration does not stop at structural and electronic analyses; it extends to understanding the antibacterial action mechanism through molecular docking and molecular dynamic simulation [7]. Molecular docking allows us to predict the binding interactions be-

* Corresponding author.
E-mail address: ddhanasekaran@bdu.ac.in (D. Dharumadurai).

https://doi.org/10.1016/j.molstruc.2024.138561
Received 16 March 2024; Received in revised form 24 April 2024; Accepted 5 May 2024
0022-2860/© 20XX

CORRECTED PROOF

Note: Low-resolution images were used to create this PDF. The original images will be used in the final composition.

tween the antibacterial compound and specific bacterial targets. Following this, molecular dynamic simulation delivers a dynamic interpretation of the compound's behaviour over time, providing valuable insights into its stability and conformational changes during interactions. This interdisciplinary approach contributes to antimicrobial research, potentially reforming antibacterial interventions. This complete approach aims to bridge the gap between theoretical insights and practical applications, facilitating a pre-clinical evaluation of the antibacterial compound. The integration of computational methods allows for a thorough examination of the compound's potential as a therapeutic agent against bacterial pathogens. Through this interdisciplinary endeavour, we strive to unlock new dimensions in antimicrobial research, fostering a deeper understanding of the compounds that hold promise in reshaping the landscape of antibacterial interventions. This computational path in lichen associated microbes, rooted in DFT principles, enhances our comprehension of the molecular aspects of antibacterial, paving the way for informed exploration of their diverse functionalities and applications in fields such as medicine, ecology, and materials science.

2. Materials and methods

2.1. Antibacterial compounds

The antibacterial compounds obtained from lichen-associated *S. mobaraensis* DRM1 and *N. synnemataformans* DRM2. Further, the compound was characterized, identified and used for the preclinical evaluation. The molecular structure of the antibacterial compound was determined through the elucidation of spectral data, including FT-IR, GC–MS, ^{1}H NMR, ^{13}C NMR, and Mass spectrometry. By analyzing these spectral data, the molecular formula and weight of the antibacterial compound were successfully determined as Phenol, 2,4-bis(1,1-dimethylethyl) and Lupeol.

2.2. Antibacterial activity

The subsequent pathogenic bacterial cultures were obtained from Bioprocess Technology Laboratory (BPTL), Department of Microbiology, Bharathidasan University, Tiruchirappalli. Multidrug-resistant bacteria(MDR) are resistant to three or more classes of antimicrobial drugs. MDR bacteria have seen an increase in prevalence in recent years and pose serious risks to public health. Therefore, we have chosen the Multidrug-resistant Gram-positive, Gram-negative clinical isolates in the experiment. The clinical isolates including the Gram-positive bacteria: *Staphylococcus aureus, Staphylococcus epidermis, Bacillus subtilis,* Gram-negative bacteria: *E. coli, S. typhi, Pseudomonas aeroginosa, Proteus vulgaris,* and *Proteus mirabilis.* Bacterial inoculum was prepared using Muller Hinton broth (MHB). The initial evaluation of antibacterial efficacy of the antibacterial compound such as Phenol, 2,4-bis(1,1-dimethylethyl) and Lupeol, involved the use of agar well diffusion method. The isolates were inoculated along the diameter on Mueller Hinton broth (MHB) for bacteria. Bacterial pathogens were uniformly spread across the plates using a sterile swab, and 4 to 5 wells were created using a well cutter. Different concentrations of Phenol, 2,4-bis(1,1-dimethylethyl) and Lupeol extracts were added to the wells, and the plates were subsequently incubated at 28 ˚C for a duration of 24 hrs. In the antibacterial evaluation, Streptomycin acted as the positive control. Acetone was used as the negative control. Following the incubation period, the plates were inspected, and the size of inhibition zones was measured and recorded.

2.3. Computational methodology

Density Functional Theory (DFT) was employed for the computation of electronic structures of the molecule, utilizing the Gaussian 09 program for DFT calculations. The standard 6–31G + (d,p) basis set was employed for the elements C, H, and O, along with the Becke three-parameter hybrid functional and Lee-Yang-gradient Parr's corrected correlation functional (B3LYP) [8]. To address the long-range dispersion effect, both Grimes' third-order correction for dispersion and Becke-Johnson damping (GD3BJ) were utilized. The geometries in the ground state (S0) of Phenol, 2,4-bis(1,1-dimethylethyl), and Lupeol were thoroughly optimized, adhering to the program's stringent convergence criteria.

Frequency determinations were conducted on the optimized geometries in the gaseous state, ensuring that all vibrational frequencies were positive to validate the global minimum of the stationary points. Gauss View was utilized to examine molecular orbital (MO) orbitals and the molecular electrostatic potential (MEP) surface. To comprehend various second-order interactions between the filled orbitals of one subsystem and vacant orbitals of another subsystem, indicative of intramolecular delocalization or hyperconjugation, natural bond orbital (NBO) calculations were performed using the NBO 3.1 program implemented in the Gaussian 09 package at the DFT/B3LYP/6–31G + (d,p) level [9].

Moreover, calculations were performed to determine the dipole moment and polarizability of the molecules. Quantum mechanical descriptors, such as the energy gap (E) between molecular orbitals, ionization potential (IP), electron affinity (EA), electronegativity (χ), chemical hardness (η), mean energy (M), chemical potential (μ), chemical softness (σ), and electrophilicity index (ω), were derived using the energies of the frontier molecular orbitals. The values for these descriptors were computed utilizing the formulas [10].

$$\Delta E = E_{LUMO} - E_{HOMO} \quad (1)$$

$$IP = -E_{HOMO} \quad (2)$$

$$EA = -E_{LUMO} \quad (3)$$

$$\chi = -\mu = (IP + EA)/2 \quad (4)$$

$$\eta = \Delta E/2 \quad (5)$$

$$\sigma = 1/\eta \quad (6)$$

$$\omega = \chi^2/2\eta \quad (7)$$

$$M = -\chi \quad (8)$$

2.4. Molecular docking and MM-GBSA calculations

Initially, to begin with, the protein data bank (PDB) IDs of enzymes sourced from various bacterial species were obtained from the Protein Data Bank repository. Subsequently, each protein, along with the two ligands, underwent pre-processing utilizing the Protein Preparation Wizard and LigPrep module. This step was crucial to eliminate any ambiguity in the 3D structure. Additionally, the pharmacokinetic and pharmacodynamic properties of both ligands were assessed using QikProp. The active sites of each protein were identified using SiteMap, and the corresponding coordinates were employed for the molecular docking process. Subsequently, the resulting compounds underwent revalidation through Prime MM-GBSA analysis. Comprehensive details of these methods were previously elucidated in our published articles [11].

2.5. Molecular dynamic simulation

Molecular dynamic simulation was conducted to examine the stability and conformational orientation of the lead complexes. In this study, simulations involving PqsA-Streptomycin (Reference), PqsA-Lupeol, and PqsA-Phenol, 2,4-bis(1,1-dimethylethyl) were executed using GROMACS 2020.2 and the CHARMM force field [12,13]. The simulation system was configured within a cubic box, incorporating a solvation shell of simple point charge (SPC) water molecules. The edges of the box were defined at a distance of 1.0 nm from the center [14]. The simulation system was neutralized by adding 4 sodium counterions. The steepest descent algorithm was employed to minimize the structure in

CORRECTED PROOF

each simulation run. Subsequently, the system underwent equilibration for 100 ps, operating in an ensemble with constant volume (NVT) at 300 K and constant pressure (NPT) at 1 atm. To restrict all bond lengths, the LINCS algorithm was utilized [15]. The maintenance of pressure and temperature was achieved using the V-rescale algorithm for temperature control and the Parrinello-Rahman algorithm for pressure control [16]. Long-range electrostatics were addressed utilizing the Particle Mesh Ewald (PME) strategy, while van der Waals interactions were computed with a cutoff of 1.4 nm. The equilibrated structures then underwent a 50 ns molecular dynamics (MD) simulation with a time step of 2 fs. Atomic coordinates were recorded every 10 ps for subsequent analysis. Structural analysis of both the reference and lead compounds was conducted using the built-in tools of the GROMACS software. Parameters such as root mean square deviation, root mean square fluctuation, and hydrogen bond interactions were considered in the analysis.

3. Result and discussion

3.1. Antibacterial activity

The antibacterial compound Phenol, 2,4-bis(1,1-dimethylethyl) and Lupeol were tested against six bacterial pathogens such as *P. vulgaris, E. coli, P. aeruginosa, B. subtilis, S. epidermis* and *S. typhi*. Two concentrations were taken such as 50 µl and 100 µl for antibacterial activity. Phenol, 2,4-bis(1,1-dimethylethyl) showed antibacterial activity against *P. vulgaris* (23 mm and 24 mm) *and S. typhi* (13 mm and 17 mm) respectively for Lupeol, *P. vulgaris* (6 mm and 6 mm), *B. subtilis* (21 mm) and *S. epidermis* (21 mm) showed more zone of inhibition at 100 µl concentration. Based on the results, *P. aeruginosa* at 100 µl concentration of both compounds showed zone of inhibition at 14 mm and 13 mm. *P. aeruginosa* is justifiably chosen for *in silico* studies for further investigation.

3.2. Optimized geometry

The antibacterial compounds obtained from lichen-associated *S. mobaraensis* DRM1 and *N. synnemataformans* DRM2 were optimized at the B3LYP level using the 6–31G + (d,p) basis set. S1 and S2 depict the optimized geometry of Phenol, 2,4-bis(1,1-dimethylethyl), and Lupeol obtained from *S. mobaraensis* DRM1 and *N. synnemataformans* DRM2, respectively. After optimization, Phenol, 2,4-bis(1,1-dimethylethyl), exhibited an energy level of −16,920.41 eV. The molecule demonstrated a polarizability of 146.62 atomic units, accompanied by a dipole moment of 2.17 Debye. Conversely, Lupeol displayed an energy of −32,895.29 eV, with a polarizability of 290.28 atomic units and a dipole moment of 1.83 Debye. Both molecules belong to the C1 point group.

This investigation explores the optimization of Phenol, 2,4-bis(1,1-dimethylethyl), and Lupeol, exposing their unique electronic characteristics. Phenol, 2,4-bis(1,1-dimethylethyl) displays an energy of −16,920.41 eV, a polarizability of 146.62 a.u., and a dipole moment of 2.17 Debye, while Lupeol exhibits an energy of −32,895.29 eV, a polarizability of 290.28 a.u., and a dipole moment of 1.83 Debye. [17] found that the dipole moment of lupeol is 1.10 Debye.

3.3. Frontier molecular orbitals

The excitation properties and electron transport capabilities may be qualitatively anticipated using the frontier molecular orbitals. Electronic absorption refers to the process of transitioning from the ground state to the first excited state, primarily marked by the movement of one electron from the highest occupied molecular orbital (HOMO) to the lowest unoccupied molecular orbital (LUMO). Essentially, the HOMO orbital serves as the electron donor, while the LUMO orbital acts as the electron acceptor. The chemical activity of the molecules is reflected in the energy levels of HOMO and LUMO as well as their energy gap. Table 1 and 2 reflects selected HOMOs and LUMOs energies of Phenol, 2,4-bis(1,1-dimethylethyl) and Lupeol respectively. Fig. 1 and 2 shows the HOMO to HOMO-4, and LUMO to LUMO + 4 orbitals computed at the B3LYP/6–31 + *G*(d,p) level for Phenol, 2,4-bis(1,1-dimethylethyl) and Lupeol. For Phenol, 2,4-bis(1,1-dimethylethyl) HOMO and LUMO energies were predicted as −5.81 eV and 0.23 eV and the energy gap between the HOMO and LUMO orbitals was found as 5.57 eV (Fig. 3 and Table 1). For Lupeol HOMO and LUMO energies were predicted as −6.68 eV and 0.61 eV and the energy gap between the HOMO and LUMO orbitals was found as 6.06 eV (Fig. 4 and Table 2).

The analysis of frontier molecular orbitals (FMOs), focusing on the Highest Occupied Molecular Orbital (HOMO) and lowest unoccupied molecular orbital (LUMO), provides insights into how a molecule interacts with other species. For Phenol, 2,4-bis(1,1-dimethylethyl), and Lupeol, specific HOMO and LUMO energies, along with the calculated energy gaps, were determined. Phenol exhibits HOMO and LUMO energies of −5.81 eV and 0.23 eV, resulting in an energy gap of 5.57 eV. In contrast, Lupeol displays HOMO and LUMO energies of −6.68 eV and 0.61 eV, with an energy gap of 6.06 eV. These values offer valuable insights into the electronic structure and reactivity of the molecules based on their energy levels. A study by [17] reported HOMO and LUMO energies of −6.33 eV and −0.83 eV, with an energy gap of 7.16 eV. Meanwhile, [18] utilized Koopmans's theorem to derive theoretical concepts such as chemical potential, hardness, electrophilicity, and electronegativity from FMOs. Their research indicated a small energy gap of 3.52 eV for the HAQ molecule, calculated using the B3LYP method, suggesting stability and reactivity comparable to reported bioactive molecules.

3.4. Molecular electrostatic potential

The molecular electrostatic potential (MEP) serves as a crucial descriptor associated with electronic density, providing valuable insights into identifying sites for electrophilic and nucleophilic reactions, as

Table 1
HOMO-LUMO values of Phenol, 2,4-bis(1,1-dimethylethyl) obtained from *Streptomyces mobaraensis* DRM1.

Serial Number	Molecular Orbital	Energy (eV)
62	LUMO + 4	2.80
61	LUMO + 3	2.55
60	LUMO + 2	1.53
59	LUMO + 1	0.40
58	LUMO	0.23
57	HOMO	−5.81
56	HOMO-1	−6.42
55	HOMO-2	−8.10
54	HOMO-3	−8.35
53	HOMO-4	−8.55

Table 2
HOMO-LUMO values of Lupeol from *Nocardiopsis synnemataformans* DRM2.

Serial Number	Molecular Orbital	Energy (eV)
120	LUMO + 4	2.23
119	LUMO + 3	2.15
118	LUMO + 2	1.99
117	LUMO + 1	1.60
116	LUMO	0.61
115	HOMO	−6.68
114	HOMO-1	−6.83
113	HOMO-2	−7.00
112	HOMO-3	−7.12
111	HOMO-4	−7.65

CORRECTED PROOF

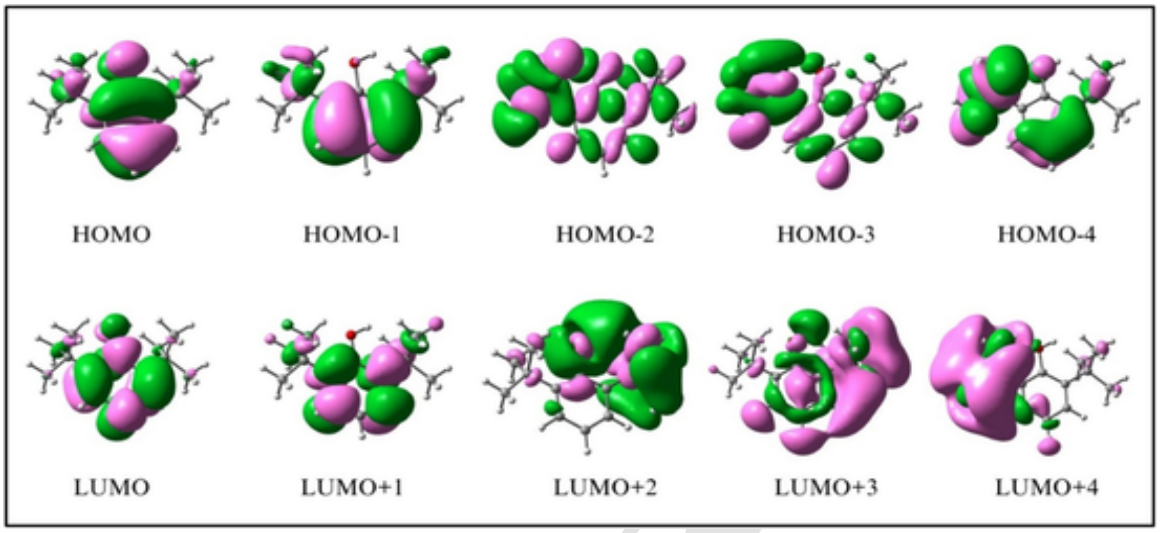


Fig. 1. The frontier molecular orbitals (FMOs) of the optimized geometry of Phenol, 2,4-bis(1,1-dimethylethyl).

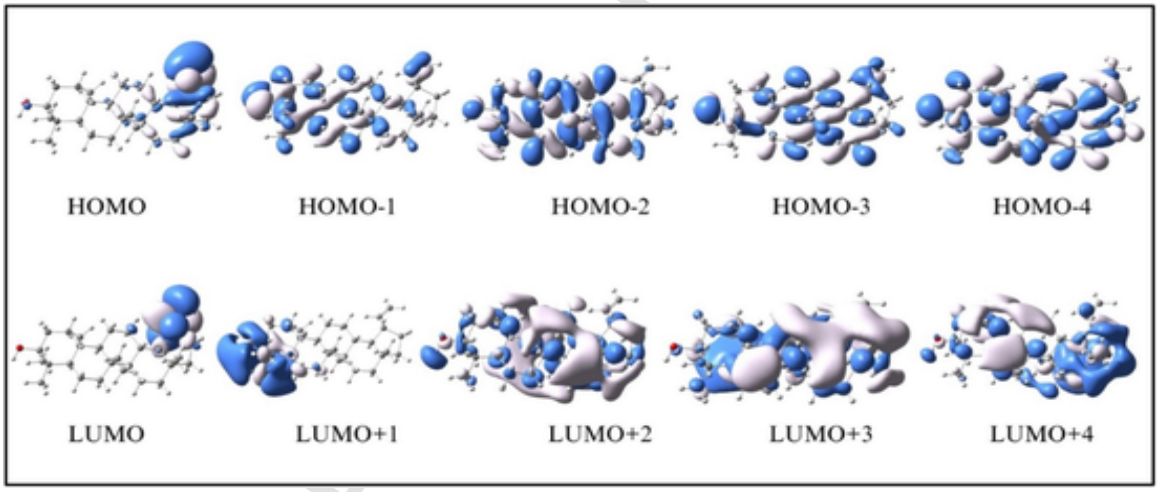


Fig. 2. The frontier molecular orbitals (FMOs) of the optimized geometry of Lupeol.

well as hydrogen-bonding interactions. In this study, MEP was employed to anticipate reactive sites susceptible to electrophilic or nucleophilic attacks within the examined molecule. Fig. 5 visually depicts the charge distributions of the molecule in three dimensions. The color-coded representation illustrates various values of the electrostatic potential at the surface: red signifies areas with the highest electronegative potential, blue designates regions with the highest positive potential, and green represents areas with zero potential. The potential progression is as follows: red < orange < yellow < green < blue. These color maps range from the deepest red (−150.86 kJ/mol) to the profoundest blue (160.16 kJ/mol), where blue denotes the strongest attraction and red denotes the strongest repulsion. Typically, regions associated with the lone pair of electronegative atoms exhibit negative potential. In the analyzed molecule, negative regions were identified around the oxygen atoms of the hydroxy group, as indicated by the MEP map of Phenol, 2,4-bis(1,1-dimethylethyl), and Lupeol. Conversely, the maximum positive regions are situated on the hydrogen atoms of the O—H groups, indicating potential sites for nucleophilic attack, with a maximum value of +160.16 kJ/mol. This information provides valuable insights into the reactivity and potential interactions of the studied molecule.

[19] reported that Molecular Electrostatic Potential (MEP) calculations at the B3LYP/6–31G(d,p) optimized geometry revealed distinctive electrostatic profiles in the investigated molecule. Negative regions concentrated over C = O bonds in anthraquinone and aldehyde groups indicated electrophilic reactivity, while positive regions predominating over C—C bonds in molecular rings suggested nucleophilic reactivity. Simultaneously, a color-coded electrostatic potential map demonstrated the variation in the molecular surface, highlighting negative potential around oxygen atoms in the hydroxy group and pinpointing maximum positive regions on hydrogen atoms of O—H groups. These findings provide valuable insights into potential sites for nucleophilic attacks, with a peak value of +160.16 kJ/mol.

3.5. NBO analysis

Natural bond orbital (NBO) calculations were carried out using the NBO 3.1 programme as implemented in the Gaussian 09 package at the DFT/B3LYP/6–31 + *G*(d,p) level in order to comprehend various sec-

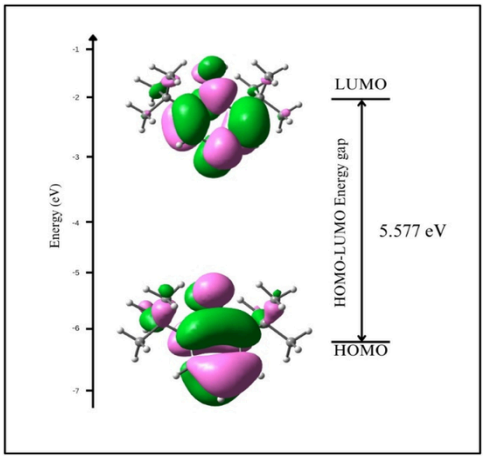


Fig. 3. HOMO-LUMO energy gap of Phenol, 2,4-bis(1,1-dimethylethyl).

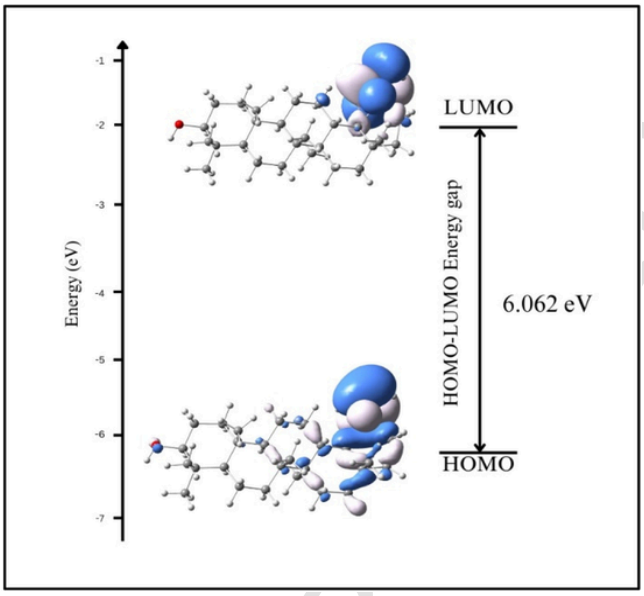


Fig. 4. HOMO-LUMO energy gap of Lupeol.

ond-order interactions between the filled orbital of one subsystem and the vacant orbital of another subsystem, which is a measure of the intermolecular delocalization or hyperconjugation. Because every orbital detail is mathematically selected to include the largest possible percentage of the electron density, NBO analysis delivers the most accurate 'natural Lewis structure' depiction of 'j'. The NBO approach has the advantage of providing data on interactions between filled and virtual orbital spaces, which could improve the analysis of intra-inter molecular interactions. Evaluation of the donor-acceptor interactions in the NBO basis was done using the second-order Fock matrix. As a result of the interactions, the localized Lewis structure's NBO loses its occupancy, turning it into an empty non-Lewis orbital. The stabilisation energy (E2) resulting from the delocalization i→j is calculated for each donor (i) and acceptor (j) as follows (Eq (9))

$$E(2) = \Delta E_{ij} = q_i \frac{\mathrm{F(i,j)}^2}{\epsilon_\mathrm{j} - \epsilon_\mathrm{i}} \tag{9}$$

The donor orbital occupancy is denoted by qi, while Ei and Ej represent the diagonal elements. Fij represents the off-diagonal NBO Fock matrix element. A substantial E(2) value in NBO analysis signifies strong contact between electron donors and acceptors, enhancing the overall system's conjugation. The potential for robust interactions is revealed through the examination of strong intramolecular hyperconjugative interactions of the p electrons, as demonstrated by the NBO basis Fock matrix analysis using second-order perturbation theory.

3.5.1. Phenol, 2,4-bis(1,1-dimethylethyl)

Intermolecular hyperconjugative interactions result from the overlap of orbitals, including bonding (C – C), (O–C), (O–H), and (C–C), as well as anti-bonding (C–C), (C–H), (*O – H*) orbitals. This overlapping leads to intramolecular charge transfer (ICT), stabilizing the molecular system and increasing electron density (ED) in the antibonding orbitals of (O–C), (O–H), and (C–C), thereby weakening the respective bonds. For instance, the intermolecular hyperconjugative interaction of σ (C5–C6) contributes to σ∗(C1–C2), resulting in a stabilization of 178.93 Kcal/mol. This extended conjugation with the anti-bonding orbital of σ*(C3–C4) leads to a strong delocalization of 252.79 Kcal/mol.

The extent of charge transfer from O7n(1) to the anti-bonding σ∗(C5–H6) and O3n(2) to the anti-bonding σ∗(C5–H6) indicates stabilization energies of 5.43 Kcal/mol and 24.03 Kcal/mol, respectively. (Supplementary Table 1 and 2)

3.5.2. Lupeol

Intermolecular hyperconjugative interactions arise from the overlapping of orbitals involving bonding (C – C), (O–C), (O–H), and (C–C), as well as anti-bonding (C–C), (C–H), and (*O – H*) orbitals. This overlap induces intramolecular charge transfer (ICT), leading to the stabilization of the molecular system and an increase in electron density (ED) in the antibonding orbitals of (O–C), (O–H), and (C–C), thereby weakening the corresponding bonds. An illustrative example is the intermolecular hyperconjugative interaction involving σ(C25–C66), which is transferred to σ∗(C26–C68), resulting in a stabilization of 101.56 kcal/mol. This heightened conjugation with σ(C26–C68) to an anti-bonding orbital of σ*(C25–C66) induces strong delocalization, contributing to a stabilization of 111.27 kcal/mol.

Furthermore, the magnitude of charge transfer from O22n(4) to the anti-bonding (C2–H3) σ∗ and from O22n(5) to the anti-bonding (C2–H33) σ∗ indicates stabilization energies of 6.42 kcal/mol and 6.17 kcal/mol, respectively (Supplementary Table 3 and 4). These findings highlight the significant role of intermolecular hyperconjugative interactions in influencing molecular stability and charge distribution within the studied system.

The investigation involves the application of natural bond orbital (NBO) analysis to Phenol and Lupeol molecules utilizing the Gaussian 09 package. Noteworthy sigma (σ) orbital interactions, specifically σ (C5–C6) to σ∗(C1–C2), play a substantial role in the molecular stabilization of Phenol, 2,4-bis(1,1-dimethylethyl). Similar hyperconjugative interactions are observed in Lupeol. Overall, the study enhances our understanding of the electronic structure and bonding patterns in Phenol, 2,4-bis(1,1-dimethylethyl) and Lupeol molecules. According to [5] suggests that local orbital interactions, particularly hyperconjugation, play a significant role in determining the spectral shifts observed in phenol-benzene complexes, while the overall electrostatics have a smaller impact. This understanding is derived from the analysis of NBO data and the correlation between hyperconjugation energies and experimental observations.

3.6. Quantum descriptor analysis

The importance of a molecule's highest occupied molecular orbital (HOMO) and lowest unoccupied molecular orbital (LUMO) stems from

CORRECTED PROOF

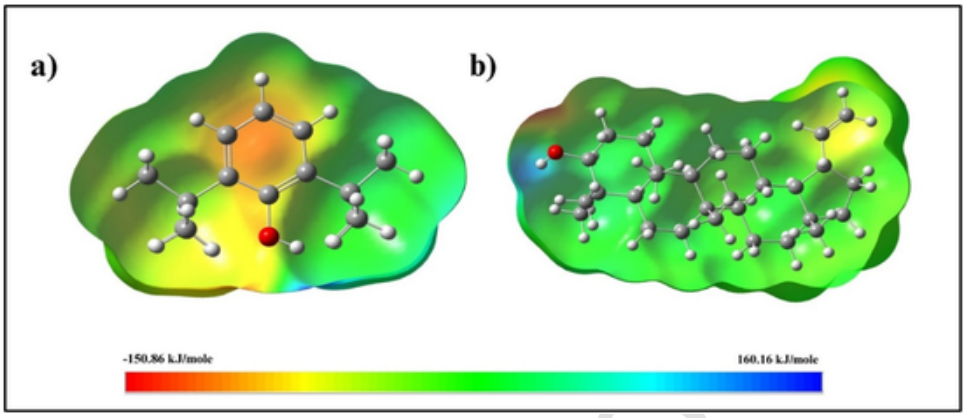


Fig. 5. Molecular electrostatic potential map of (a) Phenol, 2,4-bis(1,1-dimethylethyl) (b) Lupeol.

their crucial role in influencing the molecule's ability to acquire and donate electrons (Table 3).

3.7. ADME analysis

The pharmacokinetic/pharmacodynamic (PK/PD) properties of drug-like molecules play a vital role in the drug discovery process. In this study, the QikProp module of the Schrödinger software was utilized to assess the Absorption, Distribution, Metabolism, and Excretion (ADME) properties of Lupeol and Phenol, 2,4-bis(1,1-dimethylethyl). Table 4 reveals that both ligand molecules meet Lipinski's rule of five and Jorgensen's Rule-of-Three, indicating favourable characteristics in terms of drug-likeness. In addition, other features such as stars (≤ 5), human oral absorption (HOA > 80 %) and solubility (QPlogS –6.5 to –0.5) will be taken into consideration. Interestingly, both the ligand molecule possessed acceptable ADME properties. In their study, [20] noted that Lupeol was predicted to exhibit poor solubility (Log P = 7.27) with one molecular violation. The physicochemical properties of Lupeol suggest a likelihood of solubility issues, potentially leading to poor bioavailability and formulation challenges, as highlighted by [21]. On the other hand, [22] found that Phenol, 2,4-bis(1,1-dimethylethyl), meets all the criteria of absorption, distribution, metabolism, and excretion (ADME) as well as Lipinski's rule of 5, indicating favourable characteristics in terms of drug-likeness.

The drug-like molecules Lupeol and Phenol, 2,4-bis(1,1-dimethylethyl), underwent PK/PD analysis utilizing the QikProp module in the Schrödinger software. The findings indicate that both ligands adhere to Lipinski's rule of five and Jorgensen's Rule-of-Three, thereby meeting the established criteria for drug-likeness. Additional considerations, such as stars (≤ 5), human oral absorption (HOA > 80 %), and solubility (QPlogS –6.5 to –0.5), were taken into account, revealing that both ligands possess acceptable ADME properties. This comprehensive analysis yields valuable insights into the pharmacological potential and drug-likeness of the studied phytochemicals. Phytochemicals extracted from *Lecania brialmontii, Pseudephebe pubesecens*, and *Sphaerophorus globosus* were subjected to analysis using Osiris Data Warrior, and their properties were compared with galantamine. Evaluation against Lipinski's 'rule of five' indicated that tetrahydroxytricosanoic acid did not meet the specified criteria. Docking analysis revealed lower binding affinities for tetrahydroxytricosanoic acid. Pharmacokinetic properties, including acetylcholinesterase (TcAChE) and butyrylcholinesterase (hBChE) activity, were obtained through Osiris Data Warrior [1].

3.8. Molecular docking and MM-GBSA calculations

Molecular docking studies for various enzymes present in the bacterial species were conducted using the Glide interface within the Schrödinger suite. The binding affinities of all proteins from molecular docking were weighted using XP GScore.

[23], *Streptomyces albidoflavus* STV1572a was investigated, and 1-heneicosanol was identified as an inhibitor against the squalene epoxidase of *Tricophyton mentagrophytes*. The protein structures were modelled, validated, and selected for docking studies based on satisfactory scores (D4B2W4, D4AVJ0, A0A289Z3W9, D4ANN7, H6×152, and Q9Y736). The molecular docking results demonstrated favourable interactions of 1-heneicosanol with the target squalene epoxidase, yielding a Glide score of −8.666 kcal/mol and an MM-GBSA score of −105.85 kcal/mol. [24] focused on the "F0 ATP synthase subunit A" of Pithomyces chartarum, modelled using the template protein from *Saccharomyces cerevisiae*. [25] investigated the binding of 2,4-bis(1,1-dimethylethyl) to the LasR protein, reporting a docking score close to that of the natural ligand 3-Oxo-C12-HSL. Additionally, 1,2-benzenedicarboxylic acid, bis(2-methylpropyl) ester exhibited a strong docking score and formed two hydrogen bonds with Tyr-56 and Tyr-64. In the current study, *S. mobaraensis* DRM1-derived Phenol, 2,4-bis(1,1-dimethylethyl), was investigated as an inhibitor against Pyoverdines of *P. aeruginosa*. The modelled protein structures were validated, and structures with favourable scores (1E9Y_A, 1E9Y_B, 2GWL, 2P1W, 7EE3, 2ODJ, 2W78, 5XBW, and 5Z2V) were selected for docking studies. Molecular docking results revealed that Phenol, 2,4-bis(1,1-dimethylethyl), exhibited favourable interactions with the target Pyoverdines, yielding a Glide score of −5.330 kcal/mol and an MM-GBSA score of −29.232 kcal/mol. Comparatively, [23] obtained a Glide score of −6.201 kcal/mol and an MM-GBSA score of −40.248 kcal/mol in their study, while [24] reported a docking score of −5.355 kcal/mol and a binding free energy of −40.11 in their investigation.

In our study, we investigated *N. synnemataformans* DRM2-derived lupeol as an inhibitor against the PqsA enzyme of *P. aeruginosa*. Mod-

Table 3
Quantum characteristics for Phenol, 2,4-bis(1,1-dimethylethyl), and Lupeol were computed in electron volts (eV) using the B3LYP-631G+ (d,p) functional.

Compound	HOMO	LUMO	ΔE	IP	EA	χ	η	M	σ	Ω
Phenol, 2,4-bis(1,1-dimethylethyl)	−5.81	0.23	5.58	5.81	−0.23	2.79	2.79	−2.79	0.35	1.35
Lupeol	−6.68	0.61	6.07	6.68	−0.61	3.03	3.03	−3.03	0.33	1.51

Table 4
ADME properties of Lupeol and Phenol, 2,4-bis (1,1-diemethylethyl) from *Streptomyces mobaraensis* DRM1 and *Nocardiopsis synnemataformans* DRM2.

S. No.	Compound Name	Rule of Five	Rule of Three	Stars	Human Oral Absorption (%)	QPlogS
1.	Lupeol	1	0	5	100	−6.021
2.	Phenol, 2,4-bis (1,1-diemethylethyl)	0	0	2	100	−3.991

elled protein structures were endorsed, and structures with suitable scores (1E9Y_A, 1E9Y_B, 2GWL, 2P1W, 7EE3, 2ODJ, 2W78, 5XBW, and 5Z2V) were selected for docking studies. The molecular docking results revealed that lupeol exhibited favourable interactions with the target PqsA, with a Glide score of −3.452 kcal/mol and MM-GBSA score of −41.434 kcal/mol. In a study by [26], lupeol showed the highest binding affinity with cyclooxygenase-2 (COX-2) (−11.6 kcal/mol) and Myeloperoxidase (MPO) (−9.0 kcal/mol) compared to indomethacin, attributed to alkyl and hydrogen-bonded interactions with COX-2 and MPO residues. Lupeol also demonstrated the highest binding affinity with three cytokine targets, TNF-α (−8.4 kcal/mol), IL-1β (−6.9 kcal/mol), and IL-6 (−7.0 kcal/mol), compared to the reference standard indomethacin. [27] reported that lupeol prominently exhibited alkyl interactions and no hydrogen bonds, with a relatively high energy of −7.2 kcal/mol against the RdRp protein.

The results of molecular docking for the hit compounds with all the protein structures were organized in Table 5. The XP scores of the small molecules for different proteins ranged from −3.452 kcal/mol to −1.062 kcal/mol. Notably, the PqsA Enzyme (PDB ID: 5Z2V) from *P. aeruginosa* demonstrated a superior binding affinity of −3.452 kcal/mol. Additionally, the docking protocol was reassessed using the Prime MM-GBSA module, where the post-viewer file from XP docking was utilized for binding free energy calculations. It is noteworthy that Lupeol exhibited lower binding energy with the PqsA enzyme and actin enzyme from *P. aeruginosa* and *S. typhi*, respectively. Furthermore, the interaction scheme of Lupeol with the aforementioned proteins was analysed using PLIP software [28]. The binding poses and interaction patterns of Lupeol were emphasized in Fig. 6. The figure illustrates that Lupeol is capable of forming hydrogen bonding and hydrophobic interactions with key residues in both protein structures. Taken together, the evidence presented indicates the stable binding of Lupeol with the PqsA enzyme and actin enzyme from *P. aeruginosa* and *S. typhi*, respectively.

The Glide interface in the Schrödinger suite was employed for molecular docking studies on various enzymes in bacterial species. XP GScore was used to evaluate binding affinities, with PqsA Enzyme (PDB ID: 5Z2V) from *P. aeruginosa* displaying the best affinity at −3.452 kcal/mol. The docking protocol was re-evaluated using the Prime MM-GBSA module, revealing that Lupeol demonstrated a lower binding energy with both the PqsA enzyme from *P. aeruginosa* and the actin enzyme from *S. typhi*, respectively. Interaction analysis with PLIP software highlighted hydrogen bonding and hydrophobic interactions, indicating a stable binding of Lupeol with the mentioned proteins. The molecular docking analysis evaluated the binding affinity of eight cyanobacterial ligands with the CNR1 protein, as reported by [7]. Among the ligands, Symplocamide A exhibited the highest docking score (−7.350 kcal/mol) and the most favorable MM-GBSA binding free energy (−86.97 kcal/mol).

3.9. Molecular dynamic simulation

3.9.1. RMSD

A 50 ns molecular dynamics simulation was conducted to elucidate the structural behaviour of hit compounds within the catalytic cavity of PqsA, as detailed by [29]. The RMSD graph was employed to scrutinize the dynamics of the PqsA protein in complex with Streptomycin and lead compounds, Lupeol, and Phenol, 2,4-bis(1,1-dimethylethyl). Throughout the study, Streptomycin, the reference compound, was represented in black. Fig. 7(a) illustrates that all complexes maintained a stable backbone RMSD with low structural fluctuations during the simulation. The average RMSD values for Streptomycin, Lupeol, and Phenol, 2,4-bis(1,1-dimethylethyl) at the end of the 50 ns simulation were approximately ~1.19 nm, ~1.19 nm, and ~1.16 nm, respectively. These values, being less than 2 Å, suggest the stable nature of the PqsA protein upon ligand binding.

The identified compounds (Lupeol and Phenol, 2,4-bis(1,1-dimethylethyl)) are proposed to exhibit a similar inhibitory potential as Streptomycin against the PqsA protein. This observation aligns with previous studies, where [24] noted the stability of the interacted ligand-receptor complex (ATP synthase), [26] reported an average RMSD value for Lupeol of 4.36 Å, and [27] found that the Lupeol-protein complex initially deviated by 1.5 nm up to 20 ns and stabilized after 30 ns, with an RMSD reaching around 1 nm.

The 50 ns molecular dynamics simulation demonstrates the stable structural behaviour of PqsA in complex with Streptomycin, Lupeol, and Phenol, 2,4-bis(1,1-dimethylethyl). Overall, Lupeol and Phenol, 2,4-bis(1,1-dimethylethyl), show inhibitory potential against PqsA comparable to Streptomycin. The docking results reveal favourable interactions, especially with Lupeol exhibiting strong binding to PqsA and actin enzymes. The Prime MM-GBSA re-evaluation confirms Lupeol's stable binding. PLIP analysis further unveils hydrogen bonding and hydrophobic interactions in Lupeol-protein complexes. In summary, lupeol, calycin, and rhizocarpic acid exhibit promise as ligands for potential drug development, as reported by [30].

Table 5
The binding energetics of molecular docking and MM-GBSA for the hit molecules.

S. No.	Bacterial species	PDB ID	Enzymes	Lupeol		Phenol, 2,4-bis(1,1-dimethylethyl)	
				Glide XP GScore (kcal/mol)	MM-GBSA dG bind (kcal/mol)	Glide XP GScore (kcal/mol)	MM-GBSA dG bind (kcal/mol)
1.	*Proteus vulgaris*	1E9Y_A	Urease (alpha subunit) enzyme	−3.156	−26.345	−2.736	−25.513
		1E9Y_B	Urease (beta subunit) enzyme	−1.908	−4.700	−3.589	−15.589
2.	*S typhi*	2GWL	Actin	−3.429	−36.731	−2.643	−29.933
		2P1W	Phosphothreonine lyase	−1.062	−27.384	−4.299	−25.032
		7EE3	PltB Protein	–	–	−3.359	7.757
3.	*Pseudomonas aeruginosa*	2ODJ	Porin d	−1.277	−33.030	−2.387	−17.100
		2W78	Pyoverdines	−2.812	76.732	−5.330	−29.232
		5XBW	Pyocyanin	−2.353	−39.973	−4.084	−23.159
		5Z2V	PqsA Enzyme	−3.452	−41.434	−2.956	−29.970

CORRECTED PROOF

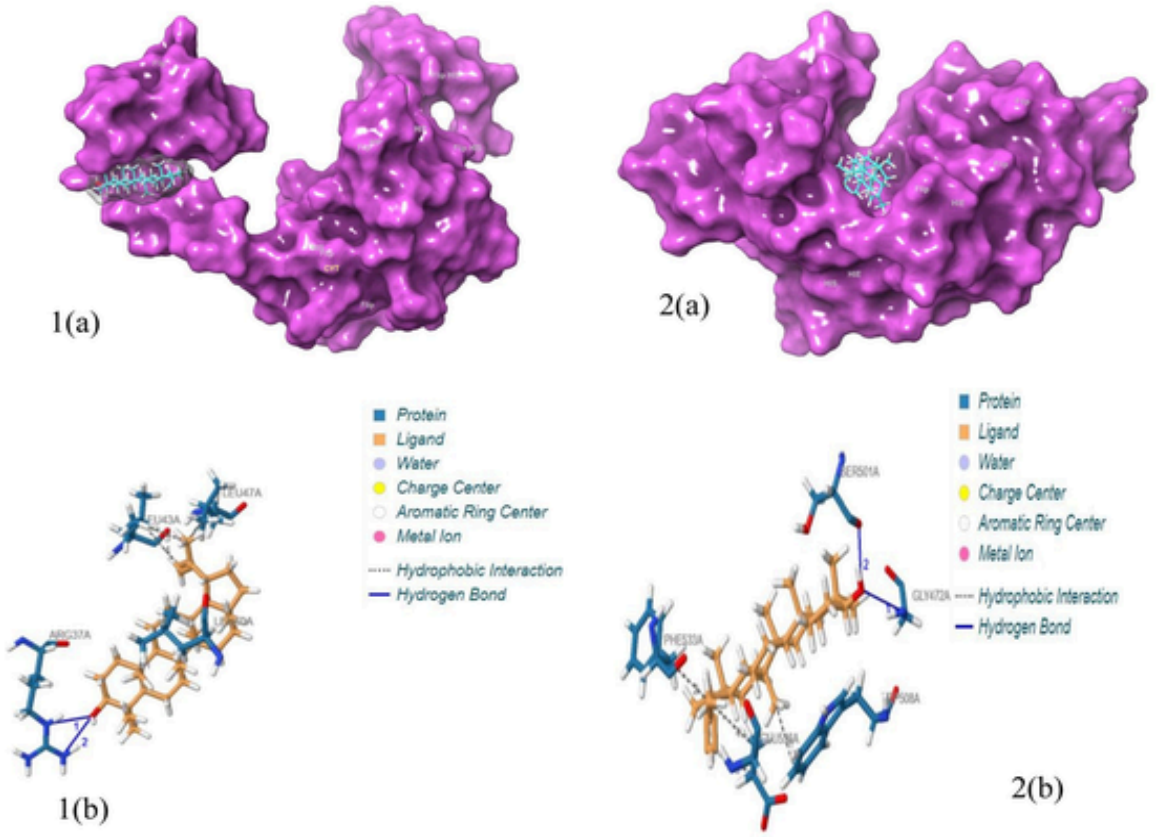


Fig. 6. Molecular docking and MM-GBSA for Lupeol and Phenol, 2,4-bis(1,1-dimethylethyl) 1(a) and 2(a) - 3D docked complex of Lupeol and Phenol, 2,4-bis(1,1-dimethylethyl) with respective protein PDB ID: 5Z2V and 2GWL 1(b) and 2(b) - 2D interaction diagram of Lupeol and Phenol, 2,4-bis(1,1-dimethylethyl) with respective protein PDB ID: 5Z2V and 2GWL, it reveals that various bonding and distance Protein and ligand connected by using hydrogen bond linkage.

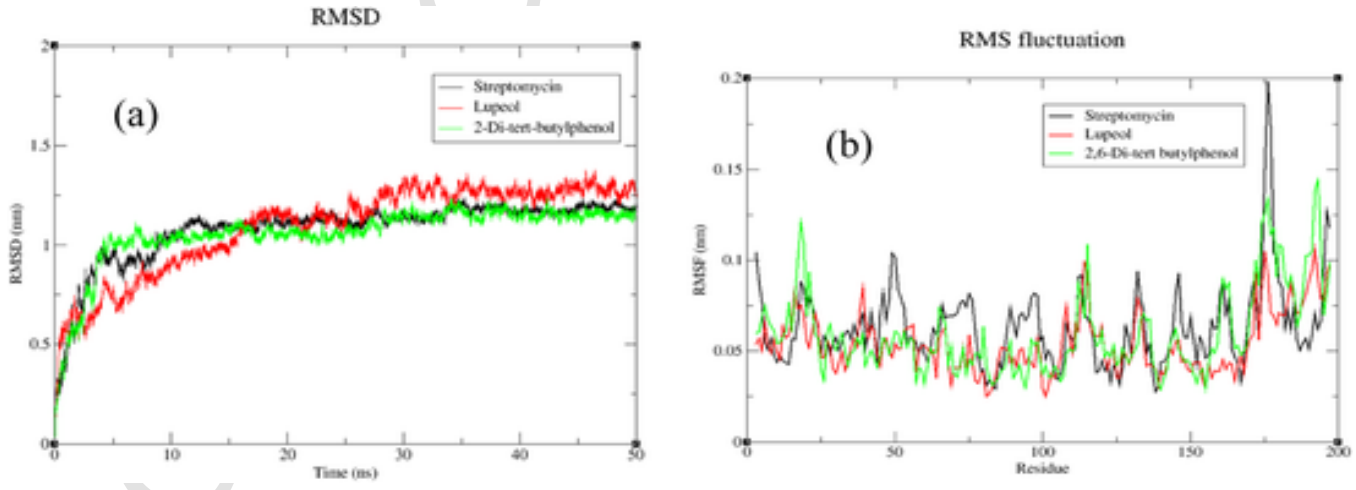


Fig. 7. (a) RMSD and (b) RMSF - residual fluctuations of the Streptomycin (black), Lupeol (red) and Phenol, 2,4-bis(1,1-dimethylethyl) (green) within the time frame of 50 ns.

3.9.2. RMSF

The RMSF plot was used to examine the flexibility and mobility of each residue within the PqsA-ligand complexes. A high RMSF value in the active site amino acids denotes weak interactions between these residues and the small molecule, which renders the binding ineffective [31]. Fig. 7(b) displays the fluctuation patterns of the reference and the hit molecules. The figure clearly depicts that the residual fluctuation profiles of both Lupeol and Phenol, 2,4-bis(1,1-dimethylethyl) was lower than the reference drug molecule. Further, the average fluctuation of Streptomycin, Lupeol and Phenol, 2,4-bis(1,1-dimethylethyl) was found to be 0.117 nm, 0.098 nm and 0.098 nm respectively. It is worth mentioning that the active site residues of PqsA when bound to the hit molecules exhibits decreased RMS fluctuations highlighting their involvement in the ligand binding.

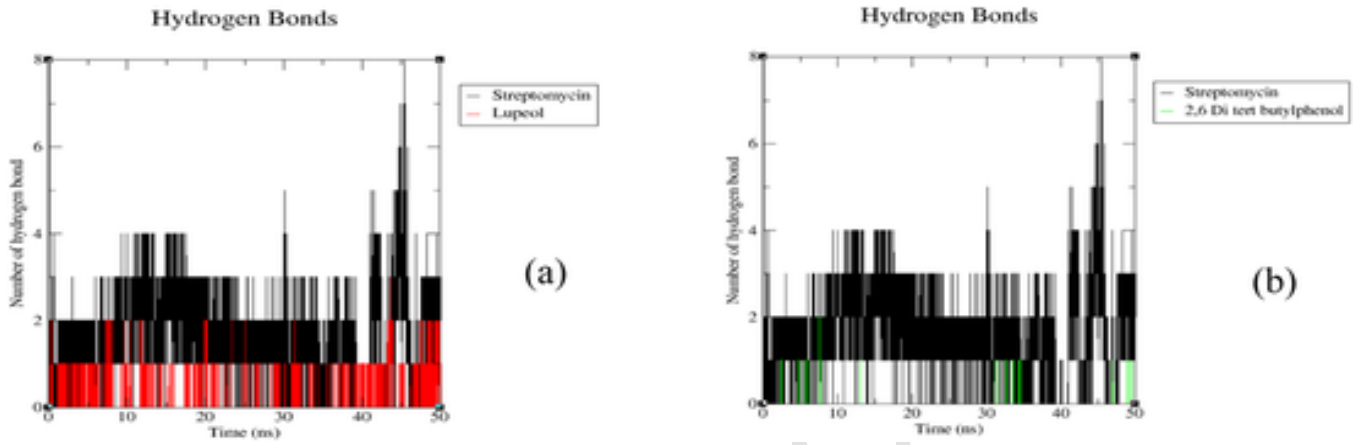


Fig. 8. The hydrogen bond interactions of PqsA protein with Streptomycin (black) (a) Lupeol (red) and (b) Phenol, 2,4-bis(1,1-dimethylethyl) (green).

The RMSF plots were utilized to analyze residue flexibility in PqsA-ligand complexes, where higher RMSF in active site amino acids may suggest weak binding. In comparison, Lupeol and Phenol, 2,4-bis(1,1-dimethylethyl), showed lower fluctuations than the reference drug Streptomycin. The average fluctuations were observed as follows: Streptomycin (0.117 nm), Lupeol (0.098 nm), and Phenol, 2,4-bis(1,1-dimethylethyl) (0.098 nm). Active site residues bound to the hit molecules exhibited reduced RMS fluctuations, indicating their involvement in ligand binding. [26] found that the average RdRp complex RMSF for lupeol was 0.95 Å. According to [30], RMSF analysis of Mpro and Mpro-ligand complexes, including Mpro-X77, Mpro-Calycin, and Mpro-Rhizocarpic acid, revealed stable secondary conformations during the 10 ns molecular dynamics simulation. The average RMSF values for Mpro protein, Mpro-X77, Mpro-Calycin, and Mpro-Rhizocarpic acid complexes were 0.07, 0.08, 0.08, and 0.09 nm, respectively, suggesting the potential of the predicted compounds to inhibit the catalytic activity of Mpro. [27] reported that Lupeol and Solasodine complexes exhibited higher residual fluctuations than Quercetin and apo-protein.

3.9.3. Hydrogen bond

The precise intermolecular interactions in protein-ligand complexes were determined using gmx H-bond. Time-dependent hydrogen bond patterns were analyzed to infer the stability of the hydrogen bonds formed between the reference and hit complexes. From Fig. 8(a) and (b), it is observed that the reference complex generated an average of about 3 hydrogen bonds throughout the simulation, while the resulting hit complexes (Lupeol and Phenol, 2,4-bis(1,1-dimethylethyl)) established ~2 and ~1 hydrogen bonds with the target protein, respectively. The interaction studies indicate that key catalytic residues were actively involved in forming hydrophobic interactions. Therefore, the analysis suggests that the presence of hydrogen bond interactions alongside hydrophobic contacts contributes to the stable binding of the reference and lead molecules [32]. [27] reported that Lupeol complexes exhibited at least one hydrogen bond throughout the simulation period, even though no hydrogen bonds were observed in the starting structure. Comparing the ligand complexes' binding energies, it was found that the Lupeol complex showed higher binding energy than other ligand complexes, favouring the formation of non-bonded interactions.

As per the findings reported by [33], the hydrogen bonding analysis of BtEcR-ZINC08952607 and BtEcR-ZINC04264850 indicates the formation of stable complexes. Specifically, ZINC08952607 forms an average of 0–5 hydrogen bonds, suggesting a more stable interaction compared to ZINC04264850, which forms 0–3 hydrogen bonds on average. Both ligands show potential for stable binding with BtEcR, with ZINC08952607 likely forming a stronger complex due to more hydrogen bonds. Thus, our study employes that gmx H-bond analysis to investigate intermolecular interactions in protein-ligand complexes. In Lupeol and Phenol, 2,4-bis(1,1-dimethylethyl) formed ~2 and ~1 hydrogen bonds with the target protein, respectively. The interaction analysis highlighted active involvement of key catalytic residues in hydrophobic interactions. The observed molecular interactions resulting from a combination of hydrogen bond interactions and hydrophobic contacts are crucial for understanding molecular interactions in drug design and molecular biology. This information provides valuable insights into the mechanisms through which molecules interact with their target proteins, aiding in the rational design of drugs and the exploration of molecular processes in biological systems. Understanding these interactions is fundamental for optimizing the efficacy and specificity of drugs and developing a deeper comprehension of the underlying biological pathways.

4. Summary and conclusions

Computational study illustrates the chemical nature of antibacterial compounds derived from *S. mobaraensis* DRM1 and *N. synnemataformans* DRM2. The findings reveal the optimized geometry, NBO analysis, molecular docking, and molecular dynamics simulations of two antibacterial compounds, Lupeol and Phenol, 2,4-bis(1,1-dimethylethyl). These investigations aim to explore electronic properties, binding affinities, and stability of these compounds with enzyme receptors in bacterial pathogens. Additionally, it is noted that Phenol, 2,4-bis(1,1-dimethylethyl) fulfills all the criteria of ADME and Lipinski's rule of 5, suggesting favorable characteristics for drug-likeness. Lupeol and Phenol, 2,4-bis(1,1-dimethylethyl) compounds inhibit the action of PqsA and actin enzymes from *P. aeruginosa* and *S. typhi* respectively, offering insights into potential pharmacological applications of antibacterial compounds derived from lichen associated actinobacteria. Further, the antibacterial compounds derived the actinobiont could be used as broad spectrum of antibacterial drug in future course of action with *in vivo* toxicity, preclinical evaluation.

CRediT authorship contribution statement

Vishnu Raja Vijayakumar: Writing – review & editing, Writing – original draft, Visualization, Methodology, Investigation, Funding acquisition, Data curation, Conceptualization. **Priyanka Jayam Rajendran:** Visualization, Data curation. **M. Poornimaa:** . **K. Ramanathan:** . **Tanmoy Saha:** Validation, Methodology, Conceptualization. **Saurabh Das:** Validation, Methodology, Conceptualization.

Dhanasekaran Dharumadurai: Writing – review & editing, Validation, Supervision.

Declaration of competing interest

The authors declare that they have no known competing financial interests or personal relationships that could have appeared to influence the work reported in this paper.

Data availability

No data was used for the research described in the article.

Acknowledgements

The first author thanks the Research Foundation of Bharathidasan University for the Fellowship (URF) (021505/URF/DIR-RES/2019 Date: 22.10.2019), DST-FIST (Department of Science and Technology-Fund for Improvement of S & T Infrastructure), New Delhi, gladly accepts the instrumentation facility (DST Sanction Order No.: SR/FIST/LSI-013/ 2012/Dt.13.08.2012). We gratefully acknowledge the Department of Science and Technology (DST) for providing funding for the research facility through the DST-Promotion of University Research and Scientific Excellence (PURSE) scheme - Phase II, Rashtriya Uchchatar Shiksha Abhiyan (RUSA)–2.O Biological Sciences (TN RUSA: 311/RUSA (2.0)/2018 Dt. December 02, 2020). We Sincerely thank the financial aid from the DBT (Govt. of India) for the establishment of the National Repository for Microalgae and Cyanobacteria – Freshwater & Marine (NRMC F & M) (Phase II) (BT/ PR29901/PBD26/694/2018), DST PURSE- Scheme DST/SR/PURSE Phase 2/16(C) and Department of Microbiology, Bharathidasan University, Tiruchirappalli, Tamil Nadu, India.

Supplementary materials

Supplementary material associated with this article can be found, in the online version, at doi:10.1016/j.molstruc.2024.138561.

References

[1] A. Torres-Benítez, J.E. Ortega-Valencia, M. Sanchez, P.K. Divakar, M.J. Simirgiotis, M.P. Gómez-Serranillos, Metabolomic profiling, antioxidant and enzyme inhibition properties and molecular docking analysis of Antarctic lichens, Molecules 27 (22) (2022) 8086.

[2] V.I.N.I.C.I.O. Galasso, Probing the molecular and electronic structure of the lichen metabolite Usnic acid: a DFT study, Chem. Phys 374 (1–3) (2010) 138–145.

[3] Z.S. Marković, N.T. Manojlović, Analytical characterization of lichexanthone in lichen: HPLC, UV spectroscopic, and DFT analysis of lichexanthone extracted from *Laurera benguelensis* (Mull. Arg.) Zahlbr, Monatshefte für Chemie-Chem. Monthly 141 (2010) 945–952.

[4] E.D. Glendening, C.R. Landis, F. Weinhold, NBO 6.0: natural bond orbital analysis program, J. Comput. Chem 34 (16) (2013) 1429–1437.

[5] P. Banerjee, T. Chakraborty, Correlation of νOH spectral shifts of phenol–benzene O–H··· π hydrogen-bonded complexes with donor's acidity: a combined matrix isolation, infrared spectroscopy, and quantum chemistry study, J. Phys. Chem. A 118 (34) (2014) 7074–7084.

[6] F. Yamashita, M. Hashida, *In silico* approaches for predicting ADME properties of drugs, Drug Metab. Pharmacokinet. 19 (5) (2004) 327–338.

[7] P. Manogar, S. Vijayakumar, S. Rajalakshmi, M. Pugazhenthi, P.K. Praseetha, S. Jayanthi, *In silico* studies on CNR1 receptor and effective cyanobacterial drugs: homology modelling, molecular docking and molecular dynamic simulations, Gene Reports 17 (2019) 100505.

[8] Frisch, M.J., Trucks, G.W., Schlegel, H.B., Scuseria, G.E., Robb, M.A., Cheeseman, J.R., Scalmani, G., Barone, V., Petersson, G.A., Nakatsuji, H., Li, X., Caricato, M., Marenich, A.V., Bloino, J., Janesko, B.G., Gomperts, R., Mennucci, B., Hratchian, H.P., Ortiz, J.V., Izmaylov, A.F., Sonnenberg, J.L., Williams-Young, D., Ding, F., Lipparini, F., Egidi, F., Goings, J., Peng, B., Petrone, A., Henderson, T., Ranasinghe, D., Zakrzewski, V.G., Gao, J., Rega, N., Zheng, G., Liang, W., Hada, M., Ehara, M., Toyota, K., Fukuda, R., Hasegawa, J., Ishida, M., Nakajima, T., Honda, Y., Kitao, O., Nakai, H., Vreven, T., Throssell, K., Montgomery, J.A., Peralta, J.E., Ogliaro, F., Bearpark, M.J., Heyd, J.J., Brothers, E.N., Kudin, K.N., Staroverov, V.N., Keith, T.A., Kobayashi, R., Normand, J., Raghavachari, K., Rendell, A.P., Burant, J.C., Iyengar, S.S., Tomasi, J., Cossi, M., Millam, J.M., Klene, M., Adamo, C., Cammi, R., Ochterski, J.W., Martin, R.L., Morokuma, K., Farkas, O., Foresman, J.B., & Fox, D.J. (2016). GAUSSIAN16. Revision C. 01. Gaussian Inc., Wallingford, CT, USA.

[9] M. Buvaneswari, R. Santhakumari, C. Usha, R. Jayasree, S. Sagadevan, Synthesis, growth, structural, spectroscopic, optical, thermal, DFT, HOMO–LUMO, MEP, NBO analysis and thermodynamic properties of vanillin isonicotinic hydrazide single crystal, J. Mol. Struct 1243 (2021) 130856.

[10] T. Saha, S. Sappati, S. Das, An insight into the mixed quantum mechanical-molecular dynamic simulation of a Zn^{II}-Curcumin complex with a chosen DNA sequence that supports experimental DNA binding investigations, Int. J. Biol. Macromol. 245 (2023) 125305.

[11] P. Murali, R. Karuppasamy, Discovery of novel and potent inhibitors against mutational variants of IDH1 protein for glioma therapy: a fragment - based approach, J. Computat. Biophy. Chem 22 (1) (2023) 43–61.

[12] D. Van Der Spoel, E. Lindahl, B. Hess, G. Groenhof, A.E. Mark, H.J. Berendsen, GROMACS: fast, flexible, and free, J. Comput. Chem 26 (16) (2005) 1701–1718.

[13] J. Huang, A.D. MacKerell Jr, CHARMM36 all-atom additive protein force field: validation based on comparison to NMR data, J. Comput. Chem 34 (25) (2013) 2135–2145.

[14] Y. Wu, H.L. Tepper, G.A. Voth, Flexible simple point-charge water model with improved liquid-state properties, J. Chem. Phys 124 (2) (2006) 024503.

[15] B. Hess, H. Bekker, H.J. Berendsen, J.G. Fraaije, LINCS: a linear constraint solver for molecular simulations, J. Comput. Chem 18 (12) (1997) 1463–1472.

[16] Y. Zhang, L. Wang, The WRKY transcription factor superfamily: its origin in eukaryotes and expansion in plants, BMC Evol. Biol. 5 (2005) 1–12.

[17] F.R. Aigbe, A.O. Adediji, C.S. Dike, E.A. Olawuyi, U.D. Akpadolu, A.A. Musa, T. Balogun, Computational evaluation of potential ACE1 inhibitors from selected antihypertensive plants, Silico Pharmacol (2023) 1–22.

[18] T. Valarmathi, R. Premkumar, A.M.F. Benial, Spectroscopic and molecular docking studies on 1-Hydroxyanthraquinone: a potent ovarian cancer drug, J. Mol. Struct 1213 (2020) 128163.

[19] R. Renjith, Y.S. Mary, H.T. Varghese, C.Y. Panicker, T. Thiemann, C. Van Alsenoy, Vibrational spectra, molecular structure, NBO, HOMO–LUMO and first order hyperpoalarizability analysis of 1, 4-bis (4-formylphenyl) anthraquinone by density functional theory, Mole. Biomole. Spectrosc 131 (2014) 225–234.

[20] S.W. Shantier, E.M. Ismail, M.S. Mohamed, W. Osman, Pharmacokinetics and molecular docking of novel antineoplastic sesquiterpene lactone from *Tarchonanthus camphoratus* L: an *in silico* approaches, Struct. Chem 34 (2) (2023) 703–712.

[21] C.A. Bergstrom, W.N. Charman, C.J. Porter, Computational prediction of formulation strategies for beyond-rule-of-5 compounds, Adv. Drug Deliv. Rev. 101 (2016) 6–21.

[22] H. Mondal, D.D.G. Silvia, I.A. Emerson, N. Chandrasekaran, A. Mukherjee, J. Thomas, Antibacterial activity of a novel compound isolated from *Bacillus licheniformis* for treating bacterial infections in fishes: an *in-silico* approach, Mol. Cell. Biochem. (2023) 1–12.

[23] A. Thekkangil, B. George, S.U. Prakash, T.V. Suchithra, Mechanism of *Streptomyces albidoflavus* STV1572a derived 1-heneicosanol as an inhibitor against squalene epoxidase of *Trichophyton mentagrophytes*, Microb. Pathog. 154 (2021) 104853.

[24] T.S. Devi, K. Vijay, R.M. Vidhyavathi, P. Kumar, M. Govarthanan, T. Kavitha, Antifungal activity and molecular docking of phenol, 2, 4-bis (1, 1-dimethylethyl) produced by plant growth-promoting actinobacterium *Kutzneria* sp. strain TSII from mangrove sediments, Arch. Microbiol. 203 (2021) 4051–4064.

[25] T. Ahmed, S. Pattnaik, M.B. Khan, D.R. Ampasala, S. Busi, V.V. Sarma, Inhibition of quorum sensing–associated virulence factors and biofilm formation in *Pseudomonas aeruginosa* PAO1 by *Mycoleptodiscus indicus* PUTY1, Brazil. J. Microbioly 51 (2) (2020) 467–487.

[26] R. Thirumalaisamy, F. Ameen, A. Subramanian, T. Selvankumar, S.S. Alwakeel, M. Govarthanan, *in vitro* and *in silico* anti-inflammatory activity of Lupeol isolated from *Crateva adansonii* and its hidden molecular mechanism, Int. J. Pept. Res. Ther 26 (2020) 2179–2189.

[27] D. Arumuganainar, P.K. Yadalam, K.J. Alzahrani, K.F. Alsharif, F.M. Alzahrani, S. Alshammeri, S.S.S.J. Ahmed, T.S. Vinothkumar, H.A. Baeshen, S. Patil, Inhibitory effect of lupeol, quercetin, and solasodine on *Rhizopus oryzae*: a molecular docking and dynamic simulation study, J. Infect. Public Health 16 (1) (2023) 117–124.

[28] M.F. Adasme, K.L. Linnemann, S.N. Bolz, F. Kaiser, S. Salentin, V.J. Haupt, M. Schroeder, Expanding the scope of the protein–ligand interaction profiler to DNA and RNA, Nucl. Acids Res. 49 (W1) (2021) W530–W534.

[29] P. Murali, R. Karuppasamy, Exploration of natural product database for the identification of potent inhibitor against IDH2 mutational variants for glioma therapy, J Mol. Model 29 (1) (2023) 1–12.

[30] T. Joshi, P. Sharma, T. Joshi, H. Pundir, S. Mathpal, S. Chandra, Structure-based screening of novel lichen compounds against SARS Coronavirus main protease (Mpro) as potentials inhibitors of COVID-19, Mol. Divers. 25 (2021) 1665–1677.

[31] S. De Vita, M.G. Chini, G. Bifulco, G. Lauro, Insights into the ligand binding to Bromodomain - containing protein 9 (BRD9): a guide to the selection of potential binders by computational methods, Molecules 26 (23) (2021) 7192.

[32] P. Murali, R. Karuppasamy, Identification of novel mutant (R132H) isocitrate dehydrogenase 1 inhibitors for glioma therapy, J. Computat. Biophys. Chem 21 (6) (2022) 647–661.

[33] H.K. Mangat, M. Rani, R.K. Pathak, I.S. Yadav, D. Utreja, P.K. Chhuneja, P. Chhuneja, Virtual screening, molecular dynamics and binding energy-MM-PBSA studies of natural compounds to identify potential EcR inhibitors against *Bemisia tabaci Gennadius*, PLoS ONE 17 (1) (2022) 0261545.

CORRECTED PROOF